

**Progress in Semiconductor
Materials for Optoelectronic
Applications**

20020703 027

Progress in Semiconductor Materials for Optoelectronic Applications

Symposium held November 26–29, 2001, Boston, Massachusetts, U.S.A.

EDITORS:

Eric D. Jones

Sandia National Laboratories
Albuquerque, New Mexico, U.S.A.

Omar Manasreh

University of New Mexico
Albuquerque, New Mexico, U.S.A.

Kent D. Choquette

University of Illinois
Urbana-Champaign, Illinois, U.S.A.

Daniel J. Friedman

National Renewable Energy Laboratory
Golden, Colorado, U.S.A.

Daniel K. Johnstone

Air Force Office of Scientific Research
Arlington, Virginia, U.S.A.



Materials Research Society
Warrendale, Pennsylvania

DISTRIBUTION STATEMENT A
Approved for Public Release
Distribution Unlimited

Effort sponsored by the Air Force Office of Scientific Research, Air Force Material Command, USAF, under F49620-01-1-0347. The U.S. Government is authorized to reproduce and distribute reprints for Governmental purposes notwithstanding any copyright notation thereon. The views and conclusions herein are those of the authors and should not be interpreted as necessarily representing the official policies or endorsements, either expressed or implied, of the Air Force Office of Scientific Research or the U.S. Government.

This work was supported in part by the Office of Naval Research under Grant Number N00014-01-1-0649. The United States Government has a royalty-free license throughout the world in all copyrightable material contained herein.

Single article reprints from this publication are available through
University Microfilms Inc., 300 North Zeeb Road, Ann Arbor, Michigan 48106

CODEN: MRSPDH

Copyright 2002 by Materials Research Society.
All rights reserved.

This book has been registered with Copyright Clearance Center, Inc. For further information, please contact the Copyright Clearance Center, Salem, Massachusetts.

Published by:

Materials Research Society
506 Keystone Drive
Warrendale, PA 15086
Telephone (724) 779-3003
Fax (724) 779-8313
Web site: <http://www.mrs.org/>

Library of Congress Cataloging-in-Publication Data

Progress in semiconductor materials for optoelectronic applications : symposium held November 26-29, 2001, Boston, Massachusetts, U.S.A. / editors, Eric D. Jones, Omar Manasreh, Kent D. Choquette, Daniel J. Friedman, Daniel K. Johnstone
p.cm.—(Materials Research Society symposium proceedings ; v. 692)
Includes bibliographical references and indexes.
ISBN 1-55899-628-1
I. Jones, Eric D. II. Manasreh, Omar III. Choquette, Kent D. IV. Friedman, Daniel J. V. Johnstone, Daniel K. VI. Materials Research Society symposium proceedings ; v. 692
2002

Manufactured in the United States of America

CONTENTS

Preface.....	xix
Materials Research Society Symposium Proceedings.....	xx

LOW CONCENTRATION NITRIDE ALLOYS I

Luminescent Characteristics of InGaAsP/InP Multiple Quantum Well Structures by Impurity-Free Vacancy Disordering	3
J. Zhao, X.D. Zhang, Z.C. Feng, J.C. Deng, P. Jin, Y.C. Wang, and G. Xu	
* Successes and Predictions of a Pseudopotential Approach in Anion-Mixed Nitrides.....	9
L. Bellaiche, A. Al-Yacoub, N.A. Modine, and E.D. Jones	
* The Role of Nitrogen-Induced Localization and Defects in InGaAsN ($\approx 2\%$ N): Comparison of InGaAsN Grown by Molecular Beam Epitaxy and Metal-Organic Chemical Vapor Deposition	21
Steven R. Kurtz, A.A. Allerman, J.F. Klem, R.M. Sieg, C.H. Seager, and E.D. Jones	
Growth of High Nitrogen Content GaAsN by Metalorganic Chemical Vapor Deposition.....	29
J.C. Roberts, B.F. Moody, P. Barletta, M.E. Aumer, S.F. LeBoeuf, J.M. Luther, and S.M. Bedair	
High Luminescence Efficiency From GaAsN Layers Grown by MBE With RF Nitrogen Plasma Source.....	35
Victor M. Ustinov, Nikolai A. Cherkashin, Nikolai A. Bert, Andrei F. Tsatsul'nikov, Alexei R. Kovsh, Jyh-Shang Wang, Li Wei, and Jim Y. Chi	
Effect of Rapid Thermal Annealing: Red and Blue Shift in Photoluminescence of GaNAs Grown By RF Plasma-Assisted Molecular Beam Epitaxy	41
W.K. Loke, S.F. Yoon, T.K. Ng, S.Z. Wang, and W.J. Fan	

*Invited Paper

**LOW CONCENTRATION NITRIDE
ALLOYS II AND PHOTOVOLTAICS**

* Electronic Structure Near the Band Gap of Heavily Nitrogen Doped GaAs and GaP	49
Yong Zhang, B. Fluegel, M. Hanna, A. Duda, and A. Mascarenhas	
InAsN Grown by Plasma-Assisted Gas Source MBE	61
Ding-Kang Shih, Hao-Hsiung Lin, and Tso-Yu Chu, and T.R. Yang	
Nature and Formation of Non-Radiative Defects in GaNAs and InGaAsN	67
W.M. Chen, N.Q. Thinh, I.A. Buyanova, P.N. Hai, H.P. Xin, C.W. Tu, Wei Li, and M. Pessa	
* Deep Centers and Their Capture Barriers in MOCVD-Grown GaN.....	73
Daniel K. Johnstone, Mohamed Ahoujja, Yung Kee Yeo, Robert L. Hengehold, and Louis Guido	
Near-Field Photoluminescence Spectroscopy of Localized States in InGaAsN Alloys.....	85
A.M. Mintairov, P.A. Blagnov, T. Kosel, J.L. Merz, V.M. Ustinov, A.S. Vlasov, and R.E. Cook	
Raman and Photoluminescence Mapping of Lattice Matched InGaP/GaAs Heterostructures.....	91
G. Attolini, P. Fallini, F. Germini, C. Pelosi, O. Martínez, L.F. Sanz, M.A. González, and J. Jiménez	

QUANTUM DOTS

* Quantum Dots of InAs/GaSb Type II Superlattice for Infrared Sensing.....	99
M. Razeghi, Y. Wei, A. Gin, and G.J. Brown	
* Quantum Dot Long-Wavelength Detectors	109
Pallab Bhattacharya, Adrienne D. Stiff-Roberts, Sanjay Krishna, and Steve Kennerly	

*Invited Paper

Enhanced Photoluminescence from Long Wavelength InAs Quantum Dots Embedded in a Graded (In,Ga)As Quantum Well.....	117
L. Chen, V.G. Stoleru, D. Pal, D. Pan, and E. Towe	
A Theoretical Study of Structural Disorder and Photoluminescence Linewidth in InGaAs/GaAs Self Assembled Quantum Dots.....	123
Yih-Yin Lin, Hongtao Jiang, and Jasprit Singh	
Electroluminescence and Spectral Shift of CdS Nanoparticles on Si Wafer	129
Eih-Zhe Liang, Ching-Fuh Lin, Sheng-Ming Shih, and Wei-Fang Su	
InAs Quantum Dots in AlAs/GaAs Short Period Superlattices: Structure, Optical Characteristics and Laser Diodes.....	135
Vadim Tokranov, M. Yakimov, A. Katsnelson, K. Dovidenko, R. Todt, and S. Oktyabrsky	

INFRARED DETECTORS

* Multi-Color Quantum Well Infrared Photodetectors for Mid-, Long-, and Very Long-Wavelength Infrared Applications.....	143
Sheng S. Li	
* A Bowtie Antenna Coupled Tunable Photon-Assisted Tunneling Double Quantum Well (DQW) THz Detector.....	155
Majid M. Khodier, Christos G. Christodoulou, and Jerry A. Simmons	
Fast Room Temperature Detection of State of Circular Polarization of Terahertz Radiation	169
Sergey D. Ganichev, Hermann Ketterl, and Wilhelm Prettl	
PbTe Flash Evaporation on Si <100> Substrates for Heterojunction Infrared Detectors.....	175
Sonia Guimarães, Sabrina de C.F.F. da Silva and João M.K. de Assis	
GaAs Photodetector for X-ray Imaging.....	181
G.C. Sun, H. Samic, V. Donchev, S. Gautrot, and J.C. Bourgoin	

*Invited Paper

Lead Telluride-Based Far-Infrared Photodetectors— A Promising Alternative To Doped Si and Ge.....	187
Dmitriy Dolzhenko, Ivan Ivanchik, Dmitriy Khokhlov, and Konstantin Kristovskiy	

INNOVATIVE DEVICES

Scatterometry for Lithography Process Control and Characterization in IC Manufacturing.....	195
Yiorgos Kostoulas, Christopher J. Raymond, and Mike Littau	

POSTER SESSION

Structural Properties and Doping of $Zn_{1-x}(Mg, Li)_xO$ Materials.....	203
R.E. Melgarejo, M.S. Tomar, A. Hidalgo, and R.S. Katiyar	
Depth Profiling of SiC Lattice Damage Using Micro-Raman Spectroscopy.....	209
Iulia C. Muntele, Daryush Ila, Claudiu I. Muntele, David B. Poker, and Dale K. Hensley	
New Approach Towards the Deposition of I-III-VI Thin Films.....	215
Mohammad Afzaal, David Crouch, Paul O'Brien, and Jin-Ho Park	
Comparison of AlGaAs Oxidation in MBE and MOCVD Grown Samples	221
Y. Chen, A. Roshko, K.A. Bertness, D.W. Readey, A.A. Allerman, M. Tan, and A. Tandon	
Hole Concentration vs. Mn Fraction in a Diluted (Ga,Mn)As Ferromagnetic Semiconductor.....	227
Raimundo R. dos Santos, L.E. Oliveira, and J. d'Albuquerque e Castro	
Photoluminescence from Er-Implanted 4H and 6H-SiC.....	233
Shin-ichiro Uekusa and Takayuki Goto	
Control of ZnO Morphology by Solution Route.....	243
Lingdong Sun, Jun Zhang, Chunsheng Liao, and Chunhua Yan	

Influence of Er and O Doses on Er-Related Emission in Al_{0.70}Ga_{0.30}As:Er.....	247
S.-I. Uekusa and T. Arai	
Intersubband Transitions in InGaAs/InAlAs Multiple Quantum Wells Grown on InP Substrate	253
Qiaoying Zhou, M.O. Manasreh, B.D. Weaver, and M. Missous	
Calculations of Dielectric Constant for AlGaInAs Quaternary Semiconductor Alloy in the Transparent Region and Above (0.4-4.0eV).....	259
M. Linnik and A. Christou	
Annealing of Some II-IV-V₂ Crystals in the Vapor of Volatile Constituents.....	265
Valeriy G. Voevodin, Olga V. Voevodina, Svetlana A. Bereznaya, Zoya V. Korotchenko, Nils C. Fernelius, Jonathan T. Goldstein, and Melvin C. Ohmer	
Radiative Recombination Processes of Thermal Donors in Silicon	275
S. Pizzini, S. Binetti, E. Leoni, A. Le Donne, M. Acciarri, and A. Castaldini	
Annealing Effect on the Nonradiative Carrier Recombination in AlGaAs/GaAs Investigated by a Piezoelectric Photothermal Spectroscopy.....	283
Atsuhiko Fukuyama, Hiroaki Nagatomo, Yoshito Akashi, and Tetsuo Ikari	
Optically Detected Magnetic Resonance Study of Core-Shell and Alloy Nanocrystals of HgTe and CdS.....	289
L. Fradkin, L. Langof, E. Lifshitz, A. Rogach, N. Gaponik, H. Weller, and A. Eychmüller	
On the Scaling of Exciton and Impurity Binding Energies and the Virial Theorem in Semiconductor Quantum Wells and Quantum-Well Wires	295
M. de Dios-Leyva and L.E. Oliveira	
Intra-Magnetoexciton Transitions in Semiconductor Quantum Wells.....	301
Z. Barticevic, M. Pacheco, C.A. Duque, and L.E. Oliveira	

Electron Scattering in Two-Dimensional Disordered Heterostructures	307
I. Gómez, E. Diez, F. Domínguez-Adame, and P. Orellana	
Exciton Diamagnetic Shifts and Magnetic Field Dependent Linewidths in Ordered and Disordered InGaP Alloys	313
E.D. Jones, K.K. Bajaj, G. Coli, S.A. Crooker, Yong Zhang, A. Mascarenhas, and J.M. Olsen	
Field Emission Enhancement of DLC Films Using Triple-Junction Type Emission Structure	319
Namwoong Paik, Michael Martin, Daeil Kim, Sungjin Kim, Steven Kim, and Kie Moon Song	
Luminescence of Quasi-2DEG in Heterostructures Based on PbS Films	325
G. Khlyap	

LASERS AND MATERIALS

* GaInNAs Material Properties for Long Wavelength Opto-Electronic Devices	333
Vincent Gambin, Wonill Ha, Mark Wistey, Seongsin Kim, and James S. Harris	
Excitonic Diamagnetic Shifts and Magnetic Field Dependent Linewidths in Al_xGa_{1-x}As Alloys	343
G. Coli, K.K. Bajaj, J.L. Reno, and E.D. Jones	
Novel AlGaAs/CaF₂ SESAM Device for Ultrashort Pulse Generation	349
Silke Schön, Lukas Gallmann, Markus Haiml, and Ursula Keller	
Optical Characterization of IV-VI Mid-Infrared VCSEL	355
F. Zhao, H. Wu, T. Zheng, P.J. McCann, A. Majumdar, Lalith Jayasinghe, and Z. Shi	

ANTIMONY-BASED DEVICES

* Sb-Based Mid-Infrared Diode Lasers	365
C. Mermelstein, M. Rattunde, J. Schmitz, S. Simanowski, R. Kiefer, M. Walther, and J. Wagner	

*Invited Paper

Thin Films of Antimony-Tin Oxide as Counter-Electrodes for Proton Working Electrochromic Devices	377
N. Naghavi, C. Marcel, L. Dupont, A. Rougier, and J-M. Tarascon	
Sb-Terminated InAs(001)-(2x4) and (2x8) Studied Using Scanning Tunneling Microscopy and <i>Ab Initio</i> Density Functional Theory	383
William Barvosa-Carter, Frank Grosse, James H.G. Owen, and Jennifer J. Zinck	
Effect of Marangoni Convection on InSb Single Crystal Growth by Horizontal Bridgman Method.....	389
K. Kodera, A. Kinoshita, K. Arafune, Y. Nakae, and A. Hirata	
Asymmetric Hybrid Al(Ga)SbAs/InAs/Cd(Mg)Se Heterostructures for Mid-IR LEDs and Lasers.....	395
S.V. Ivanov, V.A. Kaygorodov, V.A. Solov'ev, E.V. Ivanov, K.D. Moiseev, S.V. Sorokin, B.Ya. Meltzer, A.N. Semenov, M.P. Mikhailova, Yu.P. Yakovlev, and P.S. Kop'ev	

POSTER SESSION

Local Vibrational Modes of Carbon-Hydrogen Complexes in Proton Irradiated AlGaIn	403
M.O. Manasreh and B.D. Weaver	
Effects of Ion Bombarding and Nitrogenation on the Properties of Photovoltaic a-CN_x Thin Films.....	411
Z.B. Zhou, R.Q. Cui, G.M. Hadi, Q.J. Pang, C.Y. Jin, and Z.M. Ding	
Doping Profiles of n-Type GaAs Layers Grown on Si by the Conformal Method	417
Angel M. Ardila, O. Martínez, M. Avella, J. Jiménez, B. Gérard, J. Napierala, and E. Gil-Lafon	
Gallium Vacancy in GaSb Studied by Positron Lifetime Spectroscopy and Photoluminescence.....	423
W.K. Mui, M.K. Lui, C.C. Ling, C.D. Beling, S. Fung, K.W. Cheah, K.F. Li, and Y.W. Zhao	

Characterization of LiInS₂ and LiInSe₂ Single Crystals for Nonlinear Optical Applications	429
Ludmila Isaenko, Alexander Yelisseyev, Sergei Lobanov, Alexander Panich, Vitaly Vedenyapin, Julia Smirnova, Valentin Petrov, Jean-Jacques Zondy, and Guido Knippels	
Optical Constants of Annealed a-Si:H from Transmittance at Normal Incidence.....	435
Atsutoshi Doi and Yoshiyuki Matsumoto	
Field Effect Controlled Photoresistors Based on Chemically Deposited PbS Films.....	441
Eugenia Pentia, Lucian Pintilie, Ion Matei, and Ioana Pintilie	
Photo-Stimulated Rebuilding of Structure in Semiconductors	447
S.S. Rashidova, B.L. Oksengendler, N.N. Turaeva, and I.M. Aripov	
Luminescence From Erbium Oxide Grown on Silicon.....	455
E. Nogales, B. Méndez, J. Piqueras, R. Plugaru, J.A. García, and T.J. Tate	
High-Performance InAs/GaAs Quantum Dots Infrared Photodetector With/Without Al_{0.2}Ga_{0.8}As Blocking Layers.....	461
Zhengmao Ye, Joe C. Campbell, Zhonghui Chen, O. Baklenov, E.T. Kim, I. Mukhametzhanov, J. Tie, and A. Madhukar	
Current Images of CdSe Colloidal Nanodots Observed by Conductive-Tip Atomic Force Microscopy	467
Ichiro Tanaka, Eri Kawasaki, O. Ohtsuki, M. Hara, H. Asami, and I. Kamiya	
Shallow-Donor States in Spherical Quantum Dots With Parabolic Confinement	473
C.A. Duque, N. Porras-Montenegro, M. de Dios-Leyva, and L.E. Oliveira	
Continuous and Time Resolved Optically Detected Magnetic Resonance Studies of InP Nanoparticles	477
L. Langof, E. Ehrenfreund, E. Lifshitz, O.I. Micic, and A.J. Nozik	

Airplane and Drop Experiments on Crystallization of In_xGa_{1-x}Sb Semiconductor Under Different Gravity Conditions.....	483
Krishnan Balakrishnan, Yasuhiro Hayakawa, Hideki Komatsu, Noriaki Murakami, Tetsuo Nakamura, Tadashi Kimura, Tetsuo Ozawa, Yasunori Okano, Masafumi Miyazawa, Sadik Dost, Le. H. Dao, and Masashi Kumagawa	
I-V And C-V Characteristics of nGaAs-nInSb Heterojunctions Obtained by Pulsed Laser Deposition Technique	491
Karapet E. Avdjian	
Effects of Electric Fields on Cathodoluminescence From II-VI Quantum Well Light Emitting Diodes.....	495
A.Y. Nikiforov, G.S. Cargill III, M.C. Tamargo, S.P. Guo, and Y.-C. Chen	
Gas Source MBE Growth and Characterization of TiInGaAs/InP DH Structures for Temperature-Independent Wavelength LD Application.....	501
Hajime Asahi, Hwe-Jae Lee, Akiko Mizobata, Kenta Konishi, Osamu Maeda, and Kumiko Asami	
Effect of Zn Atom Diffusion in the Active Layer of InGaAlP Visible-LED Investigated by the Piezoelectric Photothermal Spectroscopy.....	507
Ryuji Ohno, Yoshihito Taiji, Shoichiro Sato, Atsuhiko Fukuyama, Shigeru Shigetomi, and Tetsuo Ikari	
Strategies For Direct Monolithic Integration of Al_xGa_(1-x)As/In_xGa_(1-x)As LEDS and Lasers on Ge/GeSi/Si Substrates Via Relaxed Graded Ge_xSi_(1-x) Buffer Layers	513
Michael E. Groenert, Christopher W. Leitz, Arthur J. Pitera, Vicky K. Yang, Harry Lee, Rajeev J. Ram, and Eugene A. Fitzgerald	
Synthesis of Nanosized Lithium Manganate CVD Diamond Thin Films for Alpha Particle Detector Application.....	519
S.G. Wang, Q. Zhang, S.F. Yoon, and J. Ahn <i>For Lithium-ion Secondary Batteries</i>	
Improved Routes Towards Solution Deposition of Indium Sulfide Thin Films for Photovoltaic Applications	525
Kuveshni Govender, David Smyth-Boyle, and Paul O'Brien	
Third Order Mode Optically Pumped Semiconductor Laser for an Integrated Twin Photon Source in Quantum Optics	531
N.G. Semaltianos, A. De Rossi, V. Berger, B. Vinter, E. Chirlias, and V. Ortiz	

On the Optical Memory of a Thin-Film pInSb-nCdTe Heterojunction Obtained by Laser Pulsed Deposition	537
Arik G. Alexanian, Nikolay S. Aramyan, Romen P. Grigoryan, Ashot M. Khachatrian, Lenrik A. Matevossian, and Arsham S. Yeremyan	
Quantitative Secondary Ion Mass Spectrometry (SIMS) of III-V Materials	543
P. Van Lierde, C. Tian, B. Rothman, and R.A. Hockett	
Preparation of CdS/ZnO Core/Shell Structured Nanoparticles by Hydrothermal Method.....	549
Chunhua Yan, Lingdong Sun, Xuefeng Fu, and Chunsheng Liao	
Development of A^{III}B^{VI} Semiconductors Doped with Cr for IR Laser Application.....	555
V.A. Kasiyan, R.Z. Shneck, Z.M. Dashevsky, and S.R. Rotman	
Oxidation Kinetics and Microstructure of Wet-Oxidized MBE-Grown Short-Period AlGaAs Superlattices.....	561
René Todt, Katharine Dovidenko, Alexei Katsnelson, Vadim Tokranov, Michael Yakimov, and Serge Oktyabrsky	

RADIATION DETECTORS AND EFFECTS

* Space Radiation Effects in Advanced Solar Cell Materials and Devices.....	569
R.J. Walters, G.P. Summers, and S.R. Messenger	
Thermal Anneal Effects on Carbon-Hydrogen LVMs in AlGaIn	581
M.O. Manasreh and B.D. Weaver	
* Irradiation Effects in Space Solar Cells Made of Multiple Absorbers.....	587
M.J. Romero, R.J. Walters, M.M. Al-Jassim, S.R. Messenger, and G.P. Summers	
* Ion Implantation Induced Interdiffusion in Quantum Wells for Optoelectronic Device Integration.....	599
L. Fu, H.H. Tan, M.I. Cohen, C. Jagadish, L.V. Dao, M. Gal, Na Li, Ning Li, X. Liu, W. Lu, and S.C. Shen	

*Invited Paper

The Influence of Annealing Temperature and Doping on the Red/Near-Infrared Luminescence of Ion Implanted SiO₂:nc-Si	607
D.I. Tetelbaum, V.A. Burdov, S.A. Trushin, A.N. Mikhaylov, D.G. Revin, and D.M. Gaponova	

GROWTH, MATERIALS, AND DOPING

* Airplane and Drop Experiments on Crystallization of In_xGa_{1-x}Sb Semiconductor Under Different Gravity Conditions	617
Krishnan Balakrishnan, Yasuhiro Hayakawa, Hideki Komatsu, Noriaki Murakami, Tetsuo Nakamura, Tadashi Kimura, Tetsuo Ozawa, Yasunori Okano, Masafumi Miyazawa, Sadik Dost, Le. H. Dao, and Masashi Kumagawa	
Photo-Assisted MOVPE Growth of ZnMgS on (100) Si.....	625
Angel Rodriguez, Jeremy Shattuck, Xiaoguang Zhang, Peng Li, David Parent, John Ayers, and Faquir Jain	
Optical Vibrational and Structural Properties of Ge_{1-x}Sn_x Alloys by UHV-CVD	631
Jennifer Taraci, S. Zollner, M.R. McCartney, Jose Menendez, D.J. Smith, John Tolle, M. Bauer, Erika Duda, N.V. Edwards, and J. Kouvetakis	
Pulsed Laser Deposition and Characterization of Zn_{1-x}Mn_xO Films.....	637
C. Jin, A. Tiwari, A. Kvit, D. Kumar, J. Muth, and J. Narayan	
* InP Self Assembled Quantum Dot Lasers Grown on GaAs Substrates by Metalorganic Chemical Vapor Deposition	643
R.D. Dupuis, J.H. Ryou, R.D. Heller, G. Walter, D.A. Kellogg, N. Holonyak Jr., C.V. Reddy, V. Narayanamurti, D.T. Mathes, and R. Hull	
Effects of As Doping on Properties of ZnO Films	649
K.S. Huh, D.K. Hwang, K.H. Bang, M.K. Hong, D.H. Lee, J.M. Myoung, M.S. Oh, and W.K. Choi	
Growth of the Single-Crystalline ZnO Films on Si (111) Substrates by Plasma-Assisted Molecular-Beam Epitaxy.....	655
Kazuto Koike, Takanori Tanite, Shigehiko Sasa, Masataka Inoue, and Mitsuaki Yano	

*Invited Paper

SYMPOSIUM K PAPERS

Properties of 2D and 3D Dielectric Structures Fabricated by Electrochemical Dissolution of III-V Compounds	663
I.M. Tiginyanu, S. Langa, M. Christophersen, J. Carstensen, V. Sergentu, E. Foca, O. Rios, and H. Föll	
Transmission Characterization of Drilled Alternating-Layer Three-Dimensional Photonic Crystals	669
Eiichi Kuramochi, Masaya Notomi, Itaru Yokohama, Jun-ichi Takahashi, Chiharu Takahashi, Takayuki Kawashima, and Shojiro Kawakami	
Interference Lithography for 3D Photonic Band Gap Crystal Layer by Layer Fabrication	675
A Feigel, Z. Kotler, B. Sfez, A. Arsh, M. Klebanov, and V. Lyubin	
Simulations of Realizable Photonic Bandgap Structures With High Refractive Contrast.....	679
Bonnie Gersten and Jennifer Synowczynski	
Optical Study of 2D Photonic Crystals in an InP/GaInAsP Slab Waveguide Structure.....	685
Rolando Ferrini, David Leuenberger, Mikaël Mulot, Min Qiu, Jürgen Moosburger, Martin Kamp, Alfred Forchel, Srinivasan Anand, and Romuald Houdré	
Fabrication of Microstructures for Microphotonic Circuit.....	691
Subhasish Chakraborty, D.G. Hasko, and R.J. Mears	
* Two Dimensional Photonic Crystal Modes and Resonances in Three-Dimensional Structures.....	697
Shanhui Fan and J.D. Joannopoulos	
Artificial Second Order Non-Linearity in Photonic Crystals.....	709
A Feigel, Z. Kotler, and B. Sfez	

*Invited Paper

SYMPOSIUM T PAPER

Atomistic Modeling of III-V Semiconductors: Thermodynamic Equilibrium and Growth Kinetics.....	717
Frank Grosse, William Barvosa-Carter, Jennifer J. Zinck, and Mark F. Gyure	
Author Index	723
Subject Index.....	729

PREFACE

Symposium H, entitled "Progress in Semiconductor Materials for Optoelectronic Applications," was held November 26–29 at the 2001 MRS Fall Meeting in Boston, Massachusetts. There were 160 papers presented in eleven sessions, including two poster sessions. The sessions were well attended and the discussions were lively.

The presentations during this four-day symposium emphasize the broad scientific and technological interest in semiconductor materials for optoelectronic applications. The objective of this symposium was to review the progress on interband and intersubband transitions in semiconductor materials including III-V, IV, and II-VI materials and quantum structures as well as to cover the progress on light sources, detectors, modulators, and other novel devices. A significant portion of the symposium addressed materials growth and processing issues for optoelectronic devices, including work on solar cell and lasers materials utilizing low nitrogen concentration compounds, VCSELs, quantum dots, and quantum wells, as well as heterostructures. Materials ranged over the III-V and II-VI semiconductors, including GaAs, GaAsN, InP, ZnSe, and others. Technological applications ranged over infrared detectors, microelectronics, optical materials, lasers solar cell applications and design and VCSELs.

Session chairs included: Salah Bedair, Yoon-Soo Park, Joe Campbell, Weng Chow, John Bruno, Steven Kurtz, Brad Weaver, Chennupati Jagadish, and Robert M. Biefeld. The organizers gratefully acknowledge their contribution.

Symposium support was provided by the Air Force Office of Scientific Research and the Office of Naval Research. The symposium organizers, proceedings editor, and the Materials Research Society gratefully acknowledge their support.

It should be noted that several selected papers from Symposium K and Symposium T were added to this proceedings.

Eric D. Jones
Omar Manasreh
Kent D. Choquette
Daniel J. Friedman
Daniel K. Johnstone

January 2002

MATERIALS RESEARCH SOCIETY SYMPOSIUM PROCEEDINGS

- Volume 664—Amorphous and Heterogeneous Silicon-Based Films—2001, M. Stutzmann, J.B. Boyce, J.D. Cohen, R.W. Collins, J. Hanna, 2001, ISBN: 1-55899-600-1
- Volume 665—Electronic, Optical and Optoelectronic Polymers and Oligomers, G.E. Jabbour, B. Meijer, N.S. Sariciftci, T.M. Swager, 2002, ISBN: 1-55899-601-X
- Volume 666—Transport and Microstructural Phenomena in Oxide Electronics, D.S. Ginley, M.E. Hawley, D.C. Paine, D.H. Blank, S.K. Streiffer, 2001, ISBN: 1-55899-602-8
- Volume 667—Luminescence and Luminescent Materials, K.C. Mishra, J. McKittrick, B. DiBartolo, A. Srivastava, P.C. Schmidt, 2001, ISBN: 1-55899-603-6
- Volume 668—II-VI Compound Semiconductor Photovoltaic Materials, R. Noufi, R.W. Birkmire, D. Lincot, H.W. Schock, 2001, ISBN: 1-55899-604-4
- Volume 669—Si Front-End Processing—Physics and Technology of Dopant-Defect Interactions III, M.A. Foad, J. Matsuo, P. Stolk, M.D. Giles, K.S. Jones, 2001, ISBN: 1-55899-605-2
- Volume 670—Gate Stack and Silicide Issues in Silicon Processing II, S.A. Campbell, C.C. Hobbs, L. Clevenger, P. Griffin, 2002, ISBN: 1-55899-606-0
- Volume 671—Chemical-Mechanical Polishing 2001—Advances and Future Challenges, S.V. Babu, K.C. Cadini, J.G. Ryan, H. Yano, 2001, ISBN: 1-55899-607-9
- Volume 672—Mechanisms of Surface and Microstructure Evolution in Deposited Films and Film Structures, J. Sanchez, Jr., J.G. Amar, R. Murty, G. Gilmer, 2001, ISBN: 1-55899-608-7
- Volume 673—Dislocations and Deformation Mechanisms in Thin Films and Small Structures, O. Kraft, K. Schwarz, S.P. Baker, B. Freund, R. Hull, 2001, ISBN: 1-55899-609-5
- Volume 674—Applications of Ferromagnetic and Optical Materials, Storage and Magnetoelctronics, W.C. Black, H.J. Borg, K. Bussmann, L. Hesselink, S.A. Majetich, E.S. Murdock, B.J.H. Stadler, M. Vazquez, M. Wuttig, J.Q. Xiao, 2001, ISBN: 1-55899-610-9
- Volume 675—Nanotubes, Fullerenes, Nanostructured and Disordered Carbon, J. Robertson, T.A. Friedmann, D.B. Geohegan, D.E. Luzzi, R.S. Ruoff, 2001, ISBN: 1-55899-611-7
- Volume 676—Synthesis, Functional Properties and Applications of Nanostructures, H.W. Hahn, D.L. Feldheim, C.P. Kubiak, R. Tannenbaum, R.W. Siegel, 2002, ISBN: 1-55899-612-5
- Volume 677—Advances in Materials Theory and Modeling—Bridging Over Multiple-Length and Time Scales, L. Colombo, V. Bulatov, F. Cleri, L. Lewis, N. Mousseau, 2001, ISBN: 1-55899-613-3
- Volume 678—Applications of Synchrotron Radiation Techniques to Materials Science VI, P.G. Allen, S.M. Mini, D.L. Perry, S.R. Stock, 2001, ISBN: 1-55899-614-1
- Volume 679E—Molecular and Biomolecular Electronics, A. Christou, E.A. Chandross, W.M. Tolles, S. Tolbert, 2001, ISBN: 1-55899-615-X
- Volume 680E—Wide-Bandgap Electronics, T.E. Kazior, P. Parikh, C. Nguyen, E.T. Yu, 2001, ISBN: 1-55899-616-8
- Volume 681E—Wafer Bonding and Thinning Techniques for Materials Integration, T.E. Haynes, U.M. Gösele, M. Nastasi, T. Yonehara, 2001, ISBN: 1-55899-617-6
- Volume 682E—Microelectronics and Microsystems Packaging, J.C. Boudreaux, R.H. Dauskardt, H.R. Last, F.P. McCluskey, 2001, ISBN: 1-55899-618-4
- Volume 683E—Material Instabilities and Patterning in Metals, H.M. Zbib, G.H. Campbell, M. Victoria, D.A. Hughes, L.E. Levine, 2001, ISBN: 1-55899-619-2
- Volume 684E—Impacting Society Through Materials Science and Engineering Education, L. Broadbelt, K. Constant, S. Gleixner, 2001, ISBN: 1-55899-620-6
- Volume 685E—Advanced Materials and Devices for Large-Area Electronics, J.S. Im, J.H. Werner, S. Uchikoga, T.E. Felter, T.T. Voutsas, H.J. Kim, 2001, ISBN: 1-55899-621-4
- Volume 686—Materials Issues in Novel Si-Based Technology, W. En, E.C. Jones, J.C. Sturm, S. Tiwari, M. Hirose, M. Chan, 2002, ISBN: 1-55899-622-2
- Volume 687—Materials Science of Microelectromechanical Systems (MEMS) Devices IV, A.A. Ayon, S.M. Spearing, T. Buchheit, H. Kahn, 2002, ISBN: 1-55899-623-0
- Volume 688—Ferroelectric Thin Films X, S.R. Gilbert, Y. Miyasaka, D. Wouters, S. Trolrier-McKinstry, S.K. Streiffer, 2002, ISBN: 1-55899-624-9

MATERIALS RESEARCH SOCIETY SYMPOSIUM PROCEEDINGS

- Volume 689— Materials for High-Temperature Superconductor Technologies, M.P. Paranthaman, M.W. Rupich, K. Salama, J. Mannhart, T. Hasegawa, 2002, ISBN: 1-55899-625-7
- Volume 690— Spintronics, T.J. Klemmer, J.Z. Sun, A. Fert, J. Bass, 2002, ISBN: 1-55899-626-5
- Volume 691— Thermoelectric Materials 2001—Research and Applications, G.S. Nolas, D.C. Johnson, D.G. Mandrus, 2002, ISBN: 1-55899-627-3
- Volume 692— Progress in Semiconductor Materials for Optoelectronic Applications, E.D. Jones, M.O. Manasreh, K.D. Choquette, D. Friedman, 2002, ISBN: 1-55899-628-1
- Volume 693— GaN and Related Alloys—2001, J.E. Northrup, J. Neugebauer, S.F. Chichibu, D.C. Look, H. Riechert, 2002, ISBN: 1-55899-629-X
- Volume 695— Thin Films: Stresses and Mechanical Properties IX, C.S. Ozkan, R.C. Cammarata, L.B. Freund, H. Gao, 2002, ISBN: 1-55899-631-1
- Volume 696— Current Issues in Heteroepitaxial Growth—Stress Relaxation and Self Assembly, E. Stach, E. Chason, R. Hull, S. Bader, 2002, ISBN: 1-55899-632-X
- Volume 697— Surface Engineering 2001—Fundamentals and Applications, W.J. Meng, A. Kumar, Y-W. Chung, G.L. Doll, Y-T. Cheng, S. Veprék, 2002, ISBN: 1-55899-633-8
- Volume 698— Electroactive Polymers and Rapid Prototyping, Y. Bar-Cohen, D.B. Chrisey, Q.M. Zhang, S. Bauer, E. Fukada, S.C. Danforth, 2002, ISBN: 1-55899-634-6
- Volume 699— Electrically Based Microstructural Characterization III, R.A. Gerhardt, A. Washabaugh, M.A. Alim, G.M. Choi, 2002, ISBN: 1-55899-635-4
- Volume 700— Combinatorial and Artificial Intelligence Methods in Materials Science, I. Takeuchi, C. Buelens, H. Koinuma, E.J. Amis, J.M. Newsam, L.T. Wille, 2002, ISBN: 1-55899-636-2
- Volume 702— Advanced Fibers, Plastics, Laminates and Composites, F.T. Wallenberger, N. Weston, K. Chawla, R. Ford, R.P. Wool, 2002, ISBN: 1-55899-638-9
- Volume 703— Nanophase and Nanocomposite Materials IV, S. Komarneni, R.A. Vaia, G.Q. Lu, J-I. Matsushita, J.C. Parker, 2002, ISBN: 1-55899-639-7
- Volume 704— Nanoparticle Materials, R.K. Singh, R. Partch, M. Muhammed, M. Senna, H. Hofmann, 2002, ISBN: 1-55899-640-0
- Volume 705— Nanopatterning—From Ultralarge-Scale Integration to Biotechnology, L. Merhari, K.E. Gonsalves, E.A. Dobisz, M. Angelopoulos, D. Herr, 2002, ISBN: 1-55899-641-9
- Volume 706— Making Functional Materials with Nanotubes, P. Nikolaev, P. Bernier, P. Ajayan, Y. Iwasa, 2002, ISBN: 1-55899-642-7
- Volume 707— Self-Assembly Processes in Materials, S. Moss, 2002, ISBN: 1-55899-643-5
- Volume 708— Organic and Optoelectronic Materials, Processing and Devices, S. Moss, 2002, ISBN: 1-55899-644-3
- Volume 709— Advances in Liquid Crystalline Materials and Technologies, P.T. Mather, D.J. Broer, T.J. Bunning, D.M. Walba, R. Zentel, 2002, ISBN: 1-55899-645-1
- Volume 710— Polymer Interfaces and Thin Films, C.W. Frank, 2002, ISBN: 1-55899-646-X
- Volume 711— Advanced Biomaterials—Characterization, Tissue Engineering and Complexity, 2002, ISBN: 1-55899-647-8
- Volume 712— Materials Issues in Art and Archaeology VI, P.B. Vandiver, M. Goodway, J.R. Druzik, J.L. Mass, 2002, ISBN: 1-55899-648-6
- Volume 713— Scientific Basis for Nuclear Waste Management XXV, B.P. McGrail, G.A. Cragnolino, 2002, ISBN: 1-55899-649-4
- Volume 714E—Materials, Technology and Reliability for Advanced Interconnects and Low-k Dielectrics II, S. Lahiri, 2002, ISBN: 1-55899-650-8

Prior Materials Research Society Symposium Proceedings available by contacting Materials Research Society

**Low Concentration Nitride
Alloys I**

Luminescent Characteristics of InGaAsP/InP Multiple Quantum Well Structures by Impurity-Free Vacancy Disordering

J. Zhao¹, X. D. Zhang¹, Z. C. Feng^{2,*}, J. C. Deng^{1,3}, P. Jin⁴, Y. C. Wang¹, and G. Xu⁵

¹ Department of Physics & Institute of Materials Science, Tianjin Normal University, Tianjin 300074, P. R. China.

² Axcel photonics, 45 Bartlett Street, Marlborough, MA 01752, USA

³ Department of Materials Science, National University of Singapore, 119260 Singapore

⁴ College of Physics, Nankai University, Tianjin 300074, P. R. China.

⁵ Department of Materials Sci. & Engineering, McMaster University, Hamilton, Canada L8S 4L7

ABSTRACT

InGaAsP/InP multiple quantum wells have been prepared by Impurity-Free Vacancy Disordering (IFVD). The luminescent characteristics was investigated using photoluminescence (PL) and photoreflectance (PR), from which the band gap blue shift was observed. Si_3N_4 , SiO_2 and SOG were used for the dielectric layer to create the vacancies. All samples were annealed by rapid thermal annealing (RTA). The results indicate that the band gap blue shift varies with the dielectric layers and annealing temperature. The SiO_2 capping was successfully used with an InGaAs cladding layer to cause larger band tuning effect in the InGaAs/InP MQWs than the Si_3N_4 capping with an InGaAs cladding layer. On the other hand, samples with the Si_3N_4 -InP cap layer combination also show larger energy shifts than that with SiO_2 -InP cap layer combination.

INTRODUCTION

In fabricating luminescent devices for integrated optoelectronic and photonic application, InGaAsP/InP multiple quantum well (MQW) structures have attracted research interests. Post-tuning of optical band gap energy can be achieved from these MQW structures, which posses the advantage to avoid the complicated post growth processing. Several technical approaches have been explored to achieve this purpose, including (1) Impurity Induced Disordering (IID) [1,2], (2) Implant Induced Composition Disordering (IICD) [3-6], and (3) Impurity-Free Vacancy Disordering (IFVD) [7,8]. Among them, IFVD technique shows more promising because it can keep high crystal quality and low optical propagation losses as well as it does not introduce free-carrier concentration. IFVD, utilizing a dielectric layer such as SiO_2 and Si_3N_4 as Ga sink at elevated temperature, could result in the redistribution of Ga vacancies in MQWs to enhance the quantum well intermixing and thus to enhance the luminescence [9,10].

* Electronic mail: zfceng@axcelphotonics.com

In this paper, a systematic investigation on luminescent characteristics of InGaAsP/InP MQW system using SiO₂, Si₃N₄ and SOG (spin on glass) as dielectric layers in IFVD is reported. Photoluminescence (PL) was measured by a Fourier Transform Infrared (FT-IR) PL system. Photorefectance (PR) measurements on these samples were used to investigate further the behavior of band gap blue shift. To our knowledge, there was no report published with measuring band gap blue shift by PR for this material system yet. We found that the different combinations of cladding layer and dielectric layer, such as InP-SiO and InP-SiN, also affect the band gap luminescent characteristics, which was also rarely reported.

EXPERIMENT

Two typical samples were chosen in this paper. Both samples A and B are InGaAsP/InP laser structures, consisting of three quantum wells, designed to emit at wavelength of 1.57 μ m and 1.55 μ m, respectively. They were grown by Gas Source Molecular Beam Epitaxy (GSMBE). The detail structures of samples are shown in Table 1, in which "1.15Q" means "InGaAsP layer with the bandgap wavelength of 1.15 μ m", and "ud" does "un-doped". Sample A was cut and divided into three groups with capped dielectric layers of SiO₂ and Si₃N₄ by PECVD and SOG by spin coating at 3000 rpm for 45 second. The thickness of all the dielectric layers is about 200 nm. Samples with the SOG cap were then baked at 200 °C for 2 hours under pure nitrogen ambient protection. Sample B was divided into two groups remarked B1 and B2. B2 was etched InP cladding layer away using corrosive solution (HCl:H₃PO₄=1:1). Then samples B1 and B2 were deposited SiO₂ and Si₃N₄, respectively, by PECVD. The thickness is also about 200nm.

Table 1. Schematic layer structure of the InGaAsP/InP MQW samples studied.

Sample A	Sample B
He*-InP p=1e18 100nm	100nm InP (ud)
InP p=6e17, 25nm	5nm InGaAs (ud)
1.15Q InGaAsP p=5e17, 80nm	200nm InP p=1e18
1.24Q 70nm	200nm InP p=5e17
1.58Q 5nm	40nm He* InP p=5e17
1.24Q 10nm	5nm InP p=5e17
1.58Q 5nm	100nm 1.15Q p=5e17
1.24Q 10nm	60nm 1.24Q (ud)
1.58Q 5nm	3*5nm QW's ; 2*10nm Barriers (QW~In _{0.758} GaAsP _{0.17}) (Barrier~In _{0.758} GaAsP _{0.475})
1.24Q 70nm	30nm 1.24Q (ud)
1.15Q n=5e17 80nm	30nm 1.15Q n=5e17
InP n=1e18 500nm	500nm InP n=1e18
n+ InP substrate	n+ InP Substrate

After the GSMBE growth, samples were then annealed in a rapid thermal annealing (RTA) furnace at the temperature ranged from 650 °C~850 °C in 50 °C steps. The annealing time for all samples was kept for 30 seconds. During the RTA the samples were covered with a piece of

semi-insulating-GaAs face to face to minimize the decomposition of InP and possible contamination. All annealing processing are under the pure nitrogen protection.

Photoluminescence measurements were performed at the temperature 300K. The excitation source was an Argon ion laser with the wavelength of 514.5 nm. The Photoreflectance (PR) spectra were measured at the optoelectronic laboratory of Nankai University. The modulation source was a He-Ne laser with the wavelength of 632.8nm.

RESULTS AND DISCUSSION

Room temperature PL spectra are shown in Figure 1 for the as-grown sample A and disordered InGaAsP multi-quantum well structures after RTA at 800°C for 30s with SiO₂ and Si₃N₄ encapsulating layer, respectively. The peak position of the PL spectrum for the as grown sample A is at 1.571 μm (0.789 eV), corresponding to the electron transition from the first level of electronic subband to the first level of heavy hole (E1-HH1) and light hole subband (E1-LH1). From the figure 1, we can find that the band gap blue shift depends on the dielectric layer. The sample A with a Si₃N₄ capped layer obtained larger blue shift. In order to find the dependence of the band gap blue shift on the annealing temperature, the samples covered with Si₃N₄, SiO₂ and SOG were annealed at the temperature of 650, 700, 750, 800 and 850°C, respectively. Figure 2 shows the annealing temperature dependence of band gap shift. It can be observed that the band gap of PL peak varies with the RTA temperature. For low annealing temperature range of 650~750°C, the PL peak has little change, however, when the annealing temperature was beyond 750°C, the PL peak moves to short wavelength evidently.

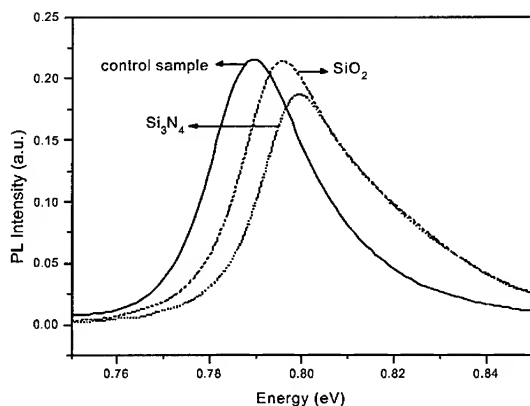


Figure 1. The PL spectra of the control sample and SiO₂, Si₃N₄ covered samples.

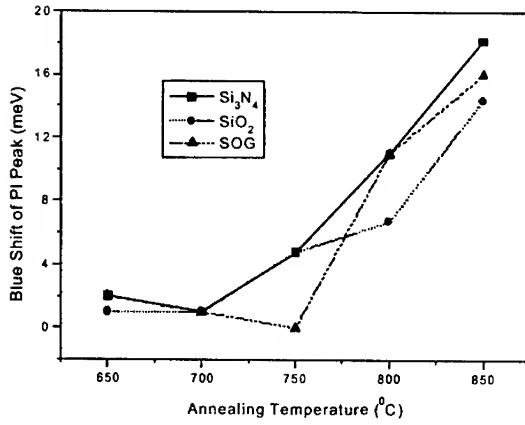


Figure 2. The temperature dependence of blue shift for different dielectric covered samples.

On the other hand, we also performed photoreflectance (PR) measurements in accordance with the results of PL spectra, as shown in Figure 3. It shows that PR results are consistent with the PL results. This indicates that PR can be used as a supplementary way to study the luminescent characteristics of the band gap shift. Furthermore, PR spectra can provide some other information, for example, some detailed data about different layer luminescent characteristics through analyzing PR spectra, which to be done in a separate paper.

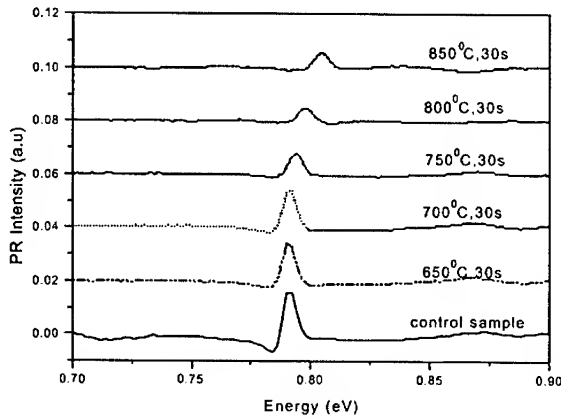


Figure 3. Band gap blue shift measured by PR with different annealing temperature.

In order to find the effects on the combination of the cladding layer and dielectric covered layer, the annealing temperature dependence of the bandgap blue shift for sample B1 and B2 with different dielectric layers were further studied, based upon the PL data. Sample B1 has an InP cladding structure, and sample B2 has an InGaAs cladding layer. Both samples B1 and B2 have the same MQWs except for the cladding layer. These two types of samples were measured under the same experimental condition, to examine their band gap blue shift. Figure 4 shows the dependences of the blue shift PL peak on the annealing temperature, caused by different covered layer of Si_3N_4 and SiO_2 , respectively. It can be observed that the induced blue shift from the sample with the InP- Si_3N_4 combination is larger than that with the InP- SiO_2 combination. For example, the blue shift of the sample with the InP- Si_3N_4 cap layer combination reaches 50 meV at 850°C , but the blue shift of the sample with the InP- SiO_2 cap layer combination is only 40 meV at the same annealing temperature. On the other hand, the combination of InGaAs- Si_3N_4 covered layer caused 20 meV, however the combination of InGaAs- SiO_2 reached 43 meV. From these results, we can conclude that the combination layer of InP- Si_3N_4 or InGaAs- SiO_2 can create larger band gap blue shift than the combination of InP- SiO_2 and InGaAs- Si_3N_4 ones. The reason for these experimental results is not very clear, but in our opinion, it can be explained as follow: The vacancies are produced in both group III and V. It is known that in GaAs material the following reactions are prompted to produce large number of vacancies at the interface:

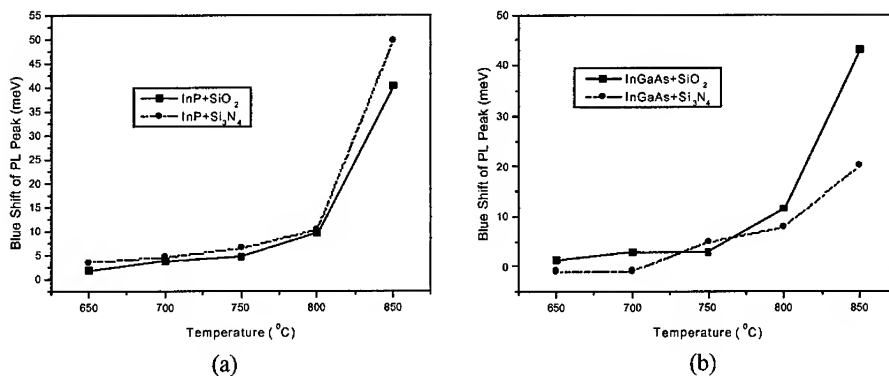
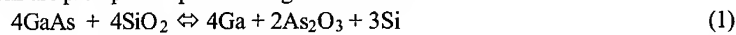


Figure 4. The temperature dependences of blue shift for the samples with (a) InP- SiO_2 and InP- Si_3N_4 combination layers, and (b) InGaAs- SiO_2 and InGaAs- Si_3N_4 combination layers.

Our results indicate that the vacancies generated by the InP- SiO_2 combination are less than that by the InGaAs- SiO_2 combination layers because of the absence of Ga. As for the group V vacancies, we can not provide the detailed reactions as to how the vacancies are produced. This may be the reason for the effects on the combination of the cladding layer and dielectric layers.

CONCLUSION

In conclusion, we have studied the dependence of the band gap blue shift on the annealing temperature and dielectric layers from the InGaAsP/InP multiple quantum wells prepared by Impurity-Free Vacancy Disorder (IFVD). Both PL and PR results, which are consistent each other, showed that this band gap blue shift increases with the annealing temperature for all samples. To our knowledge, this is a first report on the band gap blue shift measured by PR. Our results indicate that PR can also be used as a supplementary way, in addition to PL, to study the band gap blue shift. On the other hand, to obtain larger energy shift the optimal selected cap layer combination is necessary. From our experiments the combination of InP-Si₃N₄ or InGaAs-SiO₂ is better than the combination of InGaAs-Si₃N₄ or InP-SiO₂.

ACKNOWLEDGMENTS

The authors would like to thank Dr. B. Robinson at McMaster University Canada for providing the GSMBE samples. This project is supported by the Nature Science Foundation of China (NSFC) with a contract number of 69886001.

REFERENCES

1. W. D. Laiding, N. Holonyak, Jr., M. D. Camras, K. Hess, J. Coleman, P. D. Dapkus, and J. Bardeen, *Appl. Phys. Lett.* **38**, 776 (1981).
2. D. Gdepe, N. Holonyak Jr., *J. Appl. Phys.* **64**, R93 (1988).
3. J. H. Marsh, S. I. Hansen, A. C. Bryce, and R. M. De La Rue, *Opt. Quantum Electron.* **23** 941 (1991).
4. S. R. Andrew, J. H. Marsh, M. C. Holland, and A. H. Kean, *IEEE Photon Technol. Lett.* **4**, 426 (1992).
5. B. B. Elenkrig, D. A. Thompson, J. G. Simmons, D. M. Bruce, Yu. Si, Jie Zhao, J. D. Evans, and I. M. Templeton, *Appl. Phys. Lett.* **65** (10), 1239 (1994).
6. M. Paquette, J. Beauvais, J. Beerens, P. J. Poole, S. Charbonneau, C. J. Miner, and C. Blauw, *Appl. Phys. Lett.* **71** (26), 3749 (1997).
7. G. Li, S. J. Chua, S. J. Xu, X. C. Wang, A. Saher Helmy, Mao-Long Ke, and J. H. Marsh, *Appl. Phys. Lett.* **73** (23), 3393 (1998).
8. G. Li, S. J. Chua, J. H. Teng, W. Wang, Z. C. Feng, H. Huang, and T. Osipowicz, *J. Vac. Sci. Technol. B* **17** (4), 1507 (1999).
9. S. O'Brien, J. R. Shealy, D. P. Bour, L. Elbaum, and J. Y. Chi, *Appl. Phys. Lett.* **56**, 1365 (1990).
10. S. Burkner, M. Maier, E. C. Larkins, w. Rothmund, E. P. O'Reilly, and J. D. Ralston, *J. Electron. Mater.* **24**, 805 (1995).

Successes and Predictions of A Pseudopotential Approach in Anion-Mixed Nitrides

L. Bellaiche¹, A. Al-Yacoub¹, N.A. Modine² and E.D. Jones²

¹Physics Department, University of Arkansas, Fayetteville, Arkansas 72701, USA

²Sandia National Laboratories, Albuquerque, New Mexico 87185, USA

ABSTRACT

The construction and the parameters of a new-strain dependent empirical pseudopotentials method are described and provided, respectively. This method is shown to reproduce with a very high accuracy some observed unusual properties in various complex anion-mixed nitride alloys. This method is also used to predict and understand anomalous effects that remain to be experimentally discovered in $\text{Ga}_{1-y}\text{In}_y\text{As}_{1-x}\text{N}_x$ quaternaries and $\text{GaAs}_{0.5-x}\text{P}_{0.5-x}\text{N}_{2x}$ solid solutions.

INTRODUCTION

Anion-mixed nitride alloys exhibit very unusual properties. Examples of such anomalies are a large decrease of the band-gap when slightly increasing the nitrogen compositions [1-5] and a non-linear pressure behavior of the band-gap and exciton reduced masses in $\text{GaAs}_{1-x}\text{N}_x$ and $\text{Ga}_{1-y}\text{In}_y\text{As}_{1-x}\text{N}_x$ [6-10]. Other examples include the strong dependency of the optical bowing coefficient [3,4], of the interband transition intensities [11] and of the effective electronic mass with nitrogen composition [12]. Other unusual features are the huge dependency of their optical and electronic properties with nitrogen atomic arrangement [13-15], as well as, the appearance of nitrogen impurity levels near the band edges in the dilute nitrogen impurity limit of $\text{Ga}_{1-y}\text{In}_y\text{As}_{1-x}\text{P}_z\text{N}_{x+z}$ solid solutions [16-18]. Many recent studies have proposed rather different mechanisms for the microscopic effects responsible for these anomalies [3,6-9,18-21]. One possible reason for the present lack of consensus among researchers is the unprecedented difficulty of theoretically mimicking the properties of these alloys. As a matter of fact, some approximations, such as the virtual crystal approximation (VCA) [22], that can yield predictions in good agreement with measurements for conventional III-V alloys [11] are no longer valid in III-V-N solid solutions [11,23]. Similarly, the accurate description of various phenomena in anion-mixed nitride alloys requires the use of supercells that are too large to be handled by conventional first-principles calculations [18]. One computational alternative to the VCA and first-principles approaches is the so-called empirical pseudopotentials method (EPM). However, the accuracy provided by this approach strongly depends on the analytical form and on the parameters used to derive the pseudopotentials, which explains why different EPM can lead to quite different quantitative properties [3,9,10,18]. The goals of this article are (i) to describe in detail a new empirical pseudopotential method, (ii) to demonstrate that this method yields predictions in excellent agreement with measurements for various properties in complex anion-mixed nitride alloys, and (iii) to use this method to predict and understand effects that still remain to be experimentally discovered in III-V-N systems.

METHODS

Large relaxed supercells

To model a zinc-blende alloy, we use $N \times N \times N$ conventional cubic cells, where the integer N can range from 4 to 8 --- which corresponds to a number of atoms varying from 512 to 4096. For *random* solid solutions, the atoms are randomly distributed on their sublattice sites, while the atoms in *ordered* alloys are located as consistent with the atomic ordering.

The valence force field (VFF) approach [24,25] is then used to predict the relaxed atomic positions corresponding to the minimum strain energy. Specifically, we use the bond-stretching (α) and bond-bending (β) of Ref. [26] for GaN ($\alpha=96.30$ N/m and $\beta=14.80$ N/m) and InN ($\alpha=79.20$ N/m and $\beta=7.10$ N/m), and of Ref. [25] for GaAs ($\alpha=41.19$ N/m and $\beta=8.95$ N/m), InAs ($\alpha=35.18$ N/m and $\beta=5.50$ N/m), GaP ($\alpha=47.32$ N/m and $\beta=10.44$ N/m) and InP ($\alpha=43.04$ N/m and $\beta=6.24$ N/m) in these VFF calculations. Reference[3] demonstrates that the VFF approach yields a good agreement with first-principles results for the internal atomic coordinates of anion-mixed nitride alloys.

Strain-dependent empirical pseudopotentials

Having obtained a relaxed configuration of a large, periodic unit cell, we compute its band structure by using the strain-dependent empirical pseudopotential approach proposed in Ref. [10]. The crystal potential $V(\mathbf{r})$ is written as a superposition of atomic pseudopotentials $v_\gamma(\mathbf{r})$, where $\gamma = \text{Ga, In, N, P or As}$.

For the As, P or N *anions*, the Fourier transform of $v_\gamma(\mathbf{r})$ is given by:

$$v_\gamma(\mathbf{q}) = [\Omega_\gamma \sum_m a_{m\gamma} \exp(-b_{m\gamma} (\mathbf{q} - \mathbf{c}_{m\gamma})^2)] \quad , \quad (1)$$

where the m integers range from 1 to 4.

For the Ga or In cations, the analytical expression of $v_\gamma(\mathbf{q})$ becomes more complicated:

$$\begin{aligned} v_\gamma(\mathbf{q}) = & \sum_A [\Omega_{\gamma(A)} \sum_m a_{m\gamma(A)} \exp(-b_{m\gamma(A)} (\mathbf{q} - \mathbf{c}_{m\gamma(A)})^2)] [n(\gamma-A) + n(\gamma-A) d_{ma}(\gamma(A)) \\ & \text{Tr}(\epsilon_{ma}) \\ & + (x_N f_{mi}(\gamma(A)) + g_{mi}(\gamma(A))) \sum_j \text{Tr}(\epsilon_{mi}(\gamma-A_j))] \quad , \end{aligned} \quad (2)$$

where the first sum runs over the different *kinds* of anions (e.g., $A = \text{As, P and N}$) nearest neighbors of the γ cation in the alloy, ' $\gamma(A)$ ' denotes a γ cation bonding with an anion A and $n(\gamma-A)$ is the number of type A anions that are nearest neighbors of this γ cation. Furthermore, Tr denotes the trace operator and ϵ_{ma} is the *macroscopic* strain induced by an external stress, e.g., applying a hydrostatic pressure P to the alloy leads to:

$\text{Tr}(\epsilon_{\text{ma}}) = 3 (a(P) - a(P=0)) / a(P=0)$, where $a(P)$ and $a(P=0)$ are the alloy lattice constants associated with the pressure P and at equilibrium, respectively. x_N is the nitrogen composition in the alloy, and the last sum runs over the different j atoms of type A which are nearest neighbors of the γ cation. $\epsilon_{\text{mi}}(\gamma-A_j)$ is the *microscopic* strain induced by alloying, e.g., for an alloy at its equilibrium lattice constant, we have:

$$\text{Tr}(\epsilon_{\text{mi}}(\gamma-A_j)) = [(|R_x(\gamma-A_j)| - d_0(\gamma A)) / d_0(\gamma A)] + [(|R_y(\gamma-A_j)| - d_0(\gamma A)) / d_0(\gamma A)] + [(|R_z(\gamma-A_j)| - d_0(\gamma A)) / d_0(\gamma A)], \quad (3)$$

where $|R_x(\gamma-A_j)|$ (respectively, $|R_y(\gamma-A_j)|$ and $|R_z(\gamma-A_j)|$) is the absolute value of the x - (respectively, y - and z -) component of the vector position joining the γ atom to the A_j anion in the alloy. $d_0(\gamma A)$ is the corresponding equilibrium Cartesian component in the pure zinc-blende γA binary.

One can note that, unlike in Refs [3,9,18], the contribution of both the macroscopic and the microscopic strain is taken into account for the generation of the pseudopotentials.

The strain-unrelated parameters of Eqs. (1) and (2), i.e. the Ω_γ , a_{my} , b_{my} and c_{my} coefficients, are fitted carefully to *ab-initio* band structures and to the experimental band-gaps of the corresponding γA binaries at their equilibrium lattice constants a_0 (with $a_0 = 8.523, 10.300, 10.6826, 9.4108, 11.0105$ and 11.444 Bohr for GaN, GaP, GaAs, InN, InP and InAs, respectively), and are given in Table I and Table II, respectively. Some of these coefficients were already given in Ref. [3] and references therein.

Table I. Strain-unrelated empirical pseudopotentials parameters for the different anions.

Atom γ	Ω_γ (a.u.) ³	m	a_{my} (Ry)	b_{my} (a.u.) ⁻¹	c_{my} (a.u.) ²
N	75.0	1	-0.22628191	1.816012550	0.000000000
		2	0.02083001	13.51921051	2.628521803
		3	0.23728104	0.909593411	1.555913001
		4	-0.92682699	0.918842363	0.851766355
P	139.2	1	-1.02821000	0.870327000	0.000000000
		2	0.01217600	5.811450000	2.400080000
		3	-0.04943100	3.186790000	0.889644000
		4	0.11769000	0.470922000	1.028360000
As	145.2	1	-1.05821000	0.959327000	0.000000000
		2	-0.00217627	6.531450000	2.468080000
		3	-0.04343120	2.946790000	0.851644000
		4	0.10569000	0.820922000	1.224360000

Table II. Strain-unrelated empirical pseudopotentials parameters for the different cations.

Atom γ (A)	$\Omega_{\gamma(A)} \text{ (a.u.)}^3$	m	$a_{m\gamma(A)} \text{ (Ry)}$	$b_{m\gamma(A)} \text{ (a.u.)}^{-1}$	$c_{m\gamma(A)} \text{ (a.u.)}^2$
Ga(N) = Ga(P) = Ga(As)	131.4	1	-1.24498000	1.527480000	0.000000000
		2	0.03665200	0.959082000	2.097820000
		3	0.04643600	0.574047000	2.019350000
		4	-0.01333800	11.27080000	2.935810000
In(N)	131.8	1	-1.46039000	2.152539077	0.000000000
		2	0.04155672	0.567806063	2.455282992
		3	0.06009332	0.148458154	2.251294168
		4	-0.01593695	13.75237193	2.728137391
In(P)	131.4	1	-1.45986104	1.738812400	0.000000000
		2	0.05977844	0.537256952	1.788116476
		3	0.04656102	0.967274227	2.926947028
		4	-0.02482974	3.509813326	3.447074186
In(As)	131.4	1	-1.44017756	1.729912675	0.000000000
		2	0.05814899	0.503547419	1.790927031
		3	0.04869021	1.177591464	3.265606034
		4	-0.01632399	4.001886743	4.019772670

The coefficients $d_{ma}(\gamma(A))$ in Eq.(2) are fitted to reproduce the local density approximations (LDA) deformations potentials of both the valence band maximum and conduction band minimum of the pure zinc-blende γA binary [27]. On the other hand, the parameters $f_{mi}(\gamma(A))$ and $g_{mi}(\gamma(A))$ are fitted to reproduce alloy quantities, namely the experimental bowing coefficient of $\text{Ga}(\text{As}_{1-x}\text{N}_x)$ with $x=0.004$ (see Refs [4-5] and references therein), $\text{In}(\text{P}_{1-x}\text{N}_x)$ with $x=0.004$ [28] and $(\text{Ga}_{1-y}\text{In}_y)\text{N}$ with $y=0.1$ [29-30], as well as the arsenic-impurity level observed in the GaN:As system [31]. The parameters that are strain-related and that enter Eq(2) are given in Table III.

Table III. Strain-related empirical pseudopotentials parameters for the different cations.

Cation γ (A)	d_{ma}	f_{mi}	g_{mi}
Ga(N)	0.1353	-0.4233	0.5817
Ga(P)	0.1870	0.0000	0.0000
Ga(As)	0.1870	0.0000	0.0000
In(N)	0.1615	-1.1800	1.2800
In(P)	0.2000	0.0000	0.0000
In(As)	0.2000	0.0000	0.0000

Plane-wave expansion and folded spectrum method

The electronic eigenfunctions of the Hamiltonian given by the sum of the kinetic energy and the empirical pseudopotentials are developed in a plane-wave basis with a kinetic energy cutoff denoted by G_{max} . Due to the large difference in equilibrium lattice constant

between the end-member binaries, G_{\max} is chosen to be dependent on the volume of the system under investigation. More precisely, G_{\max} should correspond to 59 plane waves at the Γ point per 2-atoms zinc-blende cell. As a result, systems exhibiting an equilibrium volume per 2 atoms identical to the one of pure GaAs are associated with a G_{\max} of 5 Ry while the kinetic energy cutoff is 7.87 Ry in compounds having the equilibrium volume per 2 atoms of zinc-blende GaN. Note that the parameters displayed in Tables I-III were fitted using this volume-dependent kinetic energy cutoff.

The eigenfunctions and eigenvalues of the Schrodinger equation for the large supercells are determined by using the so-called folded spectrum method [32]. This numerical technique is a method scaling linearly with the number of atoms in the supercell, and producing single-particle eigensolutions in a given energy window.

RESULTS

Accuracy of the strain-dependent empirical pseudopotentials

In this section, we will demonstrate the accuracy provided by our numerical scheme. With the exception of the band-gap of $\text{GaAs}_{1-x}\text{N}_x$ with $x=0.4\%$ and epitaxially grown on GaAs, all the results to be shown were not included in the fitting of the EPM parameters. The first test is displayed in Table IV and consists in comparing our calculations with low-temperature measurements for the band-gaps of *disordered* $\text{Ga}_{1-y}\text{In}_y\text{As}_{1-x}\text{N}_x$ *quaternaries* that are perfectly lattice-matched to either a GaAs or InP substrate. Because of this perfect lattice-match, the microscopic strain ϵ_{mi} is the only strain turned on in the generation of the pseudopotentials in Eq. (2). Table IV indeed reveals the high accuracy offered by the strain-dependent EPM described above. In particular, one can notice that the difference between predictions and measurements does not exceed 0.03 eV for a range of band-gap as large as 0.9 eV.

Table IV. Comparison between our predictions and experiments for the band-gaps of $\text{Ga}_{1-y}\text{In}_y\text{As}_{1-x}\text{N}_x$ quaternaries perfectly lattice-matched to a GaAs^{*} or InP^{**} substrate.

(y, x) compositions of $\text{Ga}_{1-y}\text{In}_y\text{As}_{1-x}\text{N}_x$	Theoretical band-gap (eV)	Experimental band-gap (eV)
(0.00, 0.000) [*]	1.52	1.52 (Ref. 7)
(0.07, 0.022) [*]	1.18	1.15 (Ref. 7)
(0.53, 0.000) ^{**}	0.82	0.82 (Ref. 33)
(0.56, 0.010) ^{**}	0.73	0.70 (Ref. 33)
(0.59, 0.019) ^{**}	0.65	0.65 (Ref. 33)

The second test is indicated in Fig. 1, which displays the comparison between our predictions and available experimental data for the compositional behavior of the band-gap of *random* $\text{GaAs}_{1-x}\text{N}_x$ *ternaries* epitaxially grown on a GaAs substrate. In such a case, both the macroscopic ϵ_{ma} and microscopic ϵ_{mi} strains appearing in Eq (2) are activated because of the epitaxial conditions and alloying, respectively. Figure 1 also

shows the predictions of the empirical pseudopotentials when all the strain-related coefficients of Table III have been turned off. In this figure, our calculated $T=0\text{K}$ band-gaps have been shifted downward, by using the temperature-dependency measured in Ref. [34], to compare our predictions with the recent *room-temperature* experiments of Refs. [5,35,36]. Figure 1 reveals an excellent agreement between the present strain-dependent EPM theory and measurements, and clearly demonstrates that the contribution of both the macroscopic and the microscopic strains to the empirical pseudopotentials drastically improves the accuracy of the calculations for anion-mixed nitrogen systems.

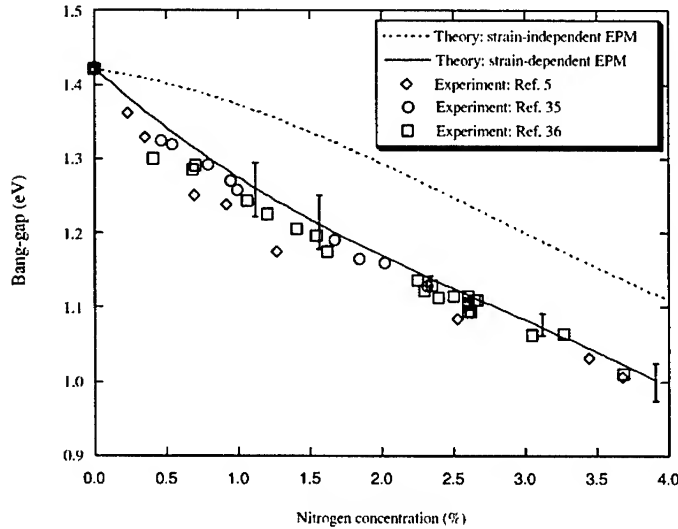


Figure 1. Comparison between our predictions, using empirical pseudopotentials methods (EPM), and experiments for the room-temperature band-gaps of $\text{GaAs}_{1-x}\text{N}_x$ alloys epitaxially grown on a GaAs substrate. Theoretical error bars are also indicated.

The result of the third test is reported in Figure 2, which shows our predictions and a low-temperature measurement [7] for the pressure-dependency of the band-gap in the random $\text{Ga}_{1-y}\text{In}_y\text{As}_{1-x}\text{N}_x$ quaternary, with $(y,x)=(0.07, 0.0023)$. Here, both macroscopic and microscopic strains are taken into account in Eq (2) because of the pressure and alloying, respectively. The calculations are corrected by multiplying the pressure-induced alloy band-gap shift by a constant number --- equal to 1.2885. This number is fitted to exactly reproduce the experimental hydrostatic deformation potential in zinc-blende GaAs. Our numerical results are once again in good agreement with measurements. In particular, one

can notice that the unusual non-linear pressure behavior of the band-gap is rather well reproduced up to 60Kbar.

The next step consists in identifying the energy of the nitrogen impurity level which is usually denoted $a_1(N)$ [9,18,21] and which is *resonant* inside the conduction band of nitrogen-dilute $\text{GaAs}_{1-x}\text{N}_x$ alloys. Such identification is realized by interpolating our results for one nitrogen atom inside a 1728 atoms-cell and inside a 4096 atoms-cell.

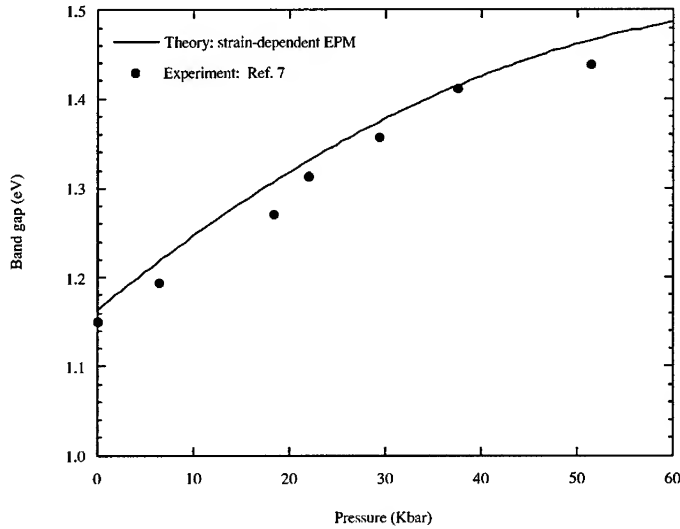


Figure 2. Comparison between our strain-dependent empirical pseudopotentials calculations and the experiment of Ref. [7] for the pressure-behavior of the band-gap in $\text{Ga}_{1-y}\text{In}_y\text{As}_{1-x}\text{N}_x$ quaternaries with $(y,x)=(0.07, 0.023)$.

$a_1(N)$ is found to be located 250 meV above the (CBM) Γ_{1c} level (or equivalently, 36 meV below the L_{1c} state) of GaAs, which is in excellent agreement with the experimental estimations of 300 meV above Γ_{1c} [37] and 30 meV below L_{1c} [38], as well as with the LDA calculations of Ref. [21] yielding 280 meV above Γ_{1c} .

The last test of this subsection is the prediction of the energy of the deep-gap impurity level occurring when adding a small amount of nitrogen to the $\text{Ga}(\text{As}_{0.5}\text{P}_{0.5})$ alloy. This

energy is found by linearly interpolating up to a null nitrogen composition the impurity levels predicted by our strain-dependent EPM for a nitrogen composition of 0.00116 and of 0.002. Such interpolation yields a nitrogen-impurity level located 115 meV below the conduction band-minimum of Ga(As_{0.5}P_{0.5}) alloy, which is in good agreement with the experimental value of 130 meV [16].

Prediction of anomalies in anion-mixed nitride alloys

The aim of this section is to review and to provide an explanation for the anomalies that were recently predicted to occur in anion-mixed nitrides, by using the present EPM [10,14,17]. Most of these anomalies remain to be experimentally discovered.

Predictions for (Ga,In)(As,N) alloys:

Ref. [10] predicted that the band-gap of the random Ga_{1-y}In_yAs_{1-x}N_x quaternaries lattice-matched to a GaAs or InP substrate strongly decreases when increasing the nitrogen composition (Note that this increase of nitrogen concentration was accompanied by a simultaneous increase in the indium composition in order to keep a perfect lattice-match to the substrate). As a result, the band-gap of both lattice-matched Ga_{1-y}In_yAs_{1-x}N_x systems crosses important technological spectral regions, namely the ones desired for optoelectronics, for solar cell applications, for designing new infrared devices and even for generating terahertz wavelengths [10]. Moreover, Ref. [10] further indicated that the band-gaps of both lattice-matched quaternaries even close for large enough nitrogen composition (namely, for x=0.12 for the InP-lattice matched quaternaries versus x=0.20 for the Ga_{1-y}In_yAs_{1-x}N_x alloys lattice matched to GaAs). In other words, these strain-dependent EPM calculations predict that it is possible to create a metallic system by mixing four semiconductors (namely, GaAs, InAs, GaN and InN)! They also demonstrate that the common empirical rule that there is a one-by-one correspondence between the value of the lattice constant and the value of the band-gap in semiconductors is completely invalid in anion-mixed nitride alloys.

Another recent article focused on the effect of *atomic ordering* on optical and electronic properties of the GaAs-lattice matched Ga_{1-y}In_yAs_{1-x}N_x solid solutions with a indium and nitrogen composition of 5% and 1.6%, respectively [14]. Three different samples were generated. The first configuration mimicks the *random* Ga_{0.95}In_{0.05}As_{0.984}N_{0.016} system. The second selected sample corresponds to the formation of one-dimensional nitrogen chains along the [001] cubic direction, such as each nitrogen atom has two other nitrogen

Table V. Band-gap of differently atomically-ordered Ga_{0.95}In_{0.05}As_{0.984}N_{0.016} alloys.

Ga _{0.95} In _{0.05} As _{0.984} N _{0.016} System	Band-gap (eV)
Random	1.27
With nitrogen chains formed along [100]	1.33
With nitrogen chains formed along [110]	1.12

atoms as *second neighbors* in the anion sublattice. The last chosen configuration also exhibits one-dimensional nitrogen chains but for which each nitrogen atom has now two other nitrogen atoms as *fourth neighbors* in the anion sublattice. The resulting direction of this chain is thus along the [110] direction. This peculiar atomic ordering was chosen because the nitrogen chains can be perceived as a bridge between the case of N-N pairs in GaAs and the case of more concentrated nitrogen alloys. Moreover, we decided to specifically choose the [100] and [110] directions as directions for the one-dimensional nitrogen chains because the formation of second neighbor N-N pair in GaAs is known to slightly increase the band-gap with respect to random Ga(As,N) alloys, while fourth neighbor N-N pair significantly decreases that band-gap [13]. We thus expected that the one-dimensional nitrogen chains formed along the [100] direction may affect the properties of (Ga,In)(As,N) quaternaries in an opposite way (with respect to the case of the disordered alloy) than the [110] nitrogen chains. Table V indeed reports that the band-gap of the ordered material exhibiting nitrogen chains arranged along the [110] direction is *smaller* (by 0.15 eV) than the band-gap of the random alloy, while the sample with one-dimensional nitrogen chains formed along the [100] direction has a band-gap *larger* by 0.06 eV than the band-gap of the disordered alloy. This variation of the band-gap with atomic ordering is quite remarkable, especially when realizing that the nitrogen composition of these alloys is as small as 1.6%.

Another finding reported in Ref. [14] is the correlation between the value of the band-gaps displayed in Table V and the wavefunction localization of the conduction band-minimum (CBM) in these alloys. In the calculations, smaller band-gaps were found to correspond to stronger localization of the alloy CBM electronic state around the nitrogen atoms.

A simple model was further proposed in Ref. [14] to provide a *qualitative* explanation for the anomalies indicated above. This model is based on the perturbation theory at the second-order in energy (and equivalently to the first-order in wavefunction), i.e. one can write the CBM energy E_{CBM} of the $\text{Ga}_{1-y}\text{In}_y\text{As}_{1-x}\text{N}_x$ alloy as:

$$E_{\text{CBM}} = E_{\Gamma,c} + \langle \Phi_{\Gamma,c} | \delta V | \Phi_{\Gamma,c} \rangle + \sum_k (\langle \Phi_{\Gamma,c} | \delta V | \Phi_{k,c} \rangle^2 / (E_{\Gamma,c} - E_{k,c})), \quad (4)$$

while the alloy CBM wavefunction Ψ_{CBM} is given by

$$\Psi_{\text{CBM}} = \alpha [\Phi_{\Gamma,c} + \sum_k \Phi_{k,c} (\langle \Phi_{\Gamma,c} | \delta V | \Phi_{k,c} \rangle / (E_{\Gamma,c} - E_{k,c}))], \quad (5)$$

where $\Phi_{\Gamma,c}$ (respectively, $E_{\Gamma,c}$) and $\Phi_{k,c}$ (respectively, $E_{k,c}$) are the conduction states (respectively, energies) of the appropriate *nitrogen-lacking system*, at Γ and at off-centers k -points, respectively. The nitrogen-lacking system is zinc-blende GaAs in the case of the $\text{Ga}_{1-y}\text{In}_y\text{As}_{1-x}\text{N}_x$ alloys lattice-matched to GaAs while it is the $\text{Ga}_{0.47}\text{In}_{0.53}\text{As}$ alloy for the InP-lattice-matched $\text{Ga}_{1-y}\text{In}_y\text{As}_{1-x}\text{N}_x$ solid solutions. Note that the difference in energy $E_{\Gamma,c} - E_{k,c}$ is negative for any off-center k -points since the CBM of both GaAs and $\text{Ga}_{0.47}\text{In}_{0.53}\text{As}$ materials occurs at the Γ point. δV is the difference of potentials between the nitride quaternaries and the nitrogen-lacking system, while α is a normalization coefficient. Ref. [14] proposes that the large band-gap redshift occurring when inserting

nitrogen atoms into the $\text{Ga}_{1-y}\text{In}_y\text{As}$ alloy is imputable to (at least) two different effects. First, the first-order perturbative term in Eq. (4) (i.e., the $\langle \Phi_{\Gamma,c} | \delta V | \Phi_{\Gamma,c} \rangle$ element) strongly shifts the energy of the alloy CBM towards the energy of the alloy valence-band-maximum. We numerically found that this first effect contributes 60% of the decrease of the band-gap of the random $\text{Ga}_{0.95}\text{In}_{0.05}\text{As}_{0.984}\text{N}_{0.016}$ alloy with respect to the band-gap of pure zinc-blende GaAs. Such a first-order term, which only involves the Γ point and the nitrogen-induced change in potential, has been overlooked in the previous studies, to our knowledge. The second effect is derived from the second-order term of Eq (4) and is therefore a manifestation of nitrogen-induced quantum coupling between different electronic states of the nitrogen-lacking system. In agreement with some recent studies [7,9,21], the most quantitatively important quantum couplings were found to occur between the Γ and L-points and between the Γ and X-points [10,14]. (Note that the effects proposed in Refs [6,9,20,21] and involving *nitrogen impurity levels* may also play a role in the decrease of the band-gap, especially for very small nitrogen concentrations). Interestingly, atomic ordering in $\text{Ga}_{1-y}\text{In}_y\text{As}_{1-x}\text{N}_x$ alloys does not affect the first-order perturbative term of Eq (4) but rather significantly changes the $\langle \Phi_{\Gamma,c} | \delta V | \Phi_{k,c} \rangle$ electronic coupling elements. In particular, it was found that some specific electronic coupling can be *turned on and off* with atomic arrangement. As it can be seen by looking at Eq. (5), the atomic-ordering dependency of $\langle \Phi_{\Gamma,c} | \delta V | \Phi_{k,c} \rangle$ also provides a “natural” explanation for the predicted change of localization of the alloy CBM state with nitrogen atomic arrangement. Note that a recent study [15], also using the present strain-dependent empirical pseudopotential technique, demonstrated that short-range atomic ordering in $\text{Ga}_{1-y}\text{In}_y\text{As}_{1-x}\text{N}_x$ affects the coupling between the Γ and L-points, which is consistent with our findings.

Predictions for Ga(As,P,N) alloys:

$\text{GaAs}_{0.5-x}\text{P}_{0.5-x}\text{N}_{2x}$ alloy differentiates itself from the $\text{Ga}_{1-y}\text{In}_y\text{As}_{1-x}\text{N}_x$ solid solution by two main features. First of all, it contains three different anions rather than two, which constitutes an additional computational difficulty. Secondly and more importantly, inserting a very small amount of nitrogen into $\text{GaAs}_{0.5}\text{P}_{0.5}$ leads to a deep impurity level located *below* the conduction band-minimum of $\text{GaAs}_{0.5}\text{P}_{0.5}$, i.e. the lowest unoccupied state of dilute $\text{GaAs}_{0.5-x}\text{P}_{0.5-x}\text{N}_{2x}$ is localized around the nitrogen atoms [16]. On the other hand, the nitrogen impurity level occurring in $\text{Ga}_{1-y}\text{In}_y\text{As}_{1-x}\text{N}_x$ alloy, with very small x , is resonant *inside* the conduction band of $\text{Ga}_{1-y}\text{In}_y\text{As}$ [16]. The aim of Ref. [17] was to follow and understand the evolution of the character and energy position of the lowest unoccupied state in $\text{GaAs}_{0.5-x}\text{P}_{0.5-x}\text{N}_{2x}$ when incorporating more and more nitrogen atoms. It was found that the evolution of this state is highly unusual. More precisely, as nitrogen is added, this lowest unoccupied state gradually evolves from an impurity localized level to a delocalized Bloch-like state. This evolution occurs over a very narrow nitrogen composition window centered around 0.4%. In other words, adding a very small amount of nitrogen drastically changes the character of the lowest unoccupied state of $\text{GaAs}_{0.5-x}\text{P}_{0.5-x}\text{N}_{2x}$. This change of character is due to two different and simultaneous quantum-mechanical processes. The first process is an *anticrossing*

between the nitrogen impurity level existing in the dilute alloy limit (for which x goes to zero) and the Γ conduction state of the nitrogen-lacking $\text{GaAs}_{0.5}\text{P}_{0.5}$ system. The second process is a repulsion between the deep-gap nitrogen levels that results in the formation of a *nitrogen subband*. One direct consequence of these double processes is that the difference in energy between the lowest unoccupied and the highest occupied levels of $\text{GaAs}_{0.5-x}\text{P}_{0.5-x}\text{N}_{2x}$ strongly decreases when increasing the nitrogen concentration. As a matter of fact, incorporating only 1% of nitrogen into $\text{GaAs}_{0.5}\text{P}_{0.5}$ leads to a difference in energy of 1.8 eV, i.e. around 300 meV smaller than the band-gap of $\text{GaAs}_{0.5}\text{P}_{0.5}$.

CONCLUSIONS

This article demonstrates that many highly unusual properties of various anion-mixed nitride alloys (including $\text{GaAs}_{1-x}\text{N}_x$ ternaries, $\text{Ga}_{1-y}\text{In}_y\text{As}_{1-x}\text{N}_x$ quaternaries and systems exhibiting three different anions such as $\text{GaAs}_{0.5-x}\text{P}_{0.5-x}\text{N}_{2x}$) can be accurately reproduced by using a new strain-dependent empirical pseudopotential method. The details of the construction of this method, as well as its parameters, are provided for the first time. Finally, this new method was used to predict and understand other anomalies, such as (i) a closing of the band-gap in $\text{Ga}_{1-y}\text{In}_y\text{As}_{1-x}\text{N}_x$ quaternaries lattice-matched to GaAs or InP substrate, (ii) a drastic change of character of the lowest unoccupied state of $\text{GaAs}_{0.5-x}\text{P}_{0.5-x}\text{N}_{2x}$ and (iii) the strong-dependency of anion-mixed nitrides' properties with the nitrogen atomic arrangement. These anomalies, which were qualitatively explained via some simple quantum mechanical effects, remain to be experimentally observed.

ACKNOWLEDGMENTS

Acknowledgment is made to the donors of The Petroleum Research Fund, administrated by the ACS, for support of this research. The authors also thank the financial assistance provided by NSF grant No. DMR-0080054, and S.-H. Wei and P. Kent for communicating their VFF results on 4096 atoms-cells.

REFERENCES

1. M. Weyers, M. Sato and H. Ando, *Jpn. J. Appl. Phys.* **31**, L853 (1992).
2. M. Kondow *et al*, *Jpn. J. Appl. Phys.* **33**, L1056 (1994).
3. L. Bellaiche, S.-H. Wei and A. Zunger, *Phys. Rev. B* **54**, 17568 (1996).
4. W.G. Bi and C.W. Tu, *Appl. Phys. Lett.* **70**, 1608 (1997).
5. K. Uesugi, N. Morooka and I. Suemune, *Appl. Phys. Lett.* **74**, 1254 (1999).
6. W. Shan, W. Walukiewicz, J.W. Ager III, E. E. Haller, J.F. Geisz, D.J.Friedman, J.M. Olson and S.R. Kurtz, *Phys. Rev. Lett.* **82**, 1221 (1999).
7. E.D. Jones, N.A. Modine, A.A. Allerman, S.R. Kurtz, A.F. Wright, S.T. Tozer and X. Wei, *Phys. Rev. B* **60**, 4430 (1999).
8. E.D. Jones, A.A. Allerman, S.R. Kurtz, N.A. Modine, K.K. Bajaj, S.T. Tozer and X. Wei, *Phys. Rev. B* **62**, 7144 (2000); E.D. Jones *et al*, *Proc SPIE* **3621**, 52 (1999); E.D. Jones *et al*, *Proc SPIE* **3944**, 80 (2000).
9. T. Mattila, S.H.- Wei and A. Zunger *Phys. Rev. B* **60**, R11245 (1999).

10. L. Bellaiche, *Appl. Phys. Lett.* **75**, 2578 (1999).
11. L. Bellaiche, S.-H. Wei and A. Zunger, *Phys. Rev. B* **56**, 10233 (1997).
12. Y. Zhang, A. Mascarenhas, H.P. Xin and C.W. Tu, *Phys. Rev. B* **61**, 7479 (2000).
13. L. Bellaiche and A. Zunger, *Phys. Rev. B* **57**, 4425 (1998).
14. Al-Yacoub and L. Bellaiche, *Phys. Rev. B* **62**, 10847 (2000).
15. K. Kim and A. Zunger, *Phys. Rev. Lett.* **86**, 2609 (2001).
16. R.J. Nelson, in *Excitons*, edited by E.I. Rashba and M.D. Sturge, North-Holland Publishing company (1982).
17. L. Bellaiche, N.A. Modine and E.D. Jones, *Phys. Rev. B* **62**, 15311 (2000).
18. P.R.C. Kent and A. Zunger, *Phys. Rev. B* **64**, 115208 (2001); *Phys. Rev. Lett.* **86**, 2613 (1996).
19. S.-H. Wei and A. Zunger, *Phys. Rev. Lett.* **76**, 664 (1996).
20. Y. Zhang, A. Mascarenhas, H.P. Xin and C.W. Tu, *Phys. Rev. B* **63**, 161303 (2001).
21. L.-W. Wang, *Appl. Phys. Lett.* **78**, 1565 (2001).
22. J.A. Van Vechten, *Phys. Rev.* **182**, 891 (1969).
23. L. Bellaiche, S.-H. Wei and A. Zunger, *Appl. Phys. Lett.* **70**, 3558 (1997).
24. P.N. Keating, *Phys. Rev.* **145**, 637 (1966).
25. R.M. Martin, *Phys. Rev. B* **1**, 4005 (1970).
26. K. Kim, W.R.L. Lambrecht and B. Segall, *Phys. Rev. B* **53**, 16310 (1996).
27. S.-H. Wei and A. Zunger, *Phys. Rev. B* **60**, 5404 (1999).
28. W.G. Bi and C.W. Tu, *J. Appl. Phys.* **80**, 1934 (1996).
29. C. Wetzel, T. Takeuchi, S. Yamaguchi, H. Katoh, H. Amano and I. Akasaki, *Appl. Phys. Lett.* **73**, 1994 (1998).
30. M.D. Cluskey, C.G. Van de Walle, C.P. Master, L.T. Romano, and N.M. Johnson, *Appl. Phys. Lett.* **72**, 2725 (1998).
31. J.I. Pankove and J.A. Hutchby, *J. Appl. Phys.* **47**, 5387 (1976).
32. L.W. Wang and A. Zunger, *J. Chem. Phys.* **100**, 2394 (1994).
33. M.R. Gokhale, J. Wei, H. Wang and S.R. Forrest, *Appl. Phys. Lett.* **74**, 1287 (1999).
34. K. Uesugi, I. Suemune, T. Hasegawa, T. Akutagawa and T. Nakamura, *Appl. Phys. Lett.* **76**, 1285 (2000).
35. L. Malikova, F.H. Pollack and R. Bhat, *J. Electron. Mater.* **27**, 484 (1998).
36. P. Gilet, L. Grenouillet, P. Duvaut, P. Ballet, G. Rolland, C. Vannuffel and A. Million, *J. Vac. Sci. Technol. B* **19**, 1422 (2001).
37. H.P. Hjalmarson, P. Vogl, D.J. Wolford and J.D. Dow, *Phys. Rev. Lett.* **44**, 810 (1980).
38. J.D. Perkins, A. Mascarenhas, Y. Zhang, J.F. Geisz, D.J. Friedman, J.M. Olson and S.R. Kurtz, *Phys. Rev. Lett.* **82**, 3312 (1999).

**The Role of Nitrogen-Induced Localization and Defects in InGaAsN ($\approx 2\%$ N):
Comparison of InGaAsN Grown by Molecular Beam Epitaxy and Metal-Organic
Chemical Vapor Deposition**

Steven R. Kurtz, A. A. Allerman, J. F. Klem, R. M. Sieg, C. H. Seager, and E. D. Jones
Sandia National Laboratories, Albuquerque, NM 87185-0601

Abstract

Nitrogen vibrational mode spectra, Hall mobilities, and minority carrier diffusion lengths are examined for InGaAsN (≈ 1.1 eV bandgap) grown by molecular beam epitaxy (MBE) and metal-organic chemical vapor deposition (MOCVD). Independent of growth technique, annealing promotes the formation of In-N bonding, and lateral carrier transport is limited by large scale (\gg mean free path) material inhomogeneities. Comparing solar cell quantum efficiencies for devices grown by MBE and MOCVD, we find significant electron diffusion in the MBE material (reversed from the hole diffusion occurring in MOCVD material), and minority carrier diffusion in InGaAsN cannot be explained by a "universal", nitrogen-related defect.

Introduction

The quaternary alloy, InGaAsN, is a novel material system with many important potential device applications. Opposite to the trend based on the respective bandgaps of GaAs (1.4 eV) and GaN (3.5 eV), addition of a small amount of nitrogen to GaAs radically *lowers* the bandgap.¹⁻³ Addition of indium to GaAsN compensates the strain induced by nitrogen, and with only 3% nitrogen incorporation, one obtains an $\text{In}_x\text{Ga}_{1-x}\text{As}_{1-y}\text{N}_y$ alloy ($x \approx 0.07$, $y \approx 0.03$) with a 1.0 eV bandgap, lattice-matched to GaAs. InGaAsN laser active regions offer the promise of longer wavelength, ≥ 1.3 μm optical transceivers grown on GaAs substrates,^{3,4} or record power efficiencies ($\approx 38\%$) would be obtained with an 1.0 eV, InGaAsN cell added in series to proven InGaP-GaAs tandem solar cells.^{5,6} However, for InGaAsN alloys grown by metal-organic chemical vapor deposition (MOCVD) or molecular beam epitaxy (MBE), photoluminescence intensity and carrier lifetime degrade with increasing nitrogen concentration, and annealing is often required to obtain useful material.^{6,7} Observation of complex annealing behavior in both MBE and MOCVD materials suggests the cause is nitrogen-related defects, not atomic impurities. In this study, we examined the defect and transport properties of MBE and MOCVD-grown InGaAsN. This comparison reveals properties which appear intrinsic to InGaAsN and other characteristics which are unique to a particular growth process. Although the minority carrier properties of MBE and MOCVD-grown InGaAsN differed, comparable solar cell performance was obtained with either growth process.

InGaAsN Growth

$\text{In}_{0.07}\text{Ga}_{0.93}\text{As}_{0.98}\text{N}_{0.02}$ (1.1 eV bandgap) was grown by MBE at a temperature of approximately 430°C. Nitrogen was supplied by a radio-frequency plasma source, while the

remainder of the constituent elements were evaporated from conventional solid sources. Ex-situ, post-growth annealing of this material at 900°C for 10 sec improved the photoluminescence efficiency and subsequent device performance. The MBE material was unintentionally doped, p-type ($\sim 10^{16}/\text{cm}^3$). N-type material was obtained with Si doping.

MOCVD samples were grown using trimethylindium, trimethylgallium, 100% arsine, and dimethylhydrazine sources. N-type material was achieved using tetraethyltin doping. MOCVD samples were annealed at 650°C for 30 minutes. For both MBE and MOCVD-grown InGaAsN, photoluminescence intensity increased $\approx 10\times$ upon annealing undoped material. Overall, photoluminescence of the MBE material displayed characteristics similar to those we have observed for MOCVD samples.⁶ However, the bandgap of the MBE material, observed through photoluminescence or absorption, increased approximately 20 meV due to incremental nitrogen loss during annealing.

Nitrogen Local-Vibrational -Mode Spectroscopy

Looking for a mechanism to explain annealing behavior, we examined nitrogen-related local-vibration-modes (LVMs). Fourier transform infrared transmission spectra are shown for an annealed and as-grown, undoped InGaAsN (1.1 eV) sample grown by MBE (Figure 1). Prior to annealing, a single LVM line is observed at 468 cm^{-1} which corresponds to the Ga-N mode at 470 cm^{-1} reported for GaAs:N.⁸ No evidence for In-N bonds was

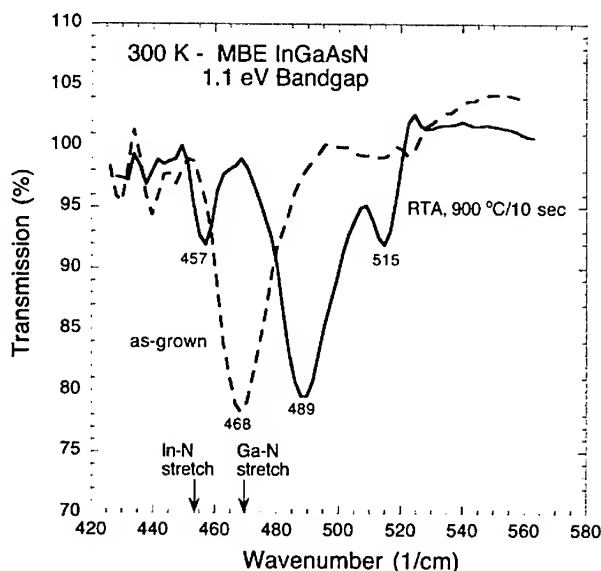


Figure 1. Infrared transmission spectra for an MBE-grown, 0.6 μm thick $\text{In}_{0.07}\text{Ga}_{0.93}\text{As}_{0.98}\text{N}_{0.02}$ sample as-grown (dashed) and ex-situ annealed (solid) at 900°C for 10 sec.

observed prior to annealing. Annealing produced In-N bonds, and three LVMs were observed at 457, 489, and 515 cm^{-1} . With the larger mass of the indium atom, the line at 457 cm^{-1} corresponds to an In-N stretch, and the Ga-N stretch is shifted to 489 cm^{-1} in a Ga_3InN cluster.⁹ Origin of the 515 cm^{-1} line is highly speculative. Similar behavior was reported by Sarah Kurtz et al. in MOCVD-grown (@ 550°C) InGaAsN samples with lower nitrogen content (0.2 %).⁹ They still observed a Ga-N, 470 cm^{-1} , peak after annealing at 700°C for 30 minutes, whereas in our MBE samples that peak disappeared after annealing which indicates that almost 100% of the nitrogen atoms formed In-N bonds. In-N pairing minimizes strain energy in the GaAs-like lattice. Our infrared studies of MOCVD-grown InGaAsN (2% N, 600°C growth) were inconclusive due to broadened and distorted ("Fano") LVM lineshapes.

Majority Carrier Transport and Localization

We examined the effect of these annealing-induced structural changes on Hall transport. Of particular interest, strong random alloy fluctuations in the InGaAsN conduction band may result in electron localization.¹⁰ Hall mobility measurements were made on a series of compensated MOCVD-grown samples with nominally the same composition, 1.6-1.9% N. N-type (Sn) doping levels were varied in this series to range from as-grown p-type to n-type, mid- $10^{17}/\text{cm}^3$. At 300 K and high carrier densities, the electron mobility curves in Fig. 2(a) converge to $\approx 300 \text{ cm}^2/\text{V}\cdot\text{s}$. Hole mobilities (Fig. 2(b)) at 300 K ranged even lower, 60-90 $\text{cm}^2/\text{V}\cdot\text{s}$. Hall mobility and carrier concentration temperature dependence are shown in Figure 3 for a single, n-type MBE-grown sample with nominally the same composition. As before, the highest mobility for the MBE material was $\approx 300 \text{ cm}^2/\text{V}\cdot\text{s}$, consistent with the limit imposed by alloy scattering at this nitrogen concentration.¹¹

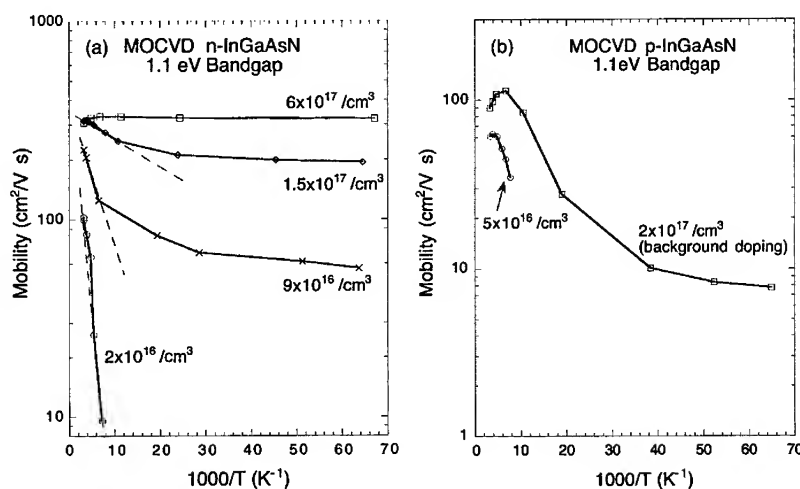


Figure 2. Hall mobility versus temperature for a series of n (a) and p-type (b), MOCVD-InGaAsN samples doped at different levels.

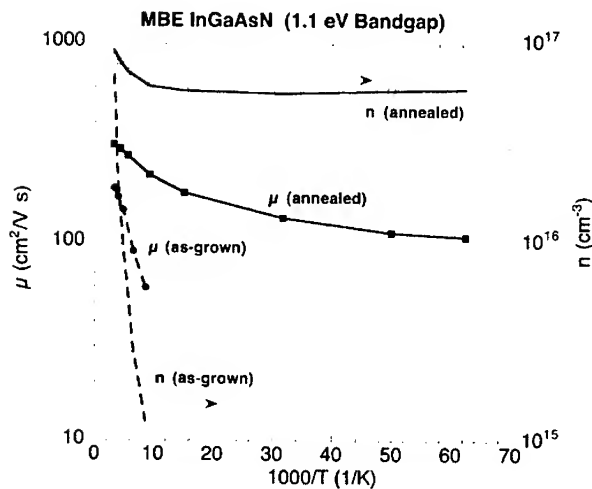


Figure 3. Temperature dependence of Hall mobilities (solid symbol) and carrier concentrations (open symbol) for an MBE-grown, n-type $\text{In}_{0.07}\text{Ga}_{0.93}\text{As}_{0.98}\text{N}_{0.02}$ sample as-grown (dashed line) and ex-situ annealed (solid line) at 900°C for 10 sec.

Hall data for the n-type, annealed MBE-grown InGaAsN (Fig. 3) were very close to those for annealed MOCVD material (Fig. 2(a)). Electron mobilities (Fig. 2(a)) were thermally activated near 300 K and became weakly temperature dependent at low temperatures. These activation energies increase with decreasing electron concentration (Fig. 2(a)). Based on limited data, we find that hole mobilities (Fig. 2(b)) were qualitatively similar to those observed for the electrons. For both electrons and holes, the carrier concentration was only weakly temperature dependent. Overall, the Hall data for annealed InGaAsN were inconsistent with an electron mobility-edge because: 1) Our Hall mobilities, not carrier concentrations, were thermally activated; 2) Holes displayed similar behavior to electrons; and 3) Low temperature mobility values were large for variable-range hopping.¹² Instead, we believe that InGaAsN carrier transport is modulated by large scale (i.e. \gg mean free path) inhomogeneities, forming potential barriers. Consistent with our data, the Hall mobility is thermally activated in such inhomogeneous materials,¹³ and Hall data for polycrystalline Si are similar to our InGaAsN results.¹⁴ Our results indicate that increased doping (i.e. increasing the Fermi energy) lowers the InGaAsN electron barriers, suggesting inhomogeneities in N concentration ($< 1\%$) produce the barriers. Contrary to reports of a random N distribution occurring in strained, GaAsN (2% N) quantum wells,¹⁵ scanning tunneling microscope images of our MOCVD-InGaAsN revealed N clustering and lateral non-uniformities.¹⁶

In the unannealed, as-grown MBE Hall sample (Fig. 3), we observed strong thermal activation of both mobility and carrier concentration. An activated carrier concentration suggests a trap-modulated mobility with a mobility edge. We associate the localization in as-grown MBE InGaAsN with structural disorder resulting from the lower temperature MBE

growth. Perhaps defects inferred from LVM spectra or excess nitrogen¹⁷ produce localization observed in InGaAsN grown at lower temperature.

Minority Carrier Diffusion and Solar Cells

Minority carrier devices are very sensitive to localization and trapping. To examine the effect of nitrogen-related defects on electron and hole diffusion lengths, we compared structurally similar solar cells, grown by MOCVD or MBE. Our non-optimized, test-cell consisted of a thick (1 μm) InGaAsN base and a thin (0.1-0.3 μm), heavily doped (mid- $10^{17}/\text{cm}^3$) InGaAsN emitter. Minority carrier diffusion lengths were determined from internal quantum efficiency (IQE) measurements performed on n-on-p and p-on-n solar cells. From the capacitance-voltage, InGaAsN optical absorption, and IQE spectral data, minority carrier diffusion lengths were determined from device simulations using the program, PC-1D.¹⁸

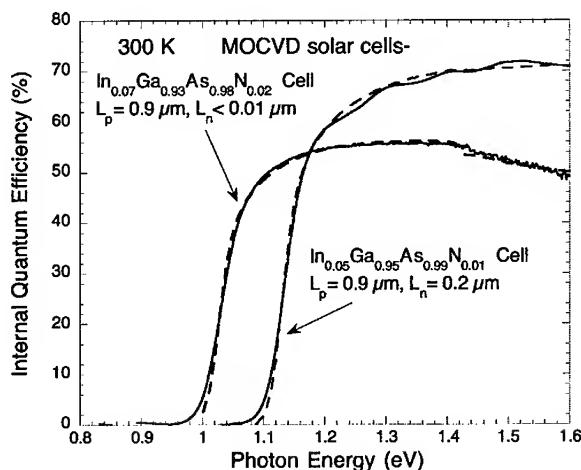


Figure 4. Spectral response of two MOCVD-InGaAsN cells with different alloy compositions (1% and 2% N). Cell simulations (dashed lines) and respective electron (L_n) and hole (L_p) minority carrier diffusion lengths are indicated in the figure.

IQE experimental results and device simulations for MOCVD-grown p-on-n, InGaAsN solar cells with 1.0 eV and 1.1 eV bandgap InGaAsN (2.1% and 1.1% N, respectively) are shown in Figure 4. In the emitter of the 1.0 eV InGaAsN cell, electrons were localized, with a diffusion length $\approx 10^{-2} \mu\text{m}$, and in the 1.1 eV InGaAsN emitter, electron diffusion had increased to 0.2 μm . In both cells, a hole diffusion length of $\approx 1 \mu\text{m}$ was obtained for the base layer. Open circuit voltages, at air-mass 0, for the 1.0 eV and 1.1 eV cells were 0.41 and 0.50 V, respectively. IQEs for the companion, n-on-p cells were low (<30%). Clearly, poor electron diffusion limited MOCVD-InGaAsN device performance.

IQE data and simulations for MBE-grown, thick p-base (n-on-p) and thick n-base (p-on-n) are shown in Figure 5. Clearly, the thick p-base devices have higher IQEs indicating

that the minority carrier, electron diffusion length was greater than that of the holes in the MBE-InGaAsN. Self-consistent fits of the cell IQEs were obtained with electron and hole diffusion lengths of 0.5 and 0.03 μm , respectively, in ex-situ annealed MBE material. The air-mass-0, open circuit voltage of the annealed, thick p-base MBE cell in Fig. 5 was 0.43 V. Overall, the IQEs and open circuit voltages of thick p-base MBE and thick n-base MOCVD solar cells were roughly comparable.

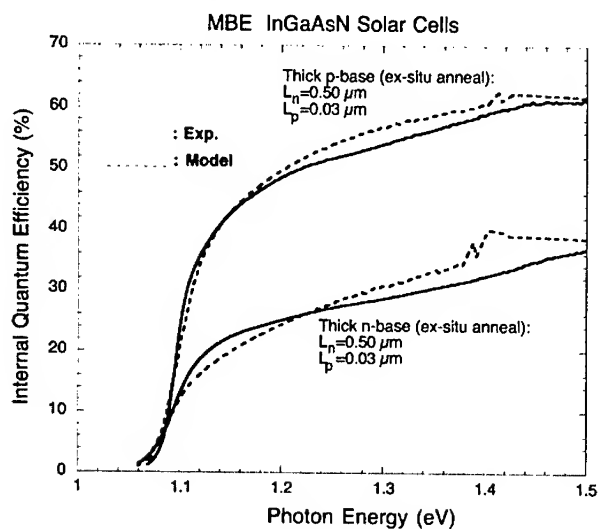


Figure 5. Spectral response of two MBE-grown InGaAsN solar cells, thick p-base (n-on-p, ex-situ annealed) and thick n-base (p-on-n, ex-situ annealed) devices. Cell simulations (dashed lines) and respective electron (L_n) and hole (L_p) minority carrier diffusion lengths are indicated for each cell.

Surprisingly, the diffusion lengths for annealed MBE material were reversed from those we reported for MOCVD-grown InGaAsN (0.01 micron for electrons and 0.9 micron for holes). Although we have presented evidence of point- defects and inhomogeneities common to MBE and MOCVD materials, this variation of minority carrier properties indicates that there are yet other traps associated with each specific growth process.

Summary

Our brief study of the properties of MBE-grown InGaAsN (≈ 1.1 eV bandgap) revealed many similarities to MOCVD material. Overall, the radiative efficiencies, Hall mobilities, device performance, and annealing behavior for MBE and MOCVD-grown InGaAsN were roughly comparable. We found evidence that annealing promotes the formation of In-N bonding like that reported for MOCVD material with lower nitrogen content. Annealed n-type, MBE-grown InGaAsN displayed a Hall mobility temperature dependence like that observed for MOCVD-grown material. We attribute the Hall mobility

temperature dependence to the presence large-scale inhomogeneities, or barriers, limiting transport. The maximum electron mobility was consistent with the limit imposed by alloy scattering, but there was no evidence of alloy-fluctuation-induced-localization. However, some transport properties were unique to a particular growth process. MBE samples grown at lower temperature displayed a strongly thermally activated mobility and carrier concentration only prior to annealing, suggesting trap-modulated transport. In annealed MBE-grown solar cells electron diffusion was dominant (electron and hole diffusion lengths of 0.5 μm and 0.03 μm , respectively), whereas in MOCVD devices the minority carrier diffusion lengths were reversed with holes dominating. In summary, a comparison of MBE and MOCVD material revealed common, intrinsic point-defects and inhomogeneities in InGaAsN, but minority carrier properties of InGaAsN remain unexplained by "universal" defect models.

Acknowledgements

The authors thank J. A. Bur and M. Bridges for technical support. Sandia is a multiprogram laboratory operated by Sandia Corporation, a Lockheed Martin Company, for the U.S. Dept. of Energy under contract DE-AC04-94AL85000.

References

1. M. Weyers, M. Sato, and H. Ando, *Jpn. J. Appl. Phys.* **31 Pt. 2**, 853 (1992).
2. W. G. Bi and C. W. Tu, *Appl. Phys. Lett.* **70**, 1608 (1997).
3. M. Kondow, T. Kitatani, S. Nakatsuka, M. C. Larson, K. Nakahara, Y. Yazawa, and M. Okai, *IEEE J. of Selected Topics in Quant. Elect.* **3**, 719 (1997), and references therein.
4. K. D. Choquette, J. F. Klem, A. J. Fischer, O. Blum, A. A. Allerman, I. J. Fritz, S. R. Kurtz, W. G. Breiland, R. M. Sieg, K. M. Geib, J. W. Scott, and R. L. Naone, *Electron. Lett.* **36**, 1388 (2000).
5. Sarah R. Kurtz, D. Myers, and J. M. Olsen, *Proc. 26th IEEE Photovoltaics Spec. Conf.* (IEEE, New York, 1997), p. 875.
6. Steven R. Kurtz, A. A. Allerman, E. D. Jones, J. M. Gee, J. J. Banas, and B. E. Hammons, *Appl. Phys. Lett.* **74**, 729 (1999).
7. E. V. K. Rao, A. Ougazzaden, Y. Le Bellego, and M. Juhel, *Appl. Phys. Lett.* **72**, 1409 (1998).
8. V. Riede, H. Neumann, H. Sobotta, R. Schwabe, W. Siefert, and S. Schwetlick, *Phys. Stat. Sol.(a)* **93**, K151 (1986).
9. Sarah Kurtz, J. Webb, L. Gedvilas, D. Friedman, J. Geisz, J. Olsen, R. King, D. Joslin, and N. Karam, *Appl. Phys. Lett.* **78**, 748 (2001).
10. Steven R. Kurtz, A. A. Allerman, C. H. Seager, R. M. Sieg, and E. D. Jones, *Appl. Phys. Lett.* **77**, 400 (2000).
11. C. Skierbiszewski, P. Perlin, P. Wisniewski, T. Suski, W. Walukiewicz, W. Shan, J. W. Ager, E. E. Haller, J. F. Geisz, D. J. Friedman, J. M. Olsen, and S. R. Kurtz, *Phys. Stat. Sol.(b)* **216**, 135 (1999).
12. N. F. Mott and E. A. Davis, *Electronic Processes in Non-Crystalline Materials*, 2nd Ed., Clarendon Press, Oxford, 1979
13. V. G. Karpov, A. Ya. Shik, and B. I. Shklovski, *Sov. Phys. Semi.* **16**, 901 (1982).

14. H. Paul Maruska, Amal K. Ghosh, Albert Rose, and Tom Feng, *Appl. Phys. Lett.* **36**, 381 (1980).
15. H. A. McKay, R. M. Feenstra, T. Schmidtling, and U. W. Pohl, *Appl. Phys. Lett.* **78**, 82 (2001).
16. H. Lyeo, C. K. Shih, A. A. Allerman, S. R. Kurtz, and E. D. Jones, to be published
17. Sylvia G. Spruytte, Christopher W. Coldren, James S. Harris, William Wampler, Peter Krispin, Klaus Ploog, and Michael C. Larson, *J. Appl. Phys.* **89**, 4401 (2001).
18. PC1D Version 5.2, Copyright P. A. Basore and D. A. Clugston, Univ. of New South Wales, Aus. (1998).

Growth of High Nitrogen Content GaAsN by Metalorganic Chemical Vapor Deposition

¹J. C. Roberts, ²B. F. Moody, ²P. Barletta, ¹M. E. Aumer, ¹S. F. LeBoeuf, ¹J. M. Luther and ¹S. M. Bedair

¹Dept. of Electrical & Computer Engineering, N. C. State University, Campus Box 7911, Raleigh, N. C. 27695-7911.

²Dept. of Materials Science and Engineering, N. C. State University, Campus Box 7907, Raleigh, N. C. 27695-7907

ABSTRACT

The incorporation of a high percentage of nitrogen in the GaAs lattice has been the subject of recent interest to reduce the bandgap while maintaining the nearly lattice matched condition to GaAs. We will report on the metalorganic chemical vapor deposition (MOCVD) of GaAsN using trimethylgallium (TMG), tertiarybutylarsine (TBA) and dimethylhydrazine (DMHy) organometallic sources in a hydrogen-free carrier gas. A nitrogen concentration as high as ~8% in GaAsN was achieved. The effect of nitrogen concentration on the structural, optical and surface properties of GaAsN films will be discussed.

INTRODUCTION

Recently, the $\text{In}_x\text{Ga}_{1-x}\text{As}_{1-y}\text{N}_y$ material system has gained attention for use in optoelectronic devices [1,2,3]. The In and N mole fractions in this quaternary system can be chosen to maintain a lattice matching condition to GaAs while achieving a ~1eV bandgap, which is of interest for increasing the efficiency of tandem solar cells by using $\text{In}_x\text{Ga}_{1-x}\text{As}_{1-y}\text{N}_y$ as the third layer in a standard GaAs/Ga_{0.5}In_{0.5}P tandem solar cell [4]. The $\text{In}_x\text{Ga}_{1-x}\text{As}_{1-y}\text{N}_y$ system is also becoming a primary material system for long wavelength laser diodes with excellent high temperature performance. However, only small nitrogen concentrations have been achieved by metalorganic chemical vapor deposition (MOCVD) of these materials due to the large miscibility gap. Several growth approaches have been applied to improve the nitrogen incorporation in this material system. High nitrogen content has been reported by using gas-source molecular beam epitaxy (GSMBE) in which radio frequency energy is used to generate active N species from an N₂ source [5]. Increases in N incorporation were achieved using dimethylhydrazine (DMHy) and replacing AsH₃ with tertiarybutylarsine (TBA). The lower cracking temperature of the column V organometallic sources DMHy and TBA allows lower temperature growth of GaAsN that can lead to higher nitrogen content [6]. The majority of research detailing the MOCVD growth of $\text{GaAs}_{1-y}\text{N}_y$ indicates the use of H₂ as the carrier gas, with nitrogen content as high as 5.6% reported [7]. In this work we will report that by substituting N₂ for H₂ as the carrier gas, nitrogen content in GaAsN as high as 8% can be achieved.

EXPERIMENTAL DETAILS

All materials were grown by MOCVD in a commercial Thomas Swan system equipped with a horizontal fused silica research reactor at pressures ranging from 700 torr to 1 atmosphere. Trimethylgallium (TMG) was used as the column III precursor, while TBA and DMHy were used as column V precursors. Column V organometallic sources were chosen not only for safety concerns, but also to take advantage of their lower cracking temperatures, which for the case of III-As-N related compounds, has been shown to result in enhanced nitrogen incorporation [8]. Ultra-high purity grade (99.999%) N_2 and H_2 were further purified with a resin-based scrubber and used as carrier gases with H_2 being varied from 0% to 67% of the total carrier gas flow. Semi-insulating GaAs substrates 2° off (100) toward [110] were solvent cleaned and then etched in a 7:1:1 solution of H_2SO_4 , deionized water, and H_2O_2 . After loading in the growth chamber, samples were cleaned for 5 minutes at $650^\circ C$ under a TBA flux to desorb remaining surface contaminants. Typical growth temperatures ranged from $575^\circ C$ to $650^\circ C$ while the reactor pressure was always maintained at 700 torr. All sample temperature values refer to the reading taken from a K-type thermocouple inserted via a 1/4" quartz tube into the graphite susceptor. The actual sample temperature may not coincide exactly with that indicated by the thermocouple. The V/III ratio was 13 and the DMHy/(DMHy+TBA) ratio was 0.88 for all samples. GaAsN layers are nominally $\sim 1\mu m$ thick with a $\sim 70nm$ GaAs cap and were annealed *in situ* for 15 minutes at $675^\circ C$ under N_2 at 700 torr immediately following deposition.

Alloy compositions were determined by examining the splitting between the (004) reflection peaks of GaAs and $GaAs_{1-y}N_y$ layers as determined from double-crystal x-ray diffraction (DCXRD) data. All $GaAs_{1-y}N_y$ layers were of sufficient thickness to be relaxed and the N content in the layers was determined by applying Vegard's Law using GaAs ($a \approx 5.65 \text{ \AA}$) and cubic GaN ($a \approx 4.52 \text{ \AA}$) as the binary end members. PL measurements were made at 77 K by mounting samples to a liquid nitrogen-cooled Cu plug with Crycon grease. The 514 nm line of an Ar ion laser was used to excite the PL signal, which was collimated, focused and dispersed through a 1/2 m monochromator and detected by a cooled photomultiplier tube. The nitrogen content measured for samples grown with H_2 as a large fraction of the carrier gas agrees well with nitrogen content reported in the literature for GaAsN samples grown under similar conditions. However, by increasing the ratio of N_2 to H_2 , the amount of nitrogen incorporated into the film increased. The total flow through the reactor was always held constant, i.e., as the H_2 flow was reduced, the N_2 flow was increased to balance the flow.

DISCUSSION

Figure 1 illustrates the importance of two fundamental parameters, growth temperature and the presence of H_2 in the carrier gas, which influence the incorporation of nitrogen in GaAsN. Two sets of samples are shown here, one set (solid circles) grown with 50% H_2 /50% N_2 as the carrier gas and the second set (solid squares) grown with no H_2 in the carrier gas (i.e., 100% N_2). We attribute the scatter in the data to several factors including some nonuniformity of nitrogen content due to lack of substrate rotation, organometallic depletion effects, and small run-to-run substrate temperature differences that can arise from variability of thermocouple placement. The

highest nitrogen content was achieved at the lowest growth temperature and with a carrier gas of 100% N₂. Efforts to further reduce the growth temperature to increase the nitrogen content resulted in very poor films without a clear defined DCXRD peak. Samples grown with 100% N₂ exhibit a similar temperature dependence for nitrogen incorporation as for those samples grown with 50% H₂/50% N₂, but also consistently show overall higher levels of nitrogen incorporation in the alloy.

Figure 2 shows the deterioration of surface morphology with increasing nitrogen content from 2.1 to 8.1%. The images are taken from an optical microscope at 40X magnification. All layers are sufficiently thick to be considered relaxed. The surface morphology for the GaAsN film with 2% nitrogen is essentially specular, while the surface takes on a cross hatched appearance for the sample with 4.9% nitrogen content. At 8.1% nitrogen content in GaAsN, the surface morphology has degraded significantly and becomes extremely rough.

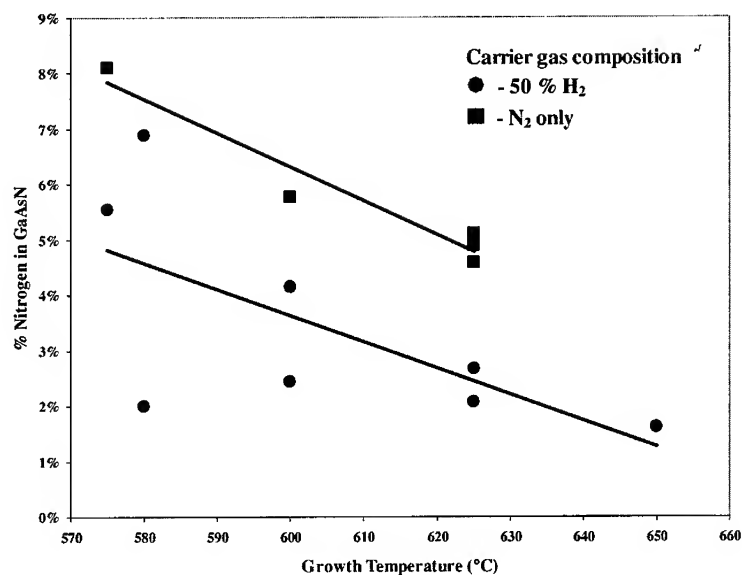


Figure 1. Percent nitrogen incorporation in thick GaAsN films vs. growth temperature (°C) for 50% H₂ in the carrier gas (●), and 0% H₂ (i.e., N₂ only) in the carrier gas (■).

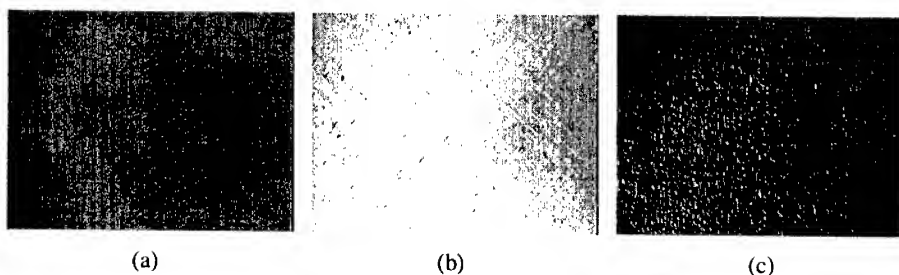


Figure 2. Variation of surface morphology for thick GaAsN films with (a) 2.1, (b) 4.9, and (c) 8.1% nitrogen content.

Figure 3 shows 77K PL data for several GaAsN films, all grown at 625 °C, whose nitrogen content has essentially been determined by the percent H₂ in the carrier gas at this constant growth temperature during the growth process. The percent nitrogen incorporation in the films is 2.7, 3.5, and 5.0% grown with 50, 40, and 25% H₂ in the carrier gas respectively. The 77K PL data indicates a bandgap red shift from ~1.37 to ~1.23 eV. Interpretation of the PL spectrum and determination of the bandgap from PL measurements is more difficult for films with higher nitrogen content as the PL signal weakens and broadens with increasing nitrogen incorporation. The relatively poor DCXRD and PL data for GaAs_{1-y}N_y films with high values of y can be the result of the deteriorated film quality, both optical and structural, with increasing nitrogen content in these metastable alloys. This is coupled with an increasing lattice mismatch between these relaxed GaAsN films and the GaAs substrate. The PL data and the deduced bandgap from this study indicate higher values of bandgap compared with other published data for strained films. This is due to the fact that PL is carried out at 77K and that the films in this study are thick and relaxed.

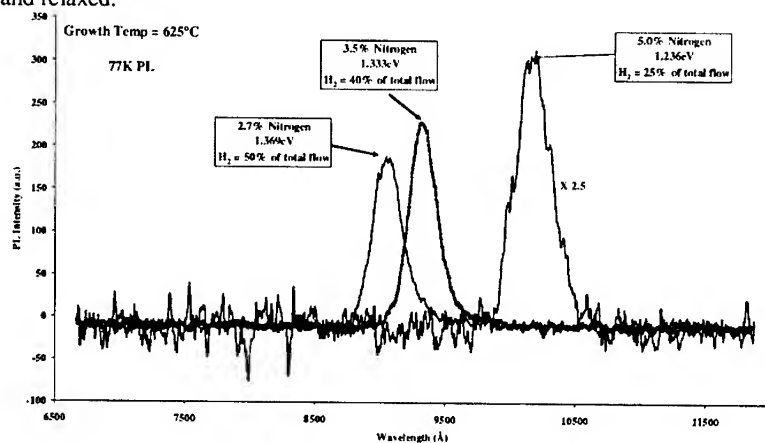


Figure 3. 77K PL for GaAsN films grown at 625 °C with nitrogen concentrations of 2.7, 3.5, and 5.0% grown with 50, 40, and 25% H₂ in the carrier gas respectively.

Figure 4 displays a plot of 77K bandgap determined from the PL peak emission of GaAsN for films grown at 600 °C. Over the composition range from ~3.5 to ~6% nitrogen a fairly linear relationship is indicated. Some discrepancy may exist between these values and other values reported in the literature due to the fact that these films are relatively thick and relaxed.

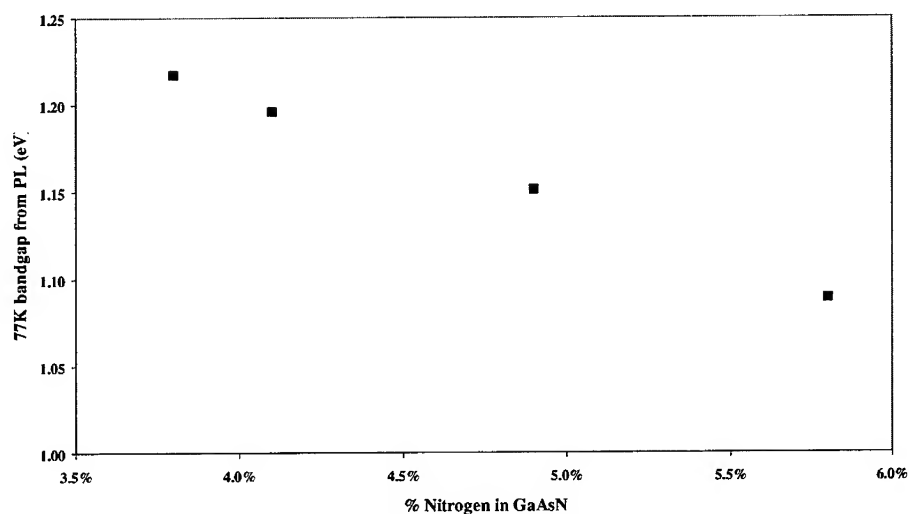


Figure 4. 77K bandgap vs. % Nitrogen content for thick GaAsN films

CONCLUSIONS

In conclusion, hydrogen has been shown to reduce the incorporation of nitrogen in GaAsN when present in the growth ambient during MOCVD. GaAsN films grown without H₂ in the growth ambient have exhibited N concentrations as high as 8.1 %. Variations in the nitrogen content in GaAsN as much as several percent have been measured when H₂ is used in the ambient in controlled amounts. A red shift and broadening of the PL is seen as the nitrogen content in these GaAsN films increases. The nature of the reduction of N in GaAsN in the presence of H₂ may include thermal and/or site-blocking effects.

ACKNOWLEDGEMENTS

The National Renewable Energy Laboratory (NREL) supported this work, contract #: AAD-9-18668-08.

REFERENCES

1. M. Kondow, S. I. Nakatsuka, T. Kitatani, Y. Yazawa, M. Okai, Jpn. J. Appl. Phys. **35**, 5711 (1996).
2. S. I. Sato, Y. Osawa, T. Saitoh, Jpn. J. Appl. Phys. - Part1, No. 5A **36**, 2671 (1997).
3. M. C. Larson, M. Kondow, T. Kitatani, K. Nakahara, K. Tamura, H. Inoue, K. Uomi, IEEE Photon. Tech. Lett. **10**, 188 (1998).
4. S. R. Kurtz, D. Myers, and J.M. Olsen, Proceedings of the 26th IEEE Photovoltaics Spec. Conference (IEEE, New York, 1997), p. 875.
5. W. G. Bi, and C. W. Tu, Appl. Phys. Lett. **70**, 1608 (1997).
6. A. Ougazzaden, Y. Le Bellego, E. V. K. Rao, M. Juhel, L. Leprince, and G. Patriarche, Appl. Phys. Lett. **70**, 2861 (1997).
7. J. Toivonen, T. Hakkarainen, M. Sopanen, H. Lipsanen, J. Crystal Growth **221**, 456 (2000).
8. S.-I. Sato, Y. Osawa, and T. Saitoh, Jpn. J. Appl. Phys. - Part 1 No.5A **36**, 2671 (1997).

High Luminescence Efficiency from GaAsN Layers Grown by MBE with RF Nitrogen Plasma Source.

Victor M. Ustinov, Nikolai A. Cherkashin, Nikolai A. Bert, Andrei F. Tsatsul'nikov, Alexei R. Kovsh^{1*}, Jyh-Shang Wang¹, Li Wei¹, and Jim Y. Chi¹

A.F.Ioffe Physico-Technical Institute, St.Petersburg 194021, Russia

¹Industrial Technology Research Institute, Hsinchu 310, Taiwan, R.O.C.

on leave from A.F.Ioffe Physico Technical Institute

ABSTRACT

(In)GaAsN based heterostructures have been found to be promising candidates for the active region of 1.3 micron VCSELs. However, (In)GaAsN bulk layers and quantum wells usually demonstrate lower photoluminescence intensity than their nitrogen-free analogues. Defects associated with lower temperature growth and N-related defects due to plasma cell operation and possible nonuniform distribution of nitrogen enhance the non-radiative recombination in N-contained layers. We studied the photoluminescence intensity of GaAsN layers as a function of N content in MBE grown samples using rf-plasma source. Increasing the growth temperature to as high as 520 °C in combination with the increase in the growth rate allowed us to avoid any N-related defects up to 1.5% of nitrogen. Low-temperature-growth defects can be removed by post-growth annealing. We achieved the same radiative efficiency of GaAsN samples grown at 520 °C with that of reference layer of GaAs grown at 600 °C. Compositional fluctuations in GaAsN layers lead to characteristic S-shape of temperature dependence of photoluminescence peak position and this feature is the more pronounced the higher the amount of nitrogen in GaAsN. Annealing reduces compositional fluctuations in addition to the increase in the photoluminescence intensity. The results obtained are important for further improving the characteristics of InGaAsN lasers emitting at 1.3 micron.

INTRODUCTION

Group-III nitride semiconductors are an area of great current interest for the development of lasers and light emitting diodes emitting in the visible to blue and UV ranges. On the other hand, addition of a small amount of nitrogen to GaAs can drastically reduce the band gap towards the infrared region [1]. This is due to the strong bowing of the energy gap in the GaAs-GaN system [2]. The large lattice mismatch between GaAs and GaN (about 21%) limits the composition range of GaAsN pseudomorphically grown on GaAs to only a few percent. The addition of In to GaAsN can lead to strain compensation, and a further decrease in the band gap of the quaternary solid solution can be obtained [3]. However, the growth of InGaAsN layers and quantum well structures of device quality appears to be a challenge even when the amount of nitrogen is less than 3 percent [4]. This is usually enough to achieve emission at 1.3 micron, which is the goal for applications in fiber optic communication systems. 1.3 micron edge-emitting lasers and VCSELs have been recently demonstrated by several research groups [5-8], however, the device characteristics are still basically inferior to those based on InGaAsP and are to be further improved. The advantage of the GaAs/InGaAsN system for laser applications is the use of well-developed AlGaAs/GaAs GRINSCH design where only active region is replaced on pseudomorphically grown InGaAsN/GaAs quantum wells. Therefore, to improve laser performance, one has to improve the quality of the nitrogen containing active region. It has been

shown previously that the nitrogen concentration, growth temperature and post-growth annealing affect the radiation efficiency of GaAsN. In addition, the specific source of nitrogen installed in the growth chamber can play a role, since, e.g., ions coming from a radio-frequency plasma source can damage the growth surface leading to the formation of additional defects. In the present work we show that the optimization of the growth regimes allows us to achieve the luminescence efficiency of $\text{GaAs}_{1-x}\text{N}_x$ very close to that of GaAs up to $x=0.015$. We also study in detail the luminescence properties of our GaAsN epilayers and we argue that the S-shape of the peak position vs temperature dependence frequently observed for InGaAsN/GaAs heterostructures can be considered as the figure of merit of uniformity of nitrogen distribution.

EXPERIMENT

The samples under investigation were grown in a Riber Epineat apparatus with solid cells for group III elements and arsenic and UNI Bulb RF Plasma Source (Applied EPI) for nitrogen. The 0.2- μm -thick layer (GaAsN or GaAs) was sandwiched by AlGaAs/GaAs superlattices. This design prevents the leakage of non-equilibrium carriers from active layer towards the substrate and the surface and allows us to have the same effective pumping for photoluminescence (PL) studies. The nitrogen composition of the samples was evaluated by x-ray diffraction. Room temperature PL measurements were carried out using a frequency doubled YAG:Nd laser ($\lambda=532\text{ nm}$). Temperature and excitation density dependences of PL were recorded under Ar+ laser excitation ($\lambda=514.5\text{ nm}$). Absorption spectra were extracted from transmission measurements.

RESULTS AND DISCUSSION

Effect of growth temperature and growth rate

In agreement with the other published data and the predictions of our thermodynamic calculations [9] we have found that the sticking coefficient of nitrogen is temperature independent over the range of 400-530 $^{\circ}\text{C}$ and decreases at higher temperatures. Therefore, we used the same characteristics of RF plasma source in this temperature interval to have equal nitrogen content for GaAsN provided the growth rate was fixed. At growth temperatures below 550 $^{\circ}\text{C}$ the 2x4 reconstruction of the pattern of reflection high-energy electron diffraction (RHEED) was observed both for GaAs and GaAsN. However, when the substrate temperature was higher than 550 $^{\circ}\text{C}$, a 3x3 RHEED pattern was observed for the GaAsN growth. It was shown that such RHEED pattern corresponds to the formation of N-rich surface [10].

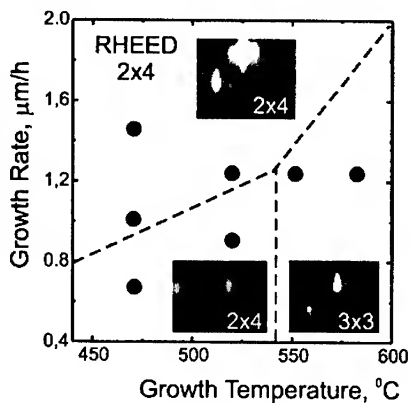


Fig.1. Growth temperature — growth rate phase diagram for the GaAsN growth. Points indicate samples grown at given growth rate and temperature. RHEED pattern pictures were taken in the $[1\bar{1}0]$ azimuth.

the growth rate. When the growth rate gets lower than a certain value the growth changes from two-dimensional to three-dimensional. We observed a steep deterioration of optical and structural properties along with this transition. The value of minimum growth rate depends on the growth temperature. These data are presented in Fig. 1 as a growth temperature vs growth rate phase diagram. The upper region corresponds to normal GaAs-like growth mode characterized by high PL intensity. We believe that the reason for the strong decrease in luminescence efficiency for the bottom two regions is associated with additional defects due to either the formation of N-rich clusters or the nitrogen segregation. Thus, there is some region of high "growth rate/growth temperature" that is free of the effects related to the phase separation. We have found that the border of top and bottom regions shifts left (or up) for higher N content. Adding even three percent of indium to match lattice parameter to GaAs also shifts the border about 40 °C left. Therefore, the presence of In enhances phase separation regardless of strain compensation.

Photoluminescence intensity of GaAs and GaAsN layers

Fig. 2a shows PL spectra (dotted lines) of $\text{GaAs}_{1-x}\text{N}_x$ layers grown at different growth temperatures, 470 and 520 °C. The luminescence intensity is about one order of magnitude higher for the samples grown at 520 °C. One can see that increasing the nitrogen content leads to the red shift of PL line. Integrated luminescence intensity is nearly constant for $x=0-0.015$ and falls about three times for $x=0.024$ (circles). PL intensity of GaAs layers also strongly depends on growth temperature (diamonds). The highest intensity shows the sample grown at 600 °C which is about one order of magnitude higher than that of the sample grown at 520 °C and 50 times higher than of the sample grown at 470 °C. It is important to note that the PL intensity of

GaAs samples grown at 520 and 470 °C is very close to that of the $\text{GaAs}_{1-x}\text{N}_x$ samples ($x < 0.015$). Fig. 2(b) shows the dependence of integrated PL intensity on excitation density measured with an Ar-laser. Data for a GaAs sample grown at 600 °C are also shown. The PL intensities are almost the same for the two samples grown at 520 °C even for very low power densities. It proves that nitrogen incorporation does not lead to formation of additional centers of non-radiative recombination. Thus, the main reason for decreasing PL intensity for GaAsN layers relative to the reference GaAs sample grown at optimal temperature 600 °C is low temperature growth rather than the presence of nitrogen.

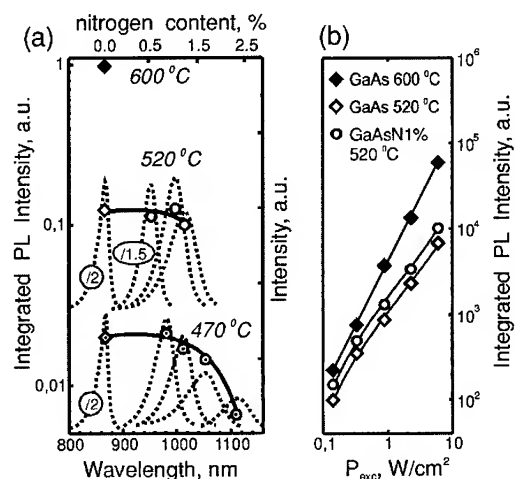


Fig.2. (a)–Dependence of integrated PL intensity of GaAs(N) layers on wavelength grown at different temperatures (left axis). PL spectra of GaAs(N) layers are shown as dotted lines (right axis). (b)–Dependence of integrated PL intensity on excitation power density for GaAs and GaAsN.

Effect of annealing

It is well known that defects related to low-temperature growth, such as arsenic antisite and/or interstitial defects, can be removed by post-growth annealing. We have investigated the effect of *in situ* annealing on our GaAsN layers. We found that the increase in luminescence intensity after annealing varied from 3 to 50 times depending on the growth temperature, Fig.3. The solid horizontal line shows intensity of GaAs grown at 600 °C, which is considered to be an optimal growth temperature for GaAs. Again one can see that PL intensity depends on growth temperature but not on the presence of N in the layers. PL intensity of samples after annealing is shown by open circles. For samples grown at 520 °C and annealed for 1 hour at 750 °C under arsenic overpressure we achieved almost the same PL intensity as GaAs grown at 600 °C.

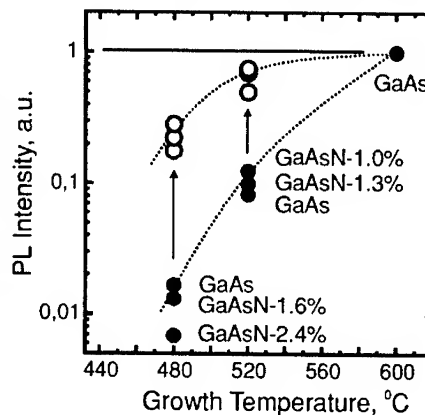


Fig.3 Dependence of integrated PL intensity of GaAs(N) layers as grown and after annealing.

Structural and optical properties of GaAsN layers

We have shown that to avoid clusterization and realize two-dimensional growth at high growth temperature (>500 °C) one can use relatively high growth rate (>1 μm/hour). PL (solid line) and absorption (dotted line) spectra of the GaAsN_{0.01} layer grown under this condition are presented in Fig.4. Insert in Fig. 4 shows cross section of transmission electron microscopy image of this sample. One can see that there is no evidence of strong compositional modulations in GaAsN layer. However, pronounced Stokes shift between the maximum of PL spectrum and absorption edge indicates that carrier recombination goes via some localized states.

Photoluminescence spectra taken at low excitation density (0.6 W/cm²) in the 10-300K range are shown in Fig. 5(a). One can see that after 100 K an additional high-energy peak (E2) appears in the spectrum and starts to dominate at higher temperatures. The temperature dependence of the positions of these low-energy (E1) and high-energy-peaks (E2) is shown in Fig. 5(b) by up-triangles and down-triangles, respectively. Only one peak at all temperatures is observed for PL spectra recorded at high excitation (100 W/cm²). Its position and absorption edge are also presented in Fig. 5(b) as solid circles and diamonds, respectively. The PL peak maximum at high excitation is close to E1 at low temperature and shifts towards E2 when the temperature is increased. Finally, at temperatures higher than 70K all data coalescence into one. The characteristic S-shape temperature dependence of the peak position is clearly seen. This S-shape temperature dependence of PL peak position after post-growth annealing is considerably less pronounced (open circles in Fig. 5(b)). To investigate the reason for this S-shaped temperature dependence, we have studied PL temperature dependences of two nominally

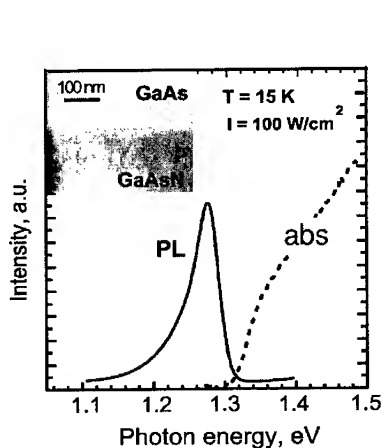


Fig.5. PL (solid line) and absorption spectra (dotted line) of GaAsN_{0.01}. Insertion shows TEM image.

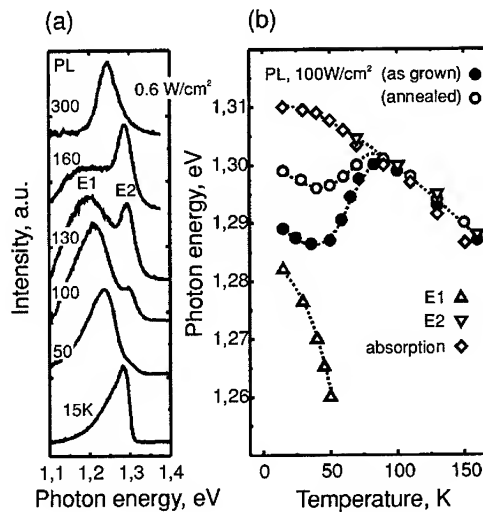


Fig.6. (a) PL spectra of GaAsN_{0.01} at different temperatures. (b) Dependence of PL peak position PL, E1 and E2 peaks, and absorption edge.

identical InGaAs QW structures grown under different growth regimes. Conventional structure with flat interfaces demonstrated usual temperature dependence of PL line following the GaAs bandgap. The structure with pronounced interface corrugation, grown under reduced As flux showed double peaked shape of the PL line and the peak intensities redistributed with the observation temperature. Fig. 6.

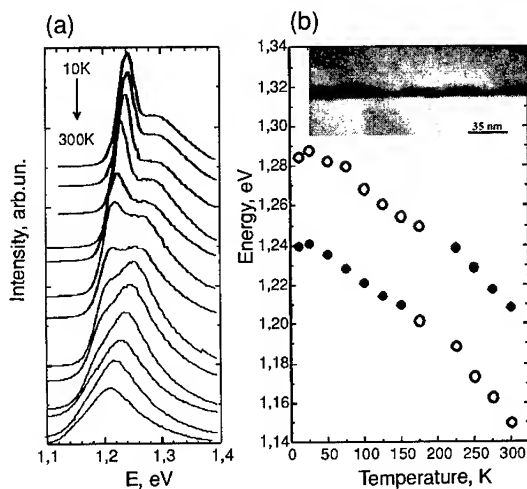


Fig.6(a)- PL spectra of corrugated InGaAs QW at different temperatures. (b) Temperature dependence of position of both PL peaks. Position of peak dominated in PL is shown as circles.

Thus, the main peak shows practically the same S-shape dependence as the GaAsN epilayers described above. Since the two InGaAs QW structures differ only in the interface corrugation leading to additional potential fluctuations we conclude that the main reason for the S-shaped temperature dependence of the PL line is potential fluctuations due to spatial nonuniformities or composition/strain modulations. Therefore, we attribute the S-shape behavior of temperature dependence of PL line in GaAsN epilayers to potential fluctuations due to nonuniformities of nitrogen distribution. Post-growth annealing reduces these inhomogeneities and the S-shape behavior becomes less pronounced. We note that these nonuniformities in nitrogen distribution are not revealed in TEM, so the shape of temperature dependence of PL line can be considered as empirical figure of merit for the extent of uniformity of nitrogen distribution in GaAsN layers.

CONCLUSIONS

Molecular beam epitaxial growth of $\text{GaAs}_{1-x}\text{N}_x$ layers has been studied as a function of nitrogen content and growth regimes. We have found that the growth at relatively high growth temperatures allows us to avoid "phase separation" or clusterization if high ($>1 \mu\text{m/h}$) growth rates are used. Up to 1.5% of nitrogen can be incorporated into GaAs without deterioration of integrated PL intensity, and for a sample containing 2.4% of nitrogen the integrated PL intensity decreases only about three times. Such layers demonstrate some compositional fluctuations leading to S-shape temperature dependence of the PL peak position. Annealing reduces compositional fluctuations and improves photoluminescence intensity.

ACKNOWLEDGEMENTS

This work is supported by the Ioffe-ITRI Joint Scientific Program. The work in Ioffe Institute was also partly supported by the NATO Science for Peace Program (grant SFP-972484).

REFERENCES

1. M. Weyers and M. Sato, *Appl. Phys. Lett.*, **62**, 1396-1398 (1993).
2. S-H- Wei and A. Zunger, *Phys. Rev. Lett.*, **76**, 664-667 (1996).
3. M. Kondow, K. Uomi, A. Niwa, A. Kitatani, S. Watahiki, and Y. Yazawa, *Japan. J. Appl. Phys.*, **35**, 1273-1275 (1996).
4. H. P. Xin and C. W. Tu, *Appl. Phys. Lett.*, **72**, 2442-2444 (1998).
5. A. Yu. Egorov, D. Bernklau, D. Livshits, V. Ustinov, Zh. I. Alferov, and H. Riechert, *Electron. Lett.*, **35**, 1643-1644 (1999).
6. M. Kawaguchi, E. Gouardes, D. Schlenker, T. Kondo, T. Miyamoto, F. Koyama, and K. Iga, *Electron. Lett.*, **36**, 1776-1777 (2000).
7. G. Steinle, H. Riechert, and A. Yu. Egorov, *Electron. Lett.*, **37**, 93-95 (2001).
8. A. W. Jackson, R. L. Naone, M. J. Dalberth, K. J. Malone, D. W. Kisker, J. F. Klem, K. D. Choquette, D. K. Serkland, and K. M. Geib, *Electron. Lett.*, **37**, 355-356 (2001).
9. V. A. Odnoblyudov, A. Yu. Egorov, A. R. Kovsh, A. E. Zhukov, N. A. Malcev, E. S. Semenova, and V. M. Ustinov, *Semicond. Sci. Technol.*, **16**, 831-835 (2001).
10. R. J. Hauenstein, D. A. Collins, X. P. Cai, M. L. O'Steen, T. C. McGill, *Appl. Phys. Lett.*, **66**, 2861 (1995).

Effect of rapid thermal annealing: red and blue shift in photoluminescence of GaNAs grown by RF plasma-assisted molecular beam epitaxy

W.K. Loke, S. F. Yoon, T. K. Ng, S. Z. Wang and W. J. Fan
Nanyang Technological University,
School of Electrical and Electronic Engineering, Block S1,
Nanyang Avenue, Singapore 639798,
Republic of Singapore

ABSTRACT

Rapid thermal annealing (RTA) of 1000Å GaNAs films grown on (100) oriented GaAs substrate by radio frequency (RF) plasma assisted solid-source molecular beam epitaxy was studied by low-temperature photoluminescence (PL) and high-resolution x-ray diffraction (HRXRD). Samples with nitrogen content of 1.3 and 2.2% have shown an overall blueshift in energy of 67.7meV and an intermediate redshift of 42.2meV in the PL spectra when subjected to RTA at 525-850°C for 10min. It is also shown that the sample, which is annealed at temperature range of 700-750°C, has the highest photoluminescence efficiency (1.7-2.1 times increase in integrated PL intensity as compared to the as-grown sample). Reciprocal space mapping of the as-grown GaNAs samples obtained by using triple-crystal HRXRD shows the presence of interstitially incorporated of N atoms with no lattice relaxation in the direction parallel to the growth surface. These results have significant implication on the growth and post-growth treatment of nitride compound semiconductor materials for high performance optoelectronics devices.

INTRODUCTION

Group III-N-As is a promising material for 1.3 and 1.55µm telecommunication optoelectronic devices grown on GaAs substrate. Hence, epitaxial growth of the nitride compound has been studied extensively. It is known that the luminescence efficiency of these alloys can be greatly improved by annealing at temperature higher than the growth temperature [1]. The same has been reported for quantum well structures of GaNAs/GaAs [2]. However, along with large improvement in the PL efficiency, a significant blueshift (9-50meV) of the maximum PL intensity position was also observed which seemed independent of the N composition. This blueshift effect in the PL peak energy has been attributed mainly to two possible reasons; (i) nitrogen out-diffusion from bulk GaNAs [3], and (ii) interdiffusion of N-As atoms near the interface of GaNAs/GaAs [4,5]. However, the results from our experiments suggest the presence of a different mechanism of diffusion. This is shown by an intermediate redshift in the PL peak energy in annealing temperature range lower than the optimum temperature. Furthermore, such changes were not accompanied by a shift towards higher Bragg angle for the GaNAs peak in HRXRD, a result different from others [6,7].

EXPERIMENTAL DETAILS

All our samples were grown by solid-source molecular beam epitaxy (SSMBE) with nominal structures of 200Å GaAs/1000Å GaNAs/3000Å GaAs buffer layer on semi-insulating GaAs (100) substrate using elemental sources of gallium (7N), arsenic (6N) and a nitrogen radio-frequency (RF) plasma source. Prior to growth of GaNAs, oxide desorption was carried out at 580°C under As overpressure, following which 300nm of GaAs buffer layer was grown. The As/Ga flux ratio was fixed at ~20 and the growth rate of GaAs at 1µm/hour. Since only a small amount of nitrogen is to be incorporated into the nitride layer, we expect no significant change in the GaNAs growth rate under the same Ga flux. A growth interruption of ~5min was used to stabilize the ignition of the nitrogen RF plasma source with N₂ background pressure of 1.0×10^{-5} Torr (at 0.10 sccm of N₂ flow). The GaNAs layer was grown at 500°C and clear (2×4) surface reconstruction was observed. GaNAs samples with different nitrogen composition were prepared by varying the RF power from 150-250W. This was followed by rapid thermal annealing (RTA) of the samples at 525-850°C for 10min under N₂ ambient. During the RTA process, the samples were capped using a GaAs wafer to minimize arsenic loss at elevated temperature. Low-temperature photoluminescence (PL) at 10K was excited by a 514.5nm ion argon laser and detected using a liquid nitrogen cooled Ge detector in conjunction with standard lock-in technique. The samples were also characterized by high-resolution x-ray diffraction (HR-XRD) for their crystalline quality (rocking curve and triple-axis scan) and the nitrogen content was determined by fitting the experimental x-ray rocking curve with the simulated rocking curve using dynamical diffraction theory.

DISCUSSION

During the growth of GaNAs at low substrate temperature of 500°C, the nitrogen atoms are incorporated into the nitride-arsenide matrix not only by substituting the As lattice site but also as interstitial nitrogen complex and/or molecular nitrogen in GaNAs. In our experiment, a (2×4) surface reconstruction was observed throughout the growth of the GaNAs layer. Since the nitrogen atom and N₂ molecule are smaller compared to the radius of the interstitial site, it is relatively easy for nitrogen to be incorporated into the interstitial site of the host lattice. As reported by Spruytte *et al.* [7], nitrogen can exist in two configurations in the GaNAs layer grown using a RF plasma nitrogen source; (i) by forming a covalent Ga-N bond (a substitutional β site: replacing As host sublattices with N atoms), an effect which primarily contributes to the band gap narrowing (redshift) due to the highly localized nature of the perturbation introduced by nitrogen atoms [8], (ii) by forming a nitrogen complex in which nitrogen is less strongly bonded to Ga atoms (an interstitial site).

The change in PL peak energy, full-width at half maximum (FWHM) and PL integrated intensity for samples with N contents of 1.3% and 2.2%, respectively, with annealing temperature from 525-850°C is shown in Fig. 1(a)-(b).

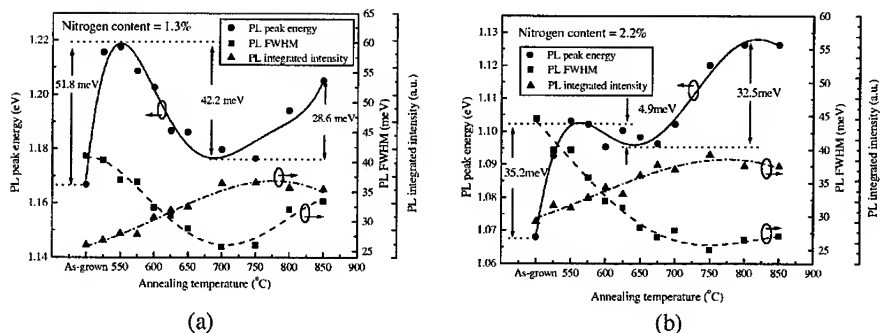


Figure 1(a)-(b). Plot of PL peak energy, integrated intensity and FWHM at different annealing temperature for samples with N content of (a) 1.3% and (b) 2.2%

Fitted lines are drawn to show the changes in these parameters following the change of annealing temperature. The thermal annealing caused an initial blue, and intermediate redshift shift in the PL peak energy, and could not be explained solely by the effect of nitrogen out-diffusion [7], or N-As atom interdiffusion across the GaNAs/GaAs heterointerface [4,5]. Because the amount of nitrogen incorporation into the GaAs lattice is very small, the nitrogen atoms adopt an impurity-like behavior in the lattice [9]. Under such a condition, it is most likely that a substitutional-interstitial diffusion mechanism [10] could take place during the thermal annealing process, which results in hopping of substitutional nitrogen atoms into interstitial sites and vice versa, according to $S \leftrightarrow I + V$, where S, I and V are the substitutional nitrogen, interstitial nitrogen and vacancy, respectively. Depending on the annealing temperature, the blueshift of the PL peak energy could have been caused by hopping of nitrogen atoms from substitutional sites to interstitial sites, or nitrogen out-diffusion, or a mixture of both mechanisms. The intermediate redshift in the PL peak energy could have been caused by a 'kick-out' effect of the substitutional arsenic atoms by interstitial nitrogen atoms.

For the sample with N content of 1.3%, grown at a lower RF plasma power of 150W, an increase in annealing temperature from 525°C to 550°C gave rise to an increase in PL peak energy from 1.166 to 1.218 eV (a total blueshift of 51.8 meV). As the annealing temperature was increased further, the PL peak energy reduces, equivalent to a total redshift of 42.2 meV (from 1.218 to 1.176 eV). The observed initial blueshift in the PL peak energy suggests a condition whereby the lattice is energetically favorable for the substitutional nitrogen atoms to diffuse into nearby interstitial sites. When the annealing temperature is increased further, the observed redshift in the PL peak energy could be due to a condition whereby it is energetically favorable for interstitial nitrogen atoms to replace As atom sites and become substitutional nitrogen atoms. Therefore, under such circumstances, the former will produce a bandgap widening effect and the latter, a bandgap narrowing effect with a change in substitutional atom sites from As to N.

In comparison, the sample with N content of 2.2% grown using higher RF plasma power of 250W, exhibit a similar trend of initial blueshift in the PL peak energy of 35.2 meV when the annealing temperature was increased to 550°C. An intermediate redshift in the PL peak energy of 4.9 meV was observed, but it is ~9 times smaller compared to that in the sample with lower

nitrogen content. The reduction in the PL peak energy reaches a minimum at annealing temperature of $\sim 650^{\circ}\text{C}$, which is lower compared to the sample with lower N content ($\sim 725^{\circ}\text{C}$). Such a difference could arise from the difference in the concentration of interstitially incorporated nitrogen atoms between these two samples. The sample with lower nitrogen content has a higher ratio of interstitial nitrogen atoms to substitutional ones, because when lower RF plasma power was used, a lower ratio of nitrogen atoms to 1st and 2nd positive molecules were generated [11] and hence, a considerable concentration of nitrogen is incorporated into the interstitial sites. Hence, the sample with lower nitrogen content of 1.3% will require higher annealing temperature in order to replace most of the substitutional As by interstitial nitrogen atoms. Therefore, the PL peak energy reaches a minimum value at higher annealing temperature of $\sim 725^{\circ}\text{C}$ compared to that of the sample with higher N content of 2.2%.

The FWHM of the PL peak for both samples showed an approximately common minimum value at annealing temperature of $700\text{--}750^{\circ}\text{C}$ (1.6 and 1.8 times reduction for sample with nitrogen content of 1.3% and 2.2% respectively, as compared to the as-grown condition). This suggests that both samples, regardless of the difference in nitrogen composition, have undergone a similar annihilation of point defects such as interstitials and vacancies in the as-grown GaNAs layer, resulting in improved crystalline quality as shown later in the HR-XRD results. Such defects are detrimental to the photoluminescence efficiency. For both samples, a 1.7–2.1 times increase in the integrated intensity of the PL peak was observed, which reaches a maximum value at annealing temperature of $\sim 770^{\circ}\text{C}$ and appear in close correlation with the respective PL FWHM improvement.

When the annealing temperature was further increased to 850°C for both samples (Fig. 1((a)-(b))), the PL peak energy continued to increase, indicating a normal blueshift in the energy caused primarily by nitrogen out-diffusion. However, such high temperature annealing could cause degradation in the crystalline quality and has a detrimental effect on the optical properties of the material, as evident by the increase in PL FWHM and reduction in the integrated PL intensity.

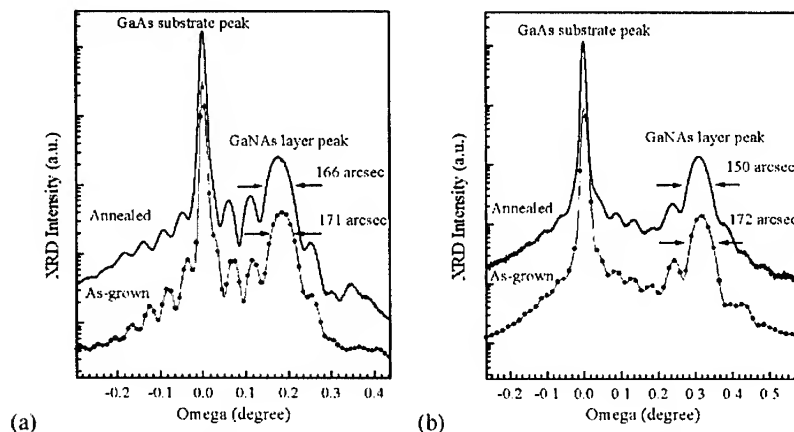


Figure 2(a)-(b). Plot of XRD rocking curves of the as-grown and annealed (750°C for 10min) GaNAs samples with N content of (a) 1.3% and (b) 2.2%

Fig. 2(a)-(b) shows the reduction in FWHM of the XRD peak of the GaNAs layer from 171 to 166 arcsec and from 172 to 150 arcsec for samples with 1.3% and 2.2% nitrogen content, respectively, when annealed at the optimized temperature for best overall optical property of 750°C for 10min (as shown in Fig. 1(a)-(b)).

The reduction in FWHM of the XRD peak is consistent with the improved PL efficiency. This is evident from the significant improvement in the PL intensity and corresponding reduction in the PL FWHM. Another noteworthy result is that there are no drastic changes to the position of the XRD peak of the GaNAs layer and the Pendellosung fringes for both samples when subjected to the thermal annealing process. This observation is notably different from that of Spruytte *et al.*³, in which a significant shift of the XRD peak position to lower Bragg angle was recorded indicating significant nitrogen out diffusion when GaNAs (with as-grown N content of 2.5%) was annealed at 760°C for 5min. This shows that in so far as the nitrogen out diffusion from the film is concerned, our samples are more stable, and the effect on the lattice parameter of the GaNAs layer and its interface with GaAs is rather minimal.

Reciprocal space mappings in (004) and (224) reflection points of the as-grown sample with 1.3% N content are shown in Fig 3(a)-(b) below.

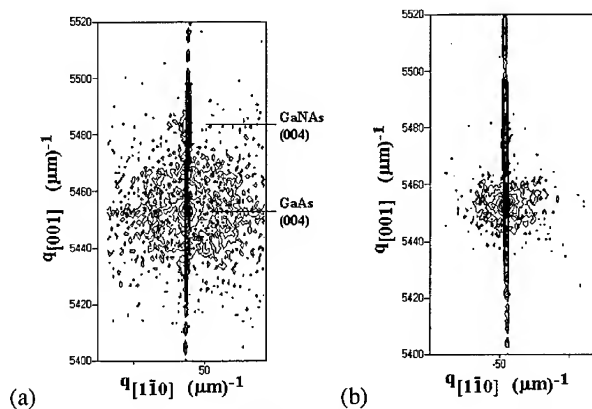


Figure 3(a)-(b). Reciprocal space map in (004) reflection points of as-grown GaNAs with N content of 1.3%, (a) As-grown and (b) Annealed 700°C for 10min.

The kinematical diffuse scattering around the (004) reflection points (Fig. 3(a)) arises from point defects such as interstitials [12]. As expected, these point defects could only be introduced during the growth of GaNAs since some nitrogen atoms are incorporated into interstitial site. When annealed at 700°C for 10min, most of these defects were annihilated as shown by the reduction of kinematical diffuse scattering in Fig 3(b).

CONCLUSION

In summary, we have presented low temperature PL measurements on GaNAs samples with nitrogen content of 1.3% and 2.2%, subjected to rapid thermal annealing from 525-850°C for 10min. The PL peak energy position, which is related to the bandgap of the GaNAs material,

showed significant blueshift and intermediate redshift in energy at annealing temperature lower than the temperature (700-750°C). These effects suggest an intermediate state of diffusion of substitutional-interstitial nitrogen atoms, whereby at certain range of annealing temperature, it is energetically more favorable for interstitial nitrogen atoms to diffuse into substitutional As sites and hence give rise to redshift in the PL peak energy. The minimum PL FWHM and maximum PL integrated intensity were observed to occur approximately at a common annealing temperature of 750°C for both GaNAs samples of different nitrogen content. The XRD results of these samples are consistent with the PL results as evident from a reduction in the FWHM of the XRD peak of the GaNAs layer corresponding to significant improvement in the PL efficiency arising from the thermal annealing process. The results also show no significant difference in the lattice parameter between the annealed and as-grown sample, indicating that the GaNAs layers are structurally more stable under thermal annealing.

REFERENCE

- [1] E. V. K. Rao, A. Ougazzaden, Y. Le Bellego, and M. Juhel, *Appl. Phys. Lett.* 72, 1409 (1998).
- [2] I. A. Buyanova, G. Pozina, P. N. Hai, N. Q. Thinh, J. P. Bergman, W. M. Chen, H. P. Xin and C. W. Tu, *Appl. Phys. Lett.* 77, 2325 (2000).
- [3] S. G. Spruytte, C. W. Coldren, J. S. Harris, W. Wampler, P. Krispin, K. Ploog and M. C. Larson, *J. Appl. Phys.* 89, 4401 (2001)
- [4] J. S. Tsang, C. P. Lee, S. H. Lee, K. L. Tsai, and H. R. Chen, *J. Appl. Phys.* 77, 4302 (1995).
- [5] Z. Pan, L. H. Li, Y. W. Lin, Z. Q. Zhou, W. Zhang, Y. T. Wang, and R. H. Wu, *J. Cryst. Growth* 209, 648 (2000).
- [6] S. Francoeur, G. Sivaraman, Y. Qiu, S. Nikishin, and H. Temkin, *Appl. Phys. Lett.* 72, 1857 (1998).
- [7] S. G. Spruytte, C. W. Coldren, J. S. Harris, W. Wampler, P. Krispin, K. Ploog and M. C. Larson, *J. Appl. Phys.* 89, 4401 (2001)
- [8] W. Shan, W. Walukiewicz, and J. W. Ager III, *Phys. Rev. Lett.*, 82, 1221 (1999)
- [9] L. Bellaiche, S.-H. Wei, and Alex Zunger, *Phys. Rev. B.* 54, 17568 (1996).
- [10] Frank, F. C. and Turnbull, D. *Phys. Rev.* 104, 617 (1956).
- [11] EPI Application Note, 97-3 (1997)
- [12] R. J. Matyi, M. R. Melloch, K. Zhang and D. L. Miller, *J. Phys. D: Appl. Phys.* 28, A139 (1995).

**Low Concentration Nitride
Alloys II and Photovoltaics**

Electronic structure near the band gap of heavily nitrogen doped GaAs and GaP

Yong Zhang*, B. Fluegel, M. Hanna, A. Duda, and A. Mascarenhas
National Renewable Energy Laboratory, 1617 Cole Boulevard Golden, CO 80401, USA
*yzhang@nrel.gov

ABSTRACT

Isoelectronic impurity nitrogen atoms have been found to generate a series of localized states in GaP and GaAs. These states can be either bound (within the band gap) or resonant (above the band gap) when in the dilute doping limit (roughly $< 10^{19} \text{ cm}^{-3}$ for GaP and $< 10^{18} \text{ cm}^{-3}$ for GaAs). With increasing nitrogen doping level, a shift of the absorption edge from the binary band gap has been observed for the so-called GaPN or GaAsN alloy. We discuss the similarity and dissimilarity between the two systems in the following aspects: (1) How does the nitrogen doping perturb the host band structure? (2) How do the nitrogen bound states evolve with increasing nitrogen doping level? (3) What are the dominant contributors to the band edge absorption? And (4) does a universal model exist for GaPN and GaAsN? Other issues that will be discussed are: how does one define the band gap for these materials, and what is the relevance of various theoretical band structure calculations to the experimentally measured parameters.

INTRODUCTION

Large band gap reductions, along with many other modifications to the band structure, have been observed in heavily nitrogen doped GaAs and GaP for nearly a decade [1,2]. Two recent reviews [3,4] have related the newer research activities in this area to a field that is more than thirty-year old, that is, isoelectronic impurities in semiconductors. These materials have frequently been referred to as dilute nitride alloys. Since GaN has a much larger band gap than either of the hosts, the observed large band gap reduction has been portrayed as “giant” bowing, using the terminology for describing conventional alloys. However, if one notes that the band alignment for GaP/GaN or GaAs/GaN is type II with the conduction band edge of the GaN lower than that of GaP by $\sim 560 \text{ meV}$ or GaAs by $\sim 200 \text{ meV}$, then the large band gap reduction is less surprising [3]. Nitrogen is one of a very distinct group of isoelectronic impurities in III-V semiconductors. Long before the finding of the large band gap reduction it was known that the impurity states associated with an isolated nitrogen and various nitrogen pairs have progressively lower energy levels in GaP [5] and GaAs [6,7]. This trend had actually already hinted at the type II band alignment between GaP or GaAs and GaN. Considering the bowing for each individual band edge instead of the entire band gap, one will find the bowing coefficient to be rather different from that given in the literature for the band gap of GaAsN or GaPN. However, the microscopic origin for the band gap reduction, i.e., its relationship with the host band structure or the nitrogen impurity states, has been an intensively debated issue in recent years. A phenomenological model, the so-called “band anti-crossing” model, suggests that the primary effect of nitrogen doping is to cause a repulsion between the isolated nitrogen level and the Γ conduction band edge [8,9], disregarding that the isolated nitrogen level is higher in GaAs and lower in GaP than the Γ point. Attempts to provide an answer using band structure calculations have been made [10-13]. A generic argument has been proposed for explaining the band gap

reduction: the nitrogen incorporation breaks the lattice symmetry and causes the bulk states at the Brillouin zone boundaries (e.g., X and L point) to fold to the Γ point, consequently, the repulsion between the folded states and the Γ point gives rise to the band gap reduction. Such an argument implies that any impurity incorporation should result in a band gap reduction, which is obviously untrue. As has been discussed in Ref.[3], an apparent reason for the large band gap reduction is simply the large type II band offset, but a more fundamental reason is that the 2s valence atomic level of N atom is much lower than that of As 4s or P 3s. Also, a recent calculation [14] indicates that the first order perturbation of the nitrogen impurity potential, which does not involve the inter-valley coupling, already results in a considerable band gap reduction for GaAsN. Although all these band structure calculations were able to yield a band gap reduction, the values scatter considerably. According to these calculations, the band edge state is bulk-like [10,11] or more simply a lowest bulk-like state is defined as the band edge [12,13]. Another suggested mechanism for the band gap reduction is the impurity band formation of the nitrogen bound states [15,16]. In GaPN, all existing experimental data seem to indicate the weak role of any perturbed host states in the band edge absorption [17-19], and instead point to the formation of an impurity band from various nitrogen bound exciton states [16,19]. However, recent theoretical calculations [12,13] claimed that the nitrogen impurity states can not interact sufficiently so as to broaden and form an impurity band, and the band gap reduction was due to the host state "plunging down" as a result of nitrogen perturbation. In GaAsN, nitrogen induced bound states have also been found to broaden and turn into a continuous spectrum [20,21]. However, it has not been clear as to how nitrogen bound states and the bulk-like states compete with each other, and which of them is the dominant contributor to the band edge absorption. This will be a major issue to be addressed in this work.

Another issue which has rarely been addressed for these so-called dilute nitride alloys is the relevant meaning of a measured parameter. Such a parameter can be, for instance, band gap and effective mass which are well-defined for an ideal crystal and meaningful for a conventional alloy. Experimentally, the band gap of GaAsN and GaPN has been derived in many different ways: photoluminescence (PL), absorption or PL excitation (PLE), derivative spectroscopy techniques which include electro- or photo-reflectance or absorption. From absorption, one can fit the absorption near the "band edge" to the lineshape function for free carrier absorption, i.e., $(E - E_g)^n$ with $n = 1/2$ for the direct transition and $n = 2$ for the indirect transition. Ambiguity in the fitting procedure has led to contradictory conclusions [4] of the same material being indirect according to one study and direct according to another study. A more fundamental concern is that the inter-band transition in an intrinsic semiconductor should always be excitonic, even if inhomogeneous broadening smears out the measured excitonic feature in some cases. However, taking the excitonic peak (if any) as the band gap versus the above mentioned fitting may give a significantly different band gap for a material like GaAsN which frequently exhibits a rather slow rising slope in its absorption curve [1]. For GaPN, since the band edge absorption originates from nitrogen bound states, it is not at all clear what kind of lineshape function can be justifiably used [16]. Regarding the various derivative spectroscopies which are commonly believed to be more accurate than the linear spectroscopies, the band gap can be determined with much less ambiguity (provided a proper lineshape function is used for fitting the experimental curve). However, the physical process that results in the measured derivative lineshape is not trivial for these strongly perturbed semiconductors. It is also unclear how well the band gaps derived from using these somewhat different criteria agree with each other.

Many attempts have been made for quantitative comparisons between experimental data and theoretical results. In many cases, it was not at all clear what exactly was being compared, although excellent agreements between experimental and theoretical results have been claimed [13].

In this work, we intend to present a comprehensive view of the so-called GaAsN and GaPN alloys. We will (1) examine the difference for the band gap measured by different techniques or using different criteria; (2) investigate how nitrogen doping affects the host band structure and the band edge excitonic absorption; (3) reveal the evolution of nitrogen bound states on increasing nitrogen doping level; and (4) discuss the relevance of comparisons between the experimental data and theoretical modeling.

EXPERIMENTS

GaAs:N samples were grown by low pressure metal-organic chemical vapor deposition (MOCVD) on semi-insulating GaAs substrates. A 50 nm AlAs layer was inserted in between for lifting off the epilayer by chemical etching. The nominal epilayer thickness is 1 μm . Transmission was measured on a film that was either van der Waals bonded to a cover glass or free standing, i.e., glued at its edge to a thin metal wire. The film on glass was found to be slightly strained at low temperature, but the "wire mounted" film remained strain-free in the area away from the wire. GaPN samples were grown by MBE on GaP substrates, as described in Ref.[16]. Some GaPN samples were thinned down to $\sim 50 \mu\text{m}$ by mechanical polishing for the transmission measurement. Transmission measurements were performed using a tungsten lamp, focused and spatially filtered to have a 50- μm spot size. 1.5 K linear absorption spectra were measured using a system with a Spex270 spectrometer and a CCD detector. Differential absorption spectra were measured using a system with a Spex 320 spectrometer and a Si-detector. A 405 nm diode laser was used as the modulation source. Nitrogen compositions were determined by either SIMS (for $x < 0.1 \%$) or x-ray measurements.

NEW "BAND GAP" OF GaAsN

Fig.1 shows a comparison of the linear and differential absorption spectra for $\text{GaAs}_{1-x}\text{N}_x$ with $x = 0, 0.2 \%$ and 2.2% . The two samples with $x = 0$ or 0.2% were measured on cover glass, and

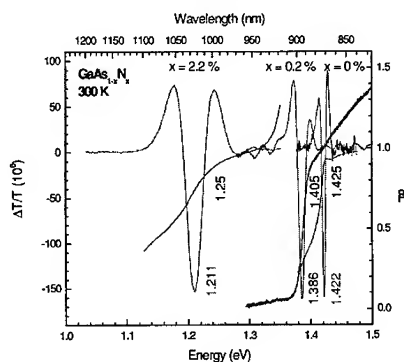


Figure 1. Linear (right) and differential (left) absorption of $\text{GaAs}_{1-x}\text{N}_x$, measured at 300 K.

the 2.2 % sample was measured on the substrate. For the $x = 0$ sample, the peak of the $\Delta T/T$ signal is shown to be very close to the excitonic absorption peak. However, the excitonic absorption peak smears out for the other two nitrogen-doped samples. Obviously, the main peak of the $\Delta T/T$ signal does not occur at the absorption "threshold" which itself is not well-defined. Thus, Fig.1 illustrates the fact that using the absorption "threshold" of the linear absorption spectrum may give rise to a rather different band gap from that determined by the differential absorption. However, there are no fundamental arguments which favor one result over the other.

Fig.2 shows 1.5 K absorption spectra for a set of relatively low nitrogen concentration samples with $x < 0.5$ %. These films were "wire mounted", thus, being nearly strain free, whereas films on cover glass show typically a ~ 2 meV splitting and shift of the absorption peaks at this temperature. The GaAs-like excitonic absorption peak is found to shift down in energy continuously with increasing nitrogen concentration. A small band gap reduction of ~ 1 meV has been observed for a sample with nitrogen concentration as low as $1 \times 10^{18} \text{ cm}^{-3}$ or $x = 0.0045$ %. When x approaches 0.5 %, the absorption peak has broadened drastically, indicating a strong interaction between the bulk-like states and the nitrogen bound states associated with nitrogen pairs or clusters. Fig.3 summarizes the band gap reduction measured by the excitonic absorption peak at 1.5 K as a function of nitrogen composition for the low x region, together with the results for the high x region obtained from electro-reflectance at 300 K [22]. There is indeed a deviation between the band gaps determined by the two techniques. Note that this deviation is not due to the temperature dependence of the band gap. There have been a few reports which suggest a significant difference for the temperature dependence of the band gap between GaAsN and GaAs (for instance, from absorption measurements [23]). However, we have found that the difference is negligible, if any, using the electro-reflectance technique.

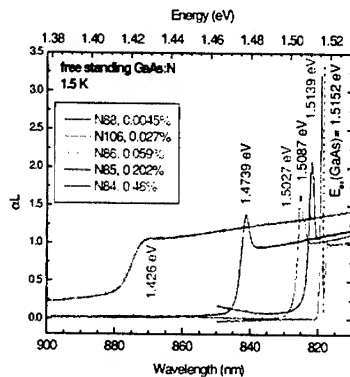


Figure 2. Linear absorption spectra of $\text{GaAs}_{1-x}\text{N}_x$ with low nitrogen concentrations, measured at 1.5 K. The absorption peak shifts monotonically with increasing nitrogen concentration.

To better understand the character of the electronic states that contribute to the absorption, for an $x = 0.1$ % sample, we have measured its PL spectra with excitation energies above and below the GaAsN band gap [20,21]. Fig.4 shows a PLE spectrum that is reconstructed from the selective excitation PL spectra, together with a few such PL spectra at representative excitation energies. As one can see, the PLE spectrum has a peak at 1.475 eV that agrees within a few meV with the band gap determined by the electroreflectance [21]. It is important to point out that with each excitation energy near but below the band gap, we observed a sharp zero-phonon line at ~ 1 meV below the excitation energy plus a TA phonon sideband and enhanced LO_Γ and TO_Γ

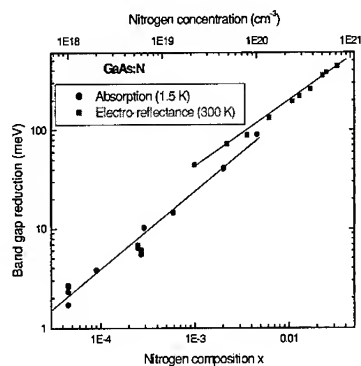


Figure 3. Band gap reduction of $\text{GaAs}_{1-x}\text{N}_x$ vs. N composition, determined by the excitonic absorption peak at 1.5 K and electroreflectance lineshape fitting at 300 K.

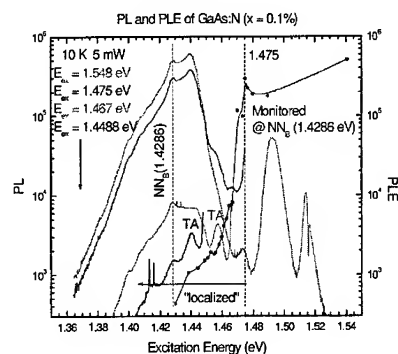


Figure 4. (left) Selective excitation PL spectra and (right) PLE spectrum reconstructed from PL intensities at the energy of NN_B peak for a $\text{GaAs}_{1-x}\text{N}_x$ sample of $x = 0.1\%$.

resonant Raman peaks, which indicates that these states behave like typical localized states [16]. Apparently, these impurity-like states exist in a spectral range at least 100 meV below the “band gap”. Thus, the existence of an impurity band is a fact, although the impurity-like states may not be the dominant contributors to the absorption near the “band gap”.

NEW “BAND EDGE” OF GaPN

For GaP:N, early studies [17,18] have indeed shown that nitrogen doping perturbs the host band structure, making the forbidden indirect band gap transition A_x partially allowed. However, the absorption at the direct band gap was found to be only $\sim 1/150$ of the A line (the isolated nitrogen state) absorption (only $\sim 1/450$ if the contribution of the A line acoustic phonon sideband is subtracted) [18]. More recent PLE measurements for nitrogen compositions up to 2 % showed absorption features near A_x as well as the direct gap energy, but no sign of any absorption feature at the L indirect gap energy [19]. Thus, it is highly unlikely that in GaPN any perturbed bulk states could make comparable contributions to the band edge absorption of the nitrogen bound states. Fig.5 shows PL spectra for a set of $\text{GaP}_{1-x}\text{N}_x$ samples with x varying 0.004 % to 0.6 % [16]. The spectrum of the most dilute sample shows the emission lines of nearly all the nitrogen induced bound states in GaPN [5]. However, on increasing nitrogen concentration,

those sharp lines due to nitrogen pairs at the higher energy side broaden and quench sequentially in the order of increasing binding energy. At the same time a broad emission band rises at the lower energy side of the NN_1 line.

Selective excitation PL is used to reveal the nature of the states that give rise to the broad emission band, while absorption measurement is used to monitor the evolution of nitrogen pair states. The results are shown in Fig.6. To the left, the PL spectra obtained under selective excitation are found to always consist of a sharp zero phonon line NN_1 together with various phonon sidebands, typical of the spectrum for a nitrogen pair like NN_1 . This indicates that the states in the broad band are nothing but nitrogen bound exciton states with different local environments. To the right, an absorption spectrum shows that the peak positions of nitrogen pair states barely move with respect to the dilute limit, but they strongly broaden and merge with each other. In fact, the absorption peak at NN_1 very much resembles an excitonic absorption peak in a conventional semiconductor. The results of Fig.5 and Fig.6 unambiguously show that for $x > 0.1$ %, nitrogen bound states in GaPN rapidly broaden into a continuous spectrum more than 300 meV wide. Fig.7 shows a set of absorption spectra for different nitrogen compositions. It is clear that the positions of nitrogen bound states remain more or less stationary until they all merge together at high nitrogen concentrations, which unambiguously disproves the $N - \Gamma$ repulsion suggested by the "band anti-crossing" model [9].

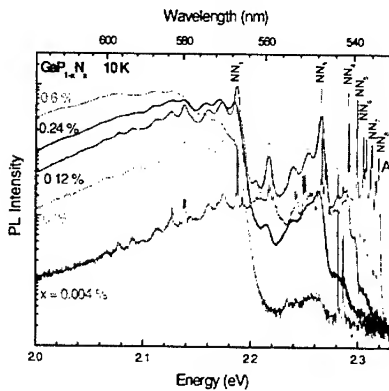


Figure 5. PL spectra of $GaP_{1-x}N_x$ with different N compositions, measured at 10 K with excitation energy of 2.33 eV.

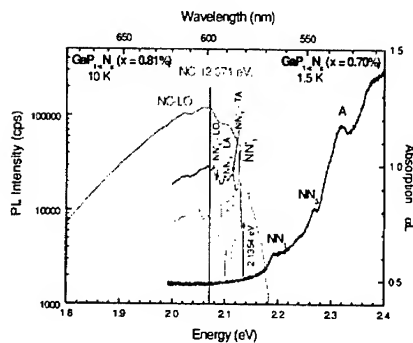


Figure 6. Left: selective excitation PL spectra for a $GaP_{1-x}N_x$ sample of $x = 0.81$ %, with excitation energies of 2.3306, 2.1354, and 2.1014 eV. Right: an absorption spectrum for a 750 nm thick $GaP_{1-x}N_x$ sample of $x = 0.70$ %.

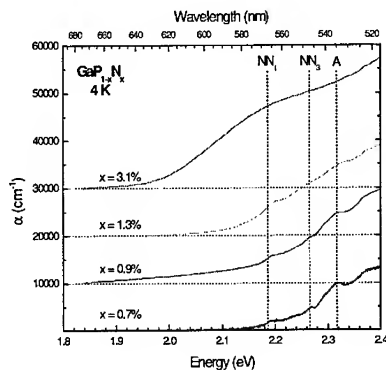


Figure 7. Absorption spectra for $\text{GaP}_{1-x}\text{N}_x$ with $x = 0.70, 0.90, 1.3$, and 3.1% , measured at 4 K (except for the $x = 0.70\%$ at 1.5 K). The curves are shifted for clarity.

DISCUSSIONS

How valid is the “band anti-crossing” model?

The “band anti-crossing (BAC)” model suggests that the band gap reduction is simply due to the isolated nitrogen state and the Γ conduction band edge repelling each other [8,9], whether or not the isolated nitrogen level is higher or lower than the Γ point and ignoring the possible role of bulk states belonging to other valleys (namely the X and L valleys) or nitrogen pair states. Although this model has been successfully used for fitting various experimental data, a number of serious internal inconsistencies have been pointed out [4], due to the over simplified nature of this model. An equal but opposite shift of the band gap and E^+ is expected by the BAC model. However, in GaAsN , this has been disproved experimentally [24,25], with one exception of the data [26] from the model’s authors. Also, there exists an inconsistency in the coupling matrix element, V_{MN} , between what was derived from the band gap pressure dependence and from composition dependence [8,26]. An extended version of this model with the k-space dispersion included is also problematic [27]. First, it is conceptually wrong to view the nitrogen level as a dispersionless band in k-space. Second, it is not clear for what range in k-space the k-independent V_{MN} model is applicable. If one simply applies the model to the whole Brillouin zone, one will have large splittings at both L and X point (e.g., 540 meV at L point and 600 meV at X point for $x = 1\%$ with $V_{\text{MN}} = 0.27\text{ eV}$), which is exactly opposite to the suggestion that the BAC model would not yield a significant splitting at the L point [26]. Although there is no reason to believe that the interaction between the nitrogen state and any bulk states is uniform, it is unreasonable to believe that the nitrogen state does not interact with the states with which it is in resonance or with the nearby L point. For GaPN , the experimental data of Fig.6 and Fig.7 have shown clearly enough that the A line is not repelled down by any bulk states, as suggested in Ref. [9]. Whether or not the Γ band edge shifts up with increasing nitrogen doping [9,19] is a different issue deserving further investigation. In fact, contradicting their own claim of the A line being repelled down starting at $x > 0\%$ in Ref.[9], the authors on a different occasion admitted that the A line energy was independent of nitrogen concentration up to $x \sim 0.5\%$ [26].

Is it possible to make quantitative comparison between experiment and theory?

It is therefore a delicate issue to make a quantitative comparison between the experimental data and the results of theoretical calculations. Along with the ambiguity of defining the band gap experimentally, it is not at all clear as to what is the exact meaning of the calculated band gap. The observed large band gap reduction in $\text{GaAs}_{1-x}\text{N}_x$ can be qualitatively understood by calculating the band structure of ordered nitrogen arrays in GaAs [10,11,28,29]. However, not only the calculated results vary significantly from one method to the other, but also neither of them agrees quantitatively with experimental results [22]. Obviously, a randomly nitrogen doped structure is expected to differ electronically from the ordered structure [16,20-22,30], which has been well demonstrated even for a conventional alloy like $\text{Ga}_{1-x}\text{In}_x\text{P}$ [31]. It has also been indicated by recent calculations [13] that merely the existence of nitrogen pair states could change the band gap of the ordered structure. Attempts to model the random structure have to contend with the issue of how to define the band gap [12,13,30,32]. Refs.[30,32] defined the band gap by averaging the lowest states (most likely being nitrogen localized states) over different randomly generated configurations. Refs.[12,13] instead tried to identify the lowest bulk-like state as the new band edge. Theoretically, one could choose different definitions for the band gap, but as to how the calculated band gap is relevant to the experimentally determined band gap would need further clarification. Thus, any claimed excellent agreements with experimental data could only be fortuitous, without actually calculating the specific quantity that is measured. For heavily nitrogen doped GaAs or GaP, the band gap is not a well defined parameter as it is for undoped GaAs or GaP. However, for a given nitrogen composition and an assumed random distribution, there will be a statistically well defined absorption profile or a distribution of impurity-like and bulk-like states. Any measurement (e.g., PL, absorption, differential absorption or electro-reflectance) will be just probing the collective behavior of these states, and these states are expected to respond to the different probes accordingly. One could define, for example, a band gap based on the technique used and a certain set of criteria. Thus, the state at the "band edge" could be either impurity-like or bulk-like.

Can an impurity band form in GaAsN and GaPN?

Impurity band formation of the nitrogen bound states has been suggested as the primary mechanism for the band gap reduction [15,16]. To disapprove this model, Refs.[12,13] claimed that the nitrogen impurity states could not interact sufficiently so as to broaden and form an impurity band. The experimental results, as summarized in the previous sections, indicate that whether the impurity band is formed or not is not really the issue. Rather, if one defines the band gap through, e.g., an absorption measurement, the key issue becomes which of the impurity-like states or bulk-like states are the dominant contributors to the absorption profile. Since GaAs is a direct gap but GaP is an indirect gap semiconductor, the relative absorption strength of the impurity-like and bulk-like states is expected to be very much different. The absorption cross section for a nitrogen bound state in GaP is known to be $\int \alpha d\nu = 9.5 \times 10^{-15} \text{ cm}$ [33], and in GaAs this is estimated to be $\int \alpha d\nu = 2.1 \times 10^{-13} \text{ cm}$ (based on the experimental data of Ref.[7] and following the detailed balance analysis of Ref.[34]). Fig.8 shows estimated peak absorption coefficients for the A line, A_x line, and NN_1 in GaPN, and for X_1 line in GaAsN, using their absorption cross sections obtained at the dilute limit and assuming no broadening. Without

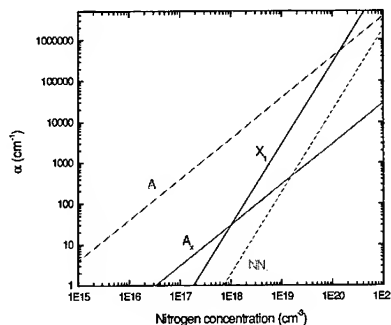


Figure 8. Estimated peak absorption coefficients for A, A_x , and NN_1 transition in GaP:N, and for X_1 in GaAs:N, using the absorption cross sections in the dilute limit and assuming no broadening.

broadening, the peak absorption of the A line in GaP could reach $98,000 \text{ cm}^{-1}$ at $x = 0.1 \%$, which is about the magnitude of the GaAs band edge excitonic absorption [35]. Similarly, for the NN_1 state at $x = 0.1 \%$, the peak absorption is estimated to be $\sim 1,100 \text{ cm}^{-1}$ in GaP and $14,000 \text{ cm}^{-1}$ in GaAs. Indeed, the absorption of the nitrogen pair bound state in GaAs would be able to reach a value comparable to the GaAs band edge excitonic absorption at such a composition, if the state remained bound and unbroadened. However, because of the fast decrease of the GaAs band edge on increasing nitrogen doping, as shown in Fig.2, a strong interaction between the shallow nitrogen pair bound states and the bulk-like states is expected. It is yet unclear how the interaction transforms the GaAs band edge and the nitrogen pair bound state from either the theoretical or experimental point of view. The recent theoretical calculation [12,13] suggested that the nitrogen states would remain more or less stationary, whereas the bulk band edge moved down and surpassed them. Since the calculations [12,13] yielded an electron binding energy of $\sim 100 \text{ meV}$ for nitrogen pairs in GaAsN, it would mean that for $x > 0.5 \%$, the nitrogen pair states should remain bound according to the data of Fig.2, which is obviously contradictory to the experimental fact [20].

How did the theoretical calculation [12,13] conclude, in contrast to the experimental results, that there is no impurity band formation in GaAsN and GaPN? To answer this question, both the intrinsic limitations and the technical inadequacy of the theory need to be examined. As summarized in Ref.[21], there are several channels for the nitrogen bound states to interact. In addition to the difficult coupling considered in Refs.[12,13,15], i.e., the coupling of the highly localized bare electron bound states, there are two other channels. One is through the excitonic states which are ultimately relevant in the experimental measurement, but not taken into account in the theoretical modeling. The other is the randomness-induced inhomogeneous broadening which can also effectively give rise to a continuous spectrum. A sincere effort has been made in Refs.[12,13] to model the random structure by using a large supercell with up to 14,000 atoms. However, such a size is still not adequate for realistically simulating the random structure in the composition range of interest. For instance, for $x = 0.1 \%$, the average pair separation is $\sim 200 \text{ \AA}$, and a 200 \AA size supercell will have $\sim 333,000$ atoms. Even for $x \sim 0.4 \%$, to statistically have just 10 pairs of the same configuration appear in a supercell in order to observe their interaction, the supercell size should be $\sim 160 \text{ \AA}$ with $\sim 180,000$ atoms [4]. Thus, the supercell used in Refs.[12,13] was not sufficiently large to generate enough nitrogen bound states with different local configurations to form a quasi continuous spectrum. In addition, the calculations [12,13] yielded an electron binding energy of $\sim 100 \text{ meV}$ for nitrogen pairs in GaAsN and of $\sim 30 \text{ meV}$ for the isolated nitrogen in GaPN, while experimental values for both cases are known to be < 10

meV [3,7,17,20]. At least to some extent, the insufficient accuracy for the impurity potential could affect the description of the impurity-impurity and the impurity-host interaction. In fact, in a recent 1,000 atom supercell calculation with improved pseudopotentials for $\text{GaAs}_{1-x-y}\text{P}_{x-y}\text{N}_{2y}$ [36], even the bare electron bound states were found to be able to form an impurity band for $x > 0.3$.

CONCLUSIONS

A band gap is not as clearly defined in the so-called dilute nitride alloys like $\text{GaAs}_{1-x}\text{N}_x$ and $\text{GaP}_{1-x}\text{N}_x$ as it is in binary semiconductors or conventional alloys. Depending on the criteria and techniques used, different band gaps may be derived. It is found that the band gaps defined in various theoretical calculations do not clearly relate to the experimentally determined band gap. Thus, any claimed excellent agreement between experiment and theory is likely to be fortuitous.

No sufficient attention has been paid in the past to recognize the difference between the host materials GaAs and GaP, one being direct gap and the other being indirect gap. Because of this major difference, the role of nitrogen impurity states and their perturbation to the host are qualitatively different in many aspects. Thus, it is unwise to attempt to find a universal model or description for these two systems.

In both GaPN and GaAsN, nitrogen bound states quickly form an impurity band on increasing nitrogen doping level from the dilute limit. The perturbed bulk states in GaPN are found to be unable to make a major contribution to the band edge absorption. It is the absorption of nitrogen bound states of isolated centers, pairs, triplets etc. that gives rise to the new band edge below the indirect band edge of the host. Whether or not the bulk-like states actually plunge down into the band gap, as predicted theoretically, is unclear and non-detectable at this time. The perturbed bulk states in GaAsN, however, remain as the dominant contributors to the band edge absorption. A well-defined, but gradually broadened, GaAs-like band edge excitonic absorption peak has been observed for nitrogen composition up to nearly 0.5 %. The interaction between the bulk-like states and the nitrogen bound states transforms the band structure near the new band edge into a mixture of localized and delocalized states.

The incorporation of nitrogen into GaAs and GaP generates a series of impurity-like states which co-exists with perturbed bulk states in a wide spectral range. Their collective behavior responds to different experimental measurements differently. Thus, arguments over which technique is more accurate or direct than the other is not always meaningful, especially, given the fact that one usually does not know the detailed mechanisms of the collective response being measured.

ACKNOWLEDGEMENTS

This work is supported by US DOE Office of Sciences, Basic Energy Sciences. We thank M. J. Seong and S. Francoeur for useful discussions and sample preparation, and J. F. Geisz, H. P. Xin and C. W. Tu for previous collaborations. SIMS measurements were performed by Charles Evans & Associates.

REFERENCES

1. M. Weyers, M. Sato, and H. Ando, *Jpn. J. Appl. Phys.* **31**, L853 (1992).
2. J. N. Baillargeon, K. Y. Cheng, G. E. Hofler, P. J. Pearah, and K. C. Hsieh, *Appl. Phys. Lett.* **60**, 2540 (1992).
3. Y. Zhang and W.-K. Ge, *J. Lumin.* **85**, 247 (2000).
4. A. Mascarenhas and Y. Zhang, *Current Opinions in Solid State and Material Science* **5**, 253 (2001).
5. D. G. Thomas, J. J. Hopfield, and C. J. Frosch, *Phys. Rev. Lett.* **15**, 857 (1965).
6. D. J. Wolford, J. A. Bradley, K. Fry, J. Thompson, and H. E. King, In *Inst. Phys. Conf. Ser. No. 65*, ed. G. E. Stillman (The Institute of Physics, Bristol, 1983), p. 477.
7. R. Scheabe, W. Seifert, F. Bugge, R. Bindemann, V. F. Agekyan and S. V. Pogarev, *Solid State Commun.* **55**, 167 (1985); X. Liu, M.-E. Pistol, L. Samuelson, S. Schwetlick and W. Seifert, *Appl. Phys. Lett.* **56**, 1451 (1990).
8. W. Shan, W. Walukiewicz, J. W. Ager III, E. E. Haller, J. F. Geisz, D. J. Friedman, J. M. Olson and S. R. Kurtz, *Phys. Rev. Lett.* **82**, 1221 (1999).
9. W. Shan, W. Walukiewicz, K. M. Yu, J. Wu, J. W. Ager III, E. E. Haller, H. P. Xin, and C. W. Tu, *Appl. Phys. Lett.* **76**, 3251 (2000).
10. E. D. Jones, N. A. Modline, A. A. Allerman, S. R. Kurtz, A. F. Wright, S. T. Tozer, and X. Wei, *Phys. Rev. B* **60**, 4430 (1999).
11. T. Mattila, S.-H. Wei, and A. Zunger, *Phys. Rev. B* **60**, R11245 (1999).
12. P. R. C. Kent and A. Zunger, *Phys. Rev. Lett.* **86**, 2613 (2001).
13. P. R. C. Kent and A. Zunger, *Phys. Rev. B* **64**, 115208 (2001).
14. A. Al-Yacoub and L. Bellaiche, *Phys. Rev. B* **62**, 10847 (2000).
15. Y. Zhang, A. Mascarenhas, H. P. Xin, and C. W. Tu, *Phys. Rev. B* **61**, 7479 (2000).
16. Y. Zhang, B. Fluegel, A. Mascarenhas, H. P. Xin, and C. W. Tu, *Phys. Rev. B* **62**, 4493 (2000).
17. D. G. Thomas and J. J. Hopfield, *Phys. Rev.* **150**, 680 (1965).
18. J. J. Hopfield, P. J. Dean, and D. G. Thomas, *Phys. Rev.* **158**, 748 (1966).
19. H. Yaguchi, S. Miyoshi, G. Biwa, M. Kibune, K. Onabe, Y. Shiraki and R. Ito, *J. Cryst. Growth* **170**, 353 (1997).
20. Y. Zhang, A. Mascarenhas, J. F. Geisz, H. P. Xin, and C. W. Tu, *Phys. Rev. B* **63**, 85205 (2001).
21. Y. Zhang, S. Francoeur, A. Mascarenhas, H. P. Xin, and C. W. Tu, *Proc. ICNS-4, Phys. Stat. Sol. (b)* **228**, 287 (2001).
22. Y. Zhang, A. Mascarenhas, H. P. Xin, and C. W. Tu, *Phys. Rev. B* **63**, R161303 (2001).
23. K. Uesugi, I. Suemune, T. Hasegawa, T. Akutagawa, and T. Nakamura, *Appl. Phys. Lett.* **76**, 1285 (2000).
24. J. D. Perkins, A. Mascarenhas, Y. Zhang, J. F. Geisz, D. J. Friedman, J. M. Olson, and S. R. Kurtz, *Phys. Rev. Lett.* **82**, 3312 (1999).
25. P. J. Klar, H. Güning, W. Heimbrodt, J. Koch, F. Höhnsdorf, W. Stolz, P. M. A. Vicente, and J. Camassel, *Appl. Phys. Lett.* **76**, 3439 (2000).
26. W. Shan, W. Walukiewicz, K. M. Yu, J. W. Ager III, E. E. Haller, J. F. Geisz, D. J. Friedman, J. M. Olson and S. R. Kurtz, *Phys. Rev. B* **62**, 4211 (2000).

27. W. Shan, W. Walukiewicz, K. M. Yu, J. W. Ager III, E. E. Haller, J. F. Geisz, D. J. Friedman, J. M. Olson, S. R. Kurtz, H. P. Xin, and C. W. Tu, *phys. stat. sol (b)* **223**, 75 (20001).
28. S.-H. Wei and A. Zunger, *Phys. Rev. Lett.* **76**, 664 (1996).
29. L.-W. Wang, *Appl. Phys. Lett.* **78**, 1565 (2001).
30. L. L. Bellaiche, S.-H. Wei, and A. Zunger, *Appl. Phys. Lett.* **70**, 3558 (1997).
31. Y. Zhang, A. Mascarenhas, and L.-W. Wang, *Phys. Rev. B* **63**, R201312 (2001).
32. L. L. Bellaiche, S.-H. Wei, and A. Zunger, *Phys. Rev. B* **54**, 17568 (1996).
33. E. C. Lightowers, J. C. North, and O. G. Lorimor, *J. Appl. Phys.* **45**, 2191 (1974).
34. M. D. Sturge, E. Cohen, and K. F. Rodgers, *Phys. Rev. B* **15**, 3169 (1977).
35. G. W. Fehrenbach, W. Schafer, J. Treusch, and R. G. Ulbrich, *Phys. Rev. Lett.* **49**, 1281 (1982).
36. L. Bellaiche, N. A. Modline, and E. D. Jones, *Phys. Rev. B* **62**, 15311 (2000).

InAsN Grown by Plasma-Assisted Gas Source MBE

Ding-Kang Shih, Hao-Hsiung Lin, and Tso-Yu Chu, National Taiwan University, Dept. of Electrical Engineering, Taipei, Taiwan, R.O.C.

T. R. Yang, National Taiwan Normal University, Dept. of Physics, Taipei, Taiwan, R.O.C.

ABSTRACT

We report the structural, electrical and optical properties of bulk InAsN alloy with various nitrogen contents deposited on (100) InP substrates by using plasma-assisted gas source molecular beam epitaxy. It is found that the fundamental absorption edge of InAsN, as compared to that of InAs, shifts to higher energy due to Burstein-Moss effect. A dramatic increase of the electron effective mass in a nitrogen-containing III-V alloy is also observed from infrared reflectivity and Hall measurement on these degenerate InAsN samples. The sizeable increase on electron effective mass is consistent with the theoretical predictions based on band-anticrossing model.

INTRODUCTION

Group III-V-nitride alloys have a very large band-gap bowing due to the large valence electron energy of the nitrogen atom when compared to other group V atoms [1]. Over the last few years, there have been numerous attempts to explain the large band gap reductions properties of the III-V-N alloys. It has been demonstrated recently that a band anticrossing (BAC) model in which localized N states interact with the extended states of the conduction band can explain the unusual properties of the III-V-N alloys [2].

The huge bowing effect on the band gap energy makes InAsN alloy a promising material for infrared applications. However, only very limited efforts were put on this materials. In this report, we have investigated a series of unintentionally doped InAsN bulk layers with various N contents grown on InP substrates by using gas source molecular beam epitaxy (GSMBE). We found that these samples are with high residual carrier concentration, which increases as N composition increases. Furthermore, the fundamental absorption edge of InAsN, as compared to that of InAs, shifts to higher energy due to the Burstein-Moss (BM) effect [3]. To deduce the 'real' band gap energy of our InAsN samples, the energy shift due to BM effect and the band gap narrowing (BGN) effect are considered by using a self-consistent approach based on the BAC model. After the correction, the 'real' band gap energy of InAsN samples decreases as N increases, and follows the bowing effect normally. In addition, we found a dramatic increase of the electron effective mass in these InAsN alloys, which is consistent with the theoretical predictions based on BAC model.

EXPERIMENTAL DETAILS

The InAsN epitaxial layers were grown on semi-insulating InP substrates using GSMBE with RF plasma source as the nitrogen source. Layers were grown at 460°C at a growth rate of 1.5 $\mu\text{m/hr}$. The ranges of RF power and nitrogen flow rate were from 300W to 480W and from 0.5 to 1.9 sccm, respectively. Detailed growth conditions has been described elsewhere [4]. The thickness of InAsN epitaxial layer was 2 μm and the nitrogen composition of the InAsN sample was determined from the double crystal X-ray diffractometer (DXRD) spectra fittings by using a

commercial dynamic simulator, RADS. The electrical and optical properties of the samples were investigated by using a home-made Hall effect system and a Bruker IFS 120 HR Fourier transform infrared (FTIR) spectrometer, respectively.

DISCUSSION

Fig.1 shows the DXRD rocking curves of InAs and InAsN samples. As plasma power increased, the diffraction peak of the InAsN, as compared with that of InAs sample, shifts closer to the InP substrate peak. It represents that N was indeed incorporated into InAs. The results from RADS fitting were also listed in the Fig.1. Although N was added into InAs successfully, its incorporation also degrades the DXRD linewidths as compared to the referential InAs. Table I shows the Hall results of the samples at room temperature. All the undoped samples exhibited n-type conduction. It was found that the more the N composition, the higher the carrier concentration. The possible origin of the high carrier concentration in N-containing sample is not quite clear at the moment. However, because of the large InAs crystal lattice constant and the small N atom size, nitrogen interstitial defects could be a possible candidate. Furthermore, since the band gap is very narrow, the defect levels in these materials could be 'effective shallow' and thus could be ionized to result in high residual carrier concentration. As compared with other samples, sample C1078 has the largest residual free carrier concentration and an extraordinary low mobility. According to BAC model, the dispersion relation of the nonparabolic subbands become flatter as the nitrogen composition is increased. This indicates a large increase of the effective mass in the subbands. Furthermore, the higher residual free carrier concentration in sample C1078 may make the nonparabolic effect on the subband more significant, and therefore results in very low mobility. Fig. 2 shows the near band edge absorption spectra converted from FTIR transmission measurement at 300K. Two points are worthy of note from this figure. First, the energy of the absorption edge of InAsN samples is always higher than that of InAs. Second, when N composition is lower than 1.6%, higher N composition results in higher absorption edge. But, the trend reverses for InAsN with N composition larger than 1.6%. The phenomenon seems controversy to the theoretical prediction. To interpret the results, BM effect should be taken into account because of the high residual carrier concentration in these InAsN samples. Samples with lower N composition have smaller effective mass and thus more significant BM effects. The two high N content samples, however, have larger effective mass and thus their BM effects are less significant. In these two samples, C1078 (2.8%) and C1077 (1.6%), the bowing effect on band gap may have overcome the BM effect, and results in red-shifted absorption edge, though the carrier concentration of the former is five times higher than that of the latter.

To deduce the 'real' band gap energy of our InAsN samples, the energy shift due to BM effect and the BGN effect which is always accompanied by the BM effect are considered by using a self-consistent approach based on the BAC model. As the BAC model described, the interaction of the N states with the extended states of the semiconductor matrix transforms them into two nonparabolic subbands E_- and E_+ given by

$$E_{\pm}(k) = \frac{1}{2} \{ [E_M(k) + E_N] \pm \sqrt{[E_M(k) - E_N]^2 + 4V_{NM}^2} \}, \quad (1)$$

where E_N is the energy of the N state, $E_M(k)$ is the dispersion relation for the conduction band of the host crystal, and V_{NM} is the matrix element coupling those two types of states. All the energies are measured relative to the top of the valence band. The downward shift of the lower subband E_- can account well for the reduction of the fundamental band gap observed in these III-V-N alloys.

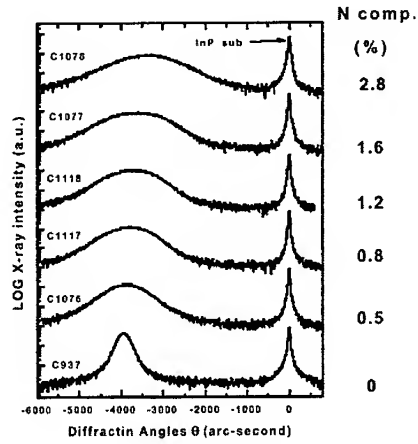


Figure1. DXRD spectra of a series $\text{InAs}_{1-x}\text{N}_x$ bulk samples with x from 0 to 0.028.

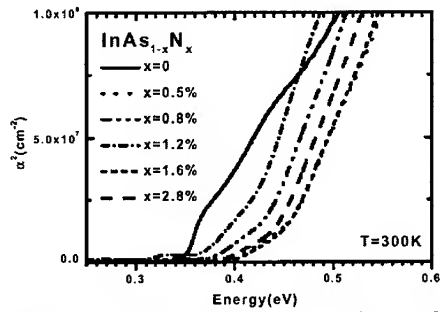


Figure 2. Plots of the square of the absorption coefficient (α^2) against the photon energy deduced from 300K IR transmission spectra recorded on a series of $\text{InAs}_{1-x}\text{N}_x$ bulk samples with x from 0 to 0.028

It is evident from Eq. (1) that the initial rate of the N-induced band gap reduction depends on the coupling parameter V_{NM} and on the energy difference $E_M - E_N$. Therefore the dependence of E_N , E_M , and V_{NM} on the nitrogen content of the InAsN bulk layer should be duly taken into account. Due to its localized nature [5], the energy E_N of the N level in InAsN case can be estimated 1.48 eV from the valence band offset, $\Delta E_V (\text{GaAs/InAs}) = 0.17$ eV [6] and $E_N = 1.65$ eV in GaAs. Concerning the dispersion relation $E_M(k)$ for the conduction band of InAs, we adopted the calculation results of Ref. 7, which is based on triple-band effective-mass approximation, and $E_M(0) = 0.35$ eV at 300K. For V_{NM} , it has been shown previously that the square of the matrix elements is proportional to the concentration of nitrogen atoms, i. e., $V_{NM} = C_{NM} x^{1/2}$, where C_{NM} is a constant dependent on the semiconductor matrix and is treated as a fitting parameter in this study.

Table I. Nitrogen composition, carrier concentration, plasma frequency, experimental, and theoretical calculated electron effective mass of the studied samples.

Sample No.	N (%)	residual carrier conc. n_D (cm^{-3})	Mobility ($\text{cm}^2/\text{V sec}$)	α_p (cm^{-1})	m^* (m_0) <i>exp.</i>	m^* (m_0) <i>cal.</i>
C937	0	2.64×10^{16}	7660	-	-	0.024 [10]
C1076	0.5	1.91×10^{17}	1740	471	0.063	0.044
C1077	1.6	3.24×10^{18}	1280	590	0.068	0.052
C1078	2.8	1.69×10^{19}	38.1	617	0.326	0.123
C1117	0.8	1.21×10^{18}	2690	390	0.055	0.039
C1118	1.2	8.85×10^{17}	3290	360	0.051	0.036
C1129	0.1	9.87×10^{17}	3530	395	0.046	0.037
C1130	1.6	1.69×10^{18}	2140	475	0.055	0.043
C1132	2.8	3.08×10^{18}	1010	593	0.058	0.046

In our case, the absorption edge E_{abs} is

$$E_{\text{abs}} = E_c + E_{\text{BM}} - E_{\text{BGN}} \quad (2)$$

where E_{BM} is the energy shift due to BM effect, E_{BGN} is the reduction energy due to BGN effect. To estimate E_{BM} , we solve the Fermi energy E_F in the conduction band from $n_D = \int f(E_-)D(E_-)dE_-$, where n_D is residual carrier concentration from the Hall measurements, $f(E_-)$ is the Fermi-Dirac distribution, and $D(E_-)$ is the density-of-states function in the lower subband conduction band, E_- . The BM shift in valence band is $E_V(k_F) = \frac{\hbar^2 k_F^2}{2m_h^*}$, where k_F is Fermi

wave number which is given by $k_F = (3\pi^2 n_D)^{1/3}$. m_h^* is the effective mass of the heavy-hole. We also assume that the perturbation induced by nitrogen on valence band can be omitted in InAsN. The absorption from the light-hole band is neglected because of its very low density of state. In addition, the band-gap narrowing due to band tails is not considered either. Now, we have the band-gap widening E_{BM} for carrier concentration n_D as $E_{\text{BM}} = E_F + E_V(k_F)$. Concerning the BGN due to the residual carrier, the shrinkage in energy is proportional to the carrier concentration and an empirical relation [8] can be represented by $E_{\text{BGN}} = \alpha_{\text{InAsN}} n_D^{1/2}$, where α_{InAsN} is BGN coefficient. With a given V_{NM} , the lower subband $E_c(k)$ can be calculated using Eq. (1). We treat the parameter V_{NM} as a fitting parameter. Once $E_c(k)$ is determined, we can further calculate the density of state $D(E_-)$ and solve E_F using $n_D = \int f(E_-)D(E_-)dE_-$ with measured n_D . E_{BM} is thus found by using $E_V(k_F) = \frac{\hbar^2 k_F^2}{2m_h^*}$ and $E_{\text{BM}} = E_F + E_V(k_F)$. With the calculated $E_c(k)$, we may also find

the conduction band effective mass, $m_{\text{InAsN}}^* = \frac{1}{\hbar^2} \frac{d^2 E_c}{dk^2}$, where \hbar is Planck's constant. The BGN

coefficient α_{InAsN} can also be found as following [9] $\alpha_{\text{InAsN}} = [(\epsilon_{\text{InAsN}}/\epsilon_{\text{InAs}})(m_{\text{InAs}}^*/m_{\text{InAsN}}^*)]\alpha_{\text{InAs}}$, where ϵ_{InAsN} is the static dielectric constant of InAs(N), and we suggest that $\epsilon_{\text{InAsN}} = \epsilon_{\text{InAs}}$ since the nitrogen composition is small in the present alloy. For InAs, $m_{\text{InAs}}^* = 0.024m_0$, where m_0 is the electron rest mass, and $\epsilon_{\text{InAs}} = 15.15$ [10]. Based on the three effects proposed in Ref.11, the estimated band-gap renormalization energy of InAs increases from ~40 meV to ~100 meV when carrier concentration increases from $n \sim 4 \times 10^{18} \text{cm}^{-3}$ to $\sim 5 \times 10^{19} \text{cm}^{-3}$. By using the empirical

formula $E_{BGN} = \alpha_{InAs} n_D^{\frac{1}{3}}$, the BGN coefficient α_{InAs} should be $\sim 2.67 \times 10^{-8}$ meV cm. This value is adopted in this study to estimate α_{InAsN} for the determination of the energy shift caused by BGN effect. Once the E_v , E_{BM} , and E_{BGN} were determined, E_{abs} was found from Eq. (2). If the difference between the calculated E_{abs} and the experimental result was larger than 10^{-4} eV, a new V_{NM} was chosen by using the bisection method to calculate a new E_{abs} .

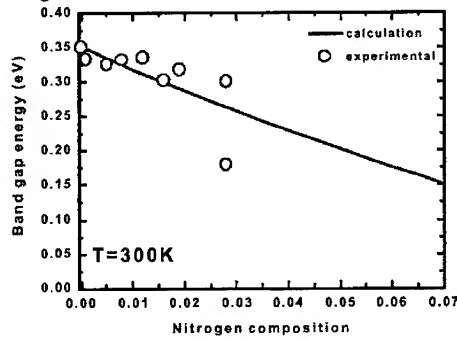


Figure 3. Composition dependence of the band gap of InAsN. The solid circles are experimental data and the solid line is calculated with the BAC model.

Table II gives the values of the E_v , E_{BM} , E_{BGN} , E_F and V_{NM} obtained from the above calculation, along with the residual carrier concentration N_D and absorption edge E_{abs} from the experiments. By fitting of $V_{NM} = C_{NM} x^{1/2}$ to the plot of V_{NM} versus the square root of nitrogen composition ($x^{1/2}$), the best fitted C_{NM} , the coupling parameter, in InAs, is 1.92eV.

Deducting the effect of E_{BM} and E_{BGN} on the band gap from the absorption peak edge gives the corrected band gap energy E_v of each InAsN sample. Fig. 3 shows the composition dependence of the corrected band gap energy of InAsN. It is clear that the bowing effect reappears in these samples. The solid line in this figure represents band gaps calculated based on BAC model carried out in this study. As can be seen, the experimental results are close to the theoretical curve calculated from BAC model. The estimated transition energy shrinkage coefficient of our bulk InAsN is -14 meV/at %.

Table II. A summary of the computed and experimental energy involved in the self-consistent approach as described in the text. All energies are in eV.

Sample No.	N (%)	E_{abs}	E_F	$E_v (k_F)$	E_{BM}	E_{BGN}	E_v
C1076	0.5	0.439	0.134	0.013	0.147	0.032	0.324
C1077	1.6	0.439	0.157	0.019	0.176	0.038	0.301
C1078	2.8	0.434	0.255	0.061	0.316	0.061	0.179
C1117	0.8	0.419	0.106	0.01	0.116	0.028	0.331
C1118	1.2	0.405	0.089	0.007	0.096	0.025	0.334
C1129	0.1	0.409	0.094	0.008	0.102	0.026	0.333
C1130	0.5	0.415	0.117	0.012	0.129	0.021	0.317
C1132	2.8	0.423	0.142	0.017	0.159	0.036	0.300

To verify the effective mass increment predicted by BAC models, we performed measurements of the infrared reflectivity and Hall effect from which the plasma frequency ω_p and Hall electron concentration n_D in these InAsN samples were determined. The plasma frequency and the calculated electron effective mass of InAsN samples are summarized in Table I. As can be seen, a very large increase of the effective mass is found in samples with higher N composition, which it is in good qualitative agreement with the predictions of the BAC model. The electron effective mass of the C1078 is extraordinary larger than other samples. This result supports the arguments we use to interpret the extraordinary low mobility for the same sample in previous Hall results.

CONCLUSION

InAsN alloys with various N compositions were successfully grown on InP substrate by using plasma-assisted GSMBE. When N composition increases, InAsN film has broader FWHM in DXRD spectrum and higher residual carrier concentration. Dramatic increase on the electron effective mass and decrease on the carrier mobility due to the N incorporation in InAsN alloy were observed. The absorption edge of InAsN alloy, as compared to that of InAs, shows blue-shift energy. After considering the energy shift due to residual carrier concentration from the absorption peak edge based on the band anticrossing theory, the bowing effect reappears in these InAsN samples.

Acknowledgement

This work was supported by the National Science Council and the Ministry of Education of the Republic of China under Contract No. NSC 89-2215-E-002 -034 and 89-N-FA01-2-4-3, in respectively.

REFERENCE

1. M. Kondow, K. Uomi, T. Kitatani, S. Watahiki, and Y. Yazawa, *J. Crystal Growth* **164**, 175 (1996).
2. W. Shan, W. Walukiewicz, J. W. Ager III, E. E. Haller, J. F. Geisz, D. J. Friedman, J. M. Olson, and S. R. Kurtz, *Phys. Rev. Lett.* **82**, 1221 (1999).
3. E. Burstein, *Phys. Rev.* **93**, 632 (1954).
4. D. K. Shih, H. H. Lin, L. W. Song, T. Y. Chu, and T. R. Yang, *Proceeding of 13th Indium Phosphide and Related Materials*, Nara, Japan (2001), p.555.
5. H.P. Hjalmarson, P. Vogl, D. J. Wolford, and J. D. Dow, *Phys. Rev. Lett.* **44**, 810 (1980).
6. Y. C. Ruan and W. Y. Ching, *J. Appl. Phys.* **262**, 2885 (1987).
7. J. Stiens and R. Vounckx, *J. Appl. Phys.* **76**, 3526 (1994).
8. X. Zhang, S. J.Chua, W. Liu, and K. B. Chong, *Appl. Phys. Lett.* **72**, 1890 (1998).
9. D. C. Reynolds, D. C. Look, and B. Jogai, *J. Appl. Phys.* **88**, 5760 (2000).
10. V. Swaminathan and A. T. Macrander, *Materials Aspects of GaAs and InP Based Structures* (Prentice-Hall, New Jersey, 1991), p.21.
11. W. Dobbelaere, J. De Boeck, P. Van Mieghem, R. Mertens, and G. Borghs, *J. Appl. Phys.* **69**, 2536 (1991).

Nature and Formation of Non-Radiative Defects in GaNAs And InGaAsN

W. M. Chen¹, N.Q. Thinh¹, I. A. Buyanova¹, P.N. Hai¹, H. P. Xin², C. W. Tu², Wei Li³, M. Pessa³

¹Department of Physics and Measurement Technology, Linköping University, S-581 83 Linköping, SWEDEN

²Department of Electrical and Computer Engineering, University of California, La Jolla, CA 92093-0407, USA

³Optoelectronics Research Center, Tampere University of Technology, FIN-33101 Tampere, Finland

ABSTRACT

The optically detected magnetic resonance (ODMR) technique has been employed to examine the nature and formation mechanism of non-radiative defects in GaNAs and InGaAsN. In both alloys, two defects were observed and were shown to be deep-level, non-radiative recombination centers. One of the defects has been identified as a complex involving an As_{Ga} antisite. These two defects gain more importance with increasing N composition up to 3%, presumably due to an increase in their concentration. With a further higher N composition, the defects start to lose importance in carrier recombination that is attributed to an increasingly important role of other new non-radiative channels introduced with a high N composition. On the other hand, effect of In composition up to 3% seems to be only marginal. Both defects were shown to be preferably introduced in the alloys during low-temperature growth by molecular beam epitaxy (MBE), but can be rather efficiently removed by post-growth rapid thermal annealing.

INTRODUCTION

N-containing III-V alloys, such as InGaAsN and GaNAs, are known to exhibit intriguing fundamental properties including giant bandgap bowing, that has attracted much interest in potential application for near infrared optoelectronic devices [1]. Unfortunately, radiative efficiency of the alloys has been shown to degrade rapidly with N incorporation largely attributed to the formation of competing non-radiative defects. However, very little is so far known about the nature of these defects and mechanism for their formation in the alloys. In this paper we shall provide some physical insight to grown-in non-radiative defects in GaNAs and InGaAsN derived from optically detected magnetic resonance (ODMR) studies.

EXPERIMENTAL DETAILS

Both GaNAs and InGaAsN alloys (either thick epilayers or multiple quantum well structures) studied in this work were grown by gas-source molecular-beam epitaxy (GS MBE). The thick GaNAs (typically 1100 Å) and InGaAsN epilayers (5000 Å) were grown at low temperatures, i.e. 420 °C and 440 °C, respectively. The N composition varies over the range 0-2.3% whereas the In composition is either 0% or 3%. The 7-period GaAs/GaNAs (200Å/70Å) multiple quantum wells (MQW), on the other hand, were grown either at a low temperature of 420 °C or at a high temperature of 580 °C. To study the effect of post-growth annealing, a piece of each low-temperature grown sample was treated by rapid thermal annealing (RTA) at 750-850 °C for 10-30 seconds in a flowing N₂ ambient.

ODMR experiments were performed at 2-5 K and with two microwave frequencies, i.e. X-band (9.28-GHz) and W-band (95-GHz), to cross-examine the contributions from various defects. The samples were illuminated by the 351 nm line of an Ar-ion laser or a tunable Ti:sapphire laser, to provide optical excitation above the GaAs bandgap or below the GaAs bandgap (resonant excitation of the GaNAs and InGaAsN alloys). The resulting photoluminescence (PL) was detected by a Ge-detector. The modulation of the PL intensity induced by the microwave radiation upon spin resonance was detected by a lock-in technique, giving rise to the ODMR signal [2].

EXPERIMENTAL RESULTS AND DISCUSSION

Nature of the non-radiative defects

Figure 1 shows typical ODMR spectra from the GaNAs and InGaAsN, obtained at two microwave frequencies. In both alloys, two non-radiative defects have been detected. The arguments for the non-radiative nature are: 1) both ODMR signals are negative in sign, meaning a spin-resonance induced decrease in PL intensity as a consequence of enhanced non-radiative recombination [2-3]; 2) the ODMR signal could be detected via any PL emissions of different origin in the alloys [2-3]. One of the ODMR signals (i.e. "1") exhibits resolved hyperfine structure, characteristic for a sizable interaction between an unpaired electron spin $S=1/2$ and a nuclear spin $I=3/2$. This provides unambiguous proof for the involvement of a defect atom with a

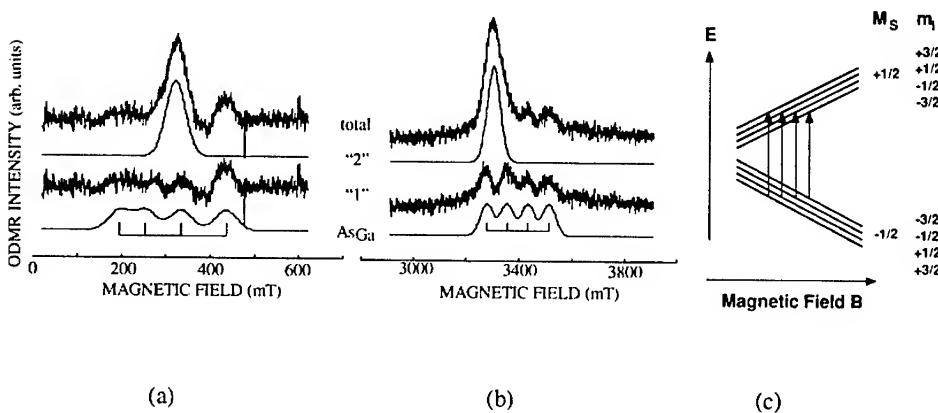


Figure 1. Typical ODMR spectra from the GaNAs and InGaAsN alloys, obtained at microwave frequencies of (a) 9.28 GHz and (b) 95 GHz. From the ODMR spectra, two ODMR signals (denoted by "1" and "2") can be deconvoluted. The former contains a four-line hyperfine structure, characteristic for a defect with an electronic spin $S=1/2$ ($M_S = -1/2, +1/2$) and a nuclear spin $I=3/2$ ($m_I = -3/2, -1/2, +1/2, +3/2$) as illustrated in (c) where the vertical arrows depict the spin resonance transitions. The ODMR signal "2" arises from a deep-level defect with $S=1/2$ and a g-factor of 2.03. The lowest curves are simulated ODMR spectra assuming the involvement of an As_{Ga} antisite complex.

nuclear spin $I=3/2$ in the defect core. The only plausible candidates in the studied materials are As or Ga atoms, both having $I=3/2$ from the isotope(s) with 100% natural abundance. Judging from the strength of the hyperfine interaction by comparing to earlier results from the parent binary compound GaAs and related ternary alloys [4-10], however, it can be concluded that the ODMR signal "1" arises most likely from a complex defect involving an As_{Ga} antisite. The other non-radiative defect has an effective electronic spin $S=1/2$ and gives rise to an isotropic ODMR signal "2". The exact chemical identity could not be obtained, unfortunately, due to the lack of resolved hyperfine structure. The g-value of the two defects was determined to be both around 2 [10], which strongly deviates from the known values for shallow-level impurities or defects and can therefore be regarded as support for the deep-level nature of the defects. Such type of defects is known to act as efficient recombination centers, very often non-radiative and harmful for optical quality of semiconductors. The results from the ODMR investigation under resonant excitation of the GaNAs and InGaAsN confirmed that both defects reside within the alloys.

Formation of the non-radiative defects

A series of GaNAs samples (both epilayers and MQW) were studied by ODMR to reveal the effect of N incorporation on the formation of the non-radiative defects. The results from the low temperature grown GaNAs MQW are presented in Fig.2. It is rather apparent that the ODMR

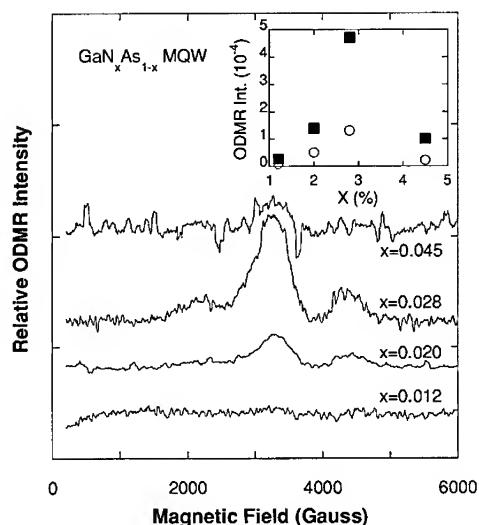


Figure 2. ODMR spectra at 9.28-GHz from the $\text{GaN}_x\text{As}_{1-x}$ MQW grown at 420 °C, as a function of N composition x . The normalized intensities of the ODMR signals "1" (the As_{Ga} antisite complex) and "2" vs. x are plotted in the inset, by the squares and circles, respectively.

intensity of both defects increases with increasing N composition up to about 3 %. This observation is believed to be largely due to an increase in the concentration of the corresponding defects. With a further increase in the N composition above 3%, the ODMR signals start to decrease. We believe that this is more likely due to a decreasing importance (rather than a decrease in the concentration) of the studied non-radiative defects, as a result of new, more efficient non-radiative defects being introduced with increasing N composition. The exact turning-point value of the N composition depends critically on growth conditions, such as growth temperature and strain.

The effect of In incorporation in the alloys on the formation of the studied non-radiative defects has, on the other hand, been found to be rather marginal at least within the range studied (<3%). This can be seen from Fig.3 where the ODMR spectrum from the InGaAsN epilayer is in a close comparison with that from the GaNAs epilayer.

In contrast, the effect of growth temperature on the formation of the studied defects is quite dramatic as shown in Fig.4. A significant reduction of the ODMR signals related to the studied non-radiative defects was observed in the MQW samples grown at 580 °C as compared to that with a similar N composition but grown at 420 °C. This provides strong evidence that these defects are preferably introduced during non-equilibrium growth at the lower temperature [11,12]. The studied non-radiative defects can be rather efficiently removed from the GaNAs and

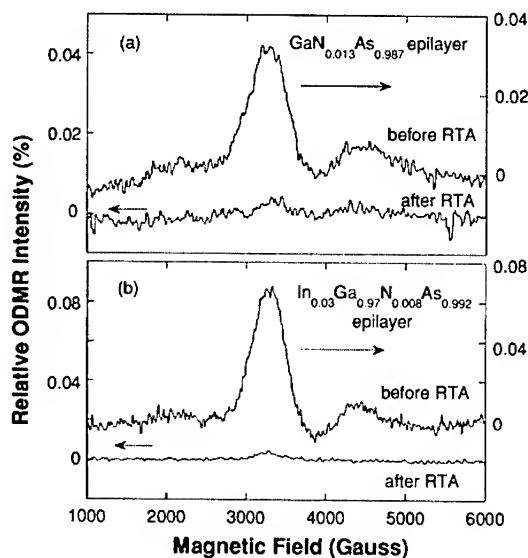


Figure 3. ODMR spectra at 9.28-GHz from the thick GaNAs and InGaAsN epilayers grown at 420 °C and 440 °C, respectively. The ODMR intensity has been normalized to the total PL intensity monitored in the ODMR experiments, and is given in percentages. The ODMR spectra from both as-grown and after the post-growth RTA treatment are shown.

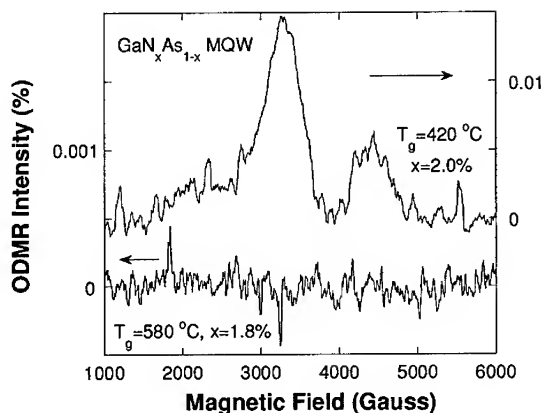


Figure 4. ODMR spectra at 9.28-GHz from two GaNAs MQW structures (with a close-match in N composition) grown at 420 °C and 580 °C, demonstrating the strong effect of growth temperature on the formation of the studied non-radiative defects.

InGaAsN alloys by RTA, see Fig.3. This is accompanied by a significant improvement in the optical quality of the alloys [13-16].

The observed anti-correlation between the ODMR intensity and the PL intensity of the alloys seems to point out that the studied defects may be among the important non-radiative recombination centers, at least within the ranges of the N compositions investigated in this work, that compete and degrade the radiative recombination processes crucial for optoelectronic device applications.

CONCLUSIONS

Two deep-level, non-radiative defects residing in the GaNAs and InGaAsN alloys were detected in the ODMR experiments. One of them exhibits characteristic hyperfine structure, arising from $S=1/2$ and $I=3/2$, which suggests a complex involving the As_{Ga} antisite as being the most likely candidate. We have shown that the introduction rate of these defects increases with decreasing growth temperature and with increasing N composition, leading to an increasingly important role in carrier recombination and thus in degrading optical quality of the material. With a further increase in nitrogen composition to 4.5% in the GaNAs/GaAs MQW structures grown at low temperature, the ODMR signals start to decrease probably due to the introduction of other competing defects that overshadow the role of the studied defects in carrier recombination. Post-growth rapid thermal annealing can significantly suppress the influence of the studied non-radiative defects in both GaNAs and InGaAsN alloys, accompanied by a drastic improvement in the efficiency of light emission.

ACKNOWLEDGEMENTS

The authors would like to acknowledge the financial support of the Swedish Natural Science Research Council (NFR). The work at UCSD is partially supported by the National Renewable Energy Laboratory (#AAD-9-18668-07)

REFERENCES

1. For a recent review, see, for example, I.A. Buyanova, W.M. Chen and B. Monemar, MRS Internet J. Nitride Semicond. Res. **6**,2 (2001).
2. For a recent review, see, for example, W.M. Chen, Thin Solid Films **364**, 45 (2000).
3. W.M. Chen and B. Monemar, Appl. Phys. **A53**, 130 (1991).
4. T.A. Kennedy and M.G. Spencer, Phys. Rev. Lett. **57**, 2690 (1986).
5. J.M. Trombetta, T.A. Kennedy, W. Tseng and D. Gammon, Phys. Rev. **B43**, 2458 (1991).
6. T. Wimbaur, M.S. Brandt, M.W. Bayerl, M. Stutzmann, D.M. Hofmann, Y. Mochizuki and M. Mizuta, Mat. Sci.Forum **258-263**, 1309 (1997).
7. For a recent review, see e.g., F.K. Koschnick and J.-M. Spaeth, phys. Stat. Sol. (b) **216**, 817 (1999).
8. H.-J. Sun, G.D. Watkins, F.C. Rong, L. Fotiadis and E.H. Poindexter, Appl. Phys. Lett. **60**, 718 (1992).
9. K. Krambrock, M. Linde, J.-M. Spaeth, D.C. Look, D. Bliss and W. Walukiewicz, Semicond. Sci. Technol. **7**, 1037 (1992).
10. N. Q. Thinh, I. A. Buyanova, P. N. Hai, and W. M. Chen, Phys. Rev. B **63**, 033203 (2000).
11. A. Ougazazaden, Y. Le Bellego, E. V. K. Rao, M. Juhel, L. L. Leprince, and G. Patriarche, Appl. Phys. Lett. **70**, 2861 (1997).
12. I.A. Buyanova, W.M. Chen, B. Monemar, H. P. Xin and C. W. Tu, Appl. Phys. Lett. **75**, 3781 (1999).
13. S. Francoeur, S. Sivaraman, Y. Qui, S. Nikishin, and H. Tempkin, Appl. Phys. Lett. **72**, 1857 (1998).
14. E. V. K. Rao, A. Ougazazaden, Y. Le Bellego, and M. Juhel, Appl. Phys. Lett. **72**, 1409 (1998).
15. I.A. Buyanova, G. Pozina, P.N. Hai, N.Q. Thinh, J.P. Bergman, W.M. Chen, H. P. Xin and C. W. Tu, Appl. Phys. Lett. **77**, 2325, (2000).
16. L. H. Li, Z. Pan, W. Zhang, Y. W. Lin, Z. Q. Zhou, and R. H. Wu, J. App. Phys. **87**, 245 (2000).

Deep Centers and Their Capture Barriers in MOCVD-Grown GaN

Daniel K. Johnstone^a, Mohamed Ahoujja^b, Yung Kee Yeo^c, Robert L. Hengehold^c, Louis Guido^d

^aAir Force Office of Scientific Research, Arlington, VA 22203, USA

^bUniversity of Dayton, Dayton, OH 45469, USA

^cAir Force Institute of Technology, Wright-Patterson AFB, OH 45433, USA

^dVirginia Polytechnic Institute and State University, Blacksburg, VA 24061, USA

ABSTRACT

GaN and its related alloys are being widely developed for blue-ultraviolet emitting and detection devices as well as high temperature, high power, and high frequency electronics. Despite the fast improvement in the growth of good quality GaN, a high concentration of deep level defects of yet unconfirmed origins are still found in GaN. For both optical and electronic devices, these deep carrier traps and/or recombination centers are very important and must therefore be understood. In the present work, deep level defects in GaN grown on sapphire substrates by metal organic chemical vapor deposition (MOCVD) have been investigated using Isothermal Capacitance Transient Spectroscopy (ICTS) and Current Voltage Temperature (IVT) measurements. Several deep level electron traps were characterized, obtaining the emission energy, concentration, and capture cross section from a fit of exponentials to the capacitance transients. ICTS was also used to reveal information about the capture kinetics involved in the traps found in GaN by measuring the amplitude of the capacitance transient at each temperature. At a reduced filling pulse where the traps were not saturated, several of them showed marked reduction in capacitance transient amplitude when compared to the transient amplitude measured under conditions where the filling pulse saturates the traps. This reduction in transient amplitude indicates that there is a barrier to carrier capture, in addition to the emission barrier. It has been found that several traps had capture barriers that were significant fractions of the emission energies up to 0.32 eV. These capture barriers may lead to persistent photoconductivity and reduced trapping. In this paper, deep level emission energies as well as capture barrier energies found in MOCVD-grown GaN will be discussed.

INTRODUCTION

In spite of considerable work to develop gallium nitride based materials, there is still much to be done to understand the nature of the defects. GaN is desirable for applications toward higher density memory,¹ high power microwave devices and high temperature devices,²⁻⁴ and UV photodetection.⁵⁻⁷ Current studies of the material include investigations of dopants to increase the carrier activation,⁸ metallizations to reduce contact resistance or improve rectifying ideality,⁹⁻¹¹ extensive efforts to improve the quality of the epitaxial material, and myriad characterization methods that have been employed to understand the origin and role of defects.¹²⁻¹⁴ Lack of high quality lattice-matched substrates for epitaxy is receiving most of the development focus. Epitaxial growth on sapphire and silicon carbide are two of the more prevalent methods. Silicon substrates are also being used. Growth is accomplished by many of the common methods including molecular beam epitaxy, metal-organic chemical vapor deposition (MOCVD), vapor phase epitaxy, and others. Circumventing the high density of threading dislocations has lead to innovative approaches such as lateral epitaxial overgrowth,^{15,16} and pendeo-epitaxy,^{17,18} but also using thick buffer layers.^{19,20} The success of these efforts has

been progressing steadily, interspersed occasionally with devices that have demonstrated record performance. However, much of the work has demonstrated the limited maturity of the material, compared to other zincblende III-Vs. Current collapse in field effect devices is one of the difficulties that are presently being addressed.^{21, 22} Limited lifetime for lasers based on nitrides also presents a vexing problem.²³ High concentrations and varied types of defects are recognized as the source of these difficulties. Understanding the characteristics of these defects is an important step in reducing their effects.

EXPERIMENTAL

ICTS diode preparation

GaN films were grown using MOCVD technique using a standard two-step growth process, beginning with a 300 Å GaN buffer layer grown at 550 °C on sapphire substrates, followed by a 2 µm thick n-type GaN test layer. Before contact fabrication, the samples were degreased in solvents, followed by an acid clean in aqua regia (HCl:nitric acid = 3:1) and a dip in de-ionized water. Ohmic contacts were made by depositing Ti(400 Å)/Al(2000 Å), and alloying them under an N₂ atmosphere at 900 °C for 30 seconds in a rapid thermal anneal system. Schottky barrier diodes were made by using a 250 µm diameter of Ni(1000 Å)/Au(1000 Å) contacts. Room temperature carrier concentration is $\sim 8 \times 10^{16} \text{ cm}^{-3}$, while the room temperature mobility is 250 cm²/V-sec.

Deep level characterization

Deep levels in epitaxial GaN were characterized using isothermal capacitance transient spectroscopy (ICTS) and by current-voltage-temperature (IVT) measurements. The ICTS experimental setup uses a data acquisition board to record the entire capacitance transient, and fits the recorded transients for one or two exponential components. The capacitance is measured using a SULA meter with minimum conversion time of 10 µsec. Data acquisition is performed by a high-resolution 16-bit National Instruments board. Representative conditions are to record ~400 points, averaged over ~1000 transients at each temperature, stepping the temperature every 2-5 K. The ICTS equipment can detect a deep level concentration of $\sim 5 \times 10^{-5} n_s$ and greater, where n_s is the shallow carrier concentration. Once the transients are acquired, they are fit using modulating functions and least squares analysis²⁴ or commercial curve fitting software. This method of exponential transient fitting has the capability of separating several overlapping emission signals. The analysis fits the capacitance as a function of time, t , given by

$$C(t)^2 = \sum_{i=0} A_i \exp(-e_i t), \quad (1)$$

where A_i is the squared amplitude of the transient due to the i^{th} energy level at a given temperature. A_0 is the steady state value of capacitance squared with $e_0=0$, and e_i is the emission rate of the i^{th} energy level. The transients can be fit for one, two, or three exponential components. Then the emission rates are taken from the fit with the smallest least squares error and used to form the Arrhenius plot. The activation energy of the trap is obtained from the slope of the Arrhenius plot, and the capture cross section is obtained from the vertical axis intercept. The trap concentration is determined from the amplitude of each transient. The method of recording and fitting the entire transient used here has been shown to be more accurate than rate-

window methods.²⁵ As data acquisition has become faster and available as an add-in board for personal computers, the method of recording and analyzing the entire transient is gradually replacing the earlier method of rate windows.

Typically, the trap energy, capture cross section, and concentration are reported characteristics. Analysis assumes that the measured characteristics of the capture cross section are not dependent on temperature. This condition is met if the filling pulse is long enough to saturate the traps over the temperature range of interest. However, several models of capture have been proposed, some of which are temperature dependent. More thorough investigation of the capture cross sections of traps will contribute to the better understanding of the materials, and contribute to the understanding of each of the models. Recording the entire transient capacitance versus time and temperature facilitates measurement of the capture barrier using a single temperature scan. Otherwise, several temperature scans must be done using the rate window method, varying the filling pulse width each time.²⁶ Adding the capture mechanisms to the other deep level characteristics that are usually reported will provide more accurate information for predicting carrier lifetimes used in device design.

Among the models for capture, three of the more prominent capture processes are cascade capture, capture by multi-phonon emission, and capture associated with Auger recombination. Lax proposed the model of capture as an electron cascading through closely spaced, extended states.²⁷ The carrier loses energy by emitting a phonon between each extended state. The process of cascade capture has negative temperature dependence as an exponent of temperature, T^{-1} . A deeper Coulombic level would have lower energy levels spaced too far apart to allow transitions accompanied by the loss of only one phonon. In this case, simultaneous emission of multiple phonons has been shown to take place.²⁸ As opposed to cascade capture, multi-phonon emission has a cross section that increases exponentially with increasing temperature, with a characteristic activation energy. The energy loss can be realized by a relaxation or a distortion of the lattice. The method used in this paper to extract the activation energy applies only to capture barriers due to multi-phonon emission.

In an ICTS experiment, a filling pulse that saturates the trap is required in order to obtain accurate trap emission energy and capture cross section from the Arrhenius plot. If saturating conditions are achieved, then the trap depth, E_T , and the capture cross section, σ , are obtained from the slope and intercept of a plot of the emission rate versus $1/kT$, respectively. Alternatively, the capture barrier can be measured by using a narrower, non-saturating filling pulse. The barrier for capture by multi-phonon emission is evident from the change in the amplitude of the capacitance transient as the temperature increases.

The concentration of filled traps, N_T^0 , is

$$N_T^0 = N_T \left[1 - \exp \left(-t_f \sigma_{\infty} v_{th} n_s e^{-\frac{E_b}{kT}} \right) \right] \quad (2)$$

N_T is the total trap concentration, t_f is the filling pulse width, σ_{∞} is the high temperature capture cross section, v_{th} is the thermal velocity, n_s is the shallow carrier concentration. E_b is the activation energy of the capture process, k is Boltzmann's constant, and T is the temperature. In practice, to measure the capture barrier, the temperature is set for maximum response from the trap. Then the pulse width is reduced until there is a reduction in capacitance transient amplitude, but wide enough so that the transient amplitude is well above the noise level. Next, the transients are recorded at temperature steps covering the entire temperature range where the trap responds. Equation (2) shows that as the temperature increases, the concentration of filled

traps increases until the exponential term goes to zero and the trap is saturated. The change in concentration of filled traps is reflected in the amplitude of the capacitance transient.

Fitting of the capacitance transients provides trap concentration versus temperature, which can then be fit according to equation (2) to obtain the capture barrier energy. This method is similar to other methods of measuring the capture barrier but doesn't require the complexities of repeated temperature scans or elaborate pulse shaping.^{29,30}

Equation (2) can be reorganized to facilitate extraction of the capture barrier energy using the familiar Arrhenius relationship, as in the analysis by Criado, et al.:²⁹

$$\ln(1 - C/C_0) = KT^{-1/2} \exp(-E_b/kT). \quad (3)$$

C is the capacitance transient amplitude at temperature T using a filling pulse of width t_f , C_0 is the transient capacitance amplitude for a very long charging time, K is a proportionality factor that is constant with temperature. This equation is appropriate if capture is by multi-phonon emission.

RESULTS

Figure 1a shows the ICTS spectra for the n-type GaN grown by MOCVD under two different filling pulse conditions. The filling pulse width was 10 msec and 50 μ sec for these rate window plots. Curve fitting analysis of the three peaks reveals four traps. The corresponding Arrhenius plot is shown in figure 1b. The characteristics of E1 and E2 are $E_T=0.190$ eV, $\sigma=3 \times 10^{-15}$ cm², and $E_T=0.253$ eV, $\sigma=9 \times 10^{-16}$ cm², respectively. The peak at 300K was deconvolved to two traps labeled E3 and E4, with characteristics $E_T=0.548$ eV, $\sigma=2 \times 10^{-15}$ cm², and $E_T=0.613$ eV, $\sigma=9 \times 10^{-15}$ cm², respectively.

The result of the IVT measurements are shown in figure 2. The energy levels are measured for three values of the reverse bias, -1 V, -2 V, and -3 V. The dominant generation center from IVT measurements is at 0.54 eV. As the reverse bias increases, the measured energy decreases, as shown in the figure. The reduction in generation center energy with increasing reverse bias reveals the donor nature of this deep level.

Reducing the filling pulse from 10 msec down to 50 μ sec was used to detect traps with a temperature dependent capture cross section. The traps at E2, E3 and E4 all showed evidence of a temperature dependent capture cross section. Further measurements were made for analyzing the transient amplitude as a function of temperature, in order to obtain more information regarding the trapping mechanism.

Further evidence is shown in plots of the concentration of filled traps as a function of temperature, which are obtained from the amplitude of the transients as they change with temperature. The amplitude obtained for the low temperature peaks is plotted in figure 3a with and without the saturating filling pulse for the traps appearing in the rate window plot between 100K and 175K. Note that trap E1 has a higher concentration with a reduced filling pulse width, although it is not evident from the rate window plot of figure 1. Trap E2 shows the behavior that is expected for reduced filling pulse width, where the curves merge at sufficiently high temperature.

The amplitude data extracted from the capacitance transients between 275K and 400K are shown in figure 3b. An interesting observation is that the two traps show competing trapping behavior. Trap E3 is filled at the expense of trap E4 over a broad range of temperature from 300 to 340K. This behavior can be explained as arising from a defect that can trap two electrons. The emission energy for the second trapped electron is reduced due to Coulomb repulsion.

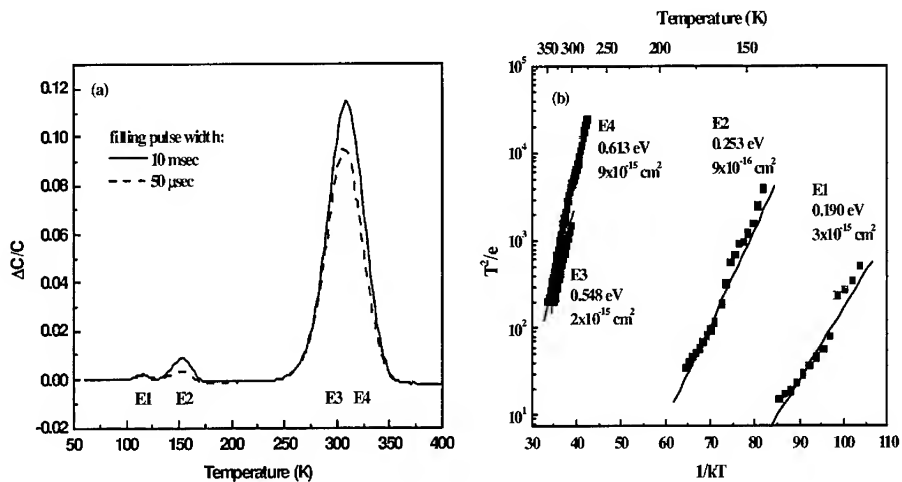


Figure 1. a. Rate-window plot for n-type GaN grown by MOCVD. The rate window is 51/sec. b. Arrhenius plots for n-GaN grown by MOCVD for each peak in figure 1a.

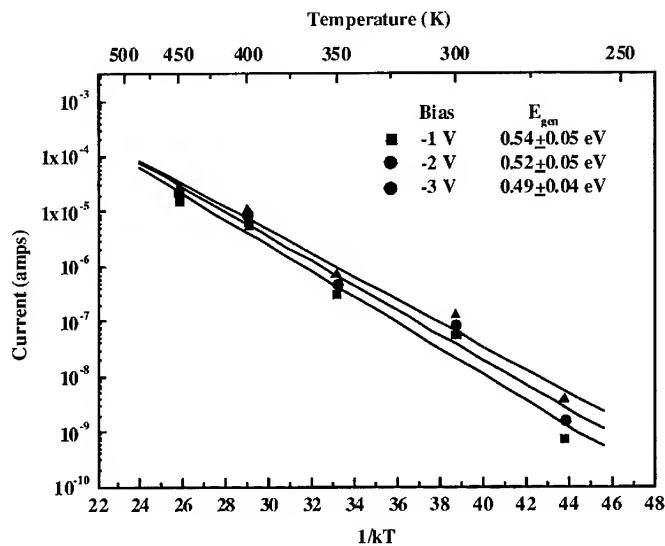


Figure 2. Arrhenius plot from the IVT measurements. The generation current activation energy decreases with increasing reverse bias.

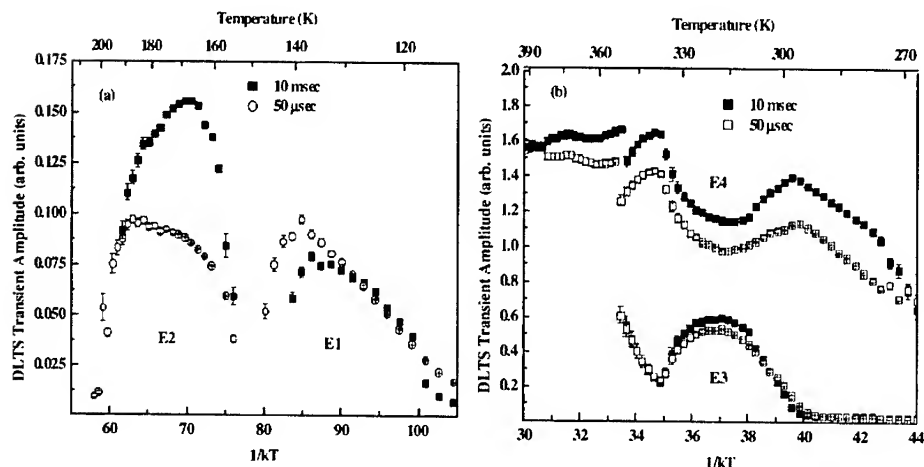


Figure 3. a) Comparison of the transient amplitude (concentration) of filled traps from a saturating 10 msec filling pulse and a non-saturating 50 μ sec filling pulse for MOCVD grown GaN for the pair of peaks shown at low temperature in figure 1a. b) Capacitance transient amplitude for GaN grown by MOCVD. The data corresponds to the peak near room temperature in the rate window plots of figure 1a. The lower curves correspond to the 0.548 eV trap and the upper curves correspond to the 0.613 eV trap.

Capture barriers for the traps were determined using equation 3. Although, the signal strength was not high enough for analysis of the capture barrier for E1 and E2. Figure 4 shows the capture barriers for E3 and E4. The trap E3 at 300K has a capture barrier of 0.32 eV as shown in the figure. Trap E4, with higher concentration, has a capture barrier of 0.12 eV.

DISCUSSION

Trap E1 is very similar to a trap that has been attributed to a nitrogen vacancy.^{31,32} If E1 and E2 are part of a defect that can trap two electrons, the reduced filling pulse preferentially fills traps with one electron. A wider filling pulse should fill the defect with two electrons. However, the emission energy of the trap filled with two electrons would be expected to be lower due to Coulomb repulsion. The observation of higher occupation of the lower energy trap, E1, at narrow filling pulse with is evidence for assignment of a negative U binding energy arrangement, where the configuration changes to make the trapping of two electrons more tightly bound than one electron. Trap E2 has been reported previously for several different growth methods, although the origin has not been determined.^{33,34}

Other studies of the electron trap E3 at 0.55 eV in various heterostructures found that the density of the trap does not change much from structure to structure or from undoped to Mg doped p-GaN.³⁵ It is a commonly reported deep level in GaN grown under many different conditions, suggesting that it is not related to impurities.^{35,36} The coupled relationship between the traps at 0.55 and 0.61 eV in the present work, labeled E3 and E4, respectively, indicate that

the trap at 0.55 eV is a defect complex with the 0.61 eV trap. Also, Hullavarad *et al.* reported that the 0.6 eV level has its origin in nitrogen vacancies and vacancy clusters.³⁷

The IVT measurement of a dominant generation center at 0.54 eV at -1 V corresponds to the trap labeled E4 at 0.61 eV measured with ICTS at -1.5 V. IVT is an equilibrium measurement, where ICTS measurements are made under nonequilibrium conditions. Therefore, IVT will measure the energy difference between the ground state of the defect and the bottom of the conduction band. The energy measured by ICTS is from the ground state of the defect to the top of the capture barrier energy, which is 0.12 eV for E4. The difference between the emission energy and the capture barrier energy measured by ICTS is thus 0.49 eV, which compares well to a value of 0.53 ± 0.05 eV for IVT, when interpolated to -1.5 V. E4 is also expected to be the dominant defect because of its position nearest to mid-gap, larger cross section, smaller capture barrier, and higher concentration compared to the other traps that are present.

The remarkable feature of these measurements is the common occurrence of capture barriers for many of the traps. Several other studies have also observed evidence for capture barriers. In other work, four energy levels were characterized in GaN on sapphire, each of which had thermal ionization energy less than the value of the optical ionization energies.³⁸ In that study, an increase in photoionization cross section with increasing illumination energy was reported, similar to the studies of the DX center in AlGaAs. The difference in optical and thermal ionization energies and the increase in photoionization cross section are due to a lattice relaxation associated with a capture barrier for the DX center. Polyakov, *et al.* has also pointed out that persistent photoconductivity (PPC), which is due to the presence of a capture barrier, is a common feature in GaN and can be responsible for the current collapse in field effect transistors.³⁹ A capture barrier of 0.2 eV was measured in their work, although the associated thermal emission energy was unknown. The reason they suggested for the capture barrier was

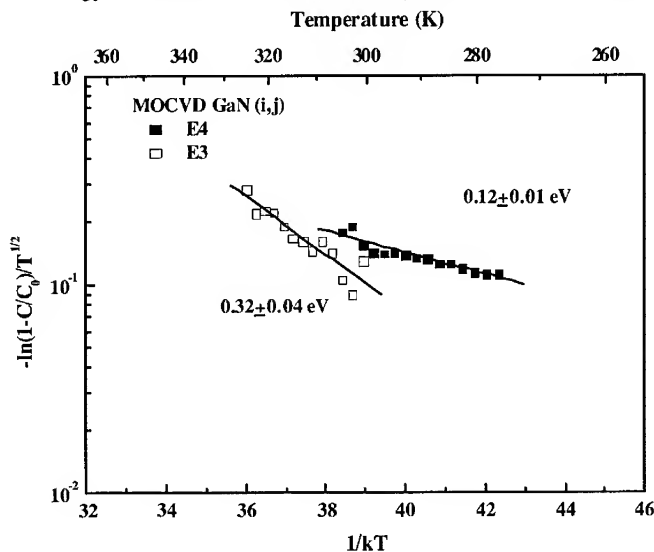


Figure 4. Arrhenius plots for GaN grown by MOCVD. The energies given are the capture barriers for the traps shown in Fig. 5.

that it is due either to a lattice relaxation, or to electrostatic potential variations in the samples resulting from non-uniformly distributed, electrically active donor and acceptor centers.

An alternative explanation for the prevalence of capture barriers could be offered by the very strong piezoelectric effect found in GaN. The lack of inversion symmetry in nitrides gives rise to piezoelectric effects when strained along [0001], which can be an order of magnitude larger than other III-Vs.⁴⁰ In addition to the strain effects, the greater screening of defects by surrounding core ion charges, reflected by the larger polarizability in GaN, needs to be taken into account. It is possible that the electrons bound to ions surrounding the defect shift toward or away from the defect to a greater extent than in other III-V materials, such as GaAs, creating a potential barrier. The effect has been addressed in applications toward nitride quantum well structures, but not for point defects or defect complexes.⁴¹

CONCLUSION

Four electron traps were measured by ICTS in MOCVD GaN. The deep levels are measured at $E1=0.190$ eV, $E2=0.253$ eV, $E3=0.548$ eV, and at $E4=0.613$ eV. The dominant generation center was determined by IVT to be the donor trap E4. Changes in the filling pulse width showed the presence of capture barriers in several of the traps. Additional analyses were performed to extract the amplitude of the capacitance transients as a function of temperature, both for saturating filling conditions and non-saturating filling conditions, in order to obtain the capture barriers. E1 and showed a behavior consistent with a defect center having a negative U binding energy arrangement. Displaying the transient amplitude as a function of temperature also revealed coupled defect behavior between E3 and E4 where E3 was filled at the expense of the occupation of E4. Capture barriers were determined to be 0.32 eV for E3, and 0.12 eV for E4. The prevalence of capture barriers is suggested to be a basic property of the nitrides, which may be due to the large polarizability, requiring further study.

REFERENCES

1. A. Hayami, M. Mochizuki, J. Tonami, H. Nakamura, and M. Itonaga, "High density optical disk system using D8-15 modulation code and new signal-processing techniques," *IEEE Transactions on Consumer Electronics* **46**, pp. 555-561, 2000.
2. L. Zhang, L. Lester, A. Baca, R. Shul, P. Chang, C. Willison, U. Mishra, S. Denbaars, J. Zolper, "Epitaxially-grown GaN junction field effect transistors," *IEEE Transactions on Electron Devices* **47**, pp. 507-511, 2000.
3. K. Kunihiro, K. Kasahara, Y. Takahashi, Y. Ohno, "Microwave performance of 0.3- μ m gate-length multi-finger AlGaIn/GaN heterojunction FETs with minimized current collapse," *Jpn. J. Appl. Phys. Suppl.* **39**, pp. 2431-2434, 2000.
4. S. Binari, W. Kruppa, H. Dietrich, G. Kelner, A. Wickenden, J. Freitas, "Fabrication and characterization of GaN FETs," *Solid-State Electron.* **41**, pp. 1549-1554, 1997.
5. A. Saxler, "A review of the electrical properties of $Al_xGa_{1-x}N$ materials for UV photodetector applications," *Proceedings of the SPIE* **3948**, pp. 330-341, 2000.
6. P. Sandvik, D. Walker, P. Kung, K. Mi, F. Shahedipour, v. Kumar, X. Zhang, J. Diaz, C. Jelen, M. Razeghi, "Solar-blind $Al_xGa_{1-x}N$ p-i-n photodetectors grown on LEO and non-LEO GaN," *Proceedings of the SPIE* **3948**, pp. 265-272, 2000.

- 7 . C. Pernot, A. Hirano, M. Iwaya, T. Detchprohm, H. Amano, I. Akasaki, "Solar-blind UV photodetectors based on GaN/AlGaIn p-i-n photodiodes," *Jpn. J. Appl. Phys., Pt.2* **39**, pp. L387-389, 2000.
- 8 . K. Kim, C. Oh, W. Lee, K. Lee, G. Yang, C. Hong, E. Suh, K. Lim, H. Lee, D. Byun, "Comparative analysis of characteristics of Si, Mg, and undoped GaN," *Journal of Crystal Growth* **210**, pp. 505-510, 2000.
- 9 . A. Zeitouny, M. Eizenberg, S. Pearton, F. Ren, "W and W/WSi/In_{1-x}Al_xN ohmic contacts to n-type GaN," *Materials Science and Engineering* **B59**, pp. 358-361, 1999.
- 10 . J. Rennie, M. Onomura, S. Nunoue, G. Hatakoshi, H. Sugawara, M. Ishikawa, "Effect of metal type on the contacts to n-type and p-type GaN," *Journal of Crystal Growth* **189/190**, pp. 711-715, 1998.
- 11 . Y. Koyama, T. Hashizume, H. Hasegawa, "Formation processes and properties of Schottky and ohmic contacts on n-type GaN for field effect transistor applications," *Solid-State Electronics* **43**, pp. 1483-1488, 1999.
- 12 . M. Johnson, S. Fujita, W. Rowland, K. Bowers, W. Hughes, Y. He, N. El Masry, J. Cook, J. Schetzina, J. Ren, J. Edmond, "MBE growth and properties of GaN on GaN/SiC substrates," *Solid-State Electronics* **41**, pp. 213-218, 1997.
- 13 . J. Chaudhuri, M. Ng, D. Koleske, A. Wickenden, R. Henry, "High resolution X-ray diffraction and X-ray topography study of GaN on sapphire," *Materials Science and Engineering* **B64**, pp. 99-106, 1999.
- 14 . M. Topf, F. Cavas, B. Meyer, B. Kempf, A. Krtschil, H. Witte, P. Veit, J. Christen, "GaN/SiC heterojunctions grown by LP-CVD," *Solid-State Electronics* **44**, pp. 271-275, 2000.
- 15 . M. Razeghi, P. Kung, P. Sandvik, K. Mi, X. Zhang, V. Dravid, J. Freitas, A. Saxler, "LEO of III-nitride on Al₂O₃ and Si substrates," *Proceedings of the SPIE* **3948**, pp. 320-329, 2000.
- 16 . Y. Song, S. Choi, J. Choi, J. Yang, G. Yang, "Lateral epitaxial overgrowth of GaN and its crystallographic tilt depending on the growth condition," *Phys. Status Solidi A* **180**, pp. 247-250, 2000.
- 17 . R. Davis, O. Nam, T. Zheleva, T. Gehrke, K. Linthicum, P. Rajogopal, "Lateral- and pendeo-epitaxial growth and defect reduction in GaN thin films," *Mater. Sci. Forum* **338-342**, pp. 1471-1476, 2000.
- 18 . T. Zheleva, S. Smith, D. Thomson, K. Linthicum, P. Rajogopal, R. Davis, "Pendeo-epitaxy: a new approach for lateral growth of gallium nitride films," *J. Electron. Mater.* **28**, pp. L5-8, 1999.
- 19 . E. Koh, Y. Ju Park, E. Kyu Kim, C. Park, S. Hun Lee, J. Hee Lee, S. Ho Choh, "The effect of N⁺-implanted Si(111) substrate and buffer layer on GaN films," *J. Cryst. Growth* **218**, pp. 214-220, 2000.
- 20 . S. Zamir, B. Meyler, E. Zolotoyabko, J. Salzman, "The effect of AlN buffer layer on GaN grown on (111)-oriented Si substrates by MOCVD," *J. Cryst. Growth* **218**, pp. 181-190, 2000.
- 21 . P. Klein, J. Freitas, S. Binari, "Photoionization spectra of traps responsible for current collapse in GaN MESFETs," *Wide-Bandgap Semiconductors for High-Power, High-Frequency and High-Temperature Applications*, pp. 547-552, 1999.
- 22 . P. Klein, J. Freitas, S. Binari, A. Wickenden, "Observation of deep traps responsible for current collapse in GaN metal-semiconductor field-effect transistors," *Appl. Phys. Lett.* **75**, pp. 4016-4018, 1999.

23. G. Hasnain, T. Takeuchi, R. Schneider, S. Song, R. Twist, M. Blomqvist, C. Kocot, and C. Flory, "On-wafer continuous-wave operation of InGaN/GaN violet laser diodes," *Electronic Letters* **36**, pp. 1779-1780, 2000.
24. P. Kirchner, W. Schaff, G. Maracas, L. Eastman, T. Chappell, C. Ransom, "The analysis of exponential and nonexponential transients in deep-level transient spectroscopy," *J. Appl. Phys.* **52**, pp. 6462-6470, 1981.
25. W. Doolittle, A. Rohatgi, "A new figure of merit and methodology for quantitatively determining defect resolution capabilities in deep level transient spectroscopy analysis," *J. Appl. Phys.* **75**, pp. 4570-4575, 1994.
26. D. Lang, "Deep-level transient spectroscopy: a new method to characterize traps in semiconductors," *J. Appl. Phys.* **45**, pp. 3023-3032, 1974.
27. M. Lax, "Cascade capture of electrons in solids," *Phys. Rev.* **119**, pp. 1502-1523, 1960.
28. C. Henry, D. Lang, "Nonradiative capture and recombination by multiphonon emission in GaAs and GaP," *Phys. Rev. B, Solid State* **15**, pp. 989-1016, 1977.
29. J. Criado, A. Gomez, E. Calleja, and E. Munoz, "Novel method to determine capture cross-section activation energies by deep-level transient spectroscopy techniques," *Appl. Phys. Lett.* **52**, pp. 660-661, 1987.
30. A. Palma, J. Jimenez-Tejada, J. Banqueri, P. Cartujo, and J. Carceller, "Accurate determination of majority thermal-capture cross sections of deep impurities in p-n junctions," *J. Appl. Phys.* **74**, pp. 2605-2612, 1993.
31. Z.-Q. Fang, D. Look, W. Kim, Z. Fan, A. Botchkarev, and H. Morkoc, "Deep centers in n-GaN grown by reactive molecular beam epitaxy," *Applied Physics Letters* **72**, pp. 2277-2279, 1998.
32. F. Auret, S. Goodman, G. Myburg, F. Koschnick, J. Spaeth, B. Beaumont, and P. Gilbert, "Defect introduction in epitaxially grown n-GaN during electron beam deposition of Ru schottky contacts," *Physica B* **273-274**, pp. 84-87, 1999.
33. C. Wang, L. Yu, S. Lau, E. Yu, W. Kim, A. Botchkarev, H. Morkoc, "Deep level defects in n-type GaN grown by molecular beam epitaxy," *Applied Physics Letters* **72**, pp. 1211-1213, 1998.
34. P. Hacke, H. Okushi, T. Kuroda, T. Detchprohm, K. Hiramatsu, N. Sawaki, "Characterization of mid-gap states in HVPE and MOVPE-grown n-type GaN," *Journal of Crystal Growth* **189/190**, pp. 541-545, 1998.
35. A. Polyakov, N. Smirnov, A. Govorkov, M. Mil'vidskii, A. Usikov, B. Pushnyi, and W. Lundin, "Deep centers in AlGaIn-based light emitting diode structures," *Solid State Electronics* **43**, pp. 1929-1936, 1999.
36. H. Cho, C. Hong, K. Kim, E. Suh, and H. Lee, "Deep levels in GaN grown by metalorganic chemical vapor depositions," *Ungyong Mulli* **12**, pp. 456-461, 1999.
37. S. Hullavarad, S. Bhoraskar, S. Sainkar, S. Badrinarayanan, A. Mandale, V. Ganesan, "Deep levels in GaN grown by nitridation of GaAs (110) surface in a electron cyclotron resonance ammonia plasma," *Vacuum* **55**, pp. 121-126, 1999.
38. T. Kang, S. Yuldashev, C. Park, C. Chi, S. Park, Y. Ryu, and T. Kim, "Deep levels in GaN epilayers grown on sapphire substrates," *Solid State Communications* **112**, pp. 637-642, 1999.
39. A. Polyakov, N. Smirnov, A. Govorkov, M. Shin, M. Skowronski, D. Greve, "Deep centers and their spatial distribution in undoped GaN films grown by organometallic vapor phase epitaxy," *Journal of Applied Physics* **84**, pp. 870-876, 1998.

-
40. H. Morkoc, R. Cingolani, B. Gil, "Polarization effects in nitride semiconductor device structures and performance of modulation doped field effect transistors," *Solid-State Electronics* **43**, pp. 1753-1771, 1999.
 41. H. Jiang and J. Singh, "Gain characteristics of InGaN-GaN quantum wells," *IEEE Journal of Quantum Electronics* **36**, pp. 1058-1064, 2000.

Near-field photoluminescence spectroscopy of localized states in InGaAsN alloys.

A. M. Mintairov^{1,2}, P. A. Blagnov², T. Kosel¹, J. L. Merz¹, V. M. Ustinov², A. S. Vlasov¹, R. E. Cook³.

¹ Electrical Engineering Department, University of Notre Dame, Notre Dame, IN, 46556

² Ioffe Physical-Technical Institute RAS, Polytechnicheskaya 26, St.Petersburg, Russia

³ Argonne National Laboratory, Argonne, IL, 60439.

ABSTRACT

We used near-field magneto-photoluminescence scanning microscopy to study structural and optical properties of quantum-dot-like compositional fluctuations in GaAsN and InGaAsN alloys. We show that these fluctuations manifest themselves by the appearance of narrow emission lines (halfwidth 0.5-2 meV) at temperatures below 70K. We estimated the size, density, and nitrogen excess of individual compositional fluctuations (clusters), revealing phase-separation effects in the distribution of nitrogen in GaAsN and InGaAsN. We found a dramatic difference in the Zeeman splitting of cluster lines between GaAsN and InGaAsN, indicating a strong effect of In on the exciton g -factor.

INTRODUCTION

$\text{In}_x\text{Ga}_{1-x}\text{As}_{1-y}\text{N}_y$ ($x \sim 0-0.08$, $y \sim 0-0.05$) alloys have recently attracted considerable attention as promising materials for laser diodes in the 1.3 -1.5 μm range as well as more efficient solar cells. These applications exploit their unusual electronic property - a "giant bowing" parameter ($b \sim 20\text{eV}$), which arises from the large electronegativity and small size of the nitrogen [1, 2]. In our recent study [3] we used temperature-dependent near-field magneto-photoluminescence spectra to observe the localization of excitons on quantum-dot-like (QD-like) compositional fluctuations of $\text{In}_{0.08}\text{Ga}_{0.92}\text{As}_{0.97}\text{N}_{0.03}$. Localization is driven by the giant bowing parameter of these alloys and manifests itself by the appearance of ultranarrow lines (halfwidth $< 1\text{ meV}$) at temperatures below 70K. We used near-field magneto-photoluminescence spectra for the estimation of the size, density, and nitrogen excess of individual compositional fluctuations (clusters) in InGaAsN, thus revealing random versus phase-separation effects in the distribution of nitrogen.

In the present paper we extend these magneto-optical measurements together with transmission electron microscope measurements to include GaAsN alloys with the same nitrogen content, allowing us to study the effect of In incorporation on the optical and structural properties of QD-like compositional fluctuation. We observed a similarity in size, N content and density of QD-like clusters in GaAsN and InGaAsN. However, Zeeman splitting was not observed for cluster emission lines in GaAsN, indicating a strong effect of In on the exciton g -factor in InGaAsN alloys.

EXPERIMENT

The $\text{GaAs}_{1-y}\text{N}_y$ and $\text{In}_x\text{Ga}_{1-x}\text{As}_{1-y}\text{N}_y$ ($x=0.08$, $y=0.03$) samples used in this study were grown by solid source molecular beam epitaxy on (001) semi-insulating GaAs substrates at $T=450^\circ\text{C}$. The layers with thickness of 0.12 μm were sandwiched between AlGaAs layers of

thickness 60 nm (bottom) and 14 nm (top). The InGaAsN layer consisted of a short period $\text{GaAs}_{0.966}\text{N}_{0.034}/\text{InAs}$ superlattice with individual layer thicknesses of 2.82 and 0.25 nm, respectively. The structure was capped by a 20 nm GaAs layer and annealed at 710°C for 10 min. The far-field PL spectrum of the layers at 5 K consisted of a single broad band (halfwidth ~ 20 meV) with peak energy 1.11 and 1.09 eV, similar to results reported in the literature [4].

Near-field photoluminescence (NPL) spectra with spatial and spectral resolution of 300 nm and 0.4 nm (0.5 meV), respectively, were taken in collection-illumination mode using uncoated tapered fiber tips. The spectra were excited by 20 μW of Ar ion laser excitation at 514.5 nm, measured in the temperature range 5-300 K and magnetic field strengths 0-10 T.

A cross-sectional specimen was prepared for transmission electron microscopy (TEM) by wedge polishing and Ar ion milling with liquid nitrogen cooling; the final accelerating energy was 500 V. TEM observations were done at 200 kV in a Philips CM30 microscope.

RESULTS AND DISCUSSION

i - Near-field spectra. In Fig. 1 a, b we present NPL spectra of our samples taken at 5 K. We see that at $T=5$ K the spectra reveal structure, consisting of the series of multiple peaks

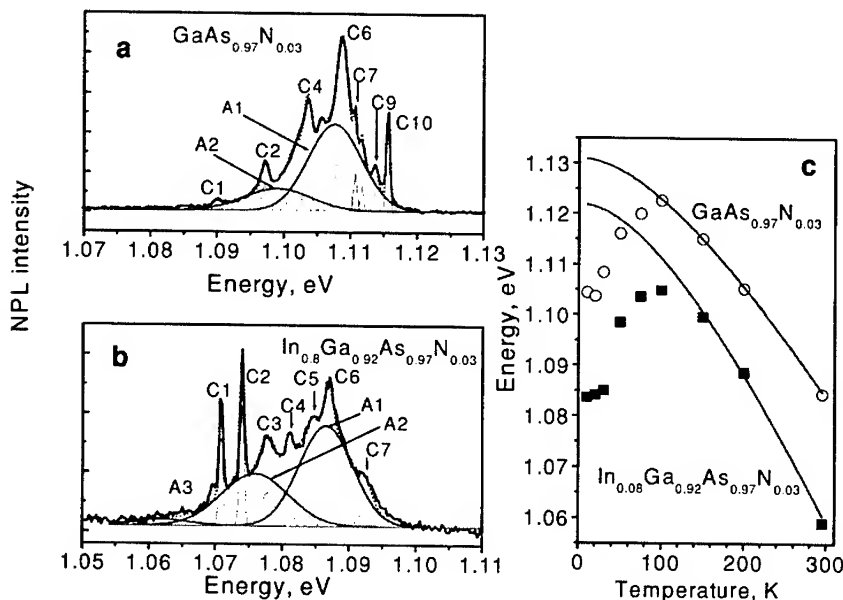


Figure 1. Experimental (thick solid) and multiple Gaussian peak modeling (dotted – whole spectra and thin solid – constituents) of 5K near-field PL spectra of $\text{GaAs}_{0.97}\text{N}_{0.03}$ (a) and $\text{In}_{0.08}\text{Ga}_{0.92}\text{As}_{0.97}\text{N}_{0.03}$ (b). (c) shows the temperature dependence of the maximum of the band A1 (solid squares – $\text{In}_{0.08}\text{Ga}_{0.92}\text{As}_{0.97}\text{N}_{0.03}$, open circles – $\text{GaAs}_{0.97}\text{N}_{0.03}$) measured in the spectra and calculated using Varshni's expression [5] (solid curve).

centered at 1.108 eV in GaAsN and at 1.087 eV in InGaAsN. For both alloys a Gaussian contour decomposition resolves up to ten narrow lines ($\gamma \approx 0.5$ –2 meV), denoted C1-C10, superimposed on the broader bands ($\gamma \approx 8$ –10 meV), denoted A1-A3. We observed [3] that the intensities of the C-lines decrease dramatically with increasing temperature, disappearing at ~ 70 K. In Fig. 1, c the temperature dependence of the energy maximum of the A1 band in GaAsN and InGaAsN is shown. We can see that this dependence is similar in both alloys. For $T > 100$ K the shift of the A1 band energy follows the behavior typical for band gap emission of a bulk semiconductor: a decrease of the emission energy with increasing temperature due to thermal expansion, which is well described by the Varshni model [3, 5]. For lower temperatures, however, the A1 band shows an inverted behavior, which indicates onset of the carrier localization. We attribute the A-bands to the emission of excitons localized on composition fluctuations having spatial extent $2r$, much greater than the exciton radius (r_{exc}) which is ~ 10 nm (weak localization regime), and we attribute the C-lines to emission of excitons localized on QD-like clusters having $r \leq r_{exc}$ (strong localization regime). The difference between Varshni's model predictions and the observed energy positions of the emission lines for $T < 150$ (Fig. 1, c) gives the exciton localization energy, which is equal to 10–60 meV for $T = 5$ K.

ii - Magneto NPL spectra. We used magneto-photoluminescence measurements to estimate the size of the composition fluctuations. In Fig. 2, a and b we present the magnetic field dependence of the C-lines in the GaAsN and InGaAsN samples. We observed Zeeman splitting of the C-lines in InGaAsN(subscript h and l denote high and low energy components in Fig2, b). The splitting energy has values of 0.6 meV for 4 T and 1.7 meV for 10 T, which is typical for GaAs [6] and InGaAs [7] QDs and corresponds to an exciton g -factor close to two. However, we did *not* observe Zeeman splitting of the C-lines in GaAsN (Fig.2,a); i.e. the g -factor is zero. Since the

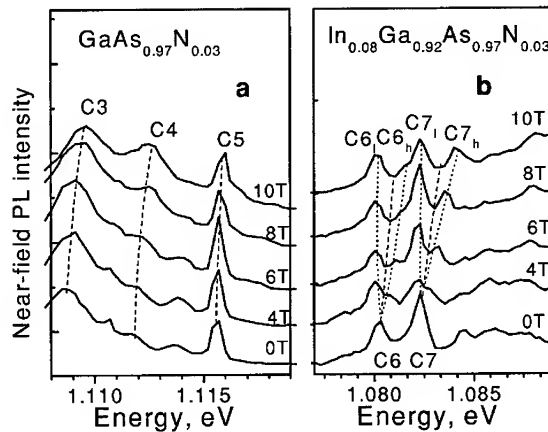


Figure 2. 5K near-field PL spectra of GaAsN (a) and InGaAsN (b) at magnetic field strengths $B=0, 4, 6, 8, 10$ T.

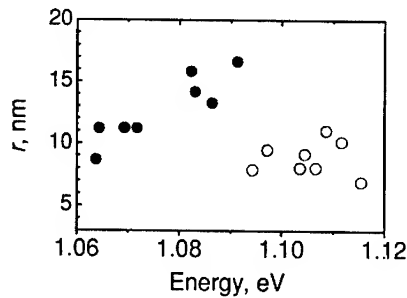


Figure 3. Cluster radius calculated from the values of the diamagnetic coefficient β [3] (open circles – GaAsN, solid circles - InGaAsN) versus emission energy of C-lines.

exciton g factor in bulk GaN is zero for a magnetic field parallel to the c -axis [8], this observation suggest a very high N content ($\Delta y \gg y$) of the clusters.

In contrast to the Zeeman splitting results, we observed a clear diamagnetic shift for the C-lines in both GaAsN and InGaAsN alloys. We measured the value of the diamagnetic coefficient to be $\beta = 3\text{--}12 \mu\text{eV/T}^2$. The cluster radius for different emission energies deduced from β [3] is presented in Fig. 3. It has a value 12 ± 5 nm for InGaAsN and 9 ± 2 nm for GaAsN.

It should be noted that in GaAsN for energy > 1.09 eV some C-lines have a low energy (paramagnetic) shift in the magnetic field, which reaches a value of 0.4 meV at 10T. The origin of such shift is not clear at this time.

We also find that the A-bands have a diamagnetic coefficient of $30\text{--}45 \mu\text{eV/T}^2$, corresponding to $2r \sim 40\text{--}60$ nm, which is consistent with the weak localization regime.

Using a calculation of the ground state energy of a particle in a spherical confining region [9] having a radius of 10 nm and localization energy of 40 meV, we calculated the value of the confining potential to be 80 meV [3]. This gives the average value of the compositional fluctuation in the cluster to be $\Delta y \sim 0.5\%$.

For $r \sim 10$ nm (80 000 bonds) and $\Delta y \sim 0.5\%$ Stirling's formula (random alloy) gives the probability of cluster formation to be as low as 10^{-15} . This corresponds to a density of the clusters of $2 \cdot 10^{-8} \mu\text{m}^{-3}$ which is too low to describe the observation of several emission cluster lines in our experiments (see below) and suggests that the formation of the clusters in our samples is spontaneous.

iii - Near-field PL imaging. The lateral distribution of the composition fluctuations was investigated using near-field PL scanning experiments. These measurements also allow us to estimate the density of the QD-like clusters in our samples to be $100 \mu\text{m}^{-3}$, which is ten orders of magnitude higher than that predicted for random alloy.

Fig.4 presents selected monochromatic NPL intensity images (scans a-e) of the $2 \times 2 \mu\text{m}$ area of the GaAsN sample taken with x/y steps of $0.2 \mu\text{m}$. The NPL spectra, measured at positions having maximum intensity in scans a-e are also presented. Simultaneous analysis of the images and the spectra shows that the spatial resolution of our experiments is 300 nm. This is clearly seen in images in the upper left section in scan c and in scan e. The higher spatial scale of the images (up to 600 nm) as well as their elongated character seen in the scans a-d are due to

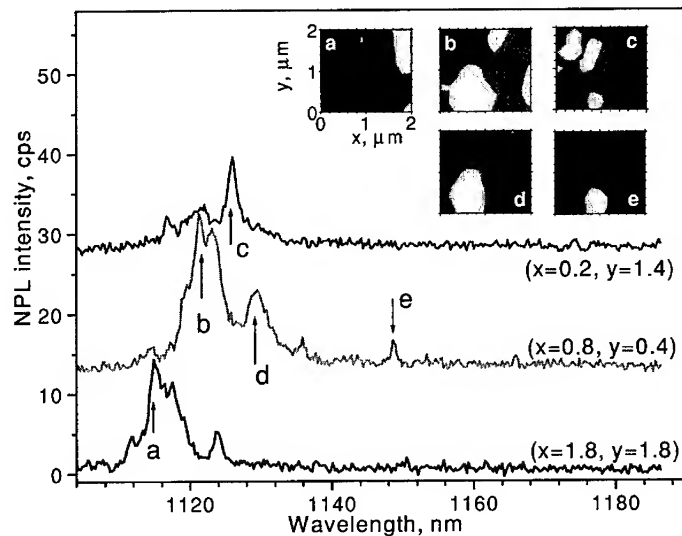


Figure 4. Monochromatic NPL intensity scans (a-e) of a $2 \times 2 \mu\text{m}$ area of $\text{GaAs}_{0.97}\text{N}_{0.03}$ together with NPL spectra (arrows show detection wavelength in corresponding scans) taken at positions (x,y), μm : (0.2,1.4), (0.8,0.4) and (1.8,1.4) with maximum intensity.

the overlapping of different lines. All scans presented (except scan e) show locations for which at least five clusters are emitting at wavelengths within 1 nm of the detection wavelength. Our measurements reveal a strong inhomogeneity of the GaAsN layer on a length scale of $1 \mu\text{m}$. Indeed, in the scan c the emission of the upper left $1 \times 1 \mu\text{m}$ section of the scan area is dominated by five clusters laterally separated by nearly $0.4 \mu\text{m}$. The emission wavelengths of these clusters occupy a very small spectral range of $\sim 2 \text{ nm}$, indicating small difference (narrow distribution) in the cluster size and N content. In contrast, in the lower left section the cluster separation is much smaller ($< 0.2 \text{ nm}$) but their wavelengths occupy spectral range $\sim 30 \text{ nm}$ (scans b-e), indicating a broad distribution of the sizes and N content. Similar long-scale inhomogeneity was observed in the InGaAsN sample.

iv – TEM study. Additional evidence of cluster formation in our samples was obtained using TEM measurements. Fig. 5, a-c shows bright-field TEM images of GaAsN and InGaAsN specimens. All images show diffraction contrast variations which we attribute to composition fluctuations. In the $g = 004$ image of InGaAsN (Fig. 5,a) this appears as a merging of the several superlattice layers and has lateral size 10-30 nm, which is in a good agreement with our estimation of the lateral cluster size from near-field magneto-PL spectra. We found that this contrast is observable only at exactly the Bragg angle ($s = 0$). Fig. 5,b shows a 2-20 image of the same specimen. The contrast variation in this case has a more vertical appearance, similar to that observed in conventional III-V alloys [10]. It has the same lateral size as seen with 004 contrast.

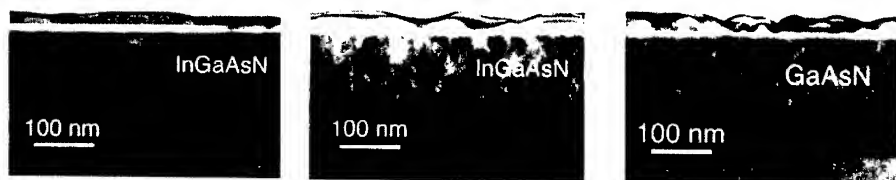


Figure 5. Bright-field TEM images of $\text{In}_{0.08}\text{Ga}_{0.92}\text{As}_{0.97}\text{N}_{0.03}$ (a- 004, b- 2-20) and $\text{GaAs}_{0.97}\text{N}_{0.03}$ (c- 2-20) structure.

The contrast extends below the InGaAsN layer, where a smaller amount of N is present. Fig.5, c is a 2-20 image of GaAsN, showing similar contrast to Fig.5, b.

CONCLUSION

Using near-field magneto-photoluminescence scanning microscopy and transmission electron microscopy we observed quantum-dot-like compositional fluctuations in GaAsN and InGaAsN alloys. These fluctuations manifest themselves by the appearance of narrow lines (halfwidth 0.5-2 meV) at temperatures below 70K. We used near-field magneto-optical scanning microscopy for the estimation of the size, density, and nitrogen excess of individual compositional fluctuations (clusters) and reveal phase-separation effects in the distribution of nitrogen. A strong effect of indium on the exciton g-factor was observed.

ACKNOWLEDGEMENTS

The authors wish to acknowledge the W. M. Keck Foundation and the NATO Science for Peace Program (Grant SFP-972484) for support of this research. The TEM work at Argonne National Laboratory was supported by the U. S. Department of Energy, Office of Science, under Contract W-31-109-Eng-38.

REFERENCES

1. S. Sakai, Y. Ueta and Y. Terauchi, Jpn. J. Appl. Phys. **32**, p. 4413 (1993).
2. S.-H. Wei and A. Zunger, Phys. Rev. Lett. **76**, 664 (1996).
3. A. M. Mintairov, P. A. Blagnov, T. Kosel, J. L. Merz, V. M. Ustinov, A. S. Vlasov, R. E. Cook, Phys. Rev. Lett. (in press).
4. E. D. Jones, A. A. Allerman, S. R. Kurz, N. A. Modine, K. K. Bajaj, S. W. Tozer and X. Wei, Phys. Rev. B **62**, 7144 (2000).
5. Y. P. Varshni, Physica **34**, 149 (1967).
6. U. Bockelman, W. Heller and A. Abstreiter, Phys. Rev. B **55**, 4469 (1997).
7. Y. Toda, S. Shinomori, K. Suzuki and Y. Arakawa, Appl. Phys. Lett. **73**, 517 (1998).
8. R. Stepniewski, M. Potemski, A. Wyszomolek, K. Pakula, J. M. Baranowski, J. Lusakowski, I. Grzegory, S. Porowski, G. Martinez and P. Wyder, Phys. Rev. B **60**, 4438 (1999).
9. D. B. Tran Thoai, Y. Z. Hu and S. W. Koch Phys. Rev. B **42**, 11261, (1990).
10. A. Zunger and S. Mahajan, in *Handbook on semiconductors*, v.3, Elsevier Amsterdam, (1994).

RAMAN AND PHOTOLUMINESCENCE MAPPING OF LATTICE MATCHED InGaP/GaAs HETEROSTRUCTURES

G. Attolini, P. Fallini, F. Germini, C. Pelosi

MASPEC-CNR Institute, Parco Area Delle Scienze, 37/A Fontanini, 43010 Parma, Italy

O. Martínez, L.F. Sanz, M.A. González, J. Jiménez

Física de la Materia Condensada, ETSII, 47011 Valladolid, Spain

ABSTRACT

The influence of the substrate on composition and CuPt-type spontaneous order of MOVPE lattice matched InGaP/GaAs layers was studied. The study was carried out by microRaman and microphotoluminescence. The order was determined by the band gap, while the Raman parameters were also contributed by the surface topography that was also related to the type of substrate. The spontaneous order increases with Si-doping of the substrates. Doping the layers with Zn randomises the alloy.

INTRODUCTION

InGaP layers lattice matched to GaAs substrates have potential applications for electronic devices, e.g. high efficiency tandem solar cells, single heterojunction bipolar transistors, tunable laser diodes, etc. It has some advantages in relation to AlGaAs ternary alloys, which are the base of many devices. Lattice matched InGaP presents a direct band gap of 1.9 eV, which is approximately equal to the maximum direct band gap that can be obtained with AlGaAs (Ga molar fraction of 0.4) [1]. InGaP is insensitive to oxygen and humidity inside the reactor, which is a well known cause of Al instability in AlGaAs [2].

InGaP is affected by other problems, in particular the composition control and the existence of an spontaneous ordered phase. $\text{In}_{1-x}\text{Ga}_x\text{P}$ matches the GaAs lattice for $x=0.516$ at room temperature; however due to the large lattice and thermal mismatches between InP, GaP and GaAs the composition is critical to avoid residual strain in the layers [3]. The second problem of interest regards the spontaneous order. InGaP can appear under a CuPt-type ordered phase [4, 5]. In the ordered phase the cations are not randomly distributed, but segregate spontaneously into alternate (111) planes giving a CuPt-type structure in the cation sublattice. This phase critically influences the optical and electrical properties of InGaP/GaAs layers. The most important is the shrinking of the band gap, which can be reduced by 100 meV for lattice matched composition [5, 6]. Also, the minority carrier lifetime and mobility are sensitive to cation order [6]. The spontaneous order is related to the growth method and the specific growth conditions, such as the substrate temperature and the V/III ratio. The nature of the substrate is shown here to influence the properties of the layers.

We present herein a detailed study of the properties of InGaP layers grown by LP-MOVPE (Low pressure metal organic vapor phase epitaxy) on different substrates aiming to understand the influence of the substrate on the spontaneous order. The analysis is carried out by High Resolution X-Ray diffraction (HRXRD), Atomic Force Microscopy (AFM), micro-Raman (μ -R) and micro-Photoluminescence (μ -PL).

EXPERIMENTAL AND SAMPLES

Layers were grown at reduced pressure (60 mBar) by MOVPE in a horizontal reactor. The precursors were trimethylgallium (TMG), trimethylindium (TMI) and Phosphine (PH_3) and Arsine (AsH_3) as main reagents; arsine was diluted in hydrogen (5%). The layers of InGaP were deposited on (100) GaAs substrates cutted 2° off towards the [110] axis. The growth conditions were the same for all runs, namely substrate temperature of 600°C and V/III ratio of 159.60 (rel.u.). The substrates were either semiinsulating (SI) or n-type (Si-doped), the doping level of the substrate was monitored by Raman spectroscopy, using the LO phonon-plasmon coupled (LOPC) modes; samples B, D, I and J were grown on semiinsulating substrates, samples F and H were grown on Si-doped substrates ($[\text{Si}] > 3 \times 10^{18} \text{ cm}^{-3}$). The InGaP layers were either undoped (B, D, F and H) Si (J) or Zn (I) doped.

The AFM images show that the surface morphology of the InGaP layers was determined by the type of substrate, figure 1. In particular, layers grown on n-type substrates present flat surfaces suggesting layer by layer growth. Instead of this, layers grown on SI substrates exhibited a rough surface, looking like an array of parallel ridges about $0.2 \mu\text{m}$ wide, which exposes (100), (101) and (111) planes.

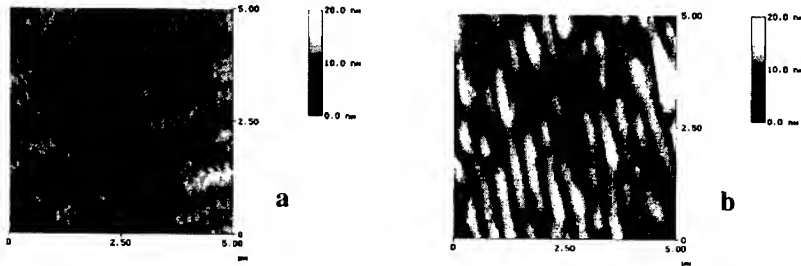


Figure 1. AFM images of samples grown on n-type substrates (Si-doped) (a), and semiinsulating substrates (b)

The layers were investigated by HRXRD. Two ($R=0, \pi$) symmetric 004 reflections, R being the azimuthal angle, have been measured from each sample to eliminate the effect of a possible miscut angle. All the diffraction profiles were recorded in the ω - 2θ scan mode. To estimate the perpendicular mismatch $(\Delta d/d)^\perp$ we used the first order formula $(\Delta d/d)^\perp = -\Delta\omega \cot\theta_B$, where θ_B is the Bragg angle of the substrate and $\Delta\omega$ the peak separation in arcsec.

μ -R measurements were carried out with a DILOR XY Raman spectrometer attached to a metallographic microscope. The 514.9 nm line of an Ar^+ laser was focused onto the sample by the large numerical aperture ($\text{NA}=0.95$) of the microscope objective, which also collected the scattered light, conforming a nearly backscattering geometry. In our usual experimental conditions the laser beam diameter at the focal plane was slightly sub-micrometric.

Room temperature luminescence spectra were obtained in the same DILOR XY Raman spectrometer, thus warranting that the same points of the samples were measured in Raman and Luminescence.

RESULTS AND DISCUSSION

The composition of the layers was estimated from HRXRD and μ -R data. The perpendicular lattice mismatches, $(\Delta d/d)^{\perp}$, estimated for the six samples studied were positive, which corresponds to compressive mismatch and therefore to slightly Ga rich stoichiometry, the composition was close to the lattice matched value since the maximum value of $(\Delta d/d)^{\perp}$ was 5.10^{-3} .

μ -R spectra were obtained on different points of the samples. The μ -PL spectra were obtained on the same points, which allowed a correlation between both measurements. The Raman spectrum of InGaP presents a two mode behaviour [7]. It consists of an LO phonon mode (GaP like) at 380 cm^{-1} (henceforth labeled LO_1), a TO phonon mode (InP-like, TO_2) at 330 cm^{-1} , which is selection rule forbidden, but is activated by alloy disorder, figure 2. Special mention should be paid to the phonon band at 365 cm^{-1} , which has been associated with the InP-like LO phonon (LO_2), the properties of this band have been reported to be sensitive to the spontaneous order. This band seems to have a complex character, in fact a TO band, GaP-like (TO_1) seems to be located in the same spectral region [8]. On the other hand, the frequencies and relative intensities of the modes are dependent on the composition.

There is a clear difference between the Raman spectra of doped and undoped layers. The phonon bands are broadened and the forbidden TO band is enhanced in the doped layers. This is the consequence of the existence of LOPC modes [8]. Therefore, a comparison between the Raman spectra of doped and undoped layers must be done with caution.

The LO_1 phonon can be used to determine the composition of the layers since its Raman shift is weakly affected by the spontaneous order [7]. The LO_1 phonon frequency shifts almost linearly with x ; it increases by $0.7\text{ cm}^{-1}/\%\text{Ga}$, in the lattice matched composition range [9]. According to the X-Ray data the samples were slightly Ga-rich. This is confirmed by Raman spectroscopy, since the Raman frequencies were all above the Raman frequency for lattice matching, which is 382 cm^{-1} ; therefore the layers were slightly Ga-rich ($\sim 52\%\text{ Ga}$). The average Raman shifts measured are 382.83 cm^{-1} (sample B), 382.85 cm^{-1} (sample D), 382.52 cm^{-1} (sample F), 382.37 cm^{-1} (sample H), 382.50 cm^{-1} (sample I) and 385.89 cm^{-1} (sample J). Samples B, D, F, H and I have compositions that differ each other by less than 1%. Sample J presents a large Raman shift that can be interpreted as a Ga rich composition ($\sim 55\%$).

The Raman scattering is sensitive to the atomic arrangement; in fact, spontaneous CuPt-type order was observed to influence the Raman spectrum. An empirical relation between the band gap and the depth of the valley between the two LO peaks in the Raman spectrum was reported [10]. The valley depth normalized to the intensity of the LO_2 phonon peak is taken as an order parameter, labeled S , see figure 2. The existence of a profound valley between the two LO bands (high S) corresponds to a large band gap (disordered layer), a value of 0.6 has been reported for fully disordered specimens. The valley depth decreases for partially ordered samples, reaching a value of 0.2 for fully ordered samples [7,10].

The Raman spectra were obtained at several points of the layers using the Raman microprobe. The Raman parameters of the spectra, that is, Raman Shifts ω_{LO_1} and ω_{LO_2} and the FWHM (Full Width at Half Maximum) of the modes were studied in relation to the valley depth aiming to establish a correlation between spontaneous order and the Raman parameters. The FWHM of the peaks is related to the phonon correlation length. In fact, the FWHM should decrease when In and Ga are randomly distributed in the cation sublattice and will increase for

clustering or in the presence of the ordered phase. The FWHM of the LO_1 band was observed to increase with the valley depth, which is controversial with the above interpretation. A good correlation is found for the frequency splitting between both LO modes, $\Delta\omega_{LO}=(\omega_{LO1}-\omega_{LO2})$, and the valley depth, figure 3. The valley depth increases when this splitting increases. This cannot be related to composition changes since the major contribution to this splitting is due to the down frequency shift of the LO_2 Raman band, the LO_1 band frequency remaining within the limits determined by the small composition variation above discussed, figure 3. According to the above discussion, a shift to the low frequency of ω_{LO2} takes place with a broadening of the LO_1 band. These data are only referred to the undoped samples, since the spectra obtained for doped samples, I and J, are influenced by the LOPC modes.

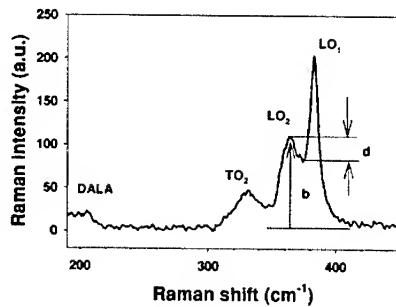


Figure 2. Typical Raman spectra of lattice matched InGaP/GaAs. The order parameter, S , is defined as the valley depth, d , normalized to the intensity of the LO_2 band, b ($S=d/b$)

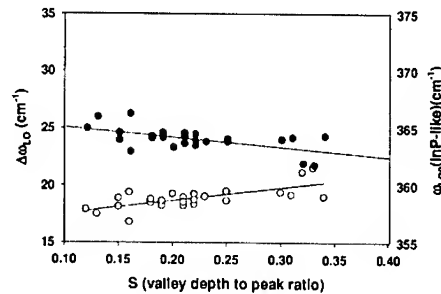


Figure 3. $\Delta\omega_{LO}(\omega_{LO1}-\omega_{LO2})$ (●) and ω_{LO2} (InP-like) (○) vs S

Taking the band gap as the peak energy of the intrinsic PL band at room temperature one obtains the following band gap average energies for the samples: 1.90 eV (sample B), 1.87 eV (sample D), 1.85 eV (sample F), 1.86 eV (sample H), 1.91 eV (sample I) and 1.89 eV (sample J). The PL spectra were measured at the same points that the Raman spectra.

The band gap is also influenced by the layer composition. In the lattice matched region the band gap is enlarged by 15 meV for an increase of 0.01 in the molar fraction of Ga [11]. However, the composition of samples B, D, F, H and I was observed to lay within less than 1% percent interval. Therefore, one can assume that the band gap differences between these samples are mostly due to the degree of spontaneous order. Only the band gap measured for sample J could be additionally contributed by composition deviation from the lattice matched value, according to the Raman data. The largest band gap and therefore the lowest degree of spontaneous order corresponds to samples B and I, followed by sample D and finally the higher degree of order corresponds to samples F and H. Taking into account the characteristics of the samples one can argue that: i) n-type substrates benefit the spontaneous order, the degree of order increases with the dopant concentration of the substrate, ii) SI substrates reduce the degree of spontaneous order, iii) Zn doping randomizes the alloy, which is a well known property of Zn [12].

If one plots the band gap vs the order parameter, S , for the undoped samples one observes that the expected correlation does not appear, figure 4. The samples with the largest band gap, B

and D, have small S , while the samples with the smallest band gap have higher values of S . This result is controversial with the results reported by other authors. This can be explained on the basis of the complex nature of the Raman band labeled LO_2 and the surface topography of our samples. The samples grown on SI substrates present a rough topography with high index planes, while the topography of the samples grown on n-type substrates was smooth, see figure 1. In our scattering geometry the TO bands are forbidden, however, they can be activated by either alloy fluctuation or the surface orientation. The presence of high index planes in samples B and D should activate the forbidden TO_1 mode, with the corresponding lineshape change of the band at 365 cm^{-1} , up to now called LO_2 , which would result on a reduction of S in spite of the lower spontaneous CuPt-type order of these samples. The smooth surface of samples F and H should reduce the contribution of the forbidden TO_1 mode to the LO_2 Raman band. An attentive observation of the spectra of samples B and D shows that the decrease of S is accompanied by an increase of the intensity of the other TO phonon band (InP-like, TO_2) at 330 cm^{-1} , figure 5, which is consistent with the activation of the TO forbidden modes and the contribution of the TO_1 mode to the value of S .

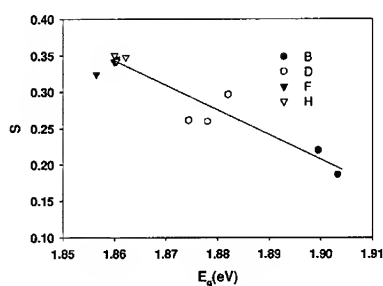


Figure 4. S vs E_g (nm). The line is a guide to the eye

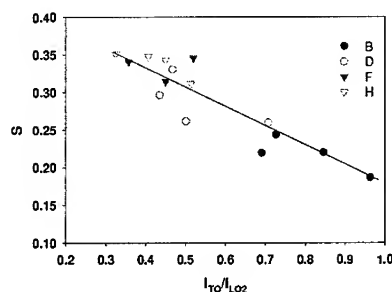


Figure 5. S vs I_{TO2}/I_{LO2} , TO_2 is the band at 330 cm^{-1} . The straight line is a guide to the eye.

Finally, monochromatic (intrinsic emission) intensity PL maps were obtained for the different samples at room temperature. Intensity fluctuations were observed, figure 6. The intrinsic PL intensity is governed by the competition between band to band recombination and non radiative recombination at deep levels. Also a decrease of the luminescence intensity has been reported (up to a factor 3) for the ordered phase [11]. Raman data did not reveal significant composition changes over a sample. However, a correlation between the PL intensity and the peak energy was observed in samples grown on n-type substrates, see Fig. 6. Therefore, the non-uniformities of the PL intensity and peak wavelength can be understood if one considers that the PL intensity and band gap energy changes are controlled by the ordered/disordered volume ratio probed by the laser beam.

The influence of the substrate on the characteristics of the samples can be tentatively explained by the change in the lattice parameter introduced by the Si impurities, since the other growth parameters were the same for all the growth runs. The smooth layer by layer growth allows the segregation of cations, while the tridimensional growth avoids it.

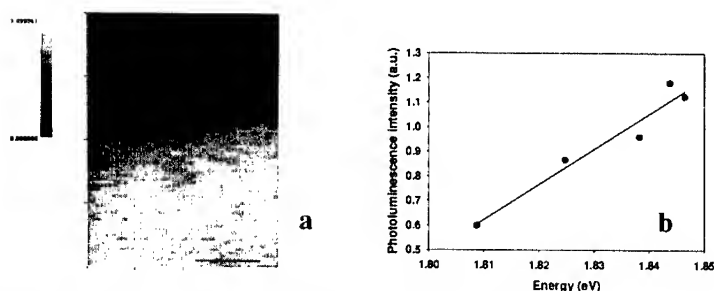


Figure 6. Monochromatic PL map (room temperature) of sample F, (a). The bar is 1 mm. I_{PL} vs E_g measured in sample F (b).

CONCLUSIONS

The influence of the type of substrate on the order of lattice matched InGaP/GaAs layers was studied by μ -R and μ -PL. The Si doping of the substrates benefits the ordering, which is related to the shrink of the band gap. The Raman parameters were demonstrated to be also influenced by the surface topography, since the S parameter was related to the activation of the forbidden TO_1 (GaP-like) Raman mode, therefore, S cannot be used as a measure of the order for samples with rough surface. Spatial inhomogeneities were related to the distribution of the ordered / disordered domains.

ACKNOWLEDGEMENTS. The Spanish group was funded by JCL (Junta de Castilla y León) and FES (Fondo Social Europeo) (Project: VA047/01). The Italian group acknowledges the financial support of the Italian Space Agency.

REFERENCES

1. J.R. Shealy, C.F. Schaus, L.F. Eastman; *Appl. Phys. Lett.* **48**, 242 (1986)
2. T.F. Kuech, D.J. Welford, E. Venhoff, V. Deline, P.M. Mooney, R. Potemski, J. Bradley; *J. Appl. Phys.* **62**, 632 (1987)
3. Y.Q. Wang, Z.L. Wang, T. Brown, A. Brown, G. May; *J. Electron. Mater.* **29**, 1372 (2000)
4. Krost, N. Esser, H. Selber, J. Christen, W. Richter, D. Bimberg, L.C. Su, G.B. Stringfellow; *J. Vac. Sci. Technol.* **12**, 2558 (1994)
5. S.F. Yoon, K.W. Mah, H.Q. Zheng; *Opt. Mater.* **14**, 59 (2000)
6. Sasaki, K. Tsuchida, Y. Narukawa, Y. Kawakami, S.G. Fujita, Y. Hsu, G.B. Stringfellow; *J. Appl. Phys.* **89**, 343 (2001)
7. F. Alsina, N. Mestres, J. Pascual, C. Geng, P. Ernst, F. Scholz; *Phys. Rev. B* **53**, 12994 (1996)
8. K. Sinha, A. Mascarenhas, S.R. Kurtz, J.M. Olson; *J. Appl. Phys.* **78**, 2515 (1995)
9. M. Zachau, W.T. Masselink; *Appl. Phys. Lett.* **60**, 2098 (1992)
10. T. Suzuki, A. Gomyo, S. Iijima, K. Kobayashi, S. Kawata, T. Hino, T. Yuasa; *Jpn. J. Appl. Phys.* **27**, 2098 (1988)
11. G.H. Olsen, C.J. Nuese, R.T. Smith; *J. Appl. Phys.* **49**, 5523 (1978)
12. T. Suzuki, A. Gomyo, K. Kobayashi, S. Kawata, S. Iijima; *Jpn. J. Appl. Phys.* **27**, L1549 (1988)

Quantum Dots

Quantum dots of InAs/GaSb type II superlattice for infrared sensing (Invited paper)

M. Razeghi^{a)}, Y. Wei, A. Gin
Northwestern University, Center for Quantum Devices, ECE Department
Evanston, IL 60208

G. J. Brown
Air Force Research Laboratory, Materials & Manufacturing Directorate, AFRL/MLPS,
Wright-Patterson AFB, OH 45433-7707

ABSTRACT

Throughout the past years, significant progress has been made in Type II (InAs/GaSb) photovoltaic detectors in both LWIR and VLWIR ranges. BLIP performance at 60K for 16 μ m photovoltaic type II detectors has been successfully demonstrated for the first time. The detectors had a 50% cut-off wavelength of 18.8 μ m and a peak current responsivity of 4 A/W at 80K. A peak detectivity of $4.5 \times 10^{10} \text{ cm} \cdot \text{Hz}^{1/2} / \text{W}$ was achieved at 80K at a reverse bias of 110mV. Detectors of cutoff wavelength up to 25 μ m have been demonstrated at 77K. The great performance of single element detectors appeals us to lower dimensional structures for both higher temperature performance and possible wavelength tunability. Simple calculations show that quantum effects will become significant when the lateral confinement is within tens of nanometers. The variation of applied gate voltage will move the electron and hole energy levels unevenly. The cutoff wavelength of the superlattice will vary accordingly. Auger recombination will also decrease and higher temperature operation becomes possible. In this talk, the latest results will be discussed.

INTRODUCTION

In recent years, extensive research has been done on infrared photodetectors for use throughout the mid to very long wavelength (3-25 μ m) range. These detectors have a wide variety of military, medical, and industrial applications. Uncooled infrared (IR) detectors are required for low-cost, lightweight sensor applications. Commercially available uncooled IR devices use ferroelectric or microbolometer detectors. These sensors are inherently slow and cannot detect rapid signal changes needed for many applications. Some of the applications which require a fast detector response time ($\tau < 30$ msec) are: free-space communication, proximity fuses, active infrared countermeasure systems, non-invasive medical monitoring, and LIDARs. Although photon detectors have frequency responses in the megahertz range, their high temperature detectivity is severely degraded due to physical limitations. The existing infrared photon detectors can be categorized as interband, which are mostly HgCdTe and InAsSb, or intersubband quantum well infrared detectors (QWIP)[1]. Unfortunately, fast Auger recombination rate in such interband detectors[2] and high thermal generation rate in the

^{a)} Electronic mail: razeghi@ccc.northwestern.edu

intersubband detectors decrease their performance for room temperature operation drastically.

As another alternative for infrared photodetectors, type-II superlattices have been studied which were originally suggested by Sai-Halaszi and L. Esaki[3]. In order to realize Auger suppression at room temperature, we have developed a new type-II superlattice detector design[4]. The experimental results show nearly one order of magnitude lower Auger recombination rate at room temperature in such detectors compared to typical intrinsic (HgCdTe) detectors with similar bandgap. Type II detectors based on InAs/GaSb superlattices have shown the potential to be the next generation of infrared sensors, surpassing HgCdTe performance over a wide range of optical wavelengths. In the VLWIR range, photodiodes based on type II InAs/GaSb superlattices with a 16 μ m 50% cutoff wavelength were reported with a detectivity of 1.5×10^{10} cmHz^{1/2}/W at 80K[5]. Photodiodes with a 22 μ m cutoff wavelength have also been demonstrated at 80K[6]. Most recently, 18.8 μ m photodiodes have shown a detectivity of 4.5×10^{10} cmHz^{1/2}/W at 80K with moderate bias of -110mV[7]. This will be discussed in more detail below. In addition, uncooled detectors with cutoff wavelengths between 8-12 μ m have been fabricated[8]. Single-element detectors[9] show a detectivity of 1.3×10^8 cmHz^{1/2}/W at 11 μ m at room temperature which is comparable to microbolometers under similar conditions. However, the measured response time of the detector is less than 68 nsec which is more than six orders of magnitude faster than microbolometers.

With the promising performance of single element detectors, researchers are attempting to increase electron confinement and wavelength tunability by moving to detectors that make use of quantum dots. Most recently in this field, others are making self-assembled quantum dot infrared photodetectors (QDIP). The dots are formed in Stranski-Krastanow growth mode in MBE. These detectors make use of the intersubband transition for detection in the wavelength range of 8-12 μ m. Peak detectivity, D^* of 3×10^9 cmHz^{1/2}/W at 100K has been reported[10]. Instead of using random self-assembled growth techniques, we plan to use electron beam lithography to create regular arrays of quantum dot infrared detectors. In this paper, we show some preliminary results towards this goal.

EXPERIMENT

The type II InAs/GaSb superlattice material is grown by an Intevac Modular Gen II molecular beam epitaxy equipped with As and Sb valved cracker sources on *p*-type epi-ready GaSb substrates. This material is used for large area detectors. The photodiode structures were grown at 396 °C according to a calibrated pyrometer. First, a 0.75 μ m GaSb buffer layer doped with Be ($p \sim 1 \times 10^{18}$ cm⁻³) was deposited. Then, InAs/GaSb:Be ($p \sim 1 \times 10^{18}$ cm⁻³) superlattice was grown, followed by a nominally undoped superlattice. Finally, InAs:Si/GaSb ($n \sim 1 \times 10^{18}$ cm⁻³) superlattice was grown and capped with InAs:Si ($n \sim 1 \times 10^{18}$ cm⁻³) top contact layer. The growth rate was 0.5 monolayer/s for InAs layers and 0.8 monolayer/s for GaSb layers. The V/III beam-equivalent pressure ratio was about 4 for InAs layers and about 1.2 for GaSb layers. The cracker temperature for As and Sb cells was 800°C. The improved material growth was achieved by greatly reduced lattice mismatch between the superlattice and the substrate, as well as reducing the growth

temperature for the n-type superlattice layers. The selected layer numbers of InAs and GaSb layers were determined for specific cutoff wavelengths using an empirical tight binding model. The lattice mismatch was predicted by the weighted average lattice constants of InAs, InSb and GaSb. InSb lattice constant is used for the interfaces between InAs and GaSb layers. For devices with a cutoff wavelength of nearly $19\mu\text{m}$ at 80K, we used 17 InAs monolayers and 7 GaSb monolayers for each superlattice period. The predicted 50% cutoff wavelength that is $18\mu\text{m}$ at 77K closely agrees with the experimental results.

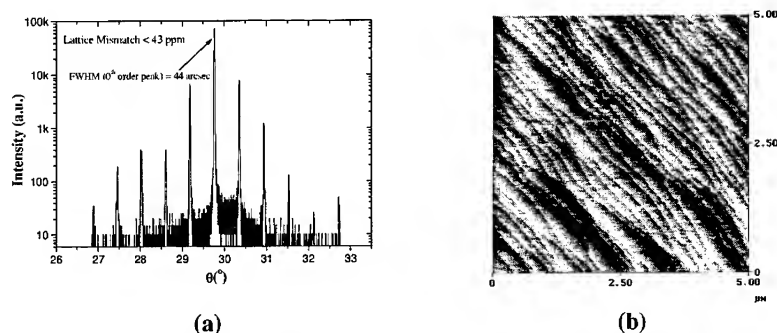


Figure 1. (a) High resolution X-ray diffraction of high quality InAs/GaSb superlattice. The lattice mismatch between the superlattice and the substrate is almost zero. **(b)** AFM image of the sample surface over $5\mu\text{m} \times 5\mu\text{m}$. Smooth atomic steps are very clear.

Structural quality of the epitaxial layers was assessed using a Phillips high-resolution x-ray diffraction system. Figure 1(a) shows the typical x-ray diffraction pattern of the photodiode structures. The mismatch between the average lattice constant of the superlattice and the GaSb substrate is below 0.0043%, while the full width at half maximum (FWHM) of the zeroth order peak is below 45 arcsec for the grown devices. The surface morphology of the samples was studied with a Digital Instruments Nanoscope IIIa atomic force microscope (AFM). The theoretical study[11] as well as experimental results[12] show the strong correlation between the surface roughness and the performance of $\text{InAs/Ga}_{1-x}\text{In}_x\text{Sb}$ superlattice photodiodes. We have achieved a root mean square (RMS) surface roughness below 1.6\AA over an area of $20\mu\text{m} \times 20\mu\text{m}$, which is the record for the type II $\text{InAs/Ga}_{1-x}\text{In}_x\text{Sb}$ material system. Figure 1(b) shows the gray-scale surface morphology of a sample. Clear and smooth atomic steps are visible over the $5\mu\text{m} \times 5\mu\text{m}$ scan area and indicate excellent surface smoothness.

The processed detectors were attached to the cold finger of a LakeShore Cryogenics helium cryostat with KRS-5 windows. The temperature was controlled precisely between 20K and 100K. Absolute spectral responsivity was calculated from the measured spectral response of the device using the Mattson Galaxy 3000 Fourier transform infrared (FTIR) spectroscopy system, and its photoresponse to a calibrated blackbody (Mikron 305) setup.

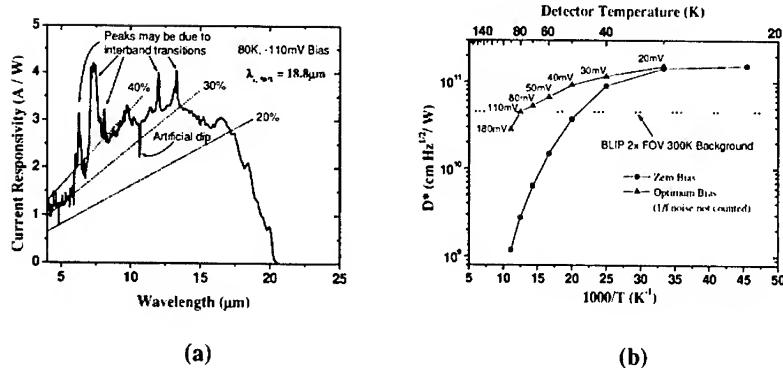


Figure 2. (a) Absolute current responsivity of the detectors at 80K under a reverse bias of 110mV. The dotted lines are equal-quantum efficiency lines. The 90% to 10% cutoff energy width is about 12meV. (b) Temperature dependent peak detectivity at 12 μm (50% cutoff is at 18.8 μm at 80K) with optimum bias and zero bias. With a reverse bias of 110mV, BLIP performance can be achieved at 80K.

Figure 2(a) shows the typical spectral responsivity of the detectors with $\lambda_{c,50\%} = 18.8\mu\text{m}$. The absorption from CO_2 and H_2O due to the small difference in the optical path length of the background measurement and the detector measurement is corrected from the measurements of the air transmission. The peak responsivity for the sample is about 4A/W under a bias of -110mV at 80K which leads to a quantum efficiency of 41.4% at 12 μm . The quantum efficiency of the detectors is obtained by dividing the current responsivity by its theoretical value which is given by,

$$R_{i,theoretical} = \frac{\eta_{ideal} \lambda e}{hc}, \quad \text{with } \eta_{ideal} = 1$$

where λ is the wavelength, e is the electron charge, h is the Plank's constant, and c is the speed of light in the air. The use of binary layers in the superlattice has significantly enhanced the uniformity and reproducibility of the energy gap. The 90% to 10% cut-off energy width of these devices is only about 2 kT, which has been maintained very well compared with previous detectors operating at different cutoff wavelength[5].

The major noise component at zero bias is the Johnson noise, and hence the detectivity of the device with current responsivity R_i at temperature T can be calculated from:

$$D^* = R_i \sqrt{\frac{R_0 A}{4kT}}$$

where R_0 is the zero bias differential resistance of the device, A is the device area, and k is the Boltzmann constant. The measured value for $R_0 A$ product for the detectors was about $0.27\Omega\text{cm}^2$ at $T = 50\text{K}$ which leads to a Johnson noise limited detectivity of about $3.71 \times 10^{10} \text{cm} \cdot \text{Hz}^{1/2} / \text{W}$. Under reverse bias, the $1/f$ noise will show up. However with appropriate modulation frequency, this noise can become negligible. The RA product goes up to $0.55\Omega\text{cm}^2$ at 80K and a reverse bias of 110mV. This lead to a Johnson noise

limited detectivity of $4.5 \times 10^{10} \text{ cm} \cdot \text{Hz}^{1/2} / \text{W}$. Figure 2(b) shows the calculated detectivity with optimum reverse bias at different temperatures without the $1/f$ noise component compared with those under zero bias. The background limited infrared photodetector (BLIP) level is achieved at temperatures near 50K under zero bias and 80K under a reverse bias of 110mV.

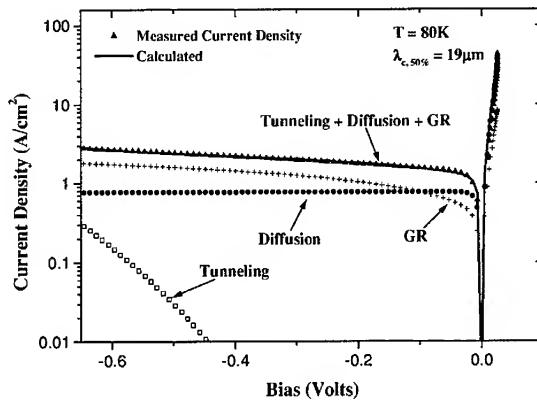


Figure 3. Comparison between measured dark current density and modeled dark current density components at 80K. At reverse bias below 100mV, the dominant dark current is the diffusion current.

The 50% cutoff wavelength decreases from $19.1 \mu\text{m}$ at 90K to $17.6 \mu\text{m}$ at 20K representing the temperature-dependent changing in bandgap of 5.5meV. For HgCdTe detectors of a similar cutoff wavelength, this change is about 23meV in the opposite direction and more than four times larger, calculated from Ref. [13]. In order to study the major components of the dark current at $T = 80\text{K}$, the current-voltage characteristic of the devices was modeled. Although the active layer of these devices consists of short period superlattices, bulk-based modeling of the dark current has been proven to give relatively accurate results [8,14,15]. We use an improved algorithm and more accurate calculations from Matlab based on formalism reported in Ref. [8]. Figure 3 shows the measured and modeled current densities versus the applied bias for devices with $\lambda_{c,50\%} = 18.8 \mu\text{m}$. The calculated current density, which consists of tunneling, generation recombination, and diffusion current densities, shows good agreement to the measured values for forward and reverse biases. We assumed an effective mass of $m_e = 0.03m_0$ for electrons and $m_h = 0.4m_0$ for holes based on previous theoretical calculations[11] and experimental results[14,16]. Based on the experimental measurements on similar devices[17], we also assumed an electron mobility parallel to the growth direction of $\mu_e = 1000 \text{ cm}^2/\text{Vs}$. The mobility of the holes is not significant in the diffusion current, since the device has an n^+p junction. The fitting parameters for the model were carrier lifetime $\tau_e = \tau_h = 24\text{ns}$, unintentional background doping level $p \sim 1 \times 10^{15} \text{ cm}^{-3}$, and generation-recombination lifetime in the depleted layer of $\tau_{gr} = 0.4\text{ns}$. In contrast to

HgCdTe, tunneling is not significant even at high values of the reverse bias due to the higher effective mass of the electrons in type-II superlattices. At low reverse bias, the dark current is dominated by diffusion current at 80K. The generation-recombination current begins to take over at reverse bias over 100mV. The value of R_0A product versus temperature shows a diffusion limit behavior down to nearly 50K, and then a generation-recombination limit behavior from 50K to 35K. Below 35K, the value of R_0A increases even slower. The ideality factor of the device was nearly 1 for small values of forward bias at 80K.

These large area detector results encourage us to move forward towards higher performance quantum dot devices. We pursued a novel method unlike the commonly used "self assembled" technique that can produce high quality, highly uniform quantum dot structures using electron beam lithography. These detectors use interband transitions in type II InAs/GaSb superlattice materials to achieve higher operating temperatures. The type II band alignment in between InAs layers and GaSb layers directly lead to lower Auger recombination rate. As the semiconductor dots get smaller, usually in tens of nanometer, the quantum confinement effect will become significant and energy levels will become increasingly discrete. This will decrease the matching energy levels for Auger recombination dramatically and much higher operating temperatures could be achieved. The material structure is shown in Figure 4(a). By using gate electrodes to apply a lateral electrical field to the detector, we can further confine the electrons in space, which changes the available energy states in the quantum dot. By assuming a parabolic potential well formed by the gate voltage, we can calculate the electron energy level shift as a function of gate bias voltage, shown in Figure 4(b). Consequently, we can control the detector cutoff wavelength by several microns by using applied voltages on the order of one volt as shown for different sized detectors in Figure 5. Also no surface grating is necessary for these quantum dots. This reduces some of the processing steps and, therefore, detector cost. This is a completely new technique to realize quantum dots.

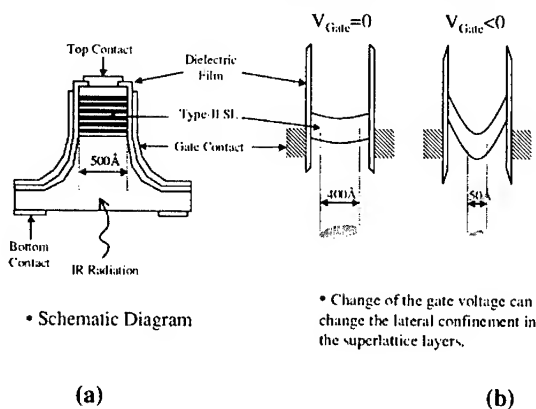


Figure 4. (a) Schematic diagram of one possible structure of the proposed quantum dot infrared detector; (b) The basic operating mechanism.

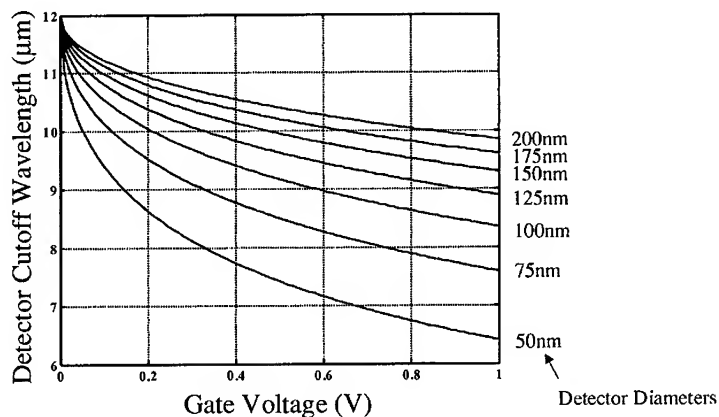


Figure 5. Preliminary modeling results for the wavelength tunability for quantum dots of various diameters.

Although the basic idea of these detectors seems elementary, the fabrication techniques needed are of critical importance. The processing for nanometer sized features is a challenge. The starting material is a type II InAs/GaSb superlattice. Stacks of high quality quantum dots can be developed by etching pillars and consequent oxide coating. In order to achieve quantum size effect, one needs to confine the electrons within tens of nanometer. However, surface leakage current will be a severe problem for such a small device, since the ratio of the surface to the volume increases dramatically. However by applying a gate voltage, not only can the cutoff wavelength be changed, the electrons will also be more confined to the center and result in less leakage.

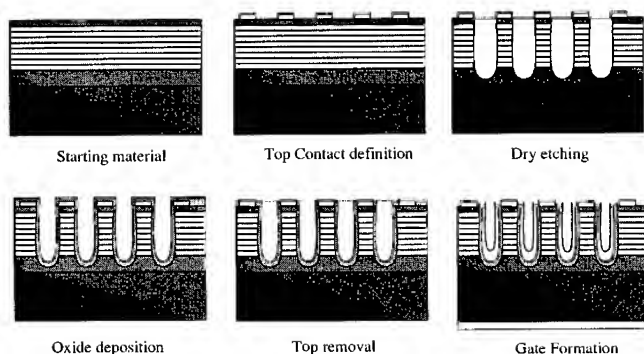


Figure 6. Interconnection of the pillars with advanced metalization and passivation techniques.

The sensitive area of such quantum pillar is very small and many detectors need to be combined to serve as a single detecting pixel. Figure 6 shows the interconnection scheme which provides a large detector area using advanced metalization and passivation techniques. A Leica LION-LVI low energy e-beam lithography system was used to produce top metal contacts. High quality metal contacts with diameter in the range of 1000 to 100nm were successfully defined on the surface of the samples. Reactive ion etching (RIE) was used to produce uniform anisotropic etching of the pillars through the material. The etching was designed for high ratio of vertical to horizontal etching rates. Figure 7(a) shows the results of such process on the 500nm diameter pillars. The vertical to horizontal ratio is in excess of five. We have produced two-dimensional arrays of this pillars with excellent uniformity over thousands of square micron. Additionally, electron beam lithography was used to create 40nm diameter holes in PMMA resist, demonstrating our high-resolution capability. The atomic force microscope scan is shown in Figure 7(b).

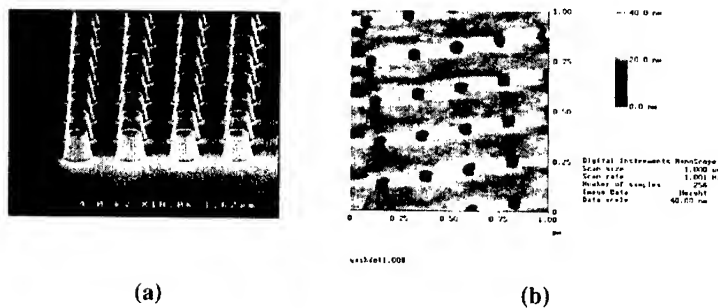


Figure 7. Current progress in processing technology. (a) Etched array of 500nm GaSb dots; (b) AFM image of 40nm diameter holes in PMMA/GaSb

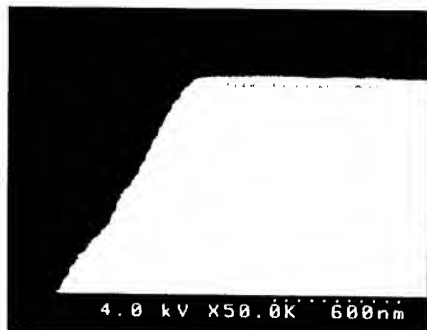


Figure 8. SEM image of the cleaved edge of a mesa covered by a uniform layer of dielectric with a thickness of about 50nm.

Passivation is one of the most important steps to control surface-induced leakage current. Surface leakage originates from unterminated, or dangling, bonds at the surface of a semiconductor. When the tetrahedral GaSb or InAs lattice is abruptly terminated along a given plane to form a surface, some of the crystal's bonds are left dangling. The formation of a native oxide terminates most of the unsatisfied bonds, but the remaining dangling bonds become interfacial traps. These traps introduce energy levels in the forbidden band gap at the semiconductor-oxide interface. They tend to pin the Fermi level near mid-bandgap and create surface leakage current. In addition, In_2O_3 , the native oxide formed on InAs or InSb, is a good conductor, which acts to decrease the resistance for the leakage path in photodiode and photoconductor devices. Therefore we need to remove the native oxides and deposit or grow a layer of insulating material to terminate all the dangling bonds and protect the surface. The key issues are the uniformity of the dielectric and the coverage of the device surface. We used plasma enhanced chemical vapor deposition (PECVD) techniques to form uniform layers of dielectrics. Figure 8 shows SEM image of a cleaved edge of a mesa covered with 50nm Si_3N_4 layer by this method.

Most of the remaining challenges with this approach are processing related. For instance, metal liftoff, the standard process for forming metal contacts, is slightly different for mesa diameters below 100nm. The surface adhesion is minimal over the small detector area and the evaporated contacts tend to peel off with the rest of the metal layer. Additionally, etching the nanopillars needs to be very carefully controlled with small devices. It becomes more challenging to achieve high aspect ratio structures by techniques such as reactive ion-etching, because the high energy plasma tends to isotropically etch at small dimensions. However, technologies will be improved to overcome these difficulties.

CONCLUSION

We have demonstrated the initial success for the processing technology of quantum dot arrays on GaSb substrates. Highly uniform dots formed by electron beam lithography have been successfully realized. Surface passivation by depositing silicon nitride has also been studied. Because the quantum confinement effects lead to much lower Auger recombination rates, this work may lead to a new generation of infrared detectors operating at much higher temperatures than previous technologies.

ACKNOWLEDGEMENTS

This work has been partially supported by Air Force and the Office of Naval Research. The authors would like to acknowledge the support of Dan Johnstone of Air Force and Y. S. Park of ONR. A. Gin is supported under a National Science Foundation Graduate Research Fellowship.

REFERENCES

1. M. A. Kinch and A. Yariv, Appl. Phys. Lett. **55**, 2093, 1989.
2. A. Rogalski, Infrared Physics & Technology **40**, 279, 1999.

3. G. A. Sai-Halasz, R. Tsu, and L. Esaki, *Appl. Phys. Lett.* **30**, 651, 1971.
4. H. Mohseni, E. Michel, J. Sandven, M. Razeghi, W. Mitchel, and G. Brown, *Appl. Phys. Lett.* **71**(10), 1403, 1997.
5. H. Mohseni, M. Razeghi, G.J. Brown, Y.S. Park, *Appl. Phys. Lett.*, **78**(15), 2107-2109, 2001.
6. Hooman Mohseni, Yajun Wei and Manijeh Razeghi, *Proc. SPIE*, **4288**, 191-199, 2001.
7. Y. Wei, A. Gin, M. Razeghi, and G. Brown, submitted to *Appl. Phys. Lett.*, Oct. 2001.
8. Hooman Mohseni, Joseph S. Wojkowski, Abbas Tahraoui, Manijeh Razeghi, G. Brown, and W. Mitchel, *Proc. SPIE*, **3948**, 153-160, 2000.
9. H. Mohseni, J. Wojkowski, M. Razeghi, *IEEE J. Of Quantum Elect.* **35**, 1041, 1999.
10. A. D. Stiff, S. Krishna, and P. Bhattacharya, *Appl. Phys. Lett.*, **79**(3), 2001.
11. G. Bastard, *Phys. Rev. B* **25**, 7584 (1982).
12. F. Fuchs, L. Burkle, W. Pletschen, J. Schmitz, M. Walther, H. Gullich, N. Herres, and S. Mueller, *Proc. SPIE* **3794**, 41 (1999).
13. W.M. Higgins, G. N. Pultz, R.G. Roy, R.A. Lancaster and J.L. Schmit, *J. Vac. Sci. Technol. A* **7** (2), 271 (1989).
14. J. L. Johnson, L. A. Samoska, A. C. Gossard, J. Merz, M. D. Jack, G. R. Chapman, B. A. Baumgratz, K. Kosai, and S. M. Johnson, *J. Appl. Phys.* **80**, 1116 (1996).
15. F. Fuchs, U. Weimar, E. Ahlswede, W. Pletschen, J. Schmitz, and M. Walther, *Proc. SPIE* **3287**, 14 (1998).
16. F. Fuchs, U. Weimar, W. Pletschen, J. Schmitz, E. Ahlswede, M. Walther, J. Wagner, and P. Koidl, *Appl. Phys. Lett.* **71**, 3251 (1997).
17. L. Burkle, F. Fuchs, R. Kiefer, W. Pletschen, R. E. Sah, and J. Schmitz, *Mater. Res. Soc. Symp. Proc.* **607**, 77 (2000).

Quantum Dot Long-Wavelength Detectors

Pallab Bhattacharya, Adrienne D. Stiff-Roberts, Sanjay Krishna¹, and Steve Kennerly²
Solid State Electronics Laboratory, Department of Electrical Engineering and Computer
Science, University of Michigan
Ann Arbor, MI 48109-2122, U.S.A.

¹Center for High Technology Materials, Department of Electrical Engineering and
Computer Engineering, University of New Mexico
Albuquerque, NM 87106, U.S.A.

²Sensors and Electron Devices Directorate, U. S. Army Research Laboratory
Adelphi, MD 20783, U.S.A.

ABSTRACT

Long-wavelength infrared detectors operating at elevated temperatures are critical for imaging applications. InAs/GaAs quantum dots are an important material for the design and fabrication of high-temperature infrared photodetectors. Quantum dot infrared photodetectors allow normal-incidence operation, in addition to low dark currents and multispectral response. The long intersubband relaxation time of electrons in quantum dots improves the responsivity of the detectors, contributing to better high-temperature performance. We have obtained extremely low dark currents ($I_{\text{dark}} = 1.7$ pA, $T = 100$ K, $V_{\text{bias}} = 0.1$ V), high detectivities ($D^* = 2.9 \times 10^8$ cmHz^{1/2}/W, $T = 100$ K, $V_{\text{bias}} = 0.2$ V), and high operating temperatures ($T = 150$ K) for these quantum-dot detectors. These results, as well as infrared imaging with QDIPs, will be described and discussed.

INTRODUCTION

Infrared detection is important in a variety of fields, such as military targeting and tracking, law enforcement, environmental monitoring, and space science. Quantum dot infrared photodetectors (QDIPs) have been widely investigated during the past few years for operation in the mid-wavelength (3-5 μm) and long-wavelength (8-14 μm) infrared ranges [1-13]. Three of the major advantages expected from QDIPs over other existing technologies are; (i) normal incidence operation, eliminating the need for external gratings and optocouplers [5,8,10], (ii) high-temperature operation, eliminating the need for expensive cooling systems presently used with mercury cadmium telluride (MCT) detectors [14,15] and quantum well infrared photodetectors (QWIPs) [16,17], and (iii) decreased dark current, increasing the background-limited performance (BLIP) of the detector. Since InAs/GaAs quantum dots are grown by molecular beam epitaxy (MBE) using the mature III-V technology, they are essentially defect-free and do not suffer from the etch-pit densities and void defects that plague MCT detectors. The main disadvantage of the QDIP is the large inhomogeneous linewidth of the quantum dot ensemble due to random variation of dot size in the Stranski-Krastanow growth mode.

Despite such challenges, QDIPs are expected to perform better at higher temperatures, especially when compared to QWIPs, due to the increased intersubband relaxation time between the phonon-decoupled ground state and excited states, increasing

the probability that a photoexcited carrier will be collected as photocurrent [9,18-20]. This long intersubband relaxation time in quantum dots results from the existence of a “phonon bottleneck” that prevents electron relaxation by a single phonon emission. Such single phonon processes dominate carrier scattering and relaxation in quantum wells, resulting in relaxation times $\sim 2-5$ ps [21]. Since, intersubband relaxation in quantum dots occurs by a multi-phonon event, which requires the satisfaction of a stringent resonant condition, this process is very slow (>1 ns). Differential transmission spectroscopy (DTS) [20,22] and high-frequency electrical impedance (HFEI) measurements [21] on $\text{In}_{0.4}\text{Ga}_{0.6}\text{As}/\text{GaAs}$ quantum dots and quantum dot laser diodes, respectively, have revealed the following picture of hot-carrier dynamics in the conduction band of quantum dots, depicted in figure 1. Electrons relax from the barrier to the excited state in 1-2 ps. Electron relaxation from the excited state to the ground state exhibits two time constants: (i) a short time constant ($\sim 6-8$ ps), due to Auger-like processes, intradot electron-hole scattering, and multi-phonon emission [23]; and (ii) a long time constant ($\sim 15-100$ ps), depending on the temperature and excitation level, which is phonon-mediated and demonstrates the phonon-bottleneck phenomenon. These studies also demonstrate that the faster relaxation is a geminate process, wherein the injected electron and hole are captured in the same dot, whereas the slow relaxation process is a non-geminate process, wherein the injected electrons and holes are captured in separate dots, by virtue of the sample temperature or scattering processes. Similar characteristics with respect to long intersubband relaxation times are expected to exist in other III-V quantum dots, such as the InAs/GaAs quantum dots used in QDIPs.

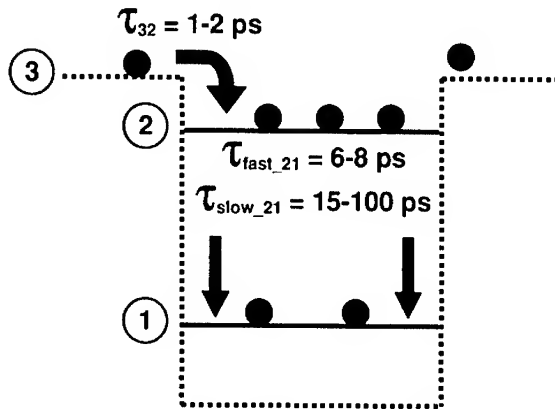


Figure 1. Schematic depiction of electron relaxation times in the conduction band of $\text{In}_{0.4}\text{Ga}_{0.6}\text{As}/\text{GaAs}$ quantum dots. The long intersubband relaxation time from level 2 to level 1 is responsible for many of the expected advantages of QDIPs.

EXPERIMENTAL DETAILS

The InAs/GaAs quantum dots comprising the active region of the vertical QDIPs were grown by solid source molecular beam epitaxy (MBE) using a Varian GEN-II machine with an uncracked As₄ source. Several generations of the device were characterized before obtaining the current best performing detector. The different conduction band profiles for these trial heterostructures are shown in figure 2(a). The results shared in this paper are for the vertical QDIP with a single 30% AlGaAs barrier at the top of ten InAs/GaAs quantum dot layers. First, a 0.5 μm silicon-doped ($n = 2 \times 10^{18} \text{ cm}^{-3}$) GaAs contact layer was deposited on a semi-insulating (100) GaAs substrate at a growth temperature of 620 °C. Next, a 250 Å intrinsic GaAs buffer was grown. The substrate temperature was decreased to 500 °C, and 2.2 ML of InAs were deposited to form the quantum dots. The reflection high-energy electron diffraction (RHEED) pattern was monitored during growth of the dots in order to observe the transition from a layer-by-layer to an island growth mode after about 1.7 ML of InAs deposition. A 250 Å intrinsic GaAs cap layer was grown on top of the InAs in order to complete the quantum dot barrier. This sequence of growth was then repeated nine times for a ten-layer InAs/GaAs quantum dot active region. After the final GaAs layer was grown, the substrate temperature was increased to 620 °C, and 400 Å of intrinsic Al_{0.3}Ga_{0.7}As were deposited in order to form a current-blocking barrier at the top of the device. Finally, a 0.1 μm silicon-doped ($n = 2 \times 10^{18} \text{ cm}^{-3}$) GaAs top contact layer was grown.

A standard, three-step photolithography and wet-etching technique was used to fabricate the device. The first step comprised Ni/Ge/Au/Ti/Au metal evaporation for the top ring contact. Next, a mesa etch ($\approx 1 \mu\text{m}$) was performed around the top contact to define the active region for a single pixel. Finally, the metal evaporation was repeated for the bottom ring contact, which was deposited around the device mesa. The device was annealed at 400 °C for approximately one minute in order to make ohmic contacts. An SEM micrograph of a fabricated device is shown in figure 2(b).

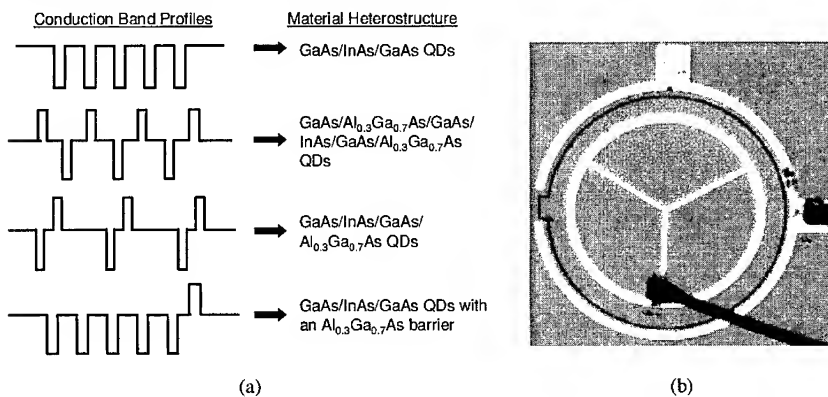


Figure 2. (a) Conduction band profiles for various vertical QDIP heterostructures; and (b) SEM micrograph of a fabricated vertical QDIP with an optical area of $2.83 \times 10^5 \text{ mm}^2$.

RESULTS AND DISCUSSION

Several measurements were conducted in order to completely characterize the vertical QDIP; namely, dark current, spectral response, noise spectra/blackbody response, and dark current uniformity measurements. These characteristics have been discussed in detail previously [24,25]. In the vertical device, at a detector temperature of 100 K, the dark current was 1.7 pA at a bias voltage of 0.1 V, which is an extremely low value. It is evident that the 30% AlGaAs barrier in the vertical QDIP successfully blocks dark current, as shown in figure 3(a), yielding lower dark currents than many other IR detectors. The spectral response was obtained for a detector temperature of 78 K in the vertical QDIP. The λ_{peak} for the response of the vertical QDIP, is 3.72 μm , and $\Delta\lambda/\lambda$ is 0.3, indicating a bound-to-continuum transition [5]. An 800 K blackbody source was used to calibrate the absolute responsivity of the QDIP to normally incident IR radiation for the noise spectra and blackbody response measurements. A germanium block was used at the shutter of the blackbody source in order to filter out near-IR radiation ($< 1.8 \mu\text{m}$) emitted by the blackbody. The vertical QDIP was characterized at 78 K, 100 K, 125 K and 150 K, and the best device performance was measured at 100 K. The maximum R_{peak} value of 2 mA/W for a bias of 0.3 V at 100 K is relatively low when compared to MCT detectors or QWIPs. The low responsivity results from the AlGaAs barrier, which not only blocks dark current, but the photocurrent as well. Despite the low R_{peak} , due to the low noise floor in the devices, a maximum D^* of $2.94 \times 10^9 \text{ cmHz}^{1/2}/\text{W}$ at a bias of 0.2 V is obtained at 100 K, which is a significant milestone in the performance of normal-incidence, vertical QDIPs. The responsivity and detectivity are shown in figure 3(b). Another important result is that the normal-incidence, vertical QDIP could be characterized up to a temperature as high as 150 K before the dark current exceeded the photocurrent, resulting in a signal-to-noise ratio less than one.

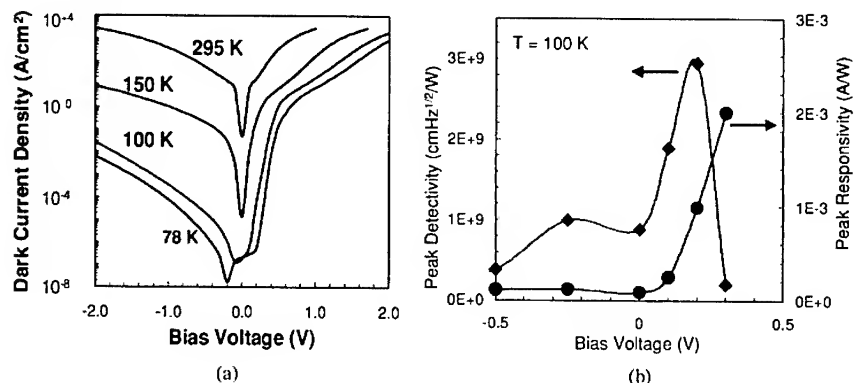


Figure 3. (a) Dark current density (A/cm^2) and (b) peak responsivity and detectivity as a function of bias voltage for InAs/GaAs vertical QDIPs with a 30% AlGaAs barrier.

The encouraging performance characteristics of discrete QDIPs motivated us to explore their application to imaging arrays. The low-bias performance and simple device structure of the vertical QDIP make it the most readily adaptable device to currently available silicon read-out circuits for the fabrication of focal plane arrays. An important factor in the success of a focal plane array is the pixel operability, which depends greatly on the uniformity of a detector array. As a preliminary study, we considered the uniformity of dark current I-V curves at room temperature across a 4x4 vertical QDIP array. The mesa size was $50\text{ }\mu\text{m}$ and the pitch was $100\text{ }\mu\text{m}$. An SEM micrograph of the fabricated array is shown in figure 4(a). As shown in the bubble diagram of figure 4(b), the dark current is fairly consistent across the array. The size of the bubble represents the magnitude of the dark current at the different pixel positions, and there is not a great variation across the array. This signifies that even though quantum dots do suffer from large inhomogeneous linewidths due to the random Stranski-Krastanow growth mode, vertical QDIPs still possess enough uniformity to make feasible the fabrication of large-area focal plane arrays.

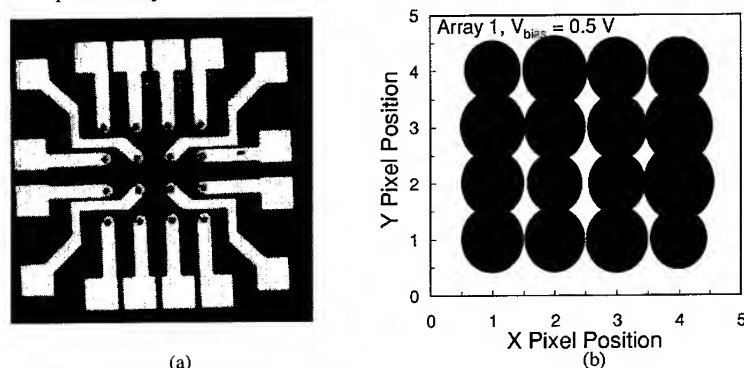


Figure 4. (a) SEM micrograph of fabricated 4x4 vertical QDIP array with $50\text{ }\mu\text{m}$ mesa size and $100\text{ }\mu\text{m}$ pitch; and (b) bubble diagram of dark current magnitude as a function of pixel position, demonstrating uniform dark current across the array.

Keeping in mind that the ultimate goal of infrared detector work is to develop an IR imaging camera, we have attempted to image a heated object with a single device, which we refer to as single pixel imaging. This allows us to demonstrate imaging with QDIPs, even though we are still in the process of designing and fabricating large area focal plane arrays, which is an expensive and time-consuming endeavor. In order to conduct the measurement, we fabricated a 13×13 interconnected vertical QDIP array with a pixel diameter of $40\text{ }\mu\text{m}$ and a pitch of $120\text{ }\mu\text{m}$. While this is not truly a single pixel, since a single average photocurrent is obtained from the entire array, the device behaves as a single pixel with a very large optical area. An X-Y pair of gold-coated mirrors servo-actuated by galvanometers is used to raster scan IR light from the object across the QDIP array. The mirror pair is mounted in a bracket whose exit window is the limiting aperture of the measurement. The QDIP array is mounted inside a cryostat with a KRS-5

window, and a lock-in amplifier is used for data acquisition. The object we chose to image is a graphite furnace igniter, which becomes red-hot when a wall current is passed through it. The image, obtained for a detector temperature of 80 K, is shown in figure 5. A very small section of the igniter is imaged due to the limiting aperture in the X-Y mirror bracket.

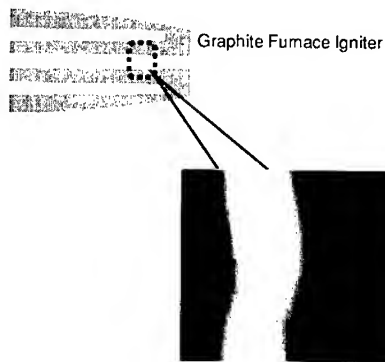


Figure 5. Raster-scanned single pixel image of a section of a graphite furnace igniter obtained at a detector temperature of 80 K for the vertical QDIP heterostructure with a single AlGaAs barrier.

CONCLUSIONS

To conclude, the properties of a vertical InAs/GaAs QDIP with a single 30% AlGaAs barrier have been investigated. This device demonstrates very high D^* values and a high operating temperature for normal-incidence. This device is also unique in that its high performance at low bias demonstrates its suitability for incorporation in a focal plane array that uses commercially available silicon read-out circuits, as demonstrated by a dark current uniformity measurement across a 4x4 vertical QDIP array. The promise of using QDIPs for infrared detection is also demonstrated by the imaging of a heated object with a single interconnected QDIP array. While the low responsivity of these devices must be improved in order to further increase the performance of the QDIPs, their high temperature operation and initially favorable imaging properties certainly motivate further investigation and development.

ACKNOWLEDGEMENTS

This work is being supported by ARO under Grants DAAD19-01-1-0462 and DAAD19-00-1-0394 (DARPA program).

REFERENCES

1. K. W. Berryman, S. A. Lyon, and M. Segev, "Mid-infrared photoconductivity in InAs quantum dots," *Appl. Phys. Lett.*, 70, pp. 1861-1863, 1997.
2. J. Phillips, K. Kamath, and P. Bhattacharya, "Far-infrared photoconductivity in self-organized InAs quantum dots," *Appl. Phys. Lett.*, 72, pp. 2020-2022, 1998.
3. S. Kim, H. Mohseni, M. Erdtmann, E. Michel, C. Jelen, and M. Razeghi, "Growth and characterization of InGaAs/InGaP quantum dots for mid-infrared photoconductive detector," *Appl. Phys. Lett.*, 73, pp. 963-965, 1998.
4. S. Maimon, E. Finkman, and G. Bahir, "Intersublevel transitions in InAs/GaAs quantum dots infrared photodetectors," *Appl. Phys. Lett.*, 73, pp. 2003-2005, 1998.
5. D. Pan, E. Towe, and S. Kennerly, "Normal-incidence intersubband (In, Ga)As/GaAs quantum dot infrared photodetectors," *Appl. Phys. Lett.*, 73, pp. 1937-1939, 1998.
6. S. J. Xu, S. J. Chua, T. Mei, X. C. Wang, X. H. Zhang, G. Karunasiri, W. J. Fan, C. H. Wang, J. Jiang, S. Wang, and X. G. Xie, "Characteristics of InGaAs quantum dot infrared photodetectors," *Appl. Phys. Lett.*, 73, pp. 3153-3155, 1998.
7. Q. D. Zhuang, J. M. Li, H. X. Li, Y. P. Zeng, L. Pan, Y. H. Chen, M. Y. Kong, and L. Y. Lin, "Intraband absorption in the 8-12 μm band from Si-doped vertically aligned InGaAs/GaAs quantum-dot superlattice," *Appl. Phys. Lett.*, 73, pp. 3706-3708, 1998.
8. A. Weber, O. Gauthier-Lafaye, F.H. Julien, J. Brault, M. Gendry, Y. Désières, and T. Benyattou, "Strong normal-incidence infrared absorption in self-organized InAs/InAlAs quantum dots grown on InP(001)," *Appl. Phys. Lett.*, 74, pp. 413-415, 1999.
9. J. Phillips, P. Bhattacharya, S. W. Kennerly, D. W. Beekman, and M. Dutta, "Self-Assembled InAs-GaAs Quantum-Dot Intersubband Detectors," *IEEE J. Quantum Electron.*, 35, pp. 936-943, 1999.
10. L. Chu, A. Zrenner, G. Böhm, and G. Abstreiter, "Normal-incident intersubband photocurrent spectroscopy on InAs/GaAs quantum dots," *Appl. Phys. Lett.*, 75, pp. 3599-3601, 1999.
11. D. Pan, E. Towe, and S. Kennerly, "Photovoltaic quantum-dot infrared detectors," *Appl. Phys. Lett.*, 76, pp. 3301-3303, 2000.
12. H. C. Liu, M. Gao, J. McCaffrey, Z. R. Wasilewski, and S. Fafard, "Quantum dot infrared photodetectors," *Appl. Phys. Lett.*, 78, pp. 79-81, 2001.
13. Y. Wang, S. D. Lin, H. W. Wu, and C. P. Lee, "Low dark current quantum-dot infrared photodetectors with an AlGaAs current blocking layer," *Appl. Phys. Lett.*, 78, pp. 1023-1025, 2001.
14. A. Rogalski, "Assessment of HgCdTe photodiodes and quantum well infrared photoconductors for long wavelength focal plane arrays," *Infrared Phys. & Technol.*, 40, pp. 279-294, 1999.
15. A. Rogalski, *Infrared Detectors*, pp. 155-650, Gordon and Breach Science Publishers, Australia, 2000.
16. B.F. Levine, "Quantum-well infrared photodetectors," *J. Appl. Phys.*, 74, pp. R1-R81, 1993.

17. S. D. Gunapala and K. M. S. V. Bandara, "Recent Developments in Quantum-Well Infrared Photodetectors," *Thin Films*, 21, pp. 113-237, 1995.
18. J. Singh, "Possibility of room temperature intra-band lasing in quantum dot structures placed in high-photon density cavities," *IEEE Photon. Technol. Lett.*, 8, pp. 488-490, 1996.
19. D. Klotzkin, K. Kamath, and P. Bhattacharya, "Quantum capture times at room temperature in high-speed $\text{In}_{0.4}\text{Ga}_{0.6}\text{As}$ -GaAs self-organized quantum-dot lasers," *IEEE Photon. Technol. Lett.*, 9, pp. 1301-1303, 1997.
20. J. Urayama, T. B. Norris, J. Singh, and P. Bhattacharya, "Temperature dependent carrier dynamics in InGaAs self-assembled quantum dots," *Phys. Rev. Lett.*, 86, pp. 4930-, 2001.
21. D. Klotzkin and P. Bhattacharya, "Temperature dependence of dynamic and dc characteristics of quantum dot and quantum well lasers: A comparative study," *IEEE J. of Lightwave Technol.*, 17, pp. 1634-, 1999.
22. T. Sosnowski, T. Norris, H. Jiang, J. Singh, K. Kamath, and P. Bhattacharya, "Rapid carrier relaxation in $\text{In}_{0.4}\text{Ga}_{0.6}\text{As}$ /GaAs quantum dots characterized by differential transmission spectroscopy," *Phys. Rev. B-Condensed Matter*, 57, pp. R9423-, 1998.
23. K. Mukai, N. Ohtsuka, H. Shoji, and M. Sugawara, "Emission from discrete levels in self-formed InGaAs/GaAs quantum dots by electric carrier injection: influence of phonon bottleneck," *Appl. Phys. Lett.*, 68, pp. 3013-, 1996.
24. A. D. Stiff, S. Krishna, P. Bhattacharya, and S. Kennerly, "High-detectivity, normal-incidence, mid-infrared ($\sim 4 \mu\text{m}$) InAs/GaAs quantum-dot detector operating at 150 K," *Appl. Phys. Lett.*, 79, pp. 421-423, 2001.
25. A. D. Stiff, S. Krishna, P. Bhattacharya, and S. Kennerly, "Normal-Incidence, High-Temperature, Mid-Infrared, InAs/GaAs Vertical Quantum-Dot Infrared Photodetector," *IEEE J. of Quant. Electron.*, 37, pp. 1412-1419, 2001.

Enhanced Photoluminescence from Long Wavelength InAs Quantum Dots Embedded in a Graded (In,Ga)As Quantum Well

L. Chen, V. G. Stoleru, D. Pal, D. Pan, and E. Towe
Department of Electrical and Computer Engineering, University of Virginia, Charlottesville,
Virginia 22904

ABSTRACT

Three sets of self-organized InAs quantum dots (QDs) embedded in an external InGaAs quantum well samples were grown by solid source molecular beam epitaxy (MBE). By modifying Indium composition profile within quantum well (QW) region, it's found the photoluminescence emission from quantum dots can be greatly enhanced when employing a graded quantum well to surround QDs. This quantum dots in a graded quantum well structure also preserves the long wavelength (1.3 μm) spectrum requirement for the future use in optoelectronics devices.

INTRODUCTION

The first GaAs-based quantum-dot laser was reported in 1994 [1]. Since then, remarkable progress has been made in the development of this device. Edge-emitting lasers operating from 1.0 to 1.3 μm with very low threshold currents have been reported [2,3,9]; in addition, vertical-cavity surface-emitting lasers (VCSELs) have also been successfully demonstrated [4].

There are currently several approaches to grow 1.3 μm (In,Ga)As quantum dots by MBE. These include (i) the alternate supply of group-III and group-V source materials to form the (In,Ga)As dots [5], (ii) very slow growth (<0.01 ML/sec) of the InAs dots at high substrate temperatures [6], (iii) burying the InAs dots with an InGaAs overlayer to reduce the strain [7], and (iv) embedding the InAs dots inside an InGaAs quantum well [8].

Most quantum-dot lasers operating at 1.3 μm appear to have two major unresolved problems: a low density of dots and a weak carrier confinement to the active region. Both of these problems imply low optical gain. In fact, the low gain is believed to prohibit the lasers from operating at the ground state without high-reflectivity coatings [3,10]. One approach to achieving tight carrier confinement is to use growth method (iv), which embeds the dots in an InGaAs quantum well. In addition to serving as a strain reducing (and hence a wavelength tuning) layer, the InGaAs quantum well also serves to confine carriers within the vicinity of the quantum-dot layer, thus promoting capture within the dots [9].

In this paper, we report a modified structure with InAs quantum dots embedded in a graded InGaAs quantum well, which not only tunes the QDs emission to 1.3 μm , but also greatly enhances the photoluminescence (PL) efficiency.

EXPERIMENT

The samples in our study were grown in a Riber 32P solid source MBE system on semi-insulating (001) GaAs substrates. The basic structure for PL study consists of a 250 nm GaAs buffer grown at a substrate temperature of 580°C, a 90 nm GaAs layer with a reduced substrate temperature at 490°C, 1~2.5 ML InAs quantum dots symmetrically sandwiched in an 8 nm

$\text{In}_x\text{Ga}_{1-x}\text{As}$ layer and a final 90 nm GaAs top layer. For Atomic-Force Microscopy (AFM), samples with similar structures, but with growth stopped after InAs deposition, were grown. The growth rate of the InAs dots was 0.05 ML/sec. The substrate holder was continuously rotated to improve the uniformity. A Coherent Argon ion laser ($\lambda=488$ nm) is used for PL and the emitted radiation was detected by a SPEX 500M spectrometer with a cooled Hamamatsu Ge detector. A Bomen MB155S FTIR is used for photocurrent (PC) measurement and a PSI AutoProbe CP is used for AFM.

RESULTS AND DISCUSSION

Fig. 1 shows the PL spectra of InAs QDs embedded in an 8 nm $\text{In}_x\text{Ga}_{1-x}\text{As}$ QW with different Indium composition x under different InAs deposition. From Fig.1, it's seen that the wavelength can be red shifted with the increase of InAs deposition. When InAs content is increased to 2.5 ML, the peak wavelength of QDs in an $\text{In}_{0.18}\text{Ga}_{0.82}\text{As}$ QW reaches 1.3 μm but with apparent decrease of PL intensity, which indicates the possible formation of defects in this highly strained structure. Our best result is from 2.5 ML InAs QDs in an $\text{In}_{0.15}\text{Ga}_{0.85}\text{As}$ QW.

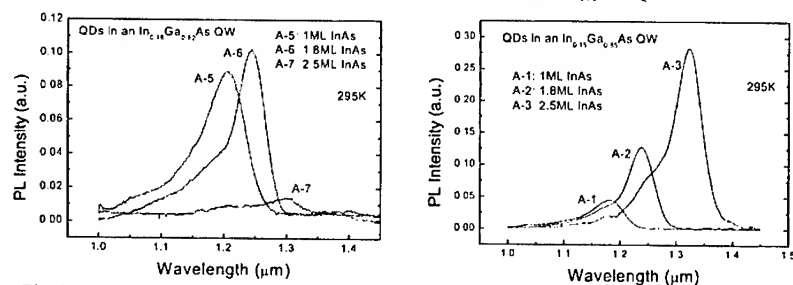


Fig. 1. Room temperature photoluminescence spectra of InAs quantum dots embedded in an 8 nm $\text{In}_x\text{Ga}_{1-x}\text{As}$ quantum well with various InAs deposition.

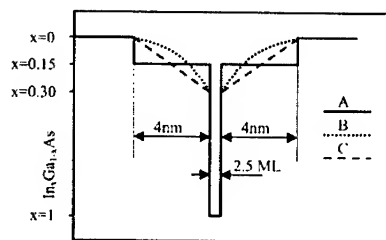


Fig. 2. Schematic structure of three different sets of quantum dot samples.

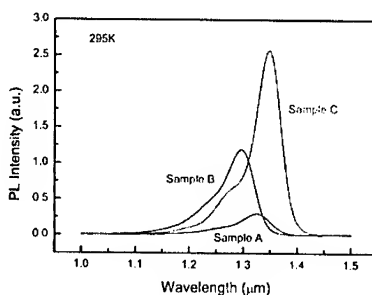


Fig. 3. Room-temperature PL spectra of QD samples at an optical excitation level of ~ 30 W/cm^2 .

To further study the influence of Indium composition profile in the $\text{In}_x\text{Ga}_{1-x}\text{As}$ QW, We modify the QW growth. A schematic of the generic structures is shown in Fig. 2. Structure A consists of 2.5 monolayers of InAs QDs sandwiched at the center of an 8 nm $\text{In}_{0.15}\text{Ga}_{0.85}\text{As}$ layer. Structure B consists of 2.5 monolayers of InAs QDs sandwiched at the center of an 8 nm $\text{In}_x\text{Ga}_{1-x}\text{As}$ layer.

x As layer; where the bottom half of the $\text{In}_x\text{Ga}_{1-x}\text{As}$ layer is graded from $x = 0.03$ to $x = 0.3$ and the top half is graded from $x = 0.3$ to $x = 0.03$. The change of Indium composition in the graded QW was achieved by gradually increasing or decreasing the Indium cell's temperature, which resulted in a curved shape of Indium distribution. The structure C is similar to structure B except that InAs/GaAs superlattice layers are used to form a quasi-linear indium distribution along the growth direction.

Room temperature photoluminescence spectra of three typical samples A, B, and C are shown in Fig. 3. The emission from the ground state transition for all three samples is at, or beyond $1.3 \mu\text{m}$, with sample C extending to $1.35 \mu\text{m}$. The spectral linewidths at half-maximum intensity for these three samples are $\Delta \lambda_A = 48 \text{ meV}$, $\Delta \lambda_B = 53 \text{ meV}$, and $\Delta \lambda_C = 39 \text{ meV}$, which shows the inhomogeneous broadening in all the samples. The grading of the $\text{In}_x\text{Ga}_{1-x}\text{As}$ QW does not have apparent effect on the uniformity of the dots. What the grading appears to do is to improve the efficiency of emission. The peak intensity of sample C, for example, is about 8.7 times higher than that of sample A. Since the only difference in the three samples is the structure of the $\text{In}_x\text{Ga}_{1-x}\text{As}$ layer into which the quantum dots are embedded, it is reasonable to speculate that the enhancement of PL intensity is due to the grading. There may be two possible reasons that account for this enhancement. One is that, in a graded QW, the energy band is also graded; this helps to drive the carriers into the quantum well, and hence into the quantum dots. Because of the three-dimensional nature of quantum dots, the graded potential also exists in the lateral direction; this enhances spatially carrier capture within the dots. The second reason for the enhancement is the smoothing effect of the InAs/GaAs superlattice. The use of superlattice causes smooth transition of the lattice parameter from the GaAs to the InAs, thus may help to reduce the defects formation. The defects, if present, would form loss channels in the electron-hole recombination process.

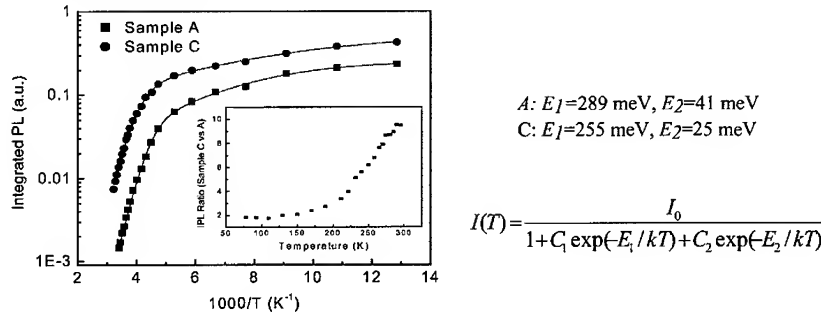


Fig. 4. The Arrhenius plots of the IPL intensity of sample A and C at an excitation level of $\sim 10 \text{ W/cm}^2$. The solid lines are fitted by the equation shown on the figure. The inset is the ratio of the IPL intensity of sample C to that of sample A as a function of temperature.

We have further studied the temperature-dependent integrated photoluminescence (IPL) intensity of samples A and C. The Arrhenius plots for these two samples are shown in Fig. 4. As seen from the figure, photoluminescence enhancement of sample C is more dramatic at higher temperatures (see the inset in Fig. 4). We fit the variation of the IPL intensity data with temperature by a generic empirical relationship [11] shown on the figure, where E_1 and E_2 are the thermal activation energies for loss mechanisms active at certain temperature ranges, k is the

Boltzmann constant, T is the temperature, and C_1 , C_2 and I_0 are fitting constants. In a physical model, these constants would take into account the recombination rates and the geometric dimensions of the dots. In Fig. 4, the solid lines are the fitting curves; the filled circles and squares represent experimental data. The extracted thermal activation energies are $E_1=289$ meV, and $E_2=41$ meV for sample A; and $E_1=255$ meV and $E_2=25$ meV for sample C. A calculation (which we will discuss later) shows that the energy difference between the ground state in the conduction band of a dot and the band-edge of the surrounding (In,Ga)As quantum well at 300 K is about 317 meV for structure A and 267 meV for sample C. These energy differences are quite close to the measured activation energies E_1 (which dominates the quenching at high temperature) for sample A and C. Note that the IPL intensity has a quenching threshold temperature ~ 190 K for sample C, and ~ 170 K for sample A. Either a fast trapping of carriers to the QDs or a reduced loss channel around QW can result in a higher quenching threshold. Our results here are similar to those of Ru *et al.* who used hydrogen passivation (in order to reduce the defect concentrations in their samples) to enhance the photoluminescence emission [12].

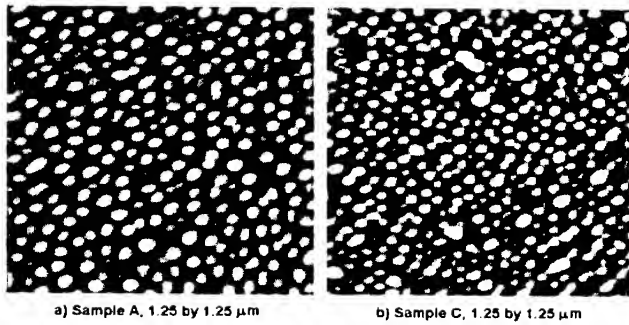


Fig.5. AFM photo-micrographs of the morphology of structure A and C.

We have also examined the possible effects of the grading on the dot density and uniformity. Two structures similar to sample A and C were grown for AFM observation. Figure 5 shows that there are no major differences in the two samples. Sample A, for example, has a dot density of around $2.5 \times 10^{10} \text{ cm}^{-2}$, while sample C has a dot density about $2.8 \times 10^{10} \text{ cm}^{-2}$. The true size of the dots cannot be determined from AFM measurement; reasonable estimates, however, can be obtained from cross-sectional TEM studies.

To show that the graded quantum well structure does not substantially modify the basic band structures, we have studied both the intensity dependent photoluminescence and photocurrent at LN_2 (78 K) temperature. In Fig. 6, we show the PL emission from sample A and sample C at high pump levels, and in Fig. 7, we show the photocurrent spectra of sample A and C excited by a broad band incident light (filtered by GaAs). There are clearly four transition energy peaks for each sample; the peaks occur at almost identical locations for both samples. To confirm these transition levels are from QDs, we have carried out some analytical calculations to determine the interband transition energies. These calculations require information on the strain distribution inside and around the dots. The strain generally depends on the shape and size of the dots, which

are difficult to determine accurately in most experimental situations. For our dots, we estimate their lateral base to be around 15 nm; the base to height ratio for sample A is about 7; and it is

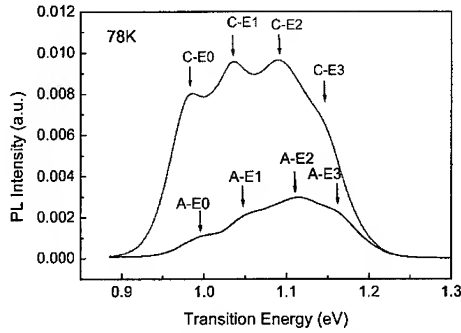


Fig. 6. Low-temperature (78 K) PL spectra of sample A and C at high optical pumping level.

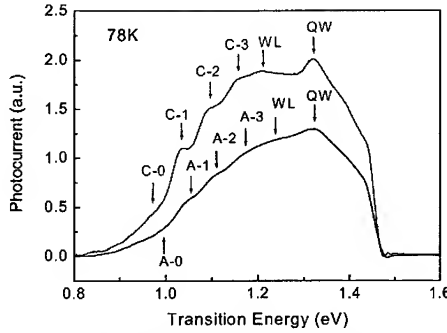


Fig. 7. Low-temperature (78 K) Photocurrent spectra of sample A and C.

5 for sample C. These estimates are based on our earlier work on buried InAs/GaAs and InGaAs/GaAs quantum dots [13], and on TEM and SEM observations. The estimate on height is further corroborated with *in-situ* RHEED observations where the thickness of an overlayer needed to completely bury an array of dots can give a rough measure of the dot height. For the calculations, we have further assumed that the dots are truncated pyramids.

Structure	Data Source	Transition Energy (eV)				
		Low Temperature (77K)				RT
		E0	E1	E2	E3	E0
A	Experimental	1.019	1.056	1.102	1.154	0.934
	Calculated	1.0162	1.0572	1.0951	1.1500	0.9405
C	Experimental	0.987	1.036	1.083	1.139	0.919
	Calculated	0.9830	1.0379	1.0809	1.1315	0.9138

Table I. Experimental and calculated transition Energies for sample A and C

The electronic spectra here are calculated in the envelope function approximation using an eight-band, strain-dependent Hamiltonian based on the $\mathbf{k}\cdot\mathbf{p}$ method [14]. The method takes into account the coupling among the light- and heavy-hole bands, and the split-off valence bands. It also includes the linear coupling between the conduction and valence bands. The lack of inversion symmetry in the zinc-blende structure, however, is neglected. The effect of strain is included via deformation potential theory [15], and the Luttinger-Kohn parameters are calculated according to the method by Pollak [16], and Bir and Pikus [17]. Because the quantum dots are in the strong confinement regime, additional binding energy from the Coulomb interaction is neglected. The bound states of QDs are found by numerically solving the Schrödinger equation, by invoking periodic boundary conditions, expanding the wavefunctions in terms of normalized

plane-wave states, and diagonalizing the obtained matrix. The calculated transition energies for sample A and C are shown in Table I. We have also shown the experimentally determined values from the photoluminescence data by multi-peaks Gaussian fitting. The experimental and the calculated transition energies are in reasonably good agreement.

CONCLUSIONS AND ACKNOWLEDGEMENT

In summary, we have shown that the photoluminescence efficiency of InAs quantum dots can be enhanced by embedding them in a graded (In,Ga)As quantum well structures. Furthermore, our proposed approach has the virtue of promoting carrier capture in potential laser structures in addition to allowing emission at the desirable telecommunications wavelength of 1.3 μm .

This work is supported under grant number DAAD19-00-1-0442 of the US Army Research Office, Research Triangle Park, North Carolina, and by the US Army Research Laboratory, Adelphi, Maryland.

REFERENCES

- [1] N. Kirkstædter, N. Ledentsov, M. Grundmann, D. Bimberg, V. Ustinov, S. Ruvimov, M. Maximov, P. Kop'ev, and Zh. Alferov, *Electron. Lett.* **30**, 1416 (1994).
- [2] G. Park, O.B. Shchekin, D.L. Huffaker, and D.G. Deppe, *IEEE Photon. Tech. Lett.* **12**, 230 (2000).
- [3] D.L. Huffaker, G. Park, Z. Zou, O.B. Shchekin, and D.G. Deppe, *Appl. Phys. Lett.* **73**, 2564 (1998).
- [4] J.A. Lott, N. Ledentsov, V. Ustinov, N. A. Malcev, A. E. Zhukov, A. R. Kovsh, M. V. Maximov, B. V. Volovik, Zh. I. Alferov, and D. Bimberg, *Electron. Lett.* **36**, 1384 (2000).
- [5] D.L. Huffaker and D.G. Deppe, *Appl. Phys. Lett.* **73**, 520 (1998).
- [6] R. Murray, D. Childs, S. Malik, P. Sivers, C. Roberts, J.M. Hartmann, and P. Stavrinou, *Jpn. J. Appl. Phys.* **38**, 528 (1999).
- [7] K. Nishi, H. Saito, and S. Sugou, *Appl. Phys. Lett.* **74**, 1111 (1999).
- [8] A. Stintz, G. T. Liu, H. Li, L. F. Lester, and K. J. Malloy, *IEEE Photon. Tech. Lett.* **12**, 591 (2000).
- [9] G. T. Liu, A. Stintz, H. Li, T.C. Newell, A.L. Gray, P.M. Varangis, K. J. Malloy, and L. F. Lester, *IEEE Journal of Quan. Electron.* **36**, 1273 (2000).
- [10] N. Hatori, M. Sugawara, K. Mukai, Y. Nakata, and H. Ishikawa, *Appl. Phys. Lett.* **77**, 773 (2000).
- [11] Y. Wu, K. Arai, and T. Yao, *Phys. Rev. B* **53**, 10485 (1996).
- [12] E. C. Le Ru, P. D. Sivers, and R. Murray, *Appl. Phys. Lett.* **77**, 2446 (2000).
- [13] V. G. Stoleru, D. Pal, and E. Towe, *Mater. Res. Soc. Proc.* Vol. **642**, J.I.7.1-6, Boston, MA (2000).
- [14] T.B. Bahder, *Phys. Rev. B* **41**, 11992 (1992).
- [15] O. Stier, M. Grundmann, and D. Bimberg, *Phys. Rev. B* **59**, 5688 (1999).
- [16] F. H. Pollak, *Semiconductors and Semimetals*, Academic Press, Inc., New York, Volume **32**, pp. 17 (1990).
- [17] G. E. Pikus and G. L. Bir, *Sov. Phys. Solid State* **1**, 1502 (1960).

A Theoretical Study of Structural Disorder and Photoluminescence Linewidth in InGaAs/GaAs Self Assembled Quantum Dots

Yih-Yin Lin, Hongtao Jiang,¹ and Jasprit Singh
Department of Electrical Engineering and Computer Science,
University of Michigan, Ann Arbor, MI 48109-2122

¹Broadcom Corporation, Irvine, CA 92618

ABSTRACT

The past few years have seen considerable efforts in growth and device application of self-assembled quantum dots. However, the photoluminescence (PL) linewidth, which represents structural fluctuations in dot sizes, is still in the range of 30-50 meV. This large linewidth has deleterious effects on devices such as lasers based on self-assembled dots. In this paper we will examine the configuration-energy diagram of self-assembled dots. Our formalism is based on: (1) an atomistic Monte Carlo method which allows us to find the minimum energy configuration and strain tensors as well as intermediate configurations of dots; (2) an 8-band $k \cdot p$ method to calculate the electronic spectra. We present results on the strain energy per unit cell for various distributions of InAs/GaAs quantum dots and relate them to published experimental results. In particular we examine uncovered InAs/GaAs dots and show that in the uncovered state a well-defined minimum exists in the configuration energy plot. The minimum corresponds to the size that agrees well with experiments.

INTRODUCTION

The use of strained epitaxy to create quasi-0 dimensional quantum dots has been widely studied over the last decade. Self-assembled quantum dots have now been fabricated using InGaAs/GaAs, SiGe/Ge, and many other strained systems [1-2]. In addition to the study of electronic and optical properties of these dots, devices lower as quantum dot interband lasers [3] and intersubband detectors [4] have been demonstrated. However, in spite of much progress in the area of self assembly, there is still a nagging issue - dot size nonuniformity. The self assembled dots vary in sizes and shapes - a variation that reflects in the electronic spectrum, photoluminescence linewidth, and gain spectrum etc. For many potential device applications, dot size nonuniformity creates deleterious effects. To understand the reason for nonuniformity and its extent, it is important to study the configuration energy of self-assembled dots.

There have been several studies on the strain tensor and energy in self-assembled dots. A useful model has emerged the valence force field (VFF) method [5,6], which allows us to calculate the strain tensor at an atomic level. It is found that the strain tensor in dots plays a key role in determining the electronic spectrum [7]. While the strain tensor of quantum dots in the covered state (i.e. with the dot buried in the large bandgap material matrix) has been examined, to our knowledge no work has been done on why certain mean dot sizes are chosen and why there is a distribution in the dot size. In this paper we use an extension of the VFF model to examine the strain tensor and energy of "covered" and "uncovered" InAs/GaAs dots. Then we apply the 8-band $k \cdot p$ model to obtain the electronic spectrum.

THEORETICAL MODEL

It is known that when a large strain exists between an overlayer and a substrate ($\epsilon > 3\%$), the growth of the overlayer is described by the Stranski-Krastanow mode. In this mode a thin "wetting layer" is followed by an island growth. For InAs/GaAs system, the wetting layer is ~ 1 monolayer, and the islands are approximately 60 \AA high with a more or less pyramidal shape. The base of the pyramid is about twice the height [8, 9]. This description of the self-assembled dots is, however, very qualitative since there is a considerable variation in the size and shape. There is substantial theoretical work on why the growth mode is island growth for high strain epitaxy. However, there is no quantitative work on why a particular size dominates the self-assembled system. To shed light on this issue, we calculate the strain tensor and energy for various sizes/shapes of InAs dots on a GaAs substrate. We examine the "uncovered" dots where the GaAs overlayer is not present and the "covered" dots where dots are embedded in a GaAs matrix.

The strained InAs/GaAs quantum dot system is shown in figure 1 for growth along the [001] direction. The InAs island is pyramidal shaped with a small square base, lying on a 1-monolayer InAs wetting layer. The InAs QDs are embedded in a GaAs matrix.

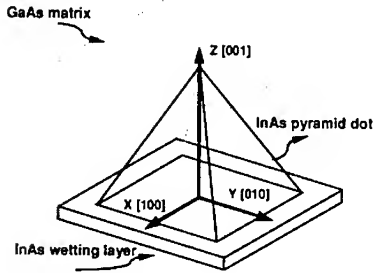


Figure 1. Schematic illustration of the Stranski-Krastanow growth mode for InAs/GaAs system.

Valence force field (VFF) model is a microscopic elastic theory, which includes the bond-stretching and bond-bending parts. The total VFF energy is taken as

$$U = \frac{1}{4} \sum_{ij} \frac{3}{4} \alpha_{ij} (d_{ij}^2 - d_{0,ij}^2)^2 / d_{0,ij}^2 + \frac{1}{2} \sum_i \sum_{j \neq k} \frac{3}{4} \beta_{ijk} (d_{ij} \cdot d_{ik} + d_{0,ij} d_{0,ik} / 3)^2 / d_{0,ij} d_{0,ik} \quad (1)$$

where i represents all atomic sites, and j, k are the nearest neighbor sites. d_{ij} is the vector joining sites i and j , d_{ij} is the bond's length, and $d_{0,ij}$ is the corresponding equilibrium bond length. α and β are the bond-stretching and bending constants. To fully understand the formation of self assembled InAs QDs, we simulate the uncovered InAs dots by replacing the GaAs cap with a virtual material by artificially reducing α and β to very small values (factor of 10 smaller). As a result, we can observe the behavior of InAs islands before the covering GaAs is deposited.

The strain tensors are solved by minimization of the total energy within the framework of the VFF model. We use the approach taken by several authors [10-12]. In the beginning all atoms are placed on the GaAs lattice. The atoms are allowed to deviate from this starting position and periodic boundary conditions are assumed in the plane perpendicular to the growth

condition. In each process, only one atom is displaced while other atoms are held fixed. All atoms are displaced in sequence. The whole sequence is repeated until the maximum distance moved is so small that there is essentially no change in the system energy. The strain energy E_{str} can then be obtained once the strain tensors can be obtained by

$$E_{str} = \frac{a^3}{4} \left[\frac{1}{2} c_{11} (\epsilon_{xx}^2 + \epsilon_{yy}^2 + \epsilon_{zz}^2) + c_{12} (\epsilon_{yy}\epsilon_{zz} + \epsilon_{zz}\epsilon_{xx} + \epsilon_{xx}\epsilon_{yy}) + \frac{1}{2} (\epsilon_{zx}^2 + \epsilon_{yz}^2 + \epsilon_{xy}^2) \right] \quad (2)$$

where a is the lattice constant, ϵ_{ij} is the strain tensor component, and c_{ij} is the elastic constant. The 8-band $k \cdot p$ method [13] is used to calculate the electronic spectra.

RESULTS

The calculated results for strain energy per unit cell as a function of dot size in a covered InAs/GaAs system are shown in figure 2. The size variation is done when the base to height ratio is maintained at 2:1. No clear preference appears in the form of a well defined energy minimum. The strain energy of InAs dots for large sizes even show higher values than forming a flat thin layer (~ 0.17 eV), which is unexpected. It is clear that the InAs dot size/shape is determined by the energies of the problem before the GaAs overlayer is deposited.

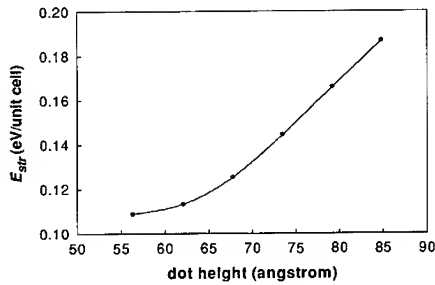


Figure 2. Strain energy per unit cell for the covered InAs dot pyramid at various dot sizes.

Figure 3 addresses the question of why certain dot sizes are preferred in high strain epitaxy. The strain energy per unit cell is illustrated as a function of the dot size. We show results for the dot alone and also the results when the wetting layer is included. Inclusion of the wetting layer is a little arbitrary since the results depend on the dot density. Nevertheless a clear minimum arises in the configuration energy plots in both cases at 62 Å dot height. This value is remarkably close to empirical observation [9]. However, due to entropy consideration we do not expect all dots to have this minimum energy size. Experimentally we know that there are variations in the dot size, causing inhomogeneous broadening of the photoluminescence line. Figure 3 also lists the values of effective bandgaps, showing how the dot size can alter the effect bandgap. We find that the effective gaps range from 0.954 to 1.2 eV as the height changes from 85 to 55 Å. The preferred size has a peak energy of ~ 1.04 eV, which agrees well with the experimental PL results [14].

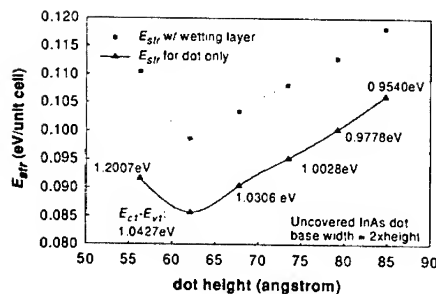


Figure 3. Strain energy per unit cell for dot only and for dot including wetting layer and effective bandgaps for the uncovered InAs dot pyramid at various dot sizes.

The electronic spectrum for different dot sizes is shown in figure 4. Here we show the ground states and the excited states of dots with heights of 56.5 Å and 62.3 Å. In each case the base is twice the height. As can be seen, the size variation will contribute to more fluctuation for higher level transitions.

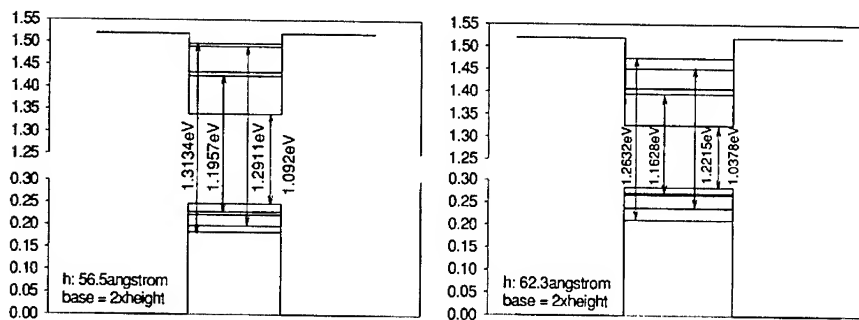


Figure 4. Electronic spectrum for InAs/GaAs dots with various heights of 56.5 Å and 62.3 Å.

Figure 5 shows how the strain energy change as a function of the shape of the dot. Here the height is fixed at the lowest configuration energy found in figure 3 while the width is adjusted. A larger base width corresponds to a wider dot pyramid and vice versa. It can be seen that when the base equals twice the island height the energy is a minimum. This result is consistent with experimental observation [9]. It is important to note that the total energy of the system would include the wetting layer strain energy and one has to then account for the dot density as well.

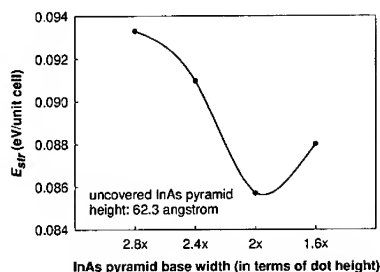


Figure 5. Strain energy of dot formation per unit cell for different dot shapes (various base).

CONCLUSION

In this paper we have examined the configuration energy profile for InAs/GaAs self-assembled dots. While it is not possible to examine the infinite possible sizes and shapes a dot can take, we find that there is a well defined size and shape as which the strain energy for the uncovered dot becomes a minimum. The shape and size calculated by us using the VFF model agree quite well with experimental findings on InAs/GaAs dots. We have also examined the configuration energy plot for covered dots, which do not show any energy minimum at the dot size observed empirically. This suggests that the dot size/shape is determined before the covering GaAs layer is deposited. Although the configuration energy is estimated assuming a pyramidal shaped dot, the calculation is done by a microscopically atomistic model. Thus this approach can be exploited to the truncated pyramidal quantum dots or even in the microlenses structure.

Another outcome of our finding is that the strain energy difference between the minimum energy configuration and other nearby dot sizes is not very large. As a result, it is expected that there will be a distribution of dots in actual growth due to entropy considerations. We have also shown how the size of dots alters the effective band-edge using the 8-band k - p method.

The good agreement of the minimum energy dot size and shape with published experimental results gives us confidence that the VFF model can be explored to understand how the dot uniformity can be controlled. This could be done by examining the role of pre-existing strains in the GaAs substrate. Further work will address these issues as well as the issue of dot size distributions.

ACKNOWLEDGEMENT

This work has been funded by US Army MURI (contract number F004658).

REFERENCES

1. J.-Y. Marzin, J.-M. Gérard, A. Izraël, D. Barrier, and G. Bastard, Phys. Rev. Lett., **73**, 716 (1994).

2. C. Teichert, M. G. Lagally, L. J. Peticolas, J. C. Bean, and J. Tersoff, *Phys. Rev. B*, **53**, 16334 (1996).
3. S. Krishna, O. Quasimeh, P. Bhattacharya, P. J. McCann, and K. Namjou, *Appl. Phys. Lett.*, **76**, 3355 (2000).
4. H. Jiang and J. Singh, *Physica E*, **2**, 720 (1998).
5. P. N. Keating, *Phys. Rev.*, **145**, 637 (1966).
6. R. M. Martin, *Phys. Rev. B*, **1**, 4005 (1969).
7. M. Grundmann, N. N. Ledentsov, O. Stier, D. Bimberg, V. M. Ustinov, P. S. Kop'ev, and Zh. I. Alferov, *Appl. Phys. Lett.*, **68**, 979 (1996).
8. M. A. Cusack, P. R. Briddon, and M. Jaros, *Phys. Rev. B*, **54**, R2300 (1996).
9. S. Krishna, J. Sabarinathan, P. Bhattacharya, B. Lita, and R. S. Goldman, *J. Vac. Sci. Technol. B*, **18**, 1502 (2000).
10. J. Bernard and A. Zunger, *Appl. Phys. Lett.*, **65**, 165 (1994).
11. F. Glas, *J. Appl. Phys.*, **66**, 1667 (1989).
12. M. R. Weidmann and K. E. Newman, *Phys. Rev. B*, **45**, 2763 (1996).
13. H. Jiang and J. Singh, *Appl. Phys. Lett.*, **71**, 3239 (1997).
14. F. Alder, M. Geiger, A. Bauknecht, F. Scholz, H. Schweizer, M. H. Pikuhn, B. Ohnesorge, and A. Forchel, *J. Appl. Phys.*, **80**, 4019 (1996).

Electroluminescence and Spectral Shift of CdS Nanoparticles on Si Wafer

Eih-Zhe Liang¹, Ching-Fuh Lin¹, Sheng-Ming Shih, and Wei-Fang Su*
Institute of Materials Science and Engineering, National Taiwan University,
Taipei, Taiwan, R.O.C.

¹Graduate Institute of Electro-Optical Engineering, National Taiwan University,
Taipei, Taiwan, R.O.C.

Abstract

Preparation of CdS nanoparticles, devices fabrication, and electroluminescence properties at room temperature of CdS nanoparticles on silicon substrates are reported. A spectral shift of 86-meV of free exciton transition was observed that was due to the passivation of p-hydroxyl thiophenol molecules around nanoparticles. Controlled process conditions such as heat treatment and/or with oxygen-rich environment are experimented and found to have significant influences on emission spectra. Radiative recombination corresponding to oxygen-impurity level, 273 meV below bandgap energy, presents in samples prepared in oxygen-rich environment. In addition to such mechanism, coalescence of nanoparticles into bulk form also exists and contributes to enhanced luminescence.

Introduction

Low-dimensional structures including nanoparticles or quantum dots (QDs) are supposed to provide significant enhancement in the density of states, so increasing the probability of light emission. Those low-dimensional structures can be epitaxially grown on bulk materials like GaAs wafers or separately formed by chemical methods. The former way is very selective on the grown substrates. Also, QDs are usually formed with only a scarce area density. In contrast, nanoparticles formed by chemical methods have many advantages. First, they can be applied on any substrates. Second, area or volume density of the material can be very high. The process to fabricate monodisperse nanoparticles is inexpensive and facile to industrial application. Stimulated emission and optical gain had been demonstrated in CdS quantum dots by methods of optical pumping[1,2]. This encourages the employment of electrical pumping to realize efficient nanoparticle-based light emitting devices.

In this work, we demonstrate the applications of CdS nanoparticles on silicon substrate. The fabrication of light emitting active layer is simply fabricated by the spin-coating technique. Electroluminescence (EL) can be easily achieved by quantum tunneling of carriers into the nanoparticles. No special care is needed, compared with thermal and chemical budgets of epitaxial technology.

Experimental

Preparation of CdS Nanoparticles

Redissolvable nanoparticles powder of CdS has been synthesized by modifying Pietro's method[3]. Cadmium acetate dihydrate ($\text{Cd}(\text{CH}_3\text{COO})_2 \cdot 2\text{H}_2\text{O}$, 0.80 g, 3.0 mmole) was dissolved in a 20 ml mixed solvent of acetonitrile, methanol, and water with a volume ratio of 1:1:2. Another solution containing disodium sulfide nonahydrate ($\text{Na}_2\text{S} \cdot 9\text{H}_2\text{O}$, 0.36 g, 1.5 mmole) and p-hydroxyl thiophenol (0.56 g, 4.4 mmole) in the same solvent system was added into vigorously stirred cadmium acetate solution. The whole system was stirred for 18 hours without light illumination. After centrifuging and washing with DI water for several times, we obtained a 0.70g yellow powder of CdS nanoparticles encapped by p-hydroxyl thiophenol.

By replacing part of cadmium acetate with manganese acetate (5 %, 10 % and 20 %, in molar ratio), we prepared Mn doped CdS nanoparticles with different concentrations of manganese. All prepared semiconductor nanoparticles can be re-dispersed in ethanol and other polar organic solvents. With ultrasonic vibration and percolation solutions for spin-coating purpose were produced by dissolving the nanoparticles in ethanol with a concentration of 1% (w/v).

Fabrication of CdS Light-Emitting Diodes on Si

The general fabrication steps of CdS light emitting diodes (LEDs) as follows. First, a low resistivity (doping $\sim 10^{15} \text{ cm}^{-3}$) silicon wafer was used as the substrate. Acetone, methanol, and DI water were used for subsequently cleaning procedure. The wafer was placed on spinner with several dips of the previously mentioned four CdS and CdS:Mn nanoparticle solutions. A spin speed of 4000 rpm for 60 sec was used. There are three different treatments with the devices. Sample A: The wafer was placed in a chamber, in which 75-mmHg air pressure and room temperature were maintained for 5 minutes to remove ethanol solvents. Sample B: The samples were subsequently treated by rapid thermal annealing (RTA) at 425°C for 5 minutes. The annealing process took place with 75-mmHg air pressure. At this temperature, the organic chemical was decomposed. Sample C: We immersed the CdS nanoparticles into high oxygen concentration environment. The nanoparticle solutions had been separately mixed with SOG (spin-on-glass) 315FX and SiO_2 nanoparticles (average diameter of 12 nm, dissolved in isopropyl alcohol). The cleaned silicon substrate was spin coated with these two kinds of mixture solutions. Both samples were treated by 425°C RTA to sinter the SiO_2 glass.

Subsequently, both top and bottom metal contacts were defined by thermal evaporation. The top semi-transparent contact layer was 10nm gold, and the bottom was 150nm gold. Before the deposition of Au layer, a 3-nm adhesion layer of chromium had been evaporated for both contacts. After voltage bias was applied, EL through top thin layer can be seen by naked eyes. Monochromator(CVI CM110) and photomultiplier were used to record the spectra. In every spectrum measurement, the slit width 0.6 mm was used for maximum detections and correct spectral measurements.

Results and Discussion

The TEM micrograph of CdS nanoparticles is shown in Figure 1(A). The average diameter

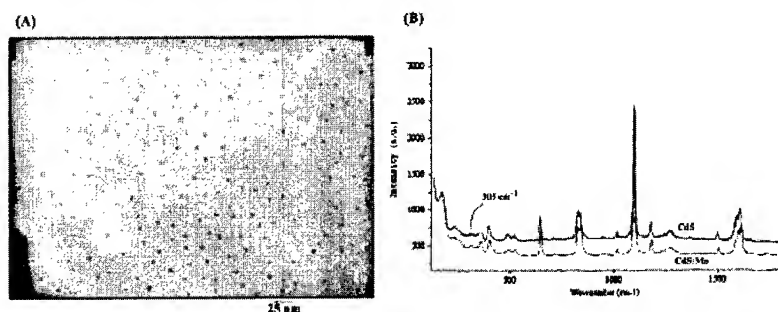


Figure 1. (A) TEM image of p-hydroxyl thiophenol capped CdS nanoparticles and (B) its Raman spectrum as compared with CdS:Mn nanoparticles.

of these spherical CdS nanoparticles is about 5 nm. Compared with the high-temperature synthesizing method by using trioctylphosphine oxygen (TOPO), this room-temperature process is easier but the particle size distribution is wider. In the case of synthesizing manganese doped CdS nanoparticles, we have used large molar percentage of Mn, 5 %, 10 % and 20 % respectively in the reaction. However, only trace doping amounts of Mn, 0.08%, 0.05% and 1.10% were detected respectively by ICP-Mass investigations. When the same approach was used to synthesize MnS nanoparticles, a very low yield was obtained. The results indicate that the reaction rate of MnS synthesis is slower than that of CdS synthesis. Therefore, the position of Cd in the lattice of CdS can not be replaced by Mn. The Mn is trapped by the hydroxyl group of p-hydroxyl thiophenol capping on the surface of CdS nanoparticles. The Raman spectra shown in Figure 1(B) proves this speculation. The Raman shift at 305cm^{-1} corresponds to the longitudinal optical phonons (LO) mode of CdS.[4] No wave number shift is observed for CdS/Mn nanoparticles, thus Mn is not in the CdS lattice. The others Raman shift peaks are from the vibrations of the organic molecules. Consequently, the EL peaks of CdS nanoparticles prepared with or without addition of Mn are the same as shown in Figure 3.

The schematic of CdS-nanoparticle LED is shown in Figure 2(A). The thickness of CdS nanoparticles layer can be as large as 500nm, verified by surface profile scan. Therefore, volume density is very high, but relative high level of resistance also presents. Samples made on n- and p-type Si wafers show different current-voltage (I-V) curves, as shown in Figure 2(B). Both have rectifying I-V curves, but with opposite polarities. This rectifying effect corresponds to metal-insulator-semiconductor tunneling effect. To be specific, the thin potential barrier of organic coating and low substrate doping level result in Schottky-diode-like behavior [5].

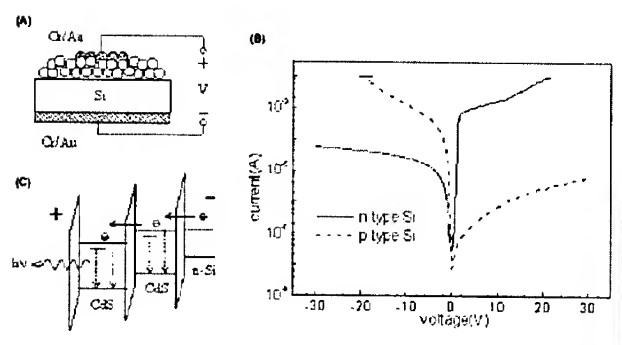


Figure 2. (A) Schematic of the CdS nanoparticles EL device on Si wafer. (B) I-V curves of devices on n-type and p-type Si, respectively. (C) Schematic of electron transport and transition in the device.

The EL can be observed only when the devices are forward biased for both types. The carriers injection and current flow for samples on the n-type substrate are illustrated in Figure 2(C). The EL spectra correspond to radiative recombination of carriers confined within CdS nanoparticles. Carriers are supplied by tunneling current. For samples on the n-type substrate, the silicon Fermi level has to be raised so that electrons are able to tunnel through the potential barrier of p-hydroxyl thiophenol group. Within CdS nanoparticles, part of the injected carriers recombine radiatively, part of them get trapped in defect levels, and part of them tunnel into the adjacent nanoparticles.

The turning point around 3V in Figure 2(B) corresponds to the start of carriers recombination process. Only after the applied bias overcoming the potential barrier of p-hydroxyl thiophenol group between the CdS nanoparticle and the metal (or silicon), the radiative recombination process could start.

In the case of sample A, both spectra of CdS and CdS doped with Mn are the same, as illustrated in Figure 3. The anterior observation of Mn in CdS nanoparticle at 585nm(2.119eV) [6] is not clearly observed in our samples. The result is consistent with our ICP-Mass analysis that the Mn atom does not enter into the CdS lattice by our synthesizing method. The emission peak at 526.5nm (2.355eV) is red-shifted from bulk CdS A-exciton transition energy, 2.441eV(508nm) at room temperature. [7] The energy with a red-shift of 86 meV does not come from quantum confinement within the nanoparticles, since such effect increases the exciton energy when the particle size decreases [8,9]. It is due to the capping p-hydroxyl thiophenol group that modifies the energy of emission peak. CdS nanoparticles coated with polyvinyl alcohol also show such energy shift in absorption spectrum.[10] Other studies[6,11] have shown different shift level with different coating treatment. The spectrum fits into Lorentzian shape with scattering time of 6 fs.

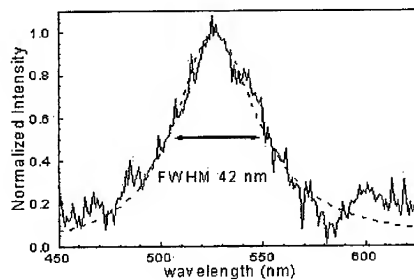


Figure 3. EL Spectrum of CdS with direct vacuum treatment

The FWHM is 42 nm. Such broad spectrum indicates dispersion of particle size. The EL spectrum of sample B depicted in Figure 4(A) shows two peaks. One is at 513.7nm and another at 571.5nm. The former peak stands for bulk CdS signal(A exciton). This spectral lobe can be fitted by Lorentzian shape with scattering time of 8 fs and FWHM 40 nm.

The peak at 571.5nm results from the trapped carriers in oxygen-impurity levels [11]. High temperature environment and the decomposition of p-hydroxyl thiophenol group cause the diffusion process of oxygen into the nanoparticles to occur. This proves p-hydroxyl thiophenol group to be effective overcoat of CdS nanoparticles against oxygen before it decomposes. The oxygen-impurity levels also induce radiative transition.

For investigating the luminescent phenomenon of oxygen impurity level, spectra of the mixture of CdS nanoparticles with SOG and SiO_2 nanoparticles(sample C) are shown in Figure 4(B). The peak at 513.7nm (2.414eV) is the A exciton signal of bulk CdS at 65°C. The peak at

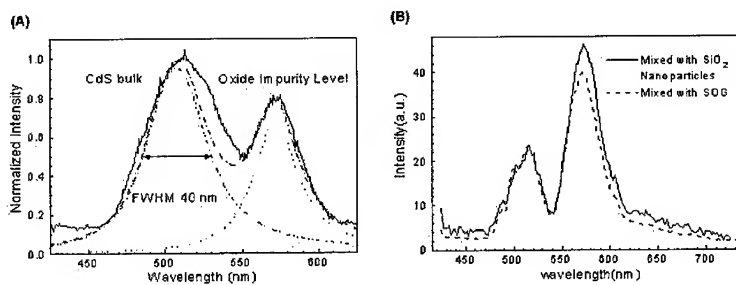


Figure 4. The EL Spectra of (A)CdS particles after heat treatment. (B)CdS nanoparticles mixed with SOG or SiO_2 nanoparticles.

571.5nm (2.414eV) corresponds to radiative transition due to carriers trapped in oxygen-impurity levels, as mentioned previously. The magnitude of light emission in these samples is ten times stronger than that from unheated samples for the same carrier injection condition. The reason for significantly enhanced EL may be twofold. First, the coalescence of CdS nanoparticles into bulk form results in less broadening spectrum around 513.7 nm. Since the potential barrier of p-hydroxyl thiophenol group disappear due to decomposition, carriers in bulk powders stay for enough time (about ns transition lifetime) to recombine radiatively between each tunneling process. Second, relative magnitude of oxygen-impurity-level luminescence is much stronger than that in previous devices. Highly increased concentration of oxygen-impurity levels, which are supplied by SOG or SiO₂ nanoparticles, contributes to the enhancement of internal quantum efficiency. The magnitude difference between mixture with SOG and SiO₂ nanoparticles comes from excess dangling Si-O bond of the latter case. With the same sintering time, the latter mixture makes oxygen diffusing easier.

Conclusions

The CdS nanoparticles prepared by chemical method are ready for spin-coating and EL device fabrication. The observed a spectral shift of free exciton transition of 86 meV is due to the passivation of p-hydroxyl thiophenol group around nanoparticles. Process modifications such as heat treatment and oxygen-rich environment are influential to intrinsic green emission of CdS nanoparticles. The p-hydroxyl thiophenol molecule has shown a protection effect to avoid the diffusion of contaminants into nanoparticles, but it cannot resist temperature deterioration above 400°C. Radiative recombination of carriers trapped in oxygen-impurity levels presents a 273 meV of below bandgap energy of bulk CdS. With the oxygen-impurity levels formed at the surface of CdS nanoparticles, luminescence increases by an order of magnitude.

References

- [1] J. Butty, Y.Z. Hu, N. Peyghambarian, Y.H. Kao, and J.D.Mackenzie, *Appl. Phys. Lett.* **67**, 2672 (1995).
- [2] V.I. Klimov, A.A. Mikhailovsky, Su Xu, A. Malko, J.A. Hollingsworth, C.A. Leatherdale, H.-J. Eisler, and M.G. Bawendi, *Science* **290**, 314 (2000).
- [3] J. G. C. Veinot, M. Ginzburg, and W. J. Pietro, *Chem. Mater.* **9**, 2117 (1997)
- [4] K.K. Nanda, S.N. Sarangi, S.N. Sahu, S.K. Deb and S.N. Behera, *Physica B* **262**, 31-39(1999).
- [5] W.E. Dahlke, and S.M. Sze, *Solid-State Electron.* **10**, 865 (1967)
- [6] L. Spanhel, E. Arpac, and H. Schmidt, *J. Non. Cryst. Solids* **147/148**, 657 (1992).
- [7] K.J. Hong, T.S. Jeong, C.J. Yoon, and Y.J. Shin, *J. Crystal. Growth.* **218**, 19 (2000)
- [8] B.G. Potter, Jr. and J.H. Simmons, *Phys. Rev. B* **37**, 10838 (1988).
- [9] M.V Rama Krishna, and R.A. Friesner, *J. Chem. Phys.* **95**, 8309 (1991)
- [10] M. Tanaka, J. Qi, and Y. Masumoto, *J. Crystal Growth* **214/215**, 410 (2000)
- [11] Y. Nosaka, K. Tanaka, and N. Fujii, *J. Appl. Polym. Sci.* **47**, 1773 (1993)

InAs quantum dots in AlAs/GaAs short period superlattices: structure, optical characteristics and laser diodes

Vadim Tokranov, M. Yakimov, A. Katsnelson, K. Dovidenko, R. Todt, and S. Oktyabrsky,
UAlbany Institute for Materials, University at Albany-SUNY, 251 Fuller Rd, Albany, NY 12203

ABSTRACT

The influence of two monolayer - thick AlAs under- and overlayers on the formation and properties of self-assembled InAs quantum dots (QDs) has been studied using transmission electron microscopy (TEM) and photoluminescence (PL). Single sheets of InAs QDs were grown inside a 2ML/8ML AlAs/GaAs short-period superlattice with various combinations of under- and overlayers. It was found that 2.4ML InAs QDs with GaAs underlayer and 2ML AlAs overlayer exhibited the lowest QD surface density of $4.2 \times 10^{10} \text{ cm}^{-2}$ and the largest QD lateral size of about 19 nm as compared to the other combinations of cladding layers. This InAs QD ensemble has also shown the highest room temperature PL intensity with a peak at 1210 nm and the narrowest linewidth, 34 meV. Fabricated edge-emitting lasers using triple layers of InAs QDs with AlAs overlayer demonstrated 120 A/cm² threshold current density and 1230 nm emission wavelength at room temperature. Excited state QD lasers have shown high thermal stability of threshold current up to 130 °C.

INTRODUCTION

Quantum dot (QD) layers were proposed as an active gain medium for semiconductor laser diodes in 1982 [1]. After the discovery of self-assembly of QDs in the InAs/GaAs system via Stranski-Krastanov growth mode, significant research efforts were directed to obtain QD ensembles with uniform size, high density, and high emission efficiency [2,3], and to fabricate QD lasers [4,5,6]. Currently, the performance of QD lasers is comparable or even better than that of quantum well (QW) lasers, e.g. room temperature threshold current density of 16 A/cm² for single- and 36 A/cm² for triple-layer QD laser [6], and long wavelength (1.3 μm) lasing on GaAs substrate [5] were obtained. However, InAs/GaAs quantum-dot lasers with the lowest threshold current density (ground level near 1.3 μm emission wavelength) have not yet achieved high-temperature stability [7].

In spite of profound studies of Stranski-Krastanov growth of In(Ga)As islands on GaAs, this self-organized formation of nanoscale islands is still not completely understood. The structural and optical properties of QD ensembles are very sensitive to the growth parameters [8,9]. This phenomenon of self-assembly is further complicated by intermixing of InAs QDs with the GaAs barrier [10], segregation of In atoms when InGaAs islands are overgrown by GaAs [11,12], complex diffusion properties of adatoms. Very recently, the top Al containing layers have been used to achieve a red shift of the InAs QDs photoluminescence band [13,14].

The primary goal of the present study is the development of the self-assembled QD active medium for laser diodes operating at elevated (>100°C) temperatures. We have investigated the influence of two monolayer - thick AlAs under- and overlayers on the formation and properties of InAs QDs in a short period superlattice (SPSL) using transmission electron microscopy (TEM) and photoluminescence (PL).

EXPERIMENTAL DETAILS

The structures were grown on GaAs(100) substrates in EPI GEN II Molecular Beam Epitaxy (MBE) system equipped with As-valved cracker source. For QD growth, InAs growth rate was maintained at 0.048 ± 0.002 ML/s, and As_2 flux was kept constant at 1.5×10^{-6} Torr. Indium flux was calibrated by InGaAs growth using reflection high energy electron diffraction oscillations. The self-assembled InAs QDs were embedded into 2ML-AlAs/8ML-GaAs SPSL barrier. The closest to the QDs four SPSL periods were grown at the QD growth temperature.

The PL and TEM measurements were carried out on the same samples with QD layers placed 30 nm below the surface. The growth was started with 500 nm of $\text{Al}_{0.45}\text{Ga}_{0.55}\text{As}$ cladding alloy followed by 280 nm SPSL grown at 650 °C. Then, the growth was interrupted to reduce the substrate temperature to that for QD growth (450 - 500 °C). InAs QDs were grown using different combinations of 2ML-AlAs and 8ML-GaAs underlayers and overlayers. The self-assembled QDs were then capped with four periods of SPSL, and after heating up the substrate by 80 °C, 3 periods of SPSL and 10 nm of AlGaAs alloy were grown on the top.

The optical properties of the self-assembled QDs were characterized using PL. The top and bottom $\text{Al}_{0.45}\text{Ga}_{0.55}\text{As}$ cladding layers were used to prevent photogenerated carriers from spreading to the substrate or to the surface. We used an Ar^+ ion laser (514.5nm) as an excitation source. The PL spectra were detected by LN_2 -cooled Ge p-i-n photodiode and recorded using lock-in techniques.

The laser diode structures were grown on n-type GaAs(100) substrates. Si and Be were used for n-type and p-type doping, respectively. n^+ -GaAs buffer layer and 1 μm - thick bottom $n\text{-Al}_{0.7}\text{Ga}_{0.3}\text{As}$ cladding layer were grown at 610°C. They were followed by an undoped 900 nm - thick SPSL waveguide structure with the QD active layers in the center. The bottom half of the SPSL waveguide and the QD layers were grown at 650 °C and 475 °C, respectively, following a similar temperature ramping procedure as for PL/TEM samples. Triple layers of InAs QDs with GaAs underlayer and AlAs overlayer, and 30 nm SPSL spacing were used as the laser active medium. Top half of the SPSL waveguide, 1 μm - thick $p\text{-Al}_{0.7}\text{Ga}_{0.3}\text{As}$ cladding layer and the top 250 nm - thick p^+ -GaAs contact layer were all grown at 570°C to prevent thermal evolution of the QD structure. Gain-guided lasers with stripe width from 10 to 200 μm and cavity lengths from 1.5 to 10 mm were fabricated from these structures. Laser diodes were fabricated by cleaving without any coating of the facets. Stripe-up laser crystals were mounted on a heatsink using In solder.

RESULTS AND DISCUSSIONS

Transmission Electron Microscopy (TEM): QDs Imbedded into Short Period SL

To optimize the properties of QD structures for the laser gain medium, we have started with the investigation of the influence of GaAs and AlAs under- and overlayers and growth temperature on size, size distribution, surface density and PL properties of QDs. We have grown a set of samples at the substrate temperature in the range of 450 - 500 °C with 2.4ML of InAs imbedded into 8ML-GaAs/2ML-AlAs SPSL. Some of the advantages of SPSL are that this is an effective wide-bandgap material grown at relatively low temperature and another variable to control the emission wavelength. We have investigated four basic QD designs: (i) with 8ML GaAs as both under- and overlayer; (ii) the same but with 2ML AlAs; (iii) with 8ML GaAs

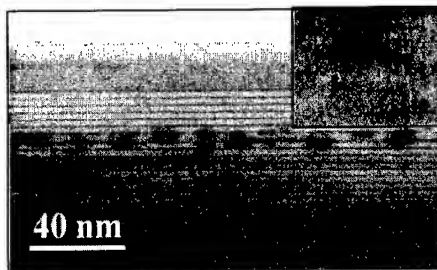


Fig. 1. Cross-sectional TEM image of QD array (2.4ML InAs with AlAs under- and overlayer). Inset: cross-sectional high-resolution TEM image of a single QD.

underlayer and 2ML AlAs overlayer; and (iv) with 2ML AlAs underlayer and 8ML GaAs overlayer.

200 keV TEM (JEOL 2010 FEG) was used for plan-view and cross-sectional studies. Fig. 1 shows a cross-sectional TEM image of a single layer 2.4ML InAs QDs with 2ML AlAs on both sides imbedded into SPSL. The strain contrast originating from the QDs is clearly visible. One can also observe that the SPSL is an effective way for structure smoothing after the QD growth. The inset in the Fig. 1 shows a cross-sectional high-resolution TEM image of a single QD demonstrating its typical pyramidal shape.

Plan-view image of a QD ensemble grown at 475 °C with 2ML AlAs under- and overlayer is presented in Fig. 2. Statistical analysis of plan-view micrographs allowed us to evaluate the surface density and average size of quantum dots. In Fig. 3, we plot the QD surface number density as a function of the growth temperature. All the studied QD designs exhibit a reduction of surface density at higher substrate temperatures, but the samples with AlAs overlayer are less sensitive to this parameter. The highest QD density of about $2 \times 10^{11} \text{ cm}^{-2}$ was obtained in the structures with AlAs underlayer and GaAs overlayer. This results from the lower diffusion rate of In adatoms on the AlAs surface as we have observed recently [15].

On the contrary, QDs with GaAs underlayer and AlAs overlayer had the lowest surface density of about $3 \times 10^{10} \text{ cm}^{-2}$ at 500 °C. The average QD size dependance on the growth temperature is shown in Fig. 4 for various QD designs. Generally, QD sizes increase with the growth temperature, and QDs on GaAs with 2ML AlAs overlayer exhibit the largest sizes. In the case of AlAs overlayer (as compared to GaAs), we have observed an increase of the average size and reduction of the surface density likely because of dissolving of small QDs and wetting layer by AlAs overlayer [14]. GaAs underlayer instead of AlAs also leads to increased size and reduced density of QDs. In this case, it is due to the higher surface diffusion of In adatoms on GaAs surface [15]. The main result from these TEM studies is that InAs QDs grown at 475 °C on GaAs underlayer and capped with AlAs overlayer exhibit the lowest QD surface density of $4.2 \times 10^{10} \text{ cm}^{-2}$ and the largest QD lateral size of about 19 nm as compared to the other combinations of the cladding layers. This QD ensemble is expected to be very promising for manufacturing of the QD medium with low ground state energy near 1.3 μm and narrow size distribution. It should be noted, that the laser applications require high density and high optical

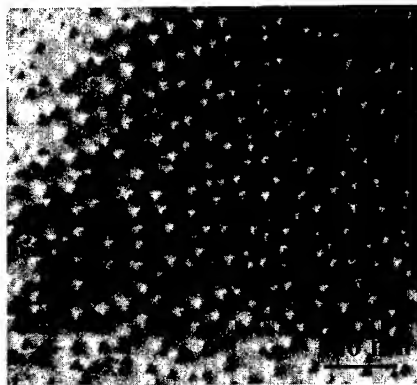


Fig. 2. TEM plan-view micrograph of QDs grown at 475 °C on AlAs with 2ML AlAs overlayer (small QDs ~14 nm).

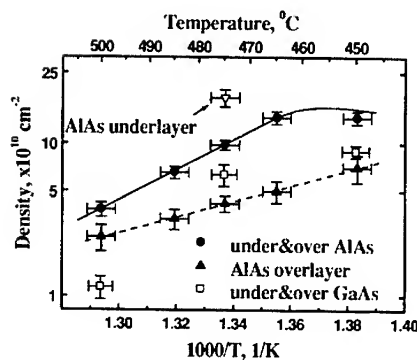


Fig. 3. Surface density of 2.4ML InAs QDs with different under- and overlayers as a function of growth temperature.

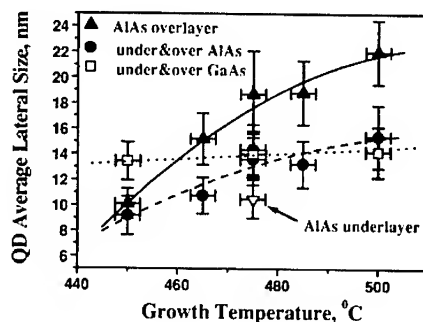


Fig. 4. Average sizes of 2.4ML InAs QDs with different under- and overlayers vs. growth temperature. Vertical error bars correspond to the QD size dispersion.

quality of the QD ensemble, which are usually quite conflicting demands. Next section is devoted to the optimization of the PL properties of the QDs.

Photoluminescence: optical properties of QDs imbedded into SPSL

Fig. 5 shows PL peak energy and FWHM of the luminescence band as a function of the average lateral size of QDs grown with different under- and overlayers at 475 °C. These data were obtained at room temperature with the excitation intensity of 10 W/cm². The PL band is found to shift towards the lower energies with increasing of QD sizes as expected from a simple quantum size effect. On the contrary, the effect of barrier bandgap is obscured by the size effect. For example, QDs capped with AlAs high-bandgap overlayers exhibit noticeable PL redshift in comparison with those overgrown by low-bandgap GaAs. Significant reduction of FWHM of the luminescence band indicates that the homogeneity of the QD sizes is also improved for large QDs. Therefore, our growth conditions with the increased In adatom diffusion length lead not only to the increase of the QD sizes, but also to the improved size distribution.

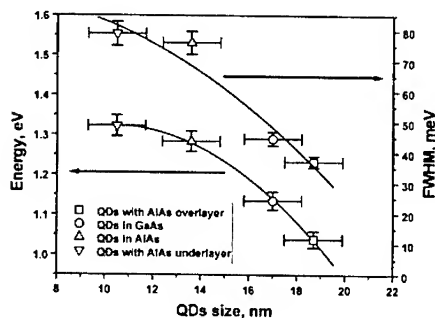


Fig. 5. Room temperature PL peak energy and band FWHM of 2.4ML InAs QDs as a function of average sizes of QD layers with different design.

QD ensemble with 2ML AlAs overlayer has demonstrated the highest room temperature PL intensity and the lowest band FWHM of 34 meV (at low excitation level, 0.1 W/cm²) in comparison with the other QD designs. The highest room temperature PL intensity indicates the reduction of density of nonradiative recombination centers in the sample with the lowest QD surface concentration grown with AlAs overlayer.

Though the AlAs layers are usually expected to have higher defect density than GaAs, we have not observed any degradation of the QD radiative recombination associated with the presence of AlAs.

Electroluminescence of triple QD layer edge-emitting lasers

All electroluminescent (EL) measurements were carried out under pulsed excitation in a temperature range 77 - 430 K. The excitation pulse width was 1 μ s with a duty cycle factor of about 0.5%. The EL spectra of an edge-emitting laser with a triple 2.2ML InAs QD layers operating on the ground state transitions are shown in Fig. 6. Light-current characteristic is plotted in the inset. Ground state lasing was obtained at a threshold current density, $J_{th} = 120$ A/cm², and wavelength, 1.23 μ m. Minimum cavity length for the ground state lasing was found to be 6 mm. We have estimated the maximum modal gain of our structure, 3.5 cm⁻¹, assuming similar intrinsic losses ($\alpha_i = 1.8$ cm⁻¹) as in the case of quantum well heterolaser with the same waveguide width (0.9 μ m). We expect that these results can be significantly improved by optimization of the laser heterostructure, especially by increasing of a potentially low optical confinement factor of the QD active medium.

The EL spectra of an edge-emitting laser with a triple 2.0ML InAs QD layers operating on excited state transitions are shown in Fig. 7, with a corresponding light-current characteristic plotted in the inset. In this case, the lasing was achieved at a higher current density, $J_{th} = 360$ A/cm², and shorter wavelength, 1.14 μ m. Minimum cavity length for ground state lasing was about 3 mm, corresponding to the maximum modal gain of the excited state of about 5 cm⁻¹ in our structure. These results can be also improved by at least 2-3 times by optimization of the laser heterostructure, such as decreasing the waveguide width down to 0.25 μ m, decreasing intrinsic losses by 20-30% down to the best reported values, 1.3 - 1.5 cm⁻¹ [6].

Thermal quenching of the laser threshold current is plotted in Fig.8. The maximum working temperature for the ground state laser was found to be 75 °C that corresponds to the currently reported values. Excited state lasers exhibited weaker temperature dependence of the threshold current with the maximum operating temperature exceeding 130 °C. The primary reason for the higher thermal stability of excited state QD lasers is the higher saturated modal gain [6]. An additional reason for poor thermal stability of the ground state QD lasers is the stress in a very long laser crystal mounted on a copper heatsink because of the difference in

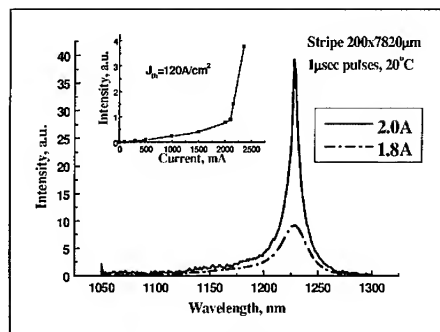


Fig. 6. EL spectra of a ground state QD laser. Inset: Ground state QD laser light-current characteristic.

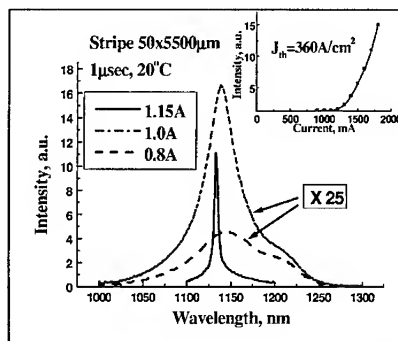


Fig. 7. EL spectra of an excited state QD laser. Inset: QD laser light-current characteristic.

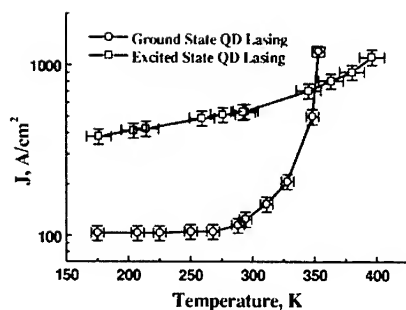


Fig. 8. Threshold current density dependence on temperature for ground state and excited state QD lasers.

thermal expansion coefficients of GaAs and copper. Therefore, synthesis of multilayered QD structures with high QD number density and low nonradiative recombination probability is still a challenging goal for low threshold QD lasers operating at high temperatures.

CONCLUSIONS

To accelerate optimization of QD growth technology and understanding of the growth mechanisms we have used QD structures suitable for both photoluminescent characterization and TEM plan-view measurements of QD density and average size.

By employing of this combined method, we

have found that 2.4ML InAs QDs with GaAs underlayer and 2ML AlAs overlayer exhibited the highest PL efficiency at room temperature, the narrowest band FWHM (34 meV), the lowest QD surface density of $4.2 \cdot 10^{10} \text{ cm}^{-2}$ and the largest QD lateral size of about 19 nm, as compared to the other combinations of cladding layers. Edge-emitting laser with triple 2.2ML InAs QD layers operating at the ground state transitions demonstrated low room temperature threshold current density of 120 A/cm² and working temperature up to 75 °C. Excited state triple 2ML InAs laser showed threshold current density of 360 A/cm², and high operation temperature up to 130 °C.

ACKNOWLEDGMENTS

The work was supported by MARCO and DARPA under the National Focus Center for Interconnects for Gigascale Integration. This support is greatly appreciated.

REFERENCES

1. Y. Arakawa, and H. Sakaki, *Appl. Phys. Lett.*, **40**, 939 (1982).
2. D. Leonard, M. Kishnamurthy, C. M. Reaves, et al., *Appl. Phys. Lett.*, **63**, 3203 (1993).
3. N. N. Ledentsov, V. M. Ustinov, A. Yu. Egorov, et al., *Semicond.*, **28**, 832 (1994).
4. D. Bimberg, N. N. Ledentsov, M. Grundmann, et al., *Physica E*, **3**, 129 (1998).
5. G. Park, D. L. Huffaker, Z. Zou, et al., *IEEE Photon. Technol. Lett.*, **11**, 301 (1999).
6. P. G. Eliseev, H. Li, A. Stintz, T. C. Newell, et al., *Appl. Phys. Lett.*, **77**, 262 (2000).
7. X. Huang, A. Stintz, C. P. Hains, et al., *IEEE Photon. Technol. Lett.*, **12**, 227 (2000).
8. L. Chu, M. Arzberger, G. Böhm, and G. Abstreiter, *J. Appl. Phys.*, **85**, 2355 (1999).
9. S. Fafard, Z. R. Wasilewski, C. Ni. Allen, D. Picard, et al., *Phys. Rev. B*, **59**, 15368 (1999).
10. P. B. Joyce, T. J. Krzyzewski, G. R. Bell, et al., *Phys. Rev. B*, **58**, R15981 (1998).
11. O. Brandt, L. Tapfer, K. Ploog, R. Bierwolf, et al., *Appl. Phys. Lett.*, **61**, 2814 (1992).
12. U. Woggon, W. Langbein, J. M. Hvam, et al., *Appl. Phys. Lett.*, **71**, 377 (1997).
13. M. Arzberger, U. Käsberger, G. Böhm, et al., *Appl. Phys. Lett.*, **75**, 3968 (1999).
14. A. F. Tsatsul'nikov, A. R. Kovsh, A. E. Zhukov, et al., *J. Appl. Phys.*, **88**, 6272 (2000).
15. M. Yakimov, V. Tokranov, and S. Oktyabrsky, *MRS Symp. Proc.*, **648**, P2.6.1 (2001).

Infrared Detectors

Multi-Color Quantum Well Infrared Photodetectors for Mid-, Long-, and Very Long- Wavelength Infrared Applications (invited)

Sheng S. Li

Department of Electrical and Computer Engineering

University of Florida, Gainesville, FL 32611

Email address: shengli@eng.ufl.edu

ABSTRACT

Quantum well infrared photodetectors (QWIPs) have been widely investigated for the 3-5 μm mid-wavelength infrared (MWIR) and 8-12 μm long-wavelength infrared (LWIR) atmospheric spectral windows as well as very long wavelength infrared (VLWIR: $\lambda_c > 14 \mu\text{m}$) detection in the past decade. The mature III-V compound semiconductor growth technology and the design flexibility of device structures have led to the rapid development of various QWIP structures for infrared focal plane arrays (FPAs) applications. In addition to the single-color QWIP with narrow bandwidth, the multi-color QWIP required for advanced IR sensing and imaging applications have also been emerged in recent years. Using band gap engineering approach, the multi-color (2, 3, and 4- color) QWIPs using multi-stack quantum wells with different well width and depth and voltage-tunable triple- coupled quantum well (TCQW) structure for detection in the MWIR, LWIR, and VLWIR bands have been demonstrated. In this paper, the design, fabrication, and characterization of a voltage-tunable 2-stack 3-color QWIP for MW/LW/LW IR detection and a 3-stack 3-color QWIP for detection in the water, ozone, and CO_2 atmospheric blocking bands are depicted.

1. INTRODUCTION

Recent advances in III-V semiconductor epitaxial layer growth techniques such as molecular beam epitaxy (MBE) [1] and metalorganic chemical vapor deposition (MOCVD) have made it possible to grow a wide variety of novel semiconductor heterostructures. Significant progress has been made in quantum wells and superlattice optoelectronic devices using these growth techniques. The quantum well is formed by using an ultra thin layer of narrow band gap semiconductor (e.g., GaAs) sandwiched between two thin wider band gap semiconductor (e.g., AlGaAs) barrier layers. The motion of the carriers perpendicular to the layers becomes quantized so that localized two-dimensional subbands of quantized states are formed inside the quantum well. [2]

Early proposals of using optical intersubband transitions in quantum wells for IR detection were made by Chang et al. [3], Esaki, Tsu, and Sakaki[4-5], and Coon and Karunasiri [6]. The intersubband absorption in GaAs quantum wells was first observed by West and Eglash [7] and followed by Harwit and Harris [8]. Levine et al. [9] demonstrated the first GaAs QWIP in 1987. Since then, QWIPs based on the bound-to-bound (B-B), bound-to-continuum (B-C) [10], and bound-to-miniband (B-M) [11] transitions have been widely investigated for the 3 to 5 μm mid-wavelength infrared

(MWIR) and 8 to 14 μm long-wavelength infrared (LWIR) detection [12-13]. Additionally, there is a considerable interest in the development of multi-stack and voltage-tunable asymmetrical coupled quantum well structures for multi-color focal plane array (FPA) applications in the MWIR and LWIR atmospheric spectral windows. [14]

One major difference between the QWIP and other IR detectors is that QWIPs use intersubband transitions either in the conduction band (n-type) or in the valence band (p-type) to detect IR radiation. The basic intersubband transition schemes for n-type QWIPs include (a) bound-to-bound (B-B), (b) bound-to-continuum (B-C), (c) bound-to-miniband (B-M), and (d) bound-to-quasi-bound (BQB) transitions. By using different well widths and barrier heights, the detection wavelengths of QWIPs can be tuned from 3 to 20 μm and beyond. Depending on where the upper excited states are located and the barrier layer structure, the intersubband transitions in a QWIP can be based on the B-B state, B-M state, BQB state, and the B-C state transitions. Among the various types of QWIPs reported, the GaAs/AlGaAs QWIP structures using the B-C and B-M transitions are the most widely used material systems and structures for the fabrication of large format FPAs for MWIR and LWIR imaging applications. Multi-color QWIPs using the multi-stack and voltage-tunable asymmetrical coupled quantum well structures such as the triple-coupled (TC-) QWIP have received considerable interest in recent years. [14-18] The multi-stack structure is usually employed to obtain multi-color detection in the MWIR and LWIR atmospheric spectral windows. Using quantum confined Stark effect, the voltage tunable TC- QWIP has also been reported for multi-color detection. [14,16]

Section 2 presents a voltage-tunable 2-stack 3-color QWIP for the MW/LW/LW IR detection using an InGaAs/AlGaAs B-C QWIP for the MWIR stack and an InGaAs/AlGaAs/GaAs TC- QWIP for the LWIR stack. A 3-stack 3-color QWIP using the graded barrier structure for detection in the water (MWIR), ozone (LWIR), and the CO_2 (VLWIR) atmospheric blocking bands is depicted in section 3. Conclusions are given in section 4.

2. A 2-STACK 3-COLOR QWIP FOR MWIR/LWIR DETECTION

A 2-stack 3-color QWIP structure used in this study was grown on a semi-insulating (SI) GaAs substrate by using the molecular beam epitaxy (MBE) technique. The bottom stack is an InGaAs/AlGaAs B-C QWIP grown on the semi-insulating (SI) GaAs substrate for MWIR detection. This MWIR QWIP consists of 3 periods of a 4.3 nm $\text{In}_{0.3}\text{Ga}_{0.7}\text{As}$ quantum well Si-doped to $N_d = 2.5 \times 10^{18} \text{ cm}^{-3}$ and an undoped 30 nm $\text{Al}_{0.3}\text{Ga}_{0.7}\text{As}$ barrier. The ohmic contact layers (Si-doped to $N_d = 2 \times 10^{18} \text{ cm}^{-3}$) were grown on the top and bottom of the MWIR stack. The top stack is a two-color TC- QWIP, which was grown on top of the MWIR stack for LWIR detection. The basic structure of the TC-QWIP is composed of 5 periods of TCQW separated by two thin (20 Å) $\text{Al}_{0.08}\text{Ga}_{0.92}\text{As}$ barrier layers. The TCQW is formed by a 65 Å Si-doped ($7 \times 10^{17} \text{ cm}^{-3}$) $\text{In}_{0.18}\text{Ga}_{0.82}\text{As}$ deep well and two 60 Å undoped $\text{In}_{0.05}\text{Ga}_{0.95}\text{As}$ shallow wells. In this structure, the well width was designed to create three subbands (i.e., E_1 , E_2 , and E_3 states) within the quantum wells with dominant transitions from the E_1 to E_3 and E_1 to E_c states, with detection peak wavelengths longer than previously reported values.[17] For ohmic contacts, two heavily

doped ($N_d = 2 \times 10^{18} \text{ cm}^{-3}$) GaAs contact layers were grown on the top and bottom of the active TCQW absorber layers. To reduce the tunneling injection current from contacts to the quantum wells, a 100 nm thick undoped GaAs spacer layer was also grown between the active TCQW absorber layers and the top/bottom contact layers.

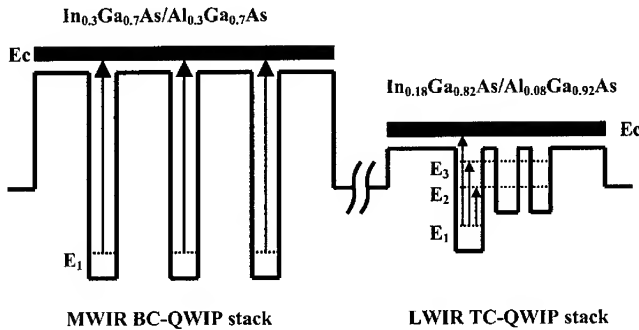


Figure 1 The schematic energy band diagram for a 2-stack 3-color QWIP

Figure 1 shows the schematic conduction band diagrams and the intersubband transition scheme for this 2-stack MWIR BC-QWIP and LWIR TC-QWIP. For the TC-QWIP, due to the strong coupling effect of the three asymmetrical QWs and two thin AlGaAs barriers, the bound states in the shallow wells and the first and second excited states in the deep well are coupled to form the second and third bound states (i.e., E_2 and E_3 states) inside the quantum wells. In this TC-QWIP stack, we observed two detection peaks in the LWIR band under negative bias condition. The first peak, which corresponds to the E_1 - E_C bound-to-continuum (BC) transition, was observed at $10 \mu\text{m}$ and shifted to $9.2 \mu\text{m}$ when the applied bias varied from -1.2 V to -1.9 V . When the bias voltage was increased above -1.4 V , a second peak appeared around $12 \mu\text{m}$, which corresponds to the bound-to-bound (BB) states transition between the E_1 and E_3 states as shown in Figure 1. By increasing the bias voltage from -1.5 V to -1.9 V we also observed the wavelength shifting from $12.2 \mu\text{m}$ to $12 \mu\text{m}$ for the second peak. As for the MWIR BC-QWIP the peak detection wavelength corresponding to the E_1 to E_C states transition is at $5.1 \mu\text{m}$.

Figure 2 (a) and (b) show the dark current density-voltage (J-V) characteristics for this QWIP device measured at different temperatures along with the 300K- background window current measured with an 180° field of view (FOV) at 20K. As expected from the asymmetrical quantum well structure, the dark current curves of the TC-QWIP stack are highly asymmetrical under positive and negative bias conditions. This asymmetrical J-V characteristic is attributed to the difference in the effective barrier height experienced by the electrons under positive and negative bias conditions. The MWIR QWIP stack is under background limited performance (BLIP) for $-0.95 \text{ V} < V_b < 0.9 \text{ V}$ at $T = 77 \text{ K}$, and the BLIP temperature is at $T = 90 \text{ K}$ for $-0.5 \text{ V} < V_b < 0.4 \text{ V}$.

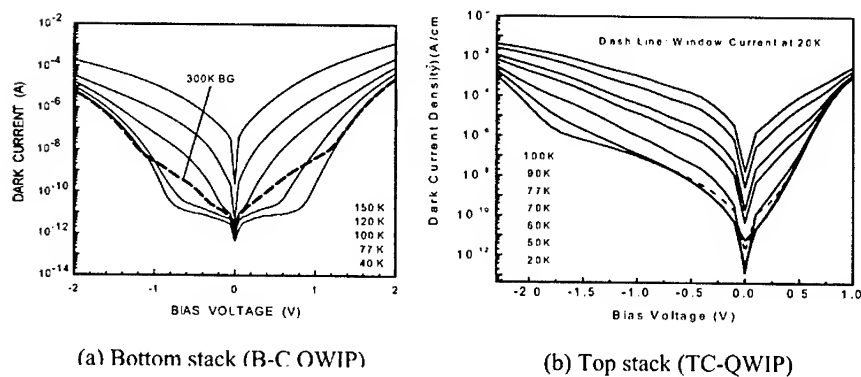


Figure 2 Dark I-V characteristics for the 2-stack 3-color OWIP.

Figure 3 (a), (b), (c), and (d) show the spectral responsivity of the MWIR QWIP stack measured at different bias voltages and temperatures. The photoresponse was due to the B-C states transition for this MWIR QWIP stack. At $T = 77$ K, the peak responsivities under negative biases were found to increase with the bias voltage up to -1.3 V and the

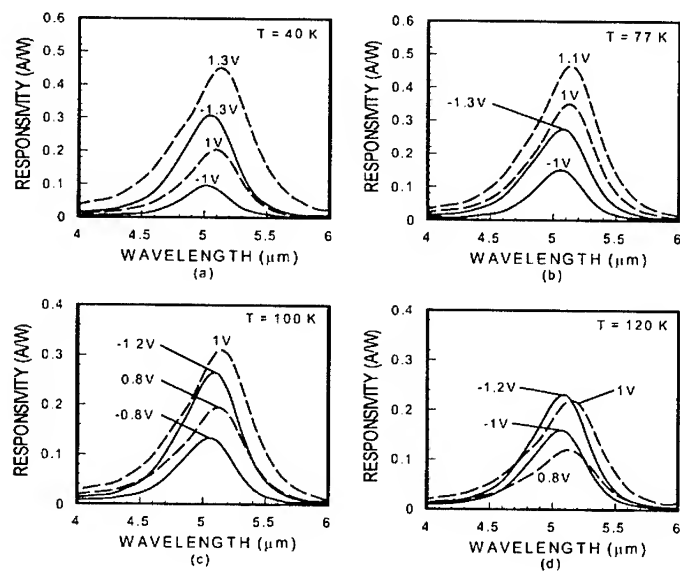


Figure 3 Spectral responsivity of the MWIR QWIP stack measured at $T = 40, 77, 100$, and 120 K for the 2-stack 3-color QWIP.

maximum responsivity was 0.27 A/W at $\lambda_p = 5.1 \mu\text{m}$ and $V_b = -1.3\text{V}$, and the peak responsivity was 0.46 A/W at $\lambda_p = 5.1 \mu\text{m}$, $V_b = 1.1\text{V}$ and $T = 77 \text{ K}$. The peak wavelength at $\lambda_p = 5.1 \mu\text{m}$ was found to be nearly independent of the bias voltage and temperature.

Figure 4 shows the spectral responsivity for the LWIR TC-QWIP stack under negative biases and at $T = 40 \text{ K}$. The peak responsivity due to the E_1-E_3 state transition under negative bias was 1.96 A/W at $\lambda_p = 12 \mu\text{m}$ and $V_b = -1.9 \text{ V}$. Under the positive bias condition, the peak responsivity due to the E_1-E_C transition was found to be 0.11 A/W at $\lambda_p = 9.5 \mu\text{m}$ and $V_b = 0.6 \text{ V}$. The relatively low responsivity observed under positive bias was attributed to the very large dark current, which makes the device easily saturated with the dark current even under very small positive bias condition.

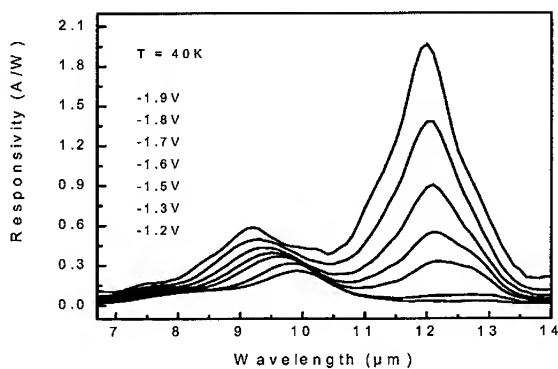


Figure 4 Spectral responsivity of the LWIR TC-QWIP stack for the 2-stack 3-color QWIP.

Figure 5 (a) and (b) show the quantum confined Stark shift of the peak detection wavelength versus applied bias for the TC-QWIP for the E_1-E_C and the E_1-E_3 transitions, which exhibit a linear dependence of the peak wavelength on the applied bias voltage. The wavelength tunability by the applied bias was achieved in the range from $9.2 \mu\text{m}$ to $10 \mu\text{m}$ and $12 \mu\text{m}$ to $12.2 \mu\text{m}$ for the E_1-E_C and E_1-E_3 transitions, respectively. The detectivity was calculated from the measured responsivity and dark current. The peak detectivity, D^* , for the TC-QWIP can be obtained by using the calculated noise gain from the zero bias dark current value and the measured responsivity, which was found to be $D^* = 1.59 \times 10^{10} \text{ cm-Hz}^{1/2}/\text{W}$ at $\lambda_p = 12 \mu\text{m}$, $V_b = -1.7 \text{ V}$, and $T = 20 \text{ K}$.

A voltage tunable 2-stack 3-color QWIP using the InGaAs/AlGaAs material systems for the MWIR stack and a voltage-tunable TC-QWIP using $\text{In}_{0.18}\text{Ga}_{0.82}\text{As}/\text{Al}_{0.08}\text{Ga}_{0.92}\text{As}/\text{In}_{0.05}\text{Ga}_{0.95}\text{As}$ material systems for LW/LW two-color detection has been demonstrated in this section. A linear dependence of the two peak wavelengths with applied bias for the TC-QWIP stack was observed in this device. By varying the bias voltages from -1.2 V to

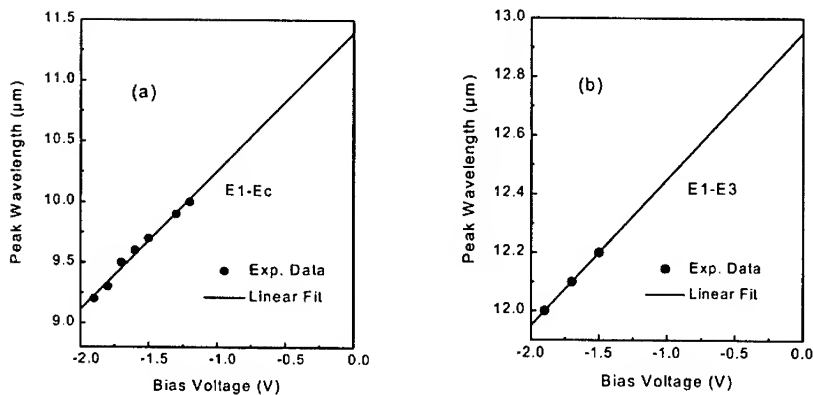


Figure 5 The peak detection wavelength vs. bias voltage for the E₁-E_c and E₁-E₃ state transition peaks for the LWIR TC-QWIP stack.

-1.9 V and -1.5 V to -1.9 V, the wavelengths of two detection peaks shift from 10 μm to 9.2 μm and 12.2 μm to 12 μm, respectively. The highest peak responsivity under negative bias was found to be 1.96 A/W at $\lambda_p = 12 \mu\text{m}$, $V_b = -1.9 \text{ V}$, and $T = 40 \text{ K}$. The maximum detectivity for the $\lambda_p = 12 \mu\text{m}$ peak was found to be $D^* = 1.59 \times 10^{10} \text{ cm-Hz}^{1/2}/\text{W}$ at $V_b = -1.7 \text{ V}$ and $T = 20 \text{ K}$. As for the MWIR QWIP stack excellent responsivity for the 5.1 μm peak was obtained up to 120 K. This 2-stack 3-color QWIP can be used for detection in the MW/LW/LW IR spectral windows for 3-color FPAs applications.

3. A 3-STACK 3-COLOR QWIP FOR H₂O, CO, AND CO₂ BANDS DETECTION

Although QWIPs have been widely investigated for detection in the 3~5 μm MWIR, and 8~14 μm LWIR atmospheric spectral windows in the past decade, however, none of the reported multi-color QWIPs have been designed specifically for detection in the atmospheric blocking bands. There are three blocking bands in the MWIR to VLWIR regions that can be used for practical IR detection. These are the water band (5.5- 7.5 μm), the ozone (O₃) band (9.4- 9.9 μm), and the CO₂ band (14- 16 μm), and none of these bands blocks the earthshine completely at exo-atmosphere. In a 3-color temperature estimation with earthshine in the exo-atmosphere, the accuracy of the earthshine ratio terms is maximized if one of the detector colors is chosen in a band where the earth atmosphere partially blocks the earthshine. [18] Therefore the sensitivity of a QWIP device with one detection wavelength in the above blocking bands will be improved if the detector is used in exo-atmospheric interceptors, space-based surveillance sensors, or satellite mapping. This technology can be used for multi-color focal plane arrays (FPAs), which is an essential application for QWIPs. In this section, we present a specially designed 3-stack, 3-color QWIP with detection wavebands in the MWIR,

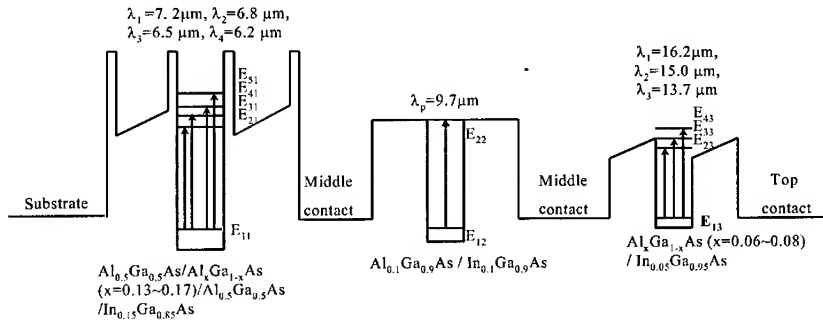


Figure 6 The schematic conduction band diagram of the 3-stack 3-color QWIP for the MW/LW/VLWIR detection covering the water, ozone, and CO₂ blocking bands.

LWIR, and VLWIR spectral ranges that cover the above three atmospheric blocking bands.

Figure 6 shows the schematic conduction band diagram and intersubband transition schemes of a 3-stack 3-color QWIP for the MW/LW/VLW IR detection. The bottom stack is designed to detect the infrared radiation with wavelengths covering the water blocking band. This stack consists of 5 periods of 500 Å Al_xGa_{1-x}As barrier and 64 Å In_{0.15}Ga_{0.85}As well doped to $N_d = 2 \times 10^{18} \text{ cm}^{-3}$. The 500 Å Al_xGa_{1-x}As barrier is composed of 460 Å Al_xGa_{1-x}As graded barrier with x varied from 0.13 on the substrate side to 0.17 and two 20 Å Al_{0.5}Ga_{0.5}As tunneling barriers grown on both sides of the graded barrier. The middle stack is designed to detect the wavelengths covering the ozone- blocking band. This stack was grown using 10 periods of 500 Å Al_{0.1}Ga_{0.9}As barrier and 63 Å In_{0.1}Ga_{0.9}As well doped to $N_d = 8 \times 10^{17} \text{ cm}^{-3}$. The detection wavelengths for the top stack cover the CO₂ blocking band, and this stack was grown with 20 periods of 500 Å Al_xGa_{1-x}As barrier and 60 Å In_{0.05}Ga_{0.95}As well doped to $N_d = 5 \times 10^{17} \text{ cm}^{-3}$. The Al_xGa_{1-x}As barrier was graded from $x = 0.06$ on the substrate side to 0.08. The three stacks are separated by a 0.5 μm and 0.6 μm thick of highly doped intermediate contact layers, and the entire stacks were sandwiched between the 0.3 μm top - and the 0.7 μm bottom- contact layers. All the contact layers were doped with silicon impurity to $N_d = 2 \times 10^{18} \text{ cm}^{-3}$ to attain low contact resistance.

The multi-layer transfer matrix method (TMM) was used to calculate the peak detection wavelengths for this 3- stack 3-color QWIP.[19] The calculated peak detection wavelength for the bottom stack is 6.5 μm, which is centered at the water- blocking band. As shown in Figure 6, the IR detection is based on the intersubband transition from the localized ground state (E₁₁) to the bound states (E₂₁, E₃₁) and the quasi-continuum states (E₄₁, E₅₁), and the peak wavelength corresponds to the E₁₁→E₄₁ transition since E₄₁ is the nearest energy state to the top of the graded barrier (i.e., Al_xGa_{1-x}As with $x = 0.17$) where

the excited state is confined inside the quantum well with the highest electron escape probability.[20] The thin $\text{Al}_{0.5}\text{Ga}_{0.5}\text{As}$ double barriers are used to increase the barrier height which gives a larger energy spacing between the ground state and the excited states for the MWIR stack. The main benefit of the graded barriers is that it creates multiple excited states, which result in a broader detection bandwidth as compared to the regular rectangular QWIP used in the MWIR band.

The calculated peak wavelength for the LWIR stack is $9.7\mu\text{m}$, which is centered at the ozone- blocking band. The IR detection is based on the intersubband transition from the ground E_{12} to the quasi-bound E_{22} states. To prevent the overlapping of IR detection wavelengths with the bottom stack (MWIR), we employ the ground to quasi-bound state intersubband transition, which has a narrower bandwidth than the ground-continuum state transition. In addition, E_{22} is in resonance with the top of the barrier to achieve maximum responsivity.

The calculated peak detection wavelength for the top stack is $15\mu\text{m}$. The dominant intersubband transitions are from the ground state E_{13} to the bound states E_{23} , quasi-bound state E_{33} , and to the continuum state E_{43} . The peak responsivity is expected from the transition of the E_{13} to E_{33} states. The major concern with a VLWIR QWIP is the high dark current caused by the thermionic emission at the desired operating temperature due to its low energy barrier. Using graded barriers can reduce the dark current under negative bias conditions as compared to the rectangular barriers.

$\text{In}_x\text{Ga}_{1-x}\text{As}$ quantum wells were used in all three QWIP stacks to enhance the intersubband absorption due to the smaller electron effective mass in this material system than that of GaAs. This in turn will increase the detection sensitivity of optical signals that are partially blocked by the water, ozone, and CO_2 bands in the atmosphere. The number of QWs, barrier widths and doping densities are chosen so that reasonable bias voltage distribution among all three stacks can be achieved without having to operate the device at very high bias voltage.

Figure 7 shows the dark current density-voltage (J-V) characteristics measured at different temperatures for the 3 stacks along with the 300K- background window current density with a 180° field of view (FOV). Figure 7 (a) shows the dark J-V curves for the bottom stack measured at $T = 40, 60, 77, 90\text{K}$. The device is under background limited performance (BLIP) for $-2.8\text{V} < V_b < 0\text{V}$, at $T = 60\text{K}$. Figure 7 (b) shows the dark J-V curves for the middle stack measured at $T = 40, 60, 77$ and 90K , and the BLIP condition occurs at $V_b = -0.5\text{V}$, $T = 77\text{K}$ and at $V_b = 1.1\text{V}$, $T = 90\text{K}$. Figure 7 (c) shows the dark J-V curves for the top stack measured at $T = 30, 40, 50, 60, 77\text{K}$, and the device is under BLIP condition over the entire range of the applied bias, at $T = 30\text{K}$. The MWIR stack, with the highest effective barrier height, has the lowest dark current density under same temperature and bias conditions as the LWIR and VLWIR stacks. The asymmetrical dark current versus bias characteristic observed in the bottom and top stacks is attributed to the asymmetrical barrier height under the positive and negative bias conditions. This asymmetrical behavior is more obvious in the bottom stack due to the steeper slope of the graded barrier. However, the asymmetrical dark J-V curves observed in the middle stack

were caused by the dopant impurity migration effect associated with the MBE growth. The photocurrent spectra were measured with a 45° facet backside illumination using a

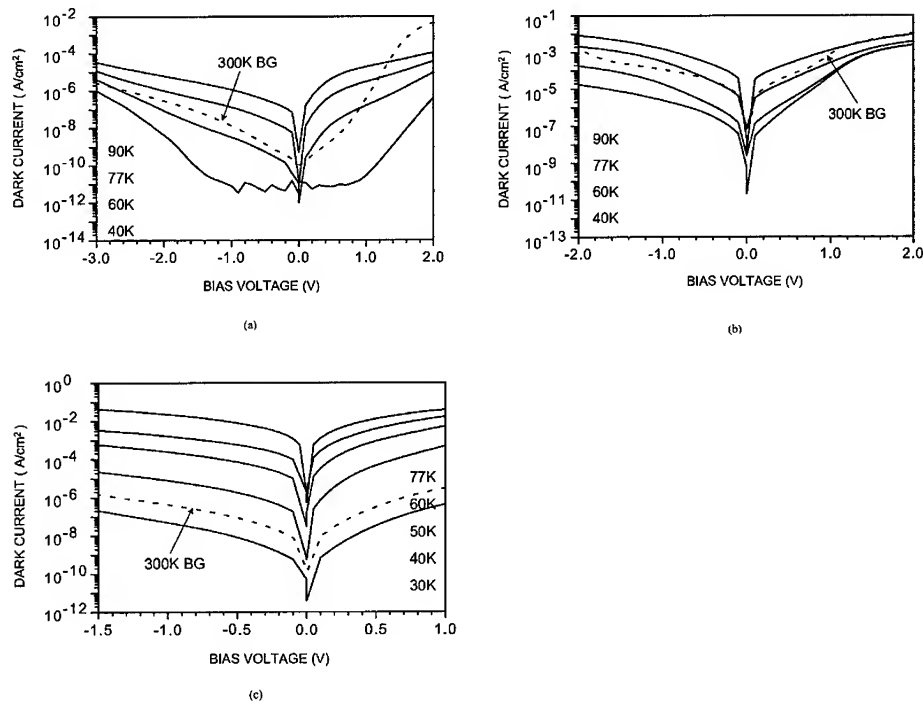


Figure 7 Dark J-V characteristics of the 3-stack 3-color QWIP: (a) MWIR stack; (b) LWIR stack, and (c) VLWIR stack.

calibrated blackbody source at 1000 K. Figure 8 (a) shows the spectral responsivity of the bottom stack measured at 40K for the MWIR stack. The peak detection wavelength is $\lambda_p = 6.5 \mu\text{m}$, which agrees well with the calculated value, and was found nearly independent of temperature and applied bias voltage. The cut-on and cut-off wavelengths for the full-width at half-maximum (FWHM) are $5.9 \mu\text{m}$ and $7.0 \mu\text{m}$, respectively, with $\Delta\lambda_p \approx 16.9\%$. The detection bandwidth for this stack covers the major portion of the water-blocking band. A peak responsivity of 0.13 A/W at $\lambda_p = 6.5 \mu\text{m}$ was obtained at $V_b = -0.13 \text{ V}$ and $T = 40 \text{ K}$, and it remains nearly constant for temperatures up to 77K. A dark-current detectivity of $D^* = 8.5 \times 10^{12} \text{ cm-Hz}^{1/2}/\text{W}$ at $V_b = -1.3 \text{ V}$, $T = 40 \text{ K}$ was obtained for this stack.

Figure 8 (b) shows the spectral responsivity measured at different biases for the middle stack at $T = 40\text{K}$. The peak detection wavelength is at $\lambda_p = 10.1\ \mu\text{m}$ for this stack. The result shows a slight red-shift compared to the calculated peak wavelength, which may be attributed to the uncertainty of the conduction band offset value used in our calculation. The FWHM for this middle stack is $9.1\ \mu\text{m} \sim 11.2\ \mu\text{m}$, with $\Delta\lambda_p = 20.8\%$, which covers the entire ozone band. A peak responsivity of $1.08\ \text{A/W}$ was obtained at $\lambda_p = 10.1\ \mu\text{m}$, $V_b = -1.4\text{V}$ and $T = 40\text{K}$, with a detectivity of $D^* = 1.5 \times 10^{10}\ \text{cm-Hz}^{1/2}/\text{W}$.

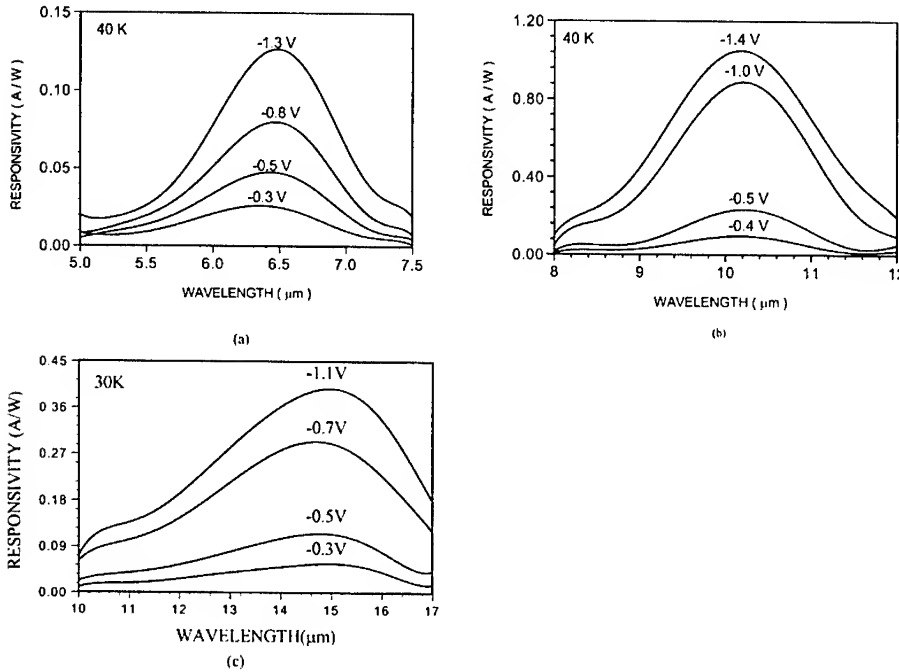


Figure 8 Spectral responsivity of the 3-stack 3-color QWIP for MW/LW/VLWIR detection: (a) MWIR stack, (b) LWIR stack, and (c) VLWIR stack.

Figure 8 (c) shows the spectral responsivity of the top stack measured at $T = 30\text{K}$. The peak detection wavelength is at $15.1\ \mu\text{m}$ for this VLWIR stack. The FWHM is from $12.2\ \mu\text{m}$ to $16.9\ \mu\text{m}$ with $\Delta\lambda_p = 31.1\%$, which covers the CO_2 band. The peak responsivity is $0.42\ \text{A/W}$ at $\lambda_p = 15.1\ \mu\text{m}$, $V_b = -1.1\text{V}$ and $T = 30\text{K}$, with $D^* = 1.2 \times 10^{11}\ \text{cm-Hz}^{1/2}/\text{W}$. The value of D^* decreases sharply with increasing temperature to $8.3 \times 10^9\ \text{cm-Hz}^{1/2}/\text{W}$ at $V_b = -0.2\text{V}$, $\lambda_p = 15.1\ \mu\text{m}$, and $T = 40\text{K}$. Reported D^* values for the VLWIR ($\lambda_p = 15 \sim 17.5\ \mu\text{m}$) InGaAs/AlGaAs QWIPs were in the $10^9 \sim 10^{12}\ \text{cm-Hz}^{1/2}/\text{W}$ range for $T = 20\text{K} \sim 40\text{K}$. [21-24] It should be pointed out that the H_2O and CO_2 bands are not

completely blocked in the atmosphere. Thus, the optical signals are not totally blocked in the atmosphere, and the ozone layer does not influence the optical signal measuring on the earth surface. As a result, a relatively large spectral responsivity can still be obtained in this 3- stack 3- color QWIP.

In summary, we have demonstrated a high performance 3-stack 3-color QWIP designed specifically for the exo- atmospheric detection with peak detection wavelength centered at the water, ozone, and CO₂ blocking bands in the atmosphere. The characteristic and performance of this 3-stack 3-color QWIP have been depicted in this section. The detection bandwidths of this QWIP over the majority or entire region of the three blocking bands in the atmosphere, and the detector can be used for the exo-atmospheric multi-color IR FPAs imaging applications.

4. CONCLUSIONS

In this paper, the design, growth, and characterization of a 2-stack 3-color QWIP for MW/LW/LW IR detection and a 3-stack 3-color QWIP for MW/LW/VLW IR detection have been depicted. Excellent performance in both QWIPs has been achieved. The flexibility of the QWIP structures by the MBE growth made the QWIP device an excellent candidate for multi-color FPAs applications in the MWIR to VLWIR spectral windows.

ACKNOWLEDGEMENT

This work was supported in part by the US Army Research Office under contract No.DAAD19-01-1-0673. The author would like to thank Dr. Bill Clark for his interest and support in this work. He would also like to thank Dr. Meimei Tidrow of BMDO for her continued support of the QWIP research at UF. The author would also like to acknowledge the contributions of Ling Jiang and Jung-Hee Moon for the characterization of QWIP devices reported in this paper.

REFERENCES

1. R. B. Emmons, S. R. Hawkins, and K. F. Cuff, Opt. Eng. **14**, 21 (1975).
2. L. Serzhenko and V. D. Shadrin, Sov. Phys. Semicond. **25**, 953 (1991).
3. L. L. Chang, L. Esaki, and G. A. Sai-Halaz, IBM Tech. Discl. Bull. **20**, 2019 (1977).
4. L. Esaki and T. Tsu, IBM J. Res. Develop. **14**, 61 (1970).
5. L. Esaki and H. Sakaki, IBM Tech. Discl. Bull. **20**, 2456 (1977).
6. D. D. Coon and R. P. G. Karunasiri, Appl. Phys. Lett. **45**, 649 (1984).

7. L. C. West and S. J. Eglash, Appl. Phys. Lett. **46**, 1156 (1985).
8. A. Harwit and J. S. Harris, Jr., Appl. Phys. Lett. **50**, 685 (1987).
9. B. F. Levine, K. K. Choi, C. G. Bethea, J. Walker, and R. J. Malik, Appl. Phys. Lett. **50**, 1092 (1987).
10. B. F. Levine, C. G. Bethea, G. Hasnain, V. O. Shen, E. Pelve, R. R. AB-Bot, and S. J. Hsieh, Appl. Phys. Lett. **56**, 851 (1990).
11. L. S. Yu and S. S. Li, Appl. Phys. Lett. **59**, 1332 (1991).
12. B. F. Levine, J. Appl. Phys. **74**, R1 (1993).
13. I. Gravé, A. Shakouri, N. Kuze, and A. Yariv, Appl. Phys. Lett. **60**, 2362 (1992).
14. Sheng S. Li and M. Z. Tidrow, "Quantum Well Infrared Photodetectors," Handbook of Nanostructured Materials and Nanotechnology, edited by H. S. Nalwa, **vol.4**, chapter 9, pp.561-619, Academic Press, Oct., 1999.
15. J. C. Chiang, Sheng S. Li, M. Z. Tidrow, P. Ho, M. Tsai, and C. P. Lee, Appl. Phys. Lett., vol. 69, pp. 2412-2414, Oct. 1996.
16. Xudong Jiang, Sheng S. Li, and M. Z. Tidrow, IEEE J. of Quantum Electronics, vol. 35, pp. 1685-1692, Nov. 1999.
17. J. C. Chiang, Sheng S. Li, and A. Singh, Appl. Phys. Lett., vol. 71, pp. 3546-3548, Dec. 1997.
18. W. R. Dyer, Electrochemical Society Proceedings Vol. 99-22, 425(1999).
19. A. K. Ghatak, K. Thyagarajan and M. R. Shenoy, IEEE J. Quantum Electronics, **24**, 1524 (1988).
20. H. C. Liu, J. Appl. Phys. **73**, 3062 (1993).
21. G.Sarusi, S.D. Gunapala, J.S. Park and B.F. Levine, J. Appl. Phys., **76**, 6001 (1994).
22. B.F.Levine, A.Zussman, J.M.Kuo and J. De Jong, J.Appl. Phys, **71**, 5130 (1992).
23. S.D. Gunapala, K.M.S.V. Bandara, B.F.Levine, G. Sarusi, D.L. Sivco and A.Y. Cho, Appl. Phys. Lett. , **64**, 2288 (1994).
24. C.Y. Lee, M.Z. Tidrow, K.K. Choi, W.H. Chang, L.F.Eastman, F.J. Towner and J.S.Ahearn, J. Appl. Phys., **75**, 4731 (1994).

A Bowtie Antenna Coupled Tunable Photon-Assisted Tunneling Double Quantum Well (DQW) THz Detector

Majid M. Khodier¹, Christos G. Christodoulou¹, and Jerry A. Simmons²

¹The University of New Mexico

Dept. of Electrical & Computer Engineering
Albuquerque, NM 87131, U.S.A.

²Sandia National Laboratories

Albuquerque, NM 87185-1415, U.S.A.

ABSTRACT

The integration of a bowtie antenna with a double electron layer tunneling transistor (DELTT) device for the purposes of THz detection is investigated in this paper. The concept of THz detection, based on photon-assisted tunneling (PAT) between the two electron layers in a double quantum well (DQW) heterostructure, will be explained. The detector is expected to have narrowband, electrically tunable, fast response, and the possibility to operate at relatively high temperatures. Since the active area of the detector is very small, which is necessary to achieve fast response, it is not efficient in collecting THz radiation. Therefore, a broadband bowtie antenna is integrated with the detector to efficiently collect the THz radiation. Characteristics of different bowtie antenna geometries at THz frequencies were studied. An equivalent circuit model of the THz detector was developed, for the first time, to estimate the impedance characteristics at THz frequencies. Such a model is crucial for achieving impedance matching between the DELTT and the antenna to increase the overall coupling efficiency.

INTRODUCTION

The last frontier in high-frequency electronics research lies in the terahertz regime (other names are submillimeter wave or far infrared, FIR) between microwaves and the infrared (i.e., 0.3-15 THz). The technical advantages of the terahertz frequency regime are many (e.g., wider bandwidth, improved spatial resolution, compactness); however, the solid-state electronics capability within the THz frequency regime remains extremely limited from a basic signal source and systems perspective (i.e., output power < mwatts). This limited development results from the confluence of two fundamental factors. First, extremely challenging engineering problems exist in this region where wavelength is on the order of component size. Second, the practical and scientific applications of this shorter-wavelength microwave region have been restricted in the past to a few specialized fields (e.g., molecular spectroscopy). On the lower frequency side, electronic devices have an upper frequency limit of several hundred GHz due to transient times and parasitic RC time constants. On the higher frequency side, photonics devices, such as interband laser diodes, can only be operated at frequencies above the material's energy gap, which is greater than 40 meV (or 10 THz). Today, more and more important applications of THz technology are rapidly emerging that have civilian and military applications. For example, the strong absorption of electromagnetic energy

by atmospheric molecules, above 300 GHz, makes any communications link impossible to achieve. On the other hand, this same fundamental interaction mechanism suggests THz electronics to be a very promising tool for the identification and interrogation of chemical and biological (CB) agents. Other important applications of THz technologies, ranging from space exploration and atmospheric studies to plasma and fusion research, appear in [1]-[8].

In all of these applications, one kind of a detector or another is needed to transform the collected radiation into a useful electrical signal that can be related to the frequency and strength of that radiation. The THz detector discussed in this paper makes use of photon-assisted tunnelling (PAT) between multiple quantum wells (QWs) when the correct biasing is established, and the radiation has the correct frequency. A general characteristic of all detectors working at THz frequencies is the difficulty of coupling THz radiation efficiently to the active part of the detector for processing, and the prohibitive material losses at such high frequencies. The efficiency of the detector can be enhanced by incorporating an antenna, and since the first work at THz frequencies, it was realized that the antenna should be integrated lithographically with the detector, and the coupling of THz radiation should be done quasi-optically. The purpose of a feed antenna is to couple power from a wave in free space into a device that is much smaller than a wavelength. Since the performance of nearly all submillimeter and IR devices (diodes, tunnel junctions, etc) improves as their physical dimensions are reduced, feed antennas are a critical component of any system that transmits or receives high frequency radiation. Since high frequency devices are manufactured lithographically, it is natural to directly integrate the feed antenna onto the same dielectric substrate. The advantages of such lithographic antenna (or quasi-optical) are many. Compared to other feeding schemes such as waveguide coupling, the fabrication is much cheaper, more accurate, more robust, and more suitable for building large arrays. General reviews of lithographic antenna engineering for mm-wave and THz frequencies can be found in [9]-[15].

The principle of operation of the detector discussed in this paper is based on photon assisted tunnelling in a Double Electron Layer Tunnelling Transistor (DELTT). A general overview of the original structure of the detector is shown in Fig. 1. It consists of a bowtie antenna integrated with a DQW PAT THz detector. Since the detector area is very small, which is necessary for fast response, it cannot collect much of the THz radiation, and therefore, the detection of such radiation is very difficult. The bowtie antenna is used to efficiently collect the THz radiation and feed it to the detector for processing. Bowtie antenna is used because of its broadband response, easy design and fabrication, and its compatibility with the detector fabrication process. In the following sections, the principle of operation of the detector and its fabrication are briefly discussed. Then, simulation results of the bowtie antenna at THz frequencies are discussed. Finally, a simple and accurate equivalent circuit model of the THz detector is developed and discussed.

PRINCIPLE OF OPERATION

The basic idea is to bias the DELTT transistor so that it is off, i.e. tunnelling cannot occur because the dispersion curves of the two QWs do not coincide (the structure of the DELTT transistor is similar to that shown in Fig. 1, but without the bowtie antenna). An infrared photon of the correct energy can then be used to complete the energy-conservation conditions, adding energy to electrons in the higher density QW so that they can resonantly

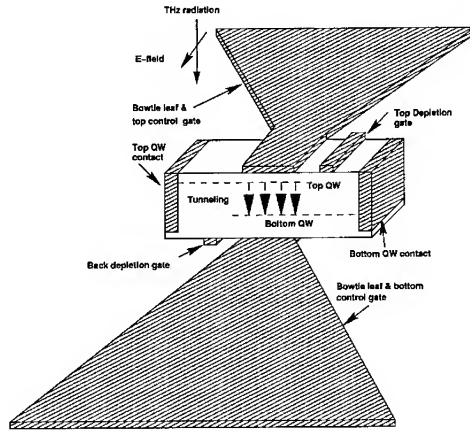


Figure 1: An overview of the DQW THz detector integrated with a bowtie antenna. The top and bottom bows are connected to the top and bottom control gates, respectively. The control gates are used to change the density of electrons in each QW, and therefore provide the electrical tunable characteristic through a DC bias. The depletion gates are used to deplete the QW the one does not wish to contact. The top QW contact is called the source, and the bottom QW contact is called the drain. The structure without the bowtie antenna is called DELTT.

tunnel into the lower density QW. Conceptually, the device behaves analogously to a p-n junction photodiode: in order for electrons to move from the high potential region to the low potential region, they must first overcome an energy barrier. In the p-n junction photodiode, this is accomplished by exciting an electron from the valence band to the conduction band, i.e. creating an electron-hole pair. In the DELTT THz detector, however, this is accomplished by exciting an electron at a given transverse momentum in one QW, to a higher energy state at the same \mathbf{k} in the other QW, as shown in Fig. 2. In the absence of photons, resonant tunnelling can only occur when there exist states in both QWs with identical energy and in-plane momentum. Because both layers are 2D, their allowed states each form a paraboloid having states only on the surface. Without THz radiation, no pairs of states of identical momentum and energy exist, and so tunnelling does not occur. A THz photon of the correct energy, however, will complete the energy-conservation conditions by exciting an electron at a given in-plane momentum \mathbf{k} in one QW, to a higher energy state at the same \mathbf{k} in the other QW. This photon-assisted tunnelling transition causes current to flow between source and drain. What is unique and exciting about the DQW photodetector is that (1) neglecting higher subbands, only a single energy will complete the energy conservation conditions for all the electrons, irrespective of their in-plane momentum values \mathbf{k} , and this results in a very narrowband response. In addition, (2) the energy of the transition can be readily controlled by a gate voltage and/or source drain bias V_{SD} , which makes it possible to obtain a tunable THz detector. A more detailed discussion about the device operation and fabrication can be found in [16]-[21].

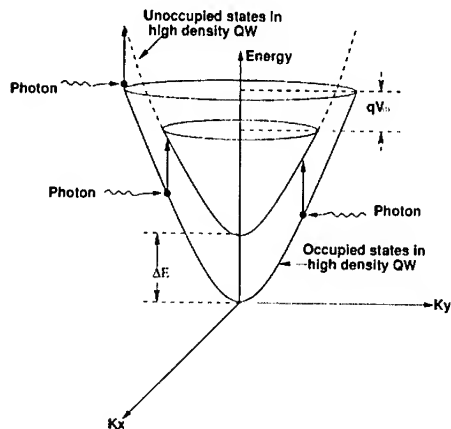


Figure 2: Sketch of the dispersion curve of a double quantum well FIR detector structure.

By applying DC bias to the top or bottom control gate, the electron density in either QW will change accordingly, and the peak of the tunneling current will change in position and magnitude. Therefore, the control gates can be used to create an electrically tunable THz detector over a broadband of THz frequencies.

The DQW structure is an MBE-grown modulation doped heterostructure using the $\text{Al}_x\text{Ga}_{1-x}\text{As}$ material system. Then, the EBASE technique [21] is used to finish the fabricate of the DQW structure by adding front and back gates. Here, we briefly discuss the basic steps involved in the device fabrication as shown in Figure 3, and a more detailed discussion about the fabrication process is found in [21]. The first step is to grow the double quantum well epitaxial structure on a sacrificial substrate. Then, the front side of the structure is processed by making the ohmic contacts and patterning the top gates using conventional methods, as shown in Figure 3(a). After processing the front side, the sample is epoxied to a host substrate as shown in Figure 3(b). Then, the original sacrificial substrate on which the active layers were grown is removed by etching as shown in Figure 3(c). Etching stops on a $\text{Al}_{0.72}\text{Ga}_{0.28}\text{As}$ stop etch layer grown at the base of the epitaxial layer structure. Finally, the back surface is processed by patterning the back gates and etching via holes through the active layers to the front side electrical contact pads for the gates and ohmic contacts as shown in Figure 3(d).

The different dielectric and metallic layers that are used to construct the detector are shown in Fig. 4. The active area of the detector is about $10\mu\text{m} \times 12\mu\text{m}$, which is only a small fraction of the whole detector area (including the antenna). The most important layers in Fig. 4 are the active layer which contains the QWs, the epoxy layer, and the GaAs substrate. The leaves of a bowtie antenna are connected to the top and bottom control gates, as shown in Fig. 1. A photo of a THz DQW detector with bowtie antenna fabricated at Sandia National Laboratory is shown in Fig. 5.

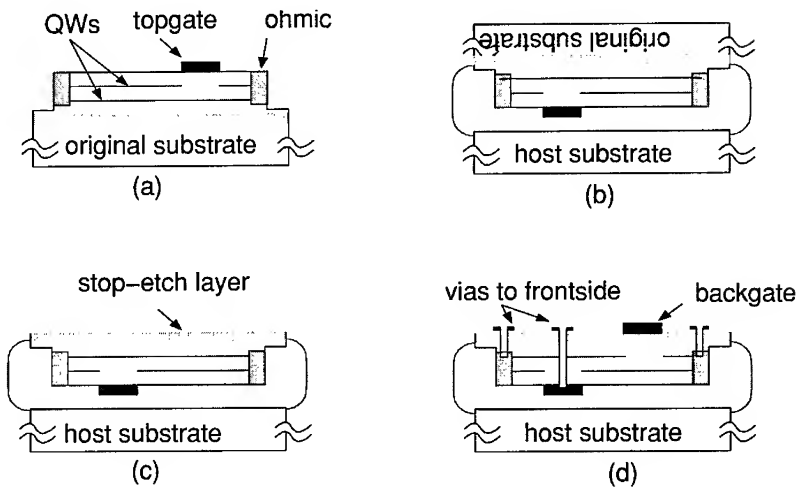


Figure 3: Main steps in the device fabrication using the EBASE technique (a) pattern frontside, (b) epoxy frontside down to host substrate, (b) remove original substrate by etching to stop-etch layer, and (d) pattern backside, including backgates and vias to frontside electrical contact pads.

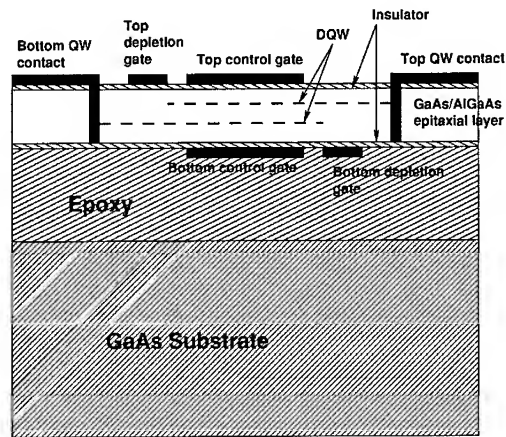


Figure 4: Cross sectional view of the DQW THz detector showing the different dielectric and metallic layers used in the device after fabrication. The GaAs substrate thickness is about $500 \mu\text{m}$, epoxy layer of about $2 \mu\text{m}$, and the epitaxial layer of about $1 \mu\text{m}$. The insulator thickness is about 200 \AA .

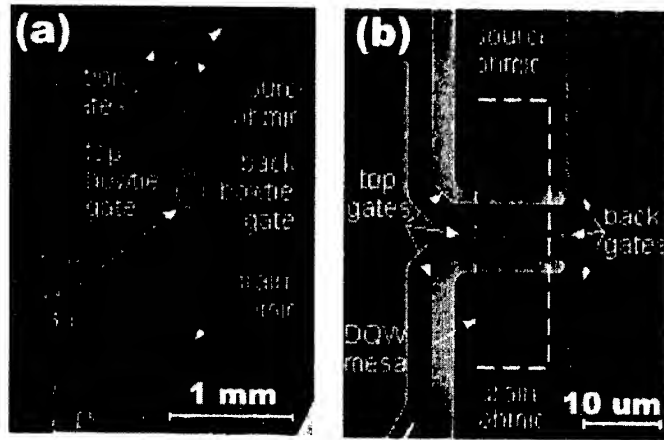


Figure 5: (a) An SEM photo of a bowtie antenna fabricated with the DQW PAT THz detector. The photo corresponds to the design shown schematically in Fig. 1, and (b) Zoomed-in view of (a), showing the active DQW mesa. The bottom gates, although beneath the semiconductor epitaxial layers, remain visible since the electron beam easily penetrates them.

BOWTIE ANTENNA SIMULATION

When the bowtie antenna shown in Fig. 5, which has a bow angle of 120° , is simulated, the results showed that the antenna does not have a broadband characteristic around the frequency of interest (2.54 THz). A new bowtie antenna layout is proposed as shown in Fig. 6(a). This antenna has a bow angle of 90° which gives a self complementary design, and therefore has a theoretical constant real input impedance equals to $60\pi \Omega$ when the antenna is suspended in free space [15]. The purpose of this antenna is to serve as a broadband antenna for coupling the THz radiation to the DQW detector. The antenna structure is simulated on top of a $500 \mu\text{m}$ GaAs substrate using the IE3D simulator [22]. The total length of the antenna is $80 \mu\text{m}$. The antenna length is chosen to be approximately two wavelengths long at 2.54 THz when the antenna is placed on top of a GaAs substrate of $\epsilon_r = 13.1$. The free space wavelength at 2.54 THz is approximately $120 \mu\text{m}$, and assuming an effective dielectric constant of 9, then the wavelength of the combined free space and substrate structure is about $40 \mu\text{m}$. The simulated values of the input impedance is shown in Fig. 6(b). The value of the real part is about 75Ω , and the magnitude of the imaginary part less than 20Ω . The theoretical value the input impedance of a self complementary antenna on a GaAs substrate is real and equals approximately to 74Ω , which is very close from the value obtained from the simulation results.

CIRCUIT MODEL

In order to achieve maximum coupling between the device and the incoming beam, the

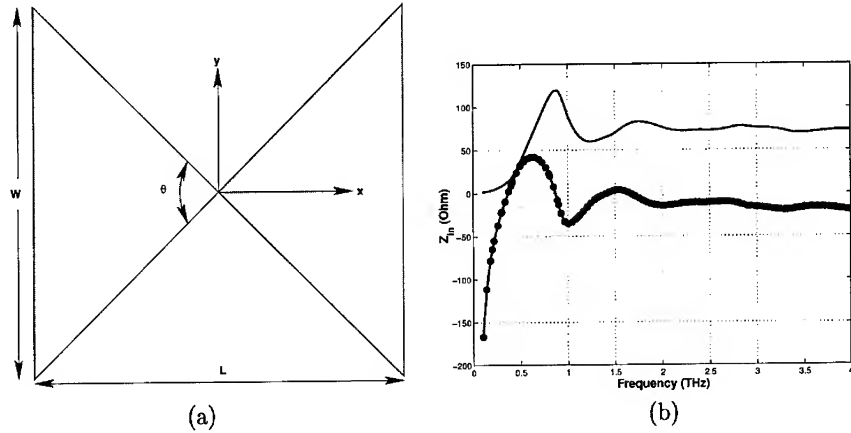


Figure 6: (a) Layout of the 90° bowtie antenna. (b) Input impedance vs. frequency. Solid line: real part, line with dots: imaginary part.

device impedance should be equal to the complex conjugate of the antenna impedance. For this purpose, a method to estimate the frequency dependent impedance of the DELTT is required. This can be achieved by developing an equivalent circuit model of the device which incorporates all the important physical processes and geometrical dimensions that affect the device operation.

A lumped circuit model for the DELTT, valid at DC, is presented in [23]. Another equivalent circuit model for a single two-dimensional electron gas (2DEG) which is capacitively contacted to metallic gates was presented in [24], based on the concept of kinetic inductance. The circuit model consists of either lumped elements or distributed elements (i.e. transmission line), depending on the structure dimensions. The validity of the model at microwave frequencies was also experimentally verified in [24]. In [25], an equivalent model for a DQW was developed using transmission line theory. However, the model did not take into consideration the presence of a gate on top or below (or both) of the DQW structure. The subject of this paper is to develop a general equivalent circuit model for the DELTT structure, which has both top and bottom gates. This work represents an extension to the work found in [24] and [25] to include the effect of the top and bottom gates.

The Drude model for the frequency dependent resistivity of a single 2DEG layer is [24]:

$$\rho(\omega) = \frac{m^*}{ne^2\tau_{mom}} (1 + j\omega\tau_{mom}) \quad (1)$$

where n is the electron density, e the electron charge, m^* the effective mass, and τ_{mom} the momentum scattering time. Equation 1 is the sum of a real part, which is the resistance, and a positive, frequency dependent, imaginary part, which can be considered as an inductive reactance. This inductance is known as the kinetic inductance, because the inductive energy is stored in the kinetic energy of the electrons. At low frequencies, the imaginary part of ρ is very small and usually neglected when developing circuit models for the 2DEG. At THz

frequencies, however, the imaginary part becomes dominant, and it is necessary to include in any circuit model. It should be mentioned that the momentum scattering time τ_{mom} in modulation doped MBE-grown, high mobility GaAs/AlGaAs structures at low temperatures ($< 4K$) is 3-4 orders of magnitude larger than in conventional, bulk doped semiconductors at room temperature.

To ease the calculation of the equivalent circuit model for the DELTT, its cross section is divided into three different regions, as shown in Figure 7. These regions are:

- Region 1: this region consists of a section of either the top or the bottom QW, and extends from the source (or drain) contact to the end of the bottom (or top) depletion gate. In this region, there is no tunneling. The equivalent circuit for this region is composed basically of a resistance in series with inductance. The length of this regions is L_1 .
- Region 2: this region consists of the section of the DELTT between the control gates and the depletions gates where there is overlap between the top and the bottom QWs, and in this region tunneling can occur. The equivalent circuit for this region is a transmission line of length L_2 . An incremental length of this region consists of a resistance R in series with an inductance L , to model each QW, and a shunt capacitance C and conductance G to model the capacitance and the tunneling conductance between the top and bottom QWs. The values of the elements in this region are per unit length.
- Region 3: this region consists of the section of the DELTT where there is overlap between the top and bottom QWs, and covered by the top and bottom control gates, and in this region tunneling can occur. The equivalent circuit for this region is also a transmission line of length L_3 . An incremental length of this region has a similar circuit as that of region 2, but with an extra top and bottom capacitors, C_t and C_b , to model the contact capacitances between the top control gate and top QW, and between the bottom control gate and bottom QW, respectively. The values of the elements in this region are per unit length.

It should be mentioned that the DELTT structure studied here is symmetrical, i.e. electron densities in both QWs are the same. The overall equivalent circuit model for the DELTT transistor, with an antenna connected between the top and bottom control gates, is shown in Figure 8. In terms of mobility μ , surface density n , the width w , dielectric permittivity ϵ of the material between the QWs, and distance between the two QWs d_{qw} , the values of R , L , and C in Figure 8 are given by:

$$R = \frac{1}{en\mu w} \quad (2)$$

$$L = \frac{m^*}{e^2 n w} \quad (3)$$

$$C = \epsilon \times \frac{d_{qw}}{w} \quad (4)$$

The small signal tunneling conductance G can be obtained from the I-V curve of the DELTT by taking the derivative of the current with respect to the applied bias. The element values,

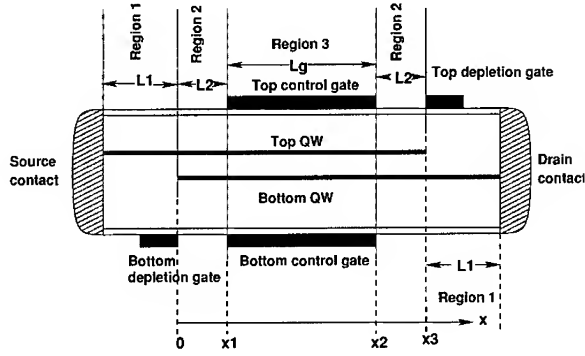


Figure 7: Cross section of the DELTT showing the three regions used in the calculation of the equivalent circuit.

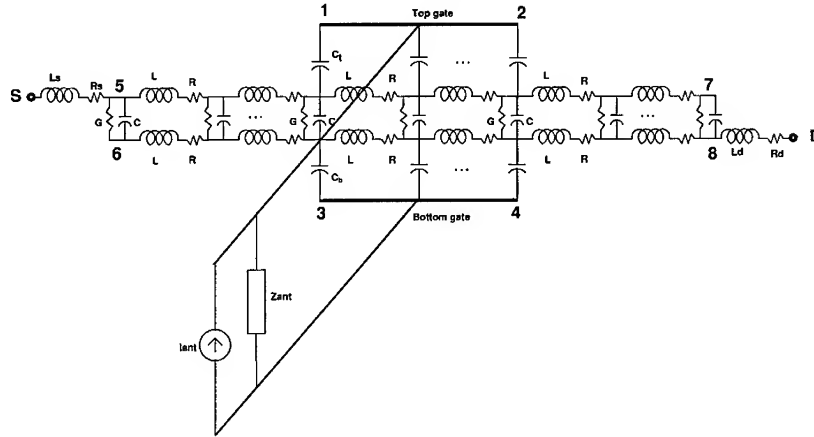


Figure 8: Equivalent circuit model of the DELTT with an antenna connected between the top and bottom control gates. The antenna is modelled as a current source in parallel with the antenna impedance.

R_s , L_s , R_d , and L_d , shown in Figure 8 can be calculated from equations 2 and 3 by multiplying the result from each equation by the length L_1 . The remaining elements, C_t and C_b , represent the geometrical capacitance between the top gate and the top QW and that between the bottom gate and bottom QW, respectively, and can be calculated as follows:

$$C_t = \epsilon \times \frac{d_t}{w} \quad (5)$$

$$C_b = \epsilon \times \frac{d_b}{w} \quad (6)$$

where d_t and d_b are the distances between the top gate and the top QW, and the bottom gate

and bottom QW, respectively, and ϵ is the dielectric permittivity of the material between each gate and the corresponding QW.

We can analyze the structure shown in Fig. 8 by assigning position dependent voltage and current for each transmission line, and then solve the resulting coupled differential equations. The result will be the position dependent voltage and current for each line. The input impedance between any two points in Fig. 8 can be found by applying the appropriate boundary conditions and solving for the unknown coefficients, and then divide the appropriate voltage and current. The details of the analysis can be found in [26]. In the following subsections, the input impedance of the DELTT between the source (S) and the Drain (D), and between the top and bottom control will be calculated using the equivalent circuit shown in Fig. 8. These are the two possible locations where an antenna can be connected to the DELTT device. Sample parameters values for a DELTT device (Sample G1717) will be used in the calculations, and these parameters are shown in Table 1.

Table 1: Sample parameters for the DELTT sample G1717. The listed parameters are QW widths (w_{qw}), tunnel barrier thickness (d_{qw}), electron densities for the top and bottom QWs (n_t and n_b measured in 10^{11} cm^{-2}), distance from top control gate to top QW (d_t) and distance from bottom control gate to bottom QW (d_b), device channel width (w_{chan}), length of the control gates (L_{cg}), length of the depletion gates (L_{dg}), and the separation between the control gates and depletion gates (L_{cg-dg}).

Sample	w_{qw} (Å)	d_{qw} (Å)	n_t	n_b	d_t (μm)	d_b (μm)	w_{chan} (μm)	L_{cg} (μm)	L_{dg} (μm)	L_{cg-dg} (μm)
G1717	150	125	2.0	1.4	0.13	2.2	500	40	10	5

Calculating Z_{SD}

To calculate the input impedance between the source and the drain, Z_{SD} , the equations of the voltages and currents in the three regions are solved for the unknown coefficients using the boundary conditions of a voltage source at point S , and a ground at the drain, D . After finding the unknown coefficients, the input current at the source is found, and then the voltage is divided by the current at the source to obtain Z_{SD} . Element values like R , L , C , C_t , C_b , R_s , R_d , L_s , and L_d are calculated from the parameters in Table 1 using equations 2-6. Applying the above procedure, we calculated Z_{SD} as a function of frequency and the result is shown in Fig. 9(b). The imaginary part of Z_{SD} increases slowly with frequency because of the source and drain conductances (L_s and L_d). The results show that the high frequency limit is basically that of an inductor. Each extra peak with increasing frequency corresponds to fitting one more wavelength into the combined length of regions 2 and 3.

Calculating Z_{13}

The impedance Z_{13} represents the impedance of the DELTT between the top and the bottom control gates where an antenna can be connected. This impedance can be calculated

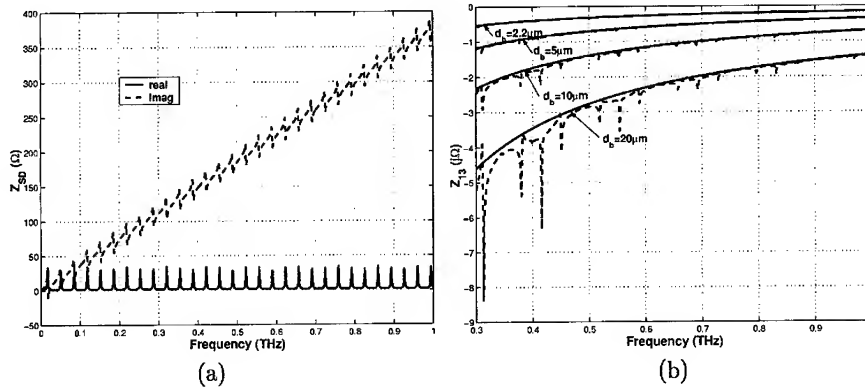


Figure 9: (a) Simulation results of Z_{SD} for the G1717 sample. (b) Simulation (solid line) and predicted (dashed line) results of Z_{13} for the G1717 sample at different values of d_b .

by applying a voltage source at point 1, grounding points 3, S, and D in Figure 8, solving the equations of the voltages and currents in the three regions for the unknown coefficients, and then dividing the voltage by the current at point 1. Simulation results for the G1717 sample are shown in Fig. 9(b) for different values of d_b . The input impedance Z_{13} has a very small real part (negligible and not shown in the figure), and a negative imaginary part that resembles the reactance of a capacitor. We propose that Z_{13} is simply the series combination of Y_t , Y , and Y_b , and therefore Z_{13} is given by:

$$Z_{13} = \frac{1}{L_{cg}} \left(\frac{1}{Y} + \frac{1}{Y_t} + \frac{1}{Y_b} \right) \quad (7)$$

where $Y = G + j\omega C$, $Y_t = j\omega C_t$, $Y_b = j\omega C_b$, and L_{cg} is the length of the control gate(s). We calculated Z_{13} using equation 7 and the results are shown in Fig. 9(b) for different values of d_b . The simulation results and the theoretical results shown in Fig. 9(b) agree very well, which suggests that equation 7 is accurate enough to predict Z_{13} of the DELTT structure.

CONCLUSIONS

The potential of THz detection based on the idea of photon-assisted tunneling in double quantum well devices was introduced. The basic principle of operation of the detector was discussed, and the detector fabrication using state-of-the-art techniques were also presented in this paper. The necessity of integrating a broadband antenna with the device was also established. Simulation results show that it is possible to achieve broadband antenna using self complementary design. This paper also presented for the first time a general equivalent circuit model for the DELTT device. Measurements at very high frequencies can be very difficult to obtain since it is extremely difficult to obtain accurate measurements of impedance at such high frequencies. However, the presented circuit model, based on the most important physical interactions that affect the device operation, can be utilized at THz frequencies,

assuming that the device parameters (like density and mobility) at these high frequencies can be determined accurately. Moreover, the simulations results of sample devices revealed that it is extremely difficult to match the DELTT impedance to the broadband band bowtie antenna impedance.

REFERENCES

- [1] J. W. Waters and P. H. Siegel, "Applications of Millimeter and Submillimeter Technology to Earth's Upper Atmosphere: Results to Date and Potential for the Future," *The 4th International Symposium on Space Terahertz Technology*, Los Angeles, CA, March 1993.
- [2] J. Farman, B. Gardiner, and J. Shanklin, "Large Losses of Total Ozone in Antarctica Reveal seasonal ClO_x/NO_x ," *Nature*, Vol. 315, p. 207, 1985.
- [3] P. B. Hays and H. E. Snell, "Atmospheric Remote Sensing in the Terahertz Regions," *Proceedings of the 1st International Symposium on Space Terahertz Technology*, p. 482, 1990.
- [4] T. G. Phillips, "Developments in Submillimeter-Wave Astronomy," *The 19th International Conference on Infrared and Millimeter Waves*, Sendai, Japan, 1994.
- [5] S. Gulkis, "Submillimeter Wavelength Astronomy Missions for the 1990s," *Proceedings of the 1st International Symposium on Space Terahertz Technology*, pp. 454-457, 1990.
- [6] N. C. Luhmann, "Instrumentation and Techniques for Plasma Diagnostics: An Overview," *Infrared and Millimeter Waves*, Vol. 2, pp. 1-65, K. J. Button, Ed., Academic Press, New York, 1979.
- [7] P. E. Young, D. F. Neikirk, P. P. Tong, and N. C. Luhmann, "Multi-channel Far-infrared Phase Imaging for Fusion Plasma," *Rev. Sci. Instrum.*, Vol. 56, pp. 81-89, 1985.
- [8] P. F. Goldsmith, "Coherent Systems in the Terahertz Frequency Range: Elements, Operation and Examples," *Proceedings of the 3rd International Symposium on Space Terahertz Technology*, pp. 1-23, 1992.
- [9] R. A. York and Z. B. Popovic, Ed., *Active and Quasi-Optical Arrays for Solid-State Power Combining*, John wiles & Sons, New York, 1997.
- [10] D. B. Rutledge, D. P. Neikirk, and D. P. Kasilingham, "Integrated-Circuit Antennas," *Infrared and Millimeter Waves*, Vol. 10, New York, Academic Press, 1983, ch. 1, pp. 1-90.
- [11] M. Rebiez, "Millimeter-Wave and Terahertz Integrated Circuit Antennas," *Proc. Of the IEEE*, Vol. 80, pp. 1748-1770, Nov. 1992.
- [12] E. N. Grossman, "Lithographic Antennas for Submillimeter and Infrared Frequencies," *IEEE International Symposium on Electromagnetic Compatibility*, pp. 102-107, 1995

- [13] D. S. Hernandez and I. Robertson, "Integrated Antennas for TeraHertz Circuits," *IEE Colloquium on Terahertz Technology*, pp. 1-7, 1995.
- [14] D. B. Rutledge, S. E. Schwarz and A. T. Adams, "Infrared and Submillimeter Antennas," *Infrared Physics*, Vol. 18, pp. 713-729, Pergamon Press Ltd, 1978.
- [15] R. C. Compton et al, "Bow-Tie Antennas on a Dielectric Half-Space: Theory and Experiment," *IEEE Trans. Antennas Propagat.*, Vol. 35, pp. 622-630, June 1987.
- [16] Sanchez, C. F. Davis, K. C. Liu and A. Javan, "The MOM Tunneling Diode: Theoretical Estimate of its Performance at Microwave and Infrared Frequencies," *J. Appl. Phys.*, Vol. 49(10), pp. 5270-5277, Oct. 1978.
- [17] H. Drexler, J. S. Scott and S. J. Allen, "Photon-Assisted Tunneling in a Resonant Tunneling Diode: Stimulated Emission and Absorption in the THz Range," *Appl. Phys. Lett.*, Vol. 67(19), pp. 2816-2818, Nov. 1995.
- [18] J. A. Simmons et al, "Planar Quantum Transistor Based on 2D-2D Tunneling in Double Quantum Well Heterostructure," *J. Appl. Phys.*, Vol. 84(10), pp. 5626-5634, Nov. 1998.
- [19] M. A. Blout et al, "Double Electron Layer Tunneling Transistor (DELTT)," *Semicond. Sci. Technol.*, Vol. 13, pp. A180-A183, 1998.
- [20] J. S. Moon et al, "Unipolar Complementary Circuits Using Double Electron Layer Tunneling Transistor," *Appl. Phys. Lett.*, Vol. 74, pp. 314-316, Jan. 1999.
- [21] M. V. Weckwerth et al, "Epoxy Bond and Stop-Etch (EBASE) Technique Enabling Backside Processing of (Al)GaAs Heterostructures," *Superlattices and Microstructures*, Vol. 20, No. 4, pp. 561-567, 1996.
- [22] IE3D is a Registered Trademark of Zeland Software, Inc.
- [23] Y. Katayama and D. C. Tsui, "Lumped Circuit Model of Two-Dimensional to Two-Dimensional Tunneling Transistors," *Appl. Phys. Lett.*, Vol. 62 (20), pp. 2563-2565, May 1993.
- [24] P. J. Burke, I. B. Spielman and J. P. Eisenstein, "High Frequency Conductivity of the High-Mobility Two-Dimensional Electron Gas," *Appl. Phys. Lett.*, Vol. 76, pp. 745-747, Feb. 2000.
- [25] P. J. Burke and J. P. Eisenstein, "Interlayer Plasmons," *unpublished report*, August 1998.
- [26] M. M. Khodier, *Analysis and Design of Broadband Antennas for the Double Quantum Well Terahertz Detector*, Ph.D. dissertation, The University of New Mexico, Albuquerque, NM, 2001.

Fast Room Temperature Detection of State of Circular Polarization of Terahertz Radiation.

Sergey D. Ganichev^{1,2}, Hermann Ketterl¹, and Wilhelm Prettl¹,

¹ Institut für Experim. und Angew. Physik, Universität Regensburg, 93040 Regensburg, Germany,

² A. F. Ioffe Physico-Technical Institute, 194021 St. Petersburg, Russia

ABSTRACT

We report on a room temperature detector which allows to determine and monitor the state of polarization of terahertz radiation with picosecond temporal resolution. The detector is based on the circular photogalvanic effect recently observed in GaAs/AlGaAs quantum wells. The circular photogalvanic effect yields in response to elliptically polarized radiation a current signal proportional to the degree of circular polarization. The peak current signal occurs in unbiased samples for circular polarization, vanishes at linear polarization and changes sign by switching the helicity from right-handed to left-handed. The detector consists of a (113)A MBE grown p-GaAs/AlGaAs multiple quantum well structure. The response has been measured in the wavelength range between 76 μm and 280 μm at normal incidence of the radiation on the sample.

INTRODUCTION

Room temperature detection of short THz laser pulses is possible using pyroelectricity [1], bulk semiconductor devices like photon drag detectors [2-5], Schottky-diodes [5], and intraband photoconductivity [6]. Recently low dimensional semiconductor structures and superlattices have been demonstrated to be very efficient for detection THz radiation with high temporal resolution. In particular photovoltaic [7], photon-drag [8], and hot electrons [9] effects in quantum well (QW) structures as well as THz radiation driving superlattices [10] are promising means of large bandwidth detection. Here we report on a new approach to THz detection applying the circular photogalvanic effect which has recently been observed in GaAs based quantum wells (QW) [11,12]. Circularly polarized radiation generates a current in the unbiased sample. Because the photogalvanic effect does not involve any charge separation, space charge regions or gradient-induced drift currents, photogalvanic detectors have the advantages of fast transient signal response at low impedance. The only physical speed limitations result from momentum relaxation times, which are in order of picoseconds at room temperature. The striking feature of this photogalvanic effect is that the current flows perpendicular to the radiation propagation and that the sign of the current reverses by changing the helicity of the radiation from right-handed to left-handed. Therefore the circular photogalvanic effect does not only trace the time dependence of a radiations pulse but it gives also the state of polarization of the electromagnetic field in a very direct way.

PHYSICAL BACKGROUND

The photogalvanic effects arise in homogeneous samples of noncentrosymmetric media [13] under homogeneous excitation due to an asymmetry of the interaction of free carriers with photons, phonons, static defects or other carriers. In the THz-range the circular photogalvanic effect occurs at intersubband or intrasubband transitions in quantum-well structures. Phenomenologically, the effect is a transfer of the angular momentum of circularly polarized photons into a directed motion of free carriers, electrons or holes. Therefore the effect depends on the symmetry of the medium.

The photogalvanic current under study can be described by the following phenomenological expression [11]:

$$j_\lambda = \chi_{\lambda\mu\nu}(E_\mu E_\nu^* + E_\nu E_\mu^*)/2 + \gamma_{\lambda\mu} i (\mathbf{E} \times \mathbf{E}^*)_\mu, \quad (1)$$

where \mathbf{E} is the complex amplitude of the electric field of the electromagnetic wave and $i(\mathbf{E} \times \mathbf{E}^*) = \hat{\mathbf{e}} P_{\text{circ}} E_0^2$ with the degree of circular polarization $P_{\text{circ}} = (|E_+|^2 - |E_-|^2)/(|E_+|^2 + |E_-|^2)$ where E_+ and E_- are the amplitudes of left and right handed circularly polarized radiation, respectively. $E_0 = |\mathbf{E}|$ is the electric field amplitude and $\hat{\mathbf{e}}$ is the unit vector pointing in the direction of the light propagation. The photocurrent given by the tensor χ describes the so-called linear photogalvanic effect (LPGE) because it is usually observed under linearly polarized optical excitation. The circular photogalvanic effect (CPGE) yielding the helicity dependent current is described by the pseudo-tensor γ and can be observed only under circularly polarized excitation.

A symmetry analysis shows that in order to obtain a helicity dependent photoresponse at normal incidence, which is convenient for detection, the symmetry of the structure must be reduced to the point group C_s . This group contains only two elements: the identity transformation and one mirror reflection. This can easily be obtained in zinc-blende based QW structures by choosing a suitable crystallographic orientation. This condition is met, for instance, in (113) grown structures. In this case the helicity dependent current flows in the direction $x \parallel [1\bar{1}0]$ being normal to the mirror plane which contains the $[110]$ axis. For the light initially polarized along x and transmitted through the $\lambda/4$ plate, as in experiments described below, we have

$$j_x = \gamma_{xz} t_p t_s \cos \Theta E_0^2 P_{\text{circ}}, \quad (2)$$

where t_p and t_s are transmission coefficients after Fresnel's formula for linear p - and s -polarizations, Θ is the angle of refraction defined by $\sin \Theta = \sin \Theta_0/n$, Θ_0 is the angle of incidence and n is the index of refraction.

Microscopically, the CPGE in MQWs is due to optical spin orientation of charge carriers and asymmetric spin-dependent scattering of spin-polarized carriers followed by an appearance of an electric current [12]. The two states of light circular polarization result in different spin orientations and, thus, in electric photocurrents of opposite directions. The principal aspect of a photon helicity driven current is the removal of spin-degeneracy in the subband states due to the reduced symmetry of the quantum well structure [12, 14]. It is related to the appearance of \mathbf{k} -linear terms in the Hamiltonian,

$$H^{(1)} = \beta_m \sigma_l k_m \quad (3)$$

where the real coefficients β_m form a pseudo-tensor subjected to the same symmetry restrictions as the pseudo-tensor γ ; σ_l are Pauli spin matrices. Spin degeneracy results from the simultaneous presence of time-reversal and spatial inversion symmetry. If one of these symmetries is broken the spin degeneracy is lifted. In (113) grown GaAs QW systems considered here the spatial inversion symmetry is broken (the point group C_s does not contain the inversion operation) and, as a consequence, spin-dependent and \mathbf{k} -linear terms appearing in the electron Hamiltonian lead to a splitting of the electronic subbands at a finite in-plane wave vector. As discussed in [14] the coupling between the spin of the carriers (σ_l) and the carrier momentum (k_m) together with spin-controlled dipole selection rules yields a net current under circularly polarized excitation. Depending on the band structure of quantum wells and the photon energy this spin photocurrent can be either due to direct or indirect intersubband transitions.

EXPERIMENTAL

The concept of the CPGE-detector was realized using quantum well structures grown by molecular beam epitaxy on semi-insulating (113) oriented GaAs substrates. The samples were

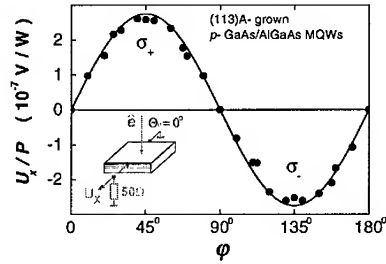


Figure 1. Photoresponse of *p*-type (113)A- grown GaAs/AlGaAs QWs structure normalized by the light power P as a function of the phase angle φ defining helicity. Measurements are presented for $T = 300$ K and normal incidence of radiation at $\lambda = 76 \mu\text{m}$. The current $j_x \propto U_x$ flows along $[1\bar{1}0]$ -direction perpendicular to the mirror plane of the C_s symmetry. Full lines are fitted to Eq. (1) using one y -axis scaling parameter. The inset shows the geometry of the experiment.

p-GaAs/AlGaAs multiple QWs containing 20 wells of 15 nm width. Samples with free hole densities of $2 \cdot 10^{11} \text{ cm}^{-2}$ were studied at room temperature. A pair of ohmic contacts was centered on opposite sample edges along the $[1\bar{1}0]$ axis (see inset in Figs. 1).

A high power pulsed THz NH_3 -laser [15] has been used as radiation source delivering 100 ns pulses with radiation power P up to 100 kW. Several lines of the NH_3 -laser between $\lambda = 76 \mu\text{m}$ and $280 \mu\text{m}$ have been applied for excitation in the THz range. Depending on the frequency the THz radiation induces direct optical transitions between heavy hole and light hole subbands and indirect optical transitions in the lowest heavy hole subband. The laser light polarization was modified from linear to circular using quartz $\lambda/4$ plates. The helicity of the incident light was varied according to $P_{\text{circ}} = \sin 2\varphi$ where φ is the angle between the initial plane of linear polarization and the optical axis of the $\lambda/4$ plate.

With irradiation of (113)-oriented samples of C_s symmetry a current signal proportional to the helicity P_{circ} is observed under normal incidence. We note that the samples were unbiased, thus the irradiated samples represent a current source. A voltage signal is obtained by applying a 50Ω load resistor in a closed circuit. The response follows the temporal structure of the laser pulse intensity and changes sign if the circular polarization is switched from left-handed to right-handed (Fig. 1). The direction of the current is determined by the symmetry of the crystal. The helicity dependent current flows always along the $[1\bar{1}0]$ -direction perpendicular to the plane of mirror reflection of the point group C_s , independent of the plane of incidence of the laser beam. In Fig. 2 we take a closer look on the dependence of the photoresponse on the angle of incidence Θ_0 of the circularly polarized laser beam. Comparison of Eqs. (1) and (2) and Figs. 1, 2 shows a good agreement between the theory and the experimental data.

In the wavelength range from $76 \mu\text{m}$ to $280 \mu\text{m}$ the voltage response of the CPGE detector depends linearly on the power up to highest intensities applied (2 MW/cm^2). The sensitivity in the range of $0.2 \mu\text{V/W}$ at 50Ω is low but enough to detect short THz pulses of sources like optically pumped molecular lasers and free-electron-lasers. It can be improved by using a larger number of quantum wells. Note that even in a large number of QWs the extinction of radiation is very low, hence the device can be used to monitor the state of circular polarization of a beam being transmitted through the sample.

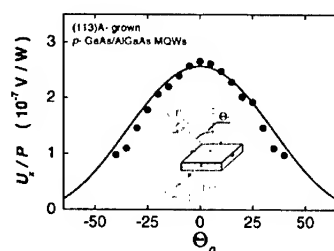


Figure 2. Photoresponse of 20 p -type (113)A-grown GaAs/AlGaAs QWs normalized by the light power P as a function of the angle of incidence Θ_0 for right circularly polarized radiation measured perpendicular to light propagation ($T = 300$ K, $\lambda = 76$ μm). Full line is fitted to Eq. (2) using one y -axis scaling parameter.

CONCLUSIONS

In conclusion we would like to point out that the detection scheme has the unique feature of being sensitive to the helicity of radiation. Combining CPGE detection with LPGE one, which is sensitive to the state of linear polarization [16], the ellipticity and the orientation of the ellipse of elliptically polarized radiation can be obtained. Finally we note that the CPGE may also occur at valence-to-conduction band transitions [14] as well at direct intersubband transitions e.g. in the case of asymmetrical (113) grown p -type Si/SiGe structures [17]. Thus the applicability of the CPGE detection scheme may well be extended the near infrared and mid infrared spectral ranges.

ACKNOWLEDGEMENTS

Financial support from the DFG, the RFFI, and the NATO linkage program is gratefully acknowledged.

REFERENCES

1. A. Hadni, *Infrared and Millimeter Waves*, vol. 3, eds. K.J. Button and J.C. Wiltse, p. 112 (Academic Press, 1980).
2. P.M. Valov, K.V. Goncharenko, Yu.V. Markov, V.V. Pershin, S.M. Ryvkin, and I.D. Yaroshetskii, *Sov. J. Quantum Electronics* **7**, 50 (1977).
3. A.F. Gibson, and M.F. Kimmitt, *Infrared and Millimeter Waves*, vol. 3, eds. K.J. Button and J.C. Wiltse, p. 182 (Academic Press, 1980).
4. S.D. Ganichev, Ya.V. Terent'ev, and I.D. Yaroshetskii, *Sov. Tech. Phys. Lett.* **11**, 20 (1985).
5. M.F. Kimmitt, *Infrared Physics* **32**, 213 (1992).
6. S.D. Ganichev, S.A. Emel'yanov, A.G. Pakhomov, Ya.V. Terent'ev, and I.D. Yaroshetskii, *Sov. Tech. Phys. Lett.* **11**, 377 (1985).

7. H. Schneider, C. Schönbein, G. Bihlmann, P. van Son, and H. Sigg, *Appl. Phys. Lett.* **70**, 1602 (1997).
8. H. Sigg, M.H. Kwakernaak, B. Margotte, D. Erni, P. van Son, and K. Köhler, *Appl. Phys. Lett.* **67**, 2827 (1995).
9. R.J. Stone, J.G. Michels, S.L. Wong, C.T. Foxton, R.J. Nicholas, and A.M. Fox, *Appl. Phys. Lett.* **69**, 3569 (1996).
10. S. Winnerl, W. Seifert, E. Schomburg, J. Grenzer, and K.F. Renk, C.J.G.M. Langerak, A.F.G. van der Meer, D.G. Pavel'ev, Yu. Koschurinov, A.A. Ignatov, B. Melzer, V. Ustinov, S. Ivanov, and P.S. Kop'ev, *Appl. Phys. Lett.* **73**, 2983 (1998).
11. S.D. Ganichev, H. Ketterl, W. Prettl, E.L. Ivchenko, and L.E. Vorobjev, *Appl. Phys. Lett.* **77**, 3146 (2000).
12. S.D. Ganichev, E.L. Ivchenko, S.N. Danilov, J. Eroms, W. Wegscheider, D. Weiss, and W. Prettl, *Phys. Rev. Lett.* **86**, 4358 (2001).
13. E.L. Ivchenko and G.E. Pikus, *Superlattices and Other Heterostructures. Symmetry and Optical Phenomena*, Springer Series in Solid State Sciences, vol. 110, Springer-Verlag, 1995; second edition 1997; Ch. 10.
14. S.D. Ganichev, E. L. Ivchenko, and W. Prettl, *Physica E*, (in press).
15. S.D. Ganichev, *Physica B* **273-274**, 737 (1999).
16. A.V. Andrianov, E.V. Beregunin, S.D. Ganichev, K.Yu. Glukh and I.D. Yaroshetskii, *Sov. Tech. Phys. Lett.* **14**, 580 (1988).
17. S.D. Ganichev, F.-P. Kalz, U. Rössler, W. Prettl, E.L. Ivchenko, V.V. Bel'kov, R. Neumann, K. Brunner, and G. Abstreiter, *Proc. of MRS Fall Meeting*, Boston (2001) (in press).

PbTe Flash Evaporation on Si <100> Substrates for Heterojunction Infrared Detectors

Sonia Guimarães, Sabrina de C. F. F. da Silva¹ and João M. K. de Assis

Instituto de Aeronáutica e Espaço, Divisão de Materiais, São José dos Campos, SP, Brazil.

¹Faculdade de Engenharia Química de Lorena, Lorena, SP, Brazil.

ABSTRACT

This work is to present results of flash evaporation of PbTe directly over single crystals p-type Si substrates, in order to produce heterojunction infrared detectors (HIRD), working at 4.3μm IR wavelength. The evaporation was performed on modified JEOL vacuum equipment, model JEE4B(a), working with vacuum pressure around 10^{-5} torr, using diffusion pump. The HIRDs produced with this method presented the same detectivity (D^*) values of HIRDs made with Hot Wall Epitaxial System (HWE)(b), in which PbTe epitaxial layers were grown directly over the same Si substrates, where an ionic pump reached about 10^{-7} torr as vacuum pressure. The best results, were obtained with PbTe layers grown with Molecular Beam Epitaxial (MBE) method(c) directly over Si substrates, where the vacuum pressure is around 10^{-9} torr, also using an ionic pump. The advantage of growing PbTe directly over Si wafers is that the HIRDs perform at room temperature. The detectivity values of HIRDs obtained with methods (a) and (b), were $D^* \approx 4,8 \times 10^5 \text{ cm.Hz}^{1/2} \text{ W}^{-1}$ and with method (c), $D^* \approx 6,7 \times 10^6 \text{ cm.Hz}^{1/2} \text{ W}^{-1}$. Different technologies: (a) very low costs, (c) high technology; not very different results.

INTRODUCTION

Single crystal semiconductor thin layers can be processed through several growth techniques. However, when it is grown for devices application, epitaxial techniques are the most used. Among the epitaxial growth methods: Hot Wall Epitaxy (HWE) [1,2], Molecular Beam Epitaxy (MBE) [3] and Flash Evaporation (FE) [4,5], are some of them.

Flash evaporation used in this work consisted of a modified vacuum equipment with three basic steps: a) solid phase source transition to gas phase, using the heat of a resistor, which contains the material to be evaporated; b) vapor transportation to the substrate surface, c) vapor condensation on the substrate surface. The modification performed in the evaporator was to provide a sample heater system, which enable us to heat, and control the Si substrates temperature till about 230 °C.

Besides PbTe, cadmium telluride (CdTe) flash evaporated layers are also attractive materials for fabrication of semiconductor devices, such as solar cells, γ and IR detectors and field effect transistors [5,6]. Rusu and Rusu [6] studied the electrical conductivity of CdTe thin films evaporated onto unheated glass substrates, and obtained <111> and amorphous structures. Domadara Das and Selvaraj [7] studied the time dependent electrical resistance of $\text{Bi}_2(\text{Te}_{0.4}\text{Se}_{0.6})_3$ flash evaporated thin films, related with the effects of oxygen adsorption. These thin films find many applications such as in small thermoelectric power generators, thermoelectric refrigerators, thermopile detectors, etc. Boustani *et al.* [8] studied the influence of the substrate temperature during CuInTe_2 flash evaporation thin films, on its properties. These films have been extensively studied because of the potential applications in multijunction thin-film solar cells [9].

In this paper metal rich alloy ($\text{Pb}_{0.502}\text{Te}_{0.498}$) with 6N pure materials (99,9999% purity), melted in tungsten boat, was flash evaporated over $\langle 100 \rangle$ and $\langle 111 \rangle$ crystal orientated, 1-10 Ω .cm resistivity Si substrate surfaces, chemically cleaned and heated at 200 and 230 °C, before and during the evaporation. The thin layers resulted of this procedure were characterized. X-ray diffraction spectrum of these thin films showed that some are single crystals, some are poli, and some are poli with strong tendency to single crystal on $\langle 100 \rangle$ orientation. Scanning Electronic Microscopy (SEM) of them showed some surface defects, like cracks, and, in some cases, they are not very flat. The experimental procedures of this work have been made in order to reach these improvements.

EXPERIMENTAL PROCEDURE

The Si wafers cleaning procedure which showed better results in layer adherence and crystal quality, was based in a chemical treatment [10-12] that first degreased the surface substrate with boiled trichloroethylene and methanol, then ammonia hydroxide, hydrogen peroxide and deionized water solution (1 NH_4OH : 1 H_2O_2 : 4 H_2O). The oxide layer was removed with HF : NH_4F (BOE - Buffered Oxide Etchant) or diluted fluoridric acid (1 HF : 10 H_2O). Afterwards, the substrate surface was passivated with boiled cloridric acid, hydrogen peroxide and deionized water (3 HCl : 1 H_2O_2 : 1 H_2O or 1 HCl : 1 H_2O_2 : 4 H_2O). Finally deoxidized by HF : NH_4F (BOE - Buffered Oxide Etchant) or diluted fluoridric acid (1 HF : 10 H_2O), once more, and put in the evaporator chamber. Inside the evaporator chamber, Si substrates distant about 3 cm from the PbTe source, were pre-heated (200 - 230 °C), during different periods of time (2 – 4.5 h), then evaporation took place, with the same pre-heating substrate temperature.

After evaporation, thickness was measured with an Alfa Step 500 Surface Profiler. X-ray diffraction spectrum of the samples was taken, with a High Resolution X-Ray Diffraction Spectrometer Philips X'Pert (PW3710), equipped with Copper anodic tube, Nickel filter, 40kV as voltage value, and 20 mA as current, $2\theta = 0.02^\circ$ step, each step taking 1 sec. Powder Diffraction Files had identified the diffraction lines, from International Center for Diffraction Data (ICDD). The SEM used to analyze the thin films surfaces under low vacuum pressure (10^{-5} torr) was a LEO 435 Vpi type; no coating was used over the samples. The PbTe/p-Si hetero structure was electrically analyzed by making electrical contacts between PbTe layers and Si substrate, in order to make the current (I) versus voltage (V) measurements, and obtain the junction characterization, I x V plot. The junctions that presented better electrical characterization had their detectivity signal measured by irradiating infrared beams at the back of the Si substrate. This IR radiation coming from a black body at 700K ($\lambda_{\text{max}} = 4.3 \mu\text{m}$), 908 Hz as modulator frequency (Lock-in) PAR 124A, and pre-amplification bandwidth frequency $\Delta f = 14\text{Hz}$.

RESULTS AND DISCUSSION

Table I shows that the cleaning treatment with (3 HCl : 1 H_2O_2 : 1 H_2O) presents better detectivity results than the cleaning treatment with (1 HCl : 1 H_2O_2 : 4 H_2O), when (1 HF : 10 H_2O) solution is used to perform the deoxidization. The opposite happens when BOE is used as deoxidizer, samples F21, F24 and F25. On the other hand, sample F19, deoxidized with HF, demonstrates that these two cleaning treatment did not make difference. Sample F23 showed that

BOE deoxidization decrease detectivity values. The first solution is more concentrated, consequently produces a thicker passivation layer than the second, consequently HF solution is probably stronger than BOE solution.

Table I – Influence of crystallographic orientation $\langle \rangle$, cleaning and thermal treatment of Si, on the detectivity values.

Samples	$\langle \rangle$	Cleaning Treatment	T_p (°C)	τ_p (hours)	$D^* \times 10^{-5}$ (cm.Hz ^{1/2} .W ⁻¹)
F12a	100	3HCl and HF	200	3	4,8
F05b	100	3HCl and HF	200	3,8	4,7
F05c	111	3HCl and HF	200	3,8	0,4
F04a	100	3HCl and HF	200	3,5	2,2
F07b	100	1HCl and HF	200	3,5	0,5
F07c	111	3HCl and HF	200	3,5	0,4
F02b	100	3HCl and HF	200	3,5	1,5
F06b	100	1HCl and HF	200	3,6	0,8
F13a	100	1HCl and HF	200	3	0,5
F20b	100	1HCl and BOE	230	2	0,7
F20a	111	1HCl and BOE	230	2	0,2
F21a	111	1HCl and BOE	230	2	0,7
F21b	100	1HCl and BOE	230	2	0,7
F25a	111	1HCl and BOE	200	2	0,4
F25c	100	1HCl and BOE	200	2	0,4
F24a	100	3HCl and BOE	200	2	0,3
F24c	111	3HCl and BOE	200	2	0,3
F19b	100	1HCl and HF	230	2	0,5
F19c	111	3HCl and HF	230	2	0,5
F23c	100	1HCl and HF	230	2	0,4
F23b	111	1HCl and BOE	230	2	0,3

T_p = pre-heating and evaporation substrate temperature, τ_p = pre-heating time
 D^* = specific detectivity.

The detectivity values also decreased when the crystal orientation changed from $\langle 100 \rangle$ to $\langle 111 \rangle$, independently of cleaning treatment, compare samples F05b and c, or F07b and c. This behavior was not observed when epitaxial layers were grown using HWE technique [13,14]. An explanation may be the substrate temperature during the evaporation. In the case of HWE [14], the substrate temperature is 300 °C, and no difference on the detectivity values was noticed, related with crystal orientation. However, samples F21, F24 and F25, where the solution used to perform the deoxidization was BOE, presented same detectivity values, independently of Si crystal orientation. The only exception is sample F20.

Results with Scanning Electronic Microscopy and X-ray Diffraction Spectrometry

Flash evaporated surface layers showed different aspects, being mirror like most of the time. The following SEM micrographs showed some surface defect, as Figure 1 cracks, caused probably due the very different crystal lattice parameters ($\text{Si} = 5,431$ and $\text{PbTe} = 6,459$, at 300K) and linear coefficient of thermal expansion ($\text{Si} = 2,6$ and $\text{PbTe} = 19,8$, at $300\text{K}(10^{-6} \text{K}^{-1})$), between substrate and evaporated layer. The same defects have been noticed when the PbTe layer was grown with HWE [14] and MBE [15] techniques.

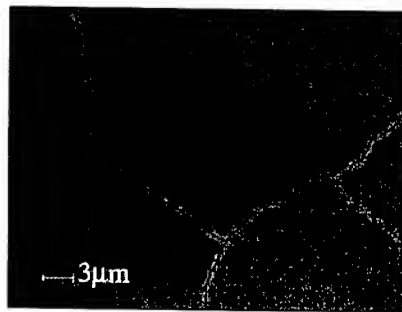


Figure 1 – SEM micrograph of sample F02b, with a $0.45 \mu\text{m}$ epilayer.

Epitaxial layers thinner than $0.9 \mu\text{m}$ probably follow the Fran-Van der Merwe epitaxial growth mechanism [16], described by a layer-by-layer growth. On the other hand, for thicker epilayers, the growth mechanism is probably dictated by Stranski-Krastanov [16], which is described by layers plus island. Meaning, after forming the first monolayer, or a few of them, the following one growth is unfavorable, and islands are formed. This second mechanism can be noticed in Figure 2, where the layer thickness is about $4 \mu\text{m}$.

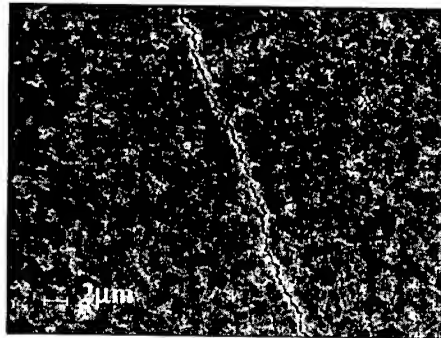
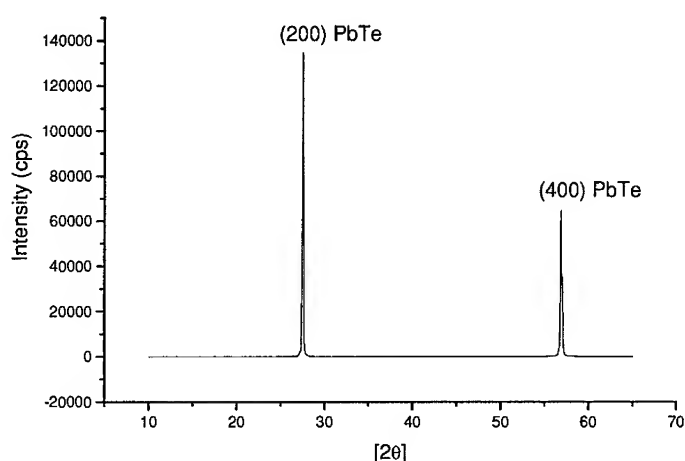


Figure 2 – SEM micrograph of sample F05c, with a $4 \mu\text{m}$ epilayer.

The thin films with single crystal characteristics, revealed X-ray diffraction spectrum as showed in Figure 3, which represents a layer evaporated over a $\langle 111 \rangle$ substrate (sample F05c),

where the Full Width at Half Maximum (FWHM) of peak (200) is 731 sec of degree. However, samples that have $\langle 100 \rangle$ crystal oriented substrates, present similar spectrum.



cps = counting per second.

Figure 3 - X-ray diffraction spectrum of sample F05c.

CONCLUSIONS

Concluding, the pre-heating temperature apparently influenced only the flash evaporation over $\langle 111 \rangle$ Si substrate, since in these cases thermal treatments at 200°C, resulted in cracks and surface defects, even in thin layers (0.2-0.4 μm). On the other hand, due to thermal treatments at 230 °C, epilayers did not present any surface defect. In both cases, the thin film resulted $\langle 100 \rangle$ crystal oriented, despite the Si wafer is $\langle 111 \rangle$.

The reason of flash evaporating PbTe over $\langle 111 \rangle$ Si wafers was that first it was very studied to growth PbTe over $\langle 111 \rangle$ BaF₂ [1-3]. According with the epitaxy definition it is epitaxial film only in case of the same orientation, substrate and layer. In the experiment you can get any orientation depending on the concrete conditions. PbTe thin layers growth with HWE techniques over $\langle 111 \rangle$ Si substrate, are $\langle 100 \rangle$ crystal orientated either [17].

Chemical oxidization, or passivation made to protect the substrate surface is a very important step, and also, its complete elimination before the flash evaporation. HF solution demonstrated to be better than BOE to remove thicker passivation layers.

Apparently all the improvements tried on this work resulted no good at all, the former devices were better than the last ones. On the other hand, it was discovered the influence of having a thicker passivation instead a thinner one when HF or BOE solution are used to deoxidize the Si surface. The substrate temperature is very important on the device performance. However, most of these results are very similar as the ones obtained with HWE and MBE

techniques. Consequently this work was able to show that a very simple technique can obtain the same results as others much more sophisticated.

ACKNOWLEDGEMENTS

The authors would like to thank Prof. Dr. Ivan Zassavitskii for the flash evaporator modification, and discussions on entire procedure. Research partially supported by the São Paulo State Research Foundation, (FAPESP - Fundação de Amparo à Pesquisa do Estado de São Paulo).

REFERENCES

- [1]. E. Abramof, S. O. Ferreira, C. Boschetti and I. N. Bandeira, *Infrared Phys.*, **30** (1): 85-91 (1990).
- [2]. S. Guimarães, I. Zassavitskii and I. N. Bandeira, *Brazilian Journal of Vacuum Applic.*, **V. 19**, 1, 15-18 (2000).
- [3]. E. Abramof, S. O. Ferreira, P. H. O Rappl, H. Closs and I. N. Bandeira, *J. Appl. Phys.*, **82** (3): 1-6 (1997).
- [4]. K. Suzuki, H. Tashiro and T. Aoyama, *Solid State Electronics* **43**: 27-31 (1999).
- [5]. M. Rusu, I.I. Nicolaescu, and G.G. Rusu, *Appl. Phys. A* **70**: 565-571 (2000).
- [6]. G.G. Rusu and M. Rusu, *Solid State Communications* **116**, 363-368 (2000).
- [7]. V. Damodara Das and S. Selvaraj, *Solid State Communications*, **V. 108**, **11**, 873-877 (1998).
- [8]. M. Boustani, K. el assali, T. Bekkay, E. Ech-Chamikh, A. Outzourhit, A. Khiara and L. Dreesen, *Semicond. Sci. Technol.*, **12**, 1658-1661 (1997).
- [9]. G. Massé and K. Djessas, *Phys. Status Solidi a*, **139** k45 (1993).
- [10]. R. C. Henderson, *J. Electrochem. Soc.: Solid-State Science and Technology*, **119**(6), 772-775 (1972).
- [11]. A. Ishizaka, K. Nakagama and Y. Shiraki, *In. Proceedings of 2nd International. Japan Society Applied Physics A-10-2*, Tokyo, 183-186 (1982).
- [12]. D. J. Eaglesham, G. S. Higashi and M. Cerullo, *Appl. Phys. Lett.* **59**(6), 685-687 (1991).
- [13]. S. Guimarães, S. C. F. F. da Silva and J. M. K. de Assis, accepted to be presented at XVIII Brazilian Society of Microscopy and Microanalyses Congress, October, 2001;
- [14]. S. Guimarães and S. C. F. F. da Silva, presented at *1st International Materials Symposium, Abstract Book A226*, Coimbra, Portugal, April, (2001).
- [15]. C. Boschetti, I. N. Bandeira, H. Closs, A. Y. Ueta, P. H. O Rappl, P. Motisuke and E. Abramof, *Infrared Physics & Technology* **42**, 91-99 (2001).
- [16]. M. A. Herman and H. Sitter, "Molecular Beam Epitaxy", New York, N.Y., (Springer, 1996) pp.12-13.
- [17]. M. K. Hwang, C. R. M. da Silva, F.C.L. de Melo, S. Guimarães and A. H. A. Bressiani, *In. Proceedings of 43rd Congresso Brasileiro de Cerâmica – 4^o Congresso de Cerâmica do Mercosul*, Article **325**, Florianópolis, Brazil, June, (1999).

GaAs Photodetector for X-ray Imaging

G. C. Sun¹, H. Samic^{1,2}, V. Donchev^{1,3}, S. Gautrot⁴ and J. C. Bourgoin¹

¹Laboratoire des Milieux Désordonnés et Hétérogènes, Université Pierre et Marie Curie, CNRS (UMR 7603), Tour 22, Case 86, 4 Place Jussieu, 75252 Paris Cedex 05, France

²Department of Physics, University of Sarajevo, Saobracajni Fakultet, Zmaja od Bosne 10, 71000 Sarajevo, Bosnia & Herzegovina

³Department of Condensed Matter Physics, Sofia University, 5, blvd. James Bourchier, 1164-Sofia, Bulgaria

⁴Centre de Spectrometrie Nucléaire et Spectrometrie de Masse, Bat. 108, Université Paris-Sud, 91405 Orsay, Paris, France

ABSTRACT

We describe briefly a cheap and non polluting technique to grow epitaxial GaAs layers, several hundred microns thick, in a matter of hour. Detectors consisting of a $p^+/i/n^+$ structure have been realised with these layers and we present their characteristics obtained from current-voltage, capacitance-voltage measurements as well as their response versus the energy and flux of X-rays.

INTRODUCTION

In the 1960s it has been suggested that GaAs could be a good alternative material for high energy photon detection [1]. Since then, various experiments have demonstrated that GaAs detectors exhibit indeed high performances in terms of charge collection efficiency and energy resolution [2-7]. These detectors were the first to demonstrate high resolution at room temperature (for a review see ref.8). However, no GaAs detector has appeared on the market although the development of a microelectronic technology for this material could have allowed an easy realization of many kinds of structures, ohmic contacts, barriers, junctions and electronics integration. The reason is the following: large thicknesses are required to detect efficiently X and γ photons, thicknesses which are only available from bulk grown materials. Unfortunately, bulk GaAs materials contain a large concentration of defects which, in addition, are not uniformly distributed (for a review see ref.9). For these reasons it has been accepted that these materials are not suitable in practice to develop detectors, in particular imaging detectors.

Only good quality materials, i.e. obtained by epitaxy, qualify for detection. All conventional epitaxial growth techniques seem to satisfy this requirement: the data claimed in ref.3 to be due to the very high purity associated with a specific epitaxial growth, are in fact similar to those reported 28 years earlier [4-7], which were obtained with other types of epitaxial growth techniques. But epitaxial layers of large enough thickness do not exist: the data reported in references 2 to 7 have been acquired on unique layers. Indeed, epitaxial growth techniques are slow: they allow to obtain a few microns thick layer in a matter of hour. Hence, to grow several hundred microns thick layers, the ones which would allow efficient absorption for X-ray, days of continuous growth are necessary, which is industrially impracticable.

However the situation could be different now that we have demonstrated that 100 to 600 μm thick epitaxial layers can be obtained in few hours using an economic and non polluting technique [10,11]. Since it has been previously demonstrated that high performances detectors can be obtained with epitaxial layers, we examine here if the new layers we produce, in large quantity, at the desired thickness, and having electronic properties similar to that of the previously used layers [12], could make detectors with similar performances.

For this we made p/i/n detectors and we investigated their response in conditions of X-ray medical examination. Here, we focus on the linearity of this response and we evaluate the efficiency of collection.

EXPERIMENTAL

We have grown non intentionally doped 200 to 300 μm thick layers on n^+ , Czochralski (Cz) grown, GaAs substrates. Briefly the technique, which is fully described in ref.10, consists in the decomposition of a source material, here GaAs originating from a semi-insulating (S.I.), Cz grown wafer, by H_2O in an H_2 atmosphere at a temperature of the order of 800 $^\circ\text{C}$. The volatile species, As_2 and Ga_2O , which are formed are transported by their partial pressure gradients to a substrate located at a short distance (typically from 1 to 2 mm) from the source. The reverse reaction takes place on the substrate because its temperature is lower than that of the source, and epitaxial growth occurs. Because the rate of material deposition is only limited by the rate of the chemical reactions taking place, the growth rate can be adjusted to very high velocities (up to 10 $\mu\text{m}.\text{min}^{-1}$). By the choice of the temperature, it is therefore possible to grow a several hundred μm thick epilayer in a matter of hours. The reactor being very simple and requesting only a small amount of pure H_2 (the volume of the reactor), this technique is cheap and non polluting.

As described elsewhere, the residual doping depends on the purity of the source material and on the ability of the reaction to induce impurity transport (as described in ref.13, only the impurities producing volatile species with the reactant, here H_2O , are transported). When using Cz, S.I. wafers as sources, the doping level achieved is in the range 10^{13} to 10^{15} cm^{-3} and can be n or p type depending on the origin of the source. In order to reduce this doping (to increase the width of space charge region for a given bias of the detector), two ways are attempted: electron irradiation which introduces defects compensating the dopants [14] and selection of the source material (which should contain only impurity which are not transported, for instance Si for the n type impurity).

We have performed ion implantation to make a p^+ layer on the surface of a 170 μm thickness layer grown on an n^+ substrate and obtain $\text{p}^+/\text{i}/\text{n}^+$ structures in which the i region is the grown layer. After deposition of ohmic contacts, on both sides, these structures were characterized by current-voltage (I-V) and capacitance-voltage (C-V) measurements, demonstrating that the current is of the order of 3 $\text{nA}.\text{mm}^{-2}$ for a reverse bias of 10 V (see figure1) and that the residual doping is in the range of 10^{13} to 10^{14} cm^{-3} . For instance figure 2 shows that the doping is $5 \times 10^{13} \text{ cm}^{-3}$; such doping level corresponds to a space charge region of 18 μm for the reverse bias of 10 V.

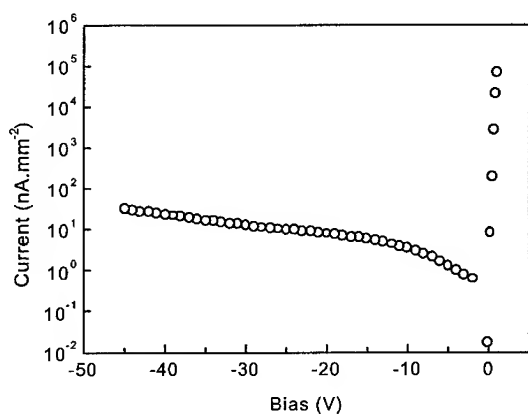


Figure 1. Current-Voltage characteristics obtained with a 27.5 mm² detector.

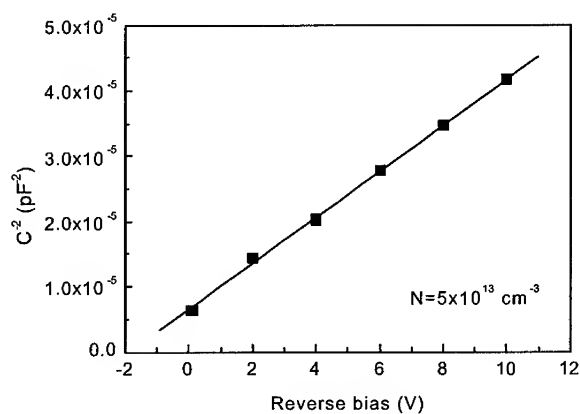


Figure 2. Typical Capacitance-Voltage characteristics obtained with a 27.5 mm² detector.

The study of the response with the fluence of X-ray has been performed using a machine whose energy is not stabilized so that the flux is modulated at 50 Hz. The current I delivered can be adjusted from 5 to 25 mA. The detector is polarized under 10 V across a 1 M Ω resistance. We monitored the modulated signal, i.e. the current flowing through this resistance, via an oscilloscope.

RESULTS AND DISCUSSION

The dependence of the signals versus the current I , monitored for accelerating voltages of 50 kV and 30 kV, at a distance of 32 cm from the X-ray source, with a detector of area 27.5 mm^2 is given in figure 3. The dependence demonstrates the linearity of the detector in the photon flux explored, up to at least $1.2 \times 10^8 \text{ photons mm}^{-2} \cdot \text{s}^{-1}$ (The number of photons is calculated with a program based on a code described in ref. 15).

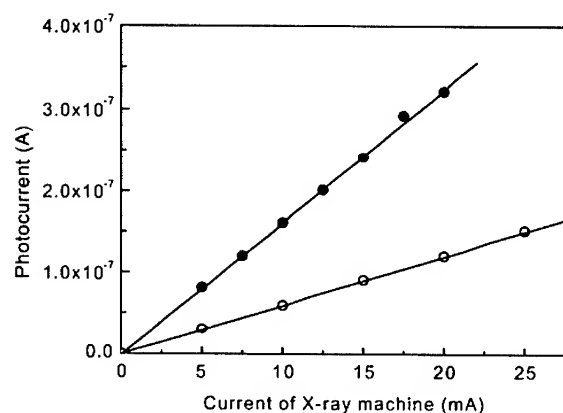


Figure 3. Current collected by the detector whose characteristics are given in figures 1 and 2 versus the current of the X-ray machine for accelerating voltage of 50 kV (●) and 30 kV (○).

Fig. 4 gives the signal dependence versus the applied reverse bias for two different value of I . As the bias, i.e. the space charge region, increases, the signal increases. For the lower value of I (10 mA) S follows the dependence expected if charge collection take place in space charge region. The fit with the calculated values is obtained assuming a charge collection efficiency of 28%. The calculation takes into account the energy distribution of the photons but makes abstraction of the photons of energy lower than 20 kV. Other data are obtained for $I=20 \text{ mA}$ with a similar charge collection efficiency (33%), but the theoretical dependence is not well reproduced at high biases. This is probably associated with signal saturation at high photon flux.

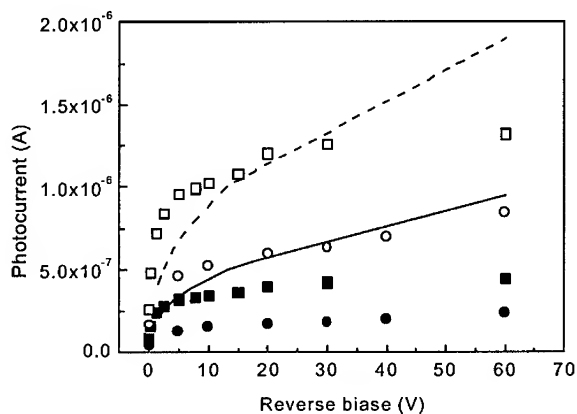


Figure 4. Current collected by the detector versus bias for currents of the X-ray machine of 10 mA (●) and 20 mA (■). The same data, but multiplied by 3.5 (○) for 10 mA, and 3 (□) for 20 mA, are shown to compare with the calculated currents (solid and dashed lines, respectively) assuming a charge collection efficiency of 1.

CONCLUSION

The data we have presented illustrate that epitaxial GaAs, known to be a good candidate to make high resolution γ detectors at room temperature, could also be used to make high efficiency for detecting X-ray. The epitaxial layers we produce, with a simple, fast, cheap and non polluting technique, qualify for this. The active thickness of the detectors we have presented are limited by the level of residual doping and efforts are now made toward decreasing this level ($5 \times 10^{13} \text{ cm}^{-3}$ has now been achieved).

REFERENCES

1. W.R. Harding, C. Hilsun, M.E. Moncaster, D.C. Northrop, O. Simpson, *Nature* **30**, 405 (1960).
2. A. Owens, M. Bavdaz, S. Kraft, A. Peacock, R. Strade, S. Nenonen, H. Andersson, M.A. Gagliardi, T. Gagliardi, and H. Graafsma, *J. Appl. Phys.* **86**, 4341(1999).
3. A. Owens, M. Bavdaz, S. Kraft, A. Peacock, S. Nenonen, H. Andersson, M.A. Gagliardi, T. Gagliardi, F. Scholze, *J. Appl. Phys.* **85**, 7522(1999).
4. J.E. Eberhardt, R.D. Ryan and T.J. Tavendale, *Nucl. Inst. and Meth.* **94**, 463(1971).
5. K. Hesse, W. Gramman and O. Hoppner, *Nucl. Inst. and Meth.* **101**, 39(1972).
6. P.E. Gibbons and J.E. Howes, *IEEE Trans. Nucl. Sci. NS* **19**, 353(1972).
7. T. Kobayashi, T. Sugita, M. Koyama and S. Takayanagi, *IEEE Trans. Nucl. Sci. NS* **19**, 324(1972).

8. D. S. McGregor, *Semiconductors and Semimetals* (Academic press, 1995) Vol.43, pp. 383-437.
9. J. C. Bourgoin, H. Jron Bardeleben and D. Strevenard, *J. Appl. Phys.* **64**, R65(88).
10. M. Hammadi, J.C. Bourgoin, H. Samic, *J. Mat. Sci.: Mat. in Electronics* **10**, 399(1999).
11. L. El Mir, M. Gandouzi, M. Hammadi, H.Samic and J.C. Bourgoin, *Current Topics in Crystal Growth Research* **5**, 131(1999).
12. H. Samic, J. C. Bourgoin, B. Pajor, R. Bisaro, C. Grattejaim, K. Khiroum, M. Pubero and M. Burle, *Proceedings 24th IEEE symposium on Compound Semiconductors* (1998) p.155
13. M. Gandouzi, J. C. Bourgoin, L. Elmir, M. Stellmacher and V. Oring, *J. Crystal growth* **234**, 279 (2002).
14. J. C. Bourgoin, N. de Angelis, K. Smith, R. Bates, C. Whiteliell and A. Meckle, *Nucl. Inst. and Meth. A* **458**, 344 (2001).
15. R.Nowotny, *Fortschr. Rontgenstr* **142**, 685(1985).

Lead telluride-based far-infrared photodetectors – a promising alternative to doped Si and Ge.

Dmitriy Dolzhenko, Ivan Ivanchik, Dmitriy Khokhlov, Konstantin Kristovskiy
Physics Department, Moscow State University, Moscow 119899, Russia

ABSTRACT

Doping of the lead telluride and related alloys with the group III impurities results in appearance of unique physical features of the material, such as persistent photoresponse, enhanced responsive quantum efficiency (up to 100 photoelectrons/incident photon), radiation hardness and many others. We review physical principles of operation of the photodetecting devices based on the group III-doped IV-VI including possibilities of fast quenching of the persistent photoresponse, construction of a focal-plane array, new readout technique, and others. Comparison of performance of the state of the art Ge(Ga) and Si(Sb) photodetectors with their lead telluride-based analogs shows that the responsivity of PbSnTe(In) photodetectors is by several orders of magnitude higher. High photoresponse is detected at the wavelength 116 micrometers in PbSnTe(In), and it is possible that the photoconductivity spectrum covers all the submillimeter wavelength range.

INTRODUCTION

Many of the sensitive photodetecting systems operating in the far infrared wavelength range (20-200) μm are based on germanium or silicon doped with shallow impurities [1]. The highest cut off wavelength reported $\lambda_{\text{co}} \approx 220 \mu\text{m}$ corresponds to the uniaxially stressed Ge(Ga) [2]. The main advantage of germanium and silicon is very well developed growth technology that allows receiving materials with perfect crystalline quality and extremely low uncontrolled impurity concentration.

An alternative possibility for construction of sensitive far-infrared photodetectors is provided by unique features of a narrow-gap semiconductor - indium-doped $\text{Pb}_{1-x}\text{Sn}_x\text{Te}$. Exciting results of fundamental research on the group III - doped lead telluride - based alloys [3] provided possibilities for construction of far-infrared photodetectors based on new physical principles [4]. Results of these activities are very promising since performance of far-infrared photodetectors based on doped lead-tin tellurides is comparable or better than for analogs based on doped Ge or Si.

INDIUM-DOPED LEAD-TIN TELLURIDES: THE MAIN PROPERTIES

Fermi level pinning.

Doping of the lead telluride with indium in amount exceeding concentration of other impurities and defects results in the Fermi level pinning effect [5]. A consequence of this effect is homogenization of electrical properties of the semiconductor. This feature results in almost absolute reproducibility of sample parameters independently on the growth technology. High sample homogeneity gives rise to enhanced carrier mobility reaching $10^5\text{-}10^6 \text{ cm}^2/\text{V}\cdot\text{s}$ at low temperatures.

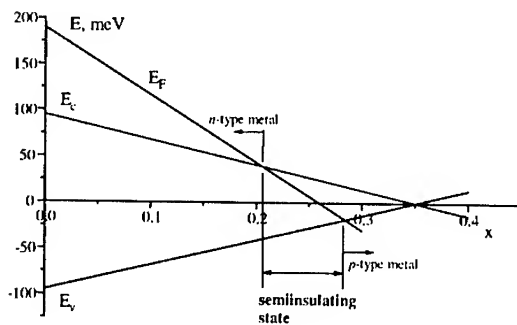


Figure 1. Energy diagram of the $\text{Pb}_{1-x}\text{Sn}_x\text{Te(In)}$ alloys for different x . E_c - conduction band bottom, E_v - valence band [6].

Position of the pinned Fermi level E_0 may be tuned by alloying (Figure 1) [6]. It crosses the gap in the tin content range ($0.22 < x < 0.28$) providing the semiinsulating state of the semiconductor for this range of alloy compositions. Conductivity of material in the semiinsulating state ($0.22 < x < 0.28$) is defined by activation from the impurity local level E_0 , and therefore the free carrier concentration is very low $n, p < 10^8 \text{ cm}^{-3}$ at temperatures $T < 10 \text{ K}$. The free carrier concentration in undoped alloys is defined by electrically active growth defects. Their concentration is never less than 10^{15} cm^{-3} . So we have a very unusual situation, when a heavily doped narrow-gap semiconductor with high number of growth defects acts as an almost ideal semiconductor with practically zero background free carrier concentration and very high electrical homogeneity. This makes very attractive the idea to use this material as an infrared photodetector.

Persistent photoconductivity.

External infrared illumination leads to the substantial increment of material conductivity at the temperatures $T < 25 \text{ K}$ (Figure 2) [7]. High amplitude of photoresponse at the low temperatures is a consequence of the persistent photoconductivity effect: the photoresponse increases linearly in time providing a kind of «internal integration» of the incident radiation flux. When the radiation is switched off, the conductivity relaxes very slowly. The characteristic relaxation time $\tau > 10^4 \text{ s}$ at $4.2 \text{ K} < T < 10 \text{ K}$, then it sharply decreases with the temperature rising, and $\tau \sim 10^{-2} \text{ s}$ at $T \approx 20 \text{ K}$. The effect is defined by the specifics of impurity states that form DX-like centers [8].

If sample temperature is so that τ is higher than the operation time required, then a photoresistor may operate only if there exists a possibility to return to the initial "darkness" state, i.e. to quench quickly the persistent photoconductivity. Moreover, periodical accumulation and successive fast quenching of the photosignal leads to the substantial gain in the S/N ratio with respect to the case of ordinary single photodetectors. The most efficient way of quenching of the

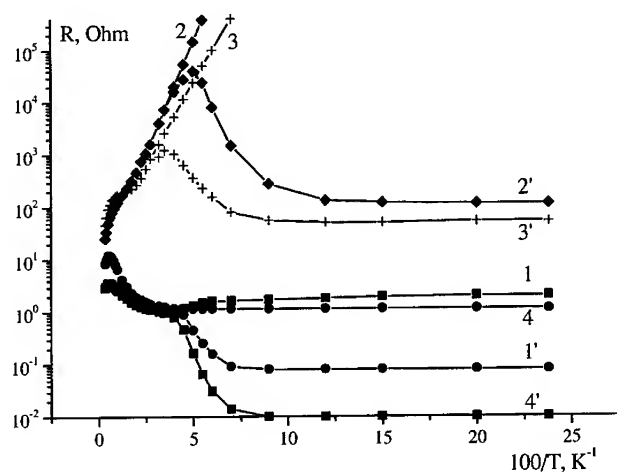


Figure 2. Temperature dependence of the sample resistance R measured in darkness (1-4) and under infrared illumination (1'-4') in alloys with $x = 0.22$ (1, 1'), 0.26 (2, 2'), 0.27 (3, 3') and 0.29 (4, 4') [7].

persistent photoconductivity in $\text{Pb}_{1-x}\text{Sn}_x\text{Te(In)}$ is application of strong microwave pulses to sample contacts [4]. Using this technique the long-living photoexcited free electrons may be localized for 10 μs . Therefore it became possible to operate in the regime of periodical accumulation and successive fast quenching of photoresponse. Moreover, application of microwave pulses in some special regime results in giant increment of the quantum efficiency up to ~ 100 [4].

Radiometric parameters.

A laboratory model of the IR-radiometer based on $\text{Pb}_{1-x}\text{Sn}_x\text{Te(In)}$ operating in the regime of periodical accumulation and successive fast quenching of the persistent photoconductivity, has been demonstrated in [4]. A helium-cooled grid filter provided effective cutting of the incident radiation spectrum at the wavelengths $\lambda > 18 \mu\text{m}$. Despite low sensitivity of the measuring electronics used, the photon flux detected in [4] was as low as $N \approx 2 \cdot 10^4 \text{ s}^{-1}$ that corresponds to $\text{NEP} \approx 2 \cdot 10^{-16} \text{ W}$ for the detector area of $0.3 \cdot 0.2 \text{ mm}^2$ and the operating rate 3 Hz.

Direct comparison of the $\text{Pb}_{0.75}\text{Sn}_{0.25}\text{Te(In)}$ photodetector, the Si(Sb) BIB structure and the Ge(Ga) photodetector using the same cryogenic equipment and measuring electronics has been performed in [9]. The responsivity S_1 of the $\text{Pb}_{0.75}\text{Sn}_{0.25}\text{Te(In)}$ photodetector at $116 \mu\text{m}$ was of the order of 10^3 A/W at 40 mV bias, that is by 2-3 orders of magnitude higher than the S_1 value obtained for a state of the art Ge(Ga) photodetector in the same measuring conditions.

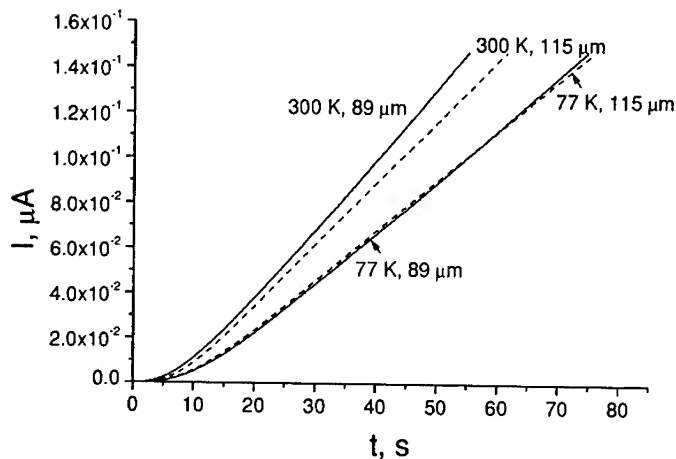


Figure 3. Photoconductivity kinetics of $\text{Pb}_{0.75}\text{Sn}_{0.25}\text{Te}(\text{In})$ film exposed to blackbody radiation filtered at $\lambda = 90$ and $116 \mu\text{m}$. Figures - the blackbody temperature and the wavelength. $T = 4.2$ K. Illumination starts at the moment $t = 0$ (with accuracy of (3-4) s) [9].

The same authors have directly observed persistent photoresponse in the $\text{Pb}_{0.75}\text{Sn}_{0.25}\text{Te}(\text{In})$ photodetector at the wavelengths of 90 and $116 \mu\text{m}$ (Figure 3) that are considerably longer than the wavelength corresponding to the thermal activation energy of the ground impurity state. Indications exist that the red cutoff wavelength for this photodetector may exceed $220 \mu\text{m}$ - the highest λ_{co} observed so far.

"Continuous" focal-plane array.

Specifics of impurity states may make very easy construction of a focal-plane array on $\text{Pb}_{1-x}\text{Sn}_x\text{Te}(\text{In})$. Local infrared illumination leads to local generation of nonequilibrium free electrons, i.e. the persistent photoconductivity effect is observed only in the illuminated part of the sample, and the photoexcitation does not propagate into the darkened regions [10]. The characteristic time of the excitation propagation is at least more than 10^4 s at $T = 4.2$ K. The spatial characteristic scale is $\sim 10 \mu\text{m}$. The physical picture of the processes involved is the following. The photoexcited free electrons cannot diffuse far away from the region of generation due to electrostatic attraction to the ionized impurity centers. On the other hand these electrons cannot recombine because of the existence of a barrier between the local and extended states.

Therefore the distribution of the radiation exposure over the sample surface reflects in a distribution of the concentration of long-living free electrons. In other words, it is possible to construct a focal plane "continuous" array, in which the signal is internally integrated in every effective element.

Readout technique is a special problem. The approach proposed in [4] seems to be the most promising. Let us consider a thin slice of $\text{Pb}_{1-x}\text{Sn}_x\text{Te}(\text{In})$ with a semitransparent electrode

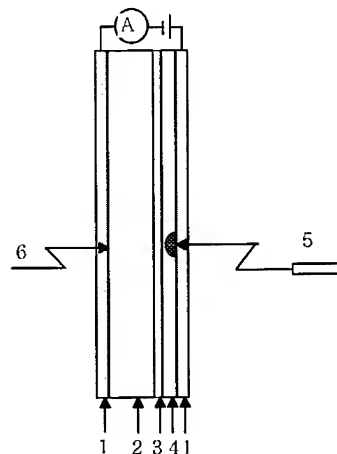


Figure 4. Device for readout of information from the "continuous" focal-plane array on $\text{Pb}_{1-x}\text{Sn}_x\text{Te}(\text{In})$. 1 - semitransparent electrodes, 2 - active $\text{Pb}_{1-x}\text{Sn}_x\text{Te}(\text{In})$ layer, 3 - fluoride buffer layer, 4 - layer of a silicon (or other semiconductor with a relatively wide gap), 5 - short-wavelength laser, 6 - incident infrared radiation flux [4].

deposited on one side (Figure 4). The investigated radiation flux illuminates the sample from the same left side in the Figure 4. A buffer insulating fluoride layer is deposited on another side of the sample followed by a thin layer of silicon or some other semiconductor with a relatively wide gap, and a second semitransparent electrode. If the sample is illuminated by a shortwavelength laser from the right side (see Figure 4), it is possible to generate a local highly conductive region in the wide-gap semiconductor. If then a bias between the electrodes is applied, the current is defined by the $\text{Pb}_{1-x}\text{Sn}_x\text{Te}(\text{In})$ sample conductivity in the region of the laser spot, because the thickness of the semiinsulating wide-gap semiconductor layer is be much less in this point. Another advantage of such a readout technique is heavy damping of the dark current in such a structure. It is analogous to certain extent to the ideas involved in BIB structures. If the recombination rate in the wide-gap semiconductor is high enough, it is easy to reconstruct the conductivity distribution over the $\text{Pb}_{1-x}\text{Sn}_x\text{Te}(\text{In})$ sample simply by scanning the laser beam over the structure surface and by measuring the respective current. Unfortunately this idea is not realized in practice so far.

Radiation hardness.

High radiation hardness is one more advantage of the photodetectors based on $\text{Pb}_{1-x}\text{Sn}_x\text{Te}(\text{In})$. This is a consequence of a very high density of impurity states ($\sim 10^{18} - 10^{19} \text{ cm}^{-3}$) that pin the Fermi level. The fast electron irradiation with fluencies up to $10^{17} - 10^{18} \text{ cm}^{-2}$ does not affect the photoresponse [11]. This value is at least by 4 orders of magnitude higher than for $\text{Hg}_{1-x}\text{Cd}_x\text{Te}$, doped Ge and Si.

SUMMARY

In summary, application of the lead-tin tellurides doped with the group III impurities as base elements for the infrared photodetectors gives a challenging opportunity to produce universal and sensitive systems. They have a number of advantageous features that allow them to compete successfully with the existing analogs: internal accumulation of the incident radiation flux, possibility of effective fast quenching of an accumulated signal, microwave stimulation of the quantum efficiency up to 10^2 , possibility of realization of a "continuous" focal-plane array, possibility of application of a new readout technique, high radiation hardness. In our opinion, these features make the $\text{Pb}_{1-x}\text{Sn}_x\text{Te}(\text{In})$ -based photodetectors ideal for the space-borne applications, for example, in the infrared astronomy.

ACKNOWLEDGMENTS

The research described in this paper was supported in part by the grant of the Russian Foundation for the Basic Research (RFBR) No. 01-02-16356.

REFERENCES

1. J.Wolf and D.Lemke, *Infrared Phys.* **25**, 327 (1985).
2. E.E.Haller, M.R.Hueschen and P.L.Richards, *Appl. Phys. Lett.* **34**, 495 (1979).
3. B.A.Akimov, A.V.Dmitriev, D.R.Khokhlov, and L.I.Ryabova, *Phys. Stat. Sol. A*: **137**, 9 (1993).
4. S.N.Chesnokov, D.E.Dolzhenko, I.I.Ivanchik, and D.R.Khokhlov, *Infrared Phys.* **35**, 23 (1994).
5. V.I.Kaidanov, R.B.Mel'nik, and I.A.Chernik, *Fiz. Tekh. Poluprov.* **7**, 759 (1973) [*Sov. Phys. Semicond.* **7**, 522 (1973)].
6. B.A.Akimov, L.I.Ryabova, O.B.Yatsenko, and S.M.Chudinov, *Fiz. Tekh. Poluprovodn.* **13**, 752 (1979) [*Sov. Phys. Semicond.* **13**, 441 (1979)].
7. B.M.Vul, I.D.Voronova, G.A.Kaluzhnaya, T.S.Mamedov, and T.Sh.Ragimova, *Pis'ma v Zh.Eksp.Teor.Fiz.* **29**, 21 (1979); B.A.Akimov, N.B.Brandt, S.O.Klimonskiy, L.I.Ryabova, and D.R.Khokhlov, *Phys.Lett.* **88A**, 483 (1982).
8. D.R.Khokhlov and B.A.Volkov, *Proc. 23 Int. Conf. Phys. Semicond.*, Berlin, Germany, July 21-26, 1996, ed. M.Scheffer, R.Zimmermann, World Sci. (Singapore), **4**, 2941 (1996).
9. D.R.Khokhlov, I.I.Ivanchik, S.N.Raines, D.M.Watson, and J.L.Pipher, *Appl. Phys. Lett.* **76**, 2835 (2000).
10. B.A.Akimov, N.B.Brandt, S.N.Chesnokov, K.N.Egorov and D.R.Khokhlov, *Solid State Commun.* **66**, 811 (1988).
11. E.P.Skipetrov, A.N.Nekrasova, and A.G.Khorosh, *Fiz. Tekh. Poluprovodn.* **28**, 815 (1994) [*Sov. Phys. Semicond.* **28**, 478 (1994)].

Innovative Devices

Scatterometry for Lithography Process Control and Characterization in IC Manufacturing

Yiorgos Kostoulas*, Christopher J. Raymond, Mike Littau
Accent Optical Technologies
3817 Academy Pkwy South NE
Albuquerque, NM 87109

ABSTRACT

As modern circuit architecture features steadily decrease in size, more accurate tools are needed to meaningfully measure critical dimensions (CD). As a general rule, a metrology tool should be able to measure 1/10 of the product tolerance. An emerging technology for high speed, high accuracy CD measurement is scatterometry. This paper describes scatterometry-based measurements of metal features of 350 nm with a space of 450 nm (pitch of 800nm) on top of a complicated layer stack and compares them with the results of an atomic force microscope (AFM). We also looked into lithography cell monitoring and trending by measuring CDs on 3 daily litho cell monitors over a period of 40 days. Our long term results show excellent agreement with those of a scanning electron microscope (CD-SEM).

INTRODUCTION

The critical dimension scanning electron microscope (CD-SEM) is the current standard for inline metrology tools. The technique however, suffers from a number of disadvantages. Due to loading wafers into a vacuum chamber, the throughput is quite limited. Surface/site charging by the electron beam can lead to inaccuracies in measurements. Finally, accuracy of results depends on interpretation algorithms used to realize the image acquired by the CD-SEM. Scatterometry, on the other hand is an optical metrology based on the principle of diffraction. By measuring and analyzing the light scattered, or diffracted, from a patterned periodic sample, the dimensions of the sample itself can be measured. Applications of the technique have included the characterization of photomasks¹, the monitoring of focus², dose³ and the post exposure bake process⁴, and even the characterization of three-dimensional features such as contact hole and DRAM arrays⁵. The method is implemented in two parts known as the 'forward' and 'inverse' problems. The forward problem is the measurement of the scatter signature and the inverse problem is fitting of the data from first principles to extract meaningful results. Although many types of scatterometers have been investigated over the years⁶, in this work we use the 2- Θ or *angle-resolved* implementation of the technique, where the intensity of the 0-th diffraction order is recorded as a function of the angle of incidence. Several different approaches have also been explored for the solution of the inverse problem⁷. The most common method has been to generate a library, or 'look-up' table, of scatter signatures using a rigorous diffraction model (Rigorous Coupled-Wave Theory). The signatures are generated in advance, and the measured scatter signature is compared against the library to find the closest match.

* Correspondence: ykostoulas@accentopto.com, 617-484-5311 (phone), 253-322-6680 (FAX)

EXPERIMENT

The samples investigated in this study were a series of 25 wafers processed by SEMATECH. Only 6 of these wafers however, were also measured with an AFM and here we will concentrate on that common set. The layer stack began with a silicon substrate, upon which was deposited 3000 Å of oxide. Next, a Ti layer (250 Å thick) was added, followed by an AlCu layer (nominal 6000 Å thick), and finally a TiN layer (350 Å thick). BARC and resist layers were added last for lithography. The targeted printed feature sizes (in photoresist) were 350 nm for the lines and 450 nm for the spaces (which results in a grating with a pitch of 800 nm). All wafers were printed at nominal dose and focus. The scatterometry measurements were carried out on a CDS-2 system from Accent Optical Technologies which uses a 632.8 nm laser as its light source while the AFM was a DEKTAK-SXM in operation at SEMATECH.

In order to show reproducibility performance of this technique, we carried out separate measurements on a daily set of 3 wafers over a period of 40 days. The grating structure consisted of 5500 Å of UV86 photoresist on a 560 Å uniform DUV30 ARC layer on a silicon substrate. For each wafer we measured CDs on 13 sites across including 5 sites within a middle die. Those sites were also measured using a CD-SEM.

Library Details

An important consideration in the generation of any scatterometry library is the number of modes, or orders, retained in the calculation. The higher the number of modes, the more accurate the theoretical results are. A large number of modes however, results in longer library computation times. The determination of the optimal number of modes is done automatically by the system software using the system's signal-to-noise as a convergence criterion. For the first part of this study, we created two libraries, one for the pre-etch (resist) study and one for the post-etch measurements. The former used four fitted parameters: resist thickness, resist sidewall angle, resist CD, and BARC thickness. The AlCu layer was thick enough to act as a substrate in this case. The later used as parameters the AlCu layer thickness, the linewidth of the metal features, the thickness of the etched part, and the thickness of the unetched part of the oxide layer. Library details can be seen in Table I and II. For the trending part of the study, we created a library that varied CDs and sidewalls.

Table I. Library parameters for the resist stack measurements.

Parameter name	Lowest iteration	Highest iteration	Resolution (step size)	Number of iterations	Lib. Size (# of signatures)
Linewidth	300 nm	360 nm	2 nm	31	31 x 11 x 37 x 11 = 138,787
Sidewall	86°	91°	0.5°	11	
Resist Thk	9800 Å	10700 Å	25 Å	37	
BARC Thk	600 Å	850 Å	25 Å	11	

Table II: Library parameters for the etched stack measurements.

Parameter name	Lowest iteration	Highest iteration	Resolution (step size)	Number of iterations	Lib. Size (# of signatures)
Linewidth	210 nm	270 nm	2 nm	31	31 x 41 x 37 x 13 = 611,351
AlCu Thk	6000 Å	7000 Å	25 Å	41	
Etch Ox Thk	100 Å	1000 Å	25 Å	37	
Unif Ox Thk	2100 Å	2400 Å	25 Å	13	

RESULTS

Metal features

Figure 1 shows the scatterometer resist (pre-etch) linewidth results in comparison to AFM data for three wafers (identified as 5, 13 and 21). In the figure results from these three wafers are grouped together in succession on the x-axis, but lines have been drawn to indicate the different wafer data. The AFM measurements are showing considerable linewidth variation for wafers 5 and 21, and to a lesser extent on wafer 13. These variations are probably an artifact due to the difficulty in performing AFM measurements on a 'sticky' material such as photoresist. A similar resist stack (APEX on BARC, also processed at SEMATECH) was measured in previous research⁸ and did not show this degree of variation. Furthermore, the sister-etched wafer (wafer 1) from this group did not exhibit this degree of variation (see figure 3, wafer 1). Overall the scatterometry results show consistent linewidth measurements across each wafer, which was to be expected for this process.

The resist sidewall angle results are shown in figure 2. In this case there is good agreement between the AFM (which are the average of the left and right wall angles) and CDS-2 results. Recall that the scatterometry model used 0.5 degree increments for the sidewall angle parameter (although this is not the ultimate resolution of the tool for performing sidewall measurements), and as a result the scatterometry data only vary between 89.0 and 89.5 degrees. The scatterometer results also seem to track the correct trends as observed by the AFM; measurement number 6, 7 and 8 (from wafer 5) show a "low-high-low" trend that was observed on both tools.

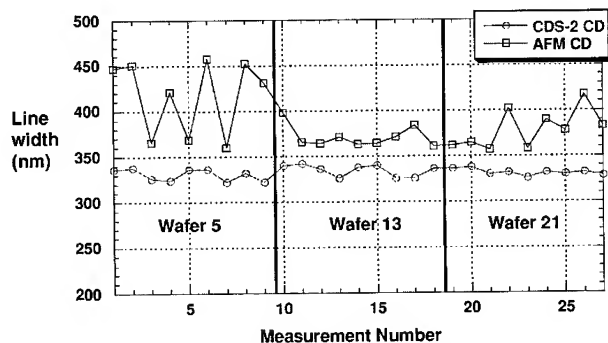


Figure 1. Scatterometer and AFM measurements of the resist (pre-etch) linewidth.

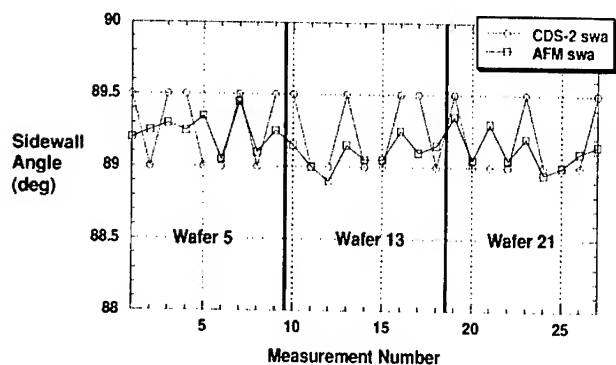


Figure 2. Scatterometer measurements of the resist (pre-etch) sidewall angle.

Figure 3 shows the etched linewidth measurements performed by both scatterometry and the AFM. The results for the first wafer in the set (wafer 1) show a good correlation with an average CD of 375 nm for the AFM and 260 nm for the scatterometer. The correlation is lower for the middle wafer (#9) and third wafer (#17). Some of the measurement sites for the third wafer were damaged as was determined by both a visible inspection and by the etched layer thickness measurements. Overall there is clearly an offset (~ 150 nm) between the two measurement types, which is best illustrated in the data from wafer 1. This offset is due to the AFM tip not being deconvolved out of this measurement (the tip width was set to 0 \AA). It is worth noting that, as one would expect, the scatterometry CD trends observed on all the individual wafers are similar to the trends observed in the resist measurements (refer back to figure 1). This is exactly what one would expect from a typical litho-to-etch process; the resist CDs are transferred into the etch. We also carried out measurements of the etched layer thickness with both the scatterometry system and the AFM and they were found to be in excellent agreement. Note that the scatterometry thickness results are the sum of the four individual layer thickness: the etched oxide region, the Ti thickness, the AlCu thickness, and the TiN thickness. The scatterometer actually determines the different thickness of these materials, whereas the AFM does not – it measures the total thickness.

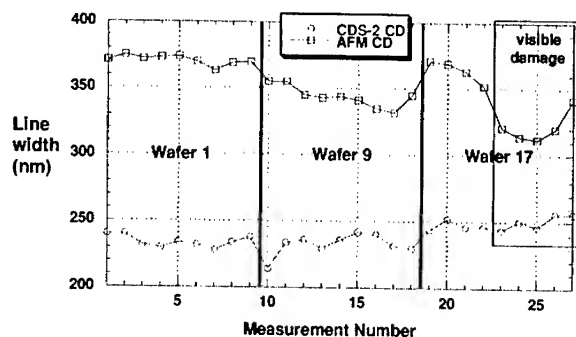


Figure 3. Scatterometer and AFM measurements of the etched metal linewidth.

Litho Cell Monitoring

Lithography cell monitors are used to monitor stepper health. The large arrays of line/space pairs make cell monitors an ideal application for scatterometry. Measurements were made on cell monitors over a 40 day period on both CD-SEM and scatterometer. Figure 4 presents CD and sidewall angle trending data for the scatterometer. Figure 5 presents CD trending data for the top-down CD-SEM.

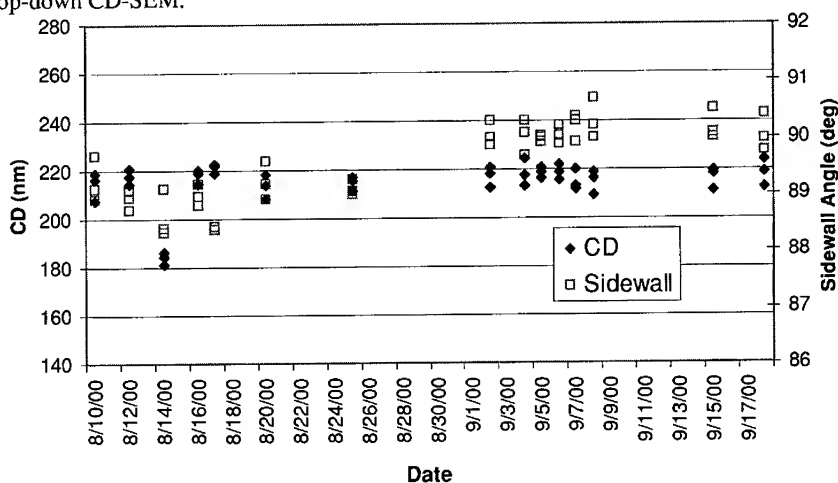


Figure 4: Lithographic cell monitor CD and sidewall angle trending data for scatterometer.

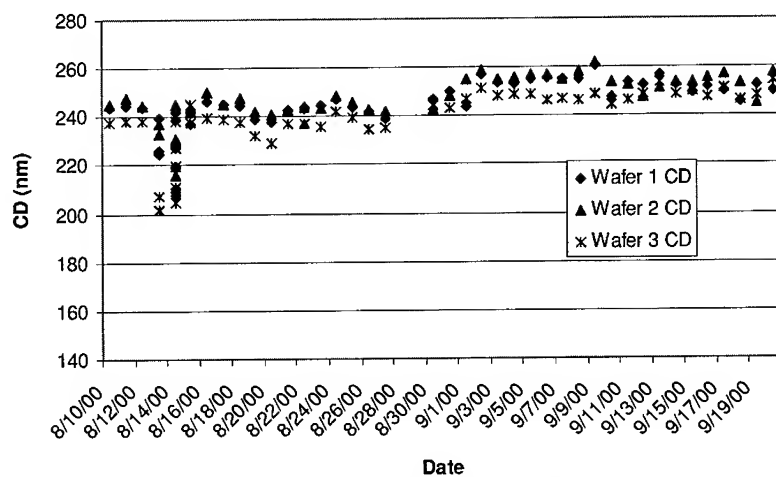


Figure 5: Lithographic cell monitor CD trending data for CD-SEM.

In comparing the results from the two metrology tools, there are three noticeable observations. The first is that there is an approximately 30 nm offset between scatterometer CD and CD-SEM CD, with the CD-SEM measuring higher. Both tools detect a temporary downward shift in the measured CD on the day of 8/14/00 (with the scatterometer also showing generally poor fits to the data for this day). The second is the response to a process shift occurring between the months of August and September. The top-down CD-SEM measured an approximate 10 nm increase in CD during the process shift, while the scatterometer measured no CD increase. However, the scatterometer does show an increase in the sidewall angle during the process shift, from an 89 degree to a 90 degree vertical sidewall. Limited cross-section CD-SEM data was taken between this process shift, which saw the sidewall angle increase from 88 degrees to 90 degrees. The trend in increasing SEM/scatterometer CD offset with more vertical sidewalls has also been observed in prior work^{4,5}, and the measured offset is consistent with what has been seen in those publications.

CONCLUSIONS

A novel, optical non-contact technique based on scatterometry was employed to measure CDs and sidewall angles on a 4 layer composite grating and the results were compared to AFM measurements. The wafers comprised both resist and etched metal samples with nominal 350 nm (resist) and 250 nm (etch) linewidth. Comparisons to AFM measurements on the same samples showed good correlation and consistency. In addition, we examined long term trending capabilities of the technique on a 40 day period and compared with the performance of a top-down CD-SEM. We found that a process shift in sidewall angles, caused the CD-SEM to report an artificially increase in CDs by 10 nm while the scatterometry measurements were able to distinguish between the CD and sidewall angle changes. Finally, the precision of these measurements were determined, and indicate that scatterometry is an attractive alternative for high volume, high precision inspections.

ACKNOWLEDGEMENTS

The authors wish to thank SEMATECH for providing these samples and their respective AFM measurements as well as Christopher Gould and Christy Gambill of Infineon Technologies for providing the trending samples and the corresponding CD-SEM results.

REFERENCES

- ¹ S. M. Gaspar-Wilson, S. Naqvi, J. R. McNeil, H. Marchman, B. Johs, R. French, F. Kalk, *Integrated Circuit Metrology, Inspection and Process Control IX, Proc. SPIE* 2439, 1995.
- ² L. M. Milner, K. P. Bishop, S. S. H. Naqvi, J. R. McNeil, *J. Vac. Sc. Tech. B* 11(4), pp. 1258-1266, 1993.
- ³ K. C. Hickman, et al., *J. Vac. Sc. Tech. B* 10(5), pp. 2259-2266, 1992.
- ⁴ J. Sturtevant et al, *Proc. SPIE* 1926, pp. 106-114, 1993.
- ⁵ Z. R. Hatab, J. R. McNeil, S. S. H. Naqvi, *J. Vac. Sc. Tech. B* 13(2), pp. 174-182, 1995.
- ⁶ S. Coulombe, P. Logofatu, B. Minhas, S. Naqvi, J. R. McNeil, *Integrated Circuit Metrology, Inspection and Process Control XII, Proc. SPIE* 3332, 1999.
- ⁷ C. J. Raymond, M. R. Murnane, S. S. H. Naqvi, J. R. McNeil, *J. Vac. Sc. Tech. B* 13(4), pp. 1484-1495, 1995.
- ⁸ C. J. Raymond, et al., *J. Vac. Sc. Tech. B* 15(2), 1997.

Poster Session

Structural Properties and Doping of $\text{Zn}_{1-x}(\text{Mg,Li})_x\text{O}$ Materials

R. E. Melgarejo, M.S. Tomar*, A. Hidalgo, R. S. Katiyar¹
Physics Department, University of Puerto Rico, Mayagüez, PR 00681,
¹Physics Department, University of Puerto Rico, Rio Piedras, PR 00931

ABSTRACT

The possibility of the solid solutions with MgO provides the opportunity in ZnO/ZnMgO quantum well structures. The recent observation that n-type conductivity in ZnO is due to hydrogen doping open the avenue for p-doping to form p-n junction devices in ZnO. We report on the synthesis and structural properties of Zn (Mg,Li)O. The possibility of p-doping by P has been explored.

INTRODUCTION

Al doped ZnO thin films increase the conductivity without sacrificing its optical properties [1]. Theoretical prediction and the recent observation [2,3] that the n type conductivity in ZnO is due to hydrogen incorporation, has attracted a lot of attention for the p doping. Zinc oxide films have been used as transparent conductors, surface acoustic wave (SAW) devices and oxygen sensors [4]. We demonstrated that $\text{Zn}_{1-x}\text{Mg}_x\text{O}$ makes a solid solution [5] for ~ 12 at % MgO without changing the wurtzite structure of ZnO. It provides the opportunity of band gap engineering for optoelectronic devices. Also, the observed small ferroelectric response [7] in $\text{Zn}_{1-x}\text{Li}_x\text{O}$ was proposed to be due to the structural modification due to off-centered dopants Li^+ (0.60\AA) on host Zn^{2+} (0.73\AA) in wurtzite structure. Thus, an understanding of the bonding character in $\text{Zn}_{1-x}(\text{Li}_y\text{Mg}_{1-y})_x\text{O}$ material is important for the development p-n junction based blue emission devices. We investigate here the structural properties of $\text{Zn}_{1-x}(\text{Li}_y\text{Mg}_{1-y})_x\text{O}$ prepared by solution chemistry synthesis route.

EXPERIMENTAL DETAILS

For the synthesis of $\text{Zn}_{1-x}(\text{Li}_y\text{Mg}_{1-y})_x\text{O}$, precursors were simple salts such as, acetates of zinc, magnesium, and lithium with methoxy ethanol and 2-ethylhexanoic acid as solvents. Stoichiometric ratios of the desired compositions were dissolved in methoxy ethanol and 2-ethylhexanoic acid. The solutions of the individual salts and solvents were mixed hot. This solution was then refluxed to form a clear solution. Part of the solution was dried on a hot plate with constant stirring to make the powder. The powder was ground in agate crucible, and annealed at different temperatures to study the evolution of chemical reaction. Another part of the solution was heated to make a denser solution for spin coating. Thin films were deposited on Pt (Pt/TiO₂/SiO₂/Si) substrate by spin coating (Headway spinner) at 3500 rpm. The materials were characterized using x-ray diffraction and Raman spectroscopy.

* Email: m_tomar@feynman.uprm.edu

Material Characterization

The Raman measurements were performed using an ISA T64000 triple monochromator with 1800 grooves/mm gratings. An optical microscope with 80X objective was used to focus the excitation radiation, a 514.5 nm line from a Coherent Innova 99 Ar⁺ laser, as well as to collect the backscattered radiation. Room temperature Raman spectra of the $\text{Zn}_{1-x}\text{Li}_x\text{O}$ for different compositions are shown in Figure 1. The new modes between 100 and 200 cm^{-1} are indeed indicative of another structural phase above $x = 0.20$. The transition for the composition $x = 0.2$ suggests a morphotropic boundary. The peaks around 1100 cm^{-1} are large, sharp, and their intensities are appreciable to consider them higher order peaks. It is quite clear that there is a definite phase transition at about $x = 0.20$ near the room temperature. The spectra beyond $x = 0.90$ show a complete transformation to a new phase dominated by Li-O modes and one could see Zn-O modes disappearing entirely. The low frequency mode around 101 cm^{-1} must be solely due to the O-O bending vibrations. The oxygen octahedra must then have the shortest edge in order for the O-O stretching frequency to be $\sim 1100 \text{ cm}^{-1}$.

X-ray diffraction patterns (CuK α line) of $\text{Zn}_{1-x}\text{Mg}_x\text{O}$ and $\text{Zn}_{1-x}\text{Li}_x\text{O}$ for different compositions and annealed at 700 °C are shown in Figure 2 and 3, respectively. For comparison, the x-ray diffraction patterns of $\text{Zn}_{0.90}(\text{Li}_{0.02}\text{Mg}_{0.08})\text{O}$ i.e. for $x = 0.10$, and $y = 0.02$ compositions and MgO are also shown in Figure 3. As evident from Figure 2, about 13 at. % Mg replaces the Zn site without changing the wurtzite structure of ZnO. In the case of $\text{Zn}_{1-x}\text{Li}_x\text{O}$, about 7 at. % of Li ion replaces the Zn ion site. Thus, band gap tailoring is possible in these materials. It can be noted in Figure 3 that for the same Zn content (i.e. $x = 0.01$) in $\text{Zn}_{1-x}\text{Li}_x\text{O}$ and $\text{Zn}_{1-x}(\text{Li}_y\text{Mg}_{1-y})_x\text{O}$, additional peak appears at about $2\theta = 43^\circ$ in the x-ray diffraction pattern of $\text{Zn}_{1-x}(\text{Li}_y\text{Mg}_{1-y})_x\text{O}$ which corresponds to MgO. This may be due to dissimilar ion sizes of Li and Mg.

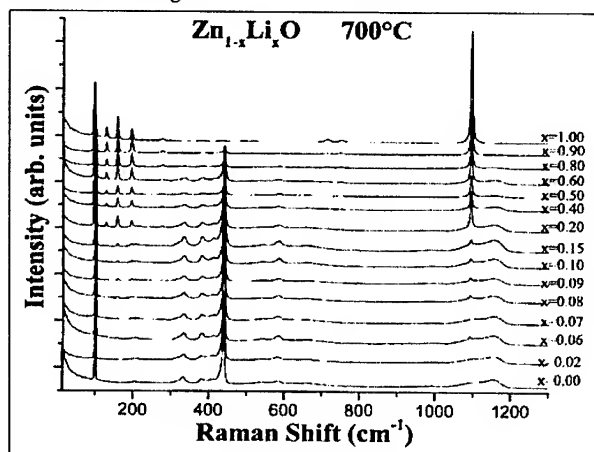


Figure 1. Raman spectra of $\text{Zn}_{1-x}\text{Li}_x\text{O}$ for different compositions and annealed at 700 °C.

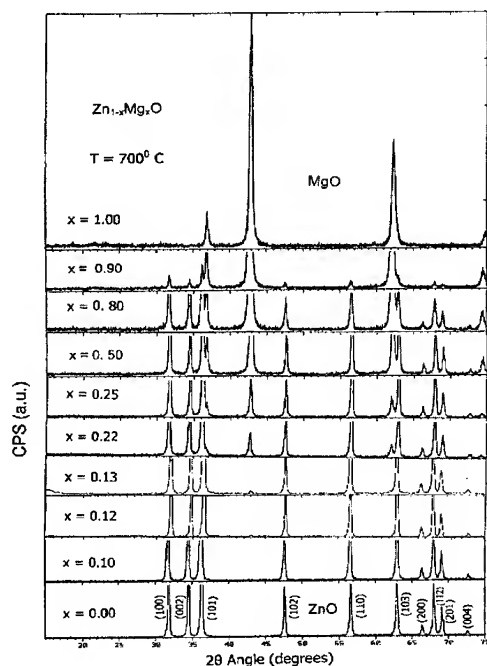


Figure 2. X-ray diffraction patterns of $\text{Zn}_{1-x}\text{Mg}_x\text{O}$ for different compositions and annealed at 700 °C.

Figure 4 shows the x-ray diffraction patterns of $\text{Zn}_{0.8}\text{Li}_{0.20}\text{O}$ and $\text{Zn}_{0.90}(\text{Li}_{0.02}\text{Mg}_{0.08})\text{O}$ and thin films deposited on Pt substrate ($\text{Pt}/\text{TiO}_2/\text{SiO}_2/\text{Si}$). One can observe that $\text{Zn}_{0.90}(\text{Li}_{0.02}\text{Mg}_{0.08})\text{O}$ film show oriented growth with dominated peak at $2\theta \approx 35^\circ$.

P-Doping

Theoretical prediction (1) and the experimental observation (2) that H^+ shallow energy levels are acting as n-dopant in ZnO, suggests that proper p-dopants such as P and N may act effectively on Zn site to avoid amphoteric behavior. The ZnO film containing P have shown p doping with poor carrier hole concentration $p = 10^{12}/\text{cm}^3$. But the Ga-N co-doping (8) has shown better hole concentrations but it also introduces undesirable defects. Therefore the gas phase doping with ionized N may be more effective, and such an effort is in progress.

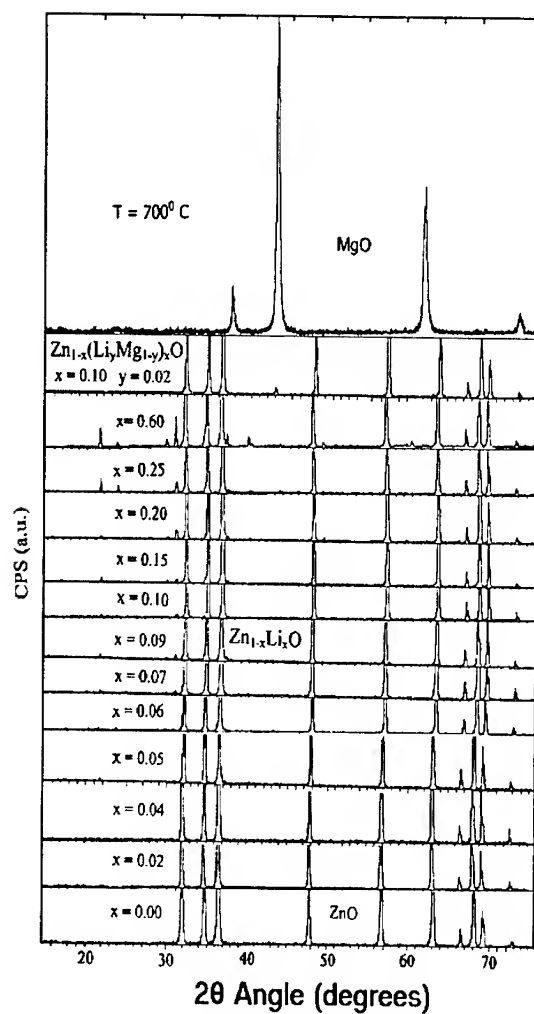


Figure 3. X-ray diffraction patterns of $\text{Zn}_{1-x}(\text{Li}_3\text{Mg}_{1-y})_x\text{O}$ for different compositions and annealed at 700°C

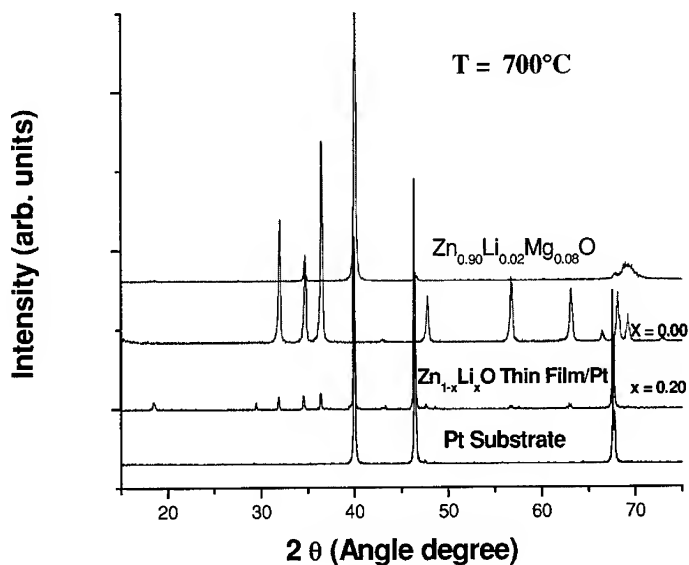


Figure 4. X-ray diffraction of $\text{Zn}_{1-x}\text{Li}_x\text{O}$ ($x = 0.00, 0.20$), and $\text{Zn}_{0.90}(\text{Li}_{0.02}\text{Mg}_{0.08})\text{O}$ thin films on Pt substrate.

CONCLUSION

We investigated the structural properties of $\text{Zn}_{1-x}(\text{Li}_y\text{Mg}_{1-y})_x\text{O}$ using x-ray diffraction and Raman spectroscopy. It is concluded that about 13 at.% of Mg does not change the wurtzite structure, and about 7 at.% of Li ion replaces Zn ion. Thin films deposited on Pt substrate by spin coating are stoichiometric. The P doped ZnO films showed poor hole density $p = 10^{12}/\text{cm}^3$.

ACKNOWLEDGEMENTS

We appreciate the support for this work by AFOSR grant No. F49620-01-1-1004.

REFERENCES

1. W.I. Park, G-C. Yi, and H.M. Jang, *Appl. Phys. Lett.* **79** (2001) 2022.
2. C.G. Van de Walle, *Phys. Rev. Lett.* **85** (2000) 1012.
2. S.F.J. Cox, E.A. Davis, S.P. Cottrell, P.J.C. King, J.S. Lord, J.M. Gil, H.V. Alberto, R.C. Vilao, J. Pirato Duarte, N. Ayres de Campos, A. Weidinger, R.L. Lichti, and S.C.J. Irvine, *Phys. Rev. Lett.* **86** (2001) 2601.
3. F.S. Hickernell, *IEEE Trans. MTT-17* (1969) 1755.
4. C. Campbell, *Surface Acoustic Wave Devices and their Signal Processing Applications*, Academic Press, San Diego, (1989).
5. M.S. Tomar, R.E. Melgarejo, P.S. Dobal and R.S. Katiyar, *J. Mater. Res.* **16** (2001) 903.
6. A. Onodera, N. Tamaki, Y. Kawamura, T. Sawada and H. Yamashita, *Jpn. J. Appl. Phys.* **35** (1996) 5160.
7. M. Joseph, H. Tabata, and T. Kawai, *Jpn. J. Appl. Phys.* **38**, (1999) L1205.

Depth Profiling of SiC Lattice Damage Using Micro-Raman Spectroscopy

Iulia C. Muntele, Daryush Ila, Claudiu I. Muntele, David B. Poker¹, Dale K. Hensley¹
Center for Irradiation of Materials, Alabama A&M University, Normal, AL – 35762, U. S. A.
¹Solid State Division, Oak Ridge National Laboratory, Oak Ridge, TN, U. S. A.

ABSTRACT

Depth profiling for the amount of lattice damage using a Confocal Micro-Raman (CMR) spectrometer is demonstrated in this paper. Samples of n-type silicon carbide were implanted with 2 MeV He and O ions at both room temperature and 500 °C, and fluences between 10^{15} and 10^{17} ions/cm². Post-implantation annealing at 1000 °C was also performed in order to study the damage evolution. Optical Absorption Spectrophotometry (OAS) was used for establishing the opacity (and therefore the probing depth) of the damaged layer to the 632.8 nm wavelength of the He-Ne laser used for CMR throughout this study. The methodology used and the results obtained are presented herein. Total dissipation of amorphous carbon islands was observed even at low annealing temperatures of the RT implanted samples, along with an increase in the size of the amorphous silicon islands.

INTRODUCTION

In device fabrication the ion implantation is usually the doping method of choice because it offers precise control over the spatial distribution and doping level using conventional masking techniques. Hot implantation of silicon carbide is a common practice aimed at reducing the damages incurred during the passage of ions through the material, reducing the needs for post-implantation annealing for crystalline lattice recovery. Although literature mentions that strong dynamical recovery has been achieved at temperatures as low as 200 °C, an annealing temperature up to 1700 °C is still necessary for an acceptable degree of lattice recovery, especially for Al-doped p-type silicon carbide. In order to predict a certain type of behavior of an electronic device, it is important to know the depth distribution of the residual damage present in the crystalline lattice. This is necessary because the carrier trapping levels introduced in the band gap by lattice damages (vacancies, interstitials, substitutionals etc.) can significantly change the electric behavior. Techniques like Positron Annihilation Spectroscopy [5,6] and Rutherford Backscattering/Channeling Spectrometry [7] have been reported in the literature as good tools for this type of investigation. This paper is intended to present an all-optical approach of this problem, using a CMR spectrometer for depth monitoring of the 400 – 600 cm⁻¹ (amorphous silicon) and 1250 – 1450 cm⁻¹ (amorphous carbon) spectral regions. Also, an UV/Vis (200 – 980 nm wavelength range) spectrophotometer was used for optical absorption measurements aimed at establishing the probing depth of the He-Ne laser (632.8 nm wavelength) used by the CMR spectrometer. The SRIM computer code was used as well, for establishing the ranges of the He and O ions into silicon carbide, and to provide a depth profile for the number of displaced atoms from the silicon carbide crystalline lattice during the implantation process.

METHODOLOGY FOR ANALYSIS

The confocal sampling mode of the micro Raman spectrometer [1] introduces the advantage of reduced/controlled depth of focus, resulting in an increased resolution on the z-axis (the normal at the surface of the sample). Experimentally, the confocality is measured usually by plotting the intensity of the only Raman line of silicon (520 cm^{-1}) as a function of the position of the focus on the z-axis. The curve obtained for a confocal hole of $200 \mu\text{m}$ has an almost gaussian shape, with the second order momentum (the square root of the variance) equal to:

$$\sigma = \frac{n\lambda}{4 \cdot NA^2} \quad (1)$$

For n-type 6H silicon carbide, considering $n=2.66$ (the refractive index), $\lambda=632.8 \text{ nm}$ (the wavelength of the He-Ne laser), and the numerical aperture of the objective $NA=0.9$ (for the 100X objective), this quantity is 520 nm . Therefore, the FWHM (full width at half maximum = the measure for confocality) of the Raman intensity curve becomes $1.22 \mu\text{m}$ ($\text{FWHM} = 2.35 \times \sigma$). This value is associated with the diameter of the spot in the sample where the laser beam is focused, and from where the Raman signal is collected. However, in implanted silicon carbide samples, the photoabsorption coefficient of the material increases to very high values, absorbing the probing light into a much lesser distance than the one given by the confocality. Therefore a "probing depth" for a particular combination target – laser beam is introduced [2] as:

$$d_p = -\frac{1}{2\mu} \ln \left(\frac{I_d}{I_s + I_d} \right) = \frac{2.3}{2\mu} \quad (2)$$

with I_s the intensity of the light scattered from the surface of the sample to the depth d_p , I_d the intensity of the light scattered from the depth d_p to infinity, and μ the photoabsorption coefficient. The number in the second part of the formula above (2.3) appears when a generally accepted 0.1 value for the ratio between the I_d and the total scattered light is considered. One can see that extrapolating for an infinite high photoabsorption coefficient (opacity of the sample), the probing depth goes to zero, and thus having analyzed only the surface of the sample.

UV/Vis Optical Absorption Spectrophotometry (OAS) was used for determining the photoabsorption coefficient of the layer damaged by ion implantation. The absorbance A measured in OAS is related to this coefficient by:

$$A = \lg(e^{\mu d}) = k\mu d \quad (3)$$

with $k = 0.4343$ and d the distance traveled by the electromagnetic radiation through the material of photoabsorption coefficient μ [8]. Assuming a constant coefficient μ' for the implanted layer of thickness d' , one can calculate it from:

$$\mu' = \mu + \frac{A' - A}{kd'} \quad (4)$$

The value for d' can be easily estimated from damage distributions given by SRIM simulations for the ion implantation process, and the two absorbances (for the sample after and before implantation, at the wavelength of the laser beam used in CMR) can be obtained from OAS.

EXPERIMENT AND RESULTS

Samples of n-type (N-doped) silicon carbide were implanted with helium and oxygen at 2 MeV and fluences between 10^{15} and 10^{17} ions/cm² at both room temperature (RT) and 500 °C. The ion implantation was carried out at the Oak Ridge National Laboratory. Table I presents the implantation conditions for the samples used in this study. The post-implantation annealing in argon at 500 and 1000 °C, and the optical analysis were performed at the Center for Irradiation of Materials of Alabama A&M University. Optical measurements (OAS and CMR) were employed before implantation and after each annealing step. Unimplanted silicon carbide samples were also annealed in identical conditions, for monitoring the original defect evolution, as a baseline for the defect densities of the implanted samples. The parameters used for the CMR spectrometer were 200 μ m confocal hole, 100X objective, 1800 g/mm grating, 20 mW He-Ne laser ($\lambda=632.817$ nm), and a Peltier cooled CCD detector. The spectra were acquired in the 300-700 cm⁻¹ region for amorphous silicon and Si-Si characteristic peaks and 1200-1700 cm⁻¹ region for amorphous carbon. OAS was performed in the 200-980 nm wavelength range, although only absorbance values at 632.8 nm were of interest for this work.

The depth scanning was performed with a 1 μ m step, starting at the surface of the sample and ending after the entire range of the implanting ions was covered, when possible (probing depth large enough). The ion ranges were obtained from SRIM. Figure 1 presents the damage profiles taken for both amorphous silicon and amorphous carbon regions for the as implanted samples. Only for two samples was possible a depth profiling, the others being opaque for 632.8 nm wavelength of the laser, therefore having Raman signal collected just from the surface. Figure 2 presents data for the RT implanted samples after annealing for 1 hour at 500 °C in argon, compared to the samples implanted at 500 °C to see the difference made by the hot implantation vs. cold implantation + annealing. Figure 3 presents the damage profiles of the samples after annealing for 1 hour at 1000 °C in argon. Damage profiling on unimplanted silicon carbide annealed in the same conditions as the implanted samples was also carried out and the results are presented in Figure 4, only for the amorphous silicon region.

Table I. Implantation parameters for the silicon carbide samples used in this work.

Parameter	Sample number							
	46	48	49	50	55	56	59	60
Ion	He	He	He	He	O	O	O	O
Energy (MeV)	2	2	2	2	2	2	2	2
Fluence (cm ⁻²)	10^{15}	10^{17}	10^{15}	10^{16}	10^{15}	10^{17}	10^{15}	10^{16}
Implantation Temperature	RT	RT	500 °C	500 °C	RT	RT	500 °C	500 °C

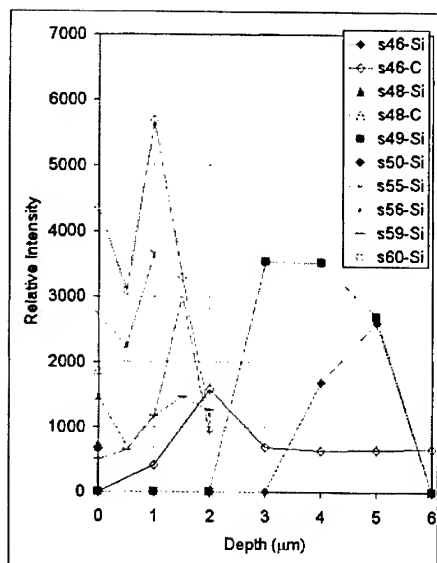


Figure 1. RT vs. 500 °C ion implantation.

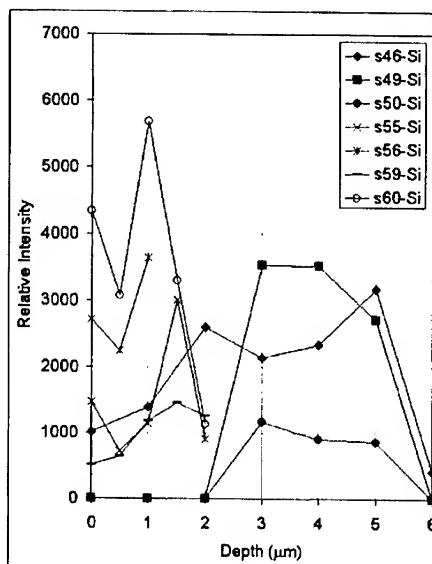


Figure 2. Implantation + annealing vs. hot implantation (all at 500 °C).

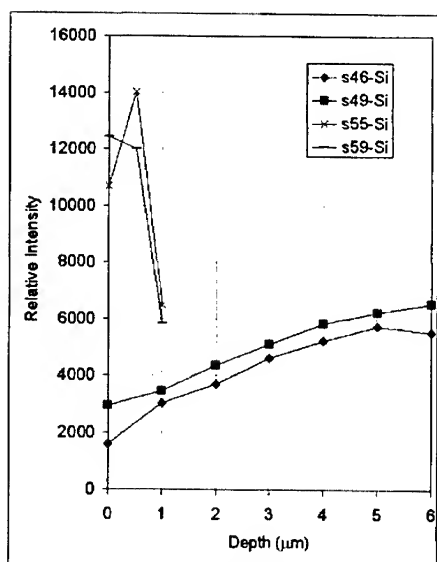


Figure 3. After annealing at 1000 °C. only).

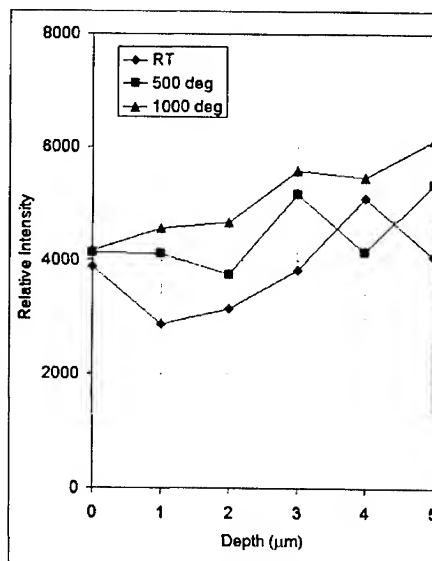


Figure 4. Pristine SiC (Si profiling

DISCUSSIONS

From Figure 1 one can see that the depth profiling was possible only for a few samples. The "Si" or "C" symbols in the legend show for which amorphous region is the respective plot taken. The plots monitoring the silicon region follow a shape mimicking the distributions given by SRIM simulations for silicon displacements, with maximum values at the depth where the helium and oxygen ions stopped in the material (4.66 and 1.6 μm , respectively). This is an unsurprising result, knowing that the damage is caused by the nuclear energy loss, which is the dominating process toward the end of the ion's range. What is surprising is that the amount of damage is greater in case of hot implantation than the RT implantation, leading to the conclusion that silicon is easier to be displaced at higher temperatures, and the damaged crystalline lattice is not recovering from this, as in the general case of other semiconductors. However, there is no amorphous carbon to be monitored for the sample that was hot-implanted, whereas for the sample implanted at RT there is a relatively massive amorphization of carbon present, with an almost uniform distribution in depth, during the entire range of helium ions. Since the sample implanted at 500 °C is more transparent to visible light than the one implanted at RT, one can conclude that the cause for losing the transparency is the amorphous carbon islands created during implantations. Post-implantation annealing to 500 °C of the samples implanted at RT (see Figure 2) presented a better transparency to visible light, allowing the depth profiling for most of the samples, also correlated to the complete disappearance of the amorphous carbon peak. However, instead of approaching the amorphous silicon distributions for the hot-implanted samples, the silicon amorphization region in sample 46 increases and spreads within the sample, showing that the situation actually worsens for the crystalline lattice. This situation is confirmed in Figure 3, where the distributions for all the samples presented there show an overall increase by a factor of 2, along with a "leveling" (more significant in the case of helium implanted samples). Also, the difference between the samples implanted at RT and the ones hot-implanted becomes negligible at this point. The confirmation that this is an effect due solely to the ion implantation, Figure 4 shows the non-implanted witness sample, whose amorphous silicon distribution remains relatively unchanged throughout the temperature range investigated.

CONCLUSIONS

The work presented here demonstrates that is possible to use a CMR setup for monitoring the depth distribution of damages in materials that are relatively transparent to the wavelength of the laser used. A methodology for estimating the depth resolution is described, and the techniques for obtaining the parameters involved are mentioned.

It has been shown that hot-implantation of silicon carbide is preferable over RT implantation followed by annealing. In addition, it was shown a complete dissipation of the amorphous carbon regions even at low annealing temperatures. As for the amorphous silicon regions in the material, it was shown that they do not dissipate, but rather increase in dimensions with the annealing temperatures. Further studies at higher temperatures are recommended for future work, for an accurate monitoring of their evolution.

ACKNOWLEDGEMENTS

This work is supported by the Center for Irradiation of Materials at Alabama A&M University and NASA-GRC Contract No. NAG3-2123. The work at ORNL was sponsored by the U.S. Department of Energy under contract DE-AC05-01OR22725 with the Oak Ridge National Laboratory, managed by UT-Battelle, LLC.

REFERENCES

1. Labram User Manual, ISA Dilor-Jobin Yvon, 1999.
2. "Raman and Luminiscence Spectroscopy for Microelectronics", Catalogue of Optical and Physical Parameters, "Nostradamus" Project SMT4-CT-95-2024, European Commission, 1998.
3. The Stopping and Ranges of Ions in Solids, J. F. Ziegler, J. P. Biersack, U. Littmark, Pergamon Press, 1985.
4. N. B. Colthup, L. H. Daly, S. E. Wiberley, "Introduction to Infrared and Raman Spectroscopy", Third Edition, Academic Press, 1990.
5. Y. Tanaka, N. Kobayashi, H. Okumura, R. Suzuki, T. Ohdaira, M. Hasegawa, M. Ogura, S. Yoshida, H. Tanoue, "Electrical and Structural Properties of Al and B Implanted 4H-SiC", Materials Science Forum Vols. 338-342 (2000), Trans Tech Publications, pp. 909-912.
6. W. Puff, A. G. Balogh, P. Mascher, "Microstructural Evolution of Radiation-Induced Defects in Semi-Insulating SiC During Isochronal Annealing", Materials Science Forum Vols. 338-342 (2000), Trans Tech Publications, pp. 965-968.
7. Handbook of Modern Ion Beam Materials Analysis, Material Research Society, 1995, Chapter 10, pp. 231-300.
8. P. D. Townsend, P. J. Chandler, L. Zhang, "Optical Effects of Ion Implantation", Cambridge University Press, 1994, pp. 71-72.

NEW APPROACH TOWARDS THE DEPOSITION OF I-III-VI THIN FILMS

Mohammad Afzaal, David Crouch, Paul O'Brien and Jin-Ho Park

The Manchester Materials Science Centre and Department of Chemistry, University of Manchester, Oxford Road, Manchester, M13 9PL, UK.

E-mail: jin-ho.park@man.ac.uk; paul.obrien@man.ac.uk

ABSTRACT

The ternary chalcopyrite semiconductor $\text{Cu}(\text{In/Ga})(\text{Se/S})_2$ is currently used as an absorber layer in high efficiency thin film solar cells. In this study, various types of I-III-VI (I = Cu, III = Ga or In, VI = S or Se) thin films (CuGaS_2 , CuInS_2 and CuInSe_2) were prepared from a series of organometallic precursors, $\text{M}[(\text{S/Se})_2\text{CNMeR}]_n$ (M = Cu, In, Ga; R = alkyl) by aerosol-assisted chemical vapour deposition (AACVD). In contrast to the metal alkyl compounds, MR_3 (M = In and Ga; R = alkyl), which are pyrophoric, the precursors are easy to synthesize by one-pot reactions and are air stable. The optimum growth temperature for the preparation of these films on glass substrates using aerosol-assisted chemical vapour deposition (AACVD) was found to be above 400 °C in terms of crystallinity, although deposition does occur at lower temperatures. The films have been characterised using XRPD, SEM and EDS. SEM analyses show all films are microcrystalline. XRPD results show evidence of the crystalline nature of these films. The results of this comprehensive study are presented and discussed.

INTRODUCTION

Ternary compound semiconductors such as copper indium/gallium disulfide/diselenide (CuInS_2 , CuGaS_2 or CuInSe_2) are promising materials for use in high efficiency solar cells. There have been only a few reports of the deposition of CuME_2 by CVD methods. A halogen transport VPE method[1] has been used to grow single crystals. CuInSe_2 films contaminated with In_2Se_3 have been deposited by MOCVD using copper(II) hexafluoroacetylacetonate mixed with trimethylamine, triethyl indium and hydrogen selenide.[2,3] A plasma enhanced process using both hexafluoroacetylacetonate copper and indium complexes and a novel selenium source 4-methyl-1,2,3-selenadiazole has also been used.[4] Chichibu has reported[5] the growth of heteroepitaxial layers of CuInSe_2 using cyclopentadienylcoppertriethylphosphine, trimethyl indium and diethylselenide as the precursors; the first successful MOVPE results.

There are also some initial reports concerning the use of single-source organometallic precursors for the deposition of CuInS_2 films.[6,7] Recently Hollingsworth *et al.* reported spray CVD of CuInS_2 films using a single-source precursor, $(\text{Ph}_3\text{P})_2\text{Cu}(\mu\text{-SEt})_2\text{In}(\text{SEt})_2$. In their study, highly orientated CuInS_2 was deposited on Si(111) substrates at 600 °C.[8]

We have been developing a range of dithio- and diseleno-carbamato complexes of various metals which have been successfully used to deposit a wide range of semiconductor materials.[9] One particularly successful modification to the sulfur/selenium containing ligands has been to develop compounds in which the parent amine is asymmetrically substituted and involves a bulky or extended alkyl substituent.[10,11] Compounds with these ligands are air stable and sufficiently volatile for the deposition of thin films of materials such as Cu_2E , In_2E_3 , Ga_2E_3 , ZnE

and CdE (E = S or Se).[12-13] Success with the binary parents of CuInE₂ has encouraged us to deposit the ternary phase. In this paper we report a simple AACVD process for copper indium/gallium disulfide/diselenide thin films.

EXPERIMENTAL DETAILS

Precursor Synthesis

The precursors were prepared by literature methods[14] and analyzed by CHN, NMR, Mass Spec. and TGA.

Cu(S₂CNMeⁿHex)₂ (1): Yield 64%, m.p. 48 °C, Elemental analysis: C₁₆H₃₂S₄N₂Cu. Calculated: C: 43.29, H: 7.2, N: 6.05%. Found: C: 42.76, H: 6.97, N: 6.05%. Mass Spectrum: m/z significant peaks [M⁺] 444, [CuS₂CNCH₃C₆H₁₃] 253, [S₂CNCH₂CH] 117, [S₂CNCH₂C] 116.

In(S₂CNMeⁿHex)₃ (2): Yield 67%, m. p. 100 °C, Elemental analysis: C₂₄H₄₈N₃S₆In. Calculated: C: 42.02, H: 6.91, N: 5.88%. Found: C: 42.27, H: 6.73, N: 6.01%. ¹H NMR (δ, C₆D₆, 300 MHz): 0.86 (t, 9H, -NCH₂CH₂CH₂CH₂CH₂CH₃), 1.18 (m, 18H, -CH₂CH₂CH₂CH₂CH₂CH₃), 1.38 (m, 6H, -NCH₂CH₂CH₂CH₂CH₂CH₃), 2.8 (s, 9H, -NCH₃), 3.3 (t, 6H, -NCH₂CH₂CH₂CH₂CH₂CH₃).

Cu(Se₂CNMeⁿHex)₂ (3): Yield 70%, Elemental analysis: C₁₆H₃₂Se₄N₂Cu. Calculated: C: 30.45, H: 5.07, N: 4.44%. Found: C: 30.84, H: 5.65, N: 4.45%. Mass Spectrum: m/z significant peaks, [CuSe₂CNCH₃CH₂C] 288, [CuSe₂CNCH₂CH₂CH] 300, [CuSe₂CNCHCH₂CH₂CH₂C] 314.

In(Se₂CNMeⁿHex)₃ (4): Yield 57%, Elemental analysis: C₂₄H₄₈N₃Se₆In. Calculated: C: 29.81, H: 4.96, N: 4.35%. Found: C: 30.83, H: 4.97, N: 4.40%. ¹H NMR (δ, C₆D₆, 300 MHz): δ 0.55 (t, 9H, -NCH₂CH₂CH₂CH₂CH₂CH₃), 0.77 (m, 18H, -CH₂CH₂CH₂CH₂CH₂CH₃), 1.00 (m, 6H, -NCH₂CH₂CH₂CH₂CH₂CH₃), 2.4 (s, 9H, -NCH₃), 2.9 (t, 6H, -NCH₂CH₂CH₂CH₂CH₂CH₃).

Ga(S₂CNMeⁿHex)₃ (5): Yield 68% m. p. 85 °C, Elemental analysis: C₂₄H₄₈N₃S₆Ga Calculated: C: 44.99, H: 7.55, N: 6.56% Found: C: 44.78, H: 8.14, N: 6.58%, ¹H NMR (δ, C₆D₆, 300 MHz): δ 0.92 (t, 9H, -NCH₂CH₂CH₂CH₂CH₂CH₃), 1.18 (m, 18H, -CH₂CH₂CH₂CH₂CH₂CH₃), 1.40 (m, 6H, -NCH₂CH₂CH₂CH₂CH₂CH₃), 2.8 (s, 9H, -NCH₃), 3.4 (t, 6H, -NCH₂CH₂CH₂CH₂CH₂CH₃).

Deposition of films and characterizations

Aerosol Assisted Chemical Vapour Deposition (AACVD): Approximately 0.25g of precursor was dissolved in 30ml Toluene (or THF) in the round-bottomed flask. Six glass substrates (1 × 2 cm) were placed inside the reactor tube. The carrier gas flow rate was controlled by Platon flow gauges. The solution in the flask is placed in a water bath above the piezoelectric modulator of a humidifier, where aerosol droplets are generated and transferred by the carrier gas into a hot-wall zone. Then both the solvent and the precursor evaporate and the precursor vapour reaches the heated substrate surface where thermally induced reactions and film deposition take place. This homemade aerosol-assisted chemical vapour deposition kit consists of a two-neck flask, a PIFCO ultrasonic humidifier (Model No. 1077) and a CARBOLITE furnace.

Film characterizations: X-ray diffraction studies were performed using Cu- K_{α} radiation on a Philips X'Pert MPD diffractometer. The sample was mounted flat and scanned from 20 - 80 ° in steps of 0.04 ° with a count time of 2 s. Samples were carbon coated before electron microscopic analysis. All EDS and electron microscopy was then carried out in a Jeol Superprobe 733 microscope.

RESULTS AND DISCUSSION

Copper Indium Sulfide by AACVD

Films of CuInS₂ were successfully grown on glass at 350 – 450 °C by AACVD. It is interesting to note that employing AACVD can reduce deposition temperature for the growth of CuInS₂ to 350 °C as compared to those grown by LP-MOCVD.[15] All films grown using compounds 1 and 2 (1:1 ratio) gave narrow and strong peaks in the X-ray powder diffraction and show characteristic tetragonal phase of CuInS₂ (Fig. 1). The XRPD patterns of the films grown at various growth temperatures show a preferred orientation along the (112) plane regardless of growth temperature. EDS analysis of films grown at 450 °C peaks corresponding to Cu, In and S and ratio was found to be close to 1:1:2.

SEM analysis for the as-deposited CuInS₂ films on glass indicates slightly different features in terms of their morphology compared to those grown by LP-MOCVD. Films grown at 450 °C show that particles are formed as randomly orientated flakes *ca.* 0.2 μm thick as compared to the relatively thick width (*ca.* 1 μm) crystallites grown by LP-MOCVD and particles grown by AACVD are laid down horizontally on the glass substrate. Also the shape of particles are very similar to those prepared on fused silica using (Ph₃P)₂CuIn(SET)₄ by spray CVD.[8]

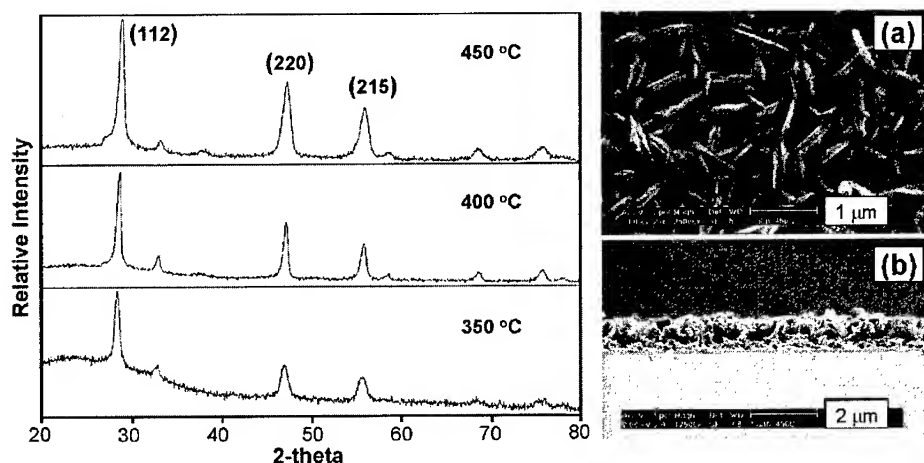


Fig. 1. XRPD patterns of CuInS₂ on glass [using compounds 1 and 2 by AACVD (temperatures indicate growth temperatures)] and SEM images of the films grown at 450 °C.

In 2 hour growth, films were found to be *ca.* 1 μm thick with 0.5 $\mu\text{m}/\text{h}$ growth rate. At lower growth temperature (350 $^{\circ}\text{C}$), a mixture of morphologies can be seen. Particle size is found to be between 0.5 – 1.6 μm .

Various ratios of compounds **1** and **2** were also utilized in order to investigate stoichiometric change of CuInSe_2 films. XRPD patterns of as-deposited films grown with different ratios show that there is no evidence to trace any by-products such as indium sulfide or copper sulfide and indicate no effect on stoichiometry of CuInSe_2 , in contrast to the LP-MOCVD work.

Copper Indium Selenide by AACVD

CuInSe_2 films have been also deposited on glass using compounds **3** and **4** by AACVD. In this case, only a 1:1 molar ratio of compounds **3** and **4** was used. Films were grown at 425 – 475 $^{\circ}\text{C}$ with constant argon flow rate of 180 sccm. XRPD analyses (Fig. 2) suggest that as-deposited films have tetragonal phase with a preferred orientation along (112) direction in all cases.

SEM images of the films show (Fig. 2) that the deposited layer is not homogenous and mainly consist of several different shapes of particles with a poor coverage at lower growth temperature (425 $^{\circ}\text{C}$). The heterogeneous morphology on thin film layer can be altered by using single crystalline substrates such as $\text{InP}(111)$ and $\text{Si}(111)$ which may lead to homogenous growth process. The observation of homogenous growth was found in the LP-MOCVD study.[16]

Copper Gallium Sulfide by AACVD

In the growth of CuGaS_2 , stoichiometric amount of compounds **1** and **5** were employed and dissolved in THF (30ml). In initial experiments, Cu/In ratio was maintained at 1:1 and growth time was kept constant for 2 hours (180 sccm/flow rate).

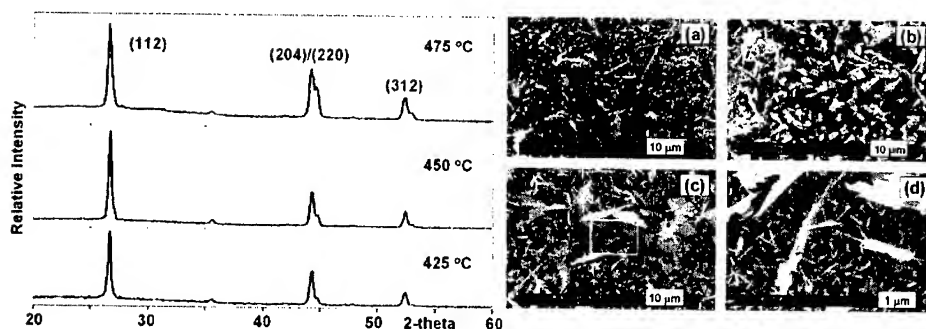


Fig. 2. XRPD patterns of CuInSe_2 films on glass by AACVD and SEM images of CuInSe_2 on glass using compounds **3** and **4** by AACVD [(a) 425 $^{\circ}\text{C}$; (b) 450 $^{\circ}\text{C}$; (c) and (d) 475 $^{\circ}\text{C}$].

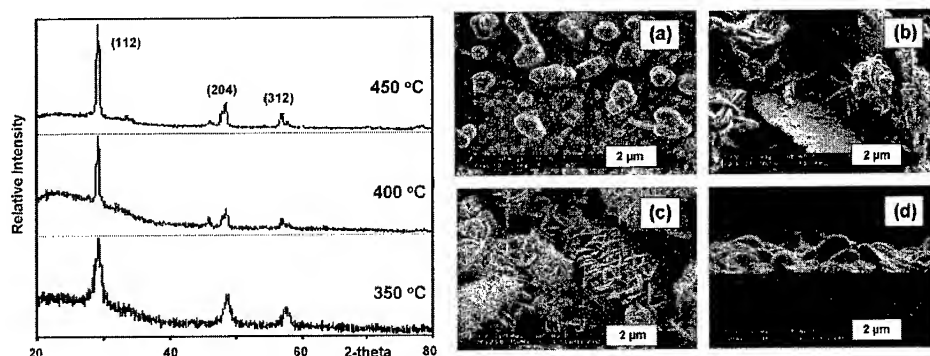


Fig. 3. XRPD patterns of CuGaS_2 films on glass by AACVD and SEM images of CuGaS_2 on glass using compounds **1** and **5** by AACVD [(a) 300 °C; (b) 400 °C; (c) and (d) 450 °C].

XRPD patterns (Fig. 3) show that deposited films by AACVD have chalcopyrite structure with a preferred orientation along (112) direction (JCPDS 27-0279). It is also conclusive that at high temperatures, the crystallinity of deposited film is highly indicated by the sharpness of peaks, whilst at low temperature (350 °C) XRPD pattern exhibits weak reflections indicating poorly crystalline films. Similar results are obtained for the films grown at lower argon flow rate (120 sccm).

SEM analysis (Fig. 3) shows that the material consists of clusters of randomly orientated platelets to the surface for films grown at 400 and 450 °C (180 sccm/flow rate). The films deposited are dense but are uneven. Growth rates are approximately 500 nm/h for films grown at 350 °C and 1 $\mu\text{m}/\text{h}$ at 450 °C. As growth temperature decrease, the growth of CuGaS_2 is significantly reduced. EDS analysis shows films are slightly copper rich with Cu 30%, Ga 24% and S 46%. However, when flow rate of argon as a carrier gas was reduced to 120 sccm, the clusters formed tended to be denser but some individual platelets can also be seen. In 2 hour growth at 450 °C, films with *ca.* 1.5 μm thickness were deposited on the glass substrate (growth rate, *ca.* 0.75 $\mu\text{m}/\text{h}$). EDS elemental atomic percent for CuGaS_2 films was found to be 29%, 23% and 48% respectively.

CONCLUSIONS

The results described herein demonstrate that AACVD using organometallic precursors results in stoichiometric CuME_2 ($\text{M} = \text{In}$ or Ga , $\text{E} = \text{S}$ or Se) films, and the quality (e.g. morphology or preferred orientations) of films are dependent on experimental parameters. Furthermore, films grown on glass by AACVD show similar XRPD patterns regardless deposited materials. It is evident that the AACVD approach leads to the deposition of I-III-IV films from the precursors used in this work. As a result, it is shown to be that a series of asymmetrical alkylthiocarbamate metal complexes can be used as precursors for the deposition of I-III-VI class films by CVD techniques.

ACKNOWLEDGEMENTS

POB acknowledges the support of Sumitomo/STS as visiting Professor of Materials Chemistry at Imperial College, London, UK. Authors thank the EPSRC, UK for the grants that have made this research possible.

REFERENCES

- [1] O. Igarashi, *J. Cryst. Growth* **130**, 343 (1993).
- [2] B. Sagnes, A. Salesse, M. C. Artaud, S. Duchemin, J. Bougnot and G. Bougnot, *J. Cryst. Growth* **124**, 620 (1992).
- [3] F. Ouchin, P. Gallon, M. C. Artaud, J. Bougnot and S. Duchemin, *Cryst. Res. Technol.* **31**, S513 (1996).
- [4] P. A. Jones, A. D. Jackson, P. D. Lickiss, R. D. Pilkington and R. D. Tomlinson, *Thin Solid Films* **238**, 4 (1994).
- [5] S. Chichibu, *Appl. Phys. Letter.* **70**, 1840 (1997).
- [6] R. Nomura, Y. Seki, K. Konishi and H. Matsuda, *Appl. Organomet. Chem.* **6**, 685 (1992).
- [7] R. Nomura, Y. Seki and H. Matsuda, *J. Mater. Chem.* **2**, 765 (1992).
- [8] J. A. Hollingsworth, A. F. Hepp and W. E. Buhro, *Chem. Vap. Deposition* **5**, 105 (1999).
- [9] M. B. Hursthouse, M. A. Malik, M. Motevalli and P. O'Brien, *J. Mater. Chem.* **2**, 949 (1992).
- [10] M. Motevalli, P. O'Brien, J. R. Walsh and I. M. Watson, *Polyhedron* **15**, 2801 (1996).
- [11] P. O'Brien, J. R. Walsh, I. M. Watson, L. Hart and S. R. P. Silva, *J. Cryst. Growth* **167**, 133 (1996).
- [12] S. W. Haggata, M. A. Malik, M. Motevalli, P. O'Brien and J. C. Knowles, *Chem. Mater.* **7**, 716 (1995).
- [13] M. R. Lazell, P. O'Brien, D. J. Otway and J. -H. Park, *Chem. Mater.* **11**, 3430 (1999).
- [14] P. O'Brien, D. J. Otway and J. R. Walsh, *Chem. Vap. Deposition* **3**, 227 (1997).
- [15] P. O'Brien, D. J. Otway and J. -H. Park, Unpublished results.
- [16] J. McAleese, P. O'Brien and D. J. Otway, *Chemical Vap. Deposition* **4**, 94 (1998).

Comparison of AlGaAs Oxidation in MBE and MOCVD Grown Samples*

Y. Chen, A. Roshko, K.A. Bertness, National Institute of Standards and Technology.
D.W. Readey, Colorado School of Mines.
A.A. Allerman, Sandia National Laboratories.
M. Tan, A. Tandon, Agilent Technologies.

ABSTRACT

Simultaneous wet-thermal oxidation of MBE and MOCVD grown $\text{Al}_x\text{Ga}_{1-x}\text{As}$ layers ($x = 0.1$ to 1.0) showed that the epitaxial growth method does not influence the oxidation rate. Nearly identical oxidation depths were measured for samples grown by both techniques. It was found, however, that the oxidation rate is very sensitive to non-uniformities in the Al concentration in the $\text{Al}_x\text{Ga}_{1-x}\text{As}$ layers, and that maintaining consistent and uniform Al concentrations is critical to achieving reproducible oxidation rates. The study also showed that the oxidation rate was not affected by the V/III ratio during growth nor by impurities at concentrations less than or equal to 10 ppm.

INTRODUCTION

Native oxides formed by wet-thermal oxidation of $\text{Al}_x\text{Ga}_{1-x}\text{As}$ are playing increasingly important roles in optoelectronic devices such as vertical cavity surface emitting lasers (VCSELs) [1, 2, 3]. They are also being considered for the gate material in field effect transistors (FET) [4]. In spite of the growing importance of these native oxides, there are several issues that complicate their use, including mechanical stability and fabrication reproducibility.

The multi-layers for VCSEL devices are fabricated by molecular beam epitaxy (MBE) [5, 6] or metal organic chemical vapor deposition (MOCVD) [7, 8]. The MBE-grown AlGaAs layers are sometimes pseudo or digital alloys, rather than the random alloys grown by MOCVD. Specifically, the MBE layers are made up of very thin (0.5 to 6 nm) alternating layers of AlAs and AlGaAs or GaAs rather than a single true AlGaAs. Other differences between these growth techniques are that MBE uses solid sources for growth under ultra high vacuum, while MOCVD uses organic precursors at pressures close to ambient. The purpose of this study is to investigate how these two growth methods and different growth systems affect the wet-thermal oxidation of AlGaAs. The effects of V/III ratio during growth and impurity concentrations on the oxidation rate are also reported.

EXPERIMENTAL PROCEDURES

Three labs provided four specimens for the study. One wafer was fabricated by MBE and the others were grown by MOCVD. In addition to the already mentioned differences between these two growth techniques, the MBE sample was grown at a lower temperature, 600°C , and at a slower rate, GaAs-0.18/AlAs-0.3/AlGaAs-0.52 nm/sec. The MOCVD samples were grown at 720°C , with MOCVD1 grown at 1.5 nm/sec, MOCVD2 at 0.6 nm/sec, MOCVD3 at 1.0 and 1.5 nm/sec. Three of the wafers had nominally identical structures with different AlGaAs layers ranging in composition from 90 % Al ($\text{Al}_{0.90}\text{Ga}_{0.10}\text{As}$) to 100 % (AlAs), in increments of 2 %. The fourth sample, MOCVD3, had three sets of

*Contribution of the U.S. government, not subject to copyright.

layers grown with V/III ratios of 90, 130 and 260. This sample had only 94, 96, 98 and 100 % AlGaAs layers.

Samples cleaved from the wafers were photolithographically patterned and wet-chemically etched, with $\text{H}_2\text{SO}_4:\text{H}_2\text{O}_2:\text{H}_2\text{O}$ (6:1:40), to form 11 parallel grooves along [011] exposing the AlGaAs layers for oxidation. Simultaneous wet-thermal oxidation of a set of samples was carried out at 460 °C for either 10 or 20 min. Nitrogen was used as the carrier gas (2.5L/min) bubbling through a water bath maintained at 75 °C. After oxidation the samples were cleaved and the oxide depths measured with scanning electron microscopy (SEM). Some difficult measurements were verified with field emission SEM (FESEM) imaging. The largest variation of oxidation depth for different grooves in a single sample was 5 %. Secondary ion mass spectroscopy (SIMS) analysis of unoxidized samples was used to obtain concentrations of potential impurities, as well as to compare relative Al and Ga concentrations.

RESULTS AND DISCUSSION

Oxidation Results

Figure 1 is an SEM image of the cleaved edge of an oxidized sample. The arrows point to the oxidized/unoxidized interface in the AlGaAs layers. The measured oxidation rates for samples MBE1, MOCVD1 and MOCVD2 are plotted in figure 2. MBE1 and

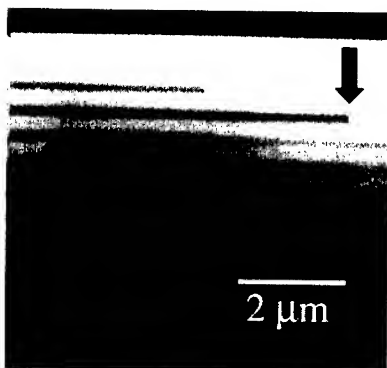


Figure 1. Oxidation front indicated by arrows in SEM image. Charging at the top surface made measurement near the surface difficult.

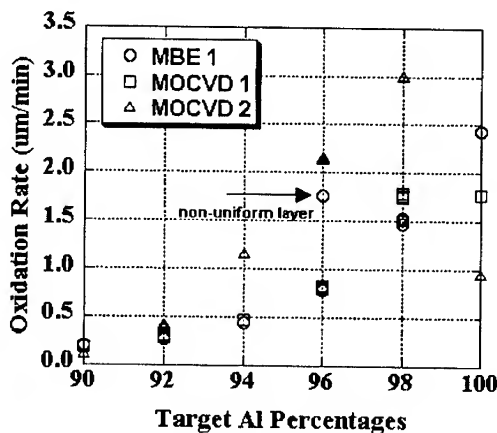


Figure 2. Oxidation rate for wafers grown by MBE and MOCVD. 20 min oxidation at 460°C with flow rate of 2.5L/min. Lower Al composition layers had very similar oxidation rates.

MOCVD1 had similar oxidation rates from 90 to 98 % Al, and the rate increased exponentially with Al composition, up to 98 %. The oxidation rates for 90 to 98 % Al layers in MOCVD2 were much higher than both the MBE1 and MOCVD1 rates, except for the AlAs layer.

Oxidation rates found for 90 to 98 % Al layers in MBE1 and MOCVD1 are in the same range as data reported previously [7,9]. The small differences in oxidation rates are probably due to the differences in oxidation process parameters such as oxidation time, oxidation temperature, bubbler temperature, gas flow rate and AlGaAs layer thickness.

Unlike those of the lower-Al-content layers, the oxidation rates of the 100 % Al layers vary widely and are quite different from those reported by other labs. The oxidation rate of the AlAs layer was highest in sample MBE1, but it is low relative to an extrapolated exponential fit to the data for lower Al concentrations. In MOCVD1 the oxidation rate was the same for the 98 and 100 % Al layers. Most unexpectedly, the oxidation rate of the AlAs layer in MOCVD 2 was lower than the rates for the 98, 96 and 94 % Al layers. These results do not agree with previous studies where the oxidation rate increased exponentially with Al composition from 90 to 100 % Al [7, 10]. While differences in the oxidation process may account for some of this variation, it is difficult to understand these results.

In order to eliminate potential sources of variation, the samples of each set were processed, etched and wet-thermally oxidized simultaneously. The oxide depths were very reproducible, with mean variations of less than 2 % for multiple samples from the same wafer. The observed variations, therefore, are unlikely to have been caused by the sample processing. The most probable cause of the variations is in the materials themselves and this likely results from the growth process. To investigate this, the V/III ratio, impurities and Al/Ga concentrations have been studied.

V/III Ratio Study

V/III ratio affects defect formation in epitaxial material, and diffusion in AlGaAs can be influenced by defect concentration [11, 12]. Therefore, V/III ratio could affect the wet oxidation rate since the oxidation process is a combination of diffusion and surface reactions.

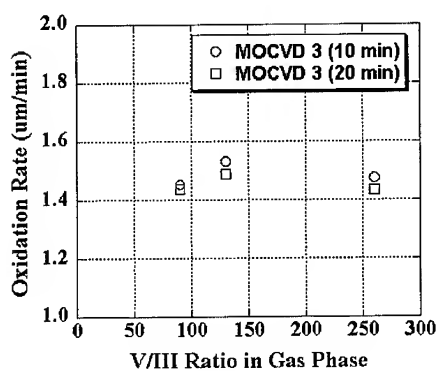


Figure 3. Dependence of oxidation rate on V/III ratio for $\text{Al}_{0.98}\text{Ga}_{0.02}\text{As}$, 460°C, 2.5 L/min, for 10 min and 20 min. No obvious correlation is evident exists between V/III ratio and oxidation rate.

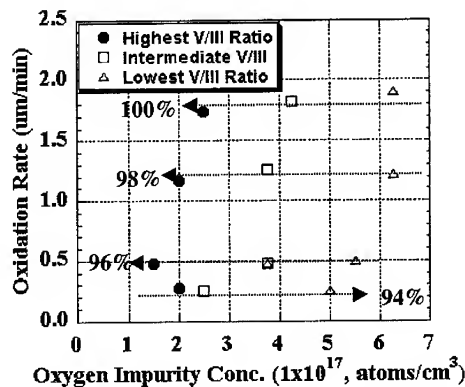


Figure 4. Oxygen impurity concentration did not affect the oxidation rate when impurity levels were less than or equal to 10 ppm. Arrows indicate the same Al% for different V/III ratios.

Wafer MOCVD3 was grown with three different V/III ratios to study the effect of V/III ratio on the oxidation rate. Figure 3 shows that the oxidation rate does not depend on the V/III ratio.

Impurity Analysis

Impurities may be incorporated in the wafers from background levels in the growth chamber or from the source materials. Oxygen and hydrogen are known to affect the oxidation process [13, 14], so their presence in the wafer as impurities may affect the oxidation rate. Low V/III ratios during growth are known to increase impurity concentrations in AlGaAs layers [15]. SIMS analysis was used to obtain the concentrations of O, H, C and Si in the un-oxidized wafers. The analysis confirmed that the impurity concentrations decreased with increasing V/III ratio (see Figure 4) and showed that, for all of the samples, the impurity concentrations were less than or equal to 10 ppm. Figure 4 shows that the oxygen impurity did not affect the oxidation rate. The rate was independent of the other impurities studied as well.

Al and Ga Concentrations

SIMS analysis was also used to examine the Al and Ga concentrations in the un-oxidized wafers. Depth profiles for MBE1 and MOCVD1 are shown in Figure 5. Both of these samples had uniform Al concentrations within each AlGaAs layer and the peak Al concentration matched the designed concentration. However, there was a spike in Al concentration in one of the 96 % AlGaAs layers in MBE1. That layer had a faster oxidation rate than the other 96 % layers in MBE1 (see Figure 2). From the SIMS analysis, the measured peak Al concentration for this particular "96 %" layer was actually 97.5 %, which is consistent with the faster oxidation rate measured for that layer.

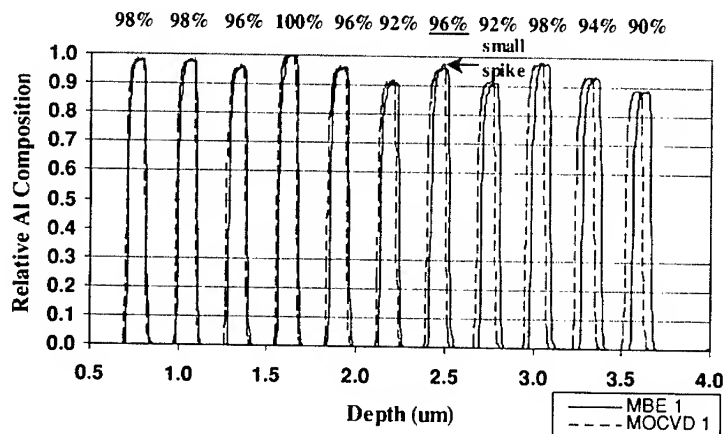


Figure 5 SIMS analysis showing uniform layer structure and Al concentration, in all but one 96 % layer in MBE1.

Non-uniformity in Al concentration was observed in almost all of the AlGaAs layers in MOCVD2 (see Figure 6). Most of the layers had a thin region with an Al content considerably higher than that of the rest of the layer and higher than the designed Al

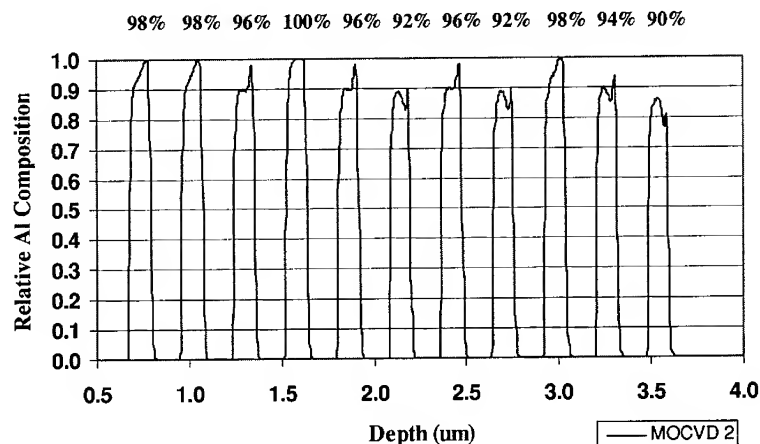


Figure 6. SIMS analysis showing MOCVD 2 has non-uniformity in Al concentration in AlGaAs layers.

concentration. This probably resulted from mass flow controller overshoot at the initiation of the layer growth. The oxidation rates for MOCVD2 were approximately twice as fast as the rates for MBE1 and MOCVD1 (see Figure 2). As shown in Figure 7, this rapid oxidation occurred in the thin region with high Al content. Oxidation rates reported in this paper were measured with reference to the section of the oxidation front that propagated the farthest.

Figure 8 is a plot of the oxidation rates as a function of the peak Al compositions

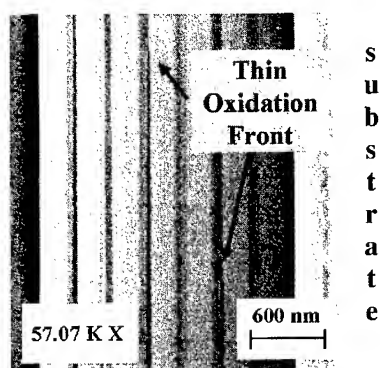


Figure 7. FESEM of MOCVD 2 showing propagation of the oxidation front through the sub-layer having elevated Al concentration.

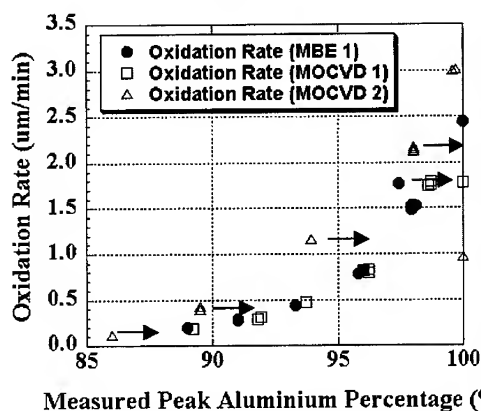


Figure 8. Oxidation rate (20 min oxidation) for all three samples are in better agreement when plotted against the peak Al concentration as measured by SIMS. Arrows indicate actual Al concentrations higher than measured by SIMS, see text.

determined from the SIMS analysis. The actual peak Al concentrations for MOCVD2 and the non-uniform 96 % Al layer in MBE1 are expected to be higher than the data measured by SIMS, as indicated with arrows. This is because intermixing and surface roughness created by sputtering during SIMS will both decrease the maximum Al concentration measured in the thin, high Al content regions. However, the extent of this effect is not certain. This new information about the actual layer compositions shows that the oxidation rates of the 90 to 98 % Al layers for all three samples are in reasonable agreement, considering the non-uniformities in MOCVD2. The cause of the variation in the rates for AlAs has yet to be found; however, experiments are underway to investigate this.

SUMMARY

In summary, it was shown that the epitaxial growth method (MBE vs. MOCVD) did not affect the wet-thermal oxidation rate of $\text{Al}_x\text{Ga}_{1-x}\text{As}$ for $x = 0.90$ to 0.98 . It was also found that the V/III ratio, for relatively clean systems, and impurity levels below 10 ppm did not affect the oxidation rate. Apparent differences between samples were found to result from compositional non-uniformities in the AlGaAs layers. These results emphasize the importance of having precise control of the Al concentration in $\text{Al}_x\text{Ga}_{1-x}\text{As}$ layers so that reproducible oxidation rates can be achieved.

¹ D.L. Huffaker, D.G. Deppe, and K. Kumar, *Appl. Phys. Lett.* **65**, 97 (1994).

² D.A. Kellogg, N. Holonyak, and R.D. Dupuis, *Appl. Phys. Lett.* **77**, 3152 (2000).

³ P.W. Evans, J.J. Wierer, and N. Holonyak, Jr., *J. Appl. Phys.* **84**, 5436 (1998).

⁴ E.I. Chen, N. Holonyak, Jr., and S.A. Maranowski, *Appl. Phys. Lett.* **66**, 2688 (1995).

⁵ Zhong Pan, Yi Zhang, Yun Du, and Ronghan Wu, *J. Appl. Phys.* **37**, 3673 (1998).

⁶ B. Koley, M. Dagenais, R. Jin, G. Simonis, J. Pham, G. McLane, F. Johnson, and R. Whaley, Jr., *J. Appl. Phys.* **84**, 600 (1998).

⁷ J.H. Kim, D.H. Lim, K.S. Kim, G.M. Yang, K.Y. Lim, and H.J. Lee, *Appl. Phys. Lett.* **69**, 3357 (1996).

⁸ M. Ochiai, G.E. Giudice, and H. Temkin, *Appl. Phys. Lett.* **68**, 1898 (1996).

⁹ K.D. Choquette, K.M. Geib, H.C. Chui, H.Q. Hou and R. Hull, *Mats. Res. Soc. Proc.* **421**, 53 (1996).

¹⁰ K.D. Choquette, K.M. Geib, C.I.H. Ashby, R.D. Twisten, O. Blum, H.Q. Hou, D.M. Follstaedt, B.E. Hammons, D. Mathes, and R. Hull, *IEEE J. Selected Topics in Quantum Elec.* **3**, 916 (1997).

¹¹ G.A. Baraff, and M. Schluter, *Physical Rev. Lett.* **55**, 1327 (1985).

¹² R.M. Cohen, *J. Appl. Phys.* **67**, 7268 (1990).

¹³ C.I.H. Ashby, M.M. Bridges, A.A. Allerman, B.E. Hammons, and H.Q. Hou, *Appl. Phys. Lett.* **75**, 73 (1999).

¹⁴ C.I.H. Ashby, J.P. Sullivan, K.D. Choquette, K.M. Geib, and H.Q. Hou, *J. Appl. Phys.* **83**, 3134, (1997).

¹⁵ G.B. Stringfellow, "Organometallic Vapor-Phase Epitaxy: Theory and Practice", Academic Press, ch. 8, 1999.

Hole concentration vs. Mn fraction in a diluted (Ga,Mn)As ferromagnetic semiconductorRaimundo R. dos Santos¹, L. E. Oliveira² and J. d'Albuquerque e Castro¹¹Inst. de Física, Univ. Fed. do Rio de Janeiro, CP 68.528, Rio de Janeiro-RJ, 21945-970, Brazil²Instituto de Física, Unicamp, CP 6165, Campinas-SP, 13083-970, Brazil**ABSTRACT**

The dependence of the hole density on that of Mn sites in $\text{Ga}_{1-x}\text{Mn}_x\text{As}$ is studied within a mean-field approach to the hole-mediated ferromagnetism in III-V Mn-based semiconductor compounds. We parametrize the hole concentration, p , as a function of the fraction of Mn sites, x , in terms of the product $m^*(J_{pd})^2$ (where m^* is the hole effective mass and J_{pd} is the Kondo-like hole/local-moment coupling), and the critical temperature T_c . By fitting $m^*(J_{pd})^2$ to experimental data for $T_c(x)$, we establish the dependence of p on x , which is interpreted in terms of a reentrant metal-insulator transition taking place in the hole gas.

INTRODUCTION

The discovery in the early 1990's of ferromagnetism in III-V materials alloyed with transition elements like Mn [1,2] has increased the interest in the study of the electronic, optical and transport properties of diluted magnetic semiconductors (DMS). Ferromagnetic semiconductors bring about the possibility of controlling both spin and charge degrees of freedom. The combination of this feature with the capability of growing low-dimensional structures has opened up new perspectives for the production of spintronic devices. Applications would include non-volatile memory systems [3] and quantum computing [4].

A great deal of attention has been focused on $\text{Ga}_{1-x}\text{Mn}_x\text{As}$ alloys, which exhibit very interesting magnetic and transport properties. When Mn atoms replace Ga in GaAs, their five 3d electrons remain localized in a core state, giving rise to $S = 5/2$ local moments. In addition, Mn atoms have one less electron in the 4s level than Ga, so they act as acceptors generating hole states in the material; for large enough doping, these states merge to form an impurity band. It should be pointed out that the equilibrium solubility of Mn atoms in GaAs is quite low [5], being only of the order of 10^{19} cm^{-3} . However, with help of molecular-beam epitaxy techniques at low temperatures, it has been possible to produce homogeneous samples of $\text{Ga}_{1-x}\text{Mn}_x\text{As}$ with x as high as 0.071. Magnetization measurements in these systems show that for $0.015 \leq x \leq 0.071$ they become ferromagnetic, with doping-dependent critical temperatures $T_c(x)$ reaching a maximum of 110 K for $x = 0.053$ [6].

The origin of ferromagnetic order in these materials is not fully understood, but there exists consensus on the fact that it results from the exchange coupling between the localized Mn moments mediated by the holes. The strength of the coupling is expected to depend on the hole concentration p , which eventually determines the Curie temperature $T_c(x)$. In principle, one would expect that each Mn would provide one hole, leading to a density of holes equal to that of the magnetic ions. However, this has not been confirmed by experiment. Although an accurate determination of the hole concentration is hindered by the anomalous Hall term, experimental data indicate that p is of the order of a 15 to 30 % fraction of that of magnetic ions [6-9]. The

mechanism responsible for the discrepancy between hole and Mn densities is not clear. Matsukura et al [7] have pointed out that such discrepancy might be due to compensation of Mn acceptors by deep donors such as As antisites, which are known to be present at high concentration in low-temperature grown GaAs [10]. However, other mechanisms such as the formation of sixfold-coordinated centers with As ($\text{Mn}^{6\text{As}}$), which would compensate Mn atoms on substitutional Ga lattice sites [11], should not be ruled out. As a consequence, no theory relating the hole concentration and that of Mn has as yet been proposed. However, this issue is of great interest for the design of new devices. The main purpose of the present work is to present a preliminary quantitative analysis on this matter.

THEORETICAL FRAMEWORK

The appearance of ferromagnetism in $\text{Ga}_{1-x}\text{Mn}_x\text{As}$ has been explained on the basis of the following picture. The Mn ions interact with the holes via a local antiferromagnetic Kondo-like exchange coupling J_{pd} between their moments [9,12-15], which results in the polarization of the hole subsystem; this, in turn, gives rise to an effective ferromagnetic coupling between the Mn moments. We point out that there has been some debate as far as the details of the above picture are concerned (e.g., whether or not such effective interaction is well described by an RKKY term [16,17]). Nevertheless, there is consensus on the fundamental role played by the hole-mediated mechanism. We emphasize, however, that the approach we follow here does not depend on the details of the effective Mn-Mn interaction.

We can thus think of two coupled subsystems (localized moments and holes) as described by the total Hamiltonian

$$H = H_{\text{Mn}} + H_{\text{h}} + J_{\text{pd}} \sum_{i,l} \mathbf{S}_i \cdot \mathbf{s}_l \delta(\mathbf{r}_i - \mathbf{R}_l). \quad (1)$$

Here H_{Mn} describes the *direct* (i.e., non-hole-mediated) antiferromagnetic exchange between Mn spins, H_{h} describes the hole subsystem, and the last term corresponds to the aforementioned Mn-hole exchange interaction, with \mathbf{S}_i and \mathbf{s}_l labeling the localized Mn spins ($S = 5/2$) and the hole spins ($s = 1/2$), respectively. As a first approach, we neglect H_{Mn} and consider H_{h} within a parabolic-band effective-mass approximation; a more general description of H_{h} may include a multi-band Kohn-Luttinger treatment [9,18], effects of impurity potentials, a site energy term arising from the Mn potential, and a correlation energy representing hole-hole repulsion.

The problem defined by the Hamiltonian in Eq. (1) is indeed quite complex, but some physical insight can be gained by a mean-field approach. Assuming that the magnetization density of the hole subsystem, $M_{\text{h}} = \langle n_{\uparrow} - n_{\downarrow} \rangle$, is uniform within the length scale of magnetic interactions, the Mn magnetization is given by

$$M = N_{\text{Mn}} g \mu_{\text{B}} M_{\text{I}} = n_{\text{Mn}} g \mu_{\text{B}} S B_{\text{S}} \left[\left(\frac{J_{\text{pd}} S}{2k_{\text{B}} T} \right) M_{\text{h}} \right], \quad (2)$$

where $n_{\text{Mn}} = x n$, is the density of Mn ions, with n , being the density of Ga lattice sites, M_{I} is the magnetization density of the Mn ions, $g = 2$ is the Mn Landé g -factor, and B_{S} is the Brillouin

function. The assumption of homogeneity of the hole magnetization allows us to evaluate M_h self-consistently by considering a Fermi sea of holes with effective mass m^* , in the presence of the mean magnetic field generated by the Mn ions. We therefore find that

$$M_h \propto m^* J_{pd} \propto M_I p^{1/3}. \quad (3)$$

RESULTS AND DISCUSSION

The critical temperature as a function of hole density and Mn composition is obtained by linearizing the self-consistency relations given by Eqs. (2) and (3), i.e.,

$$T_c \propto \left[\left(\frac{m^*}{m_e} \right) J_{pd}^2 \right] x p^{1/3}, \quad (4)$$

which leads one to write the hole concentration as

$$p = \zeta \left\{ \frac{T_c(x)}{(m^*/m_e) J_{pd}^2 x} \right\}^3, \quad (5)$$

where $\zeta = 5.29 \times 10^{-16}$, in units such that J_{pd} is given in eV nm^3 .

The sought-after relation between p and x is provided by Eq. (5). However, it depends on the parameters m^* and J_{pd} , whose values have not been determined with certainty from the experimental data. If one tentatively uses $m^* = m_e$, $J = 0.15 \text{ eV nm}^3$ [14], and the experimental transport data [6] for T_c , the resulting estimates for $p(x)$ are as given by the full circles in Fig. 1. The error bars reflect the uncertainties in the determination of T_c , as displayed in Fig. 3(c) of Ref. 6. Nevertheless, a more reliable estimate can be obtained by adopting the following strategy. Since the Hall resistance measurements [19] yield an unambiguous [20] value of $p = 3.5 \times 10^{20} \text{ cm}^{-3}$ for the sample with $x = 0.053$, for which $T_c = 110 \text{ K}$, one may use Eq. (5) to determine the value of the product $(m^*/m_e) (J_{pd})^2 = 2.4 \times 10^{-2} (\text{eV nm}^3)^2$. Thus, by taking this estimated value along with the experimental data [6] for T_c into Eq. (5), one gets the data for $p(x)$ shown as full squares over a wide range of x . The adequacy of the above procedure is confirmed by the fact that the calculated values for $p(x)$ lie below the concentration of Mn ions, shown as a dotted line, in agreement with experiment. Before accepting these estimates for $p(x)$ at face value, one should note that a closer look at the experimental data for $T_c(x)$ [6] suggests a linear behavior in the range of x of the order 0.015 - 0.035, which would imply, through Eq. (4), a constant p in that range; such constant behavior, however, should not prevail at low concentrations, $x \rightarrow 0$, where presumably one should have $p \propto x \rightarrow 0$. These considerations are incorporated in the full curves displayed in Fig. 1, which lie within the corresponding error bars of the calculated hole concentrations.

The boundaries of the metal-insulator transitions (MIT's), as determined from resistivity measurements [6], are indicated in Fig. 1 by vertical dashed lines. We remark that the present theoretical estimates for p in the insulating phases are based on the assumption that the scale

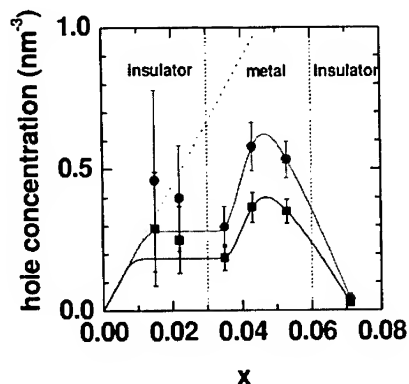


Figure 1. Theoretical results for the hole concentration as a function of the fraction of Mn sites for (Ga,Mn)As ferromagnetic alloys. The dashed line corresponds to a hole concentration equal to that of Mn sites, whereas the filled circles and squares are the present mean-field results. Full curves are obtained as reasoned in the text. I and M respectively denote insulating and metallic phases.

of localization length in insulating samples, though finite, is significantly larger than the length of magnetic interactions [9], in which case the present mean-field approach is a good starting point.

The most prominent feature of Fig. 1 is the fact that $p(x)$ displays a maximum within the metallic phase. It means that attempts to increase T_c should be carried out for samples in the metallic phase, for Mn concentrations about 0.05. Moreover, notwithstanding the considerable uncertainties [21] in the measurements of p , the present theoretical estimates for the hole concentration exhibit trends in quite good agreement with those obtained from Hall measurements by Matsukura et al [7].

The fact that the dependence of p with x is essentially related to the occurrence of MIT's taking place in the hole subsystem can be seen from the following qualitative picture. Within our approximation, the Fermi energy tracks the behavior of p , since $\epsilon_F \propto p^{2/3}$, while the exchange splitting $\Delta \propto x$. Figure 2(a) shows the schematic impurity bands for each spin channel, in the very-low doping regime in which the gas is supposed to be unpolarized. As x increases, the gas can sustain polarization and still be insulating, provided the Fermi energy lies below the mobility edge, as shown in Fig. 2(b). Further increase in x causes ϵ_F to increase and to lie within the delocalized states of the up-spin impurity band, as depicted in Fig. 2(c): The system becomes metallic. Whether or not the Fermi energy also lies within the delocalized region of the down-spin impurity band is a very interesting question, which cannot be answered by our simple model; the solution of this particular issue should have bearings on the efficiency of $\text{Ga}_{1-x}\text{Mn}_x\text{As}$ -based devices as spin filters. Once ϵ_F reaches a maximum within the metallic phase, its initial decrease upon increasing x is compensated by an increase in Δ , so that the Fermi level still lies within the delocalized states. However, with continuing increase in x the exchange splitting can no longer make up for the decrease in ϵ_F , and the latter eventually crosses the mobility edge again, lying within localized states [Fig. 2(d)]: The system reenters an insulating phase.

The simple approach used in the present work provides a straightforward and immediate estimate of the hole concentration in $\text{Ga}_{1-x}\text{Mn}_x\text{As}$ as a function of both x and T_c [22], which is an important ingredient to guide further experimental work on this subject. Clearly, the present

approach could be extended to include a more complete description of the acceptor states, taking into account the spin degrees of freedom, spin-orbit coupling, compressive/tensile strains, etc. Moreover, a proper treatment of disorder -- e.g., by explicitly considering a random, instead of continuous, distribution of Mn ions -- should lead to a more realistic description of the MIT. In this respect, many-body effects due to correlation among the holes should also influence $p(x)$, especially in the insulating phase. Of course, an appropriate description of the physical mechanisms related to As antisites and $\text{Mn}^{6\text{As}}$ centers, as far as the hole vs. Mn concentrations is concerned, is certainly a formidable task, which nonetheless deserves future theoretical attention.

In summary, we have considered a mean-field theory for the hole-mediated coupling between the localized Mn moments in $\text{Ga}_{1-x}\text{Mn}_x\text{As}$. The hole concentration as a function of the fraction of Mn sites is obtained in terms of the product $m^*(J_{pd})^2$ and the critical temperature T_c . By using experimental data for these latter quantities, we have established that the occurrence of a reentrant MIT taking place in the hole gas can be traced back to the dependence of the hole concentration with x . Although not shown here, we have also calculated the dependence of the Mn magnetization with x , for different temperatures, and found that as T increases, the width of the composition-dependent magnetization decreases dramatically, and that the magnetization maxima also decreases, indicating the need for quality-control of Mn doping composition in DMS devices.

ACKNOWLEDGMENTS

The authors are grateful to the Brazilian Agencies CNPq, FAPESP, FAEP-UNICAMP, and FAPERJ for partial financial support.

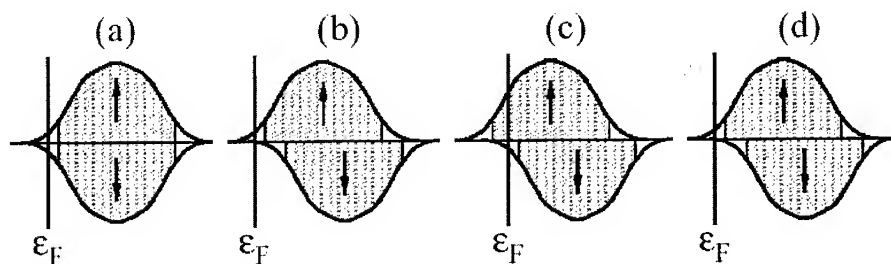


Figure 2. Schematic density of states (DOS) versus energy for the impurity band, for up- (top) and down-spins (bottom). Under each DOS curve, the hashed and empty regions correspond, respectively, to delocalized and localized states; these are separated by mobility edges. The exchange splitting is proportional to the off-set between the \uparrow and \downarrow bands, and the Fermi energy (ϵ_F) increases to the right.

REFERENCES

1. H. Ohno, H. Munekata, T. Penney, S. von Molnár, and L. L. Chang, *Phys. Rev. Lett.* **68**, 2664 (1992).
2. H. Ohno, A. Shen, F. Matsukura, A. Oiwa, A. Endo, S. Katsumoto, and Y. Iye, *Appl. Phys. Lett.* **69**, 363 (1996).
3. H. Ohno, *Science* **281**, 951 (1998); R. Fiederling, M. Kelm, G. Reuscher, W. Ossau, G. Schmidt, A. Waag, and L. W. Molenkamp, *Nature* **402**, 787 (1999); Y. Ohno, D. K. Young, B. Beschoten, F. Matsukura, H. Ohno, and D. D. Awschalom, *Nature* **402**, 790 (1999); H. Ohno, *J. Magn. Magn. Mater.* **200**, 110 (1999); T. Dietl, H. Ohno, F. Matsukura, J. Cibert, and D. Ferrand, *Science* **287**, 1019 (2000).
4. D. P. DiVincenzo, *J. Appl. Phys.* **85**, 4785 (1999).
5. T. Hayashi, M. Tanaka, and T. Nishinaga, *J. Appl. Phys.* **81**, 4865 (1997).
6. H. Ohno and F. Matsukura, *Solid State Commun.* **117**, 179 (2001).
7. F. Matsukura, H. Ohno, A. Shen, Y. Sugawara, *Phys. Rev.* **B57**, R2037 (1998).
8. J. Szczytko, W. Mac. A. Twardowski, F. Matsukura, and H. Ohno, *Phys. Rev.* **B59**, 12935 (1999).
9. T. Dietl, H. Ohno, and F. Matsukura, *Phys. Rev.* **B63**, 195205 (2001).
10. D. C. Look, *J. Appl. Phys.* **70**, 3148 (1991).
11. A. Van Esch, L. Van Bockstal, J. De Boeck, G. Verbanck, A. S. van Steenberghe, P. J. Wellmann, B. Grietens, R. Bogaerts, F. Herlach, and G. Borghs, *Phys. Rev.* **B56**, 13103 (1997).
12. T. Dietl, A. Haury, and Y. Merle d'Aubigné, *Phys. Rev.* **B55**, R3347 (1997).
13. T. Jungwirth, W. A. Atkinson, B. H. Lee, and A. H. MacDonald, *Phys. Rev.* **B59**, 9818 (1999).
14. B. Lee, T. Jungwirth, and A. H. MacDonald, *Phys. Rev.* **B61**, 15606 (2000).
15. S. P. Hong, K. S. Yi, and J. J. Quinn, *Phys. Rev.* **B61**, 13745 (2000).
16. J. König, H.-H. Lin, and A. H. MacDonald, *cond-mat/0010471*.
17. V. I. Litvinov and V. K. Dugaev, *Phys. Rev. Lett.* **86**, 5593 (2001).
18. M. Abolfath, T. Jungwirth, J. Brum, and A. H. MacDonald, *Phys. Rev.* **B63**, 054418 (2001).
19. H. Ohno, F. Matsukura, T. Omiya, and N. Akiba, *J. Appl. Phys.* **85**, 4277 (1999).
20. The currently accepted value $p = 3.5 \times 10^{20} \text{ cm}^{-3}$ is a factor 2.3 larger than the early estimate; see Ref. 3.
21. See, e.g., Fig. 2 of Ref. 7: for $x = 0.022$, the experimentally determined p has an error bar which covers over one decade, while for $x = 0.071$ the error bar runs over two decades.
22. For a treatment of the same model within spin-wave theory and dynamical mean-field theory, see J. König, H.-H. Lin, and A. H. MacDonald, *Phys. Rev. Lett.* **84**, 5628 (2000); *ibid.* **86**, 5637 (2001), and A. Chattopadhyay, S. Das Sarma, and A. J. Millis, *cond-mat/0106455*. The explicit dependence of p with x , however, is not discussed in those works.

PHOTOLUMINESCENCE FROM Er-IMPLANTED 4H AND 6H-SiC

Shin-ichiro Uekusa and Takayuki Goto

Department of Electrical and Electrical Engineering, Meiji University,
1-1-1, Higashi-mita, Tama-ku, Kawasaki-city, Kanagawa-ken, 214-8571, Japan

ABSTRACT

Erbium (Er) ions were implanted into 4H and 6H silicon carbide (SiC). The temperature-dependent photoluminescence (PL) and PL lifetime were characterized. The optimum annealing temperature for SiC : Er were 1600 °C. PL intensity decreased at 1700 °C, and the bandedge luminescence changed in relation to the luminescence of Er³⁺. Thermal quenching of the luminescence of Er³⁺ was suppressed by using SiC with a wide band gap as a host material. The Er³⁺-PL was observed at room temperature (RT). We monitored the auger effect that is believed to be the main cause of the thermal quenching process and concluded that, in the temperature range 15 K to 70 K, the thermal quenching process has a close relation to nonradiative recombination from the first excited state (⁴I_{13/2}) to the ground state (⁴I_{15/2}) of Er³⁺.

INTRODUCTION

An Erbium (Er)-doped semiconductor is a potentially useful material for light-emitting devices in optical communication systems, since the intra-4f-shell transitions of Er ions cause sharp and temperature-stable luminescence in various host materials [1], [2] at 1.54 μm, which corresponds to the minimum absorption of silica-based optical fibers.

Photoluminescence (PL) from Er³⁺ in Er-doped narrow band gap semiconductors [e.g., silicon (Si)] has been reported [3]-[7], but the PL is weak and difficult to observe at room temperature (RT). One of the reasons for difficulties in obtaining the Er³⁺-PL at RT is the low level of probability of Er excitation via recombination of free carriers, as has been theoretically explained by *Needles* et al. [8].

However, an increase of Er³⁺ luminescence could be realized by the introduction of light impurities, such as C, N, and O, and by using a wide band-gap material as a host material. The influence of the introduction of light elements on Er³⁺ luminescence in Si: Er and GaP : Er was studied by us using standard PL and photoluminescence excitation (PLE) techniques [1], [2]. We proposed that light

elements form complexes with the Er atoms and an efficient excitation of Er^{3+} occurs via a recombination of the electron-hole (e-h) pair, where one of the carriers located at Er-complex-related deep levels in the forbidden-gap [1], [2].

Silicon carbide (SiC), anticipated to be a useful material for high-temperature applications, is a very useful host material because it has a wide band gap and improves the luminescence properties of the Er^{3+} ions [9]-[12]. The aim of this work is, therefore, to investigate the effect of a wide band-gap host material on Er^{3+} luminescence. We use 4H and 6H-SiC as host materials.

EXPERIMENT

The wafers used in this work, which are single crystal SiC wafer produced by Lely method, (obtained from *Cree Research, Inc.*) were nitrogen doped hexagonal polytypes 4H and 6H-SiC. The orientation of the wafer flat is $\langle 11\bar{2}0 \rangle$ direction. The n-type wafer is uniformly predoped with nitrogen. The polished side, terminated with Si, is used for the implantation. Er implantation was carried out at 2 MeV with doses of $1 \times 10^{14} \text{ cm}^{-2}$ at RT. The projected range (R_p) and straggling (ΔR_p) for the Er implant profile were calculated by TRIM to be 505.1 and 78.8 nm, respectively. In order to be compared with SiC:Er, Ytterbium (Yb) ions were implanted into 4H-SiC. Yb implantation was carried out at 2MeV with doses of $1 \times 10^{13} \text{ cm}^{-2}$ at RT. The projected range for the implanted Yb ions was almost the same as that for the Er ions. We held their samples on carbon plate using a quartz sample holder in the rapid thermal annealing apparatus (RTA). The samples were annealed at temperatures ranging from 1400 to 1700 °C for 40 min in a pure argon (Ar) atmosphere (purity:99.999%) using a halogen flash lamp. The heating and cooling rates were 7.1 °C/s. Before annealing, the apparatus was pumped down to a base pressure of 5×10^{-6} Torr before Ar gas was fed into the vacuum chamber. Samples were placed into a closed-cycle helium gas cryostat and were held at temperatures ranging from 15 to 300 K. PL was excited using the 325-nm line of a mechanically chopped helium-cadmium (He-Cd) laser. The penetration depth of the He-Cd laser (325 nm) for SiC was approximately 520 nm. This depth value was calculated from published absorption coefficient data [13]. The PL spectrum was recorded in a standard lock-in configuration using a 1-m double monochromator, and a InGaAs photomultiplier (*Hamamatsu Photonics R5509-72*).

RESULT and DISCUSSION

Figure.1 shows greater detail of the evolution of the Er spectra in 4H-SiC:Er as warming up the sample from 15 K to R.T.. Several peaks were observed at around 1.5 μ m and the dominant peak is located at 1534.0 nm. For the hexagonal polytypes 4H-SiC and 6H-SiC, the 15 K spectrum is very similar with a dominant line at 1534.0 nm and 12 peaks or other small peaks. In order to optimize the luminescence intensity of Er³⁺, we investigated its annealing temperature dependence. As to the Er-related PL spectra of SiC:Er for different annealing temperatures, from 1400 °C to 1600 °C, the shape of Er-related spectra became sharp and the PL intensities increased on increasing the annealing temperature.

Both PL intensities in the sample annealed at 1700 °C decreased as compared with those of the sample annealed at 1600 °C. It has been reported that a layer of carbon (C) is formed on the sample surface by the sublimation of Si atoms at or above 1500 °C[14], [15]. At 15 K there is 13 peaks visible at higher energy than the peak(1) at 1515.2 nm. 2 peaks [(a), (b)] were seen at 40K, and peak(d) was seen at 160K. After all, at 300 K we have sprouted 3 peaks at higher energies of which were actually larger than the original peak(1) at 1515.2 nm. Er³⁺-related PL was observed at R.T. by using SiC with a wide band gap as a host material. These data strongly suggest that at each temperature we are seeing transitions from excited states of the crystal field spin orbit levels of Er³⁺, $^4I_{13/2} \rightarrow ^4I_{15/2}$.

Figure.2 shows the temperature dependence of the Er³⁺-related PL intensity at the dominant peak(5) of wavelength 1534.0 nm in SiC:Er. In Fig.2 the experimental data were plotted along with the theoretical (solid line) based on eq.1 [16] using the parameters (C_1 , C_2 , C_3 , E_1 , E_2 , E_3) shown in Table 1.

$$I(T)=I_0/(1+C_1\exp(-E_1/kT)+C_2\exp(-E_2/kT)+C_3(-E_3/kT)) \quad (1)$$

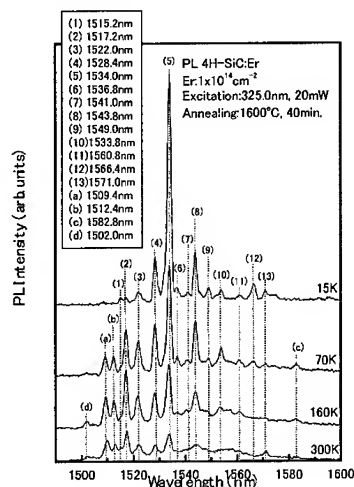


Fig.1 The temperature dependence of the Er³⁺-related PL spectra of 4H-SiC:Er

15~70K	C_1	E_1 (meV)
	4	8
70~160K	C_2	E_2 (meV)
	9.5	40
160~300K	C_3	E_3 (meV)
	100	100

Table 1. Fitting parameter for dominant peak of SiC:Er used in eq.1

In the above equation I_0 is the intensity at which the electron emission from the Er^{3+} -related trap can be neglected. Hence it corresponds to the intensity at a very low temperature. T is temperature, E_1 and E_2 are the activation energies, and k is the Boltzmann constant C_1 , C_2 and C_3 are the coupling coefficients at E_1 , E_2 and E_3 respectively. The experimental data well fitted by eq.(1). Peak(3), (4) and (12) were not able to do the fitting because the luminescence strength increased with the rise of measurement temperature. Table1 shows the activation energy (E_1 , E_2 and E_3) and fitting parameter (C_1 , C_2 and C_3).

Figure3 shows dominant peak(5) has different behavior for temperature dependence compared with other peak. Therefore it is clear that there are at least two thermal quenching processes. We can't say for certain whether Er atoms occupy the Si or C sites. It may be that Er atoms occupy

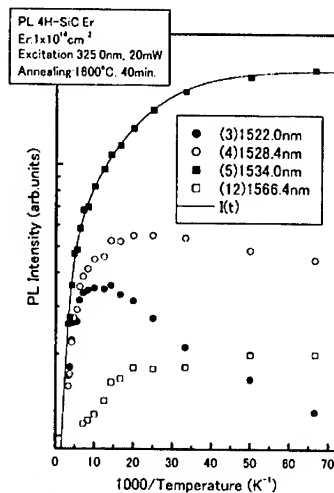


Fig.2 The temperature dependence of the Er^{3+} -related PL intensity at each peak of 4H-SiC:Er with fitting

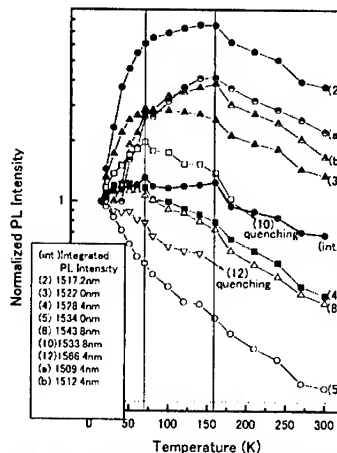


Fig.3 The temperature dependence of the Er^{3+} -related PL intensity at each peak of 4H-SiC:Er

interstitial sites. However, we have already investigated the mechanism of the luminescence of Er^{3+} in Si, which was due to the presence of Er-C complexes [2]. On these grounds, we conclude that Er forms at least two Er-C complex centers with C which contribute to the luminescence of Er^{3+} in SiC:Er.

Figure.4 shows the temperature dependence of the Yb^{3+} -related PL intensity at the dominant peak(3) of wavelength 999.8 nm in SiC:Yb. In the range 940.0 nm-1040.0 nm, 5 peaks correspond in location to the luminescence levels of the Yb ion in the 4H-SiC crystal. Yb is a typical uncontrollable impurity in SiC.

Both Er and Yb temperature dependence (shown in Fig.3 and Fig.4) are very similar characteristics. The similar feature of the observed PL of Er and Yb were the unusual temperature dependence of its intensity although Er^{3+} -related PL intensity increased with rising temperature. As the temperature increases beginning with 15K, both PL intensity of Er and Yb rapidly increase and reach a maximum value at 70 K. On the other hand, as the temperature increased beginning with 70 K, both PL intensity of Er and Yb rapidly decreased. By investigating these results, it is suggested that at more than at 70 K, electrons and excitons can't be capture by one level and the position of the level is in 6 meV under the conduction band.

Figure.5 shows the luminescence decay curve of the Er^{3+} -related PL intensity at the peak of 1534.0 nm in SiC:Er. Biexponential decay times τ was estimated via component stripping and are shown in Fig.5. We estimated the radiative decay time(τ_r) and nonradiative decay time (τ_{nr}) using eq.2, eq.3 and the value of measured lifetime τ in Fig.5. The value of τ in the luminescence decay curve, τ is shown in Figure6.

$$1/\tau(T) = 1/\tau_r(T) + 1/\tau_{nr}(T) \quad (2)$$

$$I(T) = \eta(T) \cdot I_0 \quad (3)$$

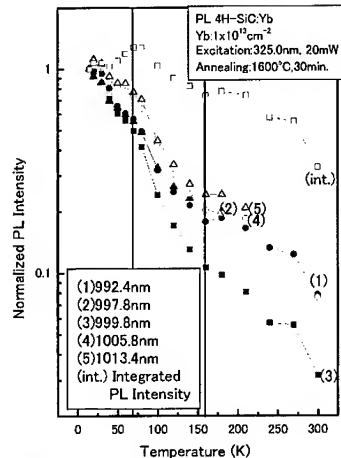


Fig.4 The temperature dependence of the Yb^{3+} -related PL intensity at each peak of 4H-SiC:Yb

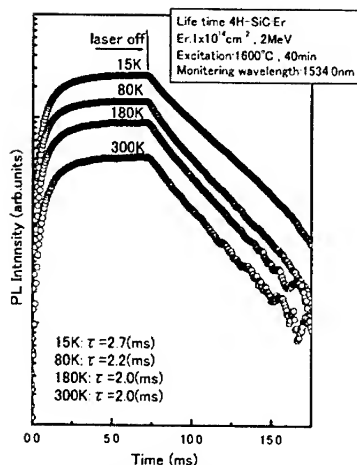


Fig.5 The temperature dependence of the luminescence curve of the Er^{3+} -related PL intensity at the peak of 1534.0 nm

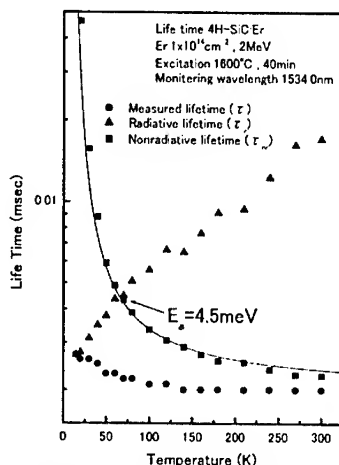


Fig.6 The temperature dependence of the τ , τ_{nr} and τ_r

In Figure.6 the experiment data were plotted along with the theoretical (solid line) based on eq.4 [17] using the parameter (E_a).

$$\tau_{nr} = (1/N_B v \sigma) \cdot \exp(E_a/kT) \quad (4)$$

As a result, $E_a = 4.5 \text{ meV}$. In the above equation, N_B is the density of nonradiative center, v is the thermal velocity of the carrier, σ is the capture cross section of nonradiative centers, E_a is the activation energy. T is temperature and k is the Boltzmann constant. The values of $E_1 (= 8 \text{ meV})$ approximately coincided with the value of E_a . Therefore we conclude that the thermal quenching process, which occurs in the low-temperature range ($15 \text{ K} < T < 70 \text{ K}$), reflects the nonradiative recombination in the transition from the first excited state ($^4I_{13/2}$) to the ground state ($^4I_{15/2}$) of Er.

To summarize we showed the proposed mechanism and scheme of these energy levels in Figure 7.

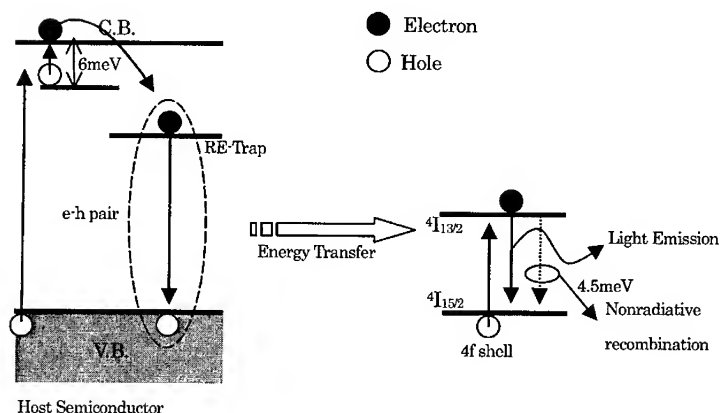


Fig.7 Possible scheme of the energy levels and mechanisms of energy transfer in the hexagonal SiC

CONCLUSION

From above results, we can conclude as follows.

- (1) It was found that the optimum annealing temperature and time for 4H and 6H-SiC were 1600 °C, 40 min., respectively.
- (2) By investigating the temperature dependence of the Er^{3+} -related PL intensity, we found that thermal quenching of the luminescence of Er^{3+} was suppressed by using SiC, instead of Si, as a host material, and that Er forms at least two Er-C complex centers with C which contribute to the luminescence of Er^{3+} in SiC:Er. Er^{3+} -related PL was observed at R.T. by using hexagonal polytypes 4H and 6H-SiC with a wide band gap as a host material.
- (3) By investigating the temperature dependence of the Er^{3+} and Yb^{3+} -related PL intensities we consider that at more than at 70K, electrons and excitons can't be capture by one level. It is suggested that the position of the level is in 6meV under the conduction band.
- (4) The thermal quenching process in the low-temperature range from 15K to 70K shows has a close relation to nonradiative recombination in the transition from the first excited state ($^4I_{13/2}$) to the ground state ($^4I_{15/2}$) of Er^{3+} .

ACKNOWLEDGMENTS

The authors thank Dr. Ken Numata of Kanagawa High-Technology Foundation for his technical support on ion implantation. This work is supported in part by Grant-in-Aids for Research Project Grant and High-Technology Research Center in Meiji University.

REFERENCES

- [1] S. Uekusa, T. Ohshima, A. Majima, and M. Kumagai, "Optical activation of the Er^{3+} emissions from GaP coimplanted with nitrogen," in Proc. 1994 Int. Workshop on Electroluminescence, Beijing, China, 1994, pp. 279-283.
- [2] S. Uekusa, K. Shimazu, A. Majima, and K. Yabuta, "Optical activation of Er^{3+} in silicon co-implanted with carbon, " Nucl. Instrum. Meth. B, vol. 106, pp. 477-479, 1995.
- [3] A. Majima, S. Uekusa, K. Abe, and M. Kumagai, "1.54 μm luminescence of Er-MeV implanted silicon, " J. Lumin., vol. 60/61, pp.595-598, 1994.
- [4] Y. S. Tang, K. C. Heasman, W. P. Gillin, and B. J. Sealy, "Characteristics of rare-earth element erbium implanted silicon, " Appl. Phys. Lett., vol.55, pp.432-433, 1989.
- [5] J. H. Shin, G. N. van den Hoven, and A. Polman, "Direct experimental evidence for trap-state mediated excitation of Er^{3+} in silicon, " Appl. Phys. Lett., vol.67, pp.377-379, 1995.
- [6] H. Przybylinska, G. Hendorfer, M. Bruckner, L. Palmetshofer, and W. Jantsch, "On the local structure of optically active Er centers in Si, "Appl. Phys. Lett., vol.66, pp.490-492, 1995.
- [7] F. Priolo, C. Fianzo, S. Coffa, A. Polman, S. Libertino, R. Barklie, and D. Carey, "The erbium-impurity interaction and its effects on the 1.54 μm luminescence of Er^{3+} in crystalline silicon," J. Appl. Phys., vol.78, pp.3874-3882, 1995.
- [8] M. Needles, M. Shluter, and M. Lannoo, "Er point defect in silicon," Phys. Rev., vol.B47, pp.15533-15536, 1993.
- [9] W. J. Choyke, R. P. Devaty, L. L. Clemen, M. Yoganathan, G. Pensl, and C. Hassler, "Intense erbium-1.54 μm photoluminescence from 2 to 525 K in ion-implanted 4H, 6H, 15R and 3C SiC," Appl. Phys. Lett., vol.65, pp.1668-1670, 1994.

- [10] S. Uekusa, K. Awahara, and M. Kumagaya, "Photoluminescence from Er-implanted polycrystalline 3C SiC," IEEE Trans. Elect. Dev., vol.46, pp572-576, 1999.
- [11] R. A. Babunts, V. A. Vetrov, I. V. Il'in, E. N. Mokhov, N. G. Romanov, V. A. Khramtsov, and P. G. Baranov, "Propertise of erbium luminescence in bulk crystals of silicon carbide" Physics of Solid State, vol.42, pp809-815.
- [12] T. Goto, S. Uekusa, "Photoluminescence from Er-implanted 4H-SiC," 48th Oyo Butsuri abstract book, pp1397 (28p-YK-2), 2001.
- [13] T. Tako, and T. Ikoma, et al., Oyo Butsuri data book, The Japan Society of AppliedPhysics, Ed., Maruzen, Japan. 1994, p.327.
- [14] S.-I. Uekusa, K. Awahara, and M. Kumagai, "Luminescence properties of Er implanted polycrystalline 3C SiC," Materials Science Forum, Silicon Carbide, III-Nitrides and Related Materials, vols.264-268, pp.505-508, 1998.
- [15] Y. Hirabayashi, M. Furuya, K. Hirai, H. Takano, K. Yabuta, and M. Kumagai, "Effect of isostatic press annealing for ion-implanted silicon carbide," Materials Science Forum, III-Nitrides and Related Materials, vols. 264-268, pp.749-752, 1998.
- [16] B. A. Wilson, W. M. Yen, J. Hegarty, and G. F. Imbusch, "Luminescence from pure MnF₂ and from MnF₂ doped with Eu³⁺ and Er³⁺," phys. Rev., vol.B19, pp.4238-4250, 1979.
- [17] J. S. Massa, G. S. Buller, A.C. Walker, J. Smpson, K. A. Prior, and B. C. Cavenett: Appl. Phys. Lett.67 (1995) 61.

Control of ZnO Morphology by Solution Route

Lingdong Sun, Jun Zhang, Chunsheng Liao, Chunhua Yan
State Key Laboratory of Rare Earth Materials Chemistry and Applications,
PKU-HKU Joint Laboratory on Rare Earth Materials and Bioinorganic Chemistry,
Peking University, Beijing 100871, China

ABSTRACT

In this paper, ZnO with a rich variety of well-defined morphologies have been achieved by solution route using different kind of precursors, which can prepare particles by only one step without calcination. The influences of solvent, and temperature on the particle size and morphology of ZnO were investigated. It was revealed by the scanning electron microscope (SEM) and transmission electron microscope (TEM) images that the morphological feature of ZnO can be controlled as rod-, polyhedron-, fluffy sphere-, snowflake- and flower-like, etc. XRD measurement showed that all of the ZnO samples with different morphologies has the same hexagonal structure, which is well consistent with electron diffraction (ED) characterization. This communication not only provides promising candidates for materials science due to the importance of shape in relationship with materials, but also presents an effective route to synthesize the well-defined inorganic materials.

INTRODUCTION

More attentions nowadays are paid on studies of the morphology control of inorganic materials, because the properties are liable to be tailored for diversified morphologies [1]. Except for focusing on sulfide or selenide nanocrystals [2-6], the studies on diversity of oxides, especially ZnO, are going on.

ZnO, as a wide band gap semiconductor, has been investigated both in fundamental and application studies [7-9]. The reports of ZnO with controlled size and morphology emerged endlessly in order to fine-tune the properties for practical applications, especially to realize the novel lasing effect [10]. Hydrothermal synthesis [3,11], as a mild reaction route, can be performed at a relatively lower temperature to produce the sufficiently crystallized products without further calcination. Previous works were extremely focused on the influence of the reaction condition on size of as-prepared ZnO, or on the simple morphologies, such as sphere- or rod-like ZnO particles [12].

In this communication, hexagonal structured ZnO with a rich variety of well-defined morphologies, have been obtained by solution routes. Some of the morphologies shown the fractal patterns and may have the potential applications for strong light scattering and localization, which are important for lasing [13]. The influences of temperature, and solvent on the particle size and morphology of ZnO were investigated.

EXPERIMENTAL DETAILS

The zinc precursor solution containing $\text{Zn}(\text{OH})_4^{2-}$ or $\text{Zn}(\text{NH}_3)_4^{2+}$ was prepared by adjusting the pH of zinc acetate solution (ZnAc_2 , 0.50 mol/L) with NaOH or ammonia to 14 and 10, respectively. The precursor was transferred into a 25 mL teflon-lined autoclave and heated to a certain temperature for a given time to form ZnO. After cooled to room temperature, the white precipitate was collected, and then washed with absolute ethanol and distilled water several times. Finally, ZnO samples were obtained by centrifugation and drying in a vacuum at 60–70 °C. In order to control the morphology, different kinds of solvent media can be selected.

The structure of all ZnO samples is wurtzite (hexagonal phase, space group $\text{P6}_3\text{mc}$) determined by XRD and ED. All of the diffraction peaks are well indexed to the hexagonal phased ZnO reported in JCPDS card (No. 36-0145).

DISCUSSION

Based on the decomposition of soluble $\text{Zn}(\text{OH})_4^{2-}$ or $\text{Zn}(\text{NH}_3)_4^{2+}$, by adjusting the reaction condition in different processes, a rich variety of ZnO with certain morphology can be obtained. For this solution route synthesis, the solvent is polarity tempered from water, ethanol to n-heptane. Polyhedron, short rod, and fluffy nanocomposite ZnO were obtained (Fig. 1) by ethanol solvent. Reacted at 100 °C for 13 h, ZnO from decomposition of the two kinds of $\text{Zn}(\text{NH}_3)_4^{2+}$ or $\text{Zn}(\text{OH})_4^{2-}$ precursors, have distinct morphologies, polyhedron and fluffy nanocomposite (Fig. 1a and 1b, respectively). The uniform fluffy nanocomposite was composed of needle-like rods with several tens of nanometers in width. Increased the reaction temperature to 180 °C, fluffy sphere evolved to uniform rod-like ZnO (Fig. 1c). The diameter of the rod is about 100 nm and the aspect ratio is about 5. The ED patterns proved the preferred growth direction is along the C-axis for the rod like ZnO crystals, which is the same as other one-dimensional ZnO materials [7]. The hexagonal like ZnO microcrystals have been reported and its growth mechanism is deduced. It is quite interesting that the nanorods can not be grow into microcrystals even with prolonged growth time.

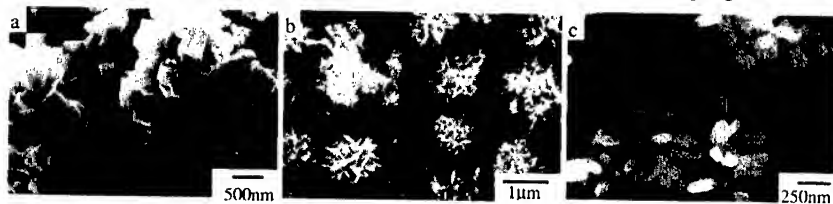


Figure 1 SEM images of ZnO prepared by using ethanol as reaction media (a) polyhedron-like ZnO (pH~10, 100 °C, 13 h), (b) fluffy sphere-like ZnO (pH~14, 100 °C, 13 h), (c) short rod-like ZnO (pH~14, 180 °C, 13 h).

The flower- and snowflake-like ZnO, shown in Fig. 2, were synthesized by using $\text{Zn}(\text{OH})_4^{2-}$ (pH~14) as precursors and H_2O or n-heptane as solvent, respectively. There are two kinds of flower-like ZnO as the two magnified images shown in the insets of Fig. 2a. It seems like they grow from a center nucleus. The different polarity of solvents, H_2O and n-heptane, sensitively determines the nucleation and shape evolution, what is the main reason caused the diversified morphology is still under active investigation.

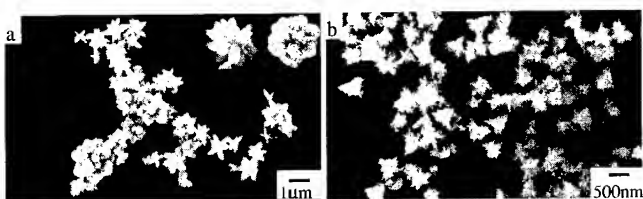


Figure 2 SEM images of ZnO prepared by using H₂O and n-heptane as reaction media, respectively. (a) flower-like ZnO using H₂O as solvent (pH~14, 180 °C, 13 h), the magnified images are the two kinds of particle patterns, (b) snow flake-like ZnO formed using n-heptane as solvent (pH~14, 180 °C, 13 h).

CONCLUSIONS

The diversiformed ZnO have been achieved by solution routes. The reaction temperature and solvent was studied for the influence on the particle size and morphology. This communication not only obtained ZnO with unusual and well-defined morphologies, which can be used as the potential candidates for the fabrication of the new application devices, but also afforded an effective way to synthesize inorganic materials with diverse morphology.

Acknowledgment This work was supported by NSFC (20001002, 20023005, 29831010), MOST (G19980613), MOE and the Founder Foundation of PKU.

References

1. Yang, H.; Coombs, D.; Ozin, G. A. *Nature*. **386**, 392 (1997).
2. Pinna, N.; Weiss, K.; Urban, Joachim.; Pileni, M. P. *Adv. Mater.* **13**, 261 (2001).
3. Yang, J.; Cheng, G. H.; Zeng, J. H.; Yu, S. H.; Liu, X. M.; Qian, Y. T. *Chem. Mater.* **13**, 848(2001).
4. Peng, X.; Manna, L.; Yang, WD; Wickham, J; Scher, E; Kadavanich, A; Alivisatos, A. P. *Nature*. **404**, 59 (2000).
5. Peng, Z. A.; Peng, X. G. *J. Am. Chem. Soc.* **123**, 1389 (2001).
6. Jun, Y. M.; Lee, S. M.; Kang, N. J.; Cheon, J. W. *J. Am. Chem. Soc.* **123**, 5150 (2001).
7. Pan, Z. W.; Dai, Z. R.; Wang, Z. L. *Science*. **291**, 1947 (2001).
8. Kong, Y. C.; Yu, D. P.; Zhang, B.; Fang, W.; Feng, S. Q. *Appl. Phys. Lett.* **78**, 407 (2001).
9. Li, Y.; Meng, G. W.; Zhang, L. D.; Phillipp, F. *Appl. Phys. Lett.* **76**, 2011 (2000).
10. Huang, M. H.; Mao, S.; Feick, H.; Yan, H. Q.; Wu, Y. Y.; Kind, H.; Weber, E.; Russo, R.; Yang, P. D. *Science*. **292**, 1897 (2001).
11. Jezequel, D.; Guenot, J.; Jouini, N.; Fievet, F. *J. Mater. Res.* **10**, 77 (1995).
12. Sekiguchi, T.; Miyashita, S.; Obara, K.; Shishido, T.; Sakagami, N. *J. Cryst. Growth*. **214/215**, 72 (2000).
13. Cao, H.; Zhao, Y. G.; Ho, S. T.; Seelig, E. W.; Wang, Q. H.; Chang, R. P. H. *Phys. Rev. Lett.* **82**, 2278 (1999).

Influence of Er and O doses in Er-related emission in $\text{Al}_{0.70}\text{Ga}_{0.30}\text{As:Er}$

Shin-ichiro Uekusa and Tomoyuki Arai

Department of Electrical and Engineering, Meiji University, 1-1-1
Higashi-mita, Tama-ku, Kawasaki, Kanagawa, Japan**ABSTRACT**

Er ions with doses ranging from $1 \times 10^{13} \text{ cm}^{-2}$ to $1 \times 10^{15} \text{ cm}^{-2}$ were implanted into $\text{Al}_{0.70}\text{Ga}_{0.30}\text{As}$ on GaAs substrates. at 800 °C. Photoluminescence (PL) intensity of Er-related emission around 1.54 μm was enhanced by co-implanted oxygen (O). The optimum dose of Er ion was $1 \times 10^{14} \text{ cm}^{-2}$ and O ion was $1 \times 10^{15} \text{ cm}^{-2}$, respectively. Furthermore, from the temperature dependence of the PL intensity of sample implanted with the optimum dose, we estimated the values of E_1 , E_2 , and E_3 , the activation energies in order to investigate the rapid thermal quenching of Er ion in $\text{Al}_{0.70}\text{Ga}_{0.30}\text{As}$. We found that PL intensity of Er-related emission, in addition to O dose, was enhanced approximately twenty two times at room temperature. And from the temperature dependence of the lifetime of the optimum dose of Er and O, the value 245meV of E_A , the activation energy for the decrease of the lifetime, was nearly equal to the value 235meV of E_3 . Based on the result, the decrease of the lifetime confirms that the radiative efficiency is lower; therefore, we propose that rapid thermal quenching occurs at temperatures above 200 K due to the decrease of the radiative efficiency.

INTRODUCTION

Rare-earth(RE) impurities in III-V semiconductors have attracted much attention due to their potential applications in new emitting devices and based on the internal emission from the 4f levels of the impurity. The intra-4f shell transitions cause sharp and temperature-stable luminescence because of shielding by outer electronic shells. [1,2] Therefore the research on the optical devices, which involves RE element, has been advanced. Er is attractive for obtaining light emitting device in silica-fiber-based optical communication systems. As a matter of fact, the luminescence from Er^{3+} ion occurs at a wavelength of 1.54 μm [3,4], which corresponds to the minimum absorption of silica-based optical fibers.

However Er-doped semiconductors have problems such as low energy transition efficiency from the host semiconductor to the intra-4f-shell of Er^{3+} ions. Therefore it is important that we understand the mechanism of the energy transition. We have

previously reported photoluminescence (PL) properties for the dependence of the composition ratio (x) in $\text{Al}_x\text{Ga}_{1-x}\text{As}$, and the influence of light elements (O, N, and C) on the low dosage $1 \times 10^{13} \text{ cm}^{-2}$ of Er. [4]

In this work, we studied the influence of O on Er^{3+} -related emission with the high Er doses ranging from $1 \times 10^{14} \text{ cm}^{-2}$ to $1 \times 10^{15} \text{ cm}^{-2}$.

EXPERIMENT

Er^{3+} ion of 1 MeV were implanted into undoped $\text{Al}_{0.70}\text{Ga}_{0.30}\text{As}$ (100) grown by molecular beam epitaxy (MBE) with doses ranging from $1 \times 10^{13} \text{ cm}^{-2}$ to $1 \times 10^{15} \text{ cm}^{-2}$ at room temperature. The projected range (R_p) and straggling (ΔR_p) for implant profile were calculated by materials computer program (TRIM) to be 205.7 and 58.4nm, respectively. O ion were implanted into $\text{Al}_{0.70}\text{Ga}_{0.30}\text{As}:\text{Er}$ with doses ranging from $1 \times 10^{13} \text{ cm}^{-2}$ to $3 \times 10^{15} \text{ cm}^{-2}$ at an energy of 130 keV. The R_p of the implanted O ions was almost the same as that of Er ions. After implantation, these samples were isochronally annealed for 10 min. at 800 °C, using the proximity cap method in H_2 atmosphere. In order to characterize the specimens, PL measurements were carried out using a 1m focal length double monochromator and photo-multiplier (Hamamatsu Photonics R5509-72). Samples were excited by the 488.0 nm line of an Ar ion laser with a power of 10 mW.

RESULTS AND DISCUSSION

In order to optimize the PL intensity of Er^{3+} , dose dependence was investigated. Figure 1 shows the Er-related PL spectra of $\text{Al}_{0.70}\text{Ga}_{0.30}\text{As}:\text{Er}$ for doses ranging from $1 \times 10^{13} \text{ cm}^{-2}$ to $3 \times 10^{15} \text{ cm}^{-2}$ measured at 15K. The several peaks were observed around 1500nm, and the dominant peak is located 1539.6 nm. PL intensity of the dominant peak increased for Er doses ranging from 1×10^{13} to $1 \times 10^{14} \text{ cm}^{-2}$ and decreased for those from 3×10^{14} to $1 \times 10^{15} \text{ cm}^{-2}$. In the sample with Er dose of $1 \times 10^{14} \text{ cm}^{-2}$, the PL intensity of the dominant peak

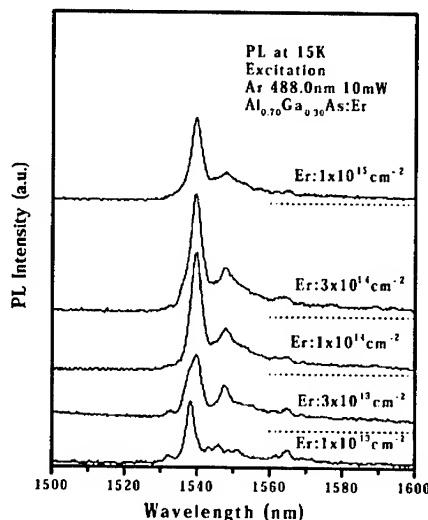


Figure 1. PL spectra of Er^{3+} ion in $\text{Al}_{0.70}\text{Ga}_{0.30}\text{As}$ corresponding to the transition $^4I_{13/2} \rightarrow ^4I_{15/2}$ recorded at 15K with Er doses ranging from $1 \times 10^{13} \text{ cm}^{-2}$ to $1 \times 10^{15} \text{ cm}^{-2}$.

at 1539.6nm was maximum. The dominant peak intensity decreased with increasing the Er doses range above $1 \times 10^{14} \text{ cm}^{-2}$.

Figure 2. shows the PL spectra of $\text{Al}_{0.70}\text{Ga}_{0.30}\text{As:Er,O}$ for different O doses and annealed at 800°C measured at 15K. As the O dose increased from $1 \times 10^{14} \text{ cm}^{-2}$ to $1 \times 10^{15} \text{ cm}^{-2}$, the dominant peak was stronger. In the sample, when O was co-implanted into the $\text{Al}_{0.70}\text{Ga}_{0.30}\text{As:Er}$ with a dose of $1 \times 10^{15} \text{ cm}^{-2}$, the PL intensity of the dominant peak became maximum. The peak intensity decreased with increasing the O doses from $1 \times 10^{15} \text{ cm}^{-2}$ to $3 \times 10^{15} \text{ cm}^{-2}$. We consider that the PL intensity in the sample with the O dose at $3 \times 10^{15} \text{ cm}^{-2}$ decreases because the defects attributed to O co-doping disturb the energy transition efficiency from the host material to the intra-4f-shell of Er^{3+} ions. Based on the results, the O dose required to obtain the maximum PL intensity at the dominant peak is concluded to be $1 \times 10^{15} \text{ cm}^{-2}$.

Figure 3 shows the temperature dependence of PL intensity for $\text{Al}_{0.70}\text{Ga}_{0.30}\text{As:Er, O}$ at Er dose of $1 \times 10^{14} \text{ cm}^{-2}$ and O dose of $1 \times 10^{15} \text{ cm}^{-2}$. From Figure.3, we can observe a peculiar three -step quenching process in PL intensity of $\text{Er:}1 \times 10^{14} \text{ cm}^{-2}$ without O and $\text{Er:}1 \times 10^{14}, \text{O:}1 \times 10^{15} \text{ cm}^{-2}$. The PL intensity rapidly decreased above 200K. Furthermore, at room temperature the PL intensity of Er-related emission from the sample co-implanted with O at a dose of $1 \times 10^{15} \text{ cm}^{-2}$ was twenty two times stronger than that from the sample implanted with

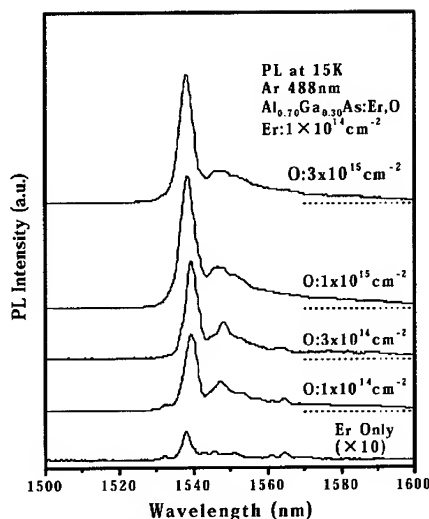


Figure 2. PL spectra measured at 15K for $\text{Al}_{0.70}\text{Ga}_{0.30}\text{As:Er,O}$ with O doses ranging from $1 \times 10^{15} \text{ cm}^{-2}$ to $3 \times 10^{15} \text{ cm}^{-2}$.

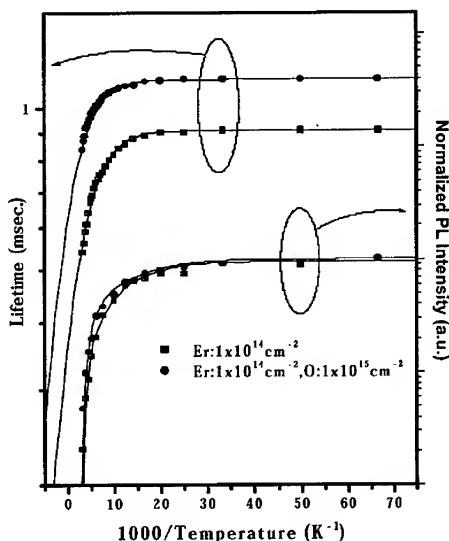


Figure 3. Er^{3+} -related PL lifetime and intensity dependence on temperature for $\text{Al}_{0.70}\text{Ga}_{0.30}\text{As:Er,O}$.

only Er: $1 \times 10^{14} \text{cm}^{-2}$. The experimental data for $\text{Al}_{0.70}\text{Ga}_{0.30}\text{As:Er,O}$ are plotted together with the theoretical lines (solid line) of the best fit obtained using Eq. (1) using parameters ($C_1, C_2, C_3, E_1, E_2, E_3$) shown in table 1.[6-8]

$$I = I_0 / \{1 + C_1 \exp(-E_1/kT) + C_2 \exp(-E_2/kT) + C_3 \exp(-E_3/kT)\} \quad (1)$$

$$1/\tau(T) = 1/\tau_r + 1/\tau_n \quad (2)$$

Where τ_n (the non-radiative lifetime) was assumed as follows:

$$1/\tau_n = C_A \exp(-E_A/kT) \quad (3)$$

Table 1. Activation energies obtained by fitting experimental results to Eqs. (1) and (2).

PL Intensity						
	C_1	$E_1(\text{meV})$	C_2	$E_2(\text{meV})$	C_3	$E_3(\text{meV})$
Er: $1 \times 10^{14} \text{cm}^{-2}$	5.0	14.0	50	50	4.0×10^5	235
Er: $1 \times 10^{14} \text{cm}^{-2}$ O: $1 \times 10^{15} \text{cm}^{-2}$	3.0	11.5	55	60	2.0×10^5	235
Lifetime						
	C_A	$E_A(\text{meV})$				
Er: $1 \times 10^{14} \text{cm}^{-2}$	1.7	235				
Er: $1 \times 10^{14} \text{cm}^{-2}$ O: $1 \times 10^{15} \text{cm}^{-2}$	0.75	245				

In the above equation, I_0 is the intensity when the electron emission from the Er-related trap can be neglected. Hence it corresponds to the intensity at a very low temperature. T is the measuring temperature, E_1, E_2, E_3 and E_A , are activation energies respectively, and k is the Boltzmann constant. C_1, C_2, C_3 and C_A are the coupling coefficient at E_1, E_2, E_3 and E_A , respectively. τ and τ_r are the lifetime and the radiative lifetime, respectively. These E_2 , and E_3 values were 50-60 meV and 235 meV, respectively. Moreover, E_A values were 235-245

meV. On the other hand, the value 235meV of E_3 , the activation energy for rapid thermal quenching, was nearly equal to the value 235-245meV of E_A , activation energy for the decrease of the lifetime. Based Eq. (2), the decrease of the lifetime confirms that the radiative efficiency is lower; therefore, we propose that rapid thermal quenching occurs above 200 K due to the decrease of the radiative efficiency. In addition, we infer that activation energy E_1 is the ionization energies of the e-h pair in the Er^{3+} -related trap level because it has been reported that the ionization energy is about 10 meV.[4,7]

CONCLUSION

In order to increase Er-related emission in $\text{Al}_{0.70}\text{Ga}_{0.30}\text{As}$, we examined dose dependence of Er and O. It was found that the optimum dose range for $\text{Al}_{0.70}\text{Ga}_{0.30}\text{As:Er}$ was $1 \times 10^{14} \text{ cm}^{-2}$, based on the dose dependence, and the optimum O dose range for $\text{Al}_{0.70}\text{Ga}_{0.30}\text{As:Er}$ was $1 \times 10^{14} \text{ cm}^{-2}$, based on the O dose dependence. The PL intensity of Er-related emission, in addition to O dose, was enhanced approximately twenty two times at room temperature. From the temperature dependence of the PL intensity and the lifetime, E_3 (235meV), the activation energy for rapid thermal quenching, was nearly equal to E_A (235-245meV) the activation energy for the decrease of the lifetime. Based on the result, the decrease of the lifetime confirms that the radiative efficiency is lower; therefore, we propose that rapid thermal quenching occurs above 200 K due to the decrease of the radiative efficiency.

ACKNOWLEDGEMENTS

The authors thank Dr. Sato of the Research of Ion Beam Technology Hosei University, and Toshihiko Kanayama of the Electrotechnical Laboratory for technical support on low-energy ion implantation. This work is supported in part by a Grant-in-Aid for Faculty Collaborative Research Grant from the Institute of Science and Technology at Meiji University High-Technology Research Center.

REFERENCES

- [1] H.Katsumata, S.Uekusa, A.Majima, M.Kumagai, J. Appl. Phys. 77 1881. (1995)
- [2] H.Katsumata, S.Uekusa, H.Sai, J. Appl. Phys. 80 2383. (1996)
- [3] A. Majima, S. Uekusa, K. Abe, and M. Kumagai, J. Luminescence 60 and 61, 595 (1994)
- [4] S.Uekusa, K.Uchiya, M.Wakutani, Nuclear Instruments and Method in Physics. Research B 148 pp.502-506 (1999)

- [5] S.Uekusa, M.Wakutani, M.Saito, and M.Kumagai Mat. Res. Soc. Symp. Vol. 484 pp. 595-600 (1998)
- [6] P. Wellmann, A. Winnacker, Matter. Res. Soc. Symp. Proc. 422 255 (1996)
- [7] A. Taguchi, K. Takahei, J. Appl. Phys. 79 (8) 4330 (1996)
- [8] T. Kimura, H. Ishida, S. Yugo, R. Saito, H. Isshiki, T.Ikoma, Matter. Soc. Symp. Proc. 301 (1993) 293.

INTERSUBBAND TRANSITIONS IN InGaAs/InAlAs MULTIPLE QUANTUM WELLS GROWN ON InP SUBSTRATE.

Qiaoying Zhou*, M. O. Manasreh*, B. D. Weaver**, and M. Missous***

*Depart of Electrical & Computer Engineering, The University of New Mexico, Albuquerque, NM 87131-1356.

**Naval Research Lab, 4555 Overlook Ave., SW, Washington, DC 20375.

***Department of Electrical Engineering and Electronics, UMIST, P. O. BOX 88, Manchester M60 1QD, England, UK.

ABSTRACT

Intersubband transitions in $\text{In}_{0.52}\text{Ga}_{0.48}\text{As}/\text{In}_{0.52}\text{Al}_{0.48}\text{As}$ multiple quantum wells grown on lattice matched InP substrates were investigated using Fourier transform infrared (FTIR) absorption and photoluminescence (FTPL) techniques. The well width was tailored to produce excited states resonant in the conduction band, at the edge of the conduction band, and confined in the quantum wells. Interband transitions were also probed using FTPL and optical absorption techniques. The FTPL spectra show that three interband transitions exist in the quantum well structures with well width larger than 30 Å. The intersubband transitions in this class of quantum wells seem to withstand proton irradiation with doses higher than those used to deplete the intersubband transitions in the GaAs/AlGaAs multiple quantum wells.

INTRODUCTION

Interband and intersubband transitions in bulk semiconductor, multiple quantum wells (MQWs), superlattices, and multiple quantum dots have been the subject of many studies (see for example Refs. [1], [2], [3], [4] and [5]) due to the fact that they form the basis for a new generation of low background and high detectivity very long, long and near wavelength infrared (IR) detectors. Additionally, IR detectors have enabled a new and a wide range of applications even though their potential is not fully realized and explored. GaAs/AlGaAs based multiple quantum well structures are the most mature of quantum well structures and have been widely studied for many applications including IR detectors (see for example Refs. [1], [6], [7] and [2]-[4]). Furthermore, these structures have been used in the development of novel high performance multi-color quantum well infrared photodetector (QWIP) for 3-5 µm mid-wavelength infrared and 8-14 µm long-wavelength infrared detection and to obtain a better understanding of the basic mechanisms that could be used to optimize the performance of these QWIPs. In case of shorter wavelength applications such as 1.55 and 1.3 µm for optical communication, the GaAs/AlGaAs MQWs may not be able to meet the demand since the conduction band offset is too small for a such wavelength range. Thus, there is a need to investigate different quantum structures with larger conduction band offset. InGaAs/InAlAs MQWs have the potential to be used as possible structures for shorter wavelength applications due to the fact that this system can be tailored with a larger conduction band offset.

In this paper, we report on the optical properties of intersubband transitions in InGaAs/InAlAs MQWs grown on lattice matched InP substrates. Photoluminescence spectra were obtained for several samples where the excited state is resonant in the conduction band or confined in the well. Additionally, proton irradiation was performed on the intersubband transition and the results will be discussed.

EXPERIMENTAL TECHNIQUES

Three $\text{In}_{0.52}\text{Ga}_{0.48}\text{As}/\text{In}_{0.52}\text{Al}_{0.48}\text{As}$ multiple quantum well structures grown on InP substrates were grown by the molecular-beam epitaxy technique. The $\text{In}_{0.53}\text{Ga}_{0.47}\text{As}/\text{In}_{0.52}\text{Al}_{0.48}\text{As}$ were both lattice matched to the InP substrates with $\Delta a/a$ less than 5×10^{-4} in each case. The growth were performed at a temperature of 450 °C which was optimal for this material system. The barrier thickness is 300 Å for all samples and the well width is 30 Å, 55 Å, and 75 Å for the three samples. The well regions were Si-doped ($[\text{Si}] = 9 \times 10^{18} \text{ cm}^{-3}$). The quality of the layers was examined by room temperature Hall effect measurements and the mobility was found 1554, 2324, 2005 $\mu \text{ (cm}^2/\text{Vs)}$ for the 30 Å, 55 Å, and 75 Å, respectively, while the Hall effect carrier concentration is consistent with growth doping profile ($\sim 9 \times 10^{18} \text{ cm}^{-3}$). The samples were also irradiated with 1 MeV protons beam. The infrared absorption spectra were recorded at the Brewster's angle of GaAs (73°) from the normal using a BOMEM Fourier-transform interferometer in conjunction with a continuous flow cryostat. The sample's cold finger holder was designed for the GaAs Brewster's angle, but the InP Brewster angle of 71° is very close to that of GaAs. The temperature was controlled within $\pm 1.0 \text{ K}$ and the spectra were measured at either 77 K or 300 K. Interband transitions were measured using the BOMEM spectrometer in conjunction with a PL attachment. Cary 500 spectrometer was also used to measure the band edge absorption of the quantum structures.

EXPERIMENTAL RESULTS AND DISCUSSIONS

The optical absorption spectra of the intersubband transitions in the three samples are shown in Fig. 1. The spectra are measured at both 77 K and 300 K. It is clear from this figure that the energy separation between the ground and excited states is decreased as the well width is increased from 30 Å [Fig. 1(a)] to 55 Å [Fig. (b)]. As the well width is increased to 75 Å, the structure seems to accommodate more than one excited states with the Fermi energy level being above the first excited state. Hence one can observe intersubband transitions from the ground state to the first excited state and from the first to the second excited states. This is illustrated in Fig. 1(c) where two intersubband transitions are clearly visible. From the shape and intensity of the intersubband transitions, one can suggest that the excited state in the sample with 30 Å wells [Fig. 2(a)] is resonant in the conduction band. The asymmetrical shape of the spectra in Fig. 1(b) indicates that the excited state is very close to the top of the barrier conduction band. This is due to the asymmetrical energy levels in the k -space. However, as the excited state is dropped inside the well by increasing its width, the line-shapes of the intersubband transitions become more symmetrical as shown in Fig. 1(c). This strongly suggests that both the ground and excited states have more or less the same

curvature in the k-space or the effective mass of the carrier is almost the same in both the ground and excited states. The positions of the energy levels in $\text{In}_{0.52}\text{Ga}_{0.48}\text{As}/\text{In}_{0.52}\text{Al}_{0.48}\text{As}$ MQWs seems to strongly depend on the well widths as compared to the GaAs/AlGaAs systems [8]. This is may be due to the fact that the conduction band offset in $\text{In}_{0.52}\text{Ga}_{0.48}\text{As}/\text{In}_{0.52}\text{Al}_{0.48}\text{As}$ MQWs is much larger than that of the GaAs/AlGaAs MQWs.

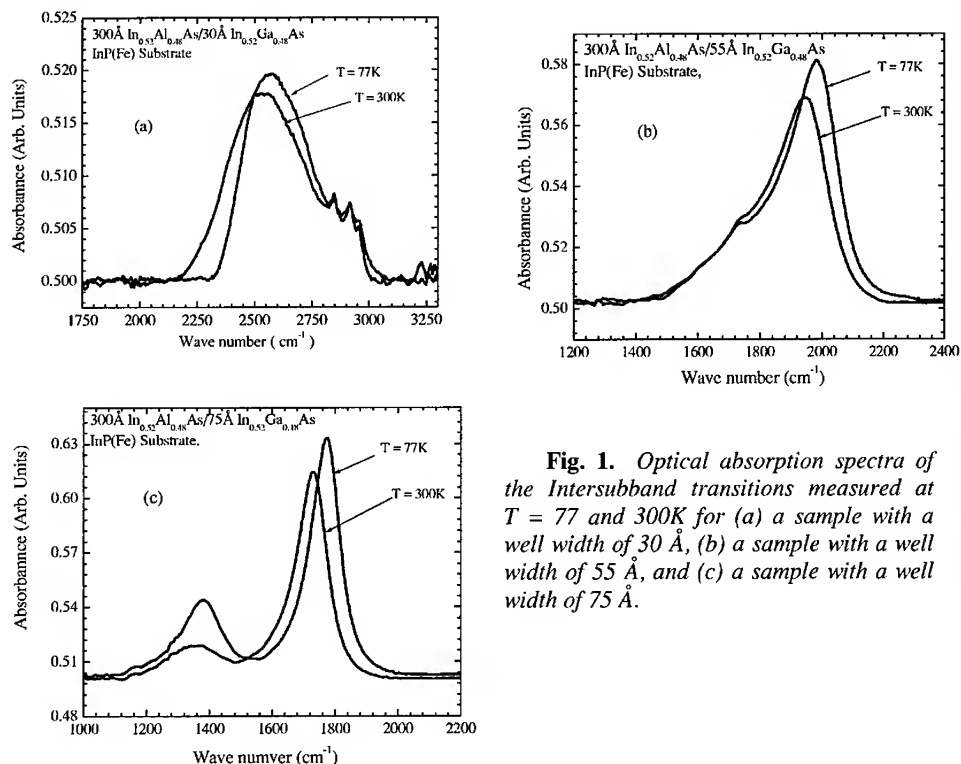


Fig. 1. Optical absorption spectra of the Intersubband transitions measured at $T = 77$ and 300K for (a) a sample with a well width of 30 Å , (b) a sample with a well width of 55 Å , and (c) a sample with a well width of 75 Å .

Interband transitions in the three MQW samples were probed using both FTPL and monochromatic light absorption. The results are shown in Fig. 2 where both the band edge absorption and PL spectra overlaid for each sample. The optical absorption threshold seems to be the same for all samples, but the PL spectra consist of only one peak for the sample with a well width of 30 Å , which suggest that there is only one confined state in the conduction band [see Fig. 2. (a)]. The PL spectra for the samples with well widths of 55 and 75 Å show structures with two peaks around 1.4 and 1.3 μm and a shoulder around 1.24 μm . The optical absorption threshold energy is about 1.17 μm (1.06 eV) while the dominant PL peak position energies for the three

samples are 1.16 μm (1.07 eV), 1.31 μm (0.947 eV), and 1.34 μm (0.925 eV). This suggests that the samples possess a small Stokes shift, which could indicate a minimal strain or distortion.

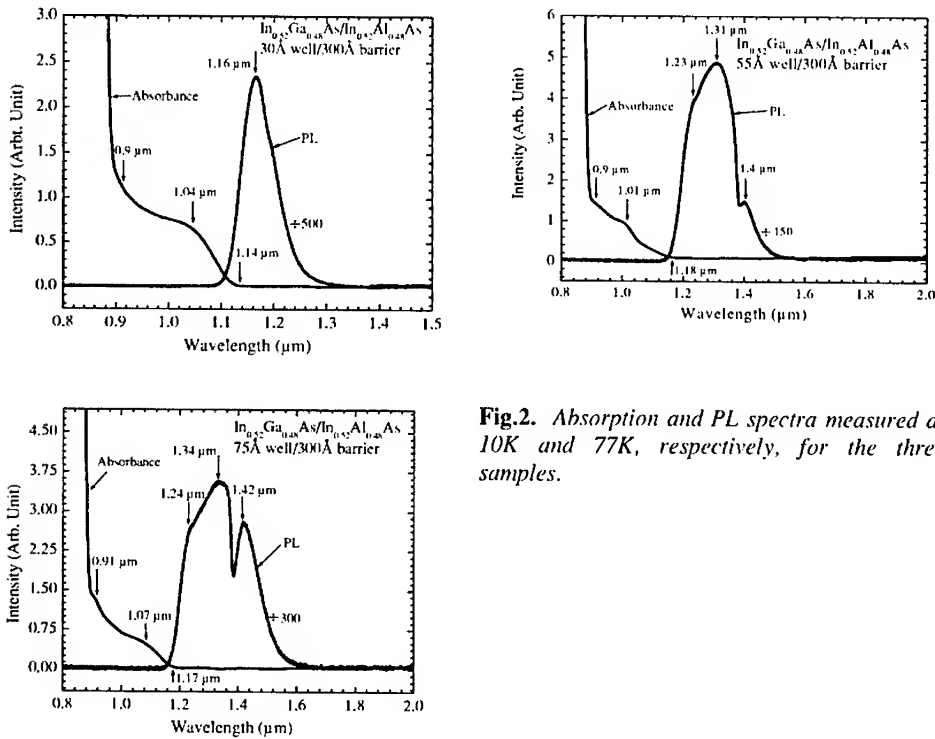


Fig.2. Absorption and PL spectra measured at 10K and 77K, respectively, for the three samples.

Two of the samples, namely 55 and 75 Å well samples, were irradiated with 1 MeV protons and found that a dose of up to $3 \times 10^{14} \text{ cm}^{-2}$ did not seem to produce a significant change in the intensity of the intersubband transitions in the samples. The results are shown in Fig. 3. Recently, proton irradiation effect on the intersubband transitions in GaAs/AlGaAs multiple quantum wells was reported [9]. It was shown that the intensity of the intersubband transitions is decreased as the proton irradiation dose is increased, which was explained in terms of trapping the two-dimensional electron gas in the GaAs quantum wells by the irradiation induced-defects such as vacancies, antisites, and more complex defects. A reduction of the intensity of the intersubband transitions in electron irradiated GaAs/AlGaAs multiple quantum wells was also observed [10] with similar results. It is noted that the intersubband transition in GaAs/AlGaAs to drastically decrease and completely deplete when the GaAs/AlGaAs MQWs were irradiated with 1 MeV and a dose of $1 \times 10^{14} \text{ cm}^{-2}$. In the present samples, a dose of $3 \times 10^{14} \text{ cm}^{-2}$ did not seem to cause the same effect which indicates that InGaAs/AlGaAs is more radiation hardness as compared to GaAs/AlGaAs systems. This subject is still under further investigation.

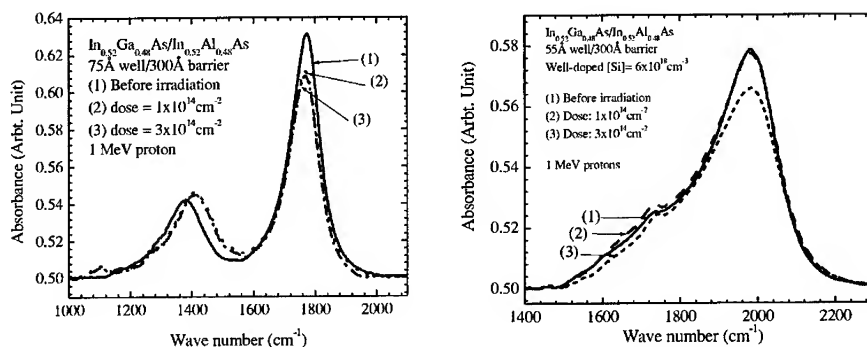


Fig. 3. Proton Irradiation effect on the intersubband transitions in two InGaAs/InAlAs MQWs samples. Less than 5% reduction was observed in the samples after irradiating them with 1 MeV protons and a dose of $3 \times 10^{14} \text{ cm}^{-2}$.

CONCLUSIONS

Intersubband transitions in InGaAs/InAlAs MQWs grown on lattice matched InP were investigated using optical absorption and photoluminescence technique. The results show that the MQWs exhibit one intersubband transition in samples with a well widths smaller than 55 Å. Two intersubband transitions, on the other hand, were observed in a sample with a well width of 75 Å suggesting that two excited states are confined in the well and the Fermi energy level is above the first excited state. The small difference in the interband transition energies observed by both the optical absorption and photoluminescence techniques suggest a small Stokes shift, which is an indicative of minimal strain. 1 MeV proton irradiation yields a small effect on the intersubband transitions in the MQWs up to a dose of $3 \times 10^{14} \text{ cm}^{-2}$.

ACKNOWLEDGEMENTS. This work was partially supported by the Air Force Office of Scientific Research Grant No. F49620-00-1-0026. We would like to thank Dr. D. Johnstone for his encouragement and support and J. Chen for the measurements.

REFERENCES

- [1] B. F. Levine, J. Appl. Phys. **74**, R1 (1993).
- [2] "Semiconductor Quantum Wells and Superlattices for Long-Wavelength Infrared Detectors," Edited by M. O. Manasreh (Artic House, Boston 1993).

- [3] "Long Wavelength Infrared Detectors," Edited by M. Razeghi, Vol. 1 in the book series "Optoelectronic Properties of Semiconductors and Superlattices," edited by M. O. Manasreh (Gordon and Breach, Amsterdam, 1996).
- [4] "Infrared Detectors," A. Rogalski, Vol. 10 in the book series "Electrocomponent Science Monographs," edited by D. S. Campbell (Gordon and Breach, Amsterdam, 2000).
- [5]. See for example the special issue on semiconductor quantum dots of Material Research Society Bulletin, February 1998, Vol. 23, No. 2.
- [6] L. J. Kozlowski *et al.*, IEEE Trans. Electron Devices **38**, 1124 (1991).
- [7] K. K. Choi, B. F. Levine, R. J. Malik, J. Walter, and C. G. Bethea, Phys. Rev. B **35**, 4172 (1987).
- [8] D. H. Huang and M. O. Manasreh, Phys. Rev. B **54**, 5620-5628 (1996).
- [9] M. O. Manasreh, P. Ballet, J. B. Smathers, G. J. Salamo, and C. Jagadish, Appl. Phys. Lett. **75**, 525 (1999).
- [10] M. O. Manasreh, H. J. von Bardeleben, A. M. Mousalitin, and D. R. Khokhlov, J. Appl. Phys. **85**, 630 (1999).

Calculations of Dielectric Constant for AlGaInAs Quaternary Semiconductor Alloy in the Transparent Region and Above (0.4-4.0eV)

M. Linnik and A. Christou

Department of Materials and Nuclear Engineering and Materials Research Science and Engineering Center, University of Maryland, College Park MD 20742

ABSTRACT

The modeling of the spectral behavior of the refractive index of AlGaInAs quaternary III-V semiconductor alloy in the energy range from 0.4 to 4eV, including the transparent region, is presented. The extended model of interband transition contributions incorporates not only the fundamental absorption edge contribution to the dielectric function, but also contributions from higher energy and indirect transitions. It is demonstrated that indirect energy transitions must be included in the calculations of the complex dielectric function of the material in the transparent region. Indirect transitions from different critical points in the Brillouin zone are treated separately. The comparison between the theoretical refractive indices and the experimental data for AlGaInAs alloy is presented. These calculations have been applied to the design of Bragg mirrors with the highest refractive index contrast for heterostructure lasers.

INTRODUCTION

The design and analysis of such devices as injection lasers, photodiodes, detectors, solar cells, multilayer structures, and microcavities requires the exact knowledge of the optical constants of III-V compound semiconductors in the region near the fundamental absorption edge as well as at the higher photon energies. In modeling of the optical constants of semiconductors in the fundamental optical region, several approaches are typically used: (1) empirical formulas, (2) damped harmonic oscillator (DHO) models, (3) standard critical point (SCP) models. Optical constants determined from empirical formulas (such as the Sellmeier dispersion equations for the refractive index and Urbach's rule for the absorption coefficient [1], or the expression for n based on interpolation of a dielectric quantity using Vegard's rule by Burkhard *et al.*[2]) are not related through the Kramers-Kronig dispersion relation and are valid only over a very limited energy range.

A semi-empirical single effective oscillator model based on quasi-classical Boltzmann equation or Drude theory proposed by Wemple *et al.*[3] does provide an analytical expression for the dispersion of the semiconductor refractive index at photon energies significantly below the direct band edge. The Drude theory ignores the carrier related effects around the band gap, and thus the results are valid only in the low optical frequency region. This model also lacks the agreement with experimental data at the band edge, which is the energy range of the most interest for semiconductor laser devices.

The standard critical point (SCP) model can determine the position of critical points of the semiconductor band structure, but cannot accurately predict the dielectric function [4]. The modified SCP model was initially proposed by Korovin [5] and Cardona *et al.*[6], and then developed by Adachi [7], and Lin *et al.*[8]. The model of interband transition contributions (ITC model) was introduced as a method to analyze the refractive index of III-V compounds at energies below and above the direct band gap by including the electron-hole pair transitions, and by adding the excitonic terms at the two lowest energy gap transitions. The comparison between

available experimental results of the spectral behavior of III-V compound semiconductors and the theoretical data calculated using the above mentioned models often reveals a lack of agreement, which is pronounced for the photon energies around the fundamental absorption edge. These differences may arise from the excitonic effects, which are largely ignored in the calculations of the real part of the dielectric constant [8].

In the present work, an extended model of interband transition contributions (EITC) is developed for the calculations of real and imaginary parts of the dielectric constant of compound semiconductors. The model introduces (1) the broadening effects, caused by phonon and defect scattering in direct and indirect transitions; (2) the strength of direct band gap transitions as a function of the effective electron, heavy hole and light hole masses of the semiconductor; (3) the exciton contributions; (4) the separate contributions of E_x and E_i indirect band gap transitions to the real and imaginary part of the dielectric constant. The importance of indirect and higher direct energy transitions is demonstrated through these calculations and through the comparison with experimental results. The detailed description of our extended ITC model is given in Reference [9], where the index of refraction for the following alloys has also been calculated and compared with the available experimental results: AlP, AlAs, AlSb, GaP, GaAs, GaSb, InP, InAs, InSb, AlGaAsSb, AlGaInAs, AlGaInP, GaInAsSb, and GaInPAs. In this work we apply the extended ITC model for the calculation of the dielectric constant of AlGaInAs alloy, which is then used for the Bragg mirror design.

THE EXTENDED ITC MODEL

The dielectric constant $\epsilon(E) = \epsilon_1(E) + i\epsilon_2(E)$ describes the optical response of the medium as a function of photon energy E . The imaginary part of the dielectric function $\epsilon_2(E)$ is calculated based on a simplified model of the band structure using the joint density of states for each Critical Point (CP) considered. The real part of the dielectric function $\epsilon_1(E)$ was calculated through the knowledge of the imaginary part, $\epsilon_2(E)$, by employing the Kramers-Kronig relation [10]. Thus, the total imaginary and real parts of the dielectric function are presented as a sum of several terms that represent the contribution of different energy CPs. These points are associated with electronic transitions in the band structure at the energies designated as E_0 , $E_0 + \Delta$, E_0^{ex} , E_1 , E_2 , and E_i . In case of quaternary, $A_xB_yC_zD$, semiconductor alloy each of the terms become a function of the alloy mole fraction, x , y and $z=1-x-y$. There are several absorption mechanisms [11] that contribute to the imaginary part of the dielectric constant, therefore $\epsilon_2(E)$ can be written as:

$$\epsilon_2(E, x, y) = \epsilon_2^{E_0}(E, x, y) + \epsilon_2^{exE_0}(E, x, y) + \epsilon_2^{E_0+\Delta}(E, x, y) + \epsilon_2^{E_1}(E, x, y) + \epsilon_2^{E_2}(E, x, y) + \epsilon_2^{E_i}(E, x, y) \quad (1)$$

where $\epsilon_2^{E_0}$ and $\epsilon_2^{E_0+\Delta}$ are contributions due to the absorption by direct interband optical transitions near the fundamental absorption edge and spin-orbit transitions, $\epsilon_2^{exE_0}$ is due to the absorption by the discrete series of excitons near the E_0 energy gap, $\epsilon_2^{E_1}$ and $\epsilon_2^{E_2}$ are contributions of the higher energy interband transitions, and $\epsilon_2^{E_i}$ is due to the indirect interband absorption effects. Similarly, the real part of the dielectric function can be presented as the following sum:

$$\epsilon_1(E, x, y) = \epsilon_1^{E_0}(E, x, y) + \epsilon_1^{exE_0}(E, x, y) + \epsilon_1^{E_0+\Delta}(E, x, y) + \epsilon_1^{E_1}(E, x, y) + \epsilon_1^{E_2}(E, x, y) + \epsilon_1^{E_i}(E, x, y) \quad (2)$$

The absorption spectrum for photon energies greater than the band gap energy is composed of many peaks correlated with Van-Hove singularities of the joint density of states [11]. For III-V zinc-blende type semiconductors, the contributions of two main peaks (E_1 and E_2) must also be included. These peaks correspond to the direct optical transitions at the L and X points of the BZ, respectively. The E_1 peak is treated as a two-dimensional M_0 type critical point, while the structure of the E_2 peak is characteristic of a damped harmonic oscillator.

The detailed description of the individual contributions to the real and imaginary parts of the dielectric constant is given in the Reference [9]. The presented model is applicable in the photon energy range from 0.4eV to about 4eV. The initial crystal parameters required for the calculations include energy band gap values, effective electron and hole masses, static dielectric constant, and the values of the bowing parameters used for the energy band gap calculations for the ternary alloys. The complex dielectric constant and refractive index of binary alloys (AlAs, GaAs, InAs) were first calculated and the results were then used in the calculation for AlGaInAs quaternary alloy. The reported model also incorporates the lifetime broadening effects of the free electron-hole pair states through the damping parameters [12].

The refractive index of a semiconductor, $n(E)$, and the extinction coefficient, $k(E)$, were calculated in terms of the complex dielectric function as follows:

$$n(E) = \left[\frac{\epsilon_1(E)}{2} + \frac{\sqrt{\epsilon_1(E)^2 + \epsilon_2(E)^2}}{2} \right]^{1/2} \quad (3)$$

$$k(E) = \left[\frac{\sqrt{\epsilon_1(E)^2 + \epsilon_2(E)^2}}{2} - \frac{\epsilon_1(E)}{2} \right]^{1/2} \quad (4)$$

There are a total of 12 unknown parameters required by the model in Eqs.(1) and (2) for the real and imaginary part of the dielectric constant of a binary alloy, which include strength and damping parameters for various transitions. These parameters are obtained by fitting through minimization of the total error function, F , over all available experimental points for each semiconductor alloy of interest, which is given below as:

$$F = \sum_{i=1}^N \left((n_{th}(E_i) - n_{exp}(E_i))^2 + (k_{th}(E_i) - k_{exp}(E_i))^2 \right) \quad (5)$$

CALCULATION RESULTS AND DISCUSSION

The present investigation of the optical properties of the III-V semiconductor alloys is centered on describing the behavior of the refractive index for the photon energies in the transparent region as well as for the higher energies. The calculated index of refraction from our extended ITC model and the available experimental data for AlGaInAs quaternary semiconductor alloy are shown in Figures 1 and 2 demonstrating excellent agreement between the two. The strongest resonance peak of the index of refraction occurs at the E_1 transition energy. The E_1 peaks in this calculation appear to be generally sharper than the experimental values, which can be explained by the absence of the lifetime broadening effects in the current model for the E_1 optical transition.

It is believed that by adding the broadening constant as well as including the exciton effects for the E_1 transition energy, better agreement for this peak can be obtained. The increase in the broadening parameter of AlGaInAs alloy is reported, which may be attributed to the

potential fluctuations resulting from random atomic placement in the quaternary alloys as compared with binary alloys. Maximum anion disorder occurs at $y=0.5$, while that for the cation occurs at $x=0.5$ and $y=1$ [13]. Therefore, the high atomic disorder in the triple-cation sublattice of $\text{Al}_{0.3}\text{Ga}_{0.16}\text{In}_{0.54}\text{As}$ alloy with compositions x, y, z close to the middle point may be responsible for the slight deviations of the calculated refractive index from the one determined experimentally. In this case the bowing parameters can no longer be represented as a quadratic function of the alloy composition. The atomic disorder and composition fluctuations are expected to broaden the optical spectra.

The valley contributions to the real part of the dielectric constant are separated according to the partition of the Brillouin zone. The L region with corresponding direct E_L and indirect E_L optical transition energy contributes approximately 65–75% to the total value of the dielectric constant while the Γ region corresponding to the E_0 transition accounts to about 5–10%, the X region, which is represented by indirect E_X energy and constant M, contributes about 15 to 30% of the total. Thus, the index of refraction is essentially determined by the band structure away from the center of the BZ, and modifications of the electronic structure at L and X points rather than Γ CPs, produce the observed variations in the index of refraction.

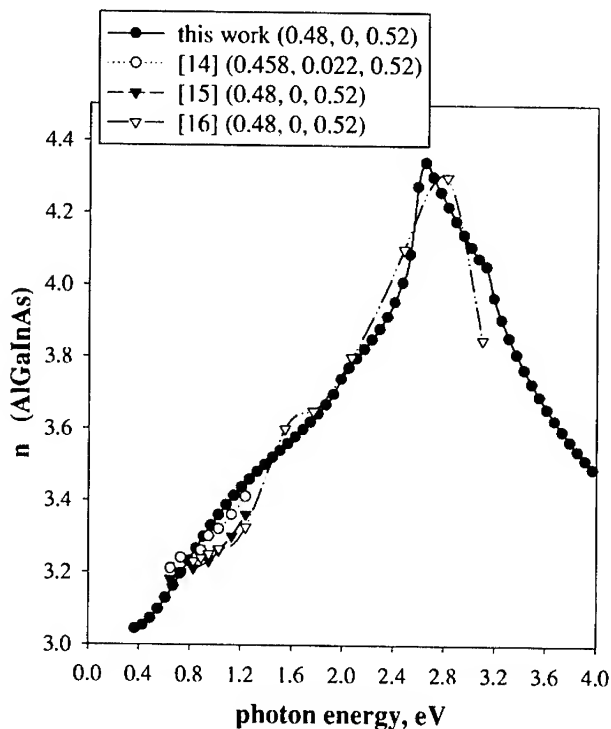


Figure 1. Refractive index of $\text{Al}_x\text{Ga}_y\text{In}_z\text{As}$ for $x=0.48, y=0, z=0.52$.

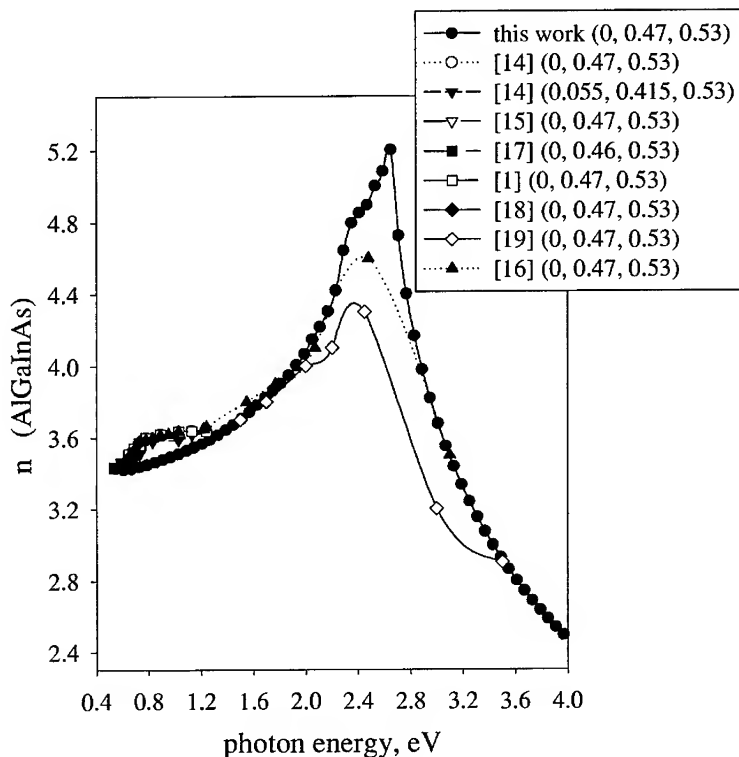


Figure 2. Refractive index of $\text{Al}_x\text{Ga}_y\text{In}_z\text{As}$ for $x=0$, $y=0.47$, $z=0.53$.

The contribution to the total dielectric function of 3D discrete exciton transitions close to the E_0 transition energy are found to be negligible, about 0.1%, due to the very narrow spectral range of such transitions.

The results of the $\text{Al}_x\text{Ga}_y\text{In}_z\text{As}$ alloy investigation were extrapolated to the different compositions of interest to photonic devices. In order to select the optimal materials for the semiconductor Distributed Bragg Reflectors (DBRs) for application in long wavelength Vertical Cavity Surface Emitting Lasers (VCSELs), the maximum and minimum refractive indices were calculated for response to the incident photon energy of 0.8eV for the alloys lattice matched to the InP substrate under the direct band gap conditions. The $\text{Al}_{0.05}\text{Ga}_{0.42}\text{In}_{0.53}\text{As}/\text{InP}$ material system with index of refraction difference of 0.46 is therefore recommended for the Bragg mirror applications.

SUMMARY

An extended ITC model and calculations of optical properties for AlGaInAs quaternary III-V semiconductor alloy are presented and the results are compared with the experimental data. The successful fit of the refractive indices in the transparent optical region as well as for the

higher photon energies was attained by combining several interband transition contributions. The largest contribution to the dielectric function is due to the direct and indirect optical transitions along $\langle 111 \rangle$ and $\langle 100 \rangle$ directions in the BZ, which accounts for 85-90% of the total contributions. Therefore, except for the optical absorption in the vicinity of the Γ gap, most of the optical properties of the material, especially the index of refraction, are determined by the electronic structure around L point, rather than at the center of the BZ. Since our model is more sensitive to the indirect band gap transitions, the nature of the indirect band gap contributions to the total dielectric function of the alloy may be better understood. The influence of the discrete exciton states around the E_0 edge at room temperature was found negligible. We have applied the results of these calculations to the AlGaInAs/InP material system for applications as semiconductor distributed Bragg reflectors.

ACKNOWLEDGMENTS

The investigation was funded by the Army Research Laboratory under the Microelectronics Research Cooperative Agreement, and partially by the University of Maryland Materials Research Science and Engineering Center.

REFERENCES

- 1 "Handbook of Optical Constants of Solids II", ed. E.Palik, 1991.
- 2 B.Broberg and S.Lindgren, *J.Appl.Phys.* **55**(9), 3376 (1984).
- 3 S.Wemple, and M.DiDomenico, *Phys.Rev.B* **3**(4), 1338 (1971).
- 4 A.Djurisic, A.Rakic, P.Kwok, E.Li, and M.Majewski, *J.Appl.Phys.* **85**(7), 3638 (1999).
- 5 L.Korovin, *Sov.Phys.Solid State* **1**, 1202 (1960).
- 6 M.Cardona, *Solid State Physics, Nuclear Physics and Particle Physics* (Benjamin, New York, 1968), p.737.
- 7 S.Adachi, *Phys.Rev.* **35**(14), 7454 (1987).
- 8 C.Lin and J.Meese, *J.Appl.Phys.* **74**(10), 6341 (1993).
- 9 M.Linnik and A.Christou, to be published in *Physica B*, 2002.
- 10 C.Alibert, M.Skouri, A.Joullie, M.Benouna, and S.Sadiq, *J.Appl.Phys.* **69**(5), 3208 (1991).
- 11 P.Paskov, *J.Appl.Phys.* **81**(4), 1890 (1997).
- 12 S.Adachi, *J.Appl.Phys.* **53**(8), 5863 (1982).
- 13 S.Kelso, D.Aspnes, M.Pollack, and R.Nahory, *Phys.Rev.B* **26**(12), 6669 (1982).
- 14 H.Dinges, H.Burkhard, R.Nickel, and W.Schlapp, *Mater.Sci.Engin.B* **21**, 174 (1993).
- 15 M.Mondry, D.Babic, J.Bowers, and L.Coldren, *IEEE Pton.Techn.Lett.* **4**(6), 627 (1992).
- 16 H.Dinges, H.Burkhard, R.Losch, H.Nickel, and W.Schlapp, *Appl.Surf.Sci.* **54**, 477, (1992).
- 17 P.Chandra, L.Coldren, and K.Strege, *Electrn.Lett.* **17**(1), 6 (1981).
- 18 "Semiconductors - Basic data", ed. O.Madelung, 1996.
- 19 C.Pickering, N.Garawal, D.Lacefield, J.Piel, and R.Blunt, *Appl.Surf.Sci.* **50**, 346 (1991).

Annealing of some II-IV-V₂ crystals in the vapor of volatile constituents

Valeriy G.Voevodin, Olga V.Voevodina, Svetlana A.Bereznaya, Zoya V.Korotchenko
Siberian Physico-Technical Institute
1 Revolution sq., 634050, Tomsk, Russia
Nils C. Fernelius, Jonathan T. Goldstein, Melvin C. Ohmer
Air Force Research Lab
Wright-Patterson Air Force Base, Dayton Ohio, 45433-7707, USA

ABSTRACT

Experiments on annealing of CdGeAs₂-, CdSnAs₂- and ZnGeP₂-crystals in the vapor of volatile constituents were carried out. Conductivity and Hall effect measurements were performed to characterize the modification of electrical properties, caused by the interaction of the crystal with the gas phase during annealing. Literature data and the results of the present work are discussed based on the results of a quasi-chemical analysis. This yielded that the results of annealing depends essentially on both the conditions of the experiment and the initial imperfection of the crystal. The most probable native structural defects becoming apparent under the annealing were the following: for CdSnAs₂ - Sn_{Cd}, V_{As}; for CdGeAs₂ - V_{As}, V_{Cd}, Cd_{Ge}, Ge_{Cd}; for CdSiAs₂ - Si_{As}, V_{As}; for CdSiP₂ - V_{Cd}, V_P; for ZnGeP₂ - Zn_{Ge}, Ge_{Zn}, V_{Zn}, V_P; and for ZnSnP₂ - Zn_{Sn}, Sn_{Zn}, V_{Zn}, V_P.

INTRODUCTION

There is great interest in the ternary compounds II-IV-V₂ (especially CdGeAs₂ and ZnGeP₂) because of their unique properties, among them their use as NLO converters for mid IR range radiation [1,2]. The widespread practical use of these materials is limited by the presence of absorption bands in their transparency range. These absorption bands are linked to deep level native defects [3-6]. For successful suppression of the undesirable influences of these defects on the properties of the material, it is necessary to define their nature. So far there have not been solutions of this task acceptable to all. Experiments on the influence of annealing in the vapor of volatile components on semiconductor electrophysical parameters may be rather informative in this respect. In this work research of such kind applied to n-CdSnAs₂, n- and p-CdGeAs₂ and p-ZnGeP₂ was fulfilled by the method of "frozen reactions".

EXPERIMENTAL RESULTS

In the case of n-CdSnAs₂ the dependence of electron concentrations on vapor pressure appear as curves with a minimum, the depth and position of which on the time axis were defined by defect parameters of the initial sample. This completely agrees with [8]. As it was reported in [9, 10], the hole concentration increased in p-CdGeAs₂ with the lapse of time under annealing in As-vapor and went to saturation at a level about $p \sim 10^{17} \text{ cm}^{-3}$ under annealing times ~ 150 hours. The electron concentration increased in n-CdGeAs₂ with the lapse of time under annealing in Cd-vapor and went to saturation at a level about $n \sim 10^{18} \text{ cm}^{-3}$ under annealing times ~ 100 hours [9]. As to ZnGeP₂, it was reported in the work [11] that the hole concentration in the material increased with increase of phosphorus pressure during synthesis

of the compound. According to data of other works, for example, [12-17], annealing in phosphorus vapor reduces the hole concentration (down to p-n conversion of the conductivity type). The results of the present work on annealing in the vapor of volatile components (saturated vapor under pure Cd or As at the temperature of the annealing for CdGeAs₂) are presented in Figures 1- 4.

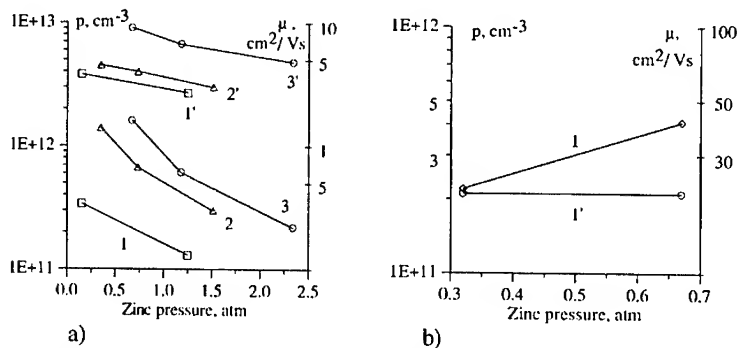


Figure 1. Dependence of concentration (1, 2, 3) and mobility (1', 2', 3') of charge carriers in ZnGeP₂ on pressure of Zn; $T_{\text{annealing}}, \text{K}$: 1-1173; 2-1223; 3-1273; $t_{\text{annealing}}, \text{hours}$: 1-110; 2-75; 3-45; a) material grown from stoichiometric melt under increased P-pressure; b) material grown from a melt containing excess Zn

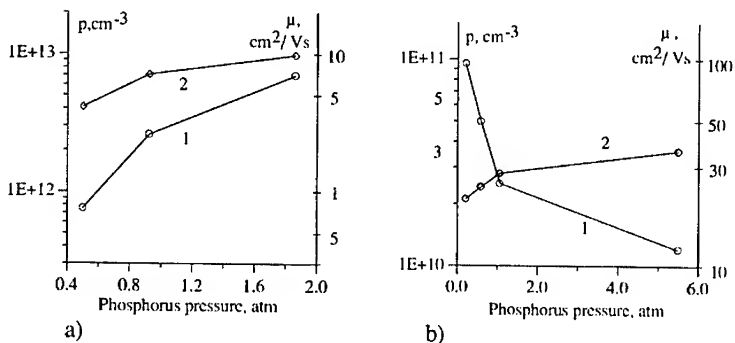


Figure 2. Dependence of concentration (1) and mobility (2) of charge carriers in ZnGeP₂ on pressure of phosphorus; $T_{\text{annealing}} = 1173 \text{ K}$; $t_{\text{annealing}} = 100 \text{ hours}$; a) material grown from stoichiometric melt under increased P-pressure; b) material grown from a melt containing excess Zn

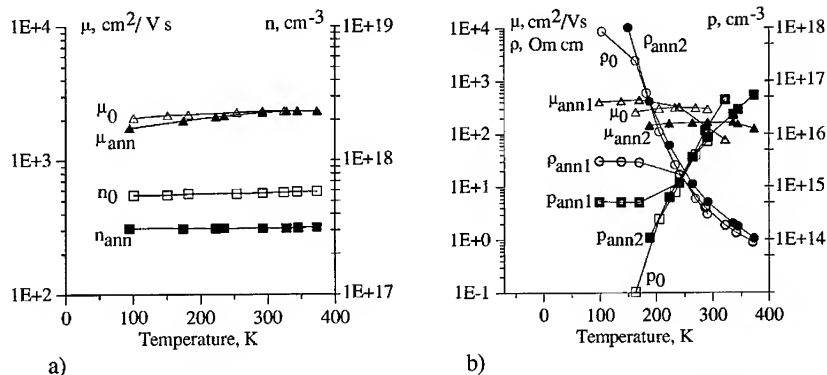


Figure 3. Influence of annealing in As_4 on parameters of $CdGeAs_2$; empty symbols - temperature dependence of initial parameters (n_0 , p_0 , μ_0 , ρ_0); filled symbols - parameters after annealing at $T_{ann} = 773$ K; square - concentration, circle - specific resistance, triangle - mobility; a) n-type, $t_{ann} = 384$ hours; b) p-type, $t_{ann1} = 190$ hours, $t_{ann2} = 384$ hours

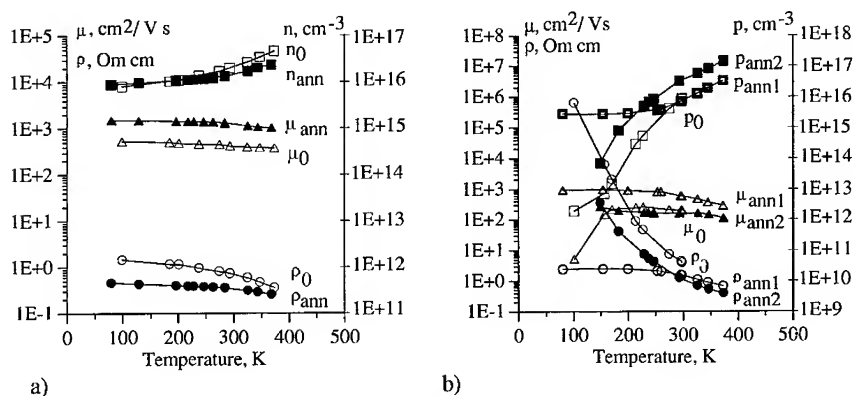


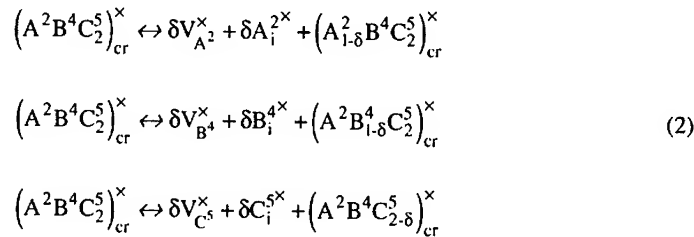
Figure 4. Influence of annealing in cadmium (saturated vapor under pure Cd at 773 K) on electrophysical parameters of $CdGeAs_2$; empty symbols - temperature dependence of initial parameters (n_0 , p_0 , μ_0 , ρ_0); filled symbols - temperature dependence of parameters after annealing at $T = 773$ K; square - hole concentration, circle - specific resistance, triangle - hole mobility; a) n-type, $t_{ann} = 190$ hours; b) p-type, $t_{ann1} = 30$ hours, $t_{ann2} = 90$ hours

SCHEME OF QUASI-CHEMICAL ANALYSIS

The processes of formation and interaction of point defects in semiconductors II-IV- V_2 , and also the processes of interaction of the crystals with a gas phase, may be described as a system of quasi-chemical reactions. The following processes were taken into consideration. Formation of Schottky defects (The Kroger designations [7] are used here and further)



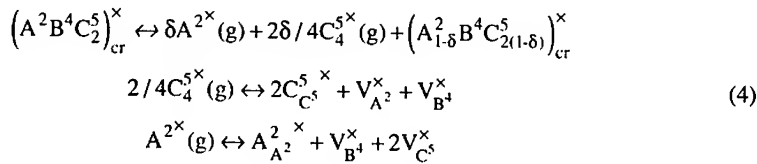
Formation of Frenkel defects



Formation processes of disorder defects in a common form



Interaction processes of crystals with a gas phase using the non-volatility of the elements B⁴ (Si, Ge and Sn) approximation



Applying the law of mass action to the quasi-chemical reactions and solving the obtained set of equations with respect to concentration of a given point defect under a choice of vapor pressure of one of the volatile components p_{A^2} or $p_{C_4^5}$ as an independent variable (for temperatures at which component C⁵ exists mainly as four-atom molecules in a gas phase) yields the following expressions

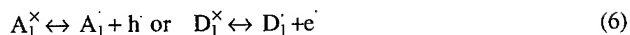
$$[N_i^x] = K_{i1} (p_{C_4^5})^{\alpha_i} \quad \text{and} \quad [N_i^x] = K_{i2} (p_{A^2})^{\beta_i}, \quad (5)$$

where $[N_i^x]$ is the concentration of neutral defects of i-type, $K_{i1,2}$ are constants at a given temperature, α_i, β_i are constants from the table I

Table I. Exponents α_i or β_i in dependencies of concentrations of neutral native point defects in semiconductors upon pressure of volatile components p_{A^2} or $p_{C_4^5}$ respectively

$[N_i^x]$	$V_{A^2}^x$	$V_{B^4}^x$	$V_{C^5}^x$	A_i^{2x}	B_i^{4x}	C_i^{5x}	$A_{B^4}^{2x}$	$A_{C^5}^{2x}$	$B_{C^5}^{4x}$	$B_{A^2}^{4x}$	$C_{A^2}^{5x}$	$C_{B^4}^{5x}$
α_i	1/2	0	-1/4	-1/2	0	1/4	-1/2	-3/4	-1/4	1/2	3/4	1/4
β_i	-1	0	1/2	1	0	-1/2	1	3/2	1/2	-1	-3/2	-1/2

Applying the law of mass action to the quasi-chemical reactions of ionization of neutral native point defects of the type



yields a set of equations

$$\begin{aligned} 1. V_{A^2} \cdot p &= K_1 \cdot V_{A^2}^x & 7. A_{B^4}^{2'} \cdot p &= K_7 \cdot A_{B^4}^{2'} \times \\ 2. V_{B^4} \cdot p &= K_2 \cdot V_{B^4}^x & 8. A_{C^5}^{2'} \cdot p &= K_8 \cdot A_{C^5}^{2'} \times \\ 3. V_{C^5} \cdot n &= K_3 \cdot V_{C^5}^x & 9. B_{C^5}^{4'} \cdot p &= K_9 \cdot B_{C^5}^{4'} \times \\ 4. A_i^{2'} \cdot n &= K_4 \cdot A_i^{2'} \times & 10. B_{A^2}^{4'} \cdot n &= K_{10} \cdot B_{A^2}^{4'} \times \\ 5. B_i^{4'} \cdot n &= K_5 \cdot B_i^{4'} \times & 11. C_{A^2}^{5'} \cdot n &= K_{11} \cdot C_{A^2}^{5'} \times \\ 6. C_i^{5'} \cdot p &= K_6 \cdot C_i^{5'} \times & 12. C_{B^4}^{5'} \cdot n &= K_{12} \cdot C_{B^4}^{5'} \times \end{aligned} \quad (7)$$

Adding to the given system written in a common form as

$$A_1 \cdot p = K_1 \cdot A_1^x \text{ or } D_1 \cdot n = K_1 \cdot D_1^x,$$

the equation for equilibrium concentration of electrons and holes

$$n \cdot p = K_{14},$$

and also the equation of an electroneutrality

$$V_{A^2} + V_{B^4} + C_i^{5'} + A_{B^4}^{2'} + A_{B^4}^{2'} + B_{C^5}^{4'} + n = V_{C^5} + A_i^{2'} + B_i^{4'} + B_{A^2}^{4'} + C_{A^2}^{5'} + C_{B^4}^{5'} + p,$$

and solving the obtained system with respect to concentration of free charge carriers using data from table I, we obtain dependencies of free electron concentration (free hole concentration) upon pressure of volatile components, such as (8) and (9).

$$n^2 = \frac{K_3' p_{C_4}^{-1/4} + K_4' p_{C_4}^{-1/2} + K_5' + K_{10}' p_{C_4}^{1/2} + K_{11}' p_{C_4}^{3/4} + K_{12}' p_{C_4}^{1/4} + K_{14}}{K_1'' p_{C_4}^{1/2} + K_2'' + K_6'' p_{C_4}^{1/4} + K_7'' p_{C_4}^{-1/2} + K_8'' p_{C_4}^{-3/4} + K_9'' p_{C_4}^{-1/4} + 1}, \quad (8)$$

where $K_1' = K_1 \cdot K_i$, $K_i'' = K_1 \cdot K_i / K_{14}$, K_i from (5).

$$p^2 = \frac{K_1'' p_{C_4}^{1/2} + K_2'' + K_6'' p_{C_4}^{1/4} + K_7'' p_{C_4}^{-1/2} + K_8'' p_{C_4}^{-3/4} + K_9'' p_{C_4}^{-1/4} + K_{14}^2}{K_3' p_{C_4}^{-1/4} + K_4' p_{C_4}^{-1/2} + K_5' + K_{10}' p_{C_4}^{1/2} + K_{11}' p_{C_4}^{3/4} + K_{12}' p_{C_4}^{1/4} + K_{14}}, \quad (9)$$

where $K_1' = K_1 \cdot K_i$, $K_i'' = K_1 \cdot K_i / K_{14}$, K_i from (5).

Analysis of the obtained dependencies of the equilibrium concentration of free charge carriers on pressure yields the following conclusions:

Increase of pressure of the component C^5 in a system leads to

a) increase in concentration of the donors, connected with disorder, that is B_A , C_A , C_B ;

b) decrease in concentration of the donors, connected with vacancies of an anion and interstitial cations, that is V_C, A_i ;
c) increase in concentration of acceptors, connected with vacancies in the cation sublattice and interstitial anions, that is V_A, C_i ;
d) decrease in concentration of acceptors, connected with disorder, that is A_B, A_C, B_C .
Therefore, it is most probable that the experimentally observed (for example, from measurements of the Hall effect on samples after annealing under high pressure of one of the volatile constituents) shift of carrier concentration in the direction of n-type conductivity with a simultaneous decrease in mobility corresponds to the situation a); the experimentally observed shift of carrier concentration in the direction of p-type conductivity with a simultaneous increase in mobility corresponds to the situation b); the shift in carrier concentration in the direction of p-type with a simultaneous decrease of mobility corresponds to the situation c); the shift in carrier concentration in the direction of n-type with a simultaneous increase of mobility corresponds to the situation d). Designating by \uparrow , the increase in defect concentration and by \downarrow , the decrease in defect concentration, the results of the analysis may be presented as the following schemes:

Table II. The scheme of the correspondence of experimentally observed shift of charge carriers concentration and mobility (a case of primary ion scattering) to a change of concentration of native structural defects after annealing under high pressure of C^5 or A^2

Annealing under high pressure of	Observation	Possible cause	Concrete definition
C^5	$n \uparrow, p \downarrow, \mu \uparrow$	$A \downarrow$	$A_B \downarrow, A_C \downarrow, B_C \downarrow$
C^5	$n \uparrow, p \downarrow, \mu \downarrow$	$D \uparrow$	$B_A \uparrow, C_A \uparrow, C_B \uparrow$
C^5	$n \downarrow, p \uparrow, \mu \uparrow$	$D \downarrow$	$V_C \downarrow, A_i \downarrow$
C^5	$n \downarrow, p \uparrow, \mu \downarrow$	$A \uparrow$	$V_A \uparrow, C_i \uparrow$
A^2	$n \uparrow, p \downarrow, \mu \uparrow$	$A \downarrow$	$V_A \downarrow, C_i \downarrow$
A^2	$n \uparrow, p \downarrow, \mu \downarrow$	$D \uparrow$	$V_C \uparrow, A_i \uparrow$
A^2	$n \downarrow, p \uparrow, \mu \uparrow$	$D \downarrow$	$B_A \downarrow, C_A \downarrow, C_B \downarrow$
A^2	$n \downarrow, p \uparrow, \mu \downarrow$	$A \uparrow$	$A_B \uparrow, A_C \uparrow, B_C \uparrow$

QUASI-CHEMICAL ANALYSIS OF EXPERIMENTAL DATA

The results of a change in electrophysical parameters under the heat treatment of some II-IV- V_2 crystals in the vapor of volatile constituents, obtained in the present work and taken from the literature, are analyzed by correlating the experimentally observed shift of charge carrier concentration and mobility (a case of primary ion scattering) to a change of concentration in native structural defects after annealing under high pressure of C^5 or A^2 from table III. The results of the analysis are given in tables III and IV.

For $CdSnAs_2$ the presence of two types of donors results from the existence of two time-stages of annealing in vapor of the both volatile components. The first annealing time-stage of $n-CdSnAs_2$ (decrease of electron concentration with sharp increase of electron mobility during annealing in As-vapor) is defined as a fast processes, (for instance, corresponding to the equations 3, 4 of system (7)) and connected mainly with the decrease in concentration of donor vacancies $[V_{As}]$. The second stage changes (increase of electron concentration during annealing in As-vapor) are affected by competitive slower processes (for instance, corresponding to the equations 10 - 12 of system (7)), connected with modifications of disorder defect concentration. Under annealing in Cd-vapor the stages traded places.

Literature data and the results of the present work concerning ZnGeP_2 testify that the conditions of the chemical and thermal history of ZnGeP_2 crystals (chemical composition of a melt, composition and pressure in a growth technological system etc.) have much influence on concentrations of native structural defects and, because of that, on properties and behavior of ZnGeP_2 under further treatments. As follows from figures 1, 2 and from the analysis the crystals ZnGeP_2 with different "previous history" have a different ensemble of native structural defects and react differently on an annealing in vapor of volatile components.

For ZnGeP_2 , the presence of both vacancies (in the present work for $\text{ZnGeP}_2 < \text{P}>$, when $[\text{V}_\text{P}]$, probably less than equilibrium concentration for conditions of annealing in Zn-vapor) and disorder defects in the cation sublattice (in the present work for $\text{ZnGeP}_2 < \text{Zn}>$) were observed.

For CdGeAs_2 the presence of at least two native acceptors has been observed in experiments utilizing radiation damage, magnetic resonance and thermal admittance spectroscopy [20]. As follows from Figures 3, 4 the annealing of n- CdGeAs_2 in both As atmosphere and Cd atmosphere, yielded a diminution of electron concentration. In the first case it was accompanied by a diminution of mobility (μ), in the second case it was accompanied by magnification of μ . In the approximation of the scheme used in table I, it corresponds to 1) magnification of concentration V_{Cd} (and, probably, As_i), 2) diminution of concentration of disorder defects such as Ge_{Cd} . We note that annealing in Cd vapor, carried out by the authors of work [9], on n- CdGeAs_2 at $T_{\text{anneal}} = 400^\circ\text{C}$, led to (from $\sim 2 \cdot 10^{16} \text{ cm}^{-3}$ to $\sim 8 \cdot 10^{17} \text{ cm}^{-3}$) the increase in the electron concentration. Probably, the less than 100°C annealing temperature in experiment [9] was the reason for the smaller activity of disorder defects. The annealing processes were defined by an extreme modification of the concentration of vacancies and led to a sharp increase in electron concentration due to a lack of a competing process, giving an opposite outcome. In the annealing of p- CdGeAs_2 a simultaneous course of several competing processes is also observed. The initial annealing stage (30 hours in As_4 vapour) gave p-n conversion of conductivity of samples under study (from $p \sim 7 \cdot 10^{15} \text{ cm}^{-3}$, $\mu \sim 290 \text{ cm}^2/\text{V}\cdot\text{s}$ to $n \sim 8 \cdot 10^{15} \text{ cm}^{-3}$, $\mu \sim 2800 \text{ cm}^2/\text{V}\cdot\text{s}$ at $T_{\text{meas}} \sim 290 \text{ K}$, and $n \sim 5 \cdot 10^{15} \text{ cm}^{-3}$, $\mu \sim 3900 \text{ cm}^2/\text{V}\cdot\text{s}$ at $T_{\text{meas}} \sim 95 \text{ K}$). Using the same approximations as in table I, the concentration of disorder defects ($\text{Cd}_{\text{Ge}} \downarrow$, $\text{Ge}_{\text{Cd}} \uparrow$) increases, or it is explained by uncontrollable doping of the samples (for example, by O_2). The outcomes of long annealing of p- CdGeAs_2 in As_4 are presented in figure 3 b). The increase in hole concentration with respective change in mobility corresponds to a stage of 190 hours of annealing. It can be described by the increase of $[\text{V}_{\text{Cd}}]$ and the decrease of $[\text{V}_{\text{As}}]$. The stage of 384 hours is characterized by an outcome ($p \downarrow$, $\mu \downarrow$). That can mean a prevalence of the first process ($\text{Ge}_{\text{Cd}} \uparrow$). Similar experiments on annealing of p- CdGeAs_2 in As_4 vapor were carried out by the authors [9, 10]. In this case the annealing temperature differed less (450°C [10] and 520°C [9]). However, the influence of the process, defined by disorder defects, which were observed in the work [9, 10] are lacking. Probably, it is possible to assume, that in this case the initial imperfection of samples under study plays a key role. A different imperfection caused different routes and different times, necessary for reaching an equilibrium condition. From an analysis of the observed modifications of electrophysical parameters, associated with annealing of p- CdGeAs_2 in Cd, we can approximate the influence of processes connected with disorder defects as follows. Such processes as $\text{A}_\text{B} \uparrow$, $\text{A}_\text{C} \uparrow$, $\text{B}_\text{C} \uparrow$ and $\text{B}_\text{A} \downarrow$, $\text{C}_\text{A} \downarrow$, $\text{C}_\text{B} \downarrow$ play a defining role. Thus, after annealing of n- and p- CdGeAs_2 under high pressure of the volatile components, we observed the influence of such native defects as V_{Cd} , V_{As} , Cd_{Ge} , Ge_{Cd} . We note that annealing in the vapor of the element A^2 (Cd) was difficult because of the high chemical activity of the element A^2 in relation to a surface of crystals $\text{A}^2\text{B}^4\text{C}^5_{12}$. This caused formation of surface layers of a different chemical nature.

Table III. The results of the quasi-chemical analysis of experimental data of the present work and also literary data on annealing in vapour of volatile components for some II-IV-V₂ (The data of the present work are marked by an asterisk)

Compound	Annealing in vapour	Observed change	Responsible native defects
CdSnAs ₂	C ⁵	1) n ↓ p ↑ μ ↑ [8],[*]	V _C ↓, A _i ↓
	C ⁵	2) n ↑ p ↓ μ ↓ [8],[*]	B _A ↑, C _A ↑, C _B ↑
	A ²	1) n ↓ p ↑ μ ↑ [8],[*]	B _A ↓, C _A ↓, C _B ↓
	A ²	2) n ↑ p ↓ μ ↓ [8],[*]	V _C ↑, A _i ↑
CdGeAs ₂	C ⁵	1) n ↓ p ↑ μ ↑ [10, 9],[*]	V _C ↓, A _i ↓
	C ⁵	2) n ↓ p ↑ μ ↓ [*]	V _A ↑, C _i ↑
	C ⁵	3) n ↑ p ↓ μ ? [*]	A _B ↓, A _C ↓, B _C ↓
			B _A ↑, C _A ↑, C _B ↑
	A ²	1) n ↑ p ↓ μ ? [10], [*]	V _C ↑, A _i ↑ or V _A ↓, C _i ↓
	A ²	2) n ↓ p ↑ μ ↑ [*]	B _A ↓, C _A ↓, C _B ↓
	A ²	3) n ↓ p ↑ μ ↓ [*]	A _B ↑, A _C ↑, B _C ↑
CdSiAs ₂	C ⁵	1) n ↓ p ↑ μ ↑ [11, 18]	V _C ↓, A _i ↓
	C ⁵	2) n ↑ p ↓ μ ↑ [11]	A _B ↓, A _C ↓, B _C ↓
	A ²	1) n ↑ p ↓ μ ↓ [11, 18]	V _C ↑, A _i ↑
	A ²	2) n ↓ p ↑ μ ↓ [11]	A _B ↑, A _C ↑, B _C ↑
CdSiP ₂	C ⁵	n ↓ p ↑ μ ? [15]	V _C ↑, A _i ↑, V _A ↓, C _i ↓
ZnGeP ₂	C ⁵	n ↓ p ↑ μ ? [11]	V _C ↑, A _i ↑, V _A ↓, C _i ↓
	A ²	n ↓ p ↑ μ ↑ [12]	B _A ↓, C _A ↓, C _B ↓
	C ⁵	n ↑ p ↓ μ ↑ [12]	A _B ↓, A _C ↓, B _C ↓
	A ²	n ↓ p ↑ μ ? [13-17]	disorder defects
	C ⁵	n ↑ p ↓ μ ? [13-17]	disorder defects
	A ²	n ↑ p ↓ μ ↓ [*]	V _C ↑, A _i ↑
ZnGeP ₂ <P>	C ⁵	n ↓ p ↑ μ ↑ [*]	V _C ↓, A _i ↓
ZnGeP ₂ <Zn>	A ²	n ↓ p ↑ μ ↓ [*]	A _B ↑, A _C ↑, B _C ↑
	C ⁵	n ↑ p ↓ μ ↑ [*]	A _B ↓, A _C ↓, B _C ↓
	C ⁵	n ↑ p ↓ μ ↑ [*]	A _B ↓, A _C ↓, B _C ↓
ZnSnP ₂	A ²	1) n ↓ p ↑ μ ↑ [19]	B _A ↓, C _A ↓, C _B ↓
	A ²	2) n ↑ p ↓ μ ↓ [19]	V _C ↑, A _i ↑
	C ⁵	1) n ↑ p ↓ μ ↑ [19]	A _B ↓, A _C ↓, B _C ↓
	C ⁵	2) n ↓ p ↑ μ ↓ [19]	V _A ↑, C _i ↑

Table IV. The most probable native structural defects in some A²B⁴C⁵₂ exhibited under heat treatment in vapor of volatile constituents and satisfying to the Hume-Rothery criterion

Compound	CdSnAs ₂	CdGeAs ₂	CdSiAs ₂	CdSiP ₂	ZnGeP ₂	ZnSnP ₂
Defects	Sn _{Cd} , V _{As}	V _{As} , V _{Cd} , Cd _{Ge} , Ge _{Cd}	Si _{As} , V _{As}	V _{Cd} , V _P	Zn _{Ge} , Ge _{Zn} , V _{Zn} , V _P	Zn _{Sn} , Zn _P , Sn _{Zn} , P _{Zn} , V _{Zn} , V _P

CONCLUSIONS

1. Experiments on annealing of CdGeAs₂-, CdSnAs₂- and ZnGeP₂-crystals in the vapor of volatile constituents were carried out. Conductivity and Hall effect measurements were performed to characterize the modification of electrical properties, caused by interaction of the crystal with the gas phase during the annealing.
2. A scheme for correlating the experimentally observed shifts of charge carrier concentration and mobility (a case of primary ion scattering) to a change in concentration of native structural defects after annealing under high pressure of C⁵ or A², based on quasi-chemical analyses was presented.
3. The literature data and results of the present work on the annealing were discussed based on the results of a quasi-chemical analysis.
4. It was noted that the outcomes of the annealing essentially depend on both the initial imperfections of the crystal and the conditions of the experiment as they define the route and time of reaching an equilibrium..
5. For some II-IV-V₂ the most probable native structural defects becoming apparent under heat treatment in the vapor of volatile constituents and satisfying to the Hume-Rothery criterion were the following: For CdSnAs₂ - Sn_{Cd}, V_{As}; for CdGeAs₂ - V_{As}, V_{Cd}, Cd_{Ge}, Ge_{Cd}; for CdSiAs₂ - Si_{As}, V_{As}; for CdSiP₂ - V_{Cd}, V_P; for ZnGeP₂ - Zn_{Ge}, Ge_{Zn}, V_{Zn}, V_P; for ZnSnP₂ - Zn_{Sn}, Sn_{Zn}, V_{Zn}, V_P.

ACKNOWLEDGEMENTS

The authors gratefully acknowledge support of the European Office of Aerospace Research and Development and the International Science and Technology Center through Project #1604p.

REFERENCES

1. N.A.Goryunova, S.Mamaev, V.D.Prochukhan, Properties of CdSnAs₂ semiconductor – an electronic analog of InAs, *Dokl. Akad. Nauk SSSR* (rus). **142**, 623-6 (1962).
2. V.D.Prochukhan, Yu.V.Rud', Potential practical applications of II-IV-V₂ semiconductors *Fiz.Tech.Polovedn* (rus) .**12**, 209 (1977)[Sov. Phys. Semiconductors **12** 121 (1977)]
3. L.E. Halliburton et al, Electron paramagnetic resonance of a native acceptor in as-grown ZnGeP₂, *Appl. Phys. Lett.* **64**, 1615 (1994).
4. R. Pandey, M.C.Ohmer, J.D.Gale, A theoretical study of native acceptors in CdGaAs₂, *J. Phys.: Condens. Matter.* **10**, 5525 (1998).
5. P.Zapol, R.Pandey, M.Ohmer, J. Gale, Atomistic calculations of defects in ZnGeP₂, *J. Appl. Phys.* **79**, 671 (1996).
6. N.C.Giles, L.E.Halliburton, Native defects in the Ternary Chalcopyrites, *MRS Bulletin.* **23**(7), 37 (July, 1998).
7. F.A. Kroger. *The chemistry of imperfect crystals* (North-Holl. Publ. Co, Amsterdam, 1964).
8. S.P.Vul', V.D.Prochukhan, Yu.V.Shmartsev, Thermal defects in CdSnAs₂, *Dokl. Akad. Nauk SSSR, Tech. Phys.* (rus). **204**(5), 1094-6 (1972).
9. B.H.Bairamov, V.Yu.Rud', Yu.V.Rud', Properties of Dopants in ZnGeP₂, CdGeAs₂, Ag-GaSe₂, AgGaSe₂, *MRS Bulletin.* **23**(7), 41 (July, 1998).
10. Ch. Dovletmuradov, A.Allanzarov, V.D. Prochukhan, Yu.V.Rud', M.Serginov, Effect of heat treatment on the electrical properties of p-CdGeAs₂, *Izv. Akad. Nauk Turkm. SSR. Ser. Fiz.-Tekh, Khim. i Geol. Nauk* (rus) **3**, 106-8 (1972).

11. V.D. Prochukhan, About the behavior of the components of a lattice of compounds $A^2B^4C_5^{5/2}$, // Some problems of chemistry and physics of multinary semiconductors: Materials of a symposium (rus). 40 (UzhGU, Uzhgorod, 1970).
12. R.V. Masagutova, Research on the influence of lattice defects on the properties of monocrystals $ZnGeP_2$: Thesis of the cand. of chem. scien. (Leningrad, 1980).
13. V.D. Prochukhan, G.K. Averkieva, Effect of intrinsic lattice defects on the properties of compound $A^{II}B^{IV}C_2^v$, *Teor. i Eksperim. Issled. Slozhn. Poluprovodn. Soedinenii* [*Theoretical and experimental research on multinary semiconductor compounds*](rus). 75-85 (Kishiniov, 1978).
14. F.P. Kesamanli, Yu. V. Rud', Wideband semiconductors $A^2B^4C_5^{5/2}$ with a chalcopyrite structure. *Ternary semiconductors and their application*. 39 (Shtiintsa, Kishiniov, 1979).
15. I.I. Tychina, Intrinsic lattice defects in the phosphides $A^2B^4C_5^{5/2}$. *Ternary semiconductors and their application*. 17 (Shtiintsa, Kishiniov, 1987).
16. V. S. Grigor'eva, V. D. Prochukhan, Yu. V. Rud', A. A. Yakovenko, Intrinsic donors in zinc germanium phosphide ($ZnGeP_2$) crystals, *Pis'ma Zh. Tekh. Fiz.* **1**(3), 130-2 (1975). [Sov. Tech. Phys. Lett. **1**(2) 61 (1975)]
17. G. A. Grishchenko, A. Sakalas, A. Sodeika, I. G. Tregub, Inversion of the conductivity type in zinc germanium phosphide ($ZnGeP_2$), *Liet. Fiz. Rinkiny*, **19**(6), 797-801 (1979).
18. A. Mamedov, M. Serginov, Lattice defects in the crystals $CdSiAs_2$. *Ternary semiconductors and their application*. 83 (Shtiintsa, Kishiniov, 1987).
19. L. V. Kradinova, V. D. Prochukhan, V. A. Radul, Effect of deviations from stoichiometry on the properties of $ZnSnP_2$ semiconductor. *Nekot. Vop. Khim. Fiz. Poluprov. Slozhn. Sostava* [*Some problems of chemistry and physics of multinary semiconductors: Materials of a symposium* (rus)]. 110-3 (UzhGU, Uzhgorod, 1970).
20. P. Zapol, R. Pandey, M. Seel, J. M. Recio, M. C. Ohmer, Density functional study of the structure, thermodynamics and electronic properties of $CdGeAs_2$, *J. Phys.: Condens. Matter*, **11**, 4517 (1999).

Radiative recombination processes of thermal donors in silicon

S. Pizzini, S. Binetti, E. Leoni, A. Le Donne, M. Acciarri, A. Castaldini(*)
INFN and Department of Materials Science, University Milano-Bicocca, Via Cozzi 53,
Milano, Italy
(*)INFN and Department of Physics, University of Bologna, Viale Berti Pichat 6/2, Bologna,
Italy

ABSTRACT

There is a recent, renewed attention on the possible development of optical emitters compatible with silicon microelectronic technology and it has been recently shown that light emitting diodes could be manufactured on dislocated silicon, where dislocations were generated by plastic deformation or ion implantation. Among other potential sources of room temperature light emission, compatible with standard silicon-based ULSI technology, we have studied old thermal donors (OTD), as the origin of their luminescence is still matter of controversy and demands further investigation.

In this work we discuss the results of a spectroscopical study of OTD using photoluminescence (PL) and Deep Level Transient Spectroscopy (DLTS) on standard Czochralsky (Cz) silicon samples and on carbon-doped samples.

We were able to show that their main optical activity, which consists of a narrow band at 0.767 eV (P line), is correlated to a transition from a shallow donor level of OTD to a deep level at $E_v+0.37$ eV which is tentatively associated to C-O complexes. As we have shown that the P line emission persists at room temperature, we discuss about its potentialities to silicon in optoelectronic applications.

INTRODUCTION

It is well known that a long dwelling at temperatures around 450°C during the cooling cycle of large diameter, crucible grown, oxygen-rich Cz silicon or any thermal annealing of Cz silicon in the same temperatures range, leads to the generation of oxygen related donors, often referred as Old Thermal Donors (OTD), to distinguish them from other types of thermal donors that can be formed in the temperature range 600–700 °C and today known as New Thermal Donors (NTD). Since their discovery generations of investigators addressed their studies to the microscopic structure, the growth and decomposition kinetics as well as the electrical and optical properties of OTDs, using all the techniques suitable for the study of electrically and optically active, paramagnetic centres.

In spite of many thousands (around 19000) of papers published on the topic, which make of the OTDs one of the most studied defect centres in semiconductors, and whose properties have been recently reviewed by Newman [1] a defect model which consistently explains all their features, including their optical properties, is still lacking.

In fact, while it is well known that oxygen rich silicon annealed at 450 °C for several hours exhibits a prominent photoluminescence spectrum with a narrow no-phonon line at 0.767 eV, generally labelled P line [2], a direct proof that oxygen is incorporated in the centre has not yet been given. Furthermore, PL measurements have cast doubts on a simple relationship between thermal donors and the P line [3]. Eventually, a carbon isotopic effect experimentally determined in the P line shows a possible involvement of carbon-oxygen complexes in the defect involved in the P line luminescence [2].

In this work we will present and discuss the results of a systematic study of the photoluminescence properties of old thermal donors, carried out on carbon-lean and carbon-doped Cz samples, with the aim looking to possible applications of the P-line in optoelectronic applications.

EXPERIMENTAL

In the experiments the following samples were examined:

- (1) n-type ($\rho = 3.5-5 \text{ Ohm cm}$) (100) Cz silicon samples with oxygen concentration of 18 ppma, carbon content below the FTIR detection limits ($<0.1 \text{ ppma}$) (kindly supplied by MEMC Electronic Materials, Italy). These samples are designed as CzM.
- (2) n-type ($\rho = 18-15 \text{ Ohm cm}$) (100) Czochralski grown silicon doped with carbon during the growth process (kindly supplied by Institute for Material Science Research of Sendai, Japan) $[\text{O}] = 24 \text{ ppma}$, $[\text{C}] = 1 \text{ ppma}$. These samples are designed as CzJ.

The samples were treated for times variable from 8 to 100 hours at 470°C in order to induce the thermal donors generation, while their dissolution has been achieved by thermal treatment at 650°C for 10'. Prior to thermal treatments, the samples were CP4 and RCA etched and then were closed under vacuum in quartz ampoules. The oxygen losses resulting from the annealing are deduced from room temperature FTIR measurements. The resistivity of all the samples, before and after any thermal treatments has been measured for OTD concentration determination according the ASTM procedure F 723-88. The values of diffusion length of minority carriers were measured by the Surface Photovoltage technique. Details are reported in [4]. The photoluminescence (PL) spectra of both sets of samples were recorded with a spectral resolution of 6 nm ($\Delta E = 4 \text{ meV}$), using standard lock-in techniques in conjunction with a grating monochromator and InGaAs as a detector. For the excitation, a quantum well laser ($\lambda = 808 \text{ nm}$) was used. The measurements were performed in the temperature range 12 - 300 K. Standard DLTS measurements have been performed by means of a SULA Tech. Inc. instrumentation. The temperature has been varied from the liquid nitrogen temperature to 350 K with reverse bias ranging from -4V to 0 and a pulse width from 1 to 10ms.

Minority carrier traps have been detected by minority carrier transient spectroscopy (MCTS). MCTS is a technique that measures the capture and emission of minority carriers at deep states within the band gap. In this technique injection of carriers is by a light pulse of above-band-gap radiation incident on a semitransparent Schottky diode. During the measurement the controlling excess carrier species are minority carriers, generated behind the depletion region by optical excitation while the sample is held under reverse bias. The electric field in the depletion region excludes majority carriers. Photogenerated minority carriers created within a diffusion length from the depletion region may then enter the depletion region and be available for capture. Schottky diode under test is maintained at a constant value of applied reverse bias, in our case 4V.

RESULTS

CzM samples

The effect of annealing time at 470°C on the concentration of interstitial oxygen $[\text{O}_i]$, and of OTDs is displayed in Figs. 1 and 2 while the time evolution of the diffusion length is reported in Fig.3.

As it is expected from earlier literature data, the concentration of OTDs increases almost linearly with the annealing time. Moreover, this increase is associated to a decrease of the diffusion length (see Fig.3), which saturates after about 20 hr. The photoluminescence spectra of these samples, collected after different annealing times at 470°C, present common features, as it is shown in Fig. 4, which reports a typical spectrum. In fact, a very intense P line is always present, together with two weak signals known in literature [2,5] as the C line at 0.789 eV and the H line at 0.925 eV and the band edge luminescence at 1.1 eV.

While the energy position of the P line has been verified to remain unaltered at increasing annealing times and by increasing the laser power within four orders of magnitude (from 0.02 mW to 60 mW), its intensity shows a typical trend, with the duration of the heat treatment.

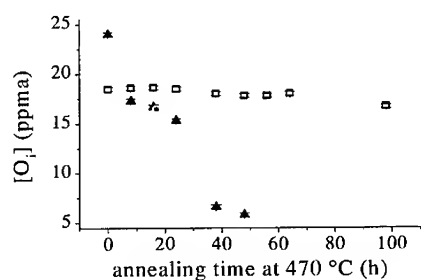


Figure 1. Evolution of the concentration of the interstitial oxygen with the annealing time at 470°C (□ CzM sample, ▲ CzJ sample).

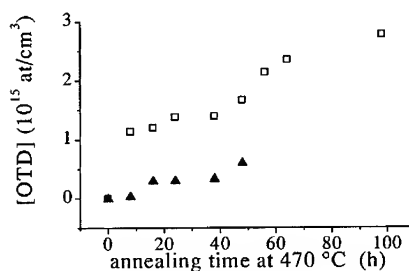


Figure 2. Evolution of the OTD concentration with the annealing time at 470°C (□ CzM sample, ▲ CzJ sample).

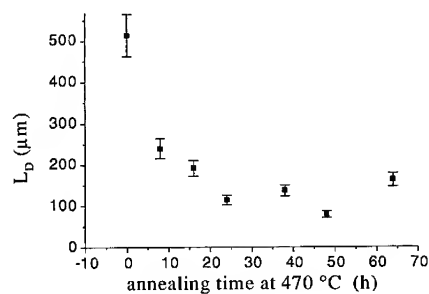


Figure 3. Evolution of diffusion length of minority carriers with the annealing time at 470 °C in the CzM sample.

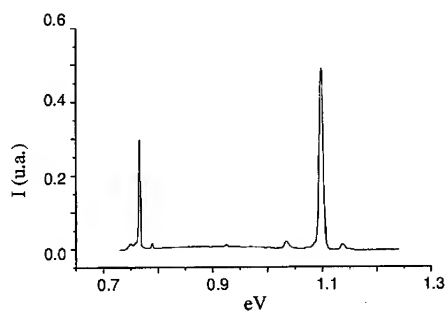


Figure 4. PL spectrum of a CzM sample after an annealing at 470 °C for 24 h ($T=12$ K, $P=6$ W/cm², $\Delta E=4$ meV).

The intensity of the P line, increases, in fact, up to a maximum after about 25 hr, and then decreases for thermal treatments of longer duration, as shown in Fig.5

It is worth to remark that this behaviour is largely uncorrelated with the total concentration of OTDs, which increases steadily (see Fig. 2), but follows almost exactly the behaviour of the PL intensity of the OTD-bound exciton emission in the TO region and the concentration of the NL8 donor, which both peak in fact at about 20 hours, as reported by Liesert et. [6] and Newman [1]. It is rather interesting, and never cited in literature, that the decrease of the diffusion length with the annealing time saturates in correspondence of the maximum of the P-line intensity, indicating a common trend with density of recombination centres and the intensity of the P-line. It is important to note that the intensities of the C and H lines remain instead constant with the entire duration of the heat treatment.

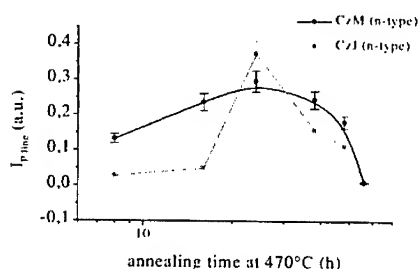


Figure 5. Evolution of the intensity of the P line with the annealing time at 470 °C (● CzM sample, ○ CzJ sample). The curves through the points are a guide for the eyes.

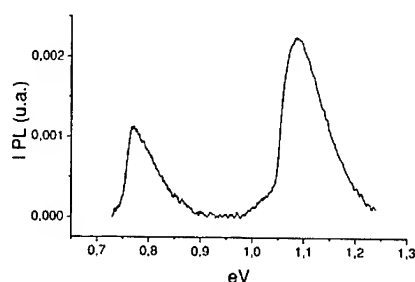


Figure 6. Typical photoluminescence spectrum of OTDs at room temperature (P=6W/cm², ΔE=4 meV).

The P line signal persists up to room temperature with a substantial decrease in intensity and an almost constant ratio with the band edge luminescence, as it is shown in Fig. 6. The thermal quenching occurs at temperatures above 50 K with a thermal dissociation energy of 31 meV (see Fig. 7.a). An increase of the P line intensity is observed between 12 and 30 K (see Fig. 7.b), in agreement to previous results of Davies [7] who explains this behaviour as a result of competition between the optical centres and other (shallow) traps. With increasing temperature the excitons freed from the traps become available for capture by photoluminescence centres. Table I displays the DLTS and MCTS results where only the traps present after the thermal treatment for 24 h and 64 h are reported. From this table we can observe the set-up of a shallow level at $E_c-0.015$ eV (related to thermal donors) after 24 hr, which permains after 64 h as well as two deep levels at $E_c-0.33$ and $E_c-0.34$ of which one sets up after 64 h. From MCTS measurements a trap at $E_v+0.37$ eV has been detected, which falls very close to the energy of the trap observed by with Hall effect measurements [10] in similarly prepared samples.

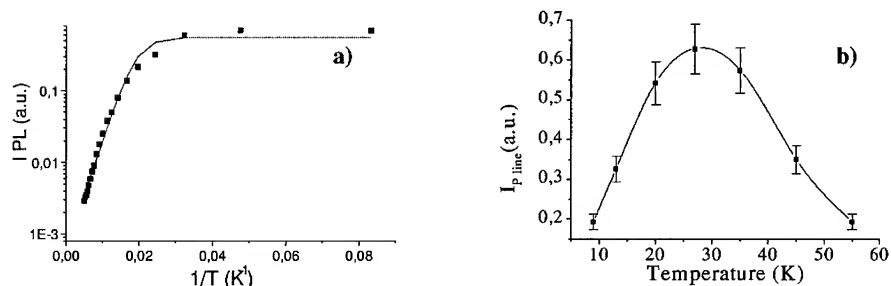


Figure 7 a) Thermal quenching of the P line b) Temperature dependence of the P line in 10-60 K range.

Samples TT 470°C	$E_c - E$ [eV]	σ [cm ²]	N_T [cm ⁻³]	Remarks
24h	0.014	4.3×10^{-21}	9.2×10^{11}	DLTS
	0.33	2.5×10^{-16}		
64h	0.015	1.7×10^{-20}	8.7×10^{11}	DLTS
	0.34	6.2×10^{-17}	1.2×10^{12}	
	0.33	2.3×10^{-18}		
Samples TT 470°C	$E_v + E$ [eV]	σ [cm ²]		Remarks
24h	0.37	1.75×10^{-18}		MCTS

Table I Summary of the properties of the majority and minority carrier traps found by DLTS and MCTS.

CzI samples

As it could be observed in Figs. 1 and 2 the effect of annealing on $[O_i]$ and OTD concentration is quite different with respect to the CzM samples. In fact, while in the former samples the oxygen concentration remains almost constant (its decrease is of the order of the donor formed, i.e. less than 1% of the initial oxygen concentration) with the annealing time, in these samples the oxygen concentration decreases down to 5 ppma, as the carbon concentration does, going below the detection limit. This can be easily explained by considering that the presence of carbon favours the oxygen precipitation as oxide. In fact, oxygen *per se* requires an excess volume to segregate as an oxide, which must be normally delivered either by vacancy absorption or self-interstitial emission. As carbon precipitation is as well volume exigent, its molar volume being half of the silicon matrix, the simultaneous presence of both oxygen and carbon favours [8] their co-precipitation.

It should be however remarked that the concentration of carbon in these samples is only little in excess over that present in former samples, indicating either a strong catalytic effect or some effect associated to an excess of IR-inactive carbon content in the oxygen segregation processes. Another striking difference is the total amount of donors formed, which is always in defect with respect to than found in CzM samples, as an indication that the overall kinetics of OTD formation is influenced by the simultaneous occurring of the oxygen segregation.

The presence of carbon has also a striking effect on the features of PL spectra, as it is shown in Fig.8. The presence of a broad band within 0.7 and 1.0 eV is clearly evident, on which the P, C and H lines [2,5] are superimposed, together with a multiplicity of other emissions of minor intensity and a strong band edge emission, which are better evidenced while removing the broad band contribution to the background, as it is shown in Fig. 9.

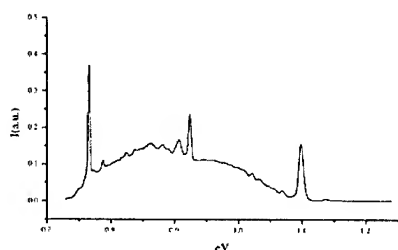


Figure 8. PL spectrum of CzJ heat treated at 470°C for 24h ($T=12$ K, $P=6$ W/cm², $\Delta E=4$ meV).

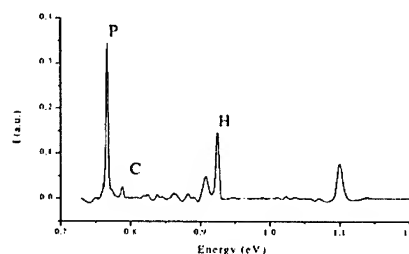


Figure 9. PL spectra of sample CzJ TT 470 °C 24 h after background subtraction.

Incidentally, a broad band in the same energy range was found as the unique PL fingerprint of the segregation of oxide nanoparticles in Cz samples annealed at 650°C for 64h [9].

It should be also remarked that the PL intensity of the P line is quite comparable with that observed in carbon-lean samples, in spite of the lesser density of donors formed and a larger integral radiative emission of the sample.

The difference between the spectral features of the PL in CzM and CzJ samples can be associated to the segregation of carbon and oxygen, which can be in fact monitored by optical microscopy after Schimmel etching (see Fig. 10). The presence of precipitates together with dislocations, where the last do however not manifest their presence in the PL spectra, is clearly evident from the triangular etch pits.

As in the case of the CzM samples, the P line disappears after a thermal dissolution treatment at 650 °C.

The evolution of the intensity of the P line in CzJ with the annealing time is reported in Fig. 5, which shows a substantial agreement with the behaviour of carbon-lean samples, both in the peak energy and in the maximum absolute intensities.



Figure 10. Optical micrograph of Schimmel etched sample CzJ TT for 24 h at 470 °C (x 1000).

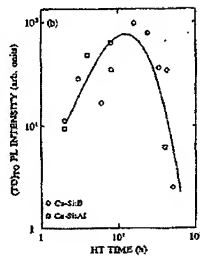


Figure 11. Annealing-time dependence of the OTD-bound exciton emission band intensity in the TO region for various boron and aluminium doped silicon crystal.

DISCUSSION

The interest of the present results is twofold, concerning both the physics of the light emission from OTD and the potentialities of the OTDs as room temperature light emitting centres. About the first issue, some main key points come from this work. At first, a shallow donor level at $E_c - 0.014$ eV and a deep level at $E_v + 0.37$ eV were detected by DLTS and MCTS measurements, where the second falls very close to the energy of the trap observed by with Hall effect measurements [10] in similarly prepared samples. The annealing time dependence of the P line luminescence follows the corresponding evolution of the NL8 donor and of the OTD-bound exciton (see Fig. 11) observed by Liesert et al. [6]. If we consider that the P-line emission correspond to a radiative transition between a donor level at $E_c - 0.0015$ eV and the deep trap at $E_v + 0.37$ eV we could fit within few meV the P line emission energy at 0.767 eV, and conclude that the P luminescence originates from a transition from a OTD level to a deep level corresponding to a C-O complexes, as already proposed by some of us in a former article [3]. About the second issue, we have demonstrated that OTDs emit light at room temperature, although with a hundredfold decrease of intensity with respect to cryogenic temperatures. The comparable values of the thermal dissociation energy (31 meV) and the energy of the shallow level which sets-up with the annealing at 470°C and which is involved in the P-line transition, calls for a quenching mechanism associated to the thermal donor ionisation. It seems therefore restricted by the physics of the PL luminescence processes of OTDs in carbon-lean samples and by the presence of non-radiative recombination centres in carbon-doped samples any possible further increase of the PL of OTDs.

REFERENCES

1. R.C. Newman, J.Phys.: Condens. Matter **12**, R335 (2000)
2. W. Kürner, R. Sauer, A. Dornen, K. Thonke, Phys. Rev. B **39**, 13327 (1989)
3. S. Pizzini, M. Guzzi, E. Grilli, G. Borionetti, J.Phys.: Condens. Matter **12**, 10131 (2000)
4. A. Castaldini, D. Cavalcoli, A. Cavallini, Appl. Phys. **A71**, 305 (2000)
5. J. Weber, R. Sauer, MRS Symp. Proc. **14**, 165 (1983)
6. B.J. Heijmink Liesert, T. Gregorkiewicz, C.A.J. Ammerlaan, Phys.Rev. B **46**(4), 2034 (1992)
7. G. Davies Physics Reports **176**, 83 (1989)
8. J.Y. Huh, U. Gösele, T.Y. Tan, J. Appl. Phys. **78**, 5926 (1995)
9. S. Binetti, S. Pizzini, E. Leoni, R. Somaschini, J. Appl. Phys. submitted (November 2001)
10. J. Weber, H.J. Queisser, MRS Symp. Proc. **59**, 147 (1986)

Annealing effect on the nonradiative carrier recombination in AlGaAs/GaAs investigated by a piezoelectric photothermal spectroscopy

Atsuhiko Fukuyama, Hiroaki Nagatomo, Yoshito Akashi, and Tetsuo Ikari
Faculty of Engineering, Miyazaki University,
1-1 Gakuen-kibanadai-nishi, Miyazaki 889-2192, Japan

ABSTRACT

Electron non-radiative recombination process of photoexcited carriers in as-grown and annealed $n\text{-Al}_{0.2}\text{Ga}_{0.8}\text{As/GaAs}$ hetero-structure samples are investigated by using a piezoelectric photothermal spectroscopy (PPTS). The PPT signal above the band-gap energy of GaAs substrate decreased when the sample was annealed at 815°C. In the frequency dependent measurements, the deviations from $1/f$ linear function are clearly observed in the AlGaAs/GaAs samples. This critical deviation frequency was found to shift to the lower frequency region by annealing. Our experimental results are explained by assuming that the sample annealing generates an unknown deep level in AlGaAs epitaxial layer region and this level effectively traps the photoexcited carriers non-radiatively.

INTRODUCTION

Pseudo-binary compound semiconductor AlGaAs is widely used for quantum electronic devices such as the light emitting diodes (LED) and the hetero bipolar transistor (HBT). Intrinsic deep defect levels in this material are known to cause a degradation of such devices. They trap the free carriers, and thus high frequency operation of electronic devices are seriously influenced. Annealing process followed by an ion-implantation is a most important process in the device fabrication. Since this annealing process affects a formation and a destruction of deep defect levels, it is very important to understand an annealing effect on the carrier generation and recombination properties through deep defect levels.

The recombination process of photoexcited carriers is commonly investigated by a photoluminescence (PL) method. This is available technique to understand a light emission mechanism such as band to band, band to impurity level, and impurity to impurity levels transitions. However, the recombination processes of carrier through the deep levels is mainly non-radiative recombination. A strong electron lattice interaction affects these carrier transitions. The PL method can detect only a radiative recombination process. Therefore, it becomes important to establish an alternative experimental technique to investigate such transitions.

Recently, we have developed the piezoelectric photo-thermal (PPT) spectroscopy that has a higher sensitivity for investigating the thermal and electronic properties of semiconductors than a conventional microphone photoacoustic method [1]. This also gives us an information of non-radiative transitions through deep defect levels. Extensive works for Si, GaAs, and AlGaAs/GaAs samples were carried out [1-3] and a metastable natures for representative deep levels in GaAs such as *EL2* and *EL6* were clearly resolved. In the present paper, we propose a model to explaining our experimental results for the non-radiative recombination process in the photoexcited carriers in the AlGaAs/GaAs hetero-structure sample. Annealing effect on the frequency dependence of the PPT signal is also explained by developing the proposed model by Todorović *et al.* [4].

EXPERIMENTAL PROCEDURES AND RESULTS

The samples were the AlGaAs/GaAs hetero-structure semiconductor cut to surface dimension of $7 \times 7 \text{ cm}^2$ from the AlGaAs epitaxial layer grown on a semi-insulating (SI) GaAs substrate wafer. The Si-doped, *n*-type $\text{Al}_{0.2}\text{Ga}_{0.8}\text{As}$ epitaxial layer ($1.4 \text{ }\mu\text{m}$ thickness) was grown by the metal organic vapor phase epitaxy (MOVPE) method. The concentration of a shallow Si donor level was $3.0 \times 10^{16} \text{ cm}^{-3}$. The substrate was the carbon-doped, liquid encapsulated Czochralski (LEC) grown SI GaAs ($600 \text{ }\mu\text{m}$ thickness). The concentrations of deep donor *EL2* and shallow carbon acceptor in the substrate were 1.3 and $0.4 \times 10^{16} \text{ cm}^{-3}$, respectively. Since the annealing process seems to generate a new defect level in the band-gap [5], two samples, as-grown and annealed (815°C for 30 min in the AsH_3 atmosphere) were prepared for the experiments. The specification of the GaAs substrates was kept constant between two samples.

The experimental configuration involving the sample and the detector is shown in the inset of figure 1. After the sample was cut from the wafer, a disk shaped PZT was attached to the surface of the GaAs substrate using a silver conducting paste. The probing light to measure the PPT signal was mechanically chopped and was always focused on the surface of the epitaxial layer side. The PPT signal generated by the nonradiative electron transitions was detected by the PZT. A detailed experimental setup has already been reported [1].

Figure 1 shows the PPT spectra of AlGaAs/GaAs at 297 K. The PPT signal intensity was recorded as a function of incident photon-energy of the probing light ranging from 1.1 to 2.8 eV. The modulation frequency was set at 200 Hz. Since the same GaAs substrates were used for two samples, the PPT signal amplitudes were normalized below the band-gap (E_g) of GaAs. This

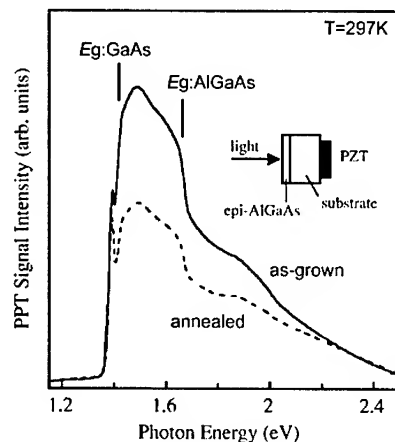


Figure 1. PPT spectra of the AlGaAs/GaAs samples at 297 K. The solid and dashed lines denote the as-grown and the annealed samples, respectively.

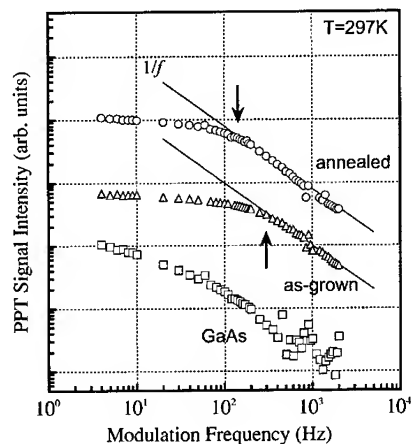


Figure 2. Frequency dependence of the PPT signal of the as-grown, annealed, and the GaAs substrate samples at 297 K.

procedure is reasonable because the PPT signal of LEC-grown SI GaAs below E_g was reported to be due to the electron non-radiative transition involving $EL2$ [2]. As shown in the figure, the PPT signal above E_g of GaAs decreased when the sample was annealed.

In the frequency dependent measurements, the PPT signal at 297 K were, then, measured as a function of the modulation frequency f between 4 and 2000 Hz. The wavelength of the probing light was set at 770 nm ($h\nu=1.65$ eV). Results are shown in figure 2. In this figure, frequency dependence of the PPT signal of LEC-grown SI GaAs substrate sample is also shown. This exhibits almost linear dependence. On the other hand, the deviations from $1/f$ linear function are clearly observed in the AlGaAs/GaAs samples. This critical deviation frequency was found to shift to the lower frequency region by annealing.

DISCUSSION

The PPT signals originated from the AlGaAs epitaxial layer are considerably large compared with that from the substrate. In our previous paper [3], we concluded that electrons photoexcited within the non-doped p-AlGaAs epitaxial layer drifted under the influence of an electric field present at the interface. These drifted electrons eventually recombined with the ionized $EL2$ in the GaAs substrate. In the present case, similar argument is possible. As shown in figure 3, an electric field and band offsets are created at the interface between the n-AlGaAs epitaxial layer and the SI GaAs substrate. Holes photoexcited within the epitaxial layer drifted and eventually recombined with the neutral $EL2$ in the GaAs substrate. Since this transition is known to have a strong non-radiative component [2], the generated heat by this transition causes the PPT signal.

The PPT signals above E_g of GaAs substrate drastically decreased when the sample was annealed at 815°C for 30 min. We, then, assume that the present annealing treatment generates an

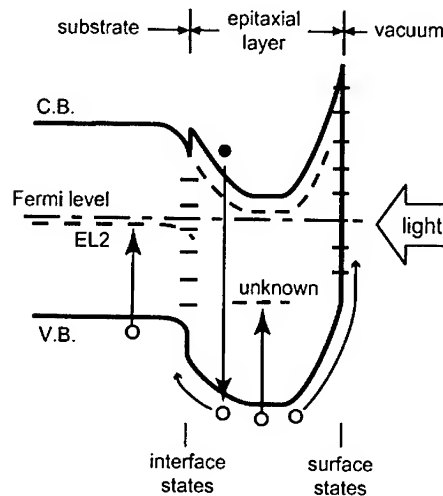


Figure 3. Schematic band diagram near the epitaxial layer and the substrate interface. A depletion region bearing an electric field and band offsets are created.

unknown deep level in the band-gap in AlGaAs epitaxial layer. Supposing that this deep level can act as a faster recombination center for holes, the photoexcited holes cannot drift to the GaAs substrate side. This results in a decrease of the PPT signal intensities in the photon-energy region above E_g of GaAs by annealing is well understood. However, if deep level acts as a non-radiative center, the capturing of the photoexcited hole by an unknown deep level generates a heat and this contributes to increase the PPT signal intensity. This is not the case for the present experimental results.

In the frequency dependent measurements, the incident photon-energy of the probing light was kept at 1.65 eV. Therefore, the signal just below the E_g of AlGaAs was measured. The PPT signal for the SI GaAs substrate exhibits almost linear dependence, as shown in the figure. However, in the AlGaAs/GaAs samples, the deviation from $1/f$ linear function is clearly observed below a critical frequency around 200 Hz. This critical deviation frequency was found to shift to the lower frequency region for the annealed sample.

To explain a shift of the critical deviation frequency observed in figure 2, we develop the theory for the photoacoustic signal generation mechanism proposed first by Todorović *et al.*, hereafter, refer to Todorović model [4]. Note that they have considered that the photoacoustic signal is detected by using a microphone, which is away from the sample surface by the air gap. However, our PZT detector is directly attached to the rear sample surface. Then, such difference should be kept in mind for further discussions. Anyway, we first assume here that the generated PPT signal at the sample surface is completely detected by PZT whichever the signal is caused by a pyro-electric or a piezo-electric effect [1].

In the Todorović model, the photoacoustic signal is caused by following three components, (a) *TD* (thermal-diffusion), (b) *TE* (thermo-elastic), and (c) *ED* (electronic deformation) components. The *TD* component is a consequence of the thermal (heat) diffusion processes in the sample, i.e.,

it depends on the periodic temperature variation on the rear sample surface. The *TE* component is the consequence of the sample surface displacement, that is, the thermo-elastic expansion and bending. This is an important effect in the photoacoustic signal generation mechanism, especially at higher frequencies. Furthermore, the photoexcited free carriers, electron and hole pairs, produce a periodic elastic deformation in the sample directly, so called an elastic deformation (*ED*), which in turn generates the photoacoustic signal. The theoretical calculation due to check a contribution of each three components to the frequency dependence of the PPT signal intensity was carried out. The *TD* component exhibits almost $1/f$ linear dependence. On the other hand, the *TE* and *ED* components show the deviation from $1/f$ linear function below a critical frequency.

In the present experimental frequency region ($f=4\sim 2000$ Hz), the *ED* component can be neglected because the intensity is very low compared with other components. Therefore, two contributions, *TD* and *TE*, may explain the present experimental results. If the *TE* component becomes dominant than *TD*, a critical deviation frequency is expected to shift to the lower frequency region. This indicates that a bending of the rear sample surface becomes large for the annealed sample than that for the as-grown sample. The photon-energy of the probing light is near the E_g of AlGaAs, and the excess free carriers are generated in the AlGaAs epitaxial layer side. If the unknown deep level fabricated by the sample annealing acts as a non-radiative center and traps the photoexcited hole, the heat generates mainly in the AlGaAs epitaxial layer side. This results in the bending term in the *TE* component may increases. This is a reason for the shift of the critical deviation frequency by the sample annealing.

CONCLUSION

The electron non-radiative recombination processes in n-AlGaAs/GaAs hetero-structure sample were investigated by using the PPT technique. Two types of the samples, as-grown and annealed sample, were used. The PPT signal above E_g of GaAs decreased by sample annealing. From the experimental results, it is considered that the annealing produces an unknown deep level in the band-gap of AlGaAs epitaxial layer. By developing the Todorović theory for the signal generation mechanism, we have explained the experimental results of the frequency dependence. Two contributions, namely thermal diffusion (*TD*) and thermo-elastic (*TE*) components, are considered. The *TE* contribution becomes large for the annealed sample. Since the deep level fabricated by the sample annealing acts as a non-radiative center and traps the photoexcited hole, the heat generates mainly in the AlGaAs epitaxial layer side. This results in the increasing of the bending term in the *TE* component. This is a reason for the shift of the critical deviation frequency by the sample annealing.

Since the PPT method does not necessitate the fabrication of electrodes, the usefulness of this method for studying the electron non-radiative recombination process non-destructively is pointed out. However, more detailed quantitative consideration is necessary for the next step.

ACKNOWLEDGMENT

The authors wish to thank Dr. Yohei Otoki of Hitachi Cable Co., Ltd. for supplying high quality GaAs samples.

REFERENCES

1. T. Ikari and A. Fukuyama, *Progress in Photothermal and Photoacoustic Science and Technology, Volume IV: Semiconductors and Electronic Materials*, edited by A. Mandelis and P. Hess (SPIE Press, Washington, 2000) p. 57.
2. A. Fukuyama, Y. Akashi, K. Yoshino, K. Maeda, and T. Ikari, *Phys. Rev. B* **58**, 12868 (1998).
3. A. Fukuyama, H. Fukuhara, S. Tanaka, A. A. Memon, K. Sakai, Y. Akashi, and T. Ikari, *J. Appl. Phys.* **90**, 4385 (2001).
4. D. M. Todorović, P. M. Nikolić, and A. I. Bojičić, *J. Appl. Phys.* **85**, 7716 (1999).
5. Y. Tokuda, K. Kamiya, and T. Okumura, *J. Crystal growth* **210**, 260 (2000).

Optically Detected Magnetic Resonance Study of Core-Shell and Alloy Nanocrystals of HgTe and CdS

L. Fradkin, L. Langof and E. Lifshitz

Dept. of Chemistry and Solid State Inst. Technion, Haifa 32000, Israel,

A. Rogach, N. Gaponik, H. Weller, and A. Eychmüller

Institute of Physical Chemistry, University of Hamburg, 20146 Hamburg, Germany

ABSTRACT

The synthesis of HgTe nanocrystals (NCs), coated with a CdS shell, presumably results in the formation of HgTe/CdS, HgTe/CdHgS core-shell structures or separated CdHgS alloys. Photoluminescence (PL), continuous-wave (cw) and time-resolved optically detected magnetic resonance (ODMR) spectroscopy examined the magneto-optical properties of the dominating resonance aforementioned products. The cw ODMR measurements indicated that the NCs exhibit a band, centered at 0.39 Tesla, corresponding to an excited state electron (e) and hole (h) spin manifold, with total angular momentum ($F=S+L$) $F_e=1/2$ and $F_h=3/2$, respectively. Theoretical simulation of the ODMR band revealed an anisotropy of the g-factor, indicating the existence of trapped carriers' at a mixed Cd-Hg tetrahedral site, confirming the formation of an alloy component. The time-resolved ODMR measurements reveal a characteristic radiative decay time and spin-lattice relaxation time of these trapped carriers of hundreds of microseconds.

INTRODUCTION

The chemical synthesis of colloidal HgTe NCs in aqueous solution was recently reported [1,2]. This novel material exhibits an emission band in the near infrared spectral regime, with giant intensity and a tunable energy, varying with the NCs' size. Therefore, these NCs are currently of great technological interest as emitting materials for thin-film electroluminescence devices, and as optical amplifier media for telecommunication networks. These recent studies [2] indicated that the bare HgTe NCs show "aging" processes and temperature instability, associated with the surface reactivity, which deteriorates the luminescence quantum efficiency. Therefore, the authors of ref. [1] and [2] suggested to improve the surface quality by capping the HgTe NCs with epitaxial layers of another semiconductor (e.g., CdS, CdHgS), to form a core-shell structure [3]. The current work shows our attempts to chemically identify carriers' trapping sites either at the core, the shell or at interface defects, by the use of photoluminescence (PL), continuous-wave and time-resolved optically detected magnetic resonance (ODMR) spectroscopy.

EXPERIMENTAL

The "bare" thioglycerol stabilized HgTe colloidal NCs were prepared in aqueous solution, at room temperature, using the method described previously [1]. The starting solution contained a 4:1 ratio of the Hg^{2+} and Te^{2-} ions. The core-shell structures were prepared by the addition of Cd-perchlorate and addition of H_2S to form a shell of CdS (> 2 nm thick) according to the synthetic conditions mentioned in reference [3]. However, the existence of excess Hg^{2+} ions in the original solution may lead to the formation of a CdHgS alloy as the coating over the "bare" NCs. This assumption will be clarified by the following

spectroscopic measurements. It should be indicated that the radius of the HgTe core was on the order of the shell thickness.

The PL and ODMR spectra were recorded at liquid helium temperature, by immersing the samples in a capillary-type Janis cryogenic Dewar. The PL spectra were obtained by exciting the sample with a 2.70 eV Ar^+ laser. The emitted light was selected by a holographic grating monochromator, and detected with a Hamamatsu Si-photodiode.

The ODMR spectra were obtained by measuring the difference in luminescence intensity (using a Si photodiode), ΔI_{PL} , induced by a magnetic resonance event at the excited state. The ODMR spectra were recorded by mounting the sample on a special probe consisting of a resonance cavity (TE_{111} , with Q-factor of 1000), coupled to a variable frequency microwave (MW) source ($\nu_{\text{MW}}=10.76$ GHz), surrounded by a split Helmholtz coil superconducting magnet, B_0 . The apertures in the cavity and in the superconducting magnet enable optical access both in the Faraday ($B_0 \parallel \text{emission}$) and Voigt ($B_0 \perp \text{emission}$) configurations.

RESULTS

A representative PL spectrum of the HgTe/CdHgS sample is shown in Fig. 1. It consists of a dominating band centered at 668 nm and additional shoulders at 820 nm, 1050 nm and 1240 nm. Most of the PL spectrum overlaps with the absorption spectrum of the size-quantized HgTe NCs which exhibit a band-edge absorption at about 1000 nm.

Magnetic resonance effects were observed in the spectral regime between 550 - 1000 nm. The corresponding non-polarized ODMR spectra, recorded in both Faraday and Voigt configurations, showed only a difference in their relative intensities (see Fig. 2a). The circular polarized ODMR spectra, recorded in the Faraday configuration with σ^+ and σ^- detection, are shown in Fig. 2b. The circular components have a similar band shape and intensity, however they are shifted one with respect to the other by 0.0055 Tesla.

The cw ODMR spectra of the studied sample, recorded with various μW modulation frequencies, are shown in Fig. 3a. It can be seen, that upon an increase in the modulation frequency, the ODMR band intensity is quenched and becomes slightly asymmetric. Furthermore, at a frequency of 819 Hz the high magnetic field component reverses its sign to

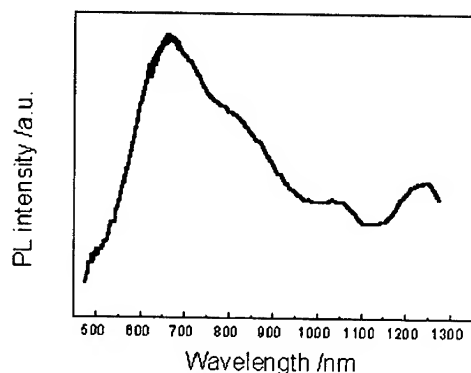


Figure 1. The photoluminescence spectrum of HgTe/CdHgS nanocrystals.

a negative signal. This suggests that the ODMR spectra actually consist of two bands, associated with two separate events with different relaxation times. A representative simulation of the ODMR spectrum with 217 Hz modulation is shown in Fig. 3b. This spectrum consists of a positive Gaussian narrow band centered at 0.395 Tesla (labeled I), overlapping a wide band, centered at 0.379 Tesla (labeled II).

A time-resolved ODMR spectrum is shown by the solid line in Fig. 4, while the MW on/off period of 967 microseconds is presented by the dashed line below. It can be seen from the figure that the PL intensity increases at the rising edge of the MW pulse, change gradually through the pulse, followed by a drastic decay at the end of the pulse.

The spin and radiative relaxation processes, leading to the transient picture and the simulated line (labeled by triangles) shown in Fig. 4, will be discussed in the next section.

DISCUSSION

The PL spectrum of the studied sample showed dominated band at 668 nm and additional shoulders at lower energies. The 1250 nm shoulder in particular resemble the typical luminescence of "bare" size-quantized HgTe NCs or a core component of a core-shell structure [3]. However, the 668 nm and the other shoulders at 820 nm and 1050 nm may correspond to the luminescence of the following species: (a) surface states in pure CdS NCs [4], (b) separate CdHgS NCs' alloys [5], or (c) emission from the shell component of HgTe/CdHgS core-shell

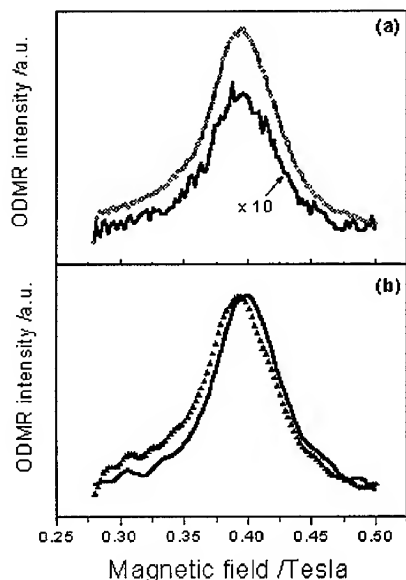


Figure 2. ODMR spectra recorded at Faraday (solid line) and Voight (open dots) configurations (a); σ^+ (solid line) and σ^- (dashed line) polarized detection of the ODMR signal at Faraday configuration

structure. The preparation of the core-shell structure involves an addition of Cd- and S-ions raising a competition between coating of the existing HgTe surfaces and a nucleation of separate CdS NCs. As indicated above, the existence of excess Hg-ions in the initial solution may lead to the formation of either separated CdHgS NCs alloys or HgTe/CdHgS core-shell NCs. The present ODMR measurements enable us to exclude the existence of pure CdS NCs, their typical magnetic resonance spectrum exhibit a different paramagnetic behavior [4]. Thus, the resonance bands shown in Fig. 2 and 3 should correspond to the CdHgS components.

The observed ODMR spectra are associated with a spin flip in the excited state of an electron and a hole. It is assumed that the electron and hole have unpaired spins of $S_e = 1/2$ and $S_h = 1/2$, an angular momentum of $L_e=0$ and $L_h=0, 1$ and a spin-orbit of $F=S+L$. The projections of F in the direction of an external magnetic field ($B||z$) have the values of $m_e = \pm 1/2$ and $m_h = \pm 3/2, \pm 1/2$. These projections split in the presence of an external magnetic field by a Zeeman interaction, $\beta g^{iso} B$ (β and g^{iso} are the Bohr magneton and isotropic g spectroscopic factor, respectively). The observation of circularly polarized ODMR signals reveals that the emitting spin state has a total spin (F_e+F_h) of ± 1 , suggesting the involvement of annihilation between an electron with $m_e=\pm 1/2$ and a hole with $m_h=\pm 3/2$, as shown in the diagram of Fig. 3c. The solid arrows in the figure correspond to the magnetic resonance transitions (consisting of a flip of the electron spins), while the dashed lines represent the optical transitions. The anticipated spectra are shown below the diagram, while the shift

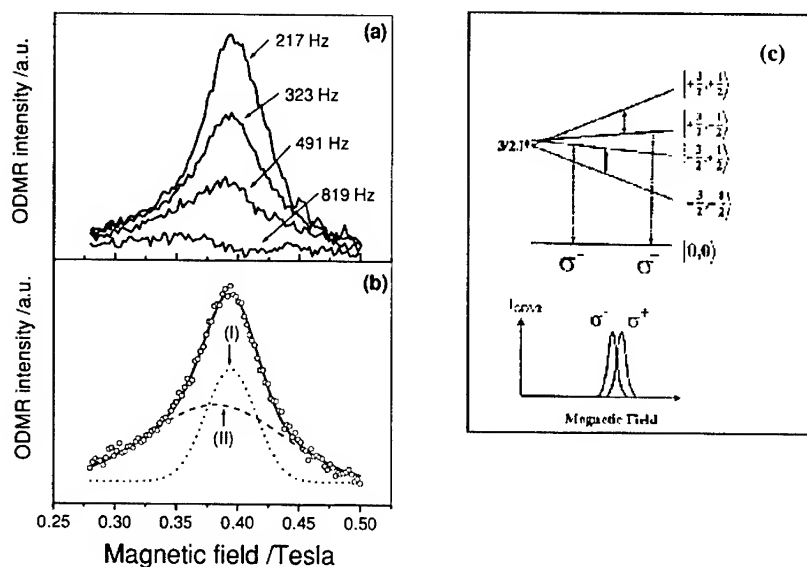


Figure 3. ODMR spectra recorded in Faraday configuration: (a) as a function of MW modulation frequencies; (b) Gaussian simulation of the ODMR signal, recorded with 217Hz MW modulation (dotted and dashed lines are representing the narrow (I) and wide (II) simulation parts, and a solid line is a total simulation (I)+(II); (c) schematic diagram of spin states and corresponding anticipated ODMR spectrum

between the σ^+ and σ^- component is $3J/\beta g_e$, when J is an isotropic electron-hole exchange interaction. Although spin states comprised of $m_e = \pm 1/2$ and $m_h = \pm 1/2$ may be populated, the theory discussed extensively in references [4, 7] predicts a negative resonance band in the Voigt configuration, which is in contradiction to the present experimental results, shown in Fig. 2a.

The present ODMR spectra were simulated with a phenomenological spin Hamiltonian containing the electron and hole Zeeman interactions as well as isotropic and anisotropic exchange interactions. The experimental results shown in Fig. 3a and the simulated spectra (Fig. 3b) suggested the existence of two overlapping events. Component I (dotted line) was simulated with the spin Hamiltonian leading to $g_{xx} = 1.995$, $g_{yy} = 1.995$, $g_{zz} = 1.845$ and $J=0.225 \mu\text{eV}$. The particularly broad component II, on the other hand, could not be simulated by a conventional spin Hamiltonian, reflecting knowledge on a contribution of an additional confinement effect of the orbit motion. The latter effect was discussed in length in a separate publication [6] and will not be extended any longer in this document.

The anisotropy in the g factor of the electron suggests its location in an asymmetric trapping site. Stoichiometric defects which can trap an electron include either M^0 ($M=\text{Cd}, \text{Hg}$) or X^{2-} ($X=\text{S}, \text{Te}$) vacancies with the latter being more common. The formation of a mixed tetrahedron formed by the substitution of a Cd into a Hg site (or vice versa) inserts an anisotropy around a X^{2-} center. Such an anisotropy is pronounced in the g value of a trapped electron. This further supports the existence of alloy components, either as a separated CdHgS or HgTe/CdHgS NCs.

The time-resolved ODMR response, shown in Fig. 4, was simulated by the following kinetic equations [7],

$$\begin{aligned}\frac{dn_1}{dt} &= -\frac{n_1}{\tau_1} + G - \frac{n_1 - (n_1 + n_2)(1 - \rho)}{T_1} - (n_1 - n_2)P_{MW} \\ \frac{dn_2}{dt} &= -\frac{n_2}{\tau_2} + G - \frac{n_2 - (n_1 + n_2)\rho}{T_1} - (n_2 - n_1)P_{MW} \\ \rho &= \frac{1}{1 + \exp(\Delta E / kT)} \quad , \quad \Delta E = \hbar \nu_{MW}\end{aligned}$$

which include a rate of the spin manifold formation (G), radiative and nonradiative processes ($\tau^{-1} = \tau_{\text{rad}}^{-1} + \tau_{\text{nr}}^{-1}$) and spin-lattice relaxation times (T_1). n_1 and n_2 correspond to $|+3/2, -1/2\rangle$ and $|+3/2, +1/2\rangle$, or $|-3/2, -1/2\rangle$ and $|-3/2, +1/2\rangle$ pair states, shown in Fig. 3c. The gradual change seen in Fig. 4 during the MW pulse is controlled by the radiative lifetime, while the sudden decay at the end of the pulse corresponds to the spin-lattice relaxation time, bringing the system back into a Boltzmann distribution of the population among the spin states. The simulated response, using the above equations, revealed a radiative decay time of 300 microseconds and a spin-lattice relaxation time of 900 microseconds. It should be noted that the ODMR experiment enables to detect relatively slow radiative processes, while the fast decay processes are not detected in the current experiment.

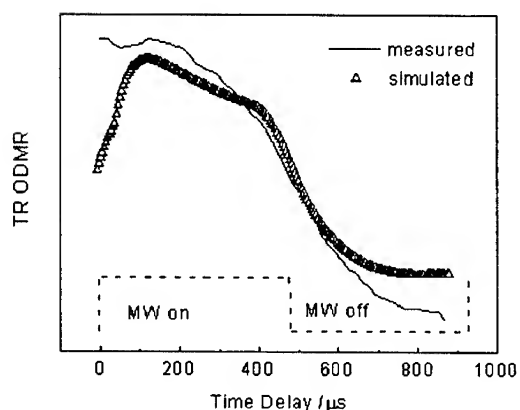


Figure 4. time-resolved ODMR spectra: measured, with the time period of the transient MW pulse (solid line); simulated (triangled line).

CONCLUSIONS

The synthetic approach of coating HgTe nanocrystals with a shell of CdS results in the formation of HgTe/CdS or HgTe/CdHgS core-shell structures or separately formed CdHgS alloys together with the preformed HgTe NCs. The cw ODMR measurements indicated that the NCs exhibit a dominating resonance band corresponding to a recombination between trapped electrons centered at mixed Cd-Hg tetrahedral sites with $F_e=1/2$ and a valence hole with $F_h=3/2$. The suggested anisotropic site indicates the existence of alloy components. The time-resolved ODMR measurements reveal relatively long (hundreds of microseconds) radiative and spin-lattice relaxation times characteristic for the radiative recombination of trapped carriers.

REFERENCES

- ¹ A. Rogach, S.Kershaw, M. Burt, M.Harrison, A. Kornowski, A. Eychmüller, and H.Weller, *Advanced Materials* 1999, **11**,552.
- ² M.Harrison, S.Kershaw, M. Burt, A. Rogach, A. Eychmüller, and H.Weller, *J.Mater.Chem*, 1999, **9**, 2721 .
- ³ M.Harrison, S.Kershaw, M. Burt, A. Rogach, A. Eychmüller, and H.Weller, *Advanced Materials* 2000, **12**,123.
- ⁴ E.Lifshitz, A.Glozman, I.D.Litvin, and H.Porteanu, *J. Phys. Chem. B* 2000, **104**, 10449
- ⁵ M.Harrison, S.Kershaw, M. Burt, A. Rogach, A. Eychmüller, and H.Weller, *Materials Science and Eng. (B)*, 2000, **69-70**, 355 .
- ⁶ E.Lifshitz, A.Glozman, K. Kohgberg, and Z.Maniv, *J. Chem. Phys.* (2001) submitted.
- ⁷ L. Langof, E. Lifshitz, O. Micic, and A. Nozik, *J. Phys. Chem. B*, (2001) submitted.

On the scaling of exciton and impurity binding energies and the virial theorem in semiconductor quantum wells and quantum-well wires

M. de Dios-Leyva¹ and L. E. Oliveira²

¹Dept. of Theoretical Physics, Univ. of Havana, San Lazaro y L, Vedado, 10400, Havana, Cuba

²Instituto de Física, Unicamp, CP 6165, Campinas, São Paulo, 13083-970, Brazil

ABSTRACT

We have used the variational and fractional-dimensional space approaches in a study of the virial theorem value and scaling of the shallow-donor binding energies versus donor Bohr radius in GaAs-(Ga,Al)As semiconductor quantum wells and quantum-well wires. A comparison is made with previous results with respect to exciton states. In the case the donor ground-state wave function may be approximated by a D-dimensional hydrogenic wave function, the virial theorem value equals 2 and the scaling rule for the donor binding energy versus quantum-sized Bohr radius is hyperbolic, both for quantum wells and wires. In contrast, calculations within the variational scheme show that the scaling of the donor binding energies with quantum-sized Bohr radius is in general nonhyperbolic and that the virial theorem value is nonconstant.

INTRODUCTION

Impurity and exciton states may be significantly modified by the barrier-potential confinement in quantum-sized semiconductor heterostructures, and much experimental and theoretical work have been devoted to the quantitative understanding of their properties in GaAs-Ga_{1-x}Al_xAs quantum wells (QWs), quantum-well wires (QWWs), and semiconductor heterostructures in general. Recently, the scaling of the exciton binding energy in semiconductor QWs and QWWs was numerically investigated by Rossi et al [1], who found that in the strong confinement limit the same potential-to-kinetic energy ratio (virial theorem value) holds for quite different wire cross sections and compositions, and claimed that a universal parameter would govern the scaling of the exciton binding energy with size. Zhang and Mascarenhas [2] reexamined the subject by calculating the exciton binding energies and the corresponding virial theorem value in QWs and QWWs with infinite confinement barriers, and found that a shape-independent scaling rule does exist for QWWs, but argued that a virial theorem value being or not a constant is irrelevant. In particular, they found that the exciton virial theorem value is not a constant for either wires or wells. The purpose of this work is to investigate the scaling rule, if any, for the donor binding energies versus Bohr radius, and the virial theorem for shallow donors in quantum-sized semiconductor heterostructures, such as GaAs-Ga_{1-x}Al_xAs cylindrical quantum wires or wells, both within the fractional-dimensional and variational approaches.

THEORETICAL FRAMEWORK

We consider a shallow donor at the position \vec{r}_i in a semiconductor GaAs-Ga_{1-x}Al_xAs heterostructure such as a QW or a cylindrical QWW, within the effective-mass and non-degenerate-parabolic band approximations. The Hamiltonian is given by

$$H = \frac{p^2}{2m^*} - \frac{e^2}{\epsilon |\vec{r} - \vec{r}_i|} + V_b(\vec{r}), \quad (1)$$

where m^* is the conduction-band effective mass and ϵ is the dielectric constant, which, for simplicity, are taken as the GaAs bulk values throughout the heterostructure [3]. $V_b(\vec{r})$ is the confining potential, which is taken as $V_b(\vec{r}) = V_b(z)$ for QWs or $V_b(\vec{r}) = V_b(\rho)$ for cylindrical QWWs. In the following, we will limit ourselves to donors located at positions where cylindrical symmetry is preserved, i.e., at any position in QWs or at the wire axis in QWWs, and will focus on the impurity 1s-like ground state. The eigenfunctions of (1) may be taken as

$$\psi_E(\vec{r}) = f(\vec{r})\phi_E(\vec{r}), \quad (2)$$

where $f(\vec{r})$ is the ground-state solution of (1) in the absence of the Coulomb interaction. In the fractional-dimensional approach, one finds that, for a given state, the "shallow donor + heterostructure" anisotropic system may be modeled by an effective isotropic hydrogenic system in a fractional D-dimensional space [4], a problem which may be solved analytically, with the D parameter chosen via the condition [5]

$$\int_0^\infty \int_0^\pi h r^2 \sin \theta \phi_E^* W \phi_j d\theta dr = 0 \quad (3)$$

where the operator W in eq. (3) includes the effects of anisotropy. In the above equation, $\phi_E(\vec{r})$ is the corresponding impurity eigenfunction, and ϕ_j (and E_j) are the exact eigenfunctions (and eigenvalues) of the D-dimensional Hamiltonian. If one is concerned with the ground-state donor binding energy, it follows [4] that

$$E_b = -E_{1s} = 4R_o/(D-1)^2 \quad (4)$$

where $R_o = \frac{m^* e^4}{2\epsilon^2 \hbar^2}$ is the donor reduced Rydberg. If the ground-state wave function is chosen as $\phi_{E,1s}^* = e^{-\lambda r}$ with $\lambda = 2/[a_o(D-1)]$, the fractional-dimensional parameter is given [5] by

$$D = 1 + 2 \sqrt{\frac{a_L}{a_o}}, \quad (5)$$

where $a_o = \frac{\hbar^2 \epsilon}{m^* e^2}$ is the reduced Bohr radius, and we have followed Rossi et al [1] and Zhang and Mascarenhas [2] and defined a "quantum-confined impurity Bohr radius" as

$$a_I = \left\langle \psi_{E,1s} \left| \frac{1}{r} \right| \psi_{E,1s} \right\rangle^{-1}, \quad (6)$$

with coordinates taken with the origin at the impurity position. Notice that (5) provides a simple relation between the fractional dimension of the effective isotropic medium and the localization of the ground-state wave function through the donor Bohr radius (6). Also, it is straightforward to demonstrate that (5) and (6) give the exact results corresponding to the 2D and 3D limits. One then obtains [5] the hyperbolic dependence of the donor binding energy on the impurity Bohr radius,

$$E_b = R_o \left(\frac{a_o}{a_I} \right) = \frac{e^2}{2\varepsilon a_I}, \quad (7)$$

and a virial theorem value of $\beta = 2$ within the fractional-dimensional space approach, for donors either in QWs or QWWs.

Alternatively, in the variational procedure, one may introduce a variational function for the donor $\phi_E(\mathbf{r})$ envelope wave function, and minimize the impurity energy with respect to the variational parameters [3]. Although one may choose a two- or three-parameter hydrogenic variational wave function for a shallow donor in a QW, the comparison between results using the fractional-dimensional space approach and the variational scheme is probably best illustrated with the simplest one-parameter hydrogenic choice [3] for the variational wave function. We choose therefore $\phi_E(\mathbf{r}) = \phi_{1s}(\mathbf{r}) = e^{-\lambda r}$ for the ground-state wave function, where λ is a variational parameter, and write

$$E_b(\lambda) = \frac{e^2}{\varepsilon a_I(\lambda)} - \frac{\hbar^2 \lambda^2}{2m^*} = \frac{e^2}{\varepsilon a_I(\lambda)} \left(1 - \frac{1}{\beta(\lambda)} \right). \quad (8)$$

By imposing the condition $\frac{\partial E_b(\lambda)}{\partial \lambda} = 0$, one obtains a transcendental equation for λ , and

$$\beta(\lambda) = \frac{\frac{a_I}{a_o}}{2 \left[\frac{\langle r \rangle}{a_o} - \frac{a_I}{a_o} \right]^2} \quad (9)$$

for the virial theorem value within the variational approach.

RESULTS AND DISCUSSION

In the following, we have used a GaAs conduction-band effective mass $m^* = 0.0665 m_0$, where m_0 is the free-electron mass, and a 60% (40%) rule for the conduction (valence) – barrier potential with respect to the total band-gap offset, with the band gap discontinuity taken

as ΔE_g (eV) = 1.247 x , where x is the Al concentration. Results are presented with energies and lengths expressed in reduced units of the impurity Rydberg (R_0) and radius (a_0), respectively.

In Fig. 1(a) we compare the theoretical fractional-dimensional calculations of the binding energies for on-center donors in GaAs-Ga_{0.7}Al_{0.3}As QWs with the corresponding results using a variational 1s-like hydrogenic envelope wave function [3]. Results are also shown for an infinite-barrier potential. Notice that the on-center donor binding energies of both fractional-dimensional and variational calculations are in excellent agreement. Figs. 1(b) and (c) show the on-center donor binding energy and corresponding virial theorem value β versus the quantum-confined donor Bohr radius [see eq. (6)], calculated in the variational [3] and fractional-dimensional [5] approaches, for GaAs-Ga_{1-x}Al_xAs QWs, both for $x = 0.30$, and infinite-barrier potentials. We notice that the fractional-dimensional approach leads to the hyperbolic dependence of the donor binding energy on the impurity Bohr radius, and to a virial theorem value of $\beta = 2$. In contrast, within the variational procedure, the virial theorem value has a strong dependence on the donor Bohr radius, and approaches the exact bulk value of 2 from above as the width of the well approaches infinite, both in the case of infinite-confining and finite-barrier potentials. One should point out that variational results for finite barriers may exhibit two different virial theorem values for a given donor Bohr radius, as a donor radius may correspond to two well widths. In the case of infinite-potential barrier in the variational scheme, the virial theorem value also approaches the exact 2D value of 2 for vanishing QW width. The above variational results for the virial theorem value in the case of shallow donors in QWs are quite similar to the results for excitons reported by Zhang and Mascarenhas [2].

The fractional-dimensional and variational results for the binding energies of donors at the axis of a cylindrical GaAs-Ga_{1-x}Al_xAs wire are presented in Fig. 2(a). A comparison between fractional-dimensional results and a donor variational calculation indicates good agreement for the binding energies in the cases of moderate and large values of the wire radius. The on-axis donor binding energy and virial theorem value are shown in Figs. 2(b) and (c) versus the quantum-confined donor Bohr radius, calculated in the variational and fractional-dimensional approaches, for both $x = 0.30$ and infinite-barrier potential GaAs-Ga_{1-x}Al_xAs QWWs. As before, the fractional-dimensional approach leads to the hyperbolic dependence of the impurity binding energy on the donor Bohr radius, and to a virial theorem value of $\beta = 2$. As in the work on excitons by Zhang and Mascarenhas [2], the virial theorem value, obtained within the variational procedure, has a significant dependence on the donor Bohr radius, and approaches the exact bulk value of 2 from above as the radius of the well approaches infinite, both in the case of infinite-confining and finite-barrier potentials, similar to the results for donors in QWs in Fig. 1. Also, in the case of infinite potential in the variational scheme, the virial theorem value approaches the exact 1D value of 2 for a vanishing QWW radius.

CONCLUSIONS

We have presented a study, within the fractional-dimensional and variational approaches, of the virial theorem value and results for the scaling of the shallow-donor binding energies versus donor Bohr radius in GaAs-(Ga,Al)As QW and QWW quantum-sized semiconductor heterostructures. In the case of the fractional-dimensional space approach, if the 3D actual anisotropic semiconductor heterostructure may be substituted by a fractional-dimensional

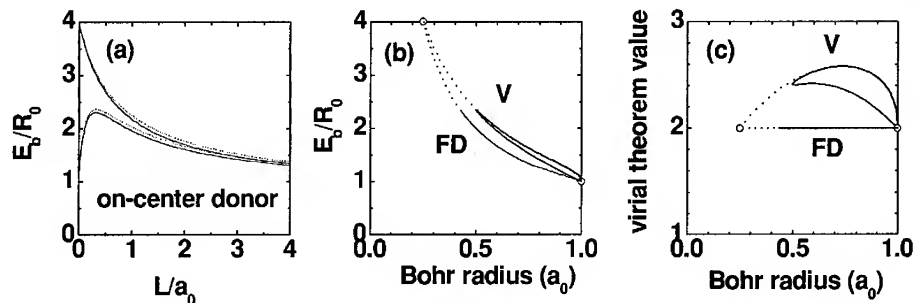


Figure 1. On-center donor binding energies as functions of the well width (a) and quantum-confined donor Bohr radius (b) in GaAs-Ga_{1-x}Al_xAs QWs, both for $x = 0.30$ and infinite-barrier potentials. The corresponding virial theorem value is shown in (c). In (a) solid curves correspond to fractional-dimensional results whereas dotted lines are calculated using a variational procedure. In (b) and (c), $x = 0.30$ results using the variational - V or fractional-dimensional - FD approaches are given as full curves, and dotted curves are in the cases of infinite-barrier potentials. Open dots correspond to exact results. Energies and lengths are expressed in reduced units of the impurity Rydberg (R_0) and radius (a_0), respectively.

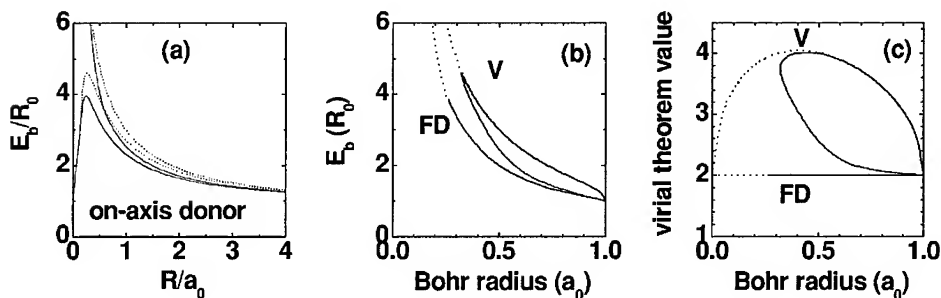


Figure 2. On-axis donor binding energies as functions of the wire radius (a) and quantum-confined donor Bohr radius (b) in GaAs-Ga_{1-x}Al_xAs cylindrical QWs, both for $x = 0.30$ and infinite-barrier potentials. The corresponding virial theorem value is shown in (c). In (a) solid curves correspond to fractional-dimensional results whereas dotted lines are calculated using a variational procedure. In (b) and (c), $x = 0.30$ results using the variational - V or fractional-dimensional - FD approaches are given as full curves, whereas results for infinite-barrier potentials are given by dotted curves. Energies and lengths are expressed in reduced units of the impurity Rydberg (R_0) and radius (a_0), respectively.

effective medium with a ground-state wave function given by $\phi_{E,1s}^* = e^{-\lambda r}$ with $\lambda = 2/[a_0(D-1)]$, the virial theorem value equals 2 and the scaling rule for the donor binding energy versus Bohr radius is hyperbolic, both for GaAs-(Ga,Al)As QWs and QWWs. In contrast, calculations within the variational scheme unambiguously show that the scaling of the donor binding energies with Bohr radius is, in general, nonhyperbolic and that the virial theorem value is nonconstant. Moreover, calculations for the donor binding energies versus QW widths or QWW radii, within both the fractional-dimensional and variational approaches, result in essentially the same binding energies with quite different virial theorem values or Bohr radii. This indicates that any general conclusion based on a given virial theorem value or donor energy versus Bohr radius scaling rule should be examined with due caution.

ACKNOWLEDGMENTS

We are grateful to Brazilian Agencies FAPESP, FAEP - UNICAMP, and CNPq for partial financial support.

REFERENCES

1. F. Rossi, G. Goldoni, and E. Molinari, *Phys. Rev. Lett.* **78**, 3527 (1997).
2. Y. Zhang and A. Mascarenhas, *Phys. Rev. B* **59**, 2040 (1999).
3. L. E. Oliveira, *Phys. Rev. B* **38**, 10641 (1988); N. Porras-Montenegro and S. T. Pérez-Merchancano, *Phys. Rev. B* **46**, 9780 (1992).
4. F. H. Stillinger, *J. Math. Phys.* **18** 1224 (1977); X-F. He, *Phys. Rev. B* **43**, 2063 (1991); P. Christol, P. Lefebvre and H. Mathieu, *J. Appl. Phys.* **74**, 5626 (1993).
5. A. Matos-Abiague, L. E. Oliveira, and M. de Dios-Leyva, *Phys. Rev. B* **58**, 4072 (1998); E. Reyes-Gómez, L. E. Oliveira, and M. de Dios-Leyva, *J. Appl. Phys.* **85**, 4045 (1999); E. Reyes-Gómez, A. Matos-Abiague, C. A. Perdomo-Leiva, M. de Dios-Leyva, and L. E. Oliveira, *Phys. Rev. B* **61**, 13104 (2000); M. de Dios-Leyva and L. E. Oliveira, *J. Phys.: Cond. Matter* **13**, 9471 (2001).

Intra-magnetoexciton transitions in semiconductor quantum wells

Z. Barticevic¹, M. Pacheco², C. A. Duque³, and L. E. Oliveira⁴

¹Depto. de Física, Universidad Técnica Federico Santa María, Casilla 110-V, Valparaíso, Chile

²Depto. de Física, Universidad de Santiago de Chile, Casilla 307, Santiago, Chile

³Depto de Física, Universidad de Antioquia, AA 1226, Medellín, Colombia

⁴Instituto de Física, Univ. Estadual de Campinas - Unicamp, CP 6165, Campinas-SP, Brazil

ABSTRACT

Highly sensitive optically detected resonance experiments have shown that magnetoexcitons in GaAs-(Ga,Al)As semiconductor quantum wells have discrete internal energy levels, with transition energies found in the far-infrared (terahertz) region. Here we are concerned with a theoretical study of the terahertz transitions of light-hole and heavy-hole confined magnetoexcitons in GaAs-(Ga,Al)As quantum wells, under a magnetic field applied in the growth direction of the semiconductor heterostructure. The various magnetoexciton states are obtained in the effective-mass approximation by expanding the corresponding exciton-envelope wave functions in terms of appropriate Gaussian functions. The electron and hole cyclotron resonances and intra-magnetoexciton transitions are theoretically studied by exciting the allowed electron, hole and internal magnetoexcitonic transitions with far-infrared radiation. Theoretical results are obtained for both the intra-magnetoexciton transition energies and oscillator strengths associated with excitations from $1s$ - like to $2s$, $2p_{\pm}$, and $3p_{\pm}$ - like magnetoexciton states, and from $2p_{\pm}$ to $2s$ - like exciton states. Present results are in overall agreement with available optically detected resonance measurements and clarifies a number of queries in previous theoretical work.

INTRODUCTION

The study of the optical properties of semiconductor heterostructures, such as GaAs-(Ga,Al)As quantum wells (QWs) and multiple quantum wells (MQWs), provides worthy information on the physical nature of confined electrons, holes, and Coulomb-bound states such as impurities and excitons. It is well known that excitons essentially dominate the optical properties of semiconductor heterostructures and, in particular, an external perturbation such as an applied magnetic field perpendicular to the GaAs and $\text{Ga}_{1-x}\text{Al}_x\text{As}$ semiconductor layers is a powerful tool which is expected to provide valuable information on carrier subbands and exciton states via magneto-optical studies. Confined excitons in GaAs- $\text{Ga}_{1-x}\text{Al}_x\text{As}$ QWs and MQWs under magnetic fields in the growth direction reveal themselves as a series of hydrogenic-like ground and excited magnetoexciton states, with the internal transition energies among the various exciton states in the far-infrared region (FIR - of the order of 10 meV or 2.4 THz). In particular, Salib et al [1] recently observed several internal excitonic transitions and found the $1s \rightarrow 2p_{+}$ heavy-hole (hh) exciton transition as dominant in GaAs- $\text{Ga}_{0.7}\text{Al}_{0.3}\text{As}$ MQWs of $L_w = 80$ Å and $L_w = 125$ Å of well width. They have also assigned a "weak" feature and a "very weak" feature in the experimental spectra to hh magnetoexciton $1s \rightarrow 3p_{+}$ and $1s \rightarrow 4p_{+}$ transitions, respectively, based primarily on the magnitude of the energy separations with respect to the $1s \rightarrow 2p_{+}$ transition. Also, some features present in the optically detected resonance (ODR) spectra

by Salib et al [1] were attributed to hole cyclotron resonances (CRs) and others termed as of uncertain origin. In a simultaneous and independent experiment, Cerne et al [2] monitored changes in the excitonic PL that are induced by FIR radiation with the electric field polarized in the plane of the QW, and observed resonant FIR absorption by confined magnetoexcitons in GaAs - Ga_{1-x}Al_xAs QWs under magnetic fields applied perpendicular to the well interfaces. The dominant resonance was assigned to the $1s \rightarrow 2p_z$ hh exciton transition, and was found to persist even when the FIR electric field was comparable to the electric field which binds the exciton. More recently, Nickel et al [3] have used ODR spectroscopy to study electron and hole CRs and various internal excitonic transitions in a number of GaAs-(Ga,Al)As MQW structures. They concluded that more work is necessary to confirm the $2p_z$ assignments, to resolve the nature of the higher energy intraexcitonic transitions, and to observe light-hole (lh) CR and associated intraexcitonic transitions. From the theoretical point of view, Duque et al [4] have performed a study of $1s \rightarrow 2p_z$, $1s \rightarrow 3p_z$, and $1s \rightarrow 4p_z$ lh and hh magnetoexcitonic transition energies in GaAs-Ga_{1-x}Al_xAs QWs within a variational procedure in the effective-mass approximation, and although some of the theoretical magnetoexciton transition energies agree quite well with experimental measurements, other calculated results only reproduce qualitative features of experiment. In order to provide a better understanding of the terahertz transitions of confined magnetoexcitons in GaAs - Ga_{1-x}Al_xAs QWs and of the ODR experimental data by Salib et al [1], Cerne et al [2], and Nickel et al [3], here we perform a more detailed theoretical study of the various intraexcitonic transitions in GaAs - Ga_{1-x}Al_xAs QWs under magnetic fields applied along the QW growth direction.

THEORETICAL FRAMEWORK

We work in the effective-mass approximation and are interested in Wannier-exciton states in GaAs-Ga_{1-x}Al_xAs QWs of width L_w in the presence of a magnetic field parallel to the growth direction of the heterostructure. We assume the spin-orbit splitting to be large enough that the interaction between $J = 3/2$ and $J = 1/2$ states may be disregarded. For simplicity, we take the relative motion of the carriers and that of the center of mass as independent, although one may only make this separation in the plane of the well [6], and write the exciton envelope wave functions as $F_{J_e^i, J_h^i}^i(\vec{r}_e, \vec{r}_h) \equiv F_{J_e^i, J_h^i}^i(\vec{\rho}, z_e, z_h)$, where $\vec{\rho}$ is the e - h relative coordinate in the plane of the QW. In what follows, we will restrict our attention to independent excitons and discard the off-diagonal elements in the hole Hamiltonian [5], i.e., we neglect effects due to hole-subband mixing in the calculation. Image-charge effects are not considered and the e - h Coulomb interaction is assumed to be screened by an average static dielectric constant of the GaAs and Ga_{1-x}Al_xAs bulk materials. The values of the square potential-well barriers $V_e(z_e)$ and $V_h(z_h)$ are determined from the Al concentration and assumed to be 65% and 35% of the total energy-band-gap discontinuity, respectively. Also, although actual measurements are for GaAs-Ga_{0.7}Al_{0.3}As superlattices (SLs), we have ignored SL tunneling effects and performed calculations for single isolated GaAs-Ga_{0.7}Al_{0.3}As QWs.

We may now expand the exciton envelope wave functions $F_{J_e^i, J_h^i}^i(\vec{\rho}, z_e, z_h)$ in terms of single-particle $f_n^{J_e^i}(z_e)$ and $f_m^{J_h^i}(z_h)$ solutions of the effective-mass equation for electron or hole motion, respectively, along the z -axis of the QW, and write [7]

$$F_{J_z^e, J_z^h}^i(\vec{p}, z_e, z_h) = \sum_{n,m} \psi_{n,m}^{J_z^e, J_z^h, i}(\rho, \phi) f_n^{J_z^e}(z_e) f_m^{J_z^h}(z_h), \quad (1)$$

with

$$\psi_{n,m}^{J_z^e, J_z^h, i}(\rho, \phi) = \sum_j C_{n,m,j}^{J_z^e, J_z^h, i} \rho^{|s|} e^{is\phi} e^{-\frac{\rho^2}{\lambda_j^2}}, \quad (2)$$

where the expansion is made in a restricted set of Gaussian functions with appropriate length parameters λ_j , and s is an integer associated with the conserved z component of the total angular momentum [7]. We assume the hh and lh exciton Hamiltonians of ref. [5], and the GaAs conduction-band effective-mass and dielectric constant as $m_e = 0.0665$ (in units of the free electron mass m_0) and $\epsilon = 12.5$, respectively; the relevant mass parameters and the Luttinger valence-band parameters are taken from Bauer and Ando [5]. In what follows, magneto-exciton energy states are labeled as $n\ell m (J_z^e, J_z^h)$ which correspond to an $n\ell m$ -like exciton state composed of a J_z^e electron (with $J_z^e = \pm 1/2$) and a J_z^h hole (with $J_z^h = \pm 1/2, \pm 3/2$).

We also note that, in the dipole approximation, the $\alpha(\omega)$ magneto-absorption coefficient for the intraexcitonic $1s \rightarrow np_{\pm}$ transitions is essentially given by

$$\alpha(\omega) \propto \frac{1}{\omega} \sum_f \left| \left\langle F_{J_z^e, J_z^h}^f(\vec{p}, z_e, z_h) \left| \hat{\epsilon} \cdot \vec{P}_r \right| F_{J_z^e, J_z^h}^{1s}(\vec{p}, z_e, z_h) \right\rangle \right|^2 \delta(E_f - E_{1s} - \hbar\omega), \quad (3)$$

where $\hat{\epsilon}$ corresponds to the photon polarization and \vec{P}_r to the relative mechanical momentum of the e - h pair.

RESULTS AND DISCUSSION

We first point out that, in the calculation by Duque et al [4], the exciton envelope wave function is described as a product of variational hydrogenic-like wave functions and electron and hole **ground-state** solutions of the effective-mass equation for motion along the z -axis of the QW. In the present approach, the exciton wave function is written in terms of products of Gaussian functions with appropriate hole and electron single-particle states [contribution of the **ground state and excited states**, cf. eq. (1)]. For allowed spin-conserving transitions involving the lowest-energy exciton states, i.e., for the hh $1s \rightarrow 2p_{\pm}$ magnetoexciton transitions, one finds very good agreement between the two calculations, whereas for higher-energy hh $1s \rightarrow 3p_{\pm}$ and lh $1s \rightarrow 2p_{\pm}$ and $1s \rightarrow 3p_{\pm}$ magnetoexciton transitions both theoretical approaches end up in quantitatively different results. Of course, the present scheme is more reliable from the quantitative point of view, and better describes higher-energy states as the exciton envelope wave function in eq. (1) includes the effects of excited electron and hole single-particle in its expansion.

The energies corresponding to lh and hh $1s \rightarrow 2p_{\pm}$ and $1s \rightarrow 3p_{\pm}$ magnetoexciton transitions are shown in Fig. 1(a) for a 80 Å GaAs-Ga_{0.70}Al_{0.30}As QW. Notice that the experimental FIR data by Salib et al [1] are in fair agreement with intraexcitonic theoretical transitions, although any assignment of the experimental higher energy FIR data to specific magnetoexciton transitions is difficult to make. Figure 1(b) displays the calculated lh and hh intraexcitonic

magneto-absorption coefficient, for left- and right-circularly polarized light in the well plane, also in the case of a $L_w = 80 \text{ \AA}$ GaAs-Ga_{0.7}Al_{0.3}As QW. It is then clear that the oscillator strength of the lh and hh $1s \rightarrow 2p_{\pm}$ intraexcitonic transitions are of the same order of magnitude and that the lh $1s \rightarrow 2p_{\pm}$ transitions should therefore be experimentally observable. The calculated results in Fig. 1(b) unambiguously indicate that, if one performs the experiment with appropriately polarized photons, both the lh and hh $1s \rightarrow 2p_{\pm}$ exciton transitions should be noticeable in the measured spectra. Also, one clearly sees [for $B = 1, 2$, and 3 T in Fig. 1(b)] that weaker, higher energy features in $\alpha(\omega)$ corresponding to lh and hh $1s \rightarrow 3p_{\pm}$ transitions should be observable, provided one is able to perform the experiment with higher spectral resolution; in fact, one notices that some of these higher energy transitions do show up in the experiment corresponding to the $L_w = 80 \text{ \AA}$ sample [see Fig. 1(a)].

Although not shown here, we have evaluated the lh and hh $1s \rightarrow 2p_{\pm}$ magnetoexciton transition energies and magneto-absorption coefficient for a 100 \AA GaAs-Ga_{0.7}Al_{0.3}As QW. Results are in quantitative agreement with FIR data and, in particular, some higher-energy experimental transitions, which Cerne et al [2] do not assign to any specific intraexcitonic transition, are found to correspond to lh $1s \rightarrow 2p_{\pm}$ magnetoexciton transitions. We have also calculated the hh $1s - 2s$ dispersion (separation of 60 cm^{-1} at zero magnetic field), and it agrees quite well with the $1s - 2s$ energy separation obtained by Cerne et al [2] with PL and PLE measurements. Moreover, we found that the lowest FIR frequency resonance is due to free-electron CR and not to hh $2p_{\pm} \rightarrow 2s$ transition energies, as suspected by Cerne et al [2].

In order to analyze the recent magnetoexciton experimental FIR data by Nickel et al [3], one should notice that, for wide wells, heavy and light holes should be strongly mixed, and hole-subband mixing must be taken into account. In order to mimic this effect, one may choose to continue to work with the parabolic one-particle Hamiltonian and adequately change the effective-mass parameters and dielectric constant in order to fit the FIR experimental transitions. Corresponding calculated results for the $1s \rightarrow 2p_{\pm}$ and $1s \rightarrow 3p_{\pm}$ magnetoexciton transition energies and magneto-absorption coefficient are shown in Fig. 2 for the $L_w = 150 \text{ \AA}$ sample, with $\epsilon(\text{GaAs})$ chosen as 13.9, and the conduction - electron effective mass chosen as $0.075 m_0$. In Fig. 2(a), the full down-triangles magnetic-field dependent experimental FIR energies correspond to $1s \rightarrow 2p_{\pm}$ calculated magnetoexciton transitions for a valence-band effective mass of $0.3 m_0$, whereas the full up-triangles FIR data correspond to the $1s \rightarrow 2p_{\pm}$ transitions for a valence-band effective masses chosen as $0.79 m_0$. The value of $0.79 m_0$ for the valence-band in the case of $L_w = 150 \text{ \AA}$ is certainly peculiar, but it reflects the unexpected experimental behavior [3], i.e., in the case of the $L_w = 150 \text{ \AA}$ sample the difference of the $1s \rightarrow 2p_{\pm}$ experimental magnetoexciton transitions (up- and down-triangles) is higher than in the $L_w = 200 \text{ \AA}$ case - see data in ref. [3] - in which the mixing of hh and lh should be stronger. Further studies are necessary to clarify this point.

Summing up, theoretical results in GaAs-(Ga,Al)As QWs are obtained for intra-magnetoexciton transition energies corresponding to excitations from $1s$ - like to $2s$ -, $2p_{\pm}$ -, and $3p_{\pm}$ - like magnetoexciton states, and from $2p_{\pm}$ - to $2s$ - like states. We have also presented results for the $\alpha(\omega)$ magneto-absorption coefficient corresponding to the intraexcitonic $1s \rightarrow np_{\pm}$ transitions, in the dipole approximation, for the case of left- and right-circularly polarized photons. Finally, we have compared the present theoretical results with available optically detected resonance measurements, and obtained good overall agreement. Nevertheless, there are still several aspects of the magnetoexciton problem that are unclear or unexpected, and quite

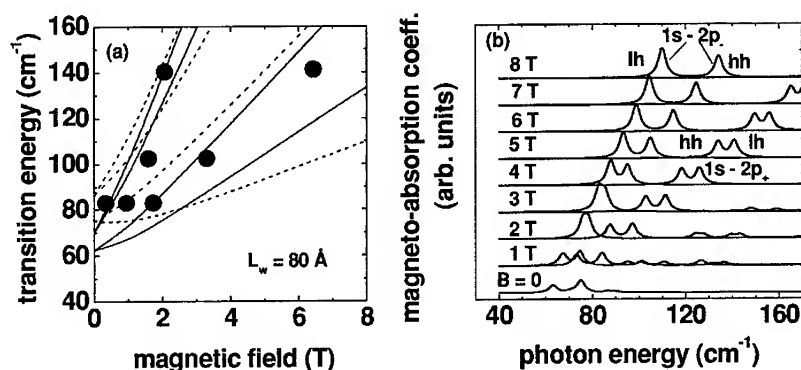


Figure 1. (a) Light-hole (dashed curves) and heavy-hole (full curves) $1s \rightarrow 2p_{\pm}$ and $1s \rightarrow 3p_{\pm}$ calculated magnetoexciton transition energies, with experimental data (full circles) taken from Salib et al [1]; (b) Intraexcitonic light-hole (lh) and heavy-hole (hh) $1s \rightarrow np_{\pm}$ magneto-absorption coefficient, for the case of left- and right-circularly polarized light in the well plane; the column of numbers on the left gives values of the applied magnetic field in Teslas (T). Results are for $L_w = 80 \text{ Å}$ GaAs-Ga_{0.7}Al_{0.3}As QWs under magnetic fields applied along the growth direction of the heterostructure.

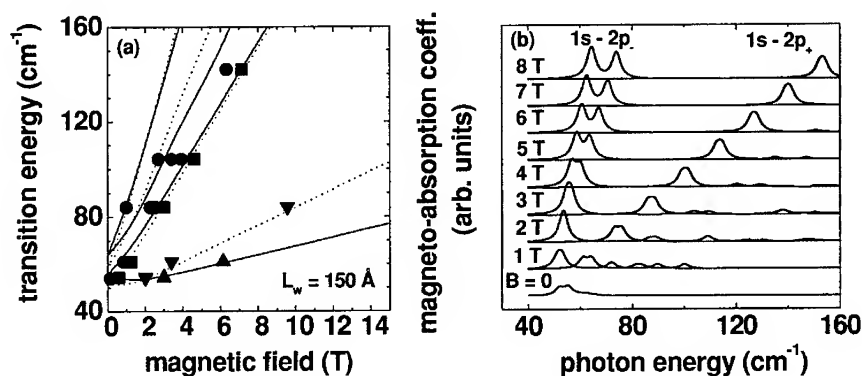


Figure 2. (a) Calculated $1s \rightarrow 2p_{\pm}$ and $1s \rightarrow 3p_{\pm}$ magnetoexciton transition energies, with experimental data (solid dots) taken from Nickel et al [3]. Calculations assume the in-plane heavy-hole mass as $0.79 m_0$ (full curve) and $0.30 m_0$ (dotted line); (b) Intraexcitonic $1s \rightarrow np_{\pm}$ magneto-absorption coefficient, for the case of left- and right-circularly polarized light in the well plane; the column on the left gives values of the applied magnetic field in Teslas (T). Results are for $L_w = 150 \text{ Å}$ GaAs-Ga_{0.85}Al_{0.15}As QWs under magnetic fields applied along the growth direction of the heterostructure.

certainly, further experimental and theoretical studies are needed. In that sense, it would be of interest to perform experimental studies with right-, left- and linearly-polarized light in the plane of the QW, and investigate the possible observation of FIR features which could be unambiguously associated to lh cyclotron resonances and lh intraexcitonic transitions.

ACKNOWLEDGMENTS

This research was partially supported by Red IX.E (CYTED), Millennium Scientific Initiative/Chile (Condensed Matter Physics, grant P 99-135-F), Fondo Nacional de Ciencias/Chile (grant 1990271), and Universidad Santa Maria (internal grant). We also acknowledge the Colombian (CODI-Universidad de Antioquia) and Brazilian Agencies (Fapesp, CNPq, and FAEP-UNICAMP).

REFERENCES

1. M. S. Salib, H. A. Nickel, G. S. Herold, A. Petrou, B. D. McCombe, R. Chen, K. K. Bajaj, and W. Schaff, *Phys. Rev. Lett.* **77**, 1135 (1996).
2. J. Cerne, J. Kono, M. S. Sherwin, M. Sundaram, A. C. Gossard, and G. E. W. Bauer, *Phys. Rev. Lett.* **77**, 1131 (1996); J. Kono, M. Y. Su, J. Cerne, M. S. Sherwin, S. J. Allen, Jr., T. Inoshita, T. Noda, and H. Sakaki, *Physica B* **249-251**, 527 (1998).
3. H. A. Nickel, G. S. Herold, M. S. Salib, G. Kioseoglou, A. Petrou, B. D. McCombe, and D. Broido, *Physica B* **249-251**, 598 (1998); H. A. Nickel, G. S. Herold, T. Yeo, G. Kioseoglou, Z. X. Jiang, B. D. McCombe, A. Petrou, D. Broido, and W. Schaff, *Phys. Stat. Sol. (b)* **210**, 341 (1998); H. A. Nickel, G. Kioseoglou, T. Yeo, H. D. Cheong, A. Petrou, B. D. McCombe, D. Broido, K. K. Bajaj, and R. A. Lewis, *Phys. Rev. B* **62**, 2773 (2000).
4. C. A. Duque, C. L. Beltrán, A. Montes, N. Porras-Montenegro, and L. E. Oliveira, *Phys. Rev. B* **61**, 9936 (2000).
5. J. M. Luttinger, *Phys. Rev.* **102**, 1030 (1956); G. E. W. Bauer and T. Ando, *Phys. Rev. B* **38**, 6015 (1988).
6. G. Bastard, E. E. Mendez, L. L. Chang, and L. Esaki, *Phys. Rev. B* **26**, 1974 (1982); J. W. Brown and H. N. Spector, *Phys. Rev. B* **35**, 3009 (1987).
7. M. Pacheco, Z. Barticevic, and F. Claro, *J. Phys. C* **5**, A393 (1993); Z. Barticevic, M. Pacheco, and F. Claro, *Phys. Rev. B* **51**, 14414 (1995); M. Pacheco and Z. Barticevic, *J. Phys.: Condens. Matter* **11**, 1079 (1999).

Electron scattering in two-dimensional disordered heterostructures

I. Gómez,¹ E. Díez,¹ F. Domínguez-Adame,¹ and P. Orellana²

¹Departamento de Física de Materiales, Universidad Complutense,
E-20840 Madrid, Spain

²Departamento de Física, Universidad Católica del Norte, Casilla 1280,
Antofagasta, Chile

ABSTRACT

The main aim of this work is to study electron scattering in imperfect semiconductor heterostructures. The source of unintentional disorder is the interface roughness at the heterojunctions occurring during growth. In order to achieve this goal we solve numerically the two-dimensional Ben Daniel-Duke equation for the electron scattering problem. Our model assumes open boundary conditions along the growth direction and periodic ones parallel to the heterojunctions. We then compute the reflection and transmission matrices that govern channel mixing due to interface roughness scattering. The knowledge of the mixing matrices allow us to calculate the transmission coefficient in any heterostructure made of wide gap semiconductors. As an example, we compute the transmission coefficient in resonant tunneling devices based on double-barrier structures.

INTRODUCTION

Electron scattering by imperfect heterojunctions reduces electron mobility due to rough surfaces even in good-quality heterostructures [1]. So far, there are analytical results concerning the propagation of wave packets in a randomly layered medium when the potential is a random function of only one coordinate [2], but for a small number of layers, as in double barrier heterostructures (DBH), in-plane disorder becomes important and one expects such approaches to fail. Realistic models of in-plane disorder usually lead to intractable analytical models; hence the importance of numerically solvable models to bridge this gap. An important contribution was already provided by Henrickson *et al.*, who applied the tight-binding Green function method to account for electron scattering by interface roughness in imperfect DBH [3]. However, in this paper electron transmission through a DBH was described by a rather artificial model of disorder, namely periodic roughness with random relative phases at the interfaces.

In the present work we introduce a two-dimensional effective-mass model to study the effects of interface roughness scattering on electron transmission through semiconductor heterostructures. To this end, the Ben Daniel-Duke equation is discretized, boundary conditions are discussed and scattering solutions are found by means of the transfer-matrix method for *any* arbitrary heterostructure made of wide gap semiconductors. The model is worked out in a two-dimensional space for computational limitations, although it will be clear that generalization to three dimensions is rather straightforward. Finally, we present the numerical results for the transmission coefficient through imperfect DBH and the main conclusions of the work.

THEORY

We consider the Ben Daniel-Duke equation with constant effective mass m^* at the Γ valley for the electron envelope function $\psi(y, z)$, where the two spatial directions are shown in Fig. 1. The whole structure is divided into three different regions, namely left (I) and right (III) contacts and the DBH (II), where scattering by lateral disorder takes place.

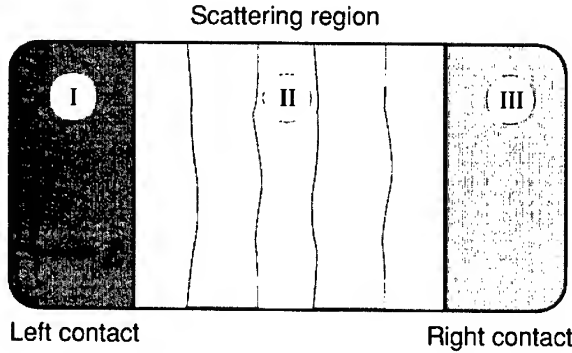


Figure 1. Schematic view of the sample. Regions I and III are the electrical contacts of the sample and electrons undergo scattering processes by lateral disorder only at region II (DBH).

We consider a mesh with lattice spacings a_y and a_z in the y and z directions, respectively. Defining $t_y \equiv -\hbar^2/(2m^*a_y^2)$ and $t_z \equiv -\hbar^2/(2m^*a_z^2)$, we obtain the discretized equation for the envelope function

$$t_z(\psi_{n+1,m} + \psi_{n-1,m}) + t_y(\psi_{n,m+1} + \psi_{n,m-1}) + (U_{n,m} - 2t_z - 2t_y)\psi_{n,m} = E\psi_{n,m}. \quad (1)$$

The potential term $U_{n,m}$ in Eq. (1) is given by the conduction-band edge energy at the point (na_y, ma_z) which, in turn, depends on the Al mole fraction in the vicinity of that position. Therefore, lateral disorder enters the equation through this diagonal term. Contacts are characterized by flat band conditions, $U(n, m) = 0$. Solutions of Eq. (1) can be determined from the appropriate boundary conditions by using the transfer matrix method. The boundary conditions are open in the z direction, and periodic on each slide, that is in the y direction. The former imply plane wave solutions in the z axis, and the latter yield an energy discretization on y . As a consequence, this discretization results in a number of transverse channels equal to the number of points in the transverse mesh direction. Once the solutions are known, the transmission coefficient is computed as a function of the electron energy.

MODEL OF DISORDER

In order to treat lateral disorder, we have considered the occurrence of islands on the interface between two consecutive layers having identical lateral sizes all of them and being consecutive one to each other. In our model, islands have heights (measured from mean position of the heterojunction) that are randomly distributed to mimic random fluctuations of local flux of atoms during growth. It is then feasible to express the rough profile of the interface between two consecutive epilayers defining the following height function

$$h(y) = \eta \sum_n w_n \{ \Theta(y - n\zeta) + \Theta[(n+1)\zeta - y] - 1 \}. \quad (2)$$

Here $h(y)$ represents the deviation from the flat surface at position y , Θ is the Heavyside theta function, ζ is the island width, w_n is a random variable associated to the n th island that controls the fluctuation around the mean value, and η is the largest deviation—in absolute value—assuming that the w_n 's are uniformly distributed between -1 and 1 . Hereafter η will be referred to as degree of *lateral disorder*. The random variables w_n take values from -1 to 1 uniformly, satisfying the following correlator $\langle w_n w_m \rangle = \delta_{nm}/3$, where the brackets indicate average over different realizations of the disorder. In particular, notice that $\langle h(y) \rangle = 0$.

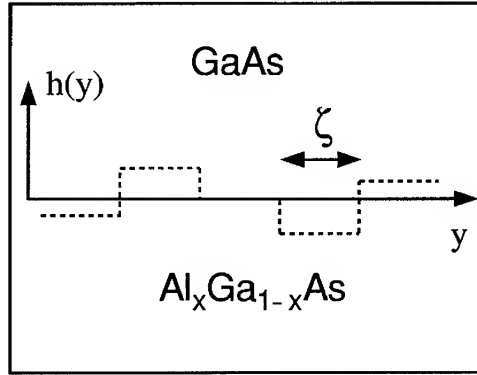


Figure 2. Islands modeling lateral disorder (roughness) at the interface between two epilayers (GaAs and $\text{Al}_x\text{Ga}_{1-x}\text{As}$).

RESULTS

We have performed several numerical calculations in order to study the effect of both lateral and compositional disorder over the transport properties of DBH made of GaAs- $\text{Al}_x\text{Ga}_{1-x}\text{As}$ heterostructures. We start by considering the effect of the interface roughness, characterized by the degree of lateral disorder η given in (2).

Figure 3 shows the transmission coefficient calculated for different values of η . Here $a_y = 10$ nm, $a_z = 0.3$ nm, $\zeta = 20$ nm, $M = 50$, and $N = 38$. The barrier widths are 2.1 nm for both the emitter and the collector, their heights are also the same, 0.3 eV, and the well width is 4.8 nm. Three different values of η were studied, namely $\eta = 0$ (perfect DBH), $\eta = 0.3$ nm (largest fluctuation of the order of one monolayer) and $\eta = 0.6$ nm (largest fluctuation of the order of two monolayers). As a main result, it can be seen in Fig. 3 that increasing the degree of lateral disorder, η , results in a decrease of the transmission probability at the resonant energy. Notice that the resonant peak slightly widens due to the fluctuations of its energy for each realization of the disorder. Besides, an additional effect can be seen, that is, as the degree of lateral disorder η increases the conductance peak shifts to smaller energies. The lowering of the energy of the resonance can be understood assuming that surface roughness makes the effective width of the quantum well larger than its nominal value. This shift would make both the threshold voltage and the negative differential resistance in the current voltage characteristic of DBH to appear at lower bias. But an effective wider well implies a higher current too, so in some statistical sense the current for the disordered DBH will be higher.

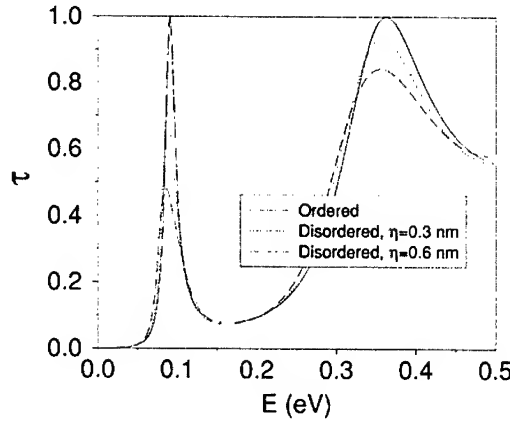


Figure 3. Transmission coefficient through an ordered DBH compared with that of a disordered DBH for two different values of the degree of lateral disorder η . The disordered results comprise 100 realizations of the disorder.

Regarding the effect of the size of the islands, ζ , we have observed that it can be neglected unless this size is of the order of the electron wavelength, that is, for $\zeta \gg \lambda_e$ the transmission coefficient does not depend on ζ . As expected, when $\lambda_e \lesssim \zeta$ the electron starts to *see* each island and then the transmission coefficient decreases as ζ increases, as shown in Fig. 4. For energies about 0.1 eV this transition takes place at sizes $\zeta \sim 10$ nm [3].

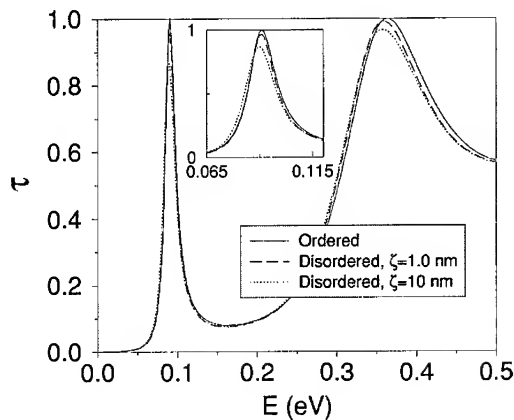


Figure 4. Transmission coefficient through imperfect DBH as a function of the size of the islands for $\zeta \sim \lambda_e$ (dotted line) and $\zeta < \lambda_e$ (dashed line). Curves comprise 50 realizations of the disorder. Inset shows an enlarged view of the main resonance peak.

CONCLUSIONS

In this paper we have presented a method to study electron transmission in unintentionally disordered heterostructures with rough interfaces. We have shown that the main effects of the lateral disorder are to decrease the transmission through DBH and to lower the resonant energy. As a consequence, our model predicts that the threshold voltage of resonance tunneling diodes becomes smaller in imperfect quantum devices.

ACKNOWLEDGMENTS

Work in Madrid was supported by DGI-MCyT (Project MAT2000-0734) and CAM (Project 07N/0075/2001). P. Orellana would like to thank Milenio ICM P99-135-F and Cátedra Presidencial de Ciencias for financial support.

REFERENCES

1. U. Penner, H. Rücker, and I. N. Yassievich, *Semicond. Sci. Technol.* **13**, 709 (1998).
2. V. D. Freilikher and S. A. Gradeskul, *Prog. Opt.* **30**, 137 (1991).
3. L. E. Henrickson, K. Hirakawa, J. Frey, and T. Ikoma, *J. Appl. Phys.* **71**, 3883 (1992).

Exciton Diamagnetic Shifts and Magnetic Field Dependent Linewidths in Ordered and Disordered InGaP Alloys

E. D. Jones¹, K. K. Bajaj², G. Coli², S. A. Crooker³, Yong Zhang⁴, A. Mascarenhas⁴, and J. M. Olsen⁴

¹Sandia National Laboratories,
Albuquerque, New Mexico 87185

²Physics Department, Emory University,
Atlanta, Georgia 30322

³National High Magnetic Field Laboratory - Los Alamos National Laboratory
Los Alamos, New Mexico 87545

⁴National Renewable Energy Laboratory,
Golden, Colorado 80401

ABSTRACT

We have measured the diamagnetic shifts and photoluminescence linewidths of excitonic transitions in ordered and disordered $\text{In}_{0.48}\text{Ga}_{0.52}\text{P}$ alloys, lattice matched to GaAs, in pulsed magnetic fields at 4 and 76K. The pulsed magnetic field ranged between 0 and 50T. The variations diamagnetic shifts with magnetic field in disordered and weakly ordered samples are considerably smaller than those calculated using a free exciton model. For a given magnetic field, the value of the diamagnetic shifts are found to increase with increasing order parameter. Furthermore, for all samples, the diamagnetic shifts at 76K are larger than at 4K suggesting that the excitons are strongly localized.

INTRODUCTION

An understanding and appreciation of the material parameters for the InGaP/GaAs system are important for laser and solar cell applications. In particular, this material system's bandgap energy can be tuned by the phenomenon known as spontaneous ordering, where, depending on the growth conditions, the InGaP crystal structure can be a randomly disordered alloy with the zincblende structure or can form a long-ranged ordered monolayer $(\text{AC})_1/(\text{BC})_1$ superlattice in the (111) orientation, known as the CuPt_2 -like crystal structure. The degree of ordering has been cast in terms of an order parameter η . For $\eta = 0$, i.e., disordered zincblende structure, the 4-K bandgap energy is nearly 2 eV while for $\eta \approx 0.5$ (CuPt_2 -like) the 4-K bandgap energy is smaller, ~ 1.9 eV. An excellent review describing this phenomena can be found in the article by Zunger and Mahajan [1].

Low-temperature photoluminescence (PL) is routinely used to assess the quality of semiconductor alloys. At liquid helium temperatures, the PL full-width-at-half-maximum (FWHM) linewidth of an excitonic transition is generally larger than those observed in their binary components. This broadening is proportional to the amount of compositional disorder [2-9] which

is inevitably present in these systems. Because alloy fluctuations are reduced in ordered structures, the PL FWHM linewidth decreases with increasing order parameter η [10].

In this paper we present PL data at 4 and 76K for the diamagnetic shifts of the excitonic transition and FWHM as a function of magnetic field in two InGaP samples, a weakly ordered and disordered $\text{In}_{0.48}\text{Ga}_{0.52}\text{P}$ alloy. For both the weakly ordered and disordered samples, we find that the observed variations of the FWHM with magnetic field are smaller than those calculated by Lee and Bajaj[7] using a free exciton model. The value of the exciton diamagnetic shift, for a given magnetic field, is also dependent on η . The values of the diamagnetic shifts are found to increase with increasing order parameter. Furthermore, for all samples, the diamagnetic shifts at 76K are larger than at 4K suggesting that the excitons are strongly localized. Previously reported magnetic field studies [11, 12] for InGaP alloys were restricted to the disordered samples.

EXPERIMENTAL

The InGaP samples were grown by metal-organic vapor-phase-deposition (MOCVD.) Substrates used were n^+ -type GaAs with a misorientation of 6° to the nearest $\langle 111 \rangle_A$ axis. A structure consisting of a epilayer of GaAs grown on top of the substrate followed by a 1- μm -thick-layer of InGaP. The order parameters were determined using polarized PL techniques described in Ref. 10. The samples are loaded directly into liquid helium in the tail of a cryostat which itself slips into the 15-mm-diameter bore of a 0.5-sec-duration 50T pulsed magnet. Light is coupled to

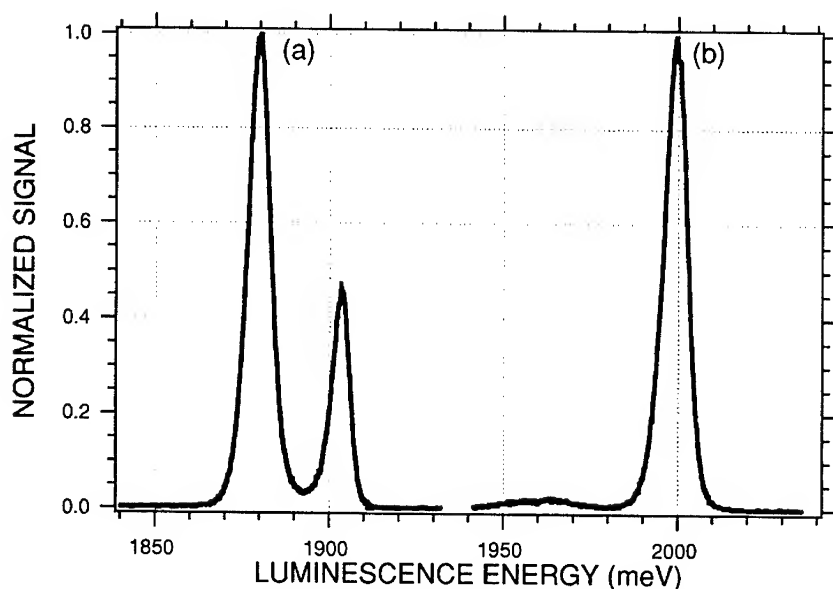


Figure 1. Low temperature ($T=4\text{K}$) photoluminescence spectra for a weakly ordered, $\eta \approx 0.5$, InGaP sample (a) and a disordered, $\eta = 0$, InGaP sample (b). As explained in the text, the lower energy peak in spectrum (a) is from an impurity bound exciton.

the sample, and PL is collected from the sample, via a single 600- μm -diameter optical fiber. The PL signal is dispersed by a 1/3M spectrometer and detected by a back-thinned CCD detector. The CCD detector collects high-resolution spectra continuously throughout the entire magnet pulse at a rate of 600Hz. In this way the entire magnetic field dependence of the PL is acquired in a single 50T magnet pulse. The magnetic field orientation was along the $\langle 100 \rangle$ crystallographic axis. Currently, it is not possible to align the magnetic field along the $\langle 111 \rangle$ direction, one of the principal axis for the CuPt₂-like structures, in the small-bore pulsed-field magnet solenoid.

Figure 1 shows 4-K spectra for the two InGaP samples discussed here. Spectrum (a) is from the weakly ordered ($\eta \approx 0.5$) sample #MA407, while (b) is from a disordered ($\eta \approx 0$) sample #MA565. For these two spectra, the laser power density was about 1 mW/cm². A study of the intensity of the two peaks as a function of laser power density (and temperature) indicates that the lower energy peak of (a) is a result of unknown impurity bound exciton luminescence.

RESULTS AND DISCUSSION

Figure 2 shows the magnetic field dependencies for the diamagnetic shifts at $T = 4\text{K}$. Also shown in Fig. 2 are calculated diamagnetic shifts for two cases: (1) The diamagnetic shift for an InGaP free exciton, reduced exciton mass $\mu_{AV} = 0.08$, and (2) the diamagnetic shift for a InGaP infinite valence-band mass exciton, $\mu_{INF} = 0.13$. The diamagnetic shift for the disordered sample (b) and the calculated diamagnetic shift for the infinite valence-band mass exciton μ_{INF} are nearly identical strongly suggesting that the valence-band holes are strongly localized in this disordered InGaP sample. On the other hand, the diamagnetic shift for the weakly ordered sample (a) falls between the two theoretical cases suggesting that the valence-band holes are less localized when compared with results from the disordered sample. Not shown here are diamagnetic shifts for InGaP samples with varying order parameters η . However, the same general conclusions are reached, i.e., for a given magnetic field, with increasing order parameter η , the value of the diamagnetic shift also increases.

Figure 3 shows the dependence of the 4-K FWHM for the weakly ordered and disordered InGaP samples. As can be seen, the value of the zero-field FWHM of about 6 meV for the weakly ordered sample, trace (a), is much less than the 8 meV zero-field FWHM disordered sample, trace (b) and as mentioned previously, the reduction in the FWHM in going from a disordered to an ordered sample is a result of reduced alloy fluctuations in ordered structures [10]. The theoretical FWHM magnetic field dependence in a semiconductor alloy has been calculated by Mena et al., [13]. Currently, a comparison between theory and experiment for the data shown in Fig. 3 are being performed and the results will be reported in detail at a later date.

The 76-K diamagnetic shift data is shown in Fig. 4. The calculated diamagnetic shifts for the two excitons with reduced masses μ_{AV} and μ_{INF} are the same as shown in Fig. 2. It is obvious from Fig. 4 that the diamagnetic shifts for both the weakly ordered and disordered samples are larger at 76K compared to the 4-K data shown in Fig. 2. One possible explanation is that the exciton center-of-mass thermal energy has overcome, somewhat, the valence-band mass confinement potential leading to an apparent "lighter" exciton reduced mass and hence a larger diamagnetic shift. In order to clarify these speculations, further experiments are needed before definite conclusions can be reached.

For completeness we show the 76-K FWHM magnetic field dependence for the two samples in Fig. 5. The increased FWHM at 76K is a result of broadening due to the higher temperatures. Because of thermal broadening, the FWHM for both samples are nearly the same.

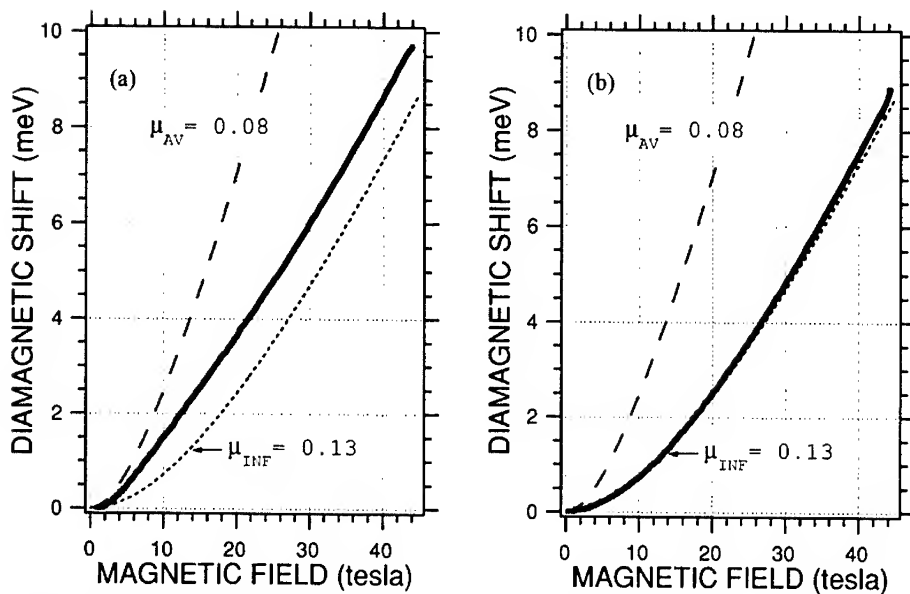


Figure 2. Magnetic field dependence of the exciton diamagnetic shift at 4K. The left graph (a) is for the partially ordered InGaP, $E_{\text{gap}} = 1903.2$ meV. The right graph (b) is for the disordered sample, $E_{\text{gap}} = 1999.2$ meV. The theoretical diamagnetic shifts for a free exciton with reduced exciton mass, $\mu_{\text{AV}} = 0.08$, and an infinite-valence band mass exciton, $\mu_{\text{INF}} = 0.13$ are shown.

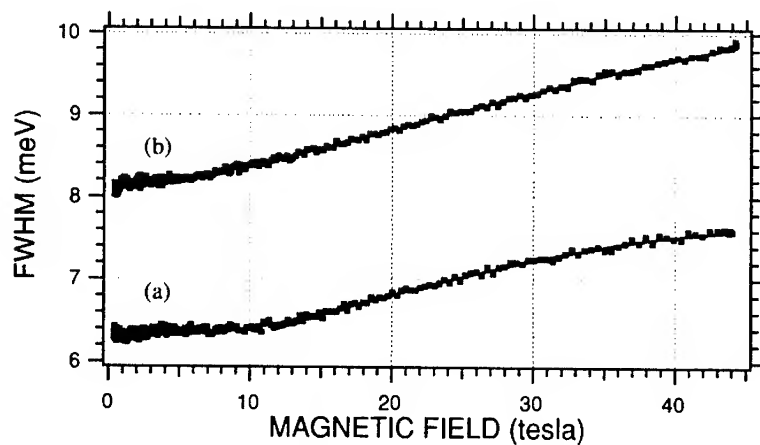


Figure 3. Magnetic field dependence of the FWHM at 4K. The upper trace (b) is for the disordered InGaP and the lower trace (a) is for the partially ordered InGaP sample.

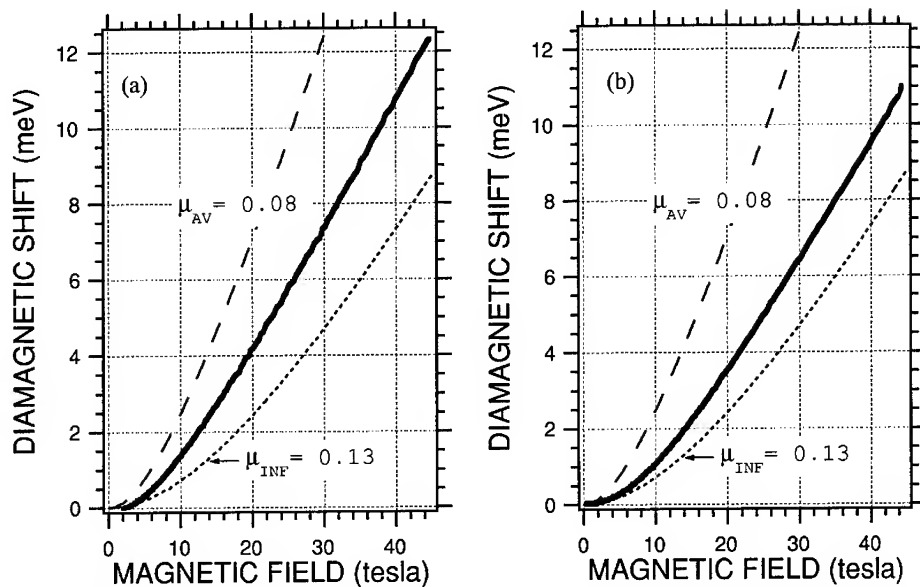


Figure 4. Magnetic field dependence of the exciton diamagnetic shift at 76K. Graph (a) is for partially ordered InGaP and graph (b) is for disordered InGaP. The 76K bandgap energies are respectively $E_{gap} = 1900$ meV and $E_{gap} = 2004.8$ meV for graphs (a) and (b). The theoretical shifts labeled μ_{AV} and μ_{INF} are the same as shown in Fig. 2.

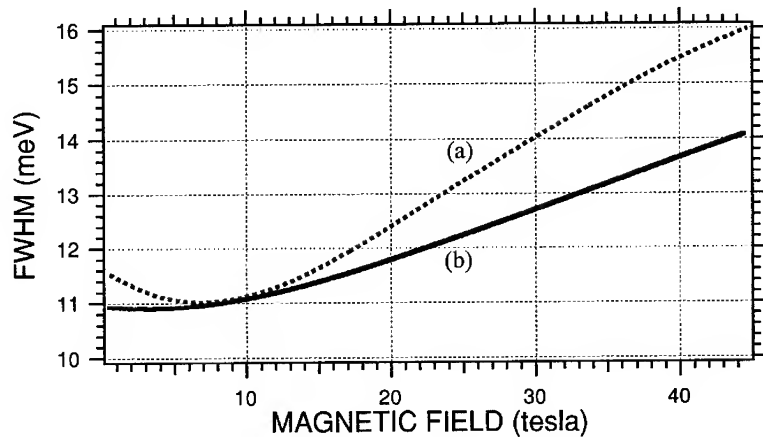


Figure 5. Magnetic field dependence of the FWHM at 76K. The dashed trace (a) is for the partially ordered InGaP and the solid trace (b) is for the disordered sample.

CONCLUSION

In summary, we have measured both the diamagnetic shifts and the linewidths of excitonic transitions in a series of weakly ordered and disordered $\text{In}_{0.48}\text{Ga}_{0.52}\text{P}$ alloys, lattice matched to GaAs, as a function of magnetic field at 4 and 76K using photoluminescence spectroscopy. The magnetic field was varied from 0 to 50T. The value of the exciton diamagnetic shift, for a given magnetic field, is also dependent on the order parameter η . The value of the diamagnetic shifts are found to increase with increasing order parameter. Furthermore, for all samples, the diamagnetic shifts at 76K are larger than at 4K suggesting that the excitons are more localized at 4K than at 76K.

ACKNOWLEDGEMENTS

Sandia is a multiprogram laboratory operated by Sandia Corporation, a Lockheed Martin Company, for the United States Department of Energy under contract DE-AC04-94AL85000. Part of this work was performed at the National High Magnetic Field Laboratory, which is supported by NSF Cooperative Agreement No. DMR-9016241 and by the State of Florida.

REFERENCES

1. A. Zunger and S. Mahajan, "Atomic Ordering and Phase Separation in Epitaxial III-V Alloys, *Handbook on Semiconductors*, edited by T.S. Moss, Volume 3, edited by S. Mahajan (Elsevier Science, 1994), pp. 1399-1514.
2. O. Goede, L. John, and D. H. Hennig, *Phys. Status Solidi B* **89**, K183 (1978).
3. J. Singh and K. K. Bajaj, *Appl. Phys. Lett.* **44**, 1075 (1984).
4. E. F. Schubert, E. O. Gobel, Y. Horikoshi, K. Ploog, and H. J. Queisser, *Phys. Rev.* **B30**, 813 (1984).
5. J. Singh and K. K. Bajaj, *Appl. Phys. Lett.* **48**, 1077 (1986).
6. J. Zimmerman, *J. Crystal Growth* **101**, 346 (1990).
7. S. M. Lee and K. K. Bajaj, *J. Appl. Phys.* **73**, 1788 (1993).
8. S. K. Lyo, *Phys. Rev.* **B48**, 2152 (1993).
9. M. E. Raikh and A. L. Éfros, *Fiz. Tverd. Tela (Leningrad)* **26**, 106 (1984) [*Sov. Phys. Solid State* **26**, 61 (1984)].
10. Y. Zhang, A. Mascarenhas, S. Smith, J.F. Geisz, J.M. Olsen, and M. Hanna, *Phys. Rev.* **B61**, 9910 (2000).
11. E. D. Jones, R. P. Schneider, S. M. Lee, and K. K. Bajaj, *Phys. Rev.* **B46**, 7225 (1992).
12. J. Zeman, G. Martinez, K. K. Bajaj, I. Krivorotov, and K. Uchida, *Appl. Phys. Lett.* **77**, 4335 (2000).
13. R. A. Mena, G. D Sanders, K. K. Bajaj, and S. C. Dudley, *J. Appl. Phys.* **70**, 1866 (1991).

Field emission enhancement of DLC films using triple-junction type emission structure

Namwoong Paik, Michael Martin, Daeil Kim, Sungjin Kim, Steven Kim and Kie Moon Song¹
SKION Corporation, Hoboken, New Jersey, 07030 U. S. A.

¹Department of Applied Physics, Konkuk University, Chungju 380-701 Korea

ABSTRACT

Negative Electron Affinity (NEA) of Diamond-like-Carbon (DLC) films has made DLC films a favorable candidate for field emission display (FED). It was suggested that triple-junction type structure could enhance the field emission characteristics. A triple junction is defined as the intersection of a semiconductor surface with a metal substrate in vacuum. In this study, field emission enhancement in triple junction type structures was investigated. As a metal substrate 5000 Å of Mo films were deposited. Then, 3000-4000 Å of DLC film was deposited as a semiconductor material. Thin film layers were made using a negative ion beam source. After the deposition, using an excimer laser, we removed the DLC layer and made circular shaped triple junction trenches with a diameter of 25–250 μm. The field emission characteristics such as I-V characteristics turn on voltage and emission lifetime data were obtained for a diode type field emission measurement system. Overall results show significantly enhanced performance of field emission characteristics such as uniform emission over patterned area, reduced turn on voltages and longer lifetimes can be achieved.

INTRODUCTION

Due to its advantages such as increased brightness, improved viewing angle and lower power consumption than Liquid Crystal Displays (LCD), Field Emission Display (FED) has become a big research and development field for the next generation display technology. In FED development, conventionally, molybdenum and Si tips were widely used as cold-cathode material¹. However, Mo can be easily contaminated and has poor mechanical properties. Silicon is rather fragile and has low thermal conductivity². Recently, DLC films become a favorable candidate for FED thanks to its Negative Electron Affinity (NEA), high thermal conductivity, chemical inertness and high hardness³. Also, field emission from DLC (diamond-like carbon) films is of particular interest because they can be made at room temperature, over large areas and on various kinds of substrates such as glass, metals, semiconductors, ceramics and polymers. Several years ago a new electron-emission mechanism so called triple-junction type emission for cold cathodes was proposed⁴. A triple junction is the intersection of a semiconductor surface with a metal substrate in vacuum. Unlike conventional mechanisms, in which electrons tunnel from a metal or semiconductor directly into vacuum, the electrons in the triple-junction type structure tunnel from a metal into diamond surface states, where they can be accelerated and ejected into vacuum.

EXPERIMENTAL SETUP

In this study, we prepared two different sets of samples; the conventional diode structure and the triple junction structure. As a metal substrate 5000 Å the Mo films were deposited. Then,

3000-4000 Å of DLC film was deposited on top of the Mo layer as a semiconductor material. Using an excimer laser, we selectively patterned the DLC layer producing circular triple junction features with diameter of 25 – 250 μm.

Film Deposition

DLC films used in this paper were made using a direct ion beam deposition technique. With a cryogenic pump (CTI-cryogenics) attached to the chamber, the base pressure was about 5×10^{-7} Torr. The chamber pressure was monitored using a thermocouple and an ion gauge. The typical operating pressure of the source with Argon plasma was on the order of 10^{-4} Torr. At the bottom, a commercial 8" magnetron sputter type negative ion source (SKION Corporation, Omnipotent series) was placed. In Molybdenum deposition, an 8-inch diameter and 0.25 inch thickness 99.999% Molybdenum target was used. At DLC deposition, the target is changed to 99.999% graphite target. The substrate holder with linear motion equipment had the capability to adjust the target-to-substrate distance. During the deposition, an 8-inch manual gate valve located between the cryo pump and the chamber controlled the pressure. To reduce the work function of the sputtering target, Cs vapor was introduced into the chamber. Detailed information about the source and mechanism of Cesium delivery is given elsewhere⁵. After the deposition, the surface morphology of the resultant DLC samples was analyzed using an AFM (Digital Instrument, Dimention3100). The typical Ra (mean roughness) of the film was 0.1nm. To create triple-junction type emission spots,

Field Emission measurement

A substantial part of this work has been the development of methods for reliable measurement of the field emission characteristics. For this purpose, we have built a field emission measurement system. All the measurement was performed inside a UHV chamber, which is capable of keep the base pressure lower than 1×10^{-7} Torr. Figure 2. is the schematic diagram of the system. The spacing between film and phosphor plate was fixed as 100 μm.

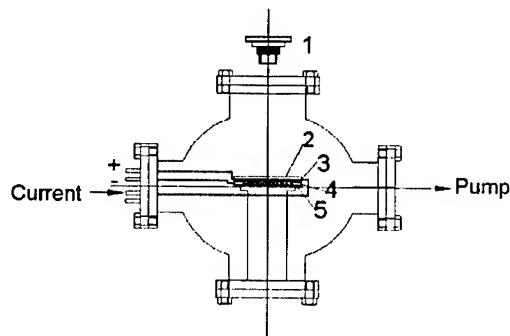


Figure 1. Field Emission measurement system: 1.Digital Camera, 2.Glass, 3.ITO, 4.Phosphor plate and 5.Laser patterned DLC

RESULTS & DISCUSSION

Emitting area analysis

During the first stage of the experiment, the emission test was performed without any modification of the film. The very smooth, un-doped DLC films are poor field emitters regardless of their sp³ content, high NEA and low surface work function. At the measurement, usually the first emission starts from the edges of film (Figure2. (a)) or at the damaged surface area. The AFM image of the emitted area is shown Figure2. (b) and (d). The emitted spot shape like a crater with some portion of DLC film is taken off. After the first emission, the emitted area can maintain stable emission even after considerable amount of time (>10hr). This suggests that this kind of emission can be considered as a triple-junction type emission. The size of the craters is from 5 up to 150 μm .

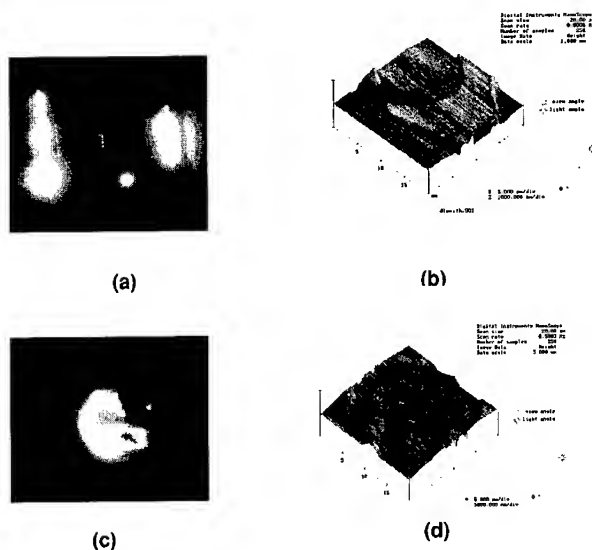


Figure 2. The field emission patterns of the DLC films and AFM images of the emitted spots: (a) DLC at 16 V/ μm , (b) an emitted spot of (a), (c) DLC 20V/ μm and (d) an emitted spot of (c).

Laser patterned DLC

Based on the results, we prepare a new sample set with laser-drilled holes. Using a laser, we took off DLC layer and produced Mo-DLC-Vacuum triple junctions. Figure 3 is the optical microscope image of the resultant film. In this case the diameter of the each hole was 100 μm and space between each hole was 300 μm .

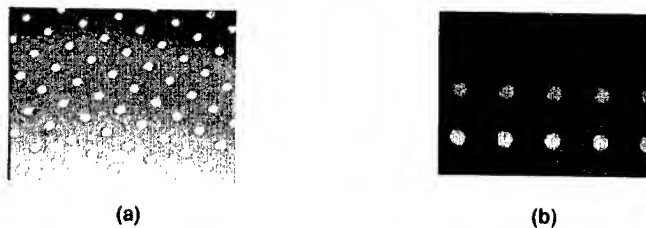


Figure 3. The optical microscope images of DLC sample:

Emission Result of Patterned Sample

Using an excimer laser, we patterned a DLC coated 4" wafer with 25 - 250 μm holes. Figure 4 shows the emission pattern of the 100 μm -hole sample at 6V/ μm (a) and at 12V/ μm (b). The result shows that even though the whole area was coated with DLC, the patterned area emitted first. Since the high voltage was applied to the center of the wafer using a wire attached with silver epoxy, the central area of the wafer is brighter than edges. In other words, since the resistivity of the film is high, the voltage drop gets larger as the distance increases. This effect decreased when we used several wires to connect different regions of the sample.

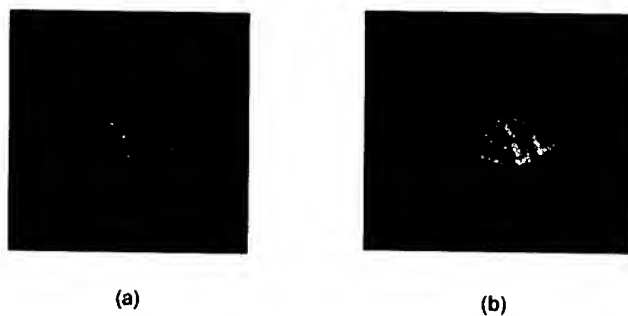


Figure 4. Emission images of the patterned DLC coating: (a) @ 6V/ μm and (b) @ 12V/ μm

Field emission measurement

The I-V characteristic of the sample was measured using a computer interfaced digital current meter (Extech, CMM-15). Figure 5 is a comparison of the J-V characteristic for DLC samples with and without patterning. Both samples were deposited at the same conditions. The result shows that the turn on voltage of the sample is enhanced from 12V/ μm to 4V/ μm with

patterning. Also the total emission current density at $15\text{V}/\mu\text{m}$ increased from $25\text{ }\mu\text{A}/\text{cm}^2$ to $300\text{ }\mu\text{A}/\text{cm}^2$ for the triple junction structure.

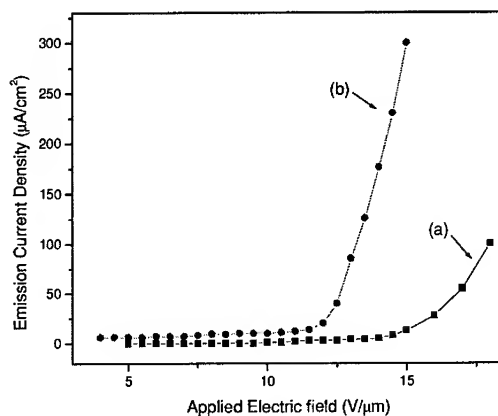


Figure 5. J-V characteristic curve of DLC films: (a) DLC without any modification, (b) Laser patterned DLC (Hole diameter $100\mu\text{m}$)

The lifetime study

In the last stage of this study, the lifetime of the emitting regions was investigated. Figure 6 shows the time dependence of a sample. Figure 6 (b) was taken after 3 hours. Total emission current decreased approximately 15% after 3 hours and stays stable after that. Also emitting area decreases as time goes by. In the case of un-patterned DLC, total emission current density dropped about 33% after 3 hours.

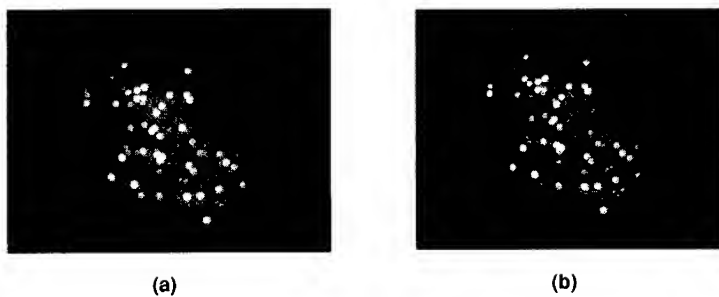


Figure 6. The emission images of the patterned DLC coating: (a) initial image and (b) image after 3 hours

CONCLUSIONS

DLC films have many encouraging characteristics such as high negative electron affinity (NEA), high thermal conductivity, chemical inertness and high hardness. However, the very smooth, un-doped DLC films are known as poor field emitters regardless of their sp³ content and high NEA. After reviewing the emitted spots, a new approach to enhance field emission was tried. The new trial is based on the triple junction type field emission theory. Using an excimer laser, we patterned the surface of DLC coatings and produced triple junction structures. The result shows that triple junction structures can reduce the turn on voltage and increase the electron current density. Also the lifetime study shows that the emitted area can maintain emission stably even after a long period of time. The overall result shows that field emission enhancement can be achieved by producing triple junction structures on DLC films.

REFERENCES

1. E.I. Givargizov, *J. Vac. Sci. Technol.* **B13** (1995) 414
2. D.S. Mao, J. Zhao, W. Li, X. Wang, X.H. Liu, Y.K. Zhu, Z. Fan, J.Y. Zhou, Q. Li and J.F. Xu *Diamond Relat. Mater.* **8** (1999) 52-55
3. J.O. Choi, J.W. Huh, Y. H. Choi, M.J. Kim, Y.R. Cho, H.S. Jeong, *J. Vac. Sci. Technol.* **B16** (1998) 1199.
4. M.W. Geis, N.N. Efremow, K.E. Krohn, J.C. Twichell, T.M. Lyszczarz, R. Kalish, J.A. Greer and M.D. Tabat *Nature* **431-435** vol393 June. 1998
5. To be published

Luminescence of quasi-2DEG in heterostructures based on PbS films

G. Khlyap, State Pedagogical University, 24 Franko str., Drohobych, 82100, Ukraine.

ABSTRACT

The paper deals with the problem of luminescence due to non-equilibrium charge carriers transfer between the quasi-2D electron system localized in the space-charge region of the heterostructures based on lead sulfide films (up to 3 μm thickness) and zinc selenide substrates surrounded by the wide gap semiconductor region. The processes of electro- and photoluminescence are studied, the band diagram is proposed and the main parameters of the structure PbS/quasi-2DEG/ZnSe are calculated.

INTRODUCTION

Highest performance of modern often requires more sophisticated structures and non-destructive methods of their properties analysis. Epitaxial techniques offer important advantages in comparison with the bulk grown ones: lower temperature, shorter growth time and reduced precipitation problems enable the growth of large-area samples with good parameters. At present, MBE (molecular-beam technology) is the most mature method of device-quality layer fabrication. In particular, semiconductor devices based on $\text{A}^2\text{B}^6\text{-A}^4\text{B}^6$ heterostructures are of special importance due to the well-known "window-effect" as well as a possibility to act as a system of quasi-2D or quasi-3D charge carriers, as it was shown earlier [1]. The paper presents results of photoluminescence studies performed at 77 K on the isotype n-n-heterojunctions PbS/ZnSe obtained by the MBE technology.

EXPERIMENTAL DETAILS

Preparation of the samples.

The investigated isotype n-n-heterostructures ZnSe/PbS were grown by the MBE technology of lead sulfide ($E_g = 0.41$ eV) films with thickness up to 3 μm on the (110)-oriented ZnSe ($E_g = 2.72$ eV) wafers under the substrate temperature $T_s = 540$ K (the vacuum level in the effusion cell was estimated to be about 10^{-9} Tor). The samples of 1.5x3.5 mm² size characterized by the film surface homogeneity were selected for the examinations. Parameters of the contacting materials are listed in Table 1.

Table 1.
Parameters of the components of the investigated heterostructures

Material	Parameter
ZnSe	$E_g = 2.72$ eV
	$a = 5.668$ Å
	$\epsilon = 9.1\epsilon_0$
	$n_e = (7.8 \cdot 10^{16} - 2.6 \cdot 10^{17}) \text{ cm}^{-3}$
PbS:Na	$E_g = 0.41$ eV
	$a = 5.940$ Å
	$\epsilon = 175\epsilon_0$
	$n_e = (2 - 8) \cdot 10^{15} \text{ cm}^{-3}$

Results of electric-field measurements.

The electrophysical studies described for the first time in [2], were shown that the heterostructures based on the materials mentioned in the present article are abrupt heterojunctions.

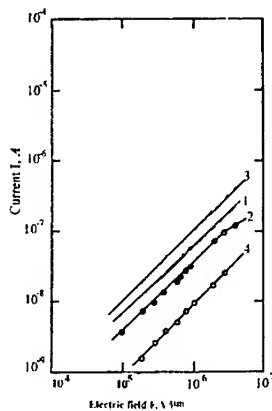


Fig. 1. Field dependencies of the examined heterostructure $n\text{-PbS}/n\text{-ZnSe}$. Functions 1, 3 are forward sections and functions 2, 4 are reverse ones at 300 and 77 K, respectively.

The further electric-field measurements (Fig. 1) carried out on the as-grown specimens demonstrated that the processes of the charge carriers transfer are strongly effected by the space-charge region of the heterojunction formed by the surface electron states at the interface. The numerical analysis of the experimental I-F-measurements (where I stands for the current flowing through the heterojunction and F denotes the external electric field) showed that the I-F-function can be expressed according to the model developed in [3]:

$$I = K_{\text{tun}} \frac{2\epsilon_0 \epsilon A_i v_{\text{sat}} F}{LW}, \quad (1)$$

where K_{tun} is the transparency coefficient of the potential barrier formed at the interface of the heterostructure depending on the energy spectrum of the surface electron states [2], ϵ is the dielectric constant, A_i is an electrical area of the investigated sample, L takes care of the sample thickness, W stands for the width of the space-charge region determining from the capacitance-voltage measurements [2] and v_{sat} is a complex function strongly influenced by the parameters of the contacting materials. Such a field dependence indicates on the inhomogeneous (quantum wells continuum, QW-continuum) structure of the potential barrier which determines not only the electric characteristics of the heterostructure but also the emission properties of the grown samples.

Electro- and photoluminescent studies.

Photoluminescence (PL) of the investigated structures was excited by the light source of the wavelength λ centered around 290 nm. Electroluminescence (EL) was excited by the electrostatic field, $F = (0.9 - 1.8) \cdot 10^6$ V/m. Both PL and EL spectra were registered at $T = 77$ K in the wavelength range from 0.48 up to 0.8 μm . As it is shown, both PL and EL spectra are appeared as the wide Gaussian-like bands in the wavelength range 0.53-0.80 μm describing by the expression [5]

$$I(\hbar\omega) \sim \omega^2 (\hbar\omega - \Delta)^{1/2} \exp\{(\hbar\omega - \Delta)/k_B T\}, \quad (2)$$

where Δ stands for the value of the integrated potential barrier consisting of the QW-continuum, ω is frequency of the excited light source.

The energy positions of the emitted radiation maximums are estimated to be about 1.97-2.00 eV; These results show that the emission processes are take place in the subsurface region of the wide-gap material, such a value corresponds neither lead sulfide nor zinc selenide energy parameters as well as the energy levels of the known and uncontrolled impurities. The previous studies [1] were shown the formation of the quasi-2D electron system at the interface of the examined heterostructures. The experimental results obtained under the electro- and photoluminescent measurements had allowed to conclude that the investigated structure presents a multi-QW continuum localized at the interface.

The experimental results are plotted in Fig. 2.

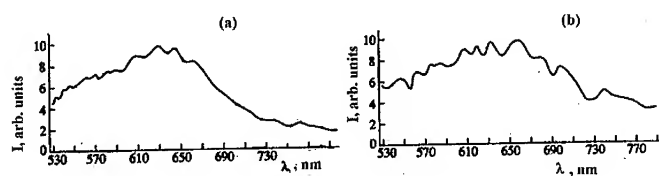


Fig. 2. Photoluminescence (a) and electroluminescence spectra of the investigated $n\text{-PbS}/n\text{-ZnSe}$ heterostructure. $T = 77$ K.

DISCUSSION

As it was mentioned above, the investigated isotype $n\text{-n}$ -heterostructure PbS/ZnSe appeared as a heterojunction with QW-continuum at the interface. The experimental data obtained from the luminescent studies showed that the non-equilibrium charge carriers were excited in the subsurface region of the wide-gap substrate adjacent to the space-charge region of the structure, then the carriers were confined in the QW-continuum and have relaxed energetically with radiative recombination. In the other words, this so-called "graded barrier" [6] acted as a suppressor of the carrier trapping at low temperatures, leading to an improved excitation transfer from the barriers to quantum wells (Fig. 3).

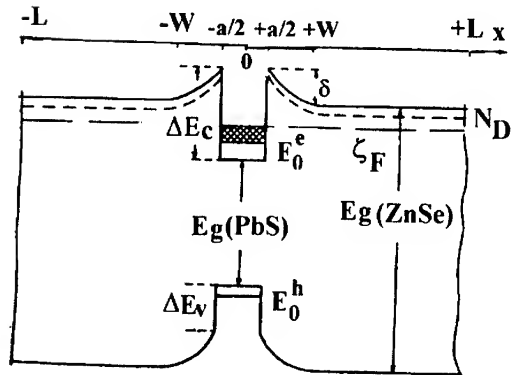


Fig. 3. Energy band diagram of the examined heterostructure constructed according to [4] (non-scaled, the main parameters are listed in Table 1)

ΔE_c and ΔE_v are the conduction band and valence band discontinuities (the method of calculation is reported in [2]), E_0^e, E_0^h are energy positions of the electron and hole levels in quantum well, respectively, a is the quantum well width ($a = (\epsilon_0 \epsilon k_B T / e^2 N_D)^{1/2}$), other notes are explained in the text.

The barrier value δ was calculated according to the measurements performed previously [1] and using the Schottky approximation for the depletion layers surrounding the quantum well, we have [4]

$$(8\epsilon_0 \epsilon N_D \delta)^{1/2} = n_s^0 + \Delta n_s - \Delta p_s, \quad (3)$$

where N_D is donor concentration in the wide-gap material, δ is the potential barrier, n_s^0 is the surface concentration of the equilibrium electrons, Δn_s stands for the concentration of the non-equilibrium electrons and Δp_s takes care for the concentration of the non-equilibrium holes.

Under equilibrium conditions $\Delta n_s = \Delta p_s = 0$ and

$$n_s^0 = \frac{m_e k_B T}{\pi \hbar^2} \ln \left[1 + \exp \left(\frac{\xi + \Delta E_c - E_0^e - \delta}{k_B T} \right) \right]. \quad (4)$$

Here ξ is the Fermi level position in the wide-gap substrate, ΔE_c is conduction band discontinuity (calculated according to the Harrison model in [2]), m_e is the electron effective mass in ZnSe, E_0^e is energy of electron level in the quantum well. The solution of the equations (3) and (4) makes it possible to calculate the equilibrium values of n_s^0 and δ . Results of the calculation are plotted in Figs. 3, 4.

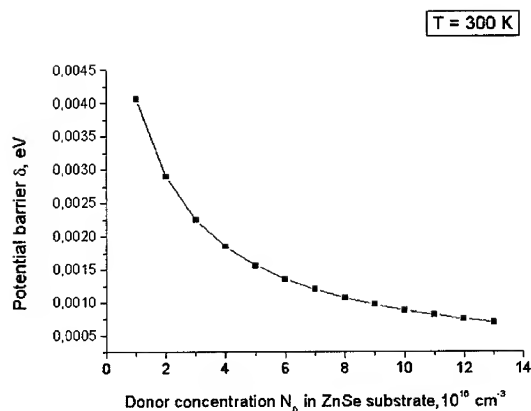


Fig. 4. Potential barrier formed by the QW-continuum localized at the interface of the heterostructure vs. donors concentration in ZnSe substrate..

As it is shown in Fig.4, the value of the barrier δ decreases as the donor concentration in the substrate increases, and the life-time of the non-equilibrium carriers has to become greater [4]. At the same time, the intensity of the luminescence spectra in long-wave interval is comparable with the same characteristic in the short-wave region. Thus, the presence of the potential barrier δ increases the effective width of the quantum well for the non-equilibrium carriers under the low level of excitation.

CONCLUSIONS

Isotype n-n-heterostructures based on thin lead sulfide films and zinc selenide demonstrated good emission characteristics under 77 K strongly depending on the properties of the space charge region. The results of luminescent (PL and EL) experiments have been shown the formation of quantum-inhomogeneous barrier at the interface of the examined n-PbS/n-ZnSe heterostructure and the technological possibility of monitoring the carriers confinement and ejection in the region of QW-continuum by means of proper doping of the substrate material.

REFERENCES

1. Andrukhiv A., Khlyap G., Andrukhiv M., Bochkariova L. *Thin Solid Films*, **267**, 126 (1995)
2. Khlyap G., Andrukhiv M. *Cryst. Res. Techn.*, **34**, 751 (1999).
3. Hernandez E. *Cryst. Res. Techn.*, **33**, 285 (1998).
4. Kozyrev S., Shik A. *Semiconductors (Russia)*, **22**, 106 (1988).
5. Sze S. M., *Physics of Semiconductor Devices, Second Edition*, John Wiley & Sons, New York, 1981.
6. Bleuse J., Bonnet-Gamard J., Mula G., Magnea N., Pautrat J.-L. *J. Cryst. Growth*, **197**, 529 (1999)

Lasers and Materials

GaInNAs Material Properties for Long Wavelength Opto-Electronic Devices

Vincent Gambin, Wonill Ha, Mark Wistey, Seongsin Kim¹, James S. Harris
Solid State and Photonics Lab, Stanford University,
Stanford, CA 94305, U.S.A.

¹Agilent Technologies
Palo Alto, CA 94303

ABSTRACT

Dilute nitrogen GaInNAs is a new promising material as an active region for use in 1.3 and 1.55 μm opto-electronic devices. It has been commonly observed that increasing the nitrogen content generally reduces the optical emission intensity and increases laser threshold. However, some non-radiative recombination defects are removed from the material during a post-growth anneal. One drawback to the anneal is that nitrogen out-diffuses from the quantum wells and blue-shifts optical emission. Using a modified active region structure, we have decreased nitrogen out-diffusion and reduced the luminescence blue-shift while still improving crystal quality. The growth consists of high nitrogen GaNAs barriers grown between lower nitrogen GaInNAs quantum wells. As an added benefit, the nitride barriers strain compensate for the compression in the high In content GaInNAs wells. Furthermore, in order to improve luminescence at long wavelengths, we have added Sb to GaInNAs and have observed high intensity photoluminescence (PL) out to 1.6 μm . We have grown and fabricated in-plane GaInNAs lasers that emit at 1.3 μm with a current threshold density of 1.2 kA/cm^2 and GaInNAsSb lasers with emissions at 1.46 μm with a current threshold of 2.8 kA/cm^2 .

INTRODUCTION

There currently is a high demand for low cost 1.3-1.55 μm diode lasers that can operate over a significant temperature range (-10 to 85°C) with moderate power (>10 mW). There are many applications for light sources in this wavelength region including telecommunication lasers, modulators and amplifiers. Current solutions based on InP have serious limitations covering the entire 1.3-1.55 μm wavelength range [1]. The GaInNAs alloy grown on GaAs has been predicted to extend over that wavelength range with several material advantages. Due to a large bandgap bowing, small amounts of nitrogen in GaAs have drastic electronic effects reducing the bandgap greater than 100 meV per atomic percent of nitrogen. Mixed with InGaAs, long wavelength light emission is possible nearly lattice-matched to GaAs. With a larger conduction band offset than InP, GaInNAs quantum wells on GaAs are thought to have improved in thermal properties. Furthermore, being based on GaAs substrates, one can take advantage of well-established processing techniques and a superior Distributed Bragg Reflector (DBR) mirror technology. GaInNAs has shown encouraging characteristics at long wavelengths, including low threshold current densities, high temperature CW operation and high T_0 in the wavelength range of 1.1-1.3 μm [2-4].

However, growing high quality GaInNAs material beyond 1.3 μm has proved challenging. Due to the low solubility of nitrogen in GaAs, nitrogen content needs to be minimized such that phase segregation does not occur. High indium content alloys with dilute nitrogen are then limited in thickness due to a large lattice mismatch. Furthermore, evidence

suggests that high indium GaInNAs tends to phase segregate, thereby drastically reducing non-radiative recombination efficiency. Two solutions exist to improve luminescence output in as-grown high indium GaInNAs. First, by growing tensile strained barriers around compressively strained quantum wells, one can strain compensate and increase the overall thickness of material feasible. Tensile GaNAs barriers can be grown in the active region to allow for an increased number of strained quantum wells increasing optical gain. Second, after thermal annealing as-grown material, photoluminescence sharply improves. However, thermal annealing tends to blue-shift emission and is less effective as wavelength increases. Optical output steadily decreases as wavelength increases, thereby limiting the performance of long wavelength GaInNAs devices.

EXPERIMENTAL DETAILS

GaInNAs/GaNAs/GaAs heterostructures were grown by elemental source molecular beam epitaxy (MBE) on N⁺ and S.I. (001) GaAs substrates. Dimeric arsenic was provided by a thermal cracker and a radio frequency (RF) plasma cell supplied atomic nitrogen. The plasma cell is operated at 250-350 W with a nitrogen gas flow of 0.1-0.5 sccm. Further details have been previously reported [5]. Nitrogen concentration was calibrated using high-resolution X-ray diffraction (HRXRD), electron probe microanalysis (EPMA), secondary ion mass spectroscopy (SIMS), and nuclear reaction analysis Rutherford backscatter spectroscopy (NRA-RBS). A thermal cracker supplied monomeric antimony and the concentration was calibrated using X-ray photoelectron spectroscopy (XPS) and RBS. All PL samples were excited with an Ar⁺ ion laser.

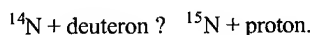
DISCUSSION

It is commonly observed that as-grown GaInNAs has poor luminescent properties. Fortunately, with high temperature anneals of 600-900°C, non-radiative recombination sites are removed and optical emission can be vastly improved. Annealing increases intensity and sharpens peaks but at the same time blue-shifts PL. The precise mechanism for defect removal on anneal is still not well understood. To help understand possible defects contributing to non-radiative recombination, atomic changes during anneal can be separated into two classifications: the reduction of point defects and atomic rearrangement.

Point Defects

Through TEM analysis, dislocation density and other two dimensional defects visible in electron microscopy are extremely low. However, with C-V analysis, deep level defects have been found in GaNAs [6,7]. The origin of these defects is unknown but likely causes include point defects such as trace contaminants, interstitials, vacancies, and antisites. In this research, we have studied interstitials and their possible contribution to the luminescent behavior of GaInNAs using nuclear reaction analysis RBS. In the RBS technique an incident He beam is accelerated at 2.275 MeV toward a thin film of GaInNAs on GaAs. A small fraction of He undergoes a direct collision with the atoms within a few microns and backscatter elastically. The energy of the detected He backscattered from the sample depends on energy lost traveling through the material and the energy lost as a result of the collision itself. Nitrogen, having such a small cross-section with respect to InGaAs, would not be easily resolved. However at certain

energies, the incident ion is absorbed by the nucleus and a variety of particles such as protons are emitted. In this analysis, the following nuclear reaction took place:



The detection of the resulting proton spectrum allows for parts per million sensitivity of nitrogen concentration. In order to study interstitial concentration, He^{++} was channeled down the (100) crystal axis. In this orientation, substitutional atoms have a very low backscattering yield and interstitial atoms are highly visible. Figure 1 shows the NRA-RBS results comparing the channeled versus random crystal orientation. The nitrogen signal, shown on channel 200 is reduced in channeled orientations. Other peaks present close to the nitrogen are surface contaminants such as carbon and oxygen that appear on both random and channeled orientations.

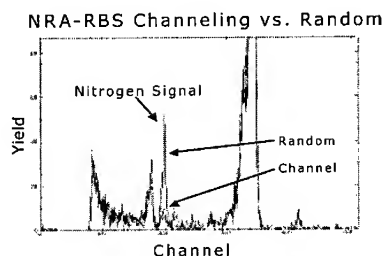


Figure 1. NRA-RBS spectrum of a 150 nm GaInNAs film. The arrows point to the nitrogen peak in both channel and random crystal orientations.

A summary of RBS analysis performed on GaNAs, GaInNAs and GaInNAsSb is shown in table I. In as-grown material, the interstitial concentration is found to be lower than 7%. After thermal anneal interstitial concentration actually increases. Possible explanations for this include a higher equilibrium concentration of interstitials at high temperatures that are quenched when rapidly cooled, or a diffusion of environmental nitrogen present in the annealing chamber into interstitial positions. Due to the low concentration of interstitials and their apparent increase during anneal, it is unlikely that this type of point defect removal is instrumental in the annealing characteristic of GaInNAs.

Vacancies are just one type of point defect effecting luminescence that could be present in GaInNAs. More information about other defects and their origin is currently being studied with other techniques such as C-V, DLTS and low temperature PL.

Table I. Total nitrogen and interstitial nitrogen content on GaNAs, GaInNAs and GaInNAsSb before and after anneal.

	%N	Interstitial %N
GaNAs	2.4	5.8
- Annealed	2.0	8.3
GaInNAs (8%In)	2.4	3.7
- Annealed	2.4	4.2
GaInNAsSb (8%In 7%Sb)	3.0	6.9
- Annealed	3.0	8.2

Atomic Rearrangement

Another possible thermally activated mechanism that could affect luminescent properties in GaInNAs is the diffusion of atoms. There are four types of diffusion that at this stage of analysis seem likely candidates. The first is the diffusion of substitutional nitrogen and the removal from its as-grown location. This has been observed in XRD through a shift of lattice constant in GaNAs films. Also SIMS analysis of GaInNAs has shown an attenuated nitrogen signal after anneal. At first this would seem the most likely candidate to explain the increase in the bandgap on anneal, however other research groups studying this material have not observed similar behavior under their growth conditions. Therefore we can conclude the events which take place during anneal are more complex than just N out-diffusion from quantum wells.

The next three diffusion mechanisms that have been investigated are the phase separation of atoms in the GaInNAs quaternary. Due to unfavorable thermodynamics for solid solubility, under certain conditions diffusion kinetics may allow phase transformations to take place. By growing high nitrogen GaNAs material under varied growth conditions, we have observed nucleation and growth of a GaN rich phase and spinodal decomposition of GaN and GaAs. This only occurs for nitrogen compositions in excess of 5%, however the majority of our material contains a nitrogen concentration less than 3.5%.

A more likely decomposition for dilute nitrogen is the segregation of In and Ga atoms. This is a very common defect in the InGaN system although is not thought to occur in nitrogen free InGaAs. TEM analysis of high In GaInNAs quantum wells however has found In segregation along the length of the wells. Figure 2 shows a low temperature PL spectrum of GaInNAs quantum wells before and after anneal taken at 30K. Two distinct peaks are seen which at higher temperatures are observed as a single peak. If phase segregation is the cause of these double luminescence peaks the diffusion of atoms would occur during growth and not caused by the high temperature anneal. Cathode luminescence (CL) was also performed at 4K on an annealed multiple GaInNAs quantum well sample with emission at 1.23 μm . A very spotty luminescence was observed with features on the order of microns, shown in figure 3. This behavior is more characteristic of InGaN and not typically observed in InGaAs. The optical CL spectrum was very similar to the one found in low temperature PL in figure 2.

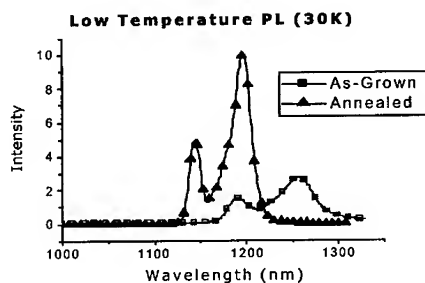


Figure 2. 30K PL of a 3-QW GaInNAs sample, before and after anneal.

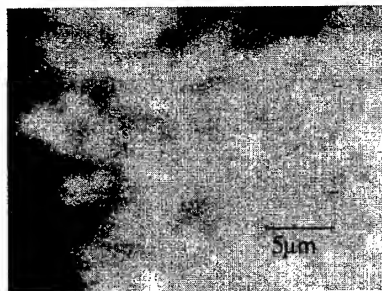


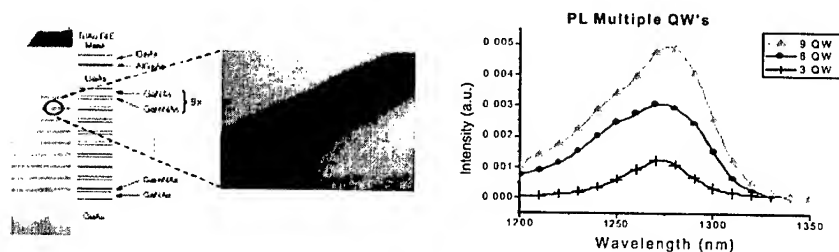
Figure 3. 4K CL surface scan of an annealed 3-QW GaInNAs sample with peak emission at 1.23μm.

The last type of atomic rearrangement that is likely to occur is the redistribution of atoms in the lattice, modifying nearest neighbor environments but without long-range phase separation. Two different driving forces and resulting atomic rearrangements have been theorized. One is the minimization of local strain, or the rearrangement of nitrogen toward indium atoms to relax stress in the lattice. The second is the diffusion of nitrogen toward gallium atoms that have lower energy bonds. Both driving forces may play a role in the reordering of atoms within the GaInNAs quaternary. By changing the overall bonding energy and strain in the system, bandgap shifts would be likely and this could explain the blue-shift of luminescence on anneal. This type of atomic rearrangement is current being investigated.

Strain Compensation

The concentration of nitrogen in GaInNAs is currently limited to under 4% with current growth techniques. Therefore, in order to extend this material to longer wavelengths, one must increase the amount of indium, compressively straining the material. While this is known to be beneficial for optical devices, the formation of dislocations will occur if the critical thickness is exceeded. This limits the number of quantum wells that can be grown and would reduce the

A nine quantum well device of highly strained 30% In, 3.3% N GaInNAs active material and GaNAs barriers has been grown dislocation free and is shown in figure 4. The resulting PL spectrum of 3, 6 and 9 quantum well structures is also shown. When we increased from 3 to 6 quantum wells, luminescence increased 2.4 times, and from 3 to 9 wells, PL increased 3.9 times. The total thickness of strained active material for the 9 quantum well sample was 63 nm, much greater than the critical thickness. A 30% InGaAs sample is known to have a critical thickness of under 10 nm. By growing tensile-strained GaNAs, a much larger active medium can be present greatly increasing optical gain in grown devices.



GaNAs/GaN Ridge Waveguide Laser Diodes

338

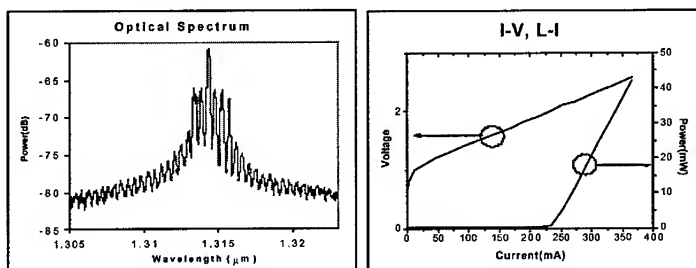


Figure 5. Optical spectrum (left) and I-V, L-I (right) of a GaInNAs/GaNAs 3-QW ridge-waveguide in-plane laser.

GaInNAsSb

As more nitrogen and indium is added into GaAs, it becomes increasingly difficult to maintain a solid solution alloy. Surface energy and high surface diffusivity plays an important role in the way atoms incorporate in the bulk. Once confined to the solid, bulk diffusivity is much lower than at the surface, thus a solid solution can be maintained during anneal. A surfactant has the ability to reduce surface energy and enhance soluble incorporation at the surface of a growing material. Antimony is a well-known surfactant aiding the incorporation of In within GaAs. A thermal cracking effusion cell provides a source of Sb during GaInNAs growth. A careful calibration of Sb growth rate and sticking coefficients in GaInNAs has not yet been completed, so for the following analysis only Sb flux has been reported.

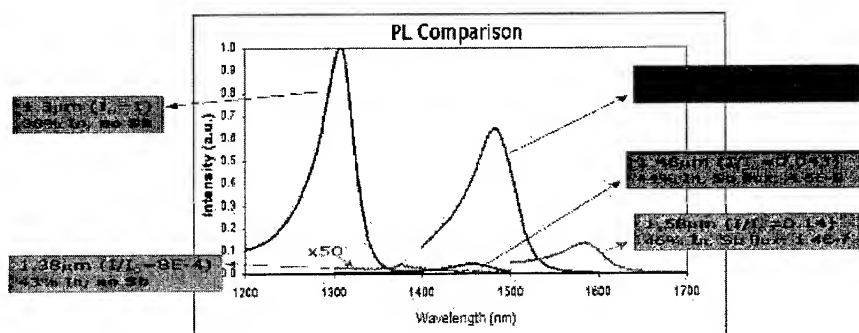


Figure 6. PL spectrum of GaInNAs and GaInNAsSb 3-QW samples, all with 2.5% N. From left to right: 1.3 μm , 38% In, Int.=1; 1.38 μm , 43% In, Int.=0.0008; 1.46 μm , 44% In, 4.6×10^{-8} torr Sb, Int.=0.043; 1.48 μm , 45% In, 7.2×10^{-8} torr Sb, Int.=0.65; 1.58 μm , 46% In, 1.4×10^{-7} torr Sb, Int.=0.14.

Figure 6 plots five different PL spectrum two without the use the Sb and three with Sb present for the entire GaInNAs/GaNAs active region growth. The leftmost, highest intensity spectrum is a 1.3 μm 38% In, 2.5% N, GaInNAs/GaNAs 3 quantum well structure with its

intensity normalized to unity. By increasing the In to 42%, 1.38 μm is measured, however the intensity is reduced over 1000 times. In the next three spectra, increased Sb was added to relatively the same GaInNAs composition. The structure of these PL samples was three GaInNAsSb quantum wells surrounded by GaNAsSb barriers. Wavelength operation was changed from 1.46 to 1.58 μm with the highest efficiency material showing a wavelength of 1.48 μm . This material had a PL intensity that was 65% of the highest intensity 1.3 μm material grown compared with 0.08% for shorter wavelength material grown without antimony. Antimony incorporation has been measured using X-ray photoelectron spectroscopy (XPS) and RBS in quantities as high as 7% in these materials, but careful calibration has not been performed. The exact mechanism for improving luminescence and red-shifting output is currently unknown. Antimony seems to be acting as both a surfactant and a significant alloy constituent improving optical emission and enabling wavelength operation as long as 1.6 μm . Table I indicates a difference in N composition with the presence of Sb. Both the increase of nitrogen content and the presence of antimony can be responsible for the longer wavelength PL shift.

Laser devices were also grown and fabricated with 44% In, 2.5% N GaInNAsSb quantum wells and GaNAsSb barriers. A flux of 6.89×10^{-8} torr of Sb was used during barrier and well growth. This flux has been measured to incorporate about 7% Sb into GaInNAs. The optical spectrum and L-I plot is shown in figure 7. A peak wavelength of 1.464 μm was taken at 1.2 times threshold. A threshold current density of 2.8 kA/cm^2 was measured for the devices with a width of 5 μm and length of a 1.3 mm. The measurements were taken with a pulsed current source at room temperature.

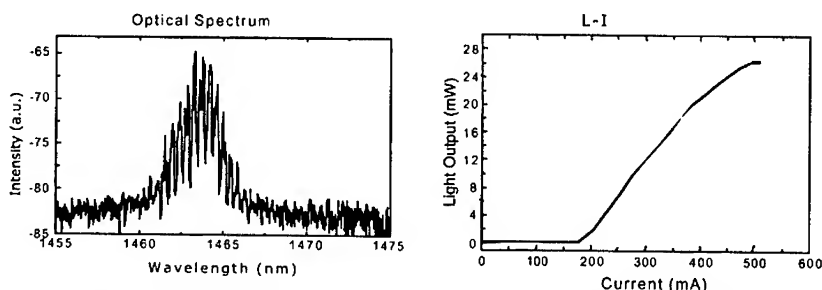


Figure 7. Optical Spectrum (left) and L-I (right) of a GaInNAsSb/GaNAsSb 3-QW ridge-waveguide device.

CONCLUSIONS

As-grown GaInNAs typically has poor optical properties due to defects incorporated during growth. Thermal anneal removes these defects but blue-shifts optical emission. This paper discusses likely defects responsible for this behavior. A new barrier structure made of tensile-strained GaNAs has been grown. These barriers increase wavelength and strain compensate compressive quantum wells. With these barriers, increased quantum well high-power lasers and modulators are now possible. A new material, GaInNAsSb, is also presented. Antimony acts as both a surfactant improving luminescence at long wavelengths and an alloy

constituent, further red shifting emission. High efficiency PL, as long as 1.6 μm , has been demonstrated. Finally, two laser structures GaInNAs/GaNAs and GaInNAsSb/GaNAsSb are shown. With low thresholds and high output powers, it further substantiates this material system's potential as a replacement for 1.3-1.55 μm opto-electronic devices.

ACKNOWLEDGMENTS

This research was supported by DARPA and ARO through contract DAAG55-98-1-0437 and by ONR through contract N00014-01-1-010. The authors would like to thank Luncun Wei of Charles Evans & Associates for the RBS data. They would also like to thank Dr. Matthias Wassermeier of the Paul-Drude-Institut fuer Festkoerperelektronik for the low-temperature PL data, Seth Bank for help with the PL data and Vincenzo Lordi for the TEM work.

REFERENCES

1. Phillips, A. F., Sweeney, S. J., Adams, A.R., and Thijs, P. J. A., IEEE J. Select. Topics Quantum Electron, **5**, 301, (1999).
2. C.W. Coldren, M.C. Larson, S.G. Spruytte, and J.S. Harris, Electron. Lett., (to be published).
3. Nakahara, K., Kondow, M., Kitatani, T., Larson, M.C., Uomi, K., IEEE Photonics Technol. Lett., **10**, 487 (1998).
4. C.W. Coldren, S.G. Spruytte, A.F. Marshall, J.S. Harris, M.C. Larson, J. Vac. Sci. Technol., (to be published).
5. S.G. Spruytte, et al., in: R. Feenstra, T. Myers, M.S. Shur, H.Amano (Eds.), Materials Research Society Symposium Proceedings, 95 (2000) W8.4.1.
6. P. Krispin, S.G. Spruytte, J. S. Harris, K. H. Ploog, J. Applied Physics, **90** (5), 2405 (2001).
7. P. Krispin, S.G. Spruytte, J. S. Harris, K. H. Ploog, Physica B, (to be published).

Excitonic Diamagnetic Shifts and Magnetic Field Dependent Linewidths in $\text{Al}_x\text{Ga}_{1-x}\text{As}$ Alloys

G. Coli¹, K. K. Bajaj¹, J. L. Reno², and E. D. Jones²

¹Physics Department, Emory University,
Atlanta, Georgia 30322

²Sandia National Laboratories,
Albuquerque, New Mexico 87185

ABSTRACT

We report measurements of both the diamagnetic shifts and the linewidths of excitonic transitions in $\text{Al}_x\text{Ga}_{1-x}\text{As}$ alloys as a function of Al concentration and magnetic field at 1.4 K using photoluminescence spectroscopy. The magnetic field was varied from 0 to 13 tesla and Al composition in our samples ranged from 0 to 30%. The samples were grown on GaAs substrates oriented along [001] direction using molecular beam epitaxy at 590°C. We find that for a given value of alloy composition, both the diamagnetic shift and excitonic linewidth increase as a function of magnetic field. To explain our experimental data we propose that the excitons are localized in a very specific manner. To simulate this localization, we assume that the exciton reduced mass is effectively increased and is obtained by using the alloy dependent heavy-hole mass along (001) direction treated isotropically. The calculated values of the variations of the diamagnetic shift and excitonic linewidth as a function of magnetic field obtained using this model agree very well with those reported here.

INTRODUCTION

One of the most commonly used optical characterization techniques to assess the quality of a semiconductor alloy is the low-temperature photoluminescence (PL) spectroscopy. At liquid helium temperatures, the linewidth of an excitonic transition defined as the full-width-at-half-maximum (σ) in semiconductor alloys as determined by PL spectroscopy is considerably larger than those observed in their components. This broadening has been attributed to the compositional disorder [1-8] which is inevitably present in these systems. In addition, the value of σ can be controlled by the application of an external magnetic field as was first pointed out independently by Raikh and Éfros [8], and Singh and Bajaj [2]. This is due to the fact that the application of a magnetic field shrinks the excitonic wave function and thus enhances the value of σ . This effect was first observed by Jones et al [9] in InGaP lattice matched to GaAs.

During the past twenty years several groups [10] have studied the variation of σ as a function of alloy composition in AlGaAs. In this paper we present an observation of the variations of the diamagnetic shift of the excitonic transition (δ) and σ as a function of magnetic field in AlGaAs at 1.4 K using PL spectroscopy. The Al composition x ranged from 0 to 0.30 and the magnetic field was varied from 0 to 13 tesla. We find that for a given value of alloy composition, both δ and σ increase as a function of magnetic field. The observed variations of δ and σ with magnetic field

are considerably smaller than those calculated by Lee and Bajaj[6] using a free exciton model. To explain our experimental data we propose that the excitons are localized in a very specific manner. In order to simulate this localization, we assume that the reduced mass of the exciton is effectively increased. In addition, we postulate that the conduction-band mass is unchanged, thereby requiring the use of a larger value for the valence-band mass. We find that the value of the heavy-hole mass along the [001] direction, when used to obtain the reduced mass, leads to the values of δ for all samples that agree very well with the calculated values. Furthermore, the observed variation of σ with magnetic field is in very good agreement with that calculated using this larger reduced mass.

EXPERIMENTAL

All of the AlGaAs samples reported here were grown on (001) oriented undoped GaAs substrates by molecular beam epitaxy at 590°C. A structure consisting of a smoothening 300-nm-thick epilayer of GaAs grown on top of the GaAs substrate followed by a double heterostructure of undoped $\text{Al}_{x+0.1}\text{Ga}_{1-x-0.1}\text{As}/\text{Al}_x\text{Ga}_{1-x}\text{As}$ with 50-nm-thick barriers and a 50-nm-thick $\text{Al}_x\text{Ga}_{1-x}\text{As}$ alloy was studied here. In this manner, the $\text{Al}_{x+0.1}\text{Ga}_{1-x-0.1}\text{As}$ barriers prevented carriers and excitons from diffusing to GaAs. A 10-nm-thick undoped cap-layer of GaAs was grown on top of the AlGaAs double heterostructure to prevent oxidation. The compositions were verified by comparing the lattice constants of the samples obtained from double x-ray scattering, with the well known composition dependence of the bandgap energy for these alloys [11]. The PL measurements were made at 1.4 K using the 514.5-nm line from an argon-ion laser. Laser power densities ranged from 0.1 $\mu\text{W}/\text{cm}^2$ to 100 mW/cm^2 . The PL lineshape and linewidth were found to be independent of excitation intensity for these low power densities.

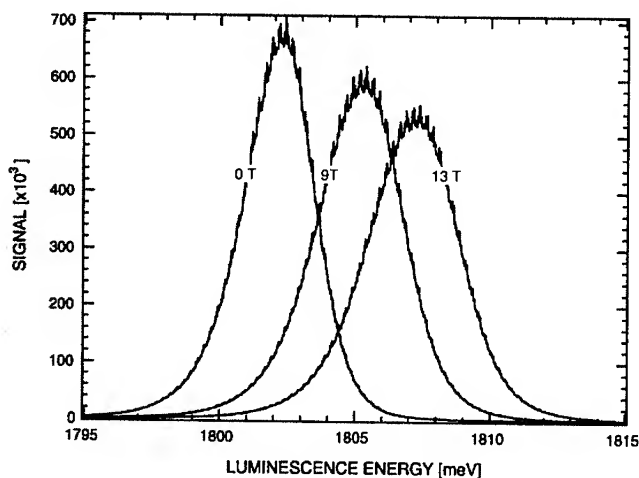


Figure 1. Photoluminescence spectrum of $\text{Al}_{0.20}\text{Ga}_{0.80}\text{As}$ at 1.4 K for different values of the magnetic field B . The leftmost spectrum is the zero-field case, the center spectrum is for $B = 9$ tesla, and the rightmost spectrum is for $B = 13$ tesla.

RESULTS AND DISCUSSION

In Fig. 1 we display typical PL spectra for $\text{Al}_{0.2}\text{Ga}_{0.8}\text{As}$ at 1.4 K for three different values of the magnetic field, namely 0, 9, and 13 tesla. The position of the zero-field excitonic transition is at 1802.3 meV. As clearly seen in Fig. 1, with increasing magnetic field, this transition broadens and shifts to higher energies. Data similar to those shown in Fig. 1 are obtained in all other samples reported here.

A number of groups have reported calculations of σ as a function of alloy composition in completely disordered semiconductor alloys both in the absence [1-6] and in the presence of magnetic field [7-8, 12]. A brief review of these calculations has been presented in Refs. 6 and 7. All these calculations are based on the premise that excitons created in different regions of the semiconductor alloy experience slightly different values of the local conduction and valence-band edges, assuming virtual crystal approximation. This leads to different values of the emission energies from the different regions of the alloy thus resulting in an inhomogeneously broadened transition.

We have calculated the variation of δ as a function of magnetic field using the formalism of Lee and Bajaj [6] using a variational wave function proposed by Fedders [13]. We have considered two cases. In the first we assume that the radiative transitions in $\text{Al}_x\text{Ga}_{1-x}\text{As}$ result from free excitons and in the second from localized excitons. To simulate the behavior of radiative transitions due to localized excitons we assume the exciton reduced mass is effectively enhanced. We further postulate that there is no change in the electron mass and only the hole mass is increased. It turns out, surprisingly, that the value of the heavy hole mass along the direction of the magnetic field, i.e., (001), when treated isotropically to obtain the exciton reduced mass yields values of the variation of δ and σ with magnetic field which agree very well with those determined experimentally as is discussed in the following.

In Figs. (2a-c) and (3a-c) we show the comparisons between the results of our measurements (squares) and those of our calculations (lines) for diamagnetic shift δ and σ , respectively, as a function of magnetic field in $\text{Al}_x\text{Ga}_{1-x}\text{As}$ alloys for $x = 0.11$, $x = 0.20$ and $x = 0.30$. Similar behavior is observed in all other samples. The values of the various physical parameters for the AlGaAs alloy system used in our calculations are obtained by linear interpolations between those of GaAs and AlAs [6]. In Figs (2a-c) we find that the variations of δ as a function of the magnetic field, reported here, agree very well with those calculated using the above mentioned localized exciton model. The calculated values using the free exciton model are considerably larger.

It is clear from Figs. (3a-c) that the observed values of σ are always larger than the calculated ones. This is due to the fact that in our calculations we consider only the broadening effect due to alloy disorder.

We have also measured the diamagnetic shift in different crystallographic directions and found no change in its value, thus suggesting that the localized excitons have spherical symmetry. The nature of the localization phenomenon is not understood at this time. Currently, experimental work is in progress to gain further insight into this phenomenon.

CONCLUSION

In summary, we have measured both the diamagnetic shifts and the linewidths of excitonic transitions in a series of $\text{Al}_x\text{Ga}_{1-x}\text{As}$ alloys as a function of Al concentration and magnetic field at 1.4 K using photoluminescence spectroscopy. The magnetic field was varied from 0 to 13 tesla

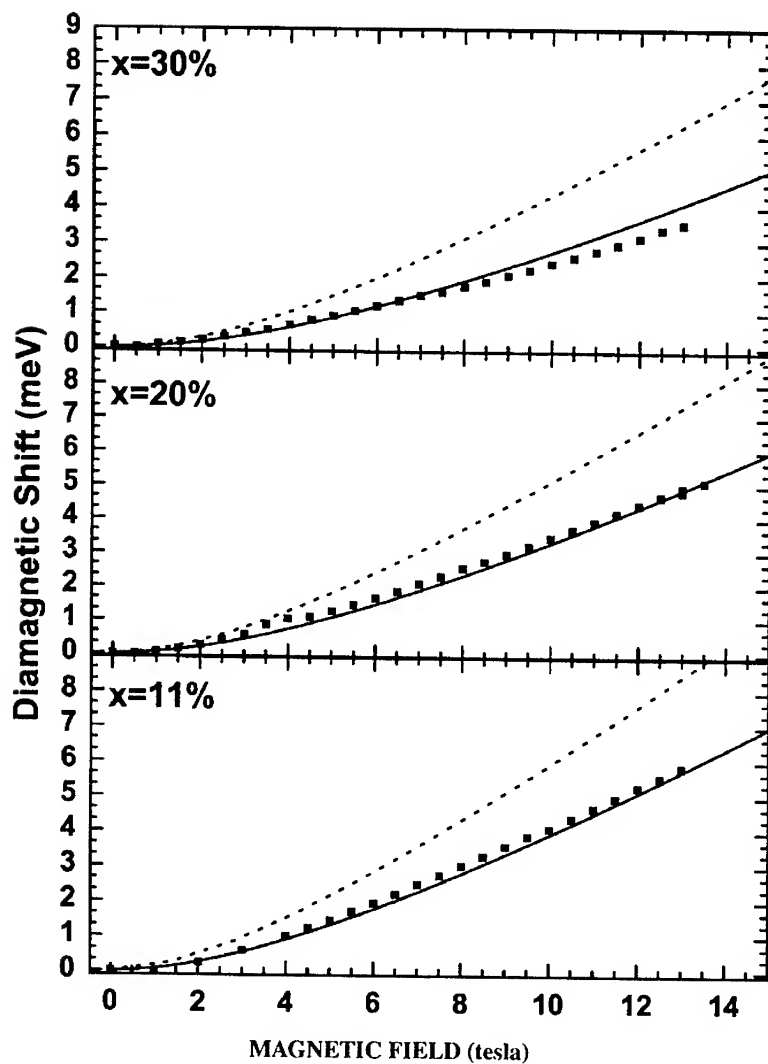


Figure 2. Variation of the diamagnetic shift of the excitonic transitions in $\text{Al}_x\text{Ga}_{1-x}\text{As}$ as a function of magnetic field for three different Al concentrations: (a) $x = 11\%$, (b) $x = 20\%$, and (c) $x = 30\%$. Dashed curves: calculated using the free exciton model; solid curves: calculated using the excitonic reduced mass obtained using heavy-hole mass along (001) direction. Symbols represent experimental data.

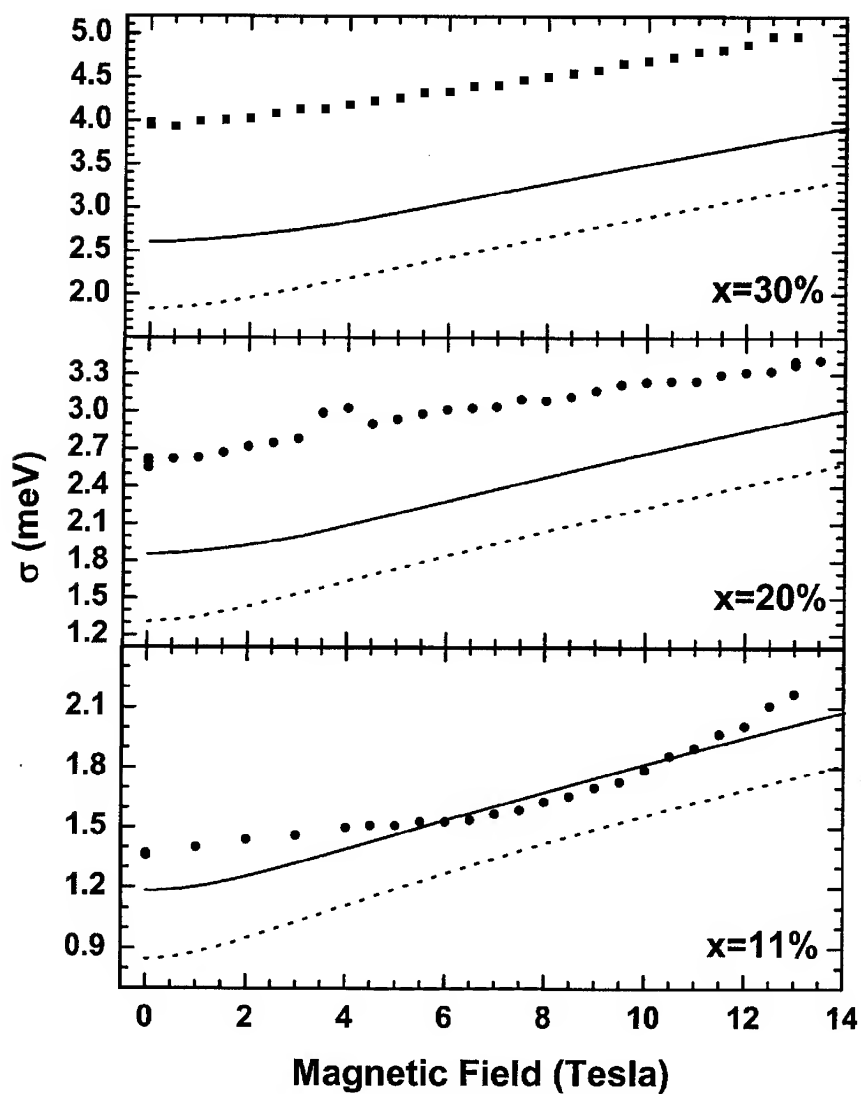


Figure 3. Variation of the excitonic linewidth (σ) in $\text{Al}_x\text{Ga}_{1-x}\text{As}$ as a function of magnetic field for three different Al concentrations: (a) $x = 11\%$, (b) $x = 20\%$, and (c) $x = 30\%$. Dashed curves: calculated using the free exciton model; solid curves: calculated using the excitonic reduced mass obtained using heavy-hole mass along (001) direction. Symbols represent experimental data.

and Al composition ranged from 0 to 30%. We find that for a given value of alloy composition, both the diamagnetic shift and excitonic linewidth increase as a function of magnetic field. To explain our experimental data we propose that the excitons are localized in a very specific manner. To simulate this localization, we assume that the exciton reduced mass is increased and is obtained by using the heavy-hole mass along (001) direction. The calculated values of the variations of the diamagnetic shift and excitonic linewidth as a function of magnetic field obtained using this model agree very well with those reported here. References

ACKNOWLEDGEMENTS

Supported by the US DOE under Contract No. DE-AC04-94AL85000

REFERENCES

1. O. Goede, L. John, and D. H. Hennig, *Phys. Status Solidi B* **89**, K183 (1978).
2. J. Singh and K. K. Bajaj, *Appl. Phys. Lett.* **44**, 1075 (1984).
3. E. F. Schubert, E. O. Gobel, Y. Horikoshi, K. Ploog, and H. J. Queisser, *Phys. Rev* **B30**, 813 (1984).
4. J. Singh and K. K. Bajaj, *Appl. Phys. Lett.* **48**, 1077 (1986).
5. J. Zimmerman, *J. Crystal Growth* **101**, 346 (1990).
6. S. M. Lee and K. K. Bajaj, *J. Appl. Phys.* **73**, 1788 (1993).
7. S. K. Lyo, *Phys Rev.* **B48**, 2152 (1993).
8. M. E. Raikh and A. L. Éfros, *Fiz. Tverd. Tela (Leningrad)* **26**, 106 (1984) [*Sov. Phys. Solid State* **26**, 61 (1984)].
9. E. D. Jones, R. P. Schneider, S. M. Lee, and K. K. Bajaj, *Phys. Rev* **B46**, 7225 (1992).
10. See for example K. S. Zhuralev, A. I. Toropov, T. S. Shamirzayev and A. K. Bakarov, *Appl. Phys. Lett.* **76**, 1131 (2000) and references cited therein.
11. See for example by L. Pavesi, "Photoluminescence Spectra of AlGaAs," *Properties of Aluminum Gallium Arsenide* edited by S. Adachi (INSPEC, the Institution of Electrical Engineers, London 1993) pp. 245-268.
12. R. A. Mena, G. D Sanders, K. K. Bajaj, and S. C. Dudley, *J. Appl. Phys.* **70**, 1866 (1991).
13. F. A. Fedders, *Phys Rev.* **B25**, 3846 (1982).

Novel AlGaAs/CaF₂ SESAM Device for Ultrashort Pulse Generation

Silke Schön, Lukas Gallmann, Markus Haiml and Ursula Keller
Swiss Federal Institute of Technology (ETH),
Physics Department / Institute of Quantum Electronics
ETH Zurich Hoenggerberg - HPT, CH-8093 Zurich, Switzerland

ABSTRACT

A novel ultrabroadband AlGaAs/CaF₂ semiconductor saturable absorber mirror (SESAM) covering nearly the entire Ti:sapphire gain spectrum is demonstrated. This device supports sub-10-fs pulse operation of a laser. In contrast to previous SESAMs of comparable bandwidth, our device can be monolithically grown by molecular beam epitaxy and requires no post-growth processing. GaAs is used as semiconductor saturable absorber material. The high defect concentration of the material is due to the lattice-mismatched growth on a fluoride surface with (111) orientation. With a time response of 1.2 ps for carrier trapping, a saturation fluence of 36 $\mu\text{J}/\text{cm}^2$ and a modulation depth of up to 2.2%, the GaAs saturable absorber is well-suited for all-optical switching in SESAM devices used for ultrashort pulse generation.

INTRODUCTION

Devices based on semiconductor materials have been found many applications in ultrafast all-optical switching, in femto- and picosecond laser pulse generation, and in optoelectronics [1]. For example, semiconductor saturable absorber layers were introduced in optical devices to explore their nonlinear optical property of an intensity depending absorption for all-optical switching [2]. A semiconductor saturable absorber mirror (SESAM) basically consists of a high reflection mirror with a reflectivity of at least 95%, and a saturable absorber material. SESAMs rely on the operation of the absorber layer as an all-optical switch that is based on changes of reflectivity due to absorption bleaching induced by a strong laser pulse allowing for the self-starting of a laser.

Conventional SESAMs have been successfully fabricated by molecular beam epitaxy (MBE) using AlGaAs/AlAs multilayer stacks and GaAs saturable absorber. Laser pulses as short as 34 fs were generated with Ti:sapphire lasers using an AlGaAs/AlAs Bragg mirror with an imbedded single GaAs quantum-well layer [3]. However, these conventional SESAMs suffer from a narrow bandwidth caused by a small difference in the refractive indices of AlAs and GaAs. Shorter pulses were obtained by replacing the AlGaAs/AlAs Bragg mirror by a silver mirror in order to increase the high reflection bandwidth. This kind of a low-finesse AFPSA device, where the top reflector is formed by the interface semiconductor/air, supported sub-6-fs pulses [4]. These pulses are some of the shortest ever generated. However, the semiconductor saturable absorber cannot be directly grown on top of a silver mirror by epitaxy. Post-growth processing has to be applied, which complicates the fabrication process and may cause additional nonsaturable losses. Moreover, the silver bottom mirror only provides a reflectivity of less than 97%. Therefore, methods are continuously in development to avoid post-growth processing and to enable the monolithic growth of ultrabroadband SESAM devices.

With the demand for a larger wavelength tuning range of monolithically grown devices, semiconductor materials have to be combined with other materials like fluorides or oxides to

increase the refractive index difference of the Bragg mirror pair [5]. In this paper, we demonstrate a monolithic ultrabroadband SESAM consisting of a two pair AlGaAs/CaF₂ Bragg mirror and a GaAs saturable absorber layer covering nearly the entire gain spectrum of a Ti:sapphire laser. The SESAM successfully started and supported mode-locking in a Ti:sapphire laser. This device was used for to generate laser pulses in the sub-10 fs range.

EXPERIMENTAL DETAILS

AlGaAs/CaF₂ SESAMs were grown by solid source molecular beam epitaxy (MBE) on GaAs (111)B oriented substrates. CaF₂ growth was carried out at a substrate temperature of 600°C and a growth rate of 0.2 μm/h. AlGaAs layers with 77% aluminum concentration were grown with 0.7 μm/h at 600°C. Growth was interrupted to anneal the surface under As₂ flux several times. The CaF₂ surface was exposed to a high energy electron beam of 20 keV at grazing incidence before the GaAs absorber overgrowth. A Varian Cary 5E spectrophotometer was used to measure the spectral reflectivity. The absorber layer was studied by saturation fluence and pump-probe measurements. All measurements were carried out at room temperature using an 80 MHz, 150 fs pulse train from a Ti:sapphire laser centered at 830 nm. A SESAM assisted Kerr-lens mode-locked Ti:sapphire laser described in Ref. [4] was operated by an AlGaAs/CaF₂ SESAM with GaAs saturable absorber layer.

DISCUSSION

The growth of AlGaAs and fluorides in multilayer stacks is governed by the lattice mismatch, by their thermal expansion properties and by the difference in their surface chemistry. The lattice mismatch is about 3.5% at room temperature but decreases to about 2.5% at growth temperature. In addition, the linear thermal expansion coefficient is three times higher for CaF₂ ($19.2 \times 10^{-6} \text{K}^{-1}$) than for GaAs ($6.4 \times 10^{-6} \text{K}^{-1}$). Therefore, large thermal strain is introduced to the layers during cooling down or temperature cycling. Severe crack formation to relax the thermal strain in (100)-oriented multilayer stacks is a consequence, which degrades the performance of an optical device. An alternative was a change in the growth orientation from (100) to (111) [6]. The (111) orientation is the preferred growth orientation of the fluorides. In addition, the mechanism of dislocation gliding allows for the relaxation of the strained layer [7]. The drawback in changing the growth direction is that GaAs has only a small growth window for the (111)-oriented growth. Furthermore, the layer quality is very sensitive to As/Ga ratio, which is much lower than that used for standard (100) GaAs growth. GaAs nucleates on CaF₂ by the formation of islands due to the low surface free energy of CaF₂ [8]. However, defects introduced to the absorber material by the growth mode offer a high density of defect states for carrier trapping. Therefore, GaAs grown on fluoride can be applied as saturable absorber material in optical devices for ultrashort pulse generation.

For the fabrication of an ultrabroadband SESAM, the AlGaAs/CaF₂ Bragg mirror and the GaAs saturable absorber needed to be combined in one device. Therefore, a two pair Bragg mirror consisting of 140 nm CaF₂ and 70 nm Al_{0.77}Ga_{0.23}As with a 170 nm CaF₂ spacer layer and a 40 nm GaAs saturable absorber layer on top was grown. This SESAM has a bandwidth of more than 300 nm for the nonsaturated reflectivity as shown in figure 1. The measured high reflection bandwidth is about five times larger than that of conventional AlGaAs/AlAs SESAMs. Furthermore, the number of mirror pairs is greatly decreased from more than 25 for

AlGaAs/AlAs to only two AlGaAs/CaF₂ pairs. The AlGaAs/CaF₂ SESAM provides a linear reflectivity of 97% due to the large difference in the refractive indices of the materials forming the mirror. The GaAs saturable absorber layer showed a higher absorption for the nonsaturated reflectivity than calculated, which indicates that the high defect concentration in the GaAs increased the absorption coefficient of the material.

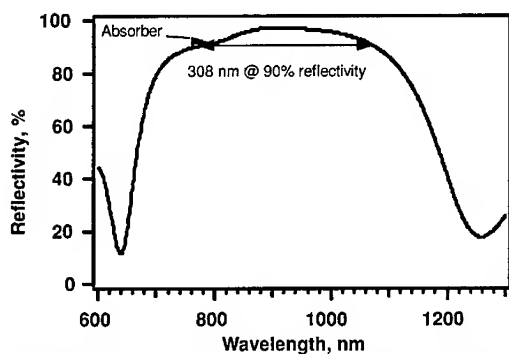


Figure 1. Reflectivity spectrum of a AlGaAs/CaF₂ SESAM with GaAs saturable absorber layer.

The saturable absorber is described in terms of the modulation depth ΔR , the nonsaturable losses ΔR_{ns} , the saturation fluence F_{sat} , and the impulse response or recovery time τ_A [9]. The modulation depth is the maximum amount of saturable losses, which can be bleached. Nonsaturable losses ΔR_{ns} are residual losses, which cannot be bleached. They are caused by scattering on interfaces or surfaces, additional absorption from defect states or reflectivity losses from the bottom mirror. The saturation fluence describes the light intensity, which is necessary to bleach the saturable losses. The recovery time is a measure for the carrier relaxation processes. The approximately biexponential recovery time has two components attributed to carrier thermalization and trapping/recombination. Epitaxially grown saturable absorber materials have typically slow recovery times on the order of nanoseconds due to the low defect concentrations in the layers. Therefore, defects have to be introduced to the material to provide additional defect states for faster carrier trapping. Methods to obtain fast saturable absorber materials are low-temperature (LT) growth by molecular beam epitaxy and ion implantation [10]. However, GaAs epitaxially grown on CaF₂ already provides high defect concentration at typical growth temperatures due to lattice-mismatched growth. Pump-probe experiments were carried out to study the impulse response. A biexponential recovery time of about 150 fs (thermalization) and 1.2 ps (carrier trapping/recombination) was measured as demonstrated in figure 2. This fast time response of the GaAs saturable absorber is excellent for the application as an all-optical switch in ultrashort pulse generation.

In general, a high defect concentration does not only contribute to the fast carrier trapping but can also cause additional absorption. Measurements of the saturation fluence and modulation depth reveal additional nonsaturable losses. A saturation fluence F_{sat} of 36 $\mu\text{J}/\text{cm}^2$ was measured for the AlGaAs/CaF₂ SESAM device, which can be compared with that of standard AlGaAs/AlAs SESAMs. A modulation depth of 2.2% and nonsaturable losses of 2.7% are

obtained. These losses can be mostly attributed to the designed bottom mirror since it consists of only two pairs.

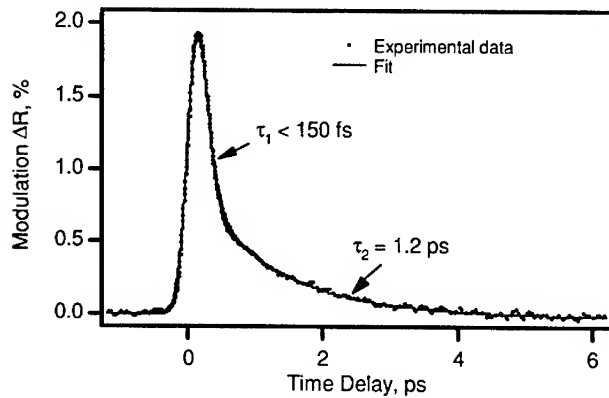


Figure 2. Nonlinear optical response and absorption modulation of the AlGaAs/CaF₂ SESAM measured in a pump-probe experiment (solid line – fit).

For short pulse generation, the SESAM was inserted in the cavity of a Ti:sapphire laser. The AlGaAs/CaF₂ SESAM successfully started and supported mode-locking in the laser. A pulse spectrum shown in figure 3 with a transform limit of 8.2 fs and pulses with a duration of 9.5 fs were measured. For the first time, the generation of ultrashort pulses below 10 fs with a AlGaAs/CaF₂ SESAM is proved. Due to the large high reflection bandwidth of more than 300 nm and the fast response time of the GaAs absorber, a broad pulse spectrum supporting sub-6-fs was measured with a different setup. That result shows the potential of AlGaAs/CaF₂ SESAM device for sub-6-fs pulse generation.

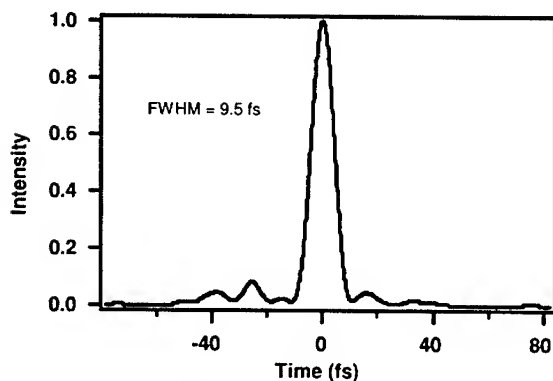


Figure 3. Sub-10-fs pulse generated by Ti:sapphire laser using an AlGaAs/CaF₂ SESAM.

CONCLUSIONS

We have shown that an ultrabroadband AlGaAs/CaF₂ SESAM device can be monolithically grown by molecular beam epitaxy. The large difference in the refractive indices of the AlGaAs and CaF₂ provide large high reflection bandwidth and makes this material combination very interesting for ultrashort pulse generation or broadband tunability. The generation of sub-10-fs pulses was possible with only six layers grown in one stack: two mirrors pairs, a spacer layer and a saturable absorber layer. The large reflection bandwidth of the AlGaAs/CaF₂ Bragg mirror, the fast recovery times and low nonsaturable losses of the GaAs saturable absorber grown on CaF₂ allow for pulse spectra supporting sub-6-fs pulses.

REFERENCES

1. U. Keller, D. A. B. Miller, G. D. Boyd, T. H. Chiu, J. F. Ferguson, and M. T. Asom, *Opt. Lett.* **17**, 505 (1992).
2. U. Keller, K. J. Weingarten, F. X. Kärtner, D. Kopf, B. Braun, I. D. Jung, R. Fluck, C. Hönniger, N. Matuschek, and J. Aus der Au, *IEEE J. Sel. Top. Quantum Electron.* **2**, 435 (1996).
3. L. R. Brovelli, I. D. Jung, D. Kopf, M. Kamp, M. Moser, F. X. Kärtner, and U. Keller, *Electron. Lett.* **31**, 287 (1995).
4. D. H. Sutter, G. Steinmeyer, L. Gallmann, N. Matuschek, F. Morier-Genoud, U. Keller, V. Scheuer, G. Angelow, and T. Tschudi, *Opt. Lett.* **24**, 631 (1999).
5. S. Schön, M. Haiml, and U. Keller, *Appl. Phys. Lett.* **77**, 782 (2000).
6. S. Schön, H. Zogg, and U. Keller, *J. Cryst. Growth* **201/202**, 1020 (1999).
7. C. C. Desai, *Surf. Technol.* **14**, 353 (1981).
8. S. Schön, M. Haiml, M. Achermann, and U. Keller, *J. Vac. Sci. Technol. B* **18**, 1701 (2000).
9. U. Keller: in *Nonlinear Optics in Semiconductors* E. Garmire, and A. Kost, Eds. (Academic Press, Inc., Boston, 1999), **59**, 211.
10. M. Haiml, U. Siegner, F. Morier-Genoud, U. Keller, M. Luysberg, R. C. Lutz, P. Specht, and E. R. Weber, *Appl. Phys. Lett.* **74**, 3134 (1999).

OPTICAL CHARACTERIZATION OF IV-VI MID-INFRARED VCSEL

F. Zhao, H. Wu, T. Zheng, P. J. McCann, A. Majumdar, Lalith Jayasinghe and Z. Shi
School of Electrical and computer Engineering
202 West Boyd, University of Oklahoma, Norman, OK 73019

ABSTRACT

PbSe/PbSrSe multiple-quantum-well (MQW) structures and PbSrSe thin films were grown on BaF₂ (111) substrates by molecular beam epitaxy (MBE) and characterized by Fourier transform infrared (FTIR) spectrometer. Strong photoluminescence without Fabry-Perot interference fringes was observed even at room temperature from the MQW structures. The peak energies for the MQW structures with different well widths shifted to high energy with increasing temperature. The absorption edge of PbSrSe layer was determined by transmission spectra. Meanwhile, we designed and fabricated $\lambda=4.1\ \mu\text{m}$ MQW vertical cavity surface emitting laser (VCSEL). A power output of 40 mW was obtained at room temperature. The room temperature threshold pump density is 200 kW/cm².

INTRODUCTION

Mid-infrared diode lasers are mainly used for trace-gas-sensing applications [1]. This is due to the fact that the numerous absorption lines of many gaseous molecules, such as CO₂, CH₄, N₂O, HCl, etc., are in the range of mid-infrared spectra. Performance requirements that are not yet available include continuous wave (cw) operation at thermoelectric cooler range ($T \geq 240\ \text{K}$), spectral purity, and reasonable output powers ($\geq 1\ \text{mW}$) with good beam quality. Although substantial advances have been made in the development of edge emitting mid-infrared diode lasers, including IV-VI lead-salt [2], quantum cascade (QC) [3,4] and type-II quantum well (QW) devices [5], there has little progress until recently in developing mid-IR vertical cavity surface emitting laser (VCSEL). This is despite the attractive performances of VCSELs, such as low-divergence circular beams, single mode operation, and the high possibility of two-dimensional monolithic integration arrays.

It is well known that the presence of the Auger recombination in narrow gap semiconductors is the major factor limiting high temperature operation of mid-infrared lasers. The major advantage of lead salt materials is that the Auger coefficients are more than one or two orders of magnitude lower than other mid-IR materials with a comparable bandgap [6,7], and it will not prevent quantum structure of these materials from achieving room temperature laser operation [6]. We proposed and demonstrated the first IV-VI VCSEL on BaF₂ (111) substrate [8]. Such VCSELs have obtained near-room-temperature pulsed operation 300mW output power [9,10] and threshold density as low as 10.5 kW/cm² [11]. In this paper, we report optical characterization of IV-VI PbSe/PbSrSe MQW structures and PbSrSe layer for VCSEL. The optical properties of the VCSEL are also given.

EXPERIMENTAL DETAIL

The PbSe/PbSrSe MQW structures and PbSrSe thin films were grown on BaF₂ (111) substrates by molecular-beam epitaxy (MBE) in an Intevac Modular Gen II system using compound sources for PbSe and BaF₂, and elemental sources for Sr and Se. The three MQW structures grown are with well layer thickness of 10, 16, 20 nm and with barrier layer thickness of 30, 40, 37 nm, respectively. A Sr-to-PbSe flux ratio of 3% was used to grow the PbSrSe barriers in PbSe/PbSrSe MQW structures. The Pb_{1-x}Sr_xSe thin film was grown with Sr-to-PbSe flux ratio from 3% up to 100%. Based on the results obtained from the samples mentioned above, we designed and grew a VCSEL structure in this MBE system. The typical structure is plotted in Fig. 1. The VCSEL structure mainly consists of a bottom mirror, a PbSe/PbSrSe MQW active layer and a top mirror. The bottom and top mirrors were fabricated with 3-pair quarter-wave stack of Pb_{0.97}Sr_{0.03}Se (188 nm)/BaF₂ (591 nm) and Pb_{0.75}Sr_{0.35}Se (282 nm)/BaF₂ (599 nm), respectively. The active layer consists of a $\lambda/2$ -cavity of 9-period PbSe (20 nm)/Pb_{0.97}Sr_{0.03}Se (20 nm) multiple QW structure. Details of the growth techniques for PbSe/PbSrSe MQW VCSEL have been published elsewhere [12]. Large difference of reflective indices between the Pb_{0.97}Sr_{0.03}Se ($n \sim 4.7$) and BaF₂ ($n=1.46$) yields more than 99% high reflectivity with only a three-pair stack for the bottom mirror. The higher strontium content of 35% is used to fabricate the top mirror for the first time so that the absorption edge of Pb_{0.75}Sr_{0.35}Se is beyond 1.064 μ m pump source. The absorption edge was determined by the transmission measurement.

The samples were characterized by the photoluminescence (PL), transmission and reflection measurements with the aid of the BRUKER IFS 66/S Fourier transform infrared (FTIR) spectrometer. Without further processing, the samples were mounted on a copper holder within a cryostat and illuminated with a 1.064 μ m Nd:YAG laser ($\tau_{\text{pulse}} \approx 50$ ns, 10 Hz) at an incident angle of 75° for PL and laser emission measurement. The standard synchronal output signal was used as trigger source during measurement. The spot size focused on the sample surface was 4 mm \times 6 mm for PL measurement. The signals coming from the samples was collected by two planar mirrors and two concave mirrors, passed through 2.47 μ m long-pass filter to cut off the signal of the pump beam and measured by the IFS 66/S spectrometer. A polarizer controlled the pump intensity by changing the angle of the polarizer, and an LN₂-cooled InSb detector with a 6 μ m cutoff wavelength detected the emission radiation. The pump power density for the PL measurement is kept about 200 kW/cm². The temperature range of the measurements is 80-300 K.

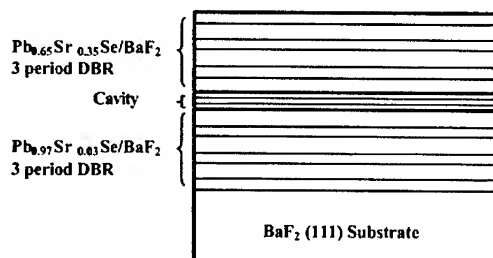


Figure 1. VCSEL structure schematic.

RESULTS AND DISCUSSION

Fig. 2 displays the temperature dependence of PL peak energies for the three MQW samples with different well layer thicknesses. Also shown is the PL energy change for the PbSe thin film grown on the (111) BaF₂ substrate. The PL peak energies increase monotonously with temperature from 80 to 300 K and decrease with the increase of the well layer thicknesses at the same temperature, which is attributed to recombination of quantum confined electron-hole pairs. The temperature coefficient is 0.43, 0.42 and 0.43 meV/K for 10, 16 and 20 nm well width, respectively. The peak energy change of bulk PbSe with temperature can be expressed theoretically as [13,14],

$$E_{g, \text{PbSe}}(\text{meV}) = 125 + (400 + 0.256T^2)^{1/2} \quad (1)$$

Where $E_{g, \text{PbSe}}$ is bandgap energy, and T is temperature. As shown in Fig. 2, the theoretical value (shown as solid square in Fig. 2) is in good agreement with the experiment data (0.498 meV/K). To optimize the VCSEL performance at a certain temperature, one needs to align the gain peak to the cavity resonance. The results above-mentioned are favorable to design and fabricate high performance VCSEL.

The measured PL spectra at 160 K and room temperature from the three MQW structures with different well layer thickness are shown in Fig. 3 (a) and (b), respectively. The spectra were collected with a resolution of 8 cm⁻¹ (1 meV) and a coaddition of 128 times. To be able to compare the PL intensities of single QW between the three samples, we divided the measured PL intensities by the corresponding QW period number in the sample. As the well layer thickness decreases, the peak energies shift towards higher energies (blueshift). At low temperature, the full width at half maximum (FWHM) decreases from 8.2 to 7.2 meV as the well layer thickness is decreased from 20 to 10 nm. However, such change of FWHM is not observed at room temperature spectra. The PL intensity is increased with decreasing well layer thicknesses and up to maximum for 10 nm well width.

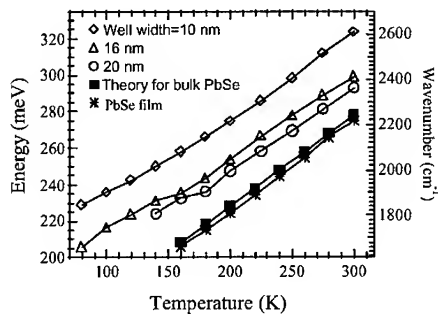


Figure 2. The PL peak energies as a function of temperature. The well width is 10 nm (diamond), 16 nm (triangle) and 20 nm (circle), respectively. The solid square and star show the calculation values from equation (1) and measured values from bulk PbSe, respectively.

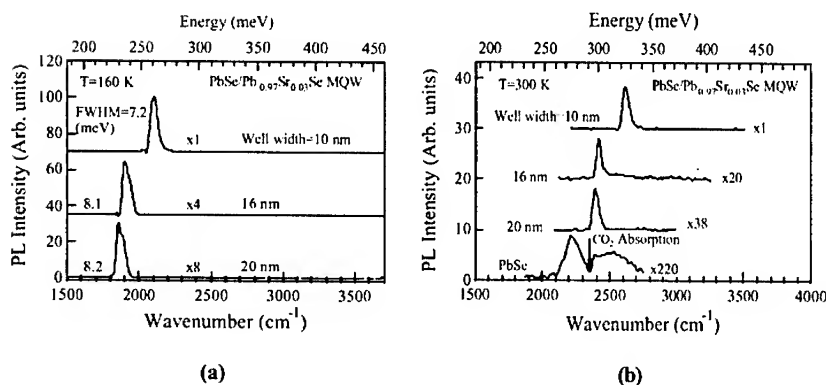


Figure 3. PL spectra for different well widths at (a) 160 K and (b) room temperature.

In comparison, the PL spectrum for PbSe thin film with thickness of 2 μm is also shown in Fig. 3 (b). The broad FWHM can be clearly observed. Note that the spectrum for bulk PbSe around 2400 cm^{-1} is distorted due to the absorption by atmospheric CO_2 in the open emission part. No interference fringes were observed for these QW samples. Normally, due to the large difference of refractive indices between the IV-VI QW layer ($n \sim 4.7$) and the BaF_2 substrate ($n=1.46$), photoluminescence (PL) signals were often merged with the interference fringes of the layer [15], which makes it very difficult to determine the net gain peak. With the aid of short pulse Nd-YAG laser at 1.06 μm being used as a pump source, the net gain peak is successfully confirmed. The strong PL signals obtained clearly showed amplified spontaneous emission (ASE) that significantly suppressed the interference fringes. The ASE at room temperature suggests that the Auger recombination does not limit IV-VI lasers operating above room temperature.

Increasing Sr content during $\text{Pb}_{1-x}\text{Sr}_x\text{Se}$ growth results in the increase of the band gap. The band gap can be obtained from the measured transmission spectra for various Sr content, shown in Fig. 4. For different pump lasers, the suitable Sr content during growth of top mirror needs

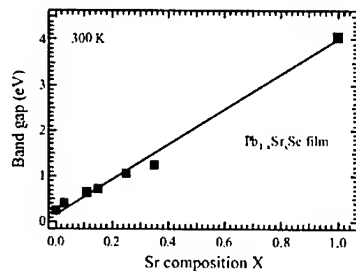


Figure 4. Band gap dependence of Sr composition.

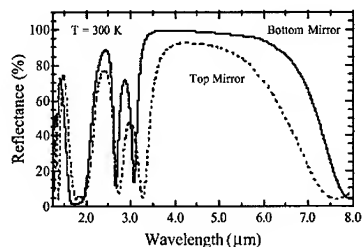


Figure 5. Room temperature reflection spectra for top mirror and bottom mirror, respectively.

to be considered so that it is transparent to pump laser. For example, if the 2.1 μm (band gap ~ 0.59 eV) pump laser is used as a pump source, more than 10% Sr content (Sr-to-PbSr flux ratio) for top mirror is required. For 1.064 μm (band gap ~ 1.165 eV) Nd:YAG pump laser, the Sr content in the top mirror has to be beyond 30% so as to be with high pump efficiency.

Based on the results above-mentioned, we designed and fabricated a VCSEL device. Fig. 5 shows the reflection spectra of the top mirror and bottom mirror for the VCSEL at room temperature. The 35% Sr content was chosen to grow the top mirror so that the top mirror is basically transparent to the 1.064 pump source, as shown in Fig. 6. However, the high Sr content results in inferior top mirror, and low reflectivity of 92%. The 9 period $\text{PbSe/Pb}_{0.97}\text{Sr}_{0.03}\text{Se}$ (20 nm/20 nm) is used as active layer. The resonance peak measured at room temperature from the reflectance of the VCSEL is well matched with the MQW gain peak of the active layer, as indicated in Fig. 6. As a result, a room temperature laser emission for the $\text{PbSe/Pb}_{0.97}\text{Sr}_{0.03}\text{Se}$ VCSEL is obtained for the first time. Fig. 7 shows light-light emission curves measured at temperatures from 290 to 310 K. As shown in Fig. 7, above-room-temperature laser emissions were clearly observed. The maximum output power of 40 mW was obtained at room

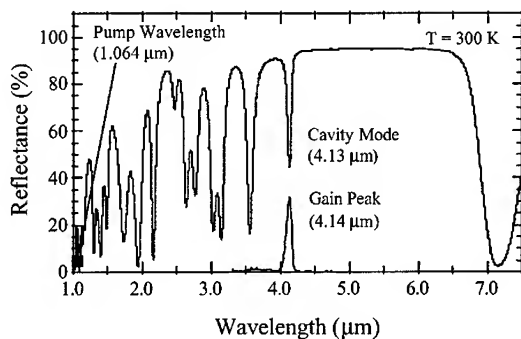


Figure 6. Room temperature reflection spectrum for the VCSEL shown in Fig. 1. Also shown is the gain peak on the bottom from PL measurement.

temperature. The room temperature threshold pump intensity is 200 kW/cm^2 . The detailed results about the VCSEL will be published elsewhere [16].

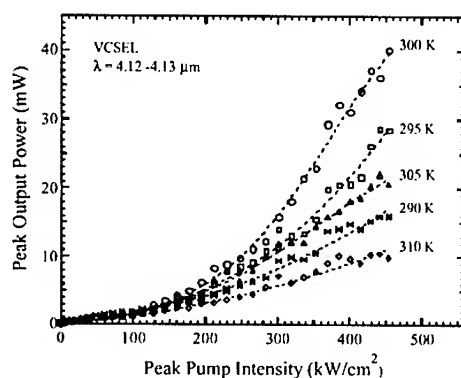


Figure 7. Peak VCSEL output power vs peak pump intensity at five temperatures, for a $1.5 \text{ mm} \times 1.5 \text{ mm}$ pump spot.

SUMMARY

The photoluminescence of PbSe/PbSrSe MQW structures grown on (111) BaF₂ substrates by MBE was measured with the IFS 66/S FTIR spectrometer. A short pulse Nd:YAG laser with the wavelength of $1.064 \text{ } \mu\text{m}$ was used as pump source. The strong ASE suppressed the Fabry-Perot interference fringes so that the net gain peak was easily obtained. Through the absorption edge measurements of PbSrSe thin films determined from the transmission spectra, a high Sr content of 35% was chosen to grow the top mirror for the VCSEL fabrication. The gain peak of the VCSEL designed and fabricated was well matched with the resonance cavity mode at room temperature. As a result, we have realized the room temperature laser emission of the IV-VI PbSe/PbSrSe MQW VCSEL for the first time. The maximum peak power output is 40 mW, which does not show saturation. The room temperature threshold pump intensity is 200 kW/cm^2 . The improvements in the crystal quality of the top mirror are required. A cw laser emission will be predicted as some suitable post-processes are applied for the VCSEL fabrication.

ACKNOWLEDGEMENTS

This work was supported by DoD AFOSR, ONR, and NSF under award numbers F49620-00-1-0291, DEPSCoR N00014-00-1-0506, and ECS-0080783, respectively.

REFERENCES

1. M. Tacke, *Infrared Phys. Technol.* **36**, 447 (1995).
2. G. Bauer, M. Kriebbaum, Z. Shi, and M. Tacke, *J. Nonlinear Opt. Phys. Mater.* **4**, 283 (1995).
3. S. Slivken, A. Matlis, A. Rybaltowski, Z. Xu, and M. Razeghi, *Appl. Phys. Lett.* **74**, 2758 (1999).
4. A. Tahraoui et al., *Appl. Phys. Lett.* **78**, 416 (2001).
5. W. W. Bewey, C. L. Felix, I. Vurgaftman, D. W. Stokes, E. H. Aifer, L. J. Olafsen, J. R. Meyer, M. J. Yang, B. V. Shanabrook, H. Lee, R. U. Martinelli, and A. R. Sugg, *Appl. Phys. Lett.* **74**, 1075 (1999).
6. R. Klann, T. Hofer, R. Buhleier, T. Elsaesser, and J. W. Tomm, *J. Appl. Phys.* **77**, 277 (1995).
7. P. C Findlay, C R Pidgeon, B N Murdin, A F G van der Meer, A F G Langerak, C M Ciesla, J Oswald, G Springholz and G Bauer, *Phys. Rev. B* **58**, 12908 (1998).
8. Z. Shi, G. Xu, P.J. McCann, and X. M. Fang, N. Dai, C. L. Felix, W. W. Bewley, I. Vurgaftman, and J. R. Meyer, *MRS 1999 Fall meeting*, Nov. 30, 1999, Boston Massachusetts.
9. Z. Shi, G. Xu, P. J. McCann, X. M. Fang, N. Dai, C. L. Felix, W. W. Bewley, I. Vurgaftman, and J. R. Meyer, *Appl. Phys. Lett.* **76**, 3688 (2000).
10. W. W. Bewley, C. L. Felix, I. Vurgaftman, J. R. Meyer, G. Xu, and Z. Shi, *Electron. Lett.* **36**, 539 (2000).
11. C. L. Felix, W. W. Bewley, I. Vurgaftman, J. R. Lindle, J. R. Meyer, H. Z. Wu, G. Xu, S. Khosravani, and Z. Shi, *Appl. Phys. Lett.* **78**, 3770 (2001).
12. H. Wu, F. Zhao and Z. Shi, *20th North American Conference on Molecular Beam Epitaxy*, Oct. 1-3, 2001, Providence, Rhode Island.
13. U. Schiessl and J. Rohr, *Infrared Technol.* **40**, 325 (1999).
14. G. Springholz, T. Schwarzl, W. Heiss, G. Bauer, M. Aigle, H. ASCHER, I. Vavra, *Appl. Phys. Lett.* **79**, 1225 (2001).
15. P. J. McCann, K. Namjou, and X. M. Fang, *Appl. Phys. Lett.* **75**, 3608 (1999).
16. F. Zhao, H. Wu, Lalith Jayasinghe and Z. Shi, accepted and to be published in *Appl. Phys. Lett.*, in Feb. 2002.

Antimony-Based Devices

Sb-Based Mid-Infrared Diode Lasers

C. Mermelstein, M. Rattunde, J. Schmitz, S. Simanowski, R. Kiefer, M. Walther, and J. Wagner
Fraunhofer-Institut für Angewandte Festkörperphysik,
Tullastrasse 72, D-79108 Freiburg, Germany

ABSTRACT

In this paper we review recent progress achieved in our development of type-I GaInAsSb/AlGaAsSb quantum-well (QW) lasers with emission wavelength in the 1.74-2.34 μm range. Triple-QW (3-QW) and single-QW (SQW) diode lasers having broadened waveguide design emitting around 2.26 μm have been studied in particular. Comparing the two designs we have found that the threshold current density at infinite cavity length as well as the transparency current density scale with the number of QWs. Maximum cw operating temperature exceeding 50°C and 90°C has been obtained for ridge waveguide lasers emitting above and below 2 μm , respectively. Ridge waveguide diode lasers emitting at 1.94 μm exhibited internal quantum efficiencies in excess of 77%, internal losses of 6 cm^{-1} , and threshold current density at infinite cavity length as low as 121 A/cm^2 reflecting the superior quality of our diode lasers, all values recorded at 280 K. A high characteristic temperature T_0 of 179 K for the threshold current along with a value of $T_1 = 433$ K for the characteristic temperature of the external efficiency have been attained for the 250-280 K temperature interval. Room temperature cw output powers exceeding 1.7 W have been demonstrated for broad area single element devices with high-reflection/antireflection coated mirror facets, mounted epi-side down. The latter result is a proof for the high power capabilities of these GaSb-based mid-ir diode lasers.

INTRODUCTION

Semiconductor diode lasers emitting at wavelengths around 2 μm and beyond are of significant current interest for an increasing number of applications, including tunable diode laser absorption spectroscopy (TDLAS) for process control and environmental monitoring, as well as materials processing such as welding of plastics and medical laser surgery. Many of the potential applications for mid-ir semiconductor lasers, in particular those involving molecular spectroscopy and remote sensing, require coherent sources with narrow linewidths. While the TDLAS related applications ask for high spectral purity and tunability of the diode laser, the two latter applications call for high output powers on the multiple watt level and concomitant high power conversion efficiency along with good beam quality. An additional key issue is the ambient or above ambient operating temperatures while maintaining high power efficiency. For the 2-3 μm wavelength interval, the conventional interband diode laser approach is adopted, employing GaInAsSb/AlGaAsSb type-I QW/barrier layers as active region grown on GaSb substrates [1, 2]. Diode lasers based on the (AlGaIn)(AsSb) material system covering the above given spectral range demonstrated excellent room temperature performances, including very low threshold current density (J_{th}), very low internal loss coefficient, and high internal quantum efficiency [3-7]. Furthermore, cw output power of 1.9 W at 15°C has been obtained from 200 μm x 2 mm broad area diode lasers emitting at 2 μm [4].

In this paper we give an overview of our results regarding the development of GaInAsSb/AlGaAsSb type-I diode lasers emitting between 1.74 and 2.34 μm , already published in part in Ref. 8-

11. The diode lasers studied in this work are based on the broadened waveguide separate confinement heterostructure concept.

EXPERIMENT

All diode laser structures described in the present paper were grown on commercial 2-inch (100) n-type GaSb:Te substrates in a solid-source molecular beam epitaxy system equipped with valved cracker effusion cells for the group V elements producing beams of As_2 and Sb_2 . The epitaxial layer sequence starts with an n^+ -GaSb:Te buffer layer, followed by an n-type digitally graded GaSb/AlGaAsSb SL transition region towards the $2\text{ }\mu\text{m}$ thick $n\text{-Al}_{0.85}\text{Ga}_{0.15}\text{As}_{0.07}\text{Sb}_{0.93}$ bottom optical cladding layer nominally lattice matched to the GaSb buffer layer. The active region of the 3-QW laser consists of three compressively strained 10 nm thick undoped $\text{Ga}_{0.70}\text{In}_{0.30}\text{As}_{0.06}\text{Sb}_{0.94}$ QWs separated by 20 nm wide undoped $\text{Al}_{0.28}\text{Ga}_{0.72}\text{As}_{0.02}\text{Sb}_{0.98}$ barriers lattice matched to the GaSb substrate. The QW region is embedded between 400 nm thick $\text{Al}_{0.28}\text{Ga}_{0.72}\text{As}_{0.02}\text{Sb}_{0.98}$ separate confinement layers, resulting in a total waveguide thickness of 870 nm. The layer sequence is completed by a $2\text{ }\mu\text{m}$ wide $p\text{-Al}_{0.85}\text{Ga}_{0.15}\text{As}_{0.07}\text{Sb}_{0.93}$ upper optical cladding layer followed by a p-type digitally graded GaSb/AlGaAsSb SL transition region towards the p^+ -GaSb:Be contact layer. The single QW laser incorporates 480 nm thick separate confinement layers and one QW in the active region, while the other parts of the structure are identical to the 3-QW laser. The entire active region and the top cladding layer are grown at a temperature of $\sim 470^\circ\text{C}$, while the bottom cladding layer at a higher temperature of $\sim 550^\circ\text{C}$. For more details regarding the growth conditions see [8, 9]. An additional set of ten diode lasers all comprising 3 QWs have been grown where the only parameters intentionally varied were the In and As contents in the QWs, from 0.07 to 0.30 and from 0 to 0.15, respectively. All other parts of the layer sequence are identical with the above mentioned structure. The energy band-edge profile of a typical 3-QW layer sequences, calculated using the Model Solid Theory [12], is shown in Figure 1.

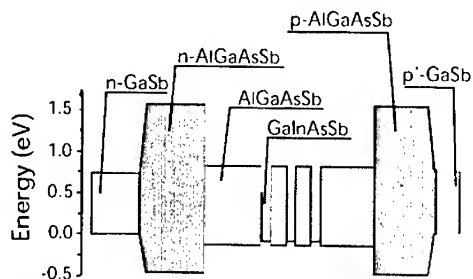


Figure 1. Schematic energy band-edge profile of a 3-QW laser structure.

After the growth the epitaxial layer structures were analyzed by high-resolution X-ray diffraction (HRXRD) and secondary ion mass spectroscopy (SIMS) in order to determine the individual layer compositions, as well as doping concentrations. Figure 2 displays a typical HRXRD profile covering the 004 reflection range of GaSb for a 3-QW diode laser. The diagram reveals well-resolved SL diffraction peak signature of the 3 QW active region along with narrow diffraction peaks associated with the AlGaAsSb cladding and separate confinement layers. The difference between the zero-order SL peak

and the GaSb buffer peak provides the net strain in the SL. In this case the zero-order peak of the SL is shifted to a diffraction angle smaller than that of the GaSb buffer layer, reflecting a compressively strained SL with $\Delta a/a = 9.5 \times 10^{-3}$. As clearly seen, the measured data are in good agreement with the simulation. The residual mismatch of both cladding layers was in most cases below 1×10^{-3} , indicating excellent lattice matching and thus high crystalline quality. All in all, these laser structures show a superior material quality indicative for our mature growth technique.

SIMS depth profiles of the group III elemental components Al, Ga, and In, along with those of the dopants Be and Te are plotted in Figure 3. The Ga and Al depth profiles clearly mark the cladding and the separate confinement layers, while the In depth profile shows the QW region. Each dopant profile was calibrated against known implants into AlGaAsSb. It can be seen that the cladding layers are heavily doped in order to minimize Ohmic losses, typically the Be is incorporated up to a level of $5.5 \times 10^{18} \text{ cm}^{-3}$, and the Te doping level is higher with a concentration of $1.4 \times 10^{19} \text{ cm}^{-3}$.

Edge-emitting index-guided Fabry-Perot diode lasers with ridge aperture varying from 6 to 64 μm have been prepared for all the structures reported in this paper, using standard optical lithography and chemically assisted ion beam etching. For high output power gain guided 150 μm broad area lasers separated by trench etch isolation have been fabricated. In the latter devices the cap etching was done by selective reactive ion etching. The etched surfaces were passivated with SiN. Ti/Pt/Au and (AuSn)Au have been deposited for the top p-contact and backside n-contact metalization, respectively. Laser bars with cavity lengths varying between 0.5 and 2 mm have been cleaved and soldered either substrate-side down or, for high output powers, epi-side down onto copper heat sink. For several laser bars, to maximize single ended output, low-reflectivity, AR (5%), and high-reflectivity, HR (95%), coatings have been applied to the cleaved mirror facets. The emission spectra were measured by focusing the laser beam into a Fourier-transform infrared (FTIR) spectrometer equipped with a cooled InSb detector, using $f/4$ collection optics and spectral resolution of 0.25 cm^{-1} ($\sim 1 \text{ \AA}$). For absolute light-power measurements the lasing emission was collected into a calibrated pyroelectric detector.

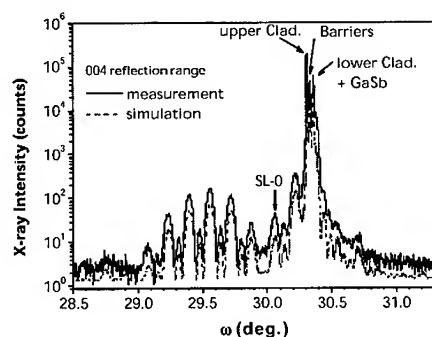


Figure 2. Experimental HRXRD profile (upper curve) and simulated profile (lower curve) covering the 004 reflection range of GaSb for a 3-QW diode laser structure.

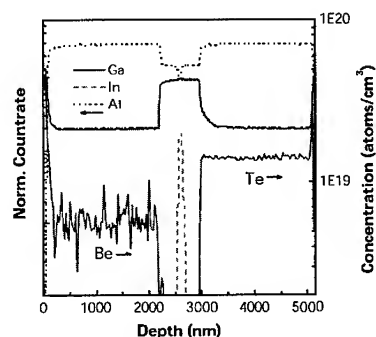


Figure 3. SIMS depth profiles of individual elemental constituents Al, Ga and In (left axis), and of the p and n dopants Be and Te, respectively (right axis), for a 3-QW laser.

RESULTS AND DISCUSSION

3-QW and SQW diode lasers emitting at 2.26 μm

The room temperature current-voltage characteristics of the devices revealed turn-on voltages around 0.7 V and low series resistances of about 300 m Ω for 64 μm x 1000 μm ridge waveguide lasers. All laser diodes were electro-optically characterized in cw operation. Additionally, for an accurate determination of the threshold current pulsed mode measurements have been performed. Current pulses of 5 μs duration at a 10 kHz repetition rate were generated by a Fastest pulsed current source. The light output power as a function of the injection current was measured at heat sink temperatures varying between 250 and 360 K for several ridge widths and cavity lengths. The power levels quoted below have been corrected for the transmission coefficients of the output optics and for the collection efficiency. Figure 4 shows cw collected optical power from a single facet and total power efficiency versus drive current, for a 64 μm x 600 μm 3-QW ridge-waveguide laser recorded at 280 and 310 K. A differential quantum efficiency (η_d) of 50% and a total power efficiency (called also wall-plug efficiency) of 23% were deduced at 280 K. The latter is the highest value reported so far for diode lasers emitting beyond 2.2 μm and equals the power efficiency of 22.5% reported for a single-QW GaInAsSb/AlGaAsSb laser with a significantly shorter emission wavelength of 2.05 μm [3]. The relatively high power conversion efficiency reflects the high η_d and low series resistance achieved for the present lasers.

The spectral characterization in cw mode yielded single mode lasing emission at several temperatures for drive currents near threshold. The inset of Figure 4 shows high-resolution single longitudinal mode cw lasing spectra, recorded at 280 and 310 K, for a 64 μm x 600 μm 3-QW diode laser, with emission close to 2.26 μm for the latter temperature. At higher injection currents the lasing spectrum exhibited multiple longitudinal modes. The temperature dependence of the lasing emission yielded a temperature tunability rate of ~ 1.3 nm/ $^\circ\text{C}$, a property linked to the temperature sensitivity of the GaInAsSb band gap. As the cavity length (L) is decreased from 1250 to 500 μm , the peak emission

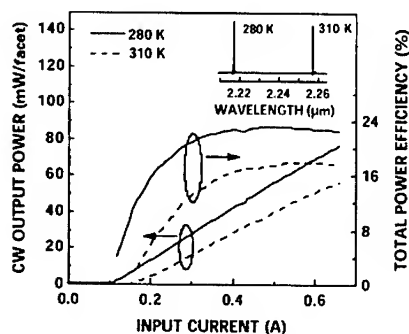


Figure 4. CW light output power per facet and total power efficiency vs injection current of a 64 μm x 600 μm 3-QW ridge laser operated at 280 and 310 K. The inset displays high resolution spectra of single longitudinal mode laser emission at the mentioned operating temperatures.

wavelength for cw operation at room-temperature decreases from 2.26 to 2.23 μm , as a result of increased band filling due to higher threshold carrier densities at shorter cavity lengths.

The threshold currents (I_{th}) are plotted as a function of the cavity length in inset of Figure 5 for the 3-QW and SQW lasers at 280 K. A linear decrease with L down to 550 μm and 1200 μm is observed for the 3-QW and SQW lasers, respectively. Further decrease in L leads to a stagnation in I_{th} due to gain saturation [13]. This behavior is more pronounced for the SQW than for the 3-QW laser due to the reduced number of QWs. Furthermore, for the SQW laser even an increase in I_{th} is noticed for the two shortest cavity lengths. The temperature sensitivity of I_{th} in the 200 - 280 K thermal range can be described by a characteristic temperature of $T_0 = 110$ K for the 3-QW laser.

Figure 5 depicts J_{th} versus reciprocal cavity length ($1/L$) together with a linear fit to the experimental data for the 3-QW and SQW lasers, both with 64 μm apertures, recorded at 280 K. Values as low as 117 A/cm^2 and 199 A/cm^2 (corresponding to 66 A/cm^2 per QW) have been achieved for the SQW and 3-QW lasers, respectively, both with 2 mm cavity length. These values compare favorably well with the 230 A/cm^2 (115 A/cm^2 per QW) reported for a double-QW laser at 2.3 μm [7]. The linear fit to the experimental data results in a J_{th} at infinite cavity of 150 A/cm^2 for the 3-QW and a value about a factor of three smaller, 55 A/cm^2 , for the SQW, as expected from the decreased number of QWs. Note that for the linear fit of the SQW data the three shortest cavity lengths were ignored because of gain saturation, as discussed above.

To deduce the standard laser parameters, namely the internal quantum efficiency (η_i) and internal loss coefficient (α_i), the inverse of η_d is plotted against the cavity length, illustrated in the inset of Figure 6 for the SQW laser with a 64 μm aperture. The η_i and α_i values were derived using the relation $\eta_d = \eta_i / [1 + \alpha_i L / \ln(1/R)]$. The linear fit results in high η_i -values of 69% and 65% for 3-QW and SQW, respectively, and α_i as low as of 7.7 cm^{-1} (3-QW) and 5 cm^{-1} (SQW). The lower loss coefficient of the SQW laser is attributed to the reduced number of interfaces in the active region. For the fit to the SQW the data point at the shortest cavity length was omitted again due to the influence of gain saturation. We point out that the data show a very low scatter even though no data averaging for a given cavity length was performed.

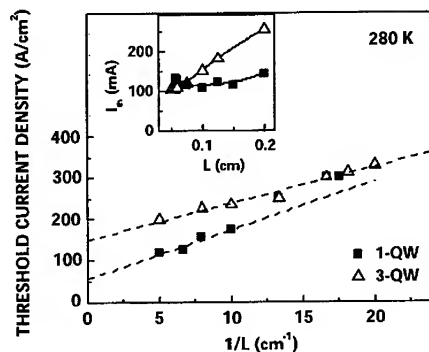


Figure 5. Threshold current density vs inverse cavity length for the 3-QW (triangles) and SQW (squares) diode lasers with 64 μm wide ridges at 280 K. The inset depicts the cavity length dependence of the threshold current for the 3-QW and SQW lasers at 280 K.

The modal gain and the transparency current density have been deduced by computing the total loss for various devices with different L . The current-dependent modal gain derived from the total losses (scattered points) and the logarithmic fit [14] to the experimental data (dashed curves) are depicted in Figure 6, for the SQW (squares) and 3-QW (triangles) lasers at 280 K. Transparency current densities of 41 A/cm² and 113 A/cm² have been obtained for the SQW and 3-QW lasers, respectively. We point out that these values of transparency current density scale with the number of QWs in the same way as the threshold current density at infinite cavity length, indicating a superior diode laser quality.

1.74 - 2.34 μm 3-QW diode lasers

Furthermore GaInAsSb/AlGaAsSb diode lasers with emission wavelengths varying from 1.74 to 2.34 μm have been investigated. The lasers have been electro-optically characterized in cw operation in order to determine the laser characteristic parameters, namely the characteristic temperature T_0 , the internal quantum efficiency η_i , and the internal loss coefficient α_i .

The cw lasing spectra recorded at 280 K heat sink temperature from nine different diode lasers, spanning the 1.84 - 2.34 μm spectral range, is shown in Figure 7. The geometry for all these diode lasers was 64 μm x 600 μm . One major peak, indicating single mode activity, has been observed in lasing spectra of several devices at low injection currents slightly above threshold. However, more peaks, reflecting multi-mode behavior, emerged at larger currents. The inset displays the spectrum of the 2.13 μm diode laser on an expanded wavelength scale. It shows well resolved multiple longitudinal mode emission with mode spacing of ~ 1 nm.

Figure 8 illustrates representative cw power output and total power efficiency plotted versus injection current, recorded at 280 K heat sink temperature for three 64 μm x 1000 μm different diode lasers emitting at 1.94, 2.21 and 2.34 μm . The light output power drops substantially upon increasing the wavelength, so does the power efficiency, due to the increase of Auger losses and QW heterobarrier leakage with increasing wavelength [11]. The maximum output powers are limited by the onset of thermal rollover due to the substrate-side-down mounting of the devices.

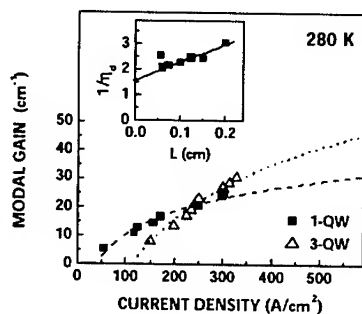


Figure 6. Modal gain vs current density for the 3-QW (triangles) and SQW (squares) diode lasers at 280 K. The inset shows the cavity length dependence of the inverse differential quantum efficiency of the SQW laser at 280 K.

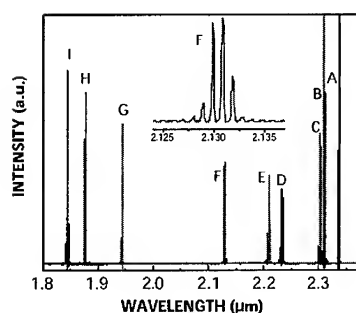


Figure 7. 280 K lasing spectra of nine different diode lasers covering the wavelength interval from 1.84 to 2.34 μm . The inset displays the emission of the 2.13 μm diode laser on an expanded wavelength scale. All lasers in this graph had a 64 μm x 600 μm size.

The maximum output power decreases approximately by a factor of three when proceeding from the shortest to the longest wavelength device, accompanied by a decrease in maximum power efficiency from 29% to 10%. Higher light output powers have been obtained by applying HR/AR coating with reflectivities of 95% and 5%, respectively, to the mirror facets of the lasers.

The characteristic temperature T_0 of the threshold current has been studied in more detail by characterizing the devices in cw as well as in pulsed operation. The temperature dependence of the threshold current measured in pulsed mode for 4 different lasers, emitting at 2.34, 2.30, 2.13 and 1.94 μm , is depicted in Figure 9. For the three diode lasers emitting on the short-wavelength side two distinct temperature regimes are visible showing different T_0 values. A study regarding the temperature dependence of the threshold current as a function of the wavelength revealed the following results: a decrease in T_0 , determined for the low temperature interval, from 179 K to 54 K is obtained for wavelengths increasing from 1.94 μm to 2.34 μm .

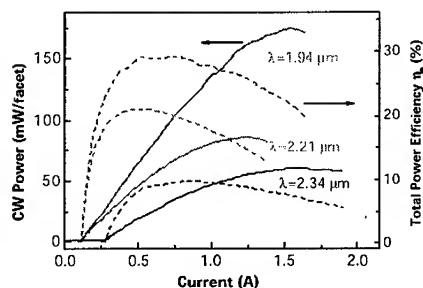


Figure 8. Power output vs current (solid lines) and power efficiency vs current (dashed lines) characteristics recorded at 280 K for three lasers emitting at 1.94, 2.21 and 2.34 μm . The 64 μm x 1000 μm ridge waveguide lasers were operated in cw mode.

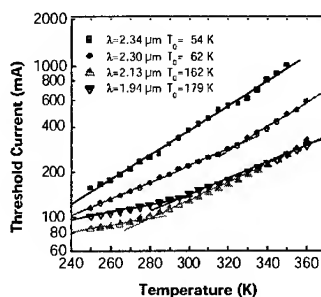


Figure 9. Pulsed threshold current vs temperature for different 64 μm x 1000 μm ridge waveguide lasers with wavelength emission between 1.94 to 2.34 μm . The T_0 values for the low temperature range are given as well in the graph.

In order to understand the decrease of T_0 with increasing wavelength, it is necessary to analyze the two main contributions responsible for the temperature sensitivity of I_{th} , namely the Auger recombination and the heterobarrier leakage. For an extensive analysis an additional diode laser, sample J, emitting at the shortest wavelength of 1.7 μm , has been included. The Auger recombination is proportional to $\exp(-\mu E_g/kT)$ [1], where E_g is the effective band gap energy and μ designates the reduced electron-hole mass. Therefore, if Auger is the dominant loss mechanism then T_0 can be expected to increase with the band gap. To test the validity of this assumption for the present set of lasers, T_0 is plotted in Figure 10 (a) against the emitted photon energy. In order to provide a higher accuracy of the experimental data, T_0 values obtained from pulsed measurements have been used since they are more precise than cw measurements, as the former prevent self-heating of the devices. Indeed, as shown in Figure 10 (a) for samples A to G, an increase in T_0 with respect to the photon energy is observed as expected from the above discussion, but all at once a decrease for lasers H, I and J, emitting on the short-wavelength side, appears which is not consistent with the view of Auger recombination limited threshold current. On the other hand, the heterobarrier leakage is proportional to $m^{1/2} \exp(-E_b/kT)$ [15], where E_b is the conduction (ΔE_c) or valence band offset (ΔE_v), whatever is smaller. Therefore, if the heterobarrier leakage is the dominant mechanism, T_0 should increase with E_b . Figure 10 (b) shows the T_0 values as a function of the conduction or valence band offset, whichever is smaller. Within the scatter of the experimental data a monotonic increase of T_0 with increasing band offset is observed, favoring the assumption that heterobarrier leakage is indeed dominant. Detailed studies of GaInAsSb/AlGaAsSb type-I QW diode lasers emitting in the 2.3 to 2.6 μm wavelength range have shown that for 2.3 μm lasers with $\Delta E_c \approx \Delta E_v$, the temperature dependence of I_{th} is governed by nonradiative two-particle recombination [16]. Thence, the current experimental results strengthened by sample J lead us to conclude that of the two mechanisms discussed above, the temperature dependence of I_{th} is governed by heterobarrier leakage, limiting the high-temperature performance of the present diode lasers.

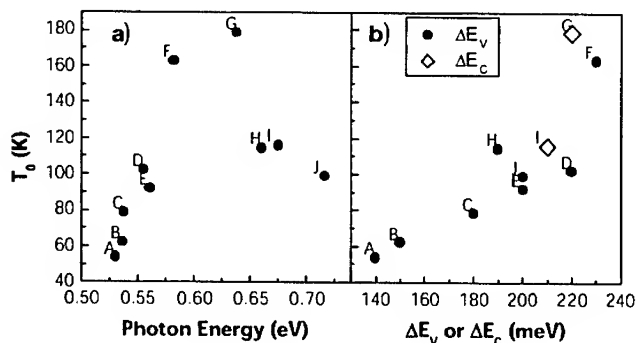


Figure 10. Characteristic temperature T_0 of the different diode lasers vs a) emitted photon energy and b) valence band offset ΔE_v (circles) or conduction band offset ΔE_c (rhombs), whichever is smaller.

Additional laser parameters, derived from the present wavelength series of diode lasers, are shown in Table I, where the values of α_i and η_i as well as the J_{th} for infinite cavity length ($J_{th,\infty}$) are compiled for the various laser structures emitting between 1.87 and 2.34 μm .

The transversal optical field has been calculated taking into account the various refractive indexes of the different epitaxial layers forming the optical waveguide. Figure 11 a) shows the refractive index and the resulting transversal optical mode intensity as a function of the transversal position, corresponding to the growth direction, for two different diode lasers emitting at 1.84 and 2.34 μm . The inset displays the same data on an expanded length scale for the active region. The calculated confinement factor of the QWs (defined by the overlap between the optical mode and the QWs) amounts to 4.7% for the 1.84 μm laser and 4% for the 2.34 μm device. The overlap with the cladding layers was calculated as well, yielding values of 8.7% and 15.5% for the short and long wavelength emitting devices, respectively.

An additional key issue for high power applications is the beam quality. To that purpose the far field (FF) distribution both along the slow and fast axis have been measured. FF scans in the transversal (fast axis) and lateral direction (slow axis) of the laser emission have been performed by rotating the diode laser placed at a distance of 20 cm in front of an extended wavelength InGaAs detector with 1 mm diameter. The diode laser has been operated at two different drive currents, 2 and 4 times the threshold. The device under investigation had a 16 μm x 1000 μm geometry and the mirror facets were HR/AR coated. All the measurements were performed at room temperature. The measured fast axis profiles for the two different injection currents, $2I_{th}$ and $4I_{th}$, were almost identical, exhibiting a Gaussian shape with full-width at half-maximum (FWHM) divergence angle of $\sim 67^\circ$, which compares well with the calculated value of 60° . Figure 11 b) displays the calculated and measured transversal FF angular distribution for the above mentioned diode lasers, emitting at 1.84 and 2.34 μm . The graph reveals a very good agreement between the calculated and experimental data. In addition, both the calculated and simulated curves show no significant dependence with respect to the wavelength.

Table I. Internal loss coefficient α_i , internal quantum efficiency η_i , as well as threshold current density for infinite cavity length $J_{th,\infty}$ for the various laser diode structures with emission wavelength given in the second column.

Wafer	λ (μm)	α_i (cm^{-1})	η_i (%)	$J_{th,\infty}$ (A/cm^2)
H	1.87	4.2	63	141
G	1.94	6.1	77	121
F	2.13	6.1	77	105
E	2.21	7.7	78	108
D	2.23	7.6	72	110
C	2.30	4.1	50	154
B	2.31	4.6	38	304
A	2.34	2.7	42	164

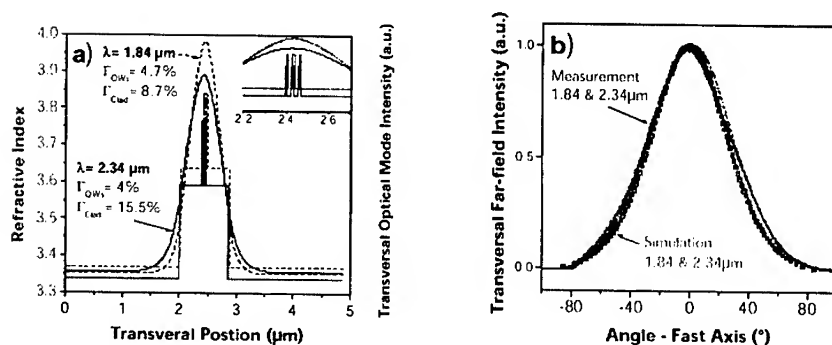


Figure 11. a) Calculated transversal optical mode intensity (right axis) and refractive index (left axis) vs transversal position, corresponding to the growth direction, for two different lasers emitting at $1.84 \mu\text{m}$ and $2.34 \mu\text{m}$. The inset zooms in the QW active region; b) Calculated (symbols) and measured (line) transversal far-field angular distributions for two different lasers emitting at $1.84 \mu\text{m}$ and $2.34 \mu\text{m}$.

The lateral optical field was calculated for a diode laser emitting at $1.94 \mu\text{m}$ with $16 \mu\text{m}$ wide ridge geometry. Figure 12 a) displays the calculated lateral optical mode profile (right axis) up to the 2nd order, together with the effective refractive index (left axis) reflecting the rectangular shape of the $16 \mu\text{m}$ ridge aperture. In contrast to the transversal pattern, however, the lateral FF shows a multi-mode behavior. Upon increasing the injection current, the profile shape changes, showing higher order side peaks, and the FWHM of the divergence angle increases somewhat from 4.8° ($2I_{\text{th}}$) to 5.6° ($4I_{\text{th}}$). Figure 12 b) illustrates the angular dispersion of the measured (upper) and simulated (lower) lateral

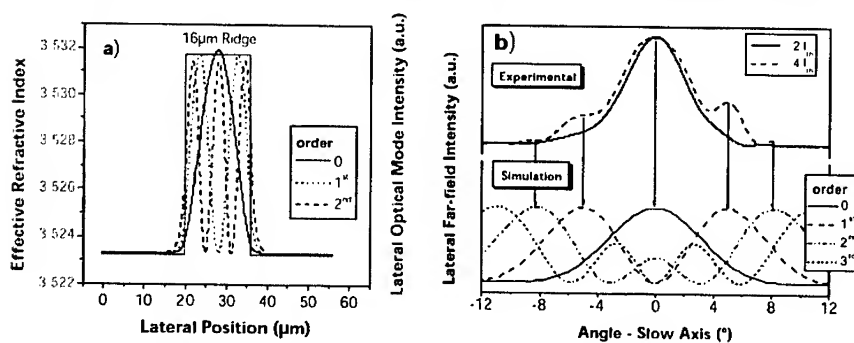


Figure 12. a) Calculated lateral optical mode spatial profiles up to the 2nd order for a $1.94 \mu\text{m}$ diode laser. The assumed etch depth is $1.9 \mu\text{m}$ and the ridge width is $16 \mu\text{m}$; b) Experimental (upper) and calculated (lower) lateral far-field mode profiles of a $16 \mu\text{m} \times 1000 \mu\text{m}$ diode laser with coated mirror facets emitting at $1.94 \mu\text{m}$. The experimental data were recorded at room temperature for two different injection currents, $2I_{\text{th}}$ and $4I_{\text{th}}$, and the calculated angular distribution is up to the 3rd order.

FF intensities of the 1.94 μm diode laser with 16 μm ridge width and 1000 μm cavity length. The measurements have been performed again at $2I_{\text{th}}$ and $4I_{\text{th}}$. The angular dependence of the lateral FF was calculated up to the 3rd order mode. Regarding the measured profiles, at $2I_{\text{th}}$ only the zero order mode is visible in the experimental FF profile, whereas at $4I_{\text{th}}$ the first and second order modes are clearly resolved. The angular position of the measured side peaks originating from higher order modes is in excellent agreement with the calculations.

To fully exploit the superior material quality of the present (AlGaIn)(AsSb) diode lasers emitting around 2 μm , broad area lasers with single ended output have been processed, and mounted epi-side down for improved heat sinking. Resulting room-temperature cw optical output and total power efficiency versus injection current is depicted in Figure 13, for a 150 μm x 1000 μm broad area laser with emission wavelength of 1.98 μm at 300 K. A maximum cw output power exceeding 1.7 W at room temperature was achieved at a drive current of 6.8 A, corresponding to a voltage drop of 1.67 V. The maximum total power efficiency amounted to 27% and decreased to a value of 15% at the maximum power of 1.7 W.

CONCLUSIONS

GaInAsSb/AlGaAsSb type-I QW lasers spanning the spectral range from 1.74 to 2.34 μm have been realized and investigated. Laser structures with 3-QWs and SQW have been studied in detail. Excellent laser performances, which become evident from high characteristic temperatures T_0 of 179 K, high internal quantum efficiency of 77%, and low internal losses of 6 cm^{-1} , have been achieved. Beside that, a comparison between the 3-QW and SQW laser structures showed that the threshold current density at infinite cavity and the transparency current density scale nicely with the number of QWs. A careful study has been conducted regarding the characteristic temperature of the threshold current with respect to the lasing wavelength in order to provide better understanding concerning the different loss mechanisms limiting the laser performances. An additional topic we have addressed was the investigation of the far field profiles related with these laser structures. Finally, 1.7 W cw optical output

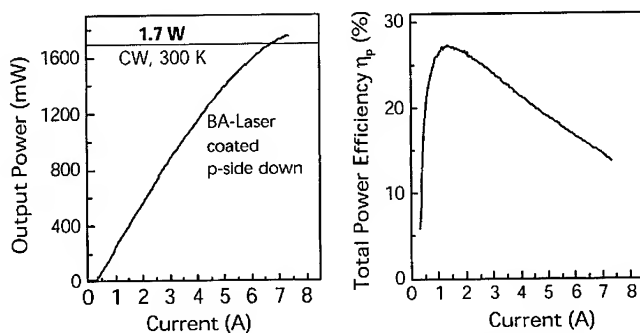


Figure 13. Room temperature cw output power vs current and total power efficiency vs current for 1.98 μm broad area diode lasers, coated and mounted epi-side down. Output powers exceeding 1.7 W cw have been achieved.

power at room temperature has been demonstrated using single ended broad area diode laser, a very promising result for high power applications of the 2 μm diode lasers.

ACKNOWLEDGMENTS

The authors would like to thank N. Herres and H. Güllich for IIRXRD measurements, as well as M. Maier and T. Fuchs for SIMS analyses. Continuous support and encouragement by G. Weimann is gratefully acknowledged. This work was supported by the German Ministry for Education and Research (BMBF).

REFERENCES

1. G. W. Turner and H. K. Choi, in *Optoelectronic Properties of Semiconductors and Superlattices*, edited by M. O. Manasreh, (Gordon and Breach, Amsterdam, 1997), p. 369, and references therein.
2. D. Z. Garbuzov, R. U. Martinelli, H. Lee, P. K. York, R. J. Menna, J. C. Connolly, and S. Y. Narayan, *Appl. Phys. Lett.* **69**, 2006 (1996).
3. G. W. Turner, H. K. Choi, and M. J. Manfra, *Appl. Phys. Lett.* **72**, 876 (1998).
4. D. Z. Garbuzov, R. U. Martinelli, H. Lee, R. J. Menna, P. K. York, L. A. DiMarco, M. G. Harvey, R. J. Matarese, S. Y. Narayan, and J. C. Connolly, *Appl. Phys. Lett.* **70**, 2931 (1997).
5. T. Newell, X. Wu, A. L. Gray, S. Dorato, H. Lee, and L. F. Lester, *IEEE Photon. Technol. Lett.* **11**, 30 (1999).
6. D. A. Yarekha, G. Glastre, A. Perona, Y. Rouillard, F. Genty, E. M. Skouri, G. Boissier, P. Grech, A. Joullie, C. Alibert, and A. N. Baranov, *Electron. Lett.* **36**, 537 (2000).
7. D. Z. Garbuzov, H. Lee, V. Khalfin, R. Martinelli, J. C. Connolly, and G. L. Belenky, *IEEE Photon. Technol. Lett.* **11**, 794 (1999).
8. S. Simanowski, N. Herres, C. Mermelstein, R. Kiefer, J. Schmitz, M. Walther, J. Wagner, and G. Weimann, *J. of Crystal Growth* **209**, 15 (2000).
9. S. Simanowski, C. Mermelstein, M. Walther, N. Herres, R. Kiefer, M. Rattunde, J. Schmitz, J. Wagner, and G. Weimann, *J. of Crystal Growth* **227-228**, 595 (2001).
10. C. Mermelstein, S. Simanowski, M. Mayer, R. Kiefer, J. Schmitz, M. Walther, and J. Wagner, *Appl. Phys. Lett.* **77**, 1581 (2000).
11. M. Rattunde, C. Mermelstein, S. Simanowski, J. Schmitz, R. Kiefer, N. Herres, F. Fuchs, M. Walther, and J. Wagner, in *Proc. of the 27th Int. Symp. on Compound Semiconductors*, (Institute of Electrical and Electronics Engineers, Inc., USA, 2001) p. 437.
12. M. P. C. M. Krijn, *Semicond. Sci. Technol.* **6**, 27 (1991).
13. R. W. H. Engelmann, C.-L. Shieh, and C. Shu, in *Quantum Well Lasers*, edited by P. S. Zory, Jr., (Academic Press, San Diego, CA, 1993), p. 170.
14. P. W. A. Mc Ilroy, A. Kurobe, and Y. Uematsu, *IEEE J. Quantum Electron.* **21**, 1958 (1985).
15. H. Schneider and K. v. Klitzing, *Phys. Rev. B* **38**, 6160 (1988).
16. D. Garbuzov, M. Maiorov, H. Lee, V. Khalfin, R. U. Martinelli, and J. Connolly, *Appl. Phys. Lett.* **74**, 2990 (1999).

Thin Films of Antimony-Tin Oxide as Counter-Electrodes for Proton Working Electrochromic Devices

N. Naghavi, C. Marcel, L. Dupont, A. Rougier and J-M. Tarascon
Laboratoire de Réactivité et Chimie des Solides, Université de Picardie Jules Verne, 80039
Amiens Cedex.

ABSTRACT

We report here on thin films proton-working electrochromic devices based on the well-known tungsten oxide as the coloring electrode, and Antimony Tin Oxide (ATO) as the ion-storage counter-electrode. We show that films deposited by Pulsed Laser Deposition (PLD) technique have an apparent Sb solubility up to 70 at %, and exhibit unusual electrochromic properties. Through potentiostatic tests we'll demonstrate that depending on the composition which influences film morphology, the Sn-Sb-O films could either present a faradic or a capacitive-like behavior, associated to a color or a neutral switching over a wide range of potentials, respectively. The structural properties of ATO films are characterized by X-ray diffraction and transmission electron microscopy (TEM). Electrochromic behavior is studied by means of cyclic voltamperometry coupled with *ex situ* optical transmittance measurements in the visible range. The maximum proton-storage capacity is observed for ATO films containing 40-50 at % Sb, while being quasi-neutral when switching over a wide range of potentials. These compositions are finally retained for the assembly of our WO₃/proton-electrolyte/ATO devices, whose performances are reported.

INTRODUCTION

In recent years, owing to their capability of persistent and reversible color changes under a reversible electrochemical process, electrochromic materials have been widely involved in optical technology, particularly in the field of display panels, antiglare car rear-view mirrors and transmission modulation through building windows [1,2]. To ensure a large-scale development for this energy conscious architecture, the cost of smart windows needs to be lowered, especially for proton-working devices, which are easier to build than lithium conducting ones. Until now, the most durable all-solid inorganic system is composed of tungsten oxide as the cathodically colored working electrode and iridium [3] as the complementary counter-electrode, both components exchanging proton ions. However, owing to the high cost of iridium oxide, research has turned on cheaper electrochromic materials such as hydrous nickel oxide [4]. But the latter also presents non-negligible drawbacks such as a poor stability in acidic electrolytes. Thus, a need for alternative and economical materials, which can be used in the composition of proton-conducting electrochromic devices, remained in order to constitute an ion-storage for WO₃, and keep the same optical density over cycling. Based on our previous works we will show that the Sn-Sb-O system may effectively satisfy that need [5].

EXPERIMENTAL DETAILS

Thin oxide films were prepared by pulsed laser deposition using a KrF excimer laser beam (Lambda Physic, Compex 102, $\lambda=248$ nm) with a laser fluence of 1-2 J/cm². The targets

were pellets of commercial SnO_2 (Aldrich 99.9%) and Sb_2O_3 (Aldrich 99.9%) mixtures in stoichiometric proportions annealed for 20 h at a relatively low temperature (700 °C) in order to avoid any antimony loss while achieving a pellet density of 60-70%. Films of 1*1 cm² area were deposited either onto (SnO_2 :F)-coated glass for electrochemical tests or onto simple glass for structural and electronic characterizations. Deposition time was fixed at 15 min with a repetition rate of 3 Hz. The thickness, determined by profilometry using a Dektak St instrument, was estimated as being in the range of 200-250 nm.

Film crystallinity was examined by X-ray diffraction (XRD) with a Philips diffractometer model PW 1710 ($\lambda_{\text{CuK}\alpha}$ = 0.15418 nm). High-resolution transmission electron microscopy (HRTEM) was carried out using a JEOL 2010 microscope equipped with an energy-dispersive X-ray spectroscopy (EDS) analyzer.

Optical transmission spectra in the UV-visible and near infrared regions (250-2500 nm) were obtained using a Varian double beam, UV-Vis-NIR spectrometer "CARY-5E".

The electrochemical properties of the films were characterized by cyclic voltammetry performed with an Autolab PGSTAT 30 system. The cell consists of the ATO film as the working electrode and of a platinum wire as the counter electrode, both immersed in a 0.1M aqueous H_3PO_4 electrolyte. The potentials were given versus the saturated calomel electrode (SCE) reference. For all these experiments, cyclic voltammograms (CV) were scanned at a rate of 10 mV/s.

RESULTS AND DISCUSSION

Films of various antimony-tin oxide compositions were grown from targets whose nominal composition was ranging between 0 and 80 at.% Sb. More specifically, the films were deposited at 200 °C under 10^{-3} mbar oxygen pressure, then annealed for 30 min at 550 °C under the same oxygen pressure, and then characterized for their electrochromic properties. Under such deposition conditions, as deduced from EDS analysis, we noted that the Sn/Sb atomic ratio was relatively well preserved between target and grown films.

Structural characterizations:

Figure 1 shows the X-ray diffraction patterns of ATO thin films deposited on glass substrate, which are typical of SnO_2 cassiterite phase. Increasing Sb amount yields a loss of crystallinity; this trend being also observed for ATO thin films deposited on FTO substrate. The absence of peaks pertaining to antimony oxide phases (whatever the oxidation states) lets suppose the complete dissolution of antimony in the nanostructured SnO_2 . Beyond 70% Sb, films become amorphous. At first such results could indicate that the "apparent solubility limit" of antimony in nanocrystalline tin oxide is reached near the 70% Sb.

At this point a legitimate question was whether these Sb-enriched ATO specimens were presenting large amounts of amorphous antimony-containing material as previously reported [6] or they were single phases. To unambiguously answer such a question, HRTEM measurements were carried out on our heavily substituted ATO films.

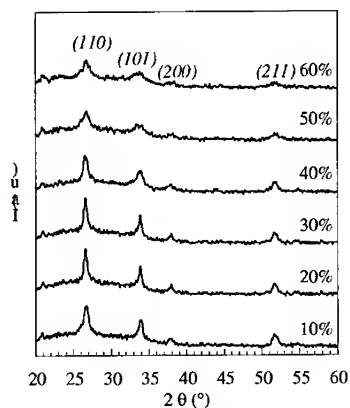


Figure 1: X-ray diffraction patterns of ATO thin films with $10 \leq \%Sb \leq 60$ having a SnO_2 -Cassiterite structure.

Figs. 2. a. and b. display HRTEM micrographs of films deposited from targets composed of 40% Sb and 60% Sb, respectively.

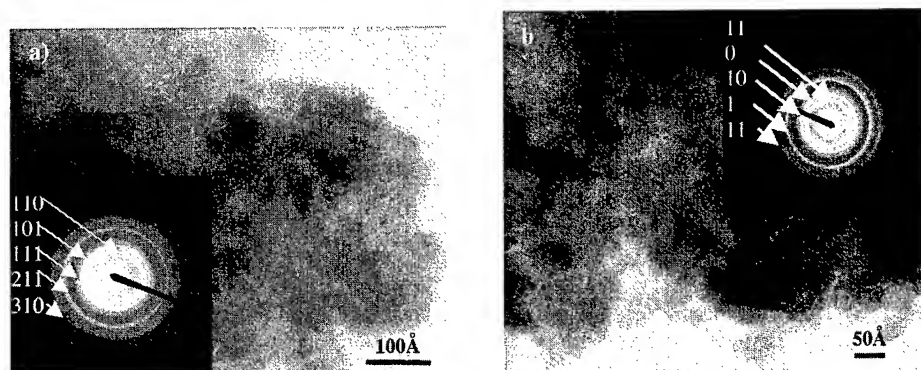


Figure 2: TEM micrographs of ATO thin films with composition of a) 40% Sb and b) 60% Sb.

The high-resolution images and the electron diffraction patterns recorded from these materials gave no evidence for the presence of any antimony oxide phase. For both compositions the diffraction pattern contains well-resolved diffraction rings characteristic of SnO_2 cassiterite phase. Indeed, films consist of small disordered crystals of a cassiterite-type solid, and no trace of amorphous materials is observed independently of antimony amount. However, changes in film texture with composition are visible: while the film with the lowest antimony content (40% Sb, Fig. 2. a.) is very dense, and exhibits a poor definition of particle shape, the film containing 60% Sb (Fig. 2. b.) appears less dense with better defined grains of about 50 Å. In short, the TEM study confirmed the formation of Sn-Sb-O solid solution with a SnO_2 cassiterite-type structure up to a concentration of 60% Sb.

Electrochemical characterizations:

Cyclic voltammograms (CV's) of our ATO films were obtained by sweeping the potential from (-0.7 to 1.5V) vs. SCE. Depending on the film Sb content two apparent types of CV traces were observed (Fig. 3). Within the 10-40% Sb range, CV curves are featureless, and the transmittance remains the same as shown for the (60%Sn-40%Sb) sample in Fig. 3. c. As the antimony contents increases up to 50%, the cyclic voltammogram of the films adopts a pseudo-capacitive like shape as previously shown by Marcel et al.⁵

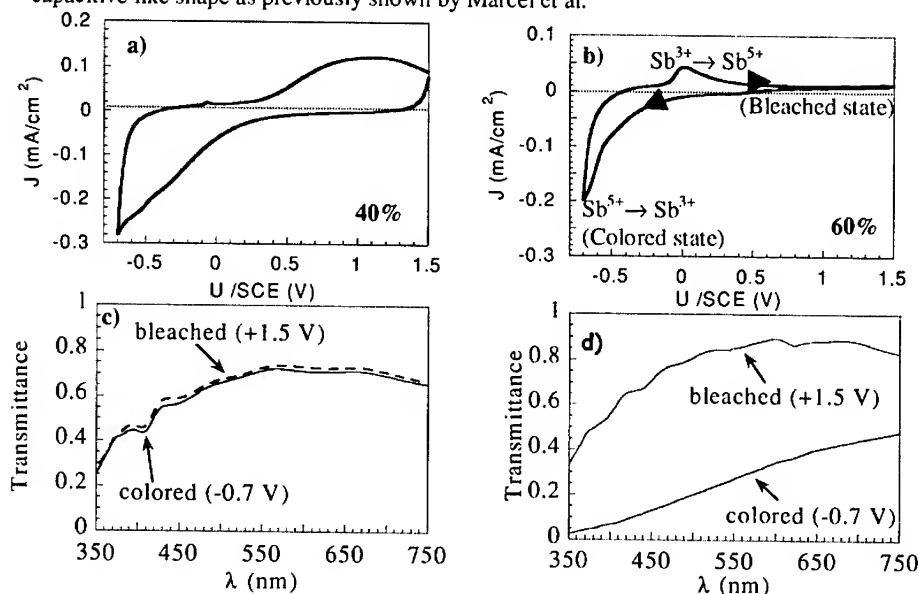


Figure 3: Voltammograms of (a) 60%Sn-40%Sb and (b) 40%Sn-60%Sb thin films. CV's were recorded between -0.7 and 1.5 V vs. SCE with a sweep rate of 10 mV/s. Optical transmittance spectra of thin films of compositions (c) 60%Sn-40%Sb and (d) 40%Sn-60% Sb, bleached at 1.5 V, and cathodically colored at -0.7 V.

From 60 to 70% Sb content, a pronounced faradic behavior appears, possibly corresponding to ($Sb^{5+} \leftrightarrow Sb^{3+}$) charge transfer with simultaneous H^+ (de)intercalation. Indeed a redox couple, visible at ca. 0V in oxidation and -0.7V in reduction, produces a dark-gray coloration with the cathodic sweep, followed by a bleaching process with anodic one. Increasing Sb amount reinforces the optical contrast (Fig. 3. d.) for the composition (40% Sn-60% Sb).

For specimens having a capacitive-like behavior (typically those containing 40% Sb) we noted that the charge density increased with cycling. The origin of this cycling-driven activation is most likely nested in the non-granular film nature that limits the proton diffusion, as neither the surface morphology nor the thickness were modified after cycling. In fact TEM measurements on films containing 40% Sb show no real change in their morphology after cycling about 100 times. These films remain very dense which may lead to a slow proton

diffusion and a capacitive behavior of these films. On the other hand, films with composition $\geq 60\%$ Sb lost their capacity after cycling. After about 100 cycles, TEM micrographs indicated a loss of density associated to a better grain definition, which may facilitate the proton diffusion leading to their "perfect" faradic behavior. Suggesting that these films tend to slightly dissolve in H_3PO_4 electrolyte, the resulting cycling lifetime is apparently short. The electrolyte was modified by either changing the concentration or its nature so as to minimize film dissolution.

Another interesting result is that the best charge density per micron thickness (volumic capacity) was obtained over the 40-60% Sb range. The best volumic capacity and the optically neutral trend of ATO 40%, make it a good candidate to be used as a counter electrode switching against the preferment electrochromic electrode, i.e. WO_3 .

An ATO-based device was so tested in H_3PO_4 (0.1 M) liquid electrolyte. Three-electrode measurements were carried out using WO_3 as the working electrode and ATO (40% Sb) as the counter electrode, first investigating the potential evolution vs the exchanged charge density for each component, then studying the stability of coloration and bleaching processes. We saw that ATO is not limiting, while the equilibrium potentials are stable for colored and bleached states. Therefore ATO (40%) is a reliable counter electrode for proton switching.

Two sorts of proton-conducting solid electrolyte were considered: A hydrated Ta_2O_5 solid electrolyte and a polymer (H_3PO_4 -doped PBI ($x=1$) gel) electrolyte. Here we will only present results for the first one.

WO_3 and Ta_2O_5 /ATO half-cells were grown separately on FTO/glass substrate using PLD, and their respective thickness was adjusted so that their capacities were balanced. The WO_3 film was deposited at RT in 10^{-1} mbar O_2 pressure ($t_{\text{WO}_3}=3000 \text{ \AA}$), whereas the ATO film was deposited as previously indicated ($t_{\text{ATO}}=5000 \text{ \AA}$), and Ta_2O_5 deposited on top with the same oxygen pressure of 10^{-2} mbar at 200°C ($t_{\text{Ta}_2\text{O}_5}=2000 \text{ \AA}$). WO_3 was first H^+ -preinserted (blue coloration) in H_3PO_4 (0.1 M) liquid electrolyte with a charge density of 15 mC/cm^2 , the stack Ta_2O_5 /ATO was cycled in the same medium in order to check its ion-storage ability. Finally the whole cell was assembled using epoxy resin.

Two-electrode potentiostatic measurements were first carried out in order to check if the pre-inserted amount of proton was effectively exchanged by the device (Fig. 5. a). Note that the scan rate was considerably reduced compared to the liquid electrolyte medium (1 mV/s) in order to enable each component to react with proton. Then optical measurements were operated through the whole cell (Fig. 5. b). Indeed for the electrochromism application, the amount of inserted species (i. e. Capacity) is not the main parameter but is linked to the resulting optical contrast yielding a figure of merit expressed by the coloration efficiency (CE)². This coloration efficiency CE is expressed as the ratio between the contrast in the bleached state (T_b) and the colored state (T_c) and the charge density (Q). See equation 1.

$$\text{CE} = (1/Q) * \log (T_b/T_c) \quad (1)$$

These measurements are yielding coloration efficiency of $35 \text{ cm}^2/\text{C}$ for our device, which is about the same as that of WO_3 half-cell. Thus ATO is an effective optically passive counter electrode. However this value can be improved whilst the overall transmission is considerably lowered by FTO/glass and ATO layers, and can be improved by using pigments such as TiO_2 .

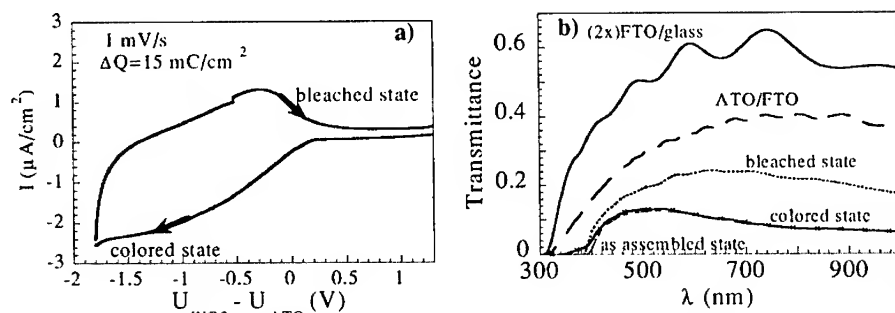


Figure 4: (a) Voltammograms of a two-electrode $\text{WO}_3/\text{Ta}_2\text{O}_5/\text{ATO}$ system. CV's were recorded between -1.8 V and 1.5 V vs. SCE with a sweep rate of 1 mV/s. (b) optical transmittance spectra of the device bleached at 1.5 V, and cathodically colored at -1.8 V.

CONCLUSION:

In summary, through a systematic study of Sn-Sb-O thin films, we gave evidence for a direct relationship between the ATO thin film electrochromic behavior and morphology via changes in Sb content. Based on a charge transfer between Sb^{3+} and Sb^{5+} , the optical contrast between bleached/colored states is thus dictated by the antimony concentration in tin oxide matrix. It increases to the detriment of electrochemical stability, which yields the most antimony-rich compositions (60-70% Sb) presenting a typical faradic behavior to be non-suitable proton-conducting switching electrodes. On the other hand, films containing 40% Sb present a neutral coloration over a wide potential scale associated to a capacitive-like behavior and a good capacity retention. These features make them good candidates in their use as cheap counter electrodes in proton-working devices. The feasibility of an all-solid electrochromic window constituted by WO_3 blue-switching electrode exchanging H^+ ions with an ATO film containing 40% Sb was studied. This device was assembled using Ta_2O_5 electrolyte. An electrochromic coloration efficiency of about $35 \text{ cm}^2/\text{C}$ was so obtained, which is about the same as that of WO_3 half-cell. Thus ATO is an effective optically passive counter electrode. However, in order to improve the transmission of such a system, and increase its switching time there is a need to improve the proton conduction for the electrolyte, and try to enlight ATO counter-electrode with pigments such as TiO_2 .

REFERENCES:

1. P. M. S. Monk, R. J. Mortimer, D. R. Rosseinsky, in *Electrochromism Fundamentals and Applications* (VCH, New York, 1995).
2. C. G. Granqvist, *Handbook of Inorganic Electrochromic Materials*, (Elsevier, Amsterdam, 1995).
3. M. A. Petit, V. Plichon, J. Electroanal. Chem., **444**, 247 (1998).
4. A. Azens, L. Kullman, G. Vairars, H. Nordborg, C. G. Granqvist, Solid State Ionics **449**, 113 (1998).
5. C. Marcel, M. S. Hegde, A. Rougier, C. Maugy, C. Guéry, J. M. Tarascon, Electrochem. Acta, **46**, 2097 (2001).
6. F. J. Berry, D. J. Smith, J. Catal., **88**, 107 (1984).

Sb-terminated InAs(001)-(2×4) and (2×8) studied using scanning tunneling microscopy and *ab initio* density functional theory

William Barvosa-Carter,^{1,*} Frank Grosse,^{1,2} James H.G. Owen,^{1,2,*} and Jennifer J. Zinck¹

¹HRL Laboratories, LLC, 3011 Malibu Canyon Road, Malibu CA 90265

²UCLA Department of Mathematics, Los Angeles, CA

© 2001 HRL Laboratories, LLC. All Rights Reserved

ABSTRACT

We have studied the structure of MBE-grown InAs(001)-(2×4) surfaces exposed to low Sb₂ fluxes by scanning tunneling microscopy (STM) and *ab initio* density functional theory (DFT). Experimentally, we observe an Sb-terminated $\alpha 2(2 \times 4)$ phase over a wide range of temperatures (400-510 °C) for low Sb₂ flux (<0.1 ML/s), whereas temperature and As₂ flux must be carefully controlled to achieve the same As-terminated surface structure. At lower temperatures, we observe indications of an Sb-terminated (2×8) symmetry surface phase, and we report briefly on its proposed structure and stability, as well as its possible role in subsequent formation of the Sb-terminated (1×3) phase found at typical Sb₂ fluxes used during heterostructure growth.

INTRODUCTION

The nearly lattice-matched 6.1Å system of III-V semiconductor materials (InAs, GaSb, and AlSb) is being investigated for use in a wide variety of novel optoelectronic and high-speed quantum devices. All of these devices incorporate very thin layers, and as a consequence, the interfaces between the constituent materials can have a disproportionate impact on device performance. Recent studies by Noshro *et al.* [1] have highlighted the need for understanding surface reconstructions and their effect on interface formation. For instance, during typical InSb-like interface formation between an AlSb or GaSb layer on an InAs layer, the transition between the (2×4) surface of the InAs and the (1×3)-like surface that results after Sb exposure can lead to monolayer-height interface roughness unless the stoichiometry between the two phases is taken into account. Even during heteroepitaxy involving GaSb and AlSb, reconstruction transitions may lead to undesirable roughness at heterostructure interfaces.[2] Hence, knowledge of surface structure under varying conditions of temperature and flux can be a valuable aid to a device grower in devising interface preparation techniques for tailored interface roughness.

In this work, we seek to extend the studies of Noshro *et al.* into the low Sb flux regime to more fully explore the stable and metastable Sb-on-InAs phases, their structure, and implications for interface formation. We find that at the lowest Sb fluxes, an $\alpha 2(2 \times 4)$ phase is present and stable on the surface up to 510°C. The desorption rate of Sb from this surface is exceedingly slow, and surfaces can be stabilized for long periods of time at lower temperatures < 480°C. As the substrate temperature is decreased, a (2×8) structure appears that apparently incorporates multiple layers of Sb and appears structurally identical to that found on GaAs. At higher Sb₂ fluxes and substrate temperatures, such as might be used for typical device growth, ($F_{Sb_2} > 1-2$ ML/s) the surface transitions fully to a (1×3)-like phase, in agreement with previous observations. At low temperatures and intermediate fluxes, the surface is comprised of a mixture of (2×4) (2×8) and (1×3) structures. Given the progression of structures with

increasing Sb flux, and their arrangement on mixed-phase surfaces, we propose a simple mechanism for formation of the (1x3)-like surface during typical interface formation techniques used in the MBE growth of InAs/III-Sb structures.

EXPERIMENT

The surfaces we report in this paper were prepared using a VG 80H MBE chamber, starting with unintentionally doped, 0.5 to 1 μm thick InAs buffer layers grown on nominally 0.05° miscut n-type (undoped) InAs(001) substrates at 470°C . As_2 flux rates were measured using the uptake method[3,4] on InAs. Sb_2 flux rates were estimated by the threshold flux needed to stabilize III-Sb growth. After various surface treatments, as described in the text, samples were quenched by simultaneously cutting the substrate heater power, shuttering all sources, rotating the sample towards the cryopanel, followed by rapid removal of the substrate from the chamber. The samples were then transferred *in vacuo* to a connected UHV chamber containing a full-wafer Omicron STM [5] where they are placed in contact with a cold metal block. After ~ 30 minutes, STM images can be acquired with little thermal drift. All filled- and empty-states STM images were acquired in constant current mode using bias voltages between 1.1 and 3.0 V and tunneling currents between 0.03 and 0.2 nA.

RESULTS AND DISCUSSION

In figure 1, we present the structure of the InAs surface at 470°C stabilized by an Sb_2 flux of ~ 0.1 ML/s. The surface prior to quench is apparently well ordered in the RHEED pattern, and this is reflected in the surface structure observed by STM. Interestingly, while the rows are well ordered in the 2x and x4 directions, there is disorder within each unit cell. From a high-resolution image of this structure, shown in figure 2, we observe that the structural units along the rows appear nearly identical to those observed on As-terminated InAs surfaces. In particular, the dominant reconstructed unit on the surface

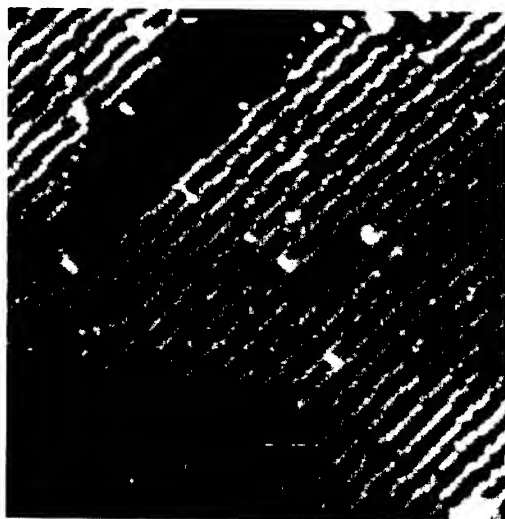


Figure 1. Structure of the surface after exposure to an Sb_2 flux of 0.1 ML/s at 470°C . Image is $50\text{nm} \times 50\text{nm}$, filled states.

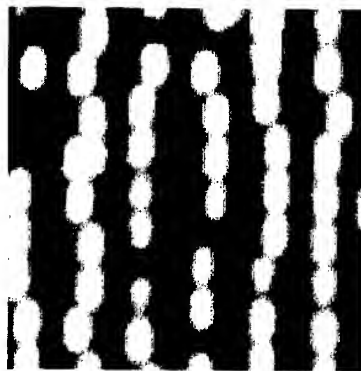


Figure 2. Higher resolution filled-states image of the $\alpha 2(2 \times 4)$ structure formed when exposing InAs(001) to Sb_2 flux.

appears to have the $\alpha 2-(2 \times 4)$ structure. Shown schematically in figure 3, the structure consists of a single Sb dimer atop a row of 3 In atoms, with a trench between each row. The In atoms at the edge of the row rebond with In atoms supporting the top As dimer. The trench dimer is also replaced with Sb. Theoretically, we find this structure to be the most stable relative to a number of other candidate structures[6].

While there are clear similarities in the structure of the unit cell between As- and Sb-terminated (2×4) surfaces, some differences emerge as well. For instance, the longer-range structure of the surface also changes dramatically. For comparison, in figure 4 we present an As-terminated $\alpha 2-(2 \times 4)$ surface, prepared by annealing an InAs(001) surface at 420°C for 20 minutes under an As₂ flux of 0.01 ML/s. Details concerning the surface phases and associated structures (e.g. the ad-

structures clearly visible atop the rows in figure 3) can be found in a forthcoming publication [7]. Briefly, on As-terminated $\alpha 2-(2 \times 4)$ surfaces, the surface structure can be characterized by a large density of point and extended, island-like defects. Additionally, many defects in the dimer rows themselves are apparent, including vacancies and occasional $\beta 2-(2 \times 4)$ reconstructed units. When the surface is converted to an Sb-

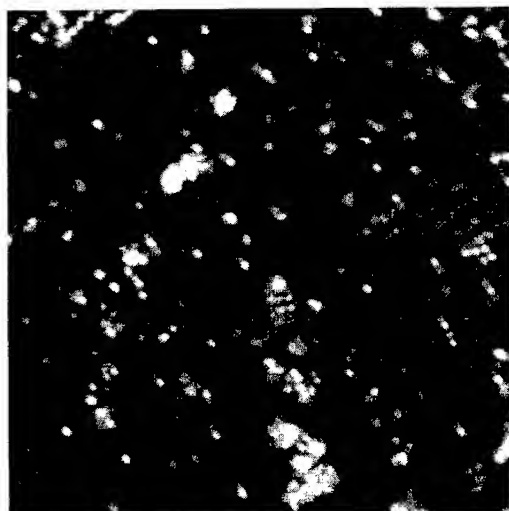


Figure 4. Structure of the InAs(001) $\alpha 2-(2 \times 4)$ surface after annealing under a flux of 0.01 ML/s at 420°C. Image is 50nmx50nm, filled states.

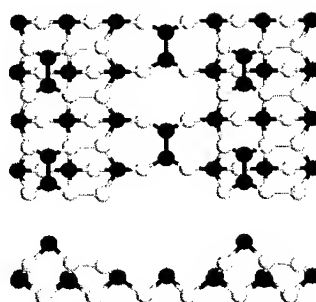


Fig. 3. Ball-and-stick model of the Sb-terminated $\alpha 2-(2 \times 4)$ structure. White balls represent In, grey balls represent As, and black balls represent Sb dimers.

terminated $\alpha 2-(2 \times 4)$, the surface appears much "cleaner" than the As-terminated surface. Additionally, we find an extremely small density of $\beta 2-(2 \times 4)$ reconstructed units – one of the few observed $\beta 2$ units can be seen in the middle left hand side of figure 2(a). This may possibly indicate that the $\beta 2-(2 \times 4)$ structure is destabilized when the As terminated InAs(001) surface is exposed to Sb.

At higher Sb fluxes (>1 ML/s) at 470°C we find that the surface makes a transition to a (1×3) structure, as measured by RHEED, in agreement with prior observations.[1] Unlike the case of Sb on GaAs(001) [8] we find no evidence in RHEED that any intermediate phases form at these temperatures. However, we find at



Fig 5: Surface after cooling to 350°C under an Sb_2 flux of ~ 0.1 ML/sec. Filled states image, 50nm \times 50nm.

lower temperatures that an additional surface structure can form which has a (2 \times 8) symmetry. Practically speaking, it is difficult to fully stabilize the surface at typical growth temperatures (420-470°C) in the (2 \times 8) structure – only at lower temperatures does this appear to be possible.

In figure 5 we show an STM image of a surface that was cooled from 470°C to 350°C with an Sb_2 flux of ~ 0.3 ML/s. As judged from the symmetry of the surface as measured by RHEED, the $\alpha 2$ -(2 \times 4) structure is maintained until $\sim 400^\circ\text{C}$, below which temperature $\times 8$ diffraction spots gradually emerge until 350°C where they appear to saturate in intensity. This observation indicates that the (2 \times 8) structure may not in fact be a thermodynamically stable structure,

but is instead metastable. Another possibility is that entropic stabilization of energetically similar structures, like the $\alpha 2$ -(2 \times 4) and (1 \times 3)-like, may squeeze out the (2 \times 8) region of stability at higher temperatures.

From the arrangement of the $\alpha 2$ -(2 \times 4) and (2 \times 8) structural units on the surface, we postulate a plausible structure and formation mechanism for the (2 \times 8) phase. We suggest a simple structure for this phase, shown in figure 6. The structure is an extension of the $\alpha 2$ -(2 \times 4) phase, with the trench between neighboring $\alpha 2$ -(2 \times 4) units

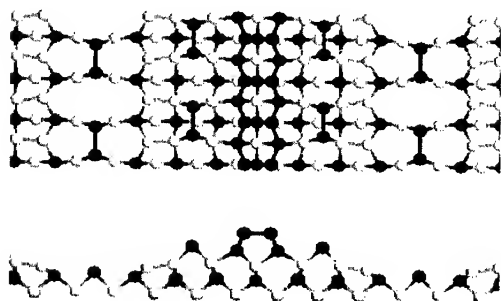


Figure 6. Proposed structure of the (2 \times 8) surface phase. White balls represent In atoms, light grey represent As atoms, and dark balls represent Sb atoms and dimers.

being filled with In, and the whole structure capped by a double layer of Sb. The structure fulfills electron-counting rules. Our structure is significantly different from the structure proposed by Whitman *et al.* [8] for Sb-on-GaAs-(2 \times 8), which incorporated Sb_{In} antisite defects, no rebonded $\alpha 2$ -like In atoms, and no trench dimer. Additionally, their structure is *asymmetric* with respect to the centerline of the unit cell, a quality that does not appear to be present in our images of this structure.

We have tested the stability of both our proposed structure and that proposed by Whitman *et al.* using

density functional theory (DFT). The DFT calculations were carried out using the FHI98MD simulation package [9] within the local density approximation using norm-conserving pseudopotentials [10]. The electronic wave functions were expanded in a plane wave basis that was truncated at a cutoff energy of 12 Ry. The equivalent of 8x8 k-points in a 1x1 unit cell were used for k-point summation, generated using the scheme proposed by Monkhorst and Pack [11].

We find that our proposed structure is more stable. This is perhaps not surprising – our proposed structure incorporates only structural motifs from known stable phases. The edges and trench of the structure are identical to those found in $\alpha 2$ -(2x4). The top of the structure, involving multiple layers of Sb, is qualitatively similar to the multilayer Sb reconstructions of the III-Sb's [12]. Additionally, while electron counting is fulfilled for both structures, Sb_{in} defects can involve a significantly higher energy cost.

At still higher Sb₂ fluxes, we begin to observe the formation of the (1x3)-like surface observed by Noshio *et al.* [1]. In figure 7, we show STM of a surface, stabilized initially at an Sb flux of ~0.1 ML/s at 490°C, and then cooled to 350°C where the surface was exposed to a higher Sb flux (~0.5 ML/s) for 10 minutes. The resulting surface clearly has $\alpha 2$ -(2x4), (2x8), and (1x3)-like structures present. There is an additional disordered structure, labeled "a" on the figure, which appears to be lower topologically than neighboring (2x4) structures, which may represent areas of the surface where In atoms have been removed for incorporation into neighboring (2x8) and (1x3)-like regions of the surface. As the In atoms in the $\alpha 2$ -(2x4) structure are removed, the underlying As is exposed. Ideally these regions can form a quasi (1x3)-like structure with Sb capping the As exposed by the departing In. In this manner, these regions would evolve into (1x3)-like regions that are topologically 1 ML lower than nearby (1x3) "islands". Subsequent desorption of top Sb and buried As dimers, followed by recapping with Sb dimers may allow these areas to eventually obtain the "ideal" multilayer Sb (1x3) or (4x3)-like surface structure.

Given the arrangement of these various structures on the mixed-phase surface in figure 7, we propose a simple mechanism for formation of the (1x3)-like surface. At typical growth temperatures, the desorption rate of As is much greater than Sb, leading to rapid conversion of the initial As-terminated (2x4) surface to an Sb-terminated $\alpha 2$ -(2x4) phase. Once formed, there may be a high driving force for incorporation and

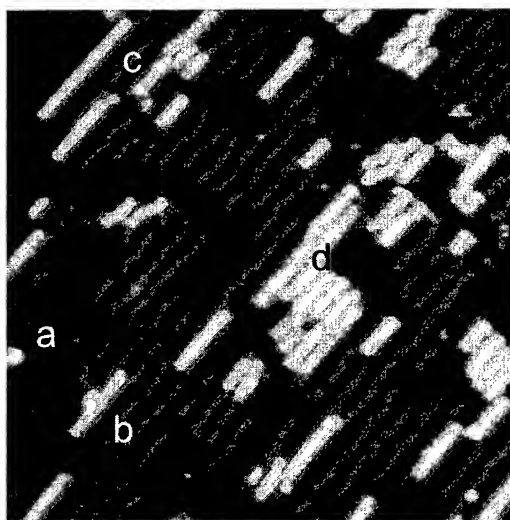


Figure 7. Surface structure after exposure to 10s Sb₂ at 350°C. All major surface phases are present: (a) disordered 1st layer, (b) $\alpha 2$ -(2x4), (c) (2x8)-like structures and (d) 2nd layer (1x3). Image is filled states, 50nm x 50nm.

capping of In adatoms by adsorbing Sb-dimers between two $\alpha 2$ rows. Once a sufficient number of In atoms are capped between these two $\alpha 2$ rows, such an arrangement is nearly identical to the (2x8) structure shown figure 6. As shown in figure 7, there do not appear to be any neighboring (2x8) units on the surface. Therefore, we speculate that once two neighboring (2x8) units are formed, the top layer Sb might either be much more mobile, or have a higher desorption rate, enabling reorganization of this layer to form the (1x3) structure. Hence, although apparently not stable as a *surface phase* at higher temperatures, it is possible that (2x8)-like structures may mediate the transition from As-terminated InAs (2x4) surface to the (1x3)-like Sb-terminated surface during typical interface formation techniques used in the MBE growth of InAs/III-Sb structures.

CONCLUSIONS

At low Sb_2 fluxes, ~ 0.1 ML/s, we find that an $\alpha 2$ -(2x4) phase is present and stable on the InAs(001) surface up to $\sim 510^\circ\text{C}$. As the substrate temperature is decreased, a (2x8) structure appears. At low temperatures and intermediate fluxes, we observe a surface comprised of a mixture of (2x4) (2x8) and (1x3) structures. The arrangement of these structures on the surface, along with our proposed structure for the (2x8), leads us to propose a simple mechanism for formation of the (1x3)-like surface during typical interface formation techniques used in the MBE growth of InAs/III-Sb structures. By tailoring the starting surface for interface formation (for instance, instead of a (1x3), use the (2x8) or the $\alpha 2$) it may be possible to advantageously change the resulting distribution of group III and group V atoms at a heterostructure interface.

+ email: wbc@hrl.com

* Present address: Electrochemical laboratories, Tsukuba Japan

Acknowledgements: This work is supported by NSF and DARPA through the Virtual Integrated Prototyping Initiative and the NSF Industrial Postdoc Program.

REFERENCES

- [1] B.Z. Noshov, W.H. Weinberg, W. Barvosa-Carter, B.R. Bennett, B.V. Shanabrook, and L.J. Whitman, *Appl. Phys. Lett.* **74** 1704 (1999).
- [2] A.S. Bracker, B.Z. Noshov, W. Barvosa-Carter, L.J. Whitman, B.R. Bennett, B.V. Shanabrook, J.C. Culbertson, *Appl. Phys. Lett.* **78** 2440 (2001).
- [3] J.H. Neave, B.A. Joyce, P.J. Dobson, *Appl. Phys. A* **34** 179 (1984).
- [4] B.F. Lewis, R. Fernandez, A. Madukhar, F.J. Grunthaner, *JVST B.* **4** 560 (1986).
- [5] J.H.G. Owen, W. Barvosa-Carter, J.J. Zinck, *Appl. Phys. Lett.* **76** 3070 (2000).
- [6] W. Barvosa-Carter, F. Grosse, J.H.G. Owen, and J.J. Zinck, *unpublished*.
- [7] W. Barvosa-Carter, R.S. Ross, C. Ratsch, F. Grosse, J.H.G. Owen, J.J. Zinck, *forthcoming in Surf. Sci. Lett.* (2001).
- [8] L. Whitman, B.R. Bennett, E.M. Kneedler, B.T. Jonker, B.V. Shanabrook, *Surf. Sci. Lett.* **436** L707 (1999).
- [9] M. Bockstedte, A. Kley, J. Neugebauer, and M. Scheffler, *Comp. Phys. Comm.* **107** 187 (1997).
- [10] M. Fuchs and M. Scheffler, *Comp. Phys. Comm.* **119** 805 (1999).
- [11] H.J. Monkhorst and J.D. Pack *Phys. Rev. B* **13** 5188 (1976).
- [12] W. Barvosa-Carter, A.S. Bracker, J.C. Culbertson, B.Z. Noshov, B.V. Shanabrook, L.J. Whitman, *Phys. Rev. Lett.* **84** 4649 (2000).

Effect of Marangoni Convection on InSb Single Crystal Growth by Horizontal Bridgman Method

K. Kodera¹, A. Kinoshita¹, K. Arafune², Y. Nakae¹, and A. Hirata¹

¹ Department of Chemical Engineering, Waseda University,
Okubo 3-4-1, Shinjuku-ku, Tokyo, 169-8555, Japan

² Research Institute of Electronics, Shizuoka Univ., Hamamatsu, Shizuoka 432, JAPAN

ABSTRACT

It is necessary to clarify the effect of Marangoni convection on single crystal growth from a melt in order to improve the quality of the grown crystal. Particularly, the deviation of crystal-melt (C-M) interface from a planar shape is a major problem because it may deteriorate the quality of the grown crystal. In this paper, we investigated the effect of thermal and solutal Marangoni convection on C-M interface shape in an In-Sb binary system by the horizontal Bridgman (HB) method. The C-M interface concavity strongly depends on the cooling rate and the temperature gradient under uniform concentration distribution conditions in the melt. A large concavity was observed at low cooling rates and high temperature gradient conditions. The concavity was found to be caused by thermal Marangoni convection, by taking Péclet number into account. Then, we varied the composition of the In-Sb binary system to induce solutal Marangoni convection intentionally. The C-M interface was kept planar in case solutal Marangoni convection occurred in the direction opposite to the thermal one. Therefore, we believe that the utilization of solutal Marangoni convection will be a new control technique to make the C-M interface planar for the HB system. From these results, it was clarified that Marangoni convection plays a significant role in the HB crystal growth system.

INTRODUCTION

At present, most of the semiconductor bulk crystals are grown by melt growth methods such as the Czochralski (CZ) or the horizontal Bridgman (HB) method. During crystal growth by these methods, convection in melt affects the quality of the grown crystals. Therefore, it is necessary to clarify the mechanism of convection in melt and to control the convection to improve the quality of the crystal. The convection can be divided into buoyancy convection and Marangoni convection. The driving force of the former is the buoyancy difference in the melt, and that of the latter is the surface tension difference on the free surface. The convection can also be divided into thermal and solutal convection because those driving forces vary with temperature and concentration. Particularly, thermal buoyancy convection has been extensively investigated since as early as the beginning of the 20th century [1]. On the other hand, the importance of Marangoni convection, which has nothing to do with gravity, was recognized after semiconductor crystal growth experiments were conducted under microgravity conditions in the 1980s [2]. Since then, Marangoni convection has been investigated by many researchers [3,4].

Regarding solutal convection, although solutal buoyancy convection has been studied as a double diffusive problem, solutal Marangoni convection had not been studied so far. Therefore, we performed some experiments to measure surface velocities caused by buoyancy convection

and Marangoni convection using a rectangular boat with a free surface. Consequently, we found that the surface velocities of solutal Marangoni convection are approximately 3-5 times higher than those of thermal Marangoni convection [5]. Moreover, in the case of coexistence of thermal and solutal Marangoni convection, solutal Marangoni convection was found to be dominant in the surface flow, and the flow direction could be opposite to that without solutal convection [6]. Also, we carried out parabolic flight experiments and found that Marangoni convection is dominant in the surface flow in case both buoyancy convection and Marangoni convection coexist [6]. From these results, we demonstrated that Marangoni convection, especially solutal Marangoni convection, is significant in a rectangular boat such as that used in the HB method. As one effect of Marangoni convection on the grown crystals, the change of C-M interface shape is often discussed. The deviation of the C-M interface shape from a planar one is a major problem because it is assumed to lower the quality of the grown crystals. Using the HB method, Lan et al. clarified numerically [7] and experimentally [8] that the effect of Marangoni convection on C-M interface shape is significant.

In this study, we performed InSb crystal growth experiments by the HB method to investigate the effects of thermal and solutal Marangoni convection on C-M interface shape. We varied the composition of the In-Sb binary system to induce solutal Marangoni convection intentionally in addition to thermal Marangoni convection. Based on the results, we suggested a simple way of controlling C-M interface shape.

EXPERIMENT

Concept of experiment

First, we discuss the interaction between thermal and solutal Marangoni convection. As described in the Introduction, Marangoni convection is induced by surface tension difference due to the difference of temperature or concentration on a free surface. In our previous study [6], it was clarified that the flow pattern of Marangoni convection could be divided into three cases as follows. Here, x denotes the composition of Sb in the In-Sb binary system ($\text{In}_{1-x}\text{Sb}_x$).

(a) Normal case ($x=0.5$)

In this case, there is no concentration difference in the melt. Flow of thermal Marangoni convection is induced in the direction shown in figure 1(a). This is because surface tension σ near the C-M interface is larger than that at the bulk of the melt.

(b) Acceleration case ($0 < x < 0.5$)

Thermal Marangoni convection is induced in the same direction as (a). When crystal growth proceeds, concentration of Indium C_{In} near the C-M interface becomes higher than that at the bulk of the melt. Because it is known that σ_{In} is larger than σ_{Sb} , surface tension near the C-M interface is larger than that at the bulk of the melt. This causes solutal Marangoni convection. Therefore, the flow direction of solutal convection is the same as that of thermal Marangoni convection.

(c) Deceleration case ($0.5 < x < 0.68$)

On the other hand, because C_{In} near the C-M interface becomes lower than that at the bulk of the melt, surface tension at the bulk of the melt becomes larger than that near the C-M interface. Therefore, the flow of solutal Marangoni convection is induced in the direction opposite to that of thermal Marangoni convection. Because it was clear that solutal Marangoni convection is stronger than thermal Marangoni convection [5], the flow direction becomes opposite to that without considering solutal Marangoni convection.

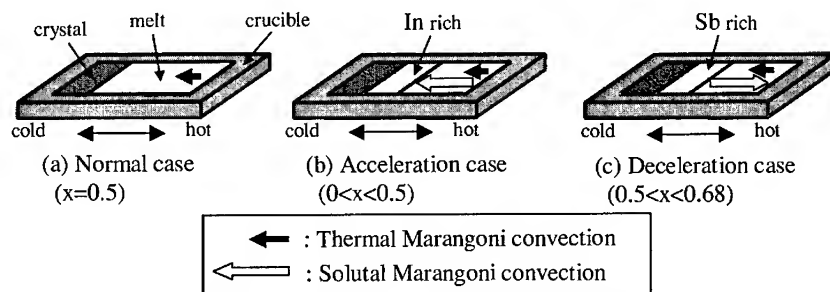


Figure 1. Flow pattern by interaction between thermal and solutal Marangoni convection

Experimental procedure

To avoid contamination and formation of metal oxide film on the free surface of the melt, special precautions were taken. In preparing the test sample, $\text{In}_{1-x}\text{Sb}_x$, In and Sb (5N, manufactured by Dowa Mining) were mixed at the desired ratio, and the mixture was dissolved and quenched in an oxygen reducing atmosphere ($\text{Ar}97\%+\text{H}_23\%$). Then, chemical etching of the test sample was carried out. Moreover, a carbon crucible was baked for degassing. Figure 2 shows the cross section of the carbon crucible. The test sample was set in the reservoir tank, and InSb, which has a length of approximately 10mm, was also set at the cold side of the observation part as a seed crystal. After heating the crucible and the reservoir tank, the melted sample flowed into the observation part through a small hole and contacted with the seed crystal. The small hole prevents efflux of the remaining metal oxides in the sample. The experimental system is shown in figure 3. The temperatures of the hot side, T_H , the cold side, T_C , and the middle of the crucible, T_M were controlled by PID temperature controllers and power controllers. The temperature difference between T_H and T_C , and cooling rates of T_H , T_M , and T_C were kept constant as shown in table 1. To reduce buoyancy convection, we used a shallow crucible. The length, width and depth of the cavity of the crucible were 48, 10, and 5 mm, respectively. The test sample was solidified unidirectionally in the crucible. C-M interface shape was observed by means of a 3-CCD video camera. C-M interface shape was evaluated in terms of the degree of concavity (figure 4).

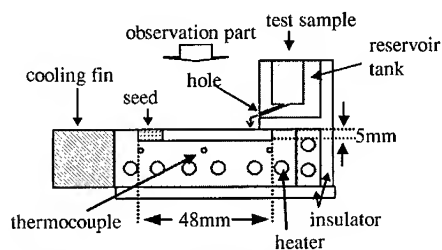


Figure 2. Cross section of the carbon crucible

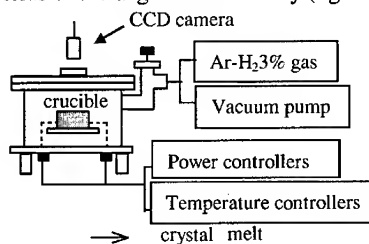


Figure 3. Experimental system

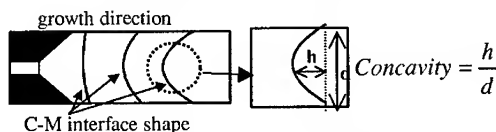


Figure 4. Top view of C-M interface shape

RESULTS AND DISCUSSION

We varied the control parameters such as cooling rate, temperature gradient, and composition of In-Sb in the experiments. The experimental conditions are shown in table 1. Figure 5 shows concavity as a function of L_c/L_0 at various cooling rates with the same temperature gradient of 14.1°C/cm . Here, L_c and L_0 denote the length of the crystal during growth, and the total crystal length after growth, respectively. Concavity increased as the growth proceeded, and then saturated at an L_c/L_0 of 0.5. Moreover, the C-M interface

concavity obtained after the growth at low cooling rates was larger than that at high cooling rates. This is because long-term exposure to thermal Marangoni convection at low cooling rates resulted in the increase of the erosion of the C-M interface. Figure 6 shows concavity as a function of temperature gradient. The temperature gradient was varied from 8.4 to 14.1°C/cm at the same cooling rate of -5°C/h . The concavity was found to depend strongly on the temperature gradient. Although in figure 5, the concavity under the temperature gradient of -5°C/h was approximately 0.55 , the concavity was kept 0 at 8.4°C/cm even if the cooling rate was -5°C/h in figure 6. The low temperature gradient indicates that thermal Marangoni convection is weak. From figures 5 and 6, there seems to be a strong correlation between driving force of Marangoni convection and C-M interface shape.

Table 1. Experimental conditions

Run No.	Cooling rate [$^\circ\text{C/h}$]	Temperature gradient [$^\circ\text{C/cm}$]	Composition x of In1-xSbx
1	-5	14.1	0.5
2	-11.7	14.1	0.5
3	-16.7	14.1	0.5
4	-19.7	14.1	0.5
5	-5	11.9	0.5
6	-5	8.4	0.5
7	-16.7	14.1	0.4
8	-16.7	14.1	0.6

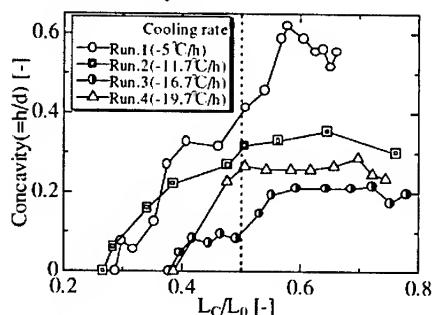


Figure 5. Concavity as a function of L_c/L_0 . The dashed line indicates the saturation point of an increase of concavity.

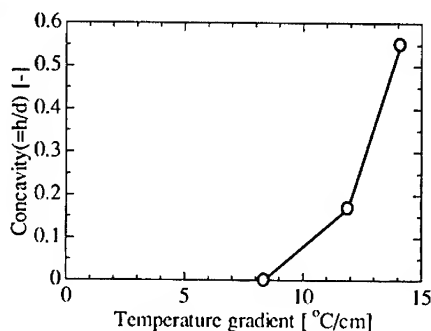


Figure 6. Concavity as a function of temperature gradient

In order to confirm this correlation, we determined Marangoni number (Ma) from temperature profiles and C-M interface position. Ma represents the driving force of Marangoni convection. Ma is defined by eq.(1).

$$Ma = \frac{\left| \frac{\partial \sigma}{\partial T} \right| \Delta T L_m}{\mu \nu} \quad \text{eq.(1)}$$

In our previous study [9], we found a relationship between Ma , Pr , and Re , as shown in eq.(2).

$$Re = 0.28 \cdot (Ma Pr^{-1/2})^{2/3} \quad \text{eq.(2)}$$

Here, Re (Reynolds number) and Pr (Prandtl number) represent flow state of fluids and heat transport phenomena, respectively. Pr is defined by eq.(3).

$$Pr = \frac{\nu}{\alpha} \quad \text{eq.(3)}$$

From eqs.(1), (2), and (3), we were able to estimate Re . After estimation of Re , we determined Péclet number (Pe) using eq.(4).

$$Pe = Pr \cdot Re \quad \text{eq.(4)}$$

Pe indicates whether convection or conduction dominates the heat transport phenomena. Therefore, Pe indicates the effect of Marangoni convection on the heat transfer through the C-M interface.

Figure 7 shows the calculated Pe as a function of L_C/L_0 . Pe decreased gradually as growth proceeded up to an L_C/L_0 of 0.5, and then abruptly decreased thereafter. In other words, the effect of thermal Marangoni convection on the heat transfer decreased abruptly at $L_C/L_0 = 0.5$. This value agrees with the saturation point of the increase of concavity shown in figure 5. From these results, it was clarified that concavity is mainly due to Marangoni convection.

As a simple way to keep C-M interface planar, we suggest that the Marangoni convection be restrained. The flow direction may be opposite to that of the normal case in the presence of solutal Marangoni convection, as reported in our previous study [6]. Therefore, we varied the composition of the In-Sb binary system to induce solutal Marangoni convection intentionally in addition to thermal Marangoni convection. Figure 8 shows the concavity as a function of L_C/L_0 . Although the increase of concavity in the case of $x=0.4$ was larger than that in the case of $x=0.5$, increase in the case of $x=0.6$ was much smaller than that in the case of $x=0.5$. This is because flow velocity was accelerated in the case of $x=0.4$ and decelerated in the case of $x=0.6$. Moreover, we could keep the C-M interface planar in the case of $x=0.6$. From these results, we found that we can keep a planar interface by inducing solutal Marangoni convection intentionally in the direction opposite to that of thermal Marangoni convection.

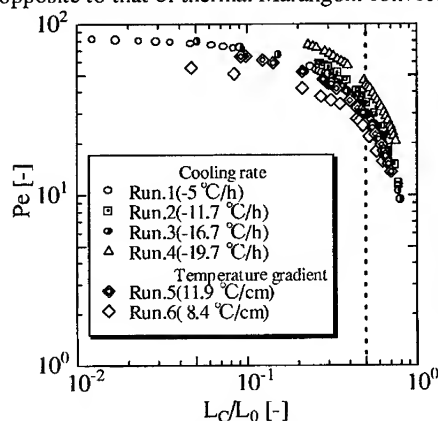


Figure 7. Pe as a function of L_C/L_0

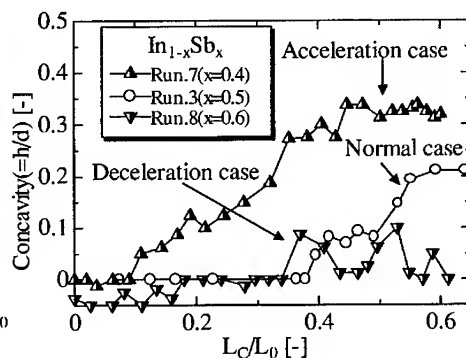


Figure 8. Concavity as a function of L_C/L_0

CONCLUSIONS

We investigated the effect of thermal and solutal Marangoni convection on crystal-melt (C-M) interface shape in the In-Sb binary system by the horizontal Bridgman (HB) method. The C-M interface concavity strongly depends on the cooling rate and the temperature gradient under uniform concentration distribution conditions in the melt. A large concavity was observed at low cooling rates and high temperature gradient conditions. The concavity was found to be due to thermal Marangoni convection, taking Péclet number into account. We varied the composition of the In-Sb binary system to induce solutal Marangoni convection intentionally. The C-M interface remained planar when solutal Marangoni convection occurred in the direction opposite to the thermal one. Therefore, we believe that the utilization of solutal Marangoni convection will be a new technique to control the planarity of the C-M interface in the HB system. From these results, it was clarified that Marangoni convection plays a significant role in the HB crystal growth system.

NOMENCLATURE

C_{In}	: concentration of Indium [at%]	Greek	
L_0	: total length of crystal [m]	ΔT	: temperature difference [K]
L_c	: length of crystal during growth [m]	α	: heat diffusion coefficient [m^2s^{-1}]
L_m	: length of melt [m]	ν	: kinematic viscosity [m^2s^{-1}]
Ma	: Marangoni number [-]	μ	: viscosity [$kgm^{-1}s^{-1}$]
Pe	: Péclet number [-]	ρ	: density [kgm^{-3}]
Pr	: Prandtl number [-]	σ	: surface tension [$kg s^{-2}$]
Re	: Reynolds number [-]	σ_{In}	: surface tension of Indium [$kg s^{-2}$]
T	: temperature [$^{\circ}C$]	σ_{Sb}	: surface tension of Antimony [$kg s^{-2}$]
T_c	: temperature at the cold side [$^{\circ}C$]	$\partial\sigma/\partial T$: temperature gradient of surface tension [$kg s^{-2}K^{-1}$]
T_{Hl}	: temperature at the hot side [$^{\circ}C$]		
T_M	: temperature at the middle of the crucible [$^{\circ}C$]		
h	: deviation of crystal-melt interface [m]		
d	: width of melt [m]		

REFERENCES

1. Rayleigh, Lord, *Phil. Mag.*, **32**, 529-546 (1916)
2. A. Eyer, H. Leist, and R. Nitsche, *J. Crystal Growth*, **71**, 173-182 (1985)
3. D. Schwabe, and J. Metzger, *J. Crystal Growth*, **97**, 23-33 (1989)
4. Y. L. Yao, F. Liu, and W. R. Hu, *Int. J. Heat Mass Transfer*, **39**, 2539-2544 (1996)
5. K. Arafune, and A. Hirata, *J. Crystal Growth*, **197**, 811-817 (1999)
6. K. Arafune, K. Yamamoto, and A. Hirata, *Int. J. Heat Mass Transfer*, **44**(13), 2405-2411 (2001)
7. M. C. Liang, C. W. Lan, *J. Crystal Growth*, **180**, 587-596 (1997)
8. C. W. Lan, M.C. Su, M.C. Liang, *J. Crystal Growth*, **208**, 717-725 (2000)
9. K. Arafune, M. Sugiura, and A. Hirata, *J. Chem. Eng. Japan*, **32**, 104-109 (1999)

Asymmetric Hybrid Al(Ga)SbAs/InAs/Cd(Mg)Se Heterostructures for Mid-IR LEDS and Lasers

S.V. Ivanov, V.A. Kaygorodov, V.A. Solov'ev, E.V. Ivanov, K.D. Moiseev, S.V. Sorokin, B.Ya. Meltzer, A.N. Semenov, M.P. Mikhailova, Yu.P. Yakovlev and P.S. Kop'ev
Ioffe Physico-Technical Institute of RAS, Politekhnikeskaya 26, St. Petersburg 194021, Russia

ABSTRACT

A hybrid double heterostructure with large asymmetric band offsets, combining AlAsSb/InAs (as a III-V part) and CdMgSe/CdSe (as a II-VI part), has been proposed as a basic element of a mid-infrared laser structure design. The p-i-n diode structure has been successfully grown by molecular beam epitaxy (MBE) and exhibited an intense long-wavelength electroluminescence at 3.12 μm (300K). A II-VI MBE growth initiation with a thin ZnTe buffer layer prior to the CdMgSe deposition results in a dramatic reduction of defect density originating at the II-VI/III-V interface, as demonstrated by transmission electron microscopy. A less than 10 times reduction of electroluminescence intensity from 77 to 300K indicates an efficient carrier confinement in the InAs active layer due to high potential barriers in conduction and valence bands, estimated as $\Delta E_c = 1.28$ eV and $\Delta E_v \sim 1.6$ eV. An increase in the pumping current results in a super-linear raising the EL intensity. The type of band line up at the coherent InAs/Cd_{1-x}Mg_xSe interface is discussed for $0 \leq x \leq 0.2$, using experimental data and theoretical estimations within a model-solid theory.

INTRODUCTION

Fabrication of room temperature cw semiconductor laser diodes for the 3-5 μm spectral range is still a big challenge. A hole leakage from an active region of pure III-V laser structures due to the particular valence band line up of InAs usually used in the active region may hamper the achievement of a low threshold current and a high output power [1].

To solve the problem of efficient hole confinement in InAs, taking a benefit of type I and type II band alignment, we have proposed a hybrid III-V/II-VI double heterostructure with large asymmetric band offsets in conduction (AlAsSb/InAs) and valence (InAs/CdMgSe) bands, as a basic element of a new mid-IR laser structure design [2]. In this case AlAsSb and CdMgSe form a strong type II heterojunction, while InAs layer interfaces are of type I, that leads, on the one hand, to high optical gain and quantum efficiency like in conventional type I double heterostructure lasers and, on the other hand, to significant suppression of both electron and hole leakage from the active region. The important feature of the proposed structure that it can be grown pseudomorphical as a whole because both AlAsSb and CdMgSe are lattice-matched to the InAs at appropriate ternary alloy compositions. An improvement of the structural quality is shown to be achieved by growing a thin ZnTe buffer layer at the III-V/II-VI interface.

EXPERIMENTAL DETAILS

The III-V part of the hybrid structures was grown by molecular beam epitaxy (MBE) in a Riber 32 chamber on a p⁺-InAs (100) substrate at temperature $T_s = 480^\circ\text{C}$. It consists of a 0.1 μm

thick p⁺-InAs:Be buffer layer, a 1 μm thick p-AlGaAsSb:Si layer followed by a 20 nm thick p-AlAsSb:Si barrier and an undoped 0.6 μm -InAs layer ($n < 10^{17} \text{ cm}^{-3}$). Thereafter, the III-V structure was transported to a separate II-VI home-made MBE chamber through air under an As cap which then was removed by annealing the sample at T_s in the 460-480°C range. A reflection high-energy electron diffraction (RHEED) system was used to monitor surface conditions. Due to the relatively high annealing temperature an intermediate $(2\times 4)\text{As}\&(4\times 2)\text{In}$ surface reconstruction has been usually obtained. Two types of growth initiation procedure at the III-V/II-VI heterointerfaces were used. At the first one, a 10 nm thick CdMgSe layer was grown in a migration enhanced epitaxy (MEE) mode at $\sim 200^\circ\text{C}$ to reduce the defects density on the InAs/CdSe interface [3], which usually resulted in a streaky RHEED patterns. The deposition times of Cd and Mg were chosen to provide desirable alloy composition. At the other, $T_s=280^\circ\text{C}$ was kept constant from the very beginning of II-VI growth which was initiated with a deposition of a ~ 5 nm thick ZnTe buffer in the MBE mode, as was proposed by Grabs et al. [4]. The growth of the following CdMgSe structure occurred at 280°C in the MBE mode under the $(2\times 1)\text{Se}$ -stabilized conditions. It consists usually of 50 nm of nominally undoped CdMgSe followed by 0.3 μm of n-type CdMgSe:Cl and capped with 10-nm-CdSe:Cl. ZnCl_2 is used as the n-doping source in this case. The electron concentration in the CdMgSe is of $4\times 10^{17} \text{ cm}^{-3}$, as indicated by C-V measurements. The Mg mole fraction in the layers ranges within 15-17%, as it follows from x-ray diffraction (XRD) measurements confirming also a pseudomorphic nature of the II-VI layers, although the $\text{Cd}_{1-x}\text{Mg}_x\text{Se}$ composition lattice-matched to InAs corresponds to $x\sim 0.10$.

Previously, photoluminescence (PL) studies of the structures have been performed over a wide spectral range at 77K, using single-grating monochromators and different excitation sources for different spectral regions [5]. An InGaAs cw laser diode emitting at 950 nm was used to excite PL in the III-V part of the structure responsible for the emission in the infra-red spectral region, whereas a 325 nm line of a cw He-Cd laser was used to excite PL from the CdMgSe layer. The bright relatively narrow peaks at the energies of 0.41 eV and ~ 2.1 eV attributed to the near-band-edge recombination in InAs and CdMgSe layers, respectively, were observed in the PL spectra. The estimation of Mg content in the CdMgSe layer from the respective PL peak position [6] gives the value of $\sim 15\%$ that corresponds well to the XRD data.

For electroluminescence (EL) studies the mesa diodes of 300 μm diameter with a 50 μm round contact were fabricated using a standard photolithography and deep wet chemical etching. A liquid N_2 -cooled InSb photodetector and a lock-in amplifier were used for light detection. EL spectra were measured both under quasi-cw conditions with pulse duration of $\tau = 2.5$ ms and filling factor of 1/2 and in a pulsed mode with pulse duration $\tau = 1\text{-}10$ μs and a repetition rate $f = 10^3\text{-}10^4$ Hz.

RESULTS AND DISCUSSION

Cross-sectional transmission electron microscopy (TEM) images of the hybrid structures with the two different interface types are presented in Fig. 1. The structure with the InAs/CdSe interface (Fig. 1a) exhibits the stacking fault (SF) density in the $10^7\text{-}10^8 \text{ cm}^{-2}$ range, which is probably due to the not completely optimized initial surface reconstruction of InAs, allowing an In-Se interaction at the heterovalent InAs/CdSe interface formation. The formation enthalpy of In_2Se_3 , characterized by a defect sphalerite structure (-344 kJ/mole [7]) is even smaller than that of Ga_2Se_3 , making the probability of In_2Se_3 nucleation at the InAs/CdSe interface very high.

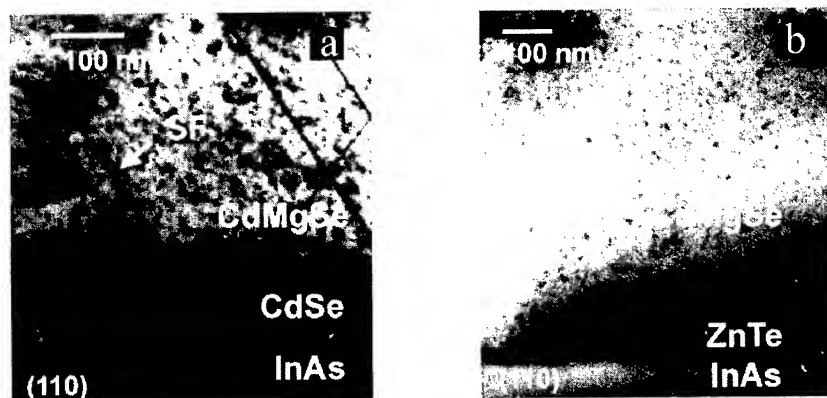


Figure 1. Cross-sectional dark-field TEM images of the hybrid structures: (a) with CdSe/InAs interface (\bar{g}_{400}) and (b) with the ZnTe buffer layer at the III-V/II-VI interface (\bar{g}_{200}). Electron beam is parallel to the [110] direction.

Lowering the temperature of As cap re-evaporation or growing an InAs buffer layer in a ultrahigh-vacuum-connected III-V MBE chamber is expected to prevent the InAs surface depletion of As, that should suppress the In-Se interaction. Contrary to that, the SF density in the structure with the ZnTe buffer layer (~ 5 nm), as illustrated in Fig. 1b, is at least two orders of magnitude lower (below 10^6 cm^{-2}), which is obviously explained by the ZnTe passivation of the InAs surface before a Cd(Mg)Se growth.

For EL studies the structures without the ZnTe buffer layer were used. Even in this case an intense electroluminescence has been observed at both 77 and 300K (Fig. 2a). The EL spectrum at 77K contains a single emission band with a photon energy maximum at 0.43 eV and a FWHM value of 40 meV. The emission band has a weakly asymmetric shape with the abrupt high-energy side. The room temperature EL spectrum contains also a single emission band with a photon energy maximum at 0.396 eV and $\text{FWHM} = 68$ meV, although the peak has a reverse asymmetry with a noticeable low-energy tail. The photon energy of the spontaneous EL slightly exceeds the InAs peak energy observed in the PL spectra perhaps due to high pumped carrier density.

The dependences of EL intensity on a drive current in a quasi-cw and pulse modes were studied both at low and room temperatures. The behavior of these dependences is similar, while more intense signal is achieved in a quasi-cw mode (Fig. 2b). The intensity of spontaneous emission at 77K increased superlinearly with the drive current rising. With the temperature increase from 77 to 300K, the maximum EL intensity decreases just by 7-10 times. This weaker temperature dependence of the spontaneous emission, as compared to that observed in conventional InAsSbP/InAs-based laser structures [8], evidences higher band offsets and better hole confinement in the hybrid structure.

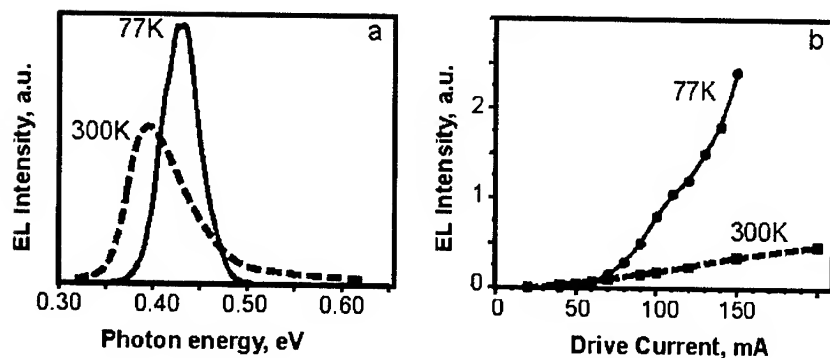


Figure 2. (a) EL spectra of the hybrid structure under quasi-cw conditions at 77K (solid curve) and 300K (dashed curve). (b) The EL intensity versus drive current in quasi-cw mode at 77K (solid curve) and 300K (dashed curve).

To estimate the band-offsets at the InAs/CdSe interface we used the known values for the CdSe-ZnSe, ZnSe-GaAs, GaAs-InAs hetero-pairs and also the "model-solid theory" of Van de Walle [9] to take into account the strain effect. As a result, type II band line-up for the InAs/CdSe interface has been obtained. InAs represents a ~ 60 meV potential barrier for electrons at the bottom of the CdSe conduction band, whereas the heavy hole band offset at the interface is as large as ~ 1.42 eV. An incorporation of a large enough content of Mg changes the situation at the InAs/CdMgSe interface from type II to type I. Our recent experimental studies of optical band bowing of the CdMgSe alloys as well as of the valence-to-conduction band offsets ratio [6] shows the conduction band offset between CdSe and $\text{Cd}_{0.9}\text{Mg}_{0.1}\text{Se}$ alloy lattice-matched to InAs as high as 150 meV, which results in the type I band alignment at the InAs/ $\text{Cd}_{0.9}\text{Mg}_{0.1}\text{Se}$ interface with $\Delta E_c \sim 90$ meV. Moreover, in the studied structures, with the Mg content in the CdMgSe layer of 15-17%, the peak energy of the CdMgSe PL band gives the CdSe/ $\text{Cd}_{0.85}\text{Mg}_{0.15}\text{Se}$ band gap difference about 350 meV. This leads to even higher band offsets as compared to those evaluated for the lattice-matched structure. Thus, the AlAsSb/InAs heterointerface with the well known $\Delta E_c = 1.28$ eV value and the InAs/CdMgSe heterointerface can readily prevent the electron and hole leakage from the InAs active layer.

To elucidate this point, comparative EL studies of the hybrid p-i-n structures with and without a 10nm-CdSe layer grown between InAs and CdMgSe layers have been carried out (samples B and A, respectively, in Fig. 3). Sample A shows the bright InAs related luminescence peak shifting to higher energies with increasing the pumping current. In contrast, sample B exhibits a 30 meV low energy shift of EL peak with respect to InAs one. Moreover, one can observe a dramatic decrease in the EL intensity of sample B. Taking into account these results, we believe that in the latter case EL is defined by electron-hole recombination at the type II InAs/CdSe heterojunction containing large enough density of non-radiative recombination defects, while in the former structures EL originates at the high quality AlAsSb/InAs interface. These conclusions have also been supported by Hall measurements of the electron transport along the respective interfaces, reported elsewhere [5].

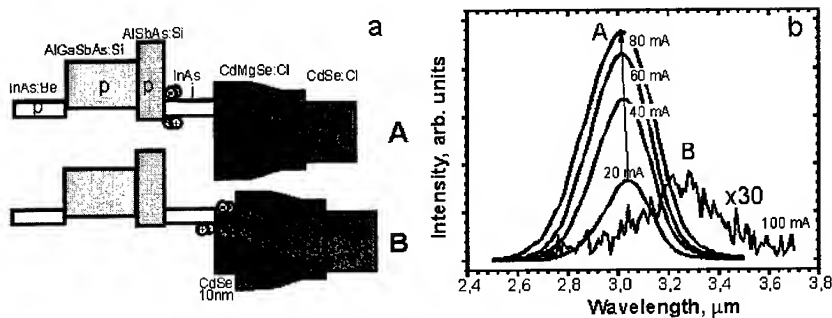


Figure 3. Schematic band diagram (a) and electroluminescence spectra at 77 K (b) of the hybrid structures with (B) and without (A) CdSe QW adjusted to InAs.

CONCLUSIONS

A double p-i-n heterostructures with high asymmetric band offsets, based on a combination of III-V (AlAsSb/InAs) and II-VI (CdMgSe/CdSe) compounds, have been proposed for mid-IR laser applications and successfully grown by MBE on InAs. Intense long-wavelength EL has been observed both at low (77K) and room temperature. Weak temperature dependence of the spontaneous emission is an evidence of the efficient carrier confinement in the InAs layer due to high potential barriers in conduction ($\Delta E_c = 1.28$ eV) and valence ($\Delta E_v \sim 1.6$ eV) bands. A change of the InAs/CdMgSe band alignment from type II to type I with the Mg content increase has been predicted and experimentally demonstrated. Significant lowering of the stacking fault density (below 10^6 cm^{-2}) has been achieved in the structures by incorporation of ZnTe buffer layer at the InAs/CdMgSe interface, preventing interaction between In and Se atoms. Laser diodes based on the hybrid III-V/II-VI double heterostructures are expected to exhibit a lower threshold current and higher characteristic temperature.

ACKNOWLEDGMENTS

This work was supported in part by ISTC 2044, RBRF Grant #00-02-17047 and Russian program "Physics of Solid-State Nanostructures" #1035 and #2014. The II-VI part of the work was also supported by INTAS Grant No. 97-31907.

REFERENCES

1. R. F. Kazarinov and M. K. Pinto, *IEEE J. Quant. El.* **30**, 49 (1994).
2. S. V. Ivanov, V. A. Solov'ev, K. D. Moiseev, I. V. Sedova, Ya. V. Terent'ev, A. A. Toropov, B. Ya. Mel'tser, M. P. Mikhailova, Yu. P. Yakovlev, P. S. Kop'ev, *Appl. Phys. Lett.* **78**(12), 1655 (2001).
3. J.M. Gaines, J. Peruzzello, B. Greenberg, *J. Appl. Phys.* **73**, 2835 (1992).
4. P. Grabs *et al.*, *Abstr. of the 11th EURO-MBE Workshop*, Hinterzarten, Germany, 9 (2001)

-
5. S. V. Ivanov, V. A. Solov'ev, A. A. Toropov, I. V. Sedova, Ya. V. Terent'ev, V. A. Kaygorodov, M. G. Tkachman, P. S. Kop'ev, L. W. Molenkamp, *J. Cryst. Growth* **227-228**, 693 (2001).
 6. V. A. Kaygorodov, I. V. Sedova, S. V. Sorokin, O. V. Nekrutkina, T. V. Shubina, A. A. Toropov, S. V. Ivanov, *Abstr. of the 10th Int. Conf. on II-VI Compounds*, Bremen, Germany, We-08 (2001)
 7. General Chemical Handbook, ed. by N. S. Zefirov (BRE, Moscow), **4**, 311 (1995) (in russian).
 8. P. N. Danilova, O. G. Ershov, A. N. Imenkov, M. V. Stepanov, V. V. Sherstnev and Yu. P. Yakovlev, *Semiconductors* **30**, 667 (1996).
 9. C. G. Van de Walle, *Phys. Rev. B* **39**, 1871 (1989).

Poster Session

LOCAL VIBRATIONAL MODES OF CARBON-HYDROGEN COMPLEXES IN PROTON IRRADIATED AlGaN

M. O. Manasreh*, and B.D. Weaver**

*Department of Electrical and Computer Engineering, University of New Mexico, Albuquerque, New Mexico 87131

**Naval Research Lab, 4555 Overlook Ave, SW, Washington, DC 20375

ABSTRACT

Local vibrational modes (LVMs) of carbon-hydrogen (C-H) complexes in proton implanted AlGaN grown on sapphire by metalorganic chemical vapor deposition (MOCVD) were investigated using Fourier transform infrared (FTIR) spectroscopy. The LVMs exhibit five distinctive peaks in the spectral region of $2846\text{--}2963\text{ cm}^{-1}$, which are due to the symmetric and asymmetric stretching modes of C-H_n ($n=1\text{--}3$). The LVMs intensities in doped AlGaN are increased as irradiation dose is increased in the entire irradiation dose range used without reaching the saturation stage. On the other hand, undoped samples show that LVMs intensity increase then either decreased or saturated as the irradiation dose is increased above $5 \times 10^{16}\text{ cm}^{-2}$. Proton irradiation causes a drastic increase in the CH_3 LVM while electron irradiation causes the opposite effect suggesting strongly that the observed LVMs are truly due to CH complexes.

INTRODUCTION

Optoelectronic devices based on III-nitrides and their ternary alloys have a broad range of application due to their wide direct band-gaps covering the spectral range from visible to ultraviolet. GaN has unique applications in blue, green and ultraviolet-blue light-emitting diodes, detectors and laser diodes [1-4]. III-nitride material system also shows tremendous potential in the field of high-temperature and high-power electronics because of their superior materials parameters [5]. Omnipresent impurities such as C, H and O play detrimental and beneficial roles in fabrication processes. For example, hydrogen can passivate the acceptor Mg [6-8] in GaN. Hydrogen can be easily incorporated into III-nitride during or after the growth of the materials [8]. Therefore, dopant incorporation remains the subject of various investigations.

Ion irradiation is a very attractive tool for several steps in III-nitride based devices' fabrication. The performance of devices such as fast switches [9] and detector [10] has been improved by subjecting them to well-controlled dose of particle irradiation. Compare to the understanding of ion beam process in mature semiconductors (i.e. Si and GaAs), the understanding of the complex ion beam process in III-nitrides is still at its infancy. Much more work is essentially needed to understand the irradiation effect on III-nitride material and device behaviors.

LVMs spectroscopy is a powerful tool in identifying impurities and dopant incorporation in semiconductors. LVMS give rise to sharp peaks in IR absorption spectra. With this method, one can identify the lattice site of the impurity atoms due to the fact that LVMs of impurities are sensitively affected by the atomic structure surrounding the dopant or impurity atom [11]. One typical example is that isotopic composition of the impurity and the surrounding atoms results in well-defined shifts in the vibrational frequencies [12-14].

LVMs of C-H complexes in a series of undoped, Si-doped, and Mg-doped AlGa_{0.4}N samples grown on sapphire substrate by the MOCVD technique have been investigated by using 1 MeV proton irradiation. Five distinctive C-H LVM frequencies were observed in the IR spectra recorded before and after proton-irradiating the samples. The evolution of the integrated areas of CH LVMs in proton-irradiated sample is presented as function of irradiation dose.

EXPERIMENT DETAILS

All the AlGa_{0.4}N samples used here were grown on sapphire with AlN buffer layer using the MOCVD technique. Al mole fraction ranges from 20% to 60%. Infrared absorbance measurements were performed with a BOMEM FTIR spectrometer, which covers the spectral range of 450–4500 cm⁻¹. A KBr beamsplitter, a globar light source, and a liquid-helium-cooled Si-B detector in conjunction with a continuous flow cryostat were used. A special sample holder was constructed to let the incident light from the spectrometer reach the sample at the Brewster's angle. This configuration proved to be very useful to avoid the interference patterns generated from the substrate as well as from the epitaxial thin film. The spectra were measured at both 300 and 77 K. The samples were irradiated with 1 MeV protons and each sample received the following sequential doses 1.0×10¹⁶, 5.0×10¹⁶ and 10.0×10¹⁶ cm⁻². Infrared absorption measurements were performed before irradiation and after each of the above irradiation doses to investigate the evolution of C-H LVMs spectra and their integrate areas.

EXPERIMENTAL RESULTS

All the samples tested before and after proton irradiation in this study were found to contain five IR peaks in the spectral range of 2846–2963 cm⁻¹. Figure 1 shows an IR spectrum for undoped Al_{0.6}Ga_{0.4}N sample implanted with 1 MeV proton and a dose of 1×10¹⁶ cm⁻². This spectrum can be resolved into five peaks at 2849, 2870, 2902, 2918 and 2960 cm⁻¹. Based on a comparison between the LVMs measurement in GaN and calculated C-H frequencies in α-Si_{1-x}C_x:H [15–18], we ascribe these five peaks to symmetric and asymmetric stretching modes of CH_n (n=1,2,3) complexes in AlGa_{0.4}N. The absorption peak at 2848 cm⁻¹ is attributed to a stretching mode of CH; the peaks at 2904 and 2916 cm⁻¹ are attributed to a symmetric and an asymmetric stretching modes of CH₂, respectively; and the peaks at 2870 and 2960 cm⁻¹ are

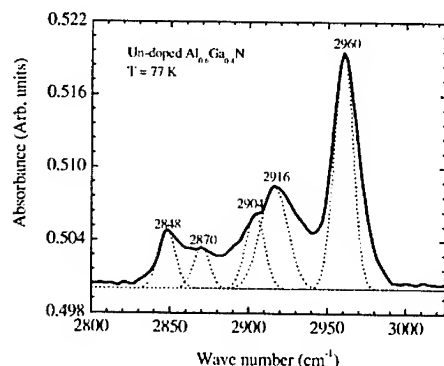


Figure 1. Infrared absorption spectrum measured at 77K for a proton irradiated Al_{0.6}Ga_{0.4}N sample. The IR absorption peaks are resolved into five peaks at 2848, 2870, 2904, 2916 and 2960 cm⁻¹. The solid line is the actual spectrum while the dotted lines are Gaussians added to the spectrum for clarification.

attributed to symmetric and asymmetric stretching modes of CH_3 . Table 1 summarizes the LVMs of C-H complexes in AlGaN, GaN and $\alpha\text{-Si}_{1-x}\text{C}_x\text{:H}$. From all the spectra of AlGaN samples tested in this study, it was noted that these five peak frequencies are sample dependent.

Table 1. LVMs frequencies of C- H_n in AlGaN, GaN: Mg and $\alpha\text{-Si}_{1-x}\text{C}_x\text{:H}$. The AlGaN sample was irradiated with 1 MeV proton and a dose of $1 \times 10^{16} \text{ cm}^{-2}$. The unit of the frequencies is cm^{-1} .

Stretching Mode	Measured frequencies in AlGaN ^a	Measured frequencies in GaN ^b	Measured frequencies in $\alpha\text{-Si}_{1-x}\text{C}_x\text{:H}$ ^{c-e}	Calculated frequencies in $\alpha\text{-Si}_{1-x}\text{C}_x\text{:H}$ ^{c-e}
CH	2848 ± 4	2853 ± 1	2860	2850
CH ₂ Asymmetric	2916 ± 6	2923 ± 1	2890-2920	2949
CH ₂ Symmetric	2904 ± 3	2900 ± 5	2870-2880	2902
CH ₃ Asymmetric	2960 ± 3	2956 ± 2	2940-2960	2950
CH ₃ Symmetric	2870 ± 3	2870 ± 5	2870-2880	2878

^aPresent work, ^bReference 15, ^cReference 16, ^dReference 17, ^eReference 18.

The LVMs spectra of $\text{Al}_{0.43}\text{Ga}_{0.57}\text{N:Mg}$ tested before and after proton irradiation were shown in Fig. 2. Spectrum (1) was obtained from the as-grown sample. Spectrum (2) and (3) were obtained for this sample after 1 MeV proton irradiation over doses of 5×10^{16} and $1 \times 10^{17} \text{ cm}^{-2}$, respectively. This figure shows that proton implantation gives rise to much more significant intensities variation of the CH_3 asymmetric stretching mode than that of other modes. All the other samples tested in this study shows similar behavior. The evolution of the LVMs integrated areas of C-H complexes in undoped, Si-doped and Mg-doped with different doses of proton irradiation is plotted in Fig. 3. Line 1, 2 and 3 are obtained for $\text{Al}_{0.6}\text{Ga}_{0.4}\text{N}$, $\text{Al}_{0.43}\text{Ga}_{0.57}\text{N:Mg}$ and $\text{Al}_{0.56}\text{Ga}_{0.44}\text{N:Si}$, respectively. The LVMs intensities of CH complexes are increased as the irradiation dose is increased in doped samples in the entire irradiation range used in this study and hydrogen atoms seem to continue to form CH complexes in doped samples without reaching the saturation stage. While the LVMs intensities of CH_n in undoped sample were increased first and then start to decrease as the proton irradiation dose is increased above $5 \times 10^{16} \text{ cm}^{-2}$.

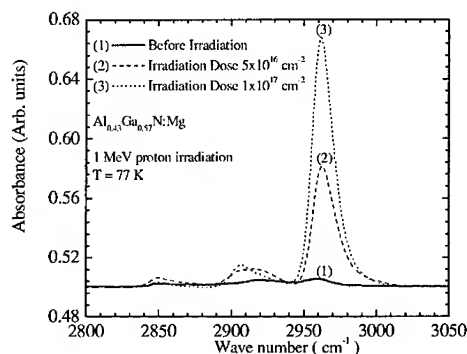


Figure 2. LVMs spectra of C- H_n measured at 77K for a Mg-doped AlGaN sample. Spectrum (1) was obtained for as-grown sample. Spectra (2) and (3) were obtained after proton irradiation with doses of 5×10^{16} and $1 \times 10^{17} \text{ cm}^{-2}$, respectively.

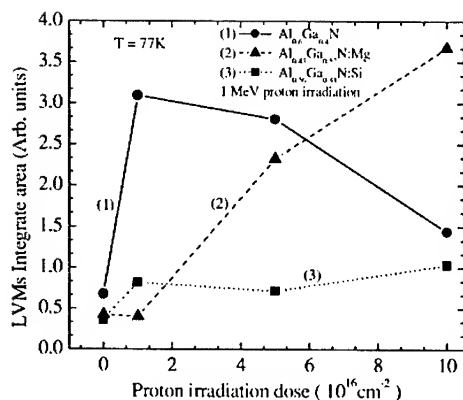


Figure 3. The integrated areas of C-H LVMs in undoped, Si-doped and Mg-doped AlGaIn samples plotted as a function of irradiation dose.

DISCUSSIONS

Theoretical studies based on the density functional approach for wurtzite [19-21] and zinc-blende [7, 20] lattices have indicated that the dominant charge state of atomic hydrogen in interstitial solution in GaN is H^+ or H^- depending upon the positions of the Fermi level, with H^0 always being less stable [7, 19-21]. H^+ is the lowest energy state in p-type GaN and H^- is the lowest state in n-type GaN. H^+ and H^0 , on the other hand, are found to be much more mobile than H^- . These studies also indicate that H can form complex by binding with neutral dopants such as acceptor Mg or donor Si on Ga sublattice as well as with residual impurities such as C. Hydrogen can also be in the form of multi-atomic hydrogen related centers (H_2 , C-H_n , $n=1,2,3$ etc.). Neutral interstitial molecular H_2 has lower formation energy than all three atomic states and was predicted to be energetically preferred for a limited range of Fermi energies near the middle of the bandgap. Energetic ion irradiation can produce gallium (V_{Ga}) and nitrogen (V_{N}) vacancies and interstitial by atomic collisions. The energetic H will initially come to rest at sites with local energy minima. Depending on its mobility, H will either remain at metastable sites or move to lower energy sites at lattice defects or dopants. In the parallel system of AlGaIn, we assume that hydrogen states have the same behaviors.

In GaN, C most likely occupies the nitrogen site. The C-H complexes formed when hydrogen passivates substitutional C (C_{N}) in GaN. Hydrogen was found to be located at a BC site between C and neighboring Ga atoms as is the case for GaAs and InAs [22,23]. Experimental results shows that the CH_n LVMs frequencies in AlGaIn are similar to that in GaN. This proves C-H complexes in AlGaIn has atomic configuration similar to that in GaN. The slight difference in LVMs frequencies of C-H_n in AlGaIn and GaN is expected. It is due to the fact that LVMs are highly sensitively to the surrounding atomic structures since Al atoms were added to the crystal, and consequently the atomic structure around C-H complexes in AlGaIn is different from that of GaN. Additionally, we observed that LVMs frequencies in AlGaIn are sample dependent. This sample dependency could be explained in terms of the presence of dislocations. The strains associated with dislocation are usually sample dependent and can affect the LVMs in a way that their frequencies are sample dependent.

To form C-H_n ($n=1-3$), n bonds of C-Ga need to be broken for hydrogen to be incorporated. It is obviously that more energy is needed if more C-Ga bonds are broken.

Therefore, after the proton implantation, the possibility to form C-H is much larger than that of forming C-H₂ and C-H₃, however we observed in all the samples tested in this proton irradiation study that the concentration of C-H₃ is much higher than that of C-H₂ and C-H. This leads to the assertion that hydrogen prefers to form C-H₃ in proton irradiated AlGaN. A possible explanation for this behavior is that there is a substantial number of V_{Ga} in the vicinity of C_N. This is quite possible since the energetic proton bombardment can produce V_{Ga} by atomic collisions, which is a good background to form C-H_n for n > 1 before V_{Ga} is annihilated.

In Fig. 3, we have shown the total integrated areas of C-H complexes LVMs as a function of irradiation dose for the three different samples (undoped, Mg-doped and Si-doped). The LVM results qualitatively provide useful information on the concentration of carbon impurity and the C-H complexes formation rate with proton irradiation dose. For different samples, it is obviously that they have different concentration of carbon impurity. For example, if a sample contains a large concentration of C and by adding H through irradiation, one would expect to observe an increase in the concentration of the C-H complexes. This is demonstrated in Fig. 3. In particular, the data labeled (2) indicates that this sample contains a larger carbon concentration as compared to the other two samples. For undoped and Si-doped samples, the carbon concentration seems to be much lower as judged by the formation of the C-H complexes. The reduction of the total integrated areas in these two samples [data labeled (1) and (3)] might be due to the decomposition of the C-H complexes by proton irradiation. This process is quite feasible in samples where the carbon atoms are completely compensated. Hence, excess proton irradiation will cause partial dissociation of C-H complexes. For the Mg-doped samples, the dominant charge state of H is H⁺ which is a faster diffuser, therefore, part of the H⁺ will form neutral complex with Mg acceptor and part of H⁺ will be attracted by the C_N which is also an acceptor. If a V_{Ga}, which is an acceptor with negative charge state, is near C_N, it may enhance the chances of forming C-H complexes since H⁺ prefer to attach itself to dangling bonds available at the vacancy site. For Si-doped samples, the dominant charge state of H is H⁻ which is less mobile compare to its other two atomic states. The formation of the C-H_n (n=1,2,3) complexes by the diffusion of H⁻ towards substitutional carbon is unlikely in n-type AlGa_{0.8}N since both are ionized acceptors whose negative charges repel one another. The V_{Ga} near C_N will also repel H⁻. For the undoped samples, major part of the energetically H atoms diffuse and combine with carbon to form C-H complexes. From this discussion, it is clear that C-H complexes as judged from the intensity of their LVMs are formed with higher rates in the proton irradiated undoped samples as compared the Mg and Si-doped samples.

Figure 3 clearly show that formation rate of

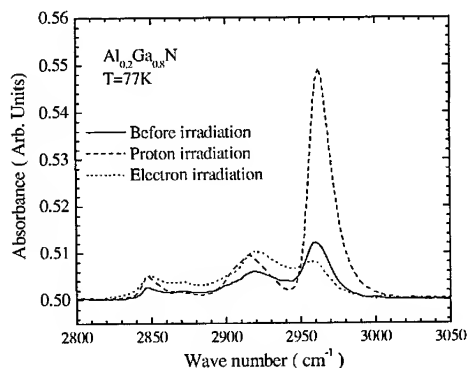


Figure 4. Local vibrational modes spectra measured for two samples cut from the same Al_{0.2}Ga_{0.8}N wafer. The solid line is the spectrum obtained for both samples before irradiation, the dashed line represents the spectrum obtained for the proton irradiated sample (dose=6x10¹⁶cm⁻²), and the dotted line represent the spectrum obtained for the electron irradiated (dose=1x10¹⁷cm⁻²) sample.

C-H complexes in the Si-doped sample is much lower than that in undoped and Mg-doped samples.

To illustrate that the observed LVMs are due to C-H complexes, we cut two pieces from an $\text{Al}_{0.2}\text{Ga}_{0.8}\text{N}$ wafer and one piece was irradiated with 1 MeV protons and the other one was irradiated with 1 MeV electrons (dose = $1 \times 10^{17} \text{ cm}^{-2}$). The results are shown in Fig. 4. The solid line is the spectrum obtained from the samples before irradiation, the dashed line is the spectrum obtained for the proton-irradiated sample, and the dotted line is the spectrum obtained from the electron irradiated sample. It is clear that proton irradiation increases the formation of C-H complexes as judged by the large increase in the stretching mode frequency of the CH_3 complex. An increase of the stretching mode frequencies for CH_2 and CH is also observed. However, the electron irradiated sample shows a noticeable decrease in the CH_3 stretching mode. This clearly demonstrates that electron irradiation break up the CH_3 complex in good agreement with others [24,25]. There is an increase of the CH_2 and CH concentrations in the electron irradiated sample as seen from the increase in the area under the LVMs stretching modes. This is most likely due to the fact that CH_3 is decomposed into C, H, CH, and CH_2 . This behavior is observed in several samples. Additionally, Hall effect measurements show a slight increase in the carrier concentration in the electron irradiation samples. This does not seem to be universal since a few samples show a slight decrease in the carrier concentration after electron irradiation.

CONCLUSION

We presented the local vibrational modes spectra of C-H complexes in proton implanted AlGaIn grown by MOCVD technique. Five distinctive C-H LVM frequencies were observed around 2848, 2870, 2904, 2916 and 2960 cm^{-1} , which are slightly different from those observed in GaN. These frequencies are related to stretching symmetrical and asymmetrical vibrational modes of CH_n ($n=1,2,3$). The evolution of the integrated areas of CH LVMs in proton irradiated samples is presented as function of irradiation dose. In the Mg-doped AlGaIn sample, hydrogen atoms (proton) seem to continue to form C-H complexes without reaching the saturation stage in the whole irradiation dose used in this study. This may be due to the fact that carbon is present with a high concentration. Si-doped samples on the other hand show a slight increase in the CH LVM intensities as the dose is increased. While proton irradiation causes a drastic increase in the CH_3 LVM, electron irradiation causes the opposite effect suggesting strongly that the observed LVMs are truly due to CH complexes.

ACKNOWLEDGEMENTS. This work was partially supported by the Air Force Office of Scientific Research Grant No. F49620-00-1-0026. We would like to thank Dr. D. Johnstone for his encouragement and support. We would like to thank D. C. Look and G. C. Farlow of Wright State University for the electron irradiation and J. Chen for the measurements.

REFERENCES

- [1] S. Nakamura, T. Mukai, and M. Smoh, *Appl. Phys. Lett.* **64**, 1687(1994).
- [2] S. Nakamura, G. Fasol, in: "The Blue Laser Diode", (Springer, New York, 1997).
- [3] M.S. Shur and M.A. Khan, GaN/AlGaIn Heterostructure devices: Photodetectors and Field Effect Transistors, *MRS Bulletin* **22**(2), pp. 44-50, Feb. (1997).

- [4] M. Razeghi and A. Rogalski, Semiconductor ultraviolet detectors, *J. Appl. Phys.* **79**(10), 7433 (1996).
- [5] K. Doverspike, A.E. Wickenden, S.C. Binari, D.K. Gaskill, J. A. Freitas, *Mat. Res. Soc. Symp. Proc.* **395** (1996) 897.
- [6] S. Nakamura, N. Iwasa, M. Senoh, and T. Mukai, *Jpn. J. Appl. Phys.*, Part 1 **31**, 1258 (1992).
- [7] J. Neugebauer and C. G. Van de Walle, *Phys. Rev. Lett.* **75**, 4452 (1995).
- [8] W. Gotz, N. M. Johnson, D. P. Bour, M. D. McCluskey, and E.E. Haller, *Appl. Phys. Lett.* **69**, 3725 (1996).
- [9] M. Lambsdorff, J. Kohl, J. Rosenzweig, A. Axmann and J. Schneider, *Appl. Phys. Lett.* **58**, 1881 (1991).
- [10] V. M. Rao, W-P Hong, C. Caneau, G-K. Chang, N. Papanicolaou, and H. B. Dietrich, *J. Appl. Phys.* **70**, 3943 (1991).
- [11] "GaN and Related Materials", edited by S. J. Pearton, Vol 2, Chapter 11, (Gordon and Breach, Amsterdam, 1997).
- [12] L. Hoffmann, E. V. Lavrov, B. Bech Nielsen, B. Hourahine, R. Jones, S. Öberg and P. R. Briddon, *Phys. Rev. B* **61** No. 24, 16659 (2000).
- [13] B. Hourahine, R. Jones, S. Öberg, R. C. Newman, P. R. Briddon and E. Roduner, *Phys. Rev. B* **57** No. 20, 12666 (1998).
- [14] P. Dixon, D. Richardson, R. Jones, C. D. Latham, S. Öberg, V. J. B. Torres, and P.R. Briddon, *Phys. Stat. Sol. (b)* **210**, 321 (1998).
- [15] G. C. Yi, and B. W. Wessels, *Appl. Phys. Lett.* **70**(3), 357 (1996).
- [16] H. Wieder, M. Cardona, and C. R. Guarnieri, *Phys. Status Solidi B* **92**, 99 (1979).
- [17] Y. Tawada, K. Tsuge, M. Kondo, H. Okamoto, and Y. Hamakawa, *J. Appl. Phys.* **53**, 5273 (1982).
- [18] B. Dischler, A. Bubenzer, and P. Koidl, *Solid State Commun.* **48**, 105 (1983).
- [19] S. M. Myers, A. F. Wright, G. A. Petersen, C. H. Seager, M. H. Crawford, W. R. Wampler, and J. Han, *J. Appl. Phys.* **88**, 4676 (2000).
- [20] A. F. Wright, *Phys. Rev. B* **60**, 5101 (1999).
- [21] Bosin, V. Fiorentini, and D. Vanderbilt, *Mater. Res. Soc. Symp. Proc.* **395**, 503 (1996).
- [22] A. Bonapasta, *Phys. Rev. B* **48**, 8771 (1993).
- [23] S. -G. Lee and K. J. Chang, *Phys. Rev. B* **53**, 9784 (1996).
- [24] J.A. van Vechten, J.D. Zook, R.D. Horning, *Jpn. J. Appl. Phys.*, **31** 3662, (1992).
- [25] J. I. Pankove P.J. Zanzucchi and C.W. Magee, *Appl. Phys. Lett.* **46**, 421, (1985).

Effects of Ion Bombarding and Nitrogenation on the Properties of Photovoltaic a-CN_x Thin Films

Z.B. Zhou *, R.Q. Cui, G.M. Hadi, Q.J. Pang

Solar Energy Institute, Department of Physics, Shanghai Jiaotong University, Shanghai 200030 China

C.Y. Jin, Z. M. Ding

Instrumental Analysis Center, Shanghai Jiaotong University, Shanghai 200030 China

ABSTRACT

Amorphous carbon nitride films (a-CN_x) were synthesized by using single ion beam sputtering of a graphite target in argon and nitrogen sputtering gases. This thin film could be used as a novel photovoltaic material. The films were characterized with the technique of laser Raman, spectroscopic ellipsometry and electron spin resonance spectrometer (ESR). In this paper we report the effects of ion impacting and nitrogenation on the microstructure, density of defect states, bonding character, optical and photovoltaic properties. Effective decreasing of intensity of the ESR signal and formation of C-N bonding were observed, which could be attributed to the increment of the impinging ions on the growing films. The nitrogenation of a-CN_x films could decrease the Tauc optical gap (0.62~0.86eV) and the intensity of ESR signal, increase photon absorption coefficient of the films ($10^6 \sim 10^4 \text{ cm}^{-1}$).

The primary photovoltaic values of the devices having Schottky structure of ITO/CN_x/Al are I_{sc} 1.56 $\mu\text{A/cm}^2$ and V_{oc} 250 mV, respectively, when exposed to AM1.5 illumination (100 mW/cm^2 , 25°C).

INTRODUCTION

The interest in carbon nitride thin films was referred to the theoretical calculation of its possible crystal structure $\beta\text{-C}_3\text{N}_4$ in 1980s [1,2]. This crystalline alloy is claimed in the ranking of hardest materials. Since that time, many efforts have carried out to synthesis this new crystal material with less success [3]. Actually, the carbon nitride films with amorphous structure might be a rather promising novel electronic material considering its electrical, optical properties can be controlled by changing the concentration of nitrogen atoms in the thin films or by choosing different deposition processes [3,4]. This new material possesses some peculiar properties, such as negative electron affinity, low dielectric constant and high photoconductive gain, so it could be used on field emitting displays, interlayer of integration circuits and photovoltaic devices [5-7]. The synthesis of carbon nitride films can be achieved with variety techniques, such as plasma enhanced CVD [8,9], unbalanced magnetron sputtering [10], ion-beam deposition [11], laser ablation and FCVA [12,13]. In all of these processes, the ion bombardment during the deposition is one of the most important factors, which affects the bonding structure, electronic and optical properties of thin films. In this work, the films we studied were deposited by the method of single ion beam sputtering process (SIBS). We mainly studied the effects of ion bombardment and nitrogenation processing conditions on the properties of the

amorphous carbon nitride thin films for photovoltaic application. We adjusted the amount of the energetic ions bombarding on the films, and successfully controlled the bonding configuration and many other properties. Some protocol Schottky thin film solar cells with the structure of ITO/a-CN_x/Al were fabricated in order to investigate the photoactive property of the a-CN_x thin film material.

EXPERIMENTAL DETAILS

The deposition equipment for a-CN_x thin films is a set of single ion beam sputtering instrument with a Kaufman ion source. The synthesizing system also consists of a diffusion pump, water-cooled target holder and substrate holder. The background and operating pressure in the vacuum chamber are better than 1×10^{-4} Pa and 3×10^{-2} Pa, respectively. A high purity graphite target (99.95%) was used as sputtering target. Nitrogen with high purity (99.999%) was used for both sputtering ions to bombard the target and nitrogen species to incorporate with carbon ions in the films. Nitrogen gas was ionized and extracted by powerful electrical field produced by accelerating grid electrode. An energetic ion beam was formed, which provided both sputtering ions and reacting nitrogen precursors. The energy and current intensity of the ions coming from the ion beam source were 740eV and 65mA/cm². The substrate holder, with an ion beam impact angle of about 80 degrees, between ion beam and normal line of substrate surface, consisted of a water-cooled copper plate, which kept substrates at ambient temperature during the deposition. We use two kinds of substrates: quartz sheets coated with ITO for Schottky solar cell processing and polished silicon wafers for characterization of a-CN_x thin film.

The structure of carbon nitride thin film solar cells ITO/a-CN_x/Al was described elsewhere [14,15]. A number of Schottky solar cells having this structure were produced based on a set of depositing conditions. We found that only a portion of these solar cells showed a testable photovoltaic performance. We tried to obtain the correlation between the process condition and their photoexcited character below.

MEASUREMENT AND DISCUSSION

In order to recognize this new material, we use some modern probes including laser Raman, ESR and spectral ellipsometry for characterization.

Spectral ellipsometry test

Table I. Deposition condition and test results for three typical samples.

	A	B	C
Incident angle θ (degree)	75	85	75
N/(N+Ar) pressure rate	0.5	0.5	1
D _r (nm)	5.67	0.11	5.43
D _{a-CN_x} (nm)	100.7	135.9	120.1
Tauc's optical band gap (eV)	0.86	0.74	0.62

In variable angle spectral ellipsometry (VASE) measurement, we can change the polarization of light as a function of angle and wavelength when light is reflected from or transmitted through a sample. The samples used for spectral ellipsometry test were

prepared on silicon substrates. The optical model for the test is composed of three layers, the first one is the surface roughness whose thickness D_r is about several nanometers, the second is a- CN_x layer described by the Lorentz model and the third is the SiO_2 substrate whose thickness is supposed to be infinite. The experimental results (including the concentration of nitrogen gas in the sputtering gases and ion impact angle θ) for three typical samples are listed in table I. The substrates would receive more bombarding ions under the condition of smaller ion impact angle θ . So the films we get have a larger thickness of roughness layer.

The spectra for the complex refractive index as a function of optical wavelength for the three typical a- CN_x films (A, B, C) are shown in figure 1.(a) (b). The curves

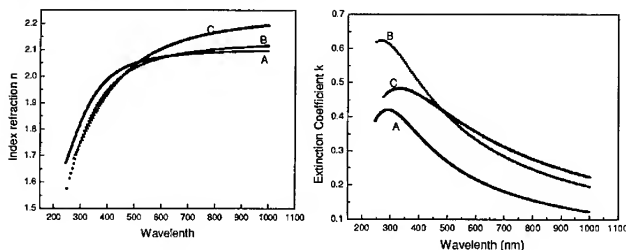


exhibit a smooth behavior, which is the characteristic of amorphous semiconductor[16]. The values of n (E) and k (E) are in the ranges 1.6~2.2 and

Figure 1. Spectra of the complex refractive index of the a- CN_x films for three typical depositing conditions (a) Refractive index n vs. wavelength (b) Extinction coefficient k vs. wavelength

0.1~0.6, respectively. In the short wavelength region, for small impact

angle θ , we observed higher values of n and lower values of k , as in Fig.1(a, b). The sample (A) shows lower extinction coefficient than the samples (B) and (C). This can be attributed to a relative low concentration of nitrogen in the sputtering gases and a smaller incident angle of the ion beam, which correlates with a trend toward better diamond-like properties. A higher concentration of nitrogen in the sputtering gases corresponds to a higher k as shown in Fig. 1(b).

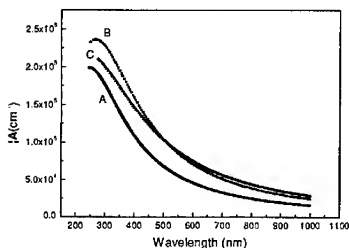


Figure 2. Variation of optical absorption with photon wavelength

Figure 2 shows the variation of optical absorption coefficient α as a function of the optical wavelength, which was obtained from ellipsometry test results. We find that the absorption coefficient in the region 500nm~1100nm is about $1 \times 10^5 \sim 2 \times 10^4 \text{ cm}^{-1}$, which is higher than that of a-Si:H thin films and arises from transitions between localized states.

We obtain the optical gap E_0 defined by the formula (1) from the curves of the $E \times \epsilon_2^{1/2}$ versus photon energy E , shown in Fig.3. Deviations of the data from linearity at low energies arise from transitions in exponential band tails below the absorption edge and are characteristic of amorphous semiconductors.

$$\omega^2 \epsilon_2(\omega) = B(h\omega - E_0)^2 \quad (1)$$

By extrapolating the linear parts to the energy axis, the values so obtained are in

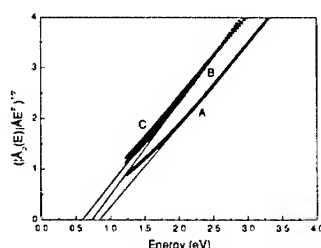


Figure 3. Tauc-plots for determining the optical band gap of three samples A, B, C

the range 0.62 ~ 0.86 eV, which depends on the different depositing conditions. Sample A, deposited with a lower nitrogen concentration in working gases and lower ion impact angle, possesses a higher optical gap 0.86 eV. Sample C, with a high concentration of nitrogen in working gas, shows a relatively smaller optical gap 0.62 eV.

Raman test

Raman spectroscopy is a non-destructive method for measuring the bonding structure of materials. Usually, the sp^2 contribution is always dominant in a Raman spectrum because the sp^2 bonding is more sensitive to visible laser light. Therefore, the Raman spectra are dominated by G peak at about 1580 cm^{-1} and D peak around about 1350 cm^{-1} . A.C. Ferrari and J. Robertson once made a full interpretation of Raman spectra for amorphous and graphitic carbon films [17]. In our work, Raman spectra of our carbon nitride films were obtained using Dilor Raman spectrometer (Ne-He laser, excitation wavelength 633 nm). Spectra were recorded from wavenumbers 800 cm^{-1} to 1800 cm^{-1} shown in Fig. 4. The 950 cm^{-1} peak arises from the silicon substrate [18].

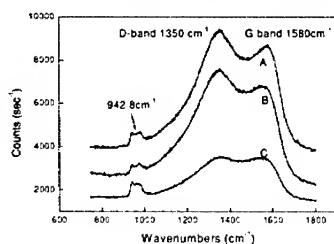


Figure 4. Raman spectra of amorphous carbon nitride thin films, D-band and G-band are located at about 1350 cm^{-1} and 1580 cm^{-1} , respectively

The conclusion of peak fitting with gaussian functions explicitly shows three peaks situated at the centers of about 1370 cm^{-1} , 1570 cm^{-1} and 1240 cm^{-1} , as seen in Fig.5 (deconvoluted spectra of sample A and B are not given here). The first two are definitely contributed from D-band (disordered band) and G-band (graphite band), respectively, which is the same as the previous research report on amorphous carbon. Here, the 1240 cm^{-1} peaks are designated the N band for the origin of 1240 cm^{-1} peak is postulated to be due to C-N stretching bonding as reference [19] mentioned.

The C=N peak in the Ref. [18] should be located at $\sim 1450 \text{ cm}^{-1}$ which was not recognized in our deconvoluted spectra. The position of N band peak was considered to shift to lower wave numbers in our sample C. The relative intensity of D and G peaks (I_D/I_G) can be taken to indicate relative sp^3/sp^2 ratio indirectly, also the relative intensity of N and G peaks (I_N/I_G) was supposed to show the nitrogen relative concentration in the films qualitatively. The conclusion was listed in table II.

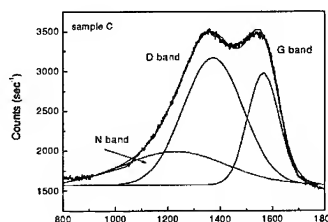


Figure 5. Deconvoluted spectra of sample C

thin film surface is to remove weak and unstable bonds. As the ion bombarding, CN trip-bond is removed easily, C=N is partially removed and C-N is preserved. This result is consistent with the known stability of the bond structure of carbon and nitrogen [20]. It also lowers the rate of I_D/I_G , however, nitrogenation can promote the rate of I_D/I_G . Therefore, the sp^3/sp^2 ratio of the sample A is higher than that of the other two. The relative nitrogen concentration in the film C is

highest among the three samples. Its atomic percentage of nitrogen is 16 % tested by XPS techniques in the Ref.[15], which have been shown in our previous work [15].

The sample C has another apparent difference compared with A and B. It has much lower N band position 1228cm^{-1} , while that of sample A and B are 1251 cm^{-1} and 1261 cm^{-1} .

The tendency of variation of the G position with the amount of bombarding ions received by substrates was coincident with the results discussed in reference [16]. Comparing sample A with C and B, we could get that the nitrogenation and ion bombarding initiate a red shift of the G band position. A higher rate of I_D/I_G corresponds to a lower ratio of sp^3/sp^2 , which was reported in the paper [16] and many other literatures [18]. The function of ion striking the

Table II.Deposition condition and Raman test results for three typical samples.

	A	B	C
Incident angle θ (degree)	75	85	75
N/(N+Ar) pressure rate	0.5	0.5	1
G band (cm^{-1})	1575	1568	1566
D band (cm^{-1})	1370	1371	1374
N band (cm^{-1})	1251	1261	1228
I_D/I_G	1.04	1.06	1.10
I_N/I_G	0.66	0.60	0.69
PV performance of Schottky solar cells	Poor	Poor	Good

Electron Spin Resonance spectra and photovoltaic property

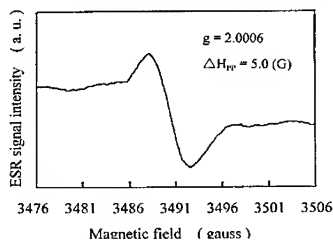


Figure 6. Electronic spin resonance spectrum of a-CN_x sample C. Sample A and B has much more intensive ESR signal than sample C

In order to compare unpaired electron densities of different samples, we measure the ESR spectra by using a conventional Bruker electron spin resonance spectrometer (ER200D-ESR X-band, Modulator frequency 100kHz). ESR measurements were made at room temperature. The g values obtained from the ESR spectra of all samples were found to be about 2.0006 and peak-to-peak width was found to lie in a wide range 5~12G as shown in Fig. 6. Sample C had a lowest relative electron spin density and a strongest photovoltaic signal among all samples. Ion bombarding and nitrogenation have a diminution function, or passivation effect, to the defect states, which

usually exist in amorphous materials. The Schottky junction made from sample C exhibited open circuit voltage 250mV and short circuit current $1.56 \mu \text{ A/cm}^2$.

CONCLUSION

Ion impacting to the films and nitrogenation during deposition play key roles on the properties of photovoltaic application orientated amorphous carbon nitride films. They could effectively decrease electron spin resonance density, promote the photo-activity. They could increase the C-N bonding which could be accountable for the photoactive character of the films. Ion impinging can increase optical band gap, decrease photon absorption while nitrogenation has an opposite effect. How to retain their advantages and diminish their negative function to meet the photovoltaic requirement is a task for the future work.

REFERENCES

1. Y. Liu and M. L. Chen, *Science* **245**, 841 (1989)
2. B.C. Yang, et al, *Chinese Physics Lett.* **16**, 847 (1999)
3. L.K. Cheah, X. Shi, et al, *Materials Science and Engineering* **B64**, 6-11 (1999)
4. Deuk Yeon Lee, Yong Hwan Kim, et al, *Thin Solid Films* **355-356**, 239-245 (1999)
5. A. Grill, *Diamond and Related Materials* **10**, 234-239 (2001)
6. T. Iwasaki, et al, *Diamond and Related Materials* **8**, 440 (1999)
7. M. Maldei, D.C. Ingram, *Solar Energy materials and Solar Cells*, **51**, 433-440 (1998)
8. S.F. Durrant, E.C. Rangel, et al, *J. Vac. Sci. Technol.* **A 13**, 361 (1995)
9. J.H. Kim, D.H. Ahn, et al, *J. Appl. Phys.* **82**, 658 (1997)
10. N. Savvides, *J. Appl. Phys.* **59**, 4133 (1986)
11. B. Enders, Y. Horino, et al, *Phys. Rev.* **B121** 73(1997)
12. Z.-M. Ren, Y.-C. Du, et al, *Appl. Phys. Lett.* **65** 1361(1994)
13. E. Liu, X. Shi, *Surface and Coatings Technology* **120-121** 601-606 (1999)
14. Z.B. Zhou, R.Q. Cui *Applied Surface Science* **172** 245-252 (2001)
15. Z.B. Zhou, R.Q. Cui and G.M. Hadi, *Solar Energy Materials and Solar Cells* **70** 487-493(2002)
16. M.H. Brodsky, *Amorphous Semiconductor*, New York (Springer-Verlag 1979) p73-109
17. A.C. Ferrari and J. Robertson, *Physical Review B* **61(20)**, 14095-14107 (2000)
18. M. Neuhaeuser, H. Hilgers, et al, *Diamond and Related Materials* **9**, 1500-1505 (2000)
19. J.H. Kaufmann, S. Metin, D.D. Saperstein, *Phys. Rev. B* **39 (18)**, 13053 (1989)
20. A.K.M.S. Chowdhury, D.C. Cameron, et al, *Thin Solid Films*, **332**, 62-68 (1998)

Doping profiles of n-type GaAs layers grown on Si by the conformal method

Angel M. Ardila^{1,2}, O. Martínez², M. Avella², J. Jiménez², B. Gérard³, J. Napierala⁴ and E. Gil-Lafon⁴

¹Depto. De Física, Facultad de Ciencias, Universidad Nacional de Colombia, Ciudad Universitaria, Santa Fe de Bogotá, Colombia

²Física de la Materia Condensada, Facultad de Ciencias, Universidad de Valladolid, Valladolid, 47011, Spain

³THALES, Corporate Research Laboratory, 91404 Orsay Cedex, France

⁴LASMEA UMR CNRS 6602, Université Blaise Pascal, Les Cézeaux, 63177 Aubière Cedex, France

ABSTRACT

We study doping profiles in selectively Si-doped GaAs layers grown by the conformal method. This growth technique allows to obtain GaAs/Si with optoelectronic quality. The samples are laterally grown, and selective doping with Si is carried out in such a way that doped stripes are intercalated with undoped ones. The study of the doping profiles was carried out by cathodoluminescence (CL) and micro-Raman (μ R) spectroscopy. Abrupt doping profiles between doped and undoped stripes were demonstrated by monochromatic CL images. Deep level related CL bands can be observed between 1000 and 1400 nm, evidencing the complex mechanism for Si incorporation at the growth temperature (730 °C). Net doping concentrations and mobilities across the layers were determined from the analysis of the phonon-plasmon coupled modes in the μ R spectra obtained with a lateral resolution better than 1 μ m.

INTRODUCTION

Matching gallium arsenide to silicon, which currently shows up in special applications, that combine the low-cost robustness of silicon with the higher optoelectronic performance of the gallium arsenide, has been a technological goal for many years [1-5]. For example, this development could permit the integration of optical components like solid state lasers with the conventional electronic devices in the same chip, enabling on-chip and chip-to-chip optical interconnects; the design of new wireless devices, like radar systems that would help automobiles avoid collisions, and new semiconductor-based lighting systems. However, the obtention of defect free epilayers is subjected to some problems because of the large lattice (4%) and thermal (55%) mismatches between Si and GaAs, as well as the difficulties of growing a polar semiconductor on a non-polar one. Nowadays, important achievements were got using different deposition techniques and treatments (annealing[2], buffering layers in vertical growth[3], or passivating layers in lateral growth[4]). In spite of this, the density of crystal defects remains high enough to render unsuitable these layers for reliable optoelectronic applications. Pribat et al. [5,6] proposed an effective method to produce GaAs layers on Si substrates that consists of a lateral epitaxial growth on the sidewall of a GaAs seed stripe previously deposited on a Si substrate.

We present in this paper the study of doping profiles in selectively Si-doped GaAs layers grown by the conformal method, using optical techniques. The carried out measurements evidence the complex mechanism of Si incorporation in the GaAs layers.

EXPERIMENTAL DETAILS

The conformal GaAs layers were prepared according to the procedure previously described [5], on 2° misoriented (001) silicon substrates. First, 0.7–1.5 μm thick GaAs layers were grown by MOVPE. These sacrificial layers usually exhibit dislocation densities above 10^8 cm^{-2} . Then, the GaAs layer is covered by a dielectric capping layer, in which either $\langle 110 \rangle$ or $\langle 1\bar{1}0 \rangle$ oriented GaAs stripes are periodically opened (10 μm wide every 200 μm). The GaAs layer is then selectively underetched using an $\text{H}_2\text{SO}_4/\text{H}_2\text{O}_2/\text{H}_2\text{O}$ solution, so as to obtain 125 μm wide GaAs seed stripes. Conformal growth is then carried out by selective hydride vapor phase epitaxy using gaseous GaCl and As₄ for the growth of GaAs and timely adding SiH₄ for the growth of doped layers intercalated with the undoped ones, see figure 1. The first layer consists of undoped GaAs whose growth is initiated on the lateral sidewalls of the GaAs seed stripes and develops laterally inside the cavity formed in between the oxidized silicon substrate and the overhanging dielectric capping layer. When this layer is about 3 μm width, silane is pushed into the reaction chamber to introduce the Si dopant in the GaAs film. This is maintained so up to growth a 3 μm wide doped stripe. Thereafter, the steps are repeated to produce up to 7 stripes at the growth temperature of 730 °C.

One has to note that the conformal growth allows for an independent control of the vertical and lateral extensions of the GaAs film, as the vertical one is settled by the thickness of the GaAs sacrificial layer. The 60° type threading dislocations initially present in the sacrificial layer cannot propagate far through the conformal GaAs growing layer as they are blocked by either the capping layer or the substrate itself. This constitutes an efficient geometrical dislocation filter as shown in figure 1. The thin SiO₂ layer formed from the oxidation of the Si substrate during the underetching step was not removed before the conformal growth step.

The optical and transport properties of the samples were studied by cathodoluminescence (CL) and micro-Raman (μR) spectroscopy. The CL measurements were done in a scanning electron microscope (SEM) using an Oxford mono-CL2 system and were carried out at liquid-nitrogen temperature. The Raman spectra were recorded using a DILOR spectrometer with a liquid-nitrogen-cooled charge coupled device (CCD) detector, attached to a metallographic microscope. The scattered light is collected by the microscope objective conforming a nearly backscattering geometry. The Raman spectra were taken at room temperature. The frequencies and linewidths of the longitudinal optic (LO) phonon and LO phonon-plasmon coupled (LOPC) modes were determined by fitting with an spectral accuracy of approximately 0.1 cm^{-1} . The spectra were calibrated using a plasma line of the laser.

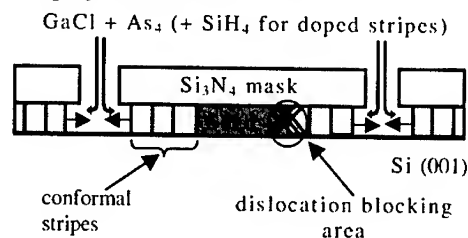


Figure 1. Schematic view of the conformal growth process showing the formation of the different doped and undoped stripes and the dislocation blocking mechanism.

DISCUSSION

Raman spectra

The Raman spectra of the GaAs conformal stripes excited under non-resonant conditions with the 514,5 Ar⁺-laser line in the backscattering geometry shows the LO-phonon mode and the forbidden by symmetry selection rules TO mode. The appearance of the TO mode is possibly due to the misalignment from the true backscattering geometry. The n-doped stripes, shows the coupled LO phonon-plasmon modes L_+ and L_- with frequencies ω_+ and ω_- , respectively; the uncoupled LO phonon mode from the depletion layer and the second-order phonon spectrum in some cases overlapping the relatively broad L_+ mode.

Figure 2 shows the typical spectra obtained from an undoped GaAs stripe (figure 2a) and from an n-type doped GaAs stripe (figure 2b). The structure near the LO peak is related to the second-order phonon bands TO+TA(X,K) associated with different crystal perfections [7]. In n-GaAs the position of the L_+ mode strongly depends on the charge carrier concentration and can be used for its calculation. The LO phonon peak intensity decreases with the carrier concentration due to the decrease of the depletion layer. The determination of the frequency of the LOPC mode is sometimes complicated by the strong damping of the high-energy L_+ mode and its superposition with the second-order phonon spectrum, specially the $2LO(\Gamma)$, $2TO(\Gamma)$ and $2TO(X,K)$ peaks. To overcome this problem and avoid confusions with possible LOPC peaks, the second-order phonon spectrum was subtracted from the spectra. In this case, the carrier concentration can be calculated using the known relation for the low (L_-) and high (L_+) frequency branches obtained by solving the system dielectric function $\epsilon(\omega) = 0$ longitudinal modes for n-type doping [8]:

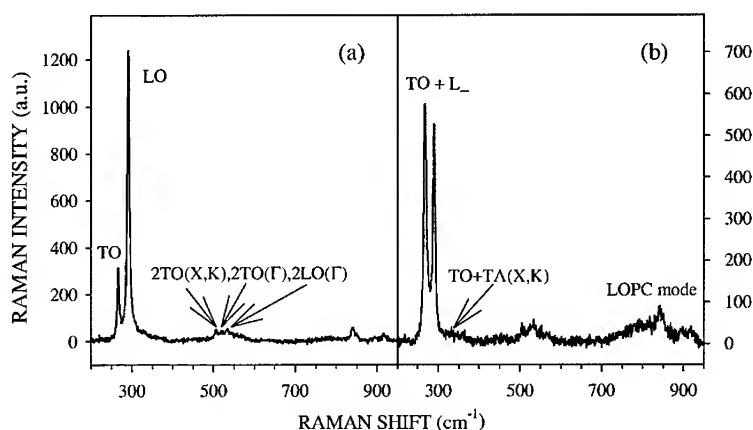


Figure 2. Typical Raman spectra obtained from (a) an undoped GaAs stripe and (b) an n-type doped GaAs stripe of the conformal layer formed with 7 different intercalated stripes.

$$\omega_{\pm}^2 = \frac{1}{2} \left[(\omega_{LO}^2 + \omega_p^2) \pm \left[(\omega_{LO}^2 + \omega_p^2)^2 - 4\omega_p^2\omega_{TO}^2 \right]^{1/2} \right] \quad (1)$$

and the expression: $\omega_p^2 = ne^2/\epsilon_0\epsilon m^*$ for the plasmon frequency, where ω_+ , ω_- , ω_{LO} , ω_{TO} and ω_p are the frequencies of the high and low LOPC branches, LO and TO phonon modes and the plasmon respectively. Using $m^* = 0.0632m_0$ and $\epsilon = 10.6$ for GaAs, the following expression can be obtained for calculating the carrier concentration:

$$n = 7.49 \times 10^{12} \omega_p^2 [\text{cm}^{-3}] \quad (2)$$

Here ω_p is given in cm^{-1} .

The calculated carrier concentration for our Si-doped GaAs conformal stripes using Eq. 2, is shown in figure 3a. These results show relatively abrupt interfaces as was expected keeping in mind that the laser spot is not punctual. The expected increase in the carrier concentration with the SiH_4 flow is also observed but the μR spectra calculated concentrations are larger than the expected values.

The free carrier mobility is obtained from the damping constant Γ_p of the high-energy branch (L_+) of the LOPC mode using the expression $\mu_{op} = e/m^*\Gamma_p$, where e is the electron charge and m^* the electron effective mass. For n-type GaAs this expression can be reduced to:

$$\mu_{op} = 1.48 \times 10^5 \left(\frac{1}{\Gamma_p} \right) \left[\frac{\text{cm}^2}{\text{Vs}} \right] \quad (3)$$

Here Γ_p is in cm^{-1} . The calculated data are represented in figure 3b and the average values of carrier concentration and mobility for the three doped stripes are summarized in table I. As can be observed from the μR spectra of the doped stripes, the high-energy branch (L_+) of the LOPC mode is highly damped, making difficult a precise calculation of the free carrier mobility. It strongly depends on the μR spectra base line.

Cathodoluminescence measurements

Figure 4 shows CL images taken at (a) 830 nm and (b) 1150 nm respectively. The band-to-band (830) emissions from the undoped GaAs conformal stripes are clearly observed in figure

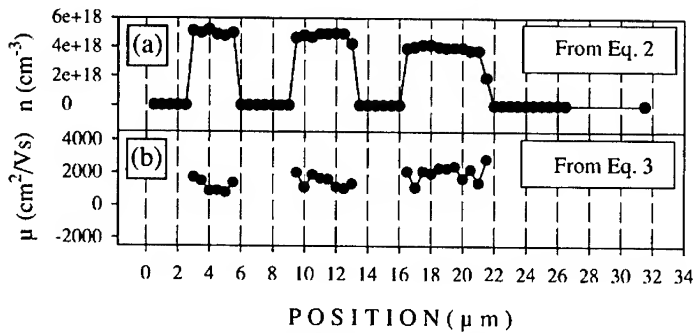


Figure 3. Calculated variations of the (a) free carrier concentration and (b) mobility, across the conformal layer, from the high-energy branch LOPC mode in the Raman spectra and using Eqs. (2) and (3).

Table I. Calculated values of the carrier concentration and mobility for the three different doped stripes in the conformal layer.

Stripe (see Fig. 5a)	SiH ₄ flow (cm ³ /min)	\bar{n} ($\times 10^{18}$ cm ⁻³) (by silane flow)	\bar{n} ($\times 10^{18}$ cm ⁻³) (by Eq. 2)	$\bar{\mu}$ (cm ² V ⁻¹ s ⁻¹) (by Eq. 3)
2	2	0.8	3.7 ± 0.2	2002 ± 652
4	4	2	4.7 ± 0.3	1451 ± 484
6	6	4	5.0 ± 0.2	1176 ± 422

4a, while the impurity related transitions (1150 nm) are observed in figure 4b. Figure 5a shows the CL intensity profiles obtained across the conformal sample in the position shown by the white line in the inset CL image. The intercalated undoped and Si-doped stripes are clearly observed and both the CL image and the CL intensity profiles show the abruptness of the inter-stripes interfaces. The slight superposition in the intensity profiles is due to the size of the incident electron beam. Figure 5b shows the CL spectra of the different doped and undoped stripes numbered in the inset image of figure 5a. The spectra of the undoped stripes 3, 5 and 7 have a 10x magnification for better observation. The broad peak observed at about 1150 nm is related to Si complexes formed as a result of doping at temperatures below 750°C. This broad emission band corresponds mainly to the so called self-activated (SA) luminescence band. The SA center responsible for this luminescence is said to be due to a deep acceptor (V_{Ga}) with a bound donor (Si_{Ga}) [9], and the emission is related to the internal transitions of electrons between the excited and ground states of the $Si_{Ga} - V_{Ga}$ complex [10].

CONCLUSIONS

The transport and optical properties of selectively doped GaAs conformal stripes grown by selective hydride vapor phase epitaxy, have been studied. The free carrier concentration and mobility were determined from the high-energy branch L_+ of the LOPC mode. Abrupt interfaces between doped and undoped stripes were revealed by CL images and intensity profiles taken at 80K. The CL spectra of the Si-doped GaAs stripes are dominated by the self-activated luminescence band produced by Si-complexes normally formed in Si-doped GaAs layers grown below 750 °C.

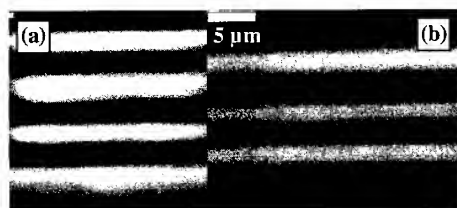


Figure 4. 80K monochromatic CL spectra taken on the GaAs conformal layer at two different wavelengths : a) 830 nm and b) 1150 nm. The bright stripes in (a) correspond to band-to-band transitions in the undoped stripes, while the bright stripes in (b) to the Si complex transitions in the doped stripes. Abrupt interfaces are clearly observed in both images.

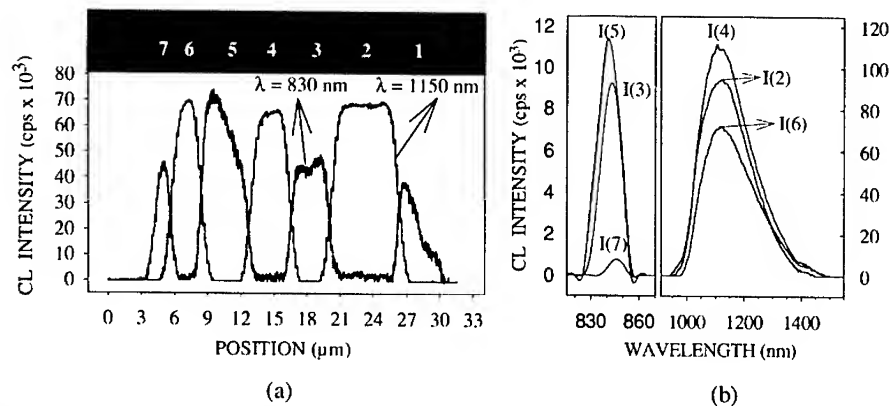


Figure 5. (a) CL intensity profiles taken across the GaAs conformal layer. (b) CL spectra from the different stripes numbered in the inset CL image of (a). The spectra were taken at 80 K.

ACKNOWLEDGMENTS

This work was done within the frame of an EU contract (BRPR – CT97 – 0512, CONFORM).

REFERENCES

1. W. I. Wang, *Appl. Phys. Lett.* **44**, 1149 (1984).
2. T. Yodo and M. Tamura, *Jpn. J. Appl. Phys.* **34**, 3457 (1995).
3. R. V. Kuz'menko, A. V. Ganzha, O. V. Bochurova, E. P. Domashevskaya, J. Schreiber, S. Hildebrandt, S. Mo, E. Peiner and A. Schlachetzki, *Semiconductors*, **34**, 73 (2000).
4. Z. R. Zytkeiwicz, *Cryst. Res. Technol.* **34**, 573 (1999).
5. D. Pribat, V. Provendier, M. Dupuy, P. Legagneux and C. Collet, *Jpn. J. Appl. Phys.* **30**, L431 (1991).
6. O. Parillaud, N. Piffault, E. Gil-Lafon and R. Cadoret, *Proc. Sixth Intern. Conf. On Indium Phosphide and Related Materials*, Santa Barbara USA, IEEE, 547 (1994).
7. M. Herms, G. Immer, J. Monecke and O. Oettel, *J. Appl. Phys.* **71**, 432 (1992).
8. G. Abstreiter, M. Cardona and A. Pinczuk, *Light Scattering in Solids IV, Topics in Applied Physics*, Vol **54** (Springer, Berlin, 1984), p. 5.
9. I. Harrison, L. Pavesi, M. Henini and D. Johnston, *J. Appl. Phys.* **75**, 3151 (1994).
10. N.H. Ky, J.D. Ganiere, F. K. Reinhart, B. Blanchard and J.C. Pfister, *J. Appl. Phys.* **74**, 5493 (1993).

Gallium vacancy in GaSb studied by positron lifetime spectroscopy and photoluminescence

W. K. Mui, M. K. Lui, C.C. Ling, C. D. Beling, S. Fung

Department of Physics, The University of Hong Kong, Pokfulam Road, Hong Kong, P. R. China

K. W. Cheah, K. F. Li

Department of Physics, Hong Kong Baptist University, Hong Kong, P. R. China

Y. W. Zhao

P.O. Box 912, Material Science centre, Institute of Semiconductors, Chinese Academy of Sciences, Beijing 100083, P. R. China

E-mail correspondence: ccling@hkucc.hku.hk

ABSTRACT

Positron lifetime technique and photoluminescence (PL) were employed to study the vacancy type defects in *p*-type Zn-doped and undoped GaSb samples. In the positron lifetime study, Ga vacancy related defect was identified in these materials and it was found to anneal out at temperature of about 350°C. For the PL measurement on the as-grown undoped sample performed at 10K, a transition peak having a photon energy of about 777meV was observed. This transition peak was observed to disappear after a 400°C annealing. Our results is consistent with the general belief that the 777meV transition is related to the $V_{Ga}Ga_{Sb}$ defect, which is the proposed residual acceptor of GaSb.

INTRODUCTION

Gallium Antimonide is a III-V semiconductor having a narrow band gap, a small effective electron mass and a high electron mobility. It is the basic material for a variety of lattice-matched materials having band gap ranging from 0.8 to 4.3 μ m. It is the potential material for fabricating optoelectronic, photovoltaic and high frequency devices. Undoped GaSb is *p*-type and has a hole concentration of 10^{16} - 10^{17} cm⁻³ [1,2]. The residual acceptor was known to be doubly ionized [3] and related to a deficiency of Sb or an excess of Ga [4-6]. Annealing the undoped GaSb for several hours converted its *p*-type conducting nature to *n*-type. It was explained by the creation of V_{Sb} upon the annealing, for which V_{Sb} was a donor compensating the residual acceptor. However, if the sample was annealed for several tens of hours, it would convert back to *p*-type with an even larger hole concentration as compared to the original as-grown value [7]. The residual acceptor has long time been attributed to the $V_{Ga}Ga_{Sb}$ defect [7-9]. The increase of hole concentration upon prolonged annealing can be understood by the formation of $V_{Ga}Ga_{Sb}$ resulting from the reaction between the V_{Sb} defect and its neighboring Ga atom. The $V_{Ga}Ga_{Sb}$ defect was also related to a luminescence signal called band A (located at about

777meV) which was commonly found in the photoluminescence and cathodoluminescence spectra of a variety of GaSb materials [7,10-15]. However, these correlations between the residual acceptor, the $V_{Ga}GaSb$ and the 777meV luminescence signal have not yet been directly confirmed by experimental observation.

Positron lifetime technique is a non-destructive defect probe which is selectively sensitive towards open volume defects [16, 17]. Positrons implanted into a solid will be rapidly thermalized and then undergo diffusion. An open volume defect in the lattice which presents as a potential well, may thus trap the diffusing positrons. The trapping process is indeed a positron state transition from the delocalized Bloch state to the localized defect state. As positrons annihilating at different states have different characteristic lifetime values, defect can thus be identified by its own characteristic lifetime after decomposing the positron lifetime spectrum. Defect information such as the concentration, the microstructure, the charge state and the ionization energy are possibly determined with the use of positron lifetime technique [16,17].

In this study, we have performed annealing studies on the undoped and the Zn-doped GaSb samples with the use of the positron lifetime and the PL techniques with an aim to investigate the correlation between the 777meV luminescence peak and the Ga vacancy positron lifetime signal.

EXPERIMENTAL

8mm×8mm samples were cut from the LEC grown GaSb wafers purchased from the MCP Wafer Technology Ltd., U.K. The thickness of the samples is 0.5mm. Two undoped samples [GaSb042Un and GaSb342Un] cut from two different ingots and one Zn-doped sample [GaSb098Zn] were investigated in the present study. The hole concentrations of the samples obtained by Hall Measurement performed at room temperature were : $p[GaSb042Un]=2.5 \times 10^{17} cm^{-3}$, $p[GaSb342Un]=2.0 \times 10^{17} cm^{-3}$ and $p[GaSb098Zn]=3.3 \times 10^{18} cm^{-3}$. The samples were degreased with acetone and ethanol, and then rinsed by deionized water. Isochronal annealing was performed in a nitrogen-hydrogen (80%-20%) forming gas atmosphere. After the 30 minute annealing, the samples were retreated out of the furnace's hot region but still kept in the forming gas atmosphere before they were cooled down.

The positron source used was $30\mu Ci$ $^{22}NaCl$ radioactive source encapsulated with kapton foil. The positron source was then sandwiched by the pair of the samples being measured. The positron lifetime spectrometer used in the present study has a resolution of $fwhm=235ps$. The positron lifetime measurements were carried out at the room temperature and in darkness. Each of the lifetime spectra contained 4 million counts.

In the PL measurements, the samples were excited by the 512 nm line of an argon laser, with typical power of 500 mW, and the excitation light was modulated at 20 Hz using a mechanical chopper. The emitted light was collected and separated by a 0.25 m focal length double monochromator, with slit width of 0.4 mm for both input and output slit, and a 800 nm long-pass filter was used to avoid any second-order light reaching the detector. A liquid nitrogen cooled InSb IR-detector converted the emitted light into electric signal, which was detected using a lock-in amplifier and was recorded with a microcomputer. All measurements were done at 10K, with the samples mounted in an Oxford Instrument closed-cycle He cryostat.

RESULTS AND ANALYSIS

Results of positron lifetime measurements

Room temperature positron lifetime measurements were performed on the samples annealed at different temperatures up to 580°C. The lifetime spectrum is the linear combination of the exponential terms contributed from the corresponding annihilating sites [16,17], i.e.

$$S(t) = \sum_i I_i \exp(-t/\tau_i) \quad (1)$$

where τ_i and I_i are respectively the characteristic lifetime and the intensity of the i -th positron trapping defect. The average lifetime of the positron lifetime spectrum is given by [16,17] :

$$\tau_{ave} = \sum_i I_i \tau_i = \int S(t) t dt / \int S(t) dt \quad (2)$$

The average positron lifetime of each of the positron lifetime spectrum annealed at different temperatures were calculated with the results shown in figure 1. For the as-grown Zn-doped sample, the average lifetime τ_{ave} was found to be 274ps. The average lifetime did not vary up to an annealing temperature of 300-400°C, at which it decreased to values of about 272ps. Afterthen, the average lifetime further decreased to about 266ps at an annealing temperature of 580°C. Ling *et al* [18] have analyzed the positron lifetime spectra of this Zn-doped sample and gave the following conclusion. The bulk lifetime of the GaSb was found to be

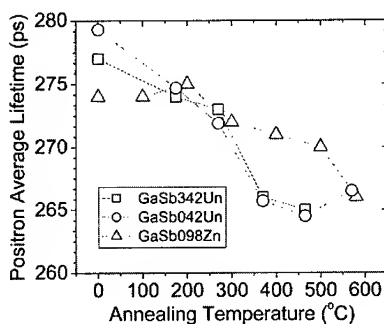


Figure 1 Positron average lifetime as a function of the annealing temperature for the three GaSb samples. The lines joining the data points are only for visual guidance.

267±1ps. A two lifetime component fit was found to give good representation to the spectra of the Zn-doped sample at all the annealing temperatures. At annealing temperatures lower than 300°C, the characteristic lifetime of the long lifetime component is constant at about 316±8ps and its intensity is also roughly constant between 50-60%. This 316ps component was attributed to positron annihilating at V_{Ga} related defect. At annealing temperatures ranging between 300° to 400°C, the characteristic lifetime of the defect component was found to increase to 368ps and the defect component intensity decreased to about 15%. This increase of lifetime value and decrease of intensity were attributed to the anneal out of the original V_{Ga} -related and the formation of a new defect D having a lifetime of 368ps. This new defect D was found to anneal out at 580°C where the defect component intensity decreased to effectively zero.

For the case of the two undoped samples, their annealing behaviors are very similar. The two undoped samples have average lifetime values higher than the bulk. This implies that there are positron trapping centres in the samples. Unlike the Zn-doped sample which has two annealing stages (namely at 300-400°C and 580°C), there is only one annealing stage at 350°C for the undoped samples. As the 350°C annealing stage in the Zn-doped sample was related to the annealing out of the V_{Ga} -related defect, it is plausible to assign the 350°C annealing observed in the undoped GaSb sample to the same process. As compared to the Zn-doped sample having an average lifetime equal to 272ps after the 350°C annealing, the average lifetime of the undoped samples reaches value of about 266ps, which is the bulk lifetime of GaSb and thus implies no

positron trapping centre exists in the undoped samples after the 350°C annealing. This indicates the formation of the defect D upon the annealing out of the V_{Ga} -related defect in the Zn-doped sample possibly involves the reaction between the V_{Ga} -related defect and the Zn dopant.

As for the undoped samples in which the defect V_{Ga} being annealed out with no formation of new defect, the simple trapping model can be used to describe the positron trapping annihilation in the sample system. The positron trapping rate κ into the Ga vacancy is given by the equation [17]:

$$\kappa = \frac{\tau_{ave} - \tau_b}{\tau_D - \tau_{ave}} \frac{1}{\tau_b} = \mu c \quad (3)$$

where $\tau_b=266ps$ is the bulk lifetime of GaSb, $\tau_D=317ps$ is the characteristic lifetime of V_{Ga} [18], $\mu=2 \times 10^{14}s^{-1}$ is the specific trapping coefficient of V_{Ga} [18] and c is the V_{Ga} concentration. The concentrations of the Ga vacancy for the two undoped samples at different annealing temperatures were calculated and shown in figure 2(a). The Ga vacancy concentrations in the two as-grown undoped samples were found to be about $2 \times 10^{17}cm^{-3}$ and then dropped to nearly zero at the annealing temperature of about 350°C.

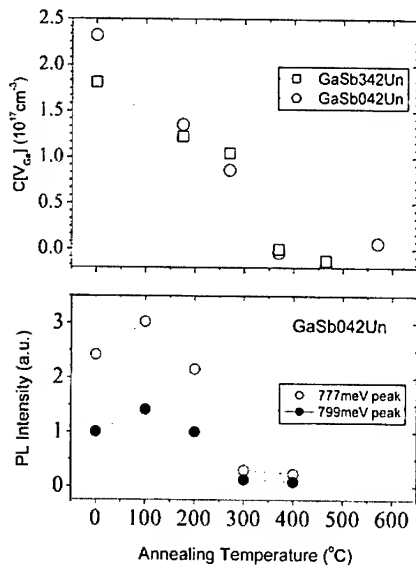


Figure 2 (a) The concentrations of the Ga vacancy related defect for the two undoped samples as a function of the annealing temperature. (b) The PL intensities of the two PL peaks (777meV and 799meV respectively) found in the undoped sample GaSb042Un as a function of the annealing temperature.

Results of PL measurements

Low temperature (10K) PL measurements have been performed on the GaSb042Un undoped samples annealed at different temperatures. Two typical PL spectra, namely those of the as-grown and the 400°C annealed samples, are shown in figure 3. For both of the spectra, the dominant luminescence signals are the peak located at about 777meV. Another two emission signals were also identified at positions of about 760meV (the low energy shoulder of the 777meV dominant emission) and 800meV. The intensities of all the peaks were found to reduce significantly after the 400°C annealing. The PL spectra taken at different annealing temperatures were fitted with the model consisting of three Gaussians. The fitted peak positions were found to be annealing temperature independent for the two stronger signals, namely at 777.36 ± 0.74 meV and 798.76 ± 1.70 meV respectively. The weak signal at about 760meV was too weak to obtain reliable fitting parameters.

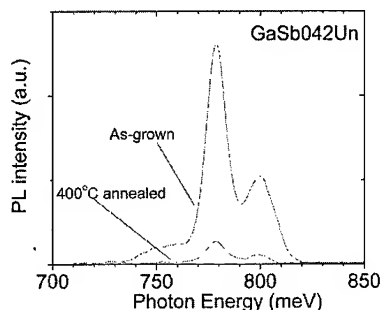


Figure 3 PL spectra of the as-grown and 400°C annealed GaSb042Un undoped GaSb samples. The measurements were performed at $T=10$ K.

The 777meV luminescence signal was found in most of the GaSb materials grown by various methods. It was related to Sb deficiency and was attributed to donor or conduction band to $V_{Ga}Ga_{Sb}$ transition [7,9,11-13]. The 799meV signal observed in the present study is close to the previous observations of PL signals attributed to exciton bound to neutral acceptor $(V_{Ga}Ga_{Sb})^0$ (792-805meV [11-13]). The intensities of the 777meV and 799meV PL signals as a function of the annealing temperature are shown in figure 2(b). From the figure, their annealing behaviors followed the identical trend and thus the two transition would involve an identical defect. This further supports the assignments of the 777meV and the 799meV signals to transitions involving the same defect

$V_{Ga}Ga_{Sb}$. Furthermore, as shown in figure 2, the intensities of the two PL peaks significantly reduce at the annealing temperature of 300°C, which is coincident with the annealing temperature of V_{Ga} related defect obtained from the positron lifetime measurements.

CONCLUSION

Positron lifetime and photoluminescence measurements were employed to study the Ga vacancy related defects in Zn-doped and undoped GaSb. By the positron lifetime technique, Ga vacancy was identified in both the Zn-doped and the undoped samples. Two luminescence signals, namely 777meV and 799meV, were identified in the PL measurement and were related to conduction band or donor to $V_{Ga}Ga_{Sb}$ transition and exciton bound with neutral $V_{Ga}Ga_{Sb}$ respectively. The two PL signals and also the positron lifetime Ga vacancy signal disappeared

at the annealing temperature of 300°C. This observation is consistent with the general viewpoint that the 777meV and the 799meV PL peaks are related to the $V_{Ga}Ga_{Sb}$ defect.

ACKNOWLEDGEMENT

This study was supported financially by the Research Grant Council, HKSAR, China [project no. HKU7134/99P] and the Committee of Research and Conference Grant, The University of Hong Kong, China.

REFERENCE:-

- [1] A.G. Milens and H.L. Polyakov, *Solid-State Electron.* **36**, 803 (1993).
- [2] P.S. Dutta and H.L. Bhat, *J. Appl. Phys.* **81**, 5821 (1997).
- [3] R.D. Baxter, R.T. Bate and F.J. Reid, *J. Phys. Chem. Solids* **26**, 41 (1965).
- [4] D. Effer and P.J. Effer, *J. Phys. Chem. Solids* **25**, 451 (1964).
- [5] E.J. Johnson and H.Y. Fan, in *Proceedings of the 6th International Conference on Physics of Semiconductors*, 1962, p. 375.
- [6] M.D'Olive Campos, A. Gouskov, L. Gouskov and J.C. Pons, *J. Appl. Phys.* **44**, 2642 (1973).
- [7] J. Allégre and M. Avérous, in *Defects and Radiation Effects in Semiconductors 1978*, Institute of Physics Conference Series No.46 (IOP, London, 1979), Chap. 5, p. 379.
- [8] M.H. Van Maaren, *J. Phys. Chem. Solids* **27**, 472 (1966).
- [9] Y.J. Van Der Meulen, *J. Phys. Chem. Solids* **28**, 25 (1967).
- [10] C. Benort a la Guillaume and P. Lavallard, *Phys. Rev. B* **5**, 4900 (1972).
- [11] W. Jakowetz, W. Rühle, K. Breuninger and M. Pilkuhn, *Phys. Stat. Solidi A* **12**, 169 (1972).
- [12] M. Lee, D.J. Nicholas, K.E. Singer and B. Hamilton, *J. Appl. Phys.* **59**, 2895 (1986).
- [13] P.S. Dutta, K.S.R. Koteswara Rao, H.L. Bhat and V. Kumar, *Appl. Phys. A* **61**, 149 (1995).
- [14] A. Bignazzi, A. Bosacchi, R. Magnanini, *J. Appl. Phys.* **81**, 7540 (1997).
- [15] B. Méndez, P.S. Dutta, J. Piqueras, E. Dieguez, *Appl. Phys. Lett.* **67**, 2648 (1995).
- [16] R. Krause-Rehberg and H.S. Leipner, *Positron Annihilation in Semiconductors, Defect Studies*, Vol. 127 of Springer Series in Solid-State Sciences (Springer-Verlag, Berlin, 1999).
- [17] P. Hautojärvi and C. Corbel, in *Positron Spectroscopy of Solids*, Proceedings of the International School of Physics, Enrico Fermi, edited by A. Dupasquier and A. P. Mills, Jr. (ISO Press, Amsterdam, 1995), p. 491.
- [18] C.C. Ling, S. Fung and C.D. Beling, *Phys. Rev. B* **64**, 075201 (2001).

Characterization of LiInS_2 and LiInSe_2 single crystals for nonlinear optical applications

Ludmila Isaenko, Alexander Yelissev, Sergei Lobanov, Alexander Panich,¹ Vitaly Vedenyapin, Julia Smirnova, Valentin Petrov,² Jean-Jacques Zondy,³ and Guido Knippels⁴

Design & Technological Institute for Monocrystals SB RAS, Novosibirsk 630058 Russia

¹Ben-Gurion University of the Negev, Dept of Physics, P.O.Box 653, 84105 Beer Sheva, Israel

²MB-Institute for Nonlinear Optics and Ultrafast Spectroscopy, D-12489, Berlin, Germany

³Laboratoire Observatoire de Paris, 61 Avenue de l'Observatoire, F 75014, Paris, France

⁴FOM-Institute for Plasma Physics, Edisonbaan 14, 3439 MN, Nieuwegein, the Netherlands

ABSTRACT

X-ray structural analysis, nuclear magnetic resonance, optical spectroscopy and second harmonic generation were used to characterize the new nonlinear crystals LiInS_2 and LiInSe_2 which possess maximum band gap (3.59 and 2.86 eV at 300 K, respectively) among ternary chalcogenides. As grown crystals are only slightly colored while color change after annealing is due to native point defects.

INTRODUCTION

Only few suitable nonlinear crystals are available for generation of coherent radiation tunable in the mid-IR (3 to 20 μm), a spectral region of great importance for vibrational molecular spectroscopy and atmospheric sensing. An active search for new nonlinear crystals for this region is in progress now. The new materials that can be successfully added to this limited list of crystals are LiInS_2 and LiInSe_2 (further LIS, LISe, respectively). The first one was first studied by Boyd and co-workers in the 70-ies [1], and has recently enjoyed renewed interest because of its attractive optical properties, such as the large transparency range from 0.35 to 13 μm and the high (estimated at 10.6 μm [1]) nonlinear susceptibility $d_{33}=15.8 \text{ pm/V}$. No information about the nonlinearity of LISe was available, but it was expected to be higher. Problems with growth of the LiInS_2 and LiInSe_2 crystals were solved recently and large crystals of high optical quality became available [2,3]. One of the typical features of ternary compounds is considerable variation of their color depending on growth or annealing conditions. Taking into account that such coloration can be due to phase transitions and affect strongly the main output parameters including nonlinear efficiency, we studied LIS and LISe samples of different color using several structurally sensitive techniques: X-ray structural analysis, nuclear magnetic resonance (NMR), frequency conversion (nonlinear susceptibility and phase-matching conditions) and optical spectroscopy and showed that color variations can be due to point defects.

EXPERIMENTAL DETAILS AND DISCUSSION

Samples: Crystal growth and annealing

The bulk LIS and LISe crystals were grown by the Bridgman-Stockbarger technique on (001) and (010) seeds. Details of LIS growth were given in [2], the growth techniques for LISe is very similar. Special attention is paid to ratios between components in the charge. A correction of the stoichiometric $\text{Li:In:S (Se)}=1:1:2$ ratios is made taking into account different stability of the

elements to weight loss during the runs because of volatilization and interaction between melt and container walls. An additional post-growth thermal treatment in chalcogen vapor at temperature close to melting point is performed to remove the small opaque inclusions of different phases. The as-grown samples are almost colorless for LIS or yellow to greenish for LISe. For as-grown samples chemical analysis indicates 1 to 3% deficit of chalcogen relative to metals (Li+In), on the other hand there is 2 to 4% Li deficit relative to In [2]. There are a lot of small inclusions inside as-grown LIS and LISe crystals which make them milky and one uses a high temperature annealing in chalcogen vapor to make samples highly transparent. It is a wide-spread technological treatment which is used for other crystals such as AgGaS_2 or AgGaSe_2 . Indeed, chemical analysis shows up to 3% surplus S or Se [2] after annealing, but in contrast to the mentioned compounds LIS and LISe change their color considerably: Annealed LIS is rose and LISe becomes dark red to opaque. Since the phase diagram can be very complicated for ternary compounds and the area of homogeneity related to a certain phase is sometimes only about 1 w.% in width, it is necessary to verify that the crystal structure remains unchanged after annealing. Thus as-grown and annealed samples of LIS and LISe were compared using different structurally sensitive techniques.

The X-ray structural analysis

The crystal structure determination for different LIS and LISe samples was performed using CAD4 diffractometer along with the SHELXL97 structure determination/refinement program. For all samples investigated identical structure (space group $\text{Pna}2_1$, wurtzite- type lattice) was established, but lattice parameters somewhat varied: they increased in line with color intensity (Table 1).

Table I. Lattice parameters for LiInS_2 and LiInSe_2 single crystals of different color determined in the present work and comparison with Ref.[1,4]

Crystal	LiInS_2			LiInSe_2			
Color	Colorless	Yellowish	Rose	Yellow	Greenish	Rose	Dark red
Space group	$\text{Pna}2_1$	$\text{Pna}2_1$	$\text{Pna}2_1$	$\text{Pna}2_1$	$\text{Pna}2_1$	$\text{Pna}2_1$	$\text{Pna}2_1$
a [Å]	6.874(1) 6.894 [1]	6.890(1)	6.896(1)	7.1917(8)	7.192	7.1939(8)	7.1934(10) 7.218 [4]
b [Å]	8.0332 8.064 [1]	8.053(1)	8.058(2)	8.4116(10)	8.412	8.4163(10)	8.4159(11) 8.441 [4]
c [Å]	6.462(1) 6.485 [1]	6.478(2)	6.484(4)	6.7926(8)	6.793	6.7926(8)	6.7971(9) 6.772 [4]
V [Å ³]	356.82 360.5 [1]	359.43	360.3	410.90(8)	410.97	411.27(8)	411.49(9) 412.6 [4]

Nuclear Magnetic Resonance: LiInSe_2

Both ^7Li ($I=3/2$) and ^{115}In ($I=9/2$) are quadrupole nuclei: their NMR line shape is sensitive to the variations of the structure of compound and to existing defects. Single crystals of LISe $3.5 \times 3.5 \times 5 \text{ mm}^3$ in size were placed into an NMR coil of 5 mm in diameter. The powder samples were prepared also from the same crystals. The ^7Li and ^{115}In spectra were measured with a Tecmag pulse

NMR spectrometer in the applied magnetic field of 8.0196 T (at resonance frequencies 132.68 and 74.84 MHz for ^7Li and ^{115}In nuclei, respectively), using Fourier transformation of the spin echo signals accumulated with the 16-phase cycled sequence. The length of $\pi/2$ pulse was 4 μs for ^7Li and 5 μs for ^{115}In . Angular dependence was measured when the crystals were rotated around their c -axis, which was perpendicular to the applied magnetic field. All samples exhibited very long spin-lattice relaxation time (around 1 h) which is characteristic for high purity compounds.

^7Li and ^{115}In NMR spectra of LiSe single crystals and powders are given in Fig. 1A and Figs. 1B-1C, respectively. Both ^7Li and ^{115}In should show quadrupolar perturbed NMR signals. In single crystal, the NMR spectrum of ^7Li nucleus with $I=3/2$ consists of three lines. Besides a single resonance at Larmor frequency ν_0 , two satellites with the first-order shift of

$$\nu_1 = e^2qQ(3\cos^2\theta - 1)/4h \quad (1)$$

occur. Here q is the electric field gradient (EFG), Q is the quadrupole moment of the nucleus, θ is the angle between applied magnetic field and the principal axis of the EFG tensor, and h is the Planck's constant. The aforementioned satellites are clearly seen in the ^7Li spectrum of single crystal (Fig. 1A). In the powder (Fig. 1B), the central line and the satellites are almost unresolved due to the overlap caused by angular dependence of the resonance frequency given by Eq.(1). For ^{115}In nucleus with $I=9/2$, nine satellites should occur. However, they are hardly excited with our $\pi/2$ pulse, and thus we show and analyze only the central line corresponding to $S \rightarrow -S$ transition.

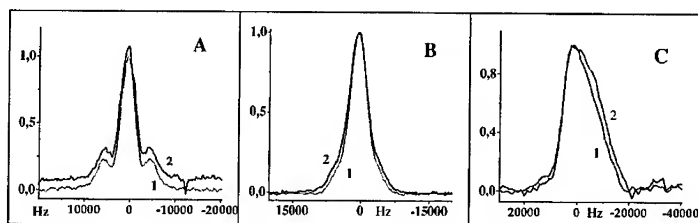


Fig. 1: A. Room temperature ^7Li NMR spectra of single crystal LiInSe_2 corresponding to the maximal splitting of the lines. Orientation of external magnetic field B_0 is: $B_0 \perp c$, angles $(B_0, a) = 22.5^\circ$, $(B_0, b) = 67.5^\circ$ (with accuracy about 2-3°). For as-grown (1) and annealed (2) samples, the spectrum of the latter is shifted upwards for clarity. B and C: Room temperature ^7Li and ^{115}In NMR spectra for as-grown (1) and annealed (2) powder LiInSe_2 , respectively.

Line width of the quadrupolar perturbed NMR signals is caused by dipole-dipole interaction of nuclei and distribution of electric field gradients existing in an imperfect crystal. The nearest neighbors of In and Li atoms are Se atoms. Due to the low natural abundance of ^{77}Se isotope (7.6%) having nuclear spin and rather large Li-Li, In-In and Li-In distances (around 4.1 Å), the dipole-dipole interactions among nuclei are weak; their contribution into the second moment of the resonance line is calculated to be around 1 kHz^2 for both ^7Li and ^{115}In . Moreover, the dipole-dipole interactions should be the same for the as-grown and annealed samples. Thus the main contribution to the line width results from the distribution of EFGs, and the difference in the line width is caused by the variation of this distribution in annealing. From Fig. 1B-C, one can see that the powder ^7Li

and ^{115}In NMR spectra of as-grown and annealed LiSe are very similar, though the resonance of the annealed sample is a little bit broader. Two reasons are suggested: 1. The EFG distributions on Li and In nuclei are broader in the annealed sample, which is less perfect than the as-grown one. It may be, for example, because surplus Se atoms occupy the unfilled tetra- or octahedral sites of the lattice. Such an imperfection of the crystal creates an additional electric field gradient at nucleus; these gradients vary from site to site and yield additional line broadening. 2. The structural parameters of the two samples are a little bit different, resulting in EFG values larger in the annealed sample than in the as-grown one. Such effect would lead to a difference in the quadrupole splitting of the NMR spectra of the two crystals, which is not obtained in the single crystalline spectra (Fig.1A). Thus one can conclude that both as-grown and annealed LiInSe_2 samples have identical crystal structure and the negligible differences in NMR spectra can be related to point defects such as surplus Se ions in different positions in crystal lattice.

Optical absorption spectroscopy

Optical transmission spectra in the whole transparency region were recorded, using Shimadzu UV-3101 UV/VIS/NIR and Bomem FTIR spectrometers (Fig.2). Both shortwave and longwave

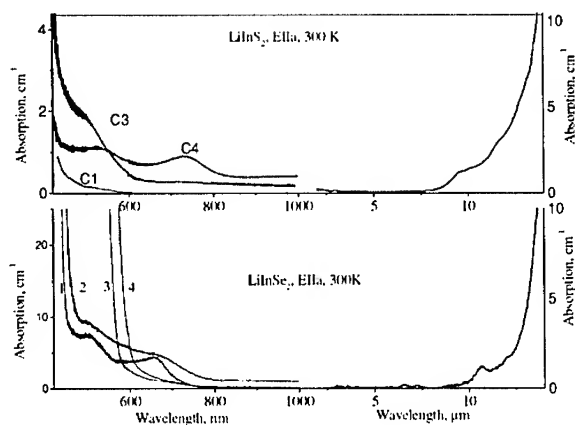


Fig.2 Absorption spectra for LIS(A) and LISe(B). In A: C1 and C4 are as-grown LIS samples; C3 was annealed [2]. In B spectra 1,2 were obtained for yellow as grown LISe and 3,4 correspond to a dark red sample. Spectra 1,3 and 2,4 were recorded at 80 K and 300 K, respectively.

edges of transparency region are important for crystal characterization. The latter is determined by lattice vibrations and one can see in Fig.2 that both for LIS and LISe it is identical in shape and position for as-grown and annealed crystals. The shortwave absorption edge characterizes band-to-band electronic transitions: in real crystals the near-edge absorption bands due to native defects mask it usually and this is the reason why thin samples, less than 0.1 mm thick are studied. For LIS this work has been reported in [2]. In both as-grown colorless and annealed rose samples the absorption spectra were found to become straight lines in $(\alpha \cdot h\nu)^2 = f(h\nu)$ coordinates and to lead

to identical band gap: $E_g = 3.72$ and 3.59 eV at 80 and 300K, respectively. The rose color of thick annealed LIS samples was due to broad bands at 420 and 540 nm [2]. For as-grown LISe the same approach gave $E_g = 3.04$ and 2.86 eV at 80 and 300K [5], respectively, but for annealed samples some additional intense bands with maxima in the 500 to 550 nm range superimpose the fundamental edge even at 0.1 mm thickness and it was necessary to decrease the thickness further. As a result annealed thin plate is red in color. It is important to note that illumination by a visible light with $\lambda \sim 400\text{--}500$ nm from 1kW Xe lamp through MDR2 diffraction monochromator was found to remove the red color of annealed LiInSe_2 crystals and to make them yellow, the effect being reversible. Such effects are typical of the recharge of point defects in solids.

Refractive indices, phase-matching and nonlinearity

For yellow and rose LIS samples tensor components of $d_{15} = 8.35$ pm/V and $d_{24} = 8.3$ pm/V were deduced both from precise gaussian beam analysis of the SHG process and also by relative measurements [6]. These values are only slightly lower than estimations based on non-phase matched methods presented in [1] at $10.6\text{ }\mu\text{m}$ ($d_{31} = 9.9$ pm/V and $d_{32} = 8.6$ pm/V, $d_{31} = d_{15}$ and $d_{32} = d_{24}$ under Kleinman symmetry). Study of the second harmonic generation for LIS showed practically identical phase-matching conditions for as-grown and annealed samples (Fig.3) which confirms that refractive indices and their dependence on wavelength are similar for these samples. Thus their structure is also the same. Some difference from [1] is likely to be due to variations in growth conditions and differences in real structure.

Refractive indices of as-grown and annealed LISe samples were measured for n_x and n_z using conventional technique of minimum deviation angles with one and the same prism which was

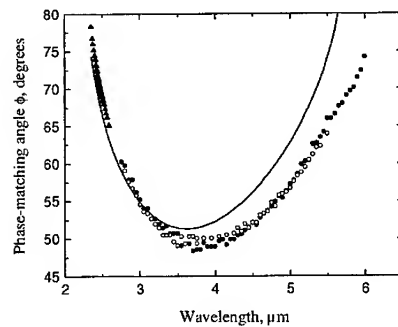


Fig.3 Measured internal phase-matching angles for the as-grown (open dots) and annealed LIS (solid dots), obtained using a free electron laser [6]. The solid triangles were measured for annealed, rose LIS with a nanosecond OPO as the pump source. The line is the calculated phase-matching curve based on Boyd's refractive index data [1].

annealed after the first stage of experiments. The indices obtained before and after annealing are given in Table 2 and one can see that they are identical within the experiment accuracy. Nonlinear parameters were measured only for as-grown LISe samples to date: they are 1.26-1.56 times higher

than those for LIS [3]. Investigation of LISe phase-matching conditions and nonlinear parameters is in progress.

Table II. Comparison of refractive indices for LiInSe_2

λ , nm	Yellow-greenish LiInSe_2		Dark red LiInSe_2	
	n_x	n_z	n_x	n_z
700	2.3627	2.4215	2.3615	2.4219
800	2.3341	2.3886	2.3347	2.3752
900	2.3130	2.3656	2.3138	2.3662
1000	2.3004	2.3507	2.3006	2.3513
1500	2.2704	2.3188	2.2709	2.3186
1900	2.2619	2.3082	2.2619	2.3090

CONCLUSIONS

Combined investigation of as-grown and colored annealed LIS and LISe crystals using X-ray structural analysis, NMR, optical absorption spectroscopy, refractive indices and phase matching conditions showed the identity of their structure and of main physical properties, which allows to associate the coloration at annealing in chalcogen vapor with native point defects: Both as-grown and annealed samples are feasible for nonlinear optical applications.

ACKNOWLEDGEMENTS

This work was partially supported by the European Community INCO-COPERNICUS program (grant No ERBIC15-CT98 0814), ISTC and CRDF (grant RE2-2222, proposal 6410).

REFERENCES

1. G. D. Boyd, H. M. Kasper, and J. H. McFee, *J. Appl. Phys.* **44**, 2809-2814 (1973).
2. L. Isaenko, I. Vasilyeva, A. Yeliseyev, S. Lobanov, V. Malakhov, L. Dovlitova, J.-J. Zondy, I. Kavun, *J. Cryst. Growth*, **218**, 313-321 (2000).
3. L. Isaenko, A. Yeliseyev, S. Lobanov, F. Rotermund, V. Petrov, G. Sleky, and J.-J. Zondy, *J. Appl. Phys.* (2001), in press.
4. T. Kamijoh and K. Kuriyama, *J. Cryst. Growth* **51**, 6-11 (1981).
5. L. Isaenko, A. Yeliseyev, J.-J. Zondy, G. Knippels, I. Thenot, S. Lobanov, *Opto-electronic review*, **9**, 135-141 (2001).
6. G. M. H. Knippels, A. F. G. van der Meer, A. M. MacLeod, A. Yeliseyev, L. Isaenko, S. Lobanov, I. Thenot, J.-J. Zondy, *Opt. Lett.* **26**, 617-619 (2001).

Optical Constants of Annealed a-Si:H from Transmittance at Normal Incidence

Atsutoshi Doi and Yoshiyuki Matsumoto

Department of Electrical Engineering, Faculty of Science and Engineering, Kinki University,
Kowakae, Higashiosaka, Osaka 577-8502, Japan

ABSTRACT

We study changes in the optical constants of a-Si:H films caused by the thermal annealing involved in solid phase crystallization. The aim is to examine the growth mechanism, since changes in refractive index are most probably caused by a change in the network structure. The refractive index change was studied from interference fringes in transmitted light at normal incidence, and shows differing dependence on temperature in different thermal ranges. DSC measurement was also performed to examine changes in the network structure with temperature. Changes in optical and thermal properties induced by an increase of temperature reveal frequent network changes of a-Si:H below 470 °C and of a-Si in the range 470 to 570 °C. We also found crystallization at about 570 °C, and grain growth above the crystallization temperature. Knowledge of network changes in a-Si film allows orientation control by an external seed.

INTRODUCTION

Solid phase crystallization of amorphous silicon films deposited on glass substrates is a potentially useful process that has received considerable attention [1,2]. However, little is known about network changes caused by the thermal annealing that takes place with crystallization. Changes in the network structure are most likely to change the refractive index. Accordingly, we investigate changes in the optical constants of annealed a-Si:H films with a view to understanding changes in crystallization of the mother network.

Optical properties of a-Si:H films have been studied by ellipsometric measurement. Standard ellipsometry measures two relative properties of orthogonally polarized radiation. Determination of the three quantities, refractive index n , absorption coefficient α , and film thickness d , therefore requires a further independent measurement that may introduce additional errors as a result of any irregularity in the thickness. In our work, optical constants were obtained by analyzing interference fringes in transmitted light at normal incidence [3,4].

Thin a-Si:H films were deposited onto quartz substrate by PECVD. Measurements were made after isochronous annealing for 16 hours, at temperatures up to 1000 °C. The refractive index depends differently on temperature in distinct ranges; the transition temperatures between these ranges are 240, 340, 450, 570, and 680 °C. The transitions at the lowest three temperatures probably involve network changes in the a-Si:H film; the transition at 570 °C is due to crystallization of a-Si; and the transition observed above the crystallization temperature is due to grain growth. Differential scanning calorimetry (DSC) is performed to examine changes in the network structure as the temperature varies. Our demonstration that external seeding can control crystalline orientation verifies the value of transmittance analysis in detecting changes in the network.

EXPERIMENT

Undoped a-Si:H films were deposited on quartz substrates for use in transmittance measurements, and also onto crystalline silicon substrates for FTIR measurements using a parallel plate PECVD apparatus. Radio-frequency electromagnetic waves (13.56 MHz) of power 2 W (power density roughly $3.7 \times 10^{-2} \text{ W/cm}^2$) were used in a glow discharge of pure silane gas fed at 3.3 sccm. The chamber pressure was maintained at 10 Pa. The deposition temperature was varied from 150 to 300 °C. Film thicknesses were between 0.7 and 0.9 μm .

The hydrogen concentration C_H in the film was determined by infrared spectroscopy (FTIR-8100, Shimadzu). The integrated intensity of the Si-H stretching mode at the wavenumbers $\nu = 2000 \text{ cm}^{-1}$ and $\nu = 2090 \text{ cm}^{-1}$ were used to determine C_H [5].

Transmittance spectra of the a-Si:H thin films on a quartz substrate of thickness 0.8 mm were measured in air at normal incidence using a double beam spectrophotometer (UV-2500PC, Shimadzu). The model of the analysis used here is essentially that of Manifacier *et al.* [3], except that a rear side surface of the substrate is incorporated to allow for multiple reflection in the substrate. The three optical parameters of the film, n , α , and d , were fitted numerically [4]. The weak absorption approximation [3] was used to generate initial iteration values for n and α . An initial value for the film thickness d was obtained by interference microscopy.

An experimental transmittance (T_{exp}) curve is shown in figure 1. Envelopes of interference maxima and minima, T_{max} and T_{min} , were modeled using spline interpolation. These three independent data suffice to determine the refractive index n , the absorption coefficient α , and the film thickness d . The refractive index and the absorption coefficient based on figure 1 are shown in figures 2(a) and 2(b). Then, we can calculate transmittance T_{cal} using these optical constants, and this is also shown in figure 1. Clearly T_{exp} and T_{cal} show excellent agreement. Accuracy of the numerical calculation for n and α was checked by comparing the experimental values with the calculated results. Calculation errors were evaluated as follows. Firstly, we obtained an exact solution of the transmittance corresponding to hypothetically introduced optical constants. Then, we determined new optical constants only from the transmittance. Finally, calculation errors were obtained by

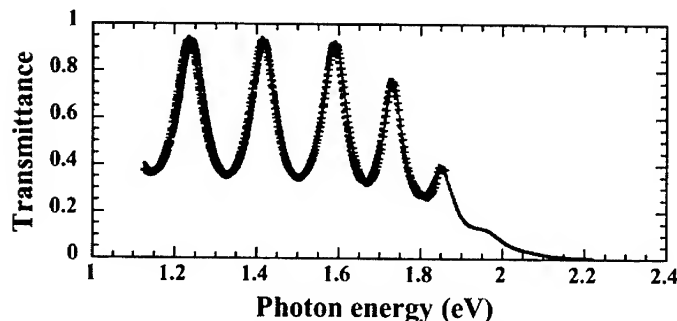


Figure 1. Transmittance of an a-Si:H film for experimental (dots) and calculated (+) values showing good agreement in the low loss region.

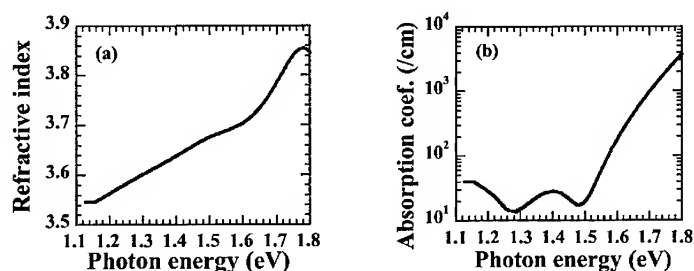


Figure 2. Optical constants for the a-Si:H film in figure 1 are shown as a function of incident photon energy; (a) refractive index and (b) absorption coefficient.

comparing the initial optical constants with newly determined ones. The calculation error for n was less than 2 % at $E = 1.15 \sim 1.85$ eV. Figure 2(a) reveals that the numerical error for n increases above $E = 1.5$ eV. We therefore determined the refractive index n at a photon energy of 1.4 eV. This is where the smallest calculation errors are expected, since the envelope curves vary slowly and the turning points of the envelopes are a long way away. Figure 2(b) shows that the numerical error for α increases in the low loss region. The error also increases in the high loss region where the interference fringes are very weak. Accuracy of the absorption coefficient was less than ± 20 % for $350 < \alpha < 4500 \text{ cm}^{-1}$. We therefore define a characteristic energy E_{1500} as the photon energy for which $\alpha = 1500 \text{ cm}^{-1}$ so as to evaluate the loss with minimum calculation error.

Thermal analysis of the a-Si:H films was carried out by DSC, using a Shimadzu DSC-50 to assess network structure changes during annealing of the film. Samples for DSC measurements were deposited at 200 °C on quartz disks (200 μm thick, 4mm in diameter) to a thickness of about 0.48 μm . Ten samples were placed in a quartz pan with an alumina sample (0.010g) in a reference pan. The DSC module was located in a helium atmosphere (35ml/min). Samples were heated at 0.5 °C/min up to 700 °C.

It is well known that the photoinduced change of electronic properties in a-Si:H, known as the Staebler–Wronski effect (SWE), is closely related to network changes [6,7]. For SWE evaluation with temperature, a set of 10 samples were irradiated by light at 300 mW/cm² for 1 hour. The first DSC measurement was performed by heating the photodegraded samples to 200 °C, and the samples were annealed in the dark by maintaining them at this temperature for 30 min. The second DSC measurement up to 200 °C followed after cooling the samples to room temperature. Differences between these measurements show network changes related to the SWE. The measurement steps were repeated twice, and an accumulation was made of the difference in order to improve the S/N ratio.

RESULTS AND DISCUSSION

Variation of refractive index with temperature is shown in figures 3. Data plots are shown for both deposited and annealed a-Si:H films. The refractive index increases with temperature up to about 570 °C. Although the data points show some irregularity, the temperature variation of the refractive index can nevertheless be partitioned into several

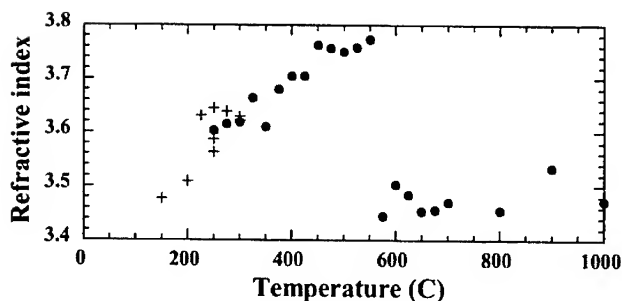


Figure 3. Refractive index of deposited a-Si:H films (+), and annealed films (●) as a function of temperature.

intervals. Approximate transition temperatures between these intervals are 240, 340, 450, and 570 °C. A weak dependence of the refractive index on temperature is observed in the ranges 240–340 and 450–570 °C, but a strong dependence in the other intervals. These changes seem to be caused by changes in the mother network.

The hydrogen concentration (C_H) measurement indicates that C_H decreases as the temperature increases, and reaches zero at about 475 °C. The transition temperatures at 240, 340, and 450 °C are therefore most probably due to network changes of the a-Si:H. Our PECVD apparatus gave device-quality a-Si:H films at a deposition temperature of about 240 °C, which is very close to the lowest critical temperature. Device-quality films relate to their defect density [8]. The present result indicates that the defect density can be related to network changes.

Variation of the characteristic energy E_{1500} with temperature is shown in figure 4(a). Data for deposited and annealed films are again both plotted in the figure. The same critical temperatures as shown in figure 3 are seen in figure 4(a). Since the turning points are not clear in this figure, however, data points up to 500 °C are plotted in figure 4(b) as a function of hydrogen concentration. The transition temperatures of 240, 340, and 450 °C correspond to critical hydrogen concentrations of about 15, 10, and 5 atomic %. It is seen

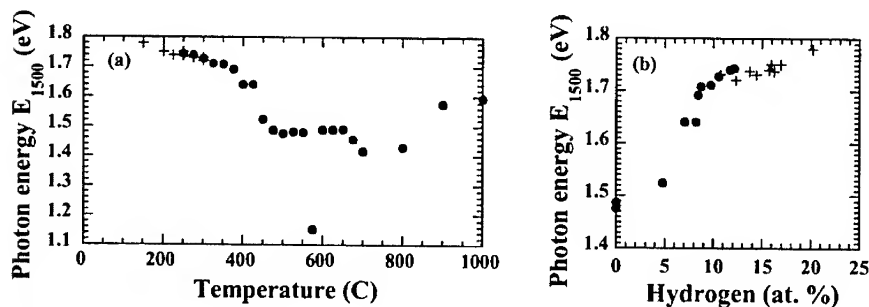


Figure 4. Change of photon energy E_{1500} with (a) temperature, and (b) hydrogen concentration. Data plots are shown for both deposited films (+), and annealed films (●).

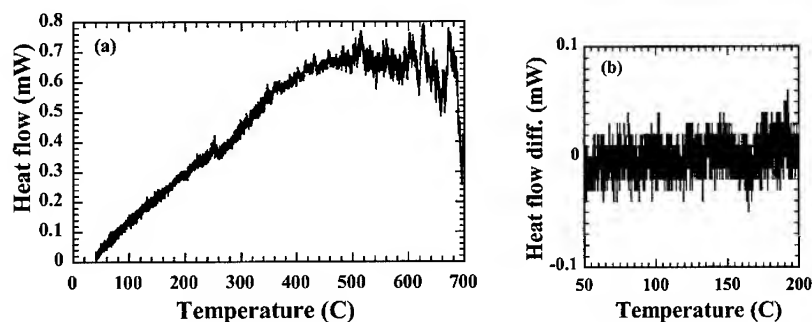


Figure 5. (a) DSC spectrum of a-Si:H films deposited at 200 °C and (b) accumulated heat flow difference between a-Si:H films with and without photoinduced network changes.

that the absorption properties of a-Si:H change at the critical temperature.

The sudden change at 575 °C in figures 3 and 4(a) is most probably caused by a crystallization. Nano-crystals reduce the refractive index and make the film opaque. Since a narrow range in particle size is responsible for the strong absorption, a low E_{1500} value is seen in a narrow temperature range in figure 4(a). The XRD spectrum of annealed films also indicated crystallization at above 570 °C. The turning points in figures 3 and 4 at above 570 °C therefore show grain growth.

Changes in the mother network in the annealed film with temperature were investigated using DSC measurements. A typical DSC spectrum is shown in figure 5. The exothermic spikes above ~ 570 °C are most probably caused by grain growth, and those below the crystallization temperature by a network change in the a-Si (around 470 and 570 °C) or a-Si:H (below 470 °C). A different DSC spectrum was observed for each measurement; however, several exothermic peaks were observed at similar temperatures: 225–250, 417, 560, 575, 610, and 670 °C. The exothermic peak at 225–250 °C varies from run to run but is the largest signal around 240 °C. Since this characteristic temperature is almost the same as that observed in figures 3 and 4, the thermal characteristics also support the hypothesis that fabrication of device-quality a-Si:H film depends on network changes. Small signals at 560 and 575 °C presumably correspond to the crystallization that generates sharp changes in optical properties as shown in figures 3 and 4. The larger signals at temperatures above the crystallization temperature in figure 5(a) most probably correspond to the growth of larger grains. The exothermic peak at 670 °C appears to correspond to the critical temperature of 680 °C in figures 3 and 4. The accumulated heat flow difference is indicated in figure 5(b). Exothermic peaks located in a range of 190–192 °C are enhanced by the accumulation. These peaks therefore correspond to the SWE.

Frequent change in the network is observed in figure 5(a) even though the temperature is well below the crystallization threshold. This suggests a possible means of control of the crystalline orientation in the film if the film is in contact with a seed crystal. Accordingly, isothermal annealing was performed with a (100)-oriented Si wafer at about 560 °C. The XRD spectrum of the film is shown in figure 6. It is well known that a crystallized a-Si film shows (111), (220) and (311) peaks in its XRD spectrum, but no (400) peak. The (400) peak in figure 6 is clearly caused by the (100)-oriented seed crystal.

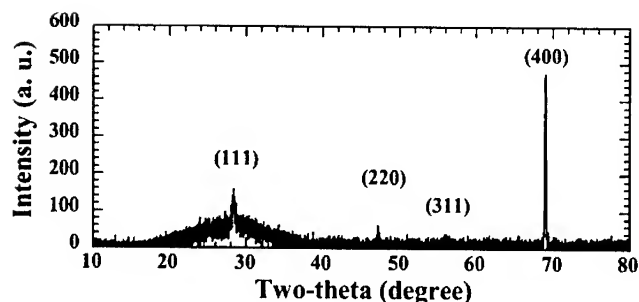


Figure 6. XRD spectrum of annealed a-Si film. The sample was maintained in contact with a (100) seed crystal during annealing.

CONCLUSIONS

We have studied changes in the Si network structure in annealed a-Si:H films from their optical and thermal properties. Optical properties were obtained from interference fringes in the transmittance at normal incidence, and thermal properties by DSC. The optical properties show differing temperature dependence in distinct temperature ranges. The transition temperatures of 240, 340, and 450 °C between these ranges correspond to network changes in a-Si:H: at 570 °C to crystallization; and at 680 °C to grain growth. The thermal properties indicate more transition temperatures arising from network changes. We highlight the fact that the SWE is related to network changes in the range 190 – 194 °C, and that the fabrication of device-quality a-Si:H film is related to a network change at around 240 °C. Finally, successful solid-phase seeding has been demonstrated, stimulated by network changes in a-Si films at temperatures around 475 and 570 °C.

REFERENCES

1. T. Aoyama, Y. Mochizuki, G. Kawachi, S. Oikawa, and K. Miyata, *Jpn. J. Appl. Phys.* **30**, L84 (1991).
2. A. Doi, M. Kumikawa, J. Konishi, and Y. Nakamizo, *Appl. Phys. Lett.* **59**, 2518 (1991).
3. J. C. Manifacier, J. Gasiot and J. P. Fillard, *J. Phys. E: Sci. Instrum.* **9**, 1002 (1976).
4. R. Swanepoel, *J. Phys. E: Sci. Instrum.* **16**, 1214 (1983).
5. H. Shanks, C. J. Fang, L. Ley, M. Cardona, F. J. Demond and S. Kalbitzer, *Phys. Stat. Sol. (b)* **100**, 43 (1980).
6. K. Shimizu, T. Tabuchi, M. Iida and H. Okamoto, *J. Non-Cryst. Solids* **227-230**, 267 (1998).
7. T. Gotoh, S. Nonomura, M. Nishio, S. Nitta, M. Kondo and A. Matsuda, *Appl. Phys. Lett.* **72**, 2978 (1998).
8. G. Ganguly and A. Matsuda, *J. Non-Cryst. Solids* **164-166**, 31 (1993).

Field Effect Controlled Photoresistors Based on Chemically Deposited PbS Films

Eugenia Pentia, Lucian Pintilie, Ion Matei, Ioana Pintilie,
National Institute of Materials Physics, Atomistilor 105 bis,
P.O. Box MG-7, 76900 Bucharest-Magurele, Romania
Fax: +401-4930267; E-mail: epentia@alpha1.infim.ro

ABSTRACT

MOS-like structures were obtained by chemical deposition of a polycrystalline PbS thin film on top of a silicon dioxide/Si substrate. Gold ohmic electrodes in coplanar configuration were subsequently deposited by vacuum evaporation on PbS surface (drain and source electrodes). The gate aluminum electrode was deposited on the back of the Si substrate. The dependence of the photoconductive signal, generated in the PbS film, on the gate voltage was studied for wavelengths ranging between 800 nm and 3000 nm at room temperature as well as at low temperatures. It was found that the relative variation of the signal could be as high as 50 % for gate voltages ranging between -30 V and +30 V. Two possible mechanisms are proposed to explain the signal variation with the gate voltage: 1) Variation of the depleted region's thickness in the PbS film, that leads to a variation of the conduction channel's resistance (the reference resistance called, also, the dark resistance), 2) The possible variation of the majority carriers (holes) life-time due to the electron blocking at the PbS/oxide interface when positive gate voltages are applied on the back electrode. Integrated IR detectors with controlled sensitivity in the 800-3000 nm range can be manufactured at a relatively low cost using the PbS/oxide/Si MOS-like structure.

INTRODUCTION

Lead sulfide (PbS) is a A_4B_6 semiconductor compound with very good photoconductive properties in the near infrared (NIR) spectrum. The sensitivity domain at room temperature is 600-3000 nm, with a maxima at around 2200-2400 nm [1,2]. The standard method used to obtain PbS thin films with good IR detection properties is the Chemical Bath Deposition (CBD) [3-5]. Other technique that started to be used in the last years for producing PbS based optoelectronic devices (laser diodes) is the hot wall epitaxy [6].

PbS films are mainly used to produce high sensitivity photoconductive cells for NIR. The spectral sensitivity could be as high as $10^{11} \text{ cmW}^{-1}\text{Hz}^{1/2}$ at maximum wavelength [7]. Even PbS was intensively studied in the past, being considered as the template of polycrystalline semiconductor compounds, further studies are under way on this material in the last years. The main target of these are: 1) to clarify the connection between bath composition, film morphology and physical properties of the film [3,8-10]; 2) to integrate PbS IR detectors with standard semiconductor technology [11,12]; 3) to develop new types of heterojunctions and heterostructures with enhanced detection properties by combining PbS with other materials (semiconductors or/and dielectrics) [11-13]. The last direction of research is particularly interesting because it offers the possibility to manufacture different type of devices, including field effect ones [14].

The paper continues the study of field effect assisted photoconductivity started in our group in the last 5 years [14,15]. It presents an enhanced PbS based heterostructure, obtained by deposition of

a PbS layer on a SiO₂/Si(n-type) substrate. A MOS-like structure was manufactured and the influence of the field effect on the photoconductive properties of PbS film were investigated.

EXPERIMENTAL DETAILS

The SiO₂ layer was grown on single crystalline n-type Si wafers. The thermal oxidation in oxygen and water vapors at 850 °C was used. The final thickness of the SiO₂ layer was of about 250 nm. The PbS film was deposited by CBD method, using lead nitrate (Pb(NO₃)₂) as Pb²⁺ ions source and thiourea as S²⁻ ions source. The deposition is performed in alkaline medium, using sodium hydroxide (NaOH), the starting solution pH being 11. Small amounts of a reducing agent (hydroxylamine chlorhydrate) and of a Bi salt are introduced in the bath in order to control the nucleation/growth process during the deposition of the PbS layer. The PbS film is then photolithographic processed, leaving an area of 2.5x3.5 mm². Gold electrodes are vacuum evaporated on PbS surface, the final active area being of 1.5x1.5 mm². After electrode deposition, the PbS films are aged at 80 °C for about 80 hours, in air. The final structure is schematically presented in fig. 1, together with the electric set-up used for field effect assisted photoconductivity measurements.

The sample was introduced in the closed-cycle He cryostat with IR optic facilities and the measurements were performed in modulated light, using the standard set-up composed by a grating monochromator model Spex270, a lock-in amplifier model SR830DSP, a d.c. voltage source (2 channels) model Grundig 300, an incandescent lamp as an IR source (30 W nominal electric power) and a mechanical chopper model Ithaco 383A. The value of the load resistance was 500 kohm.

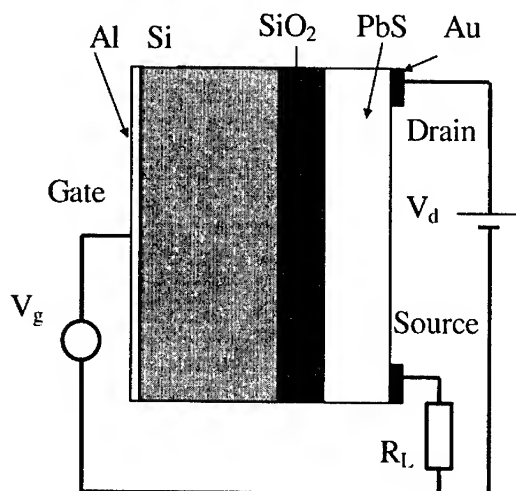


Fig. 1 The schematic of the pseudo-MOS PbS/SiO₂/Si structure and of the electrical set-up used for field effect assisted photoconductivity measurements. V_d – drain voltage; V_g – gate voltage; R_L – load resistance.

RESULTS AND DISCUSSION

In fig. 2 the spectral distribution of responsivity, for different polarities and values of the gate voltage, are presented. The responsivity is defined as the ratio between the measured signal S , expressed in Volts (V), and the incident power P_{inc} on the detector surface, expressed in Watts (W):

$$R(V/W) = \frac{S(V)}{P_{inc}(W)} \quad (1)$$

The drain voltage was in all cases +30 V. The open square curve was obtained for floating gate (the gate electrode is not connected). It can be observed that for positive gate voltages the signal increases and for negative gate voltages decreases on the entire sensitivity range of PbS. We remind that, for photoconductive measurements, a d.c. voltage is applied on the drain electrode while the signal is collected from the load resistance connected to the source electrode.

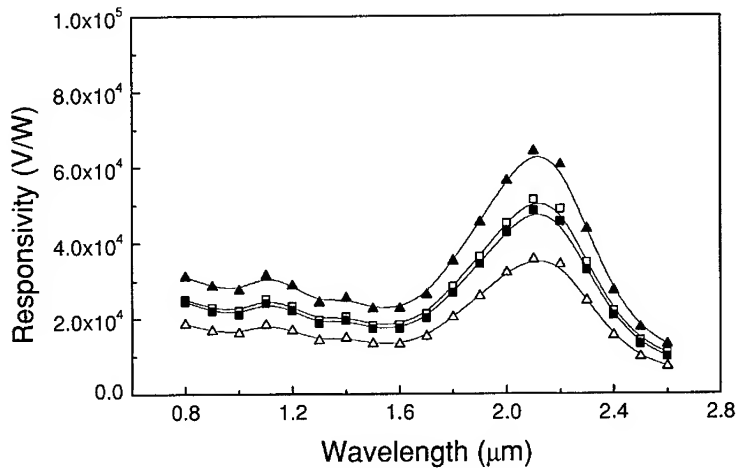


Fig. 2 Spectral distribution of responsivity in case of PbS/SiO₂/Si heterostructures, for different gate voltages. Open squares-floating gate; Solid squares-ground gate; Solid triangles- $V_g = +30$ V; Open triangles- $V_g = -30$ V. Drain voltage was +30 V.

The wavelength was then set to a certain value (1000 nm and 2000 nm) and the room temperature dependence of the photoconductive signal on the gate voltage was raised. The obtained results are presented in fig. 3. The dependence is almost linear up to about $V_g = 15$ V and then has the tendency to saturate. Finally, the temperature dependence of the photoconductive signal was raised for different gate voltages (see fig. 4).

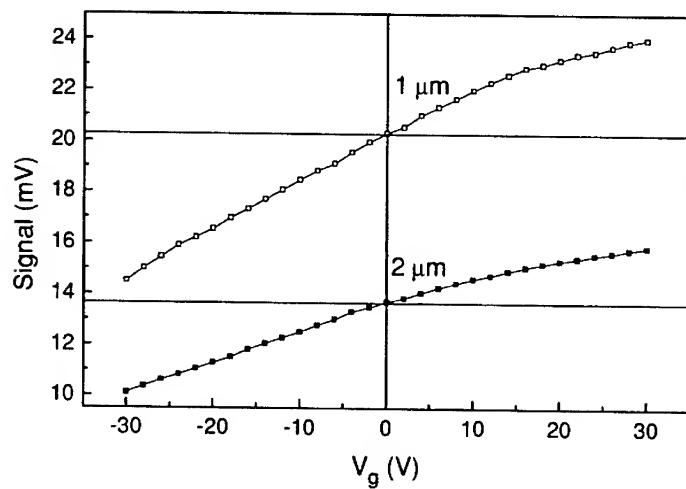


Fig. 3 The dependence of the photoconductive signal on the gate voltage.

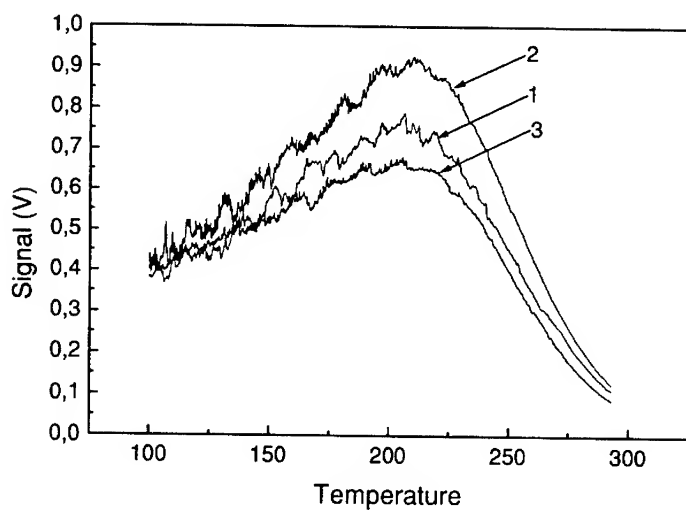


Fig. 4 The temperature dependence of the photoconductive signal, determined for different gate voltage: 1) 0 V gate voltage; 2) +30 V gate voltage; 3) -30 V gate voltage. The drain voltage was +30 V in all cases. The light was collimated on the transparent IR window of the cryostat.

From fig. 2,3 and 4 it can be seen that the photoconductive signal increases for positive gate voltage and decreases for negative ones, no matter the wavelength and temperature (at least in the 150-300 K domain). This behaviour can be explained if the influence of the field effect on the photoconductivity of PbS film is taken into consideration. The field effect is favoured by the existence of the thin SiO₂ layer that is present between the two semiconducting materials. There are two ways by which the gate voltage can change the photoconductive signal:

- a) Changing the apparent „thickness“ of the PbS film. When the gate is positive the two interfaces (PbS/SiO₂ and SiO₂/Si) go to depletion. In this case the PbS layer can be regarded as being composed of 2 distinct layers: the depleted layer, that has no free charges and, thus, no current is flowing through it; the surface conductive layer. When increasing the gate voltage V_g, the thickness of the depleted layer increases and that of the conductive layer decreases. These changes lead to an increase of photoconductive signal according with the formula:

$$\Delta v = \frac{R_L V_d}{(R_L + \frac{\rho}{d - x_{PbS}})^2} \frac{\Delta \sigma}{\sigma^2} \frac{1}{d - x'_{PbS}} \quad (2)$$

where: where: $\Delta \sigma$ is the electric conductivity variation of PbS film when it is exposed to light; σ is the dark electric conductivity of PbS film; x_{PbS} is the thickness of space charge region in PbS in dark condition; x'_{PbS} is the thickness of the space charge region in PbS when the film is exposed to light; ρ is the resistivity of the PbS film; V_d is the drain voltage; d is the total thickness of the PbS film. The quantities x_{PbS} and x'_{PbS} will depend on the gate voltage [16] (will increase with increasing V_g). x'_{PbS} will depend also on the concentration of the photogenerated carriers, as well as $\Delta \sigma$. Anyway, the dependence of the photoconductive signal on the gate voltage will be similar with that presented in fig. 3.

- b) Changing the carriers life-time. When positive gate voltage is applied electrons will be attracted to the PbS/SiO₂ interface, thus the photogenerated holes life-time will increase and same will do the photoconductive signal, according with the following formula [17]:

$$I_{foto} = q(\eta \frac{P_{opt}}{h\nu}) (\frac{\mu_n \tau E}{L}) \quad (3)$$

where: η is the quantum efficiency; P_{opt} is the incident optical power; $h\nu$ is the energy of the incident light; μ_n is the carrier mobility (holes in this case); τ is the life-time; E is the longitudinal applied electric field; L is the distance between coplanar electrodes from the surface of PbS film. If the gate voltage is negative then holes will be attracted at the PbS/SiO₂ interface. Thus the electron concentration in the conductive channel will increase, the recombination probability will be higher and the life-time of photogenerated holes will decrease, leading to a smaller photoconductive signal.

In our opinion the first mechanism is dominant for relatively small gate voltages, may be up to 10 or 15 V. After that, some inversion can occur at the PbS/SiO₂ interface. In this case, further increasing of the gate voltage will have little effect on the photoconductive signal because the negative charge accumulated at the PbS/SiO₂ interface will not allow other electrons to be attracted there. This could explain why with increasing the positive gate voltage the signal has the tendency to saturate.

CONCLUSIONS

A pseudo-MOS structure was developed on the basis of a PbS/SiO₂/Si heterostructure. It was both experimentally and theoretically shown that the photoconductive signal can be controlled by field effect. On a wide range of wavelengths and temperatures the signal variation can be as high as 50 %. From the detection point of view the most important thing is that the photoconductive signal can be increased with almost 25% if positive gate voltages are applied on the structure.

ACKNOWLEDGMENTS

The authors wish to thanks to NATO Scientific Division that supported this study through the project SFP-971970-INOWATE and to the Romanian Ministry of Education and Research, that is co-funding the above project.

REFERENCES

1. J.N.Humphrey, *Applied Optics*, **6**, 665, (1965).
2. D.E.Bode, *Physics of Thin Films*, Vol. 3, eds. G. Hass and R.E. Thun, (Academic Press, New York, 1966) pp.275
3. G.H.Blount, P.J.Schreiber, D.K.Smith and R.T.Yamada, *J.Appl.Phys.*, **44**, 978, (1973)
4. O.A. Kunze, O.G.Malan, P.A.Büger and W.Fink, *Z.Naturforsch.*, **26b**, 8, (1971).
5. T.Botila, E.Pentia and M.Mihalcea, *Patent*, nr.90272, (1986) Romania.
6. S.Abe, K.Masumoto and K.Suto, *J.of Crystal Growth*, **181**, 367, (1997).
7. "Hamamatsu Infrared Detectors" Catalog 2000, Hamamatsu Photonics, Hamamatsu City, Japan
8. P.A.Büger, O.G.Malan and O.A.Kunze, *Zeitschrift für Naturforsch.*, **26a**, 132, (1971).
9. I.Pop, C.Nascu, V.Ionescu, E.Indrea and I.Bratu, *Thin Solid films*, **307**, 240, (1997).
10. E.Pentia, L.Pintilie, C. Tivarus, I.Pintilie and T.Botila, *Mat.Sci. Eng.* **B80**, 23, (2001)
11. H.Rahnamai, H.J.Gray and J.N.Zemel *Thin Solid Films*, **69**, 347, (1980)
12. J.N.Zemel *Thin Solid Films*, **74**, 17, (1980)
13. I.Pintilie, E.Pentia, L.Pintilie, D.Petre, T.Botila and C.Constantin, *J. Appl. Phys.*, **78**, 1713, (1995).
14. L.Pintilie, I.Pintilie, D.Petre, T.Botila and E.Pentia, *Proc." 10th Meeting on Optical Engineering"*, 2-6 martie 1997, Ierusalim, Israel. vol. "SPIE" **3110**, 476, (1997).
15. L.Pintilie, E.Pentia, I.Pintilie and T.Botila, *Appl.Phys.Lett.* **76**,1, (2000)
16. C. Ravariu, A. Rusu, D. Dobrescu, F. Ravariu and L. Dobrescu, *Proc. CAS, Sinaia, Romania*, Oct. 2000, pp.307
17. S. M. Sze, "Physics of Semiconductor Devices", (John Wiley & Sons, New York, 1969), chap. 12.

Photo-stimulated Rebuilding of Structure in Semiconductors

Rashidova S.S., Oksengendler B.L., Turaeva N.N., Aripov I.M.

Institute of Polymer Chemistry and Physics, Uzbekistan

Abstract

A strong electron-phonon interaction observed in semiconductors allows to realize a special kind of atomic rebuilding under photo-irradiation of the medium. We consider three types of defective structures: one atomic, two-atomic ("dump-bell") and multi-atomic (kinks) defects. It is shown that an inversion effect of the defect potential term may be realized if there are non-equivalent neighboring positions of one-atomic and two-atomic defects. In this case the photo-excitation of electronic subsystems of these defects leads to an inversion of potential terms and a consecutive athermal rebuilding of the defective structures. The Yahn-Teller effect and psevd-effect play a special role here. It is shown for kink-structures that the photo-excitation of the electronic subsystems results in the alteration of kink nonius and the successive exponentially strong decrease of an activation barrier. Especially effects of athermal atomic rebuilding of U-negative defects are considerable.

Introduction

The possibility of stimulating atomic processes with electronic excitations is a new aspect of defect process physics. After the excitation of electronic subsystem the relaxation of this energy to the atomic degrees of freedom can lead to the atomic rebuilding with certain probability. Electron-stimulated atomic rebuildings (ESAR) [1,2] based on a strong electron-phonon interaction are well known in semiconductors of covalent and ionic characters. Types of such electronic-stimulated atomic rebuildings are rather wide and they can be subdivided into the small-scale and large-scale ones according to the quantity of defects involved into the atomic processes. In this work three models of ESAR based on different defects are considered in such systems.

Body

1. Photo-stimulated diffusion of one-atomic defect

Let us consider one-valent positively charged impurity atom (or host interstitial atom) introducing a deep local level into the forbidden band of electronic spectra. At photo-irradiation free electron and hole are produced. This electron could be trapped on the deep local level and deform the crystal around it. The impurity atom is suggested to interact with neighbor host atoms with the following potential

$$U(r) = U_{rep}(r) + U_{attr}(r), \quad (1.1)$$

where $U_{rep}(r)$ is the repulsive energy between the ion and the neighbor host atoms, $U_{attr}(r)$ is the attractive energy between them.

The total energy of the "crystal + impurity" system for two sites of symmetry with respect to the neighbor host atoms is defined by the formulas

$$\begin{aligned} U^{(1)}(r) &= U_{rep}^{(1)}(r) + U_{attr}^{(1)}(r) \\ U^{(2)}(r) &= U_{rep}^{(2)}(r) + U_{attr}^{(2)}(r) \end{aligned} \quad (1.2)$$

The activation energy of defect for its diffusion will then be given by [3]

$$\Delta Q_m = |U^{(1)}(r) - U^{(2)}(r)| = |\Delta U_{rep}(r) + \Delta U_{attr}(r)| \quad (1.3)$$

$U_{rep}(r)$ is estimated by means of Born-Mayer's equation:

$$U_{rep}(r) = A e^{\frac{r_L + r_I - r}{\rho}}, \quad (1.4)$$

where A is the scalar factor, r_L is the effective radius of the host atom, r_I is the ionic radius of the impurity, r is the distance between them, and constant ρ determines how

rapidly the repulsion falls off with distance. $U_{attr}(r)$ is connected with the effects of media polarization by the impurity:

$$|\Delta U_{attr}(r)| = |\Delta U_{pol}(r)| \leq 19B \quad [3]. \quad (1.5)$$

If $|\Delta U_{rep}(r)| > |\Delta U_{attr}(r)|$, then the equilibrium state of impurity will be the site (2), and the site (1) will be the saddle point.

The electron produced by photons can be trapped by the impurity. In this case according to the theory of auto-localization [4] neighbor atoms around the electron are deformed with the deformation potential which is defined from the equation

$$\rho(r) = \frac{\sigma}{k} |\Psi(r)|^2, \quad (1.6)$$

Here $\rho(r)$ is the relative variation of volume, σ is the constant of deformation potential, k is the elastic constant, $\Psi(r)$ is the wave function of the localizing electron. To estimate the total energy of the "crystal+electron+impurity" system we have used the following expression taking into account a role of acoustic and optical phonons in the electron-phonon interaction [5]

$$E(\mu) = L\mu^2 - A\mu^3 - B\mu \quad (1.7)$$

Here μ is the parameter of localization of the electronic wave function:

$$\Psi(r) = \left(\frac{\mu\sqrt{2}}{a} \right)^{3/2} \exp \left[-\pi \left(\frac{\mu r}{a} \right)^2 \right], \quad L = \frac{3\pi\hbar^2}{2m^*a}, \quad A = \frac{\sigma^2}{2ka^3}, \quad B = \frac{Ze^2\sqrt{2}}{\epsilon a} + \frac{e^2}{a\tilde{\epsilon}}.$$

Interaction between the electron and the acoustic vibrations leads to the deformation of crystal at total localization of the electron, $\mu=1$. In such case the repulsive energy of the impurity with neighbor atoms can be changed. For a large ion the repulsive energy will dominate $|\Delta U_{rep}(r)| > |\Delta U_{attr}(r)|$ and its activation energy of diffusion will then be defined essentially by the difference of the repulsive energies at the two sites. Therefore we can define the activation energy for its diffusion in the case of electron autolocalization

$$\Delta \tilde{Q}_m = \Delta Q_m \left(1 - \frac{U_{rep}^{(1)} d^{(1)} - U_{rep}^{(2)} d^{(2)}}{U_{rep}^{(1)} - U_{rep}^{(2)}} \xi \right) \quad (1.8)$$

$$\text{Here } \xi = \frac{\sigma}{3k\rho} \left| \Psi(r) \right|_{\mu=1}^2 \ll 1.$$

Thus it is clear from (1.8) that decreasing the activation energy of the defect is real at the electron localization in semiconductor.

2. Photo-stimulated diffusion of dumbbell defect

Semiconductor media is considered to contain a "dumb-bell" defect (two-atomic defect). It is well-known [6], that the highest engaged molecular orbital (HEMO) and the lowest empty molecular orbital (LEMO) are of even ($|g\rangle$) and odd ($|u\rangle$) characters, accordingly. These states are mixed as a result of the electron-ionic interaction. If the perturbation potential is defined by the equation

$$\hat{V} = \sum_i \frac{\partial V}{\partial Q_i} Q_i + \frac{1}{2} \sum_i \frac{\partial^2 V}{\partial Q_i^2} Q_i^2, \quad i = g, u, \quad (2.1)$$

using the Brulluen-Vigner's perturbation theory at the condition of $\langle u | \hat{V} | u \rangle / (\hat{\epsilon} - \epsilon_2) < 1$ will give the following formula for total energy of the system

$$\hat{\epsilon} = \epsilon_{gr} + \langle g | \hat{V} | g \rangle + \frac{|\langle u | \hat{V} | g \rangle|^2}{\hat{\epsilon} - \epsilon_u - \langle u | \hat{V} | u \rangle} \quad (2.2)$$

It leads to two terms with variable catching quantities of Q_g and Q_u . The value of total energy for the ground term $\hat{\epsilon}_{gr}$ allows us to estimate the radius of non-stability zone (NSZ) for a displacement of the dumb-bell defect as whole

$$\frac{\partial^2 \hat{\varepsilon}_{gr}}{\partial Q_n^2} \equiv F(Q_g, Q_n) = K_2 - 2a_{12}^2 \frac{[\Delta - (a_{11} - a_{12})Q_g]^2}{[\Delta - (a_{11} - a_{12})Q_g]^2 + 4a_{12}^2 Q_n^2} \leq 0 \quad (2.3)$$

Here $(\hat{V}Q'_j \equiv \partial \hat{V} / \partial Q_j \text{ et.al.})$ $\Delta = \varepsilon_n - \varepsilon_{gr}$, $K_1 = \langle g | \hat{V}Q'_j | g \rangle$; $K_2 = \langle u | \hat{V}Q'_j | u \rangle$;
 $a_{11} = \langle g | \hat{V}Q_g | g \rangle$; $a_{22} = \langle u | \hat{V}Q_g | u \rangle$; $a_{12} = \langle u | \hat{V}Q'_n | g \rangle$. ZNS in neighbor interstitial sites can be overlapped. The size of ZNS is defined from the condition

$$\left| Q_g - \frac{2a_{12}^2}{a_{22} - a_{11}} \right| \leq \frac{\Delta}{a_{22} - a_{11}}, \quad |Q_n - an| \leq \frac{2a_{12}^2}{3\sqrt{2}K_2}, \quad n = 0, 1, 2, \dots \quad (2.4)$$

where a is the distance between two interstitial sites.

Let us turn to the effects of laser-stimulation of the dumbbell defect diffusion. The defect is considered to be located in the interstitial site at low temperatures and the quantum number of valence vibrations tends towards zero: $N_v \rightarrow 0$. The valence vibration amplitude begins to increase under the influence of laser. After compressing the molecule to the size of $R^* = d_0 - Q_g^*$ the transference non-stability condition appears (d_0 is the equilibrium length of the defect bond). The transference to the neighbor interstitial position will be realized if the valence vibrations are excited to the following threshold energy

$$E_v = \hat{\varepsilon}_{gr}(Q_g^*) - \hat{\varepsilon}_{gr}(0) + \frac{\left(\frac{\partial \hat{\varepsilon}_{gr}}{\partial Q_g} \right)^2}{2M} \tau_+^2 \quad (2.5)$$

Here τ_+ is the minimal time of impulse accumulation [2]. The time necessary for leaving ZNS is defined by $\tilde{\tau} \approx Q_g^* / (a^2 E_0 / 4M\omega_0)$, where ω_0 is the frequency of the valence vibrations. In this case a radiation-stimulating diffusion coefficient is defined by $D \approx a^2 / \tilde{\tau}$ (it can reach a value of $10^{-6} \text{ cm}^2/\text{sec}$).

3. Photostimulated diffusion of crowdion structure

Let us consider a crowdion structure characterized by its nonius. It is well-known [7] that the barrier for collective movement of the crowdion exponentially depends upon its nonius of W_0

$$Q_m = Q_m^0 \exp\left(-\frac{\pi W_0}{a}\right) \quad (3.1)$$

where Q_m^0 is the diffusion barrier of one-atomic defect. Let an electron be trapped on the crowdion. The total energy of such system in the continuous approach is defined by the sum of potential energies

$$E_t\{u(x)\} = E_f + E_v + E_e \quad (3.2)$$

Here $E_f = (fa^2/2) \int_{-\infty}^{\infty} (\partial u(x)/\partial x)^2 dx$ is the potential energy of atoms in the interacted

chain, f is the elasticity coefficient, $E_v = (1/a) \int_{-\infty}^{\infty} U\{u(x)\} dx$ is the potential energy of

the crowdion in a field of lining; $E_e = \int_{-\infty}^{\infty} \left[(\hbar^2/2m_e) (\partial \Psi/\partial x)^2 dx + \hat{V}_{e-e} |\Psi|^2 \right] dx$ is the

electron energy localized on the crowdion, $u(x)$ is the medium displacement in the crowdion wave, $\Psi(x)$ is the electron wave function. If the option of the potential energy of lining is the Eshelbi potential [8] of $U(u) = 16u_0(u/a)^2 (1 - (u/a))^2$, and the option of $u(x)$ is the variation function of $u(x) = (a/2)[1 - \text{th}(\mu x/a)]$, besides

$\hat{V}_{e-e} = - \sum (\partial u/\partial x)$, then we have the equations

$$\begin{aligned} E_f(\mu) &= \frac{1}{6} fa^2 \mu, \\ E_v(\mu) &= \frac{4}{3} \frac{U_0}{\mu}, \\ E_e(\mu) &= -\frac{\hbar^2 \mu^2}{8m_e a^2} \left[-(1+2n) + \sqrt{1 + \frac{4m_e \Sigma a^2}{\hbar^2 \mu}} \right]^2 \end{aligned} \quad (3.3)$$

The equilibrium value of nonius of $W = 2a/\mu$ is slightly found from the condition $\partial E_c(\mu)/\partial \mu = 0$. We have the following expression at $\Sigma = 0$ (the crowdion without electron) for the crowdion nonius

$$W \rightarrow W_0 = \frac{2a}{\mu_0} = \frac{a}{(fa^2/2U_0)^{1/2}} \quad (3.4)$$

For the case of strong bond $\theta/\mu_0 \gg 1$ under the condition $1 < (\mu_0/16 - 3\xi)\mu_0 - (9\xi/\theta^{1/2})\mu_0^{5/2}$, where $\theta = \Sigma / (\hbar^2/4m_e a^2)$, $\mu_0 = 2fa^2/U_0$, $\xi = \Sigma/8U_0$, the electron localization on the crowdion increases its nonius.

We can estimate that and receive in final

$$\tilde{W} = W_0 \left[1 - \frac{1 - \left(\frac{\mu_0^2}{16} - 3\xi \right) \mu_0^2 - \frac{9\xi}{\theta^{1/2}} \mu_0^{5/2}}{2 + \frac{9\xi}{2\theta^{1/2}} \mu_0^{5/2}} \right] \quad (3.5)$$

As a result of that we can determine the barrier of the collective movement of the crowdion by the following formula

$$\tilde{Q}_m = Q_m \exp \left[- \frac{\pi W_0}{a} \frac{1 - \left(\frac{\mu_0^2}{16} - 3\xi \right) \mu_0^2 - \frac{9\xi}{\theta^{1/2}} \mu_0^{5/2}}{2 + \frac{9\xi}{2\theta^{1/2}} \mu_0^{5/2}} \right] \quad (3.6)$$

It is well known that the crowdion movement can model a number of more complicated atomic rebuildings (dislocation bend movement, inter-phase border and et. al.). Therefore the analyzed relief to such collective defect as a crowdion to migrate has its wide application.

References

1. Deep centers in semiconductors/Ed. by S.Pantelides, N.Y.Pl.Press, 1986, 950 pp.
2. Yunusov M.S., Oksengendler B.L. et.al., Subthreshold radiation effects in semiconductors, Tashkent:Phan, 1989, 224 p.
3. Weiser K., Phys.Rew.,1962, v.126, №4, p.1427-1436.
4. Toyozawa Y. Self-trapping and defect reactions // J.Semicond. and Insulat., 1983, vol.5, p.175-200.
5. Davidov A.S., Theory of solid states, Moscow:Nauka, 1976, 639 p.
6. Toyozawa Y., A proposed model of excitonic mechanism for defect formation in Acali Halides// J.Phys.Sol.Jap., 1978, vol.44, №3, p.482-488.
7. Idenbom V.L., Frenkel-Kontorova's model with accounting the discrete structure of lattice, Kristallografia, 1957, v.3, p.197-209.
8. Seger A., Shiller P., Dislocation bends and their influence on inner friction in crystals, in: Defect influence on solid states properties / Ed. by Mezon W., v.3, chapter 8, Moscow:Mir, 1969.

Luminescence from erbium oxide grown on silicon

E. Nogales¹, B. Méndez¹, J. Piqueras¹, R. Plugaru², J. A. García³ and T. J. Tate⁴

¹Universidad Complutense de Madrid, Dpto. Física de Materiales, 28040 Madrid, Spain.

²Inst. of Microtechnology, Bucharest, Romania.

³Universidad del País Vasco, Dpto. Física Aplicada II, Vizcaya, Spain.

⁴Imperial College, Dpt. of Electrical and Electronic Engineering, London, United Kingdom.

ABSTRACT

The luminescence properties of erbium oxide grown on crystalline and amorphous silicon substrates were studied by means of photo- and cathodoluminescence techniques. Differences in the luminescence spectra for samples grown on the two types of substrates used are explained in terms of the different types of erbium centers formed by taking into account the substrate properties and the thermal treatments during growth. For comparison, erbium implanted and oxygen coimplanted crystalline and amorphous silicon have been also investigated by luminescence techniques. In the implanted samples, the sharp transitions from erbium ions in the visible range were quenched and the main emission corresponds to the intraionic transitions in Er^{3+} ions in the infrared range peaked at 1.54 μm .

INTRODUCTION

The efficiency of luminescence emission associated to the intraionic Er^{3+} radiative transitions in different matrix is related to the mechanism of energy transfer from the hosts to the complexes formed by erbium and the surrounding atoms [1, 2]. The presence of other codopant elements in the Er neighborhood as well as the structure of the host matrix was found essential in determining the Er complexes formation [3, 4]. The presence of oxygen in the neighborhood of the erbium ions causes a strong enhancement of the efficiency of Er emission at 1.5 μm wavelength [5]. Other luminescence bands of the Er related transitions from visible to infrared range could be observed by a selective excitation.

In this work, the influence of the host matrix and of the excitation energies on the luminescence emission of erbium oxide grown on amorphous and crystalline substrates was investigated. The techniques used were photoluminescence (PL) and cathodoluminescence (CL) in the scanning electron microscope. The different emission bands detected are suggested to be originated at different types of Er centers formed in the erbium oxide overlayer.

EXPERIMENTAL DETAILS

Two sets of erbium doped silicon samples were investigated: erbium deposited and erbium implanted silicon films. In the former case, erbium vapor was deposited on amorphous and crystalline silicon substrates and the samples were then submitted to a thermal treatment at 950 °C during 1 hour in oxygen or nitrogen atmosphere. On the other hand, crystalline and amorphous silicon substrates were implanted with 200 keV ^{166}Er ions at doses of 5×10^{15} ions/cm². Some of the amorphous silicon substrates were coimplanted with 200 keV Er ions and 40 keV ^{16}O ions at doses of 5×10^{15} and 10^{16} ions/cm² respectively. All the implanted samples

Table I. Summary of the samples investigated.

(a) Er deposited samples			(b) Er implanted samples		
Er deposited samples	substrate	annealing atmosphere	Er implanted samples	substrate	ion implantation
c-Si:Er/O	crystalline	oxygen	c-Si:Er	crystalline	Er
a-Si:Er/O	amorphous	oxygen	a-Si:Er	amorphous	Er
a-Si:Er/N	amorphous	nitrogen	a-Si:Er,O	amorphous	Er, O

were submitted to a rapid thermal annealing (RTA) process at 1000°C for 15 s. A summary of the samples investigated in this work and their corresponding labels is displayed in table I.

All the samples were observed in the CL mode of operation in a Hitachi S2500 SEM in the temperature range of 80 - 300 K and at accelerating voltage of 20 kV. For the detection of visible light a Hamamatsu R-928 photomultiplier was used while for the near infrared light a cooled ADC germanium detector was employed. The PL measurements were performed with a CD-900 spectrometer system from Edinburgh Instruments. Samples were cooled at 10 K in a closed cryostat. The excitation sources were a He-Cd laser of 325 nm and 422 nm wavelengths with an excitation power of 50 mW and an Ar-ion laser (lines 457.9 nm, 488 nm and 514.5 nm) with an excitation power of 20 mW.

RESULTS AND DISCUSSION

Due to the low diffusivity of erbium in silicon the applied treatment leads to the formation of a thin film of erbium oxide overlayer on the sample. In order to get a better understanding of the luminescence results, we have first studied the light emission from erbium oxide pure powders. Figure 1 shows the PL spectra obtained at 10 K from Er_2O_3 in the visible range (figure 1a) and in the infrared range (figure 1b). All the peaks are attributed to intraionic transitions from different excited levels in the Er^{3+} ions to the fundamental state [6]. The set of

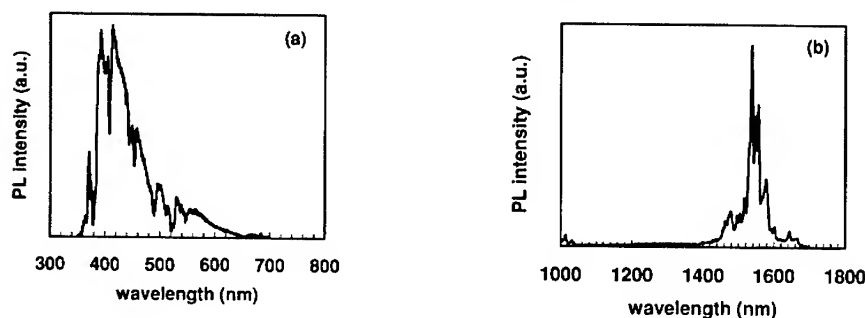


Figure 1. (a) PL spectrum from erbium oxide powder in the visible range. The excitation wavelength was 325 nm. (b) PL spectrum from erbium oxide powder in the infrared range. The excitation wavelength was 488 nm.

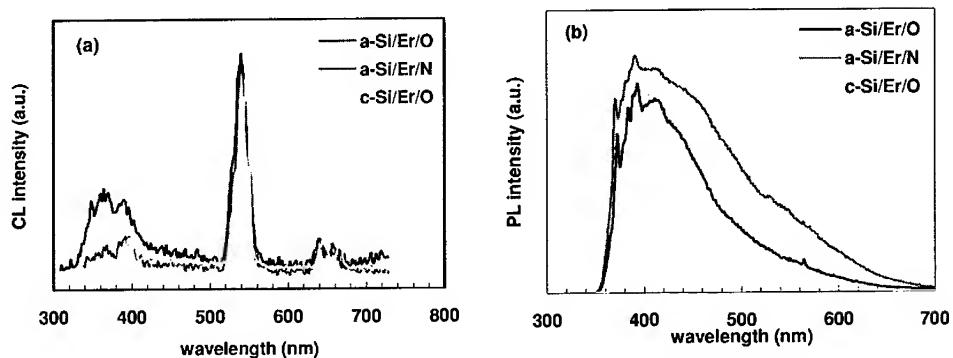


Figure 2. (a) CL spectra from Er deposited samples at 90 K. The acceleration voltage was 20 keV. (b) PL spectra from Er deposited samples obtained at 10 K.

sharp peaks around 1.54 μm has received more attention in the literature in view of further applications in optoelectronic devices and it has also been obtained when Er ions are embedded in other semiconductor matrix [7,8].

Figure 2 shows the CL and PL spectra in the visible range from the erbium deposited silicon samples. CL spectra show blue, green and red bands. The green band dominates the CL spectra at 90 K in all samples, with crystalline or amorphous substrates, (figure 2a), but at room temperature the main CL emission from the c-Si/Er/O sample corresponds to the red band, as we have reported in a previous work [9]. These green and red bands are due to intraionic Er transitions and the observed trend has been previously reported by Jaba *et al.* in other host matrix [10]. The fact that similar spectra are obtained for amorphous substrates treated in O and in N atmospheres while differences are found between amorphous and crystalline substrates, suggests that the formation of erbium oxide is determined by the oxygen content of the substrate rather

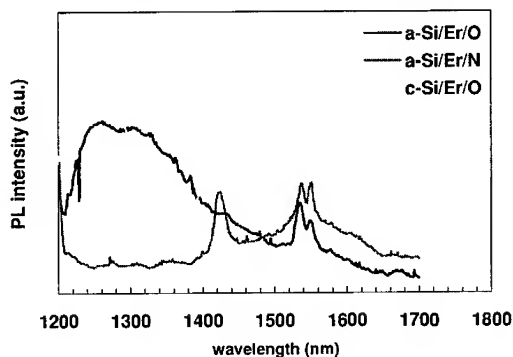


Figure 3. PL spectra from Er implanted silicon substrates, at 10 K in the infrared range. The excitation wavelength was 488 nm.

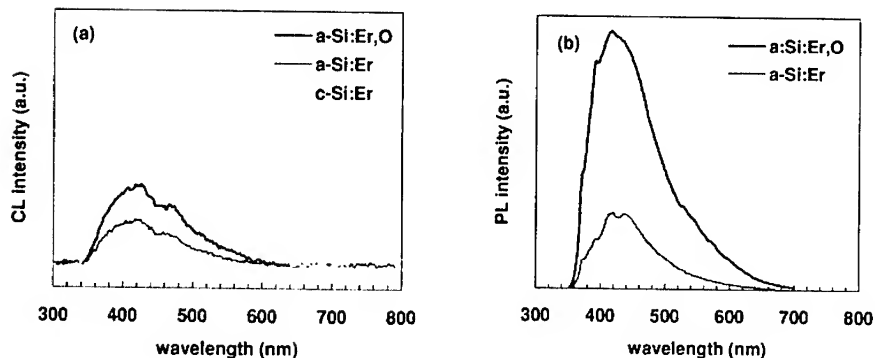


Figure 4. (a) CL spectra from Er implanted on amorphous silicon and crystalline silicon, and coimplanted with Er and O. (b) PL spectra from amorphous implanted substrates.

than the atmosphere during the treatment. The amount of oxygen provided by the substrate during growth could influence the defect structure of the layer and hence its emission properties. The difference among the samples grown on amorphous and crystalline substrates is also clearly observed in Figure 2b. Under a 325 nm laser excitation, all deposited samples show a dominant broad blue band at about 400 nm with a shoulder peaked around 540 nm (figure 2b). When we excited with the line 488 nm of the Ar laser, no significant PL signal is detected from erbium deposited on crystalline substrates, while for the amorphous substrates a sharp peak at 540 nm is clearly revealed in accordance with the CL spectra. The differences between PL and CL spectra were attributed to the different excitation energies used in both kinds of experiments and to the more selective character of the PL excitation.

In the infrared range, the CL signal was too low to record spectra with our experimental system. PL emission from deposited samples changes markedly depending on the specific substrate used. Figure 3 displays the PL spectra from the three erbium deposited samples. We observe a broad band around 1.25 – 1.30 μm in samples which were submitted to a thermal treatment in oxygen atmosphere. This band seems to be rather independent on the substrate and its maximum shifts towards lower energies when the temperature increases, similar as a near band edge emission. The origin of this band, which is not present in erbium oxide powder, could be related to defects involving oxygen introduced in the overlayers during the thermal treatment. The emission from erbium ions, peaked at 1.54 μm is well defined, but with low intensity, in the case of amorphous substrates. For crystalline substrates, however, a strong emission at 1.54 μm in form of a complex band is observed. This result suggests that in these films the erbium oxide could present a different stoichiometry, Er_2O_x , than the oxide Er_2O_3 .

The luminescence results from Er implanted and Er and O coimplanted silicon substrates are shown in figure 4. In Fig 4(a) the CL spectra is presented, whereas in Fig. 4(b) PL spectra are shown. In all implanted samples we observe contributions from the matrix to the luminescence spectra both in crystalline and amorphous substrates. From PL measurements corresponding to excitation with the line 488 nm of the Ar laser, no significant emission has been detected which shows that the green and red bands observed in erbium deposited samples have been quenched during implantation. The CL spectra are also similar to PL spectra, with broad blue band and

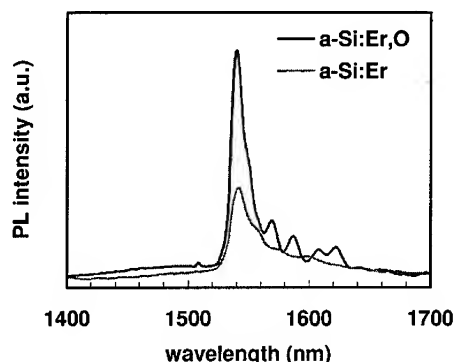


Figure 5. PL spectra at 10 K in the infrared range of implanted and coimplanted samples on amorphous substrates.

only in the case of crystalline substrates a green shoulder is appreciated in the CL spectra. In the infrared range, the strongest emission corresponds to Er and O coimplanted amorphous silicon and subsidiary peaks near 1.54 μm were clearly resolved.

CONCLUSIONS

In summary, luminescence properties of erbium deposited and erbium implanted in different silicon substrates have been studied. In erbium deposited samples the main contribution to the luminescence comes from the erbium oxide overlayer formed at the surface. In the visible range, depending on the excitation source different peaks related to intraionic transitions in erbium ions appear in the luminescence spectra. In the infrared range, the 1.54 μm peak interesting for optoelectronic applications, only dominates in the case of crystalline substrates and as a broad band. A defect related band in 1.2 – 1.3 μm range is also observed in oxygen treated samples. On the other hand, Er and O coimplanted silicon leads to the most efficiently emission of the 1.54 μm peak.

ACKNOWLEDGMENTS

This work was supported by DGI (project MAT2001-2119) and by the Scientific Cooperation Program between Spain and Romania.

REFERENCES

1. M. Fujii, M. Yoshida, S. Hayashi, and K. Yamamoto, *J. Appl. Phys.* **84**, 4525 (1998).
2. P.H. Citrin, P.A. Northrup, R. Birkhahn and A.J. Steckl, *Appl. Phys. Lett.* **76**, 2865 (2000).
3. J. Michel, J. L. Benton, R. F. Ferrante, D. C. Jacobson, D. J. Eaglesham, *J. Appl. Phys.* **70**, 2672 (1991).

4. A. Kasuya and M. Suezawa, *Appl. Phys. Lett.* **71**, 2728 (1997).
5. H. Przybylinska, W. Jantsch, Yu. Suprun-Belevitch, M. Stepikhova, L. Palmetshofer, G. Hendorfer, A. Kozanecki, R.J. Wilson, B.J. Sealy, *Phys. Rev. B* **54**, 2532 (1996).
6. A. Polman, *J. Appl. Phys.* **82**, 1 (1997).
7. J. Heikenfeld, D.S. Lee, M. Garter, R. Birkhahn, and A.J. Steckl, *Appl. Phys. Lett.* **76**, (2000).
8. A.R. Zanatta, C.T.M. Ribeiro, and U. Jahn, *Appl. Phys. Lett.* **79**, 488 (2001).
9. E. Nogales, B. Méndez, J. Piqueras, R. Plugaru, A. Coraci and J. A. García, (to be published).
10. N. Jaba, A. Kanoun, H. Mejri, A. Selmi, S. Alaya, and H. Maaref, *J. Phys.: Condens. Matter*, **12**, 4523 (2000).

High-Performance InAs/GaAs Quantum Dots Infrared Photodetector With/Without $\text{Al}_{0.2}\text{Ga}_{0.8}\text{As}$ Blocking Layers

Zhengmao Ye, Joe C. Campbell

Microelectronics Research Center, The University of Texas at Austin,
10,100 Burnet Rd., Bldg. 160, Austin, TX 78758, U.S.A.

Zhonghui Chen, O. Baklenov, E. T. Kim, I. Mukhametzhanov, J. Tie, and A. Madhukar,
Departments of Materials Science and Physics University of Southern California,
Los Angeles, CA 90089-0241, U.S.A.

ABSTRACT

InAs/AlGaAs quantum dot infrared photodetectors based on bound-to-bound intraband transitions in undoped InAs quantum dots are reported. AlGaAs blocking layers were employed to achieve low dark current. The photoresponse peaked at $6.2\ \mu\text{m}$. At 77 K and $-0.7\ \text{V}$ bias the responsivity was $14\ \text{mA/W}$ and the detectivity, D^* , was $10^{10}\ \text{cmHz}^{1/2}/\text{W}$.

INTRODUCTION

Mid and far-infrared ($3\text{--}20\ \mu\text{m}$) detection is a key technology for numerous commercial, military and space applications, e.g., night vision, thermal imaging, chemical analysis, non-destructive detecting, remote sensing, and missile guidance and defense. Due to the long carrier capture and relaxation times, quantum dot infrared photodetectors (QDIPs) have the potential for lower dark current and higher photoresponse than quantum well infrared photodetectors (QWIPs). Most importantly, the three-dimensional confinement of electrons in the quantum dots permits QDIPs to operate in the normal incidence mode, unlike QWIPs which are not sensitive to radiation that is incident perpendicular to the quantum wells [1]. To date, there have been several papers on InAs/GaAs, InGaAs/GaAs and InGaAs/InGaP QDIPs [2]–[10]. Most of the devices employed a doped active region, which resulted in high dark current. In this paper, we report an InAs/GaAs QDIP with unintentionally doped active region and AlGaAs barrier layers (sample A). The AlGaAs layers act as a blocking layer [6]–[10] for dark current, as first demonstrated in Ref. 6. The devices reported here have demonstrated low dark current, low noise, and high detectivity.

DEVICE STRUCTURES AND FABRICATIONS

The InAs QDIPs studied in this work belong to the class of n-i-n structure QDIPs (Figure 1) under examination by us [6][7]. The samples were grown on semi-insulating GaAs (001) substrates by solid-source molecular beam epitaxy. Five layers of 3 monolayer (ML) InAs quantum dots were inserted between highly Si-doped top and bottom GaAs contact layers. The punctuated island growth technique was used to grow the quantum dots [11]. The GaAs spacer layers between the contact layers and the nearest quantum dot layer had a thickness of $219 \sim 239\ \text{ML}$. 30 ML GaAs regions were used as the quantum dot cap layers. In order to reduce the dark current, four pairs of AlAs/GaAs (1 ML/ 4 ML) were introduced below the quantum dot layers and on the top of the GaAs cap layers (sample A). A similar QDIP without blocking layers

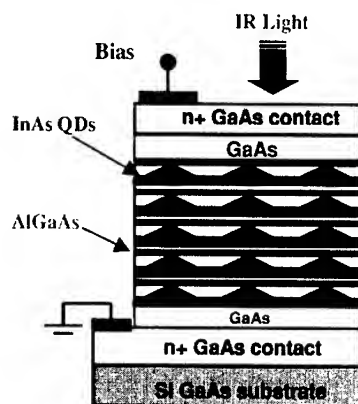


Fig. 1 Schematic of InAs/GaAs QDIP structure (e.g. with AlGaAs blocking layers).

(sample B) was also used. The sizes of the pyramidal-shaped quantum dots of sample B and A were estimated with atomic force microscopy (AFM) and a cross-sectional transmission electron microscope (XTEM): the height was 74 ± 16 Å and 59 ± 17 Å, respectively. Both dots have a base width of 210 Å. The dot densities of sample B and A was 673 ± 60 / μm^2 and 625 ± 40 / μm^2 , respectively.

Device fabrication followed standard procedure: photolithography, wet chemical etching, metal deposition and lift-off, and rapid thermal annealing. Mesas having a diameter of 250 μm and a height of ~ 1.4 μm were defined with an etch of $\text{H}_3\text{PO}_4 : \text{H}_2\text{O}_2 : \text{H}_2\text{O}$ (8:1:1). A 50 μm -diameter top contact and the bottom contact were formed by evaporation and liftoff of Au/Ni/AuGe. The contacts were then annealed at 430 °C for 20 seconds. In the following discussion, “positive” bias means that a positive voltage was applied to the top contact.

DISCUSSION

Spectral response

The normal-incidence spectral response was measured with a Nicolet Magna-IR 570 Fourier transform infrared (FTIR) spectrometer and a SRS 570 low-noise current preamplifier. Figure 2 shows the spectral response of sample A at 0.8 V bias and at temperatures of 63 K, 77 K and 100 K. The intraband photoresponse peaks occurred at 6.2 μm for all three spectra. The full width half maximum (FWHM) of the spectrum, $\Delta\lambda$, was ~ 0.4 μm , from which it follows that $\Delta\lambda/\lambda = 7.5\%$. The narrow spectral width is consistent with our previous results [7][12]. These results indicate that the electron transitions are intraband transitions from a lower bound state to a higher bound state [12]. The observed spectral width reflects the uniformity of the size of the quantum dots. The QDIP exhibits the highest photoresponse at 77 K. This can be explained as follows: As the temperature increases, more electrons occupy the lower states of the quantum dots. As long as there are unoccupied excited states available, the electrons in the lower states can participate in photon induced intraband transitions. However, further increase in the number

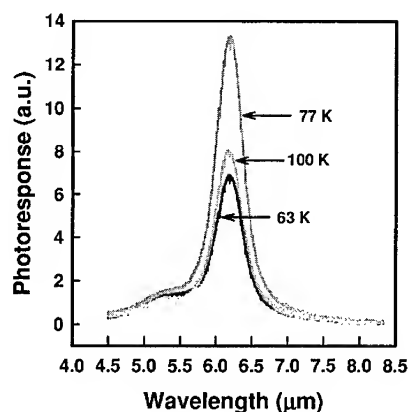


Fig.2 Normal-incident photoresponse of the QDIP sample A at the bias of 0.8 V and temperature of 63 K, 77K and 100K.

of electrons in the quantum dots, which results from the increase in dark current at higher temperature, will cause a decrease in the number of unoccupied excited states and, consequently, a decrease in the photoresponse. Additionally, a decrease in photo-excited electron lifetime at higher temperature can result in a decrease in the photoresponse, too.

Responsivity

The absolute spectral responsivity was calibrated with a blackbody source ($T = 995$ K). Since the blackbody spectrum included near infrared radiation, which could result in interband transitions, in addition to mid- and long-wavelength photons, optical filters were placed next to the aperture of the blackbody to block radiation with wavelength less than $3.5 \mu\text{m}$. Figure 3 shows the peak spectral responsivity versus bias of at temperatures of 77 K, 100 K, and 120 K. With increase in positive bias, the responsivity increased from 0.33 mA/W at 0.1 V to 280 mA/W at 1.7 V . For negative bias, the responsivity increased near four orders of magnitude from $5.2 \times 10^{-2} \text{ mA/W}$ at zero bias to 418 mA/W at -1.6 V . Negative differential responsivity, which was shown in sample B, was not observed within the bias range from -1.6 V to 1.7 V . The different responsivity curves for the positive and negative bias are attributed to the asymmetric shape of the quantum dots along the growth direction and the wetting layers beneath the quantum dots. Consequently, electrons in the quantum dots experience different barrier heights depending on whether transport is toward the top or bottom contacts. Due to the introduction of the $\text{Al}_{0.2}\text{Ga}_{0.8}\text{As}$ blocking layers, the responsivity of sample A is lower than that of sample B.

Dark current

Dark current density versus voltage characteristic of sample A is shown in Fig. 4 for temperature in the range from 60 K to 296 K. The structural asymmetry of the quantum dots also

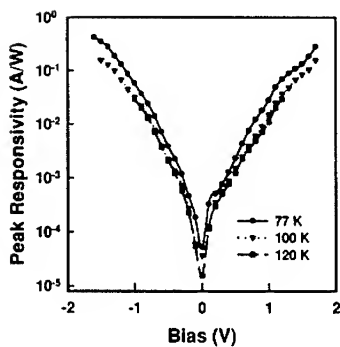


Fig. 3 Peak responsivity of sample A at 77 K, 100K, and 120K.

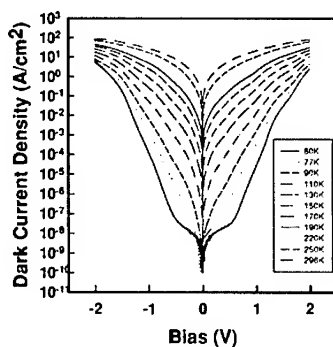


Fig. 4 Dark current density of sample A at temperature ranging from 60 K to 296K.

results in asymmetrical dark current density for positive and negative bias. At low bias, the increase in dark current density is due to the fact that as the bias increases, more electrons occupy the quantum dots, which results in an increase in the average sheet electron density. When a large fraction of the quantum dots states are occupied, further increase in bias does not significantly alter the sheet electron density. This causes a lowering of the energy barrier for injected electrons at the contact layers, which results in the nearly exponential increase of the dark current. At 0.7 V bias, the dark current density was 2.5×10^{-7} A/cm² at 60 K. With increasing temperature, it increased over seven orders of magnitude to 11.1 A/cm² at room temperature. Similarly, at -0.7 V bias, there was an increase of over eight orders of magnitude from 1.6×10^{-7} A/cm² at 60 K to 14.4 A/cm² at 296 K. Compared to the similar structure without the Al_{0.2}Ga_{0.8}As blocking layers, sample B, the dark current has been suppressed by over three orders of magnitude. For bias < 0.7 V and T > 100 K, the dark current increased exponentially with temperature, which suggests that in this temperature range the dark current originates from thermionic emission. The calculated activation energy was 196 meV at zero bias, which was close to the energy corresponding to the cutoff wavelength (193 meV) of the sample. For temperature lower than 100 K, sequential resonant tunneling and phonon assisted tunneling are probably the dominant components of the dark current.

Noise current

The noise current, i_n , was characterized with low noise current preamplifiers and a SRS 760 FFT spectrum analyzer. For $|V_B| > 0.6$ V, the noise current was measured with a SRS current preamplifier. However, below 0.6 V, the photodetector noise current of sample A was below the noise floor of the instrument. Near zero bias, a very low noise current preamplifier with high gain was used. However, restricted by the input power limitation of this current preamplifier, in the bias range from 0.1 V to 0.5 V and -0.5 V to -0.1 V, the noise current was interpolated.

Figure 4 shows the noise current of a 250 μm -diameter device at 77 K and 100 K. The calculated thermal noise current, I_{th} , at 77 K is also shown. The thermal noise current can be expressed as,

$$I_{th} = \sqrt{\frac{4 kT}{R}} \quad (1)$$

where k is Boltzmann's constant, T is the absolute temperature, and R is the differential resistance of the device, which was extracted from the dark current. At $V_B = -0.7$ V, the calculated thermal noise current (3.2×10^{-14} A/Hz^{1/2}) was very close the measured noise current (2.9×10^{-14} A/Hz^{1/2}), which indicates that thermal noise is significant in the low bias region. As the bias was increased, the noise current increased much faster than thermal noise. The noise current was greatly suppressed near three orders of magnitude by introducing $\text{Al}_{0.2}\text{Ga}_{0.8}\text{As}$ blocking layers.

Detectivity

The detectivity is given by

$$D^* = \frac{R\sqrt{A \cdot \Delta f}}{i_n} \quad (2)$$

where A is the device area, R is the responsivity, i_n is the noise current, and Δf is the bandwidth. Figure 6 shows the peak detectivity versus bias at 77 K and 100 K. The best performance was achieved at 77 K and -0.7 V where the peak detectivity was 10^{10} cmHz^{1/2}/W. The corresponding responsivity was 14 mA/W. With increase in temperature to 100 K, the peak detectivity dropped to 1.1×10^9 cmHz^{1/2}/W at 0.5 V, due to the decrease in responsivity and increase in noise current. The peak detectivity of sample B is 1.5×10^9 cmHz^{1/2}/W at 77 K. Therefore, the detectivity was enhanced over 6 times by using $\text{Al}_{0.2}\text{Ga}_{0.8}\text{As}$ blocking layers.

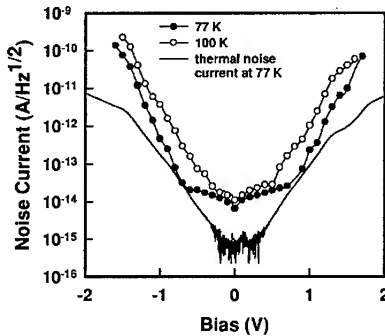


Fig. 5 Measured noise current (dots) of sample A at 77 K and 100 K, and calculated thermal noise current at 77K.

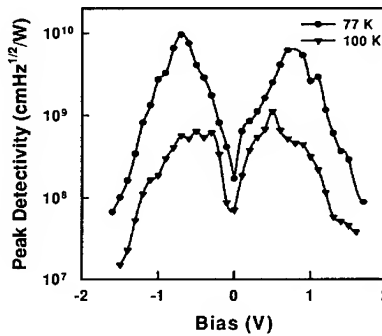


Fig. 6 Peak detectivity of sample A at 77 K and 100 K.

CONCLUSIONS

In conclusion, we have demonstrated QDIPs based on bound-to-bound intraband transitions. These QDIPs were sensitive to normal-incident infrared radiation and exhibited low dark current with $D^* = 9.6 \times 10^9$ cmHz^{1/2}/W and $R = 14$ mA/W at -0.7 V bias and 77 K. In contrast, the QDIPs with the same structure, except with GaAs barrier layer, exhibited $D^* = 1.5 \times 10^9$ cmHz^{1/2}/W at 77 K.

ACKNOWLEDGEMENTS

The authors would like to thank Dr. Jeff Beck of the DRS for help with calibration of responsivity and valuable discussions. This work was supported by AFOSR under the MURI program.

REFERENCE

- [1] V. Ryzhii, Sci. Technol. 11, 759 (1996)
- [2] D. Pan, E. Towe, and S. Kennerly, Appl. Phys. Lett. 75, 2719 (1999).
- [3] S. Kim, H. Mohseni, M. Erdtmann, E. Michel, C. Jelen, and M. Razeghi, Appl. Phys. Lett. 73, 963 (1998).
- [4] J. Phillips, Pallab Bhattacharya, S.w. Kennerly, D.W. Beekman and M. Dutta, IEEE J. Quant. Electron. 35, 936 (1999).
- [5] Jong-Wook Kim, Jae-Eung Oh, Seomg-Chul Hong, Chung-Hoon Park and Tae-Kyung Yoo, IEEE Electron Device Letter, 21, No. 7, 329 (2000).
- [6] O. Baklenov, Z.H. Chen, E.T. Kim, I. Mukhametzhanov, A. Madhukar, F. Ma, Z. Ye, B. Yang, and J. Campbell, the 58th IEEE Device Research Conference, (Denver, Colorado, June 19-21, 2000), p171; Z.H. Chen, O. Baklenov, E.T. Kim, I. Mukhametzhanov, J. Tic, A. Madhukar, Z. Ye, and J. Campbell, Proceeding of QWIP2000 Workshop, Dana Point, CA, July 2000, Infrared Physics & Technology, 42, 479 (2001)
- [7] Z.H. Chen, O. Baklenov, E. T. Kim, I. Mukhametzhanov, J. Tic, A. Madhukar, Z. Ye and J. C. Campbell, J. Appl. Phys. 89, 4558 (2001).
- [8] S. Y. Wang, S. D. Lin, H. W. Wu, and C. P. Lee, Appl. Phys. Lett., 78, 1023 (2001).
- [9] Shih-Yen Lin, Yau-Ren Tsai, and Si-chen Lee, Appl. Phys. Lett., 78, 2784 (2001).
- [10] A.D. Stiff, S. Krishna, P. Bhattacharya, and S. Kennerly, Appl. Phys. Lett. 79, 421 (2001)
- [11] I. Mukhametzhanov, Z. Wei, Rheitz, and A. Madhukar, Appl. Phys. Lett., 75, 85 (1999).
- [12] I. Mukhametzhanov, Z.H. Chen, O. Baklenov, E.T. Kim, and A. Madhukar, Phys. Status Solidi (b) 224, 697 (2001)

Current Images of CdSe Colloidal Nanodots Observed by Conductive-tip Atomic Force Microscopy

Ichiro Tanaka¹, Eri Kawasaki¹, O. Ohtsuki¹, M. Hara², H. Asami³, and I. Kamiya³

¹Department of Materials Science & Chemistry, Wakayama University,
930 Sakaedani, Wakayama 640-8510, Japan

²Frontier Research System, RIKEN, 2-1 Hirosawa, Wako, Saitama 351-0198, Japan

³Science and Technology Research Center, Mitsubishi Chemical Corp.,
1000 Kamoshida-cho, Aoba-ku, Yokohama 227-8502, Japan

ABSTRACT

We have fabricated submonolayer-thick films of CdSe colloidal nanodots in order to investigate electronic properties of individual nanodots by conductive-tip atomic force microscopy (AFM). Topographic and current images of isolated single CdSe colloidal dots on single crystalline Au (111) surface which was covered with dodecanethiol self-assembled monolayer were obtained by AFM operating in contact mode with a conductive tip under appropriate bias voltages. In the current image, it is found that the dot regions have higher electric resistances due to tunneling resistance through the CdSe dots. We also found 10 nm-scale electric inhomogeneity around the dots, which may corresponds to the previously reported etch-pits of Au (111) surfaces formed during the deposition of the dodecanethiol molecules.

INTRODUCTION

Semiconductor colloidal nanodots have been one of major research interests since they exhibit quantum effect or nano-size effect which is potentially applicable for novel optical and opto-electronic devices [1, 2]. Recently, highly monodisperse II-VI and III-V semiconductor nanodots have been synthesized by colloidal chemical techniques [3, 4]. Because they are free from the lattice mismatched substrate, the choice of materials for colloidal dots is wider than that for self-assembled quantum dots formed by Stranski-Krastanov mode growth by molecular beam epitaxy or metal organic chemical vapor deposition. The optical properties of the colloidal dots have been widely investigated, and it has been recognized that the surface termination may be playing an important role for the properties. We have reported an optical memory effect of CdSe colloidal nanodots

where the photoluminescence (PL) intensity of the nanodots spun-coat on glass substrates depends on the photoexcitation energy and duration [5]. This effect is strongly influenced by the preparation process of the sample, and the main contribution is therefore attributed to electron trap states at the interface between the CdSe nano crystals and organic molecules covering them.

In order to study the interface properties of colloidal nanodots, electronic investigation have advantages over optical since interface traps are known to be non-radiative. We thus adapted conductive-tip atomic force microscopy (AFM) [6, 7] for nano scale electronic study of CdSe colloidal nanodots. In this paper, we report on fabrication of sub-monolayer thick CdSe colloidal nanodot film for electronic investigation of individual nanodots, and observation of current images of single CdSe colloidal nanodots as well as substrate surfaces.

EXPERIMENT

The CdSe colloidal nanodots were synthesized by injecting precursor that contains Se dissolved in tributylphosphine and dimethyl cadmium into tri-*n*-octylphosphine oxide (TOPO) at temperatures ranging from 300 to 350 °C. Here, the TOPO not only act as hot soap where nucleation and growth occur but also caps and passivates the CdSe nanodot surfaces. The obtained nanodots were dispersed in toluene, and coated on substrates using a spinner at 3000 rpm for 30 sec. The average diameter of the nanodots and its distribution is estimated to be 5 nm and 10-20 %, respectively, from optical absorption measurements.

The morphology of the sample surface were measured using a high vacuum AFM system operating in contact mode, and local electric current was simultaneously mapped by applying an appropriate bias voltage between the sample and conductive tip.

RESULTS AND DISCUSSIONS

In order to investigate the electric properties of the individual CdSe colloidal nanodot by AFM, we need submonolayer-thick nanodot films where isolated nanodots exist on the substrate surface. Because the TOPO

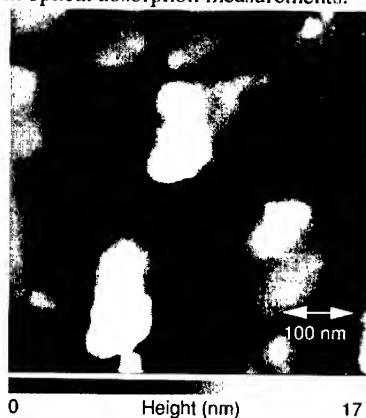


Figure 1. Topographic image of CdSe colloidal nanodots spun-coat on a Si wafer

molecules covering the CdSe nanodot surfaces are hydrophobic, the substrates with hydrophilic surfaces are not appropriate for preparing submonolayer-thick films.

Figure 1 shows an AFM image of a silicon wafer on which toluene solution containing 0.1 wt% CdSe colloidal dots is spuncoat. It is seen that single nanodots do not exist, and instead, 100 nm-scale islands which seem to consist of aggregated colloidal dots are formed, prevailing that this sample is not suitable for our purpose.

We therefore tried to prepare a substrate with hydrophobic surface. One promising candidate was gold films on which alkanethiol self-assembled monolayer (SAM) was formed, where the sulfur atom at one end of alkane chain forms a chemical bond with gold, and the alkane chains are aligned perpendicular to the gold film surface. Figure 2 shows a contact mode AFM image of Au (111) single crystalline film formed on a mica substrate by vacuum evaporation. Note that the film



Figure 2. An AFM image of Au (111) single crystalline prepared on mica

consists of sub-micron size single crystals, and the (111) surface of each crystal is so flat that single nanodots, if they are on the surface, can be easily distinguished.

After forming dodecanethiol SAM on the Au (111) surface by dipping the sample in 1 mM dodecanethiol ethanol solution for 3 hours, 0.1 wt% CdSe colloidal dots in toluene solution was spun-coat under the same conditions as on the silicon substrate. The

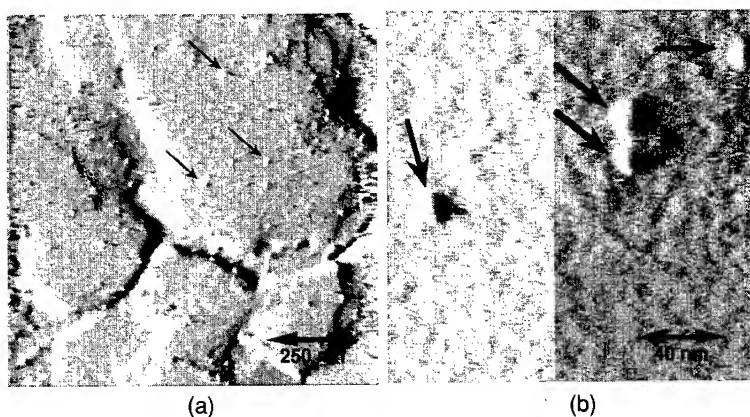


Figure 3. Single CdSe colloidal nanodots on Au (111) surface which is covered with dodecanethiol SAM: (a) low and (b) high magnification images by AFM.

differential image of the sample by contact-AFM is shown in Fig. 3 (a) and (b). In the former image, we can see that single nanodots are scattered on the Au (111) surfaces as some of them are indicated by arrows. In the latter, four single dots of about 20 nm-diameter are observed. The apparent diameter is larger than that estimated from the optical absorption measurement. We attribute this discrepancy to the large radius of the AFM tip since a 40 nm-thick metal layer is evaporated on the tip in order to ensure conductivity.

Then, we simultaneously imaged surface topography and local electric current by applying a bias voltage of 1.0 V. Figure 4 (a) is a differential image taken by contact-AFM. The three protuberances of nearly 30 nm-diameter are single nanodots as in Fig. 3 (b), and the large one near the center of the image may consists of a few dots that are aggregated. Comparing the topographic and current images, it is found that the protuberant region has larger electric resistance. Namely, the dots exhibit larger resistance since the tunneling resistance of the CdSe dots is added to that of the dodecanethiol SAM.

We can also see nm-scale electric inhomogeneity all over the substrate surface in the current image. If the substrate surface is not homogeneous on this scale, it would prohibit us from an electronic measurement of individual colloidal dots. However, it has been reported that a few nm-diameter holes of 0.3 nm depth, which are called etch-pits and observed by scanning tunneling microscopy (STM), exist on the Au (111) surfaces covered with alkanethiol SAM [8]. They are believed to be formed as a result that occurs the surface reconstruction changes during the deposition of alkanethiol SAM. We also observed those etch-pits on our substrate surface by STM, and confirmed that their depth

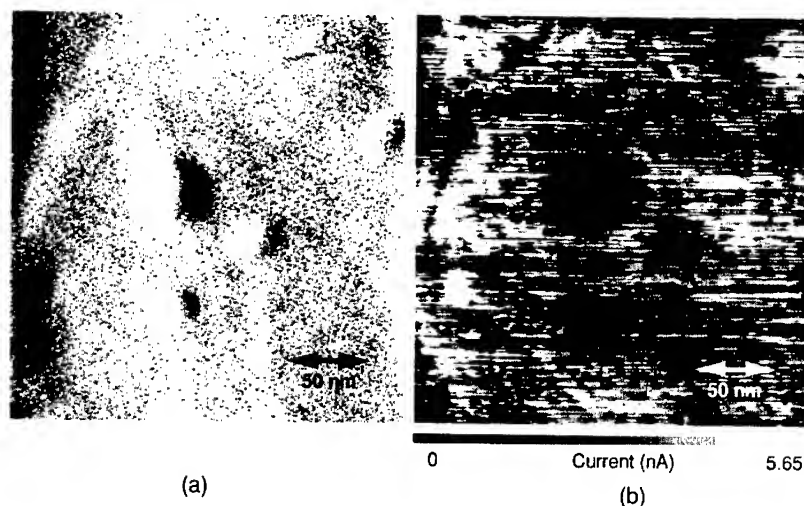


Figure 4. Simultaneously measured (a) differential topographic image and (b) current image of CdSe colloidal nanodots by AFM

was 0.3 nm. Thus, the inhomogeneous structures in the current image correspond to the etch pits.

A model that explains the correlation between the topographic and current images of our sample is described in Fig. 5. The conductive AFM tip used in our measurements has a much larger radius than that of STM tips as discussed earlier. Thus, single colloidal nanodots of about 5 nm-diameter appears as a few tens nm in both the topographic and current images. In the topographic image, however, the etch-pits are not observed because the size of the etch-pits is smaller than the resolution that can be reached with AFM tip that is employed. On the other hand, tunneling current decreases when the AFM tip is scanned over the etch-pits since the tunneling gap increases by 0.3 nm.

CONCLUSIONS

We have fabricated submonolayer-thick CdSe colloidal nanodot films on alkanethiol SAM on single crystalline Au (111) surfaces in order to investigate electronic properties of individual nanodots. Topographic and current images of the sample were successfully obtained simultaneously using a conductive-tip AFM. In the current image, the dot region has larger electric resistance due to tunneling through the dot. We have also observed nm-scale electric inhomogeneity found on the surface that corresponds to etch-pits formed by deposition of SAM on the gold surface.

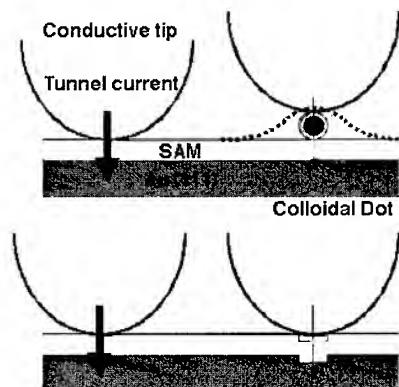


Figure 5. A model explains the topographic and current images of single CdSe colloidal nanodots on Au (111) covered with dodecanethiol SAM

REFERENCES

1. H. Sakaki, Solid State Commun., **92**, 119 (1994).
2. D. Bimberg, Semiconductors, **33**, 951 (1999).
3. C. B. Murray, D. J. Norris, and M. G. Bawendi, J. Am. Chem. Soc., **115**, 8706 (1993); M. Danek, K. F. Jensen, C. B. Murray, and M. G. Bawendi, Appl. Phys. Lett., **65**, 2795 (1994).
4. A. A. Guzelian, U. Banin, A. V. Kadavanich, X. Peng, and A. P. Alivisatos, Appl. Phys. Lett., **69**, 1432 (1994).
5. S. Maenosono, C. D. Dushkin, S. Saita, and Y. Yamaguchi, Jpn. J. Appl. Phys., **39**, 4006 (2000).
6. F. Houz , R. Meyer, O. Schneegans, and L. Boyer, Appl. Phys. Lett., **69**, 1975 (1996).
7. I. Tanaka, I. Kamiya, H. Sakaki, N. Qureshi, S. J. Allen, Jr., and P. M. Petroff, Appl. Phys. Lett., **74**, 844 (1999).
8. J. Noh, K. Kobayashi, H. Lee, and M. Hara, Chem. Lett., 630 (2000).

Shallow-donor states in spherical quantum dots with parabolic confinementC. A. Duque¹, N. Porras-Montenegro², M. de Dios-Leyva³, and L. E. Oliveira⁴¹Instituto de Física, Universidad de Antioquia, AA 1226, Medellín, Colombia²Departamento de Física, Universidad del Valle, AA 25360, Cali, Colombia³Dept. of Theoretical Physics, Univ. of Havana, San Lazaro y L, Vedado, 10400, Havana, Cuba⁴Instituto de Física, Unicamp, CP 6165, Campinas, São Paulo, 13083-970, Brazil**ABSTRACT**

The evidence of a parabolic potential well in quantum wires and dots was reported in the literature, and a parabolic potential is often considered to be a good representation of the “barrier” potential in semiconductor quantum dots. In the present work, the variational and fractional-dimensional space approaches are used in a thorough study of the binding energy of on-center shallow donors in spherical GaAs-Ga_{1-x}Al_xAs quantum dots with potential barriers taken either as rectangular [V_b (eV) = 1.247 x for $r > R$] or parabolic [$V_b(r) = \beta^2 r^2$] isotropic barriers. We define the parabolic potential with a β parameter chosen so that it results in the same E_0 ground-state energy as for the spherical quantum dot of radius R and rectangular potential in the absence of the impurity. Calculations using either the variational or fractional-dimensional approaches both for rectangular and parabolic potential result in essentially the same on-center binding energies provided the dot radius is not too small. This indicates that both potentials are alike representations of the quantum-dot barrier potential for a radius R quantum dot provided the parabolic potential is defined with β chosen as mentioned above.

INTRODUCTION

Quantum-dot heterostructures are most studied both from the theoretical and experimental point of view due to the wide possibility of applications in electronic and optoelectronic devices [1]. Such semiconductor nanostructures show interesting physical properties due to the extreme degree of confinement of electrons and holes, and the presence of impurities of course modify both the optical and transport properties of such nanostructures. For impurities in quantum dots, the ultimate goal is an artificial atom whose properties can be controlled through the material parameters and geometry.

Using variational and fractional-dimensional space approaches, Porras-Montenegro and Pérez-Merchancano [2] and Oliveira et al. [3] have calculated the binding energy for shallow-donor impurities in rectangular GaAs-(Ga,Al)As quantum dots for both finite and infinite potential confinement. As a general feature, they have found that the binding energy increases as the radius of the dot is diminished and then decreases to the three dimensional limit of the bulk in the case of finite potential confinement, whereas the binding energy always increases with the diminishing of the radius of the dot when the potential confinement is infinite.

The evidence of a parabolic potential well in quantum wires and dots was reported in the literature [4, 5], and a parabolic potential is often considered to be a good representation of the “barrier” potential in semiconductor quantum dots [6-8]. The theoretical description of the behavior of a hydrogenic on-center donor in a spherical dot for rectangular and parabolic potentials will lead to a better understanding of the properties of a spherical quantum dot, and it is

the subject of this paper. Calculations have been made within the effective mass approximation and using a variational and the fractional-dimensional space approaches.

THEORETICAL FRAMEWORK

Within the effective-mass approximation, the Hamiltonian of a system consisting of an electron bound to a donor impurity, inside a GaAs-(Ga,Al)As quantum dot of radius R for a parabolic potential confinement, may be written as

$$H = -\frac{\hbar^2}{2m^*} \nabla^2 + \frac{1}{2} m^* \omega^2 r^2 - \frac{e^2}{\epsilon_0 r}, \quad (1)$$

where r is the electron-impurity distance, ϵ_0 ($= 12.58$) is the dielectric constant of bulk GaAs, m^* ($= 0.0665 m_0$, where m_0 is the free electron-mass) is the effective electron mass, and ω is the harmonic oscillator frequency.

In the variational calculation, the trial wave function for the ground state with the impurity present is taken [8] as the product between the eigenfunction of the Hamiltonian in eq. (1) without the Coulomb interaction (third term at the right) and the hydrogenic part, i.e.:

$$\psi(r) = N \exp(-\beta r^2/2) \exp(-\lambda r), \quad (2)$$

where N is a normalization constant, λ is a variational parameter, and β is a measure of the parabolic potential, defined as

$$\beta = \frac{m^* \omega}{\hbar}. \quad (3)$$

Alternatively, one may solve the above problem in the fractional-dimensional scheme. Following Oliveira et al. [3], one finds that, for the 1s-like ground state, the "shallow donor + heterostructure" anisotropic system may be modeled by an effective isotropic hydrogenic system in a fractional D -dimensional space, a problem which may be solved analytically. Once the fractional dimension is calculated, the donor binding energies may be obtained [9, 10] through $E_b = -E_{1s} = 4R^*/(D-1)^2$, where R^* is the donor effective Rydberg. For details of calculations we refer to [3].

RESULTS AND DISCUSSION

In Figure 1 (a) we present the spherical parabolic and rectangular potential profiles for an $R = 200 \text{ \AA}$ GaAs-Ga_{1-x}Al_xAs quantum dot with an Al concentration $x = 0.3$; we have chosen β and R so that both potentials result in the same E_0 ground-state energy. In Figure 1 (b) it is displayed the parabolic-potential parameter $\beta^{-1/2}$ versus dot radius R .

Figure 2 displays the on-center donor binding energy versus quantum dot radius for a GaAs-Ga_{0.7}Al_{0.3}As quantum dot calculated both for a parabolic (dotted line) and rectangular (full curve) potentials. Calculations are performed using a variational procedure [cf. Fig. 2 (a)] and the fractional-dimensional approach [Fig. 2 (b)]. In both cases one observes that the binding energy diminishes with increasing radius of the dot, reaching the three-dimensional limit (the hydrogenic atom) for large values of the radius, as it has been reported in several works [2, 3]. As it can be seen, the agreement in the binding energy between the variational method and the fractional-dimensional approach is quite good in a wide range of the radius of the dot, independently whether the confinement is parabolic or rectangular. For radius smaller than $\approx 2 - 3 a^*$ the binding energy calculated by means of the two methods begins to differ, and the fractional-dimensional approach begins to fail [3].

CONCLUSIONS

Summing up, using the variational and fractional-dimensional approaches both for rectangular and parabolic potentials we have calculated the binding energy of an on-center donor impurity in a GaAs-(Ga,Al)As quantum dot. We find the results essentially the same provided the dot radius is not too small. This indicates that both potentials are alike representations of the quantum-dot barrier potential for a radius R quantum dot provided the parabolic potential is defined with β as it was chosen in this work. We do hope that this criteria may be of future utility in calculations

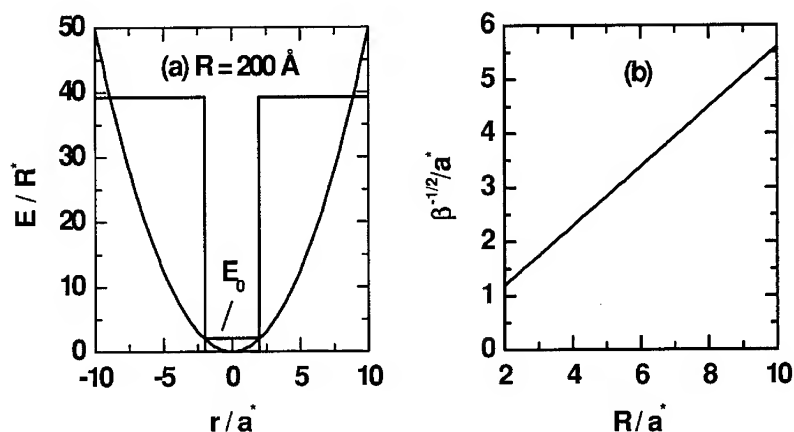


Figure 1: (a) spherical parabolic [$V_b(r) = \beta^2 r^2$] and rectangular [$V_b(\text{eV}) = 1.247 x$ for $r > R$] potential profiles for an $R = 200 \text{ \AA}$ GaAs-Ga_{1-x}Al_xAs quantum dot ($x = 0.3$); β and R are chosen so that both potentials result in the same E_0 ground-state energy; (b) parabolic-potential parameter $\beta^{-1/2}$ versus dot radius R . In the above figures, R^* and a^* are the effective Rydberg and Bohr radius, respectively.

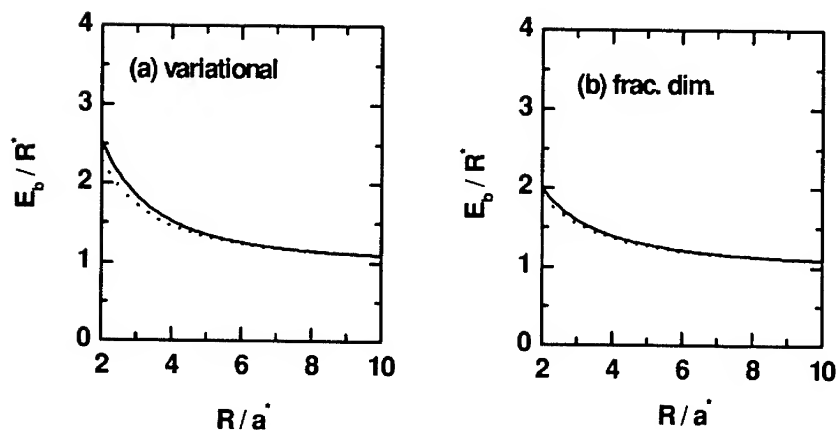


Figure 2: On-center donor binding versus quantum dot radius for a GaAs-Ga_{0.7}Al_{0.3}As quantum dot calculated both for a parabolic (dotted line) and rectangular (full curve) potentials. Calculations are performed using a variational procedure (a) and the fractional-dimensional approach (b).

using the parabolic potential for impurity-related properties in low-dimensional systems, such as impurity binding and transition energies, as well as theoretical work on photoluminescence and absorption spectra.

ACKNOWLEDGMENTS

This work was partially financed by Colombian (COLCIENCIAS and CODI-Universidad de Antioquia) and Brazilian Agencies Fapesp, Faep-Unicamp, and CNPq.

REFERENCES

1. Z. Xiao, J. Zhu, and F. He, *Superlatt. and Microstruct.* **19**, 138 (1996), and references therein.
2. N. Porras-Montenegro and S. T. Pérez-Merchancano, *Phys. Rev.* **B46**, 9780 (1992).
3. L. E. Oliveira, C. A. Duque, N. Porras-Montenegro, and M. de Dios-Leyva, *Physica* **B302-303**, 72 (2001), and references therein.
4. K. Kash, B. P. Van der Gaag, D. D. Mahoney, A. S. Gozdz, L. T. Florez, and J. P. Harbison, *Phys. Rev. Lett.* **67**, 1326 (1991).
5. M. Sopanen et al, *Appl. Phys. Lett.* **66**, 2364 (1995).
6. Z. Xiao, J. Zhu, and F. He, *Superlatt. and Microstruct.* **19**, 137 (1996).
7. C. Bose, *J. Appl. Phys.* **83**, 3089 (1998); *ibid.*, *Physica* **E4**, 180 (1999).
8. G. Murillo and N. Porras-Montenegro, *Phys. Stat. Sol. (b)* **220**, 187 (2000).
9. F. H. Stillinger, *J. Math. Phys.* **18**, 1224 (1977); X-F. He, *Phys. Rev.* **B43**, 2063 (1991).
10. H. Mathieu, P. Lefebvre, and P. Christol, *Phys. Rev.* **B46**, 4092 (1992); *ibid.*, *J. Appl. Phys.* **74**, 5626 (1993); P. Lefebvre, P. Christol, H. Mathieu, and S. Glutsch, *Phys. Rev.* **B52**, 5756 (1995).

Continuous and Time Resolved Optically Detected Magnetic Resonance Studies of InP Nanoparticles

L. Langof, E. Ehrenfreund, and E. Lifshitz
Solid State Institute, Technion – Israel Institute of Technology, Haifa 32000, Israel
O. I. Micic and A. J. Nozik
National Renewable Energy Laboratory, Golden, Colorado 80401, USA

ABSTRACT

Carriers in small colloidal InP nanoparticles are in strong quantum confinement regime. The low temperature photoluminescence spectrum of InP nanoparticles is composed of an excitonic luminescence at high energies and a non-excitonic defect emission band at lower energies. HF etching of the nanoparticles reduces the defect emission and enhances the exciton process.

In this work we apply optically detected magnetic resonance spectroscopy (ODMR) both in continuous wave and time resolved mode (TR-ODMR) to study the defect luminescence in InP nanoparticles. The results show that the defect luminescence originates from weakly coupled electron-hole pair, where the electron is trapped at the surface by phosphorous vacancy, V_p , and the hole is located at the valence band. Additionally, the results suggest that the non-etched samples are dominated by V_p at the surface. Those are mainly eliminated upon HF treatment, leaving behind small percent of V_p in the core of the nanoparticle. We also find the electron-hole exchange interaction from circular polarized ODMR measurements. The TR-ODMR measurement further clarifies the spin dynamics and characteristic of the magnetic sites. Fitting these measurements to the simulated response of the PL intensity to the square wave modulated microwave power revealed that the spin relaxation time and radiative lifetime of electron-hole pair in the nanoparticles are in the microseconds regime.

INTRODUCTION

In recent years, there has been an increase of interest in the scientific and technological aspects of colloidal semiconductor nanoparticles (NPs). These materials exhibit unique chemical and physical properties, differing substantially from those of the corresponding bulk solids. The special properties are associated with the quantum size effect and the control of surface quality. The impact of the quantum size effect in the III-V NPs is of a special interest, due to their large exciton Bohr radius (10-34 nm) and relatively narrow band gap (0.4-1.5 eV). In such a case, the Bohr radius exceeds the NP diameter, which in turn leads to strong confinement of carriers and a relatively large blue shift of the band edge.

Although carrier confinement in colloidal III-V NPs is expected to lead to enhanced PL efficiency, this is not frequently observed, presumably due to the trapping of carriers at the surface and non-radiative recombination. Indeed, Micic *et al.* [1] showed that the growth of InP colloidal NPs under excess indium produces a red luminescence band, while the growth under excess phosphorous eliminates this band. Furthermore, etching of the samples with HF partially quenches the red luminescence from surface traps. This suggests that the red band corresponds to stoichiometric defects at the surface. Thus, the ultimate goal of this work is concerned with

the identification of the surface trapping sites and their influence on the recombination processes.

EXPERIMENTAL DETAILS

Colloidal InP NPs, capped with organic ligands were prepared by wet chemical methods, while their surfaces were treated by several etching procedures. An indium chloride (InCl_3) and tris-(trimethyl-silyl)phosphine ($\text{P}(\text{SiMe}_3)_3$) were used as the starting reactants. A detailed description of the preparation procedure is given in reference [2].

In the continuous wave (cw) ODMR experiment, we monitored a change in luminescence intensity, ΔI_{PL} , resulting from a magnetic resonance event at the excited state. Thus, a plot of ΔI_{PL} versus the strength of an applied external magnetic field (B), during a simultaneous application of a microwave (MW) radiation, led to an electron spin resonance-like spectrum. The emitted beam was detected in either of the following directions: (a) parallel to the external magnetic field (Faraday configuration), or (b) perpendicular to it (Voight configuration). A total emission or a circular-polarization component (σ^+ or σ^-) was detected in both configurations. Detailed description of the cw and TR ODMR setup is given elsewhere [3].

The time-resolved ODMR (TR-ODMR) signal is a luminescence response to a microwave pulse under the resonance magnetic field.

RESULTS

The photoluminescence (PL) spectra of HF etched and non-etched InP NPs (with average diameter of 4.4 nm) at 1.4K are shown by the dashed lines in Figure 1(a) and 1(b), respectively. The PL spectrum of the etched sample is dominated by an exciton band centered at ~ 2 eV, and accompanied by a weak tail at the low energy side. On the contrary, the non-etched sample is

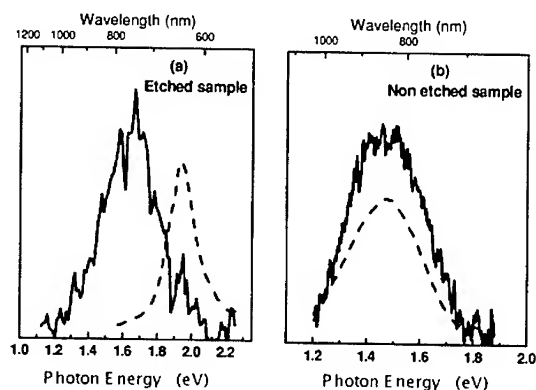


Figure 1. The photoluminescence spectra of non-etched and HF etched InP NPs (dashed line), and spectrally dependent ODMR spectra (solid line).

dominated by a deep broad band centered at 1.5 eV, with a full width half maximum (FWHM) of 0.2 eV, and a weak exciton shoulder at 1.8 eV. It should be noted that the etching process strips one or two monolayers of InP from the external surface, which reduces the NPs size and leads to a shift of the exciton band. The ODMR spectral dependence curves of both samples are shown in Figure 1 by the solid lines. They were recorded by measuring the change in PL intensity versus emission energy during an application of the resonance conditions, with an external magnetic field of 0.4 Tesla and MW radiation of $\nu_{\text{MW}}=10.8$ GHz. Both samples showed a spectral dependent ODMR band, which ranged between 1.2-2.0 eV, covering the entire non-exciton regime. In fact, this spectral dependence solely coincides with the PL spectrum of the non-etched sample, but deviates from the exciton band of the etched sample.

Representative cw ODMR spectra of the non-etched sample, recorded with circular polarizer in Faraday and Voight configurations, are shown in Figures 2(a) and 2(b), respectively. The σ^+ and σ^- detection in the Faraday configuration showed similar resonant bands, however they were shifted one with respect to the other by about 0.008 Tesla. However, the circular polarized components are indistinguishable in the Voight configuration.

The TR-ODMR spectrum of the non-etched sample, obtained with a MW transient measurement, is shown in Figure 3 by the noisy line. The solid line corresponds to a theoretical fit (*vide infra*), while the corresponding MW pulse is shown below the spectrum. This spectrum shows an instant spike of the luminescence intensity at the rising edge of the MW pulse, followed by an intensity decay, then by a sudden negative drop at the falling edge of the MW pulse, and finally, by a recovery to a steady state intensity. The spin dynamics associated with this sequence of changes will be given in the Discussion.

DISCUSSION

The PL of the etched sample is characterized by an exciton luminescence, accompanied by a tail, presumably associated with a stoichiometric defect recombination. Chemical treatment of

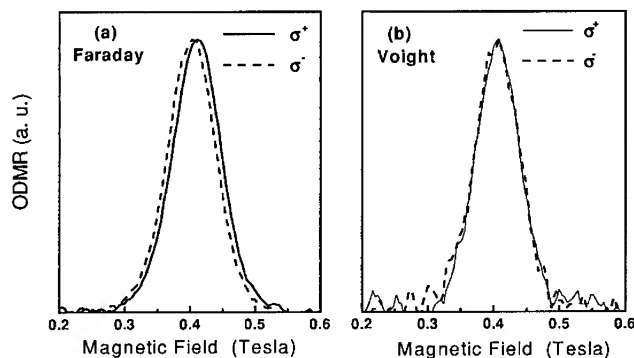


Figure 2. ODMR spectra of the non-etched sample, recorded with the circular polarizer in Faraday (a) and Voight (b) configurations.

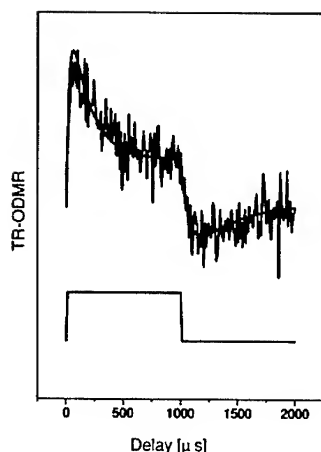


Figure 3. The TR-ODMR spectrum of non-etched sample, obtained with a MW transient measurement.

the samples with excess phosphorous during the growth or post HF etching reduces the tail recombination and enhances the exciton efficiency. Indeed, the defect recombination band dominates the PL of non-etched sample. The ODMR spectral dependence coincides solely with the defect luminescence band and thus, the magnetic resonance phenomena discussed below determine the nature of this recombination (trap-to-trap or trap-to-band), chemical identification of a defect site, electron-hole (e-h) exchange interaction and the spin dynamics.

The experimental ODMR spectra showed the existence of a single positive band, both in the Faraday and Voigt configurations, which could be fitted to a single Gaussian function. Furthermore, both the left and right circularly detected ODMR spectra are positive, but mutually shifted by about 0.008 Tesla in the Faraday configuration. This is in contradiction with the anticipation of two independent resonance bands for weakly coupled electron and hole, or a creation of a bound exciton with a negative band in the Voigt configuration [3]. Instead, the experimental evidence supports the occurrence of magnetic resonance transitions, associated with trapped electron ($F_e=1/2$) and a valence hole ($F_h=3/2$) spin system. Considering a sole spin flipping of electrons, the ODMR band could be fitted to a theoretical curve calculated by a use of conventional spin Hamiltonian including Zeeman splitting, electron hole exchange interaction J , and hyperfine interaction with the surrounding nuclei. We used $g_e=1.93$ and $J=0.28\mu\text{eV}$ for a non-etched sample, and $g_e=1.98$ for an etched sample. The increase in the g factor in the etched sample may arise from a confinement effect, due to the reduction of the NPs size upon etching or due to the existence of a different crystallographic defect. The J value was derived from the mutual shift of the σ^+ and σ^- spectra shown in Figure 2(a).

The extended wave function of the valence hole enabled a reasonable overlap with the trapped electron and indeed an e-h exchange interaction deviate from the exchange value of an exciton (30 meV) and resemble the value which was found recently for trapped electron-trapped hole recombination ($0.2\mu\text{eV}$) in colloidal NPs [4]. The magnitude of the exchange interaction is proportional to the overlap integral of the wave function of both carriers and is given by:

$$J = J_0 \exp(-2r/r_0) \quad (1)$$

where r_0 is the Bohr radius of the wave function of the less localized carrier and r is the exciton radius. It is reasonable to assume that r is close to the radius of the NPs and thus, may deviate from a single value due to the existence of a ~10% distribution in the NPs size.

The g_e value of the electron deviates considerably from that of a reported bulk value of $g_e=1.15-1.5$ at the conduction band, however, it does not approach the free electron $g_e=2.0$. This suggests that the electron is trapped at a phosphorous vacancy, but is slightly delocalized over the first next indium neighbors. The experimental lineshape could be simulated only by addition of hyperfine interactions between the trapped electron with the surrounding indium nuclei. The indium atom has a nuclear spin of $I=9/2$ with neutral abundance of 100%, while a hyperfine interaction with n next neighbors should lead to $2nI+1$ subbands. However, since the indium isotropic hyperfine constant is 390MHz [5], and the sample is studied as a powder, the detailed hyperfine lines cannot be resolved and instead, this coupling contributes to the broadening of the studied resonance band.

The time-resolved ODMR measurement further clarifies the spin dynamics and characteristics of the magnetic sites (radiative versus non-radiative). Assuming that saturation of the spin levels is avoided, the spin kinetic processes of the $|+3/2, -1/2\rangle$ and $|+3/2, +1/2\rangle$, or $|-3/2, -1/2\rangle$ and $|-3/2, +1/2\rangle$ pair states are given by the following equations:

$$\begin{aligned} \frac{dn_1}{dt} &= -\frac{n_1}{\tau_1} + G - \frac{n_1 - (n_1 + n_2)(1-\rho)}{T_1} - (n_1 - n_2)P_{MW} \\ \frac{dn_2}{dt} &= -\frac{n_2}{\tau_2} + G - \frac{n_2 - (n_1 + n_2)\rho}{T_1} - (n_2 - n_1)P_{MW} \\ \rho &= \frac{1}{1 + \exp(\Delta E/kT)} \quad , \quad \Delta E = h\nu_{MW} \end{aligned} \quad (2)$$

n_1 and n_2 correspond to the population of single pair states. G corresponds to the generation rate, while τ_1 and τ_2 are the corresponding decay times (when $\tau^{-1} = \tau_{rad}^{-1} + \tau_{nrad}^{-1}$, rad and nrad correspond to the radiative and non-radiative processes). T_1 is the spin-lattice relaxation, while P_{MW} corresponds to the MW power. $\exp(-E/kT)$ is the occupancy probability in thermal equilibrium. The analytical solution of four kinetic equations (with $P_{MW}=0$ and $P_{MW}\neq 0$) yields a theoretical change in the PL intensity due to a magnetic resonance between two states, induced by a square-wave modulation of the MW power. The experimental TR-ODMR spectrum was simulated with $\tau_{rad1}=100 \mu\text{sec}$, $\tau_{nrad1/2}=800 \mu\text{sec}$, $\tau_{rad2}\gg\tau_{rad1}$, and $T_1=250 \mu\text{sec}$, as shown by the solid smooth line in figure 3. This simulation suggests that the defect-to-band recombination is a radiative process, involving trapping of an electron at a phosphorous vacancy.

CONCLUSIONS

InP NPs prepared by colloidal techniques were investigated. The research was focused on the characterization of a defect luminescence band. cw and TR-ODMR spectroscopy was utilized in combination with conventional luminescence technique. The ODMR spectrum consists of a single broad positive resonance composed of left and right circular polarized components, mutually shifted by 0.008 Tesla in a Faraday configuration. The defect luminescence was

identified as a recombination of a valence band hole, with total angular momentum of $3/2$, and an electron trapped at a Vp site, with total angular momentum of $1/2$. The non-etched samples are dominated by Vp sites at the surface, while the etched samples are left with a small percent of vacancies at the core. The TR-ODMR measurements revealed characteristic decay times of about $100\mu\text{s}$ for the radiative and about $800\mu\text{s}$ for nonradiative spin levels. This measurement also revealed that a spin-lattice relaxation is about $250\mu\text{s}$.

REFERENCES

1. D. Bertram, O. Micic and A. Nozik, Phys. Rev. B **57**, R4265 (1998).
2. O. I. Micic, K. M. Jones, A. Cahill and A. J. Nozik, J. Phys. Chem. B **102**, 9791 (1998).
3. L. Langof, E. Ehrenfreund, E. Lifshitz, O.I. Micic, and A. J. Nozik, in press, J. Phys. Chem.
4. E. Lifshitz, A. Glozman, I. D. Litvin, and H. Porteanu, J. Phys. Chem. B **104**, 10449 (2000).
5. H. J. von Bardeleben, Solid State Commun. **57**, 137 (1986).

Airplane and Drop Experiments on Crystallization of $\text{In}_x\text{Ga}_{1-x}\text{Sb}$ Semiconductor under Different Gravity Conditions

Krishnan Balakrishnan¹, Yasuhiro Hayakawa¹, Hideki Komatsu¹, Noriaki Murakami¹, Tetsuo Nakamura¹, Tadashi Kimura¹, Tetsuo Ozawa², Yasunori Okano³, Masafumi Miyazawa³, Sadik Dost⁴, Le. H. Dao⁵ and Masashi Kumagawa¹

¹Research Institute of Electronics, Shizuoka University, 3-5-1 Johoku, Hamamatsu, Shizuoka 432-8011, Japan.

²Dept. of Electrical Eng., Shizuoka Inst. of Sci. & Tech., Fukuroi 437-8555, Japan.

³Faculty of Eng., Shizuoka University, Hamamatsu 432-8561, Japan.

⁴Dept. of Mech. Eng., University of Victoria, Victoria, BC, Canada V8W 3P6.

⁵Adv. Mat. Res. Lab., Univ. du Quebec, INRS, Verennes, Quebec, Canada J3X1S2.

ABSTRACT

Melting and crystallization experiments of InGaSb were done under the reduced gravity condition (10^{-2}G) in an airplane and at the normal gravity condition (1G) in the laboratory. Crystallized InGaSb was found to contain many needle crystals in both the cases. Reduced gravity condition was found to be more conducive for crystal growth than the normal gravity condition. Formation of spherical projections on the surface of InGaSb during its crystallization was in-situ observed using a high speed CCD camera in the drop experiment. Spherical projections showed dependence of gravity during its growth. Indium compositions in the spherical projections were found to vary depending on the temperature.

INTRODUCTION

$\text{In}_x\text{Ga}_{1-x}\text{Sb}$ is a potential optoelectronic device oriented material and it could be used to fabricate commercially viable detectors, thermo-photo-voltaic (TPV) cells. $\text{In}_x\text{Ga}_{1-x}\text{Sb}$ along with its binary counterparts GaSb and InSb are interesting III-V model materials for space ventures because of their low melting temperatures (712°C and below) and low vapour pressures. It is extremely difficult to grow high quality $\text{In}_x\text{Ga}_{1-x}\text{Sb}$ bulk crystals on earth due to gravity induced effects. As the densities of the components are different, solute transport occurs due to buoyancy. For this reason, microgravity condition in space is ideally suited to grow high quality and defect free $\text{In}_x\text{Ga}_{1-x}\text{Sb}$ crystals as the gravity induced negative effects can be overcome [1-3]. In order to investigate the effect of gravity on the dissolution and crystallization processes, we carried out two microgravity experiments. The first one was performed in the Second International Microgravity Laboratory (IML-2) in 1994 [4-7]. We studied the effects of diffusion and convection on the melt mixing of In/GaSb/Sb. One of the important observations made in this venture was the formation of many circular projections on the surface of the InGaSb spherical sample. The indium compositions in this area were different from those in the main body of the sample. The other experiment was carried out in a Chinese recoverable satellite in 1996 [8-10].

It is not always possible to venture microgravity experiments in space using space shuttles due to economic and other major constraints. Hence, it is necessary to find alternate avenues to perform this type of experiments on earth itself using the facilities like drop tower, airplane etc. It is also important to know how the crystal growth processes take place under the reduced gravity conditions like 10^{-1}G , 10^{-2}G

etc. and under the higher gravity conditions, like, 2G, 3G etc. In the present article, we discuss about the results of the airplane and drop experiments on the crystallization of InGaSb conducted under different gravity conditions.

EXPERIMENTAL

For the airplane experiment, polycrystalline $\text{In}_x\text{Ga}_{1-x}\text{Sb}$ ($x=0.05$) cut into a dimension of $5 \times 5 \times 0.2 \text{ mm}^3$ was used as the starting material. The sample was sandwiched between two thin quartz glass plates and was sealed using high temperature adhesives. Thermocouples were connected to the samples to monitor and control the temperature during the melting and crystallization processes. The sample configuration is shown in Fig.1. An equipment was designed and constructed for the airplane experiment. The sample was mounted on a movable platform so that the position of it could be changed using a motor during the experiment. The InGaSb sample was heated to a temperature of 706°C . During this time, InGaSb polycrystal melted and changed to In-Ga-Sb solution. When the gravity level changed to 10^{-2}G , the sample was moved out of the furnace and hence the temperature decreased rapidly. This process is schematically represented in Fig.2. During the rapid decrease of temperature, InGaSb crystallized. The complete experiment was videographed using a high resolution CCD camera. The same type of experiment was carried out under the normal gravity (1G) in the laboratory.

For the drop experiment, polycrystals of InGaSb were used as the starting materials. The sample structure was similar to Fig.1. This experiment was performed using a 150m drop tower facility present in the Micro-Gravity Laboratory of Japan (MGLAB). An equipment comprising a furnace to heat the sample, thermocouples, temperature controllers to control the sample and furnace temperatures, a high speed and high resolution CCD camera, and two lights, was constructed for this study and the schematic diagram of it is shown in Fig.3. The melting and crystallization of InGaSb during the experiment was videographed using the high speed and high resolution camera. The recorded images and the corresponding temperatures and gravity levels were used to study the melting and crystallization processes. InGaSb polycrystalline plate sample was heated to a temperature of 800°C at a rate of $50^\circ\text{C}/\text{min}$. and kept for 10 minutes. Later, the sample was cooled down by cutting off the power supply. During the cooling period, molten InGaSb started crystallizing. During the crystallization, the capsule was dropped in to the vacuum tower.

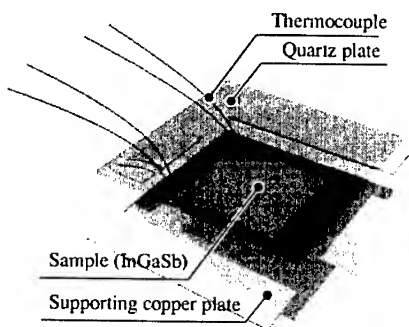


Fig.1. Sample configuration for the airplane and drop experiments.

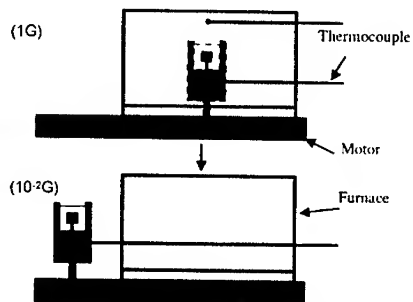


Fig.2. Change of sample position during the airplane experiment.

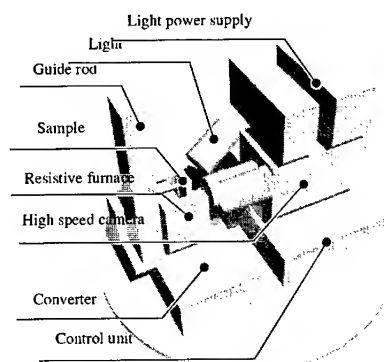


Fig.3. Schematic diagram of home-made equipment for the drop experiment.

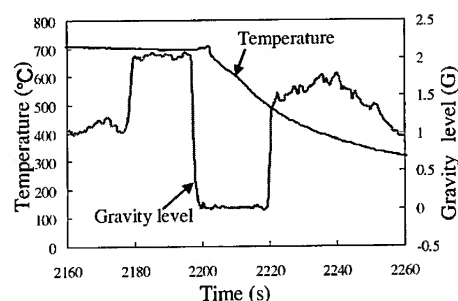


Fig.4. Variation of gravity level and sample temperature with time in the airplane experiment.

RESULTS AND DISCUSSION

Effect of gravity on the needle crystal growth

Figure 4 shows the variation of the gravity level with the flying time of the aircraft and the temperature of the InGaSb sample during the experiment. The set temperature of the sample was decreased to less than 500°C in a time of a second after the gravity became $10^{-2}G$. Figure 5 shows the photographs of the crystallized InGaSb samples under $10^{-2}G$ and 1G conditions, respectively, and the corresponding EPMA line profiles of indium composition measured on the surfaces of the samples. The needle crystals were found to have formed during the cooling of InGaSb. This result is similar to the needle crystal formed in our space experiment under microgravity condition [10]. In the case of the needle crystal formed under reduced gravity ($10^{-2}G$) and normal gravity, indium composition should be as small as 0.005. Figure 6 shows the binary phase diagram of the InSb-GaSb system. As marked in the phase diagram, the sample must be cooled down fast to get the crystal of indium composition 0.005. Hence, in the EPMA profile, the portions where the In composition is 0.005, correspond to the InGaSb needle crystal and the portions where the In composition is high, correspond to the residual solution. The needle crystal is surrounded by the residual solution and its indium composition is much more than that of the crystal. As seen in the EPMA profiles, in the case of reduced gravity processed sample, the number of indium peaks is relatively smaller than the peaks observed in the normal gravity processed sample.

Figures 7(a) and (b) show the statistics of the size of the needle crystals formed under reduced gravity and normal gravity conditions, respectively. As clearly seen in the figures, the number of smaller sized crystals formed under normal gravity conditions is much more than the number of smaller crystals formed under reduced gravity condition. It is obvious that the convective forces during the crystal growth processes behave differently depending on the gravity conditions. Under the reduced gravity condition, growth of larger sized crystals is more feasible as the negative effect of the convective forces is relatively less. In the case of the crystal growth under normal gravity, due to the convective forces, most of the needle crystals grown were smaller. This clearly indicates that the reduced gravity condition is better suited for crystal growth.

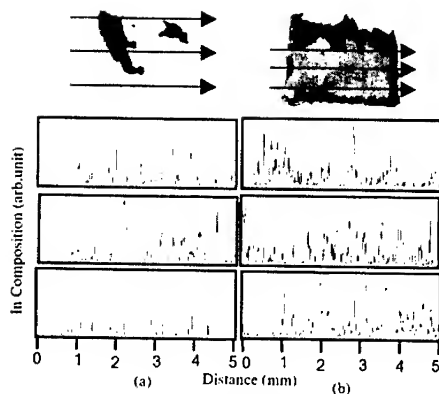


Fig. 5. EPMA line profiles for the needle crystals grown under (a) reduced gravity and (b) normal gravity.

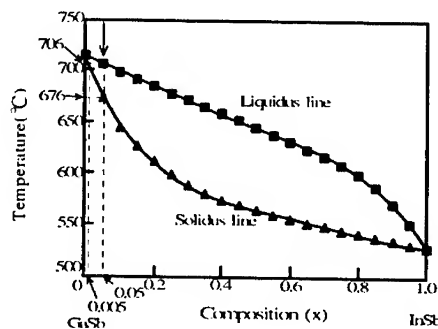


Fig. 6. InSb-GaSb binary phase diagram.

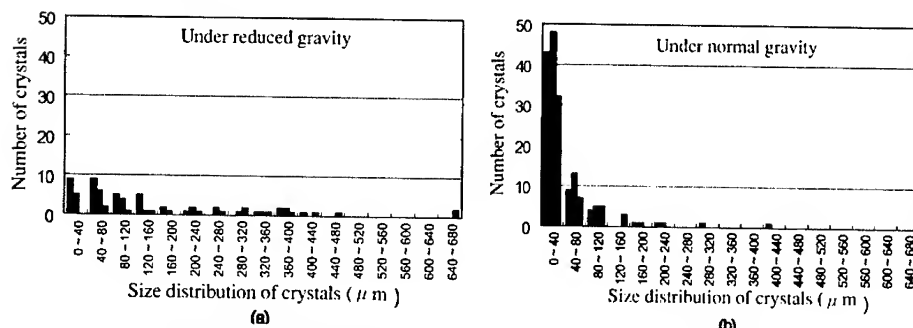


Fig. 7. Size distribution of the needle crystals grown under (a) reduced gravity ($10^{-2}G$) and (b) normal gravity conditions.

Formation of projections during InGaSb crystallization

During the crystallization of InGaSb, many spherical projections were observed on the surface of the sample. The projections emerged out during the crystallization of InGaSb from its melt due to the reason that the density of InGaSb liquid is larger than that of solid. These were similar to the projections observed in the melting and solidification experiment of In/GaSb/Sb done in IML-2 [5]. The projections in this study were found to increase in size slowly. In the present experiment, the drop of the capsule was made to coincide with the appearance and growth of spherical projections so that this process could be observed under microgravity condition. Figure 8 shows the high resolution images recorded using high speed camera during the crystallization of InGaSb in one of the drop experiments. As seen clearly in the images, the spherical projections have just started to appear and grow larger in size slowly as the time passed. The figures (a)-(f) correspond to the images recorded under microgravity condition at the timings 0s, 1s, 2s, 3s, 4s and 4.5 s, respectively. The enlarged image of the final form of the projections formed is shown in the Fig. 9. The projection A was formed under normal gravity condition and the projections B and C were formed

under microgravity condition. The projections formed under microgravity were almost spherical, whereas, the projection formed under normal gravity was not perfectly spherical. Due to gravitational pull, the top surface of the projection A tended to become flat. This shows the influence of gravity on the formation of projections.

It was found that the rate of increase of projection area was high and constant for the first 3 sec. However, in the remaining time, the increase rate became lower and this may be due to the reduction of solute supply in the final stage of projection formation. The solute supply was blocked to some extent by the already formed crystal in the lower portion of the projection.

The In compositions in the formed projection B and C were measured by EPMA and are schematically represented in Fig.10. The In composition in the projection C was found to be more than that of projection B. This is due to fact that the temperature at the time of the formation of projection B was higher than the corresponding temperature of projection C. This indicates that the In composition of the crystallized InGaSb varies depending on the existing temperature at the time of formation. This is in accordance with the InSb-GaSb ternary phase diagram [11]. Since the whole processes of melting and crystallization of InGaSb were recorded using the high speed and high resolution CCD camera (a maximum of 250 images per second) in all the experiments along with the precise values of the corresponding gravity levels and temperatures, it was possible to find the exact conditions at which the projections formed.

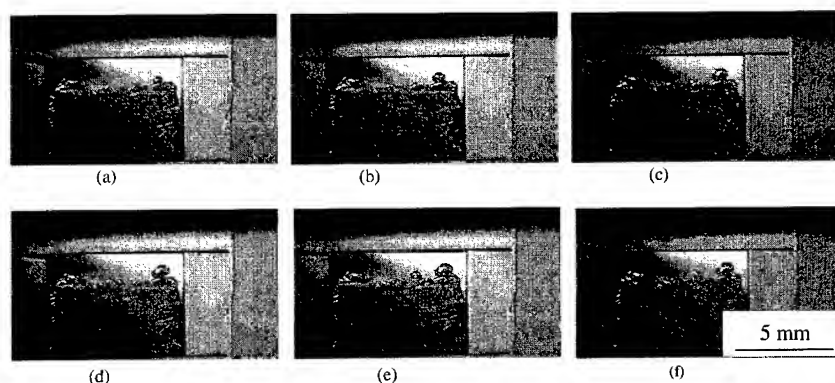


Fig.8. High resolution images recorded during the crystallization of InGaSb at the timings, (a) 0s, (b) 1s, (c) 2s, (d) 3s, (e) 4s and (f) 4.5 s, respectively.

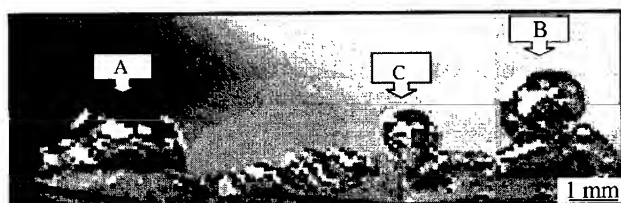


Fig.9. The enlarged images of the final shape of the projections. The projection A was formed under normal gravity condition and the projections B and C formed under microgravity condition.

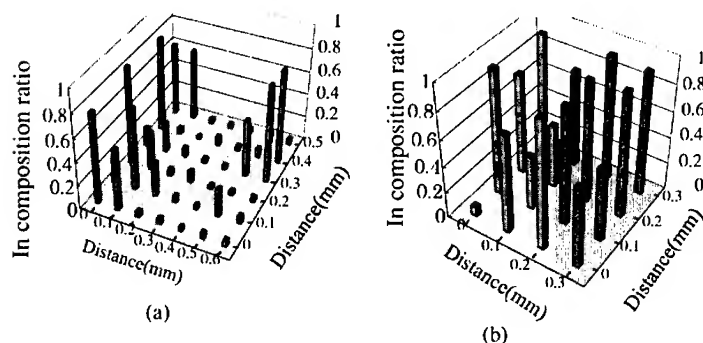


Fig.10. The 3-dimensional schematic representation of the In compositions measured on the (a) projection B and (b) projection C. The measurements were made at the selected points on the squares of areas 0.6 x 0.7 mm² and 0.4 x 0.4 mm² of projections B and C, respectively.

SUMMARY

In the airplane experiment on the crystallization of InGaSb under $10^{-2}G$ condition, needle crystal was found to have formed and the size of it was larger than the crystal obtained under normal gravity. This showed that the reduced gravity condition is more feasible for crystal growth. In the drop experiment, spherical projections of InGaSb were observed to form during its crystallization under microgravity. On the other hand, projection formed under normal gravity was not perfectly spherical. Indium composition in the projection was found to vary depending on the existing temperature condition during the formation.

ACKNOWLEDGEMENT

This study is funded by a part of "Ground Research for Space Utilization" promoted by NASDA and Japan Space Forum, and Monbusho grant-in-aid for the International scientific program and scientific encouragement fund in Shizuoka University. Technical assistance of Mr. Momose is acknowledged.

REFERENCES

1. A.F.Witt, H.C.Gatos, M.Lichtensteiger and C.J.Herman, *J.Electrochem.Soc.* 125 (1978)1832.
2. A.N.Danilewsky, K.W.Benz and T.Nishinaga, *J.Crystal Growth* 99(1990)1282.
3. T.Nishinaga, P.Ge, C.Huo, J.He and T.Nakamura, *J.Crystal Growth* 174 (1997)96.
4. K.Okitsu, Y.Hayakawa, T.Yamaguchi, K.Kumagawa, A.Hirata, M.Tachibana and N.Imaishi, *Trans.Mat.Res.Soc.Jpn.*, 16A (1995) 691.
5. K.Okitsu, Y.Hayakawa, A.Hirata, S.Fujiwara, Y.Okano, N.Imaishi, S.Yoda, T.Oida, T.Yamaguchi and M. Kumagawa, *M. Cryst. Res. and Tech.*, 31(1996) 969.
6. K.Okitsu, Y.Hayakawa, T.Yamaguchi, A.Hirata, S.Fujiwara, Y.Okano, N.Imaishi, S.Yoda, T.Oida and M. Kumagawa, *Jpn. J. Appl. Phys.* 36(1997) 3613.

7. A.Hirata, K. Okitsu, Y.Hayakawa, Y.Okano, S. Sakai, S. Fujiwara, N. Imaishi, Y. Yamaguchi, S. Yoda, T. Oida and M. Kumagawa, *Int. J. Appl. Electromagnetics and Mechanics* 10 (1999) 527.
8. A.Hirata, Y.Hayakawa, T.Wada, D.Hirose T.Yamaguchi, Y.Okano, J.Simizu, K.Arafune, N.Imaishi, Y.Kumagiri, X.Zhong, X.Xie, B.Yuan, F.Wu, H.Liu and M.Kumagawa, *Proc.of 21st International Symposium on Space Technology and Science (Oomiya, Japan, 1998.5) Vol. II*, (1998) 1243.
9. T.Kimura, Y.Hayakawa, T.Ozawa, Y.Okano, A.Hirata, M.Miyazawa, N.Imaishi, K.Arafune, T.Yamaguchi and M.Kumagawa, *J.Jpn Soc.Microgravity Appl.* 15, Supplement II (1999) 472.
10. Y.Hayakawa, Y. Okano, A. Hirata, N. Imaishi, Y. Kumagiri, X. Zhong, X. Xie, B. Yuan, F. Wu, H. Liu, T. Yamaguchi, and M. Kumagawa, *J. Crystal Growth* 213(2000)40.
11. G.B. Stringfellow, *J.Phys.Chem.Solids* 33 (1972) 665.

I-V And C-V Characteristics of nGaAs-nInSb Heterojunctions Obtained by Pulsed Laser Deposition Technique

Karapet E. Avdjian
Department of Semiconductor Electronics,
Institute of Radiophysics & Electronics, National Ac. Sci. of Armenia,
1 Brs. Alikhanian st., Ashtarak, 378410, Armenia

ABSTRACT

Using pulsed laser deposition technique, nGaAs-nInSb heterojunctions (HJs) are obtained. Their electrical properties are studied. The Current-Voltage characteristics show that obtained HJs possess rectifying properties. The rectification coefficient depends strongly on the doping level of GaAs substrate. The linear dependence of C^{-2} (V) curve in Capacitance-Voltage characteristics, as well as the change of photo-response sign with wavelength, indicates that the HJs have abrupt interface, which is, to the best of our knowledge, a novel result for these HJ materials. The full number of interface states arising due to the lattice mismatch is determined which is in agreement with Hall measurements. Current-Voltage characteristics of obtained HJs are analogous to those of metal-semiconductor junction. Based on the obtained results the energy band diagrams of nGaAs-nInSb HJ is constructed taking into account the interface states.

INTRODUCTION

Owing to its many advantages (such as technology flexibility, low temperature of crystalline growth, as well as production of thin and ultrathin layers of actually any material) the pulsed laser deposition (PLD) has its leading role in fabrication of thin semiconductor materials. In recent years, a growth of interest is observed in using the PLD for production of semiconductor heterojunctions (HJ).

Due to a large lattice mismatch (~14%) the nInSb-nGaAs type HJs refer to the class of non ideal HJs. Earlier, E.D. Hinkley and R.H. Rediker [1] reported the fabrication of nGaAs-nInSb HJs obtained by fusion of InSb into the GaAs. Nevertheless, there are no reports to our knowledge on the fabrication of crystalline nInSb-nGaAs HJs with abrupt interface using the usual techniques. This might be due to the difficulty of crystalline growth of HJ materials with large lattice mismatch. Only recently, in [2] the possibility of fabrication of crystalline nInSb-nGaAs HJs with abrupt interfaces was shown, and the results were used for analysis of an infrared (~5-6 μm) pyrometer. However, the electrical characteristics of these HJs were not presented in [2].

In the present work, crystalline nGaAs-nInSb HJs are fabricated based on the PLD technique, and their electrical properties are studied.

EXPERIMENT

The facility for fabrication of nGaAs-nInSb HJs included a Q-switched laser on Nd^{3+} (pulse length is 30 nsec., energy per pulse is 1 J, intensity in the irradiation area of the target is $\sim 10^8 \text{ W/cm}^2$) and a vacuum chamber with residual pressure of $\sim 10^{-6}$ Torr. Polished nGaAs slabs with various doping degrees ($5 \cdot 10^{16}$ – $5 \cdot 10^{18} \text{ cm}^{-3}$) were used as substrates, and nInSb pellets with doping degree 10^{14} cm^{-3} were used as target material. The nInSb layers

with $\sim 0.1 \mu\text{m}$ thickness were deposited in vacuum of $\sim 10^{-6}$ Torr at temperature of crystalline growth of $\sim 350^\circ\text{C}$. A shell of width $\sim 6 \text{ \AA}$ was deposited after each evaporating pulse. The back contact to the nGaAs substrate was made up by thermal spraying of In with protecting Ag layer and the structure was annealed during the deposition of nInSb layer. The crystallinity of the layers was checked by electron-diffraction method. In order to obtain current-voltage (I-V) and capacitance-voltage (C-V) characteristics the produced nGaAs-nInSb structures were split and placed in a purpose-built holder. All measurements were carried out at room temperature.

RESULTS AND DISCUSSION

The I-V characteristics of produced HJs at various doping levels of GaAs are shown in figure 1. As it is seen, the HJs possess rectifying properties, and the rectification coefficient depends strongly on the substrate doping level. For an HJ with $N_D(\text{GaAs}) \approx 5 \times 10^{16} \text{ cm}^{-3}$ the rectification coefficient, $k \approx 10^6$ at 0.7 V, while for $N_D(\text{GaAs}) \approx 5 \times 10^{18} \text{ cm}^{-3}$ $k \approx 40$ at the same voltage.

In figure 2, the C-V characteristics of HJs are represented at various doping levels. The essentially linear dependence of the experimental curve, $C^{-2}(V)$, is an evidence of the abruptness of the HJ interface.

The carrier concentrations in GaAs were determined from the slope of the $C^{-2}(V)$ curve. The results are in reasonable agreement with Hall measurements of concentrations in nGaAs. The extrapolation of $C^{-2}(V)$ dependence to the value $C^{-2}=0$ gives one the contact potential falling on the nGaAs. Based on these results the total equilibrium charge ($Q_{is} = -2qEN_DV_D$) on interface states originating due to the lattice mismatch, as well as the total number of these states per unit area were determined. Results are given in Table 1.

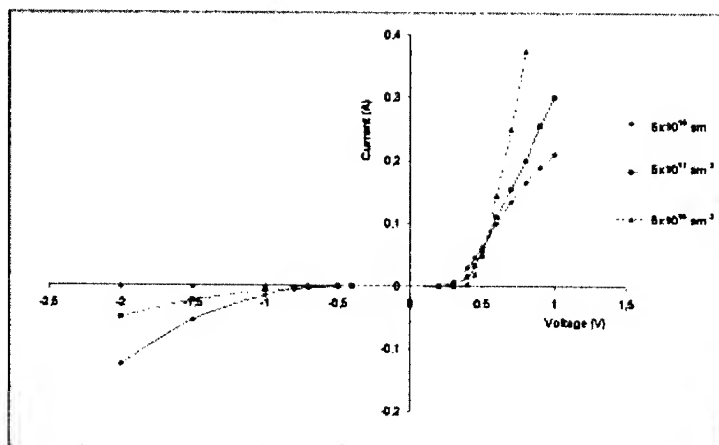


Figure 1. I-V characteristics of heterojunction nGaAs-nInSb at various doping levels of nGaAs.

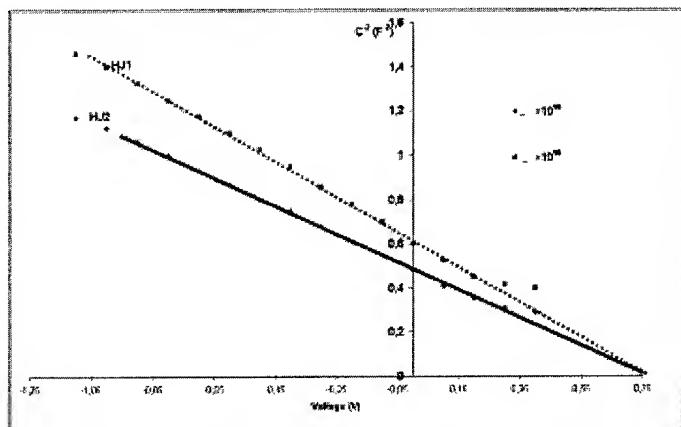


Figure 2. C-V characteristics of nGaAs-nInSb heterojunction at various doping levels of nGaAs.

Table I. Main experimental results obtained from I-V and C-V characteristics.

	$N_D(\text{GaAs})$ sm^{-3} Hall measur.	$N_D(\text{GaAs})$ sm^{-3} from C-V curves	N_{is} theor. sm^{-2}	N_{is} exper. sm^{-2}	$qV_D(\text{eV})$ from C- V curves	$\Psi(\text{eV})$ from C- V curve	η , from I-V curves	HJ surf. area (sm^2)
HJ1	$5 \cdot 10^{16}$	$6,3 \cdot 10^{16}$	$3 \cdot 10^{14}$	$\geq 1,6 \cdot 10^{14}$	0,75			$5 \cdot 10^{-3}$
HJ2	$5 \cdot 10^{17}$	$4,8 \cdot 10^{17}$	$3 \cdot 10^{14}$	$\geq 4,6 \cdot 10^{14}$	0,75	0,74	2,25	$5 \cdot 10^{-3}$

As it is seen, the obtained values of N_{is} are in good agreement with the total number of interface states of nGaAs-nInSb HJ, which was estimated from simple considerations based on the lattice mismatch of HJ materials.

The appearance of interface states also affects strongly on the mechanism of current flow through the HJ. In figure 3, the I-V characteristics of nGaAs-nInSb HJ with $N_D(\text{GaAs}) \approx 5 \cdot 10^{17} \text{ sm}^{-3}$ at room temperature is represented.

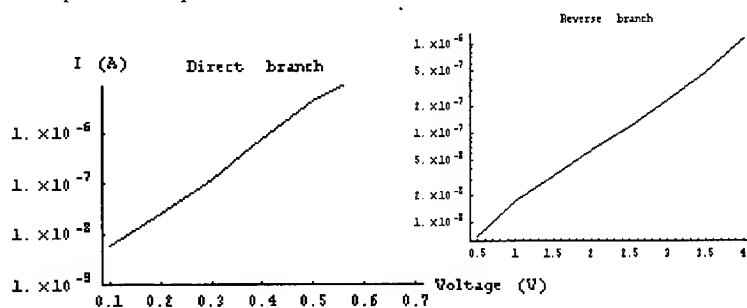


Figure 3. I-V characteristics of heterojunction nGaAs-nInSb with doping level of GaAs $N_D \approx 5 \cdot 10^{17}$ at room temperature.

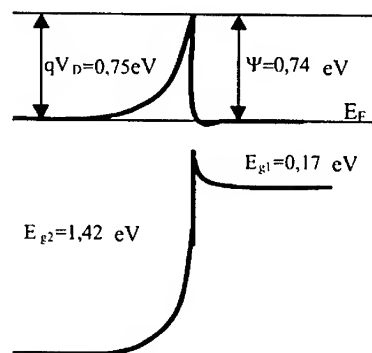


Figure 4. Energy band profile of nGaAs-nInSb heterojunction taking into account the interface states.

In spite of the large number of interface states the saturation of current was not observed in any direction. The I-V characteristics of studied HJs are similar to those of metal-semiconductor junctions.

The direct current is described by an expression $I = I_0 (\exp(qV/\eta kT) - 1)$, where $I_0 = A T^2 \exp(-\Psi/\eta kT)$ ($A = 8.64 \text{ A} \cdot \text{cm}^{-2} / \text{K}^2$, A is the effective Richardson constant, Ψ is the metal-semiconductor barrier, η is the imperfection coefficient).

The values of η and Ψ deduced from I-V curves are given in Table 1. The value of Ψ agrees well with the barrier height determined from C-V characteristics. The results of I-V and C-V characteristics were used to construct the energetic band diagram of nGaAs-nInSb HJ, which takes into account the interface states (figure 4).

CONCLUSIONS

We have studied the current-voltage and capacitance voltage characteristics of heterojunctions nGaAs-nInSb obtained by pulsed-laser deposition. We have shown that produced HJs have abrupt interfaces and possess rectification properties, which depend on the doping level of nGaAs substrates. The current transmission through HJ is similar to that through a metal-semiconductor junction. The energy band diagram of nGaAs-nInSb is constructed based on the obtained results.

REFERENCES

1. E. D. Hinkley, R. H. Rediker, Solid State Electronics, v. 10, 671 (1967).
2. A.G. Alexanian et al. The Int. Journ. IR and MM Waves, v. 18, N1 (1997).

Effects of Electric Fields on Cathodoluminescence from II-VI Quantum Well Light Emitting Diodes

A. Y. Nikiforov,¹ G. S. Cargill III,¹ M. C. Tamargo,² S. P. Guo,^{2,4} and Y.-C. Chen³

¹ Department of Materials Science and Engineering, Lehigh Univ., Bethlehem, PA 18015, U.S.A.

² Department of Chemistry, City College-CUNY, New York, NY 10031, U.S.A.

³ Department of Physics, Hunter College, CUNY, New York, NY 10021, U.S.A.

⁴ Present address: EMCORE Corp., Somerset, NJ 08873, U.S.A.

ABSTRACT

Effects of electrical bias on the cathodoluminescence (CL) have been investigated for a blue II-VI quantum well (QW) light emitting diode structure of ZnCdMgSe, lattice-matched to InP. In CL wavelength scans, the observed effects include largely reversible changes in QW CL intensity and wavelength and changes in cladding CL intensity. In CL time-based scans, the QW CL intensity showed both immediate and long term changes with bias. Irreversible, degradation-related decreases in QW CL intensity were also observed. Effects of bias on CL were modeled by calculating the rates of carrier production by electron bombardment and the resulting electron and hole currents with different applied bias fields. These model calculations do not explain many of the experimental observations, because the model does not include effects of bias on carrier escape and redistribution in the QW and effects of bias on generation and transport of atomic scale defects.

INTRODUCTION

ZnSe-based light emitting diodes have potential applications in full-color projection displays, traffic signals, and more efficient white light sources [1-5]. Although remarkable progress has been made, practical devices have not been yet achieved because of luminescent intensity degradation during device operation. The quaternary wide-gap ZnCdMgSe system (figure 1) can be grown lattice matched to (001) InP substrates by molecular beam epitaxy with a wide range of band gaps from blue to red depending on composition [3]. QW structures based on these materials exhibit excellent optical characteristics with very strong luminescence intensity and quantum confinement [4-5]. These diodes show no formation of dark line defects and have lifetimes about three orders of magnitude longer [6,7] than diodes with a comparable density of extended defects grown on GaAs substrates.

Understanding how electrical bias affects carrier transport and defect behavior may help in further improvement of performance and lifetimes of QW-based light emitting diodes (LEDs) and laser diodes [8]. Gundel et al. [8] studied the influence of reverse bias on degradation of a ZnCdSe QW-based laser diode by photoluminescence. They [8] argued that the observed changes in the degradation rate with bias were caused by the effects of bias fields on diffusion of charged defect complexes from the *p*-doped waveguide into the QW.

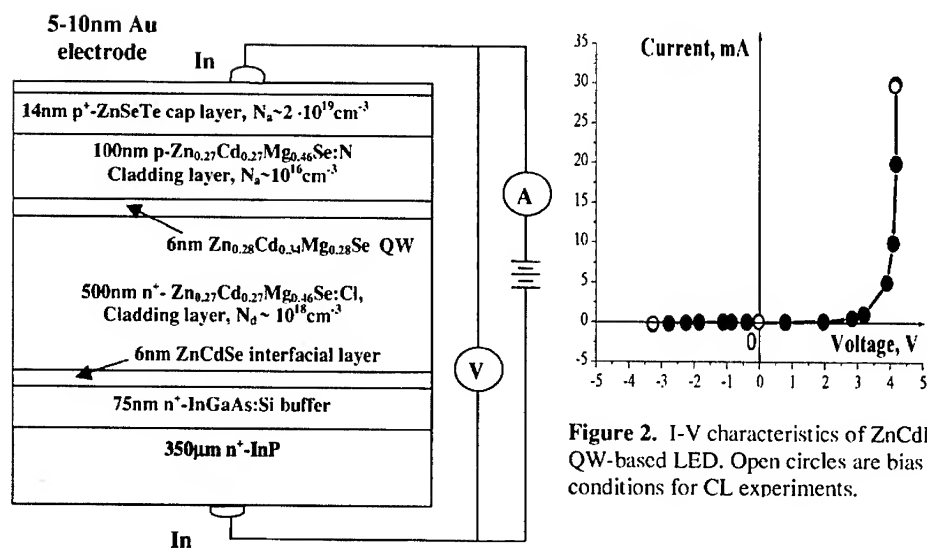


Figure 1. Schematic of ZnCdMgSe QW-based LED and experimental setup.

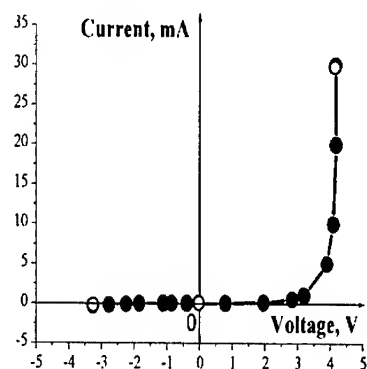


Figure 2. I-V characteristics of ZnCdMgSe QW-based LED. Open circles are bias conditions for CL experiments.

The present paper describes effects of both forward and reverse bias on CL from a ZnCdMgSe QW-based LED. Results obtained are much more extensive than those reported by Gundel et al. [8].

OBSERVED EFFECTS OF BIAS ON CATHODOLUMINESCENCE

CL measurements used a JEOL JSM-6400 SEM with an Oxford Instruments CF302 CL system. CL was studied for three biases: reverse bias of -3.2V, zero-bias, and forward bias of +4.2V, as indicated in figure 2. The electron beam voltage was 10kV and the electron beam current was ~ 50nA.

Cathodoluminescence wavelength measurements

Each wavelength scan was collected from an area of ~ 35µm × 35µm and took about 160sec. Without bias, CL wavelength scans show well resolved peaks from the QW and cladding (figures 3 and 4). Application of either forward or reverse bias causes the QW CL intensity to drop. A forward bias of +4.2V eliminates the cladding peak and shifts the QW peak to longer wavelength (figure 3). These effects appear to be fully reversible. With a reverse bias of -3.2V, the cladding peak remains unaffected and a small increase in QW CL wavelength is observed (figure 4). In contrast to forward bias, a small irreversible decrease in QW CL, but not in cladding CL, is seen after switching from reverse bias to zero bias.

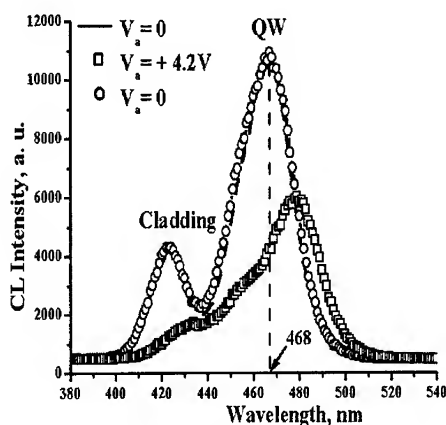


Figure 3. Forward bias CL wavelength scans.

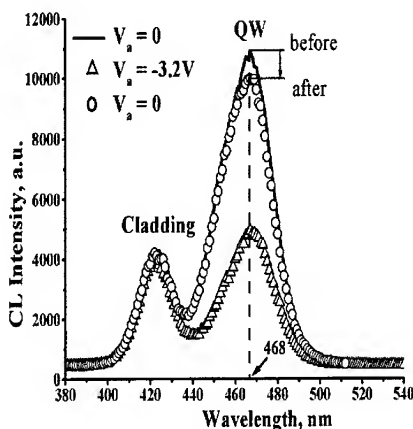


Figure 4. Reverse bias CL wavelength scans.

Time dependent effects of bias on quantum well cathodoluminescence

CL time-based scans were made with a stationary electron beam (spot mode) and with the spectrometer set to 468nm, the zero-bias QW CL wavelength. In the time-base scan without bias (figure 5), the QW intensity increased by ~10% during the initial 250s (A to B). Then the QW intensity remained nearly constant (B to C) until forward bias was applied. The decreases in the QW intensity to background level during the time-base scan, for example, at ~700s, resulted from blanking the electron beam. Forward bias led to a small, probably, instantaneous decrease (C to D), followed by a rapid decay of the QW intensity (D to F). When the bias was switched off (G), the QW intensity increased (G to H) to ~85% of its value before application of bias (C). Reverse bias caused the CL intensity to drop initially (H to I). The rate of the CL intensity decrease (I to K) for reverse bias was much slower than that for forward bias (D to F).

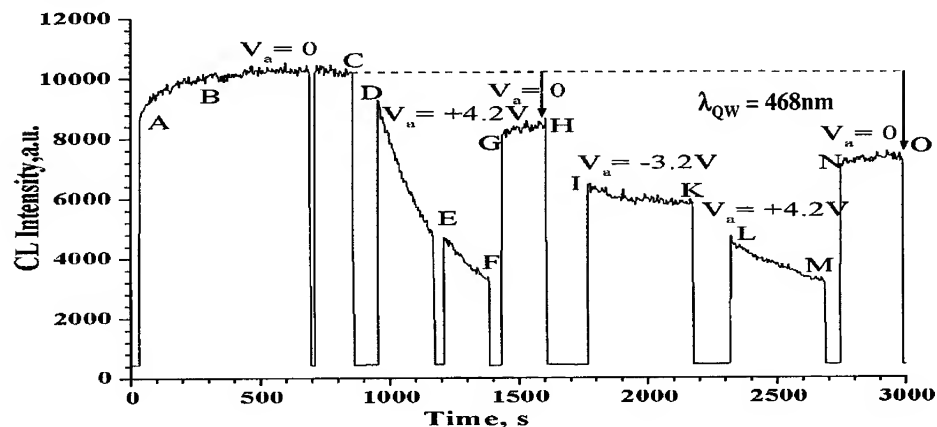


Figure 5. Bias effects in CL time-based scan. The arrows at 1600s and 3000s indicate zero-bias intensity decreases caused by electron bombardment.

Application of forward bias led to probably instantaneous QW intensity decrease (K to L) and further rapid intensity decay (L to M). After 3000s of spot mode electron irradiation with several biasing cycles, the QW intensity dropped by only ~30% (C to O). These bias effects are quite different from those reported by Gundel et al. [8] for a ZnCdSe QW-based laser diode, where rapid degradation occurred with zero bias.

MODELING EFFECTS OF BIAS ON CATHODOLUMINESCENCE FROM ZnCdMgSe QUANTUM WELL LIGHT EMITTING DIODES

Rates of electron and hole production by electron bombardment were calculated using the depth-distribution function (figure 6), which describes deposition of electron energy in depth. Effects of bias on band bending and depletion lengths were considered as well. Excess carriers, $\Delta n(\vec{r})$, generated in the specimen by continuous electron bombardment, undergo diffusion and/or drift, followed by recombination, that may give rise to luminescence. Assuming a linear dependence of CL intensity on the stationary excess carrier density, $\Delta n(\vec{r}) = n(\vec{r}) - n_0(\vec{r})$, the total CL intensity can be expressed as [9]

$$L_{CL}(\vec{r}) \propto \int_V \frac{\Delta n(\vec{r})}{\tau_{rr}} d^3r, \quad (1)$$

where τ_{rr} is the radiative recombination lifetime.

Only excess carriers created by electron bombardment in the depletion regions, $W_{n,p}$, and within the diffusion length distances, $L_{n,p}$, (figures 6 and 7), contribute to the QW intensity. With reverse or zero bias, the depletion regions are much larger than the QW width, so diffusion and drift currents of excess minority carriers, I_{diff} and I_W , are expected to be largely responsible for the QW luminescence. The diffusion of the excess minority carriers, n_p and p_n , in one-dimension, can be treated in terms of the differential equations of continuity for electrons in the p -cladding and p^+ -cap layers and for holes in the n -cladding layer (figure 1).

The local generation rate of excess carriers represents the number of electron-hole pairs generated per unit depth and per unit time [9]. This can be expressed as

$$g(z) = \frac{h(z) \times G \times I_b}{q} \left(\frac{\# \text{ pairs}}{\text{depth} \times \text{time}} \right), \quad (2)$$

where $h(z)$ with $\int_0^\infty h(z) dz = 1$ is the depth-distribution of the deposited energy as a function of depth.

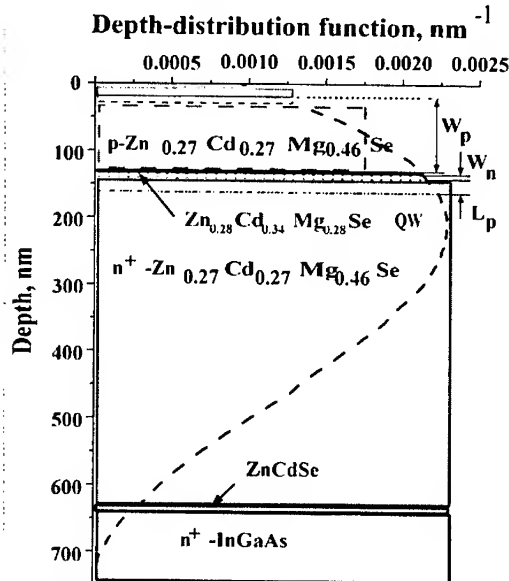


Figure 6. Depth-distribution function for ZnCdMgSe QW LED structure for 10kV electrons.

I_b is the electron beam current, and q is the electronic charge. G is the number of electron-hole pairs generated per incident electron of energy E_b ,

$$G = \frac{E_b \times (1 - \gamma)}{E_i}, \quad (3)$$

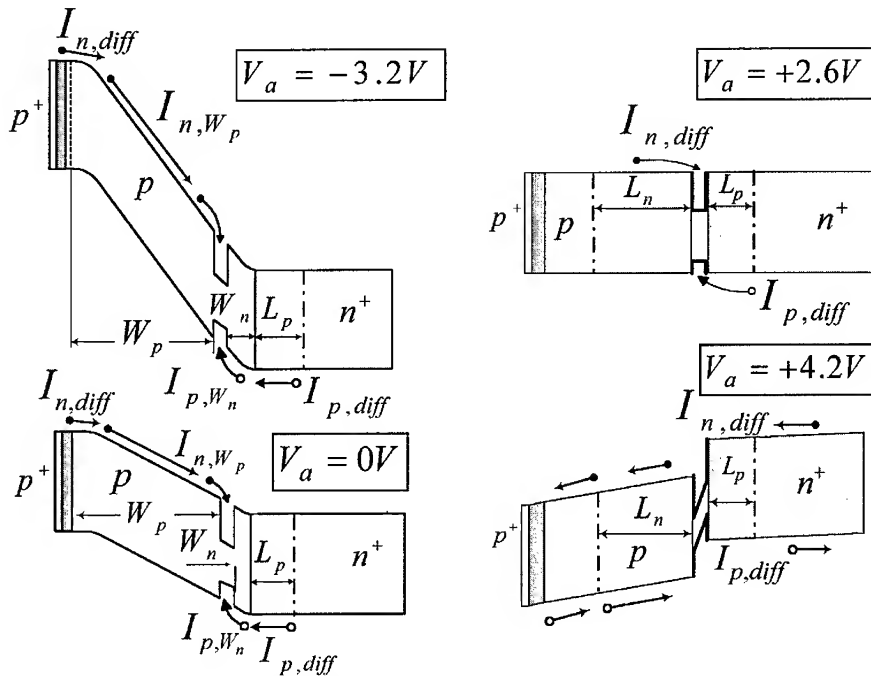


Figure 7. Illustration of electric-field-induced band bending in QW LED structure.

where γ is the fraction of electron beam energy loss due to backscattered electrons and E_i is the energy to form an electron-hole pair. Calculations of depth-distribution function (figure 6) and of minority carrier currents with and without bias were performed using structural and electrical parameters shown in figure 1. For regions W_p , W_n , L_p and L_n , the depth-distribution function was assumed to have its averaged value within each layer, as illustrated for the W_p region in figure 6. The bias dependence of drift currents enters through bias dependence of depletion widths, $W_{p,n}$, and of band bending, as shown schematically in figure 7.

Results of these calculations for bias voltages $V_a \leq 2.6V$, presented in figure 8, show that the electron current due to excess electrons excited by electron bombardment in the p -cladding layer and entering the QW is much larger than the hole current into the QW resulting from excess holes in the n -cladding layer excited by electron irradiation. This indicates that the resulting CL is a hole-limited process and should be proportional to the hole current. The calculations also indicate that luminescence should increase with reverse bias and decrease with forward bias. However, the luminescence intensity was experimentally observed to decrease with application of either forward or reverse bias (figures 3 and 4).

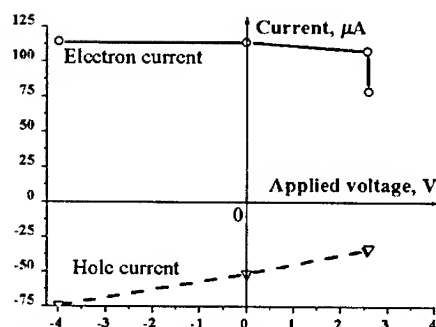


Figure 8. Minority carrier currents into the ZnCdMgSe QW.

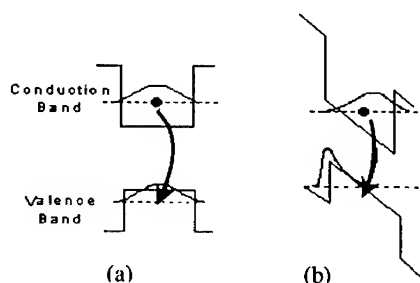


Figure 9. Expected effect of electric field on QW energy levels and wavefunctions, (a) zero field, (b) with applied field.

CONCLUSIONS

The present model does not explain many experimental observations, because it does not include forward bias levels beyond flat-band condition ($V_a \geq 2.6\text{V}$), and because it neglects effects of bias on carrier escape and redistribution in the QW (figure 9) [10]. The latter may be largely responsible for the reverse and forward bias QW CL intensity decrease and the forward bias QW CL redshift. Further CL experiments for intermediate biases, including flat-band condition, are needed to address these questions. To explain time-dependent QW CL intensity decreases and role of bias in degradation, the generation and transport of atomic scale defects must also be included in the model.

ACKNOWLEDGMENTS

Parts of this work have been supported by NSF grant DMR-9796285.

REFERENCES

1. S. Itoh, K. Nakano, and A. Ishibashi, *J. Cryst. Growth* **214/215**, 1029 (2000).
2. A. Ishibashi, *IEEE J. Select. Topics Quant. Electron.* **1**, 741 (1995).
3. M. C. Tamargo, W. Lin, S. P. Guo, Y. Guo, Y. Luo, Y. C. Chen, *J. Cryst. Growth* **214/215**, 1058 (2000).
4. M. C. Tamargo, S. P. Guo, O. Maksimov, Y. C. Chen, F. Peiris, and J. K. Furdyna, *J. Cryst. Growth* **227/228**, 710 (2001).
5. S. P. Guo, L. Zeng, and M. C. Tamargo, *Appl. Phys. Lett.* **78**, 1957 (2001).
6. W. Faschinger and J. Nurnberger, *Appl. Phys. Lett.* **77**, 187 (2000).
7. D. Albert, J. Nurnberger, V. Hock, M. Ehinger, W. Faschinger, and G. Landwehr, *Appl. Phys. Lett.* **74**, 1957 (1999).
8. S. Gundel, D. Albert, J. Nurnberger, and W. Faschinger, *Phys. Rev. B* **60**, R16271 (1999); *J. Cryst. Growth* **214/215**, 474 (2000).
9. G. Yacobi and D. B. Holt, *Cathodoluminescence Microscopy of Inorganic Solids* (Plenum, 1990).
10. G. Bastard, *Wave Mechanics Applied to Semiconductor Heterostructures* (Les Editions de Physique, Les Ulis, 1988).

Gas Source MBE Growth and Characterization of TlInGaAs/InP DH Structures for Temperature-independent Wavelength LD Application

Hajime Asahi, Hwe-Jae Lee, Akiko Mizobata, Kenta Konishi, Osamu Maeda and Kumiko Asami
The Institute of Scientific and Industrial Research, Osaka University
8-1, Mihogaoka, Ibaraki, Osaka 567-0047, Japan

ABSTRACT

TlInGaAs/InP double-hetero (DH) structures were grown on (100) InP substrates by gas source MBE. The photoluminescence (PL) peak energy variation with temperature decreased with increasing Tl composition. For the DH with a Tl composition of 13%, the PL peak energy varied only slightly with temperature (-0.03 meV/K). This value corresponds to a wavelength variation of 0.04 nm/K and is much smaller than that of the lasing wavelength of InGaAsP/InP distributed feedback laser diodes (0.1 nm/K). TlInGaAs/InP light emitting diodes with 6% Tl composition were fabricated and the small temperature variation of the electroluminescence peak energy (-0.09 meV/K) was observed at the wavelength around 1.58 μm . The results are promising to realize the temperature-independent wavelength laser diodes, which are important in the wavelength division multiplexing (WDM) optical fiber communication systems.

INTRODUCTION

Wavelength division multiplexing (WDM) technology is very important for optical fiber communication systems to drastically increase transport capacity. However, one of the problems encountered when using InGaAsP/InP laser diodes (LDs) in WDM systems is that the lasing wavelength fluctuates with ambient temperature variation mainly due to the temperature dependence of the bandgap energy. Therefore, LDs in WDM systems are equipped with Peltier elements to stabilize LD temperature. To solve this problem, the use of temperature-independent bandgap semiconductors as an active layer of LDs was proposed [1].

We have proposed III-V quaternary semiconductors, TlInGaP (Thallium Indium Gallium Phosphide) [2, 3] and TlInGaAs (Thallium Indium Gallium Arsenide) [3] as shown in figure 1. TlInGaP and TlInGaAs can be lattice-matched to InP, and cover the bandgap energies corresponding to the 1 μm wavelength range. Furthermore, we pointed out that TlInGaP and TlInGaAs are expected to show the temperature-independent bandgap energy at certain compositions because it is an alloy of semiconductor, InGaP or InGaAs, and semimetal, TIP or TIAs, similar to HgCdTe. CdTe is a semiconductor and HgTe is a semimetal. Temperature-independent bandgap energy was observed for HgCdTe at a Hg composition of 0.48 [4]. Therefore, the LDs fabricated using TlInGaP or TlInGaAs have the potential to operate without changing wavelength irrespective of

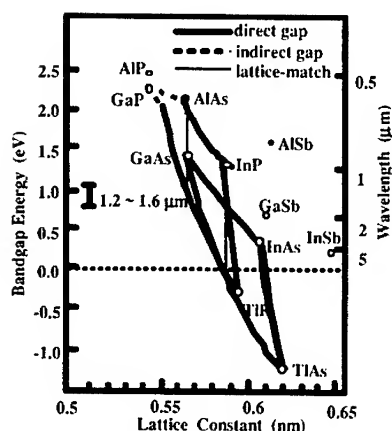


Figure 1. Bandgap energy vs. lattice constant relationship for TlInGaP and TlInGaAs .

ambient temperature variation [2, 3].

We have successfully grown TlInP , TlGaP , TlInGaP , TlInAs and TlInGaAs by gas source molecular-beam epitaxy (MBE) [2, 5-7]. In this paper, the growth of TlInGaAs/InP double-hetero (DH) structures and the observation of very small temperature variation of photoluminescence (PL) peak energy are reported. The results on the electroluminescence (EL) properties for the TlInGaAs/InP light emitting diodes (LEDs) are also described.

GAS SOURCE MBE GROWTH

TlInGaAs/InP DH structures were grown by gas source MBE. Elemental Tl (5N), In (7N) and Ga (7N) and thermally cracked AsH_3 and PH_3 were used as group III and group V sources, respectively. The substrates used were (100) InP. The substrate temperature during growth was 450 °C. Our detailed studies showed that the growth condition for alloys containing Tl is very strict. For example, growth below 400 °C resulted in segregation of Tl, and growth above 460 °C failed to incorporate Tl due to desorption of Tl atoms from the surface. During growth of InP, the reflection high-energy electron diffraction (RHEED) pattern showed (2x4) reconstruction. However, during growth of TlInGaAs the RHEED pattern showed (2x2) reconstruction.

Tl composition was estimated from the double crystal X-ray diffraction data on the TlInGaAs and InGaAs grown with the same In and Ga fluxes assuming Vegard's law and that the lattice constant of TIAs (exact value is not known) is equal to that of InAs. Concerning the lattice constant, Kajikawa *et al.* [8] recently claimed that the lattice constant of TIAs is smaller than that of InAs, though the theoretical calculation by van Schilfgaade *et al.* [9] showed the opposite result. The incorporation of Tl was confirmed

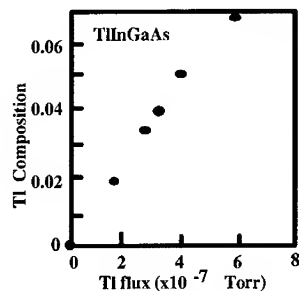


Figure 2. Dependence of Tl composition in TlInGaAs on Tl flux during growth.

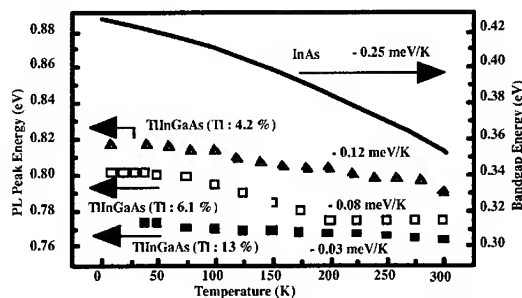


Figure 3. Temperature variation of the PL peak energy for the TlInGaAs/InP DH samples as a function of Tl composition.

with the electron probe micro-analysis (EPMA) measurement. The accuracy of the Tl concentration by EPMA was not sufficient under our experimental condition, but we measured several % to around 10% of Tl. We also observed the decrease in the RHEED intensity oscillation period during growth of TlInGaAs by the addition of Tl flux, which also indicates the incorporation of Tl into InGaAs. The Tl composition in TlInGaAs was observed to increase with the Tl flux during growth as shown in figure 2.

During the growth of TlInGaAs under our growth conditions, we think that the large part of incident Tl atoms is re-evaporating from the surface and only a small part of them is incorporating into films, very similar to the case of MBE growth of GaN under usual growth conditions. Therefore, a relatively large flux for Tl was supplied in our growth.

PL PROPERTIES

PL measurements were conducted in the temperature range from 10 K to 300 K using an Ar ion laser at 488 nm line as the excitation source. With increasing Tl composition, the PL peak energy was shifted toward lower energy [10].

The PL peak energy of the TlInGaAs/InP DH samples varied only slightly with temperature as shown in figure 3. As the Tl composition increased, the temperature variation of the peak energy decreased. For all the DH samples, the temperature variation of the peak energy was much smaller than that of InAs. It is noteworthy that the bandgap energy (~ 0.8 eV) of TlInGaAs is larger than that of InAs (0.356 eV). In general, the wider bandgap a material has, the larger variation of bandgap energy with temperature. The TlInGaAs/InP DH sample with a Tl composition of 13 % showed very small temperature variation of as small as -0.03 meV/K, which corresponds to the wavelength variation of 0.04 nm/K. This value is much smaller than those of lasing wavelengths for the InGaAsP/InP Fabry Perot LDs (0.04 nm/K) as well as the InGaAsP/InP DFB LDs (0.1 nm/K). The InGaAsP/InP DFB LDs are presently used in the optical fiber communication systems. With further increase of Tl composition, we can expect real temperature-independent bandgap energy or positive temperature-dependence.

EL PROPERTIES

TlInGaAs/InP DH LED samples were composed of (i) a Si-doped n-type InP cladding layer ($n=1 \times 10^{18} \text{ cm}^{-3}$), (ii) an undoped TlInGaAs active layer, (iii) a Be-doped p-type InP cladding layer ($p=1 \times 10^{18} \text{ cm}^{-3}$) and (vi) a Be-doped p-type InGaAs contact layer ($p=1 \times 10^{18} \text{ cm}^{-3}$). Tl composition was 6%. Two types of LEDs were fabricated; one is surface emitting LEDs and the other is edge emitting LEDs. The former has $100 \mu\text{m}$ -diameter circular p-type electrode on the p-type InGaAs contact layer and the EL light output was detected from the top surface. The latter has $70 \mu\text{m}$ -wide and $300 \mu\text{m}$ -length stripe p-type electrode and the light output was detected from the cleaved-edge surface.

Figure 4 shows the temperature variation of EL peak energies for both types of LEDs. Small temperature variation was observed; -0.09 meV/K and -0.088 meV/K. These values

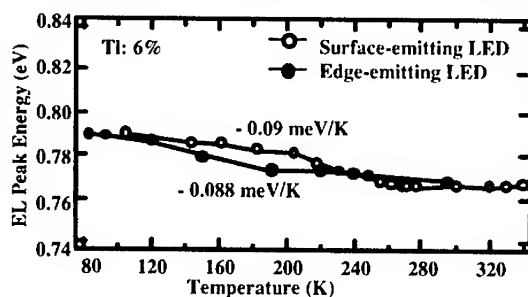


Figure 4. Temperature variation of the EL peak energies for (a) surface-emitting and (b) edge-emitting TlInGaAs/InP DH LEDs.

are the same as that of the PL peak energy for the DH sample with 6% Tl composition (figure 3). The results indicate that the small temperature variation characteristic was

confirmed also on the device level. Therefore, the TlInGaAs/InP heterostructures are promising to realize the temperature-independent wavelength LDs, which are important in the WDM optical fiber communication systems.

SUMMARY

In summary, we have grown TlInGaAs/InP DH samples on (100) InP substrates by gas source MBE. It was confirmed that the temperature variation of the PL peak energy for the TlInGaAs/InP DH sample decreased with increasing Tl composition. The PL peak energy of the 13% Tl DH sample varied only slightly with temperature (-0.03 meV/K). This value corresponds to a wavelength variation of 0.04 nm/K and is much smaller than that of the lasing wavelength of InGaAsP/InP DFB LDs (0.1 nm/K). The TlInGaAs/InP DH LEDs were also fabricated and the similar small temperature variation of the EL peak energy was observed.

ACKNOWLEDGEMENTS

This work was supported in part by the "Research for the Future" program of the Japan Society for the Promotion of Science, the Scientific Research Grant-in Aid and the Grant-in Aid for the COE from the Ministry of Education, Science, Sports and Culture of Japan.

REFERENCES

1. K. Oe and H. Asai, IEICE Trans. Electron., **E79-C**, 1751 (1996).
2. H. Asahi, K. Yamamoto, K. Iwata, S. Gonda and K. Oe, Jpn. J. Appl. Phys. **35**, L876 (1996).
3. H. Asahi, Compound Semicond. **2**, 34 (1996).
4. W.S. Pelouch and L.A. Schlie, Appl. Phys. Lett. **68**, 1389 (1996).
5. M. Fushida, H. Asahi, K. Yamamoto, H. Koh, K. Asami, S. Gonda and K.Oe, Jpn. J. Appl. Phys. **36**, L665 (1997).
6. H. Koh, H. Asahi, M. Fushida, K. Yamamoto, K. Asami, S. Gonda and K.Oe, J. Crystal Growth **188**, 107 (1998).
7. K. Takenaka, H. Asahi, H. Koh, K. Asami, S. Gonda and K. Oe, Jpn. J. Appl. Phys. **38**, 1026 (1999).
8. Y. Kajikawa, S. Asahina, and N. Kanayama, Jpn. J. Appl. Phys., Part 1, **40**, 28 (2001).
9. M. van Schilfgaarde, A.B. Chen, S. Krishnamurthy and A. Sher, Appl. Phys. Lett. **65**, 2714 (1994).
10. A. Ayabe, H. Asahi, H.-J. Lee, O. Maeda, K. Konishi, K. Asami, and S. Gonda, Appl. Phys. Lett. **77**, 2148 (2000).

Effect of Zn atom diffusion in the active layer of InGaAlP visible-LED investigated by the Piezoelectric Photothermal Spectroscopy

Ryuji Ohno, Yoshihito Taiji, Shoichiro Sato, Atsuhiko Fukuyama*, Shigeru Shigetomi** and, Tetsuo Ikari

Department of Electrical and Electronic Engineering, Miyazaki University, 1-1 Gakuen Kibanadai-nishi, Miyazaki 889-2192, Japan

*Department of Applied Physics, Miyazaki University, 1-1 Gakuen Kibanadai-nishi, Miyazaki 889-2192, Japan

**Department of Physics, Kurume University, 67 Asahiyasu, Kurume, Fukuoka 830-0011, Japan

ABSTRACT

It has been reported that Zn atoms diffused from the Zn-doped p-InAlP cladding to the active layer in InGaAlP visible-light-emitting diodes cause a degradation of light output efficiency. A doping effect of the Zn atoms was then investigated using a Piezoelectric Photothermal Spectroscopy from a nonradiative transition point of view. The results indicate that the Zn-doping unexpectedly induces a decrease of the nonradiative component of the electron transitions above the band gap of the active layer. The experimental results are explained by considering that Zn doping cause the increase of both shallow and deep acceptor levels at the same time with the different rate for generation.

INTRODUCTION

Recently, high-brightness operation from the orange to green region have been obtained for the InGaAlP LEDs using InAlP cladding layers and distributed Bragg reflectors (DBRs) grown by metal organic chemical-vapor deposition (MOCVD) method [1]. But one of the problems in the InGaAlP LEDs is a degradation of light output power, which may be caused by the presence of Zn atoms diffused from Zn-doped InAlP cladding layer during the device manufacturing processes. Since a lifetime of the injected carriers in the active layer decreased with increasing Zn concentrations, the diffused Zn was considered to create a not only shallow acceptor but also deep defect levels at the same time in the InGaAlP active layer [2]. However, details have not been clear yet.

For the semiconductors which have such deep levels, nonradiative processes may play an important role for the electron transition mechanisms. However, Photoluminescence methods can't detect such nonradiative transitions. The great advantage of the Piezoelectric Photothermal Spectroscopy (PPTS) is that it is a direct monitor of the nonradiative recombination processes of photoexcited electrons. Therefore, it is useful to clarify the effect of diffused Zn atoms in InGaAlP active layer from the nonradiative transition point of view. We have already reported [3, 4] that the nonradiative transition in semi-insulating bulk GaAs and in AlGaAs/GaAs heterostructure sample could be clearly understood by this technique. In this paper, we propose here a model for an effect of Zn doping and for an electron transition mechanism through the nonradiative pathways to explain our results. The effect of DBRs is

also taken into account. We conclude that deep defect level generated by the Zn atoms diffusion play an important role for the degradation of the LEDs.

EXPERIMENT

Two InGaAlP LEDs which have Zn-doped or not intentionally doped InGaAlP active layer were prepared to clarify an effect of Zn-doping. Figure 1 shows a schematic diagram of the present $\text{In}_{0.5}(\text{Ga}_{0.72}\text{Al}_{0.28})_{0.5}\text{P}$ LEDs samples. The $\text{In}_{0.5}(\text{Ga}_{0.72}\text{Al}_{0.28})_{0.5}\text{P}$ (hereafter, refer to InGaAlP) active, $\text{In}_{0.5}\text{Al}_{0.5}\text{P}$ (refer to InAlP) cladding and, DBRs layers were grown by MOCVD on (100) n-GaAs substrate tilted 15° off toward [011]. A DBR consisting of a pair of n-InAlP and n-GaAs is an important component to avoid a reduction of light extraction efficiency due to the light absorption in the GaAs substrate.

For the PPTS measurements, the piezoelectric transducer (PZT) was attached to the GaAs substrate side of the sample using a silver conduction paste. The probing light from a grating monochromator was mechanically chopped and focused on the epitaxial layers side. Details of the experimental procedures were reported previously [5].

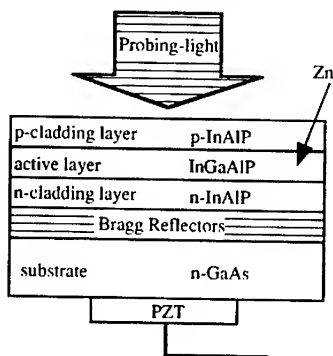


Figure 1. Schematic diagram of InGaAlP LEDs samples. For the PPTS measurements, the piezoelectric transducer (PZT) was attached to the GaAs substrate side of the sample using a silver conducting paste. The probing-light from a grating monochromator was mechanically chopped and focused on the epitaxial layers side.

RESULTS AND DISCUSSION

The PPT spectra of non- and Zn-doped InGaAlP LEDs at 297K are shown in Figure 2. For the non-doped sample, the PPT signal peaks that reflect well the optical properties of the n-GaAs substrate are observed below 1.4eV, which corresponds to the direct bandgap energy (E_g) of GaAs of 1.43eV at 297K. In the higher energy region, the PPT signals show a rapid increase and a subsequent decrease about 2.1eV and 2.6eV, respectively. These photon energies correspond to E_g of InGaAlP (2.07eV) and of InAlP (2.5eV) at 297K, respectively [6]. Therefore, it can be considered that the PPT signals ranging from 2.1eV to 2.6eV are due to the

nonradiative transition in the InGaAlP active layers. We hereafter refer this band to B-band. Figure 2 also shows the effect of Zn-doping in InGaAlP active layers. The PPT signal intensity of the Zn-doped sample decreases about 12 times smaller than that of non-doped one. If Zn-related levels induced by a doping act as a nonradiative recombination center, the PPT signal intensity should increase. This is not the case for the present result.

Additional fine structure is observed in the photon energy region between 1.5 and 2.0eV, below the band-gap of InGaAlP active layer. These are shown in Figure 3 with expanded vertical scale. We consider this signal results from DBRs. The calculated results for the reflectivity due to the presence of DBRs are shown in Fig.3 by open circles. The experimental results for Zn-doped sample were also shown in the figure. All of the photon energy positions for observed humps and dips are well corresponded to the calculated results. The same result is observed for non-doped sample. However, the PPT signal intensity of the Zn-doped sample is larger than that of non-doped one in this photon energy region. The doping effect of the PPT signal intensity is reversed below and above 2.1eV.

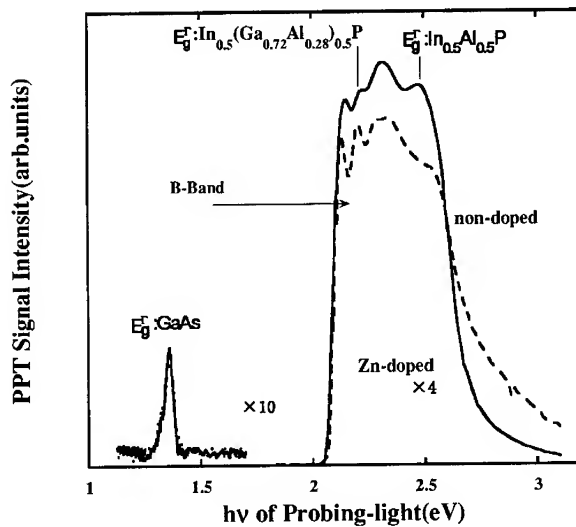


Figure 2. PPT amplitude spectra of $\text{In}_{0.5}(\text{Ga}_{0.72}\text{Al}_{0.28})_{0.5}\text{P}$ at 297K. The solid and broken curve is non-doped and Zn-doped sample, respectively.

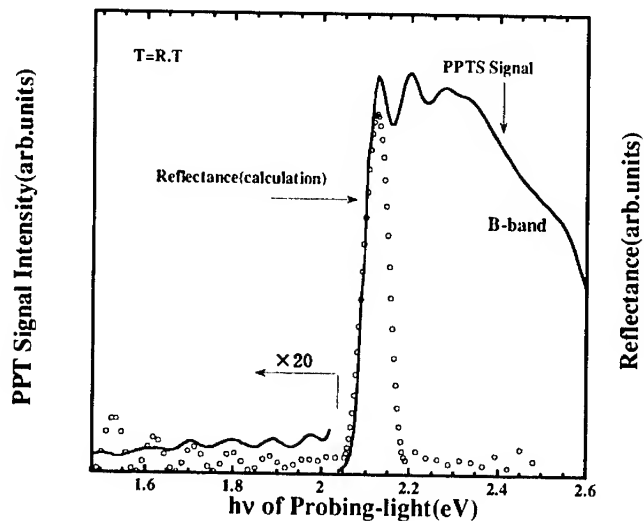


Figure 3. PPT amplitude spectra of Zn-doped sample and calculation of reflectance in DBRs at 297K. The solid curve and the open circle are experiment of Zn-doped sample and calculation of reflectance in DBRs, respectively. There is good agreement between experiment and calculation.

We, here, propose a carrier recombination model in the active layer for explaining why the PPT signal intensity of B-band decreases by doping. Supposing that the introduced Zn atom occupy the substitutional site in the active layer, it is reasonable to consider that the Zn atoms act as shallow acceptor levels even when the Zn atom resides at Ga or As site. We first propose that the transition of photo-excited electrons from conduction band to such shallow acceptor level generates the heat by the nonradiative process and cause the PPT signal. Since the Zn doping increases the concentration of those acceptor level, the PPT signal should increase with doping. However, this is not the case.

Then we consider next that the Zn atoms occupy the substitutional and the interstitial sites in the active layer. In this case, the Zn atoms form the shallow acceptor and the deep level, respectively, at the same time. The schematic model is shown in Figure 4. Transition (1) means excitation of electrons from valence to conduction band, transition (2) means radiative transition from conduction to valence band, transition (3) means radiative transition from conduction band to shallow acceptor level, transition (4) means nonradiative transition from conduction band to deep level and this cause the PPT signal. When the sample was doped with Zn atoms, the number of both shallow and deep acceptor levels increases. However, we further assume here that the increasing rate for the deeper acceptor level is small compared with that of shallow level. This is because that the Zn atom can easily reside at substitutional rather than at interstitial site. According to the present model, the number of photoexcited electrons that can recombine with

the deep level and cause the PPT signal decreases with Zn doping. Most of the photoexcited carriers may recombine with shallow acceptor through the radiative transition and the number of the electrons that can recombine with deep level decreases. This results in the decrease of the PPT signal by doping.

Photoluminescence (PL) measurements for the same sample have already been carried out [2]. Since PL lifetime, determined from a time resolved PL technique, decreased by doping of Zn, they considered that introduced Zn atom from p-type clad to the active layer formed deep defect levels and caused the degradation for the luminescence. However, our model has assumed that the increasing rate for the deeper acceptor level was small than that of the shallow acceptor level. Detailed discussion for clarifying this inconsistency is now carrying on.

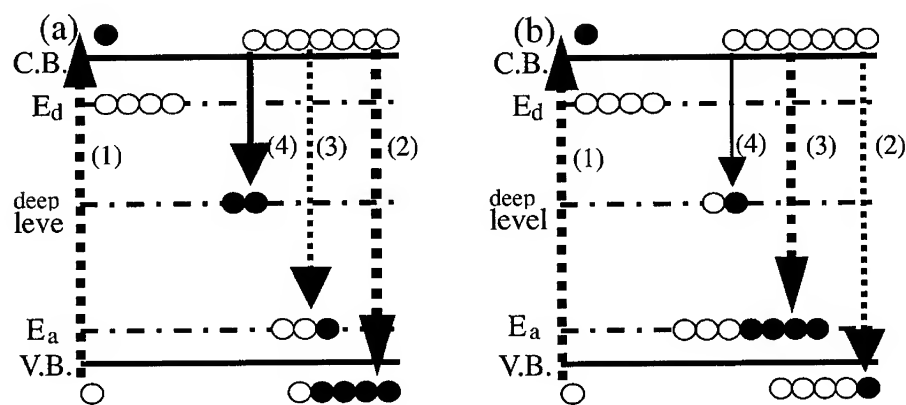


Figure 4. Schematic model of before Zn dope (a) and after Zn dope (b) in the active layer.

CONCLUSION

The PPTS measurements of InGaAlP LED with non- and Zn-doped active layers were carried out to investigate an effect of Zn-doping to the active layer. The results imply that the Zn atom doping creates not only a shallow acceptor but also deep defect levels at the same time in the InGaAlP active layer. The decrease of the PPT signal intensity with Zn doping for B band was explained by supposing that the shallow level was easily formed than the deep levels. However, the present model cannot reach the conclusion that the light emission efficiency of the present LEDs decreases with Zn doping. More detailed experiments should be carried out for further discussions.

ACKNOWLEDGMENT

The authors acknowledge Toshiba Co., Ltd. For supplying high-quality InGaAlP-LEDs.

REFERENCES

1. H. Sugawara, K. Itaya and H. Nagai, J. Appl. Phys. 74 (1982) 4928.
2. S. Washizuka and Y. Akaike, Proc. of 195th state of The Art Program on Compound Semiconductors, Seattle, 1999, p. 210.
3. A. Fukuyama, Y. Morooka, Y. Akashi, K. Yoshino, K. Maeda and T. Ikari, J. Appl. Phys. 81 (1997) 7567.
4. A. Fukuyama, H. Fukuhara, Y. Akashi, K. Yoshino, K. Maeda and T. Ikari, 1998 IEEE Ultrasonics Symp. Proc. (1998) 1235.
5. T. Ikari, K. Miyazaki, A. Fukuyama, H. Yokoyama, K. Maeda and K. Futagami, J. Appl. Phys. 71 (1992) 2408.
6. H. Asahi, Y. Kawamura and H. Nagai, J. Appl. Phys. 53 (1992) 4928.

Strategies For Direct Monolithic Integration of $\text{Al}_x\text{Ga}_{(1-x)}\text{As}/\text{In}_x\text{Ga}_{(1-x)}\text{As}$ LEDS and Lasers On Ge/GeSi/Si Substrates Via Relaxed Graded $\text{Ge}_x\text{Si}_{(1-x)}$ Buffer Layers

Michael E. Groenert, Christopher W. Leitz, Arthur J. Pitera, Vicky K. Yang, Harry Lee*, Rajeev J. Ram*, and Eugene A. Fitzgerald

Department of Materials Science and Engineering, MIT, Cambridge, MA 02139, U.S.A.

*Department of Electrical Engineering and Computer Science, MIT, Cambridge, MA 02139, U.S.A.

ABSTRACT

$\text{Al}_x\text{Ga}_{(1-x)}\text{As}/\text{GaAs}$ quantum well lasers have been demonstrated via organometallic chemical vapor deposition (OMCVD) on relaxed graded $\text{Ge}/\text{Ge}_x\text{Si}_{(1-x)}$ virtual substrates on Si. Despite un-optimized laser structures with high series resistance and large threshold current densities, surface threading dislocation densities as low as $2 \times 10^6 \text{ cm}^{-2}$ enabled cw room-temperature lasing at a wavelength of 858nm. The laser structures are oxide-stripe gain-guided devices with differential quantum efficiencies of 0.16 and threshold current densities of 1550 A/cm^2 . Identical devices grown on commercial GaAs substrates showed differential quantum efficiencies of 0.14 and threshold current densities of 1700 A/cm^2 . This comparative data agrees with our previous measurements of near-bulk minority carrier lifetimes in GaAs grown on Ge/GeSi/Si substrates. A number of GaAs/Ge/Si integration issues including thermal expansion mismatch and Ge autodoping behavior in GaAs were overcome.

INTRODUCTION

Semiconductor lasers remain a primary goal for GaAs on Si integration due to their proven usefulness in a wide variety of optoelectronic applications, but they also remain the most difficult devices to demonstrate successfully. As high-power minority carrier devices, semiconductor lasers are very sensitive to epitaxial material quality and crystal defect density. Early attempts to grow reliable GaAs lasers directly on Si using a wide variety of epitaxial techniques were unsuccessful [1]. The 4.1% lattice mismatch between GaAs and Si leads to unacceptably high densities of threading dislocation defects ($> 10^8 \text{ cm}^{-2}$) in the active regions of lasers grown directly on Si, resulting in very short device lifetimes. More recently, alternative techniques involving wafer bonding [2], epitaxial lateral overgrowth [3] and migration-enhanced epitaxy [4] were investigated for integration applications. While bonding in particular has attracted much interest, this technique is inherently cost-limited as device density increases, and faces continued difficulties with contact resistance at the bond interface.

Continuing work in our group has demonstrated an alternative approach to successful monolithic GaAs on Si integration making use of relaxed graded Ge/GeSi buffer layers [5]. Ting [6] has demonstrated high-quality diode structures on Ge/GeSi buffers on Si and has shown how past difficulties with anti-phase boundary (APB) formation at the GaAs/Ge interface can be avoided with high-temperature initiation on deliberately offset substrates. Surface threading dislocation densities in these samples have been measured at $2 \times 10^6 \text{ cm}^{-2}$ using defect selective etching and plan-view transmission electron microscopy (TEM). Minority carrier lifetime measurements for GaAs films grown on GeSi/Ge buffers [7] have shown lifetimes comparable to

bulk GaAs, indicating that the mean dislocation spacing has approached the minority carrier diffusion length in this optimized material.

The thermal expansion coefficient of Si is significantly smaller than GaAs. Consequently, growth of GaAs on Si substrates by high-temperature CVD leads to trapped tensile strain in GaAs device layers on Ge/GeSi/Si. Efforts have been taken to reduce this tensile strain by introducing deliberate compressive strain in the Ge/GeSi buffer layers [5]. This compressive strain yields cubic Ge layers on Si after cooldown at room temperature, but at the cost of increased compressive strain and imperfect GaAs/Ge lattice matching at the growth temperature. Compressive strain in the Ge buffer will limit the critical thickness for strained $\text{In}_x\text{Ga}_{(1-x)}\text{As}$ quantum wells in GaAs grown above it.

GaAs grown on Ge can introduce complications for device integration due to autodoping effects from amphoteric Ge moving into the GaAs above it. This Ge can act to compensate intentional dopants in GaAs device layers and increase free-carrier absorption in laser active regions. Work by Srinivasan [8] and others [9],[10] has shown that autodoping can occur via transport in the vapor phase during film growth, and that this gas-phase reaction depends strongly on reactor pressure and on the temperature and time of pregrowth annealing.

In the present study, GaAs/AlGaAs/InGaAs laser structures were grown on relaxed graded Ge/GeSi graded buffers on Si substrates and compared to identical lasers on commercial GaAs substrates. The initial structures and growth recipes were then modified to account for thermal expansion effects and Ge autodoping in the devices grown on Ge/GeSi/Si.

EXPERIMENTAL DETAILS

All laser structures were grown in an atmospheric organometallic chemical vapor deposition (OMCVD) reactor operating at 750 °C. Commercial (100) n+ GaAs substrates offcut 2° towards [110] were used as controls. For growth on Si, relaxed Ge on graded $\text{Ge}_x\text{Si}_{(1-x)}$ buffers on (100) Si offcut 6° towards the [110] were used. The details of the Ge/GeSi buffer growth process and its optimization for GaAs growth has been reported elsewhere [5].

The laser structures grown for these experiments were AlGaAs/GaAs/InGaAs graded index separate confinement heterostructure (GRINSCH) quantum-well devices. The structure is shown in Figure 1. The growths began with a 500nm GaAs buffer ($n = 6 \times 10^{18} \text{ cm}^{-3}$) followed by a 1.1 μm $\text{Al}_{0.6}\text{Ga}_{0.4}\text{As}$ cladding layer ($n = 4 \times 10^{18} \text{ cm}^{-3}$). After this a symmetric graded $\text{Al}_x\text{Ga}_{(1-x)}\text{As}$ structure ($x = 0.6$ to 0.2) centered around an 8 nm $\text{In}_{0.2}\text{Ga}_{0.8}\text{As}$ quantum well was

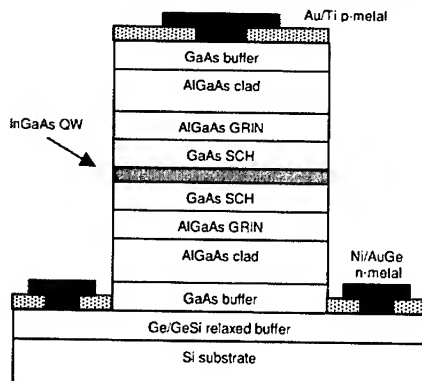


Figure 1: Schematic of laser structure used for this experiment. Devices with 10nm GaAs QWs and $\text{Al}_{0.2}\text{Ga}_{0.8}\text{As}$ SCHs were also grown to avoid misfit dislocations in the quantum wells.

grown without doping. This structure was capped with another 1.1 μm $\text{Al}_{0.6}\text{Ga}_{0.4}\text{As}$ cladding layer ($p = 2 \times 10^{17} \text{ cm}^{-3}$) and a highly doped 50nm GaAs contact layer ($p = 1 \times 10^{19} \text{ cm}^{-3}$). Film thicknesses were confirmed with TEM, and dopant concentrations were measured using secondary ion mass spectroscopy (SIMS).

Oxide-stripe gain-guided devices were fabricated from these structures with 5 μm stripe-widths. To reduce series resistance through the substrate, n-side contact stripes were etched through the GaAs layers to the Ge buffer layer, defining wide (100 μm) ridge waveguides. Devices were then thinned and cleaved into bars of varying lengths.

RESULTS AND DISCUSSION

$\text{In}_{0.2}\text{Ga}_{0.8}\text{As}$ quantum well lasers grown on GaAs substrates operated cw at room temperature and demonstrated a threshold current density of 1370 A/cm^2 and a differential quantum efficiency of 0.30 at a wavelength of 1005 nm. Identical devices grown on Ge/GeSi/Si substrates did not lase and showed a subthreshold differential quantum efficiency of 7.1×10^{-6} . Cross-sectional TEM of similar devices on Ge/GeSi/Si substrates showed misfit dislocations in the quantum well, indicating that the critical thickness for $\text{In}_{0.2}\text{Ga}_{0.8}\text{As}$ in these samples was less than 8 nm. As mentioned above, the reduced critical thickness for compressive InGaAs on a Ge/GeSi/Si substrate is likely due to the increased compressive strain in the Ge/GeSi buffer layer at the growth temperature.

SIMS scans of similar structures on Ge/GeSi/Si substrates in Figure 2a show uniform Ge contamination in all layers of the GaAs device at concentrations of $1 \times 10^{18} \text{ cm}^{-3}$ or higher. The flat Ge doping profile throughout the device structure with a small peak in the low-growth-rate quantum well region confirms the dominance of vapor-phase transport from external sources over other autodoping mechanisms such as solid-state diffusion, which would be expected to show a decreasing Ge concentration with device thickness. The high pressures and temperatures present in the OMCVD growth chamber, coupled with a 5-minute pregrowth anneal step at 700 $^{\circ}\text{C}$ provided ample opportunity for Ge substrate evolution into the vapor phase and subsequent deposition in the GaAs/AlGaAs/InGaAs device layers.

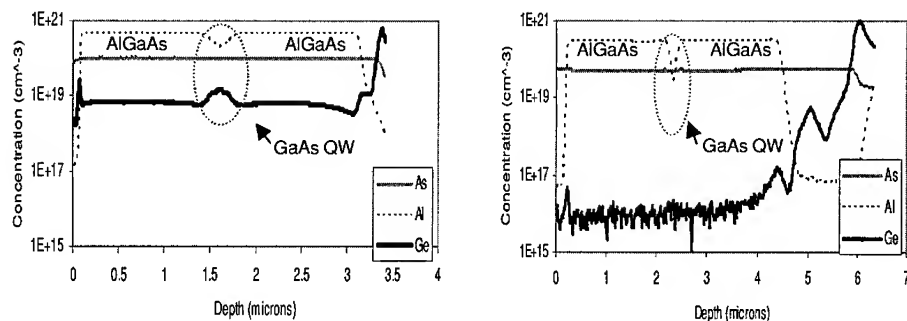


Figure 2: SIMS data showing (a.) Ge contamination in device layers and (b.) reduced contamination with the improved recipe to remove Ge vapor sources in the reactor

To avoid the difficulties with compressive strain introduced by the Ge/GeSi buffer layers, identical laser structures were grown substituting a 10nm GaAs quantum well for the 8nm InGaAs quantum well. The GaAs quantum well removes the problem of strain-induced misfit dislocations in the quantum well at the cost of reduced electrical and optical confinement and less resistance to dark-line defects [11].

To reduce the high Ge autodoping in the device layers, a series of experiments was run to pinpoint the chief sources of Ge in the growth sequence. Four steps were taken to remove potential sources for gas-phase Ge evolution: 1.) cleaning the reactor tube, 2.) changing the graphite susceptor the sample rests on during growth, 3.) capping the front Ge/GeSi surface with GaAs, and 4.) polishing the wafer backside to remove Ge underneath the device. Reducing the reactor pressure or growth temperature may reduce autodoping; but this is not possible with the available CVD reactor and our optimized APB-free GaAs on Ge nucleation recipe.

SIMS scans showed reduced Ge contamination in the GaAs device layers for the four steps mentioned above. The largest reduction came with a combination of all four techniques which then became the growth recipe used for all further GaAs growths on Ge/GeSi/Si substrates. The final recipe for controlling Ge autodoping in GaAs was to grow a thin (200nm) GaAs cap layer on the Ge/GeSi/Si substrate, remove the substrate, polish the backside mechanically to remove about 10 μm of the wafer and all Ge at this interface, then reinsert the capped and polished substrate into a cleaned reactor tube with a new graphite susceptor. Although this procedure is complicated, it reduced the Ge autodoping in the GaAs/AlGaAs device layers to undetectable limits ($< 10^{16} \text{ cm}^{-3}$) and yielded high-quality films above the regrowth interface. The SIMS data showing this reduced Ge concentration is shown in Figure 2b.

GaAs/AlGaAs quantum-well GRINSCH laser structures were then grown on Ge/GeSi/Si substrates and tested. These devices operated cw at room temperature, demonstrating a threshold current density of 1550 A/cm^2 and a differential quantum efficiency of 0.16 at a wavelength of 858 nm. Identical devices grown on GaAs substrates showed a threshold current density of 1700 A/cm^2 and a differential quantum efficiency of 0.14. The light vs. current and current vs. voltage data for the devices on Ge/GeSi/Si and GaAs are shown in Figure 3. The temperature sensitivity of both devices was also measured; the laser on Ge/GeSi/Si had a characteristic temperature T_0 of 61 K, while the device on GaAs had a measured T_0 of 128 K. The current-

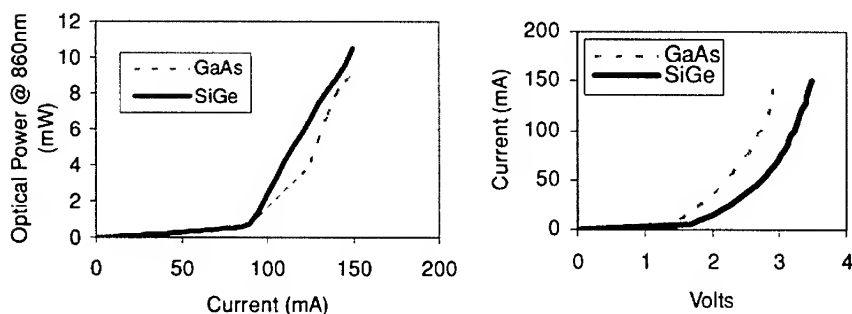


Figure 3: Side-by-side light vs. current (a.) and current vs. voltage (b.) characteristics for identical GaAs/AlGaAs GRINSCH-QW lasers grown on Ge/GeSi/Si and GaAs substrates

voltage characteristics of the device on Ge/GeSi/Si showed higher turn-on voltages and slightly larger series resistance at high current levels than the device on GaAs.

Reliability measurements were made at constant currents for both devices. The lasers on Ge/GeSi/Si showed gradual degradation after only a few minutes, and fell below threshold after a little more than 20 minutes. The device on GaAs showed no obvious degradation. A plot of the measured light intensity vs. time for two sample devices is shown in Figure 4.

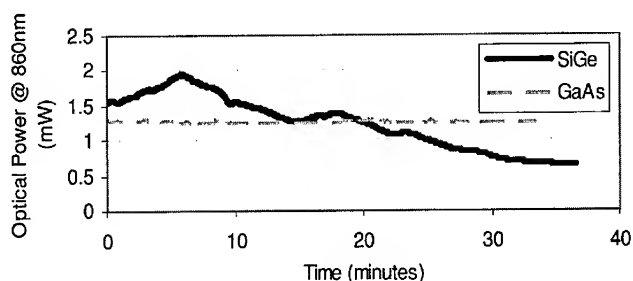


Figure 4: Lifetime measurements at constant current for representative devices on Ge/GeSi/Si and GaAs substrates. The lasing threshold power was 1mW for both devices at 860nm

The higher series resistance and lower characteristic temperature (and thus lower lifetimes) for the laser on Ge/GeSi/Si indicates that this device will require further optimization. Adding $\text{In}_x\text{Ga}_{(1-x)}\text{As}$ to the active region would increase reliability by inhibiting dark-line defect propagation, if indeed that is the responsible degradation mechanism. Care would need to be taken to avoid the thermal expansion mismatch problems encountered previously, perhaps by finding a way to relax compressive strain at the growth temperature below the quantum well interface. Improved contact geometries (to avoid contacting through the double junction at the GaAs/Ge interface) and facet coating may also be useful in reducing turn-on and threshold current densities. Further investigation of the failed devices on Ge/GeSi/Si will help to understand the exact mechanisms responsible for the observed gradual degradation behaviors.

CONCLUSIONS

AlGaAs/GaAs quantum-well lasers have been demonstrated on relaxed Ge/GeSi on Si substrates for the first time. These devices operated cw at room temperature with roughly equivalent operating characteristics to identical devices grown on commercial GaAs substrates. By avoiding super-critical InGaAs quantum wells and taking steps to avoid autodoping effects from the Ge buffer layer, these lasers showed dramatic improvement over earlier devices. Device lifetimes on Ge/GeSi/Si substrates were less than 20 min at room temperature due to a still undetermined failure mechanism. Despite this rapid degradation, measured near-bulk minority carrier lifetimes in GaAs on Ge/GeSi/Si reassure us that no fundamental materials issues stand between these devices and reliable GaAs/AlGaAs/InGaAs laser operation on Si substrates. Further optimization will seek to increase device lifetimes while improving laser performance.

ACKNOWLEDGEMENTS

The authors acknowledge the financial support of the MARCO Focused Research Center on Interconnects, which is funded at MIT through a subcontract from the Georgia Institute of Technology. This work made use of the MRSEC Shared Facilities supported by the National Science Foundation under Award DMR-9400334. Additional funding was supplied by ARO Contract No. DAAG55-97-1-0111.

REFERENCES

- 1 H. Kroemer, Liu, T.Y., and Petroff, M., *Journal of Crystal Growth* **95**, 96 (1989).
- 2 Z. Hatzopoulos, Cengher, D., Deligeorgis, G., Androulidaki, M., Aperathitis, E., Halkias, G., Georgakilas, A., *Journal of Crystal Growth* **227-228**, 193 (2001).
- 3 Z.I. Kazi, Thilakan, P., Egawa, T., Umeno, M., and Jimbo, T., *Japanese Journal of Applied Physics* **40** (8), 4903 (2001).
- 4 P.J. Taylor, Jesser, W.A., Benson, J.D., Martinka, M., Dinan, J.H., Bradshaw, J., Lara-Taysing, M., Leavitt, R.P., Simonis, G., Chang, W., Clark, W.W., and Bertness, K.A., *Journal of Applied Physics* **89** (8), 4365 (2001).
- 5 M. T. Currie, Samavedam, S. B., Langdo, T. A., Leitz, C. W., and Fitzgerald, E. A., *Applied Physics Letters* **72** (14), 1718 (1998).
- 6 S. Ting, Bulsara, M., Yang, V., Groenert, M., Samavedam, S., Currie, M., Langdo, T., Fitzgerald, E., Joshi, A., Brown, R., Wang, X., Sieg, R., Ringel, S., presented at the SPIE Conference on Optoelectronics, San Jose, CA, 1999 (unpublished).
- 7 S.A. Ringel, Carlin, J.A., Leitz, C.W., Currie, M., Langdo, T., Fitzgerald, E.A., Bulsara, M., Wilt, D.M., and Clark, E.V., presented at the 16th European Photovoltaics Solar Energy Conference and Exhibition, Glasgow, Scotland, 2000 (unpublished).
- 8 G.R. Srinivasan, *Journal of the Electrochemical Society* **127** (6), 1334 (1980).
- 9 J.O. Carlsson, Boman, M., presented at the 9th International Conference on Chemical Vapor Deposition, Cincinnati, OH, 1984 (unpublished).
- 10 H. Kasano, *Solid State Electronics* **16**, 913 (1973).
- 11 S. H. Yellen, Shepard, A.H., Dalby, R.J., Baumann, J.A., Serreze, H.B., Guido, T.S., Soltz, R., Bystrom, K.J., Harding, C.M., and Waters, R.G., *IEEE Journal of Quantum Electronics* **29** (6), 2058 (1993).

Synthesis of Nanosized Lithium Manganate For Lithium-ion Secondary Batteries

Hsien-Cheng Wang, Yueh Lin, Ming-Chang Wen, and Chung-Hsin Lu
Department of Chemical Engineering, National Taiwan University.
Taipei, Taiwan

ABSTRACT

Nanosized lithium manganate powders are successfully synthesized via a newly developed reverse-microemulsion (R μ E) process. Monophasic LiMn₂O₄ powders are obtained after calcining the precursor powders at 700°C. The particle size of the spinel compound significantly depends on the concentration of the aqueous phase. Increasing the water-to-oil volume ratio results in an increase in the particle size. While the aqueous phase is equal to 0.5 M, the size of the obtained LiMn₂O₄ powder is around 60-70 nm. It is found that the specific capacity of nanosized LiMn₂O₄ particles is greater than that of submicron particles. The large surface area of ultrafine particles is considered to facilitate the intercalation and deintercalation of lithium ions during the cycling test.

INTRODUCTION

Lately, lithium-ion secondary batteries have become one of the most promising candidates in the field of rechargeable batteries owing to their high working voltage, high energy density, steady discharging properties, and long cycle life. For perfecting the performance of lithium ion batteries, the electrochemical characteristics of cathode materials have been intensively investigated. A variety of lithiated transition metal oxides including LiCoO₂, LiNiO₂, and LiMn₂O₄ have been explored for utilizing as cathode electrodes in lithium-ion secondary batteries [1-4]. Among these cathode materials, lithium manganate with a spinel structure is of particular interest for using in the rechargeable cells because of its inexpensive material cost, acceptable environmental characteristics, and better safety compared to LiCoO₂. However, LiMn₂O₄ suffers the disadvantages of relatively low discharge capacity and serious capacity fading during the cycling process [6-8]. For optimizing the electrochemical performance of LiMn₂O₄, a great deal of efforts have been devoted to synthesize LiMn₂O₄ powders with a controlled morphology [9,10]. A new reverse-microemulsion (R μ E) process was thus to control the morphology and particle size of LiMn₂O₄ powders, developed in this study, and the electrochemical performance of the obtained powders was also evaluated.

EXPERIMENTAL DETAILS

Lithium nitrate (LiNO₃) and manganese nitrate (Mn(NO₃)₂) were chosen as the starting materials. The well-dispersed aqueous phase was mixed with the continuous phase that

comprised oil and surfactant. After emulsifying these starting compounds, a transparent R μ E system was successfully obtained. The R μ E system was heated and dried for preparing the precursors of the target spinel compound. The precursor powders were calcined in a tube furnace at 350°C with a heating rate of 10°C/min to obtain the LiMn₂O₄ powders. The powders prepared at the cationic concentration of 0.5 M and 2.0 M were named as sample A and B, respectively. The crystallinity of the formed products was identified via the powder X-ray diffraction (XRD) analysis. The morphology and the particle size of the obtained powders were measured with a field emission scanning electron microscopy (FESEM). The electrochemical cell was composed of the R μ E- derived LiMn₂O₄ powders as the cathode, lithium foil as the anode, and an electrolyte of 1 M LiPF₆ in ethylene carbonate (EC) and 1,2-dimethyl carbonate (DMC) solution. The charge and discharge characteristics of the cathode materials were investigated using a current density of 0.23 mA/cm² in the voltage range of 3.0 and 4.3 V.

RESULTS AND DISCUSSION

Figure 1 illustrates the XRD patterns of the R μ E derived specimens heated at 700°C for 1 h. After analyzing the structural characteristics, these calcined powders were identified to be monophasic spinel LiMn₂O₄ with a cubic unit cell and a space group of Fd3m. All the diffraction peaks were consistent with the data in ICDD PDF No. 35-782. It is confirmed that at the cationic concentration of 0.5 and 2.0 M, pure spinel LiMn₂O₄ powders can be effectively synthesized using the R μ E process.

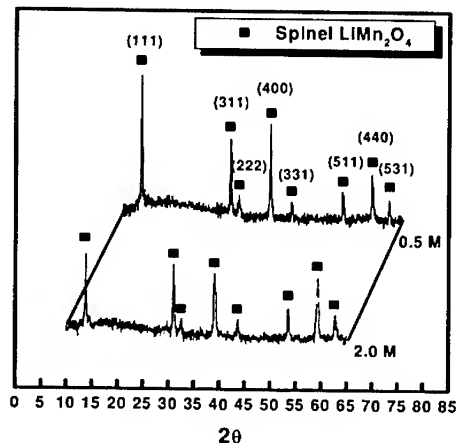


Fig. 1 XRD patterns of the R μ E-derived powders.

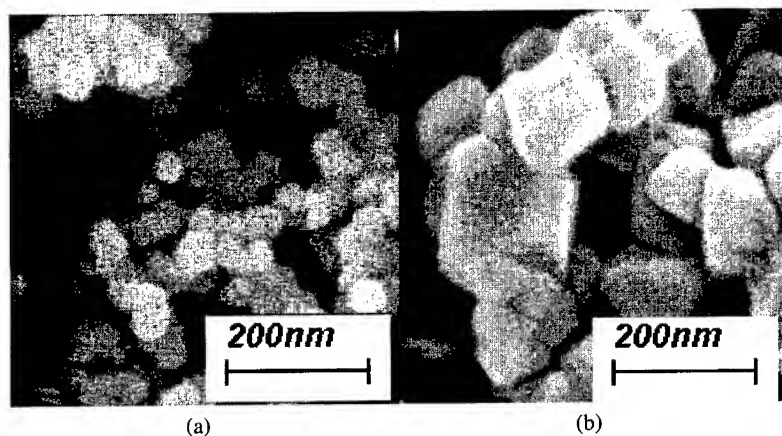


Fig. 2 The FESEM photos of the R μ E-derived powders (a) sample A and (b) sample B.

Figure 2 illustrates the field emission scanning electron microscopic photos of the pure spinel powders. Sample A has an uniform morphology and the particle sizes are around 60-70 nm with a narrow size distribution. Meanwhile, the mean particle size of sample B is 136 nm much larger than that of sample A. It was found that the particle size of the R μ E powders increased monotonously with a rise in the cationic concentration. In comparison with previous solution methods, the R μ E process significantly reduces the particle size of LiMn₂O₄ even down to a nanosized order.

Figure 3 shows the charge-discharge profiles for the 700°C-calcined samples cycled at 0.23 mA/cm². The cell consisting of sample A delivered the discharge capacity of 116 mAh/g in the first cycle at room temperature. After ten cycles, the discharge capacity retained 104.2 mAh/g. For the electrochemical characteristics of the sample B, the discharge capacity in the first cycle was 92.2 mAh/g, which was smaller than that of sample A. The superior performance of sample A was attributed to the larger surface area of smaller particles, which facilitated lithium ions to participate in the intercalation/deintercalation process.

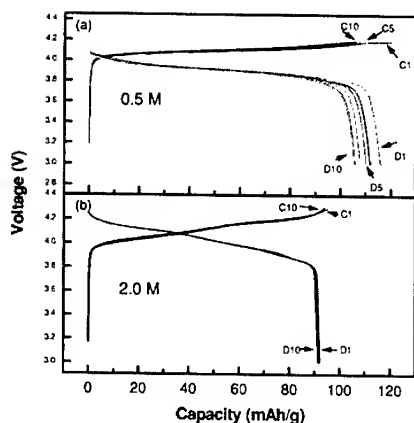


Fig. 3 Charge and discharge properties of the R μ E-derived powders cycled at the ambient temperature.

In order to investigate the cycling performance of the R μ E-derived powders at elevated temperatures, the electrochemical characteristics were also examined at 55°C. Figure 4 illustrates the charge and discharge profiles of the 700°C-calcined specimens. For sample A, the first-cycle discharge capacity was 98.8 mAh/g, while that of the 10th cycle was 81.0 mAh/g. As for sample B, the discharge capacities of the first and tenth cycles were 88.7 and 84.1 mAh/g, respectively. It was found that the R μ E-derived powder obtained at low cationic concentration demonstrated worse capacity fading than that derived from high cationic concentration.

The cycling stability at 55°C and the capacity retention of the R μ E-derived powders are shown in Fig. 5. It was found that the capacity fading of sample B was less severe than that of sample A, indicating that high cationic concentration in the R μ E system is effective in suppressing the capacity fading. Figure 5(b) depicts that the capacity retention of sample A and B after 10 cycles at this temperature were 82% and 95%, respectively. It was found that the specific capacity increased with an increase in the surface area of the obtained LiMn₂O₄ powders, however the capacity retention was completely opposite. The reason for better capacity retention of sample B at elevated temperature was its larger particle size. The enlargement of surface area facilitated the insertion and extraction of lithium ions, but also increased the dissolution of manganese ions into the electrolyte. For optimizing the electrochemical performance of the R μ E-derived LiMn₂O₄ powders, the particles size should be precisely controlled.

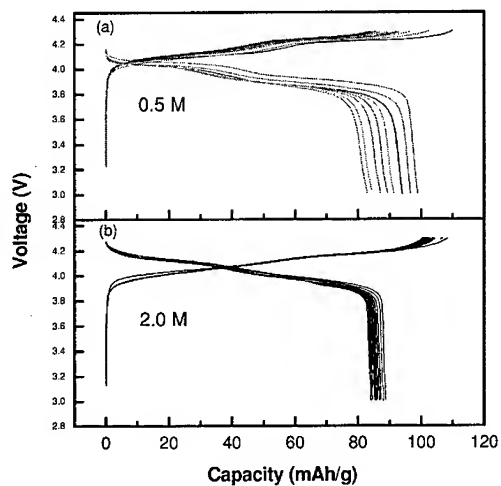


Fig. 4 Charge and discharge performance of the RμE-derived powders at 55°C. The aqueous concentration are (a) 0.5 M and (B) 2.0 M, respectively.

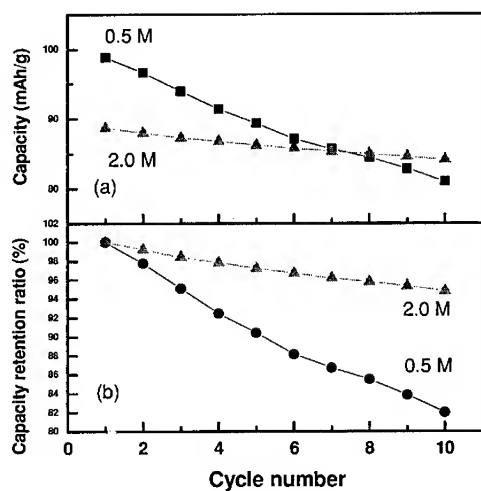


Fig. 5 Comparison of the cycling stability and the capacity retention of the RμE-derived powders at 55°C.

CONCLUSIONS

Monophasic nanosized LiMn_2O_4 powders were successfully synthesized after calcining the precursor powders at 700°C for 1 h. The electrochemical performance of the obtained LiMn_2O_4 powders was also examined. The particle size decreased and the surface area increased with a drop in the cationic concentration. It was found that LiMn_2O_4 particles with larger surface area gave rise to a greater specific capacity but a worse cyclability at elevated temperatures. The first-cycle discharge capacities of the samples prepared from cationic concentrations of 0.5 M and 2.0 M were 98.8 and 88.7 mAh/g at 55°C , and the corresponding capacity retentions after ten cycles were 82% and 95%, respectively. In order to optimize the electrochemical performance of LiMn_2O_4 , the control of particle size is necessary.

REFERENCES

1. J. M. Tarascon, E. Wang, F. K. Shokoohi, W. R. McKinnon, S. Colson, *J. Electrochem. Soc.* **138**, 2859 (1991).
2. A. Momchilov, V. Manev, A. Nassalevska, *J. Power Sources* **41**, 305 (1993).
3. Z. Jiang, K. M. Abraham, *J. Electrochem. Soc.* **143**, 1591 (1996).
4. T. Ohzuku, M. Kitagawa, T. Hirai, *J. Electrochem. Soc.* **137**, 769 (1990).
5. X. H. Hu, X. P. Ai, H. X. Yang, Sh. X. Li, *J. Power Sources* **74**, 240 (1998).
6. W. Liu, G. C. Farrington, F. Chaput, B. Dunn, *J. Electrochem. Soc.* **143**, 879 (1996).
7. Y. H. Ikuhara, Y. Iwamoto, K. Kikuta, S. Hirano, *J. Mater. Res.* **14**, 3102 (1999).
8. H. J. Kweon, S. S. Kim, G. B. Kim, D. G. Park, *J. Mater. Sci. Lett.* **17**, 1697 (1998).
9. C. H. Lu, S. K. Saha, *Mater. Sci. Eng.* **B79**, 247 (2001).
10. C. H. Lu, S. W. Lin, *J. Power Sources* **93**, 14 (2001).

Improved Routes towards Solution Deposition of Indium Sulfide Thin Films for Photovoltaic Applications:

Kuveshni Govender, David Smyth-Boyle and Paul O'Brien
Department of Chemistry and the Materials Science Centre, University of Manchester, Oxford Road, Manchester, M13 9PL, UK

ABSTRACT

Conditions necessary for the reproducible deposition of pristine In_2S_3 thin films on TO-glass substrates by low temperature solution deposition have been identified. Baths containing carboxylic acids yield adherent, specular and crystalline films, within a defined pH range, dependent on the particular acid employed. Films have been characterised by XRD, SEM, XPS and electronic spectroscopy. As-deposited films were found to crystallise as tetragonal $\beta\text{-In}_2\text{S}_3$, no evidence for incorporation of hydroxy-indium species was found by XPS measurements.

INTRODUCTION

The III-VI semiconductor indium sulfide (In_2S_3) has been the focus of much attention during the past two decades, primarily due to its optoelectronic properties. The compound has inspired applications in the preparation of green and red phosphors [1] and more recently in semiconductor-sensitized solar cells [2]. Indium sulfide is an n-type semiconductor that exists in three forms, viz. a defect cubic structure $\alpha\text{-In}_2\text{S}_3$ under ambient conditions, which transforms into a defect spinel $\beta\text{-In}_2\text{S}_3$ at 693 K and into a layered structure $\gamma\text{-In}_2\text{S}_3$ at 1013 K [3-5]. The bandgap of In_2S_3 varies between 2.0 and 2.45 eV depending upon the composition [6].

An important research goal within the photovoltaic industry is the replacement of toxic heavy metals, such as cadmium, with more benign materials. The replacement of n-type CdS layers in polycrystalline heterojunction thin film solar cells employing CIS, CIGS or CdTe absorber layers, is of particular interest. Thin films of In_2S_3 have been demonstrated to be a suitable substitute for such layers in CIGS based cells. Films are most commonly deposited by the chemical bath method (CBD). Efficiencies of 15.7 % have been obtained for such devices, comparable to 16 % obtained for the standard CBD CdS buffer layer [7].

It is known that the composition, structure and morphology of CBD films are highly sensitive to deposition conditions (e.g. bath chemistry and nature of substrate surface). Such sensitivity grants the investigator the potential for tailoring the material properties of films by judicious selection of CBD conditions. Various groups have reported CBD- $\text{In}_x(\text{OH},\text{S})_y$ [7-9] but to date, no convincing studies have been presented for the CBD of pristine and crystalline In_2S_3 . The most satisfactory films have been deposited from baths containing acetic acid.

In preliminary studies, we have identified the conditions necessary for reproducible CBD- In_2S_3 on TO-glass from baths containing carboxylic acids. Our approach may offer a general route towards low temperature deposition of crystalline thin films of $\beta\text{-In}_2\text{S}_3$ with no hydroxide incorporation.

EXPERIMENTAL DETAILS

CBD of In_2S_3 thin films

Thin films of In_2S_3 were deposited on commercial TO glass substrates (Hartford Glass, USA) immersed in baths containing InCl_3 ($0.0083 \text{ mol dm}^{-3}$), a carboxylic acid CA (0.1 mol dm^{-3}) and thioacetamide (0.1 mol dm^{-3}). A standard procedure was adopted for the cleaning of the substrates prior to the CBD process in order to achieve reproducible results. Based on results obtained from preliminary experiments, which were performed with no pH adjustment, a range of optimal CBD conditions were identified for each CA for the deposition of adherent and specular films. Subsequent work involved optimisation of each CA-based CBD system within the defined pH range. Bath conditions are given in Table 1. The pH of the final solution was adjusted accordingly by the dropwise addition of NaOH or HCl (5 mol dm^{-3}). A Mettler Toledo MA 235 pH/ ion analyser and InLab 413 electrode were used to record solution pH. The temperature of the solution was maintained at 80°C for a total deposition time of 30 minutes. Films were annealed for 30 min at 400°C under a dynamic flow of argon.

Characterisation of thin films

X-ray diffraction studies were performed using secondary graphite monochromated $\text{Cu K}\alpha$ radiation (40 kV) on a Philips X'Pert Materials Diffractometer (MPD). Measurements were taken using a glancing angle incidence detector at an angle of 3° for 2θ values over $10 - 95^\circ$ in steps of 0.04 with a count time of 2 s. Scanning electron microscopy of Au coated samples was carried out on a Philips 525 SEM instrument. The XPS measurements were performed in the ultra-high vacuum chamber (base pressure of 10^{-8} Pa) of a Kratos ES 200 spectrometer using $\text{Mg K}\alpha$ excitation (analyser pass energy of 65 eV). The energy scale was calibrated using Au and Ag as a reference. Electronic absorption spectra were obtained with a Helios Beta Thermospectronic spectrophotometer. For direct bandgap semiconductors, extrapolation of the linear region of plots of α^2 versus $h\nu$ allows determination of the optical bandgap.

RESULTS AND DISCUSSION

The pattern of results for each of the CA-based CBD systems in the present study was very similar. Films deposited from baths of pH values lower than the optimal range were orange, matt but adherent. Films formed in the optimal pH range were yellow, specular and adherent whereas at higher pH values, only white hydroxy-indium films were deposited. The induction period (T^*) for growth of films (*i.e.* the interval between the point the bath reaches the requisite temperature and the appearance of visible colloidal material) was inversely related to $\text{pK}_{\text{a}1}$ of the acid. For example, baths at $\text{pH} = 2$ containing citric acid ($\text{pK}_{\text{a}1} 3.13$) had T^* values $\sim 7 \text{ min}$, baths containing acetic acid ($\text{pK}_{\text{a}1} 4.75$) had T^* values $\sim 2 \text{ min}$. The observation could be rationalised in terms of the speciation of the carboxylate-indium species for each CA, which acts to buffer the free indium concentration to low levels in solution. The speciation studies will be reported in more detail in a future paper.

Table I. Carboxylic acids used in CBD of In_2S_3 .

Carboxylic acid	pKa ₁ Values	Unadjusted bath pH	pH range	Optimal pH range
citric acid	3.13	1.95	1.50 – 2.20	1.95 – 2.10
formic acid	3.75	2.20	1.00 – 3.00	2.00 – 2.20
succinic acid	4.19	2.30	1.60 – 2.50	2.10 – 2.35
acetic acid	4.75	2.49	1.60 – 2.60	2.10 – 2.30

X-ray diffraction

X-ray diffraction patterns obtained for CBD In_2S_3 thin films deposited on TO glass in this study indicate that films are highly crystalline. Annealing of films (400 °C under Ar) produced a colour change (yellow to pale orange for specular films, orange to light brown for matt films) and a slight enhancement in crystallinity. No significant differences were evident in XRD traces from films obtained from baths containing different carboxylic acids, within the effective pH ranges. Films were indexed to tetragonal $\beta\text{-In}_2\text{S}_3$ (JCPDS 25-0390). The lack of diagnostic reflections in the region $2\theta \sim 90\text{--}130^\circ$ was taken as evidence for the absence of $\alpha\text{-In}_2\text{S}_3$ modification. Discernible differences in preferred orientation were apparent for films grown within and lower than the optimal pH range from baths containing a given carboxylic acid. For example, films deposited from baths containing formic acid at lower pH showed preferred orientation in the (109) direction; thin specular films deposited in the optimal pH range grew preferentially along the (211) direction (see Figure 1).

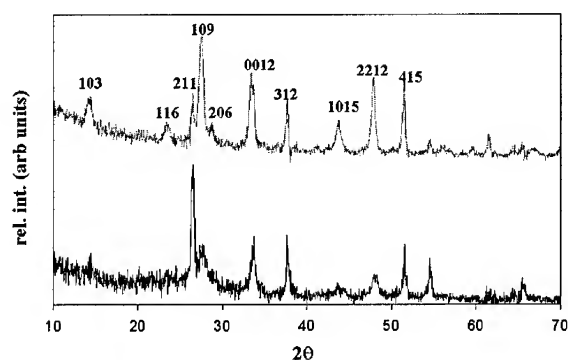


Figure 1. XRD pattern of In_2S_3 thin films deposited from baths containing InCl_3 , formic acid and thioacetamide at pH 2.2 (bottom) and 1.4 (top). Films indexed to $\beta\text{-In}_2\text{S}_3$ (JCPDS 25-0390).

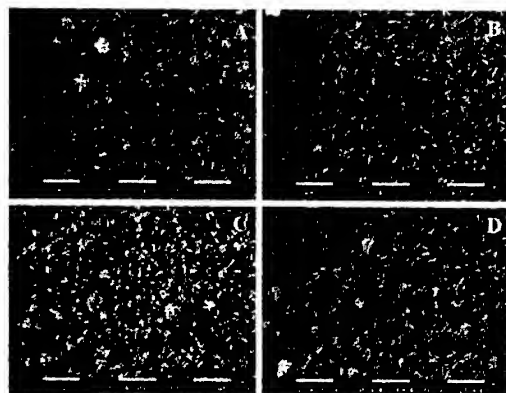


Figure 2. Scanning electron micrographs of In_2S_3 thin films deposited from baths containing InCl_3 , thioacetamide and carboxylic acid; *a.* citric (pH = 1.95); *b.* formic (pH = 2.2); *c.* succinic (pH = 2.3); *d.* acetic (pH = 2.1).

Scanning Electronic Microscopy

The effect of different carboxylic acids on CBD- In_2S_3 film morphology was probed by scanning electron microscopy (SEM). For all systems under investigation (within the optimal pH range), films were composed of dense, ribbon-like primary crystallites (Figure 2). The smallest crystallites were obtained from baths containing citric acid, which has the lowest $\text{pK}_{\text{a}1}$. Films formed from baths containing acetic or citric acid were morphologically similar and composed of spheroidal aggregates comprising primary ribbon-like crystallites. These clusters appeared to follow the underlying TO layer. The most homogeneous films, which did not conform to the underlying TO layer, were deposited from baths containing formic acid. Films deposited from baths containing succinic acid were less ordered than all others in this study.

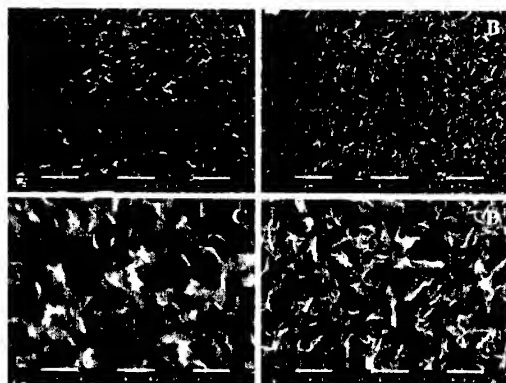


Figure 3. Scanning electron micrographs of In_2S_3 thin films deposited from baths containing InCl_3 , formic acid and thioacetamide at pH values of 2.2 (top); *a.* as deposited; *b.* annealed and 1.4 (bottom); *c.* as deposited; *d.* annealed

In order to complement the results obtained from XRD studies for films deposited from baths containing formic acid, the effect of annealing and CBD solution pH on In_2S_3 film morphology were investigated. As seen clearly in Figure 3, the pH of the deposition bath has a pronounced effect on film morphology. Films deposited at pH values lower than the optimal range (*i.e.* matt films) were composed of flaky aggregates, as opposed to the specular films obtained in the optimal pH range. Annealing of these flaky films produced pronounced changes and an improvement in crystallinity. By contrast, no significant changes in morphology were apparent upon annealing of specular films.

XPS

XPS was employed to determine photoelectron binding energies of components of annealed films. As shown in Figure 4 (left), In, S, O and C were detected. The O 1s peak, located at 533 eV, was ascribed to molecular oxygen contamination from the ambient on the basis of previous literature reports [10]. The absence of an additional peak at 530 eV was taken as evidence that oxygen was not bonded to the metal [10], although Herrero *et al.* assign this peak to C-O/H₂O [9]. No evidence for the formation of an In-O-S alloy was obtained. For example, the In Auger parameter corresponding to In_2S_3 and $\text{In}(\text{OH})_3$ is known to occur at 852.2 eV and 850.8 eV [11], whereas the feature occurs at 853 eV in our spectrum. In addition, Hariskos *et al.* state that the occurrence of an alloy results in attenuation of the feature at 404.5 eV due to an Auger contribution from In (MNN) electrons of $\text{In}(\text{OH})_3$. Expansion of the aforementioned region in our spectrum revealed no such phenomenon. Incorporation of oxy-sulfide species was discounted, as the S 2p peak binding energy (161 eV) is lower than would be expected for S-O bonds (~168 eV) [10]. The most significant feature of the spectrum, with a binding energy of 444.5 eV, was assigned to $\text{In}3d_{5/2}$ photoelectrons. The feature is consistent with literature values for In_2S_3 [12].

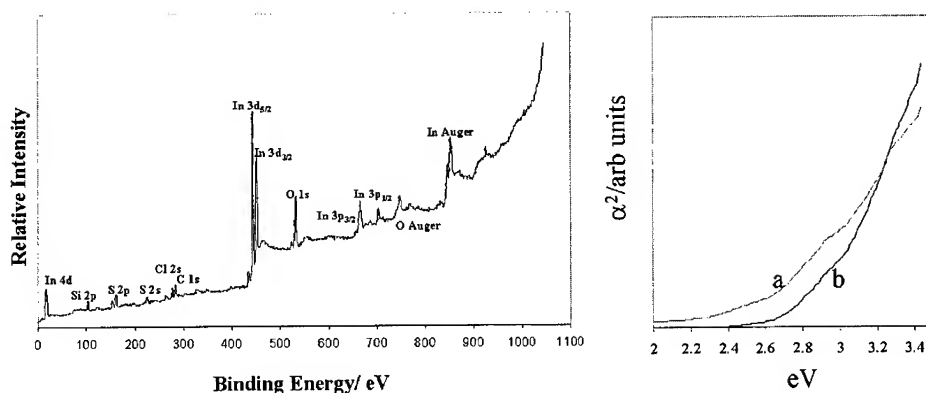


Figure 4. X-ray photoelectron (left) and electronic absorption spectra (right) of In_2S_3 thin films deposited from baths containing InCl_3 , acetic acid and thioacetamide; a. annealed, b. as-deposited (right.)

Electronic Spectroscopy

Electronic absorption spectra of as-deposited and annealed In_2S_3 films were recorded. From the extrapolation of the linear region of plots of α^2 versus $h\nu$ (eV), the bandgaps were determined. Annealed films possessed bandgaps of 2.58 eV (Figure 4, right), slightly lower than those of as-deposited films (2.78 eV). The result was very similar to values reported by Lokhande *et al* [6]. The most rational explanation for the increased bandgap values is the manifestation of quantum-size effects; the visible colour change upon annealing (*i.e.* yellow to pale orange) is also consistent with this interpretation.

CONCLUSIONS

The reproducible CBD of $\beta\text{-In}_2\text{S}_3$ thin films on TO-glass substrates has been demonstrated. Baths containing carboxylic acids yield adherent and crystalline films within a defined pH range, which is dependent on the particular acid employed.

ACKNOWLEDGEMENTS

Financial support from the NRF, SA and the Royal Society and the EPSRC, UK is gratefully acknowledged.

REFERENCES

1. S. Yu, L. Shu, Y. Qian, Y. Xie, J. Yang and L. Yang, *Mater. Res. Bull.*, **33**, 717, (1998).
2. K. Hara, K. Sata and H. Arakawa, *Solar Energy Mater. & Solar Cells*, **62**, 441, (2001).
3. W. Rehwal and G. Harbeck, *J. Phys. Chem. Solids*, **26**, 1309, (1965).
4. J.M. Giles, H. Hatwell, G. Offergeld and J. Van Cakenberghe, *J. Phys. Status Solidi*, **2**, K73, (1962).
5. R. Diehl and R. Nitsche, *J. Cryst. Growth*, **28**, 306, (1975).
6. C.D. Lockhande, A. Ennaoui, P.S. Patil, M. Giersig, K. Diesner, M. Muller and H. Tributsch, *Thin Solid Films*, **340**, 18, (1999).
7. D. Hariskos, M. Ruckh, U. Rühle, T. Walter, H.W. Schock, J. Hedström and L. Stolt, *Solar Energy Mater. & Solar Cells*, **41/42**, 345, (1996).
8. C.H. Huang, S.S. Li, W.N. Shafarman, S.H. Chang, E.S. Lambers, L. Rieth, J.W. Johnson, S.Kim, B.J. Stanberry, T.J. Anderson and P.H. Holloway, *Solar Energy Mater. & Solar Cells*, **69**, 131, (2001).
9. R. Bayón, C. Maffiotte and J. Herrero, *Thin Solid Films*, **353**, 100, (1999).
10. N. Barreau, S. Marsillac, J.C. Bernède, *Vacuum*, **56**, 101, (2000).
11. C.D. Wagner in: *Practical Surface Analysis*, Vol. 1, edited by D. Briggs and M.P. Seah (Wiley, Chichester, 1990) pp 614.
12. J.F. Moulder, W.F. Sticke, P.E. Sobol, K.D. Bomben, *Handbook of X-ray Photoelectron Spectroscopy*, Perkin-Elmer Corporation, Eden Prairie, MN, 1992.

Third Order Mode Optically Pumped Semiconductor Laser for an Integrated Twin Photon Source in Quantum Optics

N. G. Semaltianos, A. De Rossi, V. Berger, B. Vinter, E. Chirlias and V. Ortiz
Thales Research and Technology
Domaine de Corbeville
91404 Orsay, FRANCE

ABSTRACT

Lasing action on a third order waveguide mode is demonstrated at room temperature under optical pumping, in a specifically designed quantum well laser structure. The AlGaAs heterostructure involves barriers which ensure that the third order mode has a higher overlap with the single quantum well emitter than the fundamental mode. Third order mode operation of a laser structure opens the way to modal phase matched parametric down conversion inside the semiconductor laser itself. It is a first step towards the realization of semiconductor twin photon laser sources, needed for quantum information experiments.

INTRODUCTION

Twin photon sources obtained by parametric fluorescence (PF) are a useful tool in quantum cryptography or quantum optics experiments [1-3]. In these experiments PF is obtained from a laser beam with a frequency ω_p which enters into a nonlinear crystal and creates twin down generated photons at a frequency $\omega_i = \omega_s = \omega_p/2$. The whole set-up is in general complicated. The purpose of this work is to study a new type of semiconductor laser in which PF could be obtained in the semiconductor laser itself thus resulting in a highly compact twin photon source.

Two criteria must be fulfilled to obtain efficient PF: a high nonlinear coefficient and the possibility to phase match the interaction between the interacting waves [4]. Semiconductors and especially GaAs are very interesting for waveguided nonlinear parametric processes due to their high nonlinear coefficient and the possibility to integrate quantum well (QW) sources with nonlinear interactions. However, III-V semiconductors are not birefringent and alternative phase matching schemes have to be used [5]. Among the different phase matching schemes, modal dispersion phase matching (MDPM) [6,7] is attractive because it is well suited for materials grown by molecular beam epitaxy (MBE) due to the control of the layer thickness homogeneity up to the atomic level. In this method phase matching is obtained by a careful design of a multilayer waveguide in which the effective indices n_{eff} of three different guided modes i , j and k satisfy the MDPM condition: $n_{\text{eff},i}(\lambda_p) = 1/2[n_{\text{eff},j}(\lambda_i) + n_{\text{eff},k}(\lambda_s)]$. Figure 1 indicates MDPM in the laser structure which is described in detail below; in this specific design photons on the third order mode ($i = \text{TE}_2$) at $\omega_p = 775$ nm can generate through phase matched PF signal and idler photons at $\lambda_{s,i} = 2\lambda_p = 1.55$ μm on the fundamental modes ($j = \text{TE}_0$ and $k = \text{TM}_0$). In addition, the overlap integral [6] between the third order mode and the fundamental one, which gives the efficiency of this nonlinear process, is optimised.

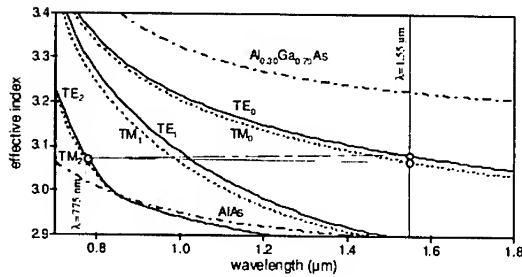


Figure 1. Effective indices of the sample as a function of wavelength. The two dash-dotted lines show the indices of the $\text{Al}_{0.30}\text{Ga}_{0.70}\text{As}$ (upper curve) and AlAs (lower curve). The triangle joining TE_2 at 775 nm (left open dot) and TE_0 and TM_0 curves at 1.55 μm (two open dots on the right) illustrates the phase matching condition: $n_{\text{TE}_2}(775\text{nm}) = 1/2[n_{\text{TE}_0}(1550\text{nm}) + n_{\text{TM}_0}(1550\text{nm})]$. Note that in this PF scheme, the two down generated photons are cross polarized, which is the best situation for quantum optics applications.

The purpose of this study is to show that a QW emitter can be used inside this waveguide as a source at ω_p , leading to lasing action on the third order mode, thus well suited for phase matched PF inside the laser cavity. Such a scheme is totally unusual for a semiconductor laser. For this, the electron-hole pairs must recombine in a place where the third order mode has a higher overlap than the two other modes in the system, as explained below.

RESULTS AND DISCUSSION

The sample was grown by a Varian MBE machine, on a semi-insulating GaAs substrate. A 1000 nm AlAs layer (C) was grown followed by a 130 nm $\text{Al}_{0.25}\text{Ga}_{0.75}\text{As}$ generation layer (G); a 140 nm $\text{Al}_{0.50}\text{Ga}_{0.50}\text{As}$ layer (B) and a 100 Å $\text{Al}_{0.11}\text{Ga}_{0.89}\text{As}$ active QW. Then the layers were repeated in the order B/G/C followed finally by a 30nm GaAs cap layer. Figure 2 shows the refractive index profile along the sample depth together with the field distributions of the third order mode (TE_2) and of the fundamental one (TE_0), for a wavelength equal to the expected lasing wavelength (775 nm).

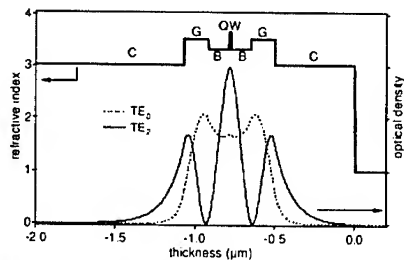


Figure 2. Refractive index profile with fundamental and third order mode field distributions, for a wavelength of 775 nm, in the TE polarization

The basic difference between this structure and other laser structures studied so far is the barriers introduced by the two 140 nm $\text{Al}_{0.50}\text{Ga}_{0.50}\text{As}$ B layers. The effect of these barriers is to

enhance the third order mode with respect to the fundamental mode at the QW location, the electric field of the fundamental being reduced in the center of the structure by these two low index layers. As a result, lasing action on the third order mode is expected. However, an additional undesirable effect of the B layers is that they introduce a physical barrier for the diffusive exchange of photogenerated carriers between the QW and the G layers, which affects the photoluminescence (PL) efficiency of the QW and of the G layers and may have consequences in the laser power threshold, optical gain and other laser parameters.

The resulting band structure of the sample structure is shown in Figure 3 by taking into account the generation and recombination of electrons and holes in the G layer, their transport to the QW, and their recombination stimulated by the third order mode.

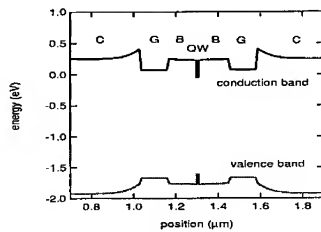


Figure 3. Band structure of the sample.

PL spectra from the sample excited by a CW low power (around 5 mW) He:Ne laser at 633 nm (1.958 eV) (Figure 4 (a)), are dominated by two peaks: at 10 K one peak at 1.70 eV related to the excitonic recombination transition between the fundamental state of the conduction band electrons to the fundamental state of the valence band heavy holes of the QW and another one at 1.85 eV related to the band edge excitonic transition from the G layers.

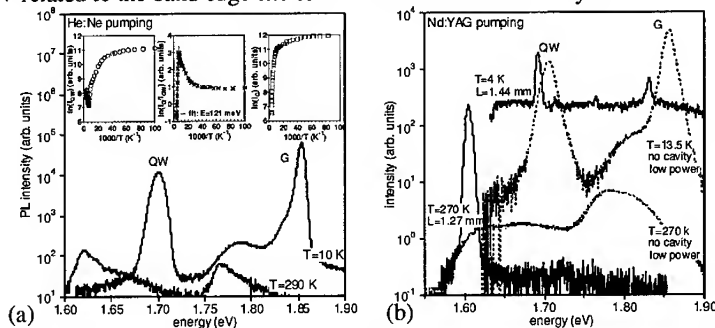


Figure 4. (a) PL spectra from the sample at low and high temperatures excited by a low power CW He:Ne laser at 633 nm. Inset shows the temperature dependence of the integrated intensities of the peaks related to the QW (I_{QW}), G layers (I_G) and of the ratio (I_G/I_{QW}). In part (b) of the figure a pulsed Nd:YAG laser at 532 nm was used. Dotted line spectra correspond to a low power excitation below threshold, while solid line spectra correspond to transverse pumping of laser bars with cavity lengths L . The lasing peak appears at the low energy side of the spontaneous emission peak.

In the temperature dependence of the integrated intensities of the two peaks (shown in the insets of Figure 4 (a)), it is seen that while the I_G decreases monotonically from low temperatures up to room temperature, the I_{QW} starts increasing above 150 K. This is due to a thermally activated transport of carriers from the G layers to the QW above 150 K with an activation energy of 121 meV estimated from the slope of the straight line behaviour of the ratio of the integrated intensities of the two peaks (I_G/I_{QW}). This energy corresponds to the conduction band offset of the $Al_{0.25}Ga_{0.75}As/Al_{0.50}Ga_{0.50}As$ subsystem (theoretically $\Delta E_{c,G}=154$ meV). By increasing the temperature further above 240 K, I_{QW} starts dropping again. This is due to an increasing importance of thermally activated non-radiative recombination processes at high temperatures, which dominate over the thermal carrier exchange between QW and G layers.

In Figure 4 (b) the sample was pumped by 6 ns pulses from a frequency doubled YAG laser at 532 nm (2.33 eV), at a frequency of 10 Hz. Dotted lines correspond to spontaneous emission spectra with a low excitation power while the solid lines correspond to transverse pumping of cleaved laser bars with cavity length L . Laser emission is observed at 772.5 nm (1.6 eV) at room temperature, near the expected wavelength of 775 nm.

Comparing Figures 4 (a) and (b) it is seen that under He:Ne pumping although at low temperatures I_G is greater than I_{QW} , at room temperature the opposite is true. On the other hand under Nd:YAG pumping I_{QW} is always weaker than I_G even at room temperature, because of the distribution of carrier population in QW and G layers before recombination. However, the inverted population required for stimulated emission is always created first in the QW rather than in the G layers, and this is so in the whole temperature region studied.

The laser power threshold at room temperature was measured equal to 10.7 KW/cm^2 for unprocessed planar samples (as-grown) and 42 KW/cm^2 for processed samples with waveguide ridges (width $10 \mu\text{m}$ and distance between them around $100 \mu\text{m}$). The higher threshold of processed samples as compared to unprocessed ones may be due to the fact that etching of photolithographically made ridges onto the sample surface has as a result oxidation of the AlAs and formation of $AlOx$ [8,9]. The characteristic temperature which expresses the threshold in the exponential empirical form versus sample temperature (Figure 5), was measured equal to 117 K which is comparable to the value reported for III-V lasers in general [10] as well as for ZnSe/ZnSse blue lasers [11].

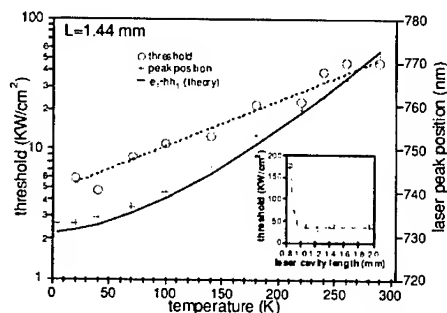


Figure 5. Laser power threshold and peak position versus temperature. The solid line (through the cross points) corresponds to the theoretically estimated energy of the e_1-hh_1 transition of the QW. Inset shows threshold versus cavity length.

Both values for the threshold reported above are higher than the value of around 1 KW/cm^2 calculated theoretically from simulations based on Figure 3. Apart from stronger recombination in the G layers than simulated, this may be explained by optical losses higher than expected due to optical leakage in the plane of the laser structure, or towards the substrate. Indeed, it can be seen in Figure 1 that the third order mode at 775 nm is near the cut-off of the waveguide (given by the refractive index of the cladding material AlAs), which implies that the mode is very sensitive to scattering processes into leaky waves in the substrate.

Experiments were carried out to measure the far field emission pattern of the semiconductor laser. The signal, shown in Figure 6 as a function of the angle in the transverse direction, starts from a maximum value at 0° , decreases with the angle of rotation to a minimum value at around $20^\circ \pm 3^\circ$ then obtains a second maximum value at an angle of $40^\circ \pm 3^\circ$ and finally decreases again to zero.

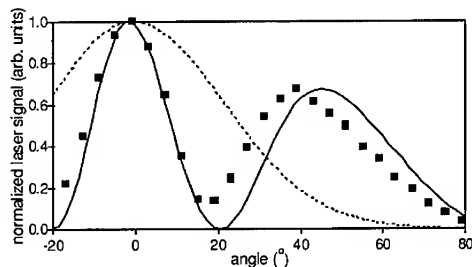


Figure 6. Laser output signal versus transverse angle of rotation (squares), compared with the calculated far field of third order (full line) and fundamental laser modes (dotted line).

The solid line in the figure corresponds to theoretical calculation using the Rayleigh-Sommerfeld integral [12] of the far field distribution for a third order mode radiation while the dashed line corresponds to the fundamental mode. As expected, the fundamental mode shows only one main lobe centered at 0° , whereas the third order mode diffraction pattern shows a strong side lobe. Similarity of the experimental points with the theoretical calculated curves for the filed distributions demonstrate that our specially designed laser sample structure emits on the third order mode, as intended.

CONCLUSIONS

We have demonstrated laser emission at 772.5 nm , on a third order waveguide mode, and at room temperature, from an optically pumped AlGaAs QW structure. The structure was characterized in detail in terms of: temperature and pumping energy dependence of photoluminescence spectra and temperature and laser cavity length dependence of power threshold and laser peak position. Further work will include the study of modal phase matching in this semiconductor laser waveguide, in order to provide through intracavity parametric fluorescence a semiconductor source of twin photons.

ACKNOWLEDGEMENTS

This work was performed within the framework of the EC project 'QUCOMM'. N.G.S. is a recipient of a Marie Curie Research Fellowship of the European Community, grant number IST-1999-80034 under the 'QLOPORT' programme.

REFERENCES

1. P. G. Kwiat, K. Mattle, H. Weinfurter, A. Zeilinger, A. V. Sergienko and Y. Shih, *Phys. Rev. Lett.* **75**, 4337 (1995).
2. D. Bouwmeester, J-W. Pan, K. Mattle, M. Eibl, H. Weifurter and A. Zeilinger, *Nature* **390**, 575 (1997).
3. J. W. Pan, D. Bouwmeester, M. Daniell, H. Weinfurter and A. Zeilinger, *Nature* **403**, 515 (2000).
4. A. Yariv, "*Quantum Electronics*" (John Wiley & Sons, New York, 1989).
5. Fiore, V. Berger, E. Rosencher, P. Bravetti and J. Nagle, *Nature* **391**, 463 (1998).
6. M. Jäger, G. I. Stegeman, M. C. Flipse, M. Diemeer and G. Möhlmann, *Appl. Phys. Lett.* **69**, 4139 (1996).
7. H. P. Wagner, S. Wittmann, H. Schmitzer and H. Stanzl, *J. Appl. Phys.* **77**, 3637 (1995).
8. J. M. Dallesasse, J. N. Holonyak, Jr., A. R. Sugg, T. A. Richard, *Appl. Phys. Lett.* **57**, 2844 (1990).
9. T. Takamori, K. Takemasa, T. Kamijoh, *Appl. Phys. Lett.* **69**, 659 (1996).
10. H. C. Casey and M. B. Panish, "*Heterostructure Lasers*", Academic, New York, Ch. 7 (1978).
11. K. Nakanishi, I. Suemune, Y. Fujii, Y. Kuroda and M. Yamanishi, *Appl. Phys. Lett.* **59**, 1401 (1991).
12. M. Born and E. Wolf, "*Principles of Optics*", (Pergamon Press, Oxford, 1980).

On the Optical Memory of a Thin-Film pInSb-nCdTe Heterojunction Obtained by Laser Pulsed Deposition

Arik G. Alexanian, Nikolay S. Aramyan, Romen P. Grigoryan*, Ashot M. Khachatryan, Lenrik A. Matevossian, and Arsham S. Yeremyan

Department of Semiconductor Electronics,
Institute of Radiophysics & Electronics, National Academy of Science of Armenia,
1 Brs. Alikhanian st., Ashtarak-2, 378410, Armenia;

*Yerevan Physics Institute, Yerevan, 375036, Armenia.

ABSTRACT

Thin film pInSb-nCdTe heterojunctions (HJs) were produced using pulsed laser deposition (PLD) technique and their photoelectric properties were studied for various thickness of the CdTe layer at nitrogen temperature and under a background radiation the photo-EMF for which was around 1.5 mV. At radiative excitation of the HJ a photo-EMF is observed, which persists when the excitation is turned off. The optical memory (OM) effect is observed in an idling regime and in a wide spectral range: (0.37–1.37) μm with "recording" (0.37–0.575) μm , (0.75–1.37) μm , and "clearing" (0.575–0.75) μm sub-regions. The maximum OM signal is observed at $\lambda=0.575\mu\text{m}$ while the minimum is at $\lambda=0.768\mu\text{m}$. In the spectral dependence of the OM signal at direct and reverse scanning of monochromatic irradiation an hysteresis is observed which is evident for the OM effect. The time dependence of OM signal is investigated at $\lambda=0.575\mu\text{m}$ and at various intensities of the radiation source. Here, an effect of saturation is clearly observed, and the time during which the OM signal runs up to saturation, depends strongly on the incident light flow power and decreases drastically as the latter is increased. The external bias applied to the HJ enhances the OM on 2 orders over its value in the idling regime. The OM signal persists for a time period no less than 10^5 sec, either with or without an external bias. The actually obtained values of "recording" sensitivity and the "recording" time are $U=0.66 \mu\text{J}/\text{mm}^2$ and $\tau=10^{-4}$ sec., respectively. The OM signal reaches its maximal value as the thickness of CdTe layer increases (up to $d=0.45 \mu\text{m}$). It is shown that the investigated HJ possess the property of integration of the radiation.

INTRODUCTION

It is well known that the effect of optical memory (OM) in semiconductors is related with the presence of inhomogeneities in a sample [1]. These inhomogeneities generally show a randomness which results in drastic changes of main characteristics of the effect from sample to sample even for the same material. This complicates the experimental studies of quantitative trends of the OM effect. The problem of reproducibility of OM-based devices is even more complicated. Therefore, observation of these effects in artificial structures with controllable parameters is very important.

The presence of a recombination barrier in semiconductor is a necessary condition of OM in semiconductors. The simplest systems containing such barriers are p-n heterojunctions (other examples are p-n homojunctions, Schottky-barrier diodes, and MOS structures).

In this work, we have studied the I-V characteristics and photoelectric properties of PLD-grown [2] pInSb-nCdTe HJs.

EXPERIMENT

pInSb-nCdTe HJs were produced by laser deposition of nCdTe layers of various thickness on the polished substrates of partially compensated pInSb ($N_A - N_D \approx 4.17 \times 10^{14} \text{ cm}^{-3}$ at $T = 77^\circ \text{K}$). The ohmic contacts on InSb and CdTe are obtained by thermal evaporation of metallic indium. The contact film of In covers the whole surface of the pInSb layer, while on the CdTe layer it has a shape of 1mm-diameter round. Surface areas of obtained HJs are in the range $(0.25 - 0.36) \text{ cm}^2$. Heterojunctions with the thickness of CdTe-layer (0.15, 0.45, 0.6, 1.2) μm were produced. In order to obtain large amplitudes of OM-signal the space charge region must take the large part of the conducting layer. The dependence of the cutoff voltage on the thickness of CdTe-layer was determined from the family of I-V curves at 77°K (by extrapolation of the linear part of an I-V curve. The value of V_c corresponding to the total bend of energy bands of HJ materials saturates at thickness of CdTe layer, $d \geq 0.5 \mu\text{m}$. The thickness of $W_n = 0.45 \mu\text{m}$ corresponds to the maximum width of space charge region in CdTe. The latter is completely depleted at smaller thickness. Using the measured values of $V_c = V_D = V_{Dn} + V_{Dp} = 0.45 \text{ eV}$ and $W_n = 0.45 \mu\text{m}$, within the Anderson model, the concentration of donor impurities in CdTe, the space charge region in InSb, as well as the band curvature for each HJ material [3] were determined. The corresponding values are the following: $N_D = 8.55 \cdot 10^{14} \text{ cm}^{-3}$, $W_p = 1.025 \mu\text{m}$, $V_{Dp} = 0.2 \text{ eV}$, and $V_{Dn} = 0.25 \text{ eV}$.

The analyses of photoelectric properties of HJs were carried out on the monochromator MDP-3, and incandescent lamps were used as radiation sources. The HJ samples were placed in nitrogen cryostats. X-Y recorder, Endim, was used to record the output signal. The effect of optical memory was observed in InSb-CdTe HJ sample when irradiated from the side of wide bandgap CdTe with a monochromatic light of a certain wavelength. The excitation of HJ resulted in a photo-EMF, which persisted when the excitation was turned off. The effect was observed in a temperature range $(77 - 165)^\circ \text{K}$, under the steady integral background radiation, the photo-EMF for which was 1.5 eV (idling regime).

The photomemory effect was observed also when an external bias was applied on the structure in accordance with I-V curves. In biased structure, the photovoltage was on 2 orders higher than that observed in idling regime. In difference with the work [4], the OM in our samples was observed either with or without an external bias, and in a wider spectral range: $\lambda = (0.37 - 1.37) \mu\text{m}$.

DISCUSSION

Figure 1 represents the spectral dependence of OM at direct and reverse scanning of the incident light spectrum, showing a hysteresis in this dependence. The studied wavelength range can be conveniently divided into 3 subranges:

- a) $\lambda = (0.37 - 0.575) \mu\text{m}$, where the OM-signal enhances with increasing incident wavelength, i.e. a "recording effect" is observed (curve AB in figure 1);

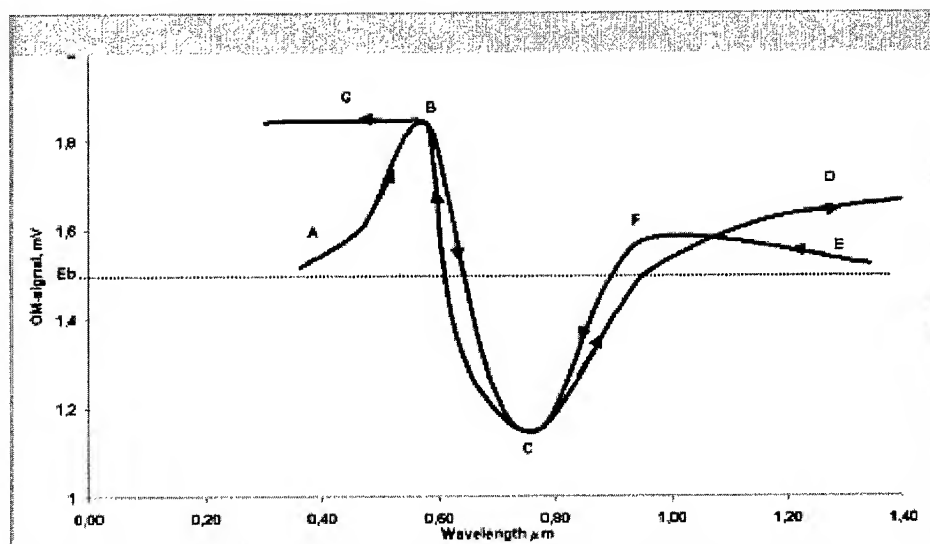


Figure 1. Wavelength dependence of optical memory signal (arrows indicate the scanning direction of external radiation).

- b) $\lambda=(0.575-0.768) \mu\text{m}$, in which the OM reduces with increasing wavelength, i.e. "clearing effect" (BC curve);
- c) $\lambda=(0.768-1.37) \mu\text{m}$, where the "recording effect" is again observed (CD curve).

The maximum of OM-signal is observed at $\lambda=0.575 \mu\text{m}$, while the minimum is at $\lambda=0.768 \mu\text{m}$. At larger thickness of the CdTe-layer the OM-signal enhances reaching a maximal value at $d=0.45 \mu\text{m}$. The further increase of d leads to decrease in OM-signal.

In figure 2, the time-dependence of OM-signal is shown at various intensities of incident radiation at $\lambda=0.575 \mu\text{m}$. The effect of saturation is clearly seen on this dependence in accordance with the population of (finite) number of interface states (traps). The saturation start-time depends strongly on the power flow of the light and decreases drastically with its enhancement. We should mention that a certain intermediate value of OM-signal could be obtained also at constant radiation intensity, by simply varying the exposition time. It is also interesting that if after the first act of illumination the HJ is not returned to its initial state, instead an additional radiation-pulse is applied, the memory voltage increases from the initial to a new value. This continues until this voltage reaches a certain maximal value, which corresponds to the saturation of traps. Thus, the produced heterojunctions possess the property of integration of incident radiation.

For "recording" samples the achieved sensitivity to the incident radiation was $\sim 0.66 \mu\text{J}/\text{mm}^2$, and the "recording time" was $\tau_0 \sim 8.3 \cdot 10^{-4}$ sec. One should note, however, that the determined τ_0 is not limited to this value and depends on the experimental capabilities. The OM-signal persists in both biased and unbiased HJs no less than 10^3 sec.

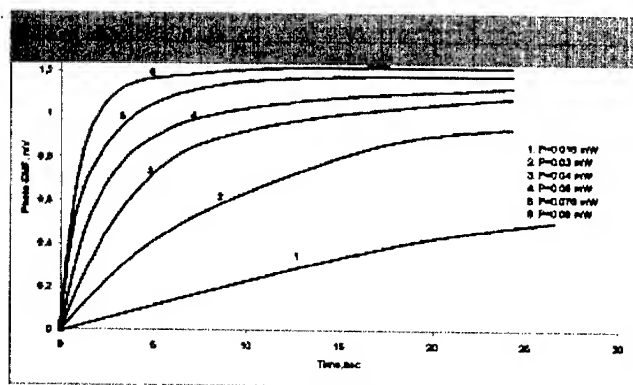


Figure 2. Time dependence of OM signal at various intensities of incident light. Incident wavelength is $\lambda=0.575 \mu\text{m}$.

The measurements of the memory photo-EMF depending on the reverse bias voltage were carried out at a fixed intensity of incident radiation at $\lambda=0.575 \mu\text{m}$. The applied voltages were in the range (100–1000) mV, where the resulting photo-EMF was in the range (9.15–65)mV (figure 3).

Thus, a reverse bias applied to the HJ increases the recombination barrier for non-equilibrium carriers (electrons) in CdTe resulting in an enhancement of memory photo-EMF more than 200 times.

The complex view of OM dependence on the incident wavelength results from the competing effects on the physical processes in HJ of such parameters as absorption coefficient, its frequency dependence, thickness of CdTe-layer, and geometrical sizes of space charge region.

The largest amplitude of OM-signal is observed in a sample with thickness comparable to the space charge region and with radiation penetration depth (the reciprocal absorption coefficient) to the incident wavelength.

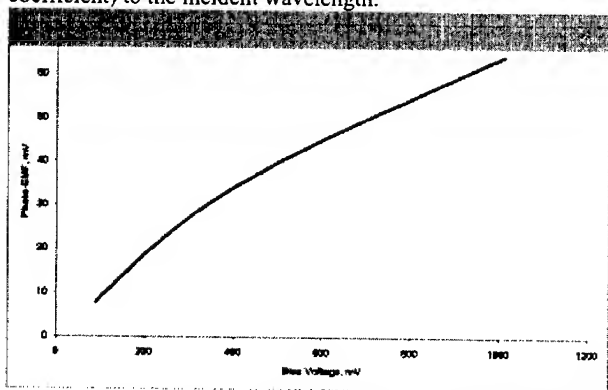


Figure 3. OM-signal in a biased sample. An incident light with fixed intensity at $\lambda=0.575 \mu\text{m}$ is used.

It follows from the OM-signal vs. wavelength dependencies that the OM appears in both cases of fundamental and impurity-related absorption. Based on this fact we assume that the absorption in CdTe occurs at interband and interface states--conduction band transitions. The HJ field separates the electron-hole pairs created by incident light: electrons move to the CdTe contact, and holes move to CdTe-InSb interface. Holes are partially captured by deep interface states (another part of holes pass to InSb) resulting in an enhancement of positive charge on the interface. After the radiation is turned off this charge remains on the surface states creating an optical memory voltage (AB curve in figure 1).

In order to remove the photo-EMF it is necessary for electrons to be able to pass over the recombination barrier and recombine with holes on surface states. Electrons in CdTe do not possess such energy so they cannot contribute to this process. With increase of the radiation wavelength the radiation partially penetrates into the InSb at $\lambda \geq d$ creating electron-hole pairs, which again does the HJ field separate. The electrons with sufficiently high energies ($E \geq E_{rec}$) pass over the barrier and recombine with holes decreasing the memory photovoltage. Thus, a maximum of photo-EMF appears in wavelength dependence. With further increase of wavelength the number of electron-hole pairs increases in InSb while decreasing in CdTe. Besides, electrons still pass over the barrier and recombine decreasing the photo-EMF (BC curve, figure 1). The latter process continues until the absorption that is related with transitions from impurity states to conduction band, becomes appreciable. The increase of impurity-related absorption with wavelength leads to the enhancement in trap charge and in the OM amplitude. This can be explained by impurity-related absorption. The latter coefficient has a maximum in spectral dependence, and is described by an expression

$$k_{imp} \sim x^{1/2} \cdot (1+x)^{-4}, \quad (1)$$

where $x = \frac{\hbar\omega - (E_g - \Delta E_a)}{\Delta E_a}$, ΔE_a is the depth of acceptor state, E_g is the bandgap width of CdTe,

and ω is the frequency of incident radiation. As it is seen, k_{imp} has a maximum at $x_{max}=1/7$:

$$\hbar\omega_{max} = E_g - \frac{6}{7}\Delta E_a. \text{ Since the OM still increases with wavelength even when } \lambda < \lambda_{max} (\lambda_{max}$$

corresponds to the maximum of the absorption coefficient), this can take place only if the energy of electrons created in InSb is not sufficient to pass over the recombination barrier. The OM amplitude continues to increase (charge accumulation occurs) and saturates. At reverse scanning of the incident wavelength after the HJ is returned to its initial state, the memory signal appears at $\lambda=1.37\mu\text{m}$ and increases with wavelength decrease, in accordance with the frequency dependence of the absorption coefficient, reaching a maximum at ω_i and then decreasing. The latter is possible when at frequencies $\omega > \omega_i$ the energy of electrons created in InSb is high enough to pass over the recombination barrier. Otherwise the OM amplitude would continue to

increase until the saturation, though the absorption coefficient still increases. Further, the decrease in OM signal continues unless the interband transitions at $\lambda \leq \lambda_2$ turn on, when the intensities of electron and hole capturing equal. The OM signal passes the minimum and increases with further increase of absorption coefficient.

CONCLUSIONS

Optical memory effect was observed in pInSb-nCdTe heterojunctions produced by pulsed laser deposition. The wavelength dependence of photo-EMF signal has the form of a hysteresis in a spectral range 0.37 to 1.37 μm . Optical memory signal was observed in unbiased, as well as in biased samples. In the latter case, the signal was on 2 orders of magnitude higher. The produced heterojunctions possess a property of integration of incident light power. Detailed description of physical mechanisms is given explaining the observed spectral and temporal dependencies of memory signal.

ACKNOWLEDGEMENT

This work was supported by the Fundamental Research Foundation of the Republic of Armenia and the ISTC Project A-102.

REFERENCES

1. M. K. Sheikman and A. Ya. Shik, Fiz. Tekh. Poluprovodn. **10**, 209 (1976).
2. A. G. Alexanian, R. K. Kazarian, and L. A. Matevossian, Elektronnaya Promyshlennost', **1**, 55 (1982).
3. A.G. Alexanian, A.I. G. Alexanian, R. K. Kazarian, and L. A. Matevossian, Int. Journ. of IR and MM waves, **14**, 2203 (1993).
4. N. V. Varlamov, L. A. V'ukov, O. V. Kulikova, O. G. Maksimova, S. I. Radautsap, A. N. Soliakov, and V. I. Filipp, Fiz. Tekh. Poluprovodn. **15**, 2423 (1981).

Quantitative Secondary Ion Mass Spectrometry (SIMS) of III-V Materials

P. Van Lierde, C. Tian, B. Rothman and R. A. Hockett
Evans Analytical Group
810 Kifer Road
Sunnyvale, CA 94086

ABSTRACT

Secondary ion mass spectrometry (SIMS) provides direct methods to characterize the chemical composition of III-V materials at major, minor and trace level concentrations as a function of layer depth. SIMS employs keV primary ions to sputter the surface and sensitive mass spectrometry techniques to mass analyze and detect sputtered secondary ions which are characteristic of the sample composition. In-depth compositional analysis of these materials by SIMS relies on a number of its unique features including: (1) keV primary ion sputtering yielding nanometer depth resolutions, (2) the use of MCs^+ detection techniques for quantifying major and minor constituents, and (3) ion implant standards for quantifying trace constituents like dopants and impurities. Nanometer depth resolution in SIMS sputtering provides accurate detection of diffusion of dopants, impurities and major constituents. MCs^+ refers to the detection of "molecular" ions of an element (M) and the Cs^+ primary beam. MCs^+ minimizes SIMS matrix effects in analysis for major and minor constituents, thus providing good quantification. This paper presents a SIMS study of $\text{Al}_x\text{Ga}_{1-x}\text{As}$ structures with three different x values. MCs^+ (M=Al or Ga) data are presented for the accurate determination of major and minor components. Rutherford backscattering spectrometry (RBS) and x-ray diffraction (XRD) data were cross-correlated with the MCs^+ results. Three specimens with different x values were ion implanted with H, C, O, Mg, Si, Zn and Se to study quantification of trace levels. SIMS data acquired on a double focusing instrument (CAMECA IMS-4f) and a quadrupole instrument (PHI ADEPT 1010) are also compared. Lastly, we discuss our efforts to improve the analysis precision for p- and n-type dopants in AlGaAs which currently is $\pm 3\%$ (1 sigma).

INTRODUCTION

The importance of using SIMS to support optoelectronics device manufacturing, and by implication the device development as well, is illustrated by a publication of Lucent Technologies in 2000 [1]. They used a CAMECA IMS-4f SIMS instrument to monitor dopant concentrations, layer thickness, and junction integrity for epitaxial layers of InP, InGaAs and InGaAsP doped with Zn, Fe and Si. These optoelectronics devices were laser diodes designed for high-speed transmission of digital and analog information through fiber optic media. They reported monitor data taken over a two and a half year period of manufacturing these devices.

Their SIMS measurements used the MCs^+ detection technique for quantifying major and minor constituents [2]. MCs^+ refers to the detection of "molecular" ions of an element (M) and the Cs^+ primary beam. MCs^+ minimizes SIMS matrix effects in analysis for major and minor

constituents, thus providing good quantification. They also used ion implanted reference materials to determine relative sensitivity factors (RSF's) to improve quantification [3].

EXPERIMENTAL

For the study of $\text{Al}_x\text{Ga}_{1-x}\text{As}$ the following samples were used: one AlGaAs/GaAs calibration sample as quantification standard and three AlGaAs/GaAs samples for the MCs^+ experiments, and two GaAs substrate samples doped with Si and Zn, respectively. The quantification standard sample was characterized by RBS and had x_{Al} value of 0.254. The samples were ion implanted with nine species representing most common dopants and impurities (Table 1). The list of implanted ions was split into four groups to minimize possible interference.

Table 1: Ion implant parameters.

Species	Energy (keV)	Dose (at/cm ²)	Species	Energy (keV)	Dose (at/cm ²)
¹ H	30	2E+15	²⁸ Si	200	1E+14
⁹ Be	100	1E+14	⁶⁴ Zn	300	2E+14
¹² C	100	1E+15	⁸⁰ Se	600	5E+13
¹⁸ O	100	5E+14	¹³⁰ Te	600	5E+13
²⁴ Mg	250	2E+14			

The data were taken using a CAMECA IMS-4f and a PHI ADEPT 1010 under various standard configurations with a Cs^+ primary ion beam. The H, C, O, Si, Se and Te species were measured as single charged negative ions, Be was measured as BeAs^+ , and Mg and Zn as a molecular ion MCs^+ (M=Mg or Zn). The sputter rates were determined from profilometry measurements of the analysis craters with an Alpha step.

RBS data were taken using a 2.275 MeV He^{2+} ion beam with detector scattering angle of 160°. The spectra were taken with 50uC charge accumulations with the sample rotated about the incident beam to avoid ion-channeling artifacts.

DISCUSSION

The relative change in the sputter rate with composition is shown in Figure 1. The data show a linear relationship between the sputter rate and the $\text{Al}_x\text{Ga}_{1-x}\text{As}$ composition for 14.5 keV Cs bombardment over the range investigated, which is in agreement with Meyer, et al. [4]. In addition, the As ion yields increase with increased Al content in Figure 2. This plot can be used for rough estimation of the Al mole fraction in AlGaAs.

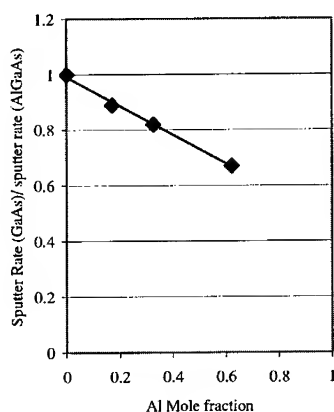


Figure 1. Relative sputter rate versus $\text{Al}_x\text{Ga}_{1-x}\text{As}$ composition for 14.5 keV Cs bombardment.

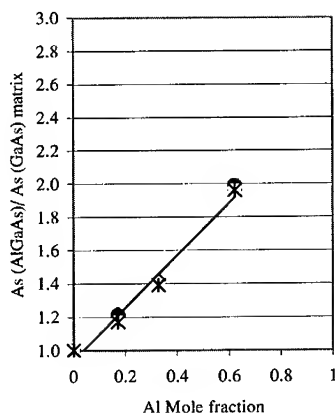


Figure 2. Relative As ion yield versus $\text{Al}_x\text{Ga}_{1-x}\text{As}$ composition for 14.5 keV Cs bombardment.

Measured ion counts are converted to concentrations by Relative Sensitivity Factors (RSF's). These are highly specific for each species and matrix as illustrated in Figure 3. Relative RSF's are plotted versus $\text{Al}_x\text{Ga}_{1-x}\text{As}$ composition. The change in relative RSF reflects changes in both the ion yield for the species and ion yield for the matrix species. For species with a high ionization potential like Se and Te, the ion yield is constant in the various AlGaAs matrixes. Therefore, the relative RSF reflects mainly the change in ion yield for the As⁻ matrix species. For species where the change in the ion yield is proportional to ion yield change of the matrix the relative RSF remains constant [5]. The MCs^+ detection technique has much reduced ion yield changes as is illustrated by the small change of relative RSF's for both Mg and Zn.

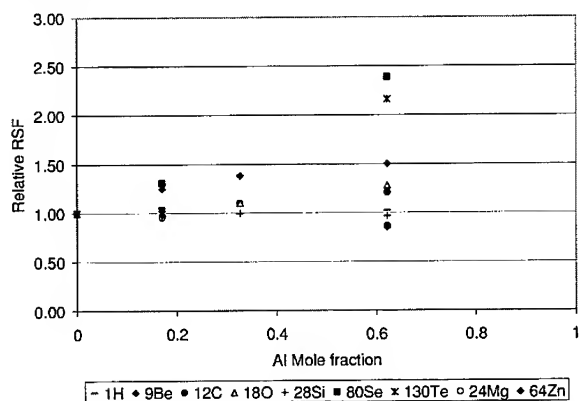


Figure 3. Relative RSF for implanted species as function of $\text{Al}_x\text{Ga}_{1-x}\text{As}$ composition

Table 2 illustrates a high precision study for SIMS data acquired from a Se doped AlGaAs

Table 2: High precision SIMS analysis of Se dopant in AlGaAs.

Se in AlGaAs (at/cm ³)			
SIMS Measurement	Reference Standard	Sample A	Sample B
1	7.54E+17	1.22E+18	1.38E+18
2	7.66E+17	1.21E+18	1.34E+18
3	7.42E+17	1.19E+18	1.35E+18
4	7.44E+17	1.20E+18	1.36E+18
5	7.30E+17		
6	7.66E+17		
7	7.45E+17		
8	7.33E+17		
9	7.64E+17		
Average	7.49E+17	1.21E+18	1.36E+18
% Standard Deviation	1.85%	1.29%	1.71%

structure. The reference standard provided the quantification for this work in which repeated measurements of this reference determined the analytical precision, in this case 1.85% (1 sigma). Samples A and B are analytical samples which yield the tabulated measurement and average concentration values. The variance of these latter values fall within the precision of the standard measurements insuring that instrumental variations are not distorting the measured concentrations of the Se dose. In addition, the high level of measurement precision demonstrates that SIMS is capable of detecting small differences in the Se concentration.

Optimal SIMS materials analysis requires statistical process control (SPC) procedures to insure the quality of the data. In our laboratory, SPC procedures utilize both calibration and control standards in which the calibration standard is used to quantify the sample while the control standards are used to evaluate reproducibility. Figure 4 illustrates a recent SPC plot for dopant concentration of p doped AlGaAs, over the past three months. This plot shows an approximate $\pm 3\%$ (1 sigma) precision over this time frame.

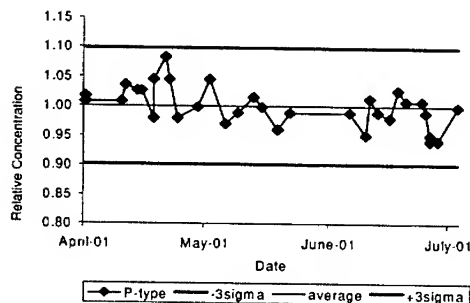


Figure 4. Relative dopant concentration of p type AlGaAs.

Table 3: Mole fraction $\text{Al}_x\text{Ga}_{(1-x)}\text{As}$

	A	B	C
	0.168	0.318	0.622
SIMS	0.173	0.332	0.621
	0.171	0.330	0.624
Avg	0.171	0.327	0.622
Std Dev	0.3%	0.8%	0.2%
RBS	0.16	0.28	0.60
XRD	0.149	0.307	0.615

A representative SIMS compositional analysis of $\text{Al}_x\text{Ga}_{1-x}\text{As}$ using a Cs^+ primary ion beam and negative secondary ion detection for three specimens having different x values is illustrated in Table 3. The SIMS data is compared to data acquired from Rutherford Backscattering Spectroscopy (RBS) and x-ray diffraction (XRD). The SIMS precision is less than 1% and the measured values correspond well with the accurate data obtained by RBS and XRD. The major advantage of the SIMS technique in this type of application is its ability to perform compositional analysis of layered structures.

Clear examples of the power of SIMS depth profiling are illustrated in Figures 5 and 6 which plot the results of a high resolution depth profile of a InP/GaAsSb/InP DHBT device using a Cs^+ primary ion beam and negative secondary ion detection. The sample had a planar structure and the relative positions and secondary ion intensities accurately map the composition of the device to a depth of 800 nanometers. High depth resolution allows dopant uniformity through thin layers to be evaluated and the location of contaminants (often at interfaces) to be determined. Figure 4 is a blow up of the central region of this depth profile illustrating the distribution of a 50nm wide C dopant from which quantitative data can be obtained.

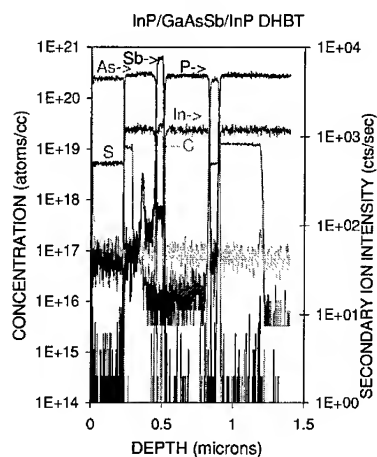


Figure 5. Sulfur and carbon profiles were collected concurrently with layer marker profiles using a 2 keV Cs primary ion beam.

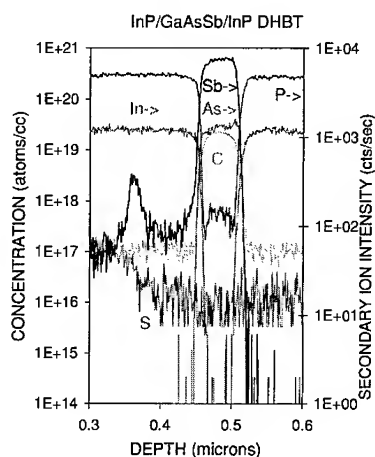


Figure 6. Detail of 50 nm C doped layer

CONCLUSIONS

State-of-the-art secondary ion mass spectrometry techniques and methods can address many of the dopant, impurity and compositional analysis issues facing the development of innovative III-V materials. The high detection sensitivity and in-depth resolution of SIMS make it one of the most powerful materials analysis techniques. The implementation of SPC protocols along with the analysis of standard materials insure a high degree of reliability in SIMS data in process monitoring applications.

REFERENCES

1. T. Bitner, E. De Chambost, P. Monsallut, B. Rasser and M. Schubmacher, "In Line SIMS Tool for Optoelectronic Device Manufacturing," *Secondary Ion Mass Spectrometry SIMS XII*, ed. A. Benninghoven, P. Bertrand, H-N. Migeon and H. W. Werner (Elsevier, 2000) pp. 731-734.
2. MCs+ in SIMS conference series
3. R. G. Wilson, F. A. Stevie and C. W. Magee, *Secondary Ion Mass Spectrometry* (Wiley & Sons, 1989).
4. C. Meyer, M. Maier and D. Bimberg, *J. Appl. Phys.* **54**, 2672.
5. S. W. Novak and R. G. Wilson, *Secondary Ion Mass Spectrometry SIMS VI*, ed. A. Benninghoven, A. M. Huber and H. W. Werner (Wiley & Sons, 1988) pp. 303-305.

Preparation of CdS/ZnO Core/shell Structured Nanoparticles by Hydrothermal Method

Chunhua Yan, Lingdong Sun, Xuefeng Fu, chunsheng Liao
State Key Laboratory of Rare Earth Materials Chemistry and Applications,
PKU-HKU Joint Laboratory on Rare Earth Materials and Bioinorganic Chemistry,
Peking University, Beijing 100871, China

ABSTRACT

CdS and ZnO capped CdS (CdS/ZnO) semiconductor nanoparticles were synthesized via hydrothermal method by thermal decomposition of the cysteine-cadmium and $\text{Zn}(\text{OH})_4^{2-}$ complex precursors. Both of the photoluminescence properties and structure characterization confirmed the core/shell structure as expected. Compared to CdS nanoparticles, the band-gap emission of CdS/ZnO was greatly improved, that means the capping layer of ZnO modified the surface of CdS and reduced the surface defects effectively. ED and XRD confirmed the formation of hexagon phased CdS and the TEM image indicated the size of CdS/ZnO was about 20 nm.

INTRODUCTION

Nanosized materials have attracted much consideration in recent years because of the unique properties different very much from the corresponding bulks [1,2]. And nanosized semiconductors have potential applications especially on novel luminescent materials. Many preparation methods have been afforded to improve the quantum efficiency [3-5]. The most successful method is inorganic shell modification, both anionic and cationic sites, are modified by the inorganic shell layer and the surface traps are removed [6-11]. The luminescence efficiency also benefits from the shell and the stability is also increased.

We reported on the formation of CdS and CdS/ZnO composite nanoparticles by hydrothermal method, which $\text{Zn}(\text{OH})_4^{2-}$ precursors was used to form ZnO capped CdS nanoparticles. These core/shell nanoparticles were characterized with florescent spectra, transmission electron microscopy (TEM), and X-ray photon spectra (XPS) to study optical properties, morphologies and structures. Compared with CdS nanoparticles, the band-gap emission of CdS/ZnO was greatly improved, that means the capping layer of ZnO modified the surface of CdS and reduced the surface defects effectively.

EXPERIMENTAL DETAILS

(1) Preparation of CdS nanoparticles

0.6 mL cadmium acetate solution was dropwised into 2.8 mL (0.005 mol/L) L-cysteine solution, and 0.15 mL (0.12 mol/L) NaOH was added to the above mixture to ensure ionization of cysteine to $^-\text{SCH}_2\text{CH}(\text{NH}_2)\text{COO}^-$, which can enhance coordination ability to Cd^{2+} . Actually, complex of $\text{Cd}-\text{SCH}_2\text{CH}(\text{NH}_2)\text{COO}^-$ is used as the precursor to form CdS

nanoparticles under hydrothermal condition. The reaction temperature and time is controlled to obtain spherical CdS nanoparticles. The resulting yellowish colloid is washed and centrifuged to remove excessive reagents.

(2) Preparation of CdS/ZnO nanoparticles

0.4 mL (0.050 mol/L) zinc chloride is diluted and pH is set to 12-13 in order to form $\text{Zn}(\text{OH})_4^{2-}$ used as precursors for ZnO capping layer [12]. It is dropwised to the Cd-SCH₂CH(NH₂)COO⁻ complex solution used in the above step. The following hydrothermal procedure and treatment is the same as the preparation of CdS nanoparticles stated above.

The fluorescent experiments were carried on a Hitachi F-4500 spectrophotometer. XPS was performed using ESCA Lab5. TEM measurement was carried on JEOL-200CX microscope operating at 200 kV. Samples for TEM observation were prepared by dipping a drop of colloid on copper grids and then they were allowed to dry at ambient conditions.

DISCUSSION

1. Formation and conformation of core/shell structured nanoparticles

(1) Morphology and structure characterization

Typical TEM images of CdS/ZnO nanoparticles prepared at 110 °C for 4 h is shown in Figure 1. Spherical particles with diameter of 20 nm were observed. Electron diffraction pattern confirmed hexagonal structured nanoparticles. But we can not distinguish the core and shell as that have been observed elsewhere [7]. The particle size does not change obviously by ZnO capping shell formation, and no extra phase was observed from X-ray diffraction for CdS/ZnO nanoparticles. It can be excluded that ZnO existed separately.

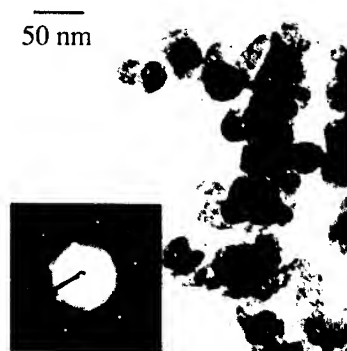


Figure1. TEM images of CdS/ZnO nanoparticles prepared at 110 °C for 4 h.

XPS is very useful in the investigation of chemical nature, i.e., valence and component of the samples. We analyzed elemental composition of CdS and CdS/ZnO nanoparticles and it also proved to be effective. Compared the XPS of the prepared CdS nanoparticles with that of the bulk, the appearance of Cd3d_{5/2} at 406.2 eV and S2p at 162.69 eV indicate the formation

of CdS. For the CdS/ZnO nanoparticles, the appearance of Cd3d_{5/2} at 404.7 eV, S2p at 160.99 eV, Zn2p_{3/2} at 1021.45 eV and O1s at 530.45 eV confirmed the existence of Cd, S, Zn and O. In our preparation procedure, S²⁻ is provided by decomposition of cysteine, but cysteine can also be oxide to S and SO₄²⁻, these species and Cl⁻ in the system will change the chemical environment of the surface of CdS nanoparticles, and led to the increase of Cd3d_{5/2} of CdS. Actually, a little amount of Cd-O bond at the interface of the CdS and capping layer ZnO existed, and Cd3d_{5/2} ranged at 404.8~405.5 eV just confirmed the formation of capping layer on the CdS nanoparticles, that is the formation of core shell structure [7].

(2) Optical properties

As we have mentioned, band edge emission is a reflection of the surface states [2]. It can be seen in Figure 2, band edge emission increased a lot for ZnO capped CdS nanoparticles. It is obviously that CdS can be formed instantly by the decomposition of Cd-SCH₂CH(NH₂)COO⁻, and Zn²⁺ appeared as Zn(OH)₄²⁻ can be adsorbed on the particle surface effectively. During the decomposition, ZnO formed and capped on CdS nanoparticles as expected. This resulted the band edge emission increased significantly.

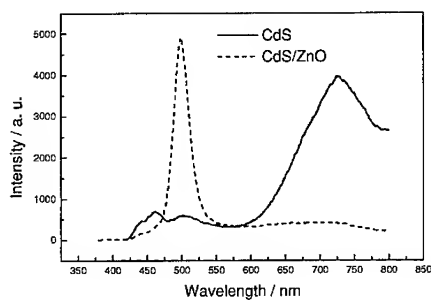


Figure 2. Photoluminescence spectra of CdS and CdS/ZnO nanoparticles prepared at 150 °C for 4 h.

2. Influence of reaction time and temperature on CdS/ZnO nanoparticles

At certain pH and reaction time, CdS/ZnO emission changed with reaction temperature is shown in Figure 3a. When the reaction temperature is 80°C, the photoluminescence of CdS/ZnO showed two separate emission bands, band edge emission at 470 nm and trap emission at 610 nm, the relative ratio is 1:1.7. As the reaction temperature increased, band edge emission increased and red-shifted with trap emission decreased. The ratio of the two emission bands increased to 4.8:1 as temperature increased to 150 °C. The relative intensity of band and trap emission mainly caused by the surface state difference. Lower temperature made the decomposition and capping much more difficult and not effective, more defects still existed. More ZnO formed as continuous capping layer on the surface of CdS nanoparticles with increasing temperature, and this made the band edge emission of CdS nanoparticles increased. The photoluminescence spectra of the samples treated at 150°C for different time is

also studied as shown in Figure 3b. Longer reaction time not only improves crystallization, but also eliminates much more surface dangling states. In fact, higher temperature and longer reaction time also increase the particle size and thus lead the band edge emission red-shift.

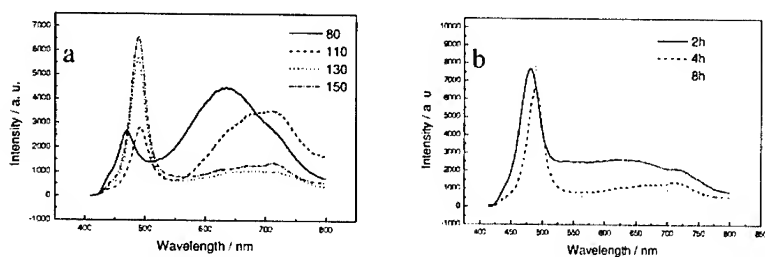


Figure 3. Photoluminescence spectra of CdS/ZnO nanoparticles prepared at (a) different temperature for 4 h and (b) 150 °C for different times.

CONCLUSIONS

$\text{Cd-SCH}_2\text{CH}(\text{NH}_2)\text{COO}^-$ and $\text{Zn}(\text{OH})_4^{2-}$ are designed as the precursors to produce CdS and ZnO capped CdS nanoparticles effectively by controlling pH and reaction conditions, which is easy to process. Capping CdS nanoparticles with ZnO layer yield a strong band edge emission, which indicate a successful and effective modification by elimination surface defects. Measurements were carried out to confirm the composition of CdS and CdS/ZnO nanoparticles.

ACKNOLEGEMENT

The author would like to thank Prof. Qinlin Guo for XPS measurements and analysis. Research is supported by NSFC (Nos. 20001002, 20023005), the State Key Project for Fundamental Research of MOST (G19980613), the foundation for University Key Teacher by MOE, and the Founder Foundation of Peking University.

REFERENCES

1. Henglein A., Chem. Rev. **89**, 1861 (1991).
2. Hasselbarth A., Eychmuller A. and Weller H., Chem. Phys. Lett. **203**, 271 (1993).
3. Tian Y., Newton T., Kotov N., Guldi D., Fendler J. J. Phys. Chem. **100**, 8927 (1996).
4. Danek M., Jensen K. F., Murray C. B., Bawendi M.G. Chem. Mater. **8**, 173 (1996).
5. Mews A., Eychmuller A., Giersig M., Schooss D., Weller H. J. Phys. Chem. **98**, 934 (1994).
6. Spahnel, L.; Haase M.; Weller H. J. Am. Chem. Soc. **109**, 5649 (1987).
7. Hoener C. F., Allan K. A., Bard A. J., Campion A., Fox M. A., Mallouk T.E., Webber S. E., White J. M. J. Phys. Chem. **96**, 3812 (1992).

8. Rodriguez-Viejo J., Jensen K. F., Mattoussi H., Michel J., Dabbousi B.O., Bawendi M.G. *Appl. Phys. Lett.* **70**(16), 2132 (1997).
9. Dabbousi B.O., Rodriguez-Viejo J., Mikulec F.V., Heine J.R., Mattoussi H., Ober R., Jensen K.F., Bawendi M.G. *J. Phys. Chem. B* **101** (46), 9463 (1997).
10. Schlamp M. C., PENG X. G., Alivisatos A. P., *J. Appl. Phys.* **82**(11), 5837 (1997).
11. Peng X. G., Schlamp M. C., Kadavanich A. V., Alivisatos A. P., *J. Am. Chem. Soc.* **119**, 7019 (1997).
12. Zhang J., Sun L. D., Pan H. Y., Liao C. S., Yan C. H., *New J Chem.*, in press.

Development of A^{II}B^{VI} Semiconductors Doped with Cr for IR Laser Application

V.A. Kasiyan, R.Z. Shneck, Z.M. Dashevsky and S.R. Rotman¹
Department of Materials Engineering, ¹Department of Electrical Engineering
Ben-Gurion University of the Negev, P.O.B. 653, Beer-Sheva 84105, Israel

ABSTRACT

Electrical and optical measurements obtained with CdSe single crystals doped with chromium from a gas source CrSe over a wide temperature range (500-1050 °C) are compared with ZnSe annealed in liquid metal (Zn). These processes are intended to control the concentrations of the impurity and intrinsic defects. The low temperature annealing of CdSe crystals in CrSe atmosphere allows obtaining high electron mobility up to 9000 cm²/Vs at 80 K and demonstrates the low native defect concentration. A high temperature annealing gives rise to increased electron concentration with decreased mobility. Optical absorption measurements show that at the high annealing temperature effective doping with Cr takes place. The impurity absorption beyond the absorption edge is interpreted by the excitation of Cr⁺⁺ and Cr⁺ deep levels.

INTRODUCTION

Compact, tunable, room-temperature, solid-state laser sources operating in the mid-IR (1.5 – 3 μm) spectral region are of interest for a number of applications such as eye safe laser radar, chemical sensing, IR counter-measures and spectroscopy. Efficient room temperature lasing has been demonstrated with Cr⁺⁺ active ions doped into II-VI chalcogenides such as ZnSe and CdSe [1, 2]. Transition metals incorporated into Zn(Cd)Se substitute metallic atoms and create deep levels in the band gap [3]. Only one strong emission at 2.67 eV is observed in the spectrum of the undoped ZnSe, which corresponds to the room temperature band gap energy in ZnSe. The luminescence of doped compounds exhibits two new bands near 2.2 and 1.4 eV corresponding to the photogeneration (Cr⁺⁺ + e_{VB} → Cr⁺) and photoionization (Cr⁺ → Cr⁺⁺ + e_{CB}) processes in ZnSe. Hence the positions of Cr⁺ and Cr⁺⁺ states were found 1.24 and 2.26 eV beneath the conduction band edge [4]. From the intensities of Cr⁺/Cr⁺⁺ related processes a relatively large capture cross section of the Cr⁺⁺ ion has been deduced.

In addition to these high energy transitions, a typical room temperature absorption spectrum of CdSe:Cr⁺⁺ reveals a peak at 1.9 μm [5] corresponding to the inter-center transition ⁵T₂ → ⁵E of Cr⁺⁺ in CdSe [6]. Mid-infrared tunable laser media based on II-VI semiconductors doped by transition metals were demonstrated in [7] based on this transition. Tetrahedrally-coordinated Cr⁺⁺ ions are especially attractive as laser centers on account of high luminescence quantum yields for emission in the 2-3 μm range. The strength of the emission depends on the concentration of the Cr⁺⁺ ions in the material. In developing of a II-VI:Cr laser material we consider two questions: (a) The total amount of the Cr dopant atoms depends on the available metallic vacancies for replacement by Cr. To investigate the vacancy replacement process we studied the annealing of ZnSe crystals in Zn melt. (b) The fraction of Cr⁺⁺ may be controlled by the free electron concentration in the crystal and its IR absorption. Annealing at different temperatures and Se vapor pressures determine the free electron concentration. In the present paper doping approached of CdSe and ZnSe crystals are investigated with the aim of optimizing

the materials for laser application. CdSe was doped with Cr and compared with ZnSe crystals annealed in Zn melt. The electronic and optical properties of the crystals were characterized.

EXPERIMENTAL DETAILS

ZnSe single crystals were grown by the high-pressure Bridgman method using ZnSe powder with a purity of 6N. All samples were cut from one as-grown ZnSe single crystal and then mechanically polished so that they have the shape of wafers with dimensions about $5 \times 5 \times 1$ mm³. CdSe crystals were grown by the Czochralski technique. Regular X-ray diffraction was used to determine the quality of crystals. The CdSe crystals have a surface orientation $\langle 0001 \rangle$ and thickness ≈ 1 mm. The *n*-ZnSe samples were prepared by long-term high temperature treatment (500 - 950 °C) of the originally high ohmic ($\rho \approx 10^{10}$ Ωcm) single crystals in zinc melt. The self diffusion coefficient is $D_{\text{Zn}} = 9.8$ (cm²/s) $\exp(-3 \text{ eV}/kT)$ [8]. Increasing of the duration of the treatment of the ZnSe crystals causes the increase of the electron concentration which reach saturation after 100 hours. Diffusion of Cr from a gaseous source (CrSe) was used for doping the CdSe specimens, allowing to maintain a constant level of surface Cr concentration during a 100 hr diffusion anneal. The selenium gaseous source generates an overpressure of Se and prevents decomposition of the crystals during the heat treatment. The concentration of Cr in CdSe crystals was varied by changing the annealing temperature between 500 to 1050 °C.

DISCUSSION

The temperature dependence of the Hall coefficient R_H and the electron mobility $R_H\sigma$ (σ is the conductivity) of ZnSe:Zn samples are shown in figures 1 and 2.

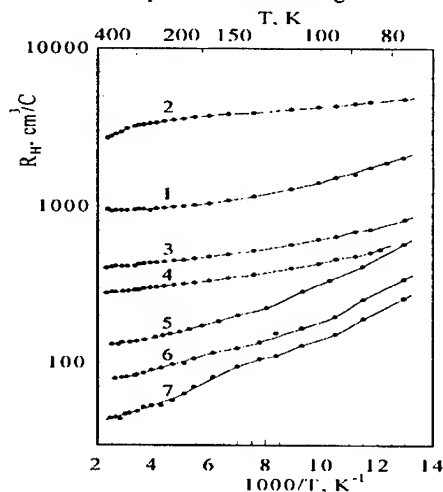


Figure 1. The temperature dependence of the Hall coefficient R_H for CdSe:Cr and ZnSe:Zn crystals annealed at different temperatures. 1- CdSe as grown, 2-4 - CdSe:Cr, 5-7 - ZnSe:Zn. Annealing temperatures: (2) 500 (3) 600, (4, 5) 700, (6) 800, (7) 950 °C.

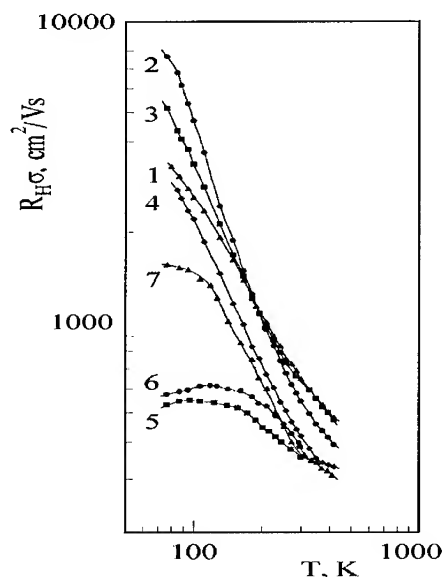


Figure 2. Hall mobility $R_H\sigma$ as a function of temperature in CdSe:Cr and ZnSe:Zn crystals. 1- CdSe as grown, 2-4 - CdSe:Cr, 5-7 - ZnSe:Zn. Annealing temperatures: (2) 500 (3) 600, (4, 5) 700, (6) 800, (7) 950 °C.

With increasing the annealing temperature, one observes increase both of the free electron concentration and of their mobility. In the low temperature range the $R_H(T)$ dependence is determined by electron activation from shallow donor states to the conduction band. The $R_H(T)$ dependence becomes weaker in the high temperature range. The donor concentration for ZnSe:Zn samples calculated by the electrical-neutrality equation reaches $N_D = 1.6 \times 10^{17} \text{ cm}^{-3}$ as the annealing temperature increases to 950 °C. The carrier concentration and therefore the concentration of donors increases with increasing of the annealing temperature, namely, the compensation ratio decreases. With temperature decrease the mobility monotonously increases in conformity with a power law (figure 2) and has a maximum only near the liquid nitrogen temperature. This indicates a combination of phonon and ion scattering. The increase of the mobility with annealing temperature indicates the decrease of electron scattering by the charged impurity ions and is caused by a decrease of the compensation.

The temperature dependence of the Hall coefficient R_H and the Hall mobility for the CdSe:Cr samples are also shown in figures 1 and 2. The Hall mobility $R_H\sigma$ in the CdSe:Cr samples annealed at low temperature (500 °C) has a high values of 9000 cm^2/Vs at 77 K and of 520 cm^2/Vs at room temperature indicating the high perfection and purity of the crystals. In the temperature range from 77 to 400 K (figure 1), the character of the $R_H = f(10^3/T)$ dependence remains similar to the ZnSe:Zn crystals and is unchanged with varying the Cr content: the Hall coefficient decreases with increasing temperature. This is caused by the activation of electrons from shallow donors (Se vacancies). The R_H dependence becomes weaker with tendency to

saturation near 400 K. Also the mobility monotonously increases in conformity with a power law, in similarity with the ZnSe crystals (figure 2).

Unlike the ZnSe:Zn crystals, the Hall coefficient and the electron mobility increase at the low treatment temperature relative to the as-grown crystal. These are explained as the result of filling of selenium vacancies by selenium from the CrSe source with a concomitant reduction of the concentration of these native defects. Doping at higher temperatures leads to a decrease of the mobility in the CdSe:Cr crystals, due to the introduction of chromium scattering centers. Indeed, the increase of chromium concentration at high doping temperatures is manifested by changes in the optical absorption.

Room temperature optical transmission near the band gap was measured for CdSe:Cr crystals annealed at different temperatures. The absorption coefficient α was calculated from the measured transmission I/I_0 , by the relation:

$$I = I_0(1 - R)^2 \exp(-\alpha d),$$

where d is the thickness of the wafer and R is the wavelength dependent reflectivity [9]. Results of the calculated α as a function of the wavelength for CdSe samples annealed at different temperatures are shown in figure 3.

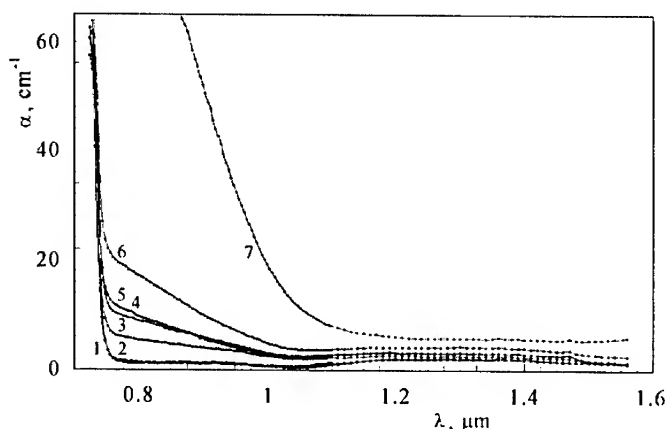


Figure 3. Optical absorption coefficient α in CdSe:Cr crystals versus wavelength for various Cr concentrations. 1- CdSe as grown, 2-7 - CdSe:Cr. Annealing temperatures: (2) 600 (3) 700, (4) 900, (5) 950 (6) 1000, (7) 1050 °C.

The doping of CdSe crystals by Cr moves the effective absorption edge to the IR range. The fundamental absorption edge does not change by doping with Cr but the absorption at energies lower than the fundamental absorption edge regularly increases with raising the annealing temperature and is remarkable after annealing at 1050 °C. This is clearly the result of the increase of Cr concentration.

CONCLUSIONS

The principal possibility to dope CdSe single crystals by Cr from gaseous CrSe source has been demonstrated. High temperature doping is the outcome of the occupation of metallic vacancies by Cr atoms thus decreasing the acceptor Cd vacancies concentration and leaving the main influence to the shallow donor Se vacancies. In these conditions the electron concentration increases to 10^{16} cm^{-3} but the electron mobility is reduced. The doping effect on carrier concentration is similar to the annealing of ZnSe crystals in Zn melt. The introduction of Cr atoms at the high doping temperatures creates strong absorption *beyond* the fundamental edge of the absorption. The magnitude of the impurity absorption grows with increasing the chromium concentration. This absorption is interpreted by the excitation of Cr^{++} and Cr^+ deep levels.

REFERENCES

1. R. H. Page, K. L. Schaffers, L.D.DeLoach, G.D.Wilke, F.D.Patel, J.B.Tassano, S.A.Payne, W.F.Krupke, K.-T.Chen, and A.Burger, IEEE J. Quantum Electron. **33**, 609 (1997).
2. K.L.Schepler, S.Kuck, and L.Shozawa, J. Lumin. **72-74**, 116 (1997).
3. S. Bnaskar, P. S. Dobal, B. K. Rai, R. S. Katiyar, H. D. Bist, J.-O. Ndup, A. Burger, J. of Appl. Phys. **85**, 439 (1999).
4. M. Godlevski and M. Kaminska, J. Phys. C **13**, 6537 (1980).
5. M. Ming Li, D. J. Strachan, T. M. Ritter, M. Tamargo and B. A. Weinstein, Phys. Rev. B **50**, 4358 (1994).
6. A. Zunger, Solid State Physics **39**, 275 (1986).
7. L. D. DeLoach, R. H. Page, G. D.Wilke, S. A. Payne, and W.F. Krupke, IEEE J. Quantum Electron. **32**, 885 (1996).
8. V. A. Kasiyan, D. D. Nedeoglo, and N. D. Nedeoglo, Phys. Stat. Sol. (b) **210**, 485 (1998).
9. W. L. Bond, J. Appl. Phys. **36**, 1674 (1965).

Oxidation Kinetics and Microstructure of Wet-Oxidized MBE-Grown Short-Period AlGaAs Superlattices

René Todt[†], Katharine Dovidenko, Alexei Katsnelson, Vadim Tokranov, Michael Yakimov, and Serge Oktyabrsky

UAlbany Institute for Materials, University at Albany-SUNY,
Albany, NY 12203, U.S.A.

[†] currently Walter Schottky Institute, Technical University Munich,
85748 Garching, Germany

ABSTRACT

The kinetics of the wet oxidation process of MBE-grown high-Al-content AlAs/Al_{0.6}Ga_{0.4}As short-period superlattices (SPSLs) was investigated and compared to AlGaAs alloys and pure AlAs. We found that alloys and superlattices (SLs) have different oxidation characteristics. These differences were attributed to traces of the superlattice structure in the oxidized material. The microstructure and chemistry of SPSLs with an equivalent composition of Al_{0.98}Ga_{0.02}As was studied, using transmission electron microscopy, energy-dispersive x-ray spectroscopy, Rutherford backscattering, and nuclear reaction analysis for hydrogen-profiling. We also report on the mechanical stability of oxidized SPSL layers in optoelectronic device structures.

INTRODUCTION

Recently, selective wet oxidation of AlGaAs alloys has gained interest for various applications in electronic and optoelectronic devices [1-3]. So far, wet oxidation has had its biggest impact on performance of AlGaAs/GaAs oxide-apertured vertical cavity surface emitting lasers (VCSELs), where devices with the lowest threshold currents and highest wall plug efficiency have been demonstrated [4]. As it is well known by now that VCSELs employing oxidized AlAs layers suffer from delamination and degradation problems [5], high-Al-content AlGaAs layers are generally preferred as wet oxidation layers. Devices employing AlGaAs alloys as wet oxidation layer were reported to be mechanically stable [5]. Also, VCSEL devices with an AlAs/GaAs superlattice (SL) oxidation layer with an equivalent Al content of 98 % were reported to be mechanically stable during post-growth processing, except for minor structural degradations on the edge of the mesa [6].

Due to the high selectivity of the wet oxidation process with respect to the Al content of the layer to be oxidized, a precise control over the composition during molecular beam epitaxy (MBE) growth of the structure is required in order to achieve reproducible oxidations [7]. The growth of high-Al-content alloys is, however, problematic with respect to reproducibility. Short-period superlattices (SPSLs), also termed digital-alloys, provide an enhanced control over the composition as compared to alloys. In addition, digital alloys of a wide variety of compositions can be grown without changing the effusion cell temperatures. Moreover, SPSLs are of great technological importance in MBE growth of optoelectronic device structures as they grow more smoothly than alloys, which is especially important when very thick structures like VCSELs with a total thickness in excess of 10 μm are grown.

This paper reports on wet oxidation kinetics, structure chemistry and mechanical stability of Al_xGa_{1-x}As SPSLs ($x = 0.90$ - 0.98), which are compared to Al_xGa_{1-x}As alloys.

EXPERIMENTAL DETAILS

The structure used for the study of the oxidation kinetics was grown by MBE on GaAs(100) substrates. The high-Al-content layers used for oxidation were 1000 Å-thick and were separated by 1000 Å $\text{Al}_{0.1}\text{Ga}_{0.9}\text{As}$ layers. The high-Al-content $\text{Al}_x\text{Ga}_{1-x}\text{As}$ layers were grown as SPSLs with equivalent Al concentrations of $x = 0.90, 0.92, \dots, 0.98$, or as alloys with $x = 0.96, 0.98$. The SPSLs were grown as periodic (3-19 ML AlAs)/(1 ML $\text{Al}_{0.6}\text{Ga}_{0.4}\text{As}$) structures with a fixed 1 monolayer thickness of the $\text{Al}_{0.6}\text{Ga}_{0.4}\text{As}$ layers.

Post growth processing started with the definition of 300 μm wide stripe mesas by standard photolithography and chemical wet etching using a solution of $\text{HCl}:\text{H}_2\text{O}_2:\text{H}_2\text{O}$ (20:1:1). Oxidations were carried out at temperatures of 350, 400 and 450 °C for 30 to 120 min in a flow of wet nitrogen at atmospheric pressure. Wet nitrogen was produced by flowing dry nitrogen at a flow rate of 2.0 slm through a bubbler filled with deionized water, which was maintained at a temperature of 93 °C. After the oxidation, the samples were cleaved and the oxidation lengths were measured using cross-sectional scanning electron microscopy (SEM).

A sample for the study of the microstructure and composition of oxidized SPSLs with an equivalent Al content of 98 % consisted of 1686 Å $\text{Al}_{0.98}\text{Ga}_{0.02}\text{As}$ layers (1ML/29MLs of $\text{Al}_{0.4}\text{Ga}_{0.6}\text{As}/\text{AlAs}$) separated by 744 Å $\text{Al}_{0.4}\text{Ga}_{0.6}\text{As}$ layers. Immediately before wet oxidation, 60 μm wide stripe mesas were etched, and oxidation was carried out at 400 °C for 90 min.

RESULTS AND DISCUSSION

Oxidation kinetics

A cross-sectional SEM image of an oxidized structure, which was used for the measurement of the oxidation lengths, is shown in Figure 1. From the measurement of the oxidation lengths as a function of oxidation time, the oxide growth was observed to proceed linearly with time and the oxidation rates were determined as plotted in Figure 2. The oxidation rates decrease with decreasing Al-content, as expected, and one can observe that the oxidation rates of SLs are significantly higher than those of alloys with the equal average Al content. This difference in the oxidation rates between SLs and alloys is decreasing with increasing oxidation temperature and they become equal within the error of the experiment at 450 °C. This observation is in agreement with a report by Pickrell et al. who observed the same trend for an AlAs/GaAs SL with an effective Al content of 98 % [6]. Using a similar model as the one developed by Deal and Grove for the oxidation of silicon [8], the linear growing oxidation length x can be described in terms of an activation energy E_A as

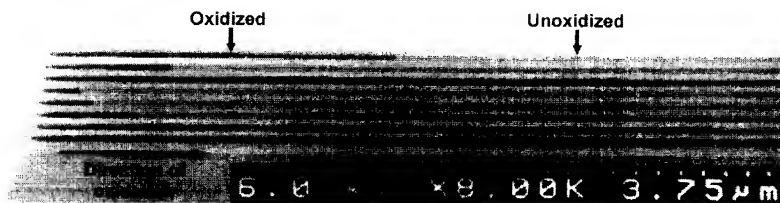


Figure 1. Cross-sectional SEM image of an oxidized multilayer structure, which contains several high-Al-content $\text{Al}_x\text{Ga}_{1-x}\text{As}$ layers. From top to bottom: $x = 0.98, 0.96$ alloys, pure AlAs, $x = 0.90, 0.92, \dots, 0.98$ SPSLs. The oxidation has been carried out at 400 °C.

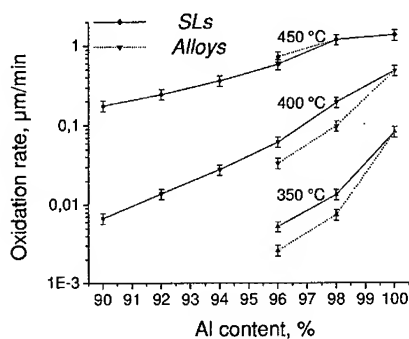


Figure 2. Oxidation rate vs. Al content.

$$x(t, T) = C t \exp\left(-\frac{E_A}{k_B T}\right), \quad (1)$$

where C is a constant. Hence, an Arrhenius plot (Figure 3) of the oxidation rate (x/t) versus the inverse of the oxidation temperature T allows to determine E_A and C (Table I). The activation energies increase with decreasing Al content and the oxidation process of a SL has a lower activation energy than that of an alloy with the equal Al content. The determined activation energies for the alloys are in good agreement with literature values [9]. Our results clearly indicate that the oxidation processes of alloys and SPSLs are not identical.

Microstructure and composition of wet-oxidized AlGaAs short-period superlattices

To gain a more thorough understanding of the wet oxidation process of SPSLs, we investigated the microstructure of an $\text{Al}_{0.98}\text{Ga}_{0.02}\text{As}$ SPSL. Figure 4 shows a cross-sectional transmission electron microscope (TEM) image of the oxidized AlGaAs SL and its interface to an adjacent unoxidized $\text{Al}_{0.4}\text{Ga}_{0.6}\text{As}$ layer. The interface (indicated by arrows in Figure 4) between the oxidized and the adjacent unoxidized layer was observed to be rough. The image also clearly shows traces of the SL structure in the oxidized layer. Certainly, the presence of an ordered structure is a significant difference between oxidized SPSLs and alloys, which can explain for the different oxidation characteristics of alloys and SLs with the equal Al content.

The wet oxidized layers are quite porous, and the reaction kinetics is usually determined by the diffusion of the reactants through the dense

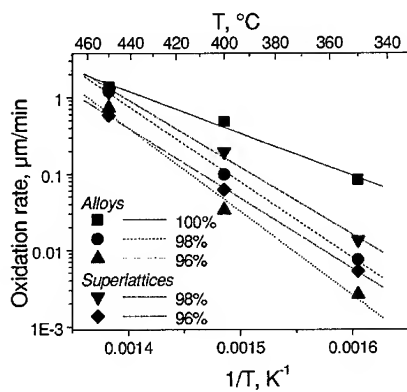


Figure 3. Arrhenius plot of the oxidation rate vs. the inverse oxidation temperature, illustrating the different temperature dependences of the wet oxidation process of SLs and alloys with the equal Al content.

Table I. Activation energies E_A and constants C as determined from an Arrhenius plot of the oxidation rates vs. the inverse temperature.

Al content	E_A , eV	C , $\mu\text{m}/\text{min}$
100 %	1.09 ± 0.11	18.0 ± 1.9
98 % alloy	1.97 ± 0.07	31.8 ± 1.1
96 % alloy	2.17 ± 0.06	34.5 ± 1.0
98 % SL	1.75 ± 0.02	28.3 ± 0.4
96 % SL	1.83 ± 0.12	28.8 ± 1.9



Figure 4. Cross-sectional bright field TEM image showing an oxidized $\text{Al}_{0.98}\text{Ga}_{0.02}\text{As}$ SPSL (upper part) and its interface (indicated by arrows) to an adjacent unoxidized $\text{Al}_{0.4}\text{Ga}_{0.6}\text{As}$ layer (lower part). Traces of the SL structure are clearly observed in the oxidized layer.

oxidation front. The properties of this oxidation front are very sensitive to the Ga content. Therefore, the presence of an ordered structure, such as the traces of the SL, provides an efficient path for diffusion of reactants (through areas without Ga) and results in an increased concentration of the oxidizing agent water at the reaction front. Hence, the oxidation rate is increased (assuming that the oxidation process is not reaction rate limited), which is in agreement with our observations at 350 and 400 °C. With increasing temperature, the diffusion through the dense oxidation front becomes faster and thus, the kinetics of the oxidation process is determined by the rate of reaction at the reaction front. Therefore, the difference in the oxidation rate of alloys and SLs with the equal Al contents will become smaller with increasing temperature until the oxidation rates of SLs and alloys finally become equal, which is also supported by our experimental results.

The oxidized $\text{Al}_{0.98}\text{Ga}_{0.02}\text{As}$ SLs have been observed to be unstable under electron beam exposure in the TEM, showing recrystallization and grain growth. This is in agreement with an earlier report in literature on the microstructure of wet oxidized AlGaAs alloys [10]. Selected area electron diffraction patterns (SADPs) taken during the observation in the TEM illustrate this crystallization process (Figure 5). At the very beginning of the observation, the SADP (Figure

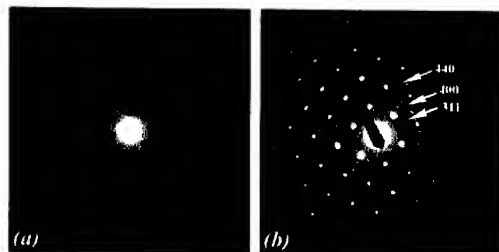


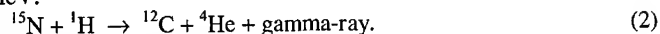
Figure 5. Selected area electron diffraction patterns from the oxidized SL showing crystallization under the electron beam. (a) At the beginning of the observation, showing an amorphous structure. (b) After several minutes of observation, showing a polycrystalline structure of cubic $\gamma\text{-Al}_2\text{O}_3$ phase.

5a) shows a diffuse pattern indicating an amorphous material. After several minutes of the electron beam exposure, a sharp ring pattern is formed (Figure 5b), corresponding to non-stoichiometric polycrystalline cubic $\gamma\text{-Al}_2\text{O}_3$ phase with a lattice constant of 7.9 Å (PDF file #74-2206).

Further investigations on the composition were carried out using energy dispersive x-ray spectroscopy (EDXS) and Rutherford backscattering (RBS). The results showed that As is evaporated upon wet oxidation and that only significant amounts of Al and O are present in the oxidized material, as was expected from

previous reports on the composition of oxidized AlGaAs alloys [10]. The composition of the oxidized $\text{Al}_{0.98}\text{Ga}_{0.02}\text{As}$ SL matches with an $\alpha\text{-Al}_2\text{O}_3$ (sapphire) standard sample within 5 %.

Also the formation of aluminum hydroxides can be expected upon wet oxidation. Nuclear reaction analysis (NRA) was employed for hydrogen profiling in the oxidized $\text{Al}_{0.98}\text{Ga}_{0.02}\text{As}$ SPSL. NRA for hydrogen was carried out using a resonant nuclear reaction of ^{15}N and ^1H at a resonance energy of 6.385 MeV:



A hydrogen depth profile was first measured for the as-oxidized sample. Subsequently, this sample was annealed at 450 °C in vacuum ($\sim 10^{-3}$ mbar) for 10 min and a second hydrogen depth profile was measured. Figure 6 shows the measured hydrogen depth profiles. In the as-oxidized sample, the hydrogen concentration in the oxidized layer was determined to be about $2 \times 10^{22} \text{ cm}^{-3}$, which corresponds to an Al-to-H ratio of about 1:0.7. After annealing in vacuum, the hydrogen concentration is reduced significantly, and the determined Al-to-H ratio is about 1:0.2. High H concentration in the as-oxidized sample is likely due to absorption of water in the porous oxide layer, though the formation of aluminum hydroxides cannot be completely ruled out. After the vacuum anneal, most of the absorbed water is evaporated, and the hydrogen concentration is determined by the chemically bound H, presumably in the form of aluminum hydroxides.

Mechanical stability of oxide-apertured VCSELs and LEDs

We used $\text{Al}_{0.96}\text{Ga}_{0.04}\text{As}$ SPSL wet oxidation layers for the fabrication of oxide-apertured AlGaAs-based VCSELs. These devices had diameters ranging from 10 to 35 μm and were oxidized at 400 °C. Oxidation lengths were varied between 4 and 10 μm . We did not observe any structural degradation of these device structures upon wet oxidation or further processing.

For the fabrication of AlGaAs-based surface-emitting LEDs, oxidation lengths in excess of 10 μm were required. We employed a 1000 Å $\text{Al}_{0.98}\text{Ga}_{0.02}\text{As}$ SPSL, which was embedded in 2 μm thick $\text{Al}_{0.1}\text{Ga}_{0.9}\text{As}$ layers, as a wet oxidation layer. Upon wet oxidation, formation of cracks was observed. These cracks originated from the wet oxidation layer and propagated towards the top of the structure (Figure 7). Also a cavity can be observed to form at the origin point of the crack. Interestingly enough, the position of the cracks were found to be independent of the oxidation length for a particular structure. For the LED structure shown in the Figure 7, the cracks always originated at 20 μm from the mesa edge, indicating the existence of a critical stress and, therefore, a critical oxidation length. Cracking occurs due to the buildup of stress caused by the shrinkage of the high-Al-concentration layer upon wet oxidation. Such structural degradations were so far known only for pure AlAs oxidation layers. We envision that the critical oxidation length is a function of the composition of the

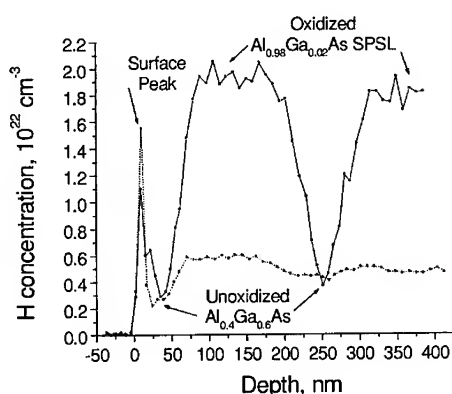


Figure 6. Hydrogen depth profiles of an as-oxidized sample (solid line) and of the same sample after annealing in vacuum (dotted line). The hydrogen concentration is strongly reduced after annealing of the sample in vacuum.

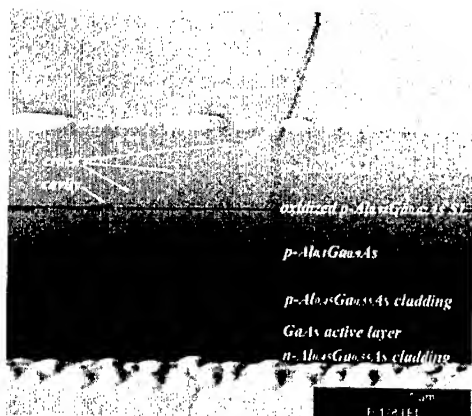


Figure 7. Focused ion beam (FIB) microscope image of the cross section of a LED structure oxidized through 40 μm . A crack (indicated by arrows) was formed upon wet oxidation and is originating from the oxidized AlGaAs SL to the surface of the structure.

found to have amorphous structure, and was recrystallized under the electron beam exposure during TEM observation to form a polycrystalline non-stoichiometric $\gamma\text{-Al}_2\text{O}_3$ phase. High hydrogen concentration (Al-to-H ratio of 1:0.7) was measured for an as-oxidized film, and we demonstrated that the hydrogen concentration was greatly reduced (3.5 times) by thermal annealing of the sample in vacuum. A critical oxidation length for the formation of cracks was observed for short-period superlattices with the equivalent composition of $\text{Al}_{0.98}\text{Ga}_{0.02}\text{As}$. Once this critical oxidation length is exceeded, cracks are formed, indicating the relaxation of the buildup stress.

ACKNOWLEDGMENT

This work has been supported by the National Focus Center for Interconnects for Gigascale Integration, funded by MARCO and DARPA.

REFERENCES

1. E. I. Chen, N. Holonyak, Jr., and S. A. Maranowski, *Appl. Phys. Lett.*, **66**, 2688 (1995).
2. F. A. Kish, S. J. Caracci, et al., *Appl. Phys. Lett.*, **59**, 1755 (1991).
3. D. L. Huffaker, D. G. Deppe, et al., *Appl. Phys. Lett.*, **65**, 97 (1994).
4. L. A. Coldren, E. Hegblom, et al., *SPIE Proc.*, **3003**, 2 (1997).
5. K. D. Choquette, K. M. Geib, et al., *Appl. Phys. Lett.*, **69**, 1385 (1996).
6. G. W. Pickrell, J. H. Epple, et al., *Appl. Phys. Lett.*, **76**, 2544 (2000).
7. J. M. Dallesasse, N. Holonyak, Jr., et al., *Appl. Phys. Lett.*, **57**, 2844 (1990).
8. B. E. Deal, and A. S. Grove, *J. Appl. Phys.*, **36**, 3770 (1965).
9. K. M. Geib, K. D. Choquette, et al., *SPIE Proc.*, **3003**, 69 (1997).
10. R. D. Twisten, D. M. Follstaedt, and K. D. Choquette, *SPIE Proc.*, **3003**, 55 (1997).

oxidation layer as well as of the geometry and mechanical properties of the whole structure. Further efforts should be applied to establish the window for the mechanically stable oxidized structures.

CONCLUSIONS

In conclusion, we characterized the kinetics of the lateral wet oxidation process of high-Al-content short-period superlattices (SPSLs), investigated the microstructure and composition of an oxidized $\text{Al}_{0.98}\text{Ga}_{0.02}\text{As}$ SPSL, and reported on the mechanical stability of VCSELs and LEDs with an AlGaAs SPSL oxide aperture. The differences in the oxidation kinetics of SLs and alloys were explained by the presence of traces of the SL structure in the oxidized SPSL layer, which results in a higher oxidation rate of the SPSLs. The oxidized layer was

Radiation Detectors and Effects

Space Radiation Effects in Advanced Solar Cell Materials and Devices

R. J. Walters and G. P. Summers
US Naval Research Laboratory, Washington, DC 20375
S. R. Messenger
SFA, Inc., Largo, MD 20000

ABSTRACT

An investigation of the physical mechanisms governing the response of III-V based solar cells to particle irradiation is presented. The effect of particle irradiation on single and multijunction solar cells is studied through current vs. voltage, spectral response, and deep level transient spectroscopy measurements. The basic radiation response mechanisms are identified, and their effects on the solar cell electrical performance are described. In particular, a detailed analysis of multijunction $\text{In}_x\text{Ga}_{1-x}\text{P}/\text{In}_y\text{Ga}_{1-y}\text{As}/\text{Ge}$ devices is presented. The MJ cell response is found to be more strongly affected by the internal cell structure than by the In content.

INTRODUCTION

This invited talk will give a brief tutorial on the effects of the space radiation environment on the electrical properties of advanced photovoltaic materials and devices. Solar cells are the basis of nearly all spacecraft power systems. The space market for commercial communications as well as military and scientific applications is driving rapid development of new solar cell technologies to provide increased power. In particular, the approach of multijunction (MJ) solar cells, where bandgap engineering is employed in layering several semiconductor junctions in a monolithic stack, has rapidly matured, attaining record, one-sun, air-mass-zero efficiencies close to 30% [1]. However, for these advanced technologies to operate efficiently in space, they must be resistant to the harsh space radiation environment. This paper will begin with a discussion of the basic mechanisms of radiation damage in solar cell materials. The talk will then describe the physics of multijunction solar cells and show how these advanced devices respond to radiation exposure. In keeping with the general symposium theme, the presentation will focus on the InGaAs and related material systems.

BASIC RADIATION DAMAGE MECHANISMS

As an energetic particle passes through the atomic lattice of a material, it transfers energy to the lattice through ionizing events in which electrons in the lattice are temporarily excited to higher energy levels and nonionizing events in which collisions between the incident particle and target atoms results in displacement of atoms in the lattice. In terms of solar cell radiation-induced degradation, ionization has little effect. It is the permanent displacement damage produced by nonionizing events that degrades the device electrical performance. A calculation of the amount of energy lost to nonionizing events (i.e. the nonionizing energy loss (NIEL)) by a proton and an electron incident upon GaAs as a function of the incident particle energy is shown in Fig. 1 [2]. The calculated NIEL values show protons to be much more damaging with the amount of damage increasing as the energy decreases until the threshold for

atomic displacement is reached. For electrons, on the other hand, the amount of displacement damage decreases as the energy decreases.

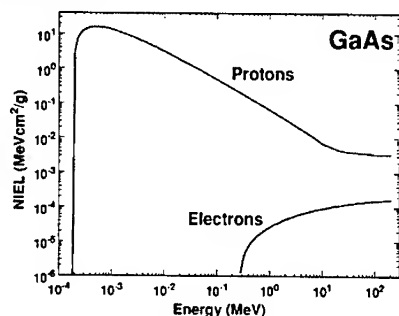


Figure 1. Calculated nonionizing energy loss (NIEL) for electrons and protons incident upon GaAs

Considering a solar cell in a space radiation environment, the primary radiation effect is the creation of point defects or defect complexes that form energy levels within the semiconductor bandgap. An example of a radiation-induced defect spectrum as measured in an InP solar cell after proton irradiation using deep level transient spectroscopy (DLTS) is shown in Fig 2 [3]. Each peak in the DLTS spectrum corresponds to a specific defect energy level acting as a trapping center for free charge carriers. A positive peak indicates a majority carrier trap and a negative peak indicates a minority carrier trap.

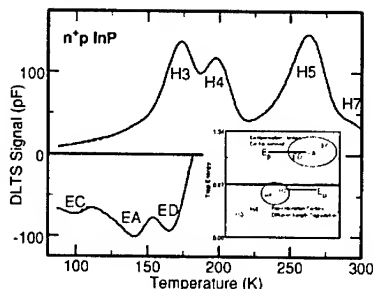


Figure 2. Deep level transient spectroscopy (DLTS) measurements made on an InP solar cell after irradiation. The positive peaks indicate a majority carrier trap, and the negative peaks indicate capture of a minority charge carrier. The inset indicates the location of the defect levels within the InP bandgap.

The effects of the radiation-induced defects on the solar cell electrical characteristics depend on the location of the defect energy level within the bandgap. Those defect levels lying nearer to mid-gap, like the defect levels labeled H4 and H5 in the spectrum of Fig. 2, tend to act as free charge carrier traps and recombination centers. The presence of such defect levels reduces the minority carrier lifetime (τ) and diffusion length (L). The decrease in L with the introduction of defects is given by [4]:

$$\frac{1}{L^2(D_d)} = \frac{1}{L_0^2} + \sum \frac{\sigma_i v_{ti}}{D} D_d = \frac{1}{L_0^2} + \kappa_L D_d \quad \text{Equ (1)}$$

where L_0 is the preirradiation value of L , σ_i is the minority carrier capture cross section of the i^{th} recombination center, I_{ti} is the introduction rate of the i^{th} recombination center, v is the thermal velocity of the minority carrier, D is the diffusion coefficient, and D_d is the displacement damage dose, which is given by the product of the particle fluence and the NIEL [5]. As shown in Eq. (1), the specific parameters for each defect are typically lumped into a single damage coefficient, κ_L . An example of measured diffusion length data and a fit of the data to Eq. (1) is shown in Fig. 3.

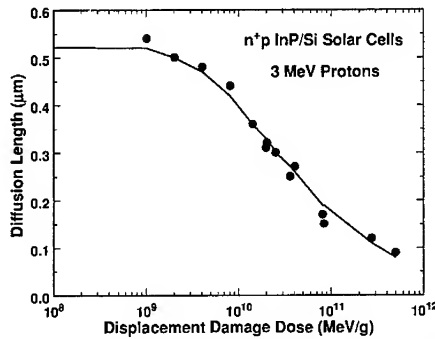


Figure 3. Degradation of the minority carrier diffusion length, L , in an InP solar cell due to proton irradiation. The line represents a fit of the data to Equ 1.

Those defects lying closer to one of the bands tend to act as majority charge carrier traps. The capture of a majority carrier can cause compensation of the material thus reducing the carrier concentration. This is referred to as carrier removal and such trapping centers are referred to as compensation centers. Carrier removal effects emerge when the radiation-induced defect concentration is on the order of the dopant concentration. Since solar cells typically have dopant levels $>10^{16} \text{ cm}^{-3}$, carrier removal effects are usually not seen until relatively higher irradiation levels. In the case of InP, the minority carrier traps labeled EA, EC, and ED (Fig. 4) have been shown to be compensation centers. A demonstration of the evolution of the carrier concentration under irradiation is shown in Fig. 4, where electrochemical capacitance (ECV) profiling has been used to measure the carrier density in an n^+p InP solar cell after increasing levels of irradiation [6]. The irradiation causes the carrier concentration in the p -type material to be reduced until the material is actually type converted and driven n -type.

BASIC RADIATION DAMAGE MECHANISMS

In this section, the radiation damage mechanisms discussed in the preceding section will be related to the degradation of the electrical output of a solar cell. The primary method for characterizing the output of a solar cell is by measuring the current vs. voltage (IV) curve under simulated solar light. An example of an IV curve measured on a single-junction InP solar cell is shown in Fig. 5. The standard IV parameters extracted from these data are the short circuit current, I_{sc} ; the open circuit voltage, V_{oc} ; and the maximum power, P_{mp} . The sunlight to

electricity conversion efficiency (Eff) is determined by dividing Pmp by the incident solar power. In this paper, all measurements were made under extraterrestrial simulated solar light, i.e. air mass zero (AM0), at one sun intensity, 136.7 mW/cm². The final IV parameter to introduce is the fill factor (FF), which is given by the ratio of Pmp to the product of Isc and Voc and gives a measure of how square the IV curve is. The closer the FF is to unity, the higher the quality of the solar cell junction.

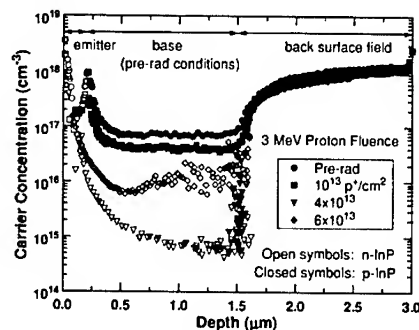


Figure 4. Electrochemical capacitance (ECV) profile of an n+p InP solar cell after proton irradiation. The radiation-induced defects act as compensation centers the deplete and then typ-convert the p-type base region.

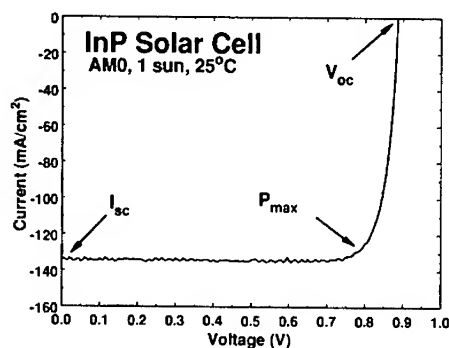


Figure 5. Current vs. voltage (IV) curve measured on an InP solar cell indicating the standard IV parameters used to characterize the solar cell electrical output.

When a solar cell is exposed to particle irradiation, the IV parameters degrade. As an example, the decrease in the PV parameters of the InP solar cell of Fig. 5 due to proton irradiation is shown in Fig. 6. For proton fluences up to about $1 \times 10^{13} \text{ cm}^{-2}$, each of the IV parameters shows steady degradation. This degradation is due almost entirely to a reduction in the minority carrier diffusion length. As the diffusion length degrades, less of the photogenerated charge carriers are able to transit the material to be collected, so Isc degrades. At the same time, an increase in the concentration of recombination/generation centers in the

depletion region causes an increase in the junction dark current, which degrades V_{oc} . The voltage and current degradation leads to degradation of P_{mp} and FF.

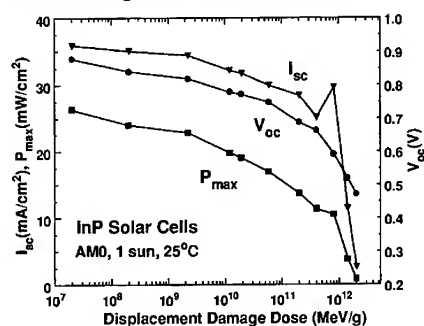


Figure 6. Degradation of the IV parameters of an InP solar cell under irradiation.

After irradiation to fluences above $1 \times 10^{13} \text{ cm}^{-2}$, significantly different behavior is observed. While V_{oc} continues to degrade in a fashion similar to that observed at lower fluences, I_{sc} shows a large increase followed by a decrease to essentially zero. As a result, P_{mp} experiences a small plateau region followed by a sharp plummet to zero. These effects are caused by carrier removal in the base region. As shown in Fig. 4, at higher fluence levels, the irradiation causes a marked decrease in the base carrier concentration resulting in an increased depletion region width until the entire base region is eventually depleted. In this condition, the carrier collection is entirely by drift along the depletion region electric field, which is much more efficient than collection by diffusion through the bulk material, especially under the condition the reduced carrier lifetime. Therefore, I_{sc} shows an increase. However, the increased size of the depletion region also results in increased recombination/generation dark current, which degrades V_{oc} . When the base material is eventually type converted, the junction is essentially destroyed, and the solar cell stops working. In addition to explaining the solar cell behavior after irradiation to high fluence levels, these results also highlight the influence that the solar cell structure can have on the device radiation response. This will be important in the discussion of multijunction solar cell response below.

BASIC MULTIJUNCTION SOLAR CELL STRUCTURE

A multijunction (MJ) solar cell is a structure, which consists of a monolithic stack of several semiconductor materials with different bandgaps. The layers are interconnected via tunnel diodes. In this configuration, the voltages of each individual junction add while the current is limited by the junction with the smallest photocurrent. The goal in designing a MJ solar cell is to choose the bandgap combination for maximum electrical conversion of the incident sunlight. A calculation of theoretical efficiencies for a two-junction device as a function of the top and bottom material band gap is shown in Fig. 7. From these calculations it is seen that even with only a two-junction device, efficiencies above 32% are theoretically achievable. However, since these are monolithic devices, the choice of material systems is constrained to ones that allow for high quality growth of one layer upon the other.

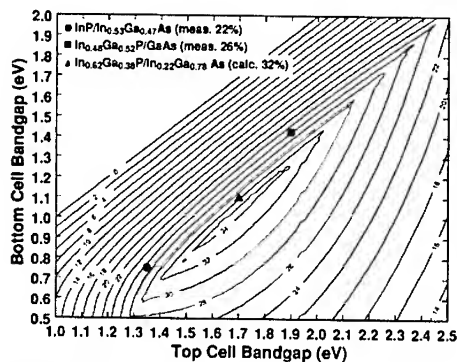


Figure 7. Calculated 1 sun, AM0 efficiency of a dual-junction solar cell as a function of top and bottom cell bandgap.

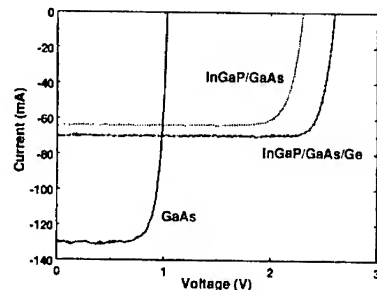


Figure 8. Example IV curves a single-junction GaAs/Ge and a dual and triple junction InGaP₂/GaAs/Ge solar cells.

By far the greatest success has been achieved with the dual and triple junction InGaP₂/GaAs/Ge system. Representative IV curves from a one-junction GaAs/Ge, two-junction InGaP₂/GaAs/Ge, and three-junction InGaP₂/GaAs/Ge cell are shown in Fig 8. Comparing these curves shows how the addition of the InGaP₂ top junction limits the current but boosts Voc by almost 1.3 V resulting in a net increase in power output. Adding a junction in the Ge bottom layer further boosts the voltage by nearly 0.3 V. Since Ge has a relatively low bandgap, the Ge sub-cell typically produces sufficient photocurrent to not limit the overall device current. The current state-of-the-art for the three-junction device has efficiencies approaching 27% (1-sun, AM0) [7].

Efforts to develop higher powered devices include the development of an appropriate 1-eV bandgap material for a forth junction as described in [8]. Other efforts are focused on applying the concept of bandgap engineering to achieve a bandgap combination that is better tuned to the AM0 spectrum (see Fig. 8). Leveraging on the success of the InGaP₂/GaAs/Ge technology, the In_xGa_{1-x}P/In_yGa_{1-y}As/Ge system is being developed at several laboratories [1,9]. These material system is showing very good results as ongoing improvements in lattice mismatched and strained layer growth techniques are significantly relaxing the lattice matching requirement [10]. Spectral response data measured in In_xGa_{1-x}P/In_yGa_{1-y}As/Ge MJ devices at two stoichiometries are shown in Fig. 9. Spectral response is a measurement of the device

response to monochromatic light. Increasing the In content within each subcell, i.e. increasing x and y , decreases the bandgap thus extending the absorption range. This results in increased photo-absorption and, hence, photocurrent, but it also results in reduced voltages. It is balancing these competing effects that yields the stoichiometry that is optimized for a given input spectrum. In addition, the effect of an increased In concentration on the cell radiation response must be considered. This aspect will be investigated in the remainder of the paper.

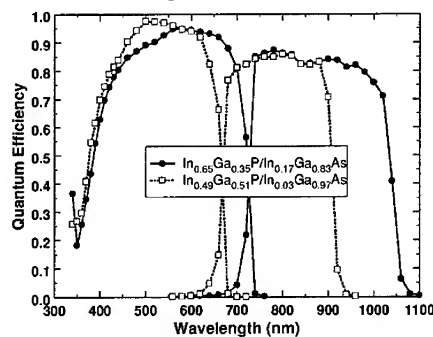


Figure 9. Example spectral response curves a dual-junction $\text{In}_x\text{Ga}_{1-x}\text{P}/\text{In}_y\text{Ga}_{1-y}\text{As}$ solar cells at two stoichiometries.

MULTIJUNCTION SOLAR CELL RADIATION RESPONSE

An example of the radiation response of MJ $\text{InGaP}_2/\text{GaAs}/\text{Ge}$ devices in both a two and a three-junction configuration is shown in Fig 10 along with data from a single junction GaAs/Ge device for comparison [11,12]. Comparing the data on an absolute scale (Fig 10a) shows that clear advantage of the MJ devices, as the MJ cells produce significantly higher power both before and after irradiation. Comparing Fig 10 with Fig. 6, the MJ cell response is seen to be controlled primarily by diffusion length degradation. Comparing the data on a normalized scale (Fig 10b) shows the degradation characteristics of the three technologies to be similar with the MJ devices showing higher radiation resistance.

The mechanisms for the MJ cell radiation response stems from the monolithic nature of the MJ device. Since the current of a MJ device is limited by the smallest photocurrent of the three sub-junctions, the most radiation sensitive sub-junction generally controls the radiation response. To show this explicitly, the spectral response of an $\text{InGaP}_2/\text{GaAs}/\text{Ge}$ three-junction cell after proton irradiation is considered (Fig 11). The integral of each of these curves with the incident spectrum yields the photocurrent. Given the wide absorption range of the Ge sub-cell, it produces significantly more photocurrent than the top two junctions, even after irradiation, so it does not limit the current. The photocurrents of the top two sub-cells, on the other hand, are quite closely matched in the as-grown device. The as-grown condition is referred to as beginning-of-life (BOL). Indeed, current matching is the condition for maximum power output, and this device was specifically designed to achieve current matching at BOL. However, under irradiation, the GaAs sub-cell degrades much faster than the InGaP_2 sub-cell so that it limits the current. This explains the similarity in the normalized radiation degradation curves (Fig 10b), since in each of the three configurations, it is the GaAs junction that controls the radiation response.

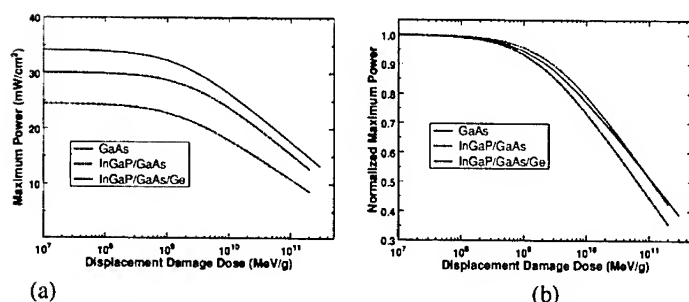


Figure 10. Radiation-induced degradation of single-junction GaAs/Ge and dual and triple-junction GaInP₂/GaAs/Ge solar cells considered on an absolute (a) and a normalized scale (b).

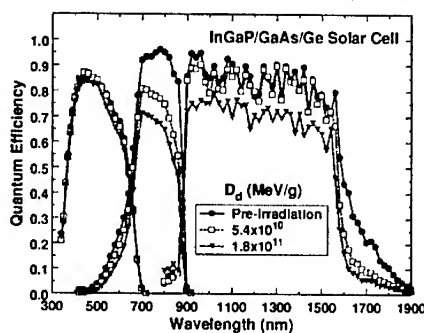


Figure 11. Radiation-induced degradation of spectral response of a triple-junction GaInP₂/GaAs/Ge solar cell.

The improved radiation resistance of the MJ cells over the single-junction GaAs cells can be explained through current matching. While the cell of Fig. 11 was designed to be current matched at BOL, the cell can also be designed to be current-matched after irradiation. The after irradiation condition is referred to as end-of-life (EOL). Since the GaAs cell degrades more rapidly, a current matched cell at EOL will be top cell limited at BOL. This will sacrifice some of the BOL power but result in optimum EOL performance. Some ways of attaining a top-cell limited device include thinning the top cell, decreasing absorption in the interconnecting tunnel junction, and extending the GaAs sub-cell absorption range. When top-cell limited at BOL, the degradation of a MJ cell will be controlled by the more radiation resistant InGaP₂ top-cell until a specific irradiation level is reached where the photocurrent of the GaAs sub-cell is degraded to the level of the top-cell leaving the device current matched. The challenge, then, is to engineer the cell structure so that the radiation level corresponding to current matching coincides with the predicted radiation level of a specific space mission.

RADIATION RESPONSE OF $\text{In}_x\text{Ga}_{1-x}\text{P}/\text{In}_y\text{Ga}_{1-y}\text{As}/\text{Ge}$ MJ SOLAR CELLS

Since the GaAs sub-cell has been shown to be the most radiation sensitive within the $\text{InGaP}_2/\text{GaAs}/\text{Ge}$ stack, significant research is being dedicated to understanding the radiation response of single-junction $\text{In}_y\text{Ga}_{1-y}\text{As}$ devices for application in the $\text{In}_x\text{Ga}_{1-x}\text{P}/\text{In}_y\text{Ga}_{1-y}\text{As}/\text{Ge}$ system. [9,13,14]. The radiation response of several configurations of this cell type is shown in Figs. 12a-c. For Dd levels up to $\sim 10^{10}$ MeV/g, the P_{mp} degradation for all of the $\text{In}_y\text{Ga}_{1-y}\text{As}$ cells is nearly equivalent to that of a conventional GaAs cell (i.e. with $y=0$). This is quite a high exposure level, being roughly equivalent to a one-year mission in the heart of the Earth's proton belts. This indicates the radiation resistance of the $\text{In}_y\text{Ga}_{1-y}\text{As}$ cells to be relatively insensitive to changes in the value of y .

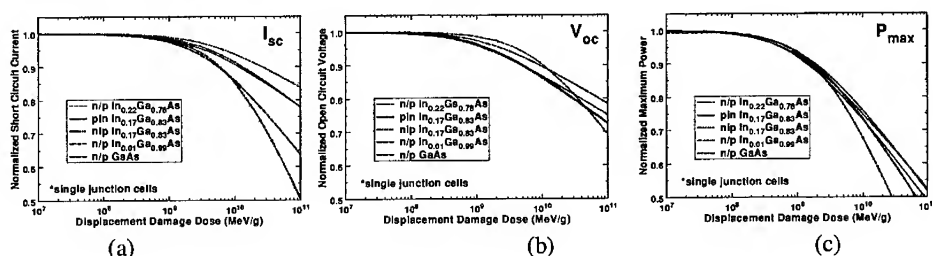


Figure 12. Radiation-response of several single-junction $\text{In}_y\text{Ga}_{1-y}\text{As}$ solar cells.

Some variation in cell response amongst the different technologies is observed at higher Dd levels. In particular, the 22% In cells showed a rapid decrease in voltage (Fig 12b) and current (Fig 12c) for $\text{Dd} > 5 \times 10^9$ MeV/g. Measurements showed the V_{oc} degradation to be due to a more rapid radiation-induced increase in dark current in the 22% In cells. This may be a direct result of the higher In content in those cells and, hence, lower band-gap and larger lattice mismatch. However, the I_{sc} response suggests that differences in cell structure also significantly impact the radiation response. The 17% In cells, which were of a p-i-n and n-i-p structure, displayed a much better blue response before irradiation, which was nearly insensitive to the irradiation, and after irradiation, those cells showed a better spectral response at nearly all wavelengths (Fig 13). This can be explained by the enhanced collection efficiency afforded by the intrinsic layer of these cells and to a better front and rear interface passivation scheme. From these results, it can be concluded that, within the range of In concentrations studied, the response of these cells are more strongly controlled by the cell structure than the In concentration.

The radiation response of several dual junction $\text{In}_x\text{Ga}_{1-x}\text{P}/\text{In}_y\text{Ga}_{1-y}\text{As}$ devices are shown in Fig 12. The device with $y = 0.49$ and $x = 0.0$ is an EOL optimized cell developed under the ManTech program [11]. Except for the $\text{In}_{0.65}\text{Ga}_{0.35}\text{P}/\text{In}_{0.17}\text{Ga}_{0.83}\text{As}$ cell in the n/p structure, the cells show generally similar radiation characteristics, independent of the In concentration. This is especially significant in the case of $y = 0.35$, $x = 17$ device, considering the large difference in In concentration and the top cell configuration. The n/p $\text{In}_{0.65}\text{Ga}_{0.35}\text{P}/\text{In}_{0.17}\text{Ga}_{0.83}\text{As}$ cell was optimized for terrestrial use under AM1.5 illumination, so the middle cell base thickness and dopant level were larger than optimal for good radiation resistance. These results are similar to those of the single junction $\text{Ga}_y\text{In}_{1-y}\text{As}$ cells, and again suggest that the cell structure may have considerably more affect on the radiation response than the In concentration.

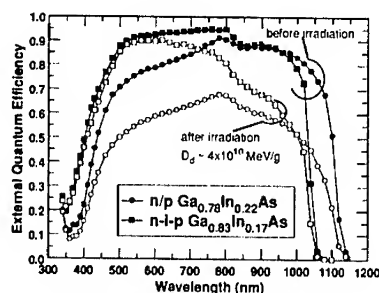


Figure 13. Radiation-response of the spectral response of two single-junction $\text{In}_y\text{Ga}_{1-y}\text{As}$ solar cells.

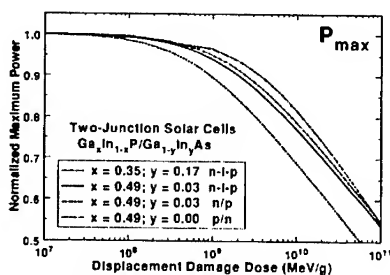


Figure 14. Comparison of the radiation-response of several dual junction $\text{In}_x\text{Ga}_{1-x}\text{P}/\text{In}_y\text{Ga}_{1-y}\text{As}$ solar cells.

The advantages of the EOL optimized $\text{InGaP}_2/\text{GaAs}$ can be seen through a study of the I_{sc} response of the cells (Fig. 13). At low D_d levels, the I_{sc} of the EOL optimized cell is limited by the top cell, and as such, degrades little since the top cell is quite resistant to irradiation. As the bottom cell degrades at higher D_d levels, the dual-junction device transitions to being bottom cell limited. At this point, the dual-junction I_{sc} degradation curve turns over and rapidly degrades down to the level of the other cells.

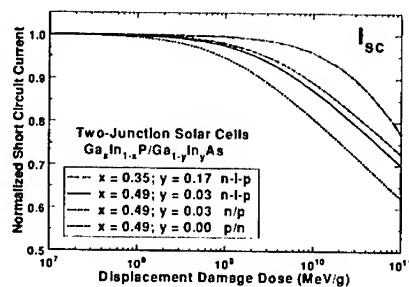


Figure 15. Comparison of the radiation-response of I_{sc} in the $\text{In}_x\text{Ga}_{1-x}\text{P}/\text{In}_y\text{Ga}_{1-y}\text{As}$ solar cells of Fig 12.

These results clearly demonstrate that, like the InGaP₂/GaAs technology, the Ga_xIn_{1-y}As sub-cell cell primarily controls the radiation response of the MJ Ga_xIn_{1-x}P/Ga_yIn_{1-y}As devices. In Fig. 14, the normalized degradation of the I_{sc} of the Ga_xIn_{1-x}P top and Ga_yIn_{1-y}As bottom cells are shown independently. These data were calculated by integrating the spectral response of each subcell over the energy dependence of the AM0 spectrum. The degradation of all the Ga_xIn_{1-x}P cells can be seen to be small up to high damage levels, independent of the stoichiometry. The Ga_{1-x}In_xAs cells, on the other hand, degrade significantly. Also, a significant difference is observed in the degradation of the different Ga_{1-x}In_xAs bottom cells. Since two cell structures, each with y = 0.03, show significantly different behavior, this difference cannot be attributed only to the cell stoichiometry. Again, the cell response appears to be more strongly controlled by the cell structure. The n-i-p Ga_{0.97}In_{0.03}As sub-cell benefits from the increased carrier collection efficiency afforded by the extended electric field of the intrinsic region. Also, in contrast to the n-i-p Ga_{0.97}In_{0.03}As, which was designed for AM0 operation, the n/p Ga_{0.97}In_{0.03}As cell was designed from AM1.5 operation, so the base dopant level was relatively high in that cell ($\sim 2 \times 10^{17} \text{ cm}^{-3}$), which results in a lower radiation resistance.

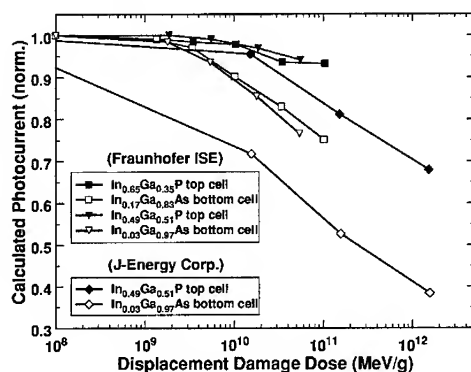


Figure 16. Comparison of the radiation-response of photocurrent of the top and bottom cells of the the In_xGa_{1-x}P/In_yGa_{1-y}As solar cells of Figs 12 and 13.

CONCLUSIONS

In this paper, an comprehensive analysis of the radiation response characteristics of III-V multijunction solar cells has been presented. The basic mechanisms governing the cell radiation response have been identified, and their impact on the cell electrical performance has been described. Results on the electrical performance and radiation hardness of tandem solar cells from the new lattice mismatched Ga_xIn_{1-x}P/Ga_yIn_{1-y}As material combination has been presented. It was shown that despite the lattice mismatch, excellent, multijunction photovoltaic devices can be produced with these material systems. Contrary to initial speculation, the radiation-response of the Ga_yIn_{1-y}As-based devices is quite good and essentially independent of In content. Instead, it is the cell structure that more significantly controls the radiation-response, and it has been shown how the cell structure may be optimized for maximum BOL and EOL performance that is equal to or better than conventional Ga_{0.49}In_{0.51}P/GaAs cells.

REFERENCES

- [1] R.R. King, N.H. Karma, J.H. Ermer, M. Haddad, P. Colter, T. Isshiki, H. Ion, H.L. Cotal, D.E. Joslin, D.D. Krut, R. Sudharsanan, K. Edmondson, B.T. Cavicchi, and D.R. Lillington, "Next-Generation, High-Efficiency III-V Multijunction Solar Cells", *Proceedings of the 28th Photovoltaic Specialists Conference*, Anchorage, AK, September, 2000, p. 998.
- [2] S.R. Messenger, E.A. Burke, G.P. Summers, M.A. Xapsos, R.J. Walters, E.M. Jackson, and B.D. Weaver, "Nonionizing Energy Loss (NIEL) for Heavy Ions", *IEEE Transactions on Nuclear Science* 46, 1595 (1999).
- [3] R.J. Walters and G.P. Summers, "Deep Level Transient Spectroscopy Study of Proton-Irradiated p-Type InP", *J. Appl. Phys.* 69, 6488 (1990).
- [4] H.Y. Tada, J.R. Carter, Jr., B.E. Anspaugh, and R.G. Downing, *Solar Cell Radiation Handbook*, 3rd Edition, JPL Publication 82-69, 1982.
- [5] G.P. Summers, E.A. Burke, and M.A. Xapsos, "Displacement Damage Analogs to Ionizing Radiation Effects", *Radiation Measurements*, 24, 1 (1995)
- [6] S.R. Messenger, E.M. Jackson, E.A. Burke, R.J. Walters, M.A. Xapsos, and G.P. Summers, "Structural Changes in InP/Si Solar Cells Following Irradiation with protons to Very High Fluences", *J. Appl. Phys.* 86, 1230 (1999).
- [7] See product literature from the three major US multijunction cell vendors at www.spectrolab.com, www.emcore.com, and www.tecstar.com.
- [8] J.M. Olson, J.F. Geisz, S.R. Kurtz, and A.G. Norman, "1-eV semiconductors for multijunction solar cells", this conference.
- [9] S.R. Messenger, R.J. Walters, G.P. Summers, A.W. Bett, F. Dimroth, C. Baur, M. Meusel, T. Takamoto, T. Agui, M. Imaizumi, and S. Matsuda, "Radiation Response Analysis of Triple Junction InGaP/InGaAs/Ge Solar Cells", *Proceedings of the 17th European Photovoltaic Science and Engineering Conference*, Munich, Germany, October, 2001.
- [10] J.A. Carlin, S.A. Ringel, and E.A. Fitzgerald, "Impact of GaAs Buffer Thickness on Electronic Quality of GaAs Grown on Graded Ge/GeSi/Si Substrates", *Appl. Phys. Lett.* 76, 1884 (2000).
- [11] D. C. Marvin, Aerospace Report: TOR-00(1210)1
- [12] B. E. Anspaugh, Proc. 22nd IEEE Photovoltaic Specialist Conference, Las Vegas, NV, Oct. 1991, p. 1593
- [13] R.J. Walters, S.R. Messenger, G.P. Summers, A.W. Bett, F. Dimroth, R.W. Hoffman, Jr., M.A. Stan, T. Takamoto, E. Ikeda, M. Imaizumi, O. Anzawa, and S. Matuda, "Radiation Response of Ga_xIn_{1-x}As Solar Cells", *Proceedings of the 16th European Photovoltaic Science and Engineering Conference*, Glasgow, United Kingdom, May, 2000.
- [14] F. Dimroth, A.W. Bett, R.J. Walters, G.P. Summers, S.R. Messenger, T. Takamoto, E. Ikeda, M. Imaizumi, O. Anzawa, and S. Matsuda, "Radiation Response of Dual-Junction Ga₃In₁₋₃P/Ga_{1-x}In_xAs Solar Cells", *Proceedings of the 28th Photovoltaic Specialists Conference*, Anchorage, AK, September, 2000, p. 1110

THERMAL ANNEAL EFFECTS ON CARBON-HYDROGEN LVMs IN AlGaN

M. O. Manasreh*, and B.D. Weaver**

*Department of Electrical and Computer Engineering, University of New Mexico,
Albuquerque, New Mexico 87131

**Naval Research Lab, 4555 Overlook Ave, SW, Washington, DC 20375

ABSTRACT

Thermal annealing effects on carbon-hydrogen (C-H) complexes defects in AlGaN grown on sapphire by metalorganic chemical vapor deposition (MOCVD) technique have been investigated using Fourier transform infrared spectroscopy (FTIR). The CH complexes in AlGaN, formed either during growth or by proton irradiation, exhibit five local vibrational modes (LVMs) due to the symmetric and asymmetric vibrational stretching modes of C-H in CH_n ($n=1-3$) defect complexes. It was found that the annealing temperature (T_a) of 500°C is sufficient enough to dissociate most of the C-H complexes in AlGaN samples. A turning point annealing temperature is found around 300°C for un-irradiated Mg-doped sample, below which the total integrated area of the C-H LVMs continued to increase with increasing annealing temperature and reach the maximum value around 300°C. At $T_a > 300^\circ\text{C}$, the total integrated area of the C-H LVMs starts to decrease and the C-H complexes seem to be completely depleted at $T_a > 600^\circ\text{C}$. The depleted C-H LVMs were observed to partially recover after thermal annealing at $T_a > 500^\circ\text{C}$ and waiting for aging periods of several days. This recovery behavior is explained in terms of the hydrogen being remained inside the crystal after the dissociation of C-H complexes, subsequent diffusion and recombining again with carbon atom to reform C-H complexes.

INTRODUCTION

Optoelectronic devices based on III-nitrides and their ternary alloys have a broad range of application due to their wide direct band-gaps covering the spectral range from visible to ultraviolet. GaN has unique applications in blue, green and ultraviolet-blue light-emitting diodes, detectors and laser diodes [1-4]. III-nitride material system also shows tremendous potential in the field of high-temperature and high-power electronics because of their superior materials parameters [5]. Omnipresent impurities such as carbon, hydrogen and oxygen play detrimental and beneficial roles in fabrication processes. For example, hydrogen can passivate the acceptor Mg [6-8] in GaN. Hydrogen can be easily incorporated into III-nitride during or after the growth of the materials [8]. Ion irradiation represents a very attractive tool for several technological steps, such as electrical and optical selective-area doping, dry etching and electrical isolation, in III-nitride based devices' fabrication. Compare to the understanding of ion beam process in mature semiconductors (i.e. Si and GaAs), the understanding of the complex ion beam process in III-nitrides is still at its infancy. Therefore, understanding of thermal annealing behavior of complexes defects will help the understanding of dopant incorporation and application of ion implantation.

In this paper, we report on some results of thermal annealing behavior of C-H complexes defects formed unintentionally or by proton irradiation in AlGaN. The evolutions of C-H LVMs

in proton irradiated sample as a function of thermal annealing and the aging effect of the sample annealed at $T_a > 500^\circ\text{C}$ are presented.

EXPERIMENT DETAILS

Furnace rapid thermal annealing was performed on three samples to investigate the thermal annealing behavior of C-H complexes in as-grown and proton irradiated AlGa_{0.4}N. All the samples used in this study were grown on sapphire substrate with AlN buffer layer using the MOCVD technique. The infrared (IR) absorption measurements were performed with a BOMEM Fourier-transform spectrometer (FTIR), which covers the spectral range of 450–4500 cm^{-1} . A KBr beamsplitter, a globar light source, and a liquid-helium-cooled Si-B detector in conjunction with a continuous flow cryostat were used. A special sample holder was constructed to let the incident light from the spectrometer reach the sample at the Brewster's angle. This configuration proved to be very useful to avoid the interference patterns generated from the substrate as well as from the epitaxial thin film. The temperature was controlled within $\pm 1.0\text{K}$ and the spectra were measured at both 300 K and 77 K.

The three samples are undoped Al_{0.6}Ga_{0.4}N sample [denoted as (A)], Si-doped Al_{0.6}Ga_{0.4}N sample [denoted as (B)] and Mg-doped Al_{0.4}Ga_{0.6}N sample [denoted as (C)]. Sample A was irradiated with 1 MeV proton and doses $5.0 \times 10^{16} \text{cm}^{-2}$. All these samples were sandwiched between two boron nitride wafers to reduce the loss of nitride and ionization and heated in a continuous flow of N₂. For Mg-doped Al_{0.4}Ga_{0.6}N sample, [sample (C)], it was heated at a sequence of temperatures from 100 to 900°C in steps of 50°C, and the annealing time was 2 minutes at $T_a \leq 700^\circ\text{C}$ and 15 minutes at $T_a \geq 750^\circ\text{C}$. IR absorbance measurements were made just after each annealing treatment on sample (C) as well as after waiting for periods of several days for each annealing treatment. This procedure allows us to observe the variation of the C-H LVM intensities and the aging effect. The aging effect was performed at each annealing temperature above 500°C.

EXPERIMENTAL RESULTS

All the samples tested in this study were found to contain five IR peaks in the spectral range of 2846–2963 cm^{-1} . Figure 1 shows FTIR spectrum for undoped Al_{0.6}Ga_{0.4}N sample implanted with 1 MeV proton and a dose of $1 \times 10^{16} \text{cm}^{-2}$. This spectrum can be resolved into five peaks at 2849, 2870, 2902, 2918 and 2960 cm^{-1} . Based on a comparison with the LVMs measurement in GaN and calculated C-H frequencies in $\alpha\text{-Si}_{1-x}\text{C}_x\text{:H}$ [9–12], we ascribe these five peaks to symmetric and asymmetric stretching modes of CH_n ($n=1,2,3$) complexes in AlGa_{0.4}N. The absorption peak at 2848 cm^{-1} is attributed to a stretching mode of CH; the peaks at 2904 and 2916 cm^{-1} are attributed to a symmetric and an asymmetric stretching mode of CH₂, respectively; and the peaks at 2870 and 2960 cm^{-1} are attributed to symmetric and asymmetric stretching mode of CH₃.

Figure 2 shows IR absorbance spectra of sample (A) (spectrum 1) and sample (B) (spectrum 2) measured before (solid line) and after 15 minutes (dotted line) thermal annealing at 500°C. Thermal annealing behavior of LVMs spectra of C-H complexes in sample (C) is shown in Fig. 3 (a), (b) and (c). Fig. 3(a) shows the LVMs spectral behavior as the annealing temperature is changed. Fig. 3(b) shows spectra for the same sample annealed at higher temperatures. These spectra were measured just after thermal annealing (dotted spectra) and

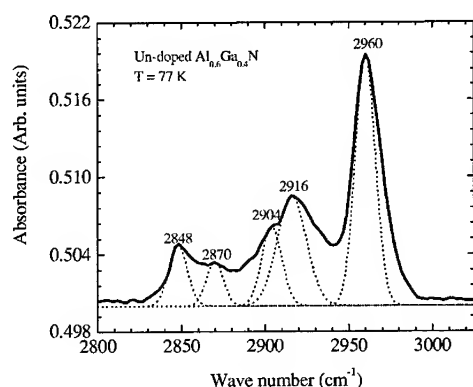


Figure 1. Infrared absorption spectrum measured at 77K for a proton irradiated $Al_{0.6}Ga_{0.4}N$ sample. The IR absorption peaks are resolved into five peaks at 2848, 2870, 2904, 2916 and 2960 cm^{-1} . The solid line is the actual spectrum while the dotted lines are Gaussians added to the spectrum for clarification.

several days after thermal annealing was performed (solid spectra). The data labeled (1) in Fig. 3 (c) show the total integrated areas of CH LVMs in sample (C) tested just after each annealing treatment. While the data for the integrated areas labeled (2) in this figure were obtained after annealing the samples and waiting for periods of 170 hours or higher as indicated in the figure. The data labeled (1) in Fig. 3(c) clearly show an increase in the total integrated area as the annealing temperature is increased from 0 to 300°C. As T_a is increased above 300°C, the integrated area starts to decrease and essentially vanished at T_a above 600°C. But then the CH LVMs seem to recover after waiting for a period of 170 hours or higher as indicated in the data labeled (2). The LVMs spectra of sample (C) in Fig. 3(b) were obtained just after each annealing (dotted spectra) and after waiting for a period of several days (solid spectra) at $T_a = 700$ (spectra 1), 800 (spectra 2) and 900°C (spectra 3). It is obvious that a partial recovery of CH LVMs occurs when the samples were tested one week after thermal annealing. It is also noted that the general trend is that the total integrated areas of the C-H LVMs is decrease as the annealing temperature is increased above 300°C for both before and after the aging [see Fig. 3(c)].

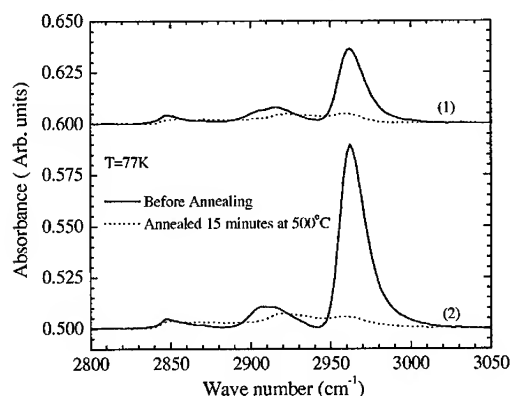


Figure 2. LVMs spectra measured before annealing (solid line) and after 15 minutes annealing at 500°C (dot line) in sample (1), (2) are shown. Sample (1) is Si-doped as-grown $Al_{0.6}Ga_{0.4}N$. Sample (2) is un-doped $Al_{0.6}Ga_{0.4}N$ with 1MeV proton irradiation at the dose of $5 \times 10^{16} cm^{-2}$. All the measurements were carried out at 77K.

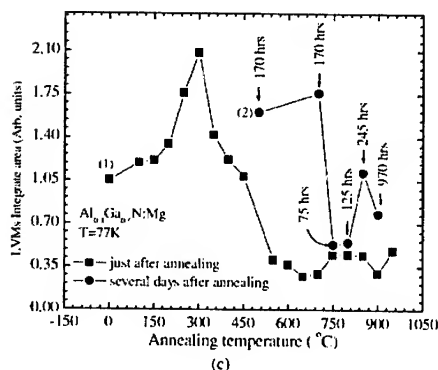
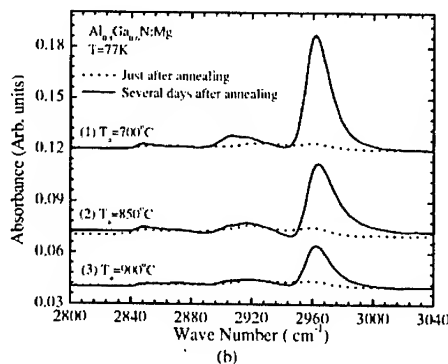
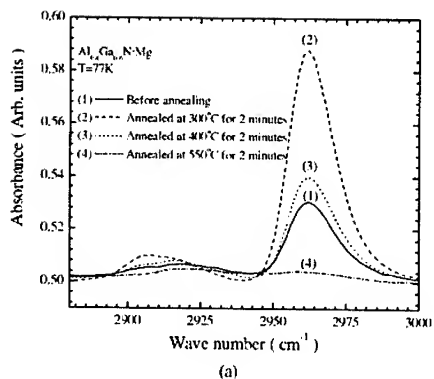


Figure 3. (a) LVMs spectra of CH complexes measured at 77K in Mg-doped $\text{Al}_{0.4}\text{Ga}_{0.6}\text{N}$ sample measured after thermal annealing at $T_a=300, 400$, and 550°C . (b) The same as (a) but $T_a=700, 850$, and 900°C . The dotted lines represents the spectra measured just after thermal annealing while the solid lines represent the spectra measured several days after thermal annealing. (c) Total integrated areas of C-H LVMs measured for the Mg-doped $\text{Al}_{0.4}\text{Ga}_{0.6}\text{N}$ sample. Data labeled (1) were obtained after thermal annealing and data labeled (2) were obtained several days after thermal annealing. The number of hours in the graph represents the waiting periods used to measure the spectra after thermal annealing.

DISCUSSIONS

To illustrate that the observed LVMs are due to C-H complexes, we cut two pieces from an $\text{Al}_{0.2}\text{Ga}_{0.8}\text{N}$ wafer and one piece was irradiated with 1 MeV protons and the other was irradiated with 1 MeV electrons (dose = $1 \times 10^{17} \text{cm}^{-2}$). The results are shown in Fig. 4. The solid line is the spectrum obtained from the samples before irradiation, the dashed line is the spectrum obtained for the proton irradiated sample, and the dotted line is the spectrum obtained from the electron irradiated sample. It is clear that proton irradiation increases the formation of C-H complexes as judged by the large increase in the stretching mode frequency of the CH_3 complex. An increase of the stretching mode frequencies for CH_2 and CH is also observed. However, the electron irradiated sample shows a noticeable decrease in the CH_3 stretching mode. This clearly demonstrates that electron irradiation break up the CH_3 complex in good agreement with others [13,14]. There is an increase of the CH_2 and CH concentrations in the electron irradiated sample as seen from the increase in the area under the LVMs stretching modes. This is most likely due to the fact that CH_3 is decomposed into C, H, CH, and CH_2 . This behavior is observed in several samples. Additionally, Hall effect measurements show a slight increase in the carrier concentration in the electron irradiation samples. This does not seem to be universal since a

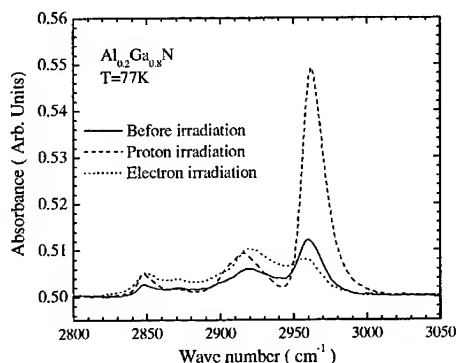


Figure 4. Local vibrational modes spectra measured for two samples cut from the same $\text{Al}_{0.2}\text{Ga}_{0.8}\text{N}$ wafer. The solid line is the spectrum obtained for both samples before irradiation, the dashed line represents the spectrum obtained for the proton irradiated sample (dose= $6 \times 10^{16} \text{ cm}^{-2}$), and the dotted line represent the spectrum obtained for the electron irradiated (dose= $1 \times 10^{17} \text{ cm}^{-2}$) sample.

few samples show a slight decrease in the carrier concentration after electron irradiation. Figure 3 (a) and (b) show the thermal annealing effect on C-H LVMS. The asymmetrical stretching mode of CH_3 is affected dramatically by thermal annealing as compared to other stretching modes of CH_2 and CH . This means that CH_3 is thermally unstable. It is observed from Fig. 3 (c) that the LVMS integrated area of C-H complexes in Mg-doped sample is increased with increasing annealing temperature and it reaches a maximum value after annealing the sample at 300°C . This proves that C-H complexes in AlGaIn are stable below 300°C . Thermal annealing at $T_a < 300^\circ\text{C}$ seems to help the formation of C-H. The C-H LVM intensities decrease after thermal annealing treatment at $T_a > 300^\circ\text{C}$ due to the dissociation of C-H complexes. After the thermal dissociation of C-H complexes, H either lose an electron and becomes H^+ , which could have a higher probability of recombining with C^- and reforming the passivated complexes, or it captures a second electron to form H^- . This of course will not recombine with C^- , and it is likely to migrate further away due to Coulomb repulsion and could eventually form either a molecule by combining with an H^+ or a larger H cluster or aggregate. C-H complexes seem to be completely depleted at $T_a > 600^\circ\text{C}$.

CONCLUSION

We presented the local vibrational modes spectra of C-H complexes in annealed AlGaIn grown by MOCVD technique. Thermal annealing at temperature around 500°C is sufficient enough to dissociate most of the C-H complexes in AlGaIn thin film. However, a partial recovery of the CH LVMS is observed in thermally annealed samples at $T_a > 500^\circ\text{C}$. This intriguing behavior is explained in terms of C-H recombination, which strongly suggests that H atoms remain trapped in the sample even after C-H decomposition. However, the integrated areas of the C-H LVMS are decreased after thermal annealing and aging as the annealing temperature is increased. While proton irradiation cause a drastic increase in the CH_3 LVM, electron irradiation cause the opposite effect suggesting strongly that the observed LVMS are truly due to CH complexes.

ACKNOWLEDGEMENTS. This work was partially supported by the Air Force Office of Scientific Research Grant No. F49620-00-1-0026. We would like to thank Dr. D. Johnstone for his encouragement and support and J. Chen for the measurements.

REFERENCES

- [1] S. Nakamura, T. Mukai, and M. Smoh, *Appl. Phys. Lett.* **64**, 1687(1994).
- [2] S. Nakamura, G. Fasol, in: "The Blue Laser Diode", (Springer, New York, 1997).
- [3] M.S. Shur and M.A. Khan, GaN/AlGaIn Heterostructure devices: Photodetectors and Field Effect Transistors, *MRS Bulletin* **22(2)**, pp. 44-50, Feb. (1997).
- [4] M. Razeghi and A. Rogalski, Semiconductor ultraviolet detectors, *J. Appl. Phys.* **79**(10), 7433 (1996).
- [5] K. Doverspike, A.E. Wickenden, S.C. Binari, D.K. Gaskill, J. A. Freitas, *Mat. Res. Soc. Symp. Proc.* **395** (1996) 897.
- [6] S. Nakamura, N. Iwasa, M. Senoh, and T. Mukai, *Jpn. J. Appl. Phys.*, Part 1 **31**, 1258 (1992).
- [7] J. Neugebauer and C. G. Van de Walle, *Phys. Rev. Lett.* **75**, 4452 (1995).
- [8] W. Gotz, N. M. Johnson, D. P. Bour, M. D. McCluskey, and E.E. Haller, *Appl. Phys. Lett.* **69**, 3725 (1996).
- [9] G. C. Yi, and B. W. Wessels, *Appl. Phys. Lett.* **70**(3), 357 (1996).
- [10] H. Wieder, M. Cardona, and C. R. Guarnieri, *Phys. Status Solidi B* **92**, 99 (1979).
- [11] Y. Tawada, K. Tsuge, M. Kondo, H. Okamoto, and Y. Hamakawa, *J. Appl. Phys.* **53**, 5273 (1982).
- [12] B. Dischler, A. Bubenzer, and P. Koidl, *Solid State Commun.* **48**, 105 (1983).
- [13] "GaN and Related Materials", edited by S. J. Pearton, Vol 2, Chapter 11, (Gordon and Breach, Amsterdam, 1997).
- [14] L. Hoffmann, E. V. Lavrov, B. Bech Nielsen, B. Hourahine, R. Jones, S. Öberg and P. R. Briddon, *Phys. Rev. B* **61** No. 24, 16659 (2000).

Irradiation Effects in Space Solar Cells Made of Multiple Absorbers

M.J. Romero, R.J. Walters,¹ M.M. Al-Jassim, S.R. Messenger,¹ and G.P. Summers¹
National Renewable Energy Laboratory (NREL), 1617 Cole Boulevard, Golden, CO 80401-3393
Phone: 303-384-6653, Fax: 303-384-6604, Email: mromero@nrel.gov

¹Naval Research Laboratory (NRL), Code 6615, 4555 Overlook Ave., S.W., Washington DC 20375

ABSTRACT

Solar cells made of multiple absorbers are a commonly used approach for improving efficiency due to their extended range of spectral sensitivity. Indeed, efficiencies nearing the theoretical maximum have been achieved with a triple-junction device made of $\text{In}_{0.51}\text{Ga}_{0.49}\text{P}$ (InGaP_2), GaAs, and Ge solar cells connected in series. For extraterrestrial applications, there is the added requirement of radiation tolerance. The main challenge for space power-generation is therefore the development of highly efficient and radiation-tolerant devices. We have investigated several aspects of the radiation response of solar cells made of multiple absorbers, such as multijunction devices and quantum-well solar cells. Novel possibilities such as quantum-dot solar cells and ordered-disordered heterostructures are proposed.

INTRODUCTION

Future satellite systems are projected to fly in orbit in or near the proton radiation belts, which extend from 2,000 to 10,000 km of altitude (MEO: Medium-Earth Orbit). Radiation effects can be very severe in these orbits, and high-efficiency solar cells with minimal degradation under cosmic particle bombardment are required.

Recent attempts to boost efficiencies are based on extending the spectral sensitivity by the use of multiple absorbers. Multijunction solar cells hold the promise of increasing the maximum attainable conversion efficiency well above the Shockley and Queisser (SQ) limit [1]. Indeed, the maximum practical efficiency for a solar cell (of 32.2% at 1-sun, AM1.5) has been achieved with a triple-junction device made of $\text{In}_{0.51}\text{Ga}_{0.49}\text{P}$ (InGaP_2), GaAs, and Ge solar cells connected in series. Quadruple-junction devices are being developed, and the search for 1-eV absorbers to add a junction to the $\text{InGaP}/\text{GaAs}/\text{Ge}$ cell is being conducted at NREL [2].

Other efforts have been made to improve solar cell efficiencies by the use of quantum wells as an intermediate level that absorbs additional lower-energy photons [3]. One question is whether quantum-well solar cells have their efficiency restricted by the SQ limit. Quantum-well solar cells have the potential to increase the maximum attainable conversion efficiency above the limit of conventional solar cells by extracting hot carriers to produce either higher photovoltages or photocurrents. However, if phonon-assisted relaxation of hot carriers is not prevented, a quantum-well solar cell ideally behaves as a single-junction solar cell.

The use of these advanced devices for space power-generation is limited by their radiation resistance. We have investigated several aspects of the radiation response of these solar cells by beam injection methods. In multijunction devices, some of the critical issues are the occurrence of a radiation-induced sublattice order-disorder transition in InGaP_2 [4], interconnecting junctions, type conversion under irradiation, and buffer-layer engineering when needed. In quantum-well solar cells, some of the matters to address are interdiffusion between the wells and the barriers and how carrier excess transport is influenced by irradiation.

We critically review these solar cells and explore novel schemes for high efficiency solar cells with improved radiation resistance.

MULTIJUNCTION SOLAR CELLS

Monolithic multijunction (MJ) solar cells consist of several single cells of different spectral sensitivity connected in series. Under irradiation with high-energy electrons and protons, as occurs in space, all junctions are degraded simultaneously. The most vulnerable junction determines the radiation response of the entire cell because the individual cells are series connected. For the lattice-matched InGaP₂/GaAs tandem, InGaP₂ has shown much higher radiation tolerance than GaAs; therefore, the radiation response of the tandem is limited by the radiation response of the GaAs sub-junction cell. At end of life, the effects of subsequent irradiation might nullify the higher power density gained from the tandem. Because the design of the multijunction devices requires matching the current density of each individual solar cell to the solar spectra irradiance, this requirement should be satisfied throughout the life of the solar cell in space. Therefore, damage coefficients under electron and proton irradiation for each individual cell should be matched as closely as possible for their use in space. In light of this, we have investigated possibilities other than the conventional InGaP₂/GaAs.

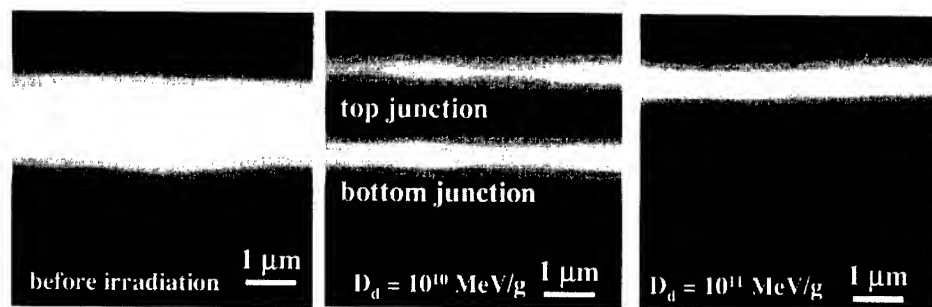


Figure 1. Cross-sectional EBIC images of the mismatched tandem cell ($\text{In}_{0.65}\text{Ga}_{0.35}\text{P}/\text{In}_{0.17}\text{Ga}_{0.83}\text{As}$) at different displacement damage doses, D_d .

Non-lattice-matched multijunction solar cells

The high-efficiency, commercially available leading technologies are the dual-junction InGaP₂/GaAs and triple-junction InGaP₂/GaAs/Ge solar cells. The challenge of these technologies is to lattice match the different semiconductors at their interfaces to prevent the generation of threading dislocations. However, InGaP₂ and GaAs are not the optimum semiconductors for the solar spectrum in space (AM0). This tandem has no degree of freedom to suit the spectral irradiance, whereas this is not the case for $\text{In}_x\text{Ga}_{1-x}\text{P}$ and $\text{In}_y\text{Ga}_{1-y}\text{As}$, where the indium content might be optimized for spectral sensitivity. Buffer engineering should then be applied to accommodate the lattice mismatch. Several dual-junction (DJ) cells have been investigated. One of them is the conventional DJ InGaP₂/GaAs of *n-p* polarity commercialized by Spectrolab. To explore other systems, $\text{In}_{0.49}\text{Ga}_{0.51}\text{P}/\text{In}_{0.03}\text{Ga}_{0.97}\text{As}$ (nearly lattice-matched) and $\text{In}_{0.65}\text{Ga}_{0.35}\text{P}/\text{In}_{0.17}\text{Ga}_{0.83}\text{As}$ (lattice mismatched) DJ devices of *n-p* polarity were fabricated on

GaAs substrates by metal-organic vapor-phase epitaxy (MOVPE) [5]. Linearly graded buffer layers of InGaAs have been used here, which is a better approach to progressively relax the strain [6,7] over step-graded or single layers. In this way, InGaAs epilayers of high quality have been achieved. Testing their radiation response is of interest for their use in space. The devices were irradiated with protons in the MeV energy range.

Figure 1 shows cross-sectional electron-beam-induced-current (EBIC) images of the mismatched tandem cell at different displacement damage doses, D_d [8]. Before irradiation, the subcells are not resolved due to the diffusion length at the base of the top cell being much longer than the base thickness. After irradiation, by the degradation of the diffusion length, both the top and bottom junctions are finally resolved. From these images, it is apparent that the bottom cell is more susceptible to irradiation than the top cell. Diffusion lengths (L) are subsequently estimated by EBIC, and the diffusion-length damage coefficient, κ_L ($\text{g cm}^{-2} \text{MeV}^{-1}$) is evaluated from fits to the diffusion-length degradation equation [9]:

$$\frac{1}{L^2(D_d)} = \frac{1}{L_0^2} + \kappa_L D_d, \quad (1)$$

where L_0 is the diffusion length prior to irradiation. The values thus determined for κ_L for the various semiconductor materials studied are given in Table I.

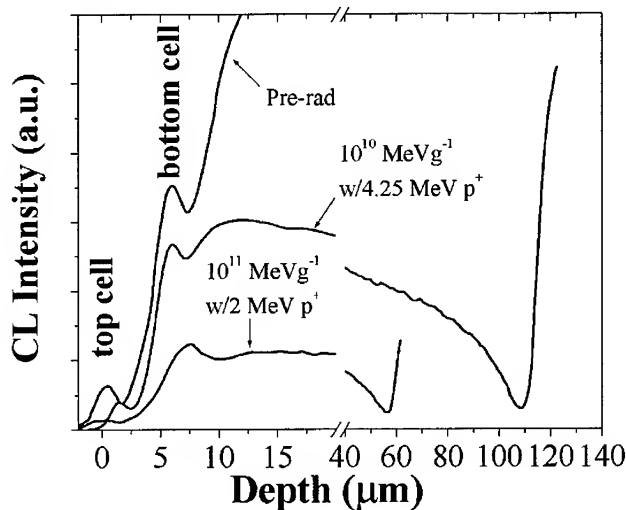


Figure 2. CL intensity measured as a function of depth into the $\text{In}_{0.49}\text{Ga}_{0.51}\text{P}/\text{In}_{0.03}\text{Ga}_{0.97}\text{As}$ cell at different damage doses (in MeVg^{-1}).

Panchromatic cathodoluminescence (CL) measured on cross-sections allows the emission from each individual junction to be resolved, as shown in Figure 2. The positive peaks in the data occur at the location of each junction. For the post-irradiation data, the large negative peaks

occurring deep into the sample are a result of the heavy damage produced when the incident protons slow-down and stop in the material. Thus, the location of the negative peaks corresponds to the range of the incident protons. The intensity of the CL is progressively degraded under proton bombardment as a result of lifetime degradation, as expressed by

$$\frac{I}{I_0} = \frac{1}{1 + \tau_0 \kappa_\tau D_d}, \quad (2)$$

where τ_0 and I_0 are the minority-carrier lifetime and the emitted intensity prior to irradiation, respectively, and κ_τ ($\text{g s}^{-1} \text{MeV}^{-1}$) is the lifetime damage coefficient. The fits from equations 1 and 2 yield the damage coefficients for L and τ for each semiconductor, as detailed in Table I.

Table I. Diffusion-length and lifetime damage coefficients under proton irradiation for different semiconductors. ‡ Lower limit for the diffusion length.

	In _{0.65} Ga _{0.35} P	InGaP ₂	In _{0.49} Ga _{0.51} P	GaAs	In _{0.03} Ga _{0.97} As	In _{0.17} Ga _{0.83} As
Carrier density (cm^{-3})	<i>p</i> -type, 1.5×10^{17}	<i>n</i> -type, 1.5×10^{16}	<i>p</i> -type, 1.5×10^{17}	<i>p</i> -type, 8×10^{16}	<i>p</i> -type, 1.5×10^{17}	<i>p</i> -type, 1.5×10^{17}
L_0 (μm)	1.40 [‡]	0.30	1.50 [‡]	2.50	2.05	1.89
κ_L ($\text{g cm}^{-2} \text{MeV}^{-1}$)	5×10^{-11}	1×10^{-10}	7×10^{-11}	8×10^{-9}	1×10^{-10}	3×10^{-11}
$\tau_0 \kappa_\tau$ (g MeV^{-1})	6×10^{-13}	1×10^{-12}	5×10^{-12}	5×10^{-11}	4×10^{-11}	6×10^{-11}

The κ_L damage coefficient is particularly useful in describing the radiation response, but this parameter is known to be sensitive to polarity, carrier density, and L_0 , making a detailed comparison amongst the samples based on this parameter difficult. Furthermore, because the top cells are relatively thin, they are nearly insensitive to diffusion length degradation. The lifetime damage coefficient, $\tau_0 \kappa_\tau$, on the other hand, is not as sensitive to these other parameters, so it provides a better means for comparing radiation tolerance. $\tau_0 \kappa_\tau$ falls into the $10^{-12} \text{ g MeV}^{-1}$ range for $\text{In}_x\text{Ga}_{1-x}\text{P}$ and is approximately $5 \times 10^{-11} \text{ g MeV}^{-1}$ for $\text{In}_y\text{Ga}_{1-y}\text{As}$, suggesting greater radiation resistance in the $\text{In}_x\text{Ga}_{1-x}\text{P}$ material. Also, the data suggest that the addition of indium to $\text{In}_x\text{Ga}_{1-x}\text{P}$ improves the radiation response while the opposite is true for $\text{In}_y\text{Ga}_{1-y}\text{As}$.

Figure 3a shows the low-temperature CL spectra of $\text{In}_{0.49}\text{Ga}_{0.51}\text{P}$ measured at different damage doses. Prior to irradiation, the spectra are characterized by the band-to-band emission (e,h) at $1.913 \pm 0.002 \text{ eV}$ and a free-to-band transition associated with Zn acceptors (e, Zn^0). After doses as high as $5 \times 10^{10} \text{ MeV g}^{-1}$, there are no evident effects on the spectra. However, at $1 \times 10^{11} \text{ MeV g}^{-1}$, the band-to-band emission peak shifts toward higher photon energies, and the recombination path related to Zn is progressively deactivated. The former effect has been successfully explained by an order-disorder transition, as we will discuss later. The role of Zn impurities has been previously investigated in InP [10], and a defect complex involving Zn after irradiation has been suggested. These results suggest that there may be a similar effect in InGaP.

The effects of proton irradiation on the CL spectra of $\text{In}_{0.65}\text{Ga}_{0.35}\text{P}$ are shown in Figure 3b. Prior to irradiation, the $\text{In}_{0.65}\text{Ga}_{0.35}\text{P}$ emission is centered at 1.728 eV . After moderate irradiation, the emission slightly shifts to lower photon energies, although the overall luminescence is not much degraded. Note that this semiconductor has shown a lifetime

degradation coefficient as low as $6 \times 10^{-13} \text{ g MeV}^{-1}$. Increasing the dose does not cause the emission to shift further, but the intensity is degraded. There is no evidence of shifting in the room-temperature spectra (not shown).

To fully interpret these results, a more extensive investigation needs to be conducted. It is believed that compositional modulation might be responsible for this effect. The higher the In content, the better the radiation resistance. Degradation is then primarily located in the gallium-rich regions of wider bandgap. Hence, after irradiation, the main emission of photons is from the indium-rich regions and the overall intensity shifts to lower energies. The effect is not observable at room temperature, as diffusion lengths are longer than the range of compositional modulation.

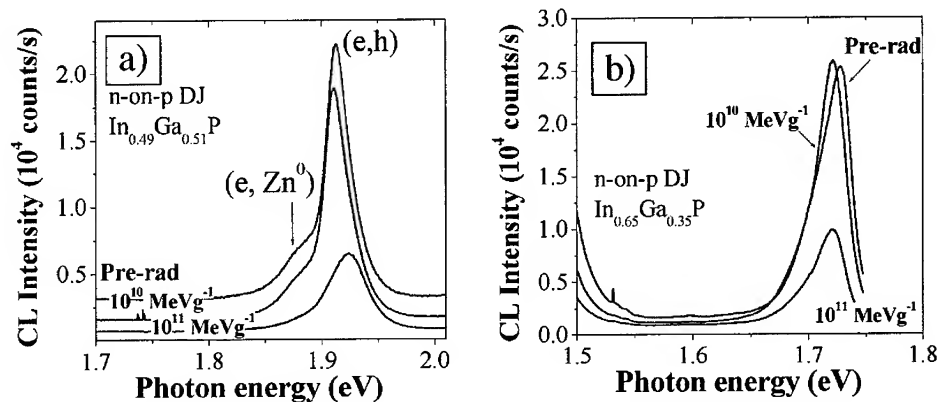


Figure 3. CL spectra measured at different damage doses (in MeVg⁻¹) for the In_xGa_{1-x}P alloys (a) In_{0.49}Ga_{0.51}P, and (b) In_{0.65}Ga_{0.35}P.

The role of dislocations

Local observations by EBIC or CL indicate that dislocations act as efficient carrier recombination centers, representing a loss mechanism for photovoltaic conversion. For space solar cells, the question arises of how irradiation influences the electrical activity of dislocations. We have recently developed an EBIC method for defect recognition in each individual sub-cell of multijunction solar cells using filtered external illumination [11]. By means of this *light-biasing EBIC*, misfit dislocations are seen at the bottom cell of the In_{0.65}Ga_{0.35}P/In_{0.17}Ga_{0.83}As tandem (Figure 4a), as well as dislocations threading through the top cell (Figure 4b). Under proton irradiation, the EBIC contrast of the misfit dislocations located at the bottom cell decreases, and the contrast for threading dislocations crossing the In_{0.65}Ga_{0.35}P eventually vanishes.

In modeling the EBIC contrast, dislocations are assumed to be regions of a recombination lifetime, τ_D , different from that in the surrounding region, τ [12]. The mechanism governing the recombination at the defect site is not considered. Lifetimes are related to diffusion lengths through the diffusion coefficient $D = L_D^2 / \tau_D = L^2 / \tau$. The EBIC contrast is then defined by:

$$c = \Gamma \times F(L, z_D, E_b), \quad (3)$$

with Γ being the defect recombination activity and F a correction factor that groups geometric factors such as the depth of the defect z_D , the spatial distribution of the electron beam excitation, and the diffusion length L of the surrounding region. Therefore, measured contrast must be corrected by F to yield the defect recombination activity Γ . In a first-order approximation [12], Γ is given by:

$$\Gamma = \frac{\pi r_D^2}{D} \frac{1}{\tau_D} \quad (4)$$

where r_D is the effective radius of the defect. Thus, the reduction of the contrast under irradiation might be due to degradation of the diffusion length in the region surrounding the dislocation, instead of differences in the defect recombination activity. By simulation of the induced currents, we have confirmed that indeed *irradiation decreases the recombination activity of dislocations*.

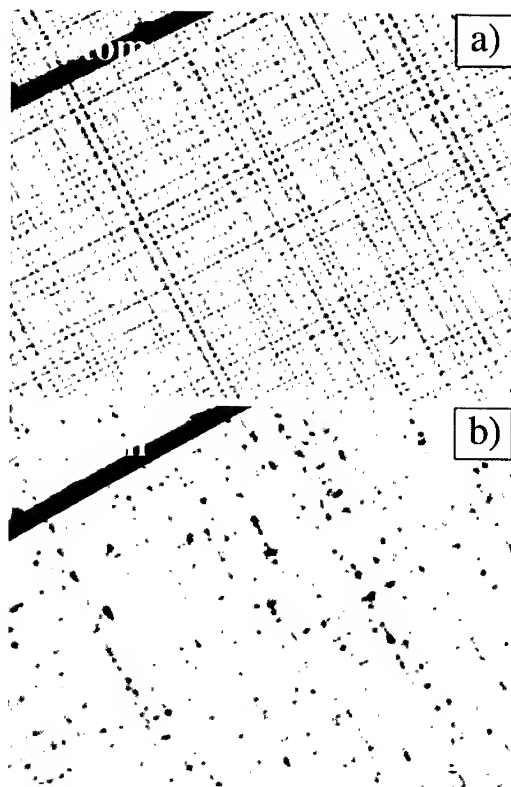


Figure 4. Defect imaging by EBIC: (a) misfit dislocations at the bottom cell, and (b) dislocations threading through the top cell of the lattice-mismatched $\text{In}_x\text{Ga}_{1-x}\text{P}/\text{In}_y\text{Ga}_{1-y}\text{As}$ structure.

Dislocations are one-dimensional disruptions of the lattice, which may be described in III-Vs by one-dimensionally distributed deep-levels and a space-charge region surrounding them. Defects induced by irradiation might either affect the density of active defect states at the dislocation or influence the surrounding space-charge region by carrier traps in the host semiconductor. Radiation effects on dislocations are considerably more in $In_xGa_{1-x}P$ than in $In_yGa_{1-y}As$.

Interconnecting junctions

Multijunction cell operation is allowed by interconnecting tunnel junctions, which are on the order of tens of nanometers in thickness. These nano-junctions connect the individual cells in series while minimizing absorption losses. High-energy electron and proton irradiations have a negligible impact on their characteristics due to their nanoscale. However, tunnel junctions are very sensitive to nuclear radiation. The highly energetic thermal pulse accompanying nuclear radiation boosts interdiffusion, which is very severe for the tunnel junction. The strength of nanoscale junctions under high-energy particle irradiation is the weakness under nuclear radiation.

Radiation-induced order-disorder transition in InGaP

MOVPE-grown $InGaP_2$ is known for the predisposition of In and Ga to order on the group III sublattice along the $\langle 111 \rangle$ direction. This phenomenon is driven by the reconstruction of the surface and step motion during the MOVPE growth, depending both on the orientation of the substrate [13] and on growth parameters such as temperature, V/III ratio [14,15], and growth rate [16]. The most attractive effect associated with ordering in $InGaP_2$ is the predicted decrease of 260 meV in the band-to-band transition [17]. Therefore, ordering effects might be used to modulate the absorption limit by modifying the growth parameters, without introducing any lattice mismatch. By exploiting this behavior, the spectral response of the $InGaP_2$ top cell, and thus, the multijunction cell output, could possibly be optimized. The radiation response of the ordered $InGaP_2$ semiconductor is thus of great interest.

Figure 5a is a monochromatic CL image showing the ordered domains in the $InGaP_2$ along the $[110]$ direction. Darker areas are possibly associated with antiphase boundaries (APBs). The CL spectra are shown in Figure 5b. A_0 is the spectrum excited on *ordered* $InGaP_2$ (o- $InGaP$) prior to irradiation. After doses as high as 10^{11} MeV g^{-1} , there is little effect on the spectrum (A_1). However, in *partially ordered* $InGaP_2$ (see spectrum B_0) the subsequent irradiation (spectrum B_1 , $D_d \sim 10^{11}$ MeV g^{-1}) disorders the structure. We have finally confirmed the occurrence of a radiation-induced order-disorder transition in $InGaP_2$ by combining CL measurements and transmission electron microscopy observations [4].

Estimates of the lifetime damage coefficient under proton irradiation lead to 10^{-12} gMeV $^{-1}$ and 10^{-13} gMeV $^{-1}$ for disordered and ordered $InGaP$, respectively. Therefore, ordered structures seem to be even more radiation tolerant than partially ordered or disordered ones. A first attempt to explain these results is from the coordination of phosphorous in ordered and disordered $InGaP$. Within ordered domains, P is coordinated to either $InGa_3$ or In_3Ga . Disordering the structure, we find additionally P coordinated to In_4 , In_2Ga_2 , and Ga_4 . Displacement of indium by irradiation should be preferential due to the mutual relationship between the energy of the In-P and Ga-P bonds. The displacement of an In atom in an In_2Ga_2 environment leads to $InGa_2^-$ that is more

electronegative and thus less stable than In_2Ga^+ from In_3Ga . A statistical approach shows then that the higher the degree of ordering, the lower is the density of vacancies produced after irradiation.

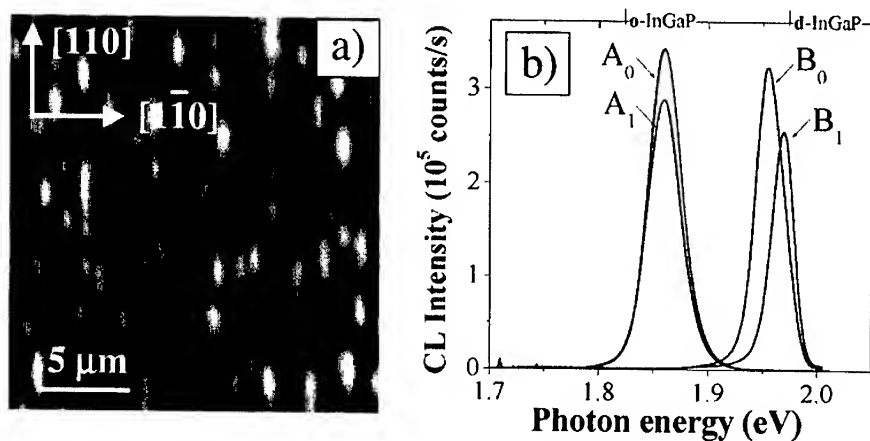


Figure 5. (a) Monochromatic CL image showing ordered domains in InGaP_2 . (b) CL spectra of InGaP_2 for *ordered* InGaP (A) and *partially ordered* InGaP (B), before and after irradiation (0 and 1 subscripts, respectively).

Summary and novel schemes

The radiation response of a multijunction device is determined by the response of the most vulnerable individual sub-cell. The use of $\text{InGaP}_2/\text{GaAs}$ cells in severe radiation environments is thereby limited by GaAs sub-cell. However, a multijunction device consisting of highly ordered InGaP_2 as a top cell and a disordered semiconductor as a bottom cell (OD InGaP_2) may increase the efficiency above single-junction InGaP_2 devices, avoid lattice mismatch, and have a much improved radiation resistance than current $\text{InGaP}_2/\text{GaAs}$ technologies. In a first estimate from the damage coefficients, the same degradation of the output after one year of service of a $\text{InGaP}_2/\text{GaAs}$ cell would be reached by the order-disordered heterostructure in as much as 10 to 100 years. The selection between $\text{InGaP}_2/\text{GaAs}$ or OD InGaP_2 would be driven by the expected dose of radiation and the requirements of power density through the lifetime of the solar panel.

QUANTUM-WELL SOLAR CELLS

Another advanced solar cell made of multiple absorbers is based on quantum wells. Quantum-well solar cells show extended spectral sensitivity by absorption of lower-energy photons. However, these cells are predicted to have the same ideal efficiencies as the single-junction solar cell in the unity quantum-efficiency limit. Hot carriers must be extracted to produce either higher photovoltages or photocurrents. Higher photovoltages require carriers to be extracted before thermalization, whereas enhanced photocurrents are associated with production of additional carriers by impact ionization. In both approaches, hot-carrier relaxation rates should be considerably reduced, making the other processes competitive with thermalization. Quantization effects may dramatically reduce hot-carrier relaxation and, therefore, quantum wells might have the potential to increase the maximum conversion efficiency predicted by Shockley and Queisser. We have investigated the carrier excess dynamics and the effects of irradiation in quantum-well solar cells by beam injection techniques. These cells are InP single-junctions, in which a ten-period, strained $InAs_xP_{1-x}/InP$ multiple quantum well is incorporated between the emitter and the base.

Carrier excess dynamics in quantum-well solar cells

Improved efficiencies are anticipated by exploiting the increase of short-circuit current densities provided by incorporating quantum wells in the depletion region of a single-junction cell. Unfortunately, an increase in efficiency is frequently not achieved because of significant degradation in the open-circuit voltage (V_{OC}), as a result of carrier relaxation in quantum wells. It has been shown experimentally that a threshold built-in electric field must be exceeded for an optimum collection of carriers [3]. Figure 6 shows EBIC scans across the quantum wells for one of the $InAs_xP_{1-x}/InP$ cells, which is representative of the cells investigated. At lower excitation densities, there is no saturation in the induced current at the quantum well-region, and therefore, carrier collection is not optimized. Saturation is attained at higher excitation levels instead. By modeling the measured EBIC, we have shown that the main loss mechanism for non-optimized cells within the intrinsic region is carrier capture at the quantum wells [18]. Table II shows the measured V_{OC} for the $InAs_xP_{1-x}/InP$ structures of different well widths and arsenic contents, as well as calculations by the ideal theory of Anderson, in the unity quantum-efficiency limit with radiative recombination [19]. For shallow quantum wells, which show optimum collection, reasonable agreement is observed. For the cells with deeper wells, better agreement is seen when capture lifetimes (as determined by EBIC) are taken into account.

Table II. Measured and calculated V_{OC} for the strained $InAs_xP_{1-x}/InP$ quantum well solar cells. The measurements were made under 1 sun, AM0 solar spectrum.

ID	Well width (Å)	Arsenic content	V_{OC} (V) exp.	V_{OC} (V) ideal theo.	V_{OC} (V) w/capture lifetimes	Optimized collection
N1	18	0.37	0.73	0.74	...	yes
N2	12	0.65	0.71	0.73	...	yes
N3	12	0.66	0.70	0.73	...	yes
N4	31	0.32	0.61	0.69	0.64	no
N5	20	0.53	0.61	0.65	0.60	no

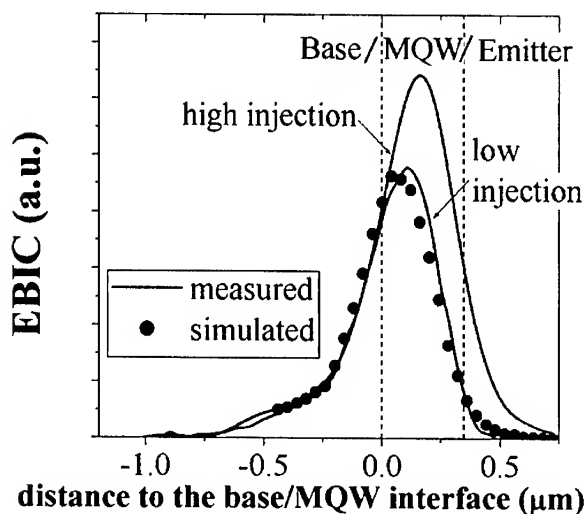


Figure 6. EBIC scans recorded under low and high excitation densities for the $\text{InAs}_x\text{P}_{1-x}/\text{InP}$ quantum-well solar cell N4.

The effect of irradiation on the operational characteristics of quantum-well solar cells can be incorporated into the ideal theory by adding the contribution of the radiation-induced defects to the nonradiative recombination lifetime. Diffusion lengths along the quantum wells were measured using the *mask method* in CL [20] before and after proton irradiation. The data suggest that solar cells with deeper quantum wells will be more sensitive to irradiation, although lifetime degradation coefficients are similar for the $\text{InAs}_x\text{P}_{1-x}/\text{InP}$ wells studied. Recombination of carriers through nonradiative transitions increases the rate of carrier capture by quantum wells. Carrier capture is detrimental for cell performance and should be avoided. The use of these solar cells in space is therefore limited by the relaxation of photogenerated carriers within the wells.

Interdiffusion

Energy transferred to the quantum wells under proton irradiation might result in interdiffusion by displacing As from the wells to the InP barriers. Indeed, we have observed a systematic shift of the quantum well-emission to lower photon energies (see CL spectra in Figure 6b), suggesting interdiffusion of arsenic. It is worth noting that although both N1 and N2 cells (see Table II) were designed to provide nearly identical energy states in the wells, the well thickness and As content are substantially different. Displacement of As from $\text{InAs}_x\text{P}_{1-x}$ requires less energy than that of P, and interdiffusion might be preferential for N2. Indeed, the quantum-well emission shifted up to 5 meV and 15 meV under irradiation for N1 and N2, respectively. For thinner wells such as N2, wave functions are expected to spread further into the barriers; hence, is the device rendered more sensitive to effects in the barriers and at the quantum-well/barrier interfaces.

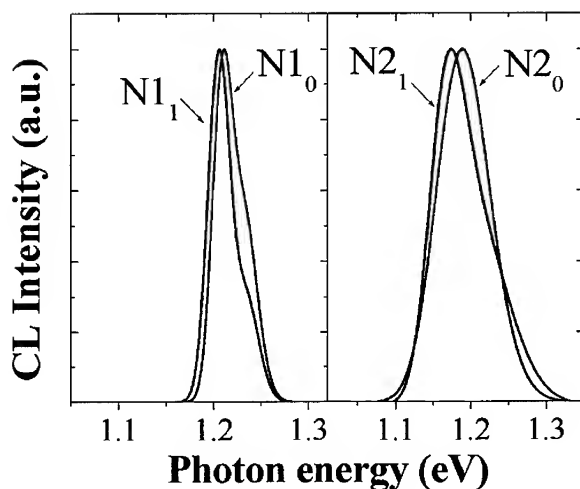


Figure 7. Effect of proton irradiation on the quantum-well luminescence for the $\text{InAs}_{1-x}\text{P}_x/\text{InP}$ structures N1 and N2 (0 and 1 subscripts correspond to before and after irradiation, respectively).

Summary and novel schemes

Quantum-well solar cells are predicted to increase the efficiency of solar cells by using hot carriers. However, a major factor limiting the performance of these cells is the capture of photogenerated carriers. Quantization in quantum wells is restricted to the confinement direction, and the other two classical dimensions possibly govern the relaxation dynamics of the carrier excess. Indeed, the ideal theory for quantum-well solar cells, which has proven to be successful in explaining their behavior, is fundamentally classical in nature. Quantum dots are quantized in three dimensions, and the probability of reducing the loss of photocarriers by recombination in the dots is much higher. Electronic minibands formed by coupling of quantum dots may dramatically increase the diffusion of carriers across the absorber. The use of quantum dots for solar energy conversion therefore becomes an attractive approach to be explored in the future.

ACKNOWLEDGMENTS

We would like to thank A. Bett of Fraunhofer ISE and A. Freundlich of the University of Houston for providing the solar cells for irradiation testing. This work was supported by the DOE at NREL and by the U.S. Office of Naval Research at NRL.

REFERENCES

1. S.R. Kurtz, D. Myers, and J.M. Olson, "Projected performance of three- and four-junction devices using GaAs and GaInP," in *Proceedings of the 26th IEEE Photovoltaic Specialists Conference*, pp. 875-878 (1997).
2. J.M. Olson, J.F. Geisz, S.R. Kurtz, and A.G. Norman, "1-eV semiconductors for multijunction solar cells" at this conference.
3. I. Serdiukova, C. Monier, M.F. Vilela, and A. Freundlich, *Appl. Phys. Lett.* **74**, 2812 (1999).
4. M.J. Romero, D. Araujo, R. García, R.J. Walters, G.P. Summers, and S.R. Messenger, *Appl. Phys. Lett.* **74**, 2684 (1999).
5. A.W. Bett, R. Adelhelm, C. Agert, R. Beckert, F. Dimroth, and U. Schubert, *Solar Energy Materials and Solar Cells* **66**, 541 (2001).
6. S.I. Molina, F.J. Pacheco, D. Araujo, R. García, A. Sacedón, E. Calleja, Z. Yang, and P. Kidd, *Appl. Phys. Lett.* **65**, 2460 (1994).
7. L. Lazzarini, C. Ferrari, S. Gennari, A. Bosacchi, S. Franchi, M. Berti, A.V. Drigo, F. Romanato, and G. Salviati, *Inst. Phys. Conf. Ser.* **157**, 149 (1997).
8. The displacement damage dose (D_d) is given by the product of the particle fluence, which is expressed in cm^{-2} , and the calculated non-ionizing energy loss (NIEL, in $\text{MeVcm}^2\text{g}^{-1}$).
9. H.Y. Tada, J.R. Carter, B.E. Anspaugh, and R.G. Downing, *The Solar Cell Radiation Handbook*, JPL Publication 82-69 (1982).
10. R.J. Walters, M.J. Romero, D. Araujo, R. García, S.R. Messenger, and G.P. Summers, *J. Appl. Phys.* **86**, 3584 (1999).
11. M.J. Romero, J.M. Olson, and M.M. Al-Jassim, "Light-biasing electron-beam-induced-current for multijunction solar cells," in *Proceedings of the NCPV Program Review Meeting*, pp. 289-290 (2001).
12. C. Donolato, *Optik* **52**, 19 (1978/79).
13. K. Sinha, A. Mascharenhas, R.G. Alonso, G.S. Horner, K.A. Bertness, S.R. Kurtz, and J.M. Olson, *Solid State Communications* **89**, 843 (1994).
14. H. Murata, I.H. Ho, G.B. Stringfellow, and J.B. Mullin, *J. Crys. Growth* **170**, 219 (1997).
15. Y.S. Chun, H. Murata, G.B. Stringfellow, and J.B. Mullin, *J. Crys. Growth* **170**, 263 (1997).
16. Y.S. Chu, S.H. Lee, I.H. Ho, and G.B. Stringfellow, *J. Crys. Growth* **174**, 585 (1997).
17. S.H. Wei, and A. Zunger, *Appl. Phys. Lett.* **56**, 662 (1990).
18. R.J. Walters, G.P. Summers, S.R. Messenger, M.J. Romero, M.M. Al-Jassim, R. Garcia, D. Araujo, A. Freundlich, F. Newman, and M.F. Vilela, *J. Appl. Phys.* **90**, 2840 (2001).
19. N.G. Anderson, *J. Appl. Phys.* **78**, 1850 (1995).
20. Y. Tang, D.H. Rich, A.M. Moy, and K.Y. Cheng, *Appl. Phys. Lett.* **72**, 55 (1998).

Ion Implantation Induced Interdiffusion in Quantum Wells for Optoelectronic Device Integration

L. FU, H.H. TAN, M.I. COHEN and C. JAGADISH

Department of Electronic Materials Engineering, Research School of Physical Sciences and Engineering, The Australian National University, Canberra, ACT 0200, Australia

L.V. DAO and M. GAL

School of Physics, University of New South Wales, Sydney, NSW 2052, Australia

NA LI, NING LI, X. LIU, W. LU and S.C. SHEN

Shanghai Institute of Technical Physics, Chinese Academy of Science, Shanghai, China

ABSTRACT

Ion implantation induced intermixing of GaAs/AlGaAs and InGaAs/AlGaAs quantum wells was studied using low temperature photoluminescence. Large energy shifts were observed with proton implantation and subsequent rapid thermal annealing. Energy shifts were found to be linear as a function of dose for doses as high as $\sim 5 \times 10^{16} \text{ cm}^{-2}$. Proton implantation and subsequent rapid thermal annealing was used to tune the emission wavelength of InGaAs quantum well lasers as well as detection wavelength of GaAs/AlGaAs quantum well infrared photodetectors (QWIPs). Emission wavelength of lasers showed blue shift whereas detection wavelength of QWIPs was red shifted with intermixing.

INTRODUCTION

Quantum well intermixing has drawn considerable attention in recent years for integration of optoelectronic devices [1-3]. Impurity induced disordering (IID) and impurity free vacancy disordering (IFVD) have been widely used to modify the shape of the quantum wells, in turn their electrical and optical properties [4-7]. However, in the case of impurity induced disordering, residual impurities are detrimental to the performance of devices. In the case of IFVD, defects are produced in the near surface region [8,9] and defect diffusion length should be large enough to reach the quantum wells in the active regions of devices which are often 1-2 micron deep. Ion implantation is a versatile technique and allows introduction of defects in selected regions with defect distribution peaking in the region of interest by choosing appropriate ion energy, dose etc. Recently, ion implantation induced intermixing has been used to tune the emission wavelength of quantum wells and to enhance light emission from V-groove quantum wires [10-12].

In this paper, we review the issues associated with implantation induced intermixing in GaAs/AlGaAs and InGaAs/AlGaAs quantum wells and apply this technique to tune the emission wavelength of quantum well lasers. Intermixing has also been used to tune the detection wavelength of quantum well infrared photodetectors.

EXPERIMENTAL

The GaAs/AlGaAs, InGaAs/GaAs and InGaAs/AlGaAs quantum well structures and InGaAs quantum well laser structures used in this study were grown by metal organic vapor phase epitaxy (MOVPE) on semi-insulating and n+-GaAs (100) substrates, respectively. Quantum well infrared photodetector structures were grown by molecular beam epitaxy on semi-insulating (100) GaAs substrates. Proton irradiation was carried out at room temperature using 40 keV Protons for quantum well structures, 220 keV protons for laser structures and 900 keV proton for QWIP structures. Proton energies for quantum well and laser structures were chosen to locate the peak of the defect profile closer to the quantum wells. In the case of QWIPs, peak of the damage profile is located in the substrate and tail of the profile is used to create uniform distribution of damage in the quantum well region consisting of 50 quantum wells doped with silicon. Half of each sample was masked during irradiation to serve as a reference region and sample was tilted 7° off the beam axis to minimise channeling effect. Rapid thermal annealing was carried out in argon ambient at temperatures in the range of 900-950°C for periods of 30-60 sec. Low temperature (12K) photoluminescence (PL) was performed to monitor energy shifts in quantum wells due to interdiffusion using green He-Ne laser (543.5 nm) as the excitation source and the luminescence was detected with a silicon CCD through a monochromator.

RESULTS AND DISCUSSION

GaAs/AlGaAs Quantum Wells

A four quantum well structure of GaAs/Al_{0.54}Ga_{0.46}As with nominal quantum well thicknesses of 1.4 nm, 2.3 nm, 4.0 nm and 8.5 nm was implanted with 40 keV protons in the dose range of 1×10^{14} to 5×10^{16} cm⁻². Samples were rapid thermally annealed at 900°C for 60 sec. Photoluminescence measurements showed blue shift of the emission peak for doses above 5×10^{14} cm⁻². Energy shifts were linear with proton dose to 5×10^{16} cm⁻² for all the quantum wells. Energy shifts as large as 200 meV were obtained without significant degradation in the PL intensity (only a factor of two lower in intensity), suggesting that proton implantation is quite effective in achieve quantum well intermixing. Results of these studies [10,11] were used to design experiments to tune detection wavelength of GaAs/AlGaAs QWIPs.

InGaAs/AlGaAs Quantum Wells

The InGaAs/GaAs and InGaAs/AlGaAs structures consisted of two quantum wells of 5 nm thickness with In_{0.15}Ga_{0.85}As and In_{0.30}Ga_{0.70}As well and GaAs and Al_{0.2}Ga_{0.8}As barriers, respectively. Proton irradiation was carried out at room temperature using 40 keV protons. Rapid thermal annealing was carried out in argon ambient at 900°C for 60 sec. The PL spectra from InGaAs/GaAs and InGaAs/AlGaAs samples implanted at doses of 1×10^{15} cm⁻² and 5×10^{15} cm⁻² are shown in Fig. 1(a) and 1(b), respectively. It can be seen that the proton irradiation and subsequent rapid thermal annealing led to blue shift of the emission wavelength from all the quantum wells. PL intensity decreased with increase in ion dose in InGaAs/GaAs samples indicating that the non-radiative recombination centers introduced by proton implantation are not removed by RTA. However, PL intensity recovery was very good (>50%) for InGaAs/AlGaAs

quantum wells and this is attributed to the dynamic annealing of defects during ion irradiation. Previous studies proposed that the presence of AlGaAs offers some protection against damage accumulation in adjacent GaAs regions due to the strong dynamic annealing of the mobile point defects generated in AlGaAs [13,14]. Accordingly, for InGaAs QW sandwiched between AlGaAs barrier layers, it is possible that during implantation a similar process might occur. This together with the simultaneous dynamic annealing in the AlGaAs layers, preventing the formation of large defect clusters, suggests that the residual defects in the sample would be predominantly point defects. These point defects have lower thermal stability and are annealed much more easily than defect clusters (in the case of InGaAs/GaAs QWs) to promote intermixing and hence the remarkable recovery of the PL intensities of the InGaAs/AlGaAs samples.

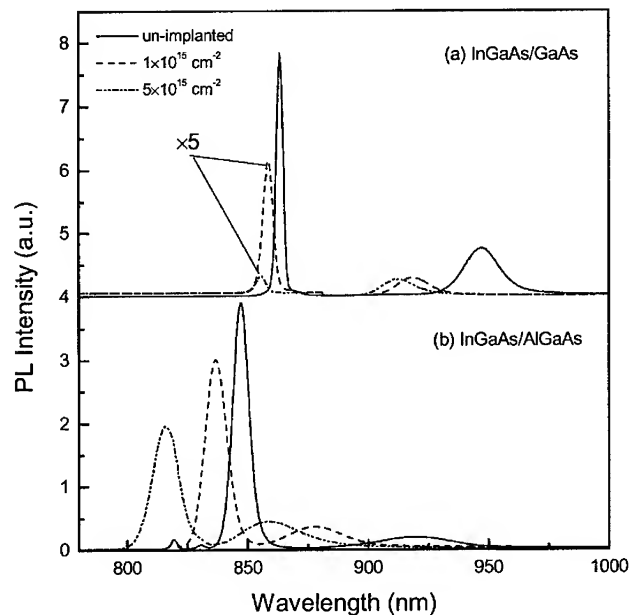


Fig. 1 Comparison of PL spectra for InGaAs QW samples with GaAs or AlGaAs barriers after proton implantation with doses of $1 \times 10^{15} \text{ cm}^{-2}$, $5 \times 10^{15} \text{ cm}^{-2}$ and RTA at 900°C , 60s. The peaks from the $\text{In}_{0.15}\text{Ga}_{0.85}\text{As}$ QWs of the implanted InGaAs/GaAs samples are multiplied by a factor of 5 in order to make clearer comparison.

Quantum Well Lasers

A standard graded-index separate confinement heterostructure (GRINSCH) laser with active region consisting of 7 nm $\text{In}_{0.2}\text{Ga}_{0.8}\text{As}$ quantum well sandwiched by 12 nm $\text{Al}_{0.2}\text{Ga}_{0.8}\text{As}$ barriers was grown by MOVPE. Laser structure was irradiated with 220 keV protons to locate the damage peak nearer to the quantum well region. Half of the sample was masked (for reference) and the other half was irradiated with a dose of $1 \times 10^{15} \text{ cm}^{-2}$ and the whole sample was annealed at 900°C for 30 sec. After RTA, these samples, together with as-grown samples were fabricated into 4 micron stripe width ridge waveguide lasers by optical lithography. Figure 2 shows the laser spectra from three different devices (as-grown, as-grown and annealed, proton implanted and annealed) at $1.5 I_{th}$ under pulsed conditions using 2 microsec pulses of 5% duty cycle at room temperature. Wavelength shifts of 30 nm and 49 nm (compared with as-grown sample) were obtained from the reference annealed sample and irradiated and annealed sample, respectively.

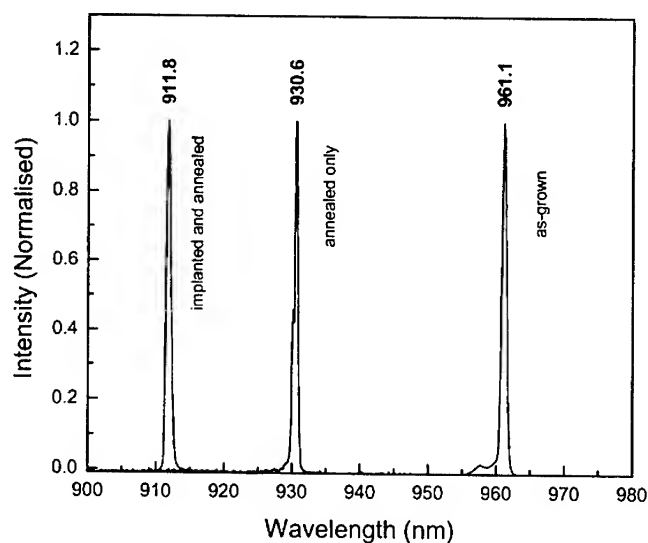


Fig. 2 Lasing spectra for the InGaAs/AlGaAs lasers before and after H implantation measured at room temperature.

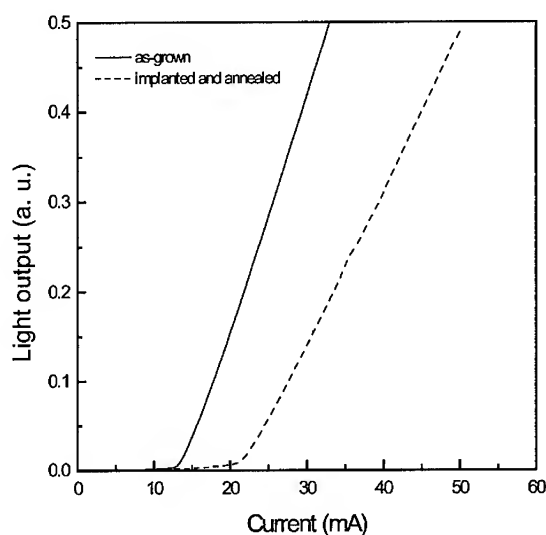


Fig. 3 L - I curves for the InGaAs/AlGaAs lasers (length of $\sim 710 \mu\text{m}$) before and after H implantation measured at room temperature.

Figure 3 shows L - I curves of the InGaAs/AlGaAs lasers measured at room temperature before and after H implantation and annealing. Though threshold current has increased in implanted and annealed samples, slope efficiency is similar that of the as-grown lasers suggesting that the laser quality is not significantly degraded due to proton implantation and annealing. Increase in threshold current is mainly due to the presence of non-radiative recombination centers. Further optimisation of implantation and annealing conditions could lead to reduction in non-radiative recombination centers. This suggests that the ion irradiation induced intermixing is a promising technique for integration of lasers operating at different wavelengths on the same chip.

Quantum Well Infrared Photodetectors.

Proton implantation and rapid thermal annealing was used to tune the detection wavelength of quantum well infrared photodetectors. The structures used in this work were n-type GaAs/AlGaAs bound to continuum QWIPS grown by molecular beam epitaxy on semi-insulating substrates. The structure contained 50 quantum wells sandwiched between $2 \mu\text{m}$ top and $1.3 \mu\text{m}$ bottom contact n⁺-GaAs layers. The quantum wells were nominally 4.5 nm Si doped ($\sim 10^{18} \text{ cm}^{-3}$) GaAs with 50 nm undoped $\text{Al}_{0.3}\text{Ga}_{0.7}\text{As}$ barriers. In order to obtain homogeneous intermixing in the quantum well region, 900 keV protons were chosen and the damage peak was located

in the substrate and a relatively uniform distribution of displacements across the quantum well region was achieved. During implantation, part of the sample was masked to serve as a reference and the rest of the sample was implanted with doses in the range of $1-4 \times 10^{16} \text{ cm}^{-2}$. All the samples were rapid thermally annealed at 950°C for 30sec under argon ambient. QWIPs were processed into $250 \times 250 \text{ } \mu\text{m}^2$ devices using standard lithography and wet etching. A 6 micron period grating was etched to allow normal incidence operation.

The spectral responses from all the samples acquired at 80K using Fourier transform infrared spectrometer are shown in Fig. 4. The peak detection wavelength has shifted from 6.8 microns for the unimplanted reference sample to 7, 7.3, 7.6 and 8.6 microns for samples implanted with doses of 1, 2, 3, $4 \times 10^{16} \text{ cm}^{-2}$, respectively. The dark current measurements have shown that the dark current increased by one to two orders of magnitude with increase in ion dose. This could be due to changes in the potential profile of the quantum well due to interdiffusion as well as due to the presence of residual defects which enhance tunneling probability of electrons. The contribution of residual defects to dark current could be reduced by carrying out multiple implant-anneal sequences [15,16].

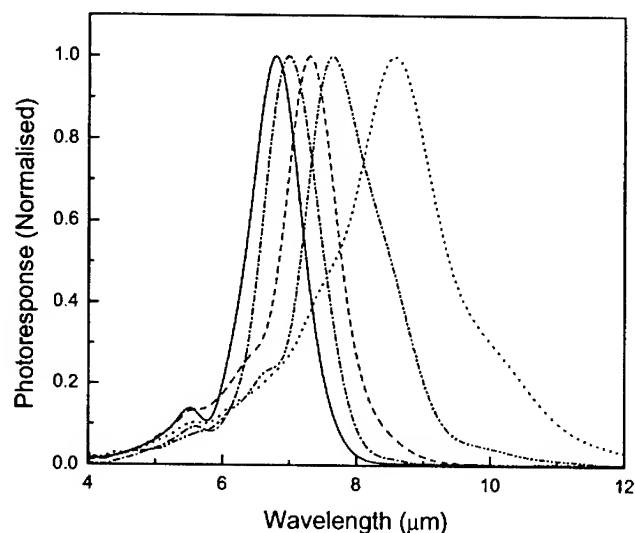


Fig. 4 Normalised photoresponse for the un-implanted sample and samples implanted with the doses of 1, 2, 3, $4 \times 10^{16} \text{ cm}^{-2}$ (from left to right) by a single high energy measured at 80 K under the bias of -6 V .

CONCLUSIONS

Proton implantation and rapid thermal annealing was used to create interdiffusion in GaAs/AlGaAs quantum wells leading to blue shift in the emission wavelength of the quantum wells. Blue shift in the emission wavelength of InGaAs quantum well lasers was achieved with modest degradation in device performance. In the case of quantum well infrared photodetectors, a red shift was obtained. In summary, suitability of implantation induced interdiffusion for optoelectronic device integration was demonstrated by fabricating multi-wavelength quantum well lasers and quantum well infrared photodetectors.

References

1. D.G. Deppe and N. Holonyak, Jr., *J. Appl. Phys.*, 64, R93 (1988).
2. E.H. Li, Ed. *Quantum Well Intermixing for Photonics*, SPIE Milestone Series, Bellingham, WA, 1997
3. E.H. Li, Ed. *Semiconductor Quantum Well Intermixing*, Gordon and Breach, Amsterdam, 2000
4. Shu Yuan, C. Jagadish, Yong Kim, Y. Chang, H. H. Tan, R. M. Cohen, M. Petravic, L. V. Dao, M. Gal, M. C. Y. Chan, E. H. Li, J. S. O, and P. S. Zory, *IEEE Journal of Special Topics in Quantum Electronics* 4, 629-635 (1998).
5. P.N.K. Deenapanray, H.H. Tan, M.I. Cohen, K. Gaff, M. Petravic and C. Jagadish, *J. ElectroChem. Soc.* 147, 1950-1956 (2000).
6. P.N.K. Deenapanray and C. Jagadish, *J. Vac. Sci. Technol. B* 19, 1962-1966 (2001).
7. L. Fu, P.N.K. Deenapanray, H.H. Tan, C. Jagadish, L.V. Dao and M. Gal, *Appl. Phys. Lett.* 76, 837-839 (2000).
8. R.M.Cohen, G. Li, C. Jagadish, P.T. Burke and M. Gal, *Appl. Phys. Lett.* 73, 803-805 (1998).
9. P.N.K. Deenapanray, H.H. Tan, C. Jagadish and F.D. Aurret, *Appl. Phys. Lett.* 77, 696-698 (2000).
10. C. Jagadish, H.H. Tan, S. Yuan and M. Gal, *Mater. Res. Soc. Symp. Proc.* 484, 397-411 (1998).
11. H.H. Tan, J.S. Williams, C. Jagadish, P.T. Burke and M. Gal, *Appl. Phys. Lett.* 68, 2401-2403 (1996).
12. Y. Kim, S. Yuan, R. Leon, C. Jagadish, M. Gal, M.B. Johnston, M.R. Phillips, M.A. Stevens Kalceff, J. Zou and D.J.H. Cockayne, *J. Appl. Phys.* 80, 5014-5020 (1996).
13. H.H. Tan, J.S. Williams, C. Jagadish, A. Skirowski, Z. Jin and D.J.H. Cockayne, *J. Appl. Phys.* 77, 87-94 (1995).
14. H.H. Tan, C. Jagadish, J.S. Williams, Z. Jin, D.J.H. Cockayne and A. Skirowski, *J. Appl. Phys.* 80, 2691-2701 (1996).
15. L. Fu, H. H. Tan, C. Jagadish, Na Li, Ning Li, X. Q. Liu, W. Lu, and S. C. Shen, *Appl. Phys. Lett.* 78, 10-12 (2001).
16. L. Fu, H.H. Tan, C. Jagadish, Na Li, N. Li, X. Liu, W. Lu and S.C. Shen, *Infrared Phys. & Technol.* 42, 171-175 (2001).

The Influence of Annealing Temperature and Doping on the Red/Near-Infrared Luminescence of Ion Implanted $\text{SiO}_2\text{:nc-Si}$

D.I. TETELBAUM, V.A. BURDOV, S.A. TRUSHIN, and A.N. MIKHAYLOV
Physico-Technical Research Institute of Nizhnii Novgorod State University, 603950,
Nizhnii Novgorod, Gagarin prospect, 23/3, Russia

D.G. REVIN, and D.M. GAPONOVA
Russian Academy of Science Institute of Physics for Microstructures, 603600 Nizhnii
Novgorod, GSP – 105, Russia

ABSTRACT

The results of an experimental research of the dependence of photoluminescence (PL) intensity in region about 800 nm for silicon nanoinclusions (quantum dots) obtained by Si ion implantation in SiO_2 on the dose of Si ions at two temperatures of an annealing $T_{\text{ann}} = 1000$ and 1100°C are presented. It is established that in both cases the dependences have the shape of the curves with a maximum. For 1100°C the maximum is shifted to the lower dose. The influence of an additional ion doping by the phosphorus on intensity of PL is investigated depending on the dose (concentration) of P and the dose of the silicon at $T_{\text{ann}} = 1000^\circ\text{C}$. It is shown, that in all the investigated region of P doses, the presence of P enhances the PL. The degree of the enhancement increases with the P dose, but the rate of the intensity enhancement goes down. With the growth of Si dose at the constant dose of P, the degree of the enhancement decreases. In an approximation of an effective mass, the energy spectra of a quantum dot are calculated at the presence of one or several P atoms for various their arrangement.

INTRODUCTION

The system of silicon nanoinclusions (NI) in SiO_2 ($\text{SiO}_2\text{:nc-Si}$) attracts the great attention in connection with the prospects of its use in the silicon optoelectronics. Ion implantation is one of the most common methods of the $\text{SiO}_2\text{:nc-Si}$ production [1-5]. The important parameter is the intensity of the photoluminescence (IPL) for the constant intensity of the excitation. This is especially important taking into account a small thickness of nc-Si layer for ordinarily ion energies. Generally, IPL depends on the several factors: NIs number, their sizes, the availability and the concentration of the centers of a nonradiative recombination. These factors are sensitive to the conditions of the ion implantation (ion energy and dose), the conditions of the annealing (temperature and time), and also the presence of the impurities. In [6,7] was shown that for a fixed annealing temperature $T_{\text{ann}} = 1000^\circ\text{C}$ (the annealing time, $t_{\text{ann}} = 2$ hours), IPL can be adjusted by the choice of a dose. At that, the sizes of NI practically do not vary, and their density grows. The IPL growth proceeds up to the dose for which the NI joining begins due to their high concentration. Also, it was established that IPL can be essentially increased by the additional implantation of phosphorus. The position of the PL peak occurs practically independent on the phosphorus doses. In the report, the results of a prolongation of these investigations are presented. The dependence of IPL on the dose of silicon was taken at the more high temperature of an annealing – 1100°C . The influence of the doping by P was investigated depending on Si and P dose. The theoretical research of the influence of impurity atoms contained in the quantum dots (QD) on the energy spectra and on the energies of the radiative interband transitions is continued.

EXPERIMENTAL

The SiO₂ layers with the thickness of 300 - 600 nm were grown up on the silicon in a "dry - wet - dry" cycle. Ion implantation by Si⁺ and P⁺ was provided at the energy of ions $E = 150$ keV and the ion current densities $j < 3 \mu\text{A}/\text{cm}^2$. The postannealing was carried out in the dry nitrogen atmosphere. The photoluminescence (PL) spectra were measured at the Ar laser excitation ($\lambda = 488$ nm) with a power density about $50 \text{ W}/\text{cm}^2$.

RESULTS AND DISCUSSION

For all the annealed after the Si⁺ implantation layers, the PL spectra with a maximum close to 800 nm are observed. Such spectrum is typical for Si NIs in SiO₂ [1-6]. In Fig. 1, the IPL dependencies on the Si dose at the $T_{\text{ann}} = 1000$ and 1100°C are presented. Earlier, it was shown [7] that for $T_{\text{ann}} = 1000^\circ \text{C}$, the dependence well coincides with the calculated one. This calculation was made on the base of the model of the NI accumulation with the dose

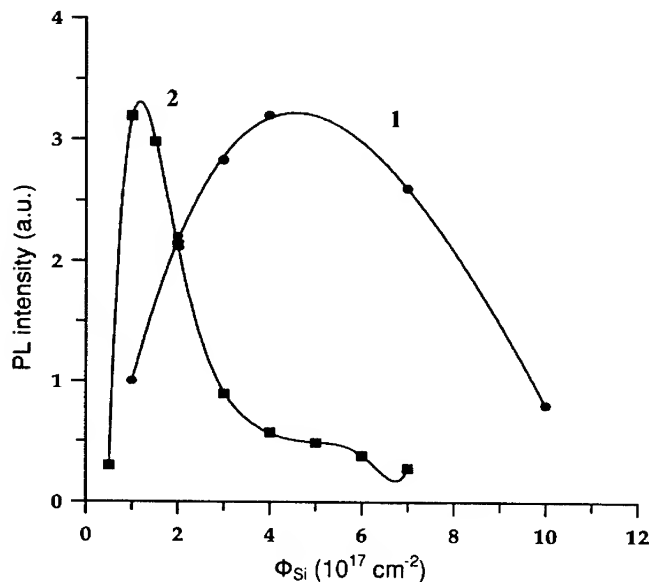


Fig. 1. The silicon dose (Φ_{Si}) dependencies of PL peak intensity at two annealing temperatures. T_{ann} : 1 - 1000°C , 2 - 1100°C .

and NI joining at higher doses. It is evident that for 1100°C the IPL dependence on the dose has a similar shape - the curve with the maximum, but the position of the maximum is shifted to the lower doses. It is naturally to explain by the fact that the rate of NI nucleation increases with the annealing temperature, therefore for the same concentration of the excess silicon atoms, the NI density is higher. However, the model used earlier for $T_{\text{ann}} = 1000^\circ \text{C}$ does not allow to explain quantitatively the IPL dependence on the dose for $T_{\text{ann}} = 1100^\circ \text{C}$. Perhaps, it is necessary to take into account other factors, such as Ostwald ripening, the role of which would increase with T_{ann} .

In Fig. 2, the dependence of $F = I_p/I_{\text{wp}}$ (the ratio of IPL for SiO₂:nc-Si additionally doped by phosphorus and those versus without phosphorus doping) on phosphorus dose is shown.

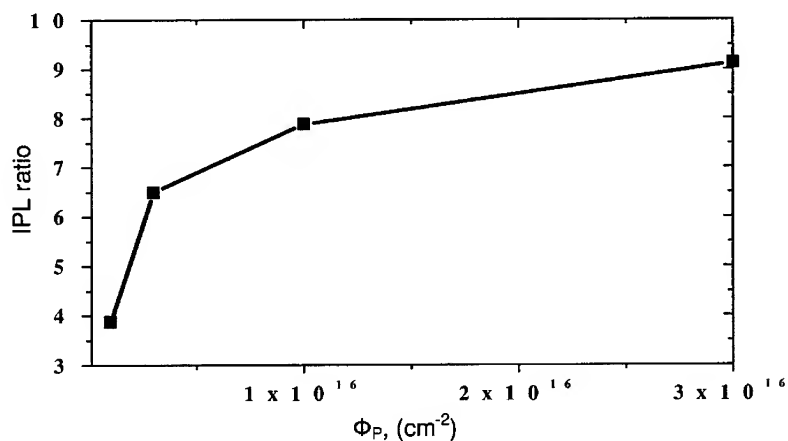


Fig.2. The phosphorus dose (Φ_P) dependence of $F = I_p/I_{wp}$ (the ratio of IPL for $\text{SiO}_2:\text{nc-Si}$ additionally doped by phosphorus and those without phosphorus doping. $\Phi_{\text{Si}} = 1 \cdot 10^{17} \text{ cm}^{-2}$, $T_{\text{ann}} = 1000^\circ \text{C}$).

With growth of the dose, the F magnitude increases. In [6,7], the model is suggested according to which the IPL enhancement at the phosphorus doping is connected with the action of two mechanisms: the passivation of the disrupted bonds (hence, the decrease of the nonradiative recombination rate) and the appearance of additional electrons in the conductivity band of QD. In our case, unlike [5], the decrease of the IPL at the high P concentration is not observed.

In Fig.3, the F dependence on the Si dose at the constant P dose is presented. The decrease of F with Si dose can be caused by the reduction of P atoms number contained in each NI with the increase of the amount of the latter. This is possible if a redistribution of the phosphorus between SiO_2 and NIs during the annealing takes place.

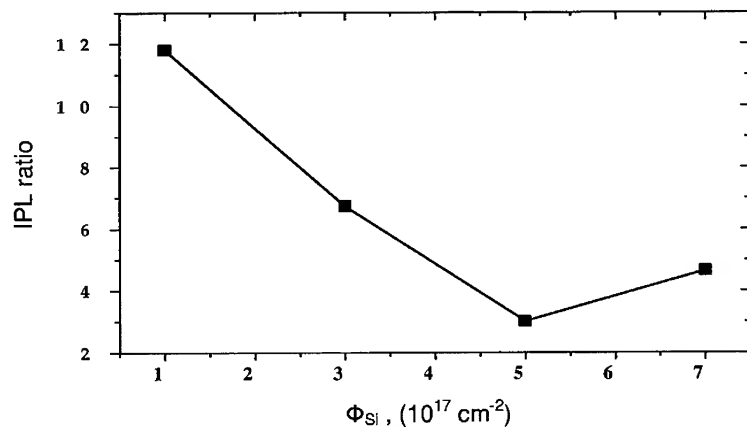


Fig.3. The dependence of $F = I_p/I_{wp}$ (IPL ratio) on the Si dose (Φ_{Si}). $\Phi_P = 1 \cdot 10^{16} \text{ cm}^{-2}$, $T_{\text{ann}} = 1000^\circ \text{C}$.

THEORETICAL ACCOUNTS

To prove theoretically the absence of the essential shifts of the PL peak at the doping by phosphorus, the calculations of the electronic energy spectra and of the optical gap of QD in the envelope function approximation were carried out. For solving the problem we were made the following assumptions: 1) the quantum dots have the spherical shape; 2) the impurity ions create a field of a hydrogen-like type; 3) spin-orbit interaction can be neglected; 4) the silicon quantum dots are placed in a dielectric matrix.

For the definition of energy levels we must solve the equation for the envelope functions $F_\mu(\vec{r})$

$$\hat{H}_{\mu\nu} F_\nu(\vec{r}) = E F_\mu(\vec{r}), \quad (1)$$

where E is the electron energy which is counted off the top of the valence band, and operator $\hat{H}_{\mu\nu}$ represents the single-electron Hamiltonian which was written in a $\vec{k} \cdot \vec{p}$ -approximation. Near the X-point in a conduction band the Hamiltonian is represented by a 2×2 matrix:

$$\begin{pmatrix} \hat{H}_{0x} + \frac{\hbar^2}{6} \left(\frac{1}{m_t} - \frac{1}{m_l} \right) (\vec{k}^2 - 3\hat{k}_z^2) + \hat{V}_c & \hbar^2 \left(\frac{1}{m_t} - \frac{1}{m_0} \right) \hat{k}_x \hat{k}_y + i \frac{\hbar^2 k_0}{m_t} \hat{k}_z \\ \hbar^2 \left(\frac{1}{m_t} - \frac{1}{m_0} \right) \hat{k}_x \hat{k}_y - i \frac{\hbar^2 k_0}{m_t} \hat{k}_z & \hat{H}_{0x} + \frac{\hbar^2}{6} \left(\frac{1}{m_t} - \frac{1}{m_l} \right) (\vec{k}^2 - 3\hat{k}_z^2) + \hat{V}_c \end{pmatrix}$$

Here

$$\hat{H}_{0x} = \Delta_{\Gamma X} + \frac{\hbar^2 \vec{k}^2}{2m_c}$$

is the isotropic operator with the electronic effective mass $m_c = 3m_t m_l / (2m_t + m_l)$, where m_t and m_l are the "transverse" and "longitudinal" mass respectively. These masses equal $0.19m_0$ and $0.92m_0$. Value $k_0 = 0.144 \cdot 2\pi/a$ is determining the distance in \vec{k} -space between X-point and the nearest minimum of the energy in Brillouin zone, $a = 0.354 \text{ nm}$ - the lattice constant, $\Delta_{\Gamma X} = 1.215 \text{ eV}$ is the difference between the energies in X-point of the conduction band and in Γ -point of the valence band. \hat{V}_c is the operator of Coulomb interaction which can be written as

$$\hat{V}_c = - \sum_{j=1}^K \frac{e^2}{\epsilon_s |\vec{r} - \vec{h}_j|} - \frac{e^2 (\epsilon_s - \epsilon_d)}{\epsilon_s R} \sum_{j=1}^K \sum_{l=0}^{\infty} \frac{h_j^l r^l}{R^{2l}} \frac{l+1}{l\epsilon_s + (l+1)\epsilon_d} P_l(\cos \Theta_j) +$$

$$\frac{e^2 (\epsilon_s - \epsilon_d)}{2\epsilon_s R} \sum_{l=0}^{\infty} \frac{r^{2l}}{R^{2l}} \frac{l+1}{l\epsilon_s + (l+1)\epsilon_d}.$$

It consists of two part: the direct Coulomb interaction between electron and impurity ions, and the interaction between electron and two image fields - of ions and of electron itself. \vec{h}_j is the radius-vector of the impurity ion with the number j , parameters ϵ_s and ϵ_d are the dielectric constants of silicon and dielectric matrix, R is the dot radius, $-e$ is the electron charge, K is the number of the impurity ions and $P_l(\cos\theta_j)$ is a Legendre polynomial.

Near the Γ -point in a valence band the Hamiltonian is represented by a 3×3 matrix

$$\begin{pmatrix} \hat{H}_{0h} + \hat{V}_x + \hat{V}_c & -N\hat{k}_x\hat{k}_y & -N\hat{k}_x\hat{k}_z \\ -N\hat{k}_x\hat{k}_y & \hat{H}_{0h} + \hat{V}_y + \hat{V}_c & -N\hat{k}_y\hat{k}_z \\ -N\hat{k}_x\hat{k}_z & -N\hat{k}_y\hat{k}_z & \hat{H}_{0h} + \hat{V}_z + \hat{V}_c \end{pmatrix}$$

Here

$$\hat{H}_{0h} = -\frac{\hbar^2 \hat{k}^2}{2m_h}, \quad \hat{V}_j = \frac{\hbar^2}{2m_0} \frac{L-M}{3} (\hat{k}^2 - 3\hat{k}_j^2)$$

and m_h is the hole effective mass which equals $3m_0/(L+2M)$. The numbers L , M , N are the empirical parameters which equal 6.8, 4.43, 8.61 respectively [8].

The Hamiltonian $\hat{H}_{\mu\nu}$ takes into account the real silicon band structure possessing rather strong anisotropy. However, in spite of this, the anisotropy of the dispersion law can be described by means of a perturbation theory, as well as a Coulomb interaction with impurity ions.

Solving equation (1) we find the several lowest energy levels in the conduction band and several highest energy levels in the valence band and also their dependence on number K for different types of an impurity distribution. Then the change of the optical gap Δ due to the presence of an impurity in the quantum dot can be written as

$$\delta(K, \vec{h}) = \Delta(K, \vec{h}) - \Delta(0), \quad (2)$$

where vector \vec{h} means the set $(\vec{h}_1, \vec{h}_2, \dots, \vec{h}_K)$.

The results of our calculations are presented in the Table. The gap $\Delta_\infty(0)$ corresponds to the case when the potential barriers height is assumed infinite. In this case the magnitude of the optical gap without impurity has the greatest value. If we have taken into account the finite height of the barriers (3.1eV for electrons and 4.4eV for holes), the gap will be less ($\Delta_1(0)$ in the Table.1). The smallest values of the gap are obtained when we take into account not only the finite height of the barriers, but also the discontinuity of the effective mass on the boundary of the quantum dot. The gap $\Delta_2(0)$ was calculated for the case when the electron effective mass in the dielectric matrix equals m_0 and does not coincides with the masses m_e or m_h in the silicon quantum dot. As we can see, the differences between $\Delta_\infty(0)$ and $\Delta_2(0)$ are rather significant. Note that the values

$\Delta_2(0)$ for different sizes of the quantum dot are in good agreement with the experimental data [9,10,11] and with the theoretical calculations of other authors who used another methods (such as local density approximation [12], tight-binding model [13,14] or pseudopotential method [15,16]).

The calculations of the optical gap shift $\delta(K, \bar{h})$ were carried out in the framework of more simple model with the infinite barriers. Another models with the finite height of the barriers are significantly more complicated for the calculations, and as the estimations have shown, the results do not differ essentially. The position of the energy levels and hence the value δ will be depend not only on the quantity of donors but also on the distribution of ions inside the quantum dot. Since it is impossible to obtain the analitical expression for the shift δ in a general case, we consider a three kinds of impurity distribution which correspond to some extreme situations.

Table.1. The magnitudes of the optical gaps (Δ) and its shifts (δ) due to the presence of the impurity atoms (eV) for different values of radius (nm).

R	$\Delta_1(0)$	$\Delta_2(0)$	$\Delta_2(0)$	δ_1			δ_2		
				K = 1	K = 3	K = 5	K = 1	K = 3	K = 5
1.5	2.63	2.28	1.90	-0.04	-0.12	-0.21	-0.08	-0.30	-0.55
2	1.98	1.83	1.64	-0.03	-0.09	-0.15	-0.06	-0.23	-0.42
2.5	1.69	1.61	1.50	-0.02	-0.07	-0.12	-0.05	-0.18	-0.34

One of these is the case, when impurity ions distributed by the centrally-simmetric way on the boundary of the quantum dot ($h_j = R$). As the calculations have shown, in this case $\delta = 0$ irrespective of the donors number K . In the other case, when all the impurity atoms are situated at the centre of the quantum dot ($h_j = 0$, actually $h_j \ll R$), the shift δ , which is denoted by δ_1 in the Table, is nonzero. The last case corresponds to the maximum asymmetric distribution with the maximum electrical dipole momentum, when all the impurity atoms are situated in one place on the boundary of the quantum dot. This distribution type gives more significant shift δ_2 (see the Table.1).

As it has been seen from the table the magnitude of the shift is rather small almost in all cases, shown in the Table, excluding the case of the maximum asymmetric distribution with the large number of donors ($K = 5$). However, it is clear, that this kind of the distribution is hardly realized in experiments and the possibility of such configurations strongly decreases with increasing K . Hence, the contribution of the asymmetric configurations with the maximum dipole momentum will be negligible.

In reality, the impurity atoms, perhaps, are randomly situated inside the NI. Therefore, the true magnitude of δ for $K \leq 5$ would be somehow averaged one between ~ -0.2 eV and zero, e.g. -0.1 eV $< \delta < 0$. For the case $K \gg 1$, the consideration becomes not justified enough because: (i) the interaction between impurity atoms must be taken into account (the approximation of isolated atoms can be not right); (ii) the validity of the perturbation theory can be violated.

Thus, the magnitude δ , obtained experimentally, can not exceed a several per cents from the magnitude of the gap and the shift of the luminescence peak in the presence of phosphorus must be rather small.

CONCLUSIONS

1. The dependences of IPL from Si doses similar character for $T_{\text{ann}}=1000^{\circ}\text{C}$ and 1100°C . However, for the latter case, unlike the first one, it can not be quantitatively described by the same model.
2. The additional phosphorus implantation causes the IPL enhancement for all the impurity doses investigated.
3. The effectivity of phosphorus related IPL enhancement drops with the silicon dose (excess silicon concentration)
4. Theoretical consideration in effective mass approximation shows that (in agreement with experiment) the phosphorus doping would not shift the luminescent peak position significantly for the interband transitions.

ACKNOWLEDGEMENTS

This work is supported by RFBR (grants No: 00-02-17488, 01-02-06399, 01-02-06397) and INTAS (grant No: 00-0064).

REFERENCES

1. P. Mutti, G. Ghisloti, S. Bertoni, L. Bonoldi, G.F. Cerofolini, L. Meda, E. Grilli, M. Guzzi, Appl. Phys. Lett., 66, 851, (1995).
2. T. Shimizu-Iwayama, K. Fujita, S. Nakao, K. Saitoh, R. Fujita, N. Itoh, J.Appl.Phys., 75, 7779, (1994).
3. K. S. Min, K.V. Scheglov, C.M. Yang, H. A. Atwater, M.L. Brongersma, A. Polman, Appl. Phys. Lett., 69, 2033, (1996).
4. G.A. Kachurin, I.E. Tischenko, K.S. Zhuravlev, N.A. Pazdnikov, V.A. Volodin, A.K. Gutakovsky, A.F. Leiser, W. Skorupa, R.A. Yankov, Nucl. Instr. Meth. B, 122, 571, (1997).
5. M. Fujii, A. Mimura, S. Hayashi, K. Yamamoto, Appl. Phys. Lett., 75, 184, (1999).
6. D.I. Tetelbaum, O.N.Gorshkov, S.A.Trushun, D.G.Revin, D.M.Gaponova, W. Eckstein, Nanotechnology, 11, 295, (2000).
7. D.I. Tetelbaum, S.A. Trushin, V.A. Burdov, A.I. Golovanov, D.G. Revin, D.M. Gaponova, B, 174, 123, (2001).
8. M. Voos, Ph. Uzan, C. Delalande, G. Bastard, A. Halimaoui, Appl. Phys. Lett., 61, 1213, (1992).
9. A. Mimura, M. Fujii, S. Hayashi, D. Kovalev, F. Koch, Phys. Rev. B, 62, 12625, (2000).
10. S. Takeoka, M. Fujii, S. Hayashi, Phys. Rev. B, 62, 16820, (2000).
11. S. Guha, B. Quadri, R.G. Musket, M.A. Wall, T. Shimizu-Iwayama, J. Appl. Phys., 88, 3954, (2000).
12. B. Delley, E.F. Steigmeier, Appl. Phys. Lett., 67, 2370, (1995).
13. S. Y.Ren, J.D. Dow, Phys. Rev. B, 45, 6492, (1992).
14. C. Delerue, M. Lannoo, G. Allan, Phys. Rev. Lett., 84, 2457, (2000).
15. S. Ogut, J.R. Chelikowsky, Phys. Rev. Lett., 79, 1770, (1997).
16. A. Franceschetti, A. Zunger, Phys. Rev. B, 62, 2614, (2000).

**Growth, Materials,
and Doping**

Airplane and Drop Experiments on Crystallization of $\text{In}_x\text{Ga}_{1-x}\text{Sb}$ Semiconductor under Different Gravity Conditions

Krishnan Balakrishnan¹, Yasuhiro Hayakawa¹, Hideki Komatsu¹, Noriaki Murakami¹, Tetsuo Nakamura¹, Tadashi Kimura¹, Tetsuo Ozawa², Yasunori Okano³, Masafumi Miyazawa³, Sadik Dost⁴, Le. H. Dao⁵ and Masashi Kumagawa¹

¹Research Institute of Electronics, Shizuoka University, 3-5-1 Johoku, Hamamatsu, Shizuoka 432-8011, Japan.

²Dept. of Electrical Eng., Shizuoka Inst. of Sci. & Tech., Fukuroi 437-8555, Japan.

³Faculty of Eng., Shizuoka University, Hamamatsu 432-8561, Japan.

⁴Dept. of Mech. Eng., University of Victoria, Victoria, BC, Canada V8W 3P6.

⁵Adv. Mat. Res. Lab., Univ. du Quebec, INRS, Verennes, Quebec, Canada J3X1S2.

ABSTRACT

Melting and crystallization experiments of InGaSb were done under the reduced gravity condition (10^{-2}G) in an airplane and at the normal gravity condition (1G) in the laboratory. Crystallized InGaSb was found to contain many needle crystals in both the cases. Reduced gravity condition was found to be more conducive for crystal growth than the normal gravity condition. Formation of spherical projections on the surface of InGaSb during its crystallization was in-situ observed using a high speed CCD camera in the drop experiment. Spherical projections showed dependence of gravity during its growth. Indium compositions in the spherical projections were found to vary depending on the temperature.

INTRODUCTION

$\text{In}_x\text{Ga}_{1-x}\text{Sb}$ is a potential optoelectronic device oriented material and it could be used to fabricate commercially viable detectors, thermo-photo-voltaic (TPV) cells. $\text{In}_x\text{Ga}_{1-x}\text{Sb}$ along with its binary counterparts GaSb and InSb are interesting III-V model materials for space ventures because of their low melting temperatures (712°C and below) and low vapour pressures. It is extremely difficult to grow high quality $\text{In}_x\text{Ga}_{1-x}\text{Sb}$ bulk crystals on earth due to gravity induced effects. As the densities of the components are different, solute transport occurs due to buoyancy. For this reason, microgravity condition in space is ideally suited to grow high quality and defect free $\text{In}_x\text{Ga}_{1-x}\text{Sb}$ crystals as the gravity induced negative effects can be overcome [1-3]. In order to investigate the effect of gravity on the dissolution and crystallization processes, we carried out two microgravity experiments. The first one was performed in the Second International Microgravity Laboratory (IML-2) in 1994 [4-7]. We studied the effects of diffusion and convection on the melt mixing of In/GaSb/Sb . One of the important observations made in this venture was the formation of many circular projections on the surface of the InGaSb spherical sample. The indium compositions in this area were different from those in the main body of the sample. The other experiment was carried out in a Chinese recoverable satellite in 1996 [8-10].

It is not always possible to venture microgravity experiments in space using space shuttles due to economic and other major constraints. Hence, it is necessary to find alternate avenues to perform this type of experiments on earth itself using the facilities like drop tower, airplane etc. It is also important to know how the crystal growth processes take place under the reduced gravity conditions like 10^{-1}G , 10^{-2}G

etc. and under the higher gravity conditions, like, 2G, 3G etc. In the present article, we discuss about the results of the airplane and drop experiments on the crystallization of InGaSb conducted under different gravity conditions.

EXPERIMENTAL

For the airplane experiment, polycrystalline $\text{In}_{1-x}\text{Ga}_x\text{Sb}$ ($x=0.05$) cut into a dimension of $5 \times 5 \times 0.2 \text{ mm}^3$ was used as the starting material. The sample was sandwiched between two thin quartz glass plates and was sealed using high temperature adhesives. Thermocouples were connected to the samples to monitor and control the temperature during the melting and crystallization processes. The sample configuration is shown in Fig.1. An equipment was designed and constructed for the airplane experiment. The sample was mounted on a movable platform so that the position of it could be changed using a motor during the experiment. The InGaSb sample was heated to a temperature of 706°C . During this time, InGaSb poly crystal melted and changed to In-Ga-Sb solution. When the gravity level changed to 10^{-2}G , the sample was moved out of the furnace and hence the temperature decreased rapidly. This process is schematically represented in Fig.2. During the rapid decrease of temperature, InGaSb crystallized. The complete experiment was videographed using a high resolution CCD camera. The same type of experiment was carried out under the normal gravity (1G) in the laboratory.

For the drop experiment, polycrystals of InGaSb were used as the starting materials. The sample structure was similar to Fig.1. This experiment was performed using a 150m drop tower facility present in the Micro-Gravity Laboratory of Japan (MGLAB). An equipment comprising a furnace to heat the sample, thermocouples, temperature controllers to control the sample and furnace temperatures, a high speed and high resolution CCD camera, and two lights, was constructed for this study and the schematic diagram of it is shown in Fig.3. The melting and crystallization of InGaSb during the experiment was videographed using the high speed and high resolution camera. The recorded images and the corresponding temperatures and gravity levels were used to study the melting and crystallization processes. InGaSb polycrystalline plate sample was heated to a temperature of 800°C at a rate of $50^\circ\text{C}/\text{min}$ and kept for 10 minutes. Later, the sample was cooled down by cutting off the power supply. During the cooling period, molten InGaSb started crystallizing. During the crystallization, the capsule was dropped in to the vacuum tower.

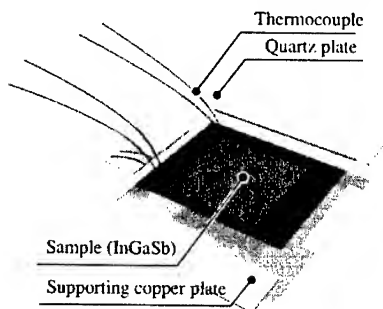


Fig.1. Sample configuration for the airplane and drop experiments.

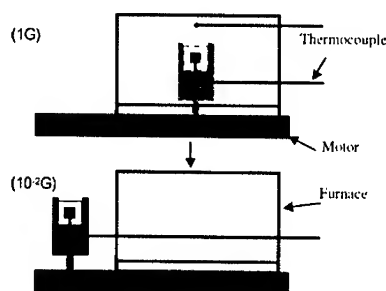


Fig.2. Change of sample position during the airplane experiment.

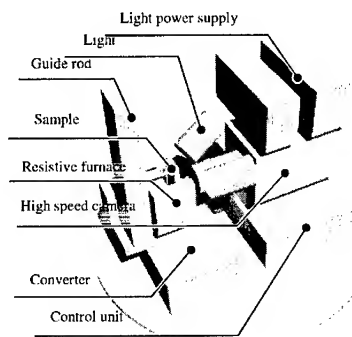


Fig.3. Schematic diagram of home-made equipment for the drop experiment.

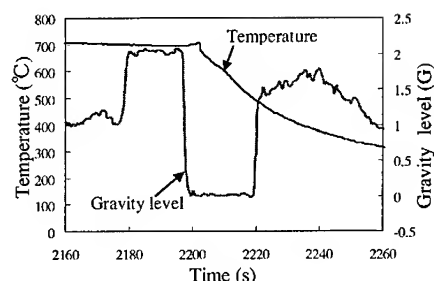


Fig.4. Variation of gravity level and sample temperature with time in the airplane experiment.

RESULTS AND DISCUSSION

Effect of gravity on the needle crystal growth

Figure 4 shows the variation of the gravity level with the flying time of the aircraft and the temperature of the InGaSb sample during the experiment. The set temperature of the sample was decreased to less than 500°C in a time of a second after the gravity became 10^{-2} G. Figure 5 shows the photographs of the crystallized InGaSb samples under 10^{-2} G and 1G conditions, respectively, and the corresponding EPMA line profiles of indium composition measured on the surfaces of the samples. The needle crystals were found to have formed during the cooling of InGaSb. This result is similar to the needle crystal formed in our space experiment under microgravity condition [10]. In the case of the needle crystal formed under reduced gravity (10^{-2} G) and normal gravity, indium composition should be as small as 0.005. Figure 6 shows the binary phase diagram of the InSb-GaSb system. As marked in the phase diagram, the sample must be cooled down fast to get the crystal of indium composition 0.005. Hence, in the EPMA profile, the portions where the In composition is 0.005, correspond to the InGaSb needle crystal and the portions where the In composition is high, correspond to the residual solution. The needle crystal is surrounded by the residual solution and its indium composition is much more than that of the crystal. As seen in the EPMA profiles, in the case of reduced gravity processed sample, the number of indium peaks is relatively smaller than the peaks observed in the normal gravity processed sample.

Figures 7(a) and (b) show the statistics of the size of the needle crystals formed under reduced gravity and normal gravity conditions, respectively. As clearly seen in the figures, the number of smaller sized crystals formed under normal gravity conditions is much more than the number of smaller crystals formed under reduced gravity condition. It is obvious that the convective forces during the crystal growth processes behave differently depending on the gravity conditions. Under the reduced gravity condition, growth of larger sized crystals is more feasible as the negative effect of the convective forces is relatively less. In the case of the crystal growth under normal gravity, due to the convective forces, most of the needle crystals grown were smaller. This clearly indicates that the reduced gravity condition is better suited for crystal growth.

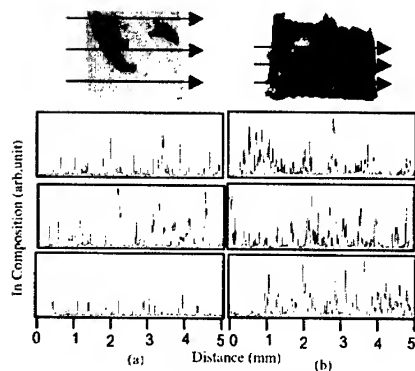


Fig. 5. EPMA line profiles for the needle crystals grown under (a) reduced gravity and (b) normal gravity.

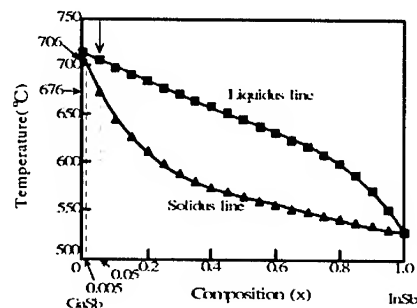


Fig. 6. InSb-GaSb binary phase diagram.

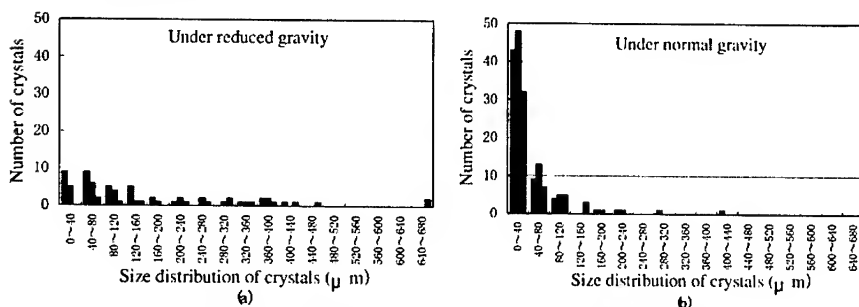


Fig. 7. Size distribution of the needle crystals grown under (a) reduced gravity ($10^{-2}G$) and (b) normal gravity conditions.

Formation of projections during InGaSb crystallization

During the crystallization of InGaSb, many spherical projections were observed on the surface of the sample. The projections emerged out during the crystallization of InGaSb from its melt due to the reason that the density of InGaSb liquid is larger than that of solid. These were similar to the projections observed in the melting and solidification experiment of In/GaSb/Sb done in IML-2 [5]. The projections in this study were found to increase in size slowly. In the present experiment, the drop of the capsule was made to coincide with the appearance and growth of spherical projections so that this process could be observed under microgravity condition. Figure 8 shows the high resolution images recorded using high speed camera during the crystallization of InGaSb in one of the drop experiments. As seen clearly in the images, the spherical projections have just started to appear and grow larger in size slowly as the time passed. The figures (a)-(f) correspond to the images recorded under microgravity condition at the timings 0s, 1s, 2s, 3s, 4s and 4.5 s, respectively. The enlarged image of the final form of the projections formed is shown in the Fig. 9. The projection A was formed under normal gravity condition and the projections B and C were formed

under microgravity condition. The projections formed under microgravity were almost spherical, whereas, the projection formed under normal gravity was not perfectly spherical. Due to gravitational pull, the top surface of the projection A tended to become flat. This shows the influence of gravity on the formation of projections.

It was found that the rate of increase of projection area was high and constant for the first 3 sec. However, in the remaining time, the increase rate became lower and this may be due to the reduction of solute supply in the final stage of projection formation. The solute supply was blocked to some extent by the already formed crystal in the lower portion of the projection.

The In compositions in the formed projection B and C were measured by EPMA and are schematically represented in Fig.10. The In composition in the projection C was found to be more than that of projection B. This is due to fact that the temperature at the time of the formation of projection B was higher than the corresponding temperature of projection C. This indicates that the In composition of the crystallized InGaSb varies depending on the existing temperature at the time of formation. This is in accordance with the InSb-GaSb ternary phase diagram [11]. Since the whole processes of melting and crystallization of InGaSb were recorded using the high speed and high resolution CCD camera (a maximum of 250 images per second) in all the experiments along with the precise values of the corresponding gravity levels and temperatures, it was possible to find the exact conditions at which the projections formed.

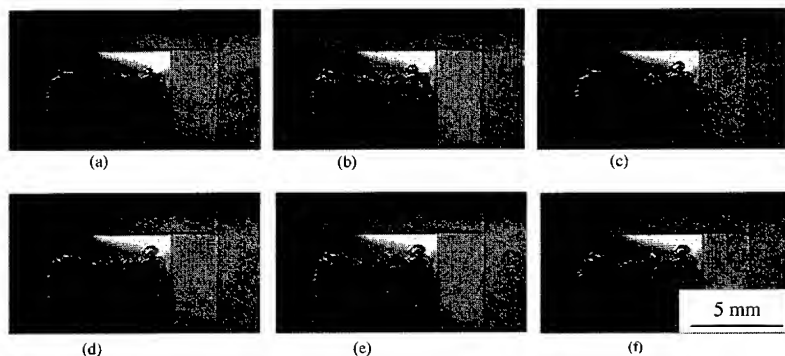


Fig.8. High resolution images recorded during the crystallization of InGaSb at the timings, (a) 0s, (b) 1s, (c) 2s, (d) 3s, (e) 4s and (f) 4.5 s, respectively.

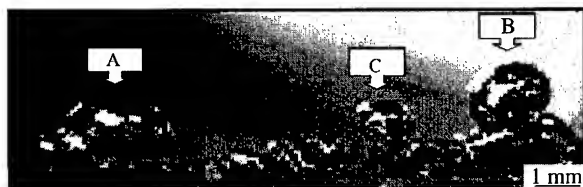


Fig.9. The enlarged images of the final shape of the projections. The projection A was formed under normal gravity condition and the projections B and C formed under microgravity condition.

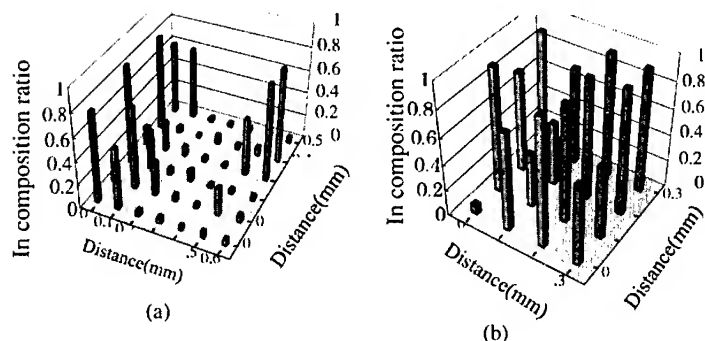


Fig.10. The 3-dimensional schematic representation of the In compositions measured on the (a) projection B and (b) projection C. The measurements were made at the selected points on the squares of areas $0.6 \times 0.7 \text{ mm}^2$ and $0.4 \times 0.4 \text{ mm}^2$ of projections B and C, respectively.

SUMMARY

In the airplane experiment on the crystallization of InGaSb under $10^{-2}G$ condition, needle crystal was found to have formed and the size of it was larger than the crystal obtained under normal gravity. This showed that the reduced gravity condition is more feasible for crystal growth. In the drop experiment, spherical projections of InGaSb were observed to form during its crystallization under microgravity. On the other hand, projection formed under normal gravity was not perfectly spherical. Indium composition in the projection was found to vary depending on the existing temperature condition during the formation.

ACKNOWLEDGEMENT

This study is funded by a part of "Ground Research for Space Utilization" promoted by NASDA and Japan Space Forum, and Monbusho grant-in-aid for the International scientific program and scientific encouragement fund in Shizuoka University. Technical assistance of Mr. Momose is acknowledged.

REFERENCES

1. A.F.Witt, H.C.Gatos, M.Lichtensteiger and C.J.Herman, *J.Electrochem.Soc.* 125 (1978)1832.
2. A.N.Danilewsky, K.W.Benz and T.Nishinaga, *J.Crystal Growth* 99(1990)1282.
3. T.Nishinaga, P.Ge. C.Huo, J.He and T.Nakamura, *J.Crystal Growth* 174 (1997)96.
4. K.Okitsu, Y.Hayakawa, T.Yamaguchi, K.Kumagawa, A.Hirata, M.Tachibana and N.Imaishi, *Trans.Mat.Res.Soc.Jpn.*, 16A (1995) 691.
5. K.Okitsu, Y.Hayakawa, A.Hirata, S.Fujiwara, Y.Okano, N.Imaishi, S.Yoda, T.Oida, T.Yamaguchi and M. Kumagawa, *M. Cryst. Res. and Tech.*, 31(1996) 969.
6. K.Okitsu, Y.Hayakawa, T.Yamaguchi, A.Hirata, S.Fujiwara, Y.Okano, N.Imaishi, S.Yoda, T.Oida and M. Kumagawa, *Jpn. J. Appl. Phys.* 36(1997) 3613.

7. A.Hirata, K. Okitsu, Y.Hayakawa, Y.Okano, S. Sakai, S. Fujiwara, N. Imaishi, Y. Yamaguchi, S. Yoda, T. Oida and M. Kumagawa, *Int. J. Appl. Electromagnetics and Mechanics* 10 (1999) 527.
8. A.Hirata, Y.Hayakawa, T.Wada, D.Hirose T.Yamaguchi, Y.Okano, J.Simizu, K.Arafune, N.Imaishi, Y.Kumagiri, X.Zhong, X.Xie, B.Yuan, F.Wu, H.Liu and M.Kumagawa, *Proc.of 21st International Symposium on Space Technology and Science* (Oomiya, Japan, 1998.5) Vol. II , (1998) 1243.
9. T.Kimura, Y.Hayakawa, T.Ozawa, Y.Okano, A.Hirata, M.Miyazawa, N.Imaishi, K.Arafune, T.Yamaguchi and M.Kumagawa, *J.Jpn Soc.Microgravity Appl.*15, Supplement II (1999) 472.
10. Y.Hayakawa, Y. Okano, A. Hirata, N. Imaishi, Y. Kumagiri, X. Zhong, X. Xie, B. Yuan, F. Wu, H. Liu, T. Yamaguchi, and M. Kumagawa, *J. Crystal Growth* 213(2000)40.
11. G.B. Stringfellow, *J.Phys.Chem.Solids* 33 (1972) 665.

Photo-Assisted MOVPE Growth of ZnMgS on (100) Si

Angel Rodriguez, Jeremy Shattuck, Xiaoguang Zhang, Peng Li, David Parent¹, John Ayers and Faquir Jain

University of Connecticut, Department of Electrical and Computer Science Engineering,
Storrs, CT 06269-2157, U.S.A.

¹San Jose State University, Department of Electrical Engineering,
San Jose, CA, U.S.A.

ABSTRACT

This paper presents for the first time photo-assisted Metalorganic vapor phase epitaxial (MOVPE) growth of ZnMgS on Si (100) substrates. The growth was done using dimethylzinc (DMZn), bismethylcyclo-pentadienyl-magnesium ((MeCP)₂Mg), and diethylsulfide (DES) as zinc, magnesium, and sulfur precursors. Epitaxial characterization by X-ray Photoelectron Spectroscopy (XPS), and low - angle X-ray Diffraction (XRD) results are presented. Mg solid phase incorporation is estimated to vary from 0 to 60 percent. The epitaxial nature of the ZnMgS layers has been verified using the low-angle X-ray diffraction eliminating any interference from the Si substrate. It can be shown with this technique that the change in the ZnMgS peak position changes from 27.35 degrees to 26.5 degrees with an increase in Mg incorporation, compared with a Si control sample peak at 27.4 degrees. XRD results obtained have been verified with XPS data. Chlorine doping of the ZnMgS layer was also studied. Concentrations up to $3 \times 10^{15} \text{ cm}^{-3}$ were observed in the ZnMgS layer. Results of the n (ZnMgS:Cl) - p (Si) diodes fabricated are also presented.

INTRODUCTION

The availability of flat panel televisions, laptop computers and many other products during the past decade has been made possible by the development of flat panel displays (FPDs). FPD technologies include electroluminescent displays (ELDs), light emitting diode arrays, plasma display panels (PDPs), liquid crystal displays (LCDs), and flat cathode ray tubes (CRTs). Their applications generally fall into two broad categories: (i) High Information Content (HIC) or high pixel count displays having 50,000 to 10^6 pixels per frame (both monochrome and color), and (ii) lower pixel count displays as used in calculators, clocks, and other consumer products.

II-VI materials such as ZnCdSe have been used and proposed in the implementation of laser diodes emitting in the red through blue spectrum [1-3]. An application for this material system includes flat panel displays, which has the advantage of enabling the realization of transistor drivers in the silicon substrate.

Another application includes higher efficiency solar cells, which are also currently under investigation [4,5]. Advantages of using wide-band gap material in solar cells include lower losses in the window region, and lower ohmic losses. In addition ZnS and Si exhibit closely matched electron affinities.

EXPERIMENT & RESULTS

A vertical, stainless steel EMCORE reactor with a rotating, resistively-heated molybdenum susceptor was used for growth. All growth runs were carried out at 250 Torr, with a susceptor rotation of 350 rpm, and 14.25 slm of palladium-diffused hydrogen as the carrier gas. The photo irradiation was achieved using an Oriel Hg arc lamp operated at 150W electrical power. The ultraviolet irradiation was brought into the reaction chamber using a mirror and a quartz window, resulting in normal incidence on the sample. Neutral density filters were used to adjust the irradiation intensity. All irradiation intensities reported were measured using an intensity meter (manufactured by HTG) outside of the reaction chamber.

Prior to growth, the native oxide on the substrates was removed by an *in-situ* dry etch [6,7,8], using a dilute flow of hydrogen sulfide (H_2S) at a temperature of 900°C for one hour prior to the epitaxial growth. Then temperature was decreased to 360°C for the ZnMgS layer growth. The reactant mole fractions for the ZnMgS layers were 10^{-4} (DMZn), 4×10^{-4} (DES) and $1.8 - 7.4 \times 10^{-6}$ ((McCP) $_2$ Mg).

The samples were characterized using a low-angle X-ray diffraction technique with a Bruker analytical X-ray System D5005 X-ray Diffractometer. The results of which are seen in Figure 1. With this technique the X-ray beam is incident on the sample at very small angles, usually $0.5^\circ - 5^\circ$, to confine the penetration of the X-ray beam to the epitaxial film only. In this system the sample is fixed, and the X-ray source is fixed after the angle of incidence as been selected. The detector head rotates from the initial 2θ angle to the final 2θ angle selected by the user.

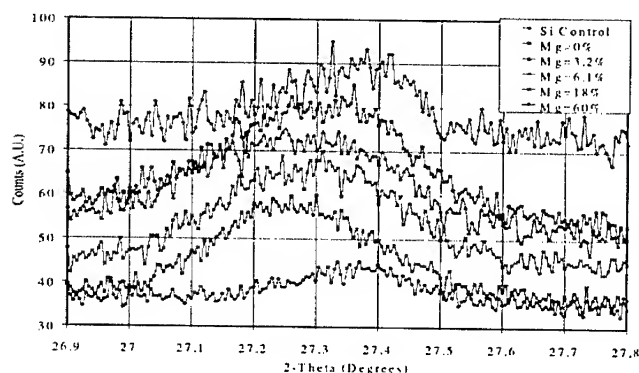


Figure 1. Low-angle X-ray diffraction curves measured at room temperature, for different Mg compositions of x for $Zn_{1-x}Mg_xS/Si(100)$ heterostructures. The $Zn_{1-x}Mg_xS$ epitaxial films were grown at 360°C with $35mW/cm^2$ UV irradiation intensity.

The samples were also sent to Evans East for XPS analysis, where the surface of the sample was examined initially by low-resolution survey scans to determine which elements were present. Then high-resolution depth profiles were acquired, as seen in Figure 2. The samples were profiled (sputtered) using a 3kV Ar^+ ion beam ($3.5 \times 3.5 \text{ mm}^2$ raster) and high-resolution scans of the elements were obtained every 37.5\AA (assuming a SiO_2 sputtering rate).

The quantification of the elements was accomplished by using the atomic sensitivity factors for a Physical Electronics Model 5700Lsci ESCA spectrometer.

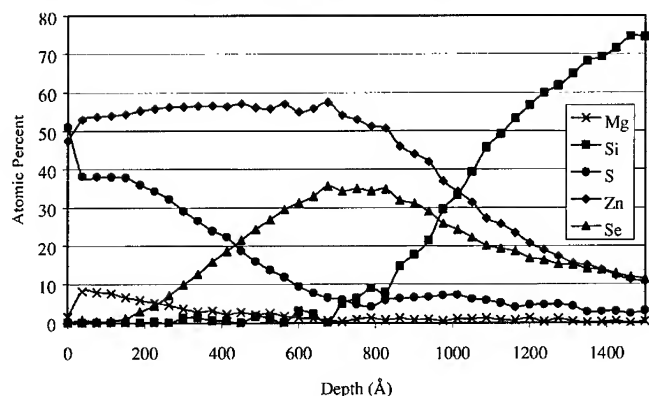


Figure 2. XPS results for run number 1261, for 6.1% composition Mg in the solid phase. The $\text{Zn}_{1-x}\text{Mg}_x\text{S}$ epitaxial film was grown at 360°C with $35\text{mW}/\text{cm}^2$ UV irradiation intensity.

From the results obtained with XPS the percent Mg in the solid phase of ZnMgS versus percent $(\text{MeCp})_2\text{Mg}$ in the gas phase was determined as seen in Figure 3.

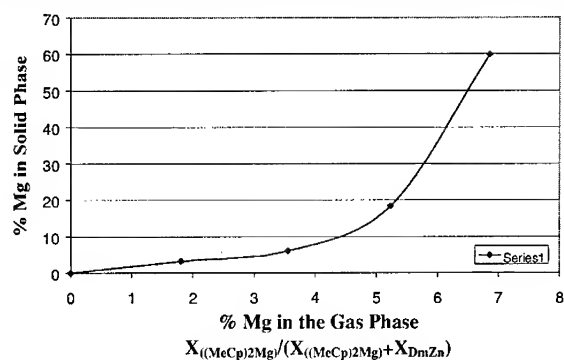


Figure 3. Percent Mg in the solid phase of ZnMgS (as determined by XPS results) versus percent $(\text{MeCp})_2\text{Mg}$ in the gas phase. The $\text{Zn}_{1-x}\text{Mg}_x\text{S}$ epitaxial films were grown at 341°C with $35\text{mW}/\text{cm}^2$ UV irradiation intensity.

Thickness measurements were done by the Filmetrics F20 system, an optical non-destructive thickness measurement system. The results of which are presented in Figure 4.

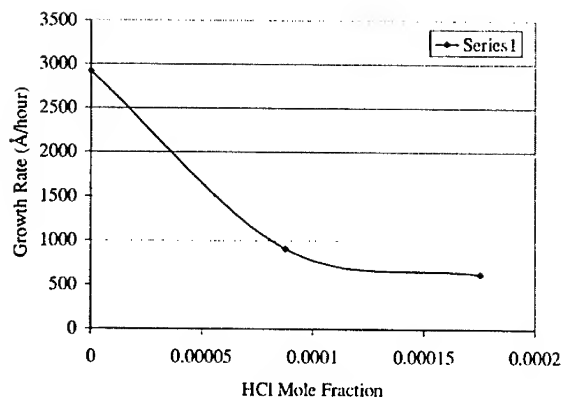


Figure 4. Growth rate of $\text{Zn}_{1-x}\text{Mg}_x\text{S}$ epitaxial films doped with HCL versus HCL mole fraction. The $\text{Zn}_{1-x}\text{Mg}_x\text{S}$ epitaxial films were grown at 360°C with no UV irradiation, and without a buffer layer.

Chlorine doping levels were measured with an AC Hall Effect setup, using the Van der Pauw Method. Since the substrate was not semi-insulating a multi-layer model[9] had to be used to extrapolate the parameters of the epitaxial layer, listed in Table 1.

Table 1. Results from Room Temperature AC Hall Effect Measurements

Sample #	#1280	#1281
Electron Hall Mobilty $\mu_n(\text{cm}^2/\text{V-s})$	2.420×10^3	2.650×10^3
Electron Carrier Concentration(cm^{-3})	2.375×10^{15}	3.058×10^{15}
Conductivity (mhos)	0.9196	1.296
$R_{\text{Hall}} (\Omega)$	2.632×10^3	2.044×10^3
Cl mole fraction	8.771×10^{-5}	1.754×10^{-4}
p-type Si Substrate Conductivity (mhos)	0.1148	

The current - voltage (I-V) characteristics were obtained with an HP 4145B Semiconductor Parameter Analyzer. The results are shown in Figure 5.

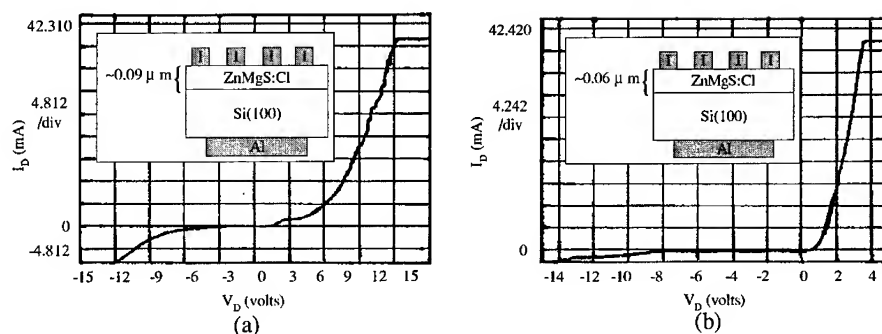


Figure 5. Current - Voltage characteristics of n-type $\text{Zn}_{1-x}\text{Mg}_x\text{S:Cl}$ / p-type Si diodes: (a) sample #1280 (b) sample #1281, (structure shown in insert).

CONCLUSION

This paper presents for the first time photo-assisted MOVPE growth of ZnMgS on Si (100) substrates. Epitaxial characterization by XPS, shows a Mg solid phase incorporation from 0 to 60 percent in the epitaxial layer. The epitaxial nature of the ZnMgS layers has been verified using the low-angle X-ray diffraction eliminating any interference from the Si substrate. It was shown with this technique that the change in the ZnMgS peak position changes from 27.35 degrees to 26.5 degrees with an increase in Mg incorporation, compared with a Si control sample peak at 27.4 degrees. XRD results obtained were verified with XPS data. Chlorine doping of the ZnMgS layer was also studied. Concentrations up to $3 \times 10^{15} \text{ cm}^{-3}$ were observed in the ZnMgS layer. Results of the n (ZnMgS:Cl) – p (Si) diodes fabricated were also presented.

REFERENCES

1. Washizuka, A. Mikami. "A 14.4-in Diagonal High Contrast Multicolor Information EL Display with 640×128 Pixels." *IEICE TRANS. Electron.* E81C (November 1998): pp. 1725-1732.
2. F. Jain. "Electroluminescent Flat Panel Displays Using MOCVD Grown ZnS and Ternary Compounds for Enhanced Blue Emission." *Proposal, University of Connecticut.* (1998).
3. G.P. Crawford. "A Bright New Page in Portable Displays." *IEEE Spectrum.* 37 (October 2000): pp. 40-46.
4. M.B. Spitzer, S.M. Vernon, and C.J. Keavney. "Passivation Techniques for Silicon Solar Cells."
5. G. Landis, J. Loferski, R. Beaulier, P. Sekula-Moisé, S. Vernon, M. Spitzer, and C. Keavney. "Wide-Bandgap Epitaxial Heterojunction Windows for Silicon Solar Cells." *IEEE Transactions on Electron Devices.* 37 (February 1990): pp. 372-380.
6. P. Smith. "Preparation and characterization of ZnS thin films produced by metalorganic chemical vapor deposition." *J. Vac. Sci. Technol.* A7 (May/June 1989): pp. 1451-1455.
7. T. Yokogawa, H. Sato, and M. Ogura. "Growth of ZnSe/ZnS strained-layer superlattices on Si substrates." *Journal of Applied Physics.* 64 (November 1988): pp. 5201-5205.

-
8. P. Rai-Choudhury, and A.J. Noreika. "Hydrogen Sulfide as an Etchant for Silicon." Journal of the Electrochemical Society: Electrochemical Technology. 116 (April 1969): pp. 539-541.
 9. L.F. Lou, and W.H. Frye. "Hall effect and resistivity in liquid-phase-epitaxial layers of HgCdTe." Journal of Applied Physics. 56 (October 1984): pp. 2253-2267.

Optical Vibrational and Structural Properties of $\text{Ge}_{1-x}\text{Sn}_x$ alloys by UHV-CVD

Jennifer Taraci¹, S. Zollner⁴, M. R. McCartney², Jose Menendez³, D. J. Smith^{2,3}, John Tolle¹, M. Bauer¹, Erika Duda⁴, N. V. Edwards⁴, and J. Kouvetakis¹

¹ Department of Chemistry, Arizona State University, Tempe AZ 85287

² Center for Solid State Science, Arizona State University, Tempe AZ 85287

³ Department of Physics and Astronomy, Arizona State University, Tempe AZ 85287

⁴ Motorola Inc, Semiconductor Products Sector, 2200 W. Broadway Rd, Mesa AZ 85502

ABSTRACT

UHV-CVD growth based on a deuterium stabilized Sn hydride and digermane produces Ge-Sn alloys with tunable bandgaps. The $\text{Ge}_{1-x}\text{Sn}_x$ ($x=2-20$ at.%) alloys are deposited on Si (100) and exhibit superior crystallinity and thermal stability compared with MBE grown films. Composition, crystal and electronic structure, and optical and vibrational properties are characterized by RBS, low energy SIMS, high resolution electron microscopy TEM, x-ray diffraction, as well as Raman and IR spectroscopies. TEM studies reveal epitaxial films with lattice constants between those of Ge and Sn. X-ray diffraction shows well-defined (004) peaks and rocking curves indicate a tightly aligned spread of the crystal mosaics. Resonance Raman indicate a E_1 bandgap reduction relative to Ge, consistent with a decrease of the E_2 critical point observed in spectroscopic ellipsometry. IR transmission spectra indicate an increase in absorption with increasing Sn content consistent with a decrease of the direct bandgap.

INTRODUCTION

The preparation of Ge-Sn alloys with cubic structures has attracted considerable attention because of reports that $\text{Ge}_{1-x}\text{Sn}_x$ heterostructures might exhibit tunable direct bandgaps [1,2]. $\text{Ge}_{1-x}\text{Sn}_x$ materials with Sn content greater than 1 at % are, however, thermodynamically unstable. This is due to the large difference in lattice constant of α -Sn (6.489 Å) and Ge (5.646 Å) and the instability of the cubic Sn above 13.2°C with respect to the β -Sn structure [3,4]. Despite this metastability considerable progress has been made in growing high quality $\text{Ge}_{1-x}\text{Sn}_x$ alloys by solid-source MBE and related physical methods [5-9]. Nevertheless major synthetic challenges still remain including segregation of Sn toward the film surface during MBE growth and low thermal stability of MBE-grown samples [9,10]. In some cases, annealing at temperatures as low as 120-300°C causes Sn precipitation and phase segregation. Recently we reported the first chemical method to prepare Ge-Sn materials utilizing precursors that incorporate single Sn atoms in the molecular structure and UHV-CVD [11,12]. Our method has afforded epitaxial, monocrystalline layers on Si (100) which display thermal stability substantially higher than that reported for MBE grown films of comparable compositions. In this report we summarize our growth results and describe in detail the optical, vibrational, and structural properties of the UHV-CVD grown materials.

RESULTS AND DISCUSSION

The depositions are conducted in a custom built UHV-CVD reactor at 350°C and 10^{-4} Torr. The substrates are Si (100) wafers prepared for deposition using a modified RCA process followed by H-passivation of the Si surface using 10% HF. The precursor is a deuterium-stabilized Sn hydride with molecular formula (Ph)SnD₃, Ph=C₆H₅. It has a vapor pressure of 3 Torr at 22°C and decomposes readily in UHV at 250°C to form Sn atoms via elimination of stable d₁-Ph and D₂ byproducts. The reaction of (Ph)SnD₃ with Ge₂H₆ produces epitaxial Ge_{1-x}Sn_x films which incorporate Sn concentrations up to 20 at%. The films adhere extremely well to the Si surface and their visual appearance is similar to that of Ge. Thermal treatment indicated that the alloys are stable up to 650°C for samples with 5 % Sn concentrations, and at least up to 750°C for samples with less than 5 at. % Sn contents. Analyses at the nanometer scale by EDX in a high-resolution electron microscope show that there is no phase segregation or formation of Sn clusters during the annealing. All of the as deposited and annealed samples were analyzed by Rutherford backscattering (RBS) and selected samples were analyzed by secondary ion mass spectrometry (SIMS). RBS was used to determine the concentration of Sn and Ge and to detect and identify any possible D, H, or C impurities as well as to estimate the film thickness. The Sn to Ge elemental concentration was obtained by utilizing 2 MeV He²⁺ ions. Forward scattering and carbon resonance [¹²C(α,α)¹²C] experiments at 4.265 MeV confirmed the absence of D, H and C impurities. To determine the quality of the epitaxial growth, and to confirm substitutionality of Sn in the Ge lattice, the random and aligned (channeled) RBS spectra were recorded and compared. Figure 1 shows the two spectra for a sample containing 5 % Sn in which both Sn and Ge atoms channel remarkably well despite the large difference in lattice dimensions between the epilayer and the Si substrate. Low energy SIMS spectra were recorded on an Atomica 4500 spectrometer with a 300 eV O₂⁺ primary ion beam. Figure 2 shows the SIMS profiles for Ge_{0.95}Sn_{0.05} and Ge_{0.88}Sn_{0.12}.

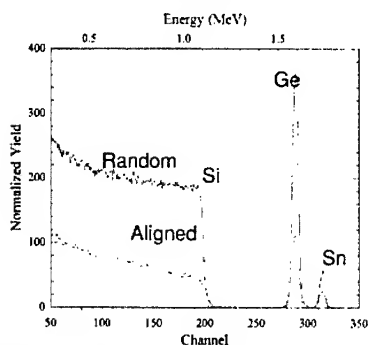


Figure 1. RBS aligned and random spectra for Ge_{0.95}Sn_{0.05}. Channeling is used to determine the crystallinity in the films.

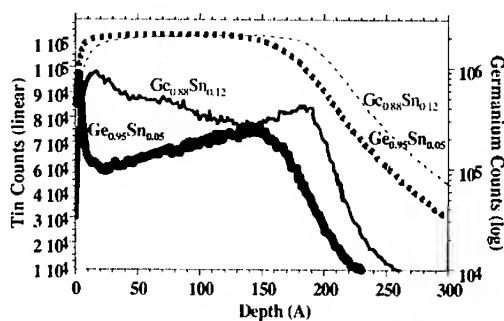


Figure 2. Low energy SIMS profiles of Ge_{0.95}Sn_{0.05} and Ge_{0.88}Sn_{0.12} showing nearly uniform Sn profile throughout the film. The slope is due to the film roughness which is about 10% of the film thickness.

The Ge and Sn profiles are constant in both samples. The slope seen in the Sn profile is due to film roughness. The SIMS spectra revealed background levels of H, and D as well as very low C and O levels primarily at the Si-film interface. The structure of the materials were determined by x-ray diffraction and high resolution TEM. X-ray analysis in the θ - 2θ mode using a rotating anode show a single alloy peak corresponding to the (004) reflection of the diamond lattice. The lattice constants are intermediate between those of Ge and α -Sn. There are no extra peaks due to other phases except for the forbidden $\text{Ge}_{1-x}\text{Sn}_x$ (002) reflection with its intensity increasing with increasing Sn concentration in the samples. This reflection is due to the breaking of the inversion symmetry and it could be related to charge transfer from Sn to Ge. Also, this peak would be expected to appear if the symmetry is broken due to local distortions. This supports local ordering with the Sn atoms perhaps being arranged as second nearest neighbors in the crystal. Figure 3 shows representative patterns for a $\text{Ge}_{0.88}\text{Sn}_{0.12}$. Rocking scans of the (004) reflection have a FWHM less than 0.5° indicating a tightly aligned spread of crystal mosaics.

Cross-sectional TEM revealed that all samples were continuous films with an average roughness of about 10% of the film thickness. The films were monocrystalline and epitaxial. Periodic arrays of edge dislocations and occasional {111} stacking faults originating at the interface were observed but the remainder of the layer was defect-free. Some strain contrast was also observed in the TEM micrographs. A typical cross-sectional electron micrograph of the interface region demonstrating defect free coherent growth of $\text{Ge}_{0.94}\text{Sn}_{0.06}$ is shown in Figure 4. SAED patterns confirm that the material has a cubic structure. There is an appreciable splitting of the spots in the diffraction pattern which is consistent with the large difference in lattice dimensions between the substrate and the film. The lattice parameter obtained from measurements of the SAED patterns from this sample was 5.70 \AA which is intermediate to those of pure Ge (5.646 \AA) and α -Sn (6.489 \AA). A similar value of 5.696 \AA was measured by x-ray diffraction. EDX with a probe size less than 1 nm was used to determine whether the elemental composition was homogeneous on the nanometer scale and to further verify phase purity. A detailed survey of the compositional profiles in cross-section and plan-view geometries showed that the constituent elements were evenly distributed throughout the sample.

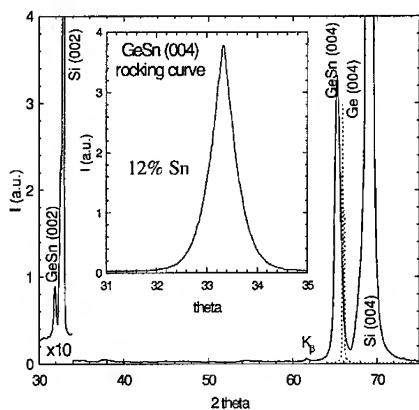


Figure 3. 2θ scan for $\text{Ge}_{0.88}\text{Sn}_{0.12}$ on Si (100). The inset shows the (004) rocking curve.

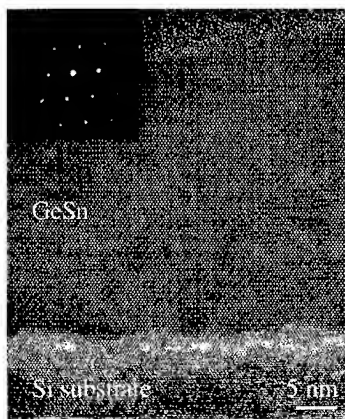


Figure 4. TEM micrograph of $\text{Ge}_{0.94}\text{Sn}_{0.06}$.

The optical properties and band structure of the $\text{Ge}_{1-x}\text{Sn}_x$ were investigated by spectroscopic ellipsometry and resonance Raman. The ellipsometric angles ψ and Δ were acquired for three samples containing 5, 12 and 16 at.% Sn. The data are displayed in the 1 to 6 eV photon-energy range as a pseudodielectric function and fitted in Figure 5 for $\text{Ge}_{0.95}\text{Sn}_{0.05}$. An examination of the imaginary part ϵ_2 shows that the absorption of GeSn rises from low values at 1 eV (just above the band gap of Ge and Si) to a broad peak (E_1) between 1.5 and 2.5 eV (which is actually a combination of an interference fringe and an interband transition) a shoulder E_0' at 3.5 eV and a knee at 4.2 eV called E_2 . The presence of these three peaks indicates a well-pronounced band structure requiring a crystalline film with long-range ordering. More information can be obtained by solving the Fresnel's equations assuming a substrate/film/overlayer sample structure and comparing simulated spectra with the experimental data. Since there is uncertainty for the optical constants below 1.5 eV and above 6 eV, only the data between 1 and 6 eV are shown. The model assumes that the epilayer is Ge (ignoring the effects of Sn alloying) and the surface overlayer is GeO_2 . Using rough Ge as the overlayer leads to similar results. The dashed lines in Figure 5 show the results of the model. The film thickness for sample $\text{Ge}_{0.94}\text{Sn}_{0.06}$ obtained from the fit is 423 Å, with 62 Å of native oxide. The model shows the Ge E_1 and $E_1+\Delta_1$ critical points (doublet) at about 2.3 eV combined with an interference oscillation in ϵ_2 at 1.8 eV. In the experimental data, the splitting between the three structures is not resolved. The reduction in peak height of ϵ_2 at 4.2 eV is due to oxidation of the film combined with roughness. While a detailed analysis of the E_1 and $E_1+\Delta_1$ critical points is not possible in the alloy (since the spin-orbit splitting and the interference fringe are not resolved), the penetration depth of the light should be small enough at higher photon energies in the E_2 region near 4.2 eV. The second derivative of the pseudodielectric function was calculated (to remove the non-resonant background) and fitted with analytical lineshapes (Figure 6). This allows an accurate determination of the E_2 critical-point energy. From the value of E_2 , the Sn content can be determined, since E_2 changes by a large amount between elemental Ge (4.368 eV) and elemental Sn (3.627 eV). We found that E_2 varies from 4.29 to 4.32 eV. The values of Sn concentration we obtain are 6.6, 8.1, and 11.1 % Sn. The corresponding RBS values are 5, 12, and 16 at. % respectively. The magnitude of shifts of E_2 found by ellipsometry are 50 to 80 meV. This method assumes a linear dependence of E_2 on Sn content. It is possible that the dependence of E_2 could be nonlinear for this unusual alloy system. Finally, the broadenings of E_2

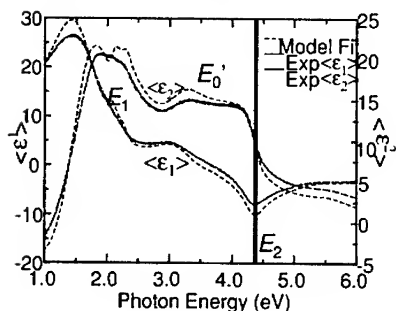


Figure 5. Experimental and model pseudodielectric functions of $\text{Ge}_{0.95}\text{Sn}_{0.05}$.

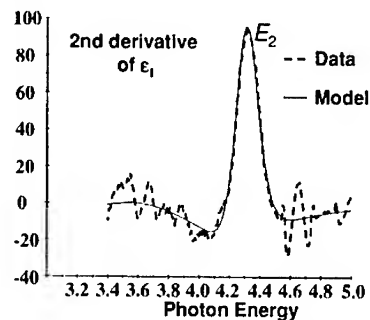


Figure 6. Second derivative of the pseudodielectric function with respect to photon energy. Fit to analytical lineshape.

Raman spectroscopy can be used to study the electronic structure of the alloys by measuring the intensity of the Raman peaks as a function of the laser wavelength. In pure Ge, it has been shown that the Raman cross section undergoes a resonant enhancement for laser photon energies near the E_1 and $E_1 + \Delta_1$ gaps. We performed similar measurements for a $\text{Ge}_{0.95}\text{Sn}_{0.05}$ alloy and a Ge reference. The net result is that we find a redshift of E_1 and $E_1 + \Delta_1$ by about 100 meV relative to pure Ge. This result combined with the redshift observed for the E_2 critical point by ellipsometry suggest that the bandgap in the alloy is reduced relative to pure Ge although it is not possible from this information to determine whether the expected indirect-direct transition has taken place. The Raman spectra of the Sn-Ge films showed a strong peak assigned to Ge-Ge lattice vibrations which is downshifted relative to the Raman peak of pure Ge. A weak peak around 240 cm^{-1} was also observed and was assigned to the Sn-Ge vibrations. The observation of Sn-Ge bands provides strong spectroscopic evidence for the presence of tetrahedral Ge-Sn coordination in our films and supports the formation of an extended random alloy with the diamond-cubic structure. Peaks corresponding to Sn-Sn vibrations were not detected in the Raman spectra. Finally we conducted transmission IR measurements in order to examine the effect of increasing Sn concentration on absorption. This should provide information of possible band gap variation with composition in the alloy. The transmission spectra of four Ge-Sn films with Sn content ranging from 9 to 18 % are shown in Figure 7. The spectrum of the Si substrate is also provided as a reference. We found that the transmission drops monotonically with increasing Sn content at about 0.8 eV . The simplest explanation for these results is a decrease of the band gap of $\text{Ge}_{1-x}\text{Sn}_x$ as a function of Sn concentration, since such a reduction is likely to result in increased absorption at a fixed photon energy above the band gap. Further experiments and data analysis aimed toward determination of the absolute band gaps and absorption coefficients are in progress.

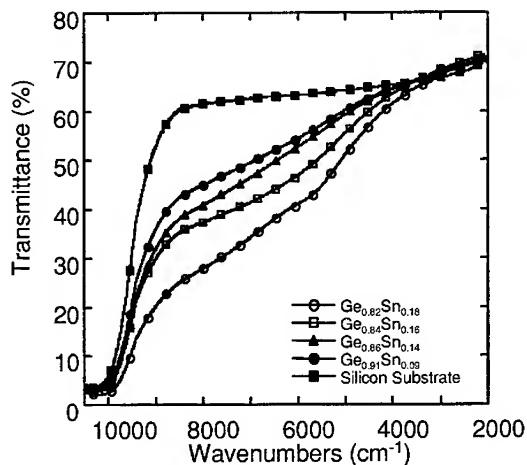


Figure 7. Transmission spectra of the Si substrate and four Ge-Sn films with Sn content ranging from 6-18%.

SUMMARY AND CONCLUSIONS

We describe UHV-CVD growth of $\text{Ge}_{1-x}\text{Sn}_x$ alloys from reactions of Ge_2H_3 with newly synthesized deuterium-stabilized Sn hydrides. Sn concentrations of 2-20 at % were measured by RBS in layers deposited on (100)Si substrates. Low energy SIMS indicated excellent uniformity of the constituent Ge and Sn elements and revealed background level contents of impurities such as H and D. High resolution TEM and XRD revealed high quality heteroepitaxial growth of films that are aligned well with the Si (001) direction. Strain relaxation by edge dislocations and some twinning was also observed in the TEM studies. High-resolution analytical electron microscopy in cross section and plan-view confirmed that the materials are highly homogeneous and are of good thermal stability. Ellipsometry studies showed that the bandgap near the X-point (E2) redshifts 50 to 80 meV compared to Ge. IR spectra showed that the absorption trough the films at 0.8eV increases due to the red shift of the lowest bandgap. Raman spectra show Ge-Ge and Sn-Ge lattice vibrations and a red shift of the E1 resonance by 100 meV.

ACKNOWLEDGEMENTS

The work at ASU was supported by NSF and Army Research Office.

REFERENCES

- 1 G. He, H. A. Atwater, *Phys. Rev. Lett.* **79**, 1937 (1997).
- 2 R. Ragan, H. A. Atwater, *Appl. Phys. Lett.*, **77**, 3418 (2000).
- 3 *Bull. Alloy Phase Diagrams*, and references therein, **5**, 266 (1984).
- 4 O. Gurdal, R. Desjardins, J. R. A. Carlsson, N. Taylor, H. H. Radamson, J.-E. Sundgren, J. E. Greene, *J. Appl. Phys.* **83**, 162 (1998).
- 5 E. A. Fitzgerald, P. E. Freeland, M. T. Asom, W. P. Lowe, R. A. Macharri, B. E. Weir, A. R. Kortan, F. A. Thiel, T.-H. Xie, A. M. Sergeant, S. L. Cooper, G. A. Thomas, L. C. Kimerling, *J. Elect. Mater.* **20**, 489 (1991).
- 6 M. T. Asom, E. A. Fitzgerald, A. R. Kortan, B. Spear, L. C. Kimerling, *Appl. Phys. Lett.* **55**, 578 (1989).
- 7 J. Piao, R. Beresfor, T. Licata, W. I. Wang, H. Homma, *J. Vac. Sci. Technol. B*, **8**, 221 (1990).
- 8 S. S. Wong, G. He, S. Nikzad, C. C. Ahn, H. A. Atwater, *J. Vac. Sci. Technol. A*, **13**, 216 (1995).
- 9 P. R. Pukite, A. Harwit, S. S. Iyer, *Appl. Phys. Lett.* **54**, 2142 (1989).
- 10 W. Wegscheider, J. Olajos, U. Menczgar, U. Dondl, G. Abstreiter, *J. Cryst Growth*, **132**, 75 (1992).
- 11 J. Taraci, J. Tolle, M. R. McCartney, J. Menendez, M. Santana, D. J. Smith, J. Kouvetakis, *Appl. Phys. Lett.* **78**, 3607 (2001).
- 12 J. Taraci, S. Zollner, M. R. McCartney, J. Menendez, M. A. Santana, D. J. Smith, G. Wolf, A. Haaland, A. Tutukin, G. Gundersen, J. Kouvetakis, *J. Am. Chem. Soc.* **132**, 10980 (2001).

Pulsed Laser Deposition and Characterization of $\text{Zn}_{1-x}\text{Mn}_x\text{O}$ Films

C. Jin, A. Tiwari, A. Kvit, D. Kumar, J. Muth, and J. Narayan

Department of Materials Science and Engineering and NSF Center for Advanced Materials and Smart Structures.

North Carolina State University, Raleigh, NC 27695-7916, U.S.A.

ABSTRACT

Here we present our results of structural, optical, and magnetic measurements of $\text{Zn}_{1-x}\text{Mn}_x\text{O}$ thin films. These films were grown epitaxially on (0001) sapphire substrates by using pulsed laser deposition technique. The maximum Mn content ($x=0.36$) is found to be much higher than allowed by thermal equilibrium limit ($x=0.13$) due to the non-equilibrium nature of the pulsed laser deposition. All the films investigated here were found to be single phase with <0001> orientation epitaxial relationship. A linear increase in the c-axis lattice constant was observed with increase in Mn concentration. Optical transmittance measurements showed an increase in the insulating band-gap (E_g) with increase in Mn concentration. DC magnetization measurements showed that there is no long range ferromagnetic ordering down to 10 K.

INTRODUCTION

ZnO is one of the promising members of II-VI semiconductor family with a bandgap of 3.27 eV at 300K. It has a higher binding energy of exciton (60 meV) compared to GaN system, which makes the material a favorable candidate for the potential applications in optical and electrical industries. ZnO based alloys have been reported for bandgap engineering to achieve the desired wavelength for certain applications. ZnO can be alloyed with MgO (8.2 eV) to increase the bandgap or with CdO (2.0 eV) to decrease it [1-2]. Another interesting ZnO-based alloy is $\text{Zn}_{1-x}\text{Mn}_x\text{O}$ which is expected to be applied in the field of spintronics as a dilute magnetic semiconductor (DMS) [3-4]. Spintronics (spin + electronics) is a fastly developing field in physics focussed on spin-dependent phenomena applied to modern electronics devices.

Recently, two groups reported the growth of ZnMnO thin films by using pulsed laser deposition [5-6]. They found that Mn can be incorporated into ZnO thin films with a large concentration (up to 35%), which is far excess the equilibrium limitation (13%). This significant increase in solubility is due to the nonequilibrium nature of the pulsed laser deposition technique, in which the average energy of laser ablated species (100-1000 kT) is 2 to 3 orders of magnitude higher than the equilibrium value.

In this work, we report the epitaxial growth of $\text{Zn}_{1-x}\text{Mn}_x\text{O}$ thin films by pulsed laser deposition. The structures of films were characterized by X-ray diffraction and transmission electron microscopy (TEM). The optical and magnetic properties of the films are also reported.

EXPERIMENTAL DETAILS

Epitaxial $\text{Zn}_{1-x}\text{Mn}_x\text{O}$ ($x=0.01-0.36$) films were grown on both-side polished (0001) sapphire substrates by pulsed laser deposition technique using a KrF excimer laser. Targets were prepared by standard solid state pressing and sintering method. Stoichiometric amount of ZnO and MnO powders were first mixed and calcined at 450 °C for six hours. The resulting powder

was then pressed into round pallets. These pallets were subjected to sintering at 900 °C for 12 hours in flowing oxygen. Depositions using these targets were carried out at 610–650°C in an ambient oxygen pressure of 5×10^{-5} Torr. The energy density and repetition rate of the laser beam were 2–3 J/cm² and 10 Hz, respectively. The Crystal structures of these films were determined by X-ray diffraction using CuK α radiation and Ni filter. The exact stoichiometry of the films was determined by Rutherford backscattering technique. Microstructural characterization of these films was performed by cross-sectional high resolution transmission electron microscopy (HRTEM) using JEOL-2010F analytical electron microscope with point to point resolution of 0.18 nm and 0.12 nm in STEM-Z mode. Optical transmittance spectra of these films were recorded at room temperature in the energy range 1–4 eV. Magnetic properties of these films were studied using superconducting quantum interference device (SQUID) magnetometer.

RESULTS AND DISSCUSION

X-ray diffraction pattern (Intensity vs. 2θ) showed the films were single phase and had wurtzite structure with c-axis of the film aligned with that of the sapphire substrate. Fig 1 shows a typical X-ray diffraction pattern of $\text{Zn}_{1-x}\text{Mn}_x\text{O}$ with $x=0.01$ and 0.20; all other alloys till $x=0.36$ exhibited similar behavior. It is clear from the figure that there are no other orientations except (0001) reflections of ZnO and sapphire. All the films were in single phase till $x=0.36$, but for $x > 0.36$ some indication of phase separation was observed in X-ray diffraction. A systematic increase in the lattice parameter 'c' was observed without any change in crystal symmetry. It is to be noted that in this work we have succeeded in doping Mn in ZnO much above the thermal equilibrium limit of $x \sim 0.13$. This became possible because the

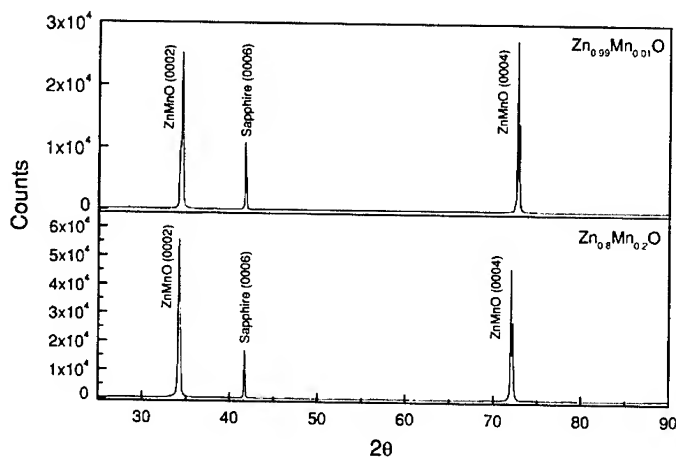


Fig. 1. X-ray diffraction patterns of $\text{Zn}_{1-x}\text{Mn}_x\text{O}$ ($x=0.20$ and 0.01) films

nonequilibrium processing was involved during the pulsed laser deposition, where the average energy of the laser ablated species is two to three orders of magnitude higher than the equilibrium value.

Fig.2 shows the Rutherford backscattering and channeling data for one of the films. From this figure we estimated the minimum channeling yield to be less than 3.0% near the surface which suggests that Mn atoms are substitutionally confined into the lattice planes rather than between the planes. From a fit to the random backscattering profile, the actual concentration of Mn in these films was determined. Mn contents in the films and the targets were found to be within $\pm 5\%$.

Fig. 3 shows the selected area diffraction pattern on the $\text{Zn}_{1-x}\text{Mn}_x\text{O}$ ($x=0.85$)/ sapphire interface area taken at $[01\ \bar{1}0]$ zone axis of ZnMnO thin film. It shows that the film was epitaxially grown on the substrate. The $\text{Zn}_{1-x}\text{Mn}_x\text{O}$ film has the following epitaxial relationships with the substrate: $\text{Zn}_{1-x}\text{Mn}_x\text{O}(0001) \parallel \text{sapphire}(0001)$, $\text{Zn}_{1-x}\text{Mn}_x\text{O}(01\ \bar{1}0) \parallel \text{sapphire}(\bar{1}2\ \bar{1}0)$, and $\text{Zn}_{1-x}\text{Mn}_x\text{O}(\bar{1}2\ 10) \parallel \text{sapphire}(01\ 10)$. Fig.4 (a) shows the results of HRTEM carried out on the $\text{Zn}_{1-x}\text{Mn}_x\text{O}$ /sapphire interface. The interface between the film and the sapphire is sharp and free from any other phase. Due to the large in-plane mismatch ($\sim 18\%$) between the film and the substrate, the epitaxial growth of the film occurs via domain epitaxy where dimensions of the domain become the repeat distance across which matching is maintained [7]. The misfit dislocations were observed at the interface as shown in Fig.4 (b). The dislocation occurs at every 6-th ($\bar{2}\ \bar{2}\ 10$) plane of sapphire (average). The unit cell of ZnMnO film was found to be rotated by 30° about the c-axis with respect to the sapphire unit cell as reported in pure ZnO on sapphire substrate [9].

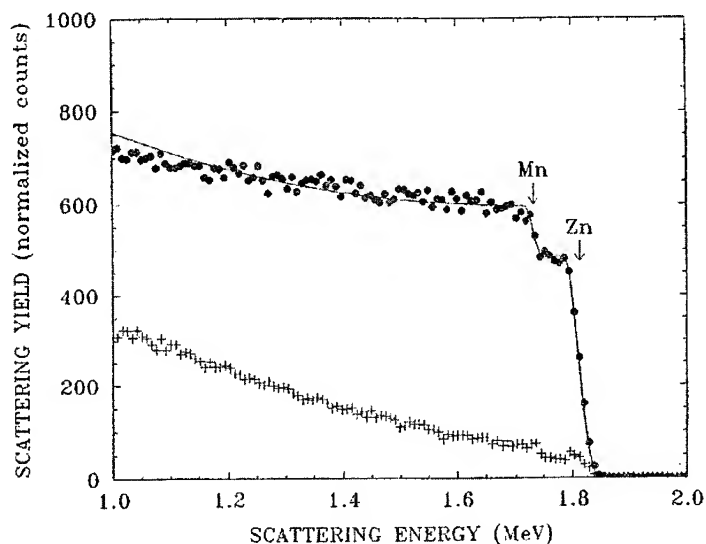


Fig. 2. Rutherford back scattering (●) and channeling (+) data for $\text{Zn}_{1-x}\text{Mn}_x\text{O}$ ($x=0.25$) film.

Optical absorbance spectra of $\text{Zn}_{1-x}\text{Mn}_x\text{O}$ films were recorded at room temperature, see Fig.5. We observed that the absorption edge moves towards the high energy side with the increase in Mn concentration. This indicates the increase in the band-gap (E_g) of the alloy. We

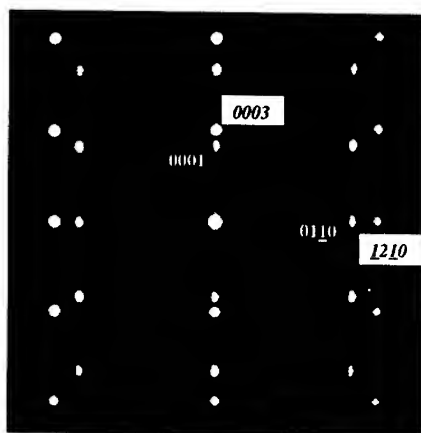


Fig.3 Selected area diffraction pattern (SAD) from $10\ \mu\text{m}$ area for $\text{Zn}_{1-x}\text{Mn}_x\text{O}$ ($x=0.15$) thin films on sapphire (0001) substrate. The white numbers correspond to ZnMnO and the black numbers in white blocks correspond to sapphire.

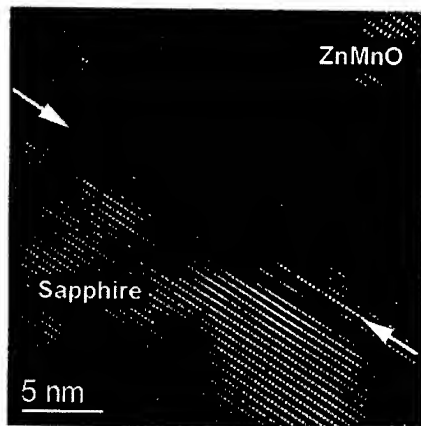


Fig. 4(a) High-resolution picture of single crystal $\text{Zn}_{1-x}\text{Mn}_x\text{O}$ ($x=15$) film grown on sapphire substrate.

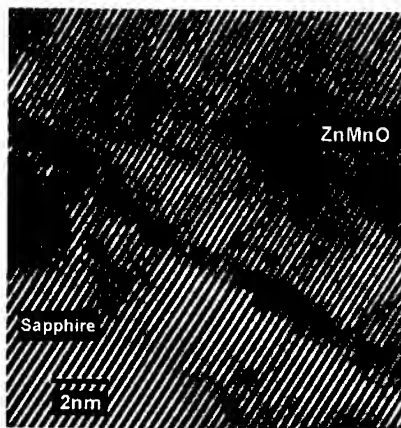


Fig. 4(b) IFFT picture from Fig. 4(a). Two reflexes ($\bar{1}2\ \bar{1}0$) and ($01\ \bar{1}0$) have been masked in corresponding FFT picture, so only ($01\ \bar{1}0$) planes of ZnMnO and ($\bar{1}2\ \bar{1}0$) planes of sapphire are observed. The places corresponding to the misfit dislocations are indicated here.

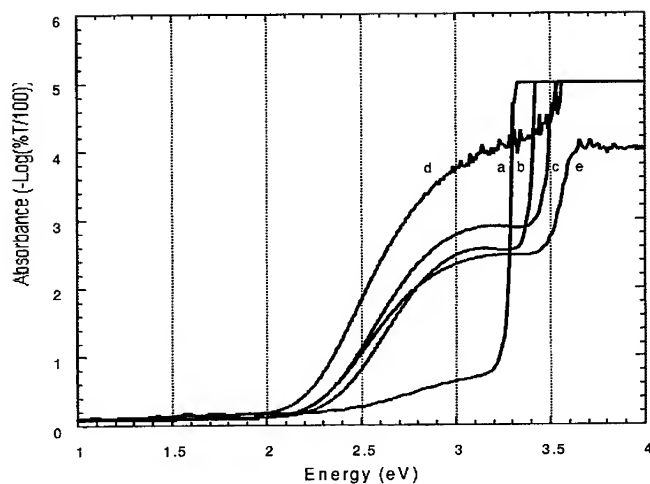


Fig. 5 Optical absorbance spectra of $\text{Zn}_{1-x}\text{Mn}_x\text{O}$ films. Symbols a, b, c, d and e correspond to $x=0.01, 0.05, 0.12, 0.18$ and 0.25 respectively. Absorbance is related to the percentage transmittance (T) by the relation $\text{absorbance} = -\text{Log}(\%T/100)$.

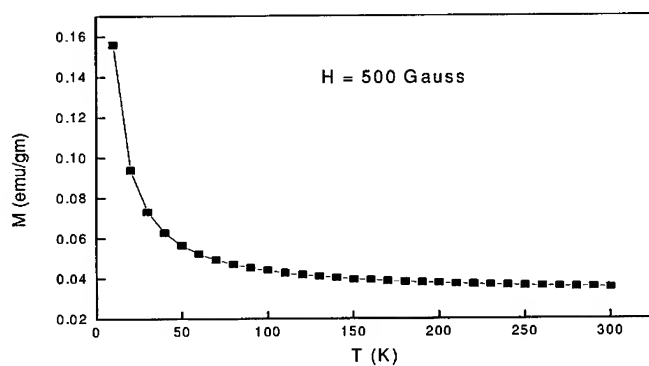


Fig.6 DC magnetization vs. Temperature for $\text{Zn}_{1-x}\text{Mn}_x\text{O}$ ($x=0.05$) film.

also observed significant amount of midgap absorption in these films which is similar to results of other groups [5]. This is believed to be due to the charge-transfer transition between donor and acceptor ionization levels of Mn ions and the band continuum [5].

DC magnetization of these magnetic films was measured using a SQUID. We found these films to be paramagnetic (see Fig6). No evidence of any long range ferromagnetic ordering could be observed in any of these films down to 10 K. This is in contradiction with the theoretical predictions of Dietl [8] et al. Magnetic susceptibility ($\chi=M/H$) data fits well in an expression of the kind $\chi=\chi_0+C/T$. Bohr magnetron number 'p' of Mn was found to be 5.9 by using expression $C=Np^2\mu_B^2/3k_B$ for Curie paramagnetism [10], which gives a value of $J\sim 5/2$ consistent with the doubly ionized ionic state of Mn, substituting Zn sites in the $Zn_{1-x}Mn_xO$ lattice.

CONCLUSION

In conclusion we have prepared high quality epitaxial $Zn_{1-x}Mn_xO$ ($x\leq 0.36$) films on sapphire using pulsed laser deposition technique. A systematic study of the microstructural characterization of these high quality epitaxial films showed a 30° rotation of the film with respect to the substrate, similar to III-nitride and pure ZnO growth on (0001) sapphire substrate. Both the c-axis lattice parameter and the band gap E_g are found to be sensitive functions of Mn content. SQUID measurements showed a paramagnetic behavior and no ferromagnetic ordering could be detected in any of these films down to 10 K.

ACKNOWLEDGMENTS

This research was supported by the US National Science Foundation Center for Advanced Materials and Smart Structure.

REFERENCES

1. A. K. Sharma, J. Narayan, J. F. Muth, C. W. Teng, C. Jin, A. Kvit, R. M. Kolbas and O. W. Holland, *Applied Physics Letters* **75**, 3327 (1999).
2. T. Makino, Y. Segawa, M. Kawasaki, A. Ohtomo, R. Shiroki, K. Tamura, Tamura, T. Tamura, T. Yasuda, and H. Koinuma, *Applied Physics Letters*, **78**, 1237(2001).
3. H. Ohno, *Science* **281**, 951 (1998).
4. J. K. Furdyna, *J. Appl. Phys.* **64**, R29 (1988).
5. T. Fukumura, Jin Zhengwu, A. Ohtomo, H. Koinuma and M. Kawasaki, *Applied Physics Letters* **75**, 3366 (1999).
6. Kenji Ueda, Hitoshi Tabata and Tomoji Kawai, *Applied Physics Letters* **79**, 988 (2001).
7. J. Narayan, P. Tiwari, X. Chen, J. Singh, R. Chowdhury and T. Zheleva, *Appl. Phys. Lett.* **61**, 1290 (1992), J. Narayan, U.S. Patent 5, 406, 123 (April 11, 1995).
8. T. Dietl, H. Ohno, F. Matsukura, J. Cibert and D. Ferrand, *Science* **287**, 1019 (2000).
9. J. Narayan, K. Dovidenko, A.K. Sharma, and S. Oktyabrsky, *Journal of Applied Physics*, **84**, 2597 (1998).
10. C. Kittel, *Introduction to Solid State Physics*, 3rd Edition, Wiley, New York 1968.

InP Self Assembled Quantum Dot Lasers Grown on GaAs Substrates by Metalorganic Chemical Vapor Deposition

R. D. Dupuis¹⁾, J. H. Ryou^{*1)}, R. D. Heller¹⁾, G. Walter²⁾, D. A. Kellogg²⁾, N. Holonyak, Jr.²⁾, C. V. Reddy³⁾, V. Narayanamurti³⁾, D. T. Mathes⁴⁾, and R. Hull⁴⁾

¹⁾ Microelectronics Research Center, The University of Texas at Austin
10100 Burnet Road, Building 160, Austin, TX 78758 USA

Phone: +1-512-471-0537, Fax: +1-512-471-0957, e-mail: dupuis@mail.utexas.edu

²⁾ Center for Compound Semiconductor Microelectronics, The University of Illinois at Urbana-Champaign, Urbana, IL

³⁾ Gordon McKay Laboratory of Applied Science, Harvard University, Cambridge, MA 02138

⁴⁾ Department of Materials Science and Engineering, The University of Virginia, Charlottesville, VA

*Now with Honeywell VCSEL Products Division, Plymouth MN 55441

ABSTRACT

We describe the operation of lasers having active regions composed of InP self-assembled quantum dots embedded in $\text{In}_{0.5}\text{Al}_{0.3}\text{Ga}_{0.2}\text{P}$ grown on GaAs (100) substrates by MOCVD. InP quantum dots grown on $\text{In}_{0.5}\text{Al}_{0.3}\text{Ga}_{0.2}\text{P}$ have a high density on the order of about $1\text{-}2 \times 10^8 \text{ cm}^{-2}$ with a dominant size of about 10-15 nm for 7.5 ML growth.[1] These $\text{In}_{0.5}\text{Al}_{0.3}\text{Ga}_{0.2}\text{P}/\text{InP}$ quantum dots have previously been characterized by atomic-force microscopy, high-resolution transmission electron microscopy, and photoluminescence.[2] We report here the 300K operation of optically pumped red-emitting quantum dots using both double quantum-dot active regions and quantum-dot coupled with InGaP quantum-well active regions. Optically and electrically pumped 300K lasers have been obtained using this active region design; these lasers show improved operation compared to the lasers having QD-based active regions with threshold current densities as low as $J_{th} \sim 0.5 \text{ KA/cm}^2$.

INTRODUCTION

III-phosphide self-assembled quantum-dot (SAQD or simply QD) structures having delta-functional behavior of the density of states and the discrete energy levels of carriers induced by three-dimensional quantum confinement offer the potential to realize injection lasers operating in the visible spectral region with improved performance characteristics, such as low threshold current density, high characteristic temperature, and high differential gain [3,4,5]. The direct growth of coherently strained defect-free self-assembled quantum dots on planar substrates using the coherent Stranski-Krastanow (SK) growth mode [6,7] offers the potential to develop QD visible laser devices with the theoretically predicted and experimentally realized improved performance. Also, the SAQD growth process can overcome the limitation of lattice matching between the substrate and epitaxial active region due to the intrinsic strain-compliant nature of the SK growth mode.

III-As quantum dot-related structures for infrared optoelectronic applications at $\lambda \sim 1.3 \mu\text{m}$ have been extensively researched for growth condition optimization, material property characterization, and device applications including lasers in the infrared spectral region. Since

the first demonstration of InAs quantum dot lasers [8], a great deal of research on III-As based quantum dot structures have led to quantum-dot lasers with improved threshold current densities and characteristic temperatures [9] as compared to more conventional quantum-well lasers. However, in comparison to the III-As material system, less research has been performed in the development of III-phosphide SAQD structures for applications in the visible-light spectral region. Initially, it was reported that the properties of III-P SAQDs had a reduced QD density and a broader size distribution than those of the III-As SAQDs. Due to the "blue-shift" effect of the emission from the SAQDs induced from multiple orders of quantum confinement and compressive strain on QDs, there is the potential to extend the wavelength of light emitters to the yellow or green spectral regions using binary and ternary III-Phosphide SAQD structures.

In the past, structures with active regions containing InP SAQDs on GaAs substrates, the QDs have generally been grown on $\text{In}_{0.49}\text{Ga}_{0.51}\text{P}$ matrix layers by MBE [10,11], MOCVD [12,13], or by hydride vapor phase epitaxy (VPE) [14]. InP SAQDs embedded in $\text{In}_{0.49}\text{Ga}_{0.51}\text{P}$ grown on GaAs (100) substrates grown by MOCVD have been reported to yield relatively low densities of SAQDs ($\sim 10^7$ - 10^9 cm^{-2}), compared to III-As SAQDs, and a bimodal size distribution of coherent islands has been reported. InP SAQDs have also been grown on GaP substrates [15] to modify the strain applied to InP QDs; however, no PL emission from the QDs was observed, possibly due to the expected Type II conduction band alignments in this system. Moreover, the growth of InP SAQDs is not as well developed as the growth of III-As SAQDs and further investigation is required.

To improve the QD density, the effect of different matrix layers lattice-matched to GaAs substrates having larger bandgap, such as $\text{In}_{0.49}(\text{Al}_x\text{Ga}_{1-x})_{0.51}\text{P}$ ($x=0.3, 0.6, 1.0$), needs to be studied to improve the carrier confinement. Furthermore, a different matrix material system is expected to change the morphology and growth characteristics of the InP SAQDs. Additionally, the matrix material affects the optical properties of SAQD structures. Recently, we studied the growth of InP SAQDs on InAlGaP matrix layers and the effect of coupling quantum dot states with the electronic states of the InGaP quantum well [20,21,22,23].

EXPERIMENT

In the present study, InP SAQD growth conditions are employed which have been optimized with various matrix layers with regards to QD size, uniformity, and density as well as optical quality to fabricate InP QD based laser operating in visible light spectral region with improved characteristics. InP quantum dots coupled to InGaP quantum wells have been studied. These lasers have lased CW optically and pulsed electrically pumped at 77K and 300K. QD material and optical properties are characterized by atomic force microscopy (AFM), photoluminescence (PL), and high-resolution transmission electron microscopy (TEM). The InAlGaP/InP QD and laser structures in this work were grown by low-pressure metalorganic chemical vapor deposition (MOCVD) in an EMCORE Model GS3200 UTM rotating disk reactor at ~ 60 Torr using a H_2 ambient. The group III precursors used are trimethylindium (TMIn), trimethylaluminum (TMAI), and triethylgallium (TEGa); the group V hydride sources are arsine (AsH_3) and phosphine (PH_3). Disilane (Si_2H_6) is used as a source of Si for *n*-type doping and bis-cyclopentadienyl magnesium (Cp_2Mg) is used for *p*-type (Mg) doping. The growth was performed simultaneously on two-inch diameter GaAs:Si (100) on-axis, (100) - 10° <111>A, and (100) - 15° <111>A substrates.

The surface morphology of SAQDs is characterized by tapping-mode AFM on the exposed QD samples to determine the QD average (or dominant) size, density, and uniformity. The QD size is expressed in terms of the height as measured by AFM. The density is taken from the multiple sets of relatively large area AFM scans. To evaluate the morphology, the $\text{In}_{0.5}\text{Al}_{0.5}\text{P}/\text{InP}$ QD structure used consists of an $\text{In}_{0.49}(\text{Al}_x\text{Ga}_{1-x})_{0.51}\text{P}$ lower matrix layer (250 nm thick) followed by an InP QD active layer all grown on a GaAs buffer layer/GaAs:Si (100) substrate. Following the QD deposition, the growth is terminated and the wafer is cooled down under a PH_3 overpressure to prevent desorption. The lattice parameters of the $\text{In}_{0.49}(\text{Al}_x\text{Ga}_{1-x})_{0.51}\text{P}$ ($x=0.3, 0.6, 1.0$) matrix layers are analyzed using a Rigaku high-resolution five double-crystal X-ray diffractometry (using a four-crystal monochromator) to determine the degree of lattice matching to the substrate. For lattice-matched matrix layers, the epitaxial layers are calibrated to have less than -200 arc-seconds of angle separation relative to the GaAs substrate measured from an (004) X-ray rocking curve. This is done in order to minimize the strain effect from the matrix layer on the growth of active QD layer. The optical properties of InP SAQDs embedded in various matrices are characterized by room-temperature and low-temperature PL. For the PL measurements, a ~ 488 nm excitation source from an Ar^+ laser operating at a constant power density (50 – 200 mW) and a GaAs photomultiplier with a GaAs photocathode are used. For these quantum-dot heterostructures (QDHs), the $\text{In}_{0.49}(\text{Al}_x\text{Ga}_{1-x})_{0.51}\text{P}$ upper matrix layer is grown on the InP SAQD layer with a certain post-purge time after the completion of SAQD layer deposition. TEM is also used to study the microscopic morphology and material quality of individual QDs with and without upper matrix layer, as shown in

The InP SAQD growth conditions are optimized by altering the growth temperature, growth time, and V/III ratio. The growth temperature of the QDs is optimized at 650°C for 1 minute (7.5 ML) with a V/III ratio $\sim 2,100$. The estimated nominal growth rate of InP has been reduced to ~ 0.125 monolayer/sec (ML/s), as calibrated by measuring the thickness of a thin InP planar layer using glancing grazing incidence X-ray reflectivity.

METHODS USED

In this study, we report some of the characteristics of the InP SAQDs. We also report the device results of optically and electrically pumped lasers based on these InP SAQDs. The InP QD growth studies are performed by altering growth temperatures and times and using various $\text{In}_{0.49}(\text{Al}_x\text{Ga}_{1-x})_{0.51}\text{P}$ matrices ($x=0.0, 0.3, 0.6$, and 1.0). The morphology changes of the exposed SAQDs depend on the growth time and the matrix material, and are characterized by atomic force microscopy (AFM). Photoluminescence (PL) spectra were taken at 4K and 300K to determine the light-emitting characteristics of the $\text{InP}/\text{In}_{0.49}(\text{Al}_x\text{Ga}_{1-x})_{0.51}\text{P}$ quantum-dot heterostructures (QDHs). 4K PL spectra from the InP SAQDs embedded in $\text{In}_{0.49}(\text{Al}_x\text{Ga}_{1-x})_{0.51}\text{P}$ cladding layers exhibit PL emission in the visible orange and red spectral regions, as shown below. Also, transmission electron microscopy is used to characterize the microscopic material quality and morphology of the individual QD and the interfaces between SAQD and cladding layers.

RESULTS OBTAINED

AFM studies of InP SAQDs grown on InAlGaP matrix layers have shown that under some conditions, a relatively high density of small quantum dots is produced, as described in Figure 1. As the QD growth proceeds with longer deposition times, the average QD height (and

base width) increases and the average density correspondingly decreases. Our work has concentrated on the 7.5ML effective QD thickness where the size and density appear to be optimal for light emitting properties determined by PL.

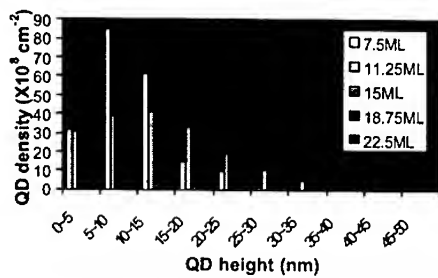


Figure 1: Variation of height and density vs. nominal layer thickness for InP SAQDs.

The 4K PL intensity vs. wavelength spectra for InP/ $\text{In}_{0.49}(\text{Al}_{0.6}\text{Ga}_{0.4})_{0.51}\text{P}$ QDHs grown for different deposition times is shown in Figure 2. The PL spectral peak position changes from 591 nm (2.10 eV for 3.75 MLs), to 653 nm (1.90 eV for 7.5 MLs) and 681 nm (1.82 eV for 15 ML), as the deposition time increases. This PL emission is at a lower energy than that observed from comparable-sized InP QDs embedded in $\text{In}_{0.49}\text{Al}_{0.51}\text{P}$.

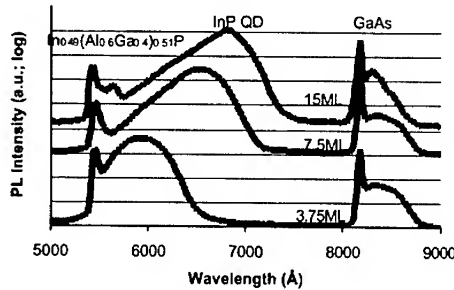


Figure 2: 4K PL spectra of InP SAQDs embedded in InAlGaP cladding layers grown at 650 °C for various deposition times.

However, InP/ $\text{In}_{0.49}(\text{Al}_{0.6}\text{Ga}_{0.4})_{0.51}\text{P}$ QDHs exhibit more efficient luminescence than InP/ $\text{In}_{0.49}\text{Al}_{0.51}\text{P}$ QDHs at room temperature, possibly due to better electron confinement. TEM studies of the InP SAQDs have shown the dislocation-free structure of single- and multiple-layer QDHs and the vertical alignment achieved for multiple QD layers, as shown in Figure 3. These InP QD active regions have been incorporated into various separate-confinement laser active regions. In the present work, we have grown three types of quantum-confined “red-emitting” active region laser structures on GaAs substrates: (1) single- and multiple-QDHs; (2) single-QW active-region QDHs; and couples QD+QW structures and compared the 300K and 77K PL emission, as shown in Figure 4. Recently, we have described the effects of coupling of the InP QD states to the electronic states of InGaP quantum wells grown below and above the quantum dots, resulting in the coupling of the quantum dots through

electronic states in the quantum wells [24]. Optically and electrically pumped 300K lasers using QD+QW active regions have been obtained using this unique design; these lasers show improved operation compared to lasers having QD-based active regions with pulsed 300K threshold current densities $J_{th} \sim 1.5 \text{ KA/cm}^2$, as shown in Figure 5. By optimizing the coupling between the quantum well and the quantum-dots, other QD+QW laser devices have been grown that exhibit pulsed J_{th} values at 300K as low as $\sim 0.5 \text{ KA/cm}^2$.



Figure 3: TEM micrograph of stacked InP SAQDs.

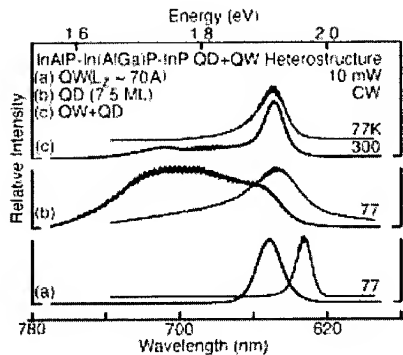


Figure 4: PL spectra for InAlP-InAlGaP-InP QW, QD, QD+QW samples.

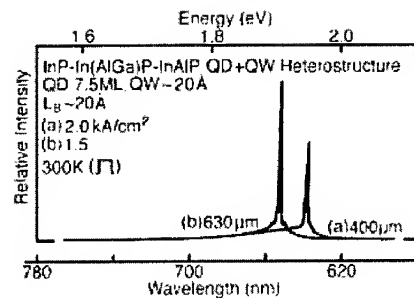


Figure 5 : InAlP-InAlGaP-InP QD+QW 300K electrically pumped optical spectra.

CONCLUSIONS

In summary, we have grown and characterized InP SAQDs embedded in $\text{In}_{0.49}(\text{Al}_x\text{Ga}_{1-x})_{0.51}\text{P}$ matrices ($x=0.0, 0.3, 0.6$, and 1.0). The InP SAQDs grown at 650C exhibit uniform morphology with a 5-10 nm dominant height and $\sim 2 \times 10^{10} \text{ cm}^{-2}$ density for 7.5 ML. As the deposition time increases, the QD size increases, while the density decreases slightly, and the PL peak position shifts to lower energy. For InP/ $\text{In}_{0.5}\text{Ga}_{0.5}\text{P}$ / $\text{In}_{0.49}(\text{Al}_{0.6}\text{Ga}_{0.4})_{0.51}\text{P}$ / $\text{In}_{0.49}\text{Al}_{0.51}\text{P}$ SQD+SQW injection lasers, we have achieved electrically pumped lasing at 681 nm at 300 K with reduced threshold current densities as low as 0.5 KA/cm^2 . We believe this approach is applicable to other QD laser materials systems.

REFERENCES

- [1] J. H. Ryou, R. D. Dupuis, G. Walter, N. Holonyak, Jr., D. T. Mathes, R. Hull, C. V. Reddy, and V. Narayanamurti, *J. Appl. Phys.*, to be published.
- [2] J. H. Ryou, Ph.D. Dissertation, The University of Texas at Austin (2001).
- [3] Y. Arakawa and H. Sakaki, *Appl. Phys. Lett.* **40**, 939 (1982).
- [4] M. Asada, Q. Miyamoto, and Y. Suematsu, *IEEE J. Quantum Electron.* **QE-22**, 1915 (1986).
- [5] N. N. Ledentsov, M. Grundmann, F. Heinrichsdorff, D. Bimberg, V. M. Ustinov, A. E. Zhukov, M. V. Maximov, Zh. I. Alferov, and J. A. Lott, *IEEE J. Select. Topic. Quantum Electron.* **6**, 439 (2000).
- [6] I. N. Stranski and L. Krastanow, *Akad. Wiss. Wien, Math-Naturwiss. Klasse* **146**, 797 (1937).
- [7] V. A. Shchukin and D. Bimberg, *Rev. Mod. Phys.* **71**, 1125 (1999).
- [8] N. N. Ledentsov, V. M. Ustinov, A. Y. Egorov, A. E. Zhukov, M. V. Maksimov, I. F. Tavatazde, and P. S. Kop'ev, *Semiconductors* **28**, 832 (1994).
- [9] G. Park, O. B. Shchekin, S. Csutak, D. L. Huffaker, and D. G. Deppe, *Appl. Phys. Lett.* **75**, 3267 (1999).
- [10] A. Kurtenbach, K. Eberl, and T. Shitara, *Appl. Phys. Lett.* **66**, 361 (1995).
- [11] A. Kurtenbach, C. Ulrich, N. Y. Jin-Phillipp, F. Noll, K. Eberl, K. Syassen, and F. Phillipp, *J. Electron. Mater.* **25**, 3 (1996).
- [12] S. P. DenBaars, C. M. Reaves, V. Bressler-Hill, S. Varma, W. H. Weinberg, and P. M. Petroff, *J. Cryst. Growth* **145**, 721 (1994).
- [13] N. Carlsson, W. Seifert, A. Petersson, P. Castrillo, M. E. Pistol, and L. Samuelson, *Appl. Phys. Lett.* **65**, 3093 (1994).
- [14] J. Ahopelto, A. A. Yamguchi, K. Nishi, A. Usui, and H. Sakaki, *Jpn. J. Appl. Phys. Part 2* **32**, L32 (1993).
- [15] Y. Nabetani, K. Sawada, Y. Fukukawa, A. Wakahara, S. Noda, A. Sasaki, *J. Cryst. Growth* **193**, 470 (1998).
- [16] K. Eberl, A. Kurtenbach, M. Zundel, N. Y. Jin-Phillipp, F. Phillipp, A. Moritz, R. Wirth, and A. Hangleiter, *J. Cryst. Growth* **175/176**, 702 (1997).
- [17] T. Riedl, E. Fehrenbacher, A. Hangleiter, M. K. Zundel, and K. Eberl, *Appl. Phys. Lett.* **73**, 3730 (1998).
- [18] Y. M. Manz, O. G. Schmidt, and K. Eberl, *Appl. Phys. Lett.* **76**, 3343 (2000).
- [19] J. Porsche, M. Ost, F. Scholz, A. Fantini, F. Philipp, T. Riedl, and A. Hangleiter, *IEEE J. Select. Topic Quantum Electron.* **6**, 482 (2000).
- [20] G. Walter, N. Holonyak, Jr., J. H. Ryou and R. D. Dupuis, *Appl. Phys. Lett.* **78**, 26, 4091 (2001).
- [21] J. H. Ryou, R. D. Dupuis, G. Walter, D. A. Kellogg, N. Holonyak, Jr., D. T. Mathes, R. Hull, C. V. Reddy, and V. Narayanamurti, *Appl. Phys. Lett.*, **79**, 4091 (2001).
- [22] J. H. Ryou, R. D. Dupuis, D. T. Mathes, R. Hull, C. V. Reddy, and V. Narayanamurti, *Appl. Phys. Lett.* **78**, 3526 (2001).
- [23] J. H. Ryou, R. D. Dupuis, C. V. Reddy, V. Narayanamurti, D. T. Mathes, R. Hull, A. Mintairov, and J. L. Merz, *J. Electron. Mat.* **30**, 471 (2001).
- [24] G. Walter, N. Holonyak, Jr., J. H. Ryou and R. D. Dupuis, *Appl. Phys. Lett.* **79**, 3215 (2001).

Effects of As Doping on Properties of ZnO Films

K.S. Huh, D.K. Hwang, K.H. Bang, M.K. Hong, D. H. Lee, J.M. Myoung
Information & Electronic Material Research Laboratory, Department of Materials Science and Engineering, Yonsei University, Seoul 120-749, Korea
M.S. Oh, W. K. Choi
Thin Film Technology Research Center, Korea Institute of Science and Technology, Seoul 130-650, Korea

ABSTRACT

A series of ZnO thin films with various deposition temperatures were prepared on (100) GaAs substrates by radio-frequency magnetron sputtering using ZnO target. The ZnO films were studied by field emission scanning electron microscope(FESEM), x-ray diffraction(XRD), photoluminescence(PL), cathodoluminescence(CL), and Hall measurements. The structural, optical, and electrical properties of the films were discussed as a function of the deposition temperature. With increasing temperature, the compressive stress in the films was released and their crystalline and optical properties were improved. From the depth profile of As measured by secondary ion mass spectrometry(SIMS), As doping was confirmed, and, in order to activate As dopant atoms, post-annealing treatment was performed. After annealing treatment, electrical and optical properties of the films were changed.

INTRODUCTION

Recently, zinc oxide (ZnO) has been emerged as an attractive material for application to the optical devices such as blue-, violet-, and UV-light emitting diodes(LEDs) and laser diodes(LDs) [1]. ZnO has very strong spontaneous emissions from bound excitons even at room temperature due to the large exciton binding energy of ~60 meV, as well as has structural and optical properties similar to GaN widely used to optical devices in present. Also, ZnO has high cohesive energy and melting temperature due to the high Zn-O bond strength, resulting in high-temperature stability during process [2,3].

For development of optical devices based on ZnO, GaAs can be used as a useful substrate material and it is attributed to the possibility of high level of monolithic system through the integration of optical components[4]. In addition, GaAs can be used as a p-type dopant source in ZnO film, which is essential to application of ZnO for optoelectronic devices [5]. However, because of the problems related to thermal stability and stress due to large lattice mismatch of about 19 % between ZnO and GaAs, a few studies of ZnO thin film on GaAs have been reported [6-9]. In general, it has known that thin films composed of polycrystalline structures are difficult to apply for optical devices due to the poor optical property originated from defect-related deep-level emissions[10].

In this study, we report on the effects of deposition temperature on properties of ZnO thin films prepared on GaAs (100) by rf magnetron sputtering. Then, effects of post-annealing treatment for ZnO films were discussed through Hall and PL measurements.

EXPERIMENTAL DETAILS

ZnO films were deposited by radio frequency(rf) magnetron sputtering. A 2-in. diameter and 5-N purity ZnO target were used to deposit the films. The substrates used were semi-

insulating (100) GaAs wafers. The sputtering chamber was evacuated to 2×10^{-6} Torr before sputtering. The ambient gases used were the mixed Ar and $O_2(1:1)$ and the working pressure was fixed at 1×10^{-2} Torr. In order to investigate the effects of the deposition temperature on the properties of ZnO film, a series of films prepared at different temperatures between room temperature(R.T.) and 450 °C. The thicknesses measured by α -step were in the ranges of 0.7 ~ 1 μm . After deposition, the surface morphology of the films was monitored by field emission scanning electron microscope (FESEM), and the crystallinity of the films was investigated by X-ray diffraction (XRD). To investigate the optical properties of ZnO films, photoluminescence (PL) and cathodoluminescence (CL) measurements were performed at R.T. In PL measurements, an excitation source was Ar laser with a wavelength of 352 nm and a power of 100 mW. The electrical properties of the ZnO films were determined by Van der Paw Hall measurements. For the films deposited at 350 and 450 °C, post-annealing treatment was performed at 500 °C for 2 hours in vacuum to activate As dopants, and their electrical and optical properties were investigated by Hall and PL measurements.

DISCUSSION

Figure 1 shows FESEM images from ZnO films deposited at different temperatures. The images showed all films consist of columnar grains perpendicular to substrates. It was clearly observed that the shape of the grains changed from needle to hexagonal and, as deposition temperature increased, the grain size of the films became larger due to the grain growth.

Figure 2 shows the root-mean-square(rms) roughness as a function of deposition temperature measured by atomic force microscope(AFM) in the $5 \times 5 \mu m^2$ area. It was observed that the rms roughness increased with increasing temperature, and it is attributed that the film surface became rough due to grain growth as shown in Fig.1. This fact indicates that deposition temperature significantly affects on the surface morphology of the films.

Figure 3 shows θ -2 θ XRD patterns of ZnO films deposited at different deposition temperatures (T_D). The peak intensities and dominant peak position were varied as different T_D . It is notable that ZnO films deposited at room temperature were predominantly deposited along (0002) direction and the peak intensity was relatively strong compared to the films deposited at 250 °C and 350 °C, and its position was shifted toward the lower-angle side than that of ZnO film deposited at 450 °C. The diffraction from (10 $\bar{1}$ 1) plane was dominant for the films deposited at 250 °C, whereas, as deposition temperature increases, the diffraction from (0002) plane became dominant. The c-axis lattices constant of the ZnO calculated from Bragg

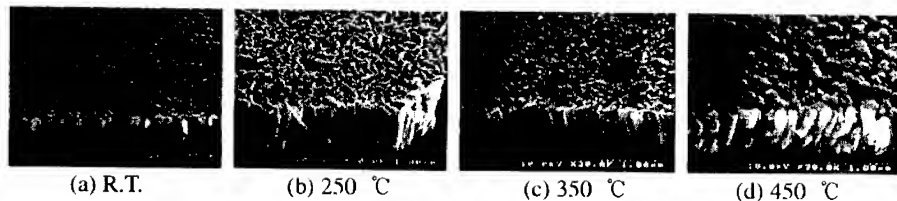


Figure 1. SEM image of the ZnO films deposited at different temperatures

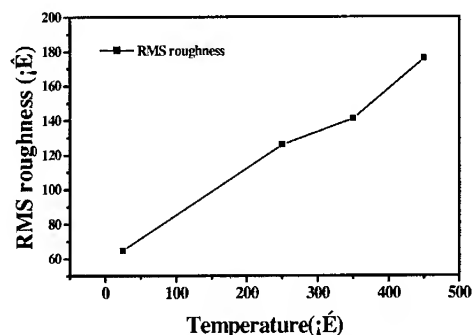


Figure 2. rms roughness of ZnO films as a function of deposition temperature.

condition for the (0002) plane are 5.226 Å for the film deposited at room temperature and 5.208 Å for 450 °C. Compared with the lattice constant of a bulk single crystal ZnO, 5.207 Å, it can be explained that the film deposited at room temperature is under compressive stress, but the stress of the film was almost relaxed for the film deposited at 450 °C [13].

In order to study the optical properties of the ZnO films, photoluminescence (PL) measurements were performed at room temperature, and the results are shown in Figure 4. It was observed that all films, except the film deposited at room temperature, showed both the near band-edge emission (NBE) at ~3.26 eV and the deep-level emission around ~2.9 eV. It is known that the near band-edge emission corresponds to the recombination of excitons bound to donors. However, the origin of the deep-level emission is not clearly understood yet. It might be attributed to both native defects like oxygen vacancies and impurities unintentionally introduced during the film deposition [14,15]. With increasing deposition temperature, intensity of the band-edge emission was increased, and the PL intensity ratio of NBE emission to the defect level emission was ~8. Considering that the epitaxial ZnO films grown by MOCVD have the ratio less than 1 and the films grown by MBE have 5~20 [15,16]. It is thought that the films in this study have relatively low defect levels.

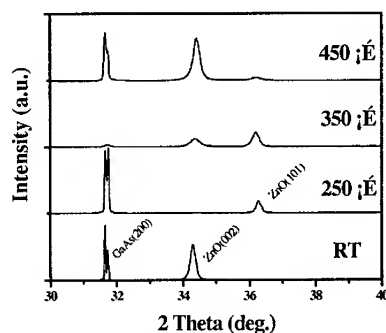


Figure 3. XRD patterns of the films with different deposition temperatures.

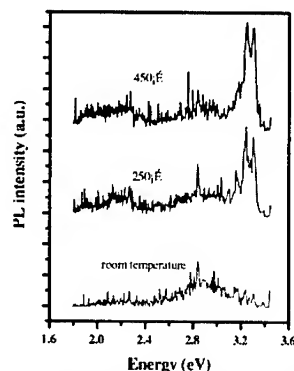


Figure 4. PL spectra of the ZnO films deposited at different temperatures.

Cathodoluminescence (CL) measurements were also performed to investigate further optical properties of the films. Figure 5 shows the CL spectra of the ZnO films deposited at room temperature and 450 °C. The films deposited at room temperature exhibited the visible emission peak located at 2.0 eV without band-edge emission. On the other hand, a strong near band-edge emission at 3.28 eV was observed at 450 °C. The emission at 2.0 eV was associated with defect level in ZnO films. However, the observation of a strong NBE for the films deposited at 450 °C implies that they are optically high-quality.

In order to investigate the dopant distribution in the films, SIMS analysis was carried for the films deposited at 350 °C and 450 °C, and the results are shown in Figure 6. The plots show that the considerable amounts of As and Ga atoms are diffused into the as-grown ZnO films from GaAs substrates. As deposition temperature increased from 350 to 450 °C, the concentrations of these atoms were increased due to the increase of vapor pressure. Vapor pressure of Ga is much lower than that of As below 500 °C, and this caused the difference of doping concentration between Ga and As atoms. It is notable that these impurities are

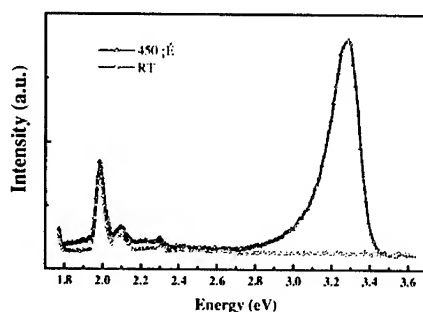


Figure 5. CL spectra of the ZnO films deposited at room temperature and 450 °C

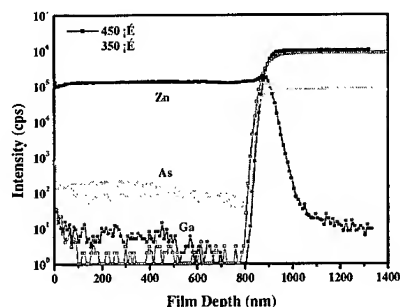


Figure 6. SIMS profiles of the ZnO films deposited at 350 °C and 450 °C

uniformly distributed through the ZnO films, and the As atom concentration is a factor 10 higher than the Ga concentration. The SIMS results indicate that the As doping method using GaAs substrate might be useful for the formation of p-type ZnO thin films. However, all as-grown films showed electrically insulating properties with high contact resistance ($>25 \text{ M}\Omega$). Considering that the films exhibited the high resistivity, it is thought that the doped As atoms were not electrically activated due to insufficient activation energy.

In order to activate As dopants, post-annealing treatment at 500 °C was performed for the films deposited at 350 °C and 450 °C. After 2-hr annealing treatment, the film deposited at 350 °C showed no change in electrical properties whereas the film deposited at 450 °C showed n-type characteristics with electron concentration of $3 \times 10^{18} / \text{cm}^3$ and resistivity of $9.65 \times 10^{-2} \Omega \cdot \text{cm}$.

However, a significant change of optical properties was observed after post-annealing treatment. Figure 7 shows the room-temperature PL spectra of ZnO films deposited at 350 °C and 450 °C after annealing treatment at 500 °C. For the film deposited at 350 °C, the intensity of NBE at 3.28 eV was much stronger than that of the as-grown films and this

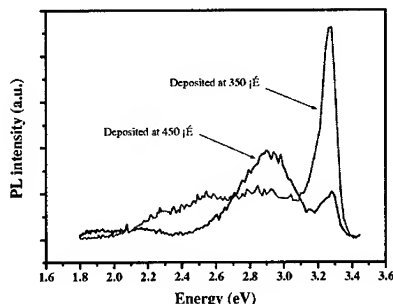


Figure 7. PL spectra of ZnO films deposited at 350 °C and 450 °C after annealing treatment at 500 °C

indicates improvement in optical properties. For the film deposited at 450 °C, however, the peak intensity related to the donor-to-acceptor pair (DAP) transition at 2.9 eV is increased. Therefore, it is thought that annealing treatment activate As dopants which act as acceptors.

CONCLUSION

ZnO films were deposited on GaAs(100) substrates by rf magnetron sputtering. As deposition temperature increased, grain growth of the films was observed from SEM images. The results of XRD analysis showed the change of preferred orientations of the film growth and the relaxation of stress in the films with increasing deposition temperature. CL measurement showed that, for the films deposited at R.T., only defect-related deep-level emission was observed while, for the films deposited at 450 °C, a strong NBE was observed, implying they are optically high-quality.

After annealing treatment for activating As dopants, the films deposited at 450 °C exhibited smaller resistivity than that of the as-grown films, although they showed n-type characteristics with $3 \times 10^{18} / \text{cm}^3$ of carrier concentration. In PL spectra of the films, DAP transition at 2.9 eV was dominant due to the activation of As dopants, which suggests the possibility of p-type doping of ZnO films when GaAs substrate is employed.

REFERENCE

- 1) D. M. Bagnall, Y. F. Chen, Z. Zhu, T. Yao, S. Koyama, M. Y. Shen, and T. Goto, Appl. Phys. Lett. **70**, 2230 (1997).
- 2) R.F. Service, Science **276**, 895 (1997).
- 3) Z. K. Tang, G. K. L. Wong, P. Yu, M. Kawasaki, A. Ohtomo, H. Koinuma, and Y. Segawa, Appl. Phys. Lett. **72**, 3270 (1998).
- 4) J. R. Choi, S. Park: Mechatronics **8**, 441 (1998).
- 5) Y. R. Ryu, S. Zhu, D. C. Look, J. M. Wrobel, H. M. Jeong and H. W. White: J. Cryst. Growth **216**, 330 (2000).
- 6) Jwo-Huei Jou, Min-Yung Han, and Duen-Jen Cheng, J. Appl. Phys. **71**, 4333 (1992).
- 7) A. B. M. Almamun Ashrafi, Akio Ueta, Adrian Avramescu, Hidekazu Kumano, Ikuo Suemune, Young-Woo Ok, and Tac-Yeon Seong, Appl. Phys. Lett. **76**, 550 (2000).
- 8) Y. R. Ryu, S. Zhu, J. D. Budai, H. R. Chandrasekhar, P. F. Miceli, and H. W. White, J. Appl. Phys. **88**, 201 (2000).
- 9) M. Dinescu and P. Verardi, Appl. Surf. Sci. **106**, 149 (1996).
- 10) H. Cao and Y.G. Zhao, S.T. Ho, E.W. Seelig, Q.H. Wang, and R.P.H. Chang, Phys. Rev. Lett. **82**, 2278 (1999).
- 11) X.L. Xu, S.P. Lau, J.S. Chen, G.Y. Chen and B.K. Tay, J. Cryst. Growth **223**, 201 (2001).
- 12) Sunglae Cho, Jing Ma, Yunki Kim, Yi Sun, George K. L. Wong, and John B. Ketterson, Appl. Phys. Lett. **75**, 2761 (1999).
- 13) H. K. Kim and M. Mathur, Appl. Phys. Lett. **61**, 2524 (1992).
- 14) D. M. Bagnall, Y. F. Chen, Z. Zhu, T. Yao, M. Y. Shen and T. Goto, J. Cryst. Growth. **184/185**, 605 (1998).
- 15) S. Bethke, H. Pan, and B. W. Wesseis, Appl. Phys. Lett. **52**, 136 (1988).
- 16) Yefan Chen, D. M. Bagnall, Hang-jun Koh, Ki-tae Park, Kenji Hiraga, Ziqiang Zhu, and Takafumi Yao, J. Appl. Phys. **84**, 3912 (1998).

Growth of the Single-Crystalline ZnO Films on Si (111) Substrates by Plasma-Assisted Molecular-Beam Epitaxy

Kazuto Koike¹, Takanori Tanite², Shigehiko Sasa^{1,2}, Masataka Inoue^{1,2}, and Mitsuaki Yano^{1,2}
Bio Venture Center¹, New Materials Research Center², Osaka Institute of Technology,
Asahi-ku Ohmiya, Osaka 535-8585, Japan

ABSTRACT

This report describes the growth of single-crystalline ZnO films on Si (111) substrates by plasma-assisted molecular-beam epitaxy. X-ray diffraction measurement shows that c-axis oriented ZnO films are easily grown on Si (111) substrates. However, in-plane random rotational domains are included in the ZnO films due to the inevitable oxidation of substrate surface at the initial stage of ZnO growth. By employing a thin CaF₂ buffer layer between the ZnO films and Si substrates, we have succeeded in suppressing the generation of rotational domains and in obtaining an intense ultraviolet photoluminescence even at room temperature. These results indicate that the use of CaF₂ buffer layer is promising for the growth of device-quality ZnO films on Si (111) substrates.

INTRODUCTION

Wide and direct band-gap semiconductor ZnO has attracted much attention to the room-temperature operating ultraviolet lasers and sensors because of its large exciton binding energy of about 60 meV [1]. To integrate these optoelectronic devices with Si-base electrical circuitry, however, high-quality ZnO growth on Si substrates is a key issue although the direct growth is apt to yield in-plane rotational domains by the oxidation of substrate surface at the initial stage of ZnO growth [2]. Recently, Iwata *et al.* demonstrated that the plasma-assisted nitridation of Si substrate prior to ZnO growth was effective to suppress the oxidation of Si surface although in-plane 30° rotational domains still remained in the ZnO films [2]. We notice the use of CaF₂ buffer layer as an alternative way to suppress the oxidation of Si surface. This idea is promoted by the recent work of Ko *et al.* that reports the growth of single-crystalline ZnO (0001) films on bulk CaF₂ (111) substrates using plasma-assisted molecular-beam epitaxy (MBE) [3]. In this heterosystem, the epitaxial relationship is reported to be $[2\bar{1}\bar{1}0]$ ZnO (0001) // $[\bar{1}10]$ CaF₂ (111) [3]. Due to the close lattice matching of about 0.6 % between CaF₂ (111) and Si (111), we can expect single crystalline MBE growth for the CaF₂ buffer layer [4,5]. In this paper, we report the effect of CaF₂ buffer layer on the ZnO films grown on Si (111) substrates.

EXPERIMENTAL PROCEDURE

The growth in this experiment was carried out using an Epiquest-MBE system equipped with effusion K-cells for Zn and CaF₂ sources and an rf-plasma cell for oxygen radical source.

The growth process was *in-situ* monitored by a reflection high-energy electron diffraction (RHEED) system operated at 15 KV. Compound CaF_2 with a purity of 4 N was used for the CaF_2 growth, and elemental Zn with a purity of 7 N and oxygen gas with a purity of 6 N were used for the ZnO growth. (111)-oriented p-type ($\sim 0.01 \Omega\text{-cm}$) Si was used as the substrates. The substrates were degreased in toluene, acetone, and ethylalcohol, and then boiled in HNO_3 bath at 130°C for 5 minutes. Subsequently, we dipped the substrates in a solution of 50 % HF for 20 minutes to remove the native oxide on the surface, and then thoroughly rinsed them in de-ionized water after dipping in a solution of NH_4F for 2 minutes. This chemical process is known to be effective to prepare a hydrogen-terminated surface with the flatness in an atomic scale [6]. By an immediate mounting on a substrate holder and loading in the MBE growth chamber, the clean surface of Si with 7×7 reconstruction was obtained in the growth chamber after elevating the substrate temperature up to 800°C . During ZnO growth, oxygen flow rate and rf power were kept at 0.30 ccm and 350 W, respectively. The base pressure was $\sim 5\times 10^{-8}$ Pa and the working pressure during ZnO growth was $\sim 1\times 10^{-4}$ Pa in the growth chamber.

In Fig. 1, (a) and (b) show the schematics of the sample structures with and without a CaF_2 buffer layer, respectively. We compare these two different samples on structural and optical properties. The ZnO film of sample (b) is directly grown on the Si clean surface without the insertion of CaF_2 buffer layer. The ZnO film of sample (a), on the other hand, is grown on a 30-nm-thick CaF_2 buffer layer. This CaF_2 buffer layer was grown at 650°C on the Si clean surface at a rate of 60 nm/h. The orientation of the resulted CaF_2 layer was (111) in agreement with that of Si substrate. Then the CaF_2 buffer layer was exposed to a defocused electron beam (15 KV, $\sim 25 \mu\text{A}$) from the RHEED gun. This exposure to electron beam was performed to remove the uppermost fluorine atoms and to generate fluorine vacancies on the CaF_2 surface [4,5]. Since fluorine-deficient CaF_2 surface is more energetically active [4,5,7], we expected the electron-beam exposure to enhance the wettability for ZnO growth.

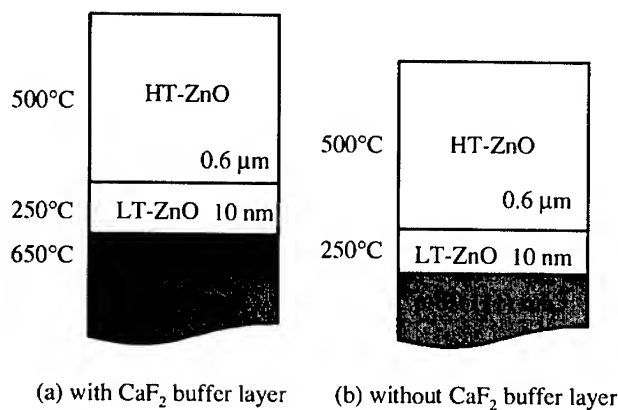


Figure 1. Schematics of two different ZnO/Si (111) heterostructures. (a) and (b) are the ZnO films with and without a CaF_2 buffer layer, respectively.

For both samples, the ZnO films of initial 10-nm-thick were deposited at 250°C using a growth rate of 200 nm/h to promote the nucleation of epitaxial growth [3]. After this low-temperature (LT) ZnO growth, the substrate temperature was elevated once up to 750°C under a Zn-beam irradiation to experience the LT-ZnO films an *in-situ* thermal annealing. Then we cooled down the substrate temperature to 500°C, and grew a high-temperature (HT) ZnO layer of 600 nm using a growth rate of 400 nm/h. We expected the combination of LT-ZnO growth and *in-situ* thermal annealing to improve both the crystalline quality and surface morphology of the ZnO films.

After the growth, these samples were characterized by atomic force microscopy (AFM) in air, x-ray diffraction (XRD) using Cu-K α radiation, and photoluminescence (PL) using the 325 nm line of a 20 mW He-Cd laser as the excitation source.

RESULTS AND DISCUSSION

In Figure 2, (a) and (b) show the RHEED patterns during growth. As seen from the pattern (1) of Figs. 2 (b), 7 \times 7 streaks were observed from the surface before growth, indicating the clean and flat surface of the Si (111) substrate [6]. When the LT-ZnO was directly grown on the Si clean surface, the streak 7 \times 7 pattern immediately changed into a ring pattern of which dependence on the direction of incident electron beam was not observed. This ring pattern essentially continued till the end of HT-ZnO growth as shown by the patterns (2) to (4) of Figs. 2 (b), although a little change to a spotty pattern was observed for the surface after HT-ZnO growth. These results indicate that polycrystalline or in-plane rotational domains are easily included in the ZnO layer due to the formation of amorphous Si-oxide on the Si surface.

On the contrary, a six-fold-symmetry pattern was observed when the LT-ZnO was grown on the CaF₂ buffer layer. At the very beginning of the LT-ZnO growth, a diffused spotty pattern like

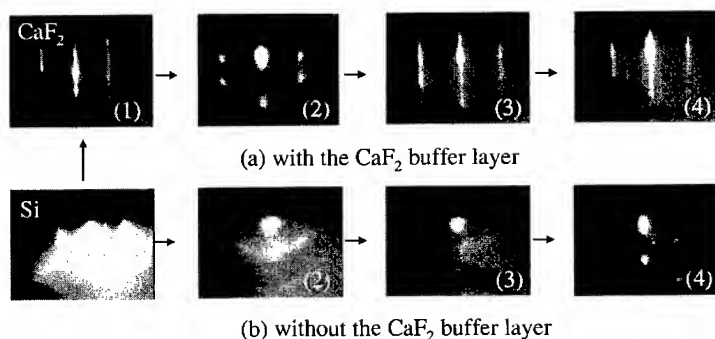


Figure 2. RHEED patterns observed from the samples with and without the CaF₂ buffer layer. In both series (a) and (b), for the samples with and without the CaF₂ buffer layer, (1) to (4) correspond to the surfaces before the LT-ZnO growth, after the LT-ZnO growth, after the annealing, and after the HT-ZnO growth, respectively.

(2) in Figs. 2 (a) appeared. The rod-spacing of the LT-ZnO is $\sim 16\%$ wider than that of the CaF_2 buffer layer, which is in good agreement with the difference in lattice constants between these two bulk materials, suggesting the strain-free growth of the ZnO epilayer. By the *in-situ* annealing at 750°C , this diffused spotty pattern was changed to a streaky one. The sharp streaks in the pattern (4) of Figs. 2 (a), from the surface after the HT-ZnO growth, indicate that both crystalline quality and surface morphology are dramatically improved by the use of the CaF_2 buffer layer.

It was revealed by AFM measurement that a typical root-mean-square (rms) roughness of the CaF_2 surface was $\sim 0.48\text{ nm}$ in $10 \times 10\ \mu\text{m}^2$ area. In agreement with the RHEED observation, the surface morphology became rough (rms roughness $\sim 4.0\text{ nm}$) after the LT-ZnO growth on the CaF_2 buffer layer. However, it was improved to be $\sim 2.5\text{ nm}$ after the HT-ZnO growth. Although similar improvement was also experienced by the sample without the CaF_2 buffer layer, the resulted morphology of the HT-ZnO surface was inferior (rms roughness $\sim 3.3\text{ nm}$) to that of the sample with the CaF_2 buffer layer.

In order to study their structural quality, we measured XRD of these two different samples. In Fig. 3 of θ - 2θ scan, (a) and (b) of which correspond to those in Fig. 1, two intense peaks located at 34.5° and 72.5° in both spectra closely agree with the (0002) and (0004) reflections from bulk ZnO, respectively. Since other peaks related to ZnO are not observed, both ZnO films with and without the CaF_2 buffer layer are considered to be highly c-axis oriented on the Si substrates. However, we found a large difference between these two samples in the in-plane crystalline quality by using the pole-figure measurement of XRD in the $\{10\bar{1}0\}$ diffraction. Note that θ - 2θ diffraction only reflects in-depth crystalline quality. In Fig. 4 of pole-figures, (a) and (b)

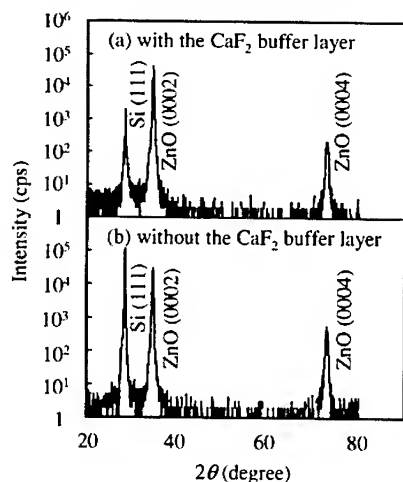


Figure 3. X-ray diffraction spectra in the θ - 2θ configuration from the ZnO films (a) with and (b) without the CaF_2 buffer layer.

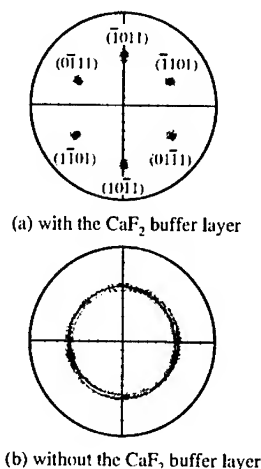


Figure 4. Pole-figures in the $\{10\bar{1}0\}$ configuration of x-ray diffraction from the ZnO films (a) with and (b) without the CaF_2 buffer layer.

are observed from the samples with and without the CaF_2 buffer layer, respectively. It is indicated that the ZnO film grown on the CaF_2 buffer layer is free from rotational domains and twins, since clear six-fold-symmetry is seen for the ZnO $\{10\bar{1}0\}$ reflection. On the contrary, the ring pattern of Fig. 4 (b) indicates that random rotational in-plane domains are included in the ZnO (0001) films when directly grown on Si substrates. Considering the RHEED pattern change in Fig. 2 (b), these random rotational domains may be predominantly included in the bottom ZnO layer.

In order to compare these two samples on their optical properties, we measured PL spectra at 20 K although the spectra are not shown here. From the sample with the CaF_2 buffer layer, only narrow and intense peaks at 3.33 eV and 3.36 eV were observed. These peaks are attributed to the excitons localized at neutral acceptors and donors, respectively [8,9]. Since the full-width at half-maximum (FWHM) of these peaks was relatively small (~ 7 meV) and there was no sign from defect-related transitions, we can conclude that high-quality ZnO growth was achieved on the CaF_2 buffer layer. On the contrary, the sample without the CaF_2 buffer layer was found to contain many defects in the ZnO film, since broad peaks from defect-related transitions appeared at around 1.8 eV and 2.2 eV. These defect-related transitions are probably associated with non-stoichiometric recombination centers such as single-ionized oxygen vacancies and/or single-negatively-charged oxygen interstitials [10].

Figure 5 shows the PL spectrum measured at 300 K from the sample with the CaF_2 buffer layer. An intense peak from the excitons in ZnO is observed at 3.29 eV. The observed energy for the peak closely agrees the previously reported value for the free excitons in the ZnO films grown on sapphire substrates [8]. As shown by the inset of Fig. 5, the intensity of defect-related emission band is quite small (less than 1/400 of the intensity of excitonic emission) even at room temperature. Note that such a stable existence of free excitons is due to the large binding energy, and is promising for short-wavelength excitonic lasers operating at room temperature.

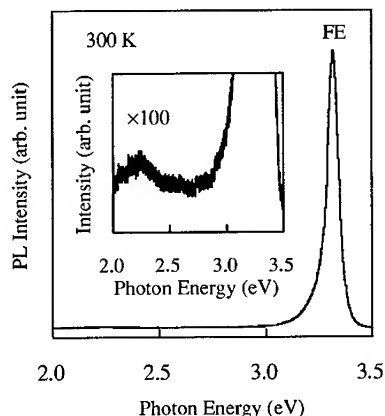


Figure 5. Room-temperature PL spectrum from the ZnO film with the CaF_2 buffer layer. An intense peak from free excitons is observed at 3.29 eV. Inset shows the vertically magnified spectrum.

This strong excitonic emission with a small FWHM of about 70 meV is a direct evidence for the high-quality of the ZnO films grown on the CaF₂ buffer layer.

CONCLUSION

We have succeeded in the MBE growth of the single-crystalline ZnO (0001) films on Si (111) substrates by using a thin CaF₂ (111) buffer layer. RHEED and XRD measurements show the growth of single-crystalline ZnO films without any rotational domains and twins. PL measurement reveals that an intense excitonic emission is dominant for the ZnO films even at room temperature. These results demonstrate that high-quality ZnO growth is achieved by using the CaF₂ buffer layer to suppress the oxidation of Si surface at the initial stage of ZnO growth.

ACKNOWLEDGEMENT

The authors wish to thank Dr. Y. Harada and Dr. H. Ochi for their help. We also thank Mr. T. Komuro for experimental assistance.

REFERENCES

1. D. G. Thomas, *J. Phys. Chem. Solids* **15**, 86 (1960).
2. K. Iwata, P. Fons, S. Niki, A. Yamada, K. Matsubara, K. Nakahara, T. Tanabe, and H. Takasu, *J. Crystal Growth* **214/215**, 50 (2000).
3. H. J. Ko, Y. F. Chen, J. M. Ko, T. Hanada, Z. Zhu, T. Fukuda, and T. Yao, *J. Crystal Growth* **207**, 87 (1999).
4. M. Tsutsui, M. Watanabe, and M. Asada, *Jpn. J. Appl. Phys.* **38**, L920 (1999).
5. K. Kawasaki and K. Tsutsui, *Jpn. J. Appl. Phys.* **38**, 1521 (1999).
6. L. T. Vinh, M. Eddrief, C. A. Sébenne, P. Dumas, A. T. Ibrahimi, R. Gunther, Y. J. Chabal, and J. Derrien, *Appl. Phys. Lett.* **64**, 3308 (1994).
7. H. C. Lee, T. Asano, H. Ishiwara, and S. Furukawa, *Jpn. J. Appl. Phys.* **27**, 1616 (1988).
8. D. M. Bagnall, Y. F. Chen, Z. Zhu, T. Yao, M. Y. Shen, and T. Goto, *Nonlinear Optics* **18**, 243 (1997).
9. H. J. Ko, Y. F. Chen, Z. Zhu, T. Yao, I. Kobayashi, and H. Uchiki, *Appl. Phys. Lett.* **76**, 1905 (2000).
10. X. L. Wu, G. G. Siu, C. L. Fu, and H. C. Ong, *Appl. Phys. Lett.* **78**, 2285 (2001).

Symposium K Papers

**Properties of 2D and 3D Dielectric Structures
Fabricated by Electrochemical Dissolution of III-V Compounds**

I.M. Tiginyanu,¹ S. Langa,¹ M. Christophersen,² J. Carstensen,² V. Sergentu,¹ E. Foca,¹ O. Rios,² and H. Föll²

¹Laboratory of Low-Dimensional Semiconductor Structures, Technical University of Moldova, Chisinau, Moldova

²Department of Engineering, Christian-Albrechts-University, Kiel, Germany

ABSTRACT

Porous layers and membranes representing 2D and 3D dielectric structures were fabricated on different III-V compounds (GaAs, InP, GaP) by electrochemical etching techniques. Nonlithographically fabricated ordered nanopore arrays in InP are reported for the first time. We show that the reflectance from nanostructured InP is lower than that from bulk InP in the spectral interval 1.5-2.2 eV. The artificial anisotropy induced by nanotexturization was studied in porous GaP membranes and the refractive indices for ordinary and extraordinary beams were evaluated.

INTRODUCTION

Electrochemistry proves to be a powerful tool for producing dielectric structures on solid-state materials. The fabrication of polycrystalline nanopore arrays with hexagonal ordering by self-organized anodization on aluminum has already been reported, e.g. [1]. The mechanical stress associated with the expansion of the aluminum during oxide formation was suggested to generate repulsive forces between neighboring pores during the oxidation process leading to self-organized formation of hexagonal pore arrays [2]. Ordered pore arrays on large areas can be prepared using prepattern-guided anodization of both aluminum and crystalline silicon [3,4]. Recently the electrochemical etching techniques were used to fabricate semiconductor sieves of gallium phosphide, i.e., two-dimensionally nanostructured membranes exhibiting a strongly-enhanced optical second harmonic generation in comparison with the bulk material [5]. Moreover, crossing pores were observed in GaAs indicating that anodic etching may be a suitable and unique tool for the production of 3D micro- and nanostructured III-V compounds [6]. In this work, we explore the possibility to produce quasi-periodic dielectric structures on III-V compounds by electrochemical etching techniques. Data concerning morphology studies and optical characterization of samples are presented.

EXPERIMENTAL

N-type (100) oriented InP, GaAs and (111)-oriented GaP wafers cut from Czochralski grown ingots were used in this work. The free carrier concentration was $n = 10^{18} \text{ cm}^{-3}$ at 300 K. The anodization was carried out in an electrochemical double cell as described elsewhere [6] in HCl and H₂SO₄ aqueous electrolytes. The area of the sample exposed to the electrolyte was 0.2 cm². The supply of holes was due to the reverse bias applied to the semiconductor/electrolyte junction, which involves the avalanche breakdown effects accompanied by generation of electron-hole pairs.

A configuration with four electrodes was used: a Pt reference electrode in the electrolyte (REE), a Pt sense electrode on the sample (SES), a Pt counter electrode (CE), and a Pt working electrode (WE). The electrodes were connected to a specially designed potentiostat/galvanostat which can deliver currents and voltages up to 200 mA and ± 80 V respectively. The temperature was kept constant at $T = 20^\circ\text{C}$ by means of a Julabo F25 thermostat. The electrolyte was pumped continuously through both cells by means of peristaltic pumps. All the equipment used in the experiments was computer controlled. The morphology of the porous layers was analyzed with a scanning electron microscope (SEM) operating at 10 kV.

RESULTS AND DISCUSSION

Study of Morphology

Figure 1 illustrates SEM images taken from n-InP samples subjected to anodic etching in 7.5 % HCl solution at different applied voltages with subsequent removal of the nucleation layer (NL) by nonselective wet etching. One can see that the degree of porosity increases with the applied potential. Apart from that, in the voltage interval 5 to 9 V a self-organized ordering of pores occurs and the highest degree of order is observed at 7-8 V. As one can see from Figure 1b, there are domains of micrometer size with nearly perfect hexagonal ordering. Two of such domains are marked in Figure 1b by solid curves.

When the samples are anodized in solution with 5 % HCl concentration, they exhibit the maximum degree of pore ordering at 9-10 V. Figure 2a presents a cleavage of a porous layer produced by anodic etching of a n-InP substrate at 10 V for 1 minute.

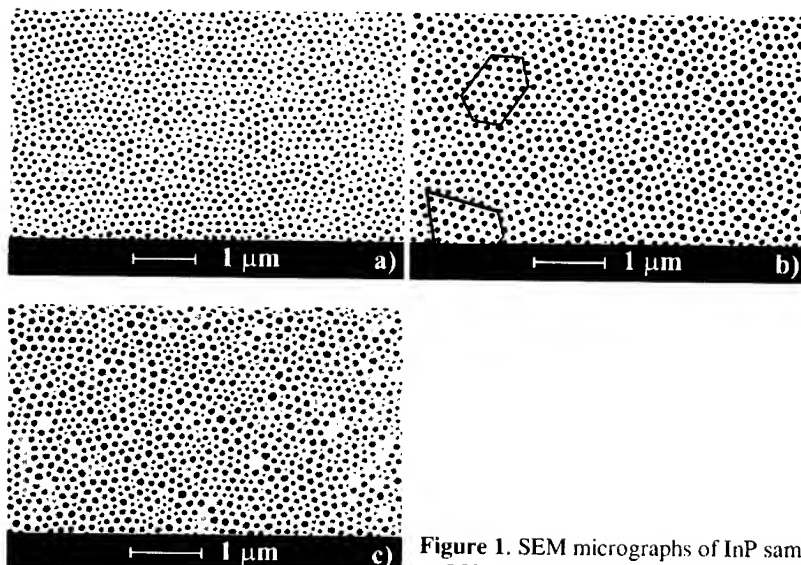


Figure 1. SEM micrographs of InP samples anodized at 5 V (a), 7 V (b) and 9 V (c).

Note that the NL layer with the thickness $1.5\ \mu\text{m}$ was removed by nonselective etching. One can see that the distribution of pores is highly uniform both along the top surface and in the depth of the porous layer. The pores grow perpendicularly to the initial surface. We believe that the interaction between pores by means of the space charge region as well as the high crystalline quality of our samples and computer-controlled accuracy of etching conditions are the primary factors leading to the observed uniformity in pore distribution. Moreover, as in the case of samples anodized in 7.5 % HCl electrolytes, the spatial distribution of pores proves to be ordered within domains of micrometer sizes (Figure 2b). The transverse sizes of pores and InP wall thicknesses equal 200 and 120 nm respectively, leading to a degree of porosity of about 55 %. An autocorrelation analysis of the pores position shows an ordering of up to the sixth neighbor. A corresponding analysis of the radial distribution of the pore position shows a 60° angle between the neighbors of one pore. Combining these data a medium range ordering of pores in a closed packet arrangement is found.

The direction of pore growth in InP strongly depends upon the anodic current density [7]. In GaAs the pores grow usually along the $\langle 111 \rangle$ crystallographic direction regardless the value of the anodic current. Moreover, $\langle 111 \rangle$ oriented pores in GaAs intersect each other without changing their direction of growth or shape [6], which is essential for producing 3D dielectric structures by intersecting quadruples of $\langle 111 \rangle$ pores starting from a common nucleus. We explored the possibility to fabricate three-dimensional photonic structures with pitting occurring on (100) surface and pores propagating along $\langle 111 \rangle$ crystallographic directions (the so-called "Moldavite" structures). Being mechanically stable for low degrees of porosity, such structures were evidenced to easily collapse at high degrees of porosity. For instance, when the pits are arranged in a two-dimensional square lattice with the lattice constant a , the material percolation proves to be broken at pore radius $r = 0.35a$. For the percolation limit, the volume of pores in the dielectric structures was found to be as high as 74 %.

We found that four $\langle 111 \rangle$ -directions of pore growth are not equivalent from the chemical/electrochemical point of view. Two of them, the so-called $\langle 111 \rangle_B$ directions, have a lower dissolution rate than the other two $\langle 111 \rangle_A$ directions.

When the $\langle 111 \rangle_A$ oriented pores are distributed close to each other, the nucleation of $\langle 111 \rangle_B$ pores is strongly inhibited. An example of high density $\langle 111 \rangle_A$ oriented pores in GaAs is shown in Figure 3. Note that the triangles result from the intersection of pores oriented along $\langle 111 \rangle_A$ directions. The insert shows the nucleation of two $\langle 111 \rangle_A$ oriented pores at the initial surface of the GaAs substrate.

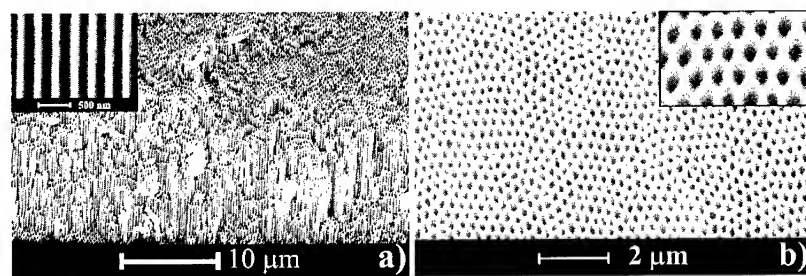


Figure 2. SEM micrographs taken from an InP sample anodized at 10 V: a) random cleavage, overview; b) top view.

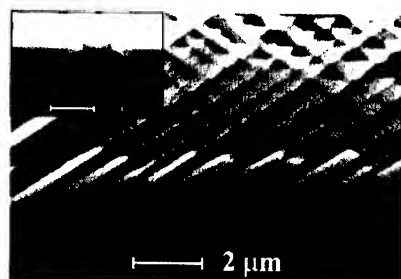


Figure 3. Cross-sectional SEM image taken from a GaAs sample anodized at a constant current density $j = 200 \text{ mA/cm}^2$. The insert illustrates the ramification of pores starting from a common nucleus.

Optical Properties

Taking into account the strongly enhanced second harmonic generation in porous GaP [5], we have studied the linear optical properties of porous membranes to evaluate the material transparency and optical anisotropy.

Figure 4 shows the transmission spectrum of a porous GaP membrane fabricated on a (111) oriented crystalline substrate as described in Ref. 5. According to SEM analysis (see Figure 1 in [5]), the membrane exhibits triangular-prism like pores with lateral average dimensions of about 50 nm. The pores are uniformly distributed and no pronounced fluctuations in their sizes exist. As one can see in Figure 4, the optical transmission spectrum of the porous membrane shows pronounced interference fringes in the spectral interval corresponding to quantum energies lower than the indirect band gap of bulk GaP ($h\nu < E_g = 2.24 \text{ eV}$).

The observation of interference fringes is indicative of the optical homogeneity of the porous medium. Due to the relatively small dimensions of both pores and skeleton entities, the porous medium proves to be optically homogeneous and, therefore, the light propagates through it without pronounced scattering.

The degree of porosity defines the value of the refractive index of the membrane and the optical anisotropy caused by the preferential orientation of pores along $\langle 111 \rangle$ crystallographic directions.

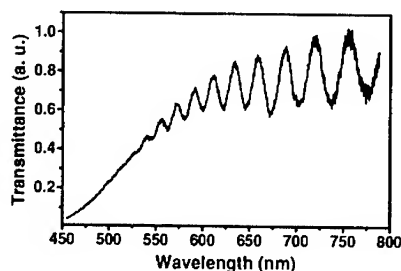


Figure 4. Optical transmission spectrum of a porous GaP membrane.

According to the effective medium theory [8], in the case of pores stretching perpendicular to the initial surface, the components of the dielectric tensor of the porous membrane can be written as follows:

$$\varepsilon_{//}(\omega) = (1 - c) \cdot \varepsilon_1 + c \cdot \varepsilon(\omega) \quad (1)$$

$$\varepsilon_{\perp}(\omega) = \varepsilon(\omega) \cdot \frac{\varepsilon_1 \cdot (2 - c) + c \cdot \varepsilon(\omega)}{\varepsilon_1 \cdot c + \varepsilon(\omega) \cdot (2 - c)} \quad (2)$$

where c is the concentration of GaP, $\varepsilon(\omega)$ is the dielectric function of GaP, and ε_1 is the dielectric constant of air. Due to $\varepsilon_{\perp}(\omega) < \varepsilon_{//}(\omega)$ for all c , porous GaP is a positive uniaxial material.

Figure 5 shows the transmission of light with $\lambda = 1064$ nm by a porous membrane with the thickness $8.2 \mu\text{m}$ as a function of the incident angle of the laser beam. The position of the maxima displayed by the interference patterns depends upon the direction of light polarization. For the ordinary beam, the maxima occurs at the incident angles 17° and 43° , while for the extraordinary beam the maxima occurs at 21° and 49° . The analysis of the interference conditions for the two beams taking into account Eqs. (1) and (2) allowed to calculate the refractive indices: $n_o = 2.43$ and $n_e = 2.67$. So, the porous membranes exhibit pronounced birefringence necessary for phase matching in the optical second harmonic generation [5]. The possibility to fabricate ordered nanopore arrays on indium phosphide looks promising for photonic crystal applications. We carried out a comparative study of reflectance spectra taken from bulk and porous InP samples (Figure 6). The samples were cleaved and the non-polarized reflectance was measured from the side. Interestingly, the porous specimen exhibits a pronounced decrease in reflection when approaching the infrared region. The analysis based on Fresnel formulas shows that the effect involved is caused by the porosity-induced decrease in the effective index of reflection and absorption coefficient of the medium.

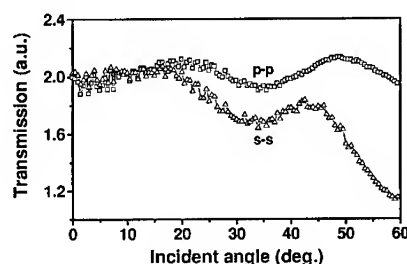


Figure 5. Transmission of light with $\lambda = 1064$ nm by a porous GaP membrane as a function of the incident angle of the laser beam for s-s and p-p polarization geometries.

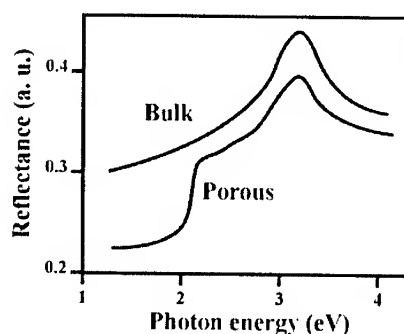


Figure 6. Reflection spectra taken from bulk and porous InP with self-organized ordering of pores.

CONCLUSIONS

Both 2D and 3D dielectric structures can be produced on III-V compounds by electrochemical etching. Under certain etching conditions self-arrangement of submicrometer parallel pores in two-dimensional hexagonal lattices occurs in InP crystalline substrates. Anodic etching of (100)-oriented GaAs results in the formation of 3D dielectric structures due to the preferential orientation of pores along $\langle 111 \rangle$ crystallographic directions. The material percolation should be taken into account when designing and producing 3D dielectric structures. 2D structures exhibit porosity-induced optical anisotropy that makes anodically etched GaP and InP perspective for advanced nonlinear optical applications.

ACKNOWLEDGMENT

This work was supported by Deutsche Forschungsgemeinschaft (DFG) under grants no. FO 258/4-1 and MOL 113/2/0-1, and by Research Council of Moldova.

REFERENCES

1. A. P. Li, F. Müller, A. Birner, K. Nielsch, and U. Gösele, *J. Vac. Sci. Technol. A* **17**, 1428 (1999).
2. O. Jessensky, F. Müller, and U. Gösele, *Appl. Phys. Lett.* **72**, 1173 (1998).
3. A. P. Li, F. Müller, and U. Gösele, *Electrochem. Solid-State Lett.* **3**, 131 (2000).
4. R. B. Wehrspohn, and J. Schilling, *MRS Bulletin* No 8, 623 (2001).
5. I. M. Tiginyanu, I. V. Kravetsky, J. Monecke, W. Cordts, G. Marowsky, and H. L. Hartnagel, *Appl. Phys. Lett.* **77**, 2415 (2000).
6. S. Langa, J. Carstensen, M. Christophersen, H. Föll, and I.M. Tiginyanu, *Appl. Phys. Lett.* **78**, 1074 (2001).
7. S. Langa, I.M. Tiginyanu, J. Carstensen, M. Christophersen, and H. Föll, *Electrochem. Solid-State Lett.* **3**, 514 (2000).
8. D.J. Bergman, *Phys. Rep.* **43**, 337 (1978).

Transmission Characterization of Drilled Alternating-Layer Three-Dimensional Photonic Crystals

Eiichi Kuramochi¹, Masaya Notomi¹, Itaru Yokohama¹, Jun-ichi Takahashi², Chiharu Takahashi^{2,3}, Takayuki Kawashima⁴, and Shojiro Kawakami⁴

¹NTT Basic Research Laboratories, NTT Corporation, 3-1 Morinosato Wakamiya, Atsugi-shi, 243-0198 Japan.

²NTT Telecommunications Energy Laboratories, NTT Corporation, 3-1 Morinosato Wakamiya, Atsugi-shi, 243-0198, Japan.

³NTT Advanced Technology Corporation, 3-1 Morinosato Wakamiya, Atsugi-shi, 243-0198, Japan.

⁴NICHE, Tohoku University, Aramaki Aza Aoba 04, Aoba-ku, Sendai, 980-8579 Japan.

ABSTRACT

We propose a new three-dimensional photonic crystal structure or drilled alternating-layer photonic crystal (DALPC), which can be fabricated by a combination of the deposition of alternating layers of dielectric films and one-time dry etching. Our band calculation predicts that the DALPC has a photonic band gap (PBG) in all directions. We fabricated a Si/SiO₂ DALPC by electron beam lithography, bias sputtering, and fluoride-gas electron cyclotron resonance etching. We measured the light transmission of the DALPC sample in both the in-plane and vertical directions. We observed a transmission minimum around the 1.4- μ m-wavelength for all measured directions and TE/TM polarizations, which demonstrated a potential of the DALPC as a three-dimensional PBG material.

INTRODUCTION

Photonic crystals (PC) [1] are now the subject of considerable attention. To pursue a full PBG or a very high Q-value, the PC structure should be three-dimensional (3D). It is relatively easy to construct the self-assembly-based 3D PCs [2,3], but it is very difficult to introduce structural modulations such as a defect to realize device functions. By contrast, device functions can be readily introduced into a lithography-based 3D structure, in which all the PC elements are defined artificially. However, the lithography-based 3D structures reported to date [4-7] require a very complicated fabrication process that needs a large number of alignment processes or sophisticated micromachining, thus making it unrealistic for use in producing commercially viable PCs.

We have proposed a novel three-dimensional photonic crystal, or drilled alternating-layer photonic crystal (DALPC), which can have a full PBG [8,9]. Our DALPC is based on a two-dimensional alternating layer structure and can be deposited by rf-bias sputtering. The automatic shaping effect that occurs in bias sputtering (autoclone) was discovered and developed by Kawakami and co-workers to fabricate 3D PCs [10,11]. We added a nanolithography to the autoclone-based alternating-layer structure to realize a full PBG by creating connectivity in the vertical direction. The main DALPC fabrication processes, namely two-time fine-line lithography, one sequential sputtering deposition, and one-time drilling by dry etching, are based on very mature technologies with few process steps. So the DALPC structure should be highly controllable and easy to fabricate.

In this paper we report the fabrication of a Si/SiO₂ DALPC focusing on the optical communication wavelength (1.5 μ m) and measurement of its transmission characteristics.

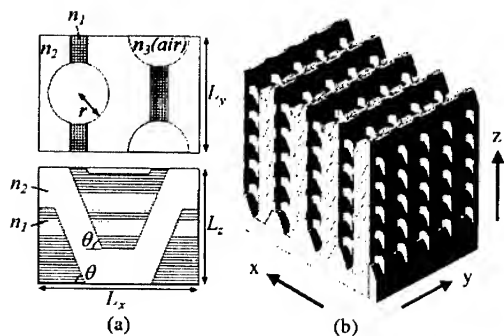


Figure 1. Schematic depiction of a DALPC.

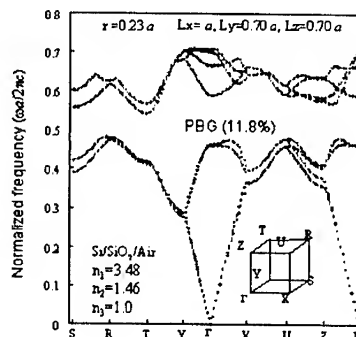


Figure 2. Photonic band structure of a DALPC obtained from a band calculation by the plane wave expansion method.

DRILLED ALTERNATING LAYER PHOTONIC CRYSTALS

Figure 1 shows a schematic depiction of a DALPC. A DALPC is composed of alternating layers (refractive index: n_1 and n_2) and cylindrical holes (index: n_3) drilled through the entire structure. The corrugated alternating layers can be formed by autocloning. This structure is equivalent to a diamond structure, which can have a full PBG. Figure 2 shows the photonic band structure of a DALPC based on a band calculation obtained by the plane wave expansion method [8]. We considered a Si/SiO₂/air DALPC ($n_1, n_2, n_3=3.48, 1.46, 1.0$) and set the lattice constant at ($x/y/z=0.7/0.5/0.5 \mu\text{m}$) to give a PBG wavelength of $1.5 \mu\text{m}$. As a result, we obtained a PC with a large gap/midgap ratio of 11.8%, which is large enough to enable us to realize various PC-based devices.

EXPERIMENTAL DETAILS

We fabricated a Si/SiO₂/air DALPC in which the lattice constant was ($x/y/z=0.7/0.5/0.3 \mu\text{m}$). The fabrication methods and technologies we used here were the same as those employed in previous report [9]. We used electron beam lithography to form grooves for autocloning the upper PC structure and to make masks for use when drilling air holes. We suppressed the alignment error of the holes we drilled in the alternating-layer structure to as little as 50 nm. The grooves were fabricated on a Si substrate with a thick surface thermal oxide cladding layer (1 μm) and then 4 periods of alternating layers of Si (0.16 μm) /SiO₂ (0.15 μm) were deposited by bias sputtering under autocloning conditions. After that we drilled air holes by means of electron cyclotron resonance plasma etching with a CF₄-SF₆ gas mixture[12], which is suitable for a Si/SiO₂ system. We used a Ni mask and minimum substrate bias voltage in the drilling because very we needed a high aspect ratio for the air holes (diameter: $\sim 300 \text{ nm}$, depth: $\sim 1.5 \mu\text{m}$).

We measured the light transmission characteristics of a DALPC sample in the in-plane direction as follows. A flat alternating-layer multilayer was formed around the DALPC so we removed most of it by dry-etching leaving 10 μm -wide mesas that acted as index guiding waveguides. We prepared two input and output waveguides for every DALPC sample. We prepared samples for two directions (Γ -X and

Γ -Y) and with transmission lengths of 2, 5, and 10 periods. To measure the transmission spectrum, we used a wavelength tunable laser as a light source and a tapered-hemispherical-end optical fiber to allow coupling with the waveguides on the sample from a cleaved facet. We detected the output light using a multimode fiber with a large spot size. To obtain the polarization characteristics, we undertook measurements using both TE-polarized and TM-polarized single-mode light as the input light.

We also measured the light transmission characteristics in the vertical direction by preparing large-area ($500 \times 500 \mu\text{m}$) DALPC samples. We used the same experimental setup that we used for the in-plane direction measurement. The light was incident from the rear of the substrate and detected at the top of the DALPC. Here TE polarization means that the electric vector was parallel to Γ -Y and TM polarization means the magnetic vector was parallel to Γ -Y.

RESULTS AND DISCUSSION

Figure 3 shows scanning electron microscope images of a DALPC sample fabricated in this study. Figure 3(a) shows a bird's eye view of the sample, which demonstrates almost exact alignment between holes and autocloning-based structure. Figure 3(b) shows a cross-section of the sample. It is obvious that the drilling reached the bottom of the PC, where the depth was about $1.5 \mu\text{m}$. This was very important because with samples where the drilling did not reach the bottom there was no clear structure related to PBG in the in-plane transmittance. However, figure 3(b) also demonstrates the air-holes were far from their ideal cylindrical shape. Especially, the undercut of the top Si layer seemed to be very serious, which was probably caused by reflected radicals at the edge of the Ni mask. We modified etching conditions from those of previous report [9] to drill deeper by increasing the selectivity of Ni to the alternate layers. The undercut seemed to increase as the Ni selectivity increased. Figure 3(b) also shows that the autocloning of the corrugated alternating-layer structure was successfully accomplished

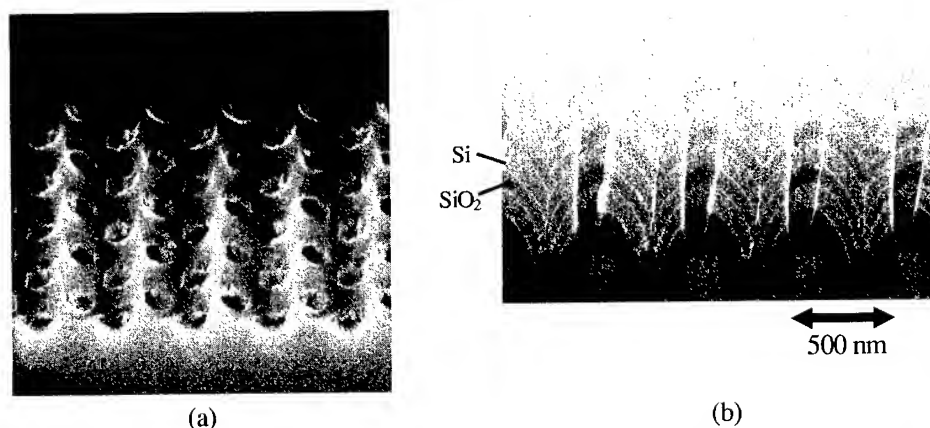


Figure 3. Scanning electron microscope images of a DALPC sample fabricated in this study. (a) A bird's eye view. (b) A cross-section.

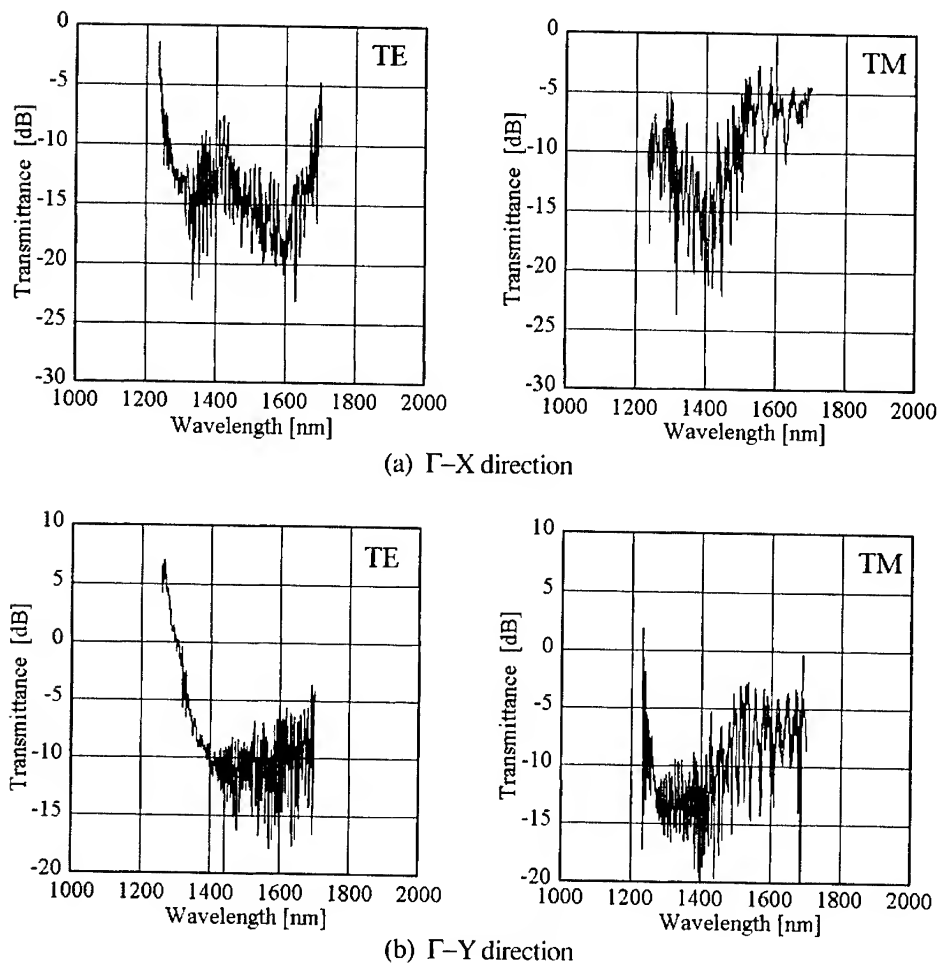


Figure 4. Transmittance of DALPC samples in in-plane directions. The transmission length of the sample was 5 periods.

Figure 4 shows in-plane light transmission spectra of the DALPC at a transmission length of 5 periods. We observed a wide (1.3-1.7 μm) transmission attenuation band for TE polarization in both the Γ -X and Γ -Y directions, where the maximum transmission loss was as large as 20 dB. We also observed an attenuation band for TM polarization although it was somewhat small, which suggested that a full PBG was not achieved in the sample. The attenuation band was considerably wider than what we estimated from the band calculation. When the transmission length was 2 periods the spectra were qualitatively similar but the attenuation band somewhat unclear compared with that of 5 pairs. When the length was 10 pairs the output light was so weak that we could not obtain reliable transmission spectra due to the

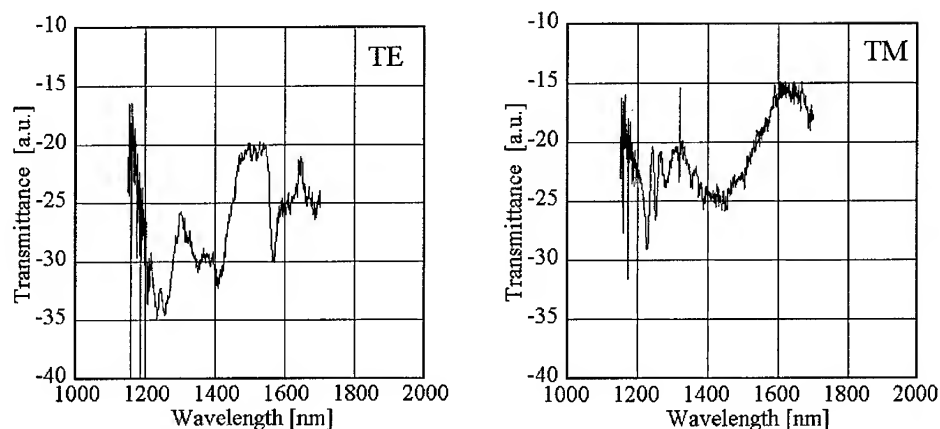


Figure 5. Vertical transmittance of the DALPC sample.

detection limit of our measurement system. Figure 5 shows vertical transmission spectra of a DALPC. Several dips were observed for both TE and TM polarization, although the origin was unclear.

Here it is noted that there was a transmission minimum about a wavelength of $1.4\ \mu\text{m}$ for all directions and polarizations. The correspondence of the transmission minimum in all the measured spectra strongly suggests that a full PBG may open at around $1.4\ \mu\text{m}$. This roughly corresponds to the PBG center we have calculated for this structure. There was no strong attenuation in the in-plane TE spectra of samples with no drilling. By contrast, in samples with air holes (the same as those of the DALPC sample) drilled into a flat alternating-layer, although the in-plane TE transmission spectra exhibited an attenuation band in the same way as the DALPC sample, there was no clear attenuation in the TM spectra. So we believe the correspondence of the transmission minimum in all the measured spectra to be an inherent characteristic of the DALPC structure. The imperfect PBG, the abnormally wide attenuation band, and the coexistence of plural dips in a transmittance were mainly due to the imperfect ion of air holes which were far from an ideal cylindrical shape. So we are currently examining ways of drilling deeper without causing any deterioration in the air hole shape.

CONCLUSION

We have fabricated Si/SiO₂ DALPCs that were designed to have a full PBG at $1.5\ \mu\text{m}$ and have reported their transmission characteristics in detail for the first time. We found a transmittance minimum at about $1.4\ \mu\text{m}$ in all directions and polarizations measured. This is a very important achievement, despite the fact that the measured sample did not have a full PBG, because it shows the possibility that a realizable DALPC can have a full PBG. We believe that after finding a way to control the shape of the drilling and optimizing the alternating-layer structure formed by autocloning we will be able to obtain a DALPC sample with a large full PBG.

ACKNOWLEDGEMENTS

We thank Dr. Akira Ozawa and Daisuke Takagi for sample preparation. We also thank Dr. Hideaki Takayanagi, Dr. Masatoshi Oda and Dr. Akinori Shibayama for their constant support.

REFERENCES

1. J. D. Joannopoulos, R. D. Meade, and J. N. Winn, *Photonic Crystals* (Princeton University Press, New Jersey, 1996).
2. A. Blanco, E. Chomski, S. Gratchak, M. Ibsate, S. John, S. W. Leonard, C. Lopez, F. Meseguer, H. Miguez, J. P. Mondla, G. A. Ozin, O. Toader, and H. M. van Driel, *Nature* **405**, 437 (2000)
3. Y. A. Vlasov, X-Z. Bo, J. C. Strum, and D. J. Norris, *Nature* **414**, 289 (2001)
4. K. M. Ho, C. T. Chan, C. M. Soukoulis, R. Biswas, and M. Sigalas, *Solid State Commun.* **89**, 413 (1994).
5. H. S. Sozuer and J. P. Dowling, *J. Mod. Opt.* **41**, 231 (1994).
6. S. Y. Lin, J. G. Fleming, D. L. Hetherington, B. K. Smith, R. Biswas, K. M. Ho, M. M. Sigalas, W. Zubrzycki, S. R. Kurtz, and J. Bur, *Nature* **394**, 251 (1998)
7. S. Noda, K. Tomoda, N. Yamamoto and A. Chutinan. *Science* **289**, 604-606, 2000.
8. M. Notomi, T. Tamamura, T. Kawashima, and S. Kawakami, *Appl. Phys. Lett.* **77**, 4256 (2000).
9. E. Kuramochi, M. Notomi, T. Tamamura, T. Kawashima, S. Kawakami, J. Takahashi, and C. Takahashi, *J. Vac. Sci. Technol.* **B18**, 3510 (2000).
10. S. Kawakami, *Electron. Lett.* **33**, 1260 (1997).
11. S. Kawakami, T. Kawashima and T. Sato. *Appl. Phys. Lett.* **74**, 463-465, 1999.
12. C. Takahashi, Y. Jin, K. Nishimura, and S. Matsuo, *Jpn. J. Appl. Phys.* **39**, 3672-3676, 2000.

Interference lithography for 3D photonic band gap crystal layer by layer fabrication.

A Feigel, Z. Kotler and B. Sfez

Electro-Optics Division, NRC Soreq, 81800 Yavne, Israel,

A. Arsh, M. Klebanov and V. Lyubin

Physics Dept, Ben-Gurion University, 84105 Beer-Sheva, Israel,

ABSTRACT

We present fabrication of 3D photonic band gap woodpile crystals from photosensitive chalcogenide glass with the help of interference lithography and layer by layer construction. The alignment method is described, which is scalable to extremely small feature sizes required for photonic crystals in the visible region.

INTRODUCTION

Optical spectrum photonic band gap crystals require high refraction index materials and technology for 3D sub-micron structure fabrication. The most flexible approaches are based on semiconductor lithography processes^{1,2}. Most of them require sophisticated equipment and are confined by the current state of the art feature size limit. Thus there is demand for scalable lithography technologies and new types of materials, offering easy treatment and high refractive index.

Chalcogenide glasses are highly promising materials for photonic crystals³. Their refractive index varies from 2.5 to 3, together with transparency from 800nm to 12 micron. They are photosensitive, and can be used as positive or negative photoresists. In addition they are amorphous materials that can be deposited on almost any other material by vacuum vapor deposition at low temperature.

EXPERIMENTAL DETAILS

Maskless interference lithography can replace classical mask lithography in the case of photonic crystals due to their periodical structure. The required periodic pattern of illuminated and dark regions can be produced by interference of two or more coherent laser beams. The advantages of interference over mask lithography are higher resolution and deep focus. The latter allows the usage of interference lithography on curved surfaces.

The woodpile photonic band gap crystal can be considered as a multi layer construction, where each different layer is a diffraction grating (see Figure 1). Hence each layer can be produced by the interference pattern of only two beams. For formation of each layer, the first

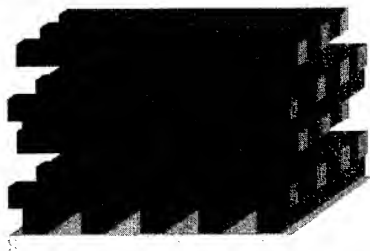


Figure 1: Woodpile Photonic Crystal

step is vacuum vapor deposition of thin chalcogenide film. The grating is obtained by using layer as a negative photoresist, after illumination and selective etching. The next step is the planarization of this grating by spin coating of Shipley photoresist, with subsequent thinning to the width of the grating. Afterwards the subsequent layers are formed in the same way. The final step is washing out of photoresist using a stripper.

All layers must be accurately aligned with each other, meaning their periods, directions and relative positions should be precisely fitted. Otherwise the desired optical properties will suffer. A technique for alignment between the two-beam interference pattern and the existing grating was developed⁴. During interference lithography the already produced layers of woodpile crystal act for incident light like an ordinary diffraction gratings, leading to several diffraction orders from each beam. The alignment can be completed in two steps, by observation of only two specific diffraction orders corresponding to different incident beams.

During the first step the period and direction of fringes are defined. When the period and direction of fringes correspond to those of the grating, some diffraction orders of different incident beams coincide. The coincidence of two beams can be verified by observation of their far field interference pattern.

The second step is fitting of the relative shift. It can be done by measurement of the total intensity of the two diffraction orders, chosen for step one. The intensity varies periodically with shift⁵.

RESULTS

Multi layer photonic crystals were constructed from AsSe (see Figure 2) and AsSeTe (see Figure 3) glasses. The third and the fourth layers of the 4-layer AsSeTe sample were successfully aligned. Shipley photoresist (planarization step) was washed out leaving dielectric/air crystals.

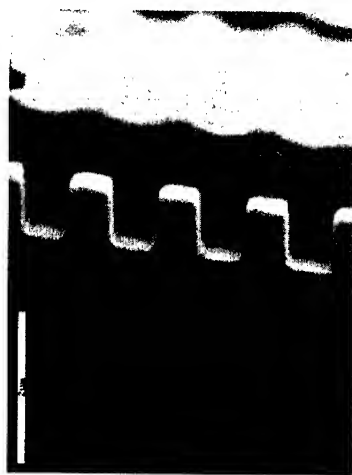


Figure 2: Two layers of woodpile photonic crystal made from AsSe chalcogenide glass and air. The period of the gratings is 1 μm .

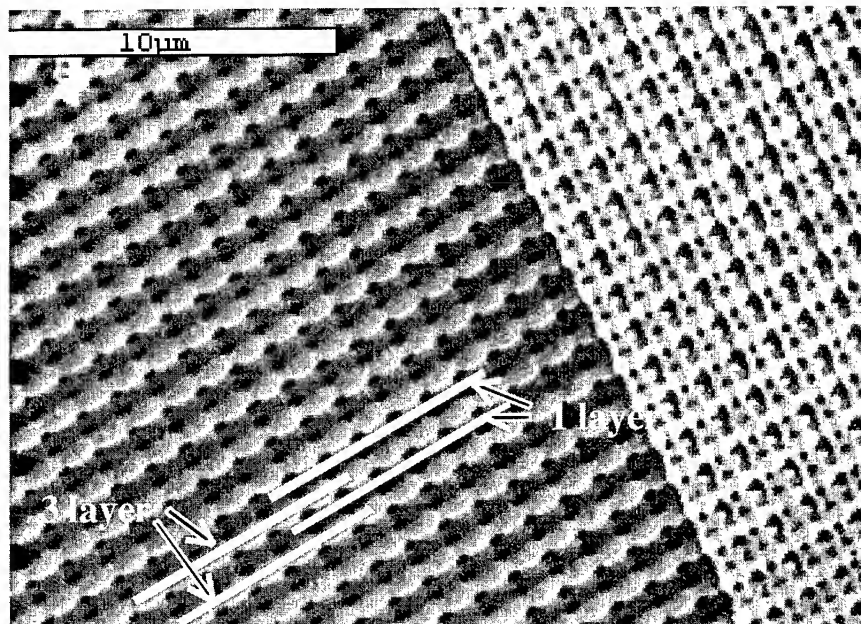


Figure 3: The 4 layer woodpile structure made from AsSeTe chalcogenide glass. The different layers are aligned with half period shift between the 1st and the 3rd layers.

DISCUSSION

The binary gratings can be obtained by interference lithography from chalcogenide glasses. There is threshold dose of illumination that converts chalcogenide glass to the insoluble state. This high sensitivity also leads to some structure fluctuations of the third and the fourth layers. The minute structure of the fourth layer can be clearly observed in Figure 3. These fluctuations are periodic due to the scattering of the incident laser beams on the previous layers. Therefore they do not contribute to the scattering losses, but definitely can change the optical properties of the crystal.

It is difficult to obtain gratings with feature size much less than half of a period. The sinusoidal laser illumination leads to more or less symmetrical patterns. However the numerical analysis of woodpile structure shows that even for 50% of the period feature size the full 3D gap can still be obtained (see Figure 4).

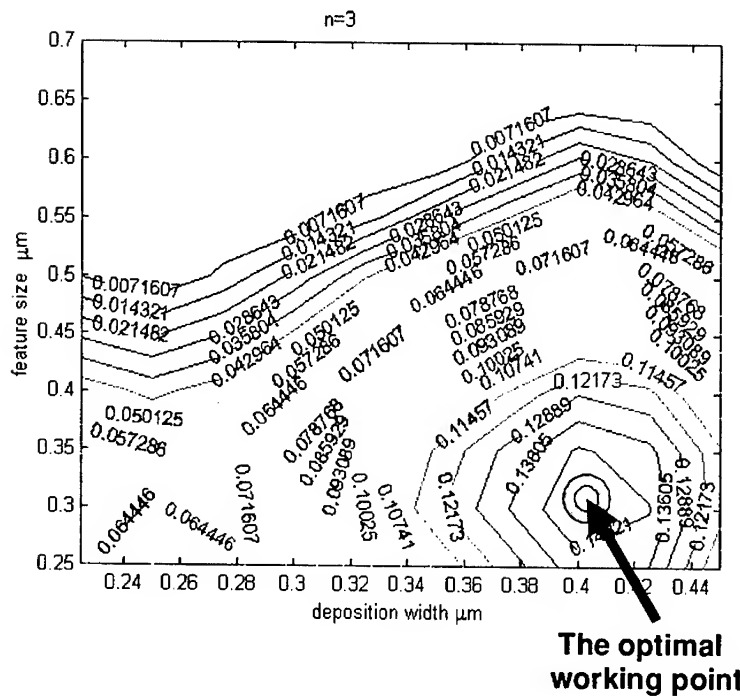


Figure 4: The gap to mid gap frequency ratio map vs. deposition width of single layer and feature size of the grating.

CONCLUSION

3D woodpile photonic crystals with 1 μm period were constructed from AsSe and AsSeTe chalcogenide glasses. The use of the interference lithography significantly simplifies the process of the fabrication. The required method of fringes alignment to some reference grating was developed.

1. S.Y. Lin, J.G. Fleming, D.L. Hetherington, B.K. Smith, R. Biswas, K.M. Ho, M.M. Sigalas, W. Zubrzycki, S.R. Kurtz and J. Blum, *Nature*, 394, 251, 1998
2. S. Noda, K. Tomoda, N. Yamamoto and A. Chutinan, *Science*, 289, 604, 2000
3. A. Feigel, Z. Kotler, B. Sfez, A. Arsh, M. Klebanov and V. Lyubin, *Appl. Phys. Lett.*, 77, 3221, 2000
4. A. Feigel, Z. Kotler and B. Sfez, submitted for publication
5. N. Yamamoto and S. Noda, *Jpn. J. Appl. Phys.*, 37, 3334, 1998

Simulations of Realizable Photonic Bandgap Structures with High Refractive Contrast

Bonnie Gersten and Jennifer Synowczynski

Weapons and Materials Research Directorate, Army Research Laboratory
Aberdeen Proving Grounds, MD 21005-5069

ABSTRACT

The transfer matrix method (TMM) software (Translight, A. Reynolds [1]) was used to evaluate the photonic band gap (PBG) properties of the periodic arrangement of high permittivity ferroelectric composite (40 wt% $\text{Ba}_{0.45}\text{Sr}_{0.55}\text{TiO}_3$ / 60 wt% MgO composite, $\epsilon_R = 80$, $\tan\delta = 0.0041$ at 10 GHz) in air (or Styrofoam, $\epsilon_R \sim 1$) matrix compared to a lower permittivity material (Al_2O_3 , $\epsilon_R = 11.54$, $\tan\delta = 0.00003$ at 10 GHz) in air. The periodic structures investigated included a one-dimensional (1D) stack and a three-dimensional (3D) face centered cubic (FCC) opal structure. The transmission spectrum was calculated for the normalized frequency for all incident angles for each structure. The results show that the bandgaps frequency increased and the bandgap width increased with increased permittivity. The effects of orientation of defects in the opal crystal were investigated. It was found by introducing defects propagation bands were introduced. It was concluded that a full PBG is possible with the high permittivity material.

INTRODUCTION

Photonic crystals (PCs) are periodic dielectric structures that exhibit frequency ranges over which an electromagnetic waves cannot propagate (called a bandgap). They are composites that are artificially engineered to have a periodic variation in the dielectric constant with a period that is on the order of the electromagnetic (EM) wavelength. When the phases have a strong refractive contrast (>3), a bandgap is created in the frequency spectrum due to the Bragg-like reflection at the interface between the two phases. PCs have many applications in optical devices including waveguides, lasers, light-emitting diodes, couplers, and filters [2]. They have also been used in microwave devices for high efficiency antenna substrates and reflectors [3] as well as waveguides, filters and delay lines. Typically, silicon has been the material of choice. It has both a high dielectric contrast ($\epsilon_R = 12.0:1$) and is compatible with fabrication methods in microelectronic and optical components. However, in this paper we propose using an even higher dielectric material, 40 wt% $\text{Ba}_{0.45}\text{Sr}_{0.55}\text{TiO}_3$ / 60 wt% MgO composite ($\epsilon_R = 80$, $\tan\delta = 0.0041$ at 10 GHz [4]). Because $\text{Ba}_{0.45}\text{Sr}_{0.55}\text{TiO}_3$ is also a ferroelectric material whose permittivity changes under an applied electric field, it is also possible to electronically tune the position and width of the bandgap.

In order to prepare a PC, the material must be periodic within less than 5% deviation. Therefore in order to obtain the correct length-scale for the desired bandgap, a model of the structure and simulation of the EM propagation must first be made. Many numerical approaches are described in the literature [5] including the plane wave method, transfer matrix method (TMM) and finite difference time domain (FDTD) method. The plane wave method was developed by expanding the EM fields as a sum of plane waves and recasting Maxwell's equations in the form of an eigenvalue problem to find the allowed eigen-frequencies. This can be represented by the equation (1):

$$-\nabla^2 E + \nabla(\nabla \cdot E) = \omega^2 \epsilon(r) E(r)$$

where E is the electric field, ω is the frequency, ϵ is the dielectric function and r is the coordinate. The disadvantages of this method are that it is inefficient in calculating complicated defects and requires significant computer time [5]. It is used to calculate the band diagrams, the field distributions and energy flows [5]. The FDTD method is the most widely used code [5] and requires less computer time [6]. However, it is inaccurate for modeling curvature and small objects. In the FDTD method, the wave propagating through the structure is found by integrating the discrete form of Maxwell's equations in the time domain. It is most often used for calculating reflection-transmission spectrums, band diagrams, field distributions, energy flows, and for coupling problems [5]. In TMM the wave-field is represented as points of real space lattice that relate the fields of one layer of the lattice to the next. The form of Maxwell's equation that this system takes on in three dimensions would be the following six equations (2-7) [7]:

$$\frac{E_y(r+a) - E_y(r)}{ia} - \frac{E_x(r+b) - E_x(r)}{ib} = \omega \mu(r) \mu_o H_z$$

$$\frac{E_z(r+b) - E_z(r)}{ib} - \frac{E_y(r+c) - E_y(r)}{ic} = \omega \mu(r) \mu_o H_x$$

$$\frac{E_x(r+c) - E_x(r)}{ic} - \frac{E_z(r+a) - E_z(r)}{ia} = \omega \mu(r) \mu_o H_y$$

$$\frac{H_z(r-b) - H_z(r)}{ib} + \frac{H_y(r-c) - H_y(r)}{ic} = -\omega \epsilon(r) \epsilon_o E_x$$

$$\frac{H_x(r-c) - H_x(r)}{ic} + \frac{H_z(r-a) - H_z(r)}{ia} = -\omega \epsilon(r) \epsilon_o E_y$$

$$\frac{H_y(r-a) - H_y(r)}{ia} + \frac{H_x(r-b) - H_x(r)}{ib} = -\omega \epsilon(r) \epsilon_o E_z$$

where μ is the permeability, a, b, c are the displacement through a distance along the x, y, z axis, respectively. TMM is most often used to calculate the reflection-transmission spectrums, and the field distributions [5].

The objective of this research was to model the PC of a 1D Bragg stack and a 3D opal using TMM comparing a high permittivity material (40 wt% $\text{Ba}_{0.45}\text{Sr}_{0.55}\text{TiO}_3$ / 60 wt% MgO composite, $\epsilon_R = 80$, $\tan\delta = 0.0041$ at 10 GHz) in air (or Styrofoam, $\epsilon_R \sim 1$) matrix compared to a lower permittivity material (Al_2O_3 , $\epsilon_R = 11.54$, $\tan\delta = 0.00003$ at 10 GHz) in air and to evaluate the effects of line defects and orientation on the propagation.

MODELING

A transfer matrix method software package called Translight [1] was used to model the PBG structures. The structures investigated were a 1D Chigrin's Stack [8] and 3D $\langle 111 \rangle$ opal [9]. The permittivities investigated were $\epsilon_R = 80, 11.54$ and $\tan\delta = 0.0041, 0.00003$, respectively, corresponding to the materials of ferroelectric 40 wt% $\text{Ba}_{0.45}\text{Sr}_{0.55}\text{TiO}_3$ / 60 wt% MgO composite

and Al_2O_3 , respectively. For both structures a lattice constant of 0.003 m was used to calculate the transmission through the structure as a function of incident angle from 0 to 90 degrees and normalized frequency, fa/c , from 0.01 to 1.0, where f is the frequency, a is the lattice constant and c is the speed of light. The results were displayed on a contour plot with transmission in gray scale. Positive incident angles correspond to TM polarized waves while the negative values correspond to TE polarized waves unless otherwise reported.

The Chigrin's stack consisted of alternating layers of air (0.5 – 0.25 thick) and dielectric (0.75 thick) see, Figure 1a. The stacks were placed in x axis orientation relative to the incident beam. The opal structure PBG was investigated for filling factors 0.25, 0.5 and 0.74. For these simulations there were twelve stacks of a group of three unit cells with twenty-seven atom spheres each (cf. Figure 1b). Because the opal cell was symmetric along x, y, and z only the affect of orientation with a defect in the structure was considered. A defect was placed on each of the unit cells at the half-way point by removing the row of atoms along the y axis.



Figure 1: PBG Structures a. Chigrin's Stack, b. Opal Unit Cell.

RESULTS AND DISCUSSION

The effect of permittivity on the Chigrin's Stack are compared for $\epsilon=80$ and $\epsilon=11.54$ in Figures 2a and 2b, respectively. As shown in the figures, as the permittivity increases the number of bandgaps increases and the bandgap width increases.

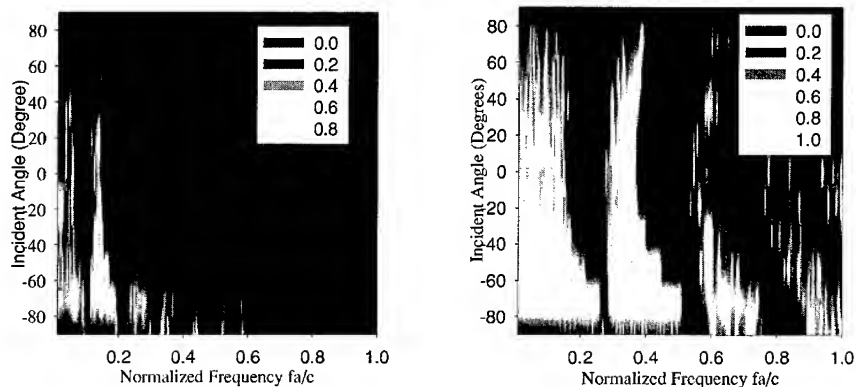


Figure 2. Chigrin's Stack with x Axis Orientation and 0.5 stack size and a. $\epsilon=80$ and b. $\epsilon=11.54$.

Similarly, the effect of increasing the stack size in a Chigrin's stack from 0.5 (cf. Figure 2a) to 0.75 (cf. Figure 3) shows an increase in the number of bandgaps as well as an increase in the bandgap width.

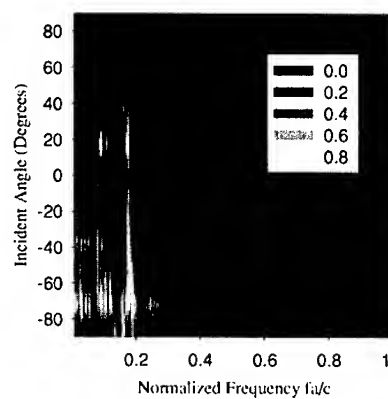


Figure 3. Chigrin's Stack Results with a Block Size of 0.75 and $\epsilon=80$ and x Axis Orientation.

A comparison of the permittivity on the PBG of the opal structure with a defect is shown in Figures 4a and 4b. Without the defect the opal structure does not have the extra propagation bands at higher frequency (cf., enclosed circle of Figure 4a). These propagation bands can be used to trap and guide the electromagnetic radiation.

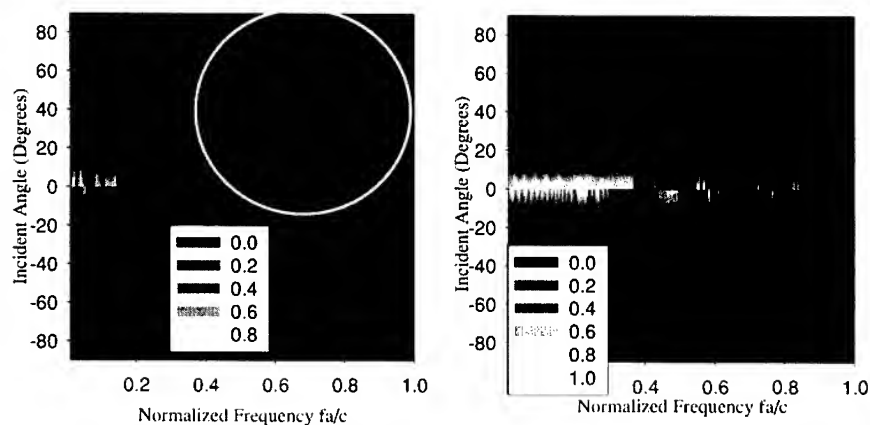


Figure 4. Opal structure PBG with 0.74 filling fractions a. $\epsilon=80$ and b. $\epsilon=11.54$.

The effect of increasing the filling fraction in the opal structure is shown in Figure 5. As the filling fraction decreases the number of bandgaps increases and the bandgap width increases.

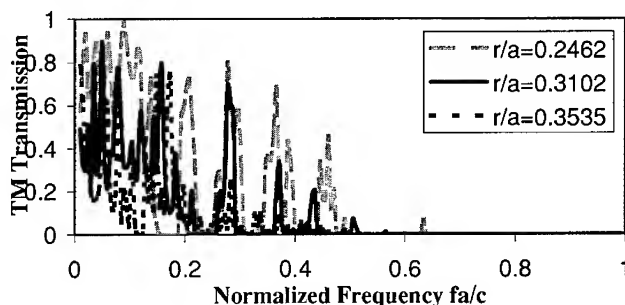


Figure 5. The effect of filling fraction on the PBG of the opal with $\epsilon=80$ and no defect.

SUMMARY

A TMM software package was used to model the PBG structures of a Chigrin's Stack and $\langle 111 \rangle$ opal. The permittivities investigated were $\epsilon_R=80$ and 11.54 and $\tan\delta = 0.0041$ and 0.00003, respectively, corresponding to the materials of ferroelectric 40 wt% $\text{Ba}_{0.45}\text{Sr}_{0.55}\text{TiO}_3$ /60 wt% MgO composite and Al_2O_3 , respectively. Calculations of the transmission through the structure as a function of incident angle and normalized frequency were performed. It was found that the bandgaps increased and the bandgap width increased with increased permittivity. The effects of orientation of defects in the crystal were investigated. It was found by introducing defects propagation bands were introduced. It was concluded that a full PBG is possible with the high permittivity material.

ACKNOWLEDGEMENTS

The authors would like to acknowledge the helpful technical discussions of Professor Azriel Genack, Bing Hue from Queens College, CUNY; Professor Dennis Prather of the University of Delaware and Dr. Mihail Sigalas of Agilent Laboratory.

REFERENCES

1. A. Reynolds, *The University Court of the University of Glasgow*, Translight (2000).
2. J. D. Joannopoulos, P.R. Villeneuve, and S. Fan, *Nature*, **386**, 14 (1997).
3. D. Sievenpiper, L. Zhang, E. Yablonovitch, IEEE MTT-S Digest **TH2C-1**, 1529 (1999).

4. J. Synowczynski et al, *Integrated Ferroelectrics*, **22**, 861 (1998).
5. A. Bjarklev, W. Bogaerts, T. Fields, D. Gallagher, M. Midrio, A. Lavrinenko, D. Mogilevtsev, T. Sondergaard, D. Taillaert, and B. Tromborg, *Report on Picco deliverable D8 for WP4* (2000).
6. J. Ward and J.B. Pendry, *Computer Physics Communications*, **128** [3], 590 (2000).
7. J. B. Pendry, *J. Phys. Condensed Matter*, **8**, 1089 (1996).
8. D. N. Chigrin, A. V. Lavrinenko, D. A. Yarotsky, S. V. Gaponenko, *J. Lightwave Tech.*, **17** [11], (1999).
9. A. Reynolds, F. Lopez-Tejiera, D. Cassagne, F.J. Garcia-Vidal, C. Jouanin, J. Sanchez-Dehesa, *Phys. Rev. B*, **60** [16], 11422, (1999).

Optical study of 2D photonic crystals in an InP/GaInAsP slab waveguide structure

Rolando Ferrini¹, David Leuenberger¹, Mikael Mulot², Min Qiu², Jürgen Moosburger³, Martin Kamp³, Alfred Forchel³, Srinivasan Anand², and Romuald Houdré¹

¹Institut de Micro et Opto-électronique, Ecole Polytechnique Fédérale de Lausanne, CH-1015 Lausanne, Switzerland.

²Department of Microelectronics and Information Technology, Royal Institute of Technology, Electrum 229, S-16440 Kista, Sweden.

³Technische Physik, University of Würzburg, Am Hubland, D-97074 Würzburg, Germany.

ABSTRACT

We report on the optical properties of two dimensional (2D) photonic crystals (PCs) deeply etched in an InP/GaInAsP step-index waveguide. Transmission (T) measurements through simple PC slabs and through one-dimensional (1D) Fabry-Pérot (FP) cavities between PC mirrors are reported and compared to theory. A 2D finite difference time-domain (FDTD) method combined to a phenomenological out-of-plane loss model is used to assess different loss contributions. The PC optical properties are deduced from the FP peak analysis. The origin of the high T level observed inside the stopgap is investigated.

INTRODUCTION

In photonic crystal (PC) structures the periodic arrangement of different elements with strong dielectric contrast affects the properties of photons forbidding light propagation along specific directions within relatively large energy bands known as *photonic band-gaps* (PBGs) [1,2]. In the last few years it has been proved that, although an omnidirectional PBG is only possible in a three-dimensional (3D) PC, a two-dimensional (2D) PC combined to a vertical step-index waveguide offers enough light control for integrated optics applications [3]. The potentials of this approach have been successfully demonstrated both in GaAs-based structures ($\lambda \approx 1.0 \mu\text{m}$) [3] and in InP-based systems at telecommunication application wavelengths ($\lambda \approx 1.5 \mu\text{m}$) [4]. In this paper we describe the optical characterization of *quasi*-2D PCs deeply etched into an InP/GaInAsP slab waveguide. The internal light source (ILS) technique is used to measure the transmission (T) spectra through simple PC slabs and one-dimensional (1D) Fabry-Pérot (FP) cavities formed between two PC mirrors. A 2D finite difference time-domain (FDTD) method is used to best fit the experimental data. The exact amount of out-of-plane losses is assessed and the hole depth/shape contributions are analyzed. The optical properties of the PC structures are determined and the origin of the high T level detected inside the stopgap is discussed.

EXPERIMENT

Quasi-2D PCs consisting of a triangular lattice of air holes were fabricated on nominally undoped GaInAsP/InP heterostructures grown by metal organic vapor phase epitaxy (MOVPE) on *n*-InP substrates (see figure 1(a)). Moderate filling factor values ($f \approx 0.30$) were chosen in order to minimize out-of-plane losses [3,4]. Such low f values result in a full gap only in the

transverse electric (TE) polarization direction. The PC structures were etched normally to an InP/GaInAsP/InP slab waveguide containing a built-in light source. The waveguide core is a 434 nm-thick $\text{Ga}_{0.24}\text{In}_{0.76}\text{As}_{0.52}\text{P}_{0.48}$ layer lattice matched to InP and sandwiched between a 200 nm-thick InP cap layer and a 600 nm-thick InP buffer layer. In the spectral region of interest (*i.e.*, $\lambda \approx 1550$ nm) the values $n_{\text{core}} = 3.35$ and $n_{\text{clad}} = 3.17$ are assumed for the refractive index of GaInAsP and InP, respectively. The resulting structure is a multimode waveguide with a fundamental guided TE mode corresponding to an effective index $n_{\text{eff}} = 3.24$ [4]. The light source consists of two different GaInAsP strain-compensated quantum well (QW) packages separated by a 30 nm spacer and located approximately in the middle of the guiding structure between two 181 nm-thick barrier layers. Due to the superimposition of the two QW signals ($\lambda_1 = 1.47 \mu\text{m}$ and $\lambda_2 = 1.55 \mu\text{m}$) a 100 nm-wide PL peak centered at 1500 nm is obtained [4].

Electron beam (e-beam) lithography was used to define the PC patterns, while dry etching techniques were applied to transfer the pattern into the semiconductor heterostructure. In order to form a durable SiO_2 etch mask for the subsequent etch process the procedure described in [4,5] was adopted. Ar/ Cl_2 chemically assisted ion beam etching (CAIBE) [4] and Cl_2 /Ar-based electron cyclotron resonance-RIE (ECR-RIE) [5] were used to pattern sample #1 and sample #2, respectively. As sketched in figure 1(a), the obtained hole shape is conical with nearly vertical walls close to the surface and a strongly tapered bottom. Figures 1(b) and (c) show the cross-section view scanning electron microscopy (SEM) micrographs of two PC test structures for sample #1 and sample #2, respectively. In sample #1 the holes have oblique walls already inside the waveguide core (z_2) and a slight bending towards the hole bottom is observed. Nevertheless, the hole pattern is "ordered": no dispersion in the hole depth $z = z_2 + \Delta z$ is found when the hole diameter (D) is kept constant. z values of $2.55 \mu\text{m}$ are obtained for the larger holes [4]. On the contrary, in sample #2 fluctuations appear in the hole depth yielding $\langle z \rangle \geq 3 \mu\text{m}$, while no bending is present and the holes have straight walls inside z_2 .

The ILS technique described in [4] was used to characterize the PC optical properties.

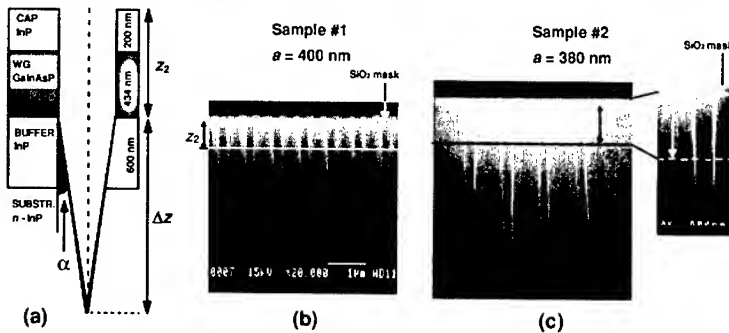


Figure 1. (a) Sketch of the InP/GaInAsP waveguide (WG) heterostructure. The hole shape model used to calculate the loss parameter value ϵ'' is illustrated. z_2 is the thickness of the cap + WG layer where the holes are assumed to be cylindrical, while Δz is the cone depth. The cone half angle α is also evidenced. (b) and (c): edge view SEM micrographs of test photonic crystal (PC) structures for sample #1 and sample #2, respectively. The images were taken before the removal of the SiO_2 mask. In the inset of figure (c) the cylindrical shape of sample #2 holes inside z_2 is evidenced.

The PL excited inside the GaInAsP QWs is used as a built-in probe beam. Part of the PL signal propagates parallel to the surface as a guided mode and interacts with the PC structure. The absolute PC T spectrum is obtained normalizing the spectrum detected after transmission through the PC structure with respect to the spectrum collected in a non-patterned region of the sample. Details on the experimental set-up and on the measurement schemes adopted for simple PC slabs and 1D FP cavities are given in [4]. Here we remind that, since ILS measurements on a single PC structure yield the T spectrum only in a narrow interval (≈ 100 nm), the "lithographic tuning" approach has to be applied in order to determine the PC optical properties within a wide spectral range. As the QW emission wavelength is fixed, the scaling property of PCs [1] is used and PC structures with different periods a are measured. If f is kept constant the whole PBG can be explored as a function of the reduced frequency $u = a / \lambda$ [3,4].

RESULTS AND DISCUSSION

T spectra through PC slabs along both ΓM and ΓK orientations and for TE polarization are shown in figures 2 (a) and (b) for sample #1 (10 rows thick slab) and #2 (8 rows), respectively. The layout of simple PC slabs is shown in figure 2 (c). Both ΓM and ΓK oriented structures were fabricated with periods a ranging from 240 to 500 nm for sample #1 ($\Delta a = 20$ nm) and from 240 to 640 nm for sample #2 ($\Delta a = 20$ nm). Well-defined PBGs appear in each spectrum with steep dielectric band edges at $u = 0.19$ and 0.22 for ΓM and ΓK orientations, respectively. On the other hand, due to the strong influence of out-of-plane losses on T at the air band edge [3], smooth T bands appear at $u \approx 0.28$ and 0.30 for ΓM and ΓK orientations, respectively. T values between 80% and 90% are reached for $u < 0.20$, while $T \leq 40\%$ for $u \geq 0.30$. Finally, an average $T \approx 3 - 5\%$ is observed inside the PBG for both samples.

The experimental T spectra are compared to theoretical spectra calculated with a 2D FDTD model [6]. The effect of the vertical confinement on the light propagating through the PC slabs

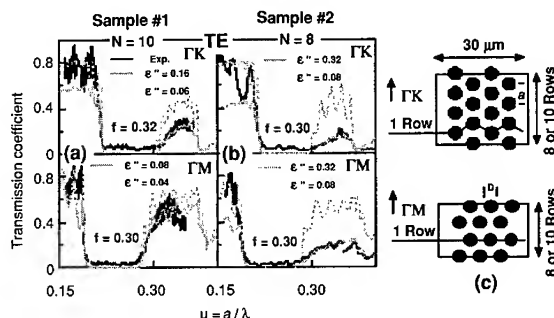


Figure 2. TE transmission spectra through ΓM and ΓK oriented photonic crystal (PC) slabs for (a) sample #1 (10 rows) and (b) sample #2 (8 rows), respectively. Experimental spectra (black lines) are compared with 2D finite difference time-domain (FDTD) calculated spectra (gray lines). (c) Sketch of the typical layout of simple PC structures along ΓM and ΓK orientations. Each slab is characterized by the period a (or hole diameter D) value. Hairlines show the single "atomic" plane for both orientations.

was taken into account assuming $n \equiv n_{eff} = 3.24$ for the dielectric matrix. Out-of-plane losses were cast into the 2D calculation by introducing the imaginary ϵ'' as a phenomenological loss parameter [4,7]. f and ϵ'' were chosen as free parameters of the fit. The best-fitted curves are reported in figures 2(a) and (b), while in table I the obtained f and ϵ'' values are listed. While for sample #2 both ΓM and ΓK spectra are fitted assuming the same f value, for sample #1 $f(\Gamma K) > f(\Gamma M)$. The latter discrepancy is due to the hole squeezing along the ΓK direction originating in the e-beam lithography of sample #1 [4]. Different ϵ'' values have to be used to fit either the dielectric or the air T band edge in both samples. As shown in [4], $\epsilon'' \propto (u^2 \times f)$: if f is constant while increasing u , higher ϵ'' values have to be introduced. Moreover, when u is fixed, $f(\Gamma K) > f(\Gamma M)$ implies $\epsilon''(\Gamma K) > \epsilon''(\Gamma M)$. Finally, the sample #2 ϵ'' values are always higher than the corresponding values of sample #1. The different out-of-plane loss level in the two samples has to be ascribed to differences in the hole morphology and in the PC pattern disorder (see below).

The ϵ'' values obtained from the best fit of the air band edge were analyzed in the framework of a loss model where the total loss parameter is expressed as $\epsilon'' = \epsilon''_{int} + \epsilon''_{hole}$ [8,9]. ϵ''_{hole} contains contributions from the finite etch depth and from the conical hole shape, while ϵ''_{int} accounts for the intrinsic losses corresponding to the ideal case of infinitely deep holes. Since for these InP-based PC structures $\epsilon''_{int} = 0.01 - 0.02$ [4], the values $\epsilon''_{hole}(\#1) = 0.105 \pm 0.045$ and $\epsilon''_{hole}(\#2) = 0.305 \pm 0.005$ derive for sample #1 and #2, respectively. Following the procedure illustrated in [9] and adopting the model hole shape sketched in figure 1(a), the theoretical value ϵ''_{hole} can be calculated. If the exponential decaying field profile $\zeta(z) = A \exp(Kz)$ is assumed in the substrate, ϵ''_{hole} is a function of K and of the cone slope α in the first $L_{decay} = K^{-1}$ [9]. From the SEM micrograph analysis $\alpha \approx 2.5^\circ \pm 0.5^\circ$ for both samples and $\epsilon''_{hole} \approx 0.30$ is obtained. While the latter value perfectly agrees with $\epsilon''_{hole}(\#2)$, it is 2 – 4 times higher than $\epsilon''_{hole}(\#1)$. As mentioned in [4], the discrepancy between the calculated and the experimental $\epsilon''_{hole}(\#1)$ values originates from the complex hole geometrical shape (e.g., hole bending, oblique walls inside the core) which does not fit the assumed model shape. On the contrary, when holes keep straight walls inside the cap + waveguide layer (z_2), the different loss contributions can be deduced from the ϵ'' experimental values and ϵ''_{hole} can be easily modeled. Extrapolating from sample #2 data, two perspectives emerge which can be considered realistic for the actual etching techniques. First, it is found that the minimum loss limit ϵ''_{int} could be reached for $\alpha \leq 0.5^\circ$, i.e. for holes with almost straight walls in some L_{decay} 's inside the substrate. On the other hand, a less critical reduction in the cone slope would make possible to get a sufficiently low loss level for good performance PC applications (e.g., $\epsilon'' \leq 0.1$ for $\alpha \leq 1.5^\circ$) [8].

In order to investigate the PC optical properties inside the PBG, 1D FP cavities were fabricated for both samples using 4 rows thick ΓM -oriented PC-based mirrors ($a = 300 - 480$ nm

Table I. Photonic crystal (PC) slabs : f and ϵ'' values (FDTD fit). 1D Fabry-Pérot (FP) cavities : optical properties of a single 4 row PC mirror and cavity parameter values (Airy's function fit).

Sample	PC slabs - FDTD fit					1D - FP Cavities - Airy's function fit					
	N		f	ϵ'' (Diel. B.)	ϵ'' (Air B.)	T (%)	R (%)	L (%)	L_p/a	m	Q
# 1	10	ΓM	0.30	0.04	0.08	$a = 340$ nm ; $W/a = 1.9$					
		ΓK	0.32	0.06	0.16	14	64	22	0.36	4	28
# 2	8	ΓM	0.30	0.08	0.32	$a = 340$ nm ; $W/a = 2.0$					
		ΓK	0.30	0.08	0.32	10	80	10	0.40	4	56

and $\Delta a = 20$ nm) separated by a spacer with a normalized width $W/a = 1.7 - 2.2$ [4]. A typical T spectrum through a 1D FP cavity is shown in figure 3(a) for sample #2 ($W/a = 2.0$). The cavity layout is sketched in figure 3(b). The two peaks appearing in the T spectrum at $u = 0.22$ and $u = 0.29$ are due to first and second-order FP resonances, respectively. The experimental spectrum is compared to the calculated 2D-FDTD T spectrum. The ΓM values derived from the best fit of simple PC slab air band edges were adopted for f and ϵ'' , while the value $W/a = 1.97$ was assumed for the cavity width. As for simple PC slabs, FDTD calculated spectra do not agree with the experimental data inside the PBG: the theoretical T value inside the gap ($T \approx 10^{-2} - 10^{-4} \%$) is higher than the detected value ($T \approx 3 - 5 \%$). While the experimental FP peaks are located at energies consistent with the calculated values, they show higher peak T and lower quality factors Q than the simulated peaks. As shown in the inset of figure 3(a) the Airy's formula for planar resonators is used to fit the first-order FP resonances [4] yielding the optical properties of a single 4 row PC mirror (see table I).

The comparison between the separate analysis of simple PC slab and 1D FP cavity spectra for both samples completes the picture given in [4]. While the fit of the T air band edges yields $\epsilon''(\#2) > \epsilon''(\#1)$, from the best fit of FP resonances inside the PBG the total loss value $L(\#2)$ is found to be lower than the corresponding $L(\#1)$ value. Moreover, in sample #2 the T level inside the stopgap decreases while reflectivity (R) increases to 80% giving $Q(\#2) = 2 \times Q(\#1)$. In order to explain this apparent discrepancy we remind that two different effects may affect light propagation through a PC structure [4]. First, the finite hole depth contributes to increase out-of-plane scattering. On the other hand, when entering the PC, the hole pattern is felt as a low refractive index contrast region and light is pushed below the guiding layer (*modal conversion*). When energies outside the stopgap are considered, light propagation is allowed and Bloch modes propagate into the PC. As pointed out in [10], Bloch modes are strongly influenced by defects and/or disorder where out-of-plane scattering can occur. Therefore, due to dispersion in the cone depth Δz (see figure 1(c)) which contributes to disorder, out-of-plane losses are found to be higher in sample #2 than in sample #1. On the contrary, the second effect becomes predominant inside the stopgap. Light propagation is forbidden and "evanescent" modes penetrate the PC.

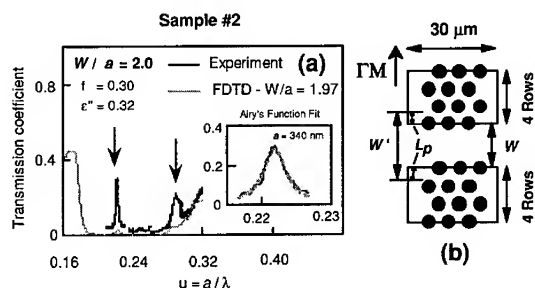


Figure 3. (a) Transmission spectrum through a 1D Fabry-Pérot (FP) cavity between two ΓM oriented 4 rows photonic crystal (PC) mirrors separated by a spacer W . Arrows indicate transmission peaks related to first and second order FP resonances. Experimental spectra (black lines) are compared with 2D finite difference time-domain (FDTD) calculated spectra (gray lines). The Airy's function best-fit (gray dashed line) of the first order peak for $a = 340$ nm is shown in the inset. (b) Sketch of the typical layout for 1D FP cavity. The actual cavity width W' taking into account the finite penetration depth L_p of the field inside the mirrors is shown.

While these modes are insensitive to defects and disorder, they are strongly influenced by the *modal conversion* and light propagation is affected by the single hole shape parameters (*e.g.*, the hole depth). Thus, since $\langle z \rangle (\#2) > z (\#1)$, inside the stopgap light transmission is lowered in sample #2 with respect to sample #1, while R and cavity Q values result to be improved.

CONCLUSIONS

We have reported on the optical properties of 2D PCs etched in InP/GaInAsP slab waveguide structures. The combination between structural analysis and optical characterization by ILS experiments makes possible to evaluate which improvements are necessary in the fabrication process. Two different regimes are identified for light propagation inside the PC structure. When light with energies outside the PBG is considered, out-of-plane losses are the limiting factor for PC performances. Improvements in the hole shape and in the ordering of the PC pattern should allow one to lower the scattering towards the substrate. On the other hand, when entering the stopgap, the hole "physical" parameters (*e.g.*, the hole depth) strongly affect the PC optical properties.

ACKNOWLEDGEMENTS

This work was supported by the European Union in the framework of the IST project PCIC (Contract n. 1999-11239).

REFERENCES

1. J.D. Joannopoulos, R.D. Meade, and J.N. Winn, *Molding the Flow of Light* (Princeton University Press, Princeton NJ, 1995).
2. E. Yablonovitch, Phys. Rev. Lett. **58**, 2059 (1987).
3. H. Benisty, C. Weisbuch, D. Labilloy, M. Rattier, C.J.M. Smith, T.F. Krauss, R.M. De La Rue, R. Houdré, U. Oesterle, and D. Cassagne, IEEE J. Lightwave Technol. **17**, 2063 (1999).
4. R. Ferrini, D. Leuenberger, M. Mulot, M. Qiu, J. Moosburger, M. Kamp, A. Forchel, S. Anand, and R. Houdré, IEEE J. Quantum Electron., submitted.
5. J. Moosburger, M. Kamp, A. Forchel, R. Ferrini, D. Leuenberger, R. Houdré, S. Anand, and J. Berggren, Nanotechnology, submitted.
6. M. Qiu, and S. He, Phys. Rev. B **61**, 12871(2000); J. Appl. Phys. **87**, 8268 (2000); Phys. Lett. A **266**, 425 (2000); *ibid.* **278**, 348 (2001).
7. H. Benisty, D. Labilloy, C. Weisbuch, C.J.M. Smith, T.F. Krauss, D. Cassagne, A. Béraud, and C. Jouanin, Appl. Phys. Lett. **76**, 532 (2000).
8. H. Benisty, Ph. Lalanne, S. Olivier, M. Rattier, C. Weisbuch, C.J.M. Smith, T.F. Krauss, C. Jouanin, and D. Cassagne, Opt. Quant. Electron., to be published.
9. H. Benisty (private communication)
10. W. Bogacrs, P. Bienstman, D. Taillaert, R. Baets, and D. De Zutter, IEEE Photonic Tech. L. **13**, 565 (2001).

Fabrication of Microstructures for Microphotonic Circuit

Subhasish Chakraborty, D G Hasko and R J Mears
University of Cambridge, Department of Engineering, Trumpington Street
Cambridge CB2 1PZ

ABSTRACT

We describe fabrication of sub-micron photonic bandgap structures on Si/SiO₂ optical waveguide, which could be used at $\lambda=1.54\mu\text{m}$.

INTRODUCTION

Control of the propagation of light using the photonic band gap (PBG) effect in photonic devices is the subject of intense international effort [1-6]. PBG materials are optical analogs of semiconductors. Main drive is towards making structures that modulate free photon dispersion as much as the same way as semiconductor crystal does for electrons. A high dielectric contrast material system is a fundamental requirement for the existence of a PBG. Silicon microphotonics, which uses Si over SiO₂ system, provides a large index difference ($\Delta n \approx 2.0 @ 1.54\mu\text{m}$) between the core and the cladding of the guide. Because of the high confinement of the optical wave, the waveguide cross-section has been miniaturised. Strip waveguides with holes of 200nm diameter have been fabricated. The cross-section of the strip waveguide is $0.26 \times 0.5 \mu\text{m}$. We have addressed some of the important issues regarding fabrication. On the simulation front, we have used commercially available software Fimmprop3D for 2D simulation of the device. Figure 1(a) and (b) shows the simulation results. Actual structure is shown in the inset of Figure 1(b).

High index contrast structures introduce a process problem because performance is limited by scattering loss from surface roughness. One important challenge towards realizing silicon microphotonics lies in making optically smooth structure to keep the scattering loss as low as possible. The dominant source of loss is the sidewall roughness scattering [7]. The increase is attributed to sidewall roughness created during the waveguide patterning process involving lithography and RIE. We have proposed combined chlorine-fluorine based plasma as a reactive ion-etching recipe for silicon microphotonics. Extremely smooth photonic structures of feature size as small as $0.1\mu\text{m}$ have been made.

FABRICATION

PBG effect devices have been made using high-resolution lithographic and pattern transfer processes, which include electron beam lithography and reactive-ion-etching. The first step is the realisation of the plasma etch mask. The poor etch resistance of PMMA is serious limiting factor for pattern transfer. The problem has been overcome by using Al as a metal etch mask.

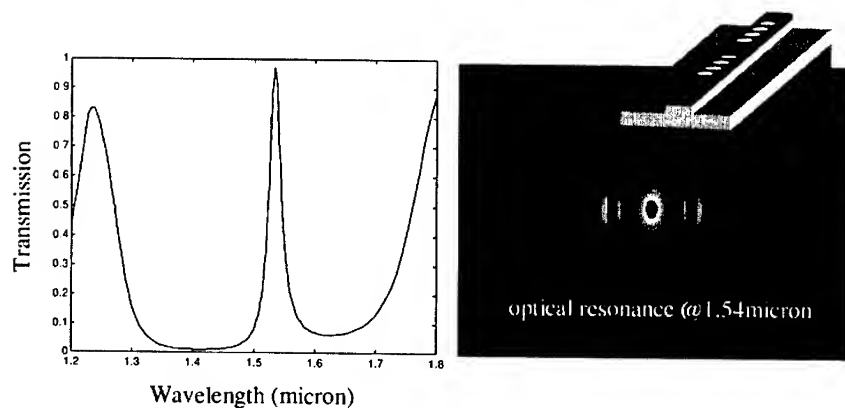


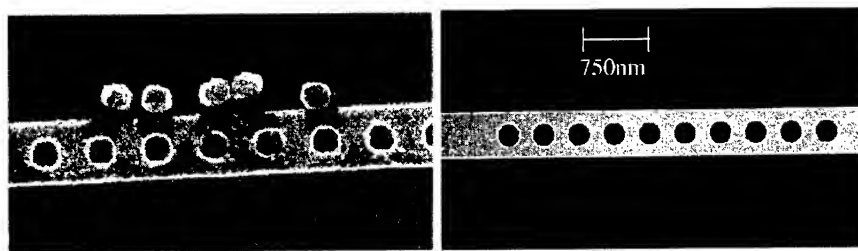
Figure 1. Simulation shows transmission for the waveguide microcavity structure designed for a resonance wavelength at 1.54 micron

In this work we have used Unibond silicon-on-insulator wafer (obtained from SOITEC, France), consisted of $0.26\mu\text{m}$ crystalline silicon layer on $1.0\mu\text{m}$ SiO_2 cladding layer on silicon substrate. Direct-write electron-beam lithography with acceleration voltage of 60 kV, and 12nm spot size is used to generate the pattern in polymethylmethacrylate (PMMA) that has been spun at 7000 rpm and baked at 180°C on to the silicon substrate. The PMMA thickness is typically 500nm. The exposed chip was then developed in 3:1 Isopropyl Alcohol and Methyl-Iso-Butyl-Ketone (IPA : MIBK=3:1) for 45 seconds at 25°C . The chip then undergoes 30seconds of oxygen plasma cleaning to remove any resist debris from exposed area.

Following the development a thin layer $\sim 70\text{nm}$ Al has been evaporated, at 0.001mTorr pressure. Soaking the sample in acetone and dissolving the PMMA then lifts off Al. Normally the sample is left in Acetone overnight. Ultrasonic agitation for approximately 10-15 seconds is also required to remove the circular Al films. Successful lift-off results an Al mask directly on to the substrate. SEM image of a typical sample after lift-off is shown in Figure 2

All RIE was performed on a STS 320PC parallel plate etcher operating at 13.56MHz. There are several plasma etching related considerations that can affect device performance. These include etch rates of Si and SiO_2 and their selectivity over Al, directionality of etching and surface damage.

Various gas combinations including CF_4/O_2 , $\text{CF}_4/\text{O}_2/\text{CHF}_3$, $\text{SiCl}_4/\text{CF}_4$ have been investigated to etch Si and SiO_2 . Plasma of CF_4 with O_2 etches silicon at a rate 200nm/minute. Etch rate of oxide is rather slow. CHF_3 could be used to etch oxide. Etching oxide with CHF_3 has a profound influence on silicon sidewall. In fact one can move from isotropic to anisotropic etch by controlling the flow rate of CHF_3 . Figure 2 (a) shows the undercut of silicon layer of SOI substrate during oxide etching.



(a) (b)
Figure 2. (a) Lift-off without any agitation, (b) Lift-off with 15 seconds of ultrasonic agitation

The $\text{CF}_4/\text{O}_2/\text{CHF}_3$ plasma is of particular interest. Directional etching has been done with 5 sccm CHF_3 , 8 sccm CF_4 , 4 sccm O_2 , at 2mTorr, 400W. These conditions were optimized to give a highly directional etch for silicon and oxide with an approximate etch rate of 150nm/minute. In such a plasma each gas has a specific influence to control the etch profile. CF_4 produces the F^* radicals for the chemical etching of the silicon forming the volatile SiF_4 . O_2 gives O^* radicals, which passivates the silicon surface with SiO_xF_y and CHF_3 produces CF_x^+ ions that removes SiO_xF_y layer by forming the volatile CO_xF_y at the bottom of the etched holes [8].

As far as directionality and etch rate is concerned $\text{SiCl}_4/\text{CF}_4$ plasma etching is another possible optimum etching process. It is quite well known to use SiCl_4 plasma for etching Si to achieve anisotropic silicon nanostructures. [9] Physical etching nature of chlorine-based plasma creates rough surface, sometimes-called “grass” effect, is unacceptable for photonic wire fabrication. Addition of CF_4 in the SiCl_4 plasma was found to reduce surface roughness or “grass” effect [10]. It is known that fluorine based etching of silicon is isotropic, while chlorine-based plasmas enable anisotropic etching because of sidewall passivation. These facts suggest that a chlorine-based plasma mixed with fluorine atoms could be used to form a user defined optimized profile. CF_4 produces F^* radicals as the dominant etching species. When clean silicon is exposed to atomic fluorine, it soon acquires “fluorinated skin”. F atoms, after penetrating the fluorinated skin, attack Si-Si bonds, resulting in stable volatile end product SiF_4 . SiCl_x from SiCl_4 induces inhibitor type anisotropy when etching silicon [9].

A mixture of 20sccm SiCl_4 and 20sccm CF_4 have been used to perform etching at a pressure 20mTorr at 300W for 3minute 30 seconds on the SOI substrates.

Extremely smooth waveguide with holes of extremely good circularity have been found, which clearly put this etching recipe as a strong candidate for silicon microphotronics fabrication. The $\text{CF}_4/\text{SiCl}_4$ system is one member of a family of etching mixtures that can be used to etch silicon anisotropically via the inhibitor mechanism. Another possible combination would be $\text{SiCl}_4/\text{CHF}_3$ at 10mTorr, 300W. Manipulation of the feed mixture composition can be used to adjust the profile contour and degree of anisotropy.

Following the etching, the Al is removed with a wet etch. Optical facet production is the next important step for the strip waveguide. Unfortunately silicon doesn't cleave easily. Yu *et al* [11] have successfully cleaved (100) silicon by thinning the silicon substrate to 90 μm

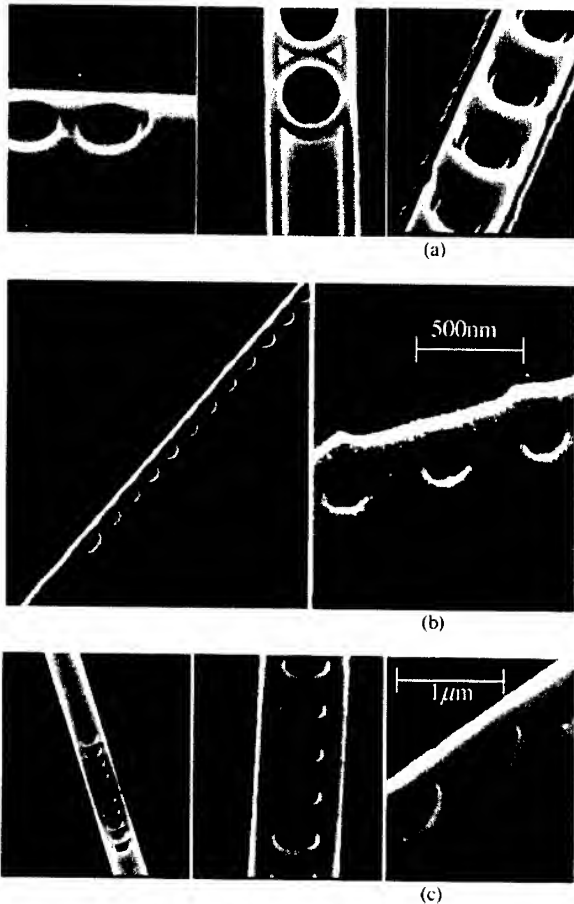


Figure 3 Scanning electron micrograph of $\lambda=1.54\mu\text{m}$ PBG waveguide. (a) Effect of CHF_3 on silicon sidewall. (b) Device made by $\text{CF}_4/\text{O}_2/\text{CHF}_3$ plasma. (c) Device made by $\text{CF}_4/\text{SiCl}_4$ plasma.

before cleaving. We have designed a special tool to cleave unthinned (100) silicon substrates. A typical sample after cleaving is shown in Figure 4.

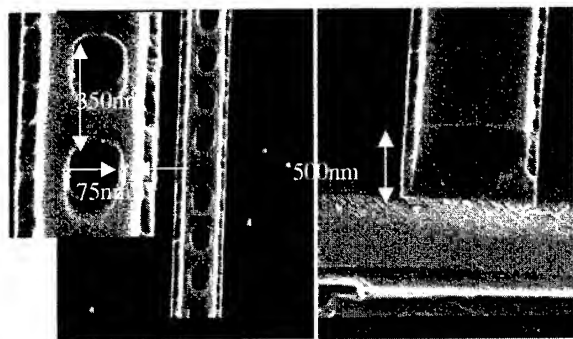


Figure 4 Scanning electron micrograph of a 1D optical cavity and of cleaved end face of $\lambda=1.54\mu\text{m}$ PBG waveguide.

CONCLUSIONS

In conclusion, a process has been described for fabricating smooth grass free structure on Unibond SOI material for use in silicon microphotonic circuit. A lift-off mask mask of Al and combined chlorine-fluorine based plasma as a reactive ion-etching recipe were used to make the structures. Optical probing of the structure to measure loss characteristics and band-gap behavior is under progress.

ACKNOWLEDGEMENTS

We wish to thank Professor H. Ahmed, Head of Research Group, Microelectronics Research Centre, University of Cambridge for giving his kind permission to use the laboratory facility. The authors gratefully acknowledge helpful discussions with Dr. A. C. Irvine of the Microelectronics Research Centre.

- [1] Joannopoulos, J. D., Villeneuve, P. R. & Fan, S. Photonic crystals: putting a new twist on light. *Nature* **386**, 143–149 (1997).
- [2] Soukoulis, C. M. (ed.) Photonic Band Gap Materials (Kluwer, Dordrecht, 1996).
- [3] Joannopoulos, J. D., Meade, R. D. & Winn, J. N. Photonic Crystals (Princeton, New York, 1995).
- [4] Krauss, T. F., De La Rue, R. & Band, S. Two-dimensional photonic bandgap structures operating at near-infrared wavelengths. *Nature* **383**, 699–702 (1996).
- [5] Yablonovitch, E. Photonic band-gap structures. *J. Opt. Soc. Am. B* **10**, 283–295 (1993).
- [6] J. S. Foresi, P. R. Villeneuve, J. Ferrera, E. R. Thoen, G. Steinmeyer, S. Fan, J. D. Joannopoulos, L. C. Kimerling, Henry I. Smith & E. P. Ippen. Photonic-bandgap microcavities in optical waveguides. *Nature* **390**, 143–145 (1997).
- [7] K. K. Lee, D. R. Lim, H. Luan, A. Agarwal, J. Foresi and L. C. Kimerling, "Effect of size and roughness on light transmission in a Si/SiO₂ waveguide: Experiments and model," *Appl. Phys. Lett.* **77** 1617 (2000).
- [8] Plasma etching: an introduction/ edited by Dennis M. Manos. Daniel L. Flamm Boston; London: Academic, Chapter 2.
- [9] P. B. Fischer and S. Y. Chou. "Sub-50 nm high aspect ratio silicon pillars, ridges, and trenches fabricated using ultrahigh resolution electron beam lithography and reactive ion etching," *Appl. Phys. Lett.* **62** 1414 (1993).
- [10] D. J. Paul, *PhD thesis*, Cambridge, 1993 Chapter 4.
- [11] L. S. Yu, Z. F. Guan, Q. Z. Liu and S. S. Lau, "Silicon on insulator photoelastic optical waveguide and polarizer," *Appl. Phys. Lett.* **66** 2016 (1995).

Two Dimensional Photonic Crystal Modes and Resonances in Three-dimensional Structures

Shanhui Fan¹ and J. D. Joannopoulos²

¹Department of Electrical Engineering, Stanford University, Stanford, CA 94305, U. S. A

²Department of Physics and Center for Material Science and Engineering, Massachusetts Institute of Technology, Cambridge, MA 02139, U. S. A

ABSTRACT

We present three-dimensional analysis of two-dimensional guided resonances in photonic crystal slab structures. This analysis leads to a new understanding of the complex spectral properties of such systems. Specifically, we calculate the dispersion diagrams, the modal patterns, and transmission and reflection spectra of these resonances. From these calculations, a key observation emerges involving the presence of two temporal pathways for transmission and reflection processes. Using this insight, we introduce a general physical model that explains the essential features of complex spectral properties. Finally, we show that the quality factors of these resonances are strongly influenced by the symmetry of the modes, and the strength of the index modulation.

INTRODUCTION

Photonic crystal slabs are a particularly important class of photonic crystal structures. A photonic crystal slab consists of a two-dimensionally periodic index contrast introduced into a high-index guiding layer (inset in Figure 1a). These structures support in-plane guided modes that are completely confined by the slab without any coupling to external radiations. These guided modes allow the control of light within the layer at the wavelength scale. Therefore, the slab structure may provide the basic substrate for large-scale on-chip integration of photonic components and circuits. [1-8]

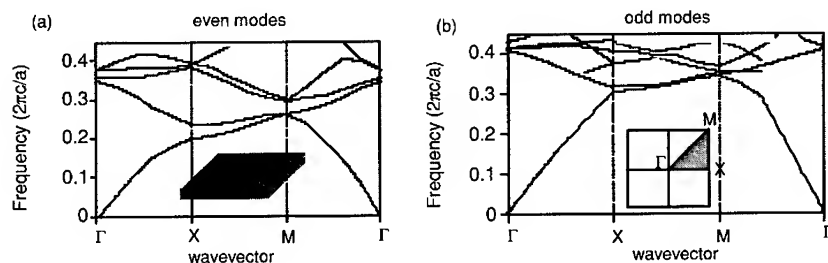


Figure 1. The band structure for (a) even and (b) odd modes in a photonic crystal slab. The structure of the slab is shown in the inset of (a), and consists of a square lattice of air holes with a radius of $0.2a$ introduced into a high-index dielectric slab with a dielectric constant of 12 and a thickness of $0.5a$. Even and odd modes are defined with respect to the mirror parallel to the slab. The gray regions are the continuum of radiation modes. Solid lines outside the gray region are guided modes. Solid lines within the gray region are guided resonances.

In addition to in-plane wave guiding, photonic crystal slabs can also interact with external radiations in complex and interesting ways. Of particular importance here is the presence of guided resonances in the structures, [9-15]. Similar to the guided mode, a guided resonance also has its electromagnetic power strongly confined within the slab. Unlike the guided mode, however, the resonance can couple to external radiations. Therefore, guided resonances can provide an efficient way to channel light from within the slab to the external environment. This property has been exploited in the designs of novel photonic-crystal based light-emitting diodes [11, 16], lasers [17, 18], and directional output couplers [19]. In addition, the guided resonances can significantly affect the transmission and reflection of externally incident light, resulting in complex resonant line shapes that are useful in filter applications, [9][20]

The purpose of this paper is to present a novel analysis of guided resonances in photonic crystal slabs. Our analysis elucidates a variety of complex spectra phenomena associated with these resonances. We compute the dispersion diagrams and the eigen-field distributions of these resonances with a plane-wave band structure computation method. We then perform finite-difference time-domain simulations to determine the transmission and reflection spectra, and to visualize in real time the interaction between the resonances and the incident light. Emerging from these simulations is a key insight that involves the presence of two temporal pathways in the transmission and reflection processes. Based upon this insight, we introduce a general and intuitive theory, which uses only interference and energy conservation arguments, to explain all the complex features in the spectral line shapes. Finally, we analyze the angular and the structural dependence of the guided resonances, and we show the wide ranges of tunability in quality factors for these resonances.

BAND STRUCTURE OF THE GUIDED RESONANCES

Since the spectral features of the guided resonances in a photonic crystal slab will turn out to depend critically on their modal properties, it is helpful to begin our discussion with a brief overview of the band structure properties of these resonances. Throughout this paper, our model system will consist of a square lattice of air holes introduced into a dielectric slab (inset in Figure 1). The thickness of the slab is $0.5a$, and the radius of the holes is $0.2a$, where a is the lattice constant. The dielectric constant of slab is 12, which roughly corresponds to the dielectric constant of Si or GaAs at optical wavelengths. For such a structure, because of the translational symmetries within the plane of the slabs, the physical properties of the slabs can be described by a band diagram that relates the frequencies of all the three-dimensional modes to the in-plane wave vectors [1][2]. The band diagram can be computed by a pre-conditioned conjugate gradient minimization of a Maxwell operator expanded on a plane wave basis [21].

For our model system as shown in the inset of Figure 1a, the band diagram for the even and odd modes are plotted in Figure 1 (a) and (b), respectively. Modes below the light line are bona-fide guided modes with infinite lifetime, in spite of the large index contrast introduced by the air holes. The guided modes above the light line, on the other hand, can couple to radiation modes and possess a finite lifetime. These modes therefore become guided resonances. They are called "guided" since they are closely related to the guided mode bands in a uniform slab, and should therefore retain significant portions of the electromagnetic power within the dielectric slab.

The presence of the air holes in the crystal also generates a discrete translational and rotational symmetry, and thereby dictates the degeneracy of the bands. At most k -points, (except

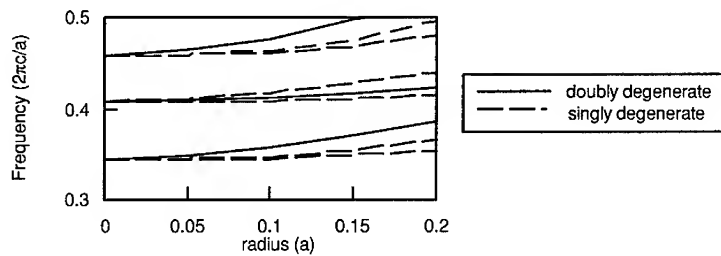


Figure 2. The frequencies of the resonances at Γ as a function of the radius of the holes in the slab. The slab has a dielectric constant of 12 and a thickness of $0.5a$. The modes are four-fold degenerate in the structure without holes. For structures with holes, the four-fold degeneracy is broken, resulting in a pair of doubly degenerate states, and two singly degenerate states.

for the special points Γ , X and M), the bands are singly degenerate. At the Γ point, the point group supports a two-dimensional irreducible representation, allowing for the existence of doubly degenerate states. Therefore, the four-fold degeneracy at the Γ point for a uniform slab splits in the presence of the air holes, as clearly seen in Figure 2, where we plot the frequencies of the resonant modes at Γ as a function of the radius of the holes. As the radius of the holes increases, the modes separate into a pair of doubly degenerate states and two singly degenerate states.

For the crystal structure with $r = 0.20a$, we show the power density distribution of the first resonant band at Γ in Figure 3. The mode is singly degenerate with a frequency $\omega = 0.35 \cdot (2\pi c/a)$. Since any singly degenerate mode should belong to a one-dimensional irreducible representation, the power density distribution of the mode should possess the full symmetry of the lattice. This can be seen in Figure 3(a), which shows the spatial distribution of the power density on a slice parallel to the slab. Also, the resonant nature of this mode is exhibited in Figure 3(b), which shows that the power density is strongly confined within the slab.

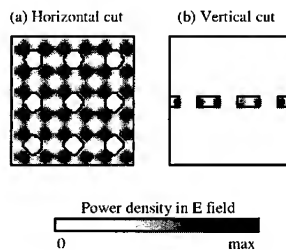


Figure 3. Spatial distribution of the power density in electric fields on (a) a horizontal slice, and (b) a vertical slice, for the lowest-order singly degenerate resonance at Γ . The lines indicate the position of the interface between dielectric and air. The white color represents low intensity and the dark color represents high intensity, as indicated by the color bar at the bottom of the figure.

The band structure computations thus allow us to examine the dispersion, the field distributions, and the symmetry properties of the guided resonances. For a complete understanding of these resonances, however, we must also study their lifetimes, and their interactions with external radiations. These questions will be addressed in the next session by finite-difference time-domain simulations.

TIME-DOMAIN ANALYSIS OF THE GUIDED RESONANCES

Computational methods

The computational domain for our finite-difference time-domain study [22] includes a single unit cell of the crystal. On the top and bottom surfaces of the computational domain, we impose the PML absorbing boundary conditions [23]. For the remaining four surfaces that are perpendicular to the slab, we impose a Bloch periodic boundary condition on the electric fields E :

$$E(r+a) = e^{ik \cdot a} E(r) \quad (1)$$

Here, a is a lattice vector of the square lattice, and k is a wavevector that is parallel to the slab. We note that by Bloch's theorem, k is a conserved quantity in the scattering process.

We generate an incident plane wave by placing a source plane consisting of oscillating dipoles near the top surface of the computational domain. For two dipoles in the plane that are separated by a distance vector r , we set the relative phase between them to be $e^{ik \cdot r}$. Therefore, in combination with the boundary condition as specified in Eq. (1), the source plane generates an incident plane wave with a parallel wavevector component k . In addition, the amplitudes of the dipole moments are set to oscillate at a constant frequency with a Gaussian profile to create a temporal pulse. This computational setup thus allows us to calculate the response functions of the structure at a given k for a wide range of frequencies in a single simulation run. (Notice that this is not a constant incidence angle calculation. At a fixed parallel wavevector k , the incidence angle changes with frequency.)

The transmission and reflection spectra are obtained by first Fourier transforming the recorded time sequence of field amplitudes at their respective monitor points. (We note that monitoring the field amplitudes only at the two monitor points is valid for the frequency range $\omega < 2\pi c/a$, where no diffraction occurs.) The spectra are then normalized with respect to the incident pulse that is calculated in an identical simulation in vacuum without the slab structure. For reflection, the normalization step is preceded by subtracting the incident pulse.

Transmission and reflection spectra

Using the computational setup as described in Section III.1, we calculate the transmission and reflection coefficients at various k -points for the structure as shown in Figure 1. In the case where $k = \hat{x} \cdot 0.2 \cdot 2\pi/a$, the calculated spectra for the s -polarized incident wave are shown in Figure 4. (An s -polarized wave has its electric field perpendicular to the plane of incidence. In this case, the electric field is polarized along the y -direction). The spectra consist of sharp resonant features superimposed upon a smoothly varying background.

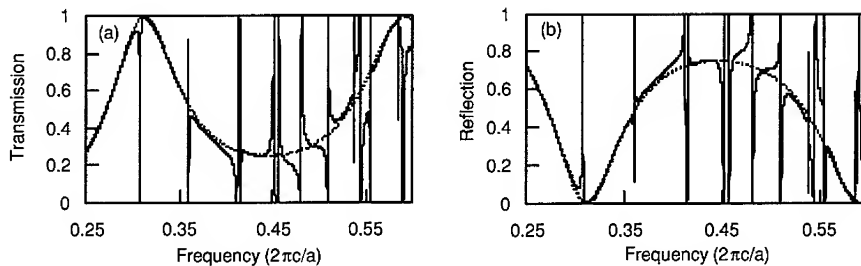


Figure 4. (a) Transmission and (b) reflection spectra. The solid lines are for the photonic crystal structure shown in the inset of Figure 1(a). The dashed lines are for a uniform dielectric slab with a frequency dependent dielectric constant, as defined in Eq. (2), and a thickness of $0.5a$. The incident wave is s -polarized, and has a parallel wavevector $k = 0.2 \cdot 2\pi/a$ along the x -direction.

The background in Figure 4 resembles the Fabry-Perot oscillations when light interacts with a uniform dielectric slab. To clearly see this, we fit the background to the spectra of a uniform slab, which are shown as dashed lines in Figure 4. The uniform slab has the same thickness of $0.5a$ as the crystal, and the light is incident with the same polarization at the same parallel wavevector. The dielectric constant of the uniform slab ϵ_1 , as obtained by the fitting procedure, represents an effective dielectric constant for the photonic crystal. Due to the presence of the holes, such ϵ_1 is a slowly varying function of the frequency. At low frequencies, the wavelength of incident light is large, and ϵ_1 for this polarization approaches the average dielectric constant ϵ_{avg} of the crystal. At higher frequencies, as the incident wave probes more details of the crystal structure, ϵ_1 starts to deviate from ϵ_{avg} . Within the frequency range in Figure 4, i.e. between $0.25 \cdot 2\pi/a$ and $0.60 \cdot 2\pi/a$, we have found that a frequency-dependent dielectric constant

$$\epsilon(\omega) = -14.16 \cdot \omega^2 + 15.18 \cdot \omega + 7.18 \quad (2)$$

gives a very good fit of the background (Figure 4). The fit here corresponds to varying ω from 10.62 at $\omega = 0.25 \cdot 2\pi/a$ to 11.5 at $\omega = 0.60 \cdot 2\pi/a$. (As a comparison, the average dielectric constant for the crystal is 10.6.) Therefore, except for the sharp resonance features, the background of the spectra for the crystal can be adequately accounted for, using the model of a uniform dielectric slab with a frequency-dependent dielectric function.

Line shape analysis

Superimposed upon the smooth background in the spectra for the crystals are sharp resonant features. Such features come from the guided resonances of the slab. In most cases, the line shapes for these resonances are asymmetric and rather complicated. Extensive experimental and theoretical work has been performed for guided resonances in structures with one-dimensionally periodic index variation. [24-31] For structures with two-dimensional periodicity, these resonances have also been studied numerically using the Rigorous Coupled Wave Analysis

(RCWA) method [20], and analytically using vector coupled-mode theory [13][15]. Here, we would like to present a novel analysis from a time-domain perspective. We will observe the important features in the time-domain signatures of the resonances. And, based upon the observation, we will introduce a general and intuitive model to account for the underlying physics.

The transmission and reflection spectra are related to the time-varying fields by a Fourier transformation. It is therefore informative to examine the time dependency of the fields. As an example, we show in Figure 5(a) the electric field amplitude at the transmission monitor point as a function of time steps, for the calculation that gives the spectra shown in Figure 4. The time sequence consists of two distinct stages: an initial pulse, and a tail of long decay.

The presence of these two stages indicates the existence of two pathways in the transmission processes. The first pathway is a direct transmission process, where a portion of the incident energy goes straight through the slab and generates the initial pulse. The Fourier transformation of the initial pulse should account for the background in the transmission spectra. The second pathway is an indirect transmission process, where the remaining portion of the incident energy excites the guided resonances. The power in the resonances then decays slowly out of the structure and produces the long decaying tail. By Fourier transforming the decaying tail, we obtain the typical symmetric Lorentzian line shapes, as shown in Figure 5(b). The analysis of the resonant line shape thus allows us to determine the quality factor Q of the resonance. A few examples of the Q values for this structure are: 360 for the resonance at $\omega = 0.31 \cdot (2\pi/a)$, and 2500 for the resonance at $\omega = 0.36 \cdot (2\pi/a)$. The interference between the direct and the indirect pathways, therefore, determine the transmission property. The same observation can be made for the reflected amplitude as well. In solid state and atomic physics, similar interference phenomena are commonly referred to as the Fano resonances [32]. Such temporal interference phenomenon has also been analyzed previously for surface plasmon in metallic thin films [33].

Taking into consideration the interference between these two pathways, we can construct a simple and intuitive model that quantitatively explains the line shape. We express the transmitted amplitude t , and the reflected amplitude r , as follows:

$$t = t_d + f \cdot \frac{\gamma}{i(\omega - \omega_0) + \gamma}, \quad (3)$$

$$r = r_d \pm f \cdot \frac{\gamma}{i(\omega - \omega_0) + \gamma}. \quad (4)$$

Here, t_d and r_d are the direct transmission coefficients, ω_0 and γ are the center frequencies and the widths of the Lorentzian from the resonance, and the factor f is the complex amplitude of the resonant mode.

The plus/minus sign in Eq. (4) corresponds to resonant modes that are even/odd with respect to the mirror plane parallel to the slab. We note that the Lorentzian functions in Eqs. (3) and (4) correspond to the decaying amplitudes of the resonances to the reflection and transmission sides of the slab, respectively. For an even mode, the decaying amplitudes to the two sides of the slab are in phase, while for an odd mode the decaying amplitudes are 180-degree out of phase. Thus, the signs in Eq. (4) are different for modes with different mirror-plane symmetry properties.

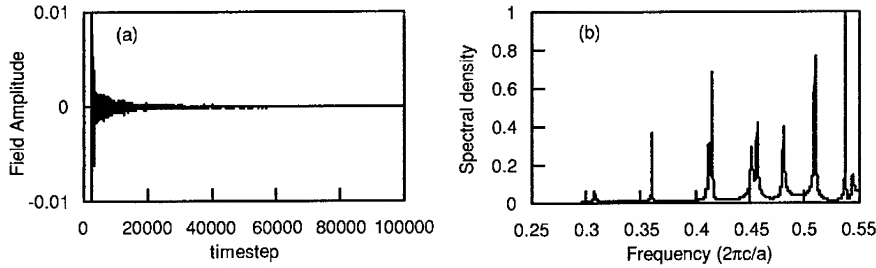


Figure 5. (a) The field amplitude at the monitor point as a function of time step, for the same calculation as shown in Figure 4. Notice the existence of two separate stages: an initial pulse, and a long decaying tail. (b) The Fourier transformation of the amplitude as shown in (a) from time step 20,000 - 100,000. The spectral intensity exhibits Lorentzian line shapes.

The factor f can in fact be determined purely by energy conservation arguments. We note that:

$$|r|^2 + |d|^2 = 1. \quad (5)$$

Moreover, since r_d and t_d are the transmission and reflection coefficients through an uniform slab with the appropriate effective dielectric constant, we should have

$$|r_d|^2 + |t_d|^2 = 1. \quad (6)$$

Constraints (5) and (6) together uniquely determine the factor f . Plugging Eqs (3), (4), and (6) into Eq. (5), we have, for any ω :

$$\begin{aligned} & -2|f|^2 \frac{\gamma^2}{(\omega - \omega_0)^2 + \gamma^2} \\ & = 2|f||t_d \pm r_d| \frac{\gamma}{\sqrt{(\omega - \omega_0)^2 + \gamma^2}} \cos \left(\arg(f) - \arg(t_d \pm r_d) - a \cos \left(\frac{\gamma}{\sqrt{(\omega - \omega_0)^2 + \gamma^2}} \right) \right), \end{aligned} \quad (7)$$

which can only be satisfied if:

$$f = -(t_d \pm r_d). \quad (8)$$

It is interesting to note here that the factor f is independent of the resonant line width γ .

The parameters r_d and t_d represent the background of the spectra. Therefore, as discussed earlier in Section III.2, such parameters can be determined by fitting the background to the response spectra of a uniform slab, as:

$$r_d = \frac{i \frac{k_{z0}^2 - k_{z1}^2}{2k_{z0}k_{z1}} \sin(k_{z1}h)}{\cos(k_{z1}h) - i \frac{k_{z0}^2 + k_{z1}^2}{2k_{z0}k_{z1}} \sin(k_{z1}h)}, \quad (9)$$

$$t_d = \frac{1}{\cos(k_{z1}h) - i \frac{k_{z0}^2 + k_{z1}^2}{2k_{z0}k_{z1}} \sin(k_{z1}h)}, \quad (10)$$

for a plane wave with parallel wavevector k_x , incident from vacuum with a dielectric constant $\epsilon_0 = 1$, through a uniform dielectric slab with a thickness h and a dielectric constant ϵ [34]. The parameters k_{z0} and k_{z1} in Equations (9) and (10) represent the wavevector components along the z -axis in the uniform slab, and are defined as:

$$k_{z0} = \sqrt{\epsilon_0 \frac{\omega^2}{c^2} - k_x^2}, \quad (11)$$

$$k_{z1} = \sqrt{\epsilon_1 \frac{\omega^2}{c^2} - k_x^2} \quad (12)$$

In obtaining Equations (9) and (10), we assume a positive frequency convention, in order to be consistent with the Lorentzian functions that we have chosen for the resonance in Equation (3) and (4).

We note, in particular, when $r_d = 0$, and $t_d = 1$, from Eqs. (3), (4), and (8), the reflection and the transmission coefficients become:

$$t = \frac{i(\omega - \omega_0)}{i(\omega - \omega_0) + \gamma}, \quad (13)$$

and

$$r = \mp \frac{\gamma}{i(\omega - \omega_0) + \gamma}. \quad (14)$$

The line shapes thus become symmetric, and the structure behaves as a narrow-band reflector with a Lorentzian reflectivity line shape. Previously, this scenario was noted by Wang and Magnusson [26]. In the general case when $r_d \neq 0$, on the other hand, the line shape becomes asymmetric. The transmission can vary from 0% to 100% within a very narrow frequency range. A small shift in the resonant frequency may therefore lead to a drastic change in the response function. This effect may be exploited in the design of optical sensors and switches.

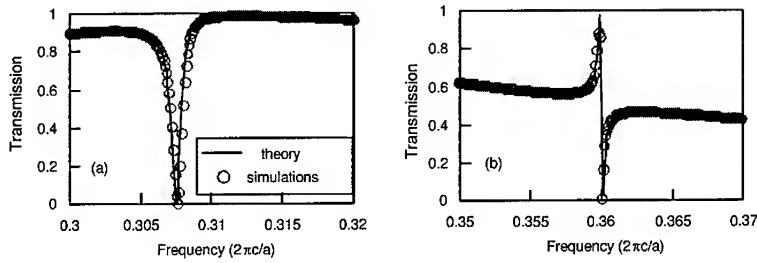


Figure 6. Comparison of theory and simulations. The empty circles in (a) and (b) are numerical results taken from Figure 5(a), which corresponds to the two lowest-frequency resonances. The solid lines are theoretical predictions from Eqs. (3), (8), (9) and (10). The parameters of the theory for the two resonances are: (a) $\omega_0 = 0.3076 \cdot 2\pi c/a$, $\gamma = 4.191 \cdot 10^{-4} \cdot 2\pi c/a$; (b) $\omega_0 = 0.3601 \cdot 2\pi c/a$, $\gamma = 7.2483 \cdot 10^{-5} \cdot 2\pi c/a$.

We compare our theoretical predictions, as defined by Eqs. (3), (4), (8), (9) and (10), to the numerical results for the first two resonances shown in Figure 5. (Both of these resonances are even.) The frequency ω and the width γ of each resonance are determined from the simulations. The only fitting parameter here is the effect dielectric constant ϵ_1 , which we take from Equation (2). The theoretical results thus obtained are shown as solid lines in Figure 6. The theory agrees completely with the numerical simulations.

Wavevector dependency of the resonances

To explore the wavevector and polarization dependency of the resonances, we performed calculations at different values of k_x , for an incident wave that is either *s*- or *p*-polarized. (The *s*-polarization has the electric field perpendicular to the plane of incidence, while the *p*-polarization has the magnetic field perpendicular to the plane of incidence). We determine the position and the width of the resonances by Fourier transforming the decaying tail, as discussed earlier in section III.3. The results are summarized in Figure 7(a), where we show the frequencies of the resonances as a function of k_x . Incident waves with different polarizations excite different resonances, since the two polarizations possess different symmetries with respect to *yz*-mirror plane.

We note that, in Figure 7(a), some of the bands do not continue to the Γ point. In other words, certain resonances at Γ do not couple to either polarization of the incident wave. A closer examination of Figure 7(a) reveals that all these uncoupled resonances are singly degenerate. Previously, this effect was observed experimentally by Pacradoni et al [14], and discussed theoretically by Paddon and Young [13], and by Ochiai and Sakoda [25]

To further explore the wavevector dependency of the resonance, in Figure 7(b) we plot the quality factors of the resonances as a function of k_x , for the four lowest bands in Figure 7(a). For bands with different symmetry properties, the behavior of the quality factors is very different. The Q factors approach a constant as k_x vanishes for the modes that connect to the doubly degenerate states at Γ . For the modes that connect to the singly degenerate states, on the other hand, the Q factors of the modes diverge. The calculation clearly demonstrates that the symmetry of the modes can significantly influence the photon lifetime of the resonances.

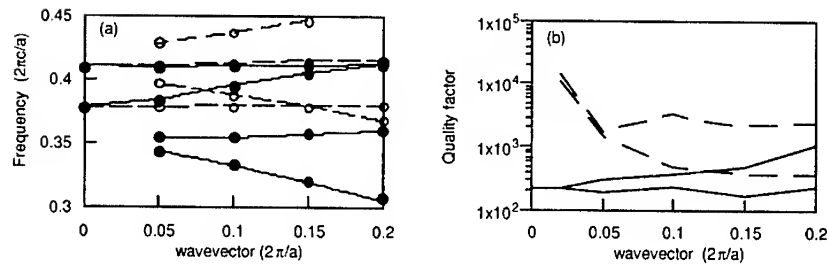


Figure 7. (a) The frequencies of the resonances as a function of wavevector, for the structure as shown in the inset of Figure 1a, as determined from the time-domain simulations. The solid circles correspond to the resonances that are excited by the p-polarized incident waves, the empty circles correspond to the resonances that are excited by the s-polarized incident waves. Notice that some of the bands do not continue to Γ , indicates the existence of uncoupled states at Γ . (b) The quality factor as a function of wavevector, for the four lowest bands in (a). The solid lines correspond to modes that connect to the doubly degenerate state at Γ point. The broken lines correspond to modes that connect to the singly degenerate state at Γ point.

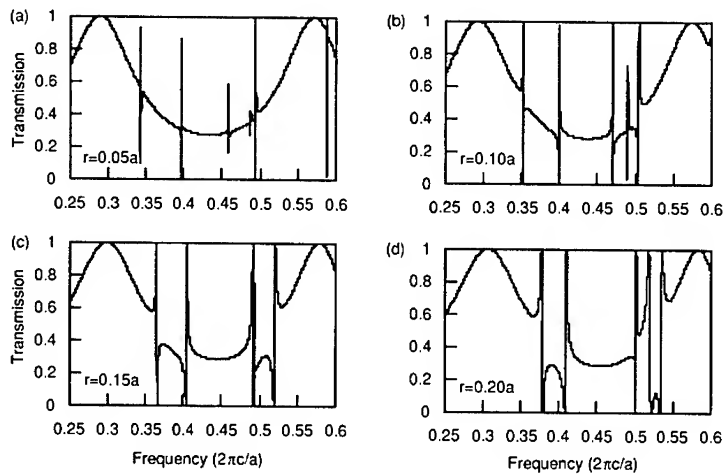


Figure 8. The transmission spectra at normal incidence, for crystal slab structures with a radius of (a) $0.05a$; (b) $0.10a$; (c) $0.15a$, and (d) $0.20a$. All the structures have a thickness of $0.5a$, and a dielectric constant of 12.

Radius dependence of the resonance.

In addition to symmetry related effects, the lifetime of the resonances is also strongly influenced by the radius of the holes. At the limit where the radius of the holes approaches zero, the Q factor for all the resonances should diverge, since the resonances asymptotically become real guided modes. To demonstrate this effect, we plot in Figure 8 the transmission spectra at normal incidence for four different structures with the radius varying from $0.05a$ to $0.20a$. The spectral feature for the resonances indeed becomes sharper as the radius becomes smaller. For the lowest-order resonances, the Q factor varies from approximately 5000 at $r = 0.05a$, to 213 at $r = 0.20a$. At a larger radius, the Q-factor should be even lower.

The tunability of the quality factor with respect to the radius of the holes is important for LED and laser applications. For photonic-crystal resonant-cavity LED structures, optimal efficiency occurs when the line width of the resonances become comparable to the line width of the emitter [35]. On the other hand, for a laser structure, a high-Q resonance is typically desirable for threshold reduction. Therefore, as we have demonstrated in this paper, photonic crystal slab structures are very versatile, and can be specifically tailored for different light emitting applications.

SUMMARY

In summary, we present a three-dimensional frequency and time-domain analysis of resonances in photonic crystal slab structures. These resonances are strongly confined with the dielectric slab, and yet at the same time are coupled to radiation modes. For external light incident upon these slabs, the transmission and reflection spectra are strongly modified by the presence of these resonances. The line shapes exhibit complex asymmetric characteristics. We show that all the complexities in the line shapes can be accounted for with a simple analytic model describing the interference between direct transmission (or reflection), and the exponential decaying amplitudes of the resonances. We also demonstrate that the quality factors of these resonances are strongly influenced by the symmetry of the modes, and the radius of the holes.

ACKNOWLEDGMENT

This work was supported in part by the Material Research Science and Engineering Center program of the National Science Foundation under Award No. DMR-9400334.

REFERENCES

1. S. Fan, P. R. Villeneuve, J. D. Joannopoulos, and E. F. Schubert, Phys. Rev. Lett. 78, 3294-7 (1997).
2. S. G. Johnson, S. Fan, P. R. Villeneuve, and J. D. Joannopoulos and L. A. Kolodzeski, Phys. Rev. B 60, 5751-8 (1999).
3. O. Painter, T. Vuckovic, and A. Scherer, J. Opt. Soc. Am. B 16, 275-85 (1999).
4. T. Baba, N. Fukaya, and J. Yonekura, Electron. Lett. 35, 654-5 (1999).
5. S. Kuchinsky, D. C. Allan, N. F. Borrelli, and J. -C. Cotteverte, Opt. Commun. 175, 147 (2000).
6. S. Y. Lin, E. Chow, S. G. Johnson, J. D. Joannopoulos, Opt. Lett. 25, 1297-9 (2000).

7. H. Benisty et al, *Appl. Phys. Lett.* 76, 531-3 (2000).
8. A. Chutinan and S. Noda, *Phys. Rev. B* 62, 4488-92 (2000).
9. M. Kanskar, P. Paddon, V. Pacradouni, R. Morin, A. Busch, J. F. Young, S. R. Johnson, J. MacKenzie and T. Tiedje, *Appl. Phys. Lett.* 70, 1438-40 (1997).
10. P. R. Villeneuve, S. Fan, S. G. Johnson, and J. D. Joannopoulos, *IEEE Proceedings: Optoelectronics* 145, 384 (1998).
11. M. Boroditsky, R. Vrijen, T. F. Krauss, R. Coccioli, R. Bhat, and E. Yablonovitch, *J. Lightwave Technol.* 17, 2096-112 (1999).
12. V. N. Astratov, I. S. Chushaw, R. M. Stevenson, D. M. Whittaker, M. S. Skolnick, T. F. Krauss, and R. M. De la Rue, *J. Lightwave Technol.* 17, 2050-8 (1999).
13. P. Paddon and J. F. Young, *Phys. Rev. B* 61, 2090-2101 (2000).
14. V. Pacardoni, W. J. Mandeville, A. R. Crown, P. Paddon, J. F. Young and S. R. Johnson, *Phys. Rev. B.* 62, 4204-7 (2000).
15. A. R. Cowan, P. Paddon, V. Pacradouni, and J. F. Young, *J. Opt. Soc. Am. A* 16, 1160-70 (2001).
16. A. A. Erchak, D. J. Ripin, S. Fan, J. D. Joannopoulos, E. P. Ippen, G. S. Petrich, and L. A. Kolodzeski, *Appl. Phys. Lett.* 78, 563-5 (2001).
17. M. Meier, A. Mekis, A. Dodabalapur, A. Timko, R. E. Slusher, J. D. Joannopoulos, *Appl. Phys. Lett.* 74, 7-9 (1999).
18. M. Imada, S. Noda, A. Chutinan, T. Tokuda, M. Murata and G. Sasaki, *Appl. Phys. Lett.* 75, 316-8 (1999).
19. A. Mekis, A. Dodabalapur, R. E. Slusher, and J. D. Joannopoulos, *Opt. Lett.* 25, 942-4 (2000).
20. S. Peng and G. M. Morris, *J. Opt. Soc. Am. A* 13, 993-1005 (1996).
21. J. D. Joannopoulos, R. D. Meade and J. N. Winn, "Photonic crystals: molding the flow of light" (Princeton University Press, Princeton, 1995).
22. For a review on finite difference time domain methods, see K. S. Kunz and R. J. Luebbers, "The finite difference time domain methods for electromagnetics", (CRC press, Boca Raton, 1993); A. Taflov and S. C. Hagness, "Computational Electrodynamics: the finite-difference time-domain method", (Artech House, Boston, 2000).
23. J. P. Berenger, *J. Computational Physics* 114, 185-200 (1994).
24. S. S. Wang and R. Magnusson, *Appl. Phys. Lett.* 61, 1022-24 (1992).
25. T. Ochiai and K. Sakoda, *Phys. Rev. B* 63, 125107-1 (2001).
26. S. S. Wang and R. Magnusson, *Opt. Lett.* 19, 919-921 (1994).
27. A. Sharon, D. Rosenblatt, A. A. Friesem, *Opt. Lett.* 21, 1564-6 (1996).
28. T. Tamir and S. Zhang, *J. Opt. Soc. Am A* 14, 1607-1616 (1997).
29. S. M. Norton, T. Erdogan and G. M. Morris, *J. Opt. Soc. Am. A* 14, 629-639 (1997).
30. S. M. Norton, G. M. Morris and T. Erdogan, *J. Opt. Soc. Am A* 15, 464-472 (1998).
31. G. Levy-Yurista and A. A. Friesem, *Appl. Phys. Lett.* 77, 1596-1598 (2000).
32. U. Fano, *Phys. Rev.* 124, 1866-77 (1961).
33. R. V. Andalaro, H. J. Simon, and R. T. Deck, *Appl. Opt.* 33, 6340-7 (1994).
34. P. Yeh, "Optical waves in layered media", (John Wiley & Sons, New York, 1988).
35. S. Fan, P. R. Villeneuve, and J. D. Joannopoulos, *IEEE J. Quantum Electron.* 36, 1123-30 (2000).

Artificial Second Order Non-Linearity in Photonic Crystals.

A Feigel, Z. Kotler and B. Sfez

Electro-Optics Division, NRC Soreq, 81800 Yavne, Israel

ABSTRACT

We describe a technique for obtaining effective second order non-linearity χ^2 in non centro-symmetric Photonic Crystal made from centro-symmetric materials (e.g. glass, Ge or Si). The effect is based on the electric quadrupole transition, strong electromagnetic mode deformation and different contributions to the volume polarization from different parts of the photonic crystal¹.

INTRODUCTION

Many new application based on different physical phenomena are feasible now with the help of photonic crystals. Possibility to design photonic density of states and spatial electromagnetic modes structure open new ways for creation of materials with extraordinary optical properties.

The second order nonlinear materials are highly required both for fundamental research and for industrial applications. Unfortunately there are many constrains that limit the choice of such materials: the value of χ^2 should be reasonably high, absorption in required spectrum should be low, high damage threshold is required and finally to possess second order non-linearity the materials has to be non-centro-symmetric. The latter immediately eliminates all amorphous materials (like glass or Silicon) and crystals from 11 of 32 symmetry classes. Hence the technology that allows fabrication of non-linear materials from previously unsuitable centro-symmetric substrates can significantly enlarge the material choice for non-linear optics.

A local second order polarization $P^{(2)}$ exists even in centro-symmetric materials due to the higher than dipole electromagnetic transitions². The asymmetry of the electromagnetic field spatial mode leads to quadrupole transition, while dipole transition is based on the asymmetry of the electron wave function. The second order polarization corresponding to a quadrupole transition is:

$$\vec{P}_Q^{(2)} = Q : \vec{E} \nabla \vec{E} \quad (1)$$

where Q is a fourth-order tensor. Generally the volume contribution of eq. (1) polarization vanishes, due to periodicity of electromagnetic mode and gradient dependence of quadrupole transition polarization. However the result in properly designed photonic crystals can be quite different.

Integration of eq. (1) over the volume in dielectric/air photonic crystal can be different from zero due to not equal contribution to volume polarization from different parts of the crystal. The polarization of the air regions can be totally neglected due to low electron density. Constructing photonic crystal in such a way that in dielectric part the quadrupole polarization has one sign and in the air the opposite, effective "structural" volume polarization can be obtained. The required symmetry breaking is introduced on the macroscale of the photonic crystal unit cell, contrary to atomic scale asymmetry in ordinary non-linear materials. Electromagnetic mode inside photonic crystal can be highly modulated³, leading to large $\nabla \vec{E}$ term.

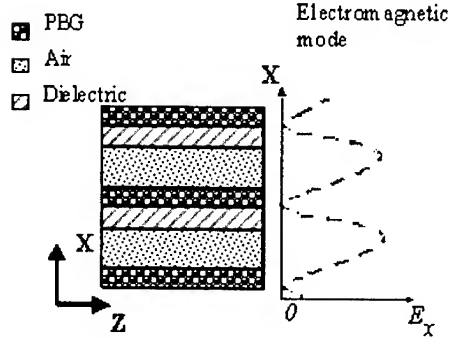


Figure 1: Array of waveguides in Photonic Band Gap Crystal. The electromagnetic mode with frequency inside the gap is strongly modulated in this structure.

The theoretical analysis leads to the following estimation for effective second order susceptibility $\chi_{str}^{(2)}$ induced by quadrupole effect:

$$\chi_{str}^{(2)} = \frac{d}{\lambda} \eta \beta_{overlap} \chi_{reul}^{(2)} \quad (2)$$

where d is characteristic interatomic dimension, λ is radiation wavelength. η is numerical coefficient (generally ≥ 10) that indicates the difference between dipole and quadrupole transition matrix elements, $\beta_{overlap}$ (generally ≈ 1) depends on electromagnetic modes structure inside the photonic crystal and $\chi_{reul}^{(2)}$ is some characteristic value for ordinary second order susceptibility. From previous experiments on the surface non-linear effects in Si and Ge, it is possible to estimate that $\chi_{str}^{(2)}$ in photonic crystals made from these substrates can be comparable with second order susceptibilities of ordinary non-linear materials. This result (2) is valid for both 2D and 3D properly designed photonic crystals¹.

Photonic crystals with strong spatial modulation of electromagnetic field are the preferred structures for the proposed method. In photonic crystal strong modulation can be obtained due to spatial photon density of states modification by defects incorporating or due to initially modulated electromagnetic mode³. We will concentrate on specific structure: the photonic crystal that consists of periodic defects lattice in the Photonic Band Gap environment. A single defect in PBG environments can possess localized modes for frequencies inside the gap. This means that for such frequencies in periodic lattices of defects, the mode might not be localized, but strongly modulated. This structure, in our opinion, should provide the maximum effect and its fabrication is feasible.

The defects should be asymmetric and possess dielectric/air structure. In this case maximum volume contribution of polarization (after integration of eq. 1) can be obtained. In our opinion the hollow cavities, partially filled with the substrate's material, are the best candidates for the proposed method.

RESULTS

The specific case of Optical Parametric Oscillations (OPO) in array of air waveguides inside Photonic Band Gap Crystal was numerically and theoretically studied. The mode modulation in such structure achieved due to lower photon state density in PBG environment and strong light confinement inside the waveguides. The required break of symmetry was introduced by partial dielectric filling of the waveguides (see Figure 1).

The numerical simulation of light propagation in such structure (see Figure 2) clearly shows that asymmetric modulated mode can be achieved leading to non-vanishing bulk quadrupole polarization. The analysis of the obtained results¹ proves that the prediction (2) is valid.

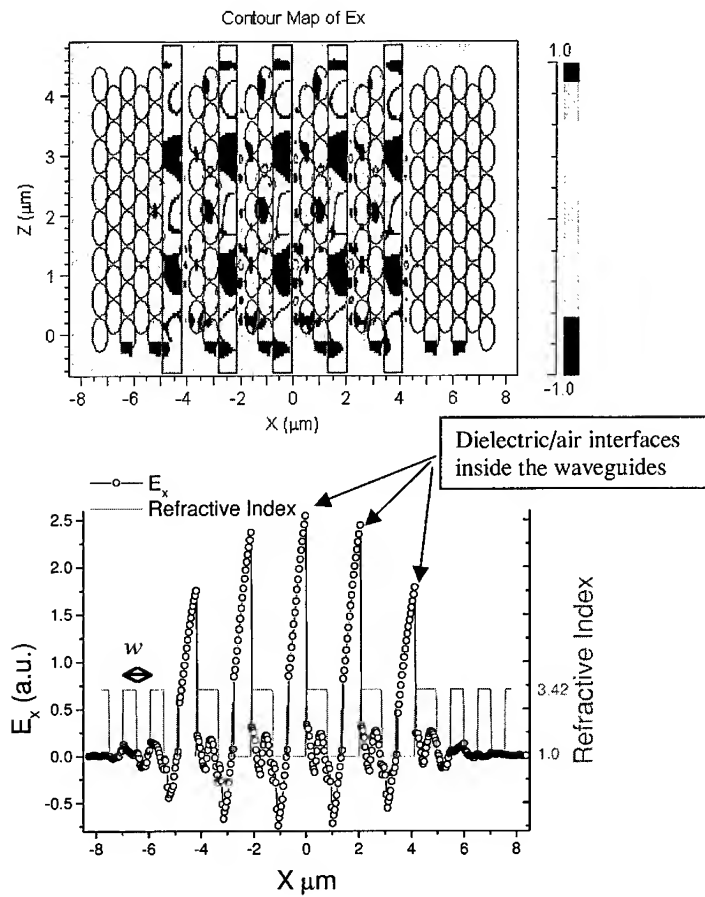


Figure 2: Numerical FDTD simulation results for TE electromagnetic mode propagation in waveguide array in 2D PBG crystal. PBG is a hexagonal array of holes in Si substrate (lattice constant $a=0.6 \mu\text{m}$, $r/a = 0.48$). Waveguides are obtained by removing of the array of the unit cells and separated by the single unit cell. They are partially air filled ($w = 0.7 \mu\text{m}$). It leads to asymmetric mode structure. The simulation was performed with FullWave commercial software.

DISCUSSION

The proposed non-linearity is the intrinsic property of photonic crystals. Indeed the spatial mode modulation can be achieved without PBG, but it is extremely difficult to create an asymmetric dielectric/air high-Q resonator. All ordinary resonators (waveguides, spheres or microdisks) are highly sensitive to any geometrical or refractive index perturbations. Defects in PBG environment are much more robust and flexible resonators, which can accomplish the task. Not surprisingly the guiding of light in air was accomplished with the help of photonic crystals⁴, by creation a defect in PBG environment or by "SuperMirror" waveguide.

For efficient non-linear process phase matching conditions have to be satisfied. Otherwise the signal from different points along propagation will be in destructive interference. Generally in most ordinary non-linear materials this condition can be influenced only by change of the propagation direction. Another method is achieving artificial phase matching by periodic modulation of the sign of non-linear tensor coefficient. It can be done e.g. in ferroelectric crystals using periodic poling. In non centro-symmetric Photonic Crystals modulation of the non-linear coefficient can be introduced during fabrication by inversion of unit cell structure (see Figure 3).

Integrated optics is one of the possible future applications for structural $\chi_{sr}^{(2)}$ materials. Broad use of ordinary non-linear materials in integrated optics is limited due to incompatibility of different processes and high production price. Creation of effective non-linearity from wafer's substrate itself can solve these problems.

The current attenuation losses in 2D waveguides are high, due to radiation losses in the third direction. It is a technical (not fundamental) problem to the implementation of the proposed method by this technology, as well as for the entire 2D technology itself. There is a great effort by many groups to bring these losses to the level of ordinary integrated optics (sub cm-1). The problem of losses is much less crucial in photonic crystal fibers and 3D photonic band gap waveguides due to all 3D confinement of the propagating light. Also some extremely deep 2D Si photonic crystals⁵ may be suitable for checking the proposed concept.

■ PBG □ Air □ Dielectric

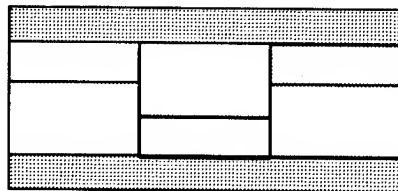


Figure 3: Unit cell inversion in non-centro-symmetric photonic crystal may be used for Quasi Phase Matching

CONCLUSION

It was shown that properly designed photonic crystals from centro-symmetric materials (glass, Si or Ge) can possess effective second order non-linearity of the same order as ordinary non-linear materials.

We want to thank the Israeli Ministry of Science and Sport for partial support of this work.

1. A. Feigel, Z. Kotler and B. Sfez, to appear in Phys. Rev. B.
2. N. Bloembergen and P.S. Pershan, Phys. Rev., 128, 606, 1962
3. O. Toader, S. Jhon and K. Busch, Optics Express, 8, 217, 2001
4. R. F. Cregan, B. J. Mangan, J. C. Knight, T. A. Birks, P. St. J. Russell, P. J. Roberts, and D. C. Allan, Science, 285, 1537, 1999; M. Ibanescu, Y. Fink, S. Fan, E. L. Thomas, and J. D. Joannopoulos, Science 289, 415, 2000
5. A. Birner, R.B. Wehrspohn, U. Gosele and K. Bush, Adv. Mater., 13, 377, 2001

Symposium T Paper

Atomistic Modeling of III-V Semiconductors: Thermodynamic Equilibrium and Growth Kinetics

Frank Grosse¹, William Barvosa-Carter², Jennifer J. Zinck², and Mark F. Gyure²

¹Department of Mathematics, University of California, Los Angeles, CA

²HRL Laboratories, LLC, Malibu, CA.

© 2001 HRL Laboratories, LLC. All Rights Reserved

ABSTRACT

Growth kinetics and thermodynamic equilibrium can both be determining factors at different stages of III-V semiconductor heteroepitaxy. We study their interplay, employing kinetic Monte Carlo simulations for the InAs(001) surface. The simulation contains atomistic details of both species, including the stability of different reconstructions and their kinetics. The behavior of the surface in thermodynamic equilibrium, including different reconstructions, is determined exclusively by extensive total energy calculations employing *ab initio* density functional theory. The continuous phase transition between the $\alpha 2(2 \times 4)$ and $\beta 2(2 \times 4)$, predicted by theory, is confirmed by experiment. At full layer coverage, a recovery of the stable reconstruction is observed. The different time scales associated with As₂ and In are discussed with respect to equilibrium and kinetics.

INTRODUCTION

Recent improvements in heteroepitaxy of III-V semiconductors enable nearly atomically flat interfaces between different layers. The reduction in width of some device layers down to a few atomic lattice constants on the other hand increases the effect of variations on the atomic scale. The complex behavior of III-V semiconductor surfaces makes investigation of atomic mechanisms challenging. Although many new insights into static surfaces, particularly concerning reconstructions, have been gained over the past few years, [1-4] the understanding of kinetics on the atomic scale is still in its infancy, even despite recent progress [5-7]. Because direct observation of microscopic processes is experimentally very difficult one relies on either *in situ* techniques like reflection high energy electron diffraction (RHEED) or photo emission (PE) that need additional interpretation to conclude microscopic morphology, or *ex situ* characterization with techniques like atomic resolution scanning tunneling microscopy (STM), where the surface is processed before it is investigated. The challenge for theoretical investigation is the determination of the large number of possible surface processes and their complex interplay. Although total energy calculations employing *ab initio* density functional theory (DFT) allow studying single processes with high accuracy [7,8], a full quantum mechanical treatment over long time scales or larger cells is not possible. These arguments suggest that computer simulations based on a combination of theory and experiment, for model construction and verification respectively, might be necessary to gain understanding in the complex dynamics of III-V semiconductors.

In this paper, we describe a new methodology that combines thermodynamic equilibrium and growth kinetics within one unified model, based on extensive DFT calculations and supported by experimental results. The achievable accuracy is demonstrated using the example of a kinetic Monte Carlo (KMC) simulation for the InAs(001) surface. Theoretical results predict a continuous transition between the $\alpha 2(2 \times 4)$ and $\beta 2(2 \times 4)$. Simulated and experimental results

agree quantitatively in the temperature dependence of the As-dimer density, directly related to this phase transition. Extending the results we reported elsewhere [9] for submonolayer deposition, we report simulation results for higher coverage exceeding one monolayer (ML) deposition. We discuss the possible use of our simulation results for surface and interface engineering.

AB INITIO DENSITY FUNCTIONAL CALCULATIONS

Atomic and electronic structure of the InAs(001) surface is studied employing *ab initio* density functional theory using the FHI98MD program package [10]. Total surface energies are calculated by modeling them in a slab geometry with periodic boundary conditions. The bottom of the slab is passivated with pseudohydrogen. Slab and vacuum thickness are converged with respect to the total energy at a length equivalent to 8 atomic layers. The local density approximation (LDA) as well as generalized gradient approximation (GGA) is used for the exchange correlation functional. Wavefunctions are expanded in plane waves up to the converged energy of $E_{cut}=12$ Ry. The k-point summation is carried out with a Monkhorst-Pack k-point set equivalent to 8x8 k-points per 1x1 unit cell.

KINETIC MONTE CARLO SIMULATION

The surface structure of InAs, including its bulk zincblende, structure is described in the simulation as follows. The simulation is carried out on a square lattice with unit vectors in the [110] and [-110] direction. Each site represents a (1x1) unit cell of the InAs(001) surface, and is characterized by its state. Allowed states are In that can have a [110], [-1-10], or no in-plane bond, and As that can have a [-110], [1-10], or no bond. The state of a site can be changed by processes describing adsorption, desorption, and diffusion on the surface. The state of site i and its neighborhood determines the local surface energy. The total surface energy is given by summing the local energy contributions of all sites.

The definition of a total surface energy in the model allows a direct mapping to total energies calculated by DFT. The parameter determination of the model energy utilizes more than 40 total energies, including those of different surface reconstructions, In adatom configurations on those reconstructions, and different As-dimer adsorption energies. By comparing energies from this model to an independent set of DFT calculations, we can test convergence with respect to interaction length, number of parameters, and parameter values. We find that energies are sufficiently converged, including interactions up to next nearest neighbor sites together with many body interactions involving up to six sites. Importantly, we find that the accuracy achieved with the model is comparable to the accuracy of the DFT calculations. A few remaining kinetic parameters (the prefactor for In and As processes, and the transition energy for In diffusion) were determined by comparing simulation results to specifically designed experiments [9]. A complete description of our KMC model will be published elsewhere.

After describing the experimental setup in the next section, we then compare simulation results for temperature dependent As-dimer densities in equilibrium with experiment. Growth kinetics is investigated for submonolayer deposition [9] and, presented here, multilayer deposition.

EXPERIMENTS

InAs(001) surfaces are prepared on undoped InAs buffer layers using conventional MBE techniques. The magnitude of the As-flux from the valved EPI As₂ source is measured by the

uptake method [11]. RHEED and PE are used as *in situ* sensors. Surfaces are annealed (In-flux $F(\text{In}) = 0$ ML/s) under fixed As-flux of $F(\text{As}) = 0.083$ ML/s at different temperatures. After achieving a steady-state annealing condition as shown by RHEED and PE the surfaces were quenched by simultaneously closing the valve and As-shutter, cutting the power to the substrate heater, and rotating the sample towards the cryopanel. The sample was transferred under UHV to the analysis chamber with an Omicron LS full-wafer STM and imaged after cooling to room temperature.

THERMODYNAMIC EQUILIBRIUM

We simulate the temperature dependence of annealed InAs(001) surfaces that is under zero In-flux. The initial surface is setup as a perfectly flat $\beta 2(2 \times 4)$ reconstructed surface. We monitor the As-density during the simulation for different temperatures using otherwise identical conditions. The As-density is determined within the simulation by counting sites that have an As state and no higher neighboring sites. Therefore the ideal $\alpha 2(2 \times 4)$ has a top As-density of 0.25 atoms per (1×1) whereas $\beta 2(2 \times 4)$ 0.5 atoms per (1×1) .

The time dependence of the As-density is plotted in Fig. 1 for temperatures between 380°C and 440°C at an As flux of 0.083 ML/s. The higher the temperature the faster the reduction and the lower the As-density. But even at higher temperatures equilibration needs a few seconds. The simulated surface morphologies after

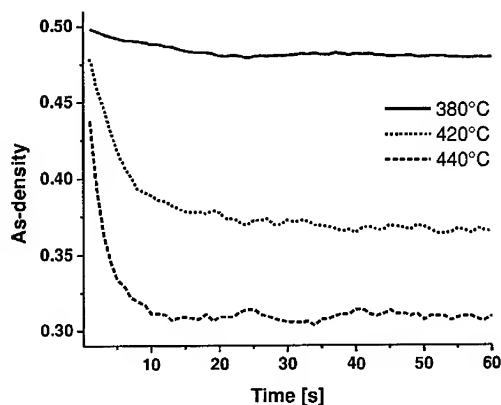


Figure 1 Simulated time dependence of As-density starting from a perfect $\beta 2(2 \times 4)$ reconstructed surface at various temperatures.

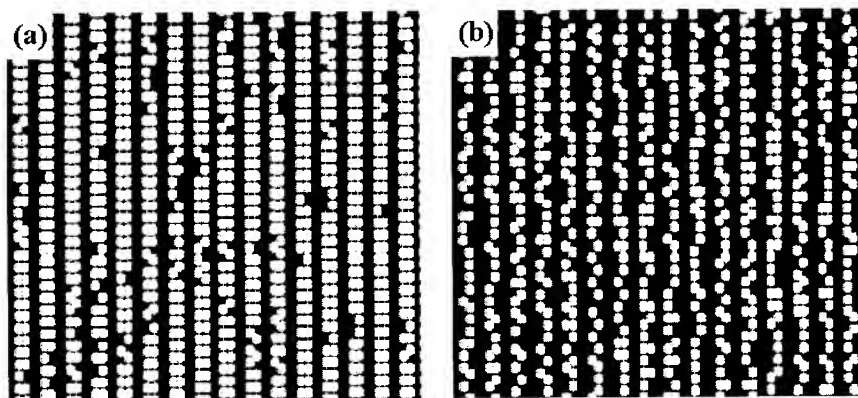


Figure 2 Simulated annealed InAs(001) surface in thermodynamic equilibrium. Parameters: As-flux $F(\text{As}) = 0.083$ ML/s, (a) $T = 380^\circ\text{C}$ (b) $T = 440^\circ\text{C}$.

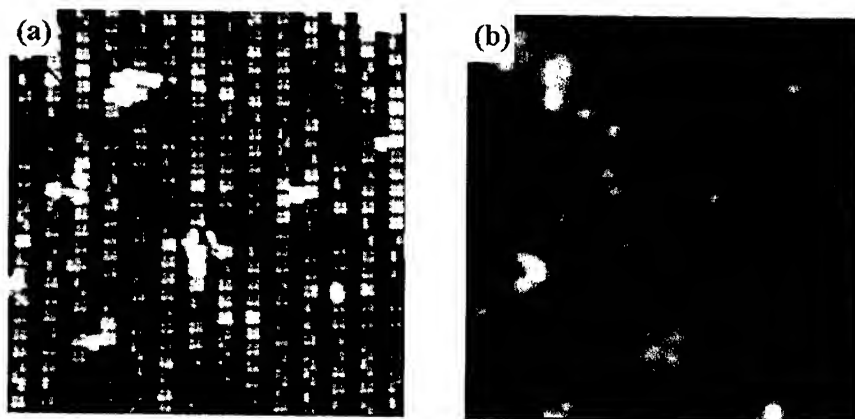


Figure 3 Annealed InAs(001) surface in experiment investigated by scanning tunneling microscopy. Conditions are identical to simulation (see Fig. 1): $F(\text{As}) = 0.083 \text{ ML/s}$, (a) $T = 380^\circ\text{C}$ (b) $T = 440^\circ\text{C}$.

100 min annealing time are plotted in Fig. 2 for two different temperatures. In both situations the surface consists mainly of $\alpha 2(2 \times 4)$ and $\beta 2(2 \times 4)$ unit cells. Additionally there are staggered dimers i.e. dimers that are phase-shifted along the dimer rows by one lattice constant. Experimental results for surfaces annealed under identical conditions are presented in Fig. 3.

GROWTH KINETICS

We present simulation results for homoepitaxial growth of InAs(001). The initial surface has the $\beta 2(2 \times 4)$ -reconstruction. The growth simulation is carried out with parameters given in caption of Fig. 4. The growth rate is determined by the In-flux equal to 0.5 ML/s . The average As-incorporation is identical balanced by adsorption and desorption. Fig. 4 presents the surface morphology after (a) half a ML and after (b) a full ML of deposition during growth. Whereas the $\beta 2(2 \times 4)$ -reconstruction nearly disappears after 0.5 ML , at ML completion patches of reconstructed unit cells become visible again. Note that these simulations should not be directly compared to existing STM pictures because we have not included the quenching process. We monitor changes in surface morphology by determining the density of certain local structures. As an example we plot the As-density during growth in Fig. 5. We find an oscillatory behavior connected to the ML coverage. The As-density has its minimum close to $1/2 \text{ ML}$ at 1 s and its maximum at ML completion at 2 s .

DISCUSSION

The $\alpha 2(2 \times 4)$ and $\beta 2(2 \times 4)$ reconstructions are stable for InAs(001), as shown experimentally and theoretically [1,4]. Due to lack of interaction between neighboring (2×4) cells, a continuous transition between both reconstructions is observed. Here we demonstrate the possibility of utilizing the substrate temperature to determine the exact As-density within the limits given by $\alpha 2(2 \times 4)$ and $\beta 2(2 \times 4)$. The resulting simulated surface morphologies (see Fig. 2) agree quantitatively with the experiment (Fig. 3). The As-density as a function of the substrate temperature is identical in simulation and experiment. The time to equilibrate the InAs(001) surface, is under typical growth conditions, at least a few seconds and exceeds typical growth rates.

Starting from a $\beta 2(2 \times 4)$ reconstructed surface, initially deposited In atoms form dimers and later smaller clusters on the As-dimer rows, leading to the reduction of the surface As-density

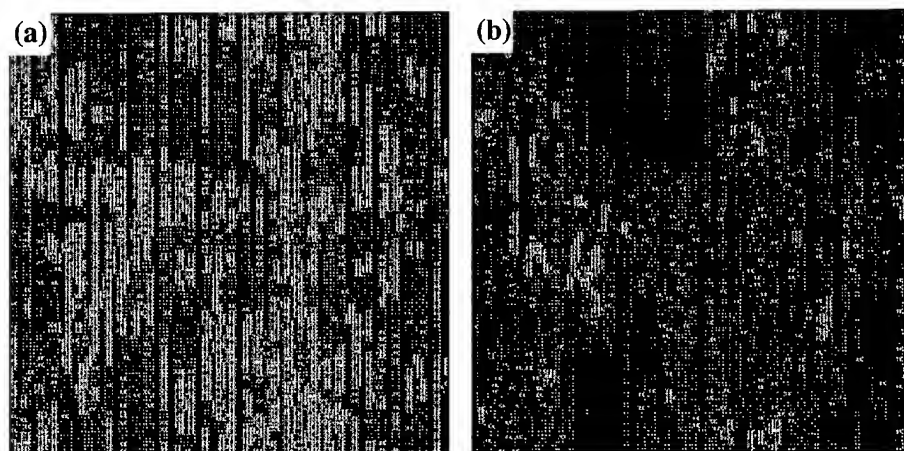


Figure 4 Surface morphologies after deposition of (a) 0.5 ML and (b) 1.0 ML (lower layer is omitted for clarity). Growth parameters $F(\text{In}) = 0.5 \text{ ML/s}$, $F(\text{As}) = 2.5 \text{ ML/s}$, $T = 380^\circ\text{C}$.

shown in Fig. 5. At later stages, more In clusters form and additional In adatoms filling the reconstruction trench. This opens adsorption sites for the simultaneously incoming As-flux. The minimum of exposed surface As-dimers is found to be close to the half ML. Related changes in local surface electronic structure could give rise to oscillations observed by *in situ* characterization techniques.

As we have demonstrated, equilibration times exceed typical growth rates. Therefore, we conclude that typical InAs(001) growth does not take place close to thermodynamic equilibrium. However, time scales associated with the dynamics of In-atoms are several orders of magnitude shorter and hence allow a partial equilibration of the In subsystem between As adsorption/desorption processes. This interplay between equilibration and non-equilibrium can be utilized for interface design. Thermodynamic equilibrium provides the possibility to continuously adjust the As-density and influence details of the initial surface. By changing the As-density, the surface kinetics and therefore the non-equilibrium behavior is directly affected.

The KMC model we present here allows investigation of detailed dynamics on the atomic scale that is difficult to achieve by experimental means. The agreement with experimental results

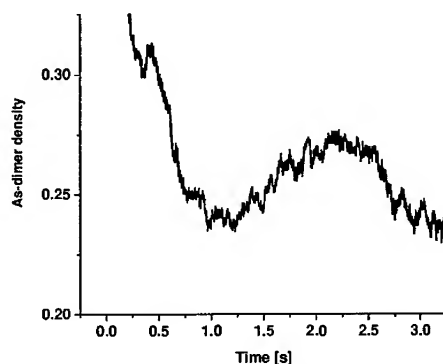


Figure 5 Time development of the As-density during growth. Identical simulation as presented in Fig. 4.

in thermodynamic equilibrium and submonolayer deposition [9] and the parameter determination by *ab initio* DFT calculations was necessary to achieve this kind of predictive capability. Modeling of *in situ* growth sensors like RHEED and PE can take advantage of the detailed microscopic information given by the KMC simulation.

SUMMARY

Simulations and experiments are presented that investigate the thermodynamic equilibrium and growth kinetics of the InAs(001) surface. We employed *ab initio* DFT based KMC simulation to study surface dynamics on the atomic scale. Theoretical and experimental results, together with simulations, suggest a unique continuous phase transition between the stable $\alpha 2(2 \times 4)$ and $\beta 2(2 \times 4)$ reconstruction. Different time scales of the As-dimers and In-atoms lead to important consequences for understanding growth of InAs(001). Equilibration times for As-dimers exceed typical growth rates. Growing surfaces are therefore globally in non-equilibrium. However, the high mobility of In-atoms compared to the slower kinetics of As processes leads to partial equilibration of the In subsystem between successive As dimer deposition events.

ACKNOWLEDGMENTS

We would like to acknowledge P. Kratzer, C. Ratsch, and R.S. Ross for valuable discussions. This work was supported by NSF and DARPA through cooperative agreement DMS-9615854 as part of the Virtual Integrated Prototyping Initiative.

REFERENCES

- [1] C. Ratsch, W. Barvosa-Carter, F. Grosse, J.H.G. Owen, and J.J. Zinck, Phys. Rev. B **62** (12) R7719 (2000).
- [2] W.G. Schmidt, S. Mirbt, and F. Bechstedt, Phys. Rev. B **62** (12), 8087 (2000).
- [3] S.-H. Lee, W. Moritz, and M. Scheffler, Phys. Rev. Lett. **85** (18), 3890 (2000).
- [4] W. Barvosa-Carter, R.S. Ross, C. Ratsch, F. Grosse, J.H.G. Owen, J.J. Zinck, *forthcoming in Surf. Sci. Lett.* (2001).
- [5] M. Itoh, G. R. Bell, A. R. Avery, T. S. Jones, B. A. Joyce, and D. D. Vvedensky, Phys. Rev. Lett. **81** (3), 633 (1998).
- [6] P. Kratzer, C.G. Morgan, and M. Scheffler Phys. Rev. B **82** (24), 4886 (1999); P. Kratzer and M. Scheffler unpublished (2001).
- [7] A. Kley, P. Ruggerone, and M. Scheffler, Phys. Rev. Lett. **79** (26), 5278 (1997).
- [8] R.H. Miwa, G.P. Srivastava Phys. Rev. B **62** (23), 15778 (2000).
- [9] F. Grosse *et al* unpublished.
- [10] M. Bockstedte, A. Kley, J. Neugebauer, and M. Scheffler, Comp. Phys. Comm. **107**, 187 (1997); M. Fuchs and M. Scheffler, *ibid.* **116**, 1 (1999).
- [11] J.H. Neave, B.A. Joyce, and P.J. Dobson Appl. Phys. A: Solids Surf. **35**, 179 (1984).

AUTHOR INDEX

- Acciarri, M., 275
 Afzaal, Mohammad, 215
 Ahn, J., 519
 Ahoujja, Mohamed, 73
 Akashi, Yoshito, 283
 Alexanian, Arik G., 537
 Al-Jassim, M.M., 587
 Allerman, A.A., 21, 221
 Al-Yacoub, A., 9
 Anand, Srinivasan, 685
 Arafune, K., 389
 Arai, T., 247
 Aramyan, Nikolay S., 537
 Ardila, Angel M., 417
 Aripov, I.M., 447
 Arsh, A., 675
 Asahi, Hajime, 501
 Asami, H., 467
 Asami, Kumiko, 501
 Attolini, G., 91
 Aumer, M.E., 29
 Avdjian, Karapet E., 491
 Avella, M., 417
 Ayers, John, 625
- Bajaj, K.K., 313, 343
 Baklenov, O., 461
 Balakrishnan, Krishnan, 483, 617
 Bang, K.H., 649
 Barletta, P., 29
 Barticevic, Z., 301
 Barvosa-Carter, William, 383, 717
 Bauer, M., 631
 Bedair, S.M., 29
 Beling, C.D., 423
 Bellaiche, L., 9
 Bereznaya, Svetlana A., 265
 Berger, V., 531
 Bert, Nikolai A., 35
 Bertness, K.A., 221
 Bhattacharya, Pallab, 109
 Binetti, S., 275
 Blagnov, P.A., 85
 Bourgoin, J.C., 181
 Brown, G.J., 99
 Burdov, V.A., 607
- Buyanova, I.A., 67
- Campbell, Joe C., 461
 Cargill III, G.S., 495
 Carstensen, J., 663
 Castaldini, A., 275
 Chakraborty, Subhasish, 691
 Cheah, K.W., 423
 Chen, L., 117
 Chen, W.M., 67
 Chen, Y., 221
 Chen, Y.-C., 495
 Chen, Zhonghui, 461
 Cherkashin, Nikolai A., 35
 Chi, Jim Y., 35
 Chirlias, E., 531
 Choi, W.K., 649
 Christodoulou, Christos G., 155
 Christophersen, M., 663
 Christou, A., 259
 Chu, Tso-Yu, 61
 Cohen, M.I., 599
 Coli, G., 313, 343
 Cook, R.E., 85
 Crooker, S.A., 313
 Crouch, David, 215
 Cui, R.Q., 411
- d'Albuquerque e Castro, J., 227
 Dao, L.V., 599
 Dao, Le. H., 483, 617
 Dashevsky, Z.M., 555
 de Assis, João M.K., 175
 de C.F.F. da Silva, Sabrina, 175
 de Dios-Leyva, M., 295, 473
 Deng, J.C., 3
 De Rossi, A., 531
 Diez, E., 307
 Ding, Z.M., 411
 Doi, Atsutoshi, 435
 Dolzhenko, Dmitriy, 187
 Domínguez-Adame, F., 307
 Donchev, V., 181
 dos Santos, Raimundo R., 227
 Dost, Sadik, 483, 617
 Dovidenko, K., 135

Dovidenko, Katharine, 561
Duda, A., 49
Duda, Erika, 631
Dupont, L., 377
Dupuis, R.D., 643
Duque, C.A., 301, 473

Edwards, N.V., 631
Ehrenfreund, E., 477
Eychmüller, A., 289

Fallini, P., 91
Fan, Shanhui, 697
Fan, W.J., 41
Feigel, A., 675, 709
Feng, Z.C., 3
Fernelius, Nils C., 265
Ferrini, Rolando, 685
Fitzgerald, Eugene A., 513
Fluegel, B., 49
Foca, E., 663
Föll, H., 663
Forchel, Alfred, 685
Fradkin, L., 289
Fu, L., 599
Fu, Xuefeng, 549
Fukuyama, Atsuhiko, 283, 507
Fung, S., 423

Gal, M., 599
Gallmann, Lukas, 349
Gambin, Vincent, 333
Ganichev, Sergey D., 169
Gaponik, N., 289
Gaponova, D.M., 607
García, J.A., 455
Gautrot, S., 181
Gérard, B., 417
Germini, F., 91
Gersten, Bonnie, 679
Gil-Lafon, E., 417
Gin, A., 99
Goldstein, Jonathan T., 265
Gómez, I., 307
González, M.A., 91
Goto, Takayuki, 233

Govender, Kuveshni, 525
Grigoryan, Romen P., 537
Groenert, Michael E., 513
Grosse, Frank, 383, 717
Guido, Louis, 73
Guimarães, Sonia, 175
Guo, S.P., 495
Gyure, Mark F., 717

Ha, Wonill, 333
Hadi, G.M., 411
Hai, P.N., 67
Haiml, Markus, 349
Hanna, M., 49
Hara, M., 467
Harris, James S., 333
Hasko, D.G., 691
Hayakawa, Yasuhiro, 483, 617
Heller, R.D., 643
Hengehold, Robert L., 73
Hensley, Dale K., 209
Hidalgo, A., 203
Hirata, A., 389
Hockett, R.A., 543
Holonyak Jr., N., 643
Hong, M.K., 649
Houdré, Romuald, 685
Huh, K.S., 649
Hull, R., 643
Hwang, D.K., 649

Ikari, Tetsuo, 283, 507
Ila, Daryush, 209
Inoue, Masataka, 655
Isaenko, Ludmila, 429
Ivanchik, Ivan, 187
Ivanov, E.V., 395
Ivanov, S.V., 395

Jagadish, C., 599
Jain, Faquir, 625
Jayasinghe, Lalith, 355
Jiang, Hongtao, 123
Jiménez, J., 91, 417
Jin, C., 637
Jin, C.Y., 411

Jin, P., 3
Joannopoulos, J.D., 697
Johnstone, Daniel K., 73
Jones, E.D., 9, 21, 313, 343

Kamiya, I., 467
Kamp, Martin, 685
Kasiyan, V.A., 555
Katiyar, R.S., 203
Katsnelson, A., 135
Katsnelson, Alexei, 561
Kawakami, Shojiro, 669
Kawasaki, Eri, 467
Kawashima, Takayuki, 669
Kaygorodov, V.A., 395
Keller, Ursula, 349
Kellogg, D.A., 643
Kennerly, Steve, 109
Ketterl, Hermann, 169
Khachatryan, Ashot M., 537
Khlyap, G., 325
Khodier, Majid M., 155
Khokhlov, Dmitriy, 187
Kiefer, R., 365
Kim, Daeil, 319
Kim, E.T., 461
Kim, Seongsin, 333
Kim, Steven, 319
Kim, Sungjin, 319
Kimura, Tadashi, 483, 617
Kinoshita, A., 389
Klebanov, M., 675
Klem, J.F., 21
Knippels, Guido, 429
Kodera, K., 389
Koike, Kazuto, 655
Komatsu, Hideki, 483, 617
Konishi, Kenta, 501
Kop'ev, P.S., 395
Korotchenko, Zoya V., 265
Kosel, T., 85
Kostoulas, Yiorgos, 195
Kotler, Z., 675, 709
Kouvetakis, J., 631
Kovsh, Alexei R., 35
Krishna, Sanjay, 109

Kristovskiy, Konstantin, 187
Kumagawa, Masashi, 483, 617
Kumar, D., 637
Kuramochi, Eiichi, 669
Kurtz, Steven R., 21
Kvit, A., 637

Langa, S., 663
Langof, L., 289, 477
LeBoeuf, S.F., 29
Le Donne, A., 275
Lee, D.H., 649
Lee, Harry, 513
Lee, Hwe-Jae, 501
Leitz, Christopher W., 513
Leoni, E., 275
Leuenberger, David, 685
Li, K.F., 423
Li, Na, 599
Li, Ning, 599
Li, Peng, 625
Li, Sheng S., 143
Li, Wei, 67
Liang, Eih-Zhe, 129
Liao, Chunsheng, 243, 549
Lifshitz, E., 289, 477
Lin, Ching-Fuh, 129
Lin, Hao-Hsiung, 61
Lin, Yih-Yin, 123
Ling, C.C., 423
Linnik, M., 259
Littau, Mike, 195
Liu, X., 599
Lobanov, Sergei, 429
Loke, W.K., 41
Lu, W., 599
Lui, M.K., 423
Luther, J.M., 29
Lyubin, V., 675

Madhukar, A., 461
Maeda, Osamu, 501
Majumdar, A., 355
Manasreh, M.O., 253, 403, 581
Marcel, C., 377
Martin, Michael, 319

Martínez, O., 91, 417	Notomi, Masaya, 669
Mascarenhas, A., 49, 313	Nozik, A.J., 477
Matei, Ion, 441	
Matevossian, Lenrik A., 537	O'Brien, Paul, 215, 525
Mathes, D.T., 643	Oh, M.S., 649
Matsumoto, Yoshiyuki, 435	Ohmer, Melvin C., 265
McCann, P.J., 355	Ohno, Ryuji, 507
McCartney, M.R., 631	Ohtsuki, O., 467
Mears, R.J., 691	Okano, Yasunori, 483, 617
Melgarejo, R.E., 203	Oksengendler, B.L., 447
Meltzer, B.Ya., 395	Oktyabrsky, Serge, 135, 561
Méndez, B., 455	Oliveira, L.E., 227, 295, 301, 473
Menendez, Jose, 631	Olsen, J.M., 313
Mermelstein, C., 365	Orellana, P., 307
Merz, J.L., 85	Ortiz, V., 531
Messenger, S.R., 569, 587	Owen, James H.G., 383
Micic, O.I., 477	Ozawa, Tetsuo, 483, 617
Mikhailova, M.P., 395	
Mikhaylov, A.N., 607	Pacheco, M., 301
Mintairov, A.M., 85	Paik, Namwoong, 319
Missous, M., 253	Pal, D., 117
Miyazawa, Masafumi, 483, 617	Pan, D., 117
Mizobata, Akiko, 501	Pang, Q.J., 411
Modine, N.A., 9	Panich, Alexander, 429
Moiseev, K.D., 395	Parent, David, 625
Moody, B.F., 29	Park, Jin-Ho, 215
Moosburger, Jürgen, 685	Pelosi, C., 91
Mui, W.K., 423	Pentia, Eugenia, 441
Mukhametzhonov, I., 461	Pessa, M., 67
Mulot, Mikaël, 685	Petrov, Valentin, 429
Muntele, Claudiu I., 209	Pintilie, Ioana, 441
Muntele, Iulia C., 209	Pintilie, Lucian, 441
Murakami, Noriaki, 483, 617	Piqueras, J., 455
Muth, J., 637	Pitera, Arthur J., 513
Myoung, J.M., 649	Pizzini, S., 275
	Plugaru, R., 455
Nagatomo, Hiroaki, 283	Poker, David B., 209
Naghavi, N., 377	Porrás-Montenegro, N., 473
Nakae, Y., 389	Prettl, Wilhelm, 169
Nakamura, Tetsuo, 483, 617	
Napierala, J., 417	Qiu, Min, 685
Narayan, J., 637	
Narayanamurti, V., 643	Ram, Rajeev J., 513
Ng, T.K., 41	Rashidova, S.S., 447
Nikiforov, A.Y., 495	Rattunde, M., 365
Nogales, E., 455	Raymond, Christopher J., 195

Razeghi, M., 99	Su, Wei-Fang, 129
Readey, D.W., 221	Summers, G.P., 569, 587
Reddy, C.V., 643	Sun, G.C., 181
Reno, J.L., 343	Sun, Lingdong, 243, 549
Revin, D.G., 607	Synowczynski, Jennifer, 679
Rios, O., 663	
Roberts, J.C., 29	Taiji, Yoshihito, 507
Rodriguez, Angel, 625	Takahashi, Chiharu, 669
Rogach, A., 289	Takahashi, Jun-ichi, 669
Romero, M.J., 587	Tamargo, M.C., 495
Roshko, A., 221	Tan, H.H., 599
Rothman, B., 543	Tan, M., 221
Rotman, S.R., 555	Tanaka, Ichiro, 467
Rougier, A., 377	Tandon, A., 221
Ryou, J.H., 643	Tanite, Takanori, 655
	Taraci, Jennifer, 631
Samic, H., 181	Tarascon, J-M., 377
Sanz, L.F., 91	Tate, T.J., 455
Sasa, Shigehiko, 655	Tetelbaum, D.I., 607
Sato, Shoichiro, 507	Thinh, N.Q., 67
Schmitz, J., 365	Tian, C., 543
Schön, Silke, 349	Tie, J., 461
Seager, C.H., 21	Tiginyanu, I.M., 663
Semaltianos, N.G., 531	Tiwari, A., 637
Semenov, A.N., 395	Todt, René, 135, 561
Sergentu, V., 663	Tokranov, Vadim, 135, 561
Sfez, B., 675, 709	Tolle, John, 631
Shattuck, Jeremy, 625	Tomar, M.S., 203
Shen, S.C., 599	Towe, E., 117
Shi, Z., 355	Trushin, S.A., 607
Shigetomi, Shigeru, 507	Tsatsul'nikov, Andrei F., 35
Shih, Ding-Kang, 61	Tu, C.W., 67
Shih, Sheng-Ming, 129	Turaeva, N.N., 447
Shneck, R.Z., 555	
Sieg, R.M., 21	Uekusa, Shin-ichiro, 233, 247
Simanowski, S., 365	Ustinov, Victor M., 35, 85
Simmons, Jerry A., 155	
Singh, Jasprit, 123	Van Lierde, P., 543
Smirnova, Julia, 429	Vedenyapin, Vitaly, 429
Smith, D.J., 631	Vinter, B., 531
Smyth-Boyle, David, 525	Vlasov, A.S., 85
Solov'ev, V.A., 395	Voevodin, Valeriy G., 265
Song, Kie Moon, 319	Voevodina, Olga V., 265
Sorokin, S.V., 395	
Stiff-Roberts, Adrienne D., 109	Wagner, J., 365
Stoleru, V.G., 117	Walter, G., 643

Walters, R.J., 569, 587	Ye, Zhengmao, 461
Walther, M., 365	Yelisseyev, Alexander, 429
Wang, Jyh-Shang, 35	Yeo, Yung Kee, 73
Wang, S.G., 519	Yeremyan, Arsham S., 537
Wang, S.Z., 41	Yokohama, Itaru, 669
Wang, Y.C., 3	Yoon, S.F., 41, 519
Weaver, B.D., 253, 403, 581	
Wei, Li, 35	Zhang, Jun, 243
Wei, Y., 99	Zhang, Q., 519
Weller, H., 289	Zhang, X.D., 3
Wistey, Mark, 333	Zhang, Xiaoguang, 625
Wu, H., 355	Zhang, Yong, 49, 313
	Zhao, F., 355
Xin, H.P., 67	Zhao, J., 3
Xu, G., 3	Zhao, Y.W., 423
	Zheng, T., 355
Yakimov, Michael, 235, 561	Zhou, Qiaoying, 253
Yakovlev, Yu.P., 395	Zhou, Z.B., 411
Yan, Chunhua, 243, 549	Zinck, Jennifer J., 383, 717
Yang, T.R., 61	Zollner, S., 631
Yang, Vicky K., 513	Zondy, Jean-Jacques, 429
Yano, Mitsuaki, 655	

SUBJECT INDEX

- AACVD, 215
- ab initio density functional theory, 383, 717
- AlGaAs, 283, 561
 - alloys, 343
 - oxidation, 221
- AlGaAs/InAs/GaAs, 461
- AlGaN, 403, 581
- alpha particle detector, 519
- aluminum gallium arsenide, 531
 - erbium, 247
- amorphous silicon, 435
- anion-mixed nitrides, 9
- anodic etching, 663
- anomalies, 9
- antimony tin oxide, 377
- atomic rebuilding, 447
- band
 - anticrossing model, 61
 - gap, 49
- beam injection methods, 587
- Bragg mirror, 259
- bridge layer, 617
- broadband mirror, 349
- CaF₂ molecular beam epitaxy, 349
- capture barrier, 73
- carbon
 - hydrogen complexes, 403
 - nitride thin films, 411
- cathodoluminescence, 417, 495
- CD process control, 195
- CdGeAs₂, 265
- CdSnAs₂, 265
- chalcogenide, 429
 - glasses, 675
- charge collection efficiency, 519
- chemical
 - bath deposition, 441, 525
 - vapor deposition, 631
- circuit model, 155
- circular photogalvanic effect, 169
- colloidal dot, 467
- complex precursors, 549
- composition conversion, 617
- concavity, 389
- conductive-tip AFM, 467
- confocal micro-Raman spectroscopy, 209
- core/shell structure, 549
- Cr doping, 555
- crystal growth under microgravity, 483
- crystallization, 435
- CuInSe₂, 215
- current image, 467
- deep level, 507
- defects, 265, 447
- DELTT, 155
- detector, 169
- diamagnetic shift, 313
- diamagnetism, 343
- diamond thin film, 519
- dielectric constant, 259
- diluted magnetic semiconductors, 227
- DLC, 319
- electrical bias, 495
- electrochemical characterization, 377
- electroluminescence, 129
- electron beam lithography, 691
- ellipsometry, 411
- epitaxial
 - GaAs, 181
 - growth, 637
- erbium, 233
 - oxide, 455
- ESR, 411
- ferroelectric, 679
- field emission display, 319
- flash evaporation, 175
- GaAs, 307, 513
 - substrate, 649
- GaAs/AlGaAs quantum wells, 169
- GaAs-(Ga,Al)As, 295, 301, 473
- GaAsN, 29, 49
- GaAs/Si, 417
- GaInNAs, 333

GaInNAsSb, 333
 GaInP, 91
 gallium
 arsenide, 599
 nitride, 35, 41
 antimonide, 423
 (GaMn)As, 227
 GaN, 73
 GaNAs and InGaAsN, 67
 GaPN, 49
 gas source molecular beam epitaxy
 (MBE), 61, 501
 GaSb, 365
 germanium, 631

 Hall mobility, 21
 heat treatments, 265
 heterojunction, 491, 537
 heterostructure, 307
 HgTe/CdHgS, 289
 high nitrogen content, 29
 hole fraction, 227
 horizontal Bridgman method, 389
 hot wall epitaxy, 175,
 hybrid III-V/II-VI heterostructures,
 395

 InAs homoepitaxy, 717
 InAs/GaAs quantum dots, 109
 InAsN, 61
 indium
 aluminum gallium phosphide,
 643
 gallium
 antimonide, 483
 arsenide, 617
 phosphide, 643
 sulfide, 525
 infrared
 detection, 109
 photodetector, 187, 461
 InGaAlP, 507
 InGaAs/InAlAs MQWs, 253
 InGaAs/InP, 3
 InGaAsN, 21
 InGaP, 313

 InP, 477
 InP/GaInAsP systems, 685
 in situ observation, 483
 interference lithography, 675
 internal light source
 photoluminescence technique,
 685
 intersubband transition, 253
 ion
 beam sputtering, 411
 implantation, 209, 599
 IR laser applications, 555
 irradiation effects, 587
 isothermal capacitance transient
 spectroscopy, 73

 kinetic Monte Carlo simulation, 717

 laser, 333, 513, 531
 diode, 135, 365
 lead
 sulfide, 325, 441
 telluride, 175, 187
 LED, 129
 linearity, 181
 local vibrational modes, 403
 of CH, 581
 luminescence, 455

 magnetoexciton, 301, 313, 343
 magneto-optics, 85
 Marangoni convection, 389
 MBE, 355, 395
 metalorganic chemical vapor
 deposition, 643
 microphotonic devices, 697
 mid-infrared laser, 395
 MOCVD, 29
 molecular beam epitaxy, 35, 41, 109,
 117, 175, 325, 655
 multi-color, 143
 multijunction(s), 569, 587
 multiple quantum well, 3
 multi-stack, 143

 nanolithography, 669

nanoparticle(s), 129, 477, 549
 native oxide, 221
 near-field spectroscopy, 85
 nGaAs-nInSb, 491
 nitride compounds, 85
 NMR, 429
 non-radiative
 defects, 67
 recombination, 283

 ODMR, 289, 477
 OMCVD, 513
 on silicon substrates, 655
 optical
 absorption, 253
 anisotropy, 663
 constants, 435
 metrology, 195
 resonances, 697
 spectroscopy, 429, 531
 optically detected magnetic
 resonance, 67

 PbSe, 355
 photoluminescence, 3, 35, 91, 233,
 247, 325, 423
 spectroscopy, 275
 photonic
 bandgap, 679
 crystal(s), 669, 697, 709
 photoresistor, 441
 photovoltaics, 525
 piezoelectric photothermal
 spectroscopy, 283, 507
 pInSb-nCdTe, 537
 porous III-V compounds, 663
 positron lifetime spectroscopy, 423
 post-annealing, 649
 precursor, 243
 pseudopotential, 9
 pulsed laser deposition, 491, 537, 637

 quadrupole electromagnetic moment,
 709

 quantum
 dot(s), 117, 135, 461, 473
 well(s), 295, 301, 365
 intermixing, 599
 wires, 295
 quaternary semiconductor, 259
 QW, 355
 QWIP, 143

 radiation
 detector, 181
 effects, 569
 Raman spectroscopy, 91, 411, 417
 reactive ion etching, 691

 Sb-terminated InAs, 383
 scanning
 electronic microscopy, 175
 tunneling microscopy, 383
 scattering, 307
 scatterometry, 195
 secondary ion mass spectrometry,
 543
 second-order non-linearity, 709
 self-assembled quantum dots, 123
 semiconductor(s), 447
 lasers, 117
 Si, 513 Ge, 513
 silicon, 175, 275, 455, 625, 669
 carbide, 209
 on insulator, 691
 simulation, 679
 size fluctuation, 123
 solar cell, 21, 569
 solution route, 243
 structural
 characterization, 377
 properties, 203
 submillimeter range, 187
 superlattices, 561
 synthesis, 203

 TEM, 135

temperature-independent wavelength
 laser diode, 501
 thermal
 annealing, 41, 581
 donors, 275
 quenching, 233, 247
 thin films, 215
 3D photonic crystals, 675
 III-V compound semiconductor, 543
 THz detector, 155
 $\text{Ti}_{1-x}\text{Co}_x\text{O}_2$, 203
 tin, 631
 TiInGaAs/InP , 501
 triple junction, 319
 2D photonic crystals, 685
 II-VI, 625
 compound semiconductors, 555
 ultrashort pulse generation, 349
 valence force field model, 123
 wet
 oxidation, 561
 thermal oxidation, 221
 x-ray diffraction, 175
 zinc oxide, 655
 ZnCdMgSe quantum well light
 emitting diode, 495
 ZnGeP_2 , 265
 ZnMgS , 625
 ZnMnO , 637
 ZnO , 243, 649